Shailendra Kumar
J. Ramkumar
Panagiotis Kyratsis   *Editors*

Recent Advances in Manufacturing Modelling and Optimization

Select Proceedings of RAM 2021

Lecture Notes in Mechanical Engineering

Series Editors

Francisco Cavas-Martínez 🔗, Departamento de Estructuras, Construcción y Expresión Gráfica Universidad Politécnica de Cartagena, Cartagena, Murcia, Spain

Fakher Chaari, National School of Engineers, University of Sfax, Sfax, Tunisia

Francesca di Mare, Institute of Energy Technology, Ruhr-Universität Bochum, Bochum, Nordrhein-Westfalen, Germany

Francesco Gherardini 🔗, Dipartimento di Ingegneria "Enzo Ferrari", Università di Modena e Reggio Emilia, Modena, Italy

Mohamed Haddar, National School of Engineers of Sfax (ENIS), Sfax, Tunisia

Vitalii Ivanov, Department of Manufacturing Engineering, Machines and Tools, Sumy State University, Sumy, Ukraine

Young W. Kwon, Department of Manufacturing Engineering and Aerospace Engineering, Graduate School of Engineering and Applied Science, Monterey, CA, USA

Justyna Trojanowska, Poznan University of Technology, Poznan, Poland

Shailendra Kumar · J. Ramkumar ·
Panagiotis Kyratsis
Editors

Recent Advances in Manufacturing Modelling and Optimization

Select Proceedings of RAM 2021

Editors
Shailendra Kumar
Department of Mechanical Engineering
S. V. National Institute of Technology
Surat, India

J. Ramkumar
Department of Mechanical Engineering
Indian Institute of Technology Kanpur
Kanpur, India

Panagiotis Kyratsis
Department of Product and Systems Design
Engineering
University of Western Macedonia
Kila Kozani, Greece

Contents

About the Editors

Dr. Shailendra Kumar is working as Professor at the Department of Mechanical Engineering, Sardar Vallabhbhai National Institute of Technology, Surat, India. He obtained his graduation in Production Engineering from NIT Jamshedpur and Doctorate in Mechanical Engineering from M.D.U. Rohtak, Haryana. He has more than 20 years of teaching and research experience. He completed five research projects funded by various national and international agencies. More than 160 research papers in reputed journals and conferences are at his credit. His current research interests include incremental sheet forming, additive manufacturing, and abrasive water jet machining of composites.

Dr. J. Ramkumar is currently working as Professor at the Indian Institute of Technology, Kanpur. He earned his B.Tech. (Production) from NIT, Trichy in 1996 and M.Tech. (Mechanical) from IIT, Madras in 1999 and Ph.D. from IIT, Madras in 2002. His current research interests include micro EDM milling, micro electrochemical milling, excimer laser micromachining, abrasive flow finishing, magnetic abrasive finishing, fabrication of composites and machining of composites. He holds 175 publications in reputed journals and 41 patents. Dr. J. Ramkumar has completed several sponsored projects and consultancy work sanctioned by various funding agencies.

Dr. Panagiotis Kyratsis is currently working as Professor at the Department of Product and Systems Design Engineering Technology, University of Western Macedonia. He obtained his Graduation in Mechanical Engineering, Aristotle University of Thessaloniki, and Ph.D. from Technical University of Crete. His major areas of research interests include CAD-based manufacturing, CAD/CAM/CAE, manufacturing and machining, product design and industrial design engineering, and reverse engineering and prototyping. Dr. Panagiotis Kyratsis holds 12 industrial designs and is Author of 120 refereed publications and 40 books/book chapters.

CFD Analysis and 3D Printing of Venturi for Vacuum-Assisted LDPE Grain Flow System

Yash R. Katkar, Aditya R. Vernekar, Anirudha K. Jahagirdar, Yash C. Waghmare, and Bhagyesh B. Deshmukh

1 Introduction

3D printing is also known as Additive Manufacturing is the technology used for manufacturing a 3D object from a given 3D model using additive processes. The additive process is the process in which the object is manufactured by laying down successive layers of material. 3D printing is the technology that enables manufacturing and rapid prototyping of highly customized parts required in various fields. It is completely reverse of subtractive or traditional manufacturing which is the process of removal of the material from the workpiece. According to the American Society for Testing and Materials (ASTM), the Additive Manufacturing process is classified into seven categories such as Directed Energy Deposition, Sheet Lamination, Powder Bed Fusion, Vat Photopolymerization, Material Jetting, Binder Jetting and Material Extrusion which includes Fused Deposition Modeling (FDM) [1].

In this paper, venturi is 3D printed which is specifically designed for vacuum-assisted LDPE (Low-Density Polyethylene) grain flow system. This system can be used to transfer the material in the molds of the Rotational Moulding Unit which is commonly used in the manufacturing of Water Tanks. In a vacuum-assisted LDPE grain flow system, a venturi is used to create a vacuum that draws the grains and causes the grains to flow along the air stream. Currently, in most of the small-scale Roto-Moulding Unit, the loading of the raw material is done manually. This manual loading process is time-consuming and also there is considerable wastage of material. This creates space for improvement and can be improved by the application of a vacuum-assisted grain flow system with a 3D printed venturi.

Y. R. Katkar (✉) · A. R. Vernekar · A. K. Jahagirdar · Y. C. Waghmare · B. B. Deshmukh
Mechanical Engineering Department, Walchand Institute of Technology, Solapur, Maharashtra 413006, India

2   Literature Review

With the use of 3D printing technology, various parts are fabricated according to their specific applications in the past. Various 3D printed parts are not only be used for prototyping but also production use cases. 3D printed parts can prove to be a replacement for metal parts under specific conditions. It was tested developing, the following parts for some of the industrial use case: Oil Sump Drain-Sieve, Air Filter Wingnut, Lubricant Flow Relay Splitter, and CNC Coolant Venturi Nozzle. And after testing it was found that 3D printed parts can replace the parts which are not subjected to unnecessary stresses [2].

3D Printed flowmeter was fabricated for the flow sensing in microfluidics, which enabled rapid and low-cost manufacturing of microfluidic flowmeter with MEMS pressure sensor. The result obtained was agreed to the CFD model developed and it was successfully concluded that 3D printing is versatile for the manufacturing of the microstructure geometry [3]. Venturi tube was 3D printed for measurements of flow rates for small fans in an electronics cooling system. It was designed according to the ASME performance test code on flow measurement. It resulted that the volumetric flow rate measured using this 3D printed venturi tube was within 4% of the manufacturer's specified flow rate. This confirms the use of 3D printing for the manufacturing of the industrial component for the desired result. It was 3D printed with 0.32 mm layer height and 0.6 mm nozzle size [4].

Feeders employed to introduce the material to be conveyed into the air stream are rotary feeder, screw feeder, and venturi feeder. In rotary feeder, the solid which is to be fed into the airstream is achieved by the rotation of the rotary valve [5]. Due to the action of gravity, the grains in the hopper flow into the rotary valve from where it is introduced into the air stream and conveyed to the system [6]. The screw feeder consists of the screw as its prime element which is in continuous rotation. This leads to the further movement of the grain which is fed to conveying air stream [7]. In screw and rotary feeder dynamic loads are involved which cannot be sustained by the 3D printed parts made by PLA or ABS. A vacuum-assisted feeder also referred to as venturi-assisted feeder can be used to introduce material into the airstream. Unlike the above methods, it has no moving parts [8, 9]. Venturi feeder as shown in Fig. 1. In this system, the venturi creates a vacuum that draws material from the hopper and conveyed with high velocity. The venturi used in this system is static and

Fig. 1 Typical venturi feeder
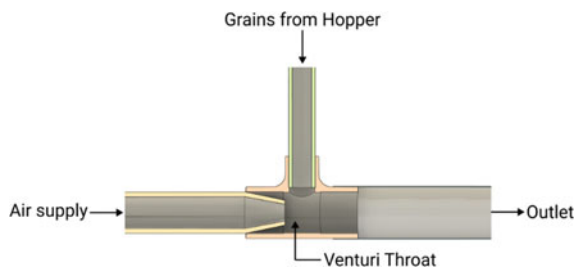
only involved in creating a vacuum which makes it more suitable and easier to 3D print it using PLA or ABS.

After a detailed literature review, it was found that screw and rotary type feeders involve moving parts. 3D printing of these moving parts (screw or rotary blade) may not ensure the desired strength. Vacuum-assisted grain flow system involves no moving parts but a venturi is used to create a vacuum that draws the grains into the system. The objective of this work was to design and model a venturi for a vacuum-assisted LDPE grain flow system. And the simulation through Computational Fluid Dynamics (CFD) was done on venturi. This venturi was further fabricated using 3D Printing.

3   CFD Analysis of Venturi

Venturi works on Bernoulli's principle, i.e., it is used for speeding the flow of the fluid, by constricting it in a cone-shaped tube. In the restriction, the fluid must increase its velocity reducing its pressure and resulting in a generation of vacuum in the throat section [10]. Small throat diameter leads to higher pressure differential. Diameter D_1 is 25.40 mm as the main pipe is 1-inch diameter. For venturi, it is assumed that throat diameter D_2 is half that of D_1. Therefore, D_2 is calculated as 12.7 mm. Applying Bernoulli's, Continuity and Discharge Equations Pressure at the throat was calculated to be -1.158 bar (vacuum) where $(-)$ signifies the vacuum pressure. Due to this vacuum pressure grains are drawn into the air stream. Using the dimensions as above a 3D model of venturi was created as shown in Fig. 2.

The previously created 3D model of venturi having the inlet diameter as 25.4 mm and outlet diameter as 12.7 mm with convergent angle (θ) of 22° was further analyzed using the Computational Fluid Dynamics (CFD) method. The mesh size for this model was kept as a fine structure with 123,577 faces, 42,714 nodes, 40,467 elements with the size of 0.8 mm. The meshed model of venturi is as shown in Fig. 3. The boundary conditions for this venturi corresponding with vacuum-assisted grain flow system were considered. The inlet of venturi with 0.06 bar pressure and outlet mass flow rate calculated analytically was 0.071 kg/s taken into account. Wall parameters are considered as no-slip conditions and standard roughness model.

Fig. 2 3D model of venturi
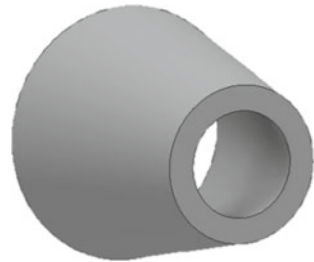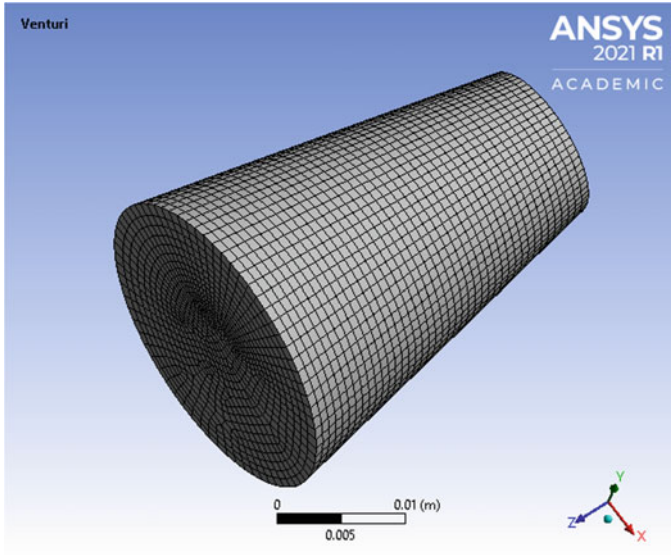
Fig. 3 Meshed model of venturi

Based on the above boundary conditions, input parameters, and meshing, Compu-
tational Fluid Dynamics (CFD) analysis was done. The result of the analysis shows
the pressure obtained at the throat was −1.193 bar as shown in Fig. 4. And there was
an increase in velocity at the outlet of this venturi as compared to the inlet section.
The velocity variation across venturi was obtained as shown in Fig. 5. This obtained
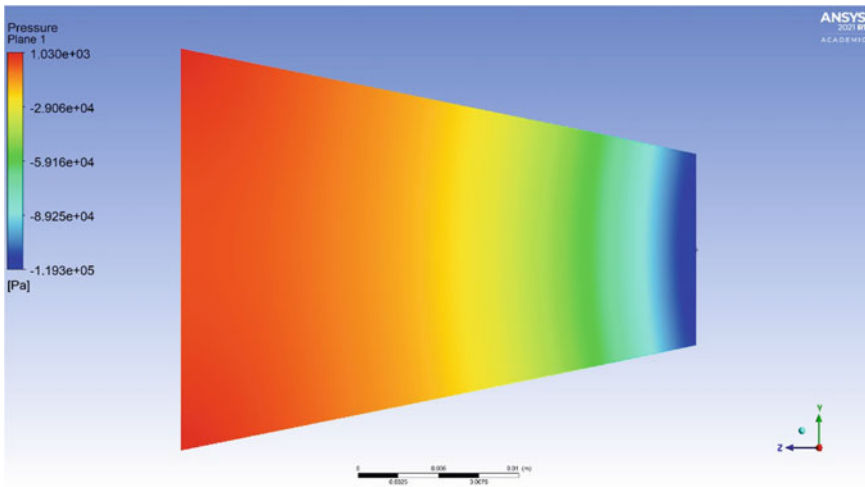
Fig. 4 Pressure variation across venturi
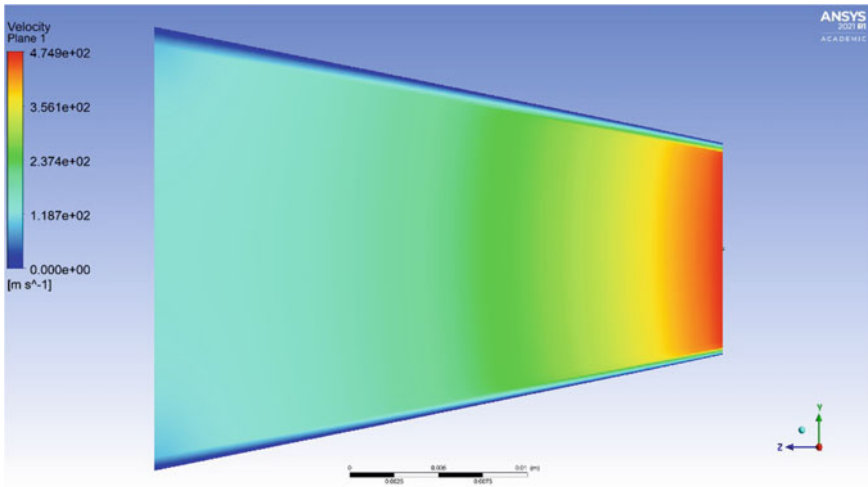
Fig. 5 Velocity variation across venturi

result deviates around 3% from the analytical calculations. The values obtained are significant for use in the vacuum-assisted grain flow system.

4 3D Printing

The 3D printing process is also referred to as rapid prototyping or rapid manufacturing [11], which makes it suitable for rapid building of venturi as per the design parameters within the given constraints. The American Society for Testing and Materials (ASTM), developed a set of standards that classify Additive Manufacturing processes. For 3D printing of venturi as per the design calculations, the Material Extrusion process which involves Fused Deposition Modeling (FDM) was used. In which, the filament is melted in the nozzle at the given temperature and it is deposited over the print bed one over the other layer which forms the 3D object in this case venturi.

For 3D printing of the venturi basically, the 3D model is required which was modeled as shown in Fig. 2. For this model to be 3D printed the topology optimization was done while modeling. The model obtained from the software was exported to Standard Tessellation Language file format generally abbreviated as *STL*. The 3D printer used for printing this venturi was a custom build desktop printer based on open-source Marlin Firmware. It has a 3D printing volume of about 100 mm × 100 mm × 150 mm with a nozzle size of about 0.4 mm.

After importing the STL file, there were certain challenges encountered. The challenges were the orientation, support generation, geometry manipulation, and selection of optimum layer height for the slicing and printing of the model. Slicing

is an essential step in 3D printing that is characterized by the use of slicing software to convert a 3D model into instructions for a 3D printer. Before slicing, the proper orientation of the model was the very crucial aspect that affects the surface finish, strength, build time, and filament required. Inappropriate orientation selected for the 3D printing process leads to unnecessary support generation utilizing more filament, decreasing layer bonding and strength of the object as shown in Fig. 6. Thus, the proper orientation is necessary. This was achieved using geometry manipulation by changing it to the proper orientation as shown in Fig. 7.

Fused Deposition Modeling works on the fused deposition of layers by laying out of nozzle the fusion between the two layers should be proper. This can be achieved by setting the optimum layer height for the specific object depending on the dimension
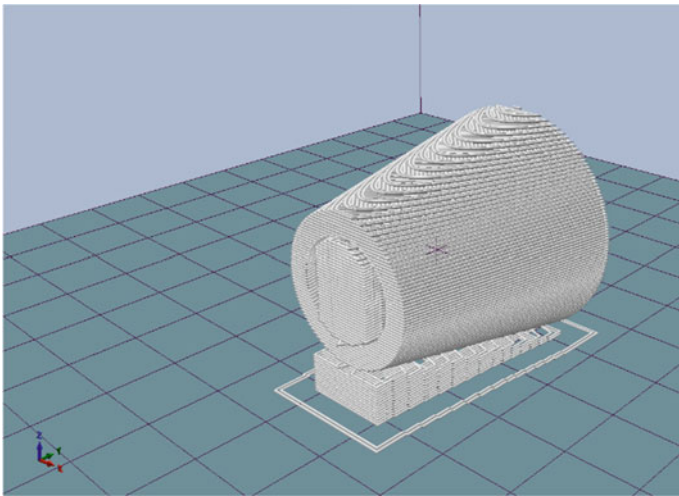
Fig. 6 Orientation of venture

Fig. 7 Sliced model of venturi
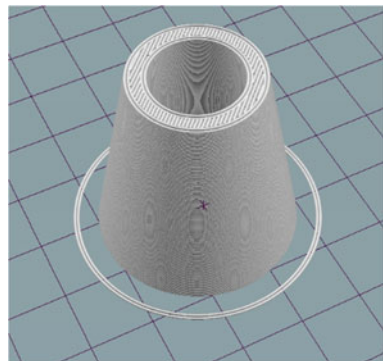
of the nozzle and the application of the object. The more or less layer height leads to the low layer bounding or over material usage without necessity.

This affects the property of the object, such as tensile strength, surface finish relating to the filament material used. As in this scope of application, the venturi was used as a stationary object which plays the role of creating pressure drop and achieving the required vacuum to draw and convey the LDPE grain in vacuum-assisted grain flow system. The layer height of 0.4 mm as discussed earlier leads to low layer bounding. Thus, the 0.2 mm layer height was selected for this application. The filament material also actively supports the strength and quality of 3D printed objects. The most common thermoplastics used as filament material are Polylactic Acid (PLA) and Acrylonitrile Butadiene Styrene (ABS) in which the PLA is biodegradable (under certain conditions). ABS has more ductility over PLA but PLA is easier to print and does not lead to wrappage during the printing process. The melting temperature of PLA is ranging from 180 to 230 °C whereas 210–250 °C for ABS also ABS is highly temperature-sensitive. For this application, the PLA is suitable but ABS can also be used. After proper orientation, optimum layer height, and material selection, the slicing was achieved by specifying certain slicing parameters as shown in Table 1.

The printing of venturi was done after slicing as shown in Fig. 8 and the completed 3D printed venturi is as shown in Fig. 9.

The 3D printed model of venturi was further incorporated into the Assembly of vacuum-assisted LDPE grain flow system as shown in Fig. 10. The vacuum-assisted LDPE grain flow system mainly consists of three prime parts: blower (air mover), venturi, and grain storage unit. The air blower is one of the most important in this system to provide the required air stream. Further Assembly consisting of 3D printed venturi was tested.

Table 1 Slicing parameters

Parameters	Unit	Values
Print speed	mm/s	30
Outer perimeter speed	mm/s	40
Infill speed	mm/s	40
Infill density	%	80
Layer height	mm	0.2
Shell thickness	mm	1
Print temperature	°C	200
Top–bottom thickness	mm	1

Fig. 8 3D printing of
venturi
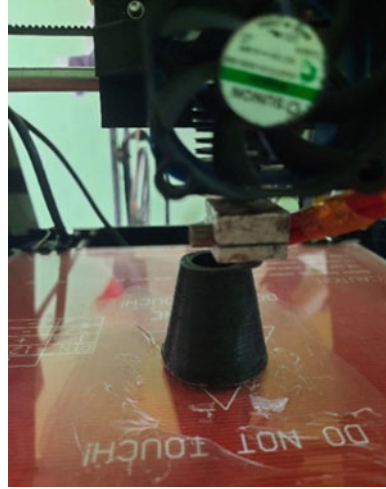
Fig. 9 3D printed venturi

5   Results

The result obtained from the Computational Fluid Dynamic (CFD) analysis of venturi
shows that there was a significant pressure drop. The pressure at the throat was
obtained -1.193 bar, whereas analytical calculations give the pressure of around $-$
1.158 bar as shown in Table 2.

The CFD results deviate by 3% from the analytical model. 3D printed venturi
after incorporating into the vacuum-assisted LDPE grain flow system resulted in the
discharge of LDPE grains. The discharge rate obtained was 2 kg/min. The pressure
condition of the system was sustained by 3D printed venturi.
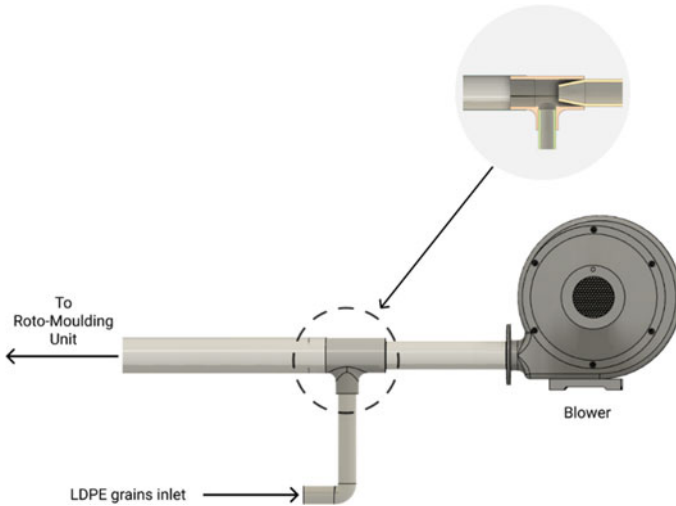
Fig. 10 Vacuum-assisted grain flow system

Table 2 Results

Parameter	Unit	Analytical	Simulation
Pressure at throat	Bar	−1.158	−1.193
Velocity	m/s	460	472

6 Conclusion

The venturi was designed and modeled for the vaccum-assisted LDPE grain flow system. The CFD of the venturi model was simulated to predict the results which validated the analytically calculated values. 3D printing was explored as a tool to manufacture or print custom-designed machine parts. FDM 3D printing process was carried out using PLA as a filament material for 3D printing of venturi. Venturi was incorporated in the system, it sustained the conditions and resulted in the discharge of about 2 kg/min of LDPE grains. 3D printing can prove to be an appropriate manufacturing process for fabricating industrial spare parts rather than a conventional manufacturing process in specific applications. It increases the scope for 3D printing applications.

References

1. ASTM International (2012) Standard terminology for additive manufacturing technologies (Withdrawn 2015)—ASTM F2792-12a. ASTM International, West Conshohocken
2. Sathish T, Vijayakumar MD, Ayyangar A (2018) Design and fabrication of industrial components using 3D printing. Mater Today Proc 5:14489–14498. https://doi.org/10.1016/j.matpr.2018.03.036
3. Adamski K, Kawa B, Walczak R (2018) 3D printed flowmeter based on venturi effect with integrated pressure sensors. Proceedings 2(13):1509. https://doi.org/10.3390/proceedings2131509
4. Hrisko J (2020) The design and characterization of a 3D printed venturi tube. http://doi.org/10.13140/RG.2.2.16963.63525/1
5. Gundogdu MY (2004) Design improvements on rotary valve particle feeders used for obtaining suspended airflows. Powder Technol 139:76–80
6. PDHengineer.com. Pneumatic conveying systems, search. http://www.pdhengineer.com/courses/m/M-5013.pdf
7. Bortolamasi M, Fottner J (2001) Design and sizing of screw feeders. Int Congr Part Technol 69
8. Ratnayake C (2005) A comprehensive scaling-up technique for pneumatic transport systems. Department of Technology, Telemark University College (HiT-TF), Norway
9. Solt PE (2001) Pneumatic points to ponder. Powder and bulk engineering. CSC Publishing, p 17
10. Dhole LP (2014) Venturi feeder system for pull push type pneumatic conveying system. Int J Adv Eng Technol. E-ISSN 0976-3945
11. Bedworth DD, Henderson MR, Wolfe PM (1991) Computer-integrated design and manufacturing. McGraw Hill, New York

Numerical Investigation of the Dimension Factor of Hairpin Coil for Sustainable Induction Heating

Sunil Kumar Biswal and Sukhomay Pal

1 Introduction

Induction heating is an effective process for surface treatment compared to conventional heating. An electromagnetic-thermal phenomenon provides a rapid non-contact localised heating without causing any environmental problem [1]. The induction heating process incorporates an alternating electromagnetic field, which induces an eddy current energy and forms heat energy. The workpiece's effective heating relies on the coil shape, position of the coil to the workpiece, coil cross-section, process parameter, and material to be heated [2]. The high frequency (HF) induction heating has certain shortcomings; the induced current is non-uniform through the workpiece, leads to localised overheating [3]. Further, planar induction heating has a different approach than wrap type induction heating. Due to its magnetic flux distribution pattern and higher air impedance, it restricts the efficient heating of the target [4, 5]. The hairpin coil is an effective coil for planar induction heating, with an efficiency of up to 60% [6]. Induction heating is a complex multiphysics problem, involves electromagnetic and thermal phenomena. Many authors numerical studied the induction heating process to understand the physical phenomena and optimise the induction heating process.

Sun et al. [7] studied the effect of parameter for hairpin coil on the temperature distribution of the cladding area. The author concluded that temperature distribution is directly proportional to current density and inversely proportional to airgap. Lee et al. [8] reported heat-induced deformation behaviour of SS400 steel using a hairpin coil. Their work focused on the interaction of the coil position and input power on the heat distribution and deformation. Similarly, Ikram et al. [9] numerically studied the

S. K. Biswal (✉) · S. Pal
Mechanical Engineering, IIT Guwahati, Guwahati, India
e-mail: biswa176103105@iitg.ac.in

S. Pal
e-mail: spal@iitg.ac.in

effect of coil design and found higher temperature distribution with a hairpin coil. Chang et al. [10] investigated the impact of coil width on the heat distribution on plate curvature and found that higher the width, lower the uniformity of temperature distribution. Zhang et al. [11] compared the feasibility of induction line hardening to conventional flame hardening based on FEM analysis. To understand the effect of magnetic flux concentrator (MFC) on the induction heating, Gao et al. [12] simulated the induction spot heating and validated it with the experimental data. They concluded that the implementation of the MFC uplifts the efficiency of heating. Similarly, Avestruz et al. [13] demonstrated the effect of one-sided magnetic shielding on the planar induction heating. The magnetic flux distribution is well-defined leads to a uniform heating zone.

As mentioned above, the temperature distribution is greatly dependent upon the induction coil geometry and process parameter. The current study aims to numerically study the effect of the coil size, input process parameter, magnetic flux concentrator on the temperature distribution to select suitable hairpin coil.

2 Establishment of FEM Analysis for Induction Heating

The simulation of the induction heating process is a coupled phenomenon involving both electromagnetic and heat transfer modelling. Hence, a coupled electromagnetic-thermal model was developed using commercial software package COMSOL 5.5. Figure 1 illustrates the model, composed of an induction coil and MFC. Also, the projected plane view is shown to understand the scheme of the coupling gap and coil gap. The dimension of the workpiece is $100 \times 100 \times 5$ mm^3, and a coupling gap of 2 mm is considered for the simulation. The flow scheme of the FEM analysis is shown in Fig. 2. The electromagnetic relationship is solved by Maxwell's equations (Eqs. 1–4) in the transient frequency domain. Eddy current can be evaluated by incorporating vector potential as given in Eq. 5.

$$\vec{\nabla}.\vec{B} = 0 \tag{1}$$
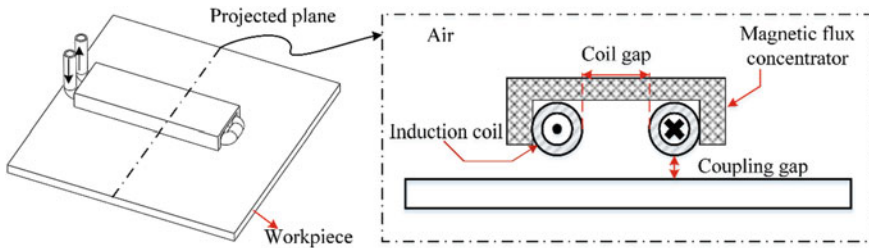
Fig. 1 Schematic representation for a physical model of induction heating
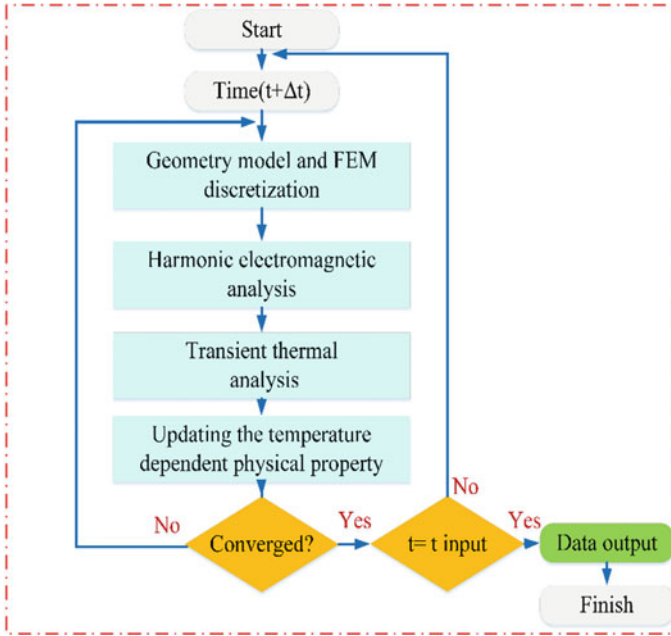
Fig. 2 Flow scheme of the calculation process for the planar induction heating

$$\vec{\nabla}.\vec{D} = \rho \tag{2}$$

$$\vec{\nabla} \times \vec{E} = -j\omega B \tag{3}$$

$$\vec{\nabla} \times \vec{H} = \vec{J} + \frac{\partial \vec{D}}{\partial t} \tag{4}$$

$$J = \sigma E = -j\omega\sigma A + \nabla \times \left(\mu^{-1} B\right) \tag{5}$$

With H is the magnetic flux intensity, J is the current density, D is the electric flux density, E is the electric field intensity, B is the magnetic flux density, μ is the permeability, ρ is the electric charge density, σ is the electrical conductivity, and ω is the angular frequency.

Heat transfer in the heating process is governed by heat diffusion, illustrated in Eq. 6. Conductive and radiative boundary conditions incorporated in the heat transfer field can be evaluated using Eq. 7.

$$\rho_m.C_p\frac{\partial T}{\partial t} - k\left(\nabla^2 T\right) = \sigma\left|E^2\right| \tag{6}$$

$$(k\nabla T).\hat{n} + h(T - T_{\text{amb}}) + \varepsilon\alpha\left(T^4 - T_{\text{amb}}^4\right) = 0 \tag{7}$$
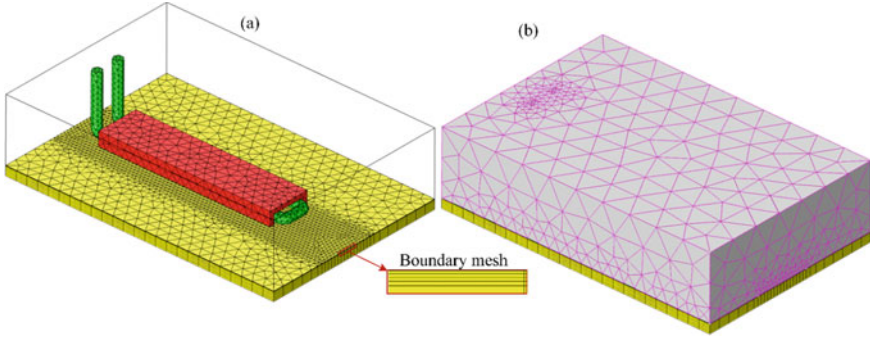
Fig. 3 Finite element meshing scheme of the model: **a** without air, **b** with air

where ρ_m is the density of the material, C_p is the heat capacity, T is the temperature, k is the thermal conductivity, $h = 50$ W/m^2. K is the convection coefficient, $\varepsilon = 0.68$ is the material's emissivity, and α is the Stefan-Boltzmann constant, which equals 5.67×10^{-8} W/m^2 K^4. and T_{amb} is room temperature, taken as 293.15 K.

The overall meshing view of the domain is shown in Fig. 3a. An additional picture is shown in Fig. 3b to visualise the meshing of the induction coil, MFC, and workpiece. Boundary layer mesh is implemented to achieve accurate result as in HF induction heating, the eddy current accumulates in the skin depth. The thickness of the boundary layer is equal to the skin depth calculated by Eq. 8, where f is the excitation frequency of the induction coil.

$$\delta = \sqrt{\frac{1}{\pi \sigma f \mu_0 \mu_r}} \tag{8}$$

The temperature-dependent electromagnetic and thermal property of the workpiece are shown in Fig. 4. AISI 1045 steel is considered as workpiece material. The thermal and electromagnetic properties of copper, MFC are shown in Table 1. The MFC used for the current analysis is FLUXTROL® alpha form MF [14] which is suitable to perform under high frequency. The properties are independent of temperature as in practical implementation, the coil and MFC are maintained at a constant temperature by using an external chiller.

Fig. 4
Temperature-dependent
electromagnetic and thermal
property of AISI 1045 steel
[12]
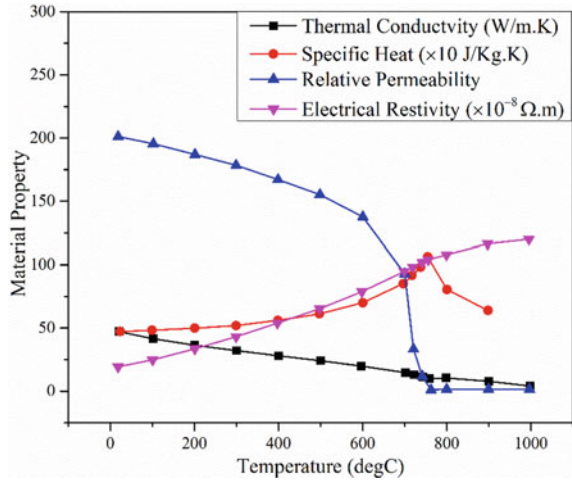
Table 1 Material property of induction coil and MFC

Material	Copper	Alpha form MF
Electrical conductivity (S/m)	5.998e7	6.667e−3
Relative permeability	1	10
Heat capacity (J/kg K)	385	–
Thermal conductivity (W/m K)	400	2

3   Results and Discussion

3.1   Effect of the Coil Gap

The coil gap has a prominent effect on the distribution of the temperature as well as the current density distribution. The effect is studied by considering 7 mm outer cross-sections for different coil gap (3–10 mm). The top surface temperature distribution on the surface induced by various coil gap at 60 s is presented in Fig. 5a. The temperature distribution trend is in the lower range for a 3 mm gap, and it increases with the increment of the gap between the adjacent coils. These results correspond to the repulsive proximity effect between in-plane and out plane induction coil. The impact is more significant on the lower gap as the opposite current cancel each other and repelled with an increase in gap. However, the temperature distribution rises till the 8 mm coil gap. There are no significant changes observed for the 9 mm and 10 mm coil gap. The current density distribution evident no substantial changes for an 8–10 mm coil gap, except shifting the peak far off due to an increase in the coil gap.
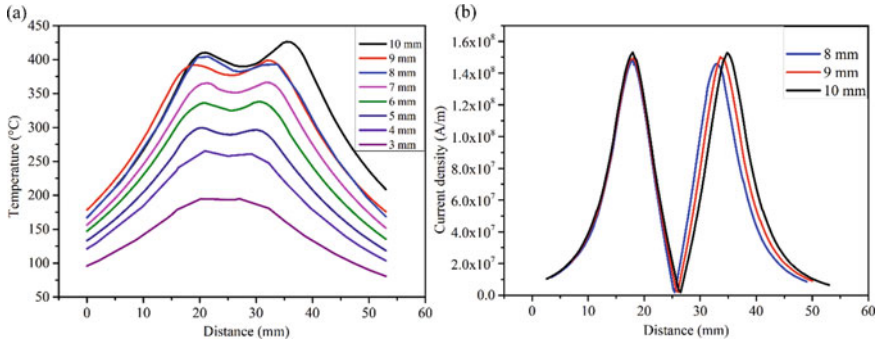
Fig. 5 **a** Surface temperature distribution, **b** current density distribution for different coil gap ($I = 700$ A, $f = 400$ kHz, $t = 60$ s)

3.2 Effect of the Coil Cross-Section

The effect of coil cross-section (5 mm, 6 mm, and 7 mm) on the surface temperature distribution beneath the coil is analysed. The analysis is carried out with constant parameter $I = 700$ A, $f = 400$ kHz, coupling gap $= 2$ mm, and coil gap $= 8$ mm. The highest peak temperature for the 5 mm coil is 1.2 times higher than the 6 mm coil, as shown in Fig. 6a. A similar pattern can also be observed from the magnetic flux density distribution as shown in Fig. 6b. The decrease in the coil diameter reduces the resistance of the coil [15] and increases the magnetic flux density that leads to a higher generation of eddy current by Joule's law in the workpiece.
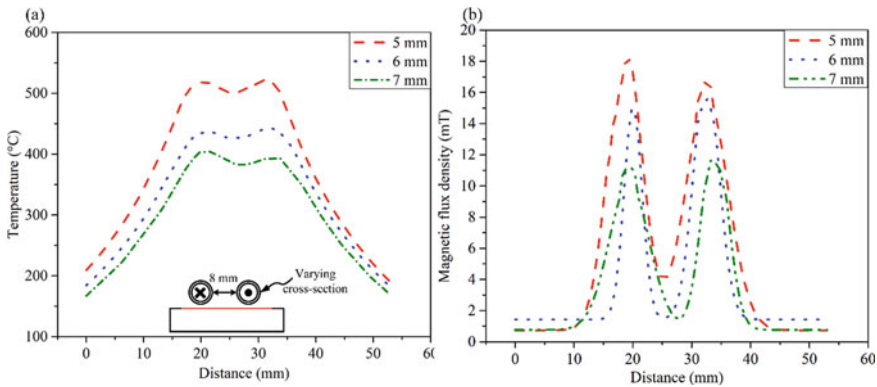
Fig. 6 Effect of the various coil cross-section on **a** temperature, **b** magnetic flux density
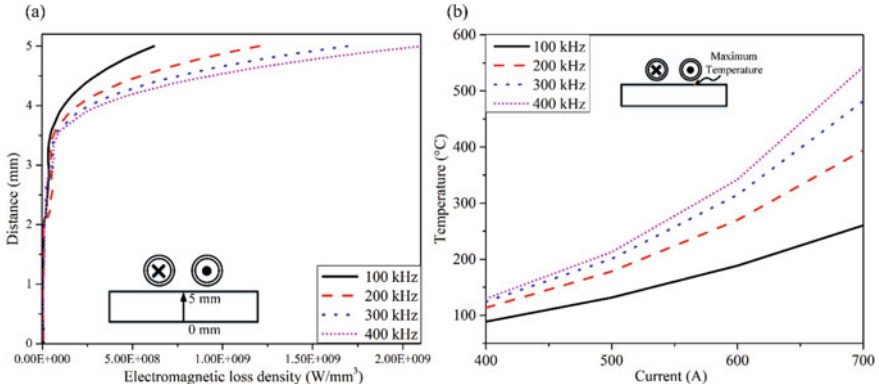
Fig. 7 Effect of frequency on **a** distribution of the current density along with the thickness of workpiece, **b** surface temperature for variation in coil current

3.3   Effect of the Coil Current and Frequency

The frequency and coil current have a striving effect on the heating of the coil for planar heating. The higher the frequency value, the more eddy current encapsulates closes to the surface (skin depth). Figure 7a shows the distribution of electrometric loss density along with the thickness. In other words, the heating rate increases with frequency due to the proximity effect on the surface closed to the induction coil. However, there is a difference in temperature between top and bottom surfaces which varies with frequency. This is because heat transfer mainly occurs by conduction mode. The coil current has a constructive effect on the temperature of the workpiece surface, as shown in Fig. 7b.

3.4   Effect of the Magnetic Flux Concentrator

The effect of the MFC on induction heating has been studied for 5 mm diameter coil and 8 mm adjacent coil gap. It is found that the maximum temperature rises by 1.95 times with the employment of MFC. Also, the uniformity of temperature distribution is broader along the length direction of the coil as shown in Fig. 8a. This is due to the concentration of the magnetic field towards the workpiece surface. The eddy current, which flows opposite in direction to the coil current, is increased enormously on the workpiece's surface, resulting in higher temperature due to joules heating. By use of MFC, the maximum current density increases from 5.24×10^7 to 6.84×10^7 A/m^2 and the temperature rose from 533 to 1043 °C. Meanwhile, the distribution is more uniform along the coil length than the regular induction heating as shown in Fig. 8b.
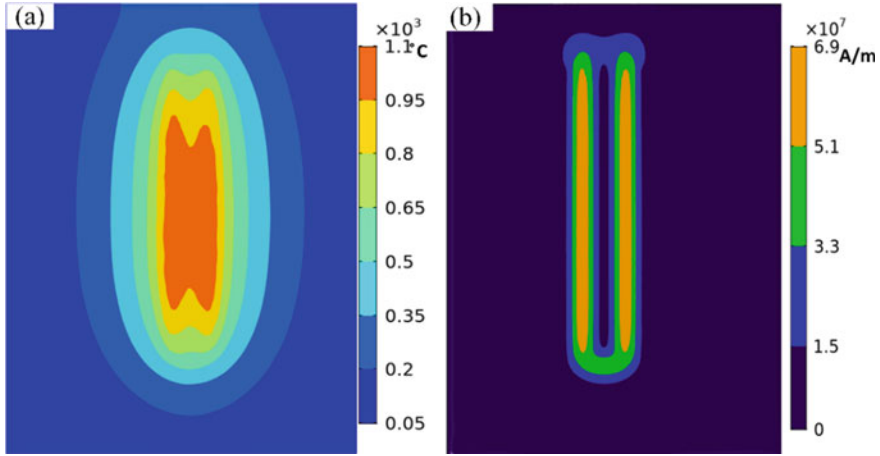
Fig. 8 a Temperature distribution, **b** current density distribution on the surface of workpiece with MFC ($I = 700$ A, $f = 400$ kHz)

4 Conclusion

The temperature distribution in planar induction heating is studied for the hairpin coil using COMSOL Multiphysics FEM software. A cylindrical induction coil with various geometric configuration is considered for the study. The aim is to select a suitable induction coil configuration by establishing the relation between electromagnetic field and thermal response of the workpiece. The following conclusion can be drawn.

1. The distance between in-plane and out plane coil has a significant effect on the heating. By analysing the temperature distribution, it can be concluded that the 8 mm coil gap is appropriate for hairpin coil configuration.
2. By comparing the surface temperature profile, it is observed that the 5 mm diameter coil generates higher temperature due to its lower resistance. In addition, increasing coil excitation frequency increases the surface temperature due to decrease in skin depth.
3. The implementation of the MFC narrowing the envelope of the magnetic field which increases the eddy current density and stiffly raises the surface temperature by 1.95 times. The temperature distribution is also relatively uniform compared to regular induction heating.

References

1. Lucía O, Maussion P, Dede EJ, Burdío JM (2013) Induction heating technology and its applications: past developments, current technology, and future challenges. IEEE Trans Industr Electron 61(5):2509–2520
2. Todaka T, Enokizono M (1996) Optimal design method with the boundary element for high-frequency quenching coil. IEEE Trans Magn 32(3):1262–1265
3. Boadi A, Tsuchida Y, Todaka T, Enokizono M (2005) Designing of suitable construction of high-frequency induction heating coil by using finite-element method. IEEE Trans Magn 41(10):4048–4050
4. Kilic VT, Unal E, Demir HV (2017) Coupling and power transfer efficiency enhancement of modular and array of planar coils using in-plane ring-shaped inner ferrites for inductive heating applications. J Appl Phys 122(1):014902
5. Bui HT, Hwang SJ (2015) Design of an induction heating coil coupled with magnetic flux concentrators for barrel heating of an injection molding machine. Proc Inst Mech Eng C J Mech Eng Sci 229(3):518–527
6. Semiatin SL (1988) Elements of induction heating: design, control, and applications. ASM International
7. Sun R, Shi Y, Pei Z, Li Q, Wang R (2018) Heat transfer and temperature distribution during high-frequency induction cladding of 45 steel plate. Appl Therm Eng 139:1–10
8. Lee KS, Eom DH, Lee JH (2013) Deformation behavior of SS400 thick plate by high-frequency-induction-heating-based line heating. Met Mater Int 19(2):315–328
9. Ikram A, Arif N, Chung H (2016) Design of an induction system for induction assisted alternating current gas metal arc welding. J Mater Process Technol 231:162–170
10. Chang L, Zhao Y, Yuan H, Hu X, Yang Z, Zhang H (2020) Effect of plate curvature on heat source distribution in induction line heating for plate forming. Appl Sci 10(7):2304
11. Zhang X, Yang Y, Liu Y (2011) Feasibility research on application of a high frequency induction heat to line heating technology. J Mar Sci Appl 10(4):456–464
12. Gao K, Qin X, Wang Z, Chen H, Zhu S, Liu Y, Song Y (2014) Numerical and experimental analysis of 3D spot induction hardening of AISI 1045 steel. J Mater Process Technol 214(11):2425–2433
13. Avestruz AT, Chang AH, Khushrushahi S, Banerjee A, Leeb SB (2013) Single-sided AC magnetic fields for induction heating. In: IECON 2013–39th annual conference of the IEEE Industrial Electronics Society, pp 5052–5057
14. FLUXTROL (2021) 2021 FLUXTROL®Inc. Retrieved at April 21, www.fluxtrol.com
15. Lope I, Acero J, Carretero C (2015) Analysis and optimisation of the efficiency of induction heating applications with litz-wire planar and solenoidal coils. IEEE Trans Power Electron 31(7):5089–5101

Numerical Modelling of Plastic Behaviour and Temperature Distribution During FSW Process

N. Kumar, M. Z. Ansari, and H. Singh

1 Introduction

The friction stir welding (FSW) is a solid state joining method, which was invented by the Welding Institute (TWI) in 1991 [1]. FSW usages a non-consumable tool with especially design tool pin and shoulder which is plunged into the workpiece and traversed along the adjoining edge to produce the weld joint. Due to its advantageous characteristic such as high weld joint quality, less welding defect and green welding process, FSW is especially applied for the welding of aluminium and magnesium [2, 3]. FSW is widely used in various industries such as automotive, shipbuilding, aerospace and construction industry [4–6]. Rajakumar et al. [7] analysed the effect of tool and process parameters on physical properties of AA7075-T6 FSW joint and concluded that the microstructure, micro-hardness of weld nugget influences the strength properties of the welded joints. Thimmaraju et al. [8] analysed the mechanical and metallurgical properties of FSW welded joints by using different types of especially designed tool and revealed that hexagonal tool pin produce finer grain size as compared to triangular and square tool pin. Further they found that the grain size is finer in weld nugget zone as compared to the base metal and also observed that the properties of the weld joint are strongly influenced by the type of tool pin used. Zhang et al. [9] developed a computational fluid dynamic model to analyse the effects of tilt angle on the mass and heat transfer in the welding

N. Kumar (✉) · M. Z. Ansari · H. Singh
Mechanical Engineering Discipline, PDPM Indian Institute of Information Technology Design & Manufacturing, Dumna Airport Road, Madhya Pradesh 482005 Jabalpur, India
e-mail: 1813303@iiitdmj.ac.in

M. Z. Ansari
e-mail: zahid@iiitdmj.ac.in

H. Singh
e-mail: hps.dme@iiitdmj.ac.in

zone of FSW process. From the numerical analysis, the authors found that by util-
ising the tool tilt angle during the FSW process, higher temperature are produced
on the advancing side of workpiece. Further, higher tool tilt angle increases the
forging force at tool/workpiece interface and better intermixing of material occurs,
resulting in better weld joint. Raouache et al. [10] developed a 3D finite element to
investigate the temperature profile developed during FSW process using COMSOL
MULTIPHYSICS using various tool profile and process parameters. The authors
concluded that tool pin geometry highly affects the weld quality and temperature
increases during tool holding time by increasing the rotational speed of the FSW
tool. However, mostly researchers focused on microstructures, mechanical proper-
ties and flow of material in FSW process. The study of the strain and stress field
during FSW is limited. Therefore, in the present paper a 3D thermo-mechanical
model is established to investigate the temperature, strain and stress profile devel-
oped during FSW process in the welding zone. Additionally, thermal and plastic
behaviour through the conventional FSW tool is compared with the stepped FSW
tool.

2   Geometric Modelling and Material Properties

The workpiece is modelled as 4 mm-thick plate of AA7075 having dimensions 60
mm × 35 mm. The plate is considered as a single continuum body to lessen compu-
tational time by neglecting the contact instabilities. Detailed configuration of the
conventional and stepped FSW tool is shown in Figs. 1 and 2, respectively. H13 tool
steel is selected as tool material.

Table 1 listed the physical characteristics of AA7075 and H13 tool steel
[DEFORM 3D manual]. Thermal conductivity and heat capacity of AA7075 is

Fig. 1 CAD model
of conventional FSW tool
(mm)
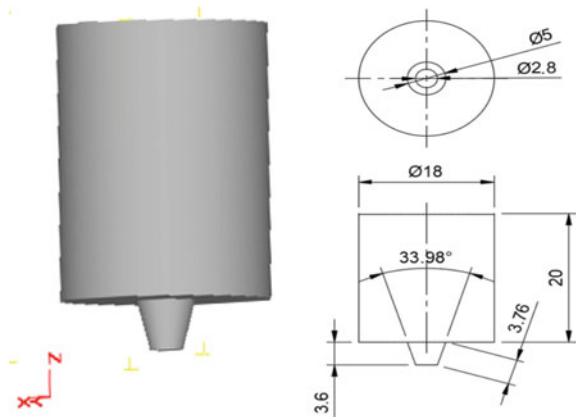
Fig. 2 CAD model of stepped FSW tool (mm)
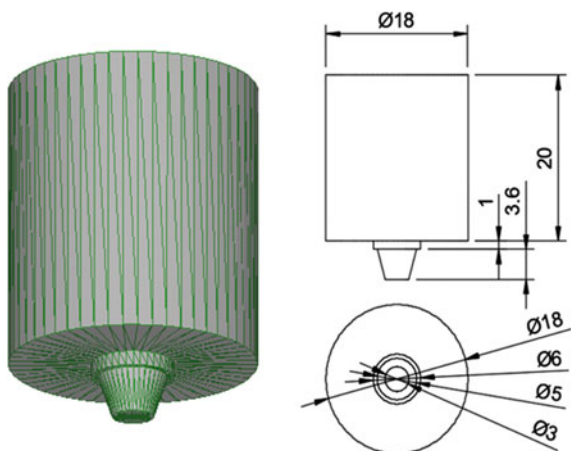
Table 1 Physical properties of AA7075 and H13 tool steel

Properties	Unit	AA7075	H13 tool steel
Young's modulus (E)	N/mm^2	71,700	210,000
Thermal conductivity (k)	N/s °C	$f(T)$	149
Heat capacity (C_p)	N/mm^2 °C	$f(T)$	2.78
Thermal expansion (α)	μ mm/mm °C		11.7
Poisson's ratio (v)		0.33	0.3

Table 2 Physical properties of AA7075

T (°C)	k (N/s °C)	C_p (N/mm^2 °C)
20	135.2	2.40
100	165.8	2.47
200	185.2	2.56
300	207.0	2.81
400	222.4	3.18
482	220.1	3.44

Table 3 Process parameters used during process

Process parameter	Unit	Value
Rotational speed	r/min	100
Traverse speed	mm/min	60
Plunge depth	mm	0.2
Tilt angle	(°) degree	0

considered as a function of temperature as listed in Table 2 [11]. Table 3 listed the process parameters used during FSW.

3   Material Modelling and Constitutive Equation

Constitutive equation for the model is defined as per the Sheppard and Wright model [12] i.e. Equation (1) and material constants for AA7075 which are fed during modelling were taken from [13], as shown in Table 4. Figure 3a depicts the flow stress of AA7075 as a function of strain rate and Fig. 3b depicts the flow stress of AA7075 as a function of temperature.

$$\dot{\epsilon} = A[\sinh(\alpha\overline{\sigma})]^n \exp\left(\frac{-\Delta H}{RT}\right) \tag{1}$$

where $\dot{\epsilon}$ is the strain rate, $\overline{\sigma}$ is the effective stress, R is the gas constant, T is the material temperature and A, α, n are material constants.

Table 4 Material constant for AA7075

A (1/s)	α	n	H (Nmm/mol)	R (Nmm/mol °C)
2.87×10^{11}	0.011	6.32	156.937×10^6	8314
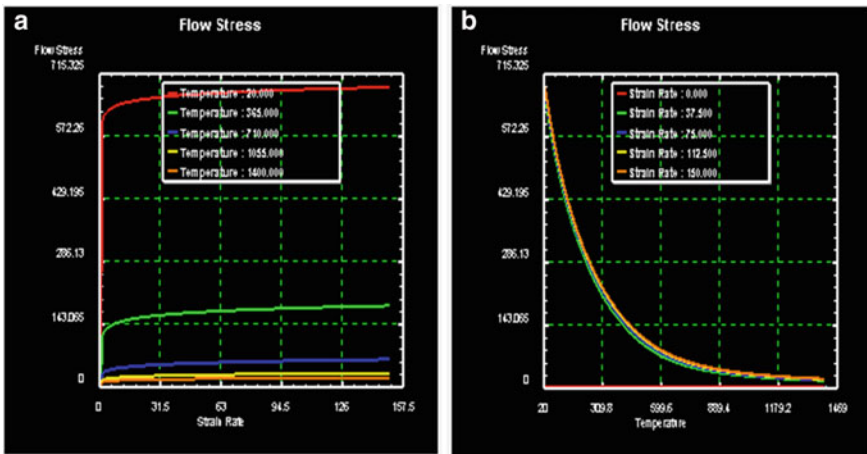
Fig. 3 Flow stress of AA7075 as a function of **a** strain rate, **b** temperature

4   Finite Element Modelling of FSW

The workpiece and tool are modelled as viscoplastic and rigid body, respectively. Conventional and stepped FSW tool meshed with tetrahedral element is shown in Fig. 4. Biased meshing is used for stepped tool. Further detail of meshing for workpiece and tools is mentioned in Table 5. After modelling, the workpiece and the tool are meshed and then assembled to depict the plunging phase which is shown in Fig. 5. The lower surface of the tool pin should be in contact with the upper surface of workpiece before starting the simulation for the ease of convergence during analysis.

Fig. 4 Meshed FSW tools
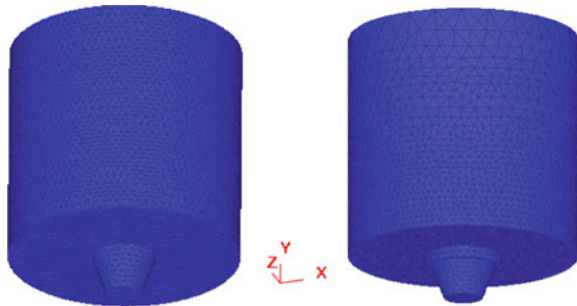
Table 5 Details of meshed workpiece and meshed tools

Process	Casting (workpiece)	Casting (tool)
Element type	Tetrahedral	Tetrahedral
Mesh size	0.6	0.5
No. of element	224,186	96,483/74,213
No. of node	63,348	5149/4862
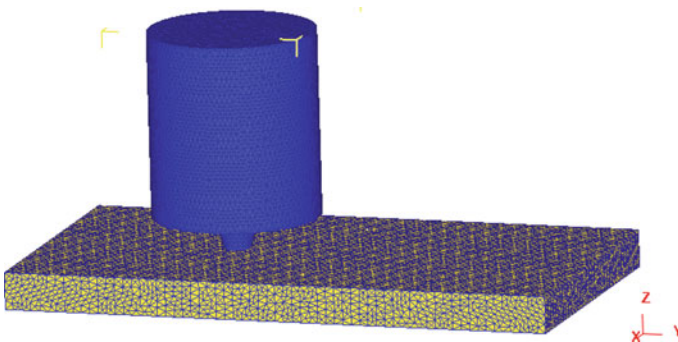
Fig. 5 Meshed assembly

Fig. 6 Mechanical boundary condition
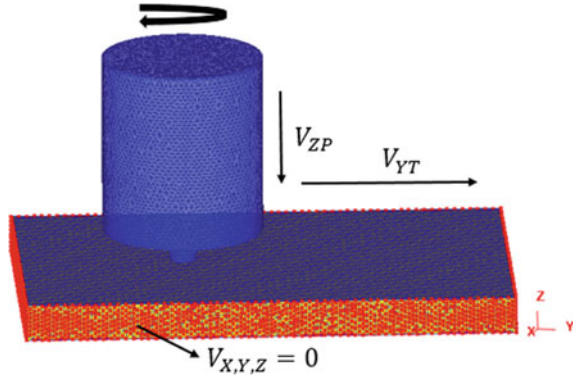
Table 6 Various convective heat transfer coefficient (h) [14]

Variables	Unit	Values
(h) for tool/workpiece to the environment	(N/mm s °C)	0.02
(h) for workpiece to the tool	(N/mm s °C)	11
(h) for workpiece bottom surface to the environment	(N/mm s °C)	11
Stefan Boltzmann constant	(N/mm °C)	5.669×10^{-11}

4.1 Boundary Conditions

The starting temperature of the ambient, tool and the workpiece is set at 25 °C. All surfaces, except bottom surface of tool pin and workpiece, interact with the ambient by convective and radiation mode of heat transfer. A convection mode of heat transfer is assumed between the workpiece and the tool and between the workpiece bottom surface and ambient as, the backing plate is not considered to reduce the computational time. Degrees of freedom are to prevent translational and rotational motion. Mechanical boundary condition defined on the workpiece and tool is shown in Fig. 6 (Table 6).

4.2 Inter-object Relation

A constant shear friction model has been used for the analysis which is represented by Eq. (2) with a friction factor of 0.5 [15].

$$\overline{\tau} = m\tau_{max} \qquad (2)$$

where $m = 0.5$.

4.3 Thermal Model

In FSW, heat generation mainly occurs due to plastic deformation and friction which is represented by Eq. (3). Frictional heating is expressed as the product of frictional stress and slip rate at the interface which is represented by Eq. (4). Heat generation due to plastic deformation is expressed as a product of flow stress and strain rate which is represented by Eq. (5). Temperature distribution is governed by the Fourier law of heat conduction which is represented by Eq. (6).

$$\dot{q} = \dot{q}_f + \dot{q}_p \tag{3}$$

$$\dot{q}_f = \varnothing(\tau_s \times \dot{\gamma}) \tag{4}$$

$$\dot{q}_p = n(\bar{\sigma} \times \dot{\epsilon}) \tag{5}$$

where $\varnothing = 0.9$ and $n = 0.9$, respectively [16].

$$k\nabla^2 T + \dot{q} = \rho c_p \frac{\partial T}{\partial t} \tag{6}$$

5 Results and Discussions

5.1 Model Validation

1. Table 7 provides information about the numerical validation of present model using the data obtained from the literature [17].
2. The maximum temperature found during process is compared with the literature's result and the model is accurately able to predict it with an error of 2.93%.

Figure 7 provides information about the temperature distribution which is obtained after simulation with all process and tool parameter (for 1000 rpm and 60 mm/min traverse speed) used in the literature and is used here to validate the present model.

Table 7 Model validation

Rotational speed (rpm)	Maximum temperature during FSW process (°C)		Percentage error (%)
	Simulation [17]	Simulation	
1000	546	530	2.93

Fig. 7 Temperature profile
of workpiece
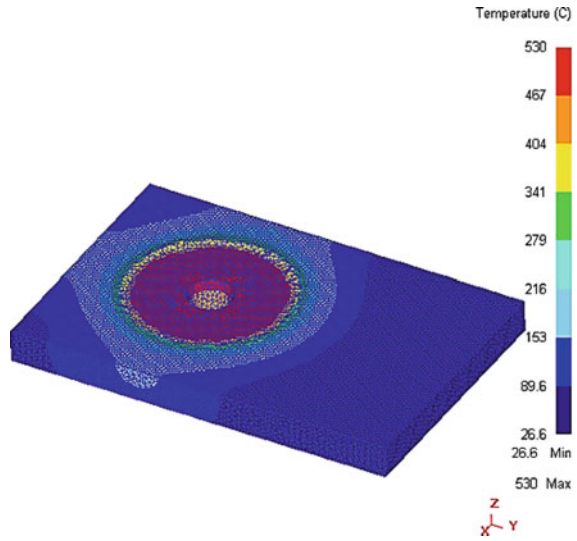
5.2 Temperature Contours

In FSW, heat generation mainly occurs due to plastic deformation and friction between tool and workpiece. Figure 8 shows the temperature profile of the upper surface and in longitudinal direction of workpiece, for a rotational speed of 1000 rpm and a traverse speed of 60 mm/min. A maximum temperature of 467 °C is observed in the stirring zone just below the shoulder, i.e. on the workpiece/shoulder interface because the tool shoulder is 3.6 times that of the tool pin and most of the heat is generated due to tool shoulder.

Figure 9 shows the selected points on top surface of the workpiece, i.e. P1, P2 and P3 and its temperature history. It is observed that when the tool pin is inserted into the
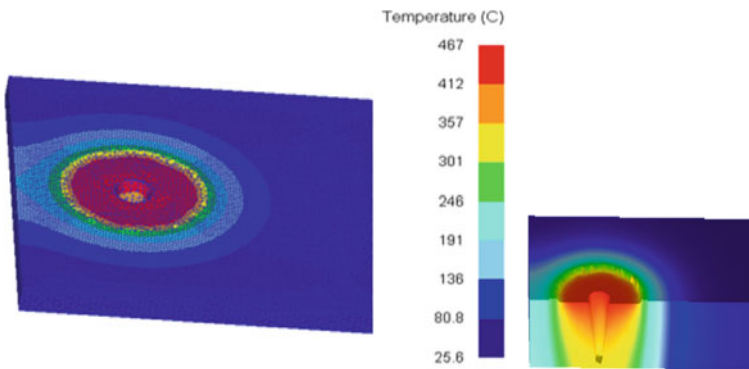
Fig. 8 Temperature profile of top surface and longitudinal direction of workpiece
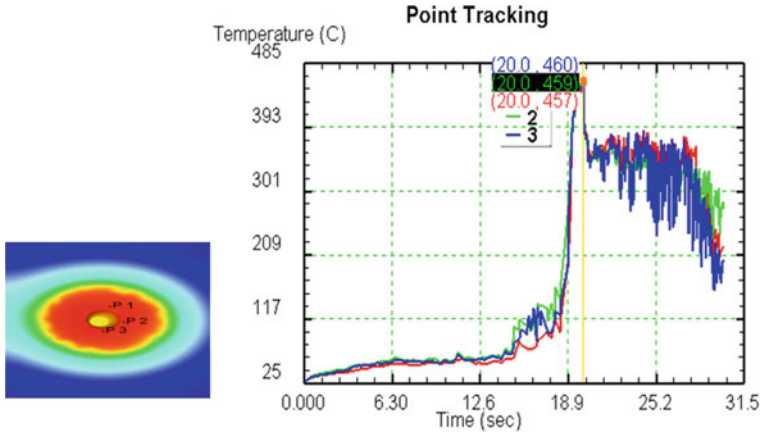
Fig. 9 Temperature history of selected points

Fig. 10 Temperature variation versus distance from weld centre
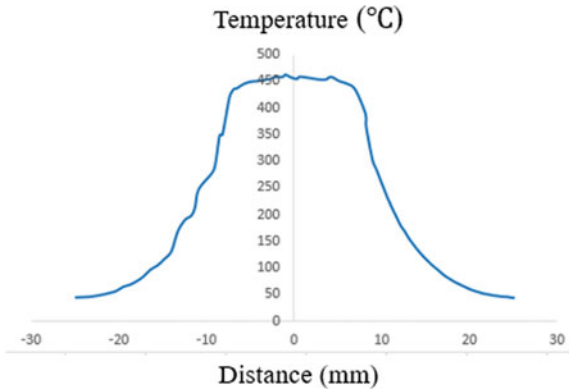
workpiece there is very small rise in temperature but when the tool shoulder is inserted into the workpiece, there is a sudden rise in temperature occurs. During plunging phase, there is continuous rise in temperature, during dwelling stage temperature the rise in temperature is very small and during welding phase a drop in temperature is observed.

From Fig. 10 it is observed that temperature distribution is nearly symmetrical in nature along the centre of the joint.

5.3 Strain Profile for Conventional FSW Tool

In FSW process plastic deformation and heat generation both strongly affect the microstructure of the weld zone so it is essential to study the strain profile during

Fig. 11 Strain developed
during welding
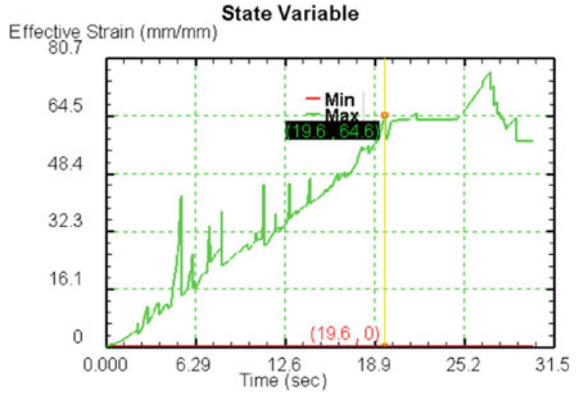
Fig. 12 Effective strain
profile
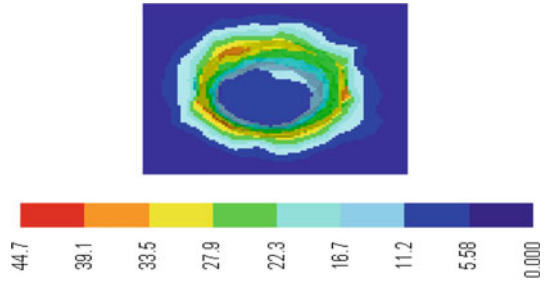
welding to optimise the weld strength and process parameters. Figure 11 shows that maximum effective strain of 75.8 is attained during the welding process. During the plunging and dwelling phase the strain increases up to maximum and after some time during the welding stage, it slightly decreases and remains almost constant for the rest of the welding.

From Fig. 12 it is observed that the effective strain are higher near the surface points as compared to other because the plastic deformation near the surface point is increased by the tool shoulder.

From Fig. 13, it is observed that the strain developed during the FSW process is more on the advancing side (AS) as compared to that of retreating side (RS) because in the advancing side rotational velocity and traverse velocity both acted in the same direction result in higher shear action of the workpiece material compared to retreating side where both the velocity acted in opposite direction. Due to higher plastic deformation in the advancing side as compared to the retreating side of the weld joint because of velocity difference on two sides of the weld makes the FSW process unsymmetrical in nature.

Fig. 13 Strain variation versus distance from weld centre
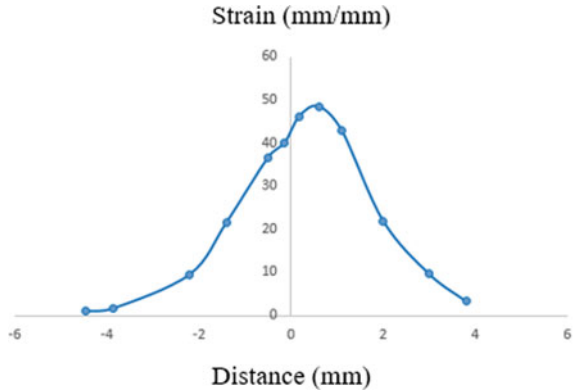
Fig. 14 Effective stress in workpiece during welding
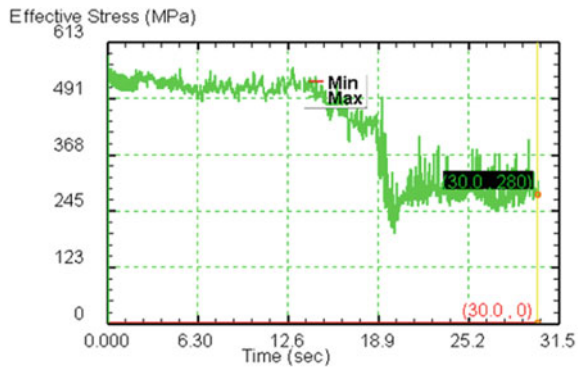
5.4 Effective Stress

From Fig. 14 it is observed that effective stress is higher in beginning but decreases with an increase in temperature during the traverse phase.

5.5 Temperature and Strain Profile for Stepped Tool

In stepped tool, the first shoulder prevented more amounts of heat formation during the FSW process, result in increase in temperature as compared to conventional FSW tool. Figure 15 shows temperature distribution on the upper surface of workpiece and a maximum temperature of 495 °C is attained at the workpiece-tool shoulder interface in the welding zone. From Fig. 16, it is concluded that maximum strain of 79.7 is attained during the stepped tool FSW process which is more than that of conventional FSW process. As it is known that temperature and strain both plays a pivotal role in

Fig. 15 Temperature distribution on the top surface of workpiece
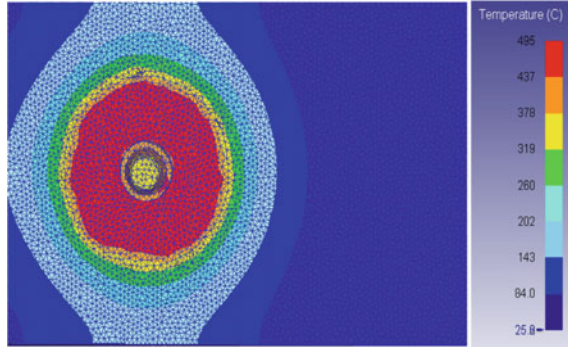
Fig. 16 Strain developed during welding through stepped tool
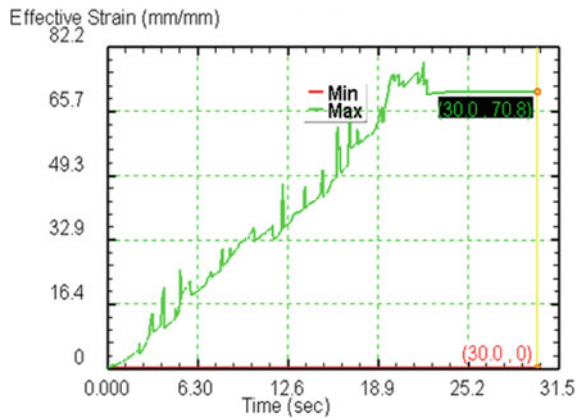
the refinement of the grains in the weld nugget zone hence a better grain refinement takes place in stepped tool FSW process result in increase in joint efficiency.

6   Conclusions

In present study, a 3D coupled thermo-mechanical is developed to investigate the temperature profile and plastic behaviour of AA7075 produce during FSW process for conventional and stepped tool using FEM software DEFORM 3D. It is found that a maximum temperature of 467 °C is attained at interface of workpiece-tool shoulder in welding zone using conventional tool. The heat generation is more on the top surface as compared to the bottom surface of workpiece due to the shoulder and temperature profile is nearly symmetrical in nature along the centre of the joint. A higher strain of 75.8 is found on the upper surface of the workpiece and also a higher strain on advancing side compared to the retreating side of the workpiece. In the weld zone, the strain distribution is uneven along the joint line which indicates

asymmetrical nature of FSW process. The strain attains maximum value during the plunging and dwelling phase and then slightly decreases during the welding phase. Stress decreases in the welding phase as compared to other plunging phase and dwelling phase. The temperature and effective strain increase up to 495 °C and 79.7, respectively, during stepped tool friction stir welding result in increase in joint efficiency.

References

1. Thomas WM, Nicholas ED, Needham JC et al (1991) Friction stir butt welding. International Patent Application No. PCT/GB92/02203 and GB Patent Application No. 9125978.8, 6
2. Wang T, Zou Y, Matsuda K (2016) Micro-structure and micro-textural studies of friction stir welded AA6061-T6 subjected to different rotation speeds. Mater Des 90:13–21
3. Threadgill PL, Leonard AJ, Shercliff HR, Withers PJ (2009) Friction stir welding of aluminium alloys. Int Mater Rev 54(2):49–93
4. Asadi P, Besharati Givi MK, Parvin N, Araei A, Taherishargh M, Tutunchilar S (2012) On the role of cooling and tool rotational direction on microstructure and mechanical properties of friction stir processed AZ91. Int J Adv Manuf Technol 63(9–12):987–997
5. Givi MKB, Asadi P (2014) Advances in friction stir welding and processing. Woodhead Publishing Limited, Elsevier
6. Barmouz M, Shahi P, Asadi P (2014) Friction stir welding/processing of polymeric materials. In: Givi MKB, Asadi P (eds) Advances in friction stir welding and processing. Elsevier, Amsterdam, pp 601–670
7. Rajakumar S, Muralidharan C, Balasubramanian V (2011) Influence of friction stir welding process and tool parameters on strength properties of AA7075-T6 aluminium alloy joints. Mater Des 32(2):535–549
8. Thimmaraju P, Arkanti K, Reddy GC, Tilak KBG (2016) Comparison of microstructure and mechanical properties of friction stir welding of Al 6082 aluminum alloy with different tool profiles. Mater Today Proc 3(10):4173–4181
9. Zhang S, Shi Q, Liu Q, Xie R, Zhang G, Chen G (2018) Effects of tool tilt angle on the in-process heat transfer and mass transfer during friction stir welding. Int J Heat Mass Transf 125:32–42
10. Raouache E, Driss Z, Guidara M, Khalfallah F (2016) Effect of the tool geometries on thermal analysis of the friction stir welding. Int J Mech Appl 6(1):1–7
11. Fratini L, Buffa G, Shivpuri R (2010) Mechanical and metallurgical effects of in process cooling during friction stir welding of AA7075-T6 butt joints. Acta Mater 58(6):2056–2067
12. Sellars CM, Tegart WM (1966) On the mechanism of hot deformation. Acta Mater 14(9):1136–1138
13. Jain R, Pal SK, Singh SB (2017) Numerical modelling methodologies for friction stir welding process. In: Davim JP (ed) Computational methods and production engineering. Elsevier, Amsterdam, pp 125–169
14. Buffa G, Hua J, Shivpuri R, Fratini L (2006) A continuum based fem model for friction stir welding—model development. Mater Sci Eng A 419(1–2):389–396
15. Tutunchilar S, Haghpanahi M, Besharati Givi MK, Asadi P, Bahemmat P (2016) Simulation of material flow in friction stir processing of a cast Al–Si alloy. Mater Des 40:415–426
16. Asadi P, Mahdavinejad RA, Tutunchilar S (2011) Simulation and experimental investigation of FSP of AZ91 magnesium alloy. Mater Sci Eng A 528(21):6469–6477
17. Jain R, Pal SK, Singh SB (2017) Finite element simulation of temperature and strain distribution during friction stir welding of AA2024 aluminium alloy. J Inst Eng (India) Ser C 98(1):37–43

Double Arrowhead Auxetic Structures: A Numerical Investigation Under Compressive Loading

Shailendra Kumar, Swapnil Vyavahare, and Harika Bogala

1   Introduction

A new class of structures named 'auxetics' got interest in recent years due to their improved mechanical properties like fracture toughness, indentation resistance and energy absorption over traditional engineering materials [1]. There is a high requirement for high-performance materials in the field of sports, safety, defence, automotive and tissue engineering [2]. The main necessity for the development of such materials is because of their tailorable combination of high strength and stiffness with a noticeable decrement in weight [3]. Evans initiated the word 'auxetics' from a Greek word 'auxetikos' signifying expanding nature of material when compressed [4]. Basically, auxetic structures are characterized by negative Poisson's ratio (NPR) [5]. Poisson's ratio is the proportion of lateral strain to longitudinal strain which is a parameter describing extent to the material gets thin when stretched [6]. Most of the traditional materials tend to exhibit a positive Poisson's ratio, i.e. when elongated they get thinner in the perpendicular direction of applied load. But the auxetic structures possess NPR, which gets elongated in the lateral direction when stretched and contracts laterally when compressed [7]. Naturally existing auxetic materials, α-cristobalite, pyrolytic graphite and α-quartz also exhibits NPR under large axial tension [8]. Based on geometrical design, auxetic structures are divided into various types like re-entrant structures, honeycombs, star-shaped, double arrowhead (DAH), chiral structures, and its variants, rotating rigid structures and its variants [9]. These auxetics are complex in nature and also difficult to manufacture through conventional processes as each structure requires a separate design tool using traditional manufacturing technique, and hence, they are easy to fabricate using additive manufacturing (AM).

S. Kumar (✉) · S. Vyavahare · H. Bogala
Department of Mechanical Engineering, Sardar Vallabhbhai National Institute of Technology, Surat, India

Various researches have performed investigations related to mechanical property improvement of auxetic structures [10]. Scarpa et al. [11] conducted finite element analysis (FEA) on honeycomb structures to find the geometrical impact on Poisson's ratio and Young's modulus. Shepherd et al. [12] carried out FEA of re-entrant, chiral, hound tooth and hexagonal honeycomb structure under impact loading with two types of drop hammer for thermoplastic polyurethane material and observed that anti-trichiral structure absorbed the highest impact energy compared to other structures. Alomarah et al. [13] investigated the effect of geometrical parameters numerically for re-entrant chiral auxetic (RCA) structures, and a large NPR is observed when the structure loaded in X-direction. Xiao et al. [14] investigated the mechanical properties of unidirectional graded auxetic honeycomb (UGAH) and bidirectionally graded auxetic honeycomb (BGAH). They observed less energy dissipation in case of UGAH. Qi et al. [15] observed that effective NPR for tetrachiral honeycombs under in-plane dynamic crushing and developed theoretical models to find the crushing strength for quasi-static and dynamic models. Vyavahare et al. [16] analysed the influence of process parameters for re-entrant auxetic structures which were fabricated using fused deposition modelling technique and showed that layer thickness and raster angle are significant for strength, stiffness and specific energy absorption (SEA) of the structures. Further, Vyavahare and Kumar [17] studied the influence of geometric parameters of re-entrant auxetic structure on mechanical properties made of two different materials, i.e. acrylonitrile butadiene styrene (ABS) and polylactic acid (PLA). They observed good strength and stiffness in PLA structures and good SEA in ABS structures. Grima and Evans [18] found that even rotating rigid squares structures can also possess NPR. Further, they improved the geometry of these structures from squares to rhombus and parallelograms [19]. Larsen et al. [20] fabricated the DAH auxetic structures while working for the development of micromechanics. They described mechanical and geometrical advantages of the developed structures. Qiao and Chen [21] developed a DAH auxetic structure having three variables, namely length, short beam angle, long beam angle with uniform thickness and out plane width. FEA was performed for the structure for high-velocity impact. They showed a good performance of DAH structure for SEA. Also, they showed that DAH structure has applications in automotive field (e.g. jounce bumper) for the improvement of the noise, vibration performance [22] and concluded that NPR jounce bumper is feasible since it achieved the mechanical performance similar to general jounce bumper. Gao et al. [23] developed a theoretical and numerical model for double v-shaped honeycomb and later considered a 3D–DAH structure by making a small modification. Further, [24] they analysed effect of three geometrical parameters in macro- and micro-scale. Also, they performed tests to find the crashworthiness of the 3D-DAH structure using steel material. They observed that when slenderness ratio of structure is greater than 2.2 results in buckling which further leads to failure of the structure. Also, crashworthiness of DAH structure is more sensitive to angles and thickness of beams. Gao et al. [25] studied impact responses of the structures for low and high velocities. They found that the effect of auxeticity is observed only at low velocity. They observed a rise in crushing strength with increase in relative density. Zhao et al. [26] developed theoretical model to predict the dynamic crushing

strength of DAH structure and observed that strength depends mainly on relative density and impact velocity. Wang et al. [27] fabricated the 3D-DAH auxetic structure by replacing the sharp vertex with a line of small width. They showed stiffer response with increase in compressive strain than normal auxetic structure.

From literature review, it is evident that most of the work related with DAH structure is concentrated on analysis structures under impact loading. Limited work has been done in investigating the influence of geometrical parameters of DAH structure under compressive loading. Therefore, in the present work a numerical investigation is performed on the quasi-static properties of DAH structures of PLA material under compressive loading. The objective of the study is to investigate the effect of geometrical parameters of DAH auxetic structures on strength, stiffness and SEA under compressive loading.

2　Experimental Details

Following is the plan of experimental work

1. Design of experiments
2. Computer-aided design (CAD)
3. Material properties
4. Finite element analysis
5. Measurement of responses.

2.1　*Design of Experiments*

A unit cell of a DAH structure has three main geometrical parameters, namely first angle (θ_1), second angle (θ_2) and half-length (l), as in Fig. 1. In the current analysis, these parameters are varied within two levels. The geometrical parameters and their range as listed in Table 1 are decided based on the literature review. A detailed experimental study is designed using Design-Expert 11 software (developed by Stat-Ease

Fig. 1 Unit cell of DAH structure
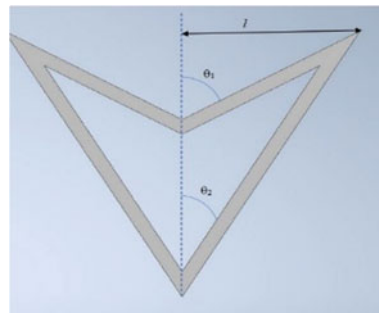
Table 1 Geometrical parameters and their range

Geometrical parameters	Units	Minimum value	Maximum value
Half-length, l	mm	8	10
First angle, θ_1	°	60	75
Second angle, θ_2	°	20	30

Table 2 Experimental design

No.	Run No.	Half-length, l (mm)	First angle, θ_1 (°)	Second angle, θ_2 (°)	Thickness, t (mm)
1	5	8	60	20	1.489
2	8	8	75	20	1.753
3	3	8	60	30	1.024
4	1	8	75	30	1.350
5	4	10	60	20	1.862
6	2	10	75	20	2.192
7	7	10	60	30	1.281
8	6	10	75	30	1.688

Inc.) by choosing the full factorial design which recommended eight experiments. The wall thickness of DAH structure is computed based on constant relative density of 35% and rearranging the parameters in Eq. 1 [21]. Table 2 gives the calculated thickness for all the eight configurations. The number of unit cells is 4 (i.e. 2 × 2) which does not have size effect as minimum number of cells to avoid the size effect is 3 [13].

$$\text{Relative density} = \rho/\rho_s = \overline{\rho} = \frac{t(\sin\theta_1 + \sin\theta_2)}{l\sin(\theta_1 - \theta_2)} \tag{1}$$

where

ρ Density of auxetic structure
ρ_s Density of solid material of which cell wall is made
$\overline{\rho}$ Relative density of auxetic structure
t Thickness of cell wall
θ_1 First angle
θ_2 Second angle
l Half-length of DAH structure.

Fig. 2 CAD model of DAH auxetic structure
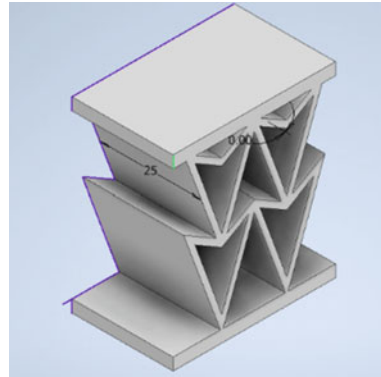
2.2 Computer-Aided Design

Autodesk Inventor 2020 tool is used to prepare the CAD models. The cellular structures are designed according to the American Society for Testing and Materials (ASTM) C365 standard [28] which is a standard test method for sandwich core structures to perform compression test. Eight configurations are modelled as per experimental design. Initially, a unit cell is designed and then arrayed in *XY* plane to get four-unit cells (2 × 2) in a structure and then extruded 25 mm in *Z*-direction to get the quasi-static models as in Fig. 2. The upper and lower support plates thickness is kept as 3 mm for all configurations, and the approximate structure size is around $45 \times 25 \times 50$ mm^3. All the models are saved in standard for the exchange of product model data (.stp) file.

2.3 Material Properties

The material properties of PLA material are adopted in the present study which is taken from the literature [17]. These material properties are given in Table 3.

Table 3 Material properties of PLA material

Material property	Value
Density	1.252 g/cm^3
Young's modulus	3.5 GPa
Poisson's ratio	0.36
Yield strength	20 MPa

Fig. 3 Boundary conditions
for DAH auxetic structure
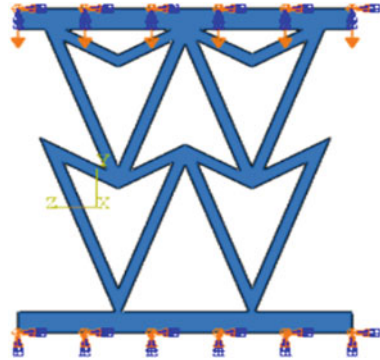
2.4 Finite Element Analysis

Finite element (FE) simulations are conducted with the help of ABAQUS/Standard
solver. Geometric files from Autodesk Inventor software are imported to ABAQUS
solver, and a 3D deformable parts are generated. PLA material is designed with
elastic, plastic properties as described in Sect. 2.3. A dynamic explicit general proce-
dure step is created for a period of 5 s. General contact interaction property is created
by considering all with self-surface pairs in contact domain with a coefficient of fric-
tion 0.15 for tangential behaviour with a penalty friction formulation. The bottom
plate is constrained in all directions by giving 'Encastre' boundary condition, and
the top plate is given a displacement boundary condition in *Y*-direction as shown in
Fig. 3. Hex element shape with sweep technique, advanced front algorithm is used for
meshing the structure. An 8-node linear brick, reduced integration, hourglass control
element type (C3D8R) is assigned. The required output variables are selected in step
module from history output requests before a job is created in job module and then
job is submitted to analysis with multiple processors to reduce the analysis time. The
structure is 60% strained.

2.5 Response Measurement

The requested history output variables, i.e. load and displacement, are extracted from
XY-data from visualization module. Then these values are transformed to stress–
strain curve. Stress is computed as the ratio of force to initial cross-sectional area
(Eq. 2) while strain is calculated as ratio of displacement to initial gauge height. The
slope of stress–strain curve gives compression modulus, while stress value at yield
point gives the compressive strength. If yield point is not observed before 10% of
strain, then the stress value at 10% strain can be considered as compressive strength
[29]. Energy absorption density (*w*) is obtained by integrating the area under curve
in Eq. 3, and SEA is calculated by using Eq. 4.

$$\sigma = E\epsilon \tag{2}$$

$$w = \int_0^\epsilon \sigma(\epsilon)\mathrm{d}\epsilon \tag{3}$$

$$\text{SEA} = \frac{w}{\overline{\rho} * \rho s} \tag{4}$$

3 Results and Discussion

The responses namely strength, modulus and SEA, are calculated and given in Table 4. Also, mean and standard deviation values of the responses are given in Table 5.

Table 4 Numerical results of DAH auxetic structures

Run No.	Conf.	First angle, θ_1	Second angle, θ_2	Half-length, l	Thickness, t	Compressive strength	Compressive modulus	Specific energy absorption
		(°)	(°)	(mm)	(mm)	(MPa)	(MPa)	(J/g)
1	4	75	30	8	1.489	0.285	9.487	483.062
2	6	75	20	10	2.192	0.317	13.233	95.016
3	3	60	30	8	1.024	0.285	13.607	425.235
4	5	60	20	10	1.862	0.211	7.355	360.75
5	1	60	20	8	1.489	0.319	21.322	124.542
6	8	75	30	10	1.868	0.323	26.924	161.353
7	7	60	30	10	1.281	0.232	9.675	175.784
8	2	75	20	8	1.751	0.244	16.637	59.890

Table 5 Mean and standard deviation of responses with respect to parameters

Geometric parameters	Units	Levels	Compressive strength (MPa)		Compressive modulus (MPa)		SEA (J/g)	
			Mean	Standard deviation	Mean	Standard deviation	Mean	Standard deviation
First angle, θ_1	°	60	0.262	0.049	12.989	6.124	271.577	144.174
		75	0.292	0.036	16.570	7.494	199.830	193.451
Second angle, θ_2	°	20	0.272	0.054	14.636	5.879	160.049	136.385
		30	0.281	0.037	14.923	8.222	311.358	166.665
Half-length, l	mm	8	0.283	0.031	15.263	4.990	273.182	211.941
		10	0.270	0.057	14.296	7.584	198.225	113.914
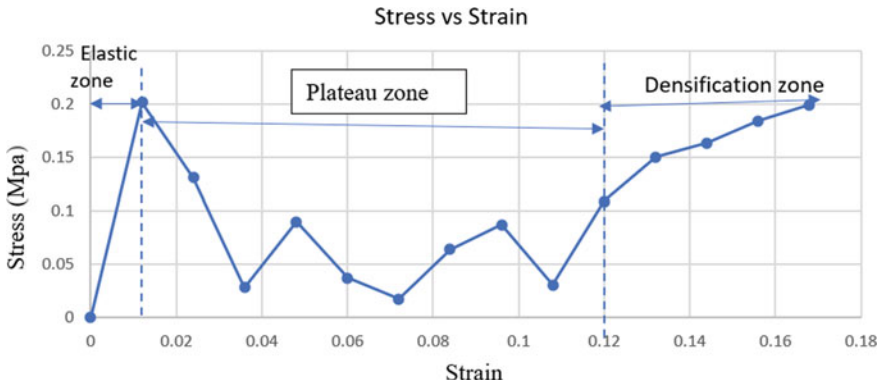
Fig. 4 Stress–strain graph of configuration 1 structure

The deformation pattern for all the configurations is observed from the simulations. It is observed that the bottom unit cells start deforming first by decreasing θ_1 which tends to move inside of the unit cell. The upper unit cells start deforming by increasing the θ_1. Lastly, all the unit cells pile upon each other causing a densification [24]. Three different deformation zones, namely elastic, plateau and densification zone, are observed in a stress–strain curve as in Fig. 4. Initial zone in stress–strain curve follows a linear equation up to a point of elastic limit which is known as elastic zone. The second region is the plateau region, where a large amount of energy absorption takes place and stress–strain curve follows waveform. Finally, there is the densification of structure with small increase in displacement values where the load exponentially increases.

Figures 5, 6, 7, 8, 9, 10, 11 and 12 show deformation patterns of different time steps for all configurations of the structure. It is observed that deformation occurs layer-by-layer and the structures get densified at the end. The primary deformation mechanism of these structures is bending of v-shaped walls. From Fig. 13, it is observed that strength of configuration 6 is highest and of configuration 5 is lowest. Figure 14 shows that configuration 5 has least, and configuration 8 has highest compression modulus. Figure 15 shows SEA that is highest for configuration 4.

Fig. 5 Deformation of configuration 1 structure

Step time 0	Step time1	Step time3	Step time 5
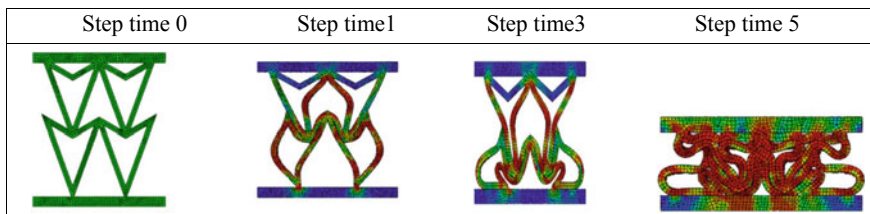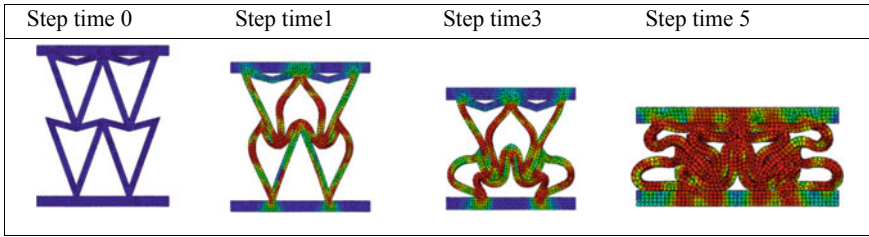
Fig. 6 Deformation of configuration 2 structure

Step time 0	Step time 1	Step time3	Step time5
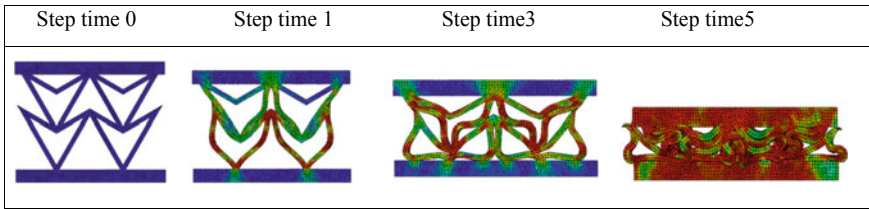
Fig. 7 Deformation of configuration 3 structure

Step time 0	Step time 1	Step time 3	Step time 5
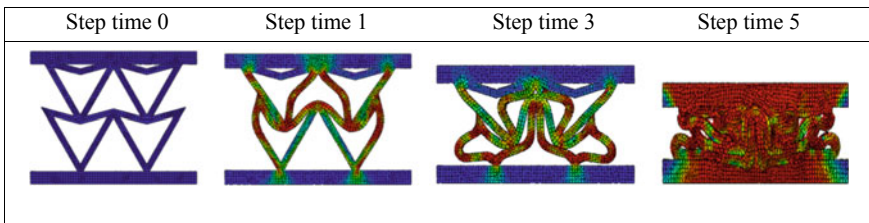
Fig. 8 Deformation of configuration 4 structure

Step time 0	Step time1	Step time 3	Step time 5
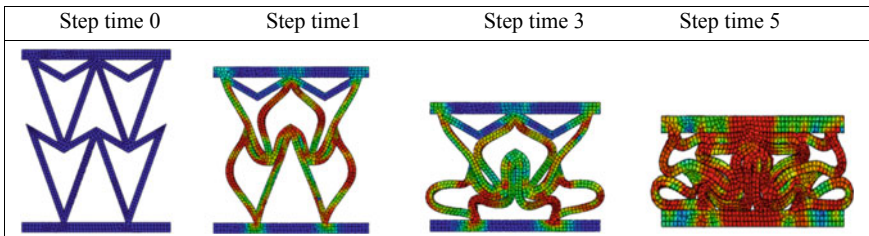
Fig. 9 Deformation of configuration 5 structure
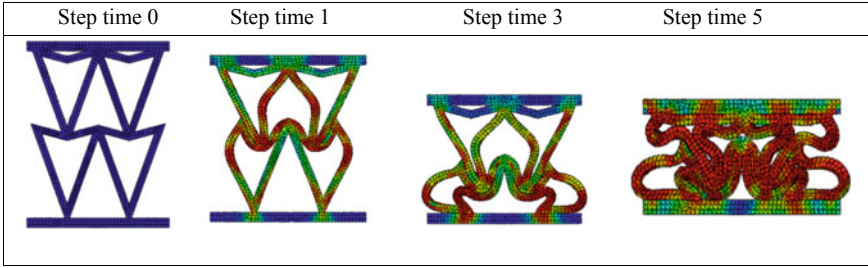
Fig. 10 Deformation of configuration 6 structure
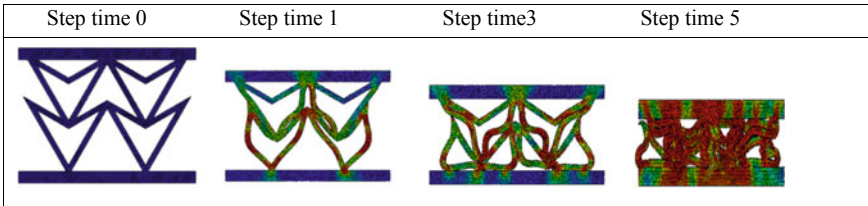
Fig. 11 Deformation of configuration 7 structure
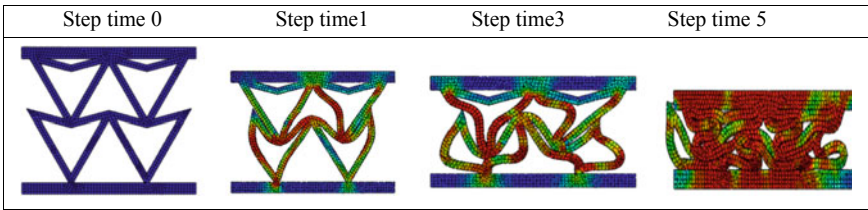
Fig. 12 Deformation of configuration 8 structure

Fig. 13 Values of compressive strength for different configurations
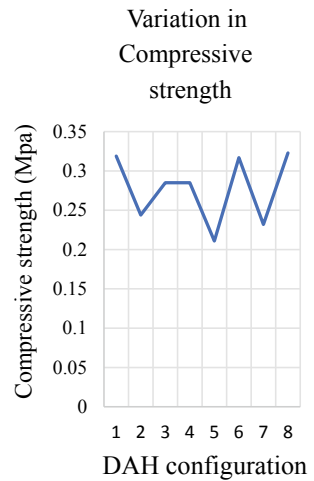
Fig. 14 Values of compressive modulus for different configurations
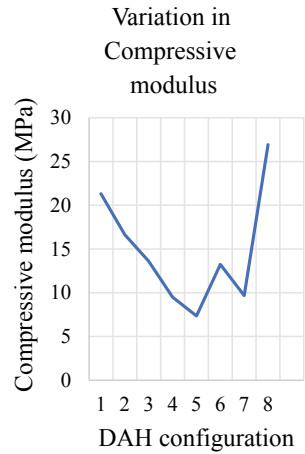
Fig. 15 Values of SEA for different configurations
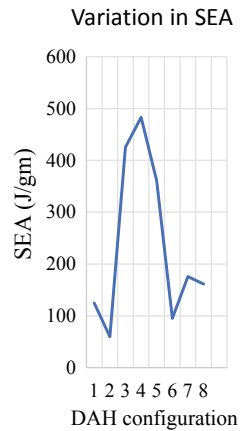
3.1 Effect of First Angle

When first angle increases, effective height slightly increases which leads to rise in strength as shown in Fig. 16 and modulus also slightly increase with increase in first angle [27] from Fig. 17. From Fig. 18, slight decrease of SEA is observed with increase of first angle. When angle is increased, lower struts have to bear more load which results in an early collapse of the structure.

Fig. 16 Plot of first angle versus mean compressive strength

Compressive strength

Fig. 17 Plot of first angle versus mean compressive modulus
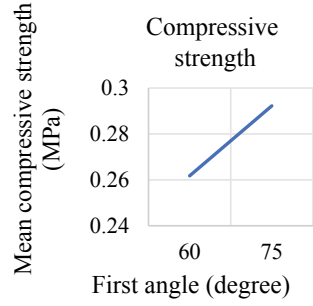
First angle vs Mean Compression modulus
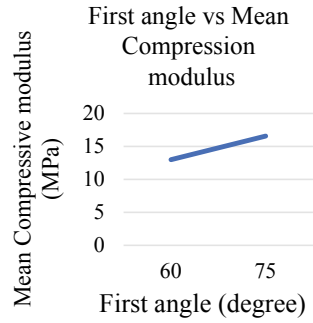
Fig. 18 Plot of first angle versus SEA

First angle vs SEA
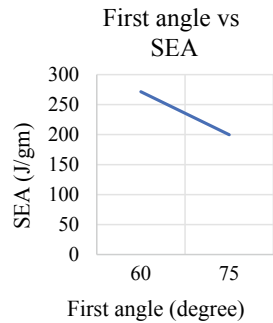
3.2 Effect of Second Angle

Second angle is the most significant parameter for strength, stiffness and SEA. From Fig. 19, it is seen that compressive strength increases with increase in second angle. When the second angle decreases, effective height increases and cell wall almost becomes vertical when compressed, which leads to easy failure of the cellular structure due to buckling. Therefore, when the second angle is increased, it takes time to become vertical which leads to increase of energy absorption. Similar observations are reported in the literature [27]. SEA increases with increase in second angle. So,

Fig. 19 Plot of second angle versus mean compressive strength

Second angle vs Mean Compressive strength

Mean Compressive strength (MPa)

0.282
0.28
0.278
0.276
0.274
0.272
0.27
0.268

20   30

Second angle (degree)
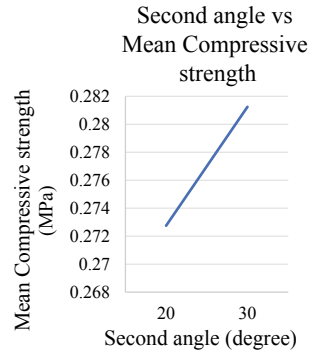
when the second angle increases, the chances to fail due to buckling decrease and stiffness also increases as shown in Figs. 20 and 21. Similar observations are reported in the literature [24].

Fig. 20 Plot of second angle versus mean compressive modulus

Second angle vs Mean Compressive modulus

Mean Compressive modulus (MPa)

15
14.9
14.8
14.7
14.6
14.5
14.4

20   30

Second angle (degree)
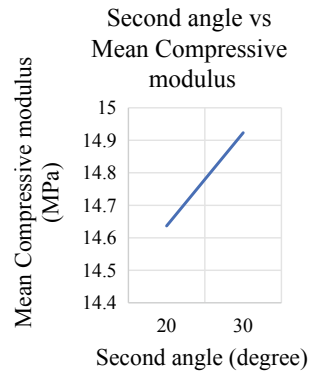
Fig. 21 Plot of second angle versus mean SEA

Second angle vs Mean SEA

Mean SEA (J/gm)

350
300
250
200
150
100
50
0

20   30

Second angle (degree)
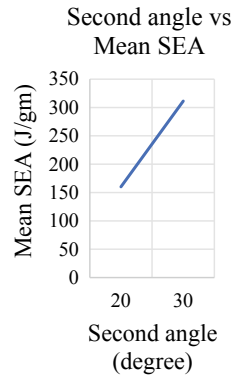
3.3 *Effect of Half-Length*

With decrease in the half-length effective height decreases, which accommodates a greater number of cells for the same size. This leads to increase in stiffness. Figure 22 shows the increment in strength for the decrement in half-length. Figure 23 shows that stiffness decreases with increase of half-length due to increase of cell size. From Fig. 24, it is noticed that SEA also decreases with expansion in half-length. Similar observations are reported in the literature [24].

Fig. 22 Plot of half-length versus mean
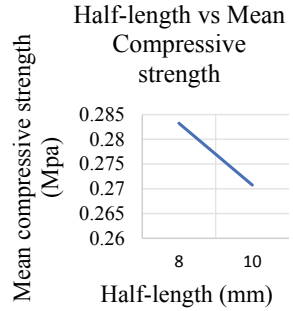
Fig. 23 Plot of half-length versus mean compressive modulus
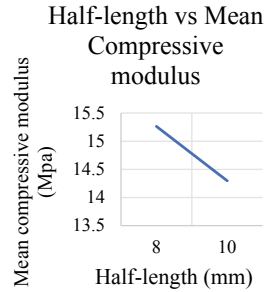
Fig. 24 Plot of half-length versus SEA
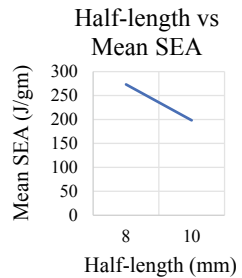
4   Conclusion

In the current study, a numerical investigation is conducted for various configurations of DAH structures under compressive loading. Deformation patterns are observed for all the configurations. Also, influence of geometric parameters (i.e. first angle, second angle and half-length) of structure on responses, namely strength, stiffness and SEA, is studied. It is found that all the geometric parameters are significantly influencing the responses of the structure. Increase in second angle and decrease in half-length lead to increase in all the responses. First angle relatively has a little significance on responses compared to other geometric parameters.

The present study is useful in selecting the best configuration of DAH structure as per the requirement of the application. Future work can be done related to fabrication and validation of the simulation results presented in this study.

References

1. Gibson LJ, Ashby MF (1999) Cellular solids: structure and properties. Cambridge University Press, Cambridge
2. Mardling P, Alderson A, Jordan-Mahy N, Le Maitre CL (2020) The use of auxetic materials in tissue engineering. Biomater Sci 8(8):2074–2083
3. Alderson A, Alderson KL (2007) Auxetic materials. Proc Inst Mech Eng Part G J Aerosp Eng 221(4):565–575. https://doi.org/10.1243/09544100JAERO185
4. Evans KE (1991) Molecular. 353(September):10065
5. Kelkar PU, Kim HS, Cho KH, Kwak JY, Kang CY, Song HC (2020) Cellular auxetic structures for mechanical metamaterials: a review. Sensors (Switzerland) 20(11):1–26. https://doi.org/10.3390/s20113132
6. Mir M, Ali MN, Sami J, Ansari U (2014) Review of mechanics and applications of auxetic structures. In: Advances in materials science and engineering, vol 2014. http://doi.org/10.1155/2014/753496
7. Ma P (2019) A review on auxetic textile structures, their mechanism and properties. J Text Sci Fashion Technol 2(1):1–10. http://doi.org/10.33552/jtsft.2019.02.000526
8. Keskar NR, Chelikowsky JR (1992) Negative Poisson ratios in crystalline SiO_2 from first-principles calculations. Nature 358:222–224
9. Kolken HMA, Zadpoor AA (2017) Auxetic mechanical metamaterials. RSC Adv 7(9):5111–5129. https://doi.org/10.1039/c6ra27333e
10. Zhang J, Lu G, You Z (2020) Large deformation and energy absorption of additively manufactured auxetic materials and structures: a review. Compos Part B Eng 201(July):108340. http://doi.org/10.1016/j.compositesb.2020.108340
11. Scarpa F, Panayiotou P, Tomlinson G (2000) Numerical and experimental uniaxial loading on in-plane auxetic honeycombs. J Strain Anal Eng Des 35(5):383–388. https://doi.org/10.1243/0309324001514152
12. Shepherd T, Winwood K, Venkatraman P, Alderson A, Allen T (2020) Validation of a finite element modeling process for auxetic structures under impact. Phys Status Solidi (B) Basic Res 257(10):1–14. http://doi.org/10.1002/pssb.201900197
13. Alomarah A, Ruan D, Masood S (2018) Tensile properties of an auxetic structure with re-entrant and chiral features—a finite element study. Int J Adv Manuf Technol 99(9):22425–2440
14. Xiao D, Dong Z, Li Y, Wu W, Fang D (2019) Compression behavior of the graded metallic auxetic reentrant honeycomb: experiment and finite element analysis. Mater Sci Eng A 758(April):163–171. https://doi.org/10.1016/j.msea.2019.04.116

15. Qi C, Jiang F, Yu C, Yang S (2019) In-plane crushing response of tetra-chiral honeycombs. Int J Impact Eng 130(April):247–265. https://doi.org/10.1016/j.ijimpeng.2019.04.019
16. Vyavahare S, Kumar S (2020) Re-entrant auxetic structures fabricated by fused deposition modeling: an experimental study of influence of process parameters under compressive loading. Polym Eng Sci 60(12):3183–3196. https://doi.org/10.1002/pen.25546
17. Vyavahare S, Kumar S (2021) Numerical and experimental investigation of FDM fabricated re-entrant auxetic structures of ABS and PLA materials under compressive loading. Rapid Prototyping J. https://doi.org/10.1108/RPJ-10-2019-0271
18. Grima JN, Evans KE (2000) Auxetic behavior from rotating squares. J Mater Sci Lett 19(17):1563–1565. https://doi.org/10.1023/A:1006781224002
19. Grima JN, Farrugia PS, Gatt R, Attard D (2008) On the auxetic properties of rotating rhombi and parallelograms: a preliminary investigation. Phys Status Solidi (B) Basic Res 245(3):521–529. http://doi.org/10.1002/pssb.200777705
20. Larsen UD, Sigmund O, Bouwstra S (1997) Design and fabrication of compliant micro mechanisms and structures with negative Poisson's ratio. Microelectromech Syst 6(2):99–106
21. Qiao J, Chen CQ (2015) Analyses on the in-plane impact resistance of auxetic double arrowhead honeycombs. J Appl Mech Trans ASME 82(5):1–9. https://doi.org/10.1115/1.4030007
22. Wang Y, Wang L, Ma ZD, Wang T (2017) Finite element analysis of a jounce bumper with negative Poisson's ratio structure. Proc Inst Mech Eng C J Mech Eng Sci 231(23):4374–4387. https://doi.org/10.1177/0954406216665415
23. Gao Q, Wang L, Zhou Z, Ma ZD, Wang C, Wang Y (2018) Theoretical, numerical, and experimental analysis of three-dimensional double-V honeycomb. Mater Des 139:380–391
24. Gao Q, Ge C, Zhuang W, Wang L, Ma Z (2019) Crashworthiness analysis of double-arrowed auxetic structure under axial impact loading. Mater Des 161:22–34. https://doi.org/10.1016/j.matdes.2018.11.013
25. Gao Q, Liao WH, Wang L (2020) On the low-velocity impact responses of auxetic double arrowed honeycomb. Aerosp Sci Technol 98:105698
26. Zhao X, Gao Q, Wang L, Yu Q, Ma ZD (2018) Dynamic crushing of double-arrowed auxetic structure under impact loading. 160:527–537. https://doi.org/10.1016/j.matdes.2018.09.041
27. Wang XT, Wang B, Wen ZH, Ma L (2018) Fabrication and mechanical properties of CFRP composite three-dimensional double arrowhead auxetic structures. Compos Sci Technol 164(May):92–102. https://doi.org/10.1016/j.compscitech.2018.05.014
28. Standard test method for flatwise compressive properties of sandwich cores 1 (2003). Current i:2–4. http://doi.org/10.1520/C0365
29. Raeisi S, Tapkir P, Ansari F, Tovar A (2019) Design of a hybrid honeycomb unit cell with enhanced in-plane mechanical properties. SAE technical paper 2019-01-0710. http://doi.org/10.4271/2019-01-0710

Simulation Study on Effect of Drill Tool Geometry on Strength and Deformation

Sehjad J. Memon, Poojan V. Fuletra, Nilay K. Degadwala, Chandresh B. Kumbhani, and Rahul Sinha

1 Introduction

Drilling is the most commonly used process for making holes with ease. Drilling is the process of making holes in hard material with drill tool made from harder material than the workpiece. Drill bit is a multi-point cutting tool with two edges often more than two.

In drilling, drill bit set against to work piece vertically and pressed down to the work piece with rotating speed of thousands of RPM.

There are mainly two types of drill for metal drilling:

1. Parallel shank
2. Taper shank.

Parallel shank drill bit generally is made in range of 1–14 mm diameter. Above this range, all the drill bit is made tapper shank drills. As per user specification, drill bit can vary in different specifications.

A feature of metal drill bit is their tip angle and helix angel, which is necessary to ensure the drilling action through the metal. Drill bit have a tip with an angle of 118° [1]. For drilling in hard metals like stainless steel, these have a slightly flatter tip angle of 135° for good centering when you start drilling action. Optimum helix angle value is about 25° [2].

While drilling into hard material, RPM of drill bit should be less to get fine cut; otherwise, drill bit will be damaged.

For handheld drilling, the most important factors are speed and precision. It must also be light and strong so as to avoid any fatigue of operator. Decisive factors in drilling are feed force, cutting speed, and speed.

S. J. Memon (✉) · P. V. Fuletra · N. K. Degadwala · C. B. Kumbhani · R. Sinha
School of Engineering, P P Savani University, Surat, Gujarat, India

2   Material

Selection of material for a drill bit is as important as the selection of proper parameters of drill bit such as helix angle, point angle, and diameter. One of the most commonly used materials to manufacture drill bit is high-speed steel (HSS). HSS has very high Rockwell hardness above 60 HR. There are various types of HSS material. It contains various materials such as tungsten, molybdenum, chromium, vanadium, and cobalt. Tungsten carbide has relatively high hardness than all the other material and manufactured with use of powder metallurgy. Tungsten carbide drill are more durable than other. The SS drill bit shown here is most commonly used in surgical uses [3]. It has anti-corrosive properties with high hardness.

The selected drill bit material is based on their usage in industries and their versatility (Table 1).

2.1   Input Parameters

Simulation of drill bit was carried out on ANSYS workbench under analysis system "Static Structural." The various parameters used to create drill on SOLIDWORKS are shown in Table 2.

1. Diameter
2. Point angle
3. Helix angle.

Table 1   Various materials properties [4]

	Name	Density (kg m^3)	Young's modulus (MPa)	Poisson ratio
M1	AISI type M2 HSS	8140	207,000	0.29
M2	Tungsten carbide	15,630	53,000	0.31
M3	Drill bit HSS	8150	230,000	0.3
M4	Drill bit SS	8000	137,000	0.3

Table 2   Various drill parameters

Diameter (mm)	Point angle	Helix angle
10	118°	25°
12	120°	32°
14	135°	35°

3   Methods

Step 1: To Create 3D model of drill bit on SOLIDWORKS modelling software as per the measurement (Fig. 1).

Step 2: Open ANSYS Workbench 2021 R1 and import the 3D model. Enter the details of all four material in the engineering data of ANSYS Workbench 2021 R1.

Step 3: Performing Simulation of the drills on ANSYS Workbench 2021 R1 in Analysis system named "Static Structural". This simulation was carried out for Deformation, Equivalent Stress and Equivalent Strain. To perform analysis, value of torque is required. Value of Torque was obtained from references [5, 6].

Step 4: In any CAE simulation there are three main important factors: Pre-Processing, Solving, Post-Processing. Meshing is a part of Pre-Processing; it has a capability to reduce the amount of time and effort to get accurate results if done right.

After importing the 3D model and defining materials for the drill bit, meshing was carried out. Taking the size of element as 1 mm for every drill bit, there is a variation in number of nodes and number of elements for every drill bit.

Number of nodes: 17,104–31,780.

Number of elements: 9037–17,323.

Step 5: After the meshing, add the parameters in the static structural such as fixed support to keep the workpiece fixed at its position and apply moment, then solve the problem (Figs. 2, 3, 4, 5, 6, 7, 8, 9, 10, 11, 12, 13, 14, 15 and 16).
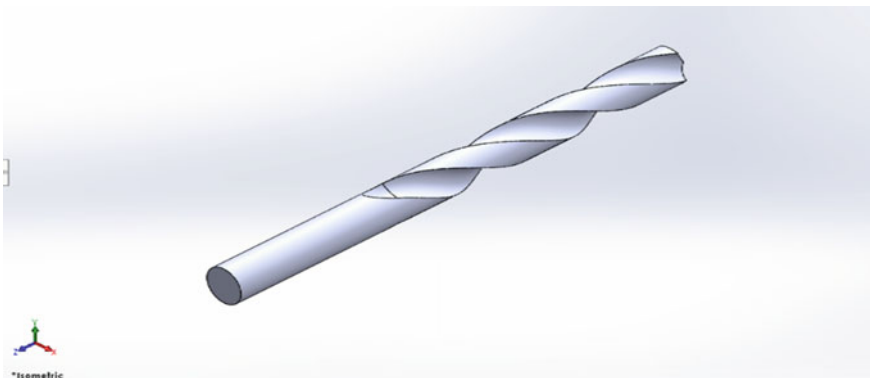
Fig. 1   Isometric view of drill bit

Fig. 2 Drill bit meshing on ANSYS
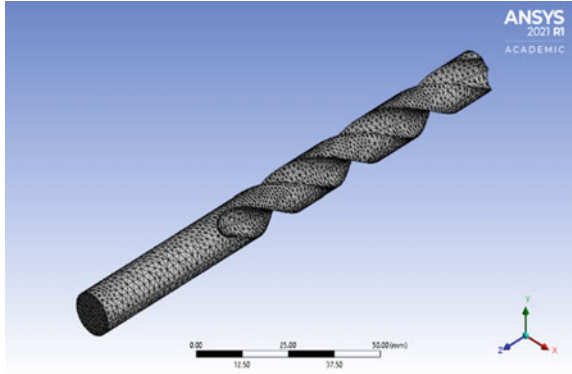
Fig. 3 Application of moment on drill bit
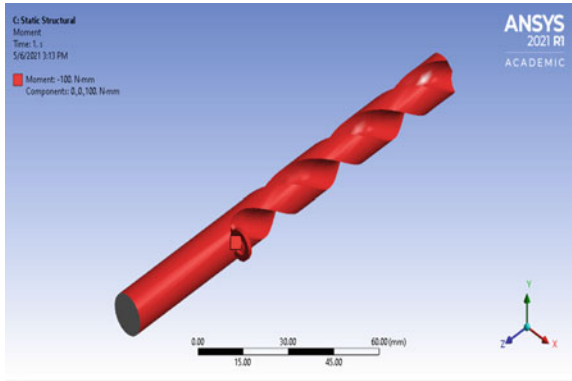
Fig. 4 Application of fixed-support on drill bit
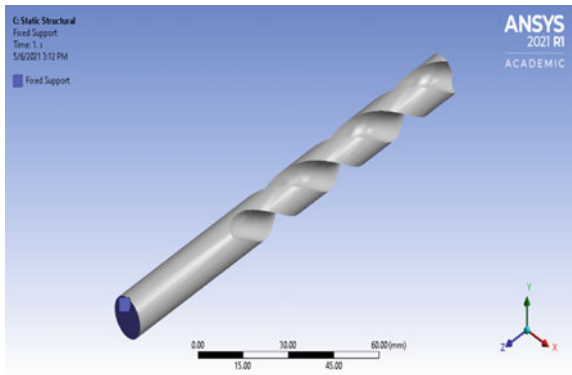
Fig. 5 Deformation in drill bit (M2)
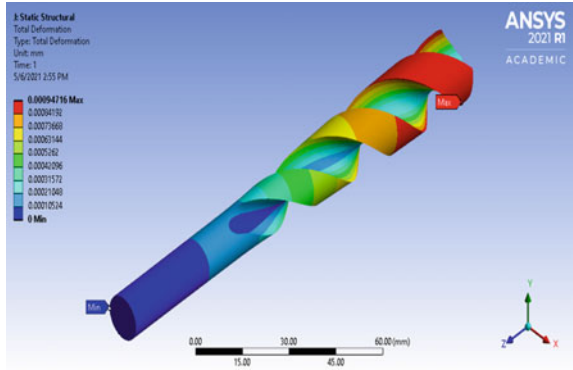
Fig. 6 Equivalent stress on drill bit (M2)
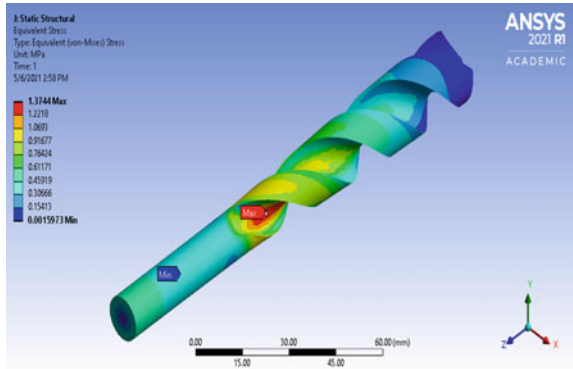
Fig. 7 Equivalent strain on drill bit (M2)
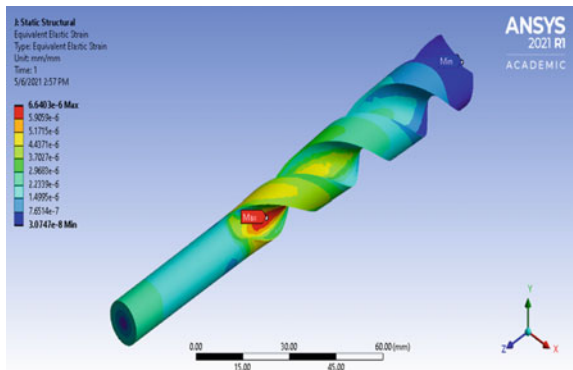
Fig. 8 Deformation in drill bit (TC)
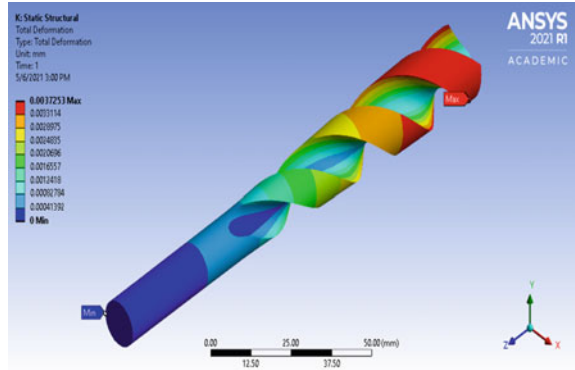
Fig. 9 Equivalent stress on drill bit (TC)
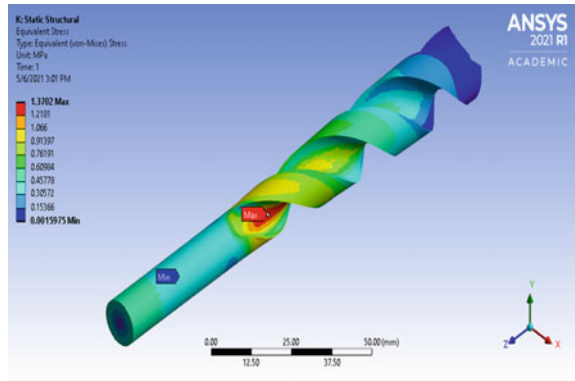
Fig. 10 Equivalent strain on drill bit (TC)
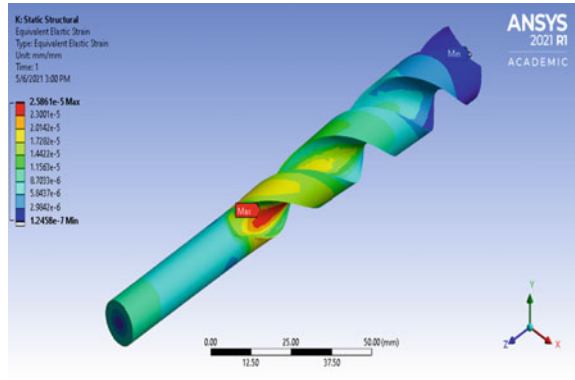
Fig. 11 Deformation in drill bit (HSS)
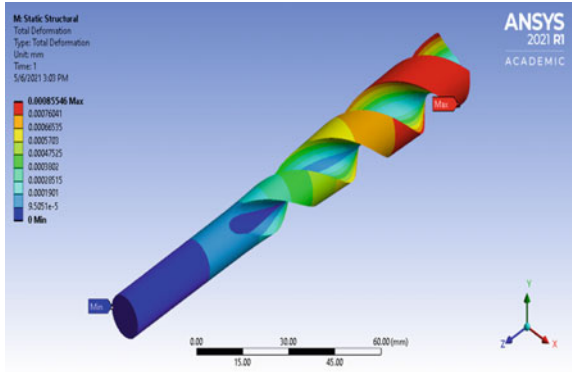
Fig. 12 Equivalent stress on drill bit (HSS)
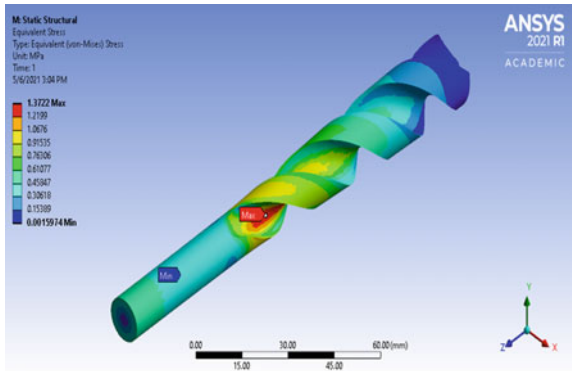
Fig. 13 Equivalent strain on drill bit (HSS)
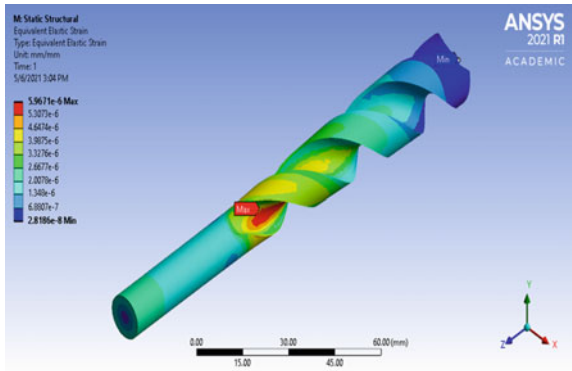
Fig. 14 Deformation in drill bit (SS)
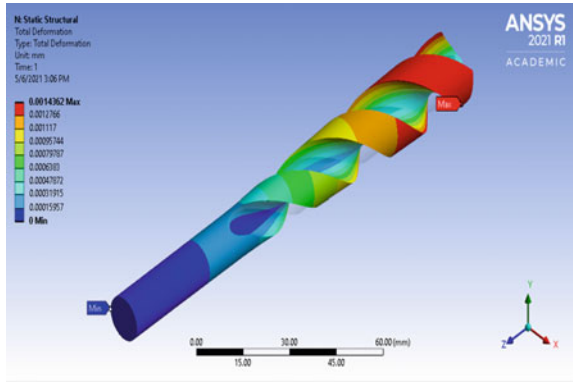
Fig. 15 Equivalent stress on drill bit (SS)
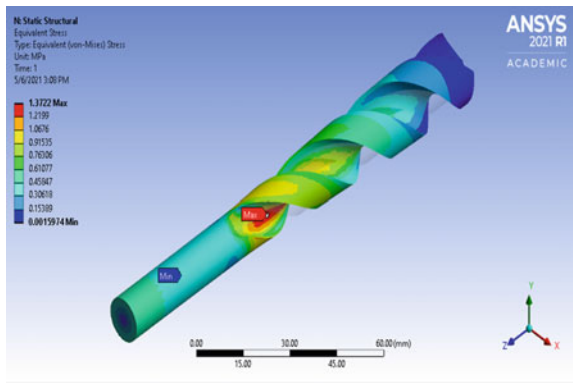
Fig. 16 Equivalent strain on drill bit (SS)
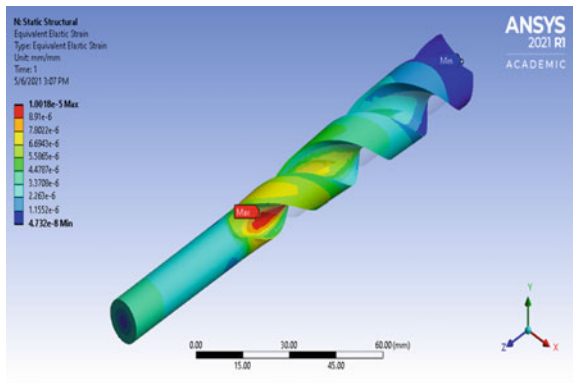
4 Results

4.1 Effect of Helix Angle on Stress Formation on Drill Bits

Helix angle has a huge effect on the cutting efficiency of the drill bits. Higher the helix angle, lesser the cross-section area. The drill bits with higher helix angle are used on softer materials and have high feed rate and low cutting speeds. They are used foe softer materials because the stress acting on the drills with higher helix angle is more, and also, with having less cross-section area, the possibility of a failure is less under softer nonferrous materials (Fig. 17) [7, 8].

For general purpose drill bit, the helix angle falls between 20° and 32°. For this experiment, consideration can be made for two helix angles that are 25° and 32°. Results generated are also quite similar per shown in the graph.
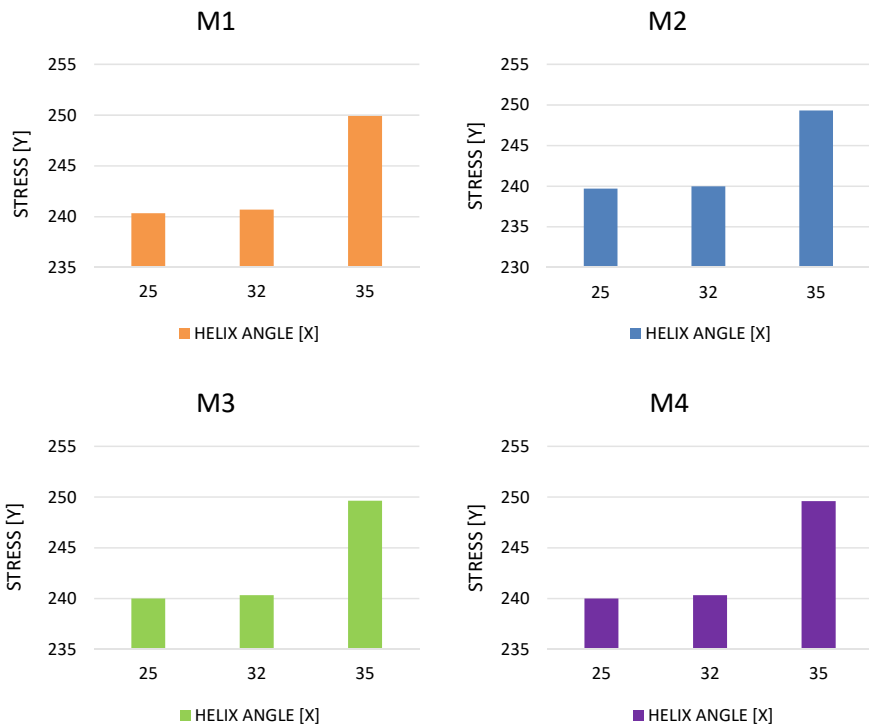
Fig. 17 Graph of helix angle versus equivalent (Von-misses) stress

4.2   Effect of Diameter on Stress Formation on Drill Bits

The stress formation on drills with different diameter is shown in the graph above as known smaller drill can operate at faster RPM compared to the larger drill. While drilling larger holes are needed to reduce the speed; while drilling, the center of the drill is travelling shorter path than the outside, and the outside edge is the most important part of the drill bit (Fig. 18).

In case of larger drill bits, the center of the drill is travelling slower than the outer edge, so the direct drilling of the large holes is not preferred. The correct procedure is to drill the hole with a small drill first and then re-drill it with the large drill, which will reduce the influence of the center of the drill.

Smaller drills working at higher RPM will be having more formation of stress on its surface comparatively with the larger drills as per shown in the graphs.
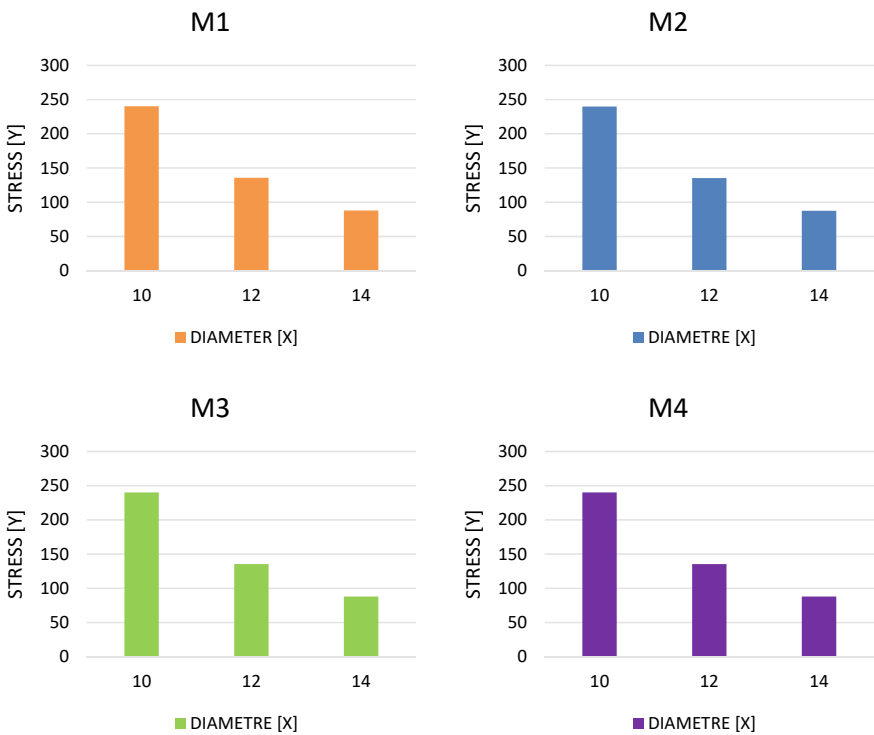
Fig. 18 Graph of diameter versus equivalent (Von-misses) stress
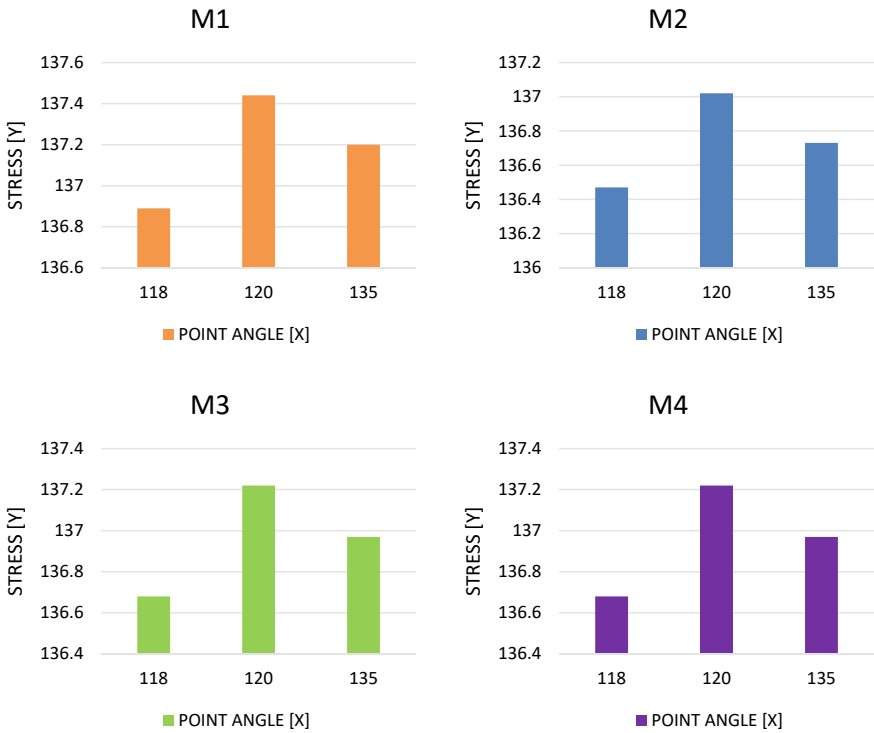
Fig. 19 Graph of point angle versus equivalent (Von-misses) stress

4.3 Effect of Point Angle on Stress Formation on Drill Bits

Drill with 135° point angle is flatter than the one with 118° so more of its cutting edge will be in contact with the materials surface sooner and will begin the process faster. Stress formation on all the above angles is quite similar to each other with a very minor difference (Fig. 19).

Stress formation on drill with the point angle of 120° is little more than both 118° and 135°.

4.4 Effect of Helix Angle on Deformation of Drill Bits

For total deformation by comparing the four different materials that are taken for the simulation. This has been seen that the deformation for the Graph M1 and M3 is quite less than that of the other two material. M1 Graph is AISI Type M2 molybdenum high-speed tool steel and M3 is drill bit HSS. Both of this materials are a type of HSS
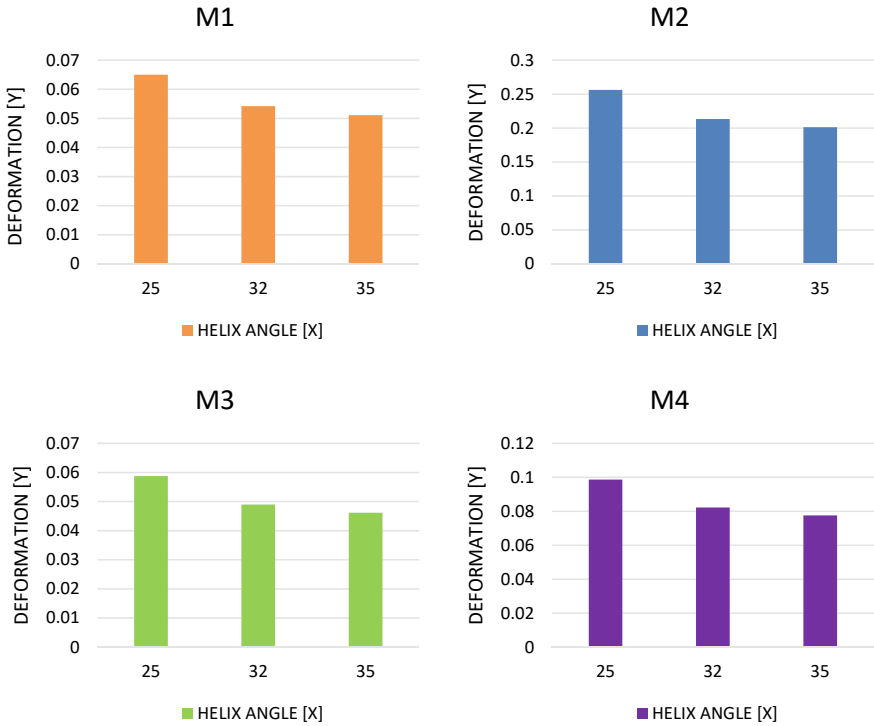
Fig. 20 Graph of helix angle versus total deformation

which is the most common material which is used to manufacture drill bit (Fig. 20) [9].

M2 Graph which is for tungsten carbide, tungsten is also found in the composition of HSS, but combining tungsten with carbide steel makes it harder, which enables drill to machined harder materials.

While drilling with TC drill bits makes it easy to drill hard materials, it is prone to most deformation compare to other three material.

As increasing the helix angle the deformation decreases.

4.5 Effect of Diameter on Deformation of Drill Bits

This result is also similar to that of the previously taken drills with helix angle of about 32° and point angle of about 118°. As there is an increase in the value of diameter, there is a decrease in the deformation (Fig. 21).
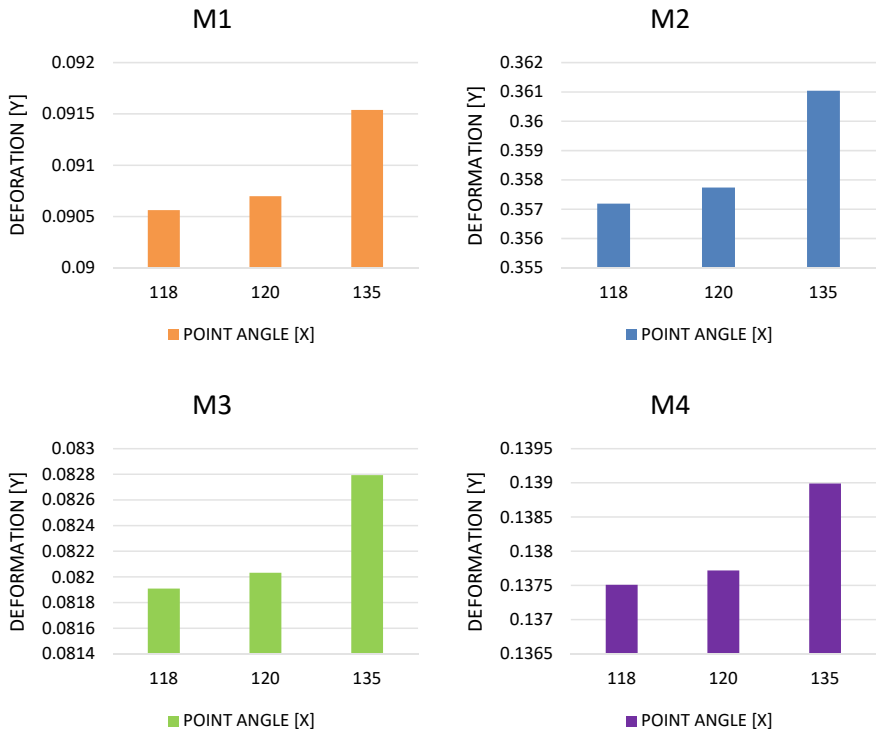
Fig. 21 Graph of diameter versus total deformation

4.6 Effect of Point Angle on Deformation of Drill Bits

In case of point angle, the deformation for drill bits with point angle 118° and 120° is lower than the one with point angle 135° (Fig. 22) [10, 11].

5 Conclusion

This study shows that the commonly used drilling tool was analyzed with the help of ANSYS software. The main objective of this research was to know about the stress formation, deformation acting on the various types of drill bit by changing various parameters describe above. By performing 108 simulations on drill bit of various parameters such as diameter, helix angle, and point angle and made up of four different materials named above on ANSYS 2021 R1. Following conclusion can be made from results generated by compiling all the simulation carried out with different variation:
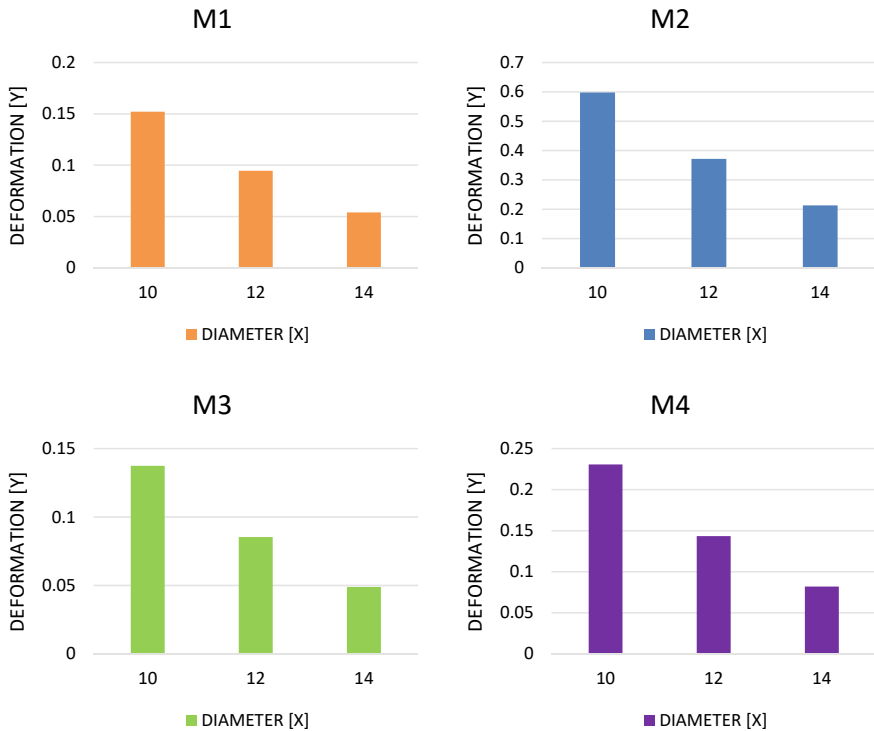
Fig. 22 Graph of point angle versus total deformation

1. By increasing the helix angle, there is an increase in stress formation on the drill bit.
2. By increasing the diameter, there is a decrease in stress formation on the drill bit.
3. That initially, as increasing the point angle the stress formation on drill bit increases, but it starts to decrease after 120°.
4. By increasing the helix angle, there is a decrease in deformation of drill bit, but value of deformation differs from material to material for M1, M3, and M4; the value of deformation is less than 0.1 mm, and for M2 material, it exceeds up to 0.25 mm (Diameter = 10 mm, Point angle = 120°).
5. By increasing the diameter, there is a decrease in deformation of drill bit, but this value differs for every material. It is maximum for M2 material.
6. By increasing the point angle, there is an increase in the value of deformation.

References

1. Dixit PK, Titariya VK (2018) Modeling and simulation of the drilling cutter by using finite element method. Int J Sci Res Dev 5(12):71–76
2. Hariharan G, Moorthi NSV, Senthilkumar N (2015) A numerical simulation study on drill bit point angle and helix angle during drilling AISI 1045 steel. In: Proceedings of ICAME-2015, UCEV, Villupuram, Tamil Nadu, 15–16 Oct 2015
3. Hassanalideh HH, Gholampour S (2020) Finding the optimal drill bit material and proper drilling condition for utilization in the programming of robot-assisted drilling of bone. CIRP J Manuf Sci Technol. https://doi.org/10.1016/j.cirpj.2020.09.011
4. Srinivas V (2018) Design and analysis of drill with various materials using ANSYS. J Eng Appl Sci. http://doi.org/10.36478/jeasci.2018.5218.5221
5. Shivani DL, Yadav A (2019) Modelling and analysis of drill bit with different materials. Int Res J Eng Technol (IRJET) 6(8):194–199
6. Yıldız A, Kurt A, Yağmur S (2020) Finite element simulation of drilling operation and theoretical analysis of drill stresses with the deform-3D. Simul Model Pract Theor. https://doi.org/10.1016/j.simpat.2020.102153
7. Reddy GM, Reddy DP, Jagadeesh K, Sai M, Rao YVH (2019) Finite element stress analysis of drill bit in ANSYS. Int J Innov Technol Exploring Eng (IJITEE) 8(7):463–467
8. Pryhorovska T, Pryhorovskyi O (2020) Finite-element simulation of PDC drill bit's operational stress-strain state. Sci J Ternopil National Tech Univ. http://doi.org/10.33108/visnyk_tntu
9. Selvam SM, Sujatha C (1995) Twist drill deformation and optimum drill geometry. Comput Struct. https://doi.org/10.1016/0045-7949(94)00615-A
10. Heisel U, Pfeifroth T (2012) Influence of point angle on drill hole quality and machining forces when drilling CFRP. Procedia CIRP. https://doi.org/10.1016/j.procir.2012.04.084
11. Feito N, Díaz-Álvarez J, Díaz-Álvarez A, Cantero JL, Miguélez MH (2014) Experimental analysis of the influence of drill point angle and wear on the drilling of woven CFRPs. Materials. https://doi.org/10.3390/ma7064258

Numerical Modeling of Die-sinking EDM for Evaluation of Material Removal Rate and Surface Roughness

B. M. Barua, S. Chang, E. Shylla, V. S. Chauhan, P. Kumar, M. Rahang, and D. K. Sarma

1 Introduction

Various non-conventional material removal methods are progressively employed for manufacturing complex parts and components of different machines. Among all the non-conventional approaches for material removal, electrical discharge machining (EDM) has accentuated many researchers due of its wide range of industrial applications [1]. The phenomenon in EDM process takes place through periodic discharge between the electrode pairs which remain dipped into a dielectric medium [2]. Between these electrodes, a small discharge zone is created where electrical energy of the sparks is transformed into intense heating which leads to melting, vaporization and incineration of the substrate material. Workpiece material that gets removed which is in the form of lumped powders is flushed away with the help of dielectric medium forced into the machining area [3]. For this study, nickel silver Grade 55-18 (composition: copper—55%, zinc—27% and nickel—18%) also known as German silver has been considered because of certain properties like high electrical resistance, high conductivity, high corrosion resistance. Owing to its good mechanical properties, it is extensively used for making keys, plumbing fixtures and marine fittings. Because of its higher values of electrical conductivity, nickel silver is mostly used in heating coils, electrically conductive railway tracks and electrical part components such as electromagnetic shielding [4, 5]. Study of EDM process has been carried out by many researchers through three well-known approaches, i.e.,

B. M. Barua (✉) · S. Chang · E. Shylla · V. S. Chauhan · P. Kumar · M. Rahang · D. K. Sarma
Department of Mechanical Engineering, National Institute of Technology Meghalaya, Shillong
793003, India
e-mail: bhargabmadhab@nitm.ac.in

M. Rahang
e-mail: maneswar_rahang@nitm.ac.in

D. K. Sarma
e-mail: dksarma@nitm.ac.in

experimental, analytical and numerical approaches. The first model of numerical simulation proposed by Erdenet and Kaftanoglu [6] used one-dimensional thermal models. Later for more expounded approaches, two-dimensional heat transfer models were utilized. Van Dijik and Dutre [7] developed a heat flow model with constant heat source for both semi-infinite and finite bodies. Beck [8] reported an approach in which they explored the study for a continuous heat source over a semi-infinite domain and also domain with insulated conditions having cylindrical-shaped area. Di Bitonto et al. [9] established a study on heat transfer in a spherical symmetry with cathode erosion model. They found that the predicted results are close to that of the experimental results, and this model became the benchmark for EDM numerical model which is still used by many researchers. Marafona and Chousal [10] used FEM analysis to develop an electro-thermal model in which Joule heating effect has been considered, and the quantity material removed per discharge pulse was related to that of the experimental data as reported by Di Bitonto et al. [9]. Joshi and Pande [11] developed a model with thermo-physical properties where analysis of single spark has been carried out in an axisymmetric continuum with Gaussian heat source. Also, investigational studies were performed to acquire the MRR and crater shape, and it was found that the predicted results from the numerical analysis are nearer to that of the experimental outcomes. Kansal et al. [12] suggested a model in which they also considered heat source of Gaussian distribution with constant spark radius. Singh and Puri [13] reported a work in which they developed a two-dimensional cross-sectional model for single spark. They found the height and diameter of the crater formed from the finite element simulation. Krishna Kiran along with Joshi [14] established a theoretic model in which they considered a cavity with single discharge to predict the surface roughness. Salonitis et al. [15] presented a work in which they developed a theoretical model to anticipate MRR and the R_a from the single discharge carter generation. Razeghiyadaki et al. [16] developed a model considering two-dimensional heat conduction through an axisymmetric rectangular domain. Their studies predicted the different values of MRR and R_a. From the previous works, it has been found that comparison of numerical analysis with experimental results is made for material removal rate (MRR). But, few researchers have reported the calculation of surface roughness (R_a) from the numerical analysis. So, in this study, an effort has been made to analyze the material removal mechanism of nickel silver Grade 55-18 through temperature distribution along with the calculation of R_a.

2 Modeling Process for EDM Operation

The modeling method of the die-sinking EDM operation for thermal analysis depends on several process such as conduction, convection, the fraction of energy, thermal properties of nickel silver, Gaussian type of heat flux and the plasma channel radius. COMSOL Multiphysics version 5.5, which is a commercial FEA software, has been utilized to develop and study the heat transfer in die-sinking EDM process. For the

ease of analysis, two-dimensional model has been considered. The prediction of MRR has been evaluated using a discharge of single pulse over the upper surface of the workpiece with cylindrical shape.

2.1 Assumptions

To simplify the study of the model, the following assumptions are made:

1. The means of heat transfer to the workpiece from the plasma is assumed to be through conduction up to spark radius beyond that the heat transfer is contemplated through convection.
2. The material of the workpiece is isotropic and homogeneous.
3. The Gaussian heat flux distribution is considered over certain part of the domain for conduction.
4. Radius of the spark produced is considered to be a function which is dependent upon the two parameters which are discharge current and pulse on time.
5. The region for spark influence is considered to be of axisymmetric nature.
6. The whole analysis is accomplished for a single discharge.
7. The efficiency of flushing is perpended to be 100%; i.e., there will be no deposition of tool material over the workpiece or formation of recast layer.
8. The room temperature is ascertained as the initial temperature for the whole domain.

2.2 Governing Equation

Fourier equation for heat conduction is considered for thermal analysis of die-sinking EDM process in 2D cylindrical Cartesian coordinate system, which is represented by Eq. (1)

$$\rho C_p \frac{\partial T}{\partial t} = \left[\frac{1}{r} \frac{\partial}{\partial r} \left(Kr \frac{\partial T}{\partial r} \right) + \frac{\partial}{\partial z} \left(K \frac{\partial T}{\partial z} \right) \right] \tag{1}$$

where ρ refers the density, C_p refers the specific heat, T refers the temperature, t refers the time, K refers the thermal conductivity of the material used as workpiece, while r and z refer the coordinate axis displayed in Fig. 1.

2.3 Boundary Conditions

An axisymmetric domain of the workpiece is selected which is positioned to be symmetric about the z direction of the axis. In this domain, Gaussian heat flux is

Fig. 1 Model of heat
transfer with all the required
boundary conditions
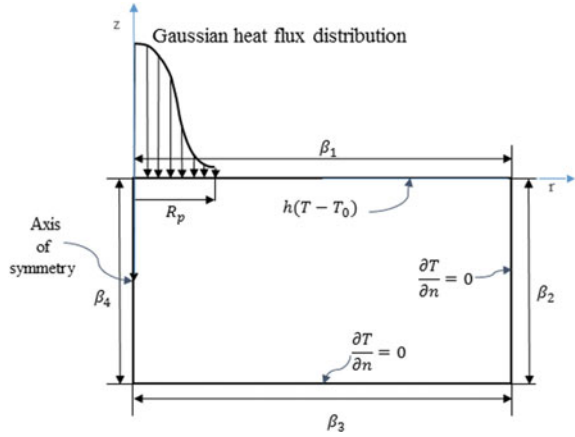
adapted over the surface β_1 for a single spark up to the spark radius R_p, beyond that
the radius of spark convection heat transfer acts over the surface β_1. This is because
of the presence of dielectric fluid, a cooling effect presides over the surface β_1. As
the boundaries referred to as β_2 and β_3 are far away from R_p and also the pulse on
time is very less, so heat transfer is assumed to be zero for these two surfaces. For the
boundary β_4, it is considered to be symmetry, so here, the heat transfer is considered
to be zero. The boundary conditions acting over the domain are illustrated in Fig. 1.

Summarized boundary conditions are given as:

1. For boundary β_1:

   (a) Till the radius of spark R_p:

$$K\frac{\partial T}{\partial z} = q(r) \tag{2}$$

   where $q(r)$ represents the heat flux produced as a result of spark.

   (b) Beyond the radius of spark R_p:

$$K\frac{\partial T}{\partial z} = h(T - T_0) \tag{3}$$

   where h refers the heat transfer coefficient between the dielectric and the
   workpiece, T refers the temperature, and T_0 refers the initial temperature.

2. For boundaries β_2, β_3 and β_4

$$\frac{\partial T}{\partial n} = 0 \tag{4}$$

   where n refers the normal vector.

2.4   Heat Source

Various types of heat source modeling have been proposed by different researchers. As for calculation of MRR and SR, heat source plays an important role. Van Dijik et al. and Beck et al. considered uniform disk-like heat source, while Di Bitonto et al. suggested point heat source. Taking the above two condition into account for temperature measurement of plasma channel, it has been found that ununiformed temperature distribution takes place in the plasma channel. To curb this problem, many researchers [1, 11, 16, 17] have proposed Gaussian distribution of heat source, as it turns out to be more convincing heat source model. In this study, a Gaussian distribution heat source model has been considered, and the mathematical representation of heat flux is given by Eq. (5)

$$q(r) = q_0 \exp\left(-4.5 \times \frac{r^2}{R_p^2}\right) \tag{5}$$

where q_0 refers the maximum heat flux at radius $r = 0$ and is indicated by Eq. (6)

$$q_0 = \frac{4.55 F_c V I}{\pi R_p^2} \tag{6}$$

where F_c refers the fraction of total energy transferred to the workpiece, V refers the discharge voltage in Volts, I refers the discharge current in Ampere, and R_p refers the spark radius in μm. The unit of q_0 is W/m^2.

2.5   Spark Radius

Experimentally, the measurement of the spark radius is a very difficult process as the spark is considered for a very less duration, i.e., in order of few millisecond. Many researchers proposed different types of approaches, some considered it as a function of time, and others considered as a function of time and current [11]. Dibitonto et al. [9] considered R_p in fundamental form for pulses of rectangular type. Ikai et al. [18] successfully derived a semi-empirical equation of R_p which is called "equivalent heat input radius", and this equation is a dependent function of pulse on time (t_{on}) and discharge current (I). Many researchers working in the field of EDM simulation used the equation derived by Ikai et al. [18]. For the current study, the equation used by Razeghiyadaki et al. [16] which is based on the equation of Ikai et al. [18] has been used and is given by Eq. (7). Analogized with other approaches, this equation is found to be much pragmatic.

$$R_p = 2.04 \times I^{0.43} \times t_{on}^{0.44} \tag{7}$$

3   Establishment of the Model

Single spark generation in EDM involves interaction of various physical phenomenon which makes it a very intricate thermal process. For simulation of temperature distribution and change in the workpiece dimensions, finite element method (FEM) needs to be implemented. Different researchers have utilized different types of analytic tools for FEM modeling and simulation. In this work, COMSOL Multiphysics has been used, as this software has large number of finite element competencies, ranging from static to time-dependent studies, analysis in the field of heat transfer, fluidics, electromagnetics, acoustics, structural dynamics, etc. The work geometry has been created with dimensions 200 μm × 200 μm using all the necessary boundary conditions. As single spark is considered and the spark duration is also very less, so the small-size domain is selected. Mesh with triangular domain was generated, and for better accuracy, smaller elements were selected over the conduction heat transfer area.

The following steps outline the process undertaken for modeling and simulation of EDM process:

Step 1: Aim: The main aim of this study is to determine the change in temperature distribution throughout the work model in EDM process.
Step 2: Analytic tool selection: COMSOL Multiphysics version 5.5.
Step 3: Model selection and application: Selection of 2D space dimension; physics selection (heat transfer in solids); study selection (time dependent); define parameters (current, voltage, fraction of energy, pulse on time, etc.); define variables; define function; geometry modeling; selection of material; heat transfer boundary conditions selection; selection of mesh and finally simulation by selecting the compute button under study.

The simulation is computed over complete mesh of 25,264 domain elements with 414 boundary elements. About 50,943 degrees of freedom (DOF) is solved with 26,097 internal DOF.

The properties of German silver and the input parameters to model the process of material removal in die-sinking EDM are exhibited in Tables 1 and 2, respectively.

Table 1 Material properties of German silver

Property	Unit	Values
Density	kg/m^3	8700
Thermal conductivity (@20 °C)	W/m-K	29
Poisson's ratio		0.34
Elastic modulus	MPa	117
Melting point	°C	1085
Heat capacity at constant pressure	J/kg-K	380

Table 2 Input parameters

Parameters	Unit	Values
Current	Ampere (A)	10, 15, 20, 25
Voltage	Voltage (V)	40
Pulse on time (t_{on})	Microseconds (µs)	100
Pulse of time (t_{off})	Microseconds (µs)	20
Fraction of energy		0.183

4 Results and Discussion of Simulation

From the simulation, it has been found that with the variation of discharge current, the temperature distribution also varies. For a single spark with different values of current impacts the formation of crater. The formation of craters and distribution of temperature for particular values of current have been presented in Fig. 2.

4.1 Effect of Current on MRR

Figure 3 displays the variation of MRR with increment in the values of current, while keeping the values of voltage and pulse on time as constant. The main concept behind the rise in the value of MRR is that with the accretion in the values of current, the concentration of heat surges and more quantity of heat gets transferred into the

(a) For 10 A current   (b) For 15 A current

(c) For 20 A current   (d) For 25 A current
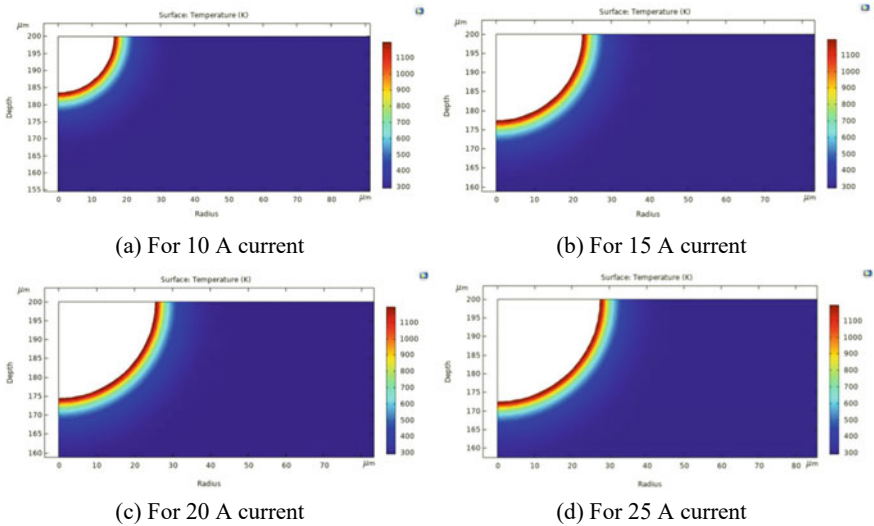
Fig. 2 Variation in crater depth and crater radius with variation in current

Fig. 3 Transition in MRR with current
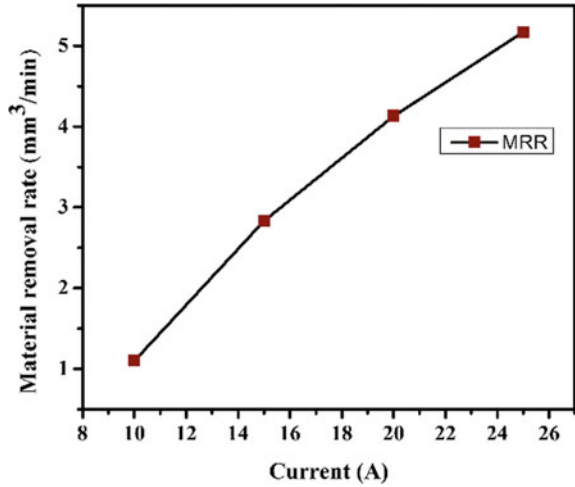
surface of the workpiece, and thus, the rate of melting and evaporation increases [17]. The shape or contour of the crater can be estimated by eliminating the components or elements having larger values of melting point temperature. Many researchers have reported how to find the crater geometry, and Dibitonto et al. [9] reported from their study that the crater shape has been numerically anticipated to be hemispherical, while Salonitis et al. [15] proposed that crater shape is to be circular paraboloid. In this study, the crater geometry is selected as of circular paraboloid in nature. The calculation of crater volume (V_c) in mm^3 can be computed when the values of radius and depth of the crater formed are familiar, and the volume of carter is given by Eq. (8) [15]

$$V_c = \frac{1}{2}\pi h r_c^2 \tag{8}$$

where h refers the depth and r_c refers the radius of crater in millimeters (mm).

The material removal rate calculation has also been studied by many researchers [11, 16, 19]. The formula for MRR calculation has been selected as stated by Razeghiyadaki et al. [16] which is given by Eq. (9)

$$MRR = \frac{60 V_c}{t_{on} + t_{off}} \tag{9}$$

4.2   Effect of Current on Surface Roughness

The R_a also depends upon the heat induced into the surface of the workpiece with the surge in discharge current. The observations from Fig. 4 indicate that with the surge in current, the surface roughness also surges. For the calculation of surface roughness, an empirical equation has been reported by Salonitis et al. [15] which has been utilized by researchers [19]. In this present study, the equation suggested by Salonitis et al. [15] has been used which is given by Eq. (10)

$$R_a = \frac{1}{4}\left(1 + \frac{R_p}{r_c}\right)^2 h \tag{10}$$

Based on the results obtained from FEM analysis, it can be observed form Fig. 3 that the R_a tends to increase in a straight path with the increase in the load of current. While from Fig. 4, it can be perceived that surface roughness inclines in a parabolic path with the surge in current (Table 3).

Fig. 4 Transition in R_a with current
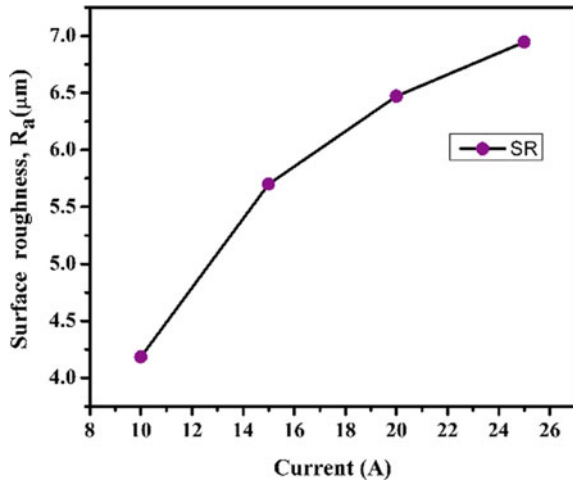
Table 3 Values of MRR and R_a for different values of current

Expt. no.	Current (A)	r_c (μm)	h (μm)	V_c (mm³)	MRR (mm³/min)	R_a (μm)
1	10	16.42	16.55	2.23×10^{-6}	1.12×10^{-6}	4.19
2	15	22.41	22.57	5.67×10^{-6}	2.83×10^{-6}	5.70
3	20	25.40	25.3	8.27×10^{-6}	4.13×10^{-6}	6.47
4	25	27.42	27.50	1.03×10^{-6}	5.17×10^{-6}	6.95

(a) Variation of temperature along z axis.   (b) Variation of temperature along r axis.
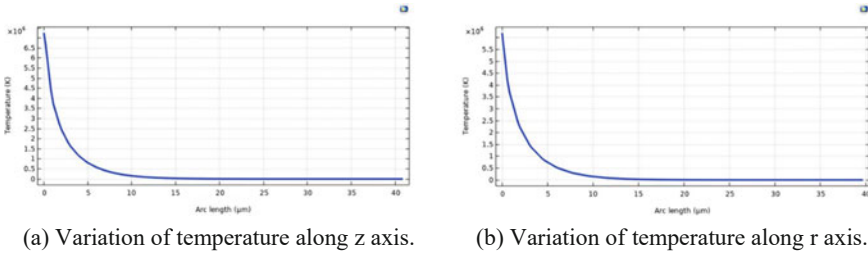
Fig. 5 Variation of temperature along the axis

4.3 Temperature Distribution Along the Axis

The observation from Fig. 5 indicates that the temperature drops as the arc radius increases. The value of temperature gets reduced as it moves along the axis for both the cases of radius and depth for the German silver workpiece. The variation of temperature is almost same for all values of current, i.e., for 10 A, 15 A, 20 A and 25 A, respectively. The main reason for drop in the values of temperature along the axis is because of t_{on}, as t_{on} is very less than the plasma that is produced because of the spark can only penetrate a few micrometers. Thus, the temperature produced because of the plasma can move up to a certain distance.

5 Conclusion

A two-dimensional cross-sectional thermal model for German silver Grade 55-18 has been developed by means of FEM. Single spark discharge study of the process of EDM for material removal of German silver has been simulated using heat transfer physics of COMSOL Multiphysics version 5.5. Convective heat flux along with conduction as a function of Gaussian distribution of heat source is taken into account for this study. Also, for the simulation, time-dependent material properties are selected, i.e., density, thermal conductivity and specific heat. Different values of MRR and R_a were found with the variation in discharge current of 10 A, 15 A, 20 A, 25 A, respectively. As it is known that for MRR, the higher the material removal is better, so the optimum condition for material removal is observed at 25 A current. At the same time, for R_a, the lesser the value is better, so the optimum condition for machining is observed at 10 A current. It can be concluded from this study that with the increment in discharge current, the depth and radius of crater increase which results in increase of MRR and R_a. Further variations in input parameters can be executed to achieve an optimum setting for maximization of MRR and minimization of R_a. The developed thermo-physical model will be compared with experimental results for material removal of German silver, and this will be the motivation for work to be carried out in the future.

References

1. Xie BC, Wang YK, Wang ZL, Zhao WS (2011) Numerical simulation of titanium alloy machining in electric discharge machining process. Trans Nonferrous Metals Soc China 21:434–439
2. Rahang M, Patowari PK (2020) Selective area deposition for pattern generation in EDM using masking technique. Surf Rev Lett 27(10)1950218:1–16
3. Khan AA (2008) Electrode wear and material removal rate during EDM of aluminum and mild steel using copper and brass electrodes. Int J Adv Manuf Technol 39(5):482–487
4. Deka S, Kar S, Patowari PK (2020) Machinability of silicon and German silver in micro electrical discharge machining: a comparative study. Silicon 1–13
5. Sortino M, Belfio S, Totis G, Kuljanic E, Fadelli G (2015) Innovative tool coatings for increasing tool life in milling nickel-coated nickel-silver alloy. Procedia Eng 100:946–952
6. Erden A, Kaftanoglu B (1981) Heat transfer modelling of electric discharge machining. In: Proceedings of the twenty-first international machine tool design and research conference, London, pp 351–358
7. Van Dijck FS, Dutre WL (1974) Heat conduction model for the calculation of the volume of molten metal in electric discharges. J Phys D Appl Phys 7(6):899–910
8. Beck JV (1981) Transient temperatures in a semi-infinite cylinder heated by a disk heat source. Int J Heat Mass Transf 24(10):1631–1640
9. DiBitonto DD, Eubank PT, Patel MR, Barrufet MA (1989) Theoretical models of the electrical discharge machining process. I. A simple cathode erosion model. J Appl Phys 66(9):4095–4103
10. Marafona J, Chousal JAG (2006) A finite element model of EDM based on the Joule effect. Int J Mach Tools Manuf 46(6):595–602
11. Joshi SN, Pande SS (2010) Thermo-physical modeling of die-sinking EDM process. J Manuf Process 12(1):45–56
12. Kansal HK, Singh S, Kumar P (2008) Numerical simulation of powder mixed electric discharge machining (PMEDM) using finite element method. Math Comput Model 47(11–12):1217–1237
13. Singh H, Puri YM (2018) Finite element analysis of electric discharge machining process. COMSOL Results 1–5
14. Krishna Kiran MPS, Joshi SS (2007) Modeling of surface roughness and the role of debris in micro-EDM. J Manuf Sci Eng 129(2):265–273
15. Salonitis K, Stournaras A, Stavropoulos P, Chryssolouris G (2009) Thermal modeling of the material removal rate and surface roughness for die-sinking EDM. Int J Adv Manuf Technol 40(3):316–323
16. Razeghiyadaki A, Molardi C, Talamona D, Perveen A (2019) Modeling of material removal rate and surface roughness generated during electro-discharge machining. Machines 7(2):1–17
17. Choubey M, Maity KP, Sharma A (2020) Finite element modeling of material removal rate in micro-EDM process with and without ultrasonic vibration. Grey Syst Theor Appl 10(3):311–319
18. Ikai T, Fujita I, Hashiguchi K (1992) Heat input radius for crater formation in the electric discharge machining. IEEJ Trans Ind Appl 112(10):943–949
19. Singh MA, Das K, Sarma DK (2018) Thermal simulation of machining of alumina with wire electrical discharge machining process using assisting electrode. J Mech Sci Technol 32(1):333–343

Numerical Analysis of Tool Material in Ultrasonic Machining Process

M. M. Mirad and B. Das

1   Introduction

The progress of brittle and hard materials for textile, medical, and aerospace industries is challenged in the manufacturing industry. It is difficult to machining the hard and fragile materials by using a conventional machining process. These materials can be machined by using advanced machining processes. Ultrasonic machining (USM) is one of the most suitable methods for machining these materials owing to its higher accuracy and good surface appearance. The USM process is influenced by various parameters such as types of abrasives, types of tool and workpiece materials, different types of horn and tool geometries, frequency, amplitude. The tool is one of the foremost components used in the USM process.

There are two types of horns designed, namely conical and exponential horns. The resonant frequency of the conical horn is higher than the exponential horn, whereas the magnification of the conical horn is lower than the exponential horn [1]. Based on the piezoelectric effect, the performance is monitored. With the help of proper selection of the electric impedance and the location, the horn performance can be improved [2]. The cup-shaped horn can be utilized as an ultrasonic tool as well as a displacement amplifier [3]. An axisymmetric ultrasonic horn is designed, and characterization for this proposed horn is carried out which is held by its amplification factor, working frequency, and nodal point position [4]. An innovative horn profile with higher displacement magnification for ultrasonic machining is proposed. The displacement magnification of the suggested horn is 8.6% and 41.4% higher than the

M. M. Mirad (✉) · B. Das
Department of Mechanical Engineering, National Institute of Technology Silchar, Silchar, Assam, India
e-mail: mehdi_rs@mech.nits.ac.in

B. Das
e-mail: bipul@mech.nits.ac.in

Bezier-profile horn and traditional catenoidal horn, respectively, with the same end surface diameter and length [5].

The experimental and numerical modelling of longitudinal vibration of several horn profiles: Gaussian, cylindrical, catenoidal, Bezier, and stepped are proposed. It is found that the Bezier and stepped horns are suitable for plastic welding. But between the two, the Bezier horn is preferred as it generates lower von Mises stress in the abruptly changing region compared to stepped horn [6]. The expression of displacement amplification and the resonance frequency equation of a full-wave barber ultrasonic horn are proposed. It is revealed that the outcome from numerical and theoretical analysis is extremely closer to the experimental observations [7]. The modal analysis is carried out to obtain the mode shapes as well as natural frequencies of different horn profiles [8]. The study of exponential horn in torsional and axial mode of vibration is carried out. It is observed that the calculated resonance frequency of the proposed horn is closer to the measured results [9]. The design of stepped and conical horns made of stainless steel and aluminium is proposed with the help of finite element analysis. It is observed that the conical horn is preferable over the stepped horn, as the stepped horn generates comparatively large stress in the abruptly changing region which is prone to failure of the horn [10].

The investigation of tool design and different types of tool material during ultrasonic machining is carried out. There are limited works which have been carried out on the effect of several tool materials in the USM process. In the present study, a stepped tool with varying different materials, i.e. tungsten carbide (WC), stainless steel (SS), and titanium (Ti) is considered. The suitable ultrasonic tool material is obtained which is preferred in the industrial applications.

2 Numerical Analysis

Numerical analysis is carried out using finite element modelling of the stepped tool for the investigation. Commercial COMSOL Multiphysics software is used for obtaining the modal as well as harmonic analysis. The framework followed for the numerical analysis is existing in the following sections.

2.1 Tool Design

Design and selection of a tool profile are a complicated process. An ultrasonic stepped tool of two different diameters, i.e. 5 mm and 3 mm along with the length 16 mm is developed as shown in Fig. 1. For a particular model, mesh generation is prepared to achieve the optimal solution of the theoretical model. The free tetrahedral element with finer size is considered to mesh all the present geometries. The meshed model of stepped tool is shown in Fig. 2. During the meshing of the model, the following records are generated: a number of vortex elements are 16, a number of edge elements

Fig. 1 Schematic representation of a stepped tool
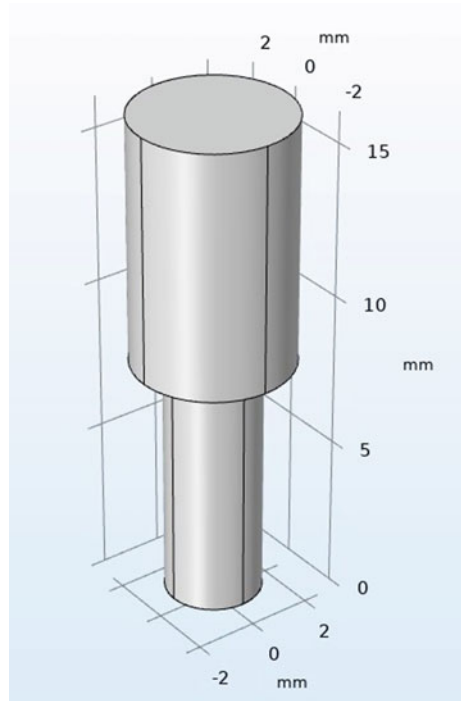
are 164, a number of boundary elements are 1282, a number of elements are 6174, free meshing time is 0.47 s, and minimum element quality is 0.235. Once the mesh generation is completed, the numerical analysis (modal and harmonic analysis) is performed.

There are three different tool materials considered, i.e. tungsten carbide, stainless steel, and titanium. The properties of the tool materials are tabulated in Table 1.

There are few assumptions considered for the numerical solution of stepped tool as follows:

1. The frequency range of the ultrasonic tool is subjected to around 20 kHz.
2. Motion of the tool is irrotational.
3. Displacement magnitude is equal to the wavelength of the tool.
4. The effect of factors like gravity, viscosity, friction, and external force has not been considered.
5. The proposed materials are supposed to be linearly elastic in nature.

2.2 *Boundary Condition*

The following boundary conditions are proposed which are influenced during numerical analysis.

Fig. 2 Schematic
representation of a meshed
stepped tool
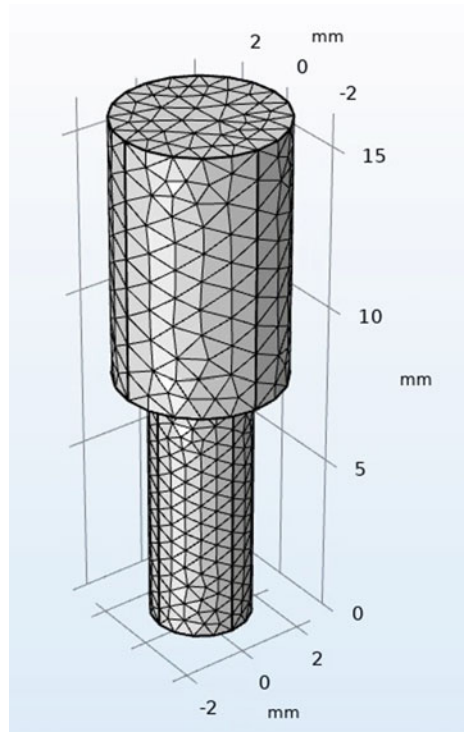
Table 1 Properties of different tool materials

S. No.	Material	Density (kg/m^3)	Young's modulus (GPa)	Poisson's ratio
1	Tungsten carbide	15,630	530	0.31
2	Stainless steel	7900	200	0.3
3	Titanium	4430	114	0.34

1. Tool is assumed to be one side fixed with the ultrasonic horn end, and other side is free.
2. Velocity and acceleration of the boundary components are considered as zero.
3. The damping of the proposed tool materials is considered as zero.
4. Applied frequency is transmitted through the transducer-ultrasonic horn-ultrasonic tool.

3 Results and Discussion

The numerical investigation of the ultrasonic tool with the influence of different materials is presented through modal and harmonic analysis. Stress analysis is furnished

to recognize the behaviour of the tool with the influence of materials and loading conditions experienced in the USM process.

3.1 Modal Analysis

The mode shapes and natural frequencies are obtained through modal analysis. The vibration of the tool in the USM process should possess to the longitudinal axis. The proposed ultrasonic tool is designed through a commercial software, i.e. COMSOL Multiphysics. There are three different tool materials selected to verify the modes and frequencies during USM process. The deformation profile and the eigen frequency of stepped tool with proposed tool materials are shown in Fig. 3 where the longitudinal mode of vibration is generated.

The present work exposes that there are six different eigen frequencies created at different six modes in all the tool materials. The preferred mode where axial mode of vibration is followed in the sixth mode for all the tool materials. Remaining five modes for all the respective tool materials have improper axial mode of vibration. The comparison of eigen frequencies of respective mode shapes for all the tool materials is shown in Table 2. The maximum eigen frequency (i.e. 1.3418E5 Hz) is generated in the ultrasonic tool which is made of tungsten carbide.

3.2 Harmonic Analysis

The harmonic analysis of the stepped horn is considered to determine the stress proficiency of the tool experienced for a particular frequency in the USM process. The boundary conditions are applied as mentioned above. The different tool materials are considered to reveal the effect of von Mises stress on the particular tool materials. The maximum stress is generated in the tool which is made of stainless steel, i.e. 233 MPa. Remaining tools which are made of tungsten carbide and titanium generated maximum stress as 231 MPa and 229 MPa, respectively. No significant variation is observed for the proposed tool materials. The different stress profile of the different tool materials is shown in Fig. 4.

3.3 Graphical Analysis

The centre line is selected to plot the line graph with its coordinates $x(0, 0)$, $y(0, 0)$, and $z(0, 16)$. Two frequencies are considered 20,000 Hz (min) and 30,000 Hz (max) to reveal the effect of stress and percentage of elongation with respect to tool length during ultrasonic machining. The effect of von Mises stress with respect to tool length at different tool materials is shown in Fig. 5. No significant variation is observed in

(a) Tungsten carbide

(b) Stainless steel

(c) Titanium
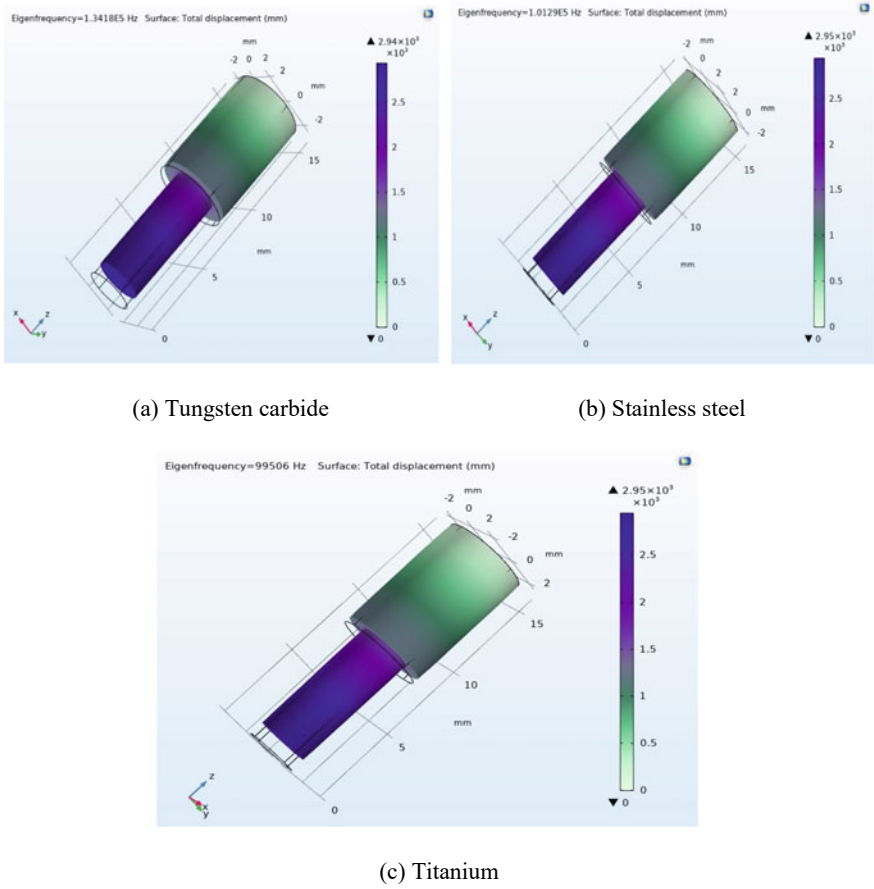
Fig. 3 Deformation profile and eigen frequency of stepped tool with proposed tool materials where axial mode of vibration is generated

Table 2 Mode shapes with respective eigen frequencies (Hz) for different tool materials

Material	Mode shape (1)	Mode shape (2)	Mode shape (3)	Mode shape (4)	Mode shape (5)	Mode shape (6)
Tungsten carbide (WC)	23,566	23,573	70,536	70,551	1.0212E5	1.3418E5
Stainless steel (SS)	17,795	17,799	53,105	53,115	74,846	1.0129E5
Titanium (Ti)	17,489	17,494	52,105	52,114	72,290	99,506
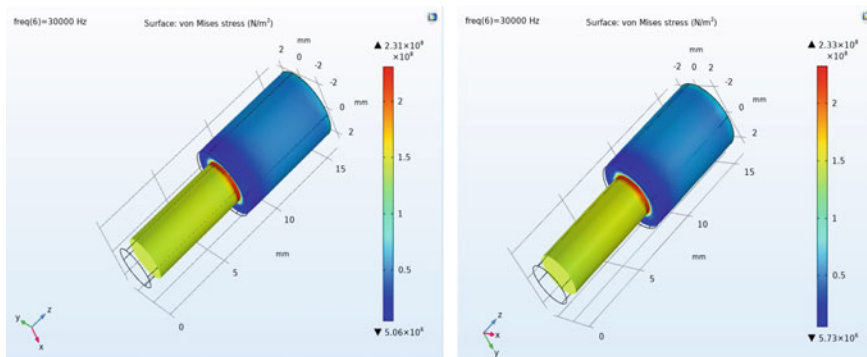
(a) Tungsten carbide   (b) Stainless steel
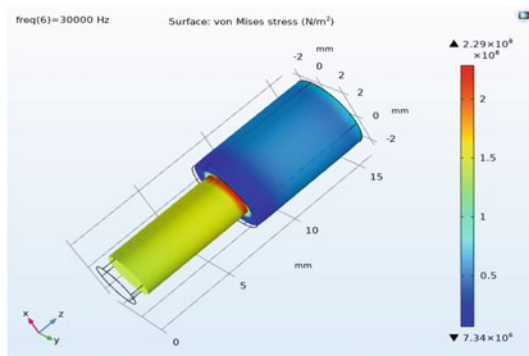
(c) Titanium

Fig. 4 Different stress profile of stepped tool with different materials
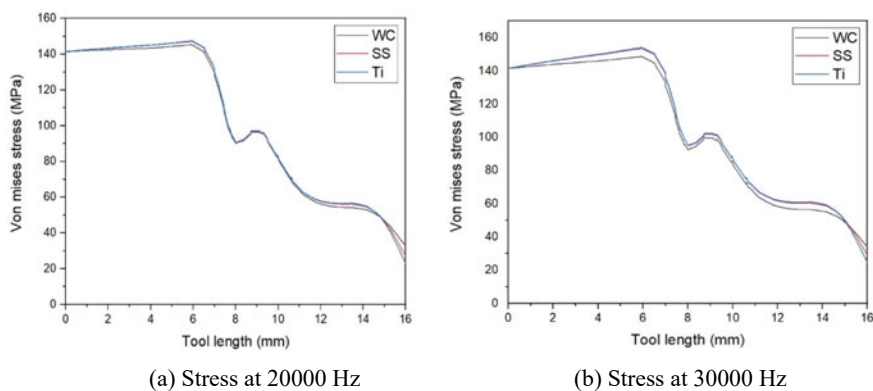
(a) Stress at 20000 Hz   (b) Stress at 30000 Hz

Fig. 5 Effect of von Mises stress with respect to tool length at different tool materials

(a) Strain at 20000 Hz (b) Strain at 30000 Hz
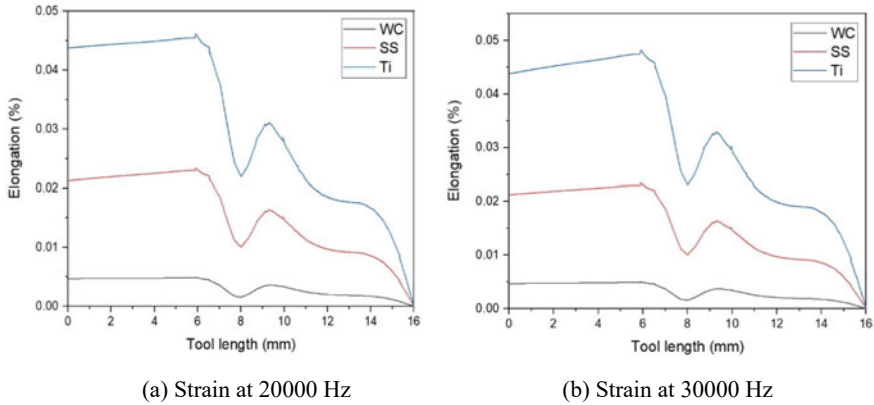
Fig. 6 Effect of elongation with respect to tool length at different tool materials

both the frequencies (min and max) for all the three different tool materials. The effect of elongation with respect to tool length at different tool materials is shown in Fig. 6. It is revealed that the frequency is not a foremost parameter to effect the elongation with respect to tool length in the USM process. The ultrasonic tool made of titanium is generated maximum elongation, while the ultrasonic tool made of tungsten carbide is generated minimum elongation.

4 Conclusion

The ultrasonic tool is an essential component for the proper functioning of the USM process. The present study is considered as the design of a stepped tool using dissimilar materials (tungsten carbide, stainless steel, and titanium) in dynamic conditions. In the modal analysis, there are six different axial and non-axial modes generated for all the tool materials. The preferred mode at which axial mode of vibration is generated at the sixth mode for all the tool materials. The axial mode has a frequency of 1.3418E5 Hz, 1.0129E5 Hz, and 99,506 Hz for the tool made of tungsten carbide, stainless steel, and titanium, respectively. In the harmonic analysis, the maximum stress is generated in the tool which is made of stainless steel, i.e. 233 MPa. Remaining tools which are made of tungsten carbide and titanium generated maximum stress as 231 MPa and 229 MPa, respectively. No significant variation is observed for the proposed tool materials through harmonic analysis. Tungsten carbide is perceived to be one of the best materials among the proposed materials due to its high axial mode of vibration.

References

1. Xiao CF, Han B (2019) Research and design of ultra-long ultrasonic horn. J Inst Eng (India) Ser C 100(6):1015–1022
2. Lin S, Guo H, Xu J (2018) Actively adjustable step-type ultrasonic horns in longitudinal vibration. J Sound Vib 419:367–379
3. Xu L (2015) Investigation of a cup-shaped ultrasonic transducer operated in the full-wave vibrational mode. Ultrasonics 59:109–118
4. Rosca IC, Pop MI, Cretu N (2015) Experimental and numerical study on an ultrasonic horn with shape designed with an optimization algorithm. Appl Acoust 95:60–69
5. Nguyen HT, Nguyen HD, Uan JY, Wang DA (2014) A nonrational B-spline profiled horn with high displacement amplification for ultrasonic welding. Ultrasonics 54(8):2063–2071
6. Rani MR, Rudramoorthy R (2013) Computational modeling and experimental studies of the dynamic performance of ultrasonic horn profiles used in plastic welding. Ultrasonics 53(3):763–772
7. Fu Z, Xian X, Lin S, Wang C, Hu W, Li G (2012) Investigations of the barbell ultrasonic transducer operated in the full-wave vibrational mode. Ultrasonics 52(5):578–586
8. Nad' M (2010) Ultrasonic horn design for ultrasonic machining technologies. Appl Comput Mech 4:79–88
9. Lin S (1996) Study on the longitudinal-torsional composite mode exponential ultrasonic horns. Ultrasonics 34(7):757–762
10. Seah KHW, Wong YS, Lee LC (1993) Design of tool holders for ultrasonic machining using FEM. J Mater Process Technol 37(1–4):801–816

Investigation of Gear Profile Deviations in Gear Planning Process Through CAD-Based Simulation

Nikolaos Tapoglou and Panagiotis Kyratsis

1 Introduction

The production of gear components is one of the important manufacturing processes in shop floors. Gear components have to be manufactured to high specifications as they are parts that have to perform under high stresses in demanding environments. Gear manufacturing processes are complex in nature compared to traditional milling and turning operations owing to the complexity of the kinematic chain, the tool geometry and the chip formation mechanism.

Researchers have focused on the creation of simulation models for traditional machining processes like milling, turning and drilling using different methods. Altintas et al. [1] presented an overview of the simulation techniques employed in the simulation of machining processes. Manufacturing processes such as milling [2, 3], drilling [4] and turning [5] have been studied with 3D solid modeling approaches as well as dexel-based and finite element simulation codes.

Simulation of gear manufacturing processes has also been the subject of studies including gear hobbing [6, 7], power skiving [8, 9] and gear shaping [10]. The main focus of these models is the prediction of the gear characteristics prior to the machining process in order to minimize expensive trials.

Gear planning is one if the well-established processes for manufacturing external high-precision gears. The process was studied by Epureanu et al. [11] who developed a mechanism for distributing the cutting energy equally among the cutting teeth that are involved in the cutting process.

N. Tapoglou (✉)
Department of Industrial Engineering and Management, International Hellenic University, Thessaloniki, Greece
e-mail: ntapoglou@iem.ihu.gr

P. Kyratsis
University of West Macedonia, Kozani, Greece
e-mail: pkyratsis@uowm.gr

This paper presents a novel simulation model that is able to simulate the cutting process by using a CAD kernel to produce high accuracy results. The developed model uses data provided by the user of the application and models the cutting process using a solid modeling approach. The reminder of the paper is as follows: Sect. 2 presents the kinematics of the cutting process along with the modeling approach followed. Section 3 presents the results and analysis of the simulation model, whereas Sect. 4 presents the concluding remarks and future developments.

2 Gear Planning Simulation

Machining of gears by means of gear planning is a cutting process with a translator primary cutting motion. The kinematic chain of gear planning consists of four distinct motions that are presented in the left side of Fig. 1. The positioning stroke (1) positions cutting tool into the correct position radially in relation to the gear. The cutting stroke (2) is the main cutting motion of the process along the axis of the gear. The motion
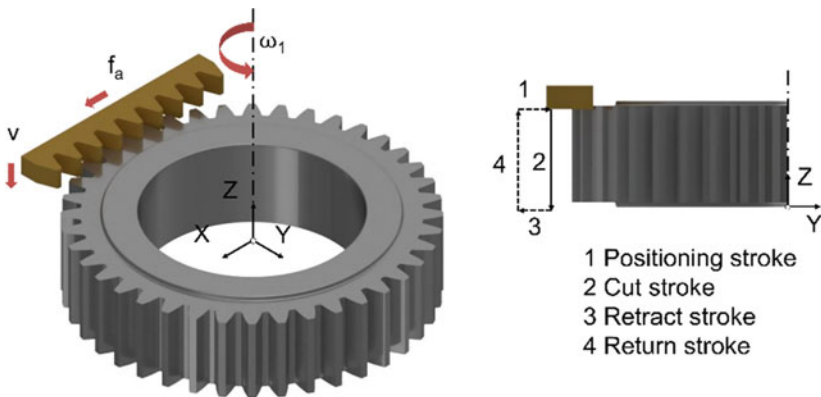
Fig. 1 Gear planning kinematics

starts above the top surface of the gear, and during the first part of the motion, the cutting tool is accelerated to the required cutting speed, then the cutting tool performs the cutting motion and exits under the gear after which part it is decelerated. During the retract stroke (3), the cutting tool clears the gear radially to prevent any damage to the gear surface as the tool advances to the next position. The return stroke (4) repositions the cutting tool to the correct position axially for the next cut. The four motions are repeated until the finished gear geometry is achieved. The gear and the cutting tool are positioned so that a rack-gear relation exists between the cutting tool and the workgear. In the case of spur gears, the cutting motion is parallel to the rotational axis of the gear, whereas in the case of helical gears, the cutting motion is angled in relation to the axis of the gear to match the helix angle of the workgear. In the case of helical gears, two variations exist depending on the machine tool and cutting tool configurations as presented in the lower right part of Fig. 1.

In the configuration on the left, the tool is configured as a helical rack and the tool profile is generated on the transverse plane. In the configuration on the right, the cutting tool has a spur rack configuration. In this case, the tool has a profile that is generated on the normal plane. In both cases, the tool trajectory follows the helix angle of the gear.

As in every gear machining process involving a generating motion, in gear planning, the tooth profile is created by the successive passes of the tool in the gear gap. Each of these passes machines the gear gap in a unique way thus producing a different chip geometry. In spur gears, the geometry remains the same throughout the cutting stroke, whereas in helical gears, this geometry changes during the cutting stroke to create a 3D chip geometry. In order to simulate the cutting process and calculate the geometry of the cutting process, a novel simulation code was developed. This code was embedded in a CAD environment in order to take advantage of the increased accuracy, analysis and visualization capabilities of these platforms. The simulation, as presented in Fig. 2, begins with the input by the user of the data required for the simulation of the cutting process. The simulation code using the data designs the profile of the cutting tool. After the cutting tool profile has been designed, the code positions of the rake face in the 3D space according to the kinematic chain of the process in consecutive positions. The tool profiles are combined to form a trajectory that describes the movement of the tool during the cutting process. This trajectory is used to extract the gear geometry after each pass as well as the chip geometry for this pass. After the end of the simulation, all the chip solid geometries as well as
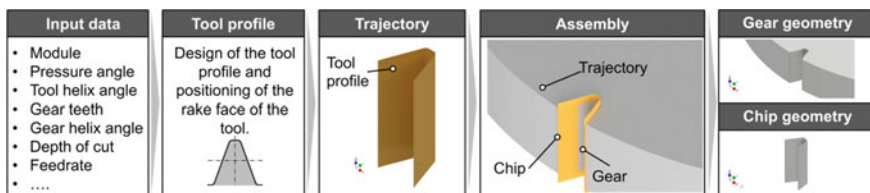
Fig. 2 Gear planning simulation approach

Fig. 3 Comparison between
theoretical and simulation
gear profiles

Input Data: m=3.79mm, a_n=20°, h_a=0°, z_1=56,
fa=2mm/stroke.
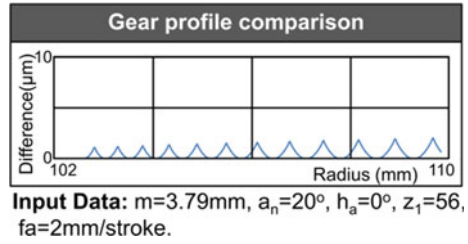
the final workgear geometry are acquired. By using this approach, both standard and
novel gear profile geometries can be simulated in a fast and cost-effective manner.

3   Simulation Results

The simulation approach presented can be used to realize the virtual production of
gears produced through gear planning. In order to validate the results of the simulation
code, a series of simulations was performed for standard involute gear geometries.
The resulting gear gap was compared against the profile generated by the analytical
involute gear equations. Figure 3 presents the results of the comparison of the profile
of the simulated gear against the analytical profile curve. As it can be observed, both
the leading and trailing flanks of the gear show good agreement against the theoretical
profile with the difference between the profiles in the order of 2 μm attributed to the
kinematics of the process. With regards to the chip geometries produced during the
simulation process, they are presented in the top part of Fig. 4. As it can be observed,
the cutting process starts from the head of the cutter before entering the full cut
area where the leading and trailing edges enter the cut. After that point, both the
leading and trailing edges are involved in the cutting process with the chips getting
progressively thinner and longer until the end of the cut. In terms of the metrics of
the process, in the lower part of Fig. 4, the cross-section area of the chips as well as
the maximum chip thickness in the simulated case, the results show an initial heavy
load in the first generating positions that gradually drops off toward the end of the
gear gap formation, in fact that agrees with the findings of Epureanu et al. [11].

4   Conclusion

A novel approach for the simulation of gear planning has been presented in this
paper. The simulation is based on a CAD environment thus taking full advantage
of the increased accuracy that is provided by these environments. The simulation
model is able to create the solid geometries of the gear and the chips produced in
the cutting process. The results acquired can be further analyzed in FEA packages
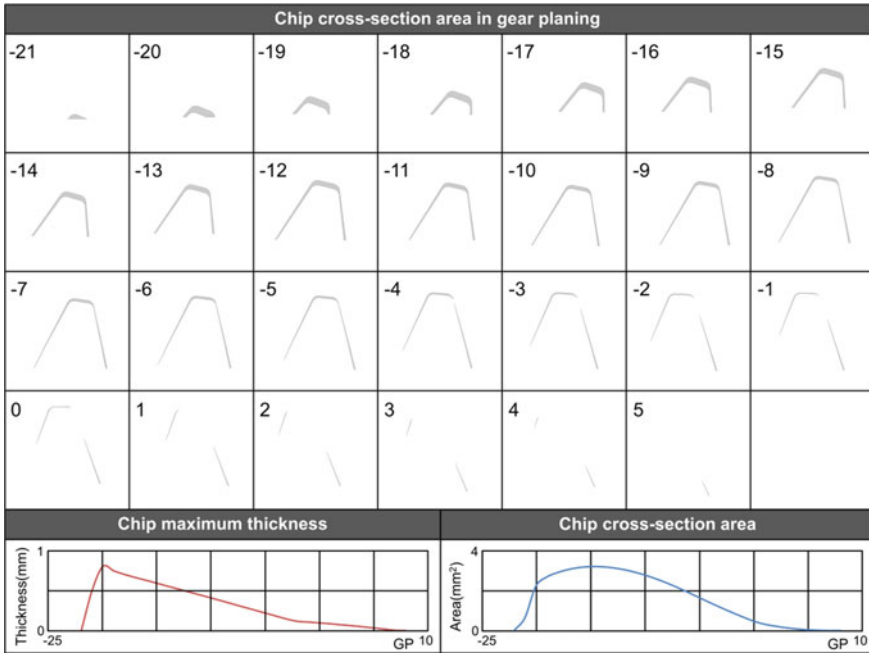
Input Data: m=3.79mm, a_n=20°, h_a=0°, z_1=56, fa=2mm/stroke.

Fig. 4 Solid chip geometries

to investigate the quality of the gear design. With the use of the proposed simulation model, custom as well as standard gear profiles can be generated, and the final quality characteristics of the gear can be predicted. This can lead in the optimization of the cutting process as well as the design of the gear profile.

References

1. Altintas Y, Kersting P, Biermann D, Budak E, Denkena B, Lazoglu I (2014) Virtual process systems for part machining operations. Ann CIRP 63(2):585–605
2. Tapoglou N, Antoniadis A (2012) 3-dimensional kinematics simulation of face milling. Measurement 45(6):1396–1405
3. Vakondios D, Kyratsis P, Yaldiz S, Antoniadis A (2012) Influence of milling strategy on the surface roughness in ball end milling of the aluminum alloy Al7075-T6. Measurement 45(6):1480–1488
4. Kyratsis P, Tapoglou N, Bilalis N, Antoniadis A (2011) Thrust force prediction of twist drill tools using a 3D CAD system application programming interface. Int J Mach Mach Mater 10(1–2):18–33
5. Kyratsis P, Tzotzis A, Markopoulos A, Tapoglou N (2021) CAD-based 3D-FE modelling of AISI-D3 turning with ceramic tooling. Machines 9(1):4
6. Tapoglou N, Antoniadis A (2012) CAD-based calculation of cutting force components in gear hobbing. J Manuf Sci Eng 134(3):031009-1-8

7. Tapoglou N, Mammas A, Antoniadis A (2013) Influence of machining data on developed cutting forces in gear hobbing. Int J Mach Mach Mater 14(1):66–76
8. Tapoglou N (2019) Calculation of non-deformed chip and gear geometry in power skiving using a CAD-based simulation. Int J Adv Manuf Technol 100(5):1779–1785
9. Tapoglou N (2021) Development of cutting force model and process maps for power skiving using CAD-based modelling. Machines 9(5):95. https://doi.org/10.3390/machines9050095
10. Erkorkmaz K, Katz A, Hosseinkhani Y, Plakhotnik D, Stautner M, Ismail F (2016) Chip geometry and cutting forces in gear shaping. CIRP Ann Manuf Technol 65(2):133–136
11. Epureanu A, Teodor V, Dima M, Oancea N (2009) A reconfigurated rack-tool for the generation of gears. Int J Adv Manuf Technol 40:662–668

Numerical Investigation and Comparison of Stress Concentration Factor in Threaded Bolts

Athul Vijay, Manas P. Vinayan, A. Hafsana, and T. Jagadeesha

1 Introduction

Individual parts of the machine are joined into assemblies with the help of various joints. There are mainly two types of joints: permanent joints and temporary joints. Threaded fasteners (screws and bolts) are temporary joints widely used in machine assemblies. Due to the easiness of use and diverse availability of threads, they are being used in applications like automobiles, machine tools, pressure vessels. Different varieties of threads are buttress, metric, square, ACME thread, etc.

A screw thread in which the driving face is made perpendicular to the axis of the screw, while the back face which makes an angle with the axis is known as buttress thread. A screw thread with V-shaped cut, 55° included angle between the screw thread flank, and a radius at both the root and crust of the thread is known as Whitworth thread. The metric threads are similar to Whitworth threads, the only difference being the included angle, which is 60° in metric threads. Another type of screw thread is square thread, commonly used in power screws and applications where high-power transmission efficiency and high load capacity are required. ACME threads are trapezoidal threads with 29° thread angle and are much stronger than square threads.

A. Vijay (✉) · M. P. Vinayan · A. Hafsana · T. Jagadeesha
Department of Mechanical Engineering, National Institute of Technology Calicut, Calicut, Kerala 671603, India
e-mail: athul_b180096me@nitc.ac.in

M. P. Vinayan
e-mail: manas_b180068me@nitc.ac.in

A. Hafsana
e-mail: hafsana_b180045me@nitc.ac.in

T. Jagadeesha
e-mail: jagdishsg@nitc.ac.in

The stress concentration is an essential factor to be considered during the design of all machine elements. Stress concentration effects in threaded bolts play a crucial role in the performance of the joint and the assembly. When the stresses developed due to unequal and fluctuating loading are not distributed evenly and are concentrated around a particular region, it can lead to the formation and propagation of a crack in that region, leading to the threaded bolts' failure. Hence, the stress concentration of different threaded bolts must be considered during design. The stress concentration factor is a term that indicates the distribution of stress in a machine element. It is the ratio of maximum stress developed in the machine element to the nominal applied tensile stress.

2 Research Background

Threaded fasteners (nuts and bolts) are an integral part of most machines, as they are widely used for temporary joints. However, these are subjected to unequal and fluctuating loads, which can cause the joint to fail, ultimately leading to the failure of the machine. Hence, it is essential to study and understand the stress concentrations in threaded fasteners for developing safe and reliable designs. Govindu et al. [1] conducted a study using finite element methods to design and optimize screwed fasteners to reduce stress concentration factors. Lehnhoff and Bunyard [2] conducted a linear finite element analysis to determine the stress concentration factors for the threads and bolt heads in a bolted connection. Although this study was conducted using linear material models, it does provide an insight into the behavior of bolted connections. Venkatesan and Kinzel [3] studied the various methods to reduce stresses in bolted joints. The effect of the relative position of the threads of the bolt and nut, shank diameter of the bolt, filet radius, and coefficient of friction between the threads on the stress concentration factor was studied. Mushtaq and Sheik [4] carried out an experimental evaluation of the effect of thread angle on the fatigue life of bolts. The study focused on plotting the *S–N* curves for various thread geometries of bolts under cyclic loading to determine the fatigue strength. Osakue and Anetor [5] studied the design of elastic screw fasteners under tensile load by presenting an equivalent stress approach.

3 Mathematical and Design Aspects

3.1 Material Considerations

The bolts used in the study are made of AISI 1018 low-carbon steel. This variant of steel imparts better mechanical properties along with exceptional machinability to bolts, rendering it quite suitable and economical for structural applications. The

Table 1 Composition of AISI 1018 carbon steel

Element	Scientific notation	Content %
Manganese	Mn	0.60–0.90
Carbon	C	0.15–0.20
Sulfur	S	0.05 (max)
Phosphorous	P	0.04 (max)
Iron	Fe	Balance

Table 2 Mechanical properties of AISI 1018 carbon steel

Properties	Unit	Value
Tensile strength	MPa	440
Yield strength	MPa	370
Poisson's ratio		0.29
Shear modulus	GPa	205
Modulus of elasticity	GPa	80

composition and mechanical properties of AISI 1018 carbon steel are summarized in Tables 1 and 2, respectively.

3.2 Calculations

M10 bolts are considered for the study throughout this paper. The diameter of the bolt (d) is 10 mm. The maximum force that the bolt can withstand is found using the material's tensile yield stress.

For the simplicity of the calculation, we assume that the principal stress in the uniaxial tension test is equivalent to the tensile yield strength of the material of the bolt.

$$\sigma = S_{yt}$$

Here, σ is the principal stress in the uniaxial tension test. S_{yt} is the tensile yield strength of the AISI 1018 carbon steel. Based on this assumption, we can find the force acting on the bolt.

The area of the bolt is calculated as, $A = \frac{\pi d^2}{4}$.

The maximum force that can be applied to the bolt, $F = S_{yt} \times A = 370 \times \frac{\pi \times 0.01^2}{4} = 29$ kN.

As the maximum force that can be handled is 29 kN, an appreciably less force is considered for the analysis. The force used for analysis is 25 kN. In order to calculate the stress concentration factors for each bolt, the nominal stress of the bolt is also evaluated.

Table 3 Number of nodes for each model

	Metric	ACME	Square	Buttress	Whitworth
Normal	19,836	16,252	15,715	16,937	21,239
Grooved	29,461	19,199	13,347	29,370	23,989
Reduced shank	29,201	14,628	14,131	22,619	20,516
Undercut	32,223	15,973	14,689	15,857	22,235
Filet	18,474	16,828	16,160	17,485	21,637

Table 4 Number of elements for each model

	Metric	ACME	Square	Buttress	Whitworth
Normal	11,053	8564	8152	8775	11,189
Grooved	17,188	10,201	7010	17,054	13,003
Reduced shank	17,371	7685	7313	12,884	11,113
Undercut	19,245	8132	7433	8228	11,987
Filet	9468	8932	8420	9132	11,378

Nominal stress of the bolt, $\sigma_o = \frac{F}{A_0}$.

For M10 bolt, pitch $= 1.5$ mm, $A_o = 56.745$ mm^2.

Therefore, $\sigma_o = 440.56$ MPa, for normal threads.

4 Finite Element Modeling

All the permutations of the considered thread structures and geometry are numerically analyzed using finite element methods in ANSYS 2020 R1. The threads are modeled in SolidWorks 2020 and are simulated using ANSYS Workbench, where the bolts are meshed and solved for equivalent stress values. A tensile force of 25 kN is applied to the bolt. Tetrahedral mesh is selected for each of the models for mesh generation. The number of nodes and elements for each model is given in Tables 3 and 4, respectively. The equivalent stress is found using the stress tool available in the solution tab in ANSYS mechanical.

5 Results and Analysis

The Von Misses stresses and stress concentration factors for various bolt designs are compiled in Table 5.

The basic design of all five threads has been analyzed. Some more modifications are made in the geometries of the threads to study the variation in stress concentration

Table 5 Von Misses and stress concentration factors for various bolt designs

S. No.	Design variant	Von Misses stress (MPa)	Stress concentration factor	Image
1	Metric normal	790.76	1.795	
2	Metric grooved	1213.8	2.440	
3	Metric reduced shank	645.51	1.298	
4	Metric undercut	1007.3	2.025	
5	Metric filet	824.69	1.658	

Table 5 (continued)

S. No.	Design variant	Von Misses stress (MPa)	Stress concentration factor	Image
6	ACME normal	658.38	1.494	
7	ACME grooved	933.22	1.876	
8	ACME reduced shank	667.4	1.342	
9	ACME undercut	978.27	1.967	
10	ACME filet	629.9	1.266	

Table 5 (continued)

S. No.	Design variant	Von Misses stress (MPa)	Stress concentration factor	Image
11	Square normal	650.41	1.476	
12	Square grooved	1006.9	2.024	
13	Square reduced shank	715.78	1.439	
14	Square undercut	679.51	1.366	
15	Square filet	674.4	1.356	

Table 5 (continued)

S. No.	Design variant	Von Misses stress (MPa)	Stress concentration factor	Image
16	Buttress normal	749.94	1.702	
17	Buttress grooved	1106.2	2.224	
18	Buttress reduced shank	820.62	1.650	
19	Buttress undercut	678.57	1.364	
20	Buttress filet	762.04	1.532	

Table 5 (continued)

S. No.	Design variant	Von Misses stress (MPa)	Stress concentration factor	Image
21	Whitworth normal	1211.7	2.750	
22	Whitworth grooved	1236.6	2.486	
23	Whitworth shank reduced	857.773	1.725	
24	Whitworth undercut	918.83	1.847	
25	Whitworth filet	1125.4	2.263	
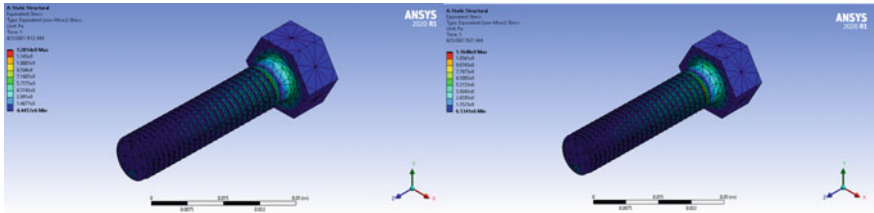
Fig. 1 **a** 20% decrease in filet. **b** 20% increase in filet

factors. The modification in geometries includes a 20% increase in filet, 20% decrease in filet, 20% decrease in undercut, and 20% increase in the undercut. The analysis is carried out for these design variants. The results for Whitworth threads are shown in Figs. 1, 2, and Table 6.
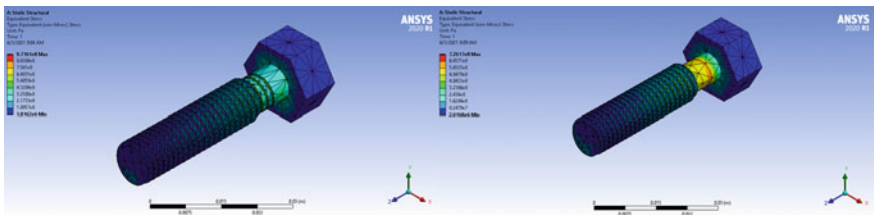
Fig. 2 **a** 20% decrease in undercut. **b** 20% increase in undercut

Table 6 Results for analysis of Whitworth thread variants

S. No.	Design variants	Von Mises stress	Stress concentration factor
1	Normal	1211.7	2.750
2	Filet	1125.4	2.263
3	Filet—20% decrease	1285.4	2.584
4	Filet—20% increase	1164.8	2.342
5	Undercut	918.83	1.847
6	Undercut—20% decrease	971.6	1.953
7	Undercut—20% increase	726.1	1.460

6 Conclusions

The various geometries of the bolts with five standard types of threads were numerically analyzed through simulations in ANSYS to obtain maximum stress and stress concentration factors for each. The study revealed that the problem–solution could be optimized by altering the dimensions of the threads used in the study. A comparison among all the thread types conveys that the stress concentration factor for square thread has relatively less concentration factor than the others, particularly the undercut variant of the thread. Out of all the threads studied, Whitworth threads are found to show a more effective reduction in stress concentration factor, while square and metric threads show less. The effectiveness of change in the stress concentration factor of Whitworth thread was depicted clearly in the analysis of 20% decrease and increase of undercut and filet forms of Whitworth thread. The 20% increase in undercut decreased the equivalent stress and the stress concentration factor. The 20% decrease in undercut increased the equivalent stress and the stress concentration factor. Similarly, for filet Whitworth threads, an increase in the equivalent stress and stress concentration factor for both increase and decrease of filet dimension is observed. The observations are made by analyzing different bolts fabricated in SolidWorks 2020, and numerical analysis is done using ANSYS 2020 R1. The values obtained in the study may not be optimal and have to be experimentally verified by performing a tension test on these geometries. However, the work provides an insight into the rough estimates and helps us understand the effect of dimensional alterations on the stress concentration of bolts.

References

1. Govindu N, Jayanand Kumar T, Venkadesh S (2015) Design and optimization of screwed fasteners to reduce stress concentration factor. J Appl Mech Eng 4(4)
2. Lehnhoff TF, Bunyard BA (2000) Bolt thread and head fillet stress concentration factors. ASME J Press Vessel Technol 122(2):180–185
3. Venkatesan S, Kinzel GL (2005) Reduction of stress concentration in bolt-nut connectors. ASME J Mech Des 128(6):1337–1342
4. Mushtaq ES, Sheik NA (2013) Experimental evaluation of the effect of thread angle on the fatigue life of bolts. IOSR J Mech Civ Eng 7(1):12–19
5. Osakue EE, Anetor L (2017) Design of elastic screw fasteners under tensile load. Mech Eng Res 7(1)

Comparative Analysis and Simulation of Routing Protocols for Wireless Body Area Networks

Rounak A. Patil, Maneetkumar R. Dhanvijay, Sudhir Madhav Patil, and Mrinai M. Dhanvijay

1 Introduction

Wireless sensory network is an important field of communication engineering. With the passing time, size of equipment used in the technology is increasing. The boom in the field of Micro Electro-Mechanical Systems (MEMS) has led to the possibility of manufacturing sensors and actuators with low power consumption and smaller size which in turn has given rise to a new field called as Wireless Body Area Network or WBAN.

WBAN is also sometimes referred as medical body area network, body area network or body sensor network. It can be defined as interconnection of wearable computing devices deployed on/in the human body for sensing different parameters such as blood sugar, electro cardiograph, heart rate, lactic acid formation, human fatigue etc. WBAN sensors are generally divided into two types: On-body and in-body sensors. On-body sensors are simply mounted on the surface of body while in-body sensors are to be implanted inside patient's body using surgical methods.

In a short amount of time, WBAN has attracted a lot of attention in several fields including medical, military, fitness and sports. Simplest example for a WBAN sensor can be fit bit which is used by people to track their calorie consumption and pulse rate. The main advantage of using WBAN technology is that it provides mobility to its users unlike wired sensors which do not let its user to move freely.

R. A. Patil · M. R. Dhanvijay (✉) · S. M. Patil
Department of Manufacturing Engineering and Industrial Management, College of Engineering, Pune (COEP), Wellesley Road, Shivajinagar, Pune 411 005, India
e-mail: mrd.mfg@coep.ac.in

M. M. Dhanvijay
Department of Electronics and Telecommunication Engineering, Modern Education Society's College of Engineering, Pune 411 001, India
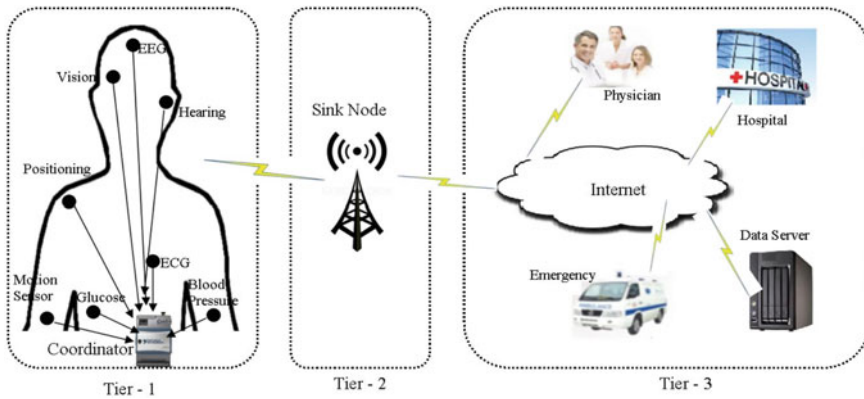
Fig. 1 WBAN architecture [1]

2 Architecture

WBAN architecture includes several small sensory nodes which are deployed on certain significant locations on the human body, which results in WBAN, and is fit for observing diverse indispensable signs. These crucial signs are communicated to a clinical specialist or any end client. The architecture of WBAN is a three-tier one which is given in Fig. 1.

The tier-1 comprises of biosensors introduced on the surface of body or embedded inside body. Their activity is detecting and sending or getting different physiological data about the human body. This may incorporate pulse, circulatory strain, glucose level, body vibration and so forth.

The tier-2 comprises of PCs, advanced cells or other canny gadgets. The data gathered and communicated by the sensory nodes is conveyed to the end server farm or worker remotely.

The tier-3 of WBAN mainly comprises of distant workers giving different applications. Its work is to gather and handle the detected information to give a unique reaction. Its importance increments if the sensor nodes gather unusual information. In the event that unusual information is distinguished, crisis transmission and disturbing is completed, which can speed up the salvage and crisis reaction.

3 Challenges

WBAN is a developing technology, but there are still a lot of issues faced by WBAN which needs to be solved and problems which needs a better solution than the existing ones. For example, security is one such issue with WBAN which needs more and more updating with time as user requires better privacy. Few challenges and issues faced by WBAN are given below.

3.1 Power Source

Due to small size of WBAN devices, the power source installed in them are also small. That's why there is an issue of low initial energy of the devices. Most of the WBAN devices are operated on batteries which are harder to replace in case of WBAN implants. As wireless charging technology is not fully developed yet, we need to rely on better power source development so the batteries can last longer.

3.2 Energy Consumption

All WBAN devices require power to sense, process, transmit or receive a signal from one node to another. As the initial energy of WBAN device is very low, it is necessary to develop energy efficient algorithms or protocols for WBAN communication so that the devices use minimum energy to operate. Energy harvesting or energy scavenging methods are being used to power WBAN devices which generates energy through body movements and vibrations.

3.3 Computational Capacity

WBAN has both limited memory as well as power, therefore only a limited number of computations can be done. Unlike WSN devices, WBAN devices lack the high computing power. Most of WBAN power is reserved for transmission and reception which results in very less power available for signal processing and computation. A solution can be the use of heterogeneous devices in a WBAN network, i.e., devices with different energy levels.

3.4 Security

Security is a major concern in field of WBAN as the data is very sensitive. The data transmission over Internet should be very confidential and private that's why it needs to be encrypted. The data related to person's health should not be tampered with. Security mechanism consumes a significant amount of energy, therefore should be energy efficient.

3.5 *Path Loss*

The body structure of a human is vital factor in case of path loss and signal attenuation. The parameters of path loss for on-body sensors and implants are different due to their location of deployment. Path loss assumes a significant part in energy utilization while transmission of signal. Hence, the study of human body path loss becomes necessity.

4 Applications of WBAN

WBAN has a vast field application. Some of them are currently used while some are still under study. The application of WBAN in medical field is too vast and crucial in modern era. The possible use of WBAN includes treatment and diagnosis of diseases. Sensors are deployed on the human physique to monitor blood pressure, motion, etc. Various diseases and the sensors to detect them are given in the Table 1.

If the WBAN sensors detect any abnormalities or the readings cross a certain threshold limit, concerned party or medical advisor is informed of called out sending a signal to their smart phone or computer. Thus, a patient can be immediately diagnosed by a medical expert or doctor.

WBAN sensors can be deployed on an athlete's body and his or her readings are noted for their performance enhancements. This application requires development of wearable computing devices installed with WBAN technology. These devices may include WBAN shirts, WBAN skin, WBAN helmet, WBAN socks, etc. Health and fitness is crucial in military and defense. A WBAN gear which measures all vital signs of a soldier can be installed on each soldier during a mission. It will continuously monitor soldier's vitals and location for immediate backup. This gear should be as light as possible so the movement of a soldier is not compromised.

Table 1 Diseases and WBAN sensors

S. No.	Disease	Sensor
1	Cardio-vascular diseases	Oximeter ECG sensor Heart rate sensor
2	Cancer	Nitric acid sensor
3	Diabetes	Diabetic sensor Insulin actuator
4	Blood pressure	Blood pressure sensor
5	Continuous monitoring	Temperature, heart rate, ECG, blood pressure, etc.

5   Routing Protocols in WBAN

A protocol is a set of rules which governs a system. Routing protocols in WBAN decides the procedure in which sensory nodes communicate with each other so as to consume energy in an efficient manner. The routing protocols also ensures that the complete energy of given interconnecting nodes resulting in a network is uniformly divided among all the nodes depending on their functionality, i.e., an advance node will have more energy than a normal mode as advance nodes need to transmit more data and require high computational capacity.

There are various routing protocols in WBAN. They are used depending on requirements of human conditions. Figure 2 gives a detailed classification of a few WBAN routing protocols and their brief description follows.

5.1   *QoS-Aware Routing Protocols*

These protocols are significant in any technology which can be applied to the real world, especially in WBAN, where resources are limited. Development of these

Fig. 2   Classification of routing protocols

protocols is very difficult and challenging as this is modular-based protocol. The Quality of Services which are considered while developing a WBAN network are: Data reliability, data security, transmission delay, network throughput, node temperature, etc. [2–10].

LAEEBA [3], Co-LAEEBA [4] and SIMPLE are examples of this type.

5.2 Temperature-Aware Routing Protocols

These protocols mainly deal with the sensors which are implanted inside human body. Like any other electronic device, WBAN devices also generate heat when energy is consumed. If the sensors or nodes are heated above a certain threshold, it may cause tissue damage. The main parameter of path selection is temperature so that no node faces a temperature rise.

Earlier these protocols were vastly studied but now energy is main concern, use of these protocols has been slightly reduced [11–20].

M2E2 [11], THSR [15] and ATTEMPT are examples of this type.

5.3 Cluster-Based Routing Protocols

These protocols can be considered analogous to cellular network protocols in terms of their architecture. In these protocols, a network is divided into one or multiple clusters of WBAN nodes and a cluster head is selected for each independent cluster. The data is gathered by all the sensory nodes in a cluster and transmitted to the base station also known as sink via corresponding cluster head to save energy [21–23].

CBBAP [21] and HIT [23] are examples of this type.

5.4 Postural-Movement-Based Routing Protocols

Bodily movements play an important role in WBAN topology as the body movements, distance between sensory nodes varies. Limbs movement might improve or worsen the network topology. These types of protocols can be used in the improvement of development of dynamic WBAN systems [24–26].

ETPA [24] and PSR [25] are examples of this type.

5.5   Cross-Layered Routing Protocols

These protocols merge different protocol layers and combine the advantages of each and every protocol stack resulting in a better network performance [27–29].

CICADA [27], TICOSS [28] and WASP [29] are examples of this type.

6   Simulation

In a wireless body area network, each node communicates through a cluster head, which is chosen using a clustering method. Cluster heads gather data and send it to sink, where the user may utilize it.

Simulation for two routing protocols: SIMPLE [7] and ATTEMPT [12] are carried out and discussed. Both the protocols contain 8 nodes and a single sink. The area covered is 0.8×1.8 m. All the nodes in network have same initial energy that is why it is called as a homogenous network. Both protocols are QoS based protocols. The simulation parameters, transceiver energy ($E_{\text{TX-Elec}}$, $E_{\text{RX-Elec}}$) and amplifier constant (E_{amp}) values are given in Table 2 and results of simulation using MATLAB as simulation tool are presented.

6.1   Performance Parameters

6.1.1   Stability Period

The time lapse from the beginning of the network till the demise of the very first node while the network is in operational mode is known as stability period. The unstable period is the time elapsed between the demise of the very first node and the demise of the end node.

6.1.2   Residual Energy

During network operation, it is the difference between initial energy of nodes and energy utilized by nodes.

Table 2 Simulation parameters

Parameters	Value	Unit
$E_{\text{TX-Elec}}$	16.7	nJ/bit
$E_{\text{RX-Elec}}$	36.1	nJ/bit
E_{amp}	1.97	nJ/bit/mm

6.1.3   Network Lifetime

It is the total time taken by the network to stay operational, i.e., it is time taken till the last node of the network is dead.

6.1.4   Throughput

It represents the number of packets received at the sink after successful transmission of the packets via nodes.

6.1.5   Path Loss

At the receiving node, the difference between the sent and received power of the transmitting node is called path loss. It is expressed in decibels (dB).

The energy parameters used in simulation are hardware-dependent. A single chip and low power transceiver Nordic nRF2401A, and Chipcon CC2420 transmitter–receiver are two commonly used transceivers in WBAN technology. Both have the same 2.4 GHz bandwidth. The most common parameters of Nordic nRF2401A transceivers are used in equations and simulations.

6.2   Results and Discussion

6.2.1   Stability Period

It is the time in which network operates till first nodes dies. From Fig. 3, it is seen that for ATTEMPT, stability period is around 2094 rounds while for SIMPLE, it is 3782 rounds. Here, one round represents a single process which includes the total time from sensing the data from body to transmitting that data to sink. Various functions are performed in a single round such as sensing, transmitting, receiving, aggregating, processing, etc. As a result, the SIMPLE protocol's stability period is greater than the ATTEMPT protocol's.

6.2.2   Network Lifetime

It is a significant parameter in WBAN simulation. It is defined as the total time for which the network operates, i.e., it is time from start of network till the final node dies which is 7321 rounds for SIMPLE and 7228 rounds for ATTEMPT as shown in Fig. 3. Thus, SIMPLE protocol will operate for longer period than ATTEMPT.
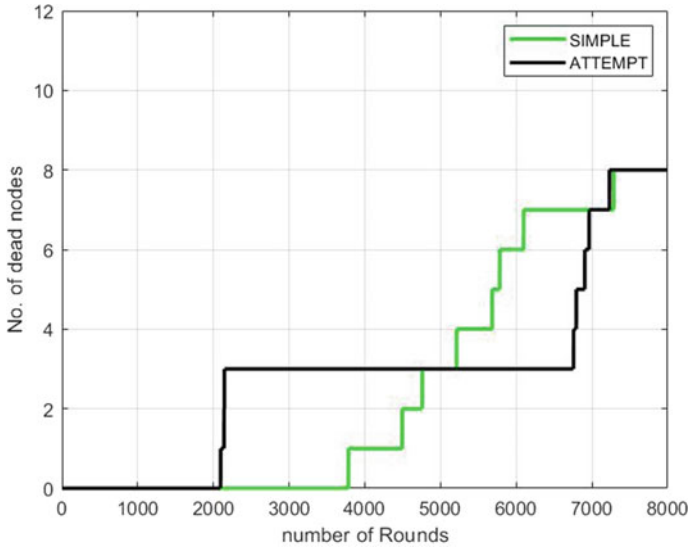
Fig. 3 Number of dead nodes per round

6.2.3 Throughput

The number of data packets received successfully per second at the sink is known as throughput. Throughput for SIMPLE and ATTEMPT is show in Fig. 4. For SIMPLE protocol the number of packets received at the sink is 2.15×10^4 and for ATTEMPT the value of throughput reduces to 0.78×10^4.

6.2.4 Path Loss

The path loss analysis for SIMPLE and ATTEMPT is shown in Fig. 5. We use a 2.4 GHz constant frequency and 3.38 as path loss coefficient for both routing protocols. The initial path loss for SIMPLE is around 451 dB and that of ATTEMPT is 434 dB. So, the path loss value for SIMPLE is slightly greater than that of ATTEMPT.

6.2.5 Residual Energy

During network activity, it is the deviation between a sensor node's initial energy and the energy utilized by the same node while operating. The total initial energy of both the networks is 4 J as shown in Fig. 6 and which is depleted over time as the number of rounds increases as each node requires energy to transmit and receive data in each round.
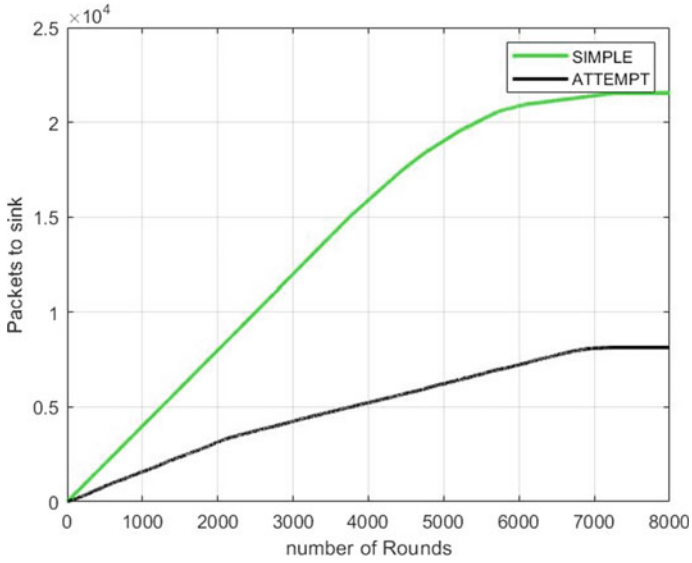
Fig. 4 Packets received at sink per round
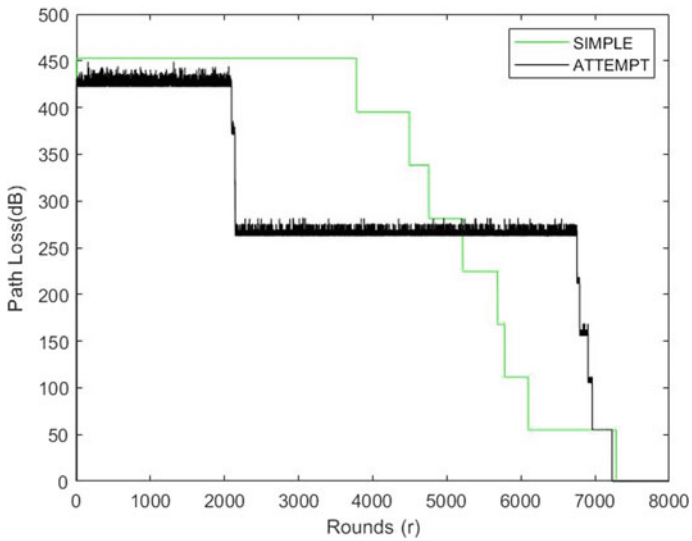
Fig. 5 Path loss
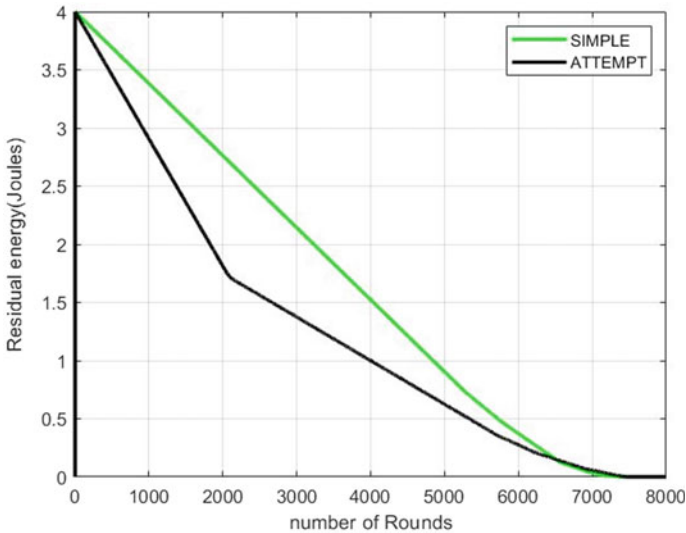
Fig. 6 Residual energy of the network

As the number of rounds increase, it is observed that SIMPLE protocol consumes less energy, since it uses cost function to select the cluster head while ATTEMPT uses best path selection depending on the temperature of the forwarder node. Hence, SIMPLE is better than ATTEMPT than in terms of energy consumption.

7 Conclusions

(i)   The SIMPLE protocol's stability period (3782 rounds) is greater than the ATTEMPT protocol's which is highly desirable.
(ii) SIMPLE protocol will operate for longer period than ATTEMPT as it completes 7321 rounds before all the nodes die out as compared to the ATTEMPT protocol.
(iii) For SIMPLE protocol the number of packets received at the sink is 2.15×10^4.
(iv) The total initial energy of both the networks is 4 J.

Based on the simulation results, it can be concluded that SIMPLE protocol is better in overall WBAN performance.

References

1. Bangash J, Abdullah AH, Anisi MH, Khan AW (2014) A survey of routing protocols in wireless body sensor networks. Sensors 14(1):1322–1357. https://doi.org/10.3390/s140101322
2. Kaur HP, Goyal K (2015) Cost based efficient routing for wireless body area networks. Int J Comput Sci Mob Comput 4(8):295–300
3. Ahmed S, Javaid N, Akbar M, Iqbal A, Khan ZA, Qasim U (2014) LAEEBA: link aware and energy efficient scheme for body area networks. In: Proceedings of the 28th IEEE international conference on advanced information networking and applications (AINA'14), Victoria, BC, pp 435–440. https://doi.org/10.1109/AINA201454
4. Ahmed S, Javaid N, Yousaf S, Ahmad A, Sandhu MM, Imran M, Khan ZA, Alrajeh N (2015) Co-laeeba: cooperative link aware and energy efficient protocol for wireless body area networks. Comput Hum Behav 51(Part B):1205–1215. https://doi.org/10.1016/j.chb201412.051
5. Sheth Mahammed Ovesh I, Sharma AK (2014) Modified LAEEBA routing in WBAN. Int J Sci Res Dev 2(8):348–351
6. Auqir A, Javaid N, Akram S, Rao A, Mohammad SN (2013) Distance aware relaying energy-efficient: DARE to monitor patients in multi-hop body area sensor networks. In: Proceedings of the IEEE 8th international conference on broadband and wireless computing, communication and applications (BWCCA'13), Compiegne, France, pp 206–213. https://doi.org/10.1109/BWCCA201340
7. Nadeem Q, Javaid N, Mohammad SN, Khan MY, Sarfraz S, Gull M (2013) Simple: stable increased-throughput multi-hop protocol for link efficiency in wireless body area networks. In: Proceedings of the eighth international conference on broadband and wireless computing, communication and applications (BWCCA'13). Compiegne, pp 221–226. https://doi.org/10.1109/BWCC201342
8. Ababneh N, Timmons N, Morrison J, Tracey D (2012) Energy-balanced rate assignment and routing protocol for body area networks. In: Proceedings of the 26th IEEE international conference on advanced information networking and applications workshops. Fukuoka, pp 466–471. https://doi.org/10.1109/WAINA201234
9. Gupta S, Kaur P (2015) WBAN health monitoring system using TEEN protocol: threshold sensitive energy efficient network protocol. Int J Innov Sci Eng Technol 2(10):20–25
10. Kumaria J, Prachia (2015) An energy efficient routing algorithm for wireless body area network. Int J Wirel Microw Technol 5:56–62
11. Rafatkhah O, Lighvan MZ (2014) M2E2: a novel multi-hop routing protocol for wireless body sensor networks. Int J Comput Netw Commun Secur 2(8):260–267
12. Ahmed A, Javaid N (2014) RE-ATTEMPT: energy-efficient routing protocol for wireless body area sensor networks. Int J Distrib Sens Netw. https://doi.org/10.1155/2014/464010
13. Monowar MM, Mehedi HM, Bajaber F, Hamid MA, Alamri A (2014) Thermal-aware multi-constrained intrabody QoS routing for wireless body area networks. Int J Distrib Sens Netw. https://doi.org/10.1155/2014/676312
14. Javaid N, Abbas Z, Fareed MS, Khan ZA, Alrajeh N (2013) M-ATTEMPT: a new energy-efficient routing protocol for wireless body area sensor networks. Proc Comput Sci 19:224–231
15. Tabandeh M, Ahourai F, Moradi S, Jahed M (2009) A thermal-aware shortest hop routing algorithm for in vivo biomedical sensor networks. In: Proceedings of the IEEE sixth international conference on information technology: new generations. Las Vegas Naveda, pp 1612–1613. https://doi.org/10.1109/ITNG2009274
16. Bag A, Bassiouni MA (2007) Hotspot preventing routing algorithm for delay sensitive biomedical sensor networks. In: Proceedings of the IEEE international conference on portable information devices. Orlando, FL, pp 1–5. https://doi.org/10.1016/j.inffus200702.001
17. Anirban B, Bassiouni MA (2008) Routing algorithm for network of homogeneous and id-less biomedical sensor nodes (RAIN). In: Proceedings of the IEEE sensors applications symposium, Atlanta, GA, USA, pp 68–73

18. Takahashi D, Xiao Y, Hu F (2007) LTRT: least total-route temperature routing for embedded biomedical sensor networks. In: Proceedings of the IEEE global telecommunications conference. Washington, DC, USA, pp 641–645. https://doi.org/10.1109/GLOCOM2007125

19. Anirban B, Bassiouni MA (2006) Energy efficient thermal aware routing algorithms for embedded biomedical sensor networks. In: Proceedings of the IEEE international conference mobile ad hoc and sensor systems (MASS'06). Vancouver, BC, Canada, pp 604–609. https://doi.org/10.1109/MOBHOC2006278619

20. Tang Q, Tummala N, Gupta SK, Schwiebert L (2005) TARA: thermal-aware routing algorithm for implanted sensor networks. In: Proceedings of the 1st IEEE international conference distributed computing in sensor systems. Marina del Rey, CA, USA, pp 206–217. https://doi.org/10.1007/11502593_17

21. Alghamdi TA (2016) Cluster based energy efficient routing protocol for wireless body area networks. Trends Appl Sci Res 11(1):12–16. https://doi.org/10.3923/tasr.2016.12.18

22. Watteyne T, Augé-Blum I, Dohler M, Barthel D (2007) Anybody: a self-organization protocol for body area networks. In: Proceedings of the ICST 2nd international conference on body area networks (BodyNets'07). Brussels, ICST Belgium, pp 6:1–6:7

23. Culpepper BJ, Dung L, Moh M (2004) Design and analysis of hybrid indirect transmissions (HIT) for data gathering in wireless micro sensor networks. ACM SIGMOBILE Mob Comput Commun Rev 8(1):61–83. https://doi.org/10.1145/980159.980169

24. Movassaghi S, Abolhasan M, Lipman J (2007) Energy efficient thermal and power aware (ETPA) routing in body area networks. In: Proceedings of the IEEE 23rd international symposium on personal, indoor and mobile radio communications. Sydney, NSW, pp 1108–1113. https://doi.org/10.1109/PIMRC20126362511

25. Liang X, Shen Q, Lu R, Lin X, Shen X, Zhuang W (2012) Exploiting prediction to enable secure and reliable routing in wireless body area networks. In: Proceedings of the 31st annual IEEE international conference on computer communications. Orlando, FL, USA, pp 388–396. https://doi.org/10.1109/INFCOM20126195777

26. Maskooki A, Soh CB, Gunawan E, Low KS (2011) Opportunistic routing for body area networks. In: Proceedings of the IEEE consumer communications and networking conference (CCNC'11). Las Vegas, NV, USA, pp 237–241. https://doi.org/10.1109/CCNC20115766463

27. Latre B, Braem B, Moerman I, Blondia C, Reusens E, Joseph W, Demeester P (2007) A low-delay protocol for multihop wireless body area networks. In: Proceedings of the 4th annual international conference mobile and ubiquitous systems: networking and services. Philadelphia, PA, USA, pp 1–8. https://doi.org/10.1109/MOBIQ.2007.4451060

28. Ruzzelli AG, Jurdak R, O'Hare GM, Van Der Stok P (2007) Energy-efficient multi-hop medical sensor networking. In: Proceedings of the 1st ACM SIGMOBILE international workshop on systems and networking support for healthcare and assisted living environments. San Juan, Puerto Rico, ACM New York, USA, pp 37–42. https://doi.org/10.1145/1248054.1248064

29. Braem B, Latre B, Moerman I, Blondia C, Demeester P (2006) The wireless autonomous spanning tree protocol for multihop wireless body area networks. In: Proceedings of the 3rd annual international IEEE conference on mobile and ubiquitous systems: networking and services. San Jose, CA, USA, pp 1–8. https://doi.org/10.1109/MOBIQ.2006.340421

Numerical Investigations of Mixing Performance in Split and Recombine Micromixer

Ekta Tripathi, Promod Kumar Patowari, and Sukumar Pati

1 Introduction

In this modern era, quick and uniform mixing is essential in various microfluidic areas such as LOC (lab on the chip) devices, μ-total analysis systems, biological and chemical synthesis [1–4]. In microfluidic devices, the mixing of fluids depends on molecular diffusion that reduces the mixing time of fluids due to laminar characteristics of flow. Various active and passive micromixers have been designed by several researchers with the purpose of increasing the mixing performance. Active micromixers require an external drive to generate energy for stirring the fluids to achieve fast mixing [1, 3–5], whereas in passive micromixers, mixing can be upgraded by designing or altering the geometries and shapes of the micromixers.

Several numerical and experimental studies have been performed in various micromixers as these micromixers are easy to fabricate by soft lithography techniques [6–8]. Mixing characteristics are analyzed in various micromixers by implementing various design concepts such as multiwave, square wave, zigzag, C-type, spiral contours. Channel walls are modified by ribs and grooves, placing the obstacles in the micromixers to disturb the flow are also introduced in order to enhance the mixing [9–14]. Sudarsan and Ugaz [15] considered planar split and recombine (S-R) and asymmetric serpentine micromixers to examine the mixing and flow characteristics of fluids. Both micromixers are found efficient in short downstream length. Hossain and Kim [16] analyzed mixing performance of water and ethyl alcohol in 3D serpentine S-R micromixer having special type segments (OH segments) and

E. Tripathi (✉) · P. K. Patowari · S. Pati
Mechanical Engineering Department, NIT Silchar, Silchar, Assam, India
e-mail: ekta_rs@mech.nits.ac.in

P. K. Patowari
e-mail: ppatowari@mech.nits.ac.in

S. Pati
e-mail: sukumar@mech.nits.ac.in

reported that SAR micromixer is more efficient than serpentine one. Hossain et al.
[17] proposed an unbalanced three split rhombic sub-channel-based micromixer for
studying the mixing and flow characteristics for $30 \leq Re \leq 80$ and reported high
mixing efficiency. Raza et al. [18] also used the concept of S-R in 3D serpentine
micromixers with crossing channels by generating saddle type flow arrangement,
which increases the chaotic advection even at low Reynolds numbers.

Numerous studies have been performed in S-R micromixers by various
researchers. From the literature, it has been observed that nominal work has been
done on different configurations of S-R geometry. In this paper, various types of
S-R micromixers are designed by changing the shape of wall boundaries and inside
grooves to examine the effect of shapes of S-R micromixers on the mixing perfor-
mance of fluids in the micromixers. Mixing characteristics and pressure drop of
mixing fluids are compared in these micromixers for low ranges of Re.

2 Problem Statement

First, a split and recombine (S-R) micromixer is designed having a square inner
groove and square wall boundaries as shown in Fig. 1a, and the geometry is abbrevi-
ated as SiSo. Two fluids enter the micromixers in two opposite sides. The main width
of the micromixers is 0.1 mm. After traveling 0.5 mm in the main mixing chamber,
fluids split and again recombine in the square grooves-based chamber. Both width
and depth of the outer square grooves are 0.2 mm whereas the width and depth of
inner grooves are 0.1 mm. Eight such chambers are designed at 0.1 mm distance.
The exit length is 0.5 mm. Figure 1b represents the second S-R geometry (TiTo) with
triangular inner grooves and triangular outer wall boundaries. Figure 1c represents
the S-R geometry (abbreviated as SiTo) in which the inner grooves are square and
outer wall boundaries are triangular. The fourth micromixer (abbreviated as TiSo) is
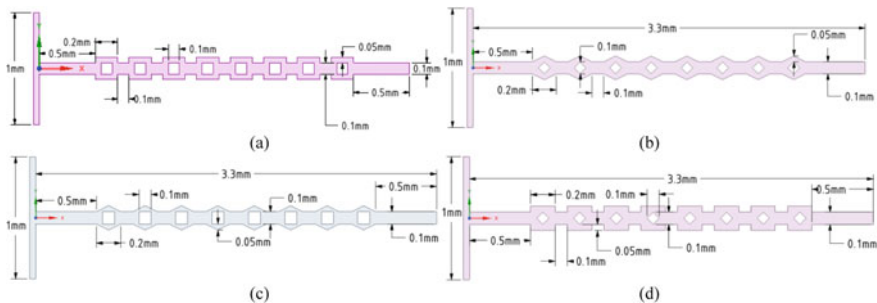
Fig. 1 Schematics of S-R micromixers. (**a**) Both outer boundary and inner grooves of square shape
(SiSo), (**b**) Both outer boundary and inner grooves of triangular shape (TiTo), (**c**) Outer boundary
of triangular and inner of square shape (SiTo), (**d**) Outer boundary of square shape and inner of
triangular shape (TiSo)

designed with triangular inner grooves and square outer wall boundaries. The sizes of all these grooves are taken exactly the same.

3 Mathematical Formulation

The velocity and pressure fields for a two-dimensional, steady-state, laminar, incompressible, isothermal, and single-phase flow in the micromixers are acquired using equations of continuity and Navier stokes for Newtonian fluids.

$$\nabla.\left(\vec{U}\right) = 0 \tag{1}$$

$$\left(\vec{U}.\nabla\right)\vec{U} = -\frac{1}{\rho}\nabla P + \nu\left(\nabla^2\vec{U}\right) \tag{2}$$

Here, $\vec{U}$ is the velocity vector, ρ is the fluid density (kg m^{-3}), P is pressure (Pa), ν is kinetic viscosity of fluids (ms^{-2}).

The concentration field is obtained by solving the species transport equation as follows:

$$\left(\vec{U}.\nabla\right)C = \alpha\left(\nabla^2 C\right) \tag{3}$$

Here, C is the concentration of the species (mol-m^{-3}) and α is the coefficient of diffusion (m^2 s^{-1}).

Uniform inlet velocity and atmospheric pressure at the outlet and 0 slip boundary conditions at the walls are considered.

The mixing quality is quantified by the mixing index. It is determined by calculating the standard deviation of species in the perpendicular plane to the fluid flow. The standard deviation of the mass fraction of the fluid in any mixture at a cross-sectional plane is considered as

$$SD = \sqrt{\frac{\sum_{j=1}^{r}(C_j - \overline{C_k})^2}{r}} \tag{4}$$

where SD is standard deviation of mass fraction in the particular cross-sectional area, r is overall number of sampling points, C_j is the mass fraction at sampling point j, and $\overline{C_k}$ is average mixing mass fraction. After calculating the SD, the mixing index (MI) is calculated as

$$MI = 1 - \frac{SD}{SD_{max}} \tag{5}$$

where SD_{max} is the standard deviation of the completely unmixed state. It may be noted that the range of MI is 0 for fully unmixed fluids to 1 for fully mixed fluids.

4 Numerical Simulations

Numerical simulations are performed in Ansys-18.1 (Fluent). Water and water-dye solution are used as fluids for mixing. The viscosity of water is 0.9×10^{-3} Pa-s and density is 1000 kg/m^3. The diffusion coefficient for water and water-dye solution is taken as 1.2×10^{-9} m^2/s. The SIMPLEC algorithm is applied for the pressure and velocity compounding. Second order upwind scheme is selected for discretization of the advection terms. For convergence, root mean square (RMS) residual is set as 10^{-5}.

A detailed grid independency test is carried out to select the grid for actual simulation in order to minimize the computational cost and time without compromising the accuracy. A graph has been plotted (Fig. 2) between pressure drop and mixing index with the total number of elements for each micromixer configuration. From the graph, it is obvious that pressure drop and mixing index are constant after a certain value of elements. From the graph plot, grids with 326,903, 195,108, 328,959, and
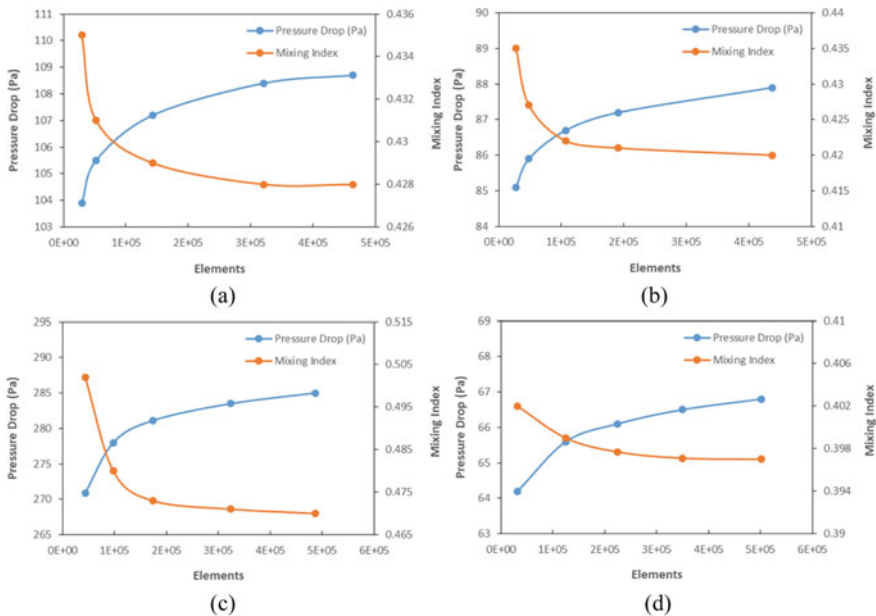
Fig. 2 Variation of pressure drop (on the primary vertical axis) and mixing index (on the secondary vertical axis) with grid elements (on the horizontal axis) for grid-independent test for micromixer **a** SiSo, **b** TiTo, **c** SiTo and **d** TiSo
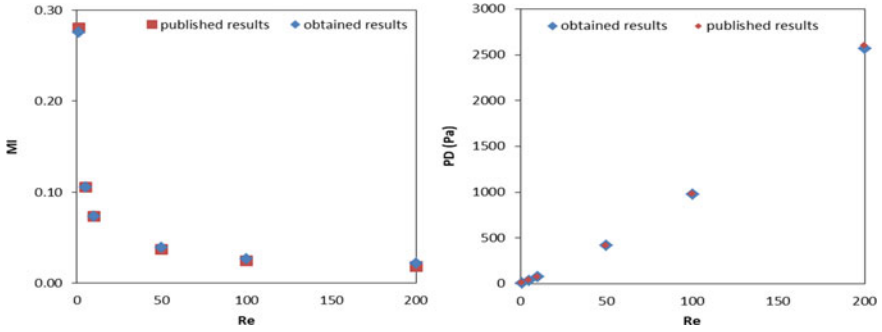
Fig. 3 Validation of (**a**) MI (mixing index) and (**b**) pressure drop with Re with the results reported in [19]

354,679 number of elements are selected for SiSo, TiTo, SiTo, and TiSo micromixers, respectively, for further calculations.

To ensure the accuracy of adopted numerical methodology in the present work, the solver is validated by comparing the mixing index and pressure drop with the results reported in [19] for a T-shape micromixer as presented in Fig. 3. As shown in Fig. 3a, b obtained and published results are compared, and it shows that both results are approximately the same, which proves the authenticity of the simulation work.

5   Result and Discussion

The focus of the work is to analyze the effect of groove shapes on the mixing characteristics of fluids and pressure-drop in the split and recombine (S-R) microchannels
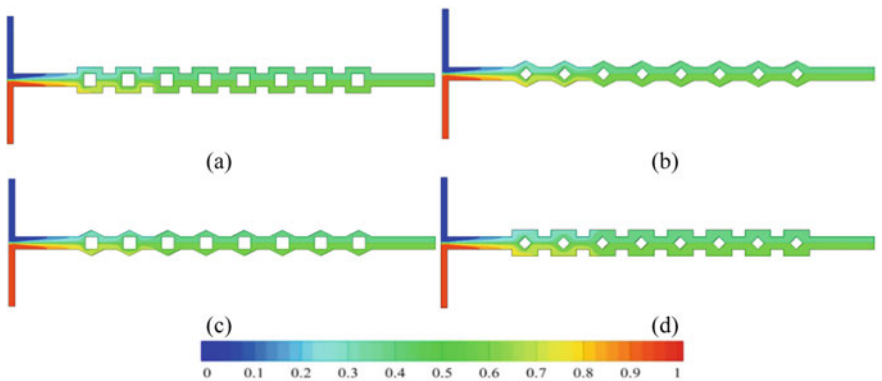
Fig. 4 Concentration contours of water at Re = 0.1 in (**a**) SiSo, (**b**) TiTo, (**c**) SiTo and (**d**) TiSo

for Reynolds number in the range of $0.1 \leq Re \leq 1$. Figure 4 represents the concentration contours of fluids at $Re = 0.1$ in each micromixer. Two fluids enter into the microchannel. For ideal mixing, the concentration plot should be uniform at the outlet of the channel throughout the cross-section. It is seen that at $Re = 0.1$, from chamber 3 onwards, almost green color appears, indicating the proper mixing in the channel. It is because of the low velocities of fluids at $Re = 0.1$, mixing or diffusion time to mix the fluids is more. Figure 5 represents the concentration contours of fluids at $Re = 0.6$ in all the micromixers. Here, mixing is diminished than that of $Re = 0.1$ as when Re is increased to 0.6, the significant difference in the concentration can be seen in each micromixer. For $Re = 1$, the difference in the concentration increases more, as shown in Fig. 6. It indicates the lower mixing efficiency of the fluids at a higher Reynolds number. The trends of concentration contours in all the micromixers are almost the same with Re.
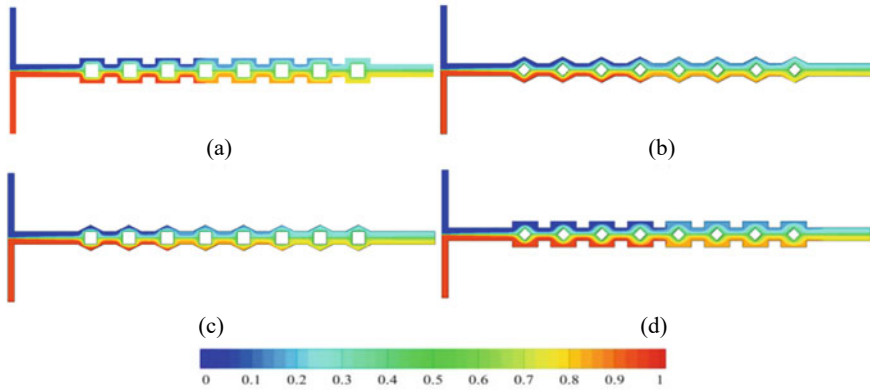
Fig. 5 Concentration contours of fluids at $Re = 0.6$ in (**a**) SiSo, (**b**) TiTo, (**c**) SiTo and (**d**) TiSo
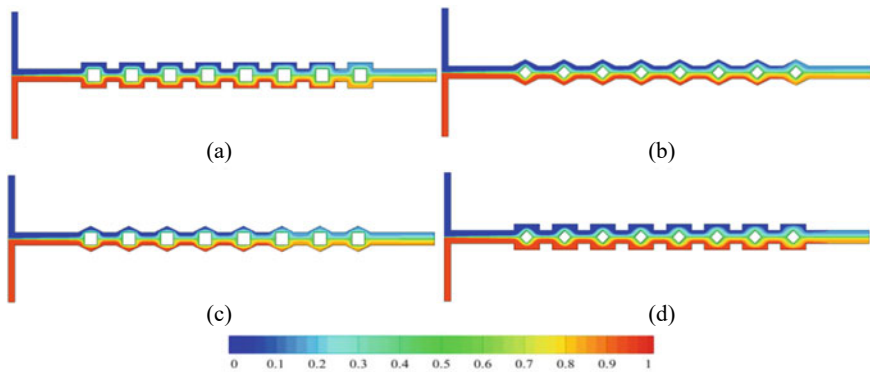
Fig. 6 Concentration contours of fluids at $Re = 1$ in (**a**) SiSo, (**b**) TiTo, (**c**) SiTo and (**d**) TiSo
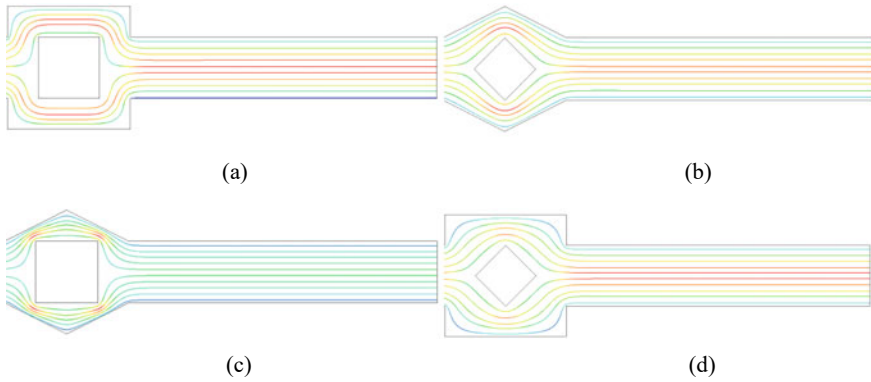
Fig. 7 Streamlines distribution in micromixers at Re = 1 in (**a**) SiSo, (**b**) TiTo, (**c**) SiTo and (**d**) TiSo micromixers

For the more comprehensive detail, streamlines distribution near the outlet in each micromixer is shown in Fig. 7 at Re = 1. Streamlines distribution are almost identical in SiSo and TiTo, as represented in Fig. 7a, b. It is clearly depicted that streamlines in SiTo (Fig. 7c) are closely packed near to the grooves, whereas in TiSo as shown in Fig. 7d, these streamlines maintain an almost equal distance from each other. This representation of streamlines in the microchannel shows the cause of different mixing indexes in the microchannel. Closely packed streamlines result in higher mixing than that of others.

The mixing index for different micromixers is compared at various Reynolds numbers in Fig. 8a. At Re = 0.1, the value of MI is the maximum, and it is almost the same for all the geometry. The change in the flow path has almost no influence because of the sufficient time for diffusion. It is observed that MI decreases with an increase in Re. It is due to a reduction in the diffusion mixing time with Re, and the homogeneity is completely diffusion controlled. The value of the mixing index is the highest in SiTo, whereas in TiSo, it is the lowest for Re $\geq$ 0.2. The values
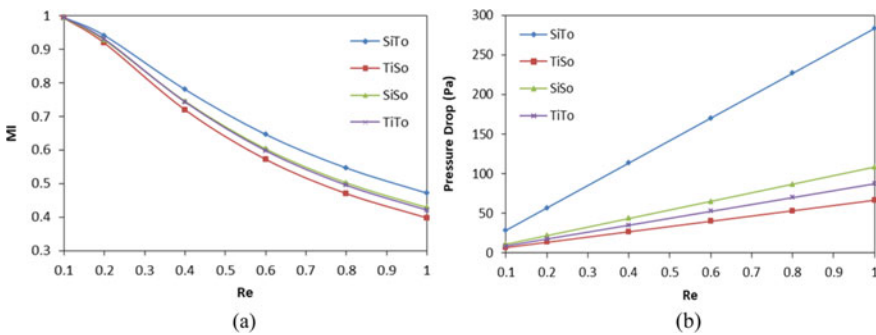
Fig. 8 Variation of (**a**) mixing index with Re and (**b**) pressure drop with Re for different micromixers

of the mixing index are almost the same for SiSo and TiTo micromixers, even for
Re ≥ 0.2. The flow passages of two fluids in the micromixers are divided and again
recombined and importantly, the shape of the groves modulates the same. In SiTo,
more fluids come in contact because of the confined passage, and the fluids mixing
takes place as it comes in contact more rapidly. That is why the mixing index in SiTo
is more than that of other micromixers. On the other hand, in TiSo, fluids do not have
enough contact to diffuse into each other, leading to the lower mixing index.

It is also vital to analyze the pressure drop in each micromixer. A pressure drop
indicates the required driving force for fluid flow inside the micromixers. The pressure
drop and Re graph for various micromixer geometry are demonstrated in Fig. 8b.
From Fig. 8b, it is clear that the pressure drop increases with an increase in Re.
The high value of Re means an increase in velocity that leads to the high-pressure
drop irrespective of any geometrical parameters. On comparing, the pressure drop
in different micromixer geometry for any values of Re, the pressure drop is the
maximum in SiTo due to the more losses incurred in the flow as shown by the curva-
ture of the streamlines (Fig. 7c). The difference of pressure drop between different
configurations increases with Reynolds number.

6 Conclusion

In this present paper, pressure drop and flow characteristics are analyzed for two-
dimensional, Newtonian, incompressible, steady flows in various split and recombine
(S-R) micromixers. Four different configurations of micromixers are designed by
considering the different shapes of grooves. The mixing characteristics and pressure
drop for Re ranges from 0.1 to 1 are analyzed in the designed micromixers. The main
outcomes of this research are concluded as:

- The mixing index reduces at higher Reynolds number in all the micromixers. At
  Re = 0.1, the mixing is the maximum, and the value is almost the same for all the
  geometry.
- The pressure drop increases with the Reynolds number for all the micromixers.
  Maximum pressure drop of 283 Pa at Re = 1 and minimum of 28 Pa at Re =
  0.1 is observed in SiTo, whereas maximum pressure drop of 66 Pa at Re = 1 and
  minimum of 6.7 Pa at Re = 0.1 are observed in TiSo.
- The mixing quality is the highest in SiTo, whereas in TiSo, it is the lowest for
  Re ≥ 0.2. The mixing index values are approximately equal for SiSo and TiTo
  micromixers, even at Re ≥ 0.2.
- Even though SiTo shows highest mixing index but due to the high-pressure drop, it
  is not recommended whereas TiTo shows second-best mixing index and relatively
  much lower pressure drop in the channel than that of SiTo. Thus, TiTo could be
  used for industrial mixing purposes.

References

1. Nguyen N (2011) Micromixers: fundamentals, design and fabrication. Elsevier Science, Netherlands
2. Ingham CJ, van Hylckama Vlieg JE (2008) MEMS and the microbe. Lab Chip 8(10):1604–1616
3. Hessel V, Löwe H, Schönfeld F (2005) Micromixers—a review on passive and active mixing principles. Chem Eng Sci 60(8–9):2479–2501
4. Nguyen NT, Wu Z (2005) Micromixers—a review. J Micromech Microeng 15:R1
5. Mehta SK, Pati S, Mondal PK (2021). Numerical study of the vortex induced electroosmotic mixing of non-Newtonian biofluids in a non-uniformly charged wavy microchannel: effect of finite ion size. Electrophoresis. https://doi.org/10.1002/elps.202000225
6. Tripathi E, Patowari PK, Pati S (2019) Fabrication of spiral micromixer using mold machined by CO_2 assisted laser machine. In: Paper presented at 11th international conference on precision, meso, micro and nano engineering (COPEN 11). IIT Indore, 12–14 Dec 2019
7. Mondal B, Pati S, Patowari PK (2020) Fabrication of wavy micromixer using soft lithography technique. Mater Today Proc 26:1271–1278
8. Mondal B, Pati S, Patowari PK (2021) Serpentine square wave microchannel fabrication with WEDM and soft lithography. Mater Today Proc. https://doi.org/10.1016/j.matpr.2021.03.519
9. Mondal B, Mehta SK, Patowari PK, Pati S (2019) Numerical study of mixing in wavy micromixers: comparison between raccoon and serpentine mixer. Chem Eng Process Process Intensifi 136:44–61
10. Mondal B, Pati S, Patowari PK (2020) Numerical analysis of mixing performance in microchannel with different ratio of outlet to inlet width. In: Techno-societal 2018. Springer, Cham, pp 257–266
11. Tripathi E, Patowari PK (2020) Design and computational analysis of spiral microchannel for mixing of fluids. In: Techno-societal 2018. Springer, Cham, pp 305–313
12. Tripathi E, Patowari PK, Pati S (2021) Comparative assessment of mixing characteristics and pressure drop in spiral and serpentine micromixers. Chem Eng Process Process Intensifi 162:108335
13. Mondal B, Pati S, Patowari PK (2019) Analysis of mixing performances in microchannel with obstacles of different aspect ratios. Proc Inst Mech Eng Part E J Process Mech Eng 233(5):1045–1051
14. Mondal B, Pati S, Patowari PK (2020) Influence of confluence angle between inlets on the mixing performance of micro-mixer with obstacles. In: Techno-societal 2018. Springer, Cham, pp 275–283
15. Sudarsan AP, Ugaz VM (2006) Multivortexmicromixing. Proc Natl Acad Sci 103(19):7228–7233
16. Hossain S, Kim KY (2015) Mixing analysis in a three-dimensional serpentine split-and-recombine micromixer. Chem Eng Res Des 100:95–103
17. Hossain S, Kim KY (2014) Mixing analysis of passive micromixer with unbalanced three-split rhombic sub-channels. Micromachines 5(4):913–928
18. Raza W, Hossain S, Kim KY (2018) Effective mixing in a short serpentine split-and-recombination micromixer. Sens Actuators B Chem 258:381–392
19. Solehati N, Bae J, Sasmito AP (2014) Numerical investigation of mixing performance in microchannel T-junction with wavy structure. Comput Fluids 96:10–19

FEA Investigation of Repaired Composite Under Low Velocity Impact

Punita Kumari [ORCID]**, Ashraf Alam, Saahil, and Jihui Wang**

1 Introduction

Glass fiber reinforced polymer (GFRP) is being used in wind turbine, naval, space, sports and vehicle industries. GFRP has numerous advantages such as light weight, anti-corrosion resistance properties and high stiffness, due to this properties it is been taken a good option against traditional metals. Several type of repair of composite is used but scarf repair is widely applicable for wind turbine, boat and automobile due to less extra addition of material weight and smooth surface. Besides several advantages GFRP are prone to impact load these load developed due to bird strike, collision with object, etc. [1–3]. These impact incidents lead to damages such as matrix damages, fiber damage, fiber failure [4–6]. Simply replacement of the composite is not option if the stiffness and strength could be restoring by repair.

Extensive study was reported about progressive damage approach [7], besides few study was reported based upon inter laminar, intra laminar and delamination study [8, 9]. While FEA model for different velocities was studied [10]. Few researchers have developed VUMAT model for low velocity impact [11–14]. There are very limited investigation was done on the scarf angle or ratio effect of the repaired GFRP

P. Kumari (✉)
School of Aeronautical Sciences, Hindustan University, Chennai, Tamil Nadu 603103, India
e-mail: punita@whut.edu.cn

P. Kumari · Saahil · J. Wang
School of Material Science and Engineering, Wuhan University of Technology, 122 Luoshi Road, Wuhan 430070, China
e-mail: saahil@whut.edu.cn

J. Wang
e-mail: jhwang11@whut.edu.cn

A. Alam
Rekhi Centre of Excellence for the Science of Happiness, Indian Institute of Technology, Kharagpur, India

composite laminates. Hence, this paper concentrated on scarf angle of the repaired laminate under drop weight impact test. Novelty of this research work is to explore Hashin's failure criteria on scarf repaired laminates with different ranging of scarf ratio. In order to get this finite element model for scarf repair composite was created with various scarf angle and subjected to low velocities impact.

2 Finite Element Model

Hashin failure criteria is generally used by several researches because it is easy implementation [15–20]. A FE model was developed for unidirectional fiber composite during fiber and matrix failure criteria taken into account. Generated model give information about matrix tension, matrix compression, fiber tension and fiber compression damages inside every ply that reduces the stiffness of structure. Traction–separation laws and the Benzeggah-Kenane (BK) mixed-mode law [16, 17] taken in account in order to calculate the damage and failure behavior.

Tensile fiber mode

$$\widehat{\sigma_{11}} \geq 0$$
$$\left(\frac{\widehat{\sigma_{11}}}{X_t}\right)^2 + \left(\frac{\widehat{\sigma_{12}}}{S_L}\right)^2 = 1 \tag{1}$$

Compressive fiber mode

$$\widehat{\sigma_{11}} \leq 0$$
$$\left(\frac{\widehat{\sigma_{11}}}{X_c}\right)^2 = 1 \tag{2}$$

Tensile matrix mode

$$\widehat{\sigma_{22}} \geq 0$$
$$\left(\frac{\widehat{\sigma_{22}}}{Y_t}\right)^2 + \left(\frac{\widehat{\sigma_{12}}}{S_L}\right)^2 = 1 \tag{3}$$

Compressive matrix mode

$$\widehat{\sigma_{22}} \leq 0$$
$$\left(\frac{\widehat{\sigma_{22}}}{2S_t}\right)^2 + \left[\left(\frac{Y_c}{2S_T}\right)^2 - 1\right]\frac{\widehat{\sigma_{22}}}{Y_c} + \left(\frac{\widehat{\sigma_{12}}}{S_L}\right)^2 = 1 \tag{4}$$

$$K_1 = \frac{2G_{13}}{e}; \quad K_2 = \frac{2G_{23}}{e}; \quad K_3 = \frac{E_3}{e}$$

In order to achieve better results, FE-model (Parent, patch and impact ball) was produced in ABAQUS/CAE 2018 with an explicit analysis was selected in this
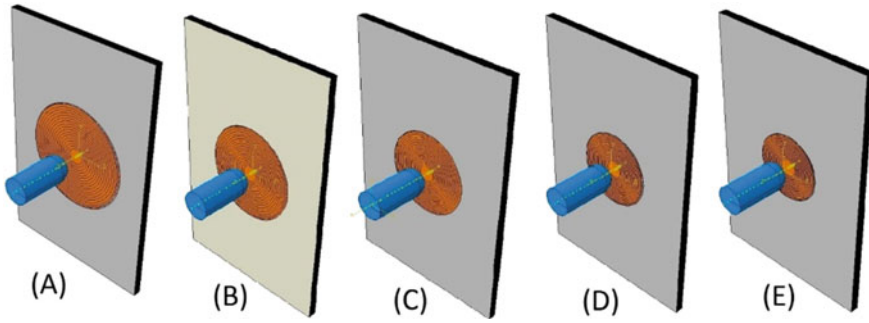
Fig. 1 FE model of composite with **a** 10° **b** 12° **c** 14° **d** 16° **e** 18°

research work. A FE-model was created that contains three different sub-parts: parent laminate, patch and impact dart (Fig. 1). Dimension was assigned to parent sample, i.e., 150 mm length 100 mm width 4.8 mm thickness additionally 5 mm radius base hole with range of scarf angle (10°–18°) circular scarf hole was generated. Same architecture is used for parent and scarf patch was laminates was generated and $[0/90/90/0]_{2s}$ ply sequence assigned. The material parameters were used to perform the numerical simulation was calculated through experimental testing, author was done all additional experimental tests [5, 6, 20]. A same material property was assigned to parent and patch laminates mentioned in Tables 3 and 4. Both parent and patch were distributed into 16 sections and been allocated to fiber angle as per stacking sequence. A scarf patch was generated with 10 mm diameter base hole and scarf angle given as per parent laminate. Continuum shell elements (SC8R) was used for meshing both parent and patch. An impact dart was developed with 16 mm diameter and 8.9 kg reference mass assigned to it addition more rigid element R3D4 was used to meshing. Full composite laminate was meshed with the coarse element size while fine meshed was done at impact zone. The mesh convergence study was done showed in Fig. 2. Moreover, to control the instabilities of mesh an hourglass
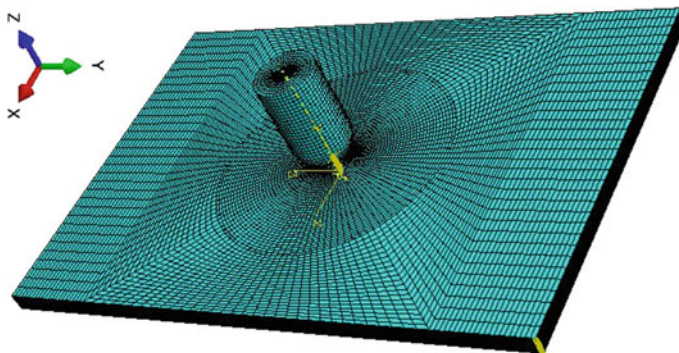
Fig. 2 Meshing of the composite sample

Table 1 Details of test laminates

Laminate series	GFRP code	Scarf angle (°)	Impact location	Impact energy (J)	Number of samples
S-series	S1	10	At center	12	3
	S2	12			3
	S3	14			3
	S4	16			3
	S5	18			3

Table 2 Impact ball details [20, 22–25]

Weight of impact ball	8.9 kg
Diameter of impact ball	16 mm
Number of fibers layers	16

control was chosen in this study. In order to avoid the case of large deformation issue, unpredictable element distortion frequently take place at integration point are assigned zero that is tends to abort the running simulation of impact test.

Movement of the impact dart was fixed to all axis except for Z-direction. Impact ball free to move in Z-direction and amplitude verse time (calculated from earlier experimental), these value normalized [21]. Boundary condition around the composite laminate edge was made fix (Tables 1, 2, 3 and 4).

Table 3 Material properties of composite (E-glass/sw905-2 lamina) [20, 22–25]

E_1 (GPa)	$E_2 = E_3$ (GPa)	$\upsilon_{12} = \upsilon_{13}$	υ_{23}	$G_{12} = G_{13}$ (GPa)	G_{23} (GPa)
45.6	8.20	0.278	0.365	5.83	3
S12 = S13 (MPa)	S23 (MPa)	G_{1t} (mJ/mm^2)	G_{1C} (mJ/mm^2)	G_{2T} (mJ/mm^2)	G_{2C} (mJ/mm^2)
65.26	46.00	2691.68	5431.05	69.83	1244.4
X_T (MPa)	X_C (MPa)		$Y_T = Z_T$ (MPa)		$Yc = Zc$ (MPa)
566.67	241.38		20.69		82.96
K_{11}	Ks		Kt		Density (kg/m^3)
41e13	29.15e13		29.15e13		2089.34

Table 4 Cohesive parameter used for composite [20, 22–25]

t_n (MPa)	T_s (MPa)	t_t (MPa)	GIC (mJ/mm^2)	GIIC (mJ/mm^2)	GIIIC (mJ/mm^2)	β	Density (kg/m^3)
126	252	252	162.66	325.32	325.32	1.45	1366.05

2.1 Mesh Convergence Study

A proper meshing analysis method approach was carried out; therefore, a performance of mesh convergence was done in order to obtain good and reliable result. The mesh element was for the repaired composite laminates assembly containing a scarf hole parent laminate, a scarf patch laminate and impact ball together around 285,259. Simulation time taken by each model was 29 h. The mesh convergence study was carried out and result is displayed in Figs. 2, 3, 4, 5 and 6. It was noticed that 285,259 elements is enough for FE model and simulation time taken by model is 29 h. Because of poor mesh around the curvatures, mass scale was introduced to the model to make sure the bad or poor mesh element does not affect the steady time increment.
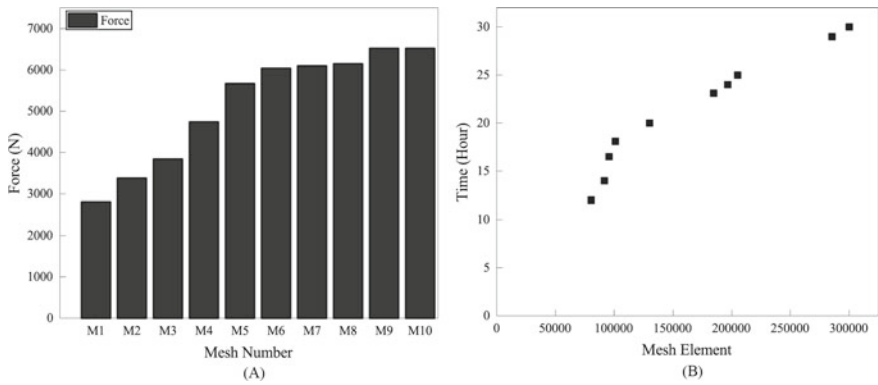
Fig. 3 **a** Force value obtained through various meshing element and compared. **b** Time taken during simulation with refine mesh

Fig. 4 FE-result force–time of composite sample S1
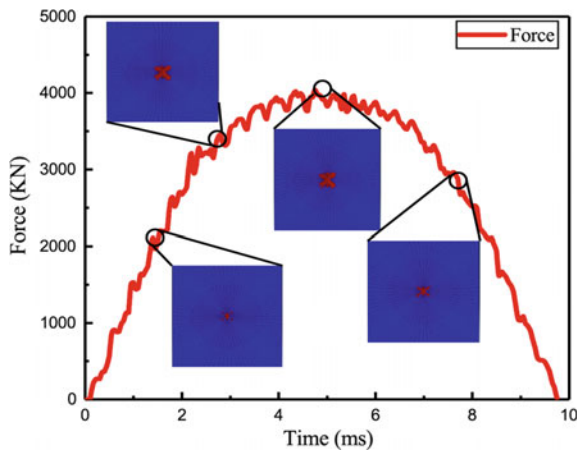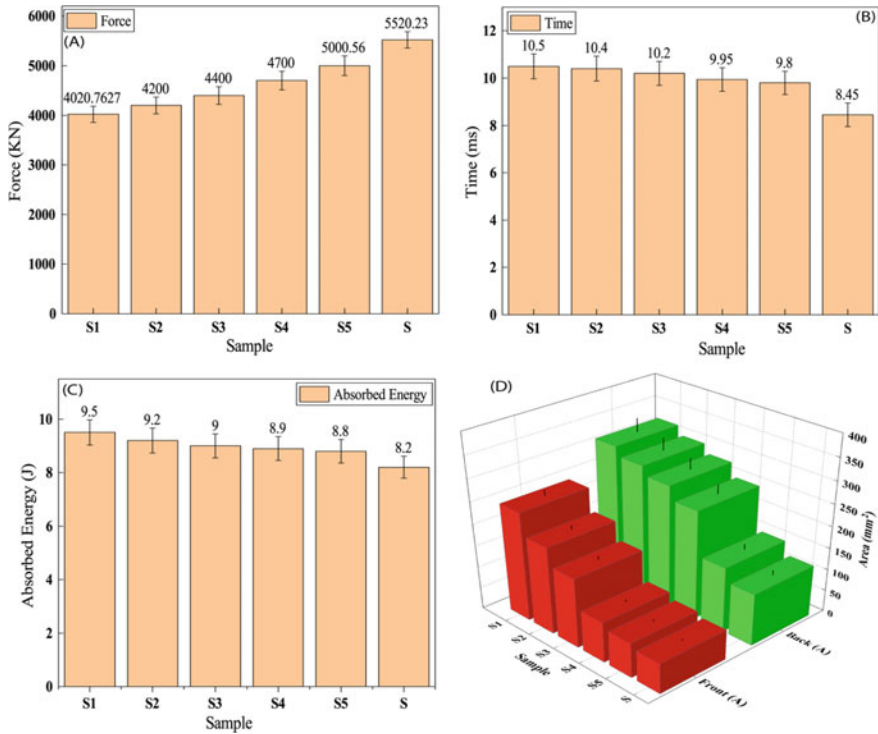
Fig. 5 FE-simulation performance of **a** peak force, **b** time interval, **c** absorbed energy **d** damaged area

3 Result and Discussion

Impact test at the scarf angle variation laminates was studied and presented in previous sub-section. The force–time, curve result of repaired laminate under low velocity impact investigated through FE and presented Fig. 4. A dynamic response of the repaired laminate subjected 10 J impact energy was demonstrated in Fig. 4. It was also observed that the maximum force obtained through the FE-analysis starts gradually dropping after the attainment the peak force value. A result values attained of peak force, time duration, damage region, through FE-simulation for repaired laminate is shown in Table 5 and Fig. 5.

From the Fig. 5a it is clearly demonstrated the contact force values that is listed as per following order is: S1 > S2 > S3 > S4 > S5 > S. The impact time interval during impact drop procedure also illustrated in Fig. 5b and that is given ranking as follow S < S5 < S3 < S4 < S2 < S1. The energy absorption through the repaired and original (non-repaired) laminates was investigated from graph shown in Fig. 5c. The absorb energy of S-series laminates was given in the order as follow: S1 > S2 > S3 > S4 > S5 > S.
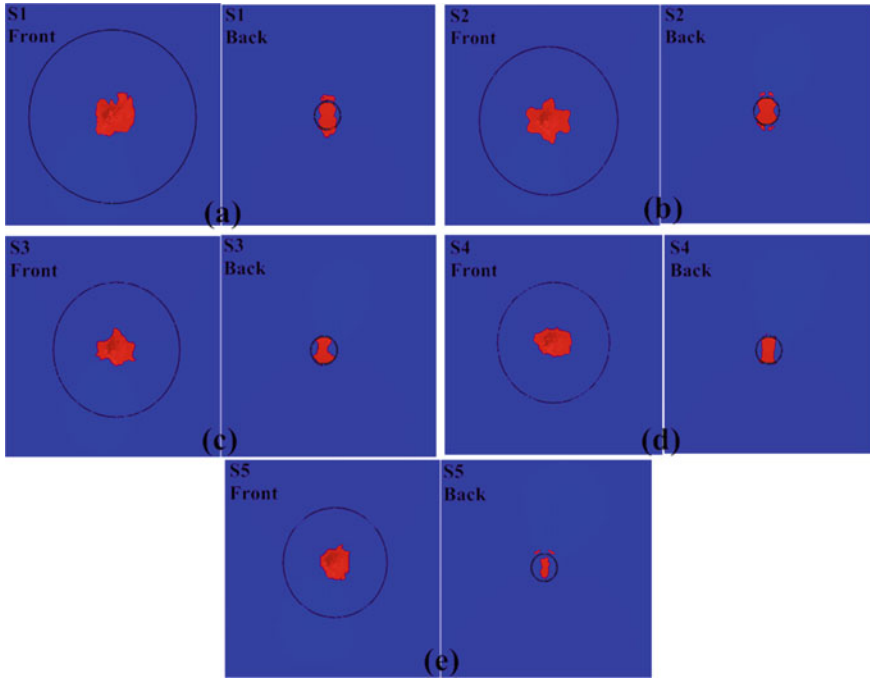
Fig. 6 Failure at the frontal and rear surface of samples **a** S1 **b** S2 **c** S3 **d** S4 and **e** S5

Table 5 FE-simulation performance of impact test

Samples	Peak force (N)	Impact time interval (ms)	Absorbed energy (J)
S	5520.23	8.45	8.2
S1	4020.7627	10.5	9.5
S2	4200	10.4	9.2
S3	4400	10.2	9
S4	4700	9.95	8.9
S5	5000.56	9.8	8.8

Impact position was selected at the center of the repaired laminate for S-series. Figure 5 demonstrated the analysis of each case of S-series repaired composite and original through FE-analysis figures. All frontal face of samples displayed the dent during impact. An elastic phenomenon of the composite sample was discovered through force–time history; during FE-simulation, impact ball strikes at the repaired laminate and after transferring impact energy to the laminate it rebound back. Moreover force–time curve verified these presents a good argument that is shown in Fig. 4. The peak contact force, time interval, absorbed energy, damage area of repaired laminated determined through the FE-analysis result shown in Fig. 5. The force, impact

time interval and absorbed energy assimilated using FE-analysis was plotted to in Table 5. The upper top ply of composite patch obtained matrix cracks and first failure investigates in numerical analysis. A peanut shape of the damaged was developed on the patch and after impact ball was subjected to the laminates later on it spreads progressively as exposed in failure simulation photographs (Fig. 6). Induced stress at the front and back face of laminates are illustrated in Fig. 6. It was seen through the analysis, profile of the impact damage is progress after impact ball strike the composite laminates and enlarge with the impact time.

However, from non-destructive inspection test (NDT) it was clear that there is progressive crack occurred while collision of impact-laminate and only small crack showed up on the impacted outer surface through the thickness. It was determined that once failure attained to the last fiber sheet, shear failure shifts to matrix dominating tensile failure. Moreover, the results of FE-simulation of repaired and impacted attained more damage than the original sample (S) impacted that is understandable. The original samples exposed slightest damage compare to repaired ones while least scarf angle (10°) demonstrated maximum damage due to material removal from the parent laminate. For repaired laminates the sample repaired with less scarf angle and impacted at the center showed up extreme damages among all S-series samples, and the repaired with high scarf angle has performed attained least damages. Sample S5 showed most favorable result and demonstrated more similar and close result as original samples.

The absorbed energy variation by the repaired laminates S1, S2, S3, S4 and S5 compare to original laminate are—15.85%, 12.19%, 9.75%, 8.53% and 7.31% computed, respectively. The oscillation in the graph curves specify the internal and hidden damage of the repaired composites which can be identify through NDT test. The similar finding is comes up in reference [13, 26]. Figure 5, demonstrated FE results tests comparison. The contact force experienced by laminates, the absorbed energy, contact time interval, damage dent and damage FE values are plotted for comparison. From the bar graph Fig. 6 it is clear that the values are close and displayed same trend.

4   Conclusion

Scarf repair when done with scarf angles 10°, 12°, 14°, 16° and 18° is capable to recover impact strengths 15.85%, 12.19%, 9.75%, 8.53% and 7.31%, respectively. The increase in tensile strength due to the energy that was absorbed during the process exhibited the strength competence of scarf repair and disclosed that it upsurges with rise in scarf angle. Looking at impact results, it is implied that when the scarf angle is minimum then it has an enhanced potential to carry maximum force and consequently least amount of damage is incurred. While on the contrary, when the scarf repair of composite laminates is highest, it shows that damage is maximum in this case and usually takes long impact time when compared with all other samples. There is quite a sizeable conformity between energy that is absorbed and damage that is

induced in the process when experimented for diverse range of scarf angles under multiple variation of impact loads. It was also observed that matrix compression and fiber damage showed a relative increase when scarf angles were reduced. Meshing element with shell, however, did not provide any evidence for exact damage mode and occurrence of delamination was observed only among different samples of fiber ply. Had we instead used meshing with solid elements, it possibly would have provided relatively more detail.

Credit Authorship Contribution Statement Punita Kumari—Visualization, Writing manuscript draft, Software Analysis, Validation, Conceptualization, Simulation work, Investigation, Funding Procurement, and Data Curation. Ashraf Alam—Visualization, Validation, Formal Analysis, Conceptualization, and Review and Editing. Saahil—Writing manuscript draft, Validation, Software Analysis work, partially Methodology, and Investigation. Jihui Wang—Resource Procurement, Supervision, funding and Project administration.

Conflicts of Interest Authors while conduction of this research found no probable and latent conflict of interest.

References

1. Vishwas M, Joladarashi S, Kulkarni SM (2018) Modelling and analysis of material behaviour under normal and oblique low velocity impact. Mater Today Proc 5(2):6635–6644. https://doi.org/10.1016/j.matpr.2017.11.319

2. Mahesh V, Joladarashi S, Kulkarni SM (2020) Influence of laminate thickness and impactor shape on low velocity impact response of jute-epoxy composite: FE study. Mater Today Proc. https://doi.org/10.1016/j.matpr.2019.12.216

3. Raut NP, Kolekar AB, Gombi SL (2020) Methods of damage detection on composites under low velocity impact: review. Mater Today Proc. https://doi.org/10.1016/j.matpr.2019.12.406

4. Bogenfeld R, Kreikemeier J, Wille T (2018) Review and benchmark study on the analysis of low-velocity impact on composite laminates. Eng Fail Anal 86:72–99. https://doi.org/10.1016/j.engfailanal.2017.12.019

5. Kumari P, Wang J, Khan S (2018) Residual tensile strength of the multi-impacted scarf-repaired glass fiber-reinforced polymer (GFRP) composites. Materials (Basel) 11(12). https://doi.org/10.3390/ma11122351

6. Kumari P, Wang J, Saahil (2019) Tensile after impact test of scarf-repaired composite laminates. Arab J Sci Eng 44 (9):7677–7697. https://doi.org/10.1007/s13369-019-03857-z

7. Caputo F, Luca AD, Lamanna G, Borrelli R, Mercurio U (2014) Numerical study for the structural analysis of composite laminates subjected to low velocity impact. Compos Part B, 296–302. https://doi.org/10.1016/j.compositesb.2014.07.011

8. Caputo F, De Luca A, Lamanna G, Lopresto V, Riccio A (2015) Numerical investigation of onset and evolution of LVI damages in carbon-epoxy plates. Compos B Eng 68:385–391. https://doi.org/10.1016/j.compositesb.2014.09.009

9. Long S, Yao X, Zhang X (2015) Delamination prediction in composite laminates under low-velocity impact. Compos Struct 132:290–298. https://doi.org/10.1016/j.compstruct.2015.05.037

10. Caputo F, De Luca A, Sepe R (2015) Numerical study of the structural behaviour of impacted composite laminates subjected to compression load. Compos B Eng 79:456–465. https://doi.org/10.1016/j.compositesb.2015.05.007

11. Bienias J, Jakubczak P, Dadej K (2016) Low-velocity impact resistance of aluminium glass laminates—experimental and numerical investigation. Compos Struct 152:339–348. https://doi.org/10.1016/j.compstruct.2016.05.056

12. Liu PF, Liao BB, Jia LY, Peng XQ (2016) Finite element analysis of dynamic progressive failure of carbon fiber composite laminates under low velocity impact. Compos Struct 149:408–422. https://doi.org/10.1016/j.compstruct.2016.04.012

13. Liao BB, Liu PF (2017) Finite element analysis of dynamic progressive failure of plastic composite laminates under low velocity impact. Compos Struct 159:567–578. https://doi.org/10.1016/j.compstruct.2016.09.099

14. Zhang C, Duodu EA, Gu J (2017) Finite element modeling of damage development in cross-ply composite laminates subjected to low velocity impact. Compos Struct 173:219–227. https://doi.org/10.1016/j.compstruct.2017.04.017

15. Farooq U, Myler P (2016) Finite element simulation of damage and failure predictions of relatively thick carbon fibre-reinforced laminated composite panels subjected to flat and round noses low velocity drop-weight impact. Thin-Wall Struct 104:82–105. https://doi.org/10.1016/j.tws.2016.03.011

16. Khan SH, Sharma AP, Parameswaran V (2017) An impact induced damage in composite laminates with intra-layer and inter-laminate damage. Proc Eng 173:409–416. https://doi.org/10.1016/j.proeng.2016.12.039

17. Li Z, Khennane A, Hazell PJ, Brown AD (2017) Impact behaviour of pultruded GFRP composites under low-velocity impact loading. Compos Struct 168:360–371. https://doi.org/10.1016/j.compstruct.2017.02.073

18. Sotoa A, González EV, Maimí P, Mayugo JA, Pasquali PR, Camanho PP (2018) A methodology to simulate low velocity impact and compression after impact in large composite stiffened panels. Compos Struct 204:223–238. doi:https://doi.org/10.1016/j.compstruct.2018.07.081

19. Gliszczynskia A, Kubiaka T, Rozylob P, Jakubczakc P, Bieniaśc J (2019) The response of laminated composite plates and profiles under low-velocity impact load. Compos Struct 207:1–12. https://doi.org/10.1016/j.compstruct.2018.09.005

20. Kumari P, Alam A, Saahil (2020) Influence of the impact position on scarf repair composite under low velocity impact: FEA investigation. Mater Today Proc https://doi.org/10.1016/j.matpr.2020.09.323

21. Thorsson SI, Waas AM, Rassaianc M (2018) Low-velocity impact predictions of composite laminates using a continuum shell based modeling approach Part B: BVID impact and compression after impact. IJSS 155:201–212. https://doi.org/10.1016/j.ijsolstr.2018.07.018

22. Kumari P, Alam A, Saahil (2021) Multi-impact on scarf repaired composite laminates: FE investigation. Mater Today Proc 46:645-650. https://doi.org/10.1016/j.matpr.2020.11.584

23. Kumari P, Alam A, Saahil (2021) Analysis of the composite sample under low velocity multi-impact test: FEA investigation. In: Advances in engineering materials. Lecture notes in mechanical engineering, pp 505–514. https://doi.org/10.1007/978-981-33-6029-7_47

24. Kumari P, Alam A, Saahil WJ (2021) Estimation of low velocity impact on the scarf repair GFRP composite: experimental method. Mater Today Proc 43:731–739. https://doi.org/10.1016/j.matpr.2020.12.853

25. Kumari P, Alam A, Saahil WJ, Sankar SS (2021) Tensile after impact response on the scarf repaired glass fiber reinforced polymer samples—experimental approach. Mater Today Proc 43:112–123. https://doi.org/10.1016/j.matpr.2020.11.223
26. Tie Y, Hou Y, Li C, Zhou X, Sapanathan T, Rachik M (2018) An insight into the low-velocity impact behavior of patch-repaired CFRP laminates using numerical and experimental approaches. Compos Struct 190:179–188. https://doi.org/10.1016/j.compstruct.2018.01.075

Mapping Uncertain Surface Roughness of Inconel 718 in WEDM

S. Saha, S. R. Maity, and S. Dey

1 Introduction

Wire EDM is emerged as a versatile and potential advanced machining process in generating intricate and complex shaped products with high-dimensional accuracy and tight tolerances as demanded by the high-end industries like aerospace, automobile, medical, and nuclear industries [1–4]. Material removal mechanism relies on discrete spark discharges taking place between the electrically conductive wire and the workpiece of electrically conductive material. Dielectric fluid is introduced in the opening between the wire–workpiece combinations through a nozzle, which is essential to initiate the spark erosion process. Thus, hardness in particular and other mechanical properties of material is not imposing any practical constraint on this machining process. Further, there is no physical contact that exists between the tool (wire) and the workpiece material in the WEDM process driving toward complete elimination of mechanical stresses and formation of unwanted burrs on the machined surfaces. So, researchers in this domain are tempted to explore the WEDM machinability of newly developed electrically conductive materials of any hardness.

Wire EDM is an attractive option in machining fir tree slots of gas turbine disks as an alternative to traditional broaching [5, 6]. Besides, the material often employed in those critical areas is Inconel 718 (Ni-based superalloy) because it offers lucrative mechanical properties for a wider temperature window (cryogenic to elevated temperatures) compared to other candidate materials. However, the major challenge is to achieve desired level of accuracy and surface finish. Surface roughness is a vital parameter in the production of critical feature like fir tree slots as it affects its

S. Saha (✉) · S. R. Maity · S. Dey
Mechanical Engineering Department, National Institute of Technology Silchar, Silchar, India

S. R. Maity
e-mail: srmaity@mech.nits.ac.in

S. Dey
e-mail: sudip@mech.nits.ac.in
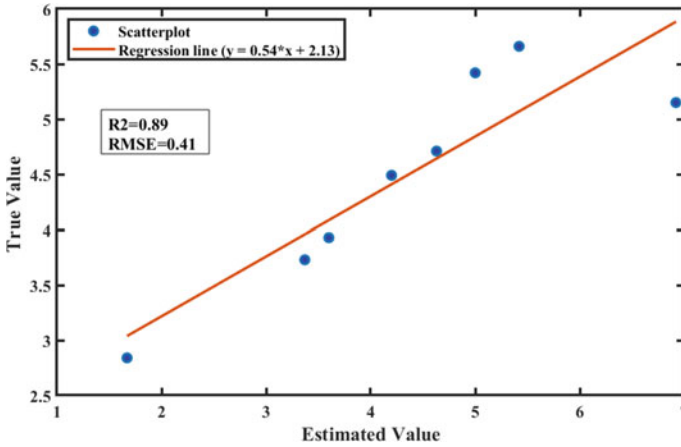
Fig. 1 Scatter plot

mechanical and tribological performances. Therefore, restricting the surface roughness to minimal value and studies pertaining to observe the effect of input factors on surface roughness have always been a research interest for the researchers and practitioners [7–9]. However, scarce literatures exist on wire EDM which sheds light on the random variations of process parameters and its subsequent impact on the responses. In this paper, wire tension, discharge current, wire speed, and pulse on time are considered as random factors. The randomness in those input factors is justified because of the complexity and unpredictable nature of the entire process mechanism, uncertainty in the gap conditions, uncertainty in the wire transport system due to unbalanced mechanical forces, the interactions between large numbers of process parameters. Therefore, it is attempted in this work to study the comprehensive probabilistic description of the surface roughness (SR) by considering the individual and compound effect of stochasticity in the input factors.

2 Mathematical Modeling

The correlation between the surface roughness (SR) and the process variables is developed using multiple linear regression (MLR) in MINITAB-17 statistical software based on data taken from the literature [10]. Out of the 27 number of samples, 19 samples are employed for building the model and the rest are employed for model validation. The developed model is presented below (Eq. 1). Besides, the scatter plot between the true value and the estimated value reveals that the model has good predictive capability ($R^2 = 0.89$ and RMSE $= 0.41$) (Fig. 1).

$$SR = -2.31 - 0.191 * WT - 0.0076 * WS + 0.132 * I + 0.604 * Ton$$

$$+ 0.00165 * WT * WS + 0.0262 * WT * I - 0.0293 * WT * Ton$$
$$- 0.000328 * WS * I - 0.000356 * WS * Ton - 0.01014 * I * Ton \quad (1)$$

where SR = surface roughness, WT = wire tension, WS = wire speed, and I = discharge current.

3 Effect of Parametric Uncertainty on Surface Roughness

3.1 Individual Effect of Stochasticity

Figure 2a–d shows the stochastic behavior of the surface roughness (SR) by means of probability density function plots corresponding to variations in the stochastic input factors. It is evident from the plots in Fig. 2a that the expected value of SR increases with increase in the mean value of discharge current. This is due to the formation of a large crater size because of higher discharge energy rendered by the higher discharge current in the spark gap. Furthermore, with the increase in the discharge current (I), the sparsity in the probability density function plots increases along with the decrease in the steepness of the distribution which endorses that the realizations tend to become more uniformly distributed at higher value of discharge current, thus jeopardizing the accuracy and precision of the expected SR. Figure 2b predicts that SR decreases with the increase in the wire tension which is primarily due to the reduction in the
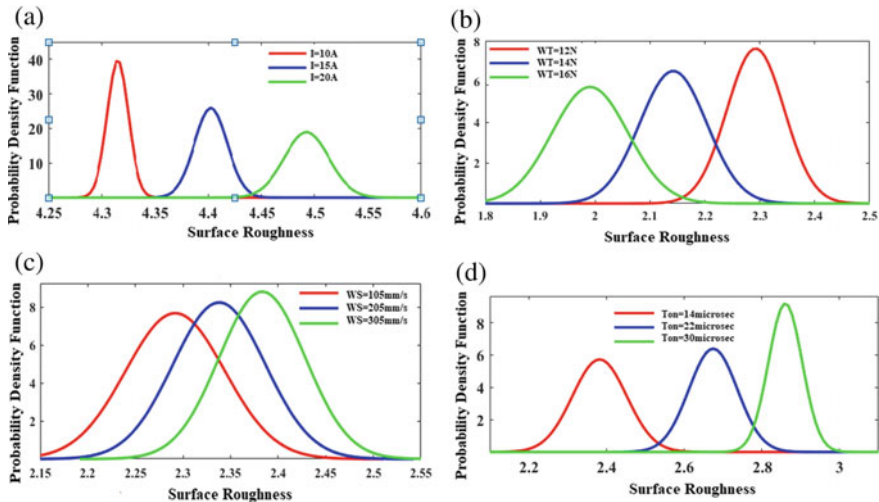
Fig. 2 **a** Effect of variations of stochastic current (I); **b** effect of variations of stochastic wire tension (WT); **c** effect of variations of stochastic wire speed (WS); **d** effect of variations of stochastic pulse on time (Ton)

vibrations of the wire. Besides, the stochastic behavior of the wire tension is seen to have no deleterious effect on the response as the surface roughness (SR) decreases with the increase in the wire tension. As shown in Fig. 2c, the probability density plots hint that the expected value of SR goes on increasing with the increment in the wire speed. With higher magnitude of wire speed, more and more fresh wire can be continuously exposed to the workpiece with appreciable removal of debris from the spark gap, thus promoting the number of effective discharges which eventually results in larger accumulation of thermal energy in the spark gap, thus resulting in larger crater sizes which can be directly linked to higher surface roughness (SR). However, high degree of overlapping between the PDF plots substantiates minimal treatment effects produced on SR by the variations in the wire speed from the point of deterministic approach but certainly gives a clue of high degree of uncertainty of SR which can be explained from the sensitivity analyses discussed later. From Fig. 2d, it can be inferred clearly that the SR with the increase in pulse on time as the amount of cumulative discharge energy increases with the increase of pulse on time but it is noticed that the plots become less scattered at higher values of pulse on time which indicates that SR becomes less sensitive to stochastic variations at higher values of pulse on time.

3.2   Compound Effect of Stochasticity

Figure 3 delineates the stochastic behavior of surface roughness (SR) produced due to the compound effect of the input parameters' random variations at varying degrees of stochasticity (dos) (1%, 2%, 3%). This information is crucial for practical considerations as it provides an understanding of the sensitivity of the surface roughness (SR) on the face of inherent randomness in the process parameters.

It can be depicted that (shown in Fig. 3) at a higher degree of stochasticity, the PDF plots become wider, reflecting that the outcomes become more uniformly distributed
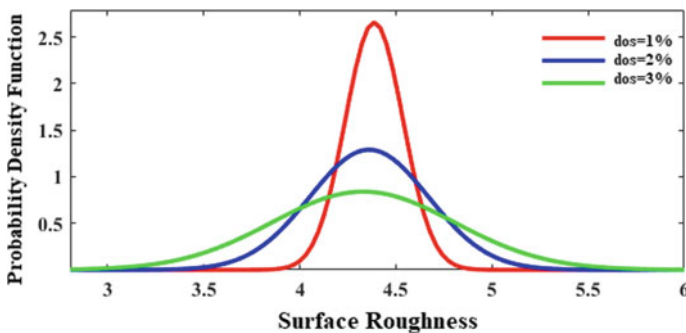
Fig. 3 Compound effect of stochastic input parameters at different degrees of stochasticity
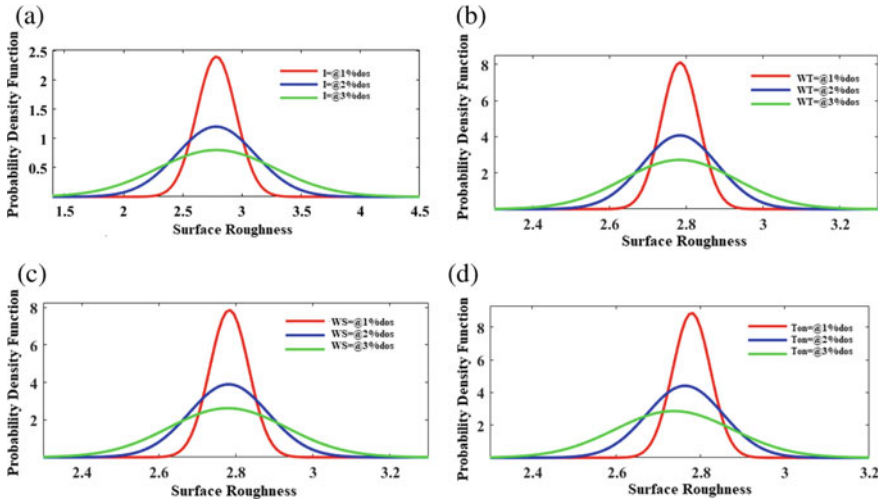
Fig. 4 **a** Stochastic variations of SR at different degrees of stochasticity of current (*I*); **b** stochastic variations of SR at different degrees of stochasticity of wire tension (WT); **c** stochastic variations of SR at different degrees of stochasticity of wire speed (WS); **d** stochastic variations of SR at different degrees of stochasticity of pulse on time (Ton)

around the expected outcome, thereby describing that arithmetic mean roughness of the machined surface might attain values beyond the actual tolerance limits.

4 Sensitivity Analysis

Figure 4a–d portrays the mapping of stochastic variations of individual input parameters to the sensitivity of surface roughness (SR) by varying the extent of stochasticity. It is observed that the sparsity is more pronounced in case of Fig. 3a. Thus, discharge current (*I*) is found to be the most influential stochastic parameter. Wire speed (WS), wire tension (WT), and pulse on time (Ton) are equally sensitive.

5 Conclusion

Firstly, it can be inferred from the overall analyses that MLR in conjunction with MCS is a novel tool to study the effect of variability of the process parameters on the output quantity of interest (QoI). Secondly, this study provides information that the effect of randomness of discharge current (*I*) is the maximum, while wire speed (WS), pulse on time (Ton), and wire tension (WT) are observed to be equally affecting the output response parameter.

References

1. Spedding TA, Wang ZQ (1997) Parametric optimization and surface characterization of wire electrical discharge machining process. Precis Eng 20(1):5–15
2. Puri AB, Bhattacharyya B (2003) An analysis and optimisation of the geometrical inaccuracy due to wire lag phenomenon in WEDM. Int J Mach Tools Manuf 43(2):151–159
3. Puri AB, Bhattacharyya B (2003) Modelling and analysis of the wire-tool vibration in wire-cut EDM. J Mater Process Technol 141(3):295–301
4. Das S, Joshi SS (2010) Modeling of spark erosion rate in microwire-EDM. Int J Adv Manuf Technol 48(5):581–596
5. Welling D (2014) Results of surface integrity and fatigue study of wire-EDM compared to broaching and grinding for demanding jet engine components made of Inconel 718. Proc CIRP 13:339–344
6. Anurag S (2018) Wire-EDM: a potential manufacturing process for gamma titanium aluminides in future aero engines. Int J Adv Manuf Technol 94(1):351–356
7. Aspinwall DK, Soo SL, Berrisford AE, Walder G (2008) Workpiece surface roughness and integrity after WEDM of Ti–6Al–4V and Inconel 718 using minimum damage generator technology. CIRP Ann 57(1):187–190
8. Yan MT, Lai YP (2007) Surface quality improvement of wire-EDM using a fine-finish power supply. Int J Mach Tools Manuf 47(11):1686–1694
9. Li L, Guo YB, Wei XT, Li W (2013) Surface integrity characteristics in wire-EDM of Inconel 718 at different discharge energy. Proc CirP 6:220–225
10. Kumar A, Mishra H, Vivekananda K, Maity KP (2017) Multi-objective optimization of wire electrical discharge machining process parameters on Inconel 718. Mater Today Proc 4(2):2137–2146

Damage Identification in Composite Structure Using Machine Learning Techniques Based on Acoustic Emission Waveforms

Pankaj Chaupal and R. Prakash

1 Introduction

GFRP composite materials extensively utilised in various engineering industries including aerospace, automotive, civil, and marine, because of their high specific strength and stiffness. When compared to conventional materials, it possesses exceptional functional characteristics such as high strength and stiffness, low weight, corrosion resistance, and long durability [1, 2]. When composite structures are subjected to mechanical and thermal loading which result damage initiation and propagation that lead to catastrophic failure [3]. In composite structures, two types of damages occur, i.e. interlaminar damage and intralaminar damage. Interlaminar damage occurs between two laminae, i.e. lamina separates; this phenomenon is known as DL, whereas FB, MC, and FMD are intralaminar damage that occurs within a lamina [4].

There are several non-destructive evaluation techniques such as ultrasonic, magnetic particle, liquid penetration, AE, which have been employed to damage detection. Out of the above techniques, AE is a widely used method due to its reliability. It detects damages in various components based on released energy. Many researchers have employed AE technique synergetic integrated with mechanical test and microstructural visualisation method for damage identification. Nikbakth et al. [5] conducted a double cantilever beam test on the different orientation of composite laminate integrated with AE sensor and micro visualisation to evaluate DL and different damages in the composite structure. Mohammadi et al. [6] investigated fatigue damage characteristics in carbon and epoxy laminate under the mode

P. Chaupal (✉) · R. Prakash
Department of Mechanical Engineering, National Institute of Technology, Tiruchirappalli, Tamil Nadu 620015, India
e-mail: 411120006@nitt.edu

R. Prakash
e-mail: rprakash@nitt.edu

II loading condition using AE and scanning electron microscope (SEM). Several researchers have also predicted the localisation and propagation of damages in composite structures under static and fatigue tensile loading conditions using AE testing accomplished by micro-computed tomography, infrared thermography, x-ray thermography, and digital image correlation [7, 8]. Few works have been done on identification of damages in composite structures based on AE testing under different environmental conditions. Denghong and Yong [9] used AE technology under a random vibration environment to analyse the damage in carbon fibre-reinforced silicon composite. Mouzakis and Dimogianopoulos [10] applied the AE method to detect the damage and study the effect of simulated environmental ageing on carbon fibre-reinforced composite under the flexural test. It is observed in AE techniques the types of damages can be classified based on the sound amplitude. Therefore, Czigany [11] described the development of damage in composite constructions using AE characteristics such as amplitude and energy. It has been discovered that various types of damage occur in composite structures at the following frequency ranges: MC (21–35 decibel (dB)), DL (35–45 dB), fibre pull-out (45–60 dB), and FB (over 60 dB).

In recent years, ML algorithms combined with AE have emerged as more precise and powerful methods for damage detection. Several research works have been carried out to predict damage in composite structures based on AE and ML techniques. Xu et al. [12] conducted tensile and AE test on the adhesive composite joint for both ageing and non-ageing specimens under regular and hypothermal environments. Furthermore, they combined ML techniques such as time-domain analysis, frequency-domain analysis and clustering analysis, to analyse the AE data for damage detection. Using AE waveforms and ML, Xu et al. [13] detected damages in the adhesive joint of a composite wind turbine blade. In this, they have used the fast search and find of density peaks method for clustering the AE signals to identify the damages. It is observed that the k-means approach is one of the most popular methods used for differentiating clustering solutions. Jiang et al. [1] studied the damage in pultruded fibre-reinforced composite using an unsupervised ML algorithm, k-mean based on AE test under flexural loading. Yong et al. [14] extracted AE features from AE waveforms and used a k-mean clustering algorithm to identify three damage modes in carbon fibre-reinforced silicon carbide composite structure under constant loading condition. Monti et al. [15] used k-mean as an unsupervised ML pattern recognition technique to identify the damage in flax-fibre of different orientation based on obtained AE signals. Saidane et al. [16] predicted damages for example MC, FMD, and FB in aged and unaged, hybrid and non-hybrid composite based on AE amplitude range using k-mean classification techniques. Godin et al. [17] proposed synergetic integration of the k-NN and k-means algorithms to categorise the AE signals while performing the tensile tests of GFRP composites. The drawback of k-means clustering is to define the centroid before the operation begins. Therefore, to overcome this problem k-means++ technique is developed.

In this study, AE data computed by Choudany et al. [18] under tensile testing was used to identify the damages in GFRP composite structure. These data are processed using unsupervised ML algorithms, k-means++ and AHC to classify into the clusters

corresponding to different type of damages. Further, a supervised ML technique *k*-NN is used to predict the performance and reliability of the *k*-means++ clustering and AHC.

This scientific study is formulated as follows: Sect. 2, gives a brief explanation of the methodology for predicting damages in composite structures. Section 3 describes the different types of ML algorithms. The results and discussion are explained in Sect. 4, and Sect. 5 describes concluding remarks.

2 Methodology

Figure 1 illustrates the flowchart for predicting damages in composite structures based on AE waveforms. AE features such as amplitude and time are taken from Choudany et al. [18]. For obtaining these parameters they were conducted AE testing under tensile loading on a universal testing machine as per ASTM D3039. Damage represents the change in geometric and material properties of structure that adversely affects its performance, safety, reliability and operational life. Thus damage identification is quite important to overcome the failure of the structures. In recent years, ML algorithms have emerged as more precise and powerful alternatives tool for damage identification based on obtained datasets from different mechanical testing.
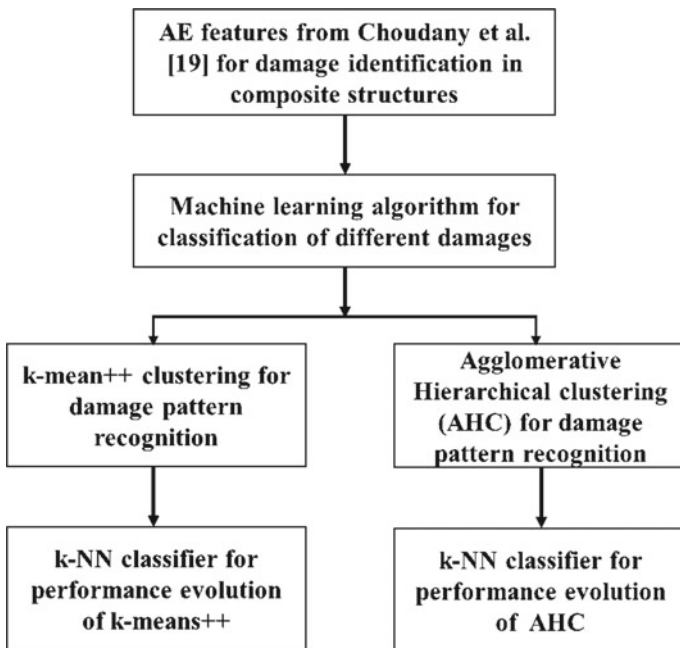
Fig. 1 Flowchart for predicting damages in the composite structures

Table 1 Basic steps of *k*-means++ algorithm

Step-1. Choose the optimum number of cluster *k* based on the elbow method. In this, we are initialising *k*-mean++ to speed up the convergence
Step-2. Compute the distance between cluster centre and each data point using either Euclidean or Manhattan distance
Step-3. Based on the shortest distance between the cluster centres and vector, assign each data point to the nearest centroid
Step-4. Take an average of the same cluster to update the new cluster centre
Step-5. Compute the distance between the new cluster centre and each data point again
Step-6. If there are no data points to reassigned, the algorithm has converged and the process should be stopped; otherwise, repeat steps 3–5

In this, the unsupervised ML algorithms *k*-mean++ and AHC are used to classify the different damages based on the AE features. Further, a supervised ML algorithm *k*-NN was trained using *k*-means++ and AHC dataset to evaluate the performance and reliability of unsupervised ML algorithms.

3   Machine Learning Algorithms

In this section, *k*-means++ and AHC are used as unsupervised ML techniques for pattern recognition. The *k*-NN was used as a supervised ML algorithm to predict the accuracy and reliability of the unsupervised ML algorithm based on a confusion matrix.

3.1   *k-means++ clustering*

In data processing, the *k*-means++ clustering technique is used to overcome the drawback of *k*-means clustering. It is an iterative method for dividing a dataset into clusters by finding the minimum square distance between the cluster's centroid and the individual data points. Suppose we have a dataset $\{x_1, x_2, x_3 \ldots x_n\}$ consist of '*n*' observation of random *D*-dimensions. The following step can be taken to divide the dataset into clusters as explained in Table 1 [19].

3.2   *Agglomerative Hierarchal Clustering*

Hierarchical clustering algorithms are designed to address some of the drawback associated with *k*-means clustering. To achieve the clustering solution, *k*-means required a predefined value of the number of clusters which is often non-destructive

Table 2 Basic steps of agglomerative hierarchical clustering algorithm

Step-1. Calculate either Euclidean distance or Manhattan distance, compute a dissimilarity matrix between all the data points
Step-2. Choose a minimum value in the dissimilarity matrix and merge clusters
Step-3. Insert the new row and column containing the least distance between the remaining clusters and the new cluster
Step-4. Continue the process until only one maximal cluster remains

in nature. Hence, agglomerative hierarchical algorithms were developed to provide a more deterministic and adaptable method for clustering data objects. There are two types of hierarchical clustering approaches those are agglomerative and divisive clustering methods. Agglomerative approaches begin with singleton clusters at the bottom level and proceed by combining two clusters at a time to create a cluster hierarchy from the bottom up. Divisive methods, on the other hand, begin with all of the data objects in a large macro-cluster and constantly divide them into two classes, resulting in a top-down hierarchy of clusters. In this section, AHC is used to solve the damage identification problem in a composite laminate. The basic steps of the AHC algorithm are discussed in Table 2 [20].

3.3 k-NN Algorithm

The k-NN classifier is the most technically elegant and simple supervised ML classification technique. This algorithm gives excellent prediction of classification when a labelled training database is properly available. The k-NN approach assigns new unclassified objects to the class which contains mainly k-nearest neighbours. Table 3 describes the basic steps of the k-NN algorithm [21].

Table 3 Basic steps of k-NN algorithm

Step-1. Pick out the number of k-neighbours
Step-2. Consider the k-NN of new data points based on shortest Euclidian distance between chosen k-neighbours points and vectors
Step-3. Calculate the number of data points in each set among the k-neighbours
Step-4 New data point is allocated to the class that has the greatest number of neighbours

4 Results and Discussions

In this section, acoustic emission testing under tensile loading is integrated with unsupervised ML algorithms such as k-means++ and AHC for assessment of various damages in the composite structure. Further, the supervised ML algorithm like k-Nearest Neighbour is used on k-means++ and AHC data to evaluate the performance and reliability of the algorithm.

4.1 k-means++ Versus Agglomerative Hierarchal Clustering

In this section, the results of k-means++ and AHC methods on the AE dataset are compared. In the first part of the comparison, elbow and dendrogram methods are used to find out the optimal value of cluster for k-mean++ and AHC. In the second part, it is shown that how acoustic AE signals are varying with different damages in composite structure and represented in the form of clusters.

A critical step in any unsupervised ML algorithms is to determine the optimal number of clusters into which the data can be clustered. The optimal number of clusters in k-means++ and AHC is shown in Fig. 2a, b, respectively. The elbow methods select several clusters heuristically in a data set by plotting a graph between several clusters and WCSS. From Fig. 2a it is observed that the elbow is formed corresponds to the fourth cluster. As a result the optimal number of clusters for the k-means++ clustering method is four. A dendrogram is a visual representation of the hierarchical relationship between the data points. In Fig. 2b a graph is plotted between cluster points and Euclidian distance, it also examined that the optimal number of cluster is four in the dendrogram.
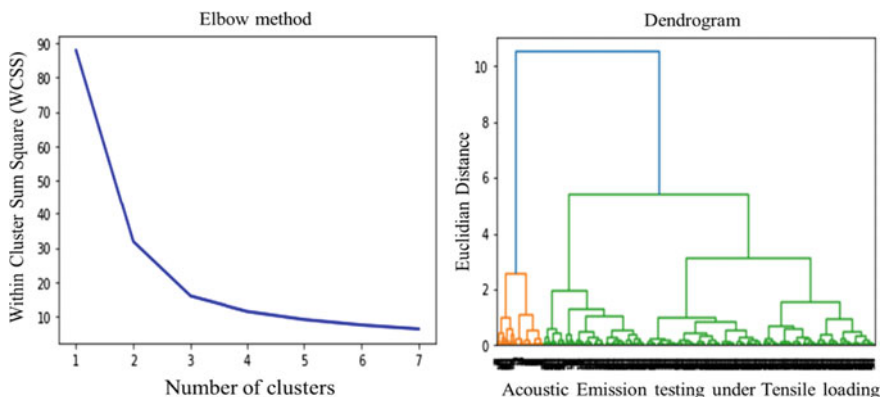
Fig. 2 Optimal number of cluster **a** k-means++ clustering. **b** Agglomerative hierarchical clustering
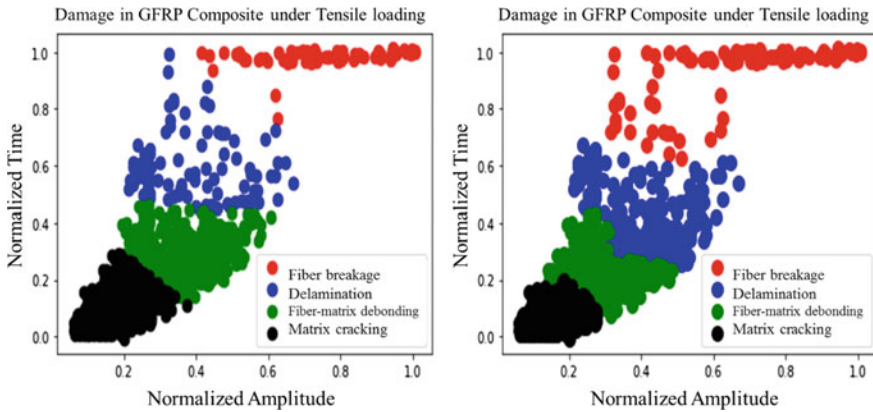
Fig. 3 **a** *k*-means++ clustering. **b** Agglomerative hierarchical clustering

AE parameters such as rise time, duration, counts, amplitude, and energy were estimated using the obtained signal waveforms. The computed descriptors were normalised by standard deviation in the range [0; 1]. To summarise the obtained results, the graph is plotted only between the normalised amplitude and the normalised time. The graph plotted in Fig. 3a, b shows four clusters, which are MC, FMD, DL, and FB, respectively. Comparing Fig. 3a, b, a minor difference is observed between *k*-means++ and AHC. The partitioning of datasets in both clusters is almost same. There is no overlapping between the clusters, the only difference is the number of acoustic emission data points in each cluster. The percentages of MC, FMD, DL, and FB in *k*-mean++ clustering are, 41.698%, 37.515%, 11.153%, and 9.632%, respectively, whereas in. AHC, MC, FMD, DL, and FB observed are 31.051%, 29.657%, 26.742%, and 12.547%, respectively.

4.2 Confusion Matrix Using k-NN Supervised Classifier

In this section, the labelled data generated by *k*-means++ clustering and AHC are used as learning data for training and testing the *k*-NN supervised classifier. The confusion matrix diagram is used to assess the classifier's performance using the learning database.

The k-NN classifier was trained using *k*-mean++ and an AHC dataset. The material is considered to have four damages: MC, FMD, DL, and FB which are represented by the numbers 0, 1, 2, and 3 accordingly. Figure 4 represents the performance of the k-NN model for which the true value is known. In Fig. 4a performance of the *k*-means++ algorithm is 100% for MC, DL, and FMD and 98% for FB. Hence, there is 2% misclassification for FB. As shown in Fig. 4b performance of the AHC algorithm is 100% for FMD and FB whereas 94% and 97% for MC and DL, respectively. Hence, there are 6% and 3% misclassification for MC and DL.
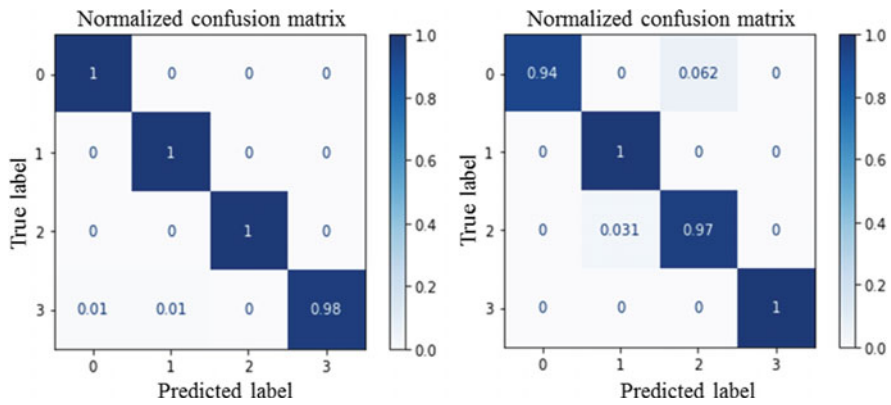
Fig. 4 Confusion matrix using *k*-NN, **a** *k*-mean++ clustering. **b** Agglomerative hierarchical clustering

4.3 Comparison of Different Algorithms

The result obtained in Fig. 5 shows that the *k*-means++ and AHC both can be used to predict the different types of damages in composite structures. For various composite damages such as MC, DL, and FMD, the accuracy of the *k*-means++ clustering algorithm is somewhat greater than AHC and incremental clustering and for FB, the accuracy of AHC is higher than *k*-means++ and incremental clustering.
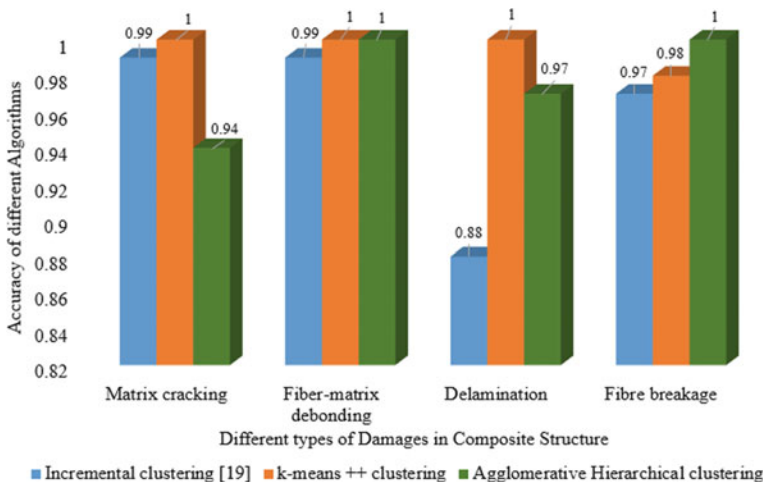
Fig. 5 Comparison of accuracy of different algorithms

5 Conclusion

This research work presents how acoustic emission signals and ML approaches may be combined to predict various damages in composite structures under tensile loading. Based on the above study, the following conclusions are made:

- k-means++ algorithm is more efficient than incremental and AHC.
- Computation time for k-means++ algorithm is quite less than AHC.

References

1. Jiang W, Zhang Q, Zhang Y, Guo Z, Tu ST (2020) Flexural behavior and damage evolution of pultruded fiber-reinforced composite by acoustic emission test and a new progressive damage model. Int J Mech Sci 188:105955
2. Abrate S (1991) Matrix cracking in laminated composites: a review. Compos Eng 1(6):337–353
3. Wei Q, Zhu L, Zhu J, Zhuo L, Hao W, Xie W (2020) Characterization of impact fatigue damage in CFRP composites using nonlinear acoustic resonance method. Compos Struct 253:112804
4. Zhou W, Qin R, Han KN, Wei ZY, Ma LH (2021) Progressive damage visualization and tensile failure analysis of three-dimensional braided composites by acoustic emission and micro-CT. Polym Test 93:106881
5. Nikbakht M, Yousefi J, Hosseini-Toudeshky H, Minak G (2017) Delamination evaluation of composite laminates with different interface fiber orientations using acoustic emission features and micro visualization. Compos B Eng 113:185–196
6. Mohammadi R, Najafabadi MA, Saghafi H, Saeedifar M, Zarouchas D (2021) The effect of mode II fatigue crack growth rate on the fractographic features of CFRP composite laminates: an acoustic emission and scanning electron microscopy analysis. Eng Fract Mech 241:107408
7. Kelkel B, Popow V, Gurka M (2020) Inline quantification and localization of transverse matrix cracking in cross-ply CFRP during quasi-static tensile testing by a joint event-based evaluation of acoustic emission and passive IR thermography. Compos Sci Technol 190:108013
8. Djabali A, Toubal L, Zitoune R, Rechak S (2019) Fatigue damage evolution in thick composite laminates: combination of X-ray tomography, acoustic emission and digital image correlation. Compos Sci Technol 183:107815
9. Denghong X, Yong G (2020) Damage monitoring of carbon fiber reinforced silicon carbide composites under random vibration environment by acoustic emission technology. Ceram Int 46(11):18948–18957
10. Mouzakis DE, Dimogianopoulos DG (2019) Acoustic emission detection of damage induced by simulated environmental conditioning in carbon fiber reinforced composites. Eng Fract Mech 210:422–428
11. Czigány T (2006) Special manufacturing and characteristics of basalt fiber reinforced hybrid polypropylene composites: mechanical properties and acoustic emission study. Compos Sci Technol 66(16):3210–3220
12. Xu D, Liu PF, Li JG, Chen ZP (2019) Damage mode identification of adhesive composite joints under hygrothermal environment using acoustic emission and ML. Compos Struct 211:351–363
13. Xu D, Liu PF, Chen ZP, Leng JX, Jiao L (2020) Achieving robust damage mode identification of adhesive composite joints for wind turbine blade using acoustic emission and ML. Compos Struct 236:111840
14. Yong G, Denghong X, Tian H, Ye L, Naitian L, Quanhong Y, Yanrong W (2019) Identification of damage mechanisms of carbon fiber reinforced silicon carbide composites under static loading using acoustic emission monitoring. Ceram Int 45(11):13847–13858

15. Monti A, El Mahi A, Jendli Z, Guillaumat L (2016) Mechanical behaviour and damage mechanisms analysis of a flax-fiber reinforced composite by acoustic emission. Compos A Appl Sci Manuf 90:100–110
16. Saidane EH, Scida D, Assarar M, Ayad R (2017) Damage mechanisms assessment of hybrid flax-glass fiber composites using acoustic emission. Compos Struct 174:1–11
17. Godin N, Huguet S, Gaertner R, Salmon L (2004) Clustering of acoustic emission signals collected during tensile tests on unidirectional glass/polyester composite using supervised and unsupervised classifiers. NDT and E Int 37(4):253–264
18. Ech-Choudany Y, Assarar M, Scida D, Morain-Nicolier F, Bellach B (2017) Unsupervised clustering for building a learning database of acoustic emission signals to identify damage mechanisms in unidirectional laminates. Appl Acoust 123:123–132
19. Bishop CM (2006) Pattern recognition and ML. Springer, pp 423–455
20. Aggarwal CC, Reddy CK (2014) Data clustering. In: Algorithms and applications. Chapman & Hall/CRC data mining and Knowledge Discovery series. Londra, pp 100–106
21. Kuncheva LI (2014) Combining pattern classifiers: methods and algorithms. Wiley, p 47

An Adaptive Neural-Fuzzy Approach for Modeling of Droplet Frequency in E-Jet-Based Micro-additive Manufacturing

Adrija Biswas, Ananya Nath, and Shibendu Shekhar Roy

1 Introduction

Nowadays, there are a huge variety of microproducts for biomedical, aircraft, automobile, and other engineering application. The diversity in materials and the complication of 3D microstructures having high aspect ratios are the major characteristics of the chief microproducts existing today. The major varieties of microproducts include microelectromechanical systems (MEMS), microsensors, [1] thin film transistors (TFTs), [2, 3] micro-opto-electro-mechanical systems (MOEMS), and microelectronic products and micro-optical electronics systems (MOES). The ability of processing a broad range of materials for the fabrication of geometrically complicated 3D microstructures provides some supplementary profits to the process of 3D micro-additive manufacturing over traditional processes like lithography-based or micromachining-based processes. The demand of 3D micro-additive manufacturing increases more and more with the development of the modern microelectronic industry [4]. One such method of additive manufacturing is the inkjet printing process which includes arrangement and layer-by-layer deposition of liquid material in droplet form. It uses thermal or piezo-electric energy to create droplets of functional materials [5]. Its major drawbacks include its inability to print nano-level structures, nozzle clogging [6] and it was not possible to achieve higher print resolution and droplet frequency. This can be overcome by EHD inkjet printing technology. Electrohydrodynamic or EHD inkjet printing is a non-contact, mask-less additive manufacturing method for printing materials on any substrate in order to obtain microscopic patterns. The e-jet printing process relies on 'pulling' [7] the liquid from the nozzle tip by applying an electric field, rather than pushing it out of the nozzle like that of the traditional inkjet techniques [8, 9]. The chief advantages

A. Biswas · A. Nath · S. S. Roy (✉)
Department of Mechanical Engineering, National Institute of Technology Durgapur, Durgapur, West Bengal, India
e-mail: shibendu.roy@me.nitdgp.ac.in

of this methodology lie in the higher resolution of printing and high frequency of droplets [10]. The influence of several experimental parameters on the drop diameter and the drop generation rate has been investigated. Up to a certain limit, a one-to-one relationship between drop generation frequency and applied voltage frequency has been found. Due to the time lag between the time required for Taylor cone formation and the voltage pulse duration time, beyond a certain point, the drop generation frequency cannot be maintained along with that of the applied voltage frequency. It was later concluded that, with the reduction in nozzle dimension, the drop generation frequency can be increased by enhancing the applied voltage frequency.

However, Chen et al. [11] experimented and successfully printed droplets with less diameter than nozzle which can result in high resolution printing by conventional method. Kim et al. [12] investigated for the right selection of process parameters to get desired droplet formation, droplet size, and frequency. Barton et al. [13] used e-jet frequency as e response to design some control system for EHD inkjet printing. An and associates [14] investigated the influence of ink material on e-jet droplet frequency. Li et al. [15] investigated the applied voltage effect on mode of droplet formation. Different kind of mode of droplet formation is seen for different voltage value like pulsating mode, dripping mode, etc.

In EHD process, a voltage is applied between the nozzle and the substrate material which is mounted over the CNC control bed. Due to the voltage difference, the fluid inside the reservoir gets deformed and pressurized and at the tip end of the nozzle a Taylor cone [16] is formed from where the ink droplet pulled out. As the ink droplet is formed at the tip of the Taylor cone and not from the nozzle tip, very less diameter of droplet can be possible to form. That is why EHD technique is very much popular in micro-manufacturing field. However, the right selection of ink and substrate material is also very important for attaining desired resolution.

Statistical approaches are always good to start for analyzing and understanding any experimental process parameters and their relationship with the output parameter. So, at first, the design of experiment (DOE) is done which gives the minimum number of experiments that is to be executed to get quality input–output data sets. DOE is used to save time as well as material and all experimental resources. In this paper, three process parameters have been chosen for the input or predictors, i.e., nozzle-substrate gap, applied voltage, and the ink flow rate. Response or output to be measured is droplet frequency. To model the droplet frequency in terms of input parameters, Adaptive Neuro Fuzzy Inference System (ANFIS) is built.

2   Experimentation

In this study, material supply system, electrical system, positioning, and visualization system are namely the three major components of EHD printing system. A syringe pump is connected with the ink nozzle. It acts as an ink reservoir and helps to deliver the ink to the nozzle by the virtue of pressure difference. A function generator is used to generate the specific frequency analog pulse with the required duty cycle. It

is connected with the nozzle and substrate over which the deposition of ink material will occur. Thus a voltage is being generated between these two. An amplifier is used to amplify this DC power analog voltage signal up to 1000 times to deposited the ink onto the print bed (substrate). This amplified voltage is then supplied between the nozzle and substrate Flexible Polyethylene terephthalate (PET) is used as the substrate material which is mounted over a 3 axis (X–Y–Z) CNC controlled stage. Right material selection of nozzle, ink, and substrate is very important for a desired deposition. The print bed can move at up to 205 mm/s speed with a resolution of 0.1 μm. A support column is provided for Z axis movement of print head, i.e., nozzle part. Nozzle is made up of stainless steel of an internal diameter of 0.836 mm and length of 51 mm. the z axis movement of nozzle and bed movement is controlled by the CNC command in a very specific manner. An optical microscope is used to inspect a magnified view of the proper droplet deposition. Deposited droplet characteristics, droplet diameter, or droplet frequency can directly be monitored with the help of processing software with the microscope. In this paper, a water soluble polymer material, such as poly(3,4-ethylenedioxythiophene) polystyrene sulfonate (PEDOT: PSS), has been used as the ink material for the deposition [17] (Fig. 1).
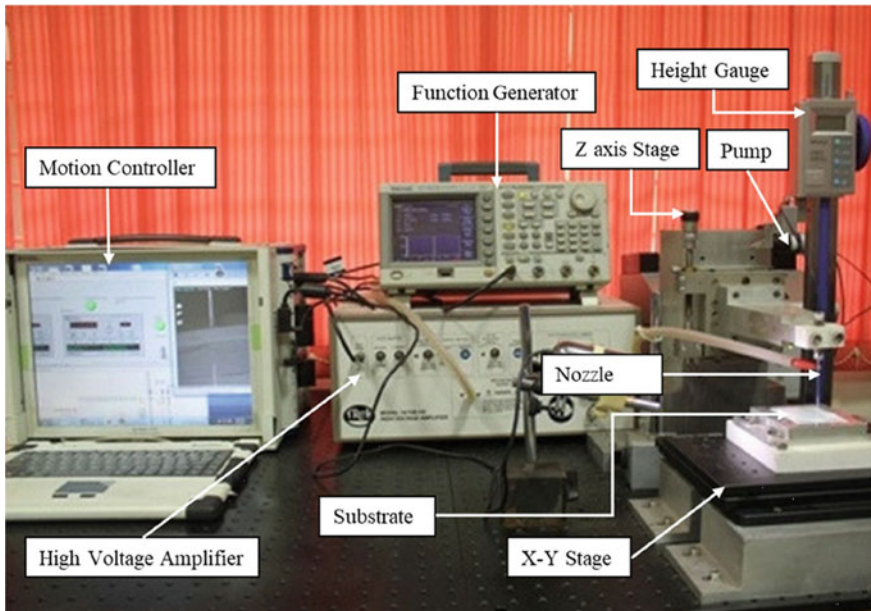
Fig. 1 Experimental setup

3 Proposed Methodology

3.1 Regression Modeling

To model any output of an experiment in terms of its input parameters, it is very important to build a relationship between the predictor and response parameters, where predictors are the input parameters and response is the output parameter. Statistical methods are easy to attain the same. In this study, the main concern is to model the response parameter, i.e., droplet frequency (Hz) of EHD printing in terms of its input parameters like nozzle-substrate gap (mm), applied potential difference (kV), and ink flow rate (µl/s). After a careful study, the range of input parameters are also set, which is shown in Table 1.

In this paper, 27 real experiments have been done. Regression models are generated to build a relationship between the input parameters (predictors) and output parameter(s) (response). Real experimental data are used for this purpose. To make the regression model more accurate, nonlinear equation are chosen and formed. With the experimental input–output data sets, the regression equations are generally formed. A generalized formulation for the aforementioned can be written as:

$$y = \beta_0 + \sum_{j=1}^{k} \beta_j X_j + \sum_{j=1}^{k} \beta_{jj} X_j^2 + \sum \sum_{j<i}^{k} \beta_{ji} X_j X_i + \varepsilon \tag{1}$$

where y is the process response, X is the process control parameter; β is the regression coefficient; the experimental error is denoted by ε; and the investigated process control parameters are represented by j and i. In Eq. (1), the linear effect of process parameters is captured by X_j; the nonlinear effect is represented by X_j^2, and parametric interaction is exhibited by $X_i X_j$. Equation (1) is then expanded one response variable and three control parameters. Thus, the equation will be expressed as:

$$y = \beta_0 + \beta_1 X_1 + \beta_2 X_2 + \beta_3 X_3 + \beta_{11} X_1^2 + \beta_{22} X_2^2 + \beta_{33} X_3^2 + \beta_{12} X_1 X_2$$
$$+ \beta_{13} X_1 X_3 + \beta_{23} X_2 X_3$$

β factors are can be determined by least square method by solving some normal set of equations. For more detail, interested readers can refer to [18].

Table 1 Input parameters with operating range

Process control parameters	Code	Operating range		
		Low (1)	Medium (2)	High (3)
Nozzle-substrate gap (mm)	A	4.5	5.0	5.5
Applied potential difference (kV)	B	3.8	4.4	5.0
Ink flow rate (µl/s)	C	10	25	40

3.2   Adaptive Neuro Fuzzy Inference System (ANFIS)

ANFIS is a machine learning algorithm which uses the artificial neural network along with fuzzy logic system to operate. It is used to build a relationship between the inputs and outputs of the data that are fed to the ANFIS architecture to train it. ANFIS consists of five layers out of which two layers are adaptive in nature where the optimization of the required parameters happens. Each of the layers has its specific governing equations by which each layer output is got. In the first (fuzzy) and fourth (de fuzzy layer) layer, some weight factors get multiplied with the layer input which are thereafter get minimized at the time of optimization. ANFIS uses a fuzzy logic-based inference system where the input membership functions are chosen by the user. The ANFIS predicted outputs also depend upon the type of membership functions.

Also, at the time of training the network, the number of levels of input parameters is given by the users which can be calibrated according to the requirement. The Accuracy of output can also be varied by the right selection of each input parameters' level. The different types of MFs of output parameters can also be varied.

After the system gets optimized, real experimental inputs are fed to the system and ANFIS predicts some output in respect of the given test (experimental) inputs. The more accurate predicted output with the experimental outputs indicates high-quality architecture or a correct training of the system.

The five layers of ANFIS are fuzzy layer, product layer, normalized layer, de fuzzy layer, and total output layer. Here, fuzzy and de fuzzy layers are adaptive in nature, where optimization occur. The predicted output of ANFIS is sent back to the system as feedback to optimize the error after each loop. Optimization refers to the minimization of the weight factors of two adaptive layers. The number of loops is called epoch. The number of epochs can be changed or increased as per need for a better result. For a detailed description of ANFIS architecture, its layers, outputs, and working principles, please refer to some relevant study materials [19, 20].

3.3   Learning Algorithm

As discussed earlier, there are two adaptive layers present in ANFIS architecture such as the first (fuzzy) layer and the fourth (de fuzzy) layer. In the fuzzy layer, the parameters present in input membership functions get minimized in adaption and in the fourth layer, randomly generated values parameters present in output governing equation of that respective layer get optimized. This optimization is very important step to build an appropriate network which can predict very similar output like experimental outputs. So, to serve this purpose, difference algorithm is used. In this modeling, droplet frequency is modeled in terms of three input parameters by build an accurate ANFIS architecture using two different algorithms. A brief introduction of those algorithms are as follows.

3.3.1 Approach 1

The first approach is using backpropagation (BP) method where error signals are generated to modify the network as per the needs by minimizing the error. Predicted output by the system is validated with the expected output by the system itself and the error signal is generated and the design parameters of adaptive layers get updated according to the need. This loop is continued for several times. Here, in this study the loop ran 1000 times and the architecture was thus formed. Gradient descent method is used here to update the system.

3.3.2 Approach 2

The second approach is a hybrid method where it uses gradient descent and least square method to update the system as per need by minimizing the design parameters. In fuzzy logic-based system, the output design parameters of fuzzy layers are called premise parameters and in the defuzzy layer, the randomly generated parameters of respective layer outputs are called consequent parameters. In this algorithm, the consequent parameters get adopted at first by least square method where premise parameters are kept fixed. Once the consequent parameters get optimally updated, it is fixed. The premise parameters get updated by gradient descent method. The error between the network predicted outputs and training output is then used to update the premise parameters by using standard gradient descent method.

4 Simulation Results and Discussion

Using 27 real experimental input–output values, a second order nonlinear regression equation is formed using MINITAB.

$$\begin{aligned}
\text{Droplet frequency} = &-15.3 + 8.64 \times G + 4.7 \times V - 0.0615 \times F \\
&- 0.862 G \times G - 0.418 \times V \times V - 0.000032 F \times F \\
&- 0.097 G \times V + 0.01244 V \times F - 0.00093 F \times G
\end{aligned}$$

where G is the nozzle-substrate gap (mm), V is applied potential difference (kV) and F is ink flow rate (μl/s).

The designed second order nonlinear regression equation is used to generate a set of input–output training data for training the ANFIS architecture. At first this training data set is fed to the system. Input–output membership function types are selected. Triangular, trapezoidal, Gaussian, and bell-shaped are some of the examples of membership functions already present in ANFIS architecture. Among them triangular, Gaussian and bell-shaped membership functions are chosen for this study. Then the levels of each input parameter are set. By the combination of three and four

levels of each input parameters such as gap, voltage and flow rate, the network is trained. At first, using backpropagation algorithm, the ANFIS architecture is trained by grid partition. Weight factors get minimized in two adaptive layers. For each MF with different levels, the system runs for 1000 epochs. Then in each optimized system, the real experimental inputs are fed to test the architecture. Predicted outputs are compared with the experimental outputs. Absolute error percentage is calculated for each of the membership functions (Table 2). The same process is repeated using hybrid algorithm. Again, in this case, predicted output is compared with that of the experimental outputs, and absolute error percentage is calculated and it has been shown in Table 3.

ANFIS architecture with hybrid algorithm outperforms the backpropagation. And among all the levels with different types of membership functions, bell-shaped MF with three levels of each input parameter has shown the most accurate results for its nonlinear behavior.

5 Conclusion

To measure the efficiency of EHD inkjet printing in terms of printing resolution, droplet frequencies are very significant. It is required to be modeled properly to attain the desired performance. In this paper, fuzzy logic-based neural networking system is used which is also known as ANFIS, to model the output parameter, i.e., droplet frequency with the help of input parameters such as nozzle-substrate gap, applied voltage, and ink flow rate. For the two different algorithms, namely backpropagation and hybrid, the network is trained, and the predicted output of the network is validated with the experimental output. Three different membership functions such as triangular, Gaussian, and bell-shaped are used for each algorithm. Error percentage for three MF came to be as 2.356299%, 2.42706195% and 2.541965%, respectively, for hybrid and 0.896212%, 0.86761% and 0.866456%, respectively, for backpropagation method. So, it is clearly visible that hybrid outperforms backpropagation method and among three membership functions, Gaussian MF with hybrid algorithm has shown the most accurate result.

Table 2 Comparison between experimental output and ANFIS predicted output using backpropagation algorithm for three different membership functions

Nozzle-substrate gap (mm)	Applied potential difference (kV)	Ink flow rate (μl/s)	Droplet frequency (Hz) (experimental output)	ANFIS predicted output using backpropagation algorithm					
				Triangular MF	Abs. error (%)	Gaussian MF	Abs. error (%)	Bell shaped MF	Abs. error (%)
4.5	3.8	10	16.34	15.5501	4.834149	15.1717	7.1499388	15.2019	6.965116
4.5	3.8	25	15.86	15.8624	0.015132	16.1408	1.7704918	15.9722	0.70744
4.5	3.8	40	15.7	16.091	2.490446	16.5219	5.23503185	16.552	5.426752
4.5	4.4	10	16.53	16.1232	2.46098	15.7435	4.75801573	15.8252	4.263763
4.5	4.4	25	16.82	16.008	4.827586	16.3525	2.77942925	16.3661	2.698573
4.5	4.4	40	16.21	16.1128	0.59963	16.6273	2.57433683	16.7388	3.262184
4.5	5	10	16.63	16.6962	0.398076	16.3151	1.89356584	16.3776	1.517739
4.5	5	25	16.43	16.1537	1.68168	16.5641	0.8161899	16.7152	1.735849
4.5	5	40	16.68	16.1346	3.269784	16.7326	0.31534772	16.8969	1.30036
5	3.8	10	16.24	16.0279	1.306034	15.6504	3.63054187	15.7104	3.261084
5	3.8	25	15.86	15.8874	0.172762	16.2465	2.4369483	16.2426	2.412358
5	3.8	40	16.22	16.0507	1.043773	16.5591	2.09062885	16.6499	2.650432
5	4.4	10	16.7	16.6009	0.593413	16.2221	2.86167665	16.3335	2.194611
5	4.4	25	16.64	16.0331	3.647236	16.4582	1.09254808	16.6365	0.021034
5	4.4	40	16.56	16.0725	2.943841	16.6644	0.63043478	16.8367	1.670894
5	5	10	17.02	17.174	0.904818	16.7938	1.32902468	16.8835	0.801998
5	5	25	16.91	16.1787	4.32466	16.6698	1.42046127	16.9843	0.439385
5	5	40	16.53	16.0943	2.635814	16.7697	1.45009074	16.9943	2.808832
5.5	3.8	10	15.86	16.5057	4.071248	16.1046	1.54224464	15.9582	0.619168
5.5	3.8	25	16.14	15.9125	1.409542	16.3363	1.21623296	16.3411	1.245973

(continued)

Table 2 (continued)

Nozzle-substrate gap (mm)	Applied potential difference (kV)	Ink flow rate (μl/s)	Droplet frequency (Hz) (experimental output)	ANFIS predicted output using backpropagation algorithm					
				Triangular MF	Abs. error (%)	Gaussian MF	Abs. error (%)	Bell shaped MF	Abs. error (%)
5.5	3.8	40	15.98	16.0104	0.190238	16.586	3.7922403	16.6575	4.239675
5.5	4.4	10	16.1	17.0787	6.078882	16.6754	3.57391304	16.5706	2.922981
5.5	4.4	25	16.34	16.0582	1.724602	16.5477	1.27111383	16.7285	2.377601
5.5	4.4	40	16.39	16.0323	2.182428	16.6913	1.83831605	16.8414	2.754118
5.5	5	10	16.62	17.6518	6.208183	17.2461	3.76714801	17.1086	2.939832
5.5	5	25	16.43	16.2038	1.37675	16.759	2.00243457	17.069	3.889227
5.5	5	40	16.42	16.0541	2.22838	16.7964	2.29232643	16.9957	3.50609

Table 3 Comparison between experimental output and ANFIS predicted output using hybrid algorithm for 3 different membership function

Droplet frequency (Hz) (experimental output)	ANFIS predicted output using hybrid algorithm					
	Triangular MF	Abs. error (%)	Gaussian MF	Abs. error (%)	Bell shaped MF	Abs. error (%)
16.34	16.1961	0.880661	16.1903	0.916157	16.1886	0.926561
15.86	16.0435	1.156999	16.0366	1.113493	16.0346	1.100883
15.7	15.8765	1.124204	15.8703	1.084713	15.8683	1.071975
16.53	16.6921	0.980641	16.6857	0.941924	16.6849	0.937084
16.82	16.5311	1.717598	16.5242	1.758621	16.5228	1.766944
16.21	16.3557	0.898828	16.3489	0.856878	16.3478	0.850093
16.63	16.8871	1.546001	16.8796	1.500902	16.8767	1.483464
16.43	16.7177	1.751065	16.7101	1.704808	16.707	1.68594
16.68	16.534	0.8753	16.5261	0.922662	16.5228	0.942446
16.24	16.2995	0.366379	16.2866	0.286946	16.2848	0.275862
15.86	16.2402	2.397226	16.2271	2.314628	16.2249	2.300757
16.22	16.1665	0.32984	16.154	0.406905	16.1523	0.417386
16.7	16.7664	0.397605	16.7539	0.322754	16.7522	0.312575
16.64	16.6987	0.352764	16.6861	0.277043	16.6841	0.265024
16.56	16.6166	0.341787	16.6045	0.26872	16.6029	0.259058
17.02	16.9323	0.515276	16.9183	0.597532	16.9153	0.615159
16.91	16.8563	0.317564	16.8427	0.397989	16.8394	0.417504
16.53	16.7658	1.426497	16.7521	1.343618	16.7491	1.325469
15.86	15.9719	0.705549	15.9591	0.624842	15.9599	0.629887
16.14	16.0059	0.830855	15.9925	0.913879	15.9929	0.9114
15.98	16.0255	0.284731	16.0132	0.20776	16.0143	0.214643
16.1	16.4097	1.923602	16.3963	1.840373	16.3978	1.849689
16.34	16.4353	0.583231	16.4218	0.500612	16.4227	0.50612
16.39	16.4465	0.344722	16.4335	0.265406	16.4353	0.276388
16.62	16.5465	0.442238	16.53	0.541516	16.5294	0.545126
16.43	16.5637	0.813755	16.5484	0.720633	16.5475	0.715155
16.42	16.5666	0.892814	16.5504	0.794153	16.55	0.791717

References

1. Kim T, Pang C, Lee G-Y (2012) A fexible and highly sensitive strain-gauge sensor using reversible interlocking of nano fibers. Nat Mater 11:7
2. Choi J, Lee S, Kim J (2012) Patterned oxide semiconductor by electrohydrodynamic jet printing for transparent thin film transistors. Appl Phys Lett 100:102108. https://doi.org/10.1063/1.3691177

3. Kwack Y-J, Choi W-S (2013) Electrohydrodynamic jet spraying technique for oxide thinfilm transistor. IEEE Electron Device Lett 34:78–80. https://doi.org/10.1109/LED.2012.2226557

4. Vaezi M, Seitz H, Yang S (2012) A review on 3D micro-additive manufacturing technologies. Springer, London

5. Calvert P (2001) Inkjet printing for materials and devices. Chem Mater 13:3299–3305

6. Onses MS, Sutanto E, Ferreira PM et al (2015) Mechanisms, capabilities, and applications of high-resolution electrohydrodynamic jet printing. Small 11:4237–4266

7. Yin ZP, Huang YA, Bu NB, Wang XM, Xiong YL (2010) Inkjet printing for flexible electronics: materials, processes and equipments. Chin Sci Bull 55:3383–3407. https://doi.org/10.1007/s11434-010-3251-y

8. Gao D, Zhou JG, (2019) Designs and applications of electrohydrodynamic three-dimensional printing. Int J Bioprint 5(1):172. https://doi.org/10.18063/ijb.v5i1.172

9. Raje PV, Murmu NC (2014) A review on electrohydrodynamic inkjet printing technology. Int J Emerg Technol Adv Eng 4(5)

10. Park J-U, Hardy M, Kang SJ, Barton K, Adair K, Mukhopadhyay DK, Lee CY, Strano MS, Alleyne AG, Georgiadis JG, Ferreira PM, Rogers JA (2007) High-resolution electrohydrodynamic jet printing. https://doi.org/10.1038/nmat1974

11. Chen C-H, Saville DA, Aksay IA (2006) Electrohydrodynamic "drop-and-place" particle deployment. Appl Phys Lett 88:154104. https://doi.org/10.1063/1.2191733

12. Kim J, Oh H, Kim SS (2008) Electrohydrodynamic drop-on-demand patterning in pulsed cone-jet mode at various frequencies. J Aerosol Sci 39:819–825. https://doi.org/10.1016/j.jaerosci.2008.05.001

13. Barton K, Mishra S, Alleyne A (2011) Control of high-resolution electrohydrodynamic jet printing. Control Eng Pract 19:1266–1273. https://doi.org/10.1016/j.conengprac.2011.05.009

14. An S, Lee MW, Kim NY (2014) Effect of viscosity, electrical conductivity, and surface tension on direct-current-pulsed drop-on-demand electrohydrodynamic printing frequency. Appl Phys Lett 105:214102. https://doi.org/10.1063/1.4902241

15. Li JL (2006) On the meniscus deformation when the pulsed voltage is applied. J Electrostat 64:44–52. https://doi.org/10.1016/j.elstat.2005.04.005

16. Taylor G (1964) Disintegration of water drops in an electric field. Proc R Soc A Math Phys Eng Sci 280:383–397

17. Das R, Roy SS, Murmu NC (2020) An experimental investigation for parametric appraisal of electrohydrodynamic-driven microfabrication approach using teaching and learning-based optimization. J Braz Soc Mech Sci Eng 42:257. https://doi.org/10.1007/s40430-020-02349-8

18. Shucai Y, Chunsheng H, Minli Z (2018) A prediction model for titanium alloy surface roughness when milling with micro-textured ball-end cutters at diferent workpiece inclination angles. Int J Adv Manuf Technol 100(5–8):2115–2122

19. Armaghani DJ, Hajihassani M, Sohaei H, Mohamad ET, Marto A, Motaghedi H, Moghaddam MR (2015) Neuro-fuzzy technique to predict air-over pressure induced by blasting. Arab J Geosci 8:10937–10950

20. Najafzadeh M, Azamathulla HM (2015) Neuro-fuzzy GMDH to predict the scour pile groups due to waves. J Comput Civ Eng 29:4014068

Significance of Machine Learning in Industry 4.0 Scenario—A Review

M. B. Kiran

1 Introduction

Industry 4.0 includes machine learning, big data analytics, sensors, RFID, Internet, cyber-physical systems (CPS), mobile devices, camera, wireless network, cloud, robotics, machine learning, and artificial intelligence (Fig. 1). With the introduction of Industry 4.0, it has become possible to connect different machines connected with sensors (CPS) used in manufacturing, over a wireless network, for interaction, data sharing and independent decision making, without human intervention. The use of Industry 4.0 in manufacturing would help in achieving operational excellence. Figure 2 shows the different functions of a manufacturing company that can be benefitted from Industry 4.0. Machine learning is a set of algorithms that are used to automatically detect the hidden patterns in the given data set either for making predictions or for making decisions under uncertainties [1]. Machine learning may also be defined as exploring knowledge from a given data set for making future decisions/predictions.

Machine learning is applicable in different domains, viz. manufacturing, agriculture, food processing, pharma companies, space applications, etc. In this research work, machine learning is studied as applied to manufacturing.

While modeling by machine learning technique, the given data set is sliced into the training set and a test set. The training set is a portion of data used for training the model. Whereas, the test set is a portion of data used for testing a model.

Supervised learning (S) is a type of training model where both input and output are given to the model. Whereas, in unsupervised learning, the model is required to identify the classes (output) by looking at the data (input) features.

M. B. Kiran (✉)
Department of Mechanical Engineering, Pandit Deendayal Petroleum University, Gandhinagar, Gujarat, India
e-mail: MB.Kiran@sot.pdpu.ac.in
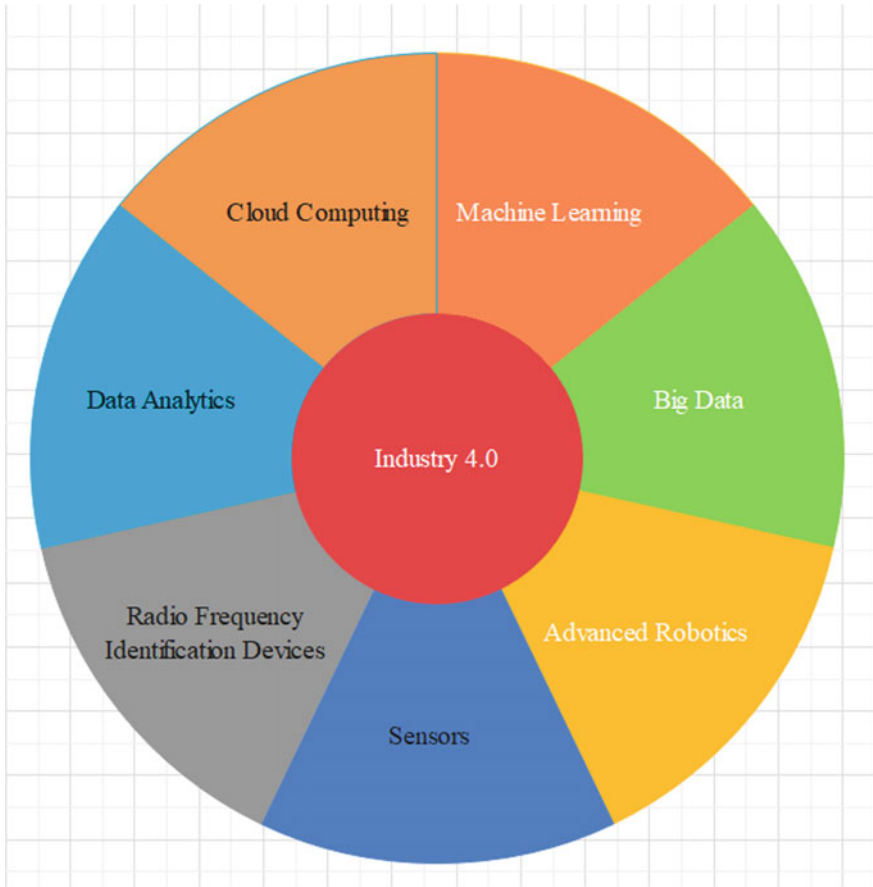
Fig. 1 Industry 4.0 technologies

Section 2 highlights how these technologies can be implemented in a manufacturing company for making it smart.

The objective of any manufacturing company is to transform raw materials into a finished product in the most economical way possible. So that the company can sell its products easily to its customers against the competition. Thus, a company sells its product only if it can attract a customer amid competition. Attracting customers is possible only if the product has better quality than the competitor and the price of the product is reasonable. Manufacturing companies were using mass production-based techniques to sell the product to the customer at a cheaper price than the competitor. This sounds good if there is a huge demand for the product. However, the scenario is changing nowadays. Today expectations are different for different customers. In this scenario, manufacturing companies cannot manufacture products in bulk, using large batch sizes, by mass production techniques. This scenario has compelled companies to devise new methods for solving the problem.
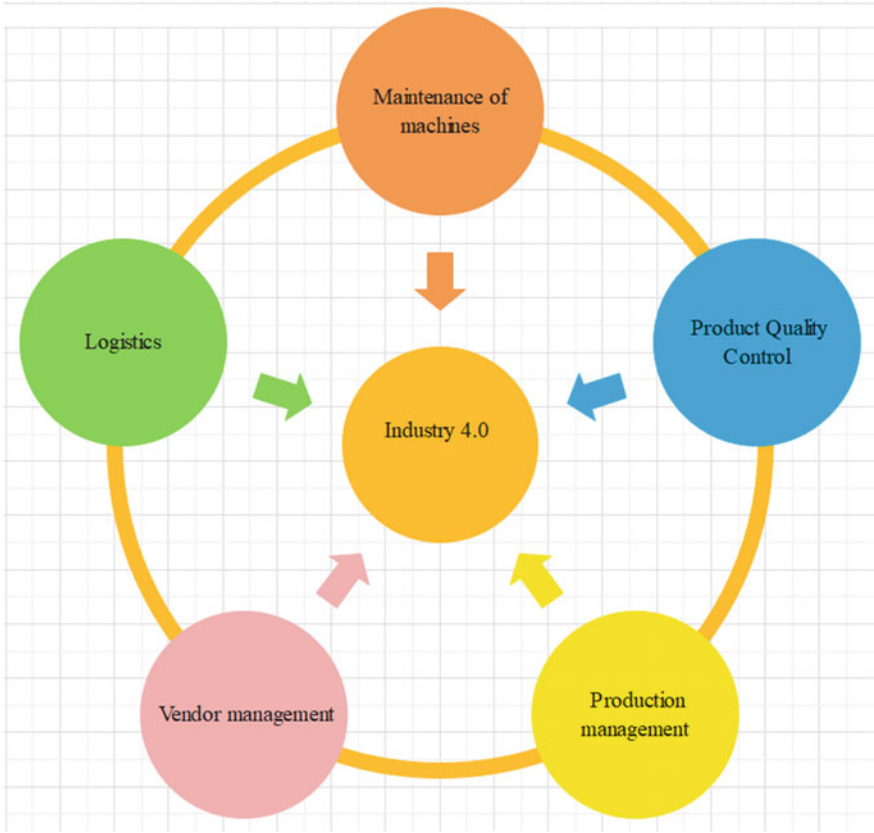
Fig. 2 Significance of Industry 4.0 in a manufacturing company

Additionally, manufacturing companies were storing large amounts of raw materials in the storeroom, for protecting themselves against the supply side variation. That is, companies want to play safely in case of failure of suppliers from supplying raw materials on time. As this will affect the manufacturing and subsequently the customer. Companies used to maintain large amounts of inventory of raw materials. Maintaining large amounts of inventory is costly and is very risky. Thus, companies are expecting new ways of solving the problem.

Companies are also facing difficulty in producing consistent quality products over some time. This may be due to multiple reasons. One of the significant reasons is the lack of standardization.

The study also showed that there is a significant amount of waiting time for the work-in-process. That is, the material had to wait for subsequent processing. This involves a significant amount of space for storing work-in-process and would clutter the workplace. However, companies have been regularly maintaining their machine

tools. The total cost of maintenance is becoming very high. Companies are looking for new ways of reducing the overall maintenance cost.

Many of the existing product inspection techniques in industries are post-process in nature. That is, the product inspection is being done only after product manufacturing. This means that statistical quality-based sampling inspection is being done for product quality testing. Sampling-based inspections are not foolproof, and there are chances of accepting a defective product or rejecting a quality product. Thus, there is a chance of defective products reaching the customer. When this happens, this would result in customer dissatisfaction and will affect the company's reputation. Therefore, manufacturers are again looking for new ways of inspecting products to achieve 100% inspection at the same time bring down the cost of the inspection.

An attempt has been made, in the above paragraphs, to highlight only a few problems being faced by manufacturing companies. Likewise, manufacturing companies are being faced with a multitude of challenges. The manufacturers are looking for new technologies, new techniques, and tools for addressing their problems. In this context, the present study assumes special significance.

2   Literature Review

Many manufacturing companies are looking for solving their problems using Industry 4.0. Many researchers have been working on using Industry 4.0 for solving industry problems. The following paragraphs try to explain how the different Industry 4.0 technologies, including machine learning, are being used in addressing the different problems in manufacturing companies.

2.1   Maintenance of Machines

Cho et al. [2] have studied the milling process. They collected data about cutting forces and the power consumed during the machine, by using sensors. They used support vector (SVM) regression for identifying the tool breakage identification. The method uses a supervised classification technique, for classifying the defects. Saxena and Saad [3] had studied the health of a roller bearing. Data is collected by using sensors. They proposed a technique that combines both genetic algorithms and neural networks (NN) for feature selection and subsequent classification. Kankar et al. [4] devised a scheme of using both NN and SVM for analyzing defects in ball bearings. They have concluded that the method is feasible. The method again is a supervisory classification technique. Azadeh et al. [5] have studied on performance data of a centrifugal pump. They proposed a method that makes use of NN, GA, and SVM techniques for defect classification. The method is based on the supervisor learning technique. The authors claim that the method works even with corrupted data of centrifugal pumps.

Zhang et al. [6] designed a method which makes use of SVM and ant colony-based supervisory methods for defect identification in roller bearings of a locomotive. Li et al. [7] have proposed an ensemble learning technique based on machine learning for tool wear classification. The authors have claimed very good accuracy in classification. Bukkapatnam et al. [8] designed a supervisory-based technique for the prediction of machine failures based on random forest technique. Authors have claimed good accuracy in prediction. Alegeh et al. [9] have proposed a method for maintenance prediction using the machine learning technique. The method is a supervisory learning technique. The method is based on the K-nearest neighbor and SVM method. Susto et al. [10] have applied machine learning in solving maintenance problems. The method gave a maintenance schedule for minimizing maintenance costs. The method is based on a supervised learning technique. They had used KNN and SVM for classification.

Wan et al. [11] proposed a technique based on NN for assessment of the remaining life of different parts of machine tools. They proposed a preventive maintenance method in a big data environment. Kuhnle et al. [12] proposed a method for reducing maintenance cost and downtime. The method is based on the reinforcement learning approach. The main advantage of this technique is that simulation has produced complementary data in addition to the historical data obtained through sensors. Liu et al. [13] have proposed a scheme for fault diagnostics for the FDM process, using the machine learning method. They have used acoustic signals for data collection.

2.2 Product Quality Control

Kusiak and Kurasek [14] have studied the printed circuit board manufacturing process. They proposed a technique for identifying and classification of defects. They have successfully identified different types of solder defects by using the machine learning (ML) technique. Specifically, they employed rough set technique for classifying defects. They have also used data mining techniques for identifying the cause of defects. Kim et al. [15] have worked in a semiconductor (wafer) manufacturing company. They observed different types of defects and proposed a scheme for identifying different types of defects. They have used ML algorithms for the identification and classification of defects related to wafers. They have achieved a very high classification accuracy in classification. Figure 3 shows the types of inspection systems.

Çaydas et al. [16] have studied the CNC machining process. They tried to estimate surface roughness in CNC machining using the SV technique. They had used austenitic stainless steel as raw material for turning operation. They have successfully estimated surface roughness during the turning operation. The authors have also used NN-based technique for comparison. They concluded that SV-based techniques gave higher prediction accuracies. This technique is based on supervisor classification. Ye et al. [17] have studied printed circuit board manufacturing. They have used a combination of NN decision trees and SVM for identifying defects in the printed
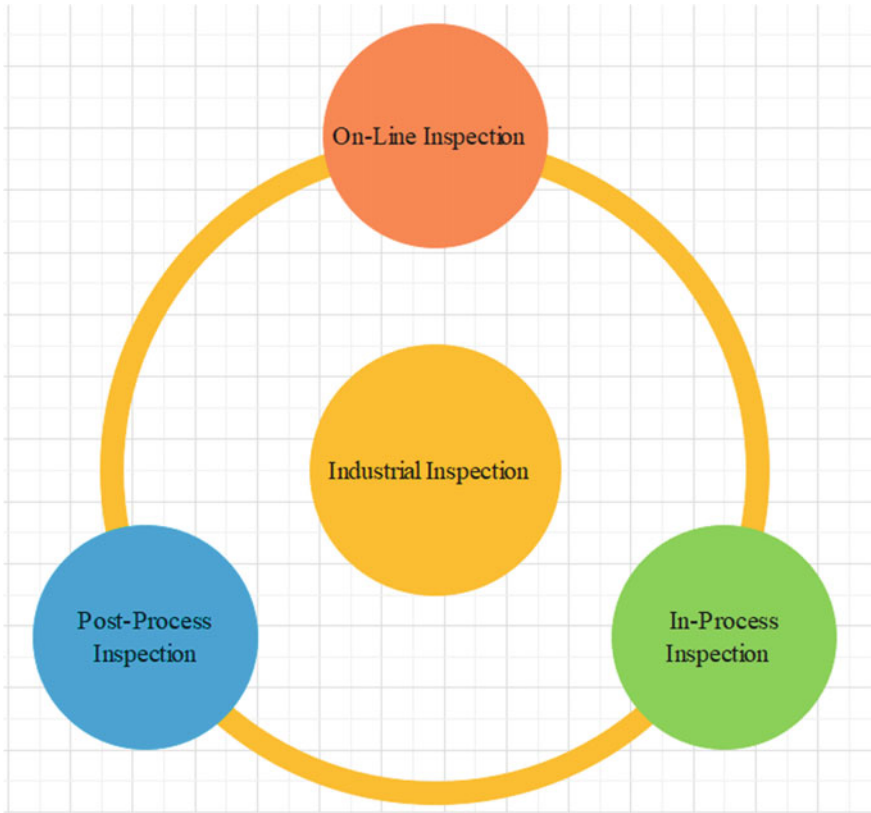
Fig. 3 Types of industrial inspection system

circuit board. This is a supervisor learning method. The method was successfully used for estimating the dielectric thickness in the manufacturing of semiconductors.

Lenz et al. [18] have worked in the semiconductor industry and studied defects and proposed a technique for defect identification. This is a supervised classification technique. They have used a combination of NN decision trees and SVM for identifying defects in wafer manufacturing. The authors have claimed high classification rates. Tan et al. [19] have also proposed a technique based on supervised classification technique for defect classification. The method makes use of an evolutionary neural network for classification. Gao et al. [20] have studied metal manufacturing companies. They proposed an unsupervised learning technique for the classification of defects. The method uses a non-negative matrix factorization method. When the different classes are not represented equally in a classification problem, it would result in an imbalanced data set. Lee et al. [21] have studied different supervised-based learning techniques for process fault detection and classification. Authors have claimed that Random forests offer very good results, especially with the imbalanced data set. Wang et al. [22] have used SVM for predicting quality in an abrasion-resistant

manufacturing process. They have achieved good results. Ko et al. [23] have worked on anomaly detection problems using machine learning and have claimed to have got very good results. The authors have rightly identified the anomalies in different machinery systems.

Tusar et al. [24] have proposed a supervisory technique that is based on machine learning and decision tree for predicting the quality of machined components. Liu et al. [25] proposed an unsupervised learning method for fault detection as well as an isolation method. Kim et al. [26] have proposed a new scheme for identifying defects. The method is based on the supervised learning method. They used die-cast data set. They have shown that the decision tree-based technique works superior to other types of classifiers. Khanzadeh et al. [27] designed algorithm based on in supervised learning method. The method uses a self-organizing map for defect detection. They studied additive manufacturing molten pool, and Manohar et al. [28] have studied aircraft assembly. They proposed an unsupervised learning method based on machine learning for defect identification by looking at the molten pool. Zhu et al. [29] designed a supervised learning algorithm for identifying defects in additive manufacturing.

2.3   Production Management

Shin et al. [30] have studied manufacturing systems for process control using a fuzzy reinforcement learning algorithm. The method is a reinforcement learning algorithm. The main characteristic of the method is that it can dynamically set goals. Garcia Nieto et al. [31] designed a supervisory learning algorithm which uses SVM and NN to control the manufacturing process of a paper mill. Wang et al. [22] designed a prediction model for tool wear prediction in a manufacturing company. They claim that they got high accuracy in tool wear prediction.

Maggipinto et al. [32] have designed a supervised learning algorithm using CNN for manufacturing process control. Mezzogori et al. [33] have proposed a supervisory learning-based technique for controlling the manufacturing process. The method uses a deep learning-based neural network and regression model to predict the throughput time after knowing current state of system. Authors have claimed higher prediction accuracies.

2.4   Vendor Management

The following paragraphs highlight the significance of machine learning in vendor management. Zan et al. [34] have proposed a supervisor-based learning method using both CNN and NN for process control.

2.5   *Logistics*

Logistics operation consists of different activities—delivering goods as per customer requirement, receiving customer order, etc. Manufacturing companies are currently facing many problems and in-efficiencies, concerning logistics and the companies are exploring means for addressing them through Industry 4.0. Digitization through Industry 4.0 has helped in reducing the carbon emission [35]. Industry 4.0 is also helping in making the logistics more reliable [36].

3   Conclusion

With the advent of Industry 4.0, many industries including manufacturing have attempted implementing machine learning for operational excellence and to meet customer expectations. Current research work attempts to study the different machine learning algorithms being proposed by many researchers for solving many production-related problems/ or challenges. From the above paragraphs, it is clear that there is an increase in the use of machine learning in the manufacturing sector. It is also evident from the above paragraphs that a significant number of researchers have implemented machine learning in addressing problems related to maintenance and quality. Researchers have proposed algorithms for designing effective maintenance strategies using machine learning. Researchers have also proposed techniques for assessing the remaining useful life of a machine tool. However, the accuracy of prediction requires improvement. Also, none of the papers reported the repeatability of measurement machine learning-based systems to help a manufacturing organization in selecting the right maintenance policy for a given machine tool. Machine learning algorithms are also widely used in automated product inspection. By using machine learning, researchers have demonstrated that 100% product inspection are possible in product inspection by making use of machine learning. Only 100% inspection techniques are capable of ensuring quality product reaching the customer. This will also make the customer happy and will improve company's reputation. This is a significant contribution of machine learning in improving the productivity of manufacturing organization. Table 1 shows the problem areas that are to be addressed by researchers.

However, many researchers have been contributing to defect identification and classification. The accuracy and robustness of classification algorithms require improvement. There is a huge need for designing and developing new and novel techniques for defect detection and classification. It is also evident that the machine learning algorithms are being applied in designing effective production schedules, to determine the best route for manufacturing a given product, scheduling, dispatching, and expediting activities. Many of the machine learning techniques proposed by researchers are based on supervisory and un-supervisory learning techniques. The least number of techniques was reported based on reinforcement learning techniques.

Table 1 Directions for further research

Area	Problems to be addressed	Remarks
Product quality assessment	Online quality assessment of manufactured products in the context of Industry 4.0	Inspection time reduction, Improved and effective quality metrics
	In-process quality assessment of manufactured products in the context of Industry 4.0	
	Product quality assessment of moving parts with fixed orientation/random orientation	Design and development of effective deblurring algorithms
	Defect identification and classification	Robustness, accuracy improvement
Machine maintenance	To assess the remaining life of components	To minimize the overall maintenance cost
	To select appropriate maintenance policy for a given machine/or material handling equipment	Accuracy and robustness in prediction
	To make use of the merits of different supervised/unsupervised/and reinforcement learning methods	
	To reduce the requirement of data sets for training the neural network	
	Assessment of maintenance policy effectiveness	
	Condition-based maintenance	To improve effectiveness
	Data mining and artificial intelligence-based techniques for prediction	
	Maintenance budget performance estimation	
	Effectiveness of preventive maintenance schedules	
	Reliability assessment and productivity enhancement	
	Customer satisfaction prediction using maintenance policies	
Vendor management	Vendor effectiveness assessment	

Table 1 (continued)

Area	Problems to be addressed	Remarks
	Integration of manufacturing with vendor management for achieving supply chain excellence	
	Items tracking and inventory management	
	Vendor selection/switching effectiveness	
	Assessment of waste and developing standards for continuous improvement	
	Direct/or indirect integration with customers	
Production planning and production control	Effectiveness of routing prediction	
	Process capability assessment	
	Tool wear assessment and predicting tool life in the context of Industry 4.0	
	In-process material inspection and integrating with vendor assessment	
	Effectiveness of dispatching methods	
	Machine selection for performing machining of components	
	Cutting tool selection and estimation of tool life	Robustness of prediction model
	Reducing the number of trips required by automated guided vehicles	
Supply chain	Post-delivery customer support or reverse logistics	
	To measure supply chain leanness/or effectiveness	
	Assessment of supply chain flexibility	
	Supplier–company relationship assessment	
	Assessment of supply chain	Through metrics

Table 1 (continued)

Area	Problems to be addressed	Remarks
	Predicting customer satisfaction of the company's supply chain	
	Enhance the effectiveness of company's supply chain	
	Measuring supply chain volatility in terms of misaligned corporate goals	
	Assessment of government policy effect on supply chain volatility	
	Supply lead time prediction	Accuracy improvement
	Assessment of reliability of business processes	

Thus, there is a need to explore the benefits of reinforcement learning techniques in solving production-related problems. The least number of research works have been reported, in literature, on vendor selection, vendor management, vendor assessment area, integrating operations and procurement, designing the best supply chain for a given organization, and designing effective logistics. Not much research work is reported in the use of both simulation and machine learning-based systems for improving operational productivity. With the advent of Industry 4.0, CPS is made available. There is a huge potential for designing robust security infrastructure for cyber-physical systems by making use of machine learning techniques. Also, protecting CPS is a dynamic problem and it is very challenging. There is also a need for identifying and classifying different types of intruders in the case of protecting cyber-physical systems. One more requirement for protecting cyber-physical systems is that the security application should be robust and foolproof.

References

1. Murphy K (2012) Machine learning: a probabilistic perspective. The MIT Press, Cambridge
2. Cho S, Asfour S, Onar A, Kaundinya N (2005) Tool breakage detection using support vector machine learning in a milling process. Int J Mach Tools Manuf 45(3):241–249
3. Saxena A, Saad A (2007) Evolving an artificial neural network classifier for condition monitoring of rotating mechanical systems. Appl Soft Comput 7(1):441–454
4. Kankar PK, Sharma SC, Harsha SP (2011) Fault diagnosis of ball bearings using machine learning methods. Expert Syst Appl 38(3):1876–1886

5. Azadeh A, Saberi M, Kazem A, Ebrahimipour V, Nourmohammadzadeh A, Saberi Z (2013) A flexible algorithm for fault diagnosis in a centrifugal pump with corrupted data and noise based on ANN and support vector machine with hyperparameters optimization. Appl Soft Comput 13(3):1478–1485

6. Zhang Y, Harik R, Fadel G, Bernard A (2019) A statistical method for build orientation determination in additive manufacturing. Rapid Prototyp J 25(1):187–207

7. Li S, Liu G, Tang X, Lu J, Hu J (2017) An ensemble deep convolutional neural network model with improved D-S evidence fusion for bearing fault diagnosis. Sensors 17(8):1729

8. Bukkapatnam STS, Afrin K, Dave D, Kumara SRT (2019) Machine learning and AI for long-term fault prognosis in complex manufacturing systems. CIRP Ann 68(1):459–462

9. Alegeh N, Shagluf A, Longstaff AP, Fletcher S (2019) Accuracy in detecting a failure in Ballscrew assessment towards machine tool servitization. Int J Mech Eng Robot Res 8(5):667–673

10. Susto GA, Schirru A, Pampuri S, McLoone S, Beghi A (2015) Machine learning for predictive maintenance: a multiple classifier approach. IEEE Trans Industr Inf 11(3):812–820

11. Wan J, Tang S, Li D, Wang S, Liu C, Abbas H, Vasilakos AV (2017) A manufacturing big data solution for active preventive maintenance. IEEE Trans Industr Inf 13(4):2039–2047

12. Kuhnle A, Jakubik J, Lanza G (2018) Reinforcement learning for opportunistic maintenance optimization. Prod Eng Res Devel 13(1):33–41

13. Liu J, Hu Y, Wu B, Wang Y (2018) An improved fault diagnosis approach for FDM process with acoustic emission. J Manuf Process 35:570–579

14. Kusiak A, Kurasek C (2001) Data mining of printed-circuit board defects. IEEE Trans Robot Autom 17(2):191–196

15. Kim D, Kang P, Cho S, Lee H, Doh S (2012) Machine learning-based novelty detection for faulty wafer detection in semiconductor manufacturing. Expert Syst Appl 39(4):4075–4083

16. Çaydas U, Ekici S (2010) Support vector machine models for surface roughness prediction in CNC turning of AISI 304 austenitic stainless steel. J Intell Manuf 23(3):639–650

17. Ye F, Zhang Z, Chakrabarty K, Xinli GU (2013) Board-level functional fault diagnosis using artificial neural networks, support vector machines, and weighted majority voting. IEEE Trans Comput Aided Des Integr Circuits Syst 32(5):723–736

18. Lenz B, Barak B, Muhrwald J, Leicht C, Lenz B (2013) Virtual metrology in semiconductor manufacturing through predictive machine learning models. In: 2013 12th international conference on machine learning and applications

19. Tan SC, Watada J, Ibrahim Z, Khalid M (2015) Evolutionary fuzzy ARTMAP neural networks for classification of semiconductor defects. IEEE Trans Neural Netw Learn Syst 26(5):933–950

20. Gao B, Woo WL, Tian GY, Zhang H (2016) Unsupervised diagnostic and monitoring of defects using waveguide imaging with adaptive sparse representation. IEEE Trans Industr Inf 12(1):405–416

21. Lee T, Lee KB, Kim CO (2016) Performance of machine learning algorithms for class-imbalanced process fault detection problems. IEEE Trans Semicond Manuf 29(4):436–445

22. Wang J, Yan J, Li C, Gao RX, Zhao R (2019) Deep heterogeneous GRU model for predictive analytics in smart manufacturing: application to tool wear prediction. Comput Ind 111:1–14

23. Ko T, Lee JH, Cho H, Cho S, Lee W, Lee M (2017) Machine learning-based anomaly detection via integration of manufacturing, inspection, and after-sales service data. Ind Manag Data Syst 117(5):927–945

24. Tusar T, Gantar K, Koblar V, Zenko B, Filipič B (2017) A study of overfitting in optimization of a manufacturing quality control procedure. Appl Soft Comput 59:77–87

25. Liu Z, Jia Z, Vong C-M, Bu S, Han J, Tang X (2017) Capturing high discriminative fault features for electronics-rich analog systems via deep learning. IEEE Trans Ind Inf 13(3):1213–1226

26. Kim A, Oh K, Jung J-Y, Kim B (2018) Imbalanced classification of manufacturing quality conditions using cost-sensitive decision tree ensembles. Int J Comput Integr Manuf 31(8):701–717

27. Khanzadeh M, Rao P, Jafari-Marandi R, Smith BK, Tschopp MA, Bian L (2017) Quantifying geometric accuracy with unsupervised machine learning: using the self-organizing map on

fused filament fabrication additive manufacturing parts. J Manuf Sci Eng 140(3). https://doi.org/10.1115/1.4038598

28. Manohar K, Hogan T, Buttrick J, Banerjee AG, Kutz JN, Brunton SL (2018) Predicting shim gaps in aircraft assembly with machine learning and sparse sensing. J Manuf Syst 48:87–95

29. Zhu Z, Anwer N, Huang Q, Mathieu L (2018) Machine learning in tolerancing for additive manufacturing. CIRP Ann 67(1):157–160

30. Shin M, Ryu K, Jung M (2012) Reinforcement learning approach to goal regulation in a self-evolutionary manufacturing system. Exp Syst Appl 39(10):8736–8743

31. García Nieto PJ, Martínez Torres J, Araújo Fernandez M, Ordonez Galan C (2012) Support vector machines and neural networks used to evaluate paper manufactured using Eucalyptus globulus. Appl Math Model 36(12):6137–6145

32. Maggipinto M, Terzi M, Masiero C, Beghi A, Susto GA (2018) A computer vision-inspired deep learning architecture for virtual metrology modeling with 2- dimensional data. IEEE Trans Semicond Manuf 31(3):376–384

33. Mezzogori D, Zammori F (2019) An entity embeddings deep learning approach for demand forecast of highly differentiated products. Proc Manuf 39:1793–1800

34. Zan T, Liu Z, Wang H, Wang M, Gao X (2019) Control chart pattern recognition using the convolutional neural network. J Intell Manuf 31(3):703–716

35. Engelhardt-Nowitzki C (2012) Improving value chain flexibility and adaptability in build-to-order environments. Int J Phys Distrib Log Manag 42:318–337

36. Christopher M, Holweg M (2017) Supply chain 2.0 revisited: a framework for managing volatility-induced risk in the supply chain. Int J Phys Distrib Log Manag 47:2–17

Accelerated Defective Product Inspection on the Edge Using Deep Learning

Dimitris Tsiktsiris, Theodora Sanida, Argyrios Sideris, and Minas Dasygenis

1 Introduction

The process of pouring molten metal into a mold cavity in order to create metal objects is called casting [1]. However, as in any manufacturing process, defects or unwanted irregularities can occur and are a common problem in casting products [2]. Quality control is responsible for examining those products and ensures that they meet the requirements [3]. Products with defects and irregularities should be discarded from the supply chain before reaching the final customer. Failures to quality inspection can cause rejection, revenue and reputation loss for the companies [4].

One of the most common techniques to detect defected products and perform quality inspection is through visual analysis [5]. Usually, a human operator performs a manual inspection of each test unit and classifies them as defective or non-defective. However, the classification can be prone to errors and is time consuming, due to the human-dependent nature of the technique. A single error in this process can lead to waste of resources and revenue loss as the company has to reject the whole production order.

In this paper, a Convolutional Neural Network (CNN) is trained to analyze images of a casting product and classify defective castings from the normal ones. The deep learning algorithm is deployed to a Jetson AGX Xavier embedded system that

D. Tsiktsiris (✉) · T. Sanida · A. Sideris · M. Dasygenis
Department of Electrical and Computer Engineering, University of Western Macedonia, 50131 Kozani, Greece
e-mail: dtsiktsiris@uowm.gr

T. Sanida
e-mail: thsanida@uowm.gr

A. Sideris
e-mail: asideris@uowm.gr

M. Dasygenis
e-mail: mdasyg@ieee.org

enables seamless integration due to the low power consumption and small dimensions. Deep learning optimizations and acceleration through TensorRT and NVIDIA Deep Learning Accelerators (DLAs) that are embedded on Jetson platform, allow for top-end classification and runtime performance. The system achieves 99.72% classification accuracy, and it is able to process up to 136 product images per second with about 28 W of peak power consumption. The system can operate standalone due to the high accuracy or can be used conjunctively with a human operator. The main contributions of our work can be summarized as follows:

- We present a deep learning approach for quality inspection that achieves high accuracy
- As proof of concept, we deployed our algorithms on the Jetson AGX Xavier platform using industrial hardware for seamless integration to the assembly lines
- We optimize our system using TensorRT and DLAs for achieving top-end performance with low power consumption.

This paper is organized as follows. Section 2 enlists the related work in the field while Section. 3 describes the dataset used, the proposed network architecture and the training process to employ the AI algorithm. Section 4 presents the results of this work while Sect. 5 concludes the paper.

2   Related Work

Several research activities have been performed in order to employ machine vision and machine learning for automating quality control and product inspection. Here we will present the prominent ones related to our work.

Ireri et al. [6] proposed a tomato grading machine vision system based on RGB images. Initially, image subtraction techniques were applied in order to eliminate the background. Calyx and stalk scars were detected, and defects were segmented by histogram thresholding based on the mean g–r value of these regions of interest. Finally, common classifiers such as support vector machine (SV) and random forest algorithms were applied for the classification of different tomato categories. The obtained results indicate that the RBF-SVM algorithm outperformed all the other models with the highest accuracy of 97.09% for the healthy and defected categories. However, the accuracy of classification decreased as the number of grading categories increased.

Wang et al. [7] proposed an AI model for quality control based on deep learning and the Hough transform. The proposed approach identifies irregular units through three stages: preprocessing, region of interest (ROI) extraction and classification. The Hough transform technique was used to detect features and extract the ROI from filtered images. Finally, a convolutional neural network was used as a classifier. The proposed approach achieves good accuracy and requires 47.60 ms of processing each image.

   Although there are several similar approaches for quality control, it is hard to find a solution that provides high accuracy, sufficient performance for evaluating multiple assembly lines and the ability to operate on the edge as a separate and seamless module.

3   Implementation

The proposed system is designed to perform automated quality control via visual inspection. A camera sensor is being used in order to acquire image data of the product. The input images are then preprocessed and forwarded into a visual analysis module to detect irregular and defected products.

3.1   Dataset and Preprocessing

For training of our model, we use the excellent dataset provided by Ravirajsinh Dabhi [8]. The dataset contains a total of 7348 images of impellers at 300×300 image resolution. The dataset is splitted with a 0.9 split ratio for training and testing. The images are converted to grayscale, and each pixel value is normalized to [0–1]. An example of the training batch is depicted in Fig. 1 while Fig. 2 shows the normalized pixel intensities after preprocessing.
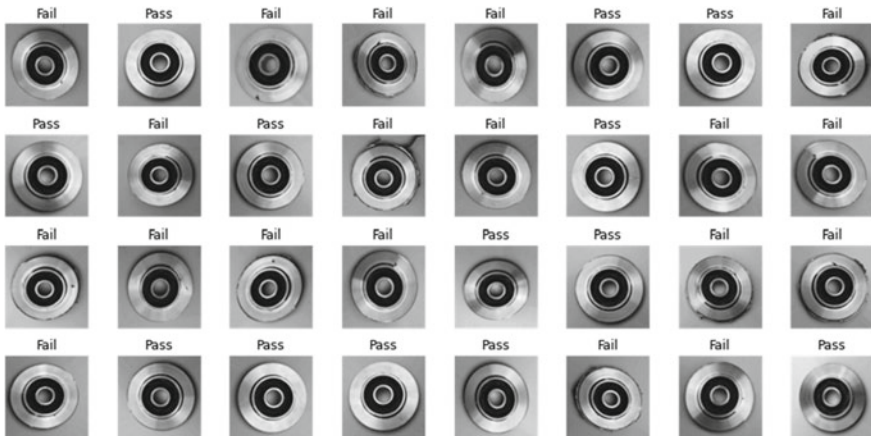
Fig. 1 Overview of the first batch of training images along with the corresponding class they belong
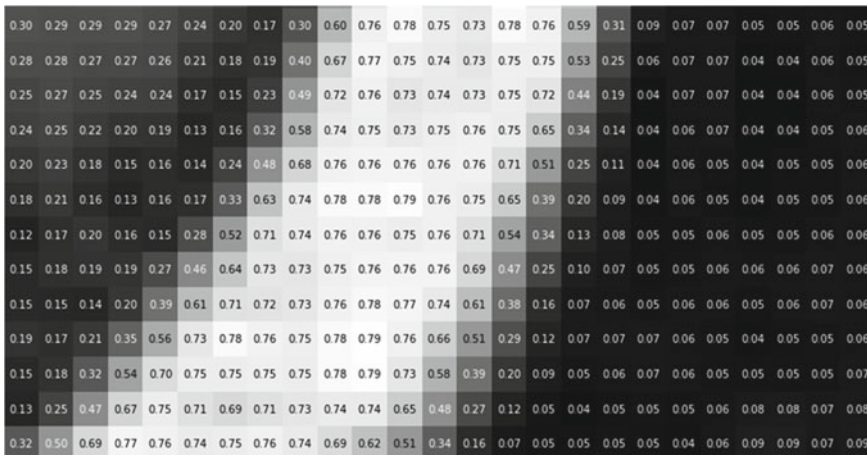
Fig. 2 Preview of image data after preprocessing. The input RGB image is converted to grayscale, and the individual pixel intensities [0–255] are normalized to [0–1]

3.2 Network Architecture

In Fig. 3, we can see an overview of the proposed network architecture. The models consist of three convolutional stages, each one followed via a MaxPooling operation in order to reduce dimensionality while increasing convolutional filters by a factor of 2. Finally, the features are flattened and passed into the final dense layers for the classification.
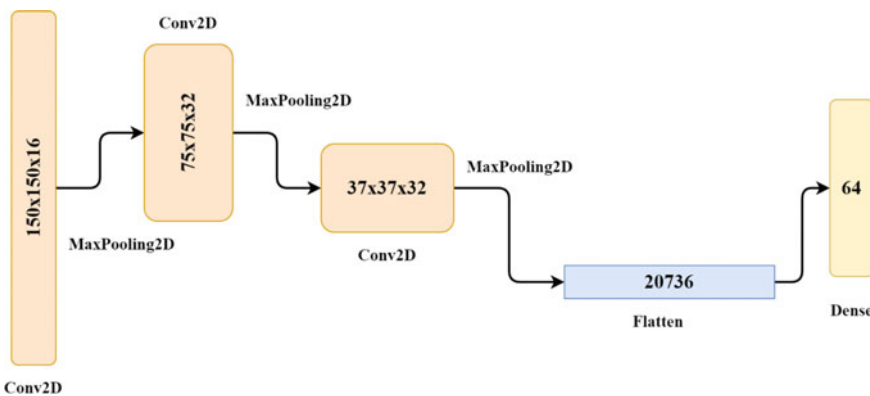
Fig. 3 Network architecture of the proposed model. Each convolutional layer is followed by a max pooling operation to reduce dimensionality. Convolutional filters are being increased by a factor of 2 at each stage, and the extracted features are being flattened and passed into the final dense layers for the classification

3.3 Training

We trained the model for 25 epochs using Adam optimizer with a learning rate of 0.001 and binary cross entropy loss function. Random spatial augmentation techniques are used for scaling, translating and rotating the images. Random color transformations for brightness and contrast are also applied.

4 Results

As Fig. 4 depicts, training the model for 25 epochs achieves 0.0351 training loss and 0.03265 validation loss. Table 1 shows the classification report with the two classes achieving an f1-score of 0.9962 and 0.9978 respectively. The combined accuracy is 99.72%.

The confusion matrix at Fig. 5 depicts the confused predictions during the evaluation of 715 samples. The model did not discard any of the non-defective products
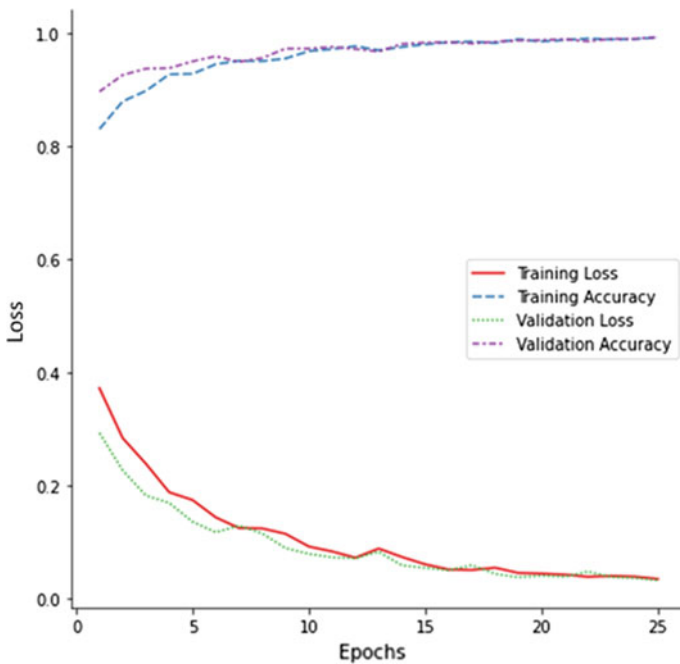
Fig. 4 Training and validation loss/accuracy per epoch. At 25 epochs the model achieves 0.0351 training loss and 0.03265 validation loss. The final accuracies are 0.9921 for the training process and 0.9932 for the validation. Adam optimizer is used along with binary cross entropy loss function

Table 1 Classification report

	Precision	Recall	F1-score	Support
Pass	0.9924	1.0000	0.9962	262
Fail	1.0000	0.9956	0.9978	451
Accuracy			0.9972	715
Macro avg.	0.9962	0.9978	0.9970	715
Weighted avg.	0.9972	0.9972	0.9972	715

Fig. 5 As indicated by the confusion matrix, the model has missed only 2 from a total of 453 defective products while did not discard any of the non-defective products
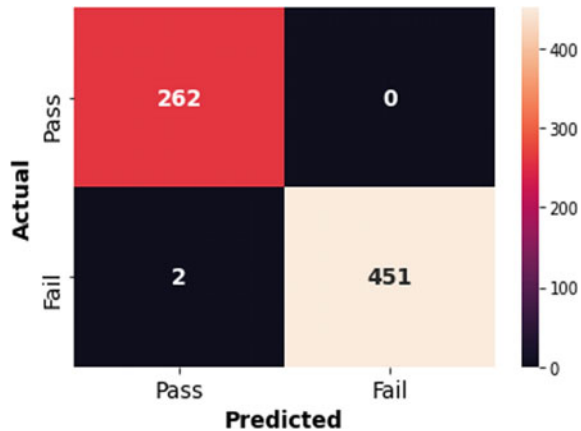
while missed only 2 from a total of 453 defective productions. The percentage of missed defective units is about 0.44% and is considered acceptable (Fig. 6).

The optimized using Nvidia's TensorRT model achieves about 7.3 ms inference latency per image. The system can process about 136 images in total per second.

5   Conclusion

Experiments have shown that the proposed solution achieves sufficient accuracy and performance. The proof-of-concept embedded system, that we specifically designed for industrial use, utilizes several underlying optimization techniques for top-end classification accuracy of 99.72%, runtime performance (136 units per second) and low power consumption (28 W under peak usage). We believe that our research will be a stepping stone toward the quality assurance and eventually lead to reduced errors in the quality control process assisting in faster inspection rates.

Fig. 6 Predicted samples with the actual/predicted label and the confidence score of each detection

References

1. Sulaiman S, Hamouda AMS, Abedin S, Osman MR (2000) Simulation of metal filling progress during the casting process. J Mater Process Technol 100(1–3):224–229
2. Joshi A, Jugulkar LM (2014) Investigation and analysis of metal casting defects reduction by using quality control tools. Int J Mech Product Eng 2092–2320
3. Kassie AA, Assfaw SB (2013) Minimization of casting defects. IOSR J Eng (IOSRJEN) 3(5):31–38
4. Mitra A (2016) Fundamentals of quality control and improvement. Wiley
5. Vernon D (1991) Machine vision-automated visual inspection and robot vision. NASA STI/Recon Tech Rep A 92:40499
6. Ireri D, Belal E, Okinda C, Makange N, Ji C (2019) A computer vision system for defect discrimination and grading in tomatoes using machine learning and image processing. Artif Intell Agric 2:28–37
7. Wang J, Fu P, Gao RX (2019) Machine vision intelligence for product defect inspection based on deep learning and Hough transform. J Manuf Syst 51:52–60
8. Dabhi R (2021) Casting product image data for quality inspection. https://www.kaggle.com/ravirajsinh45/real-life-industrial-dataset-of-casting-product

Machine Learning and Real-Time Signal Features Integration for Strength Modelling in Friction Stir Welding Process

B. Das and Jasper Ramon

1 Introduction

The friction stir welding (FSW) process by virtue of many advantages over conventional fusion welding processes has placed itself in a safe position in industrial applications. The demand in industries in industry 4.0 philosophy is an automated production system. In automated system, one of the concerns is to ensure the quality of the products with less human intervention. FSW being a critical sub process of many industrial production system such as automotive, shipbuilding, the need to develop a reliable process monitoring system is quite essential. The current research work is a contribution in the domain of developing a process monitoring system for the prediction of joint strength which is considered as a benchmark in welded part quality assessment criteria. Researchers in the recent past have attempted to achieve a reliable monitoring model for FSW process to monitor different output factors. Sensor information based control and monitoring of weld quality in FSW process have gained significant attention in the past. Boldsaikhan et al. [1] devised a methodology based on frequency information of force signals acquired during FSW process for classification of defective welds from defective welds. Importance of force signals in control and monitoring of FSW process was also attempted in the technical articles [2–5]. Importance of acoustic emission signal was highlighted in the research work reported by Chen et al. [6] for monitoring of welds in FSW process. Similar works on acoustic emission signal were also reported in the relevant technical articles [7–9]. Other remarkable sensor based control and monitoring of FSW process can be found in the pertinent technical articles [10–12]. Das et al. [13] have presented few methodologies with real-time signal information with various sensors for weld quality prediction and defect identification in FSW process.

B. Das (✉) · J. Ramon
Department of Mechanical Engineering, National Institute of Technology Silchar, Silchar, Assam 788010, India

The current study deals with developing a standalone modelling approach for prediction of ultimate tensile strength (UTS) of the welded samples in a non-destructive approach. Vertical force signals are acquired during the welding process, and later time domain statistical features are computed and the effective feature domain is formed. The same is used for training and testing machine learning model for predicting the strength of the joints.

2 Experimental Investigation and Signal Acquisition

In the current investigation, FSW of aluminium alloy AA1100 is carried out in butt joint configuration. Two workpiece having dimensions of 6 mm × 110 mm × 160 mm are joined using a vertical milling machine developed for FSW process. The experiments are carried out by controlling three significant parameters in FSW process in four levels. The detailed list of parameters with its selected ranges are shown in Table 1. Experiments are designed using full factorial design approach and a total of 64 experimental conditions are obtained. The list of designed experiments are presented in Table 2.

Experiments are performed in random order to reduce the experimentation bias. Tensile samples are prepared as per the standard available in ASTM E8M manual, and tests are carried out in universal tensile testing machine (Make: INSTRON; Model: 8801) to obtain the ultimate tensile strength (UTS) of the welded samples. The UTS of the joint against each experimental condition is also presented in Table 2.

In the current study during the welding experiments, an array of sensors are also integrated with the welding system in order to acquire the real-time signals. In this respect, a force sensor is used for the real-time signal acquisition vertical force signal during the welding experiments. A representative process setup is shown in Fig. 1. Signal acquisition is performed at a sampling frequency of 10 kHz with a 16-bit, 16 channel data acquisition system (Make: National Instrument; Model: USB-6259 BNC). The acquired signals are processed using MATLAB software package, and relevant features are obtained.

Table 1 Process parameters selected in this research work

Process parameters	Level			
	1	2	3	4
Tool rotational speed (TRS, rev/min)	600	815	1100	1500
Welding speed (WS, mm/min)	36	63	98	132
Shoulder diameter (SD, mm)	16	20	24	28

Table 2 List of experiments with coded parameters and experimental strength values

Exp. No.	TRS	WS	SD	UTS
#	rev/min	mm/min	mm	MPa
1	1	1	1	94.05
2	1	1	2	85.87
3	1	1	3	78.56
4	1	1	4	65.69
5	1	2	1	88.42
6	1	2	2	84.64
7	1	2	3	88.12
8	1	2	4	71.88
9	1	3	1	82.45
10	1	3	2	85.24
11	1	3	3	73.6
12	1	3	4	67.55
13	1	4	1	95.89
14	1	4	2	81.89
15	1	4	3	81.95
16	1	4	4	84.09
17	2	1	1	92
18	2	1	2	77.34
19	2	1	3	85.48
20	2	1	4	80.33
21	2	2	1	94.63
22	2	2	2	78.22
23	2	2	3	83.13
24	2	2	4	78.48
25	2	3	1	73.87
26	2	3	2	77.9
27	2	3	3	87.86
28	2	3	4	65.74
29	2	4	1	88.05
30	2	4	2	75.15
31	2	4	3	92.62
32	2	4	4	77.83
33	3	1	1	74.54
34	3	1	2	83.45
35	3	1	3	76.3

(continued)

Table 2 (continued)

Exp. No.	TRS	WS	SD	UTS
#	rev/min	mm/min	mm	MPa
36	3	1	4	51.15
37	3	2	1	91.86
38	3	2	2	82.69
39	3	2	3	89.91
40	3	2	4	76.12
41	3	3	1	81.41
42	3	3	2	77.86
43	3	3	3	75.35
44	3	3	4	79.28
45	3	4	1	95.95
46	3	4	2	77.55
47	3	4	3	63.91
48	3	4	4	77.86
49	4	1	1	88.42
50	4	1	2	64.95
51	4	1	3	92.22
52	4	1	4	81.08
53	4	2	1	92.59
54	4	2	2	81.65
55	4	2	3	88.92
56	4	2	4	68.57
57	4	3	1	71.38
58	4	3	2	77.17
59	4	3	3	87.12
60	4	3	4	81.81
61	4	4	1	80.29
62	4	4	2	83.93
63	4	4	3	59.12
64	4	4	4	83.64

3 Signal Processing and Feature Extraction

In this investigation, vertical force signal (F_z) is acquired using specific sensor integrated with the welding system. The acquired signals are then processed to extract the useful time length that carry effective information related to the welding process. A comparison of vertical force signals acquired against experiment number 16 and
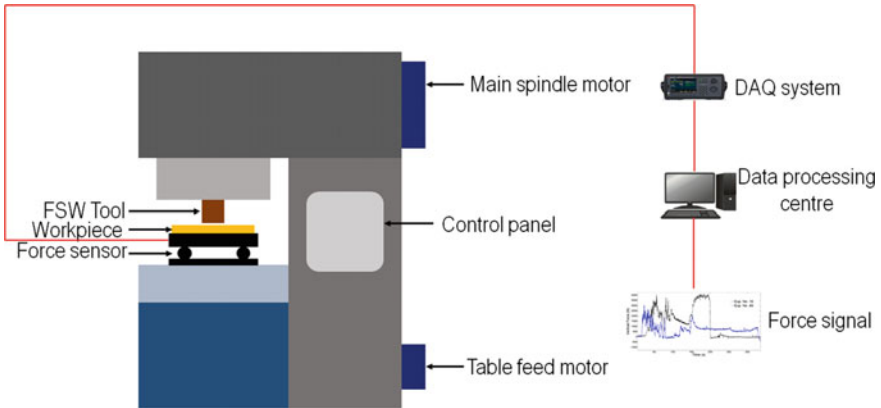
Fig. 1 Schematic representation of the FSW setup integrated with real-time sensor

experiment number 49 is shown in Fig. 2. It is to consider that these experiments are carried out in different experimental conditions as reflected in Table 2.

In Fig. 2, it is evidential that the change incurred due to the variation in process parameters in the welding process is well captured through the force signals. Exp. No. 16 is carried out at low tool rotational speed, high welding speed with tool having large shoulder diameter compared to the parameters used in Exp. No. 49. Low tool rotational speed results in low heat generation due to friction and leads to less plastic deformation. It offers resistance to the system and results in high force requirement. On the other hand, high welding speed results in low heat content per unit weld length and further contribute towards more material resistance and contributing towards the increase of force requirement for the material movement. The physical conditions of the weld are effectively captured in the acquired signals as the cases show substantial variation in the force signal amplitude. Thus, it can
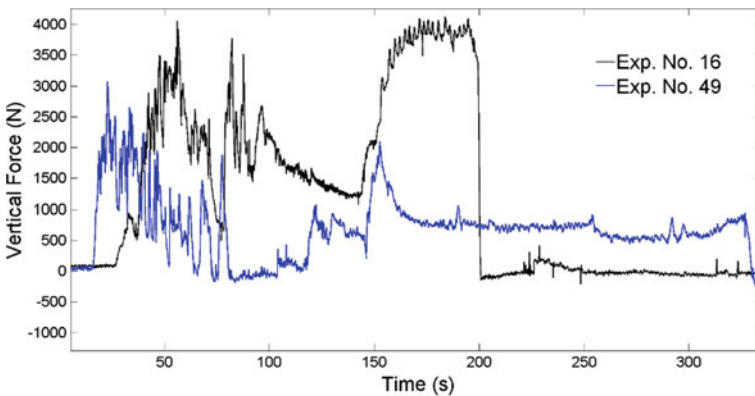
Fig. 2 Acquired force signals during friction stir welding process

be seen that real-time force signal can offer a better visualization of the process. Moreover, not only the predicted changes can be observed through the real-time signals but also the variation due to factors that are beyond human control can also be observed through the signals. This is the key motivation behind dragging the signal information in the strength modelling and optimization framework to extract better performance of the established algorithms. The acquired signals are trimmed in time domain to extract the effective time window representing the welding information. The time window of all the three signals is kept the same to maintain the data order. The signals are then analyzed using MATLAB in time domain and time frequency domain.

The sample signals shown in Fig. 2 provide the insight that the process variation during the welding is effectively captured. The variation in the amplitude of the signal is the testimony of the fact that real-time signal can be an efficient indicator of the process variation for its monitoring and control. In order to convert the information retained by the signal, effective features need to be extracted so that data processing can be easily achieved. In order to retain the information of the signal characteristics, single valued indicators are computed from the signal in the time domain. Root mean square (RMS) and kurtosis (K) values are computed against each experimental conditions of the time domain signals acquired during the experiments as given in Eqs. (1) and (2) respectively. The extracted features are presented in Fig. 3 against the experimental cases for better visibility.

$$\text{RMS} = \sqrt{\frac{1}{n} \sum_{i=1}^{n} s_i^2} \tag{1}$$

$$K = \frac{\sum_{i=1}^{n} (s_i - \bar{s})^4}{\left(\sum_{i=1}^{n} (s_i - \bar{s})^2\right)^2} \tag{2}$$

where, n is the total number of data samples under consideration, s_i is the ith sample in the data set, $\bar{s}$ is the mean of the distribution.
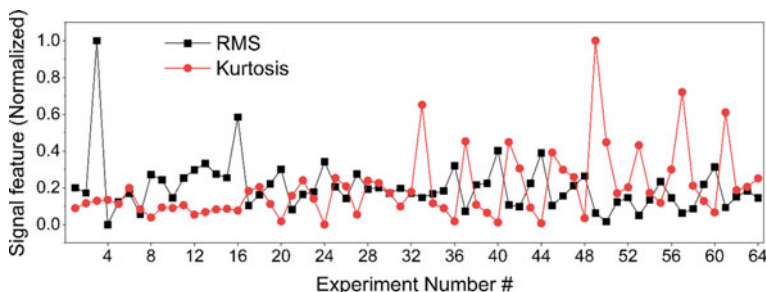
Fig. 3 Time domain statistical features against the experimental conditions

The variation of the extracted features signifies the process variation against the experimental conditions under the influence of factors that are beyond human control during the welding process.

4 Strength Modelling Using SVR

In machine learning technique support vector machine (SVM) is found to be an effective tool in modelling nonlinear functions and mostly data driven functions. SVM proved its capability in multi class problems for classification [14]. However, the effectiveness of SVM can be extended further to prediction problems with model variations. The prediction model of SVM is often referred as support vector regression (SVR) model with all the advantages of SVM. The idea of SVR lies in modelling a nonlinear problem into a linear model with the features in the input space. The mathematical approach for the construction of SVR model is presented in Eq. (3) for reference.

$$p(s, \omega) = \sum_{k=1}^{t} \omega_k h_k(s) + c \tag{3}$$

where, $h_k(s)$; $k = 1, \ldots, t$, represents transformations made into the nonlinear space and c is the constant terms associated with model bias, and ω represents the weight vector against the feature space. The performance of the estimation is often observed through an estimated loss function $L(y, p(s, \omega))$ presented in Eq. (4) and the function associated with estimation risk is given in Eq. (5).

$$L_\varepsilon(y, p(s, \omega)) = \begin{cases} 0 & \text{if } |y - p(s, \omega)| \leq \varepsilon \\ |y - p(s, \omega)| & \text{otherwise} \end{cases} \tag{4}$$

$$R_{\text{emp}}(\omega) = \frac{1}{n} \sum_{i=1}^{n} L_\varepsilon(y_i, p(s_i, \omega)) \tag{5}$$

The advantage of SVR is that it can be useful for linear and nonlinear modelling in the input feature space using the estimated loss function modelled as an optimization problem. The reduced form of the SVR model can be seen in Eq. (6).

$$\min \frac{1}{2}\omega^2 + C \sum_{i=1}^{n} (\xi_i + \xi_i^*)$$

$$\text{s.t.} \begin{cases} y_i - p(s_i, \omega) \leq \varepsilon + \xi_i^* \\ p(s_i, \omega) - y_i \leq \varepsilon + \xi_i \\ \xi_i, \xi_i^* \geq 0, \quad i = 1, \ldots, n \end{cases} \tag{6}$$

Table 3 Optimized parameter for grid search algorithm in SVR model

Parameters #	C	Γ	ε
Range of parameters	1–100	0.01–5	0.001–1
Model I (with signal features)	90	1.85	0.007
Model II (with only process parameters)	85	1.67	0.004

The above mathematical model is further formulated into a dual problem and the solution of which can be seen in Eq. (7).

$$p(s) = \sum_{i}^{n_{sv}} (\alpha_i - \alpha_i^*) K(s_i, s)$$

$$\text{s.t.}\, 0 \leq \alpha_i, \quad \alpha_i^* \leq C \tag{7}$$

where, k represents the kernel function adopted in the modelling and η_{sv} represents the number of points considered as the support vector for the hyperplane modelling.

The performance of the SVR model lies in selecting the suitable model parameters known as the meta parameters. The set of these parameters is C, ε and γ. These parameters need to be optimized in order to get a generalized SVR model. In the current study, popular grid search algorithm [15, 16] is used to obtain the set of optimized parameters. Effective range of these parameters is set in the model in the range as presented in Table 3. Iterations are carried out against all the combinations of the parameters over the selected range a set of optimized values are found for the model. The optimized set of the meta parameters is presented in Table 3. Two separate SVR models are trained for modelling the UTS of the joints. Model I is responsible for predicting the UTS with the parameters and signal features in the input domain, whereas, model II is responsible for the prediction of UTS using only process parameters in the input domain. The accuracy of the developed models against the testing data samples is presented in the results and discussion section.

5   Results and Discussion

In the development of the SVR models, the effectiveness of the signal features is tested in order to test the performance of the model in terms of prediction accuracy of the UTS of the joints. Two separate SVR models are trained and tested with two data set containing the parameters with the features and other one contains only the process parameters. The prediction accuracies of both the models are presented in Fig. 4, and the error in prediction is presented in Table 4. It is observed that with the integration of the signal features extracted from real-time vertical force signals in the machine learning model plays an effective role in improving the prediction performance. The SVR model with signal features yields a maximum absolute percentage error of 1.30
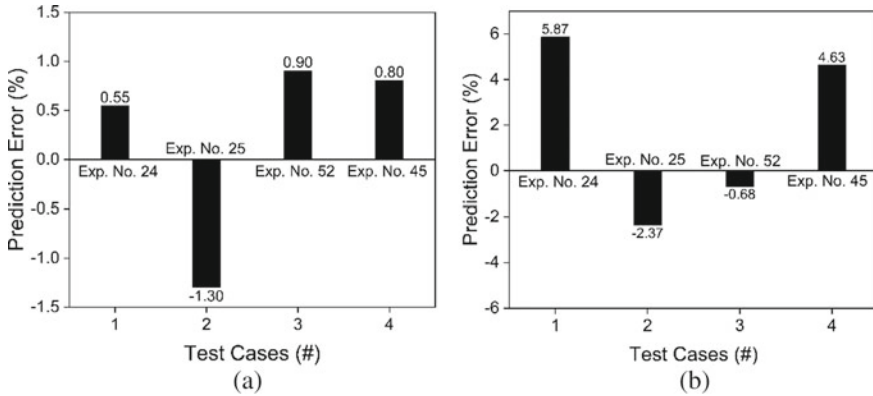
Fig. 4 Performance of SVR models in terms of prediction error **a** with signal features **b** without signal features

Table 4 Performance of SVR models

SVR model	Mean absolute prediction error (%)
Model I (with signal features)	0.88
Model II (with only process parameters)	3.38

whereas the model without the signal feature yields a maximum absolute percentage error of 5.87. This is effective in decision-making regarding the strength of the joints produced through FSW process. The reason for getting better prediction accuracy using signal features lies in the fact that the vertical force signals can capture the process change with factors that are affecting the process beyond the control of the user.

6 Conclusions

In the current study, machine learning approach has been adopted for predicting the ultimate tensile strength of the friction stir welded samples. Experimental investigations are carried out using friction stir welding system with integrating real-time force monitoring system. Force signals are acquired in real time and processes in time domain to extract statistical features. The extracted features are later presented to SVR model to predict the joint strength. In the investigation, SVR models are developed with signal features in the input domain of the model. The model developed with signal features yields a prediction accuracy of 99.12% compared to the prediction accuracy of 96% by the SVR model developed with only process parameters. It

is evident that integration of the signal features in the input domain of the machine learning model results in better performance. The presented work can be extended to develop independent system for monitoring the joint quality in a non-destructive approach.

References

1. Boldsaikhan E, Corwin EM, Logar AM, Arbegast WJ (2019) The use of neural network and discrete Fourier transform for real-time evaluation of friction stir welding. Appl Soft Comput 11:4839–4846
2. Mehta M, Chatterjee K, De A (2013) Monitoring torque and traverse force in friction stir welding from input electrical signatures of driving motors. Sci Technol Weld Joining 18(3):191–197
3. Pew JW, Nelson TW, Sorensen CD (2007) Torque based weld power model for friction stir welding. Sci Technol Weld Joining 12(4):341–347
4. Kumar U, Yadav I, Kumari S, Kumari K, Ranjan N, Kesharwani RK (2015) Defect detection in friction stir welding using discrete wavelet analysis. Adv Eng Softw 85:43–50
5. Singh KV, Hamilton C, Dymek S (2010) Developing predictive tools for friction stir weld quality assessment. Sci Technol Weld Joining 15(2):142–148
6. Chen C, Kovacevic R, Jandgric D (2003) Wavelet transform analysis of acoustic emission in monitoring friction stir welding of 6061 aluminum. Int J Mach Tool Manuf 43:1383–1390
7. Soundararajan V, Atharifar H, Kovacevic R (2006) Monitoring and processing the acoustic emission signals from the friction-stir welding process. Proc Inst Mech Eng 220:1673–1685
8. Subramaniam S, Narayan S, Ashok SD (2013) Acoustic emission-based monitoring approach for friction stir welding of aluminum alloy AA6063-T6 with different tool pin profiles. Proc Inst Mech Eng 227(3):407–416
9. Kumar SS, Ashok SD (2014) Development of acoustic emission and motor current based fuzzy logic model for monitoring weld strength and nugget hardness of FSW joints. Proc Eng 97:909–917
10. Fleming P, Lammlein D, Wilkes D, Fleming K, Bloodworth T, Cook G (2008) In process gap detection in friction stir welding. Sens Rev 28(1):62–67
11. Yang Y, Kalya P, Landers RG, Krishnamurthy K (2008) Automatic gap detection in friction stir butt welding operations. Int J Mach Tool Manuf 48(10):1161–1169
12. Fleming PA, Lammlein DH, Wilkes DM, Cook GE, Strauss AM, DeLapp DR (2009) Misalignment detection and enabling of seam tracking for friction stir welding. Sci Technol Weld Joining 14(1):93–96
13. Das B, Bag S, Pal S (2017) Torque based defect detection and weld quality modelling in friction stir welding process. J Manuf Process 27:8–17
14. Cortes C, Vapnik V (1995) Support-vector networks. Mach Learn 20:273–297
15. Bao Y, Hu Z, Xiong TA (2013) PSO and pattern search based memetic algorithm for SVMs parameters optimization. Neurocomputing 117:98–106
16. Bergstra J, Bengio Y (2012) Random search for hyper-parameter optimization. J Mach Learn Res 13:281–305

Machine Learning Application for Prediction of Surface Roughness of Milled Surface

Chaitanya Palande, Rajhdiwakar Nadar, Prashant Ambadekar, Karthick Sridhar, and Tapas Vashistha

1 Introduction

In machine vision innovation, picture-based information is utilized to review the nature of the surface. Surface quality of a component is an important feature from functional as well as aesthetics aspect. Surface roughness is a segment of surface texture. It is the height of micro and macro asperities, i.e. roughness present on the machined component. Surface roughness is a widely accepted measure of how good the quality of surface is. The most common method to measure roughness is by use of a mechanical stylus-based equipment. In this traditional method of stylus-based measurement, the operator has to stop the machining in order to measure the roughness. A stylus-based method is a contact type method. If the operator measures the roughness value frequently then he/she has to stop machining frequently, which leads to down time. In industries, stringent steps are taken in order to reduce the down time as much as possible to increase the efficiency as well as reduce the operator and machining cost. There are non-contact type measurement methods, also referred to as indirect methods but they are inaccurate [1].

The use of image processing in the field of machining is advantageous as it can help to reduce the down time introduced by the traditional techniques of measurement. In the picture processing, the surface can be characterized as the spatial variety in the splendour or force of the pixels [2–4]. Texture analysis plays a very important role in vision-based techniques such as edge detection, crack detection or variation on the surfaces [2]. Hence, extraction of the texture feature is an important step in vision-based techniques. GLCM is a very popular second order statistical technique for characterizing the surface texture using image data. Authors developed an artificial neural network for measurement of surface roughness using surface image features like contrast, homogeneity, standard deviation, entropy and range [2]. Dutta et al.

C. Palande (✉) · R. Nadar · P. Ambadekar · K. Sridhar · T. Vashistha
Department of Mechanical Engineering, SIES Graduate School of Technology, Nerul,
Maharashtra, India

[3] studied vision-based techniques for calculating surface roughness and found that there is a relation between surface roughness and GLCM parameters contrast and homogeneity. Such features were most suitable for condition monitoring [3]. Gadelmawla [4] found the relation between the surface roughness values and GLCM parameters like energy, contrast, mean, correlation, homogeneity, entropy, etc. The values predicted showed agreement with the actual values. In the recent work, authors [5] used GLCM texture features to calculate principal components and developed a regression model based on those principal components for hand grinding operation. Authors performed ANOVA test and found that contrast, homogeneity, energy, and correlation were responsible for most of the fluctuation in the data.

In the proposed work, a machine vision approach for evaluation of the surface roughness using multiple regressions is implemented for milling operation. It works on the principle of extracting the grey level co-occurrence matrix parameters of decomposed discrete wavelet transform of images followed by regression analysis. This developed regression model is capable of predicting the surface roughness value and can be proven advantageous over traditional methods. The remaining paper is categorized as follows: techniques used are described in Sect. 2. Section 3 explains the methodology, experimentation is explained in Sect. 4. Section 5 shows cases the results and Sect. 6 concludes the work.

2 Explanation of Techniques Used

2.1 Grey Level Co-occurrence Matrix (GLCM)

The likelihood of co-occurring pixel values for a particular offset and angle is represented by a co-occurrence matrix, which is a matrix of an image. A grey level co-occurrence matrix is a matrix that shows the co-occurrence of two grey levels across a certain offset. Because of its increased accuracy, GLCM is a particularly popular approach. GLCM is a square matrix having dimensions equal to that of the intensity levels present in the image. GLCM was first introduced by [6] Harlick in 1979 to extract texture features from an image. According to Harlick, the offset for computing GLCM should be d and direction θ can be 0°, 45°, 90° and 135°.

Contrast, homogeneity, angular second moment (energy), correlation, mean and maximum probability are some of the popular features of GLCM.

2.1.1 Contrast

Contrast is the difference in the grey levels of the two pixels in consideration. It is the measure of contrast or local variation present over an image for considered spatial distance d and angle θ. For a machined surface if the surface roughness value is high contrast value comes higher and vice versa.

$$\text{CON} = \sum_{i=0}^{N-1} \sum_{j=0}^{N-1} [(i-j)]^2 [P(i,j)] \qquad (1)$$

2.1.2 Energy

Energy is the measure of pixel pair repetition for a given GLCM. It measures the uniformity of the image. For a machined surface if surface roughness value is higher uniformity will be lower and hence energy value will be lower and vice versa.

$$\text{ENE} = \sum_{i=0}^{N-1} \sum_{j=0}^{N-1} [P(i,j)]^2 \qquad (2)$$

2.1.3 Correlation

Correlation is the measure of grey level linear dependencies or probability of occurrence of a specific pixel pair. For a lower surface roughness value, there will be less variation in grey levels, and hence the correlation value will be less and for higher surface roughness value it is vice versa.

$$\text{CORR} = \sum_{i=0}^{N-1} \sum_{j=0}^{N-1} [P(i,j)] \frac{(i-\mu_i)(j-\mu_j)}{\alpha_x \alpha_x} \qquad (3)$$

2.1.4 Homogeneity

Homogeneity is the measure of closeness of the distribution of elements in the GLCM to its diagonal. Homogeneity is also known as Inverse Difference Moment. For a machined surface, if the surface roughness is lower then the grey level variation is low and homogeneity value is higher. Alternatively, for a high surface roughness value non-uniformity increases and thus homogeneity value is lower

$$\text{IDM} = \sum_{i=0}^{N-1} \sum_{j=0}^{N-1} \frac{[P(i,j)]}{1+(i-j)^2} \qquad (4)$$

Sebastian et al. [7] defined a new feature called trace extracted from the GLCM matrix and its implication in texture analysis. Mohanaiah et al. [8] introduced a utilization of the grey level co-occurrence matrix (GLCM) to extract second order

quantifiable surface characteristics for evaluating picture movement Xilinx FPGA is used to process the four features: Angular Second Moment, Correlation, Inverse Difference Moment, and Entropy. The findings revealed that these surface highlights had good separation precision, required less computation time, and could thus be effectively used for ongoing pattern acknowledgement applications.

Nathan et al. [9] studied the relation between surface roughness and image texture features. GLCM features like contrast, correlation, homogeneity and energy were considered for the study. It was concluded that for milled surfaces at constant pixel pair distance the image features showed a similar trend with surface roughness for any orientation.

2.2 Discrete Wavelet Transform (DWT)

In a digital image for a machined surface, the edge is the most significant detail. The traditional filter reduces the noise but with that it also tends to make the image blurry. So, it is necessary to protect the quality of the edge while reducing the noise. To overcome this problem wavelet transform comes into the play.

The meaning of wavelet is small wave. Wavelets are continuous or discrete and hence there are two transforms, mainly continuous wavelet transform and discrete wavelet transform. The discrete wavelet transform (DWT) is a computerized method for computing quick transforms of a signal. It is the most efficient way to reduce computing time and is simple to operate and execute. In discrete wavelet transform, the image is first passed through high pass filter and low pass filter for decomposition to give low pass version and high pass version which are further passed through low and pass filters to get LL, LH, HL and HH band as shown in Fig. 1. LL band of image is an approximate of the input image. LL band can be used for further decomposition of images. Horizontal features of the input image are extracted by the LH band. The HL band helps in extracting the vertical features of the input image. And finally, the HH band gives the diagonal features of the input image as shown in Fig. 2.

Cevik et al. [10] made a comprehensive analysis on fingerprint detection using three methods which were GLCM-based feature extraction and classification, DWT-based feature extraction and classification and lastly GLCM-based feature extraction on decomposed DWT images. It was concluded that the last method gave the best identification accuracy of 93% [10].

Elgargni et al. [11] used principal component analysis and discrete wavelet transform to develop a neural network for tracking correct installation of cutting tools

Fig. 1 Decomposition level of DWT
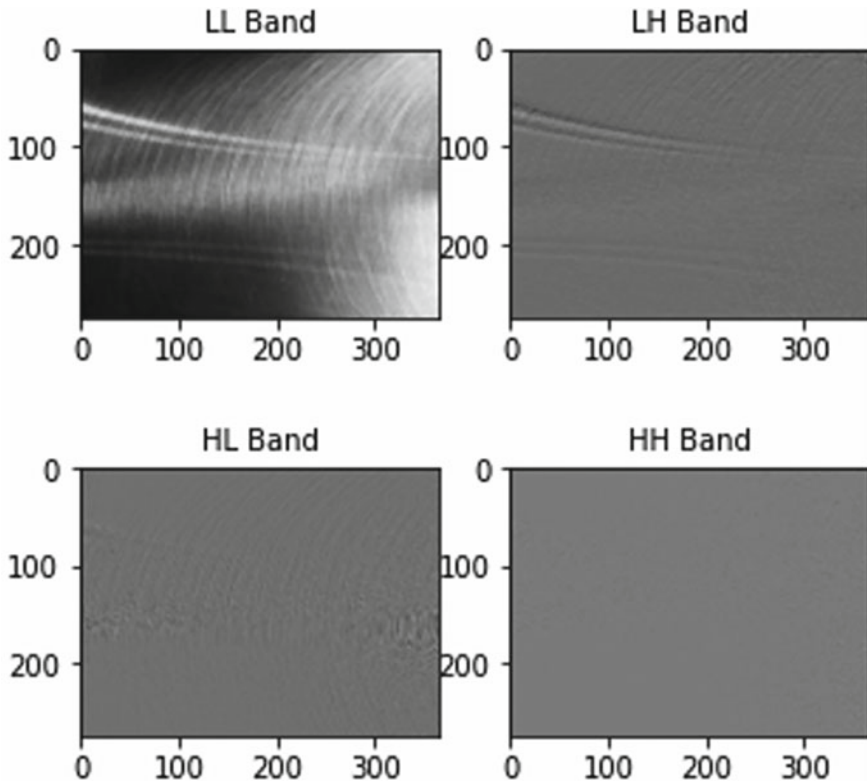
Fig. 2 LL, LH, HL, HH bands of milled surface using Haar wavelet and 1 level decomposition DWT

and fault diagnosis. DWT was used in image processing to obtain required features from the image which was further used to train the classifier for the classification purpose in combination with principal component analysis. The DWT features were obtained for low pass as well as high pass filters [11].

Danesh and Khalili [12] used undecimated wavelet transform and feature extraction to determine the tool wear for the turning process. They first calculated the wavelet transform and then extracted the GLCM features namely, energy, contrast, correlation, entropy and homogeneity. It was observed that wavelet transform was an effective tool for decomposition of the original image to subbands facilitating the identification of texture features related to tool wear [12].

For computing the DWT, Haar wavelet was selected. The Haar sequence was first proposed by Alfred Haar in 1909. The sequence is known as a first basis wavelet and is extensively used. As seen in Fig. 3, the downside of a Haar wavelet is that it is not continuous and hence not differentiable. However, this drawback might be advantageous in the analysis of signals with abrupt transitions. Haar wavelets are
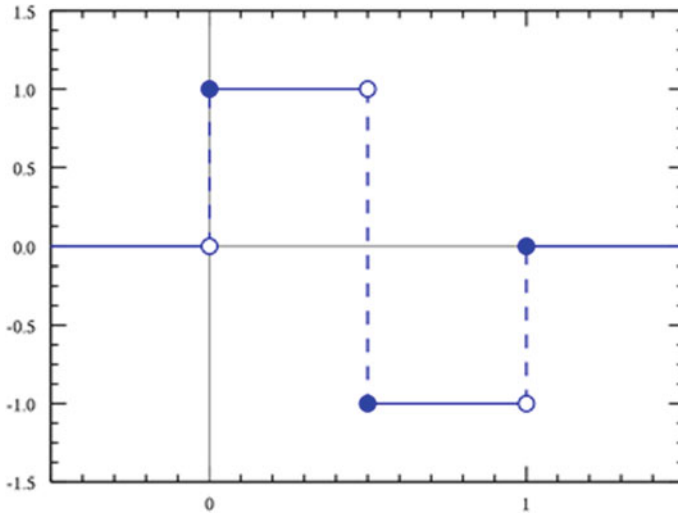
Fig. 3 Representation of Haar wavelet

also good at distinguishing closed spaced features very well. All the above features make the haar wavelet good for analysis of surface roughness.

2.3 *Multiple Linear Regression*

Multiple linear regression gives relation between a single dependent variable and number of independent variables. The reliability of the regression model is determined by the R2 score also known as the R square, then there is the adjusted R square method and Root Mean Square method.

General form of the multiple regression is given as

$$Y = b_0 + b_1 X_1 + b_2 X_2 + \cdots + b_n X_n$$

where Y = output, X_i = input parameters, b_0 = intercept b_i = regression coefficients.

In this paper, surface roughness is dependent variable and GLCM texture features contrast, homogeneity, correlation and energy are the independent variables.
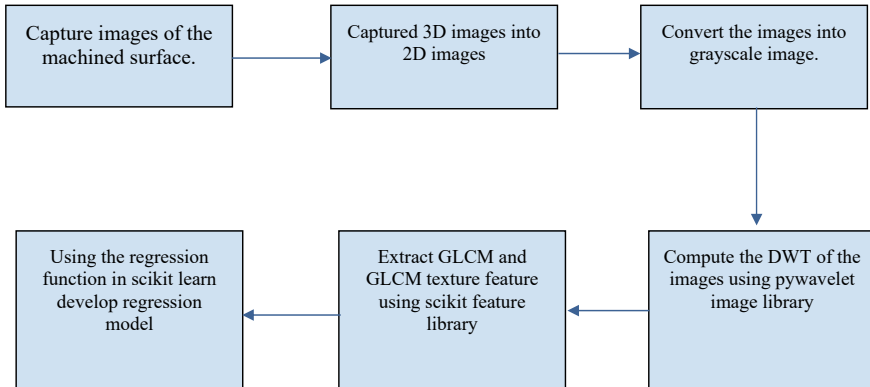
Fig. 4 Methodology for developing regression model for predicting surface roughness value

3   Methodology

The major steps involved were converting the image into greyscale, computing its discrete wavelet transform followed by calculating the GLCM and then texture feature extraction using Python programming (Fig. 4).

The images of milled surface were first preprocessed to convert colour images into greyscale images using the openCV library. Each image was converted to size 256×256. After the conversion to greyscale image, discrete wavelet transforms of the images were found with the help of pywavelet library using Haar wavelet. From this DWT the LL band image, i.e. the approximate image was used to compute the GLCM using scikit image library. After this, using features from scikit image library the GLCM texture features were extracted for pixel pair spacing i.e. $d = 4$ and orientation $\theta = 0°$ as at constant pixel pair spacing the image features showed similar trends irrespective of the orientation θ [9]. The GLCM feature values were stored for further regression analysis.

The training and testing of the regression model were done by using sklearn library. The dataset was split into training data and test data. Using the training data a regression model was developed and then tested using the test data. From sklearn.metrics R2 score, mean square error and adjusted R2 score were calculated. GLCM parameters from a new image were provided to the regression model for validation.

4   Experimentation

Milling process was performed on the universal milling machine as shown in Fig. 5. The job was to flatten the surface of the workpiece. Multi-point cutting tool was used for machining. Also the cutting parameters were kept fixed to obtain accurate results.
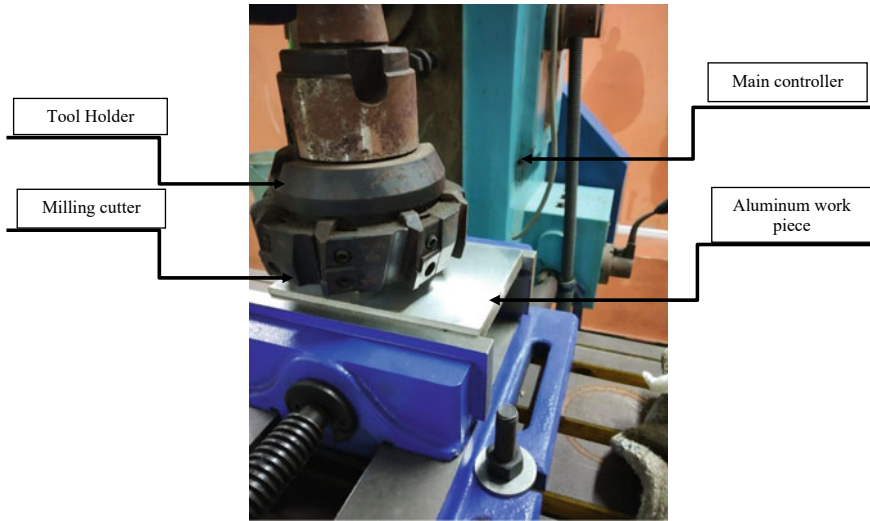
Fig. 5 Universal milling machine on which experimentation was performed

Aluminium material was used as a work piece to perform face milling. Seven work pieces were machined. Work piece dimensions were $100 \times 50 \times 20$ mm.

The milling operation was performed using an HSS shell milling cutter having 8 numbers of teeth over its circumference. Condition for performing the machining was dry. During the machining process after every two minutes, the images of the surface were taken with the camera and the surface roughness was measured using a digital surface roughness tester and the roughness value was recorded. The total number of images taken during experimentation were 95. The machining parameters for the face milling operation are shown in Table 1. The feed given to machining was 100 m/min while the depth of cut was given as 0.5 mm. The images of the surface are shown in Fig. 6.

Table 1 Machining parameters

S. No.	Parameters	Unit	Value
1	Spindle rpm	rpm	2000
2	Cutting speed	m/min	158.8
3	Feed	mm/min	100
4	Depth of cut	mm	0.5
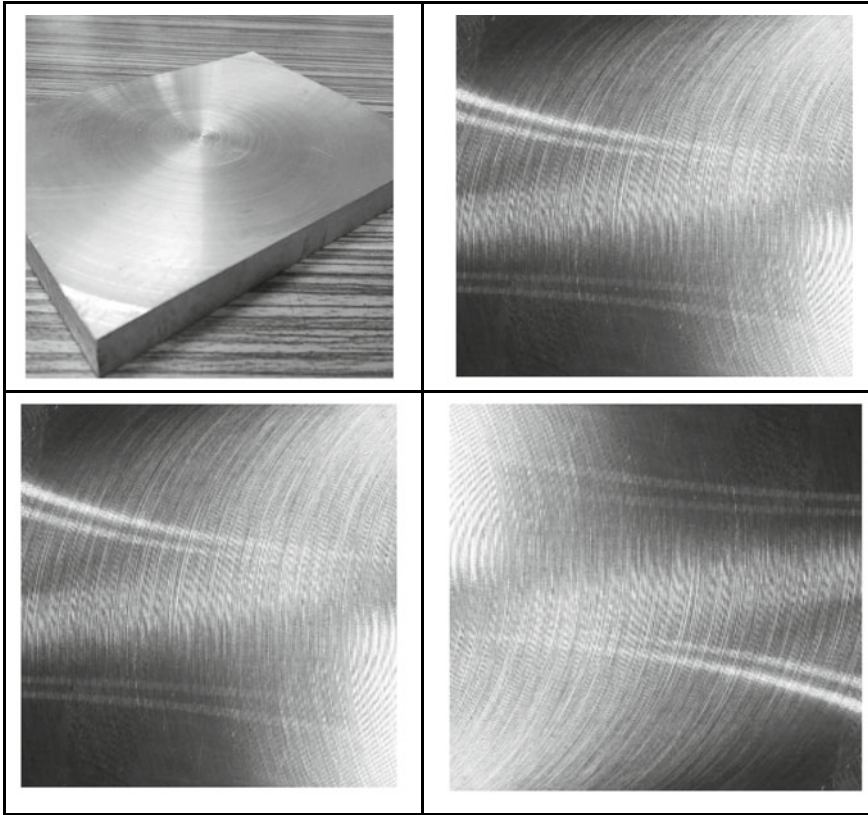
Fig. 6 Images of surface after machining

5 Result and Discussion

As explained in the methodology, GLCM and its texture feature were computed with the help of scikit image library and for computing DWT, pywavelet library was used. The data is then subjected to multiple regression analysis by scikit-learn software. The results obtained are discussed in Figs. 7, 8 and 9.

Fig. 7 Image of milled surface
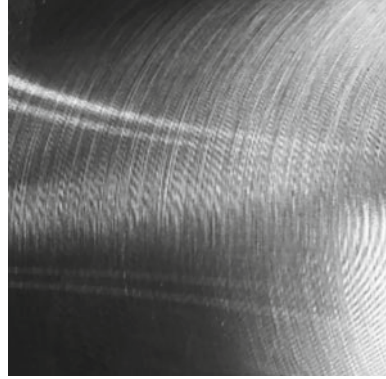
Fig. 8 DWT of milled surface
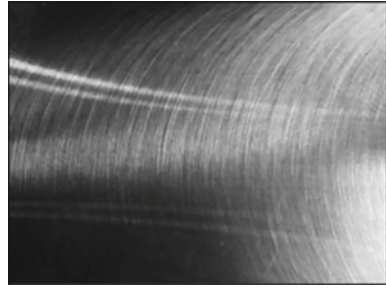
Fig. 9 Image used for validation
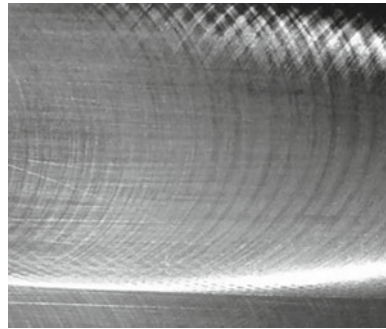
5.1 Analysis by GLCM Technique

5.1.1 GLCM Texture Feature of Faced Milled Surface Without DWT and Regression Analysis

Table 2 gives the values for the GLCM parameters of the milled surfaces from the dataset. These values were further used for developing a regression model.

Table 2 GLCM texture feature without DWT

Homogeneity	Energy	Contrast	Correlation
0.7714	0.2622	0.5848	0.9122
0.83	0.349	0.5447	0.876
0.834	0.35	0.544	0.879
0.822	0.346	0.547	0.874
0.828	0.346	0.547	0.874
0.819	0.339	0.551	0.869
0.771	0.2622	0.584	0.912
0.797	0.319	0.567	0.857
0.809	0.327	0.559	0.862
0.825	0.347	0.551	0.861

5.1.2 The Regression Model for GLCM Only

This gave a regression score of 0.8080, which means that 80.8% of the variance for a dependent variable is explained by the independent variables. The adjusted regression score was found to be 78.2%. The Regression Model also gave Root Mean Squared Error of 0.000204 mm which is acceptable.

Table 3 GLCM texture feature with DWT

Homogeneity	Energy	Contrast	Correlation
0.866	0.293	0.272	0.965
0.88	0.384	0.31	0.918
0.892	0.395	0.303	0.929
0.871	0.376	0.324	0.914
0.869	0.359	0.316	0.908
0.874	0.361	0.345	0.884
0.867	0.296	0.275	0.967
0.883	0.387	0.314	0.921
0.87	0.372	0.328	0.917
0.875	0.362	0.347	0.887

5.2 Analysis by GLCM and DWT Technique

5.2.1 GLCM Texture Feature of Faced Milled Surface with DWT and Regression Analysis

Table 3 gives the values for GLCM parameters for DWT computed images. These values are further used to develop a regression model.

5.2.2 The Regression Model for GLCM + DWT

This gave a regression score of 0.8418, which means that 84.18% of the variance for an independent variable is explained by the independent variables. The adjusted regression score was found to be 80.84%. The regression model also gave a Root Mean Square Error of 0.000152 mm which is better than the 'GLCM only' regression model.

5.3 Analysis of Validating Image Using GLCM and DWT Technique

Figure 9 shows the image used for validation of the developed regression model. The GLCM texture parameters values were first extracted using both techniques. The values of the GLCM parameters were then used in the developed regression models and surface roughness was predicted. GLCM texture feature for validation images without and with DWT is provided in Tables 4 and 5.

The surface roughness value for the validation image using mechanical means came out to be 0.00525 mm. The predicted roughness value with GLCM model

Table 4 GLCM texture feature for validation images without DWT

Homogeneity	Energy	Contrast	Correlation
0.828	0.346	0.547	0.874
0.768	0.257	0.587	0.902
0.831	0.347	0.544	0.876
0.829	0.321	0.527	0.881
0.809	0.327	0.559	0.862
0.822	0.342	0.549	0.872
0.805	0.325	0.556	0.860
0.832	0.35	0.544	0.875
0.758	0.257	0.591	0.896
0.828	0.346	0.547	0.874

Table 5 GLCM texture feature for validation images with DWT

Homogeneity	Energy	Contrast	Correlation
0.871	0.376	0.324	0.914
0.883	0.293	0.239	0.973
0.846	0.272	0.329	0.962
0.869	0.329	0.314	0.962
0.888	0.361	0.264	0.959
0.847	0.338	0.324	0.935
0.845	0.321	0.326	0.927
0.892	0.308	0.316	0.944
0.802	0.294	0.317	0.927
0.845	0.329	0.323	0.947
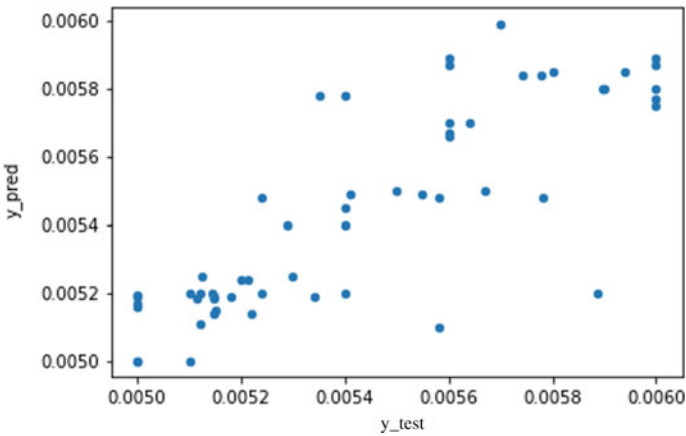
Fig. 10 Predicted value versus actual value

came out to be 0.005178 mm and for GLCM feature extraction of DWT applied images came out to be 0.005201 mm.

Figure 10 shows variation in the predicted value versus the actual surface roughness value of the test dataset for the combined method of DWT and GLCM. It can be observed that for lower surface roughness values the model predicted the roughness value with lesser error. Only a few predictions had larger errors in prediction. The corresponding error percentage for the given test data is shown in Table 6.

Figure 11 shows a graph of predicted value versus error, i.e. (actual value—predicted value). It was observed that mostly errors are from −2.5 to 2.5%. For the given test dataset most of the predicted values were within 5% error and only some of the predicted values showed an error percentage of more than 10%.

Table 6 shows percentage error of predicted value for the validation images, i.e. (actual value—predicted value). It was observed that mostly errors are from −5 to
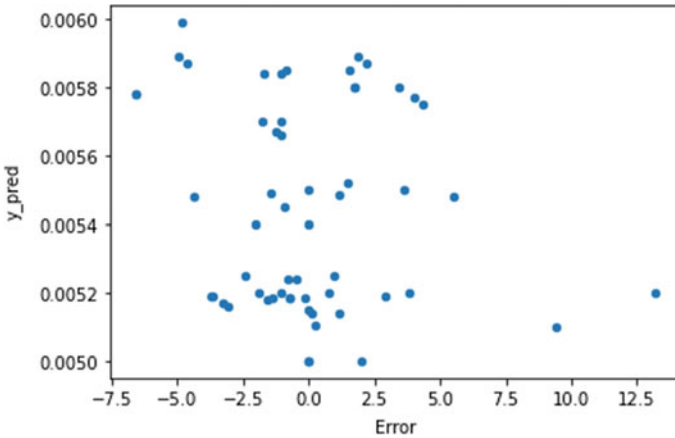
Fig. 11 Graph of predicted value versus percentage error of surface roughness value

5%. For the given test dataset most of the predicted values were within 5% error and only some of the predicted values showed an error percentage of more than 10%.

Figure 12 shows the variation of the predicted roughness value from the actual roughness values while Fig. 13 shows the corresponding percentage error for the same.

6　Conclusion

The research provided a novel machine learning-based method for determining surface roughness values. A camera was used to collect images of the milled surface, which were then analysed in Google Colab. Cropped and processed images were used to extract GLCM and texture features such as contrast, energy, homogeneity and co-relation along 0° direction. For computing DWT, a Haar wavelet is used. The DWT of an image is calculated by passing the image through a series of filters. The output gives detailed coefficients (from high pass filter) and approximate coefficient (from low pass filter).

Two different methods were used to predict the surface roughness value. First method considered GLCM-based feature extraction of the images. While the second method considered GLCM-based feature extraction of DWT computed images. Further, multiple regression analysis was carried out for both methods to compare the results obtained from the GLCM and GLCM-DWT model. The accuracy of the model increases with the use of DWT.

The research may be expanded to include additional machining techniques and additional modelling methods for prediction.

Table 6 Percentage error for predicted values for new milled surfaces

Surface roughness value with surface roughness tester	0.0051	0.0062	0.005	0.005	0.0055	0.0052	0.0055	0.0051	0.0062	0.0053
Surface roughness values predicted with model	0.0052	0.00642	0.00512	0.0048	0.0056	0.00533	0.00557	0.00499	0.0065	0.00519
Surface roughness values predicted with model	1.96	3.55	2.4	4	1.82	2.5	1.27	2.15	4.8	2.08
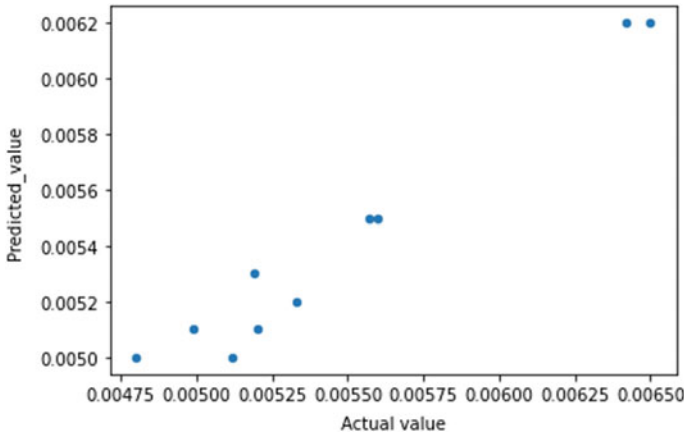
Fig. 12 Graph of predict values versus actual values of new milled surfaces
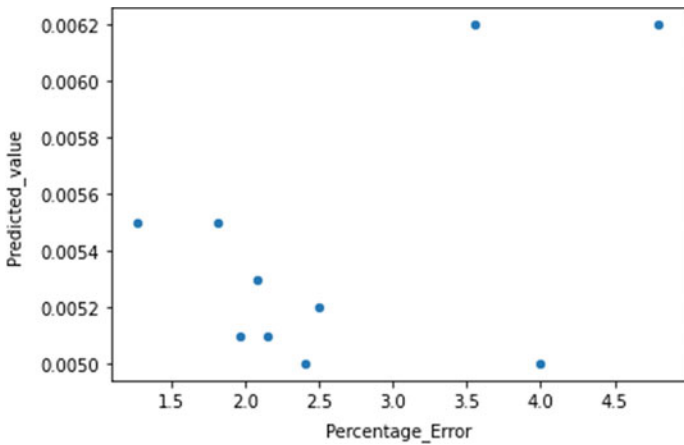
Fig. 13 Graph of predicted values versus percentage error for new milled surfaces

References

1. Ratnam MM, Shahabi HH (2010) Noncontact roughness measurement of turned parts using machine vision. Int J Adv Manufact Technol 46(1–4):275–284
2. Mahanty B, Ray PK, Shome D (2009) Non-contact estimation of surface roughness in turning using computer vision and artificial neural networks. Int J Ind Syst Eng 4(4):349–367
3. Datta A, Sen R, Datta S, Mukhopadhyay S, Pal SK (2012) Texture analysis of turned surface images using grey level co-occurrence technique. In: Advanced materials research, vol 365. Trans Tech Publications, pp 38–43
4. Gadelmawla ES (2011) Estimation of surface roughness for turning operations using image texture features, Proc IMechE Part B J Eng Manuf 225:1281–1292
5. Patil B, Joshi K (2019) Prediction of surface roughness by machine vision using principal components regression analysis. In: Paper presented at international conference on

computational intelligence and data science (ICCIDS 2019). Springer, pp 382–391

6. Haralick RM (1979) Statistical and structural approaches to texture. Proc IEEE 67(5):786–804
7. Unnikrishnan A, Bino Sebastian V, Balakrishnan K (2012) Gray level co-occurrence matrices: generalisation and some new features. Int J Comput Sci Eng Inf Technol 2:151–157
8. Gurukumar L, Mohanaiah P, Sathyanarayana P (2013) Image texture feature extraction using GLCM approach. Int J Sci Res Publ (IJSRP) 3(5). ISSN 2250-3153
9. Nathan D, Thanigaiyarasu G, Vani K (2014) Study on the relationship between surface roughness of AA6061 alloy end milling and image texture features of milled surface. Proc Eng 97:150–157. ISSN 1877-7058
10. Cevik T, Alshaykha A, Cevik N (2018) A comprehensive performance analysis of GLCM-DWT-based classification on fingerprint identification. Int J Comput Appl 180:42–47. https://doi.org/10.5120/ijca2018916909
11. Al-Habaibeh A, Elgargni M, Lotfi A (2015). A cutting tool tracking and recognition based on infrared and visual imaging systems using principal component analysis (PCA) and discrete wavelet transform (DWT) combined with neural networks. Int J Adv Manuf Technol 77:1965–1978. https://doi.org/10.1007/s00170-014-6576-y
12. Khalili K, Danesh M (2015) Determination of tool wear in turning process using undecimated wavelet transform and textural features. Proc Technol 19:98–105. ISSN 2212-0173

Predictive Maintenance Control and Automation in Plastic Injection Molding Machine

Anmol Bhagat and Sneh Soni

1 Introduction

Our main purpose is to design the control of injection molding machines using (PLC) and (SCADA) system and perform predictive maintenance on it.

The injection molding process was adapted in the late 1800s at very first they started production containing molds of a simple design like combs, buttons to many complex designs. The main concept of plastic molding is "with the help of changing temperature and pressure the polymer comes into a molten state so that polymer can take the essential shape." There are four types of molding process, blow molding, injection molding, rotational molding, and compression molding having their advantages [1]. In this work, an injection molding process is of prime focus (Fig. 1).

PLC is controller used in manufacturing and processes for high reliability and precise control. In this project, the MELSEC F series PLC module made by Mitsubishi Electric Corporation is used. The software used to interface with this PLC Module is GXWorks3. This module consists of a power supply unit, CPU module, I/O modules, and the base unit.

SCADA refers to the mixture of telemetry and acquisition of data. It consists of gathering info, transferring it to the control side, carrying out required control and analysis, then presenting this data on several operator screens. It is used to control and monitor plant equipment's. In this project, Intouch Wonderware Scada software is used for visualization and control purposes [2].

Technological development caused increased difficulty in industrial machinery and production systems. The recent industry is continuously increasing work at more

A. Bhagat

Instrumentation and Control Engineering Department, Institute of Technology, Nirma University, Ahmedabad, India

S. Soni (✉)

Instrumentation and Control Department, Nirma University, Ahmedabad, India
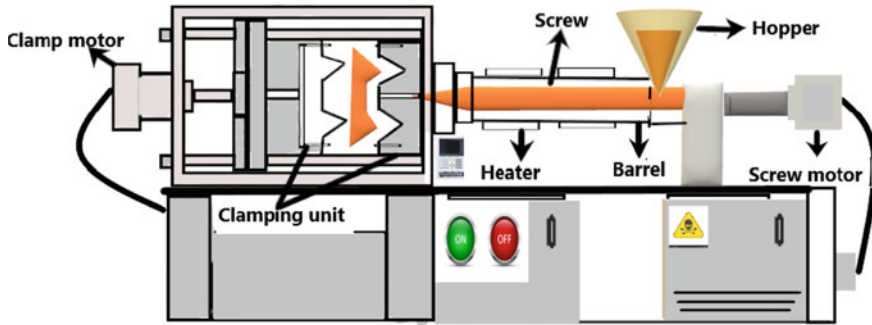
Fig. 1 Injection molding machine

reliability, less environmental risks, and human safety [3]. Therefore, the useful operating life of the machine is increased by preventing failures through early detection of fault occurrence [4].

There are six types of maintenance perfective, corrective, preventive, predictive, and adaptive. Due to bad planning, 1/3 of the maintenance value is estimated to occur, badly executed preventive maintenance, and overtime costs which lead to needlessly bigger production costs. With a proper maintenance plan, the maintenance cost and downtime can be drastically reduced [5].

2 Injection Molding Machine

Injection molding is a process of forming plastic goods from thermoplastic materials by feeding the substance through the machine components called the hopper. This material is injected into a mold at high temperature and pressure by screw assembly through the nozzle. In this process, it is mandatory to keep constant pressure until the material is injected. This is the common way of producing plastic goods in desired size and shape [5]. It permits mass production with net shape manufacturing [6].

This machine consists of two processes in a loop first injection followed by clamping where injection consists of force clamping and material heating as sub-process along with mold close and ejection as sub-process of clamping [7] (Fig. 2).

2.1 Injection Machine Components

This machine comprises main four components: hopper, screw assembly, barrel, and injection nozzle.
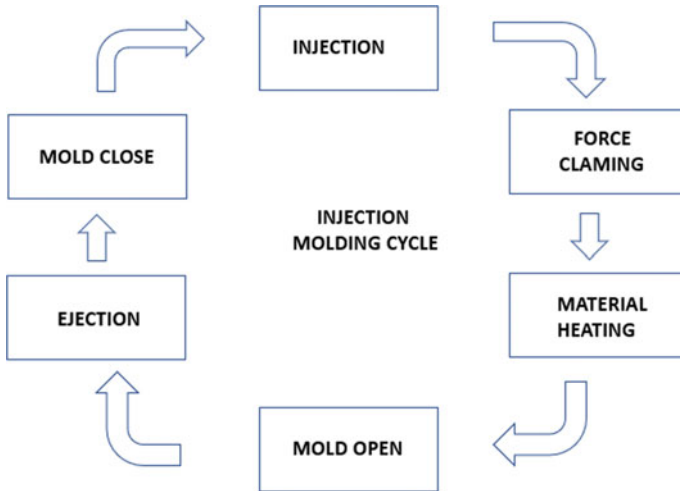
Fig. 2 Injection molding cycle

Hopper: In this plastic materials are supplied in the form of small pellets. The idea is to hold plastic pellets and feed them to the barrel.

Barrel: The main function of the barrel is to provide support for the screw. The barrel contains heater bands. It also records the temperature for each barrel section (Fig. 3).

Screw: The main function is conveying, compressing, and melting the plastic material.

It consists of three zones: the feed zone, the transition zone, and the metering zone. In the feed zone, there is no change in plastic material and it will transfer to the transition zone, the melting of pellets will start to heat and they are transferred to the next zone, which is the metering zone over here this material is ready for injection [9].

Nozzle: The main purpose of a nozzle is to link the barrel to the brushing of screw assembly, which provides a connection between barrel and mold. Nozzle temperature must be set as material melting temperature for proper result and uniform product quality [8].
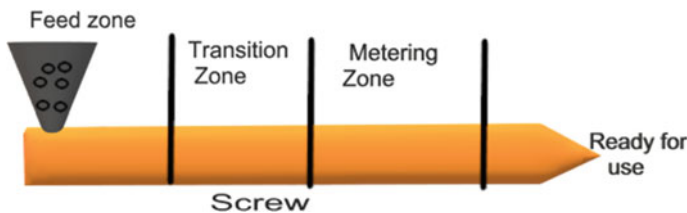
Fig. 3 Different zones of the screw [8]

2.2 Heater Band

See Fig. 4.

Zone-temperature control is performed, when one of the regions on the barrel (not nozzle) is hotter. When the controller does not ask to turn on the heater band then also zone temperature is maintained [11]. Temperature controllers must on and off cycle to control the zone temperature. All zones will have different cycles because each barrel zone has dissimilar functions [8]

3 Development of PLC and SCADA System

As the start push button is pressed the lamp is latched to on condition, then the heater will turn ON when the value in D0 is greater than or equal to 275 then the timer T1 will turn ON after 1 min forward screw motor will be turned ON, which loads the material toward clamping unit with the help of screw and nozzle assembly. A counter counts the value of forwarding operation by screw motor for 55 rotation, by a proxy sensor. As the counter is reached forward screw motor will stop and material is injected into the clamping unit then the cooling pump will turn ON for 1 min to cool down the material for a time set by timer T2 and during this time reverse screw motor is turned ON until counter C2 reach its value. Then to discharge the final product the clamping reverse motor is turned ON. And When L2 limit switch sensed the clamping reversed motor will stop, thereafter a minute whole cycle is repeated (Fig. 5).

The same process is also controlled via a SCADA having functionality to easily change process variables like timer, setpoints, and counters limit using sliders provided.

Fig. 4 Heater band in injection machine [10]
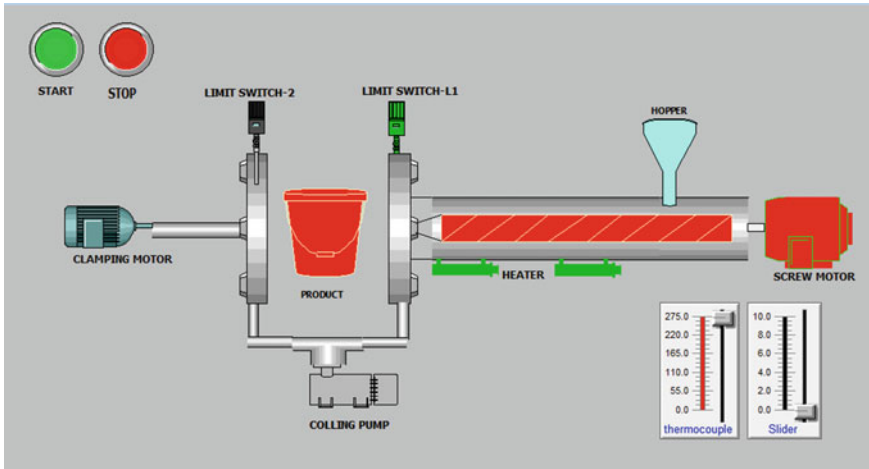
Fig. 5 SCADA Mimic

4 Maintenance and Calibration of Machine

There are many types of maintenance [12] program running in the machine as mentioned below:

Daily: In the daily maintenance first machine is clean properly then all the safety equipment and control panel are checked properly followed by the auto lubrication process and oil temperature check which should be less than 55 °C. The water tank and oil tank levels are maintained if any low level is detected then it is filled finally checking all the LEDs in working condition.

Weekly: The weekly maintenance is a little bit more than the daily maintenance in weekly at the very first all leakage is checked properly and rectified where ever it's necessary. The lubrication system is also checked where the lubrication rod is cleaned properly along with the nozzle and injection unit. The gaskets are checked for any damage if not found the cooling process is maintained properly at last, the filter was cleaned properly [13].

Monthly: In the monthly maintenance, the electrical parts are main where the heater circuit for each zone is checked individually. The earthing is checked if connections are found loose then they are fixed. The suction filter and return line of the filter is also important they must be checked at last, all the nut bolts and screws of the machine are checked if found loose then proper tightness is maintained and all manual solenoid valves are also maintained.

Fortnightly: This maintenance is cover after every 500 h of the running of a machine this all-hydraulic valve of the machine is checked along with the pressure filter of the hydraulic system.

Table 1 Example for 5 "why" analysis

What is problem	WHY-1	WHY-2	WHY-3	WHY-4	WHY-5	Verify true cause	Remarks
Machine overheats	Lack of awareness	Operator oversee	New operator			False	Only experience and skill can set temp
	Wrong setting	Lack in training	No evaluation after training			false	Evaluation after every 4 months

4.1 Predictive Maintenance Control Strategy for Machine

In this project, the predictive maintenance was embedded and selected with a "5-why" analysis to detect the problem arriving in the machine. To analysis this maintenance management, first methods should be considered properly. Industrial and process plants classically do two kinds of maintenance management which are predictive maintenance or run-to-failure.

Now it is consistent monitoring of real mechanical state, working condition, and many other indicators in machine-trains and process systems will deliver the data fulfill to ensure the maximum gap among repairs and decrease the no. and cost of unprepared outages generated by machine-train failure-based higher. It states that improving productivity, product value, and total efficiency of production plants and manufacturing by a single data set that supports the maintenance in defining the real requirement for maintenance [12].

Table 1 below represents the "5 why" study of injection molding machines at the plant. Based on the various find in the "5 why" analyze the main fault enters from the machine other than the element. The production stopped due to the controller. In this sense, the machine becomes overheat and to analyze this fault, upcoming action needs to be a plan [12].

Run-to-failure management is simple and straight forward, which states that when an interruption comes in the machine, fix it, and "If interruptions did not then don't fix it." A industries and plant using run-to-failure management will not pay high money on maintenance until a machine or system fails to work [12].

4.2 Predictive Maintenance Algorithm

At 1st, we identify injection machine equipment and components and their process parameter and also impact the relationship between the process parameter and equipment, 2nd we analyzed the process parameter data series using statistical analysis,

from this analysis result we recognized the process parameter if they not significantly disturb the response and then we eliminate from process parameter list for maintenance method, 3rd for significant process parameter the prediction model is used in this we used real-time monitoring data of parameter for prediction, 4th we checked real-time data series of process parameter and evaluated them, 5th for the detection of parameter the real-time model to predict the pattern of each parameter and to decide its maintenance point of time when a pattern is detected, finally using real-time monitored parameter data series and predicted value, we assess the patterns against nelson formula and when abnormal patterns are detected the maintenance info is informed to workers on display (Fig. 6).
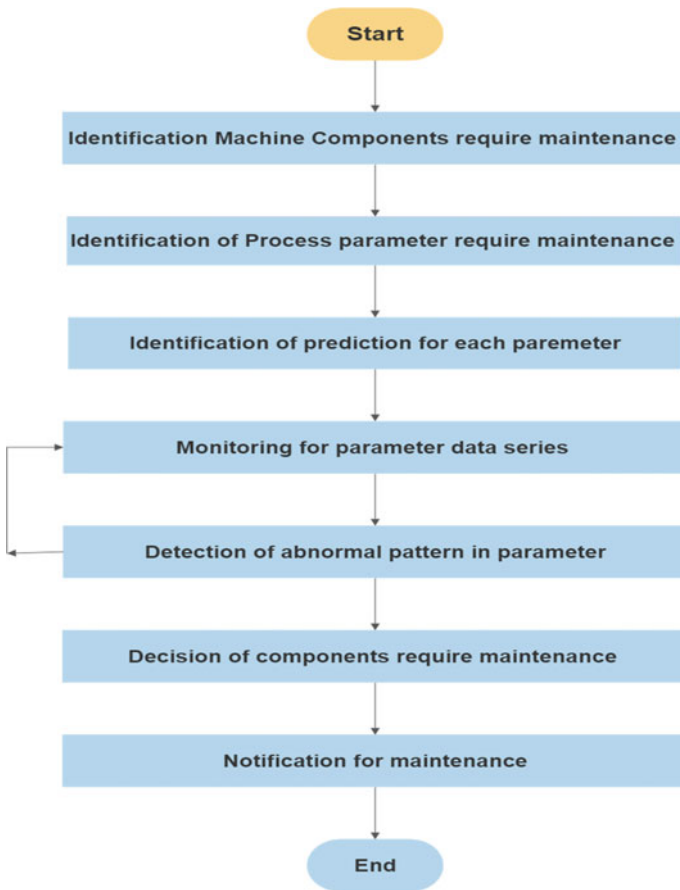
Fig. 6 Algorithm for maintenance

Table 2 Comparison of systems

	Comparison	Existing machine	Expected results
1	Accuracy	Less	More
2	Controlling	Relay Board	PLC and SCADA
3	Safety	Less	Highest
4	Quality	Less	Highest
5	Control system	manual	Manual and Automatic

5 Safety of Machine

These are the various safety parameters that are followed in the machine:

Mobile safety guard of the injection nozzle area: These safety devices prevent access to the nozzle danger area and stop contact with the hot surface or melted plastic also the safety devices stop the movement of the nozzle and the movement of a screw inside the barrel [4].

Interlock devices: Interlock devices stop the machine or disable starting of the machine if it is not in a safe condition. For example, a limit switch that detects the movable position is an interlock device.

Electro-sensitive protection system: Devices that cause stoppage of the machine or disable starting of the machine if they detect the presence of an exposed person in certain dangerous areas are (called ESPS). For example, the sensitive footboards [4].

Emergency Stop: The emergency stop is controlled by a button. This allows the operator to stop the machine in event of an emergency stop, cutting off the electrical circuits and opening actuator supply circuits (Table 2).

6 Conclusion

In this paper, we have successfully developed the injection molding machine ladder diagram program for PLC also discussed the cycle of the injection molding process for smooth running as we have seen important components of the machine and its working. For visualization and control of the process, the SCADA has been developed successfully. Some major steps are highlighted for maintenance and calibration.

- We have analyzed the predictive maintenance control strategy for this machine to overcome breakdown problems. "5 why" analysis method is used for the same, by using this method it can be concluded that it has a high strength to detect the problem which is missing out in other maintenance methods.

- We have also developed the algorithm for predictive maintenance in which accurate fault is detected by using the real-time monitoring of components in the machine. Various safety devices and protocols for the machine are discussed where we have also compared the old system with modern PLC-based machines.

References

1. Yasue A, Araki K, Nakagawa K, Chiba H (2013) Introduction to injection machine 64:75–78
2. Murti B (2010) Simulation and analysis of injection molding products and rapid prototyping. Bachelor. Arcada University, Finland
3. Chiang MH, Yang FL, Chen YN, Yeh YP (2005) Int J Adv Manuf Technol 27:53–62. https://doi.org/10.1007/s00170-004-2138-z
4. Nasiri S, Khosravani MR (2019) Received: 14 December 2018/Accepted: 3 April 2019 © Springer-Verlag London Ltd., part of Springer Nature 2019
5. Hassan MF, Jalaluddin IM (2010) iDECON 2010—international conference on design and concurrent engineering university Teknikal Malaysia Melaka (UTeM) 20–21 Sept 2010
6. Kohara Y (2011) Why-Why Analysis with five layers methodology for IT projects. Recommendation for both members and their organizations to solve problems together. In: 5th world congress for software quality, Shanghai, China
7. Roseto (2017) IOP Conf. Series "injection process loop": Conference Series 90:012067. https://doi.org/10.1088/1742-6596/908/1/012067, research gate
8. Bacau R (2018) J Eng Stud Res—"the heating system from an injection molding machine" 24 (2)
9. Havard N, Fournier J-E, Lacrampe M-F, Ryckebusch M, Krawczak P (2006) _Adaptive_Process_Control_for Thermoplastic injection moulding machines relationship between control mode weight dimensions and impact toughness 26(5)
10. Digamber GM, Akbar SM, Govind DD, Ashokrao RS, Angadrao BM, Rajkumar DA (2019) 06(03) (IRJET)
11. Froehlich C, Kemmetmüller W, Kugi A (2020) IEEE transactions on control systems technology, 28(5)
12. Ben-Daya M (2009) Failure mode and effect analysis. In: Ben-Daya M, Duffuaa SO, Raouf A, Knezevic J, Ait-Kadi D (eds) Handbook of maintenance management and engineering, Chapter 4. Springer, London, UK, ISBN: 978-1-84882-471-3, pp 75–90
13. Ohba Y, Sazawa M, Ohishi K, Asai T, Majima K, Yoshizawa Y, Kageyama K (2009) IEEE transactions on industrial electronics 56(8)

Selection of Passenger Car Using TOPSIS Method

S. Y. Borole, P. U. Malu, and A. G. Kamble

1 Introduction

In today's world, cars are one of the essential accessories for human life. Cars consist of different types like passenger cars, sports cars, jeeps, etc. The car companies have evolved themselves with the technology, finding new ideas for the design and features which will attract more people to buy the car. Today everyone wants to have a car which has all good features. The people select a car by considering the main criteria like price range, mileage, safety of the car and other features. There are many car manufacturers in India like TATA, Toyota, Hyundai, Suzuki, Honda, KIA, etc. which are always trying to make one of the best cars.

Multi-attribute decision-making methods (MADM) are used in different areas of decision-making between different alternatives. These techniques are useful when enough information about the attributes is available on behalf of which the alternatives are compared. This technique is used for the evaluation of the rankings of the different alternatives. It defines how attribute information is to be processed in order to arrive at the selection. Srikrishna et al. [1] worked on the different cars selection in India like Swift, Tata Indica, Ertiga and Alto800 with different attributes like Fuel Economy, Cost, Life span and Style. Sahu and Shukla [2] proposed the MADM method to compare the different alternatives with attributes like looks, performance, features and value for money. Babu and Manoj [3] proposed application of Analytical Hierarchy Process (AHP) and Technique for order of preference by similarity to

S. Y. Borole (✉) · P. U. Malu · A. G. Kamble
School of Mechanical and Civil Engineering, MIT Academy of Engineering, Alandi, Pune, Maharashtra 412105, India
e-mail: syborole@mitaoe.ac.in

P. U. Malu
e-mail: pumalu@mitaoe.ac.in

A. G. Kamble
e-mail: agkamble@mitaoe.ac.in

ideal solution (TOPSIS) to select a four-wheeler passenger car based on various attributes. Many findings have shown that the applications of MADM methods like Multi-Objective Optimization Method by Ratio Analysis (MOORA), Complex Proportional Assessment (COPRAS), VlseKriterijumska Optimizacija I Kompromisno Resenje (VIKOR), Analytical Hierarchy Process (AHP), Multi-Attribute Border Approximation Area Comparison (MABAC) have been widely used in the decision-making process. TOPSIS is widely used technique to prioritize selection. This approach is chosen because it offers the qualitative and quantitative study of the problem and furthermore it additionally offers excellent and brief decisions to our problems.

2   Literature Survey

Many researchers and industries are working on MADM techniques also many researchers have done on these techniques by using various problem statements. The short literature survey in area of implementation of MADM is given below:

Fei et al. [4] implemented a changed TOPSIS approach primarily based totally on *D* Numbers and had additionally labored on Applications in Human Resources Selection with the assist of evaluating one-of-a-kind applicants primarily based totally at the rankings of various subjects and have updated the classical TOPSIS method to solve the problem statement naming their process as D TOPSIS. Elsayed et al. [5] have employed the TOPSIS method to evaluate alternatives with entropy weight. The paper proposed the TOPSIS method on different banks with classifying their main criterias which were mostly needed by the customers. It involved twelve banks with five attributes. Kumar et al. [6] proposed the TOPSIS approach for choice of refrigerant. The paper detailed the rating in their options on the premise of various properties of refrigerants. The calculations have been achieved on C programming. Ebrahim et al. [7] have carried out the TOPSIS approach for the assessment and prioritization of social balance in rural regions and taken into consideration the attributes like Literacy Index, Demographic Index, Poverty Index and more three attributes for their evaluation. It helped the rural areas to have development in their way. Roszkowska [8] proposed the TOPSIS technique to interval data for a few easy issues with regard to actual conditions displaying realistic packages of various factors of this technique. Rahim et al. [9] have applied MCDM method on the attributes work discipline, work quality, job responsibilities and behavior for the ranking of employees. Five employees were considered as alternatives for the problem.

Zhongyou [10] had carried out the TOPSIS Method to the Introduction of Foreign Players in CBA Games and explored this discipline with the aid of using the use of the TOPSIS approach of decision-making technology to offer an extra medical and quantitative decision-making approach for the CBA groups to choose abroad players. Bulgurcu [11] proposed the TOPSIS method for the economic overall performance assessment of era corporations in Istanbul inventory alternate market. The paper comprised the economic overall performance of 13 era corporations buying and

selling in Istanbul Stock Exchange with the assist of ten attributes. Jamil et al. [12] have achieved a observe of multicriteria selection making for dealer choice within side the automobile enterprise with an assessment of various kinds of motors in step with the years with the assist of AHP and TOPSIS on this observe and feature in comparison 4 kinds of motors on this paper. Zulqarnain et al. [13] have proposed the TOPSIS Method for comparing different cars on the basis of different attributes like Style, Safety, Fuel Efficiency, Expanses. The paper detailed a step by step procedure for solving the problem statement. Govil et al. [14] proposed identifying of the Best Indian Entry–Level Segment SUV by the TOPSIS method with different car attributes mostly needed by any customer are taken and the alternatives are evaluated. Study of four alternatives with their four attributes is done. Jozaghi et al. [15] have done the selection of Dam Site by applying AHP and TOPSIS method. The paper aimed to display a case study in Sistan and Baluchestan Province, Iran. It worked on different criteria which are needed by dams. Moradian et al. [16] have done material selection of brake booster valve body by applying multi criteria decision-making techniques like MOORA, TOPSIS and VIKOR methods for finding the best brake booster valve body and also compared the results from the three methods.

From the above literature review, it's been determined that many researchers have worked on diverse MADM strategies for specific hassle statements. But, few researchers have worked on the selection of excellent automobiles among specific cars. Therefore in the present work, the TOPSIS technique is used for the choice of the best automobile from the alternatives.

3 TOPSIS Method

The approach was evolved by Ching-Lai Hwang and Yoon in 1981. This approach is primarily based totally on the evaluation among all of the options primarily based totally on the problem. This approach is used to discover the rankings of the options which might be to be compared.

The following steps are used to find weights for attributes and checking the consistency of the decision matrix:

Step 1   The objective and evaluation attributes determination is processed. Develop a hierarchical data structure with an objective at the highest level, the attributes at the second level and therefore the alternatives at the third level.

Step 2   Find out the relative importance of various attributes with relation to the goal. Construct a pair-wise comparison matrix employing a scale of relative importance. An attribute compared with it's always assigned the worth 1, therefore the principal diagonal entries of the pair-wise comparison matrix are all 1. The assumption of M attributes, and the pair-wise comparison of attribute i with attribute j yields a matrix BM $\times$ M where, *aij* denotes the comparative importance of attribute i with relevance attribute j within the matrix, $b_{ij} = 1$ once $i = j$ and b_{ji}. Find the relative normalized weight (w_j)

of every attribute by calculating the ith row mean and normalization of the
geometric means of rows in the comparison matrix.

Step 3   The geometric mean method of AHP is used to discover the relative normal-
ized weights of the attributes due to its simplicity and easiness to find out
the maximum eigen value and to lessen the inconsistency in the answer.

$$GM_j = \left[\Pi b_{ij}\right]^{1/M} \tag{1}$$

$$W_j = GM/\Sigma GM_j \tag{2}$$

- Calculate matrices $A3$ and $A4$ specified $A3 = A1 \times A2$ and $A4 = A3/A2$, where, $A2 = [w_1, w_2... w_j]T$ and $A1 = $ Decision matrix
- Find out the utmost Eigen value λmax (average of matrix $A4$). Calculate the consistency index $CI = (\lambda max - M)/(M - 1)$. The smaller the worth of CI, the smaller is that the deviation from the consistency and M is matrix size. Obtain the random index (RI) for the amount of attributes employed in deciding.
- Calculation of the consistency ratio by formula, $CR = CI/RI$. Generally, a CR value of 0.1 or less is taken into account as acceptable because it reflects an informed judgment that might be attributed to the knowledge of the analyst about the matter under study.

The steps for the TOPSIS method are as follows:

Step 1   Normalized decision matrix construction.

$$a_{ij} = y_{ij}/(\Sigma y_{ij}^2)^{1/2}\text{for } i = 1 \ldots m;\ j = 1 \ldots n \tag{3}$$

Step 2   Weighted normalized decision matrix construction.

Assuming that we have a set of weights for each criteria w_j for $j = 1\ldots n$. Each
column of the normalized decision matrix is multiplied by the weight associated to
it.

$$Z_{ij} = w_j * a_i \tag{4}$$

Step 3   Determination of positive ideal and negative-ideals solutions.

Positive ideal (best) solution:	Negative ideal (worst) solution:
(Maximum value for beneficial and Minimum for non-beneficial)	(Minimum value for beneficial and Maximum for non-beneficial)

Step 4   Separation measure calculation.

$$\text{Positive separation measures } S_i^+ = \left[\sum \left(V_j^+ - V_{ij}\right)^2\right]^{1/2} \tag{5}$$

$$\text{Negative separation measures } S_i^- = \left[\sum \left(V_j^- - V_{ij}\right)^2\right]^{1/2} \tag{6}$$

Step 5   Finding out the relative closeness to the ideal solution.

$$P_i = S_i^- / \left(S_i^- + S_i^+\right) \tag{7}$$

Step 6   Ranking the preference order.

Thus the alternatives are ultimately ranked in descending order, and the ranking is acquired. The first rank acquired is the nearest approach to the ideal solution and farthest from the negative ideal solution.

4   Problem Statement

Passenger car choice is one of the tough responsibilities in today's life. In the world, there are different types of cars and a customer is always confused about buying the correct car. Therefore there is a mathematical process which can be applied for the selection of cars. In the present work, the car selection problem is solved while comparing five passenger cars which consist of Tata Nexon, Vitara Brezza, Jeep compass, Harrier, Creta with five attributes like cost, mileage, safety, transmission and brake horse power. There are many more attributes which can also be selected for cars comparison but these five attributes are selected because of their higher preference while purchasing a car. People mostly focus these five attributes. The five cars are selected as customers mostly use them in day-to-day life. The cost is the only non-beneficial attribute, and all others are the beneficial attributes. Table 1 shows the information about the alternatives and attributes for different cars.

5   Solution by Using TOPSIS Method

The comparative importance of each alternative with each other is shown in Table 2.

The geometric mean is calculated using the Eq. (1) and then the weights are calculated using Eq. (2).

Table 1 Problem statement

Alternatives	Car name	Cost (Lakhs)	Mileage (Km/hr.)	Safety Rating (Out of 5 star)	Transmission (Gears)	Brake horse power (BHP)
1	Vitara Brezza	7.39	17.03	4	5	103
2	Tata Nexon	7.10	17.4	5	6	118
3	Harrier	14.00	16.35	4	6	168
4	Jeep Compass	17.02	17	5	6	161
5	Creta	10.31	20	4	6	113

Table 2 Pair-wise decision matrix

	Cost	Mileage	Safety	Transmission	BHP
Cost	1	3	0.33	5	5
Mileage	0.33	1	0.25	4	5
Safety	3	4	1	7	5
Transmission	0.2	0.25	0.14	1	0.33
BHP	0.2	0.2	0.2	3	1

$GM_1 = 1.8998$, $GM_2 = 1.1053$, $GM_3 = 3.3470$, $GM_4 = 0.2970$, $GM_5 = 0.4743$.

$W_1 = 0.2667$, $W_2 = 0.1552$, $W_3 = 0.4699$, $W_4 = 0.0417$, $W_5 = 0.0666$ (Table 3).

The maximum eigen value is calculated by taking the average of matrix A4 i.e., $\lambda max = A4/5 = 5.4253$ and the size of matrix $M = 4$. Therefore, CI $= 0.1063$.

The value of RI for the four attributes from the standard table is 1.12 therefore CR $= 0.0957$. As the CR less than 0.1 hence decision is correct and weights are acceptable.

The construction of normalized decision matrix using Eq. (3) and shown in Table 4.

Similarly, weighted normalized decision matrix is constructed using Eq. (4) and displayed in Table 5.

Table 3 Values of A2, A3, A4 matrix

A2 (Weights)	A3 = A1 * A2	A4 = A3/A2
0.2667	1.4286	5.3566
0.1552	0.8603	5.5443
0.4699	2.5154	5.3536
0.0417	0.2216	5.3148
0.0666	0.3700	5.5571

Table 4 Normalized decision matrix

Alternatives	Car name	Cost	Mileage	Safety Rating	Transmission	BHP
1	Vitara Brezza	0.2799	0.4326	0.4040	0.3846	0.3406
2	Tata Nexon	0.2689	0.4420	0.5050	0.4615	0.3902
3	Harrier	0.5302	0.4154	0.4040	0.4615	0.5555
4	Jeep Compass	0.6446	0.4319	0.5050	0.4615	0.5324
5	Creta	0.3905	0.5081	0.4040	0.4615	0.3736

Table 5 Weighted normalized decision matrix

Alternatives	Car name	Cost	Mileage	Safety Rating	Transmission	BHP
1	Vitara Brezza	0.0747	0.0672	0.1899	0.0160	0.0227
2	Tata Nexon	0.0717	0.0686	0.2373	0.0192	0.0260
3	Harrier	0.1414	0.0645	0.1899	0.0192	0.0370
4	Jeep Compass	0.1719	0.0670	0.2373	0.0192	0.0355
5	Creta	0.1042	0.0789	0.1899	0.0192	0.0249

Table 6 Positive and negative ideal solutions

Attribute	Cost	Mileage	Safety Rating	Transmission	BHP
V_j^+	0.0717	0.0789	0.2373	0.0192	0.0370
V_j^-	0.1719	0.0645	0.1899	0.0160	0.0227

The positive ideal and negative-ideals solutions for each attribute are calculated and shown in Table 6.

The separation measures are calculated by Eqs. (5) and (6) and relative closeness by Eq. (7). The rankings are based on the relative closeness values. The separation measures, relative closeness and ranks for the alternatives are displayed in Table 7.

6 Results and Discussion

The present work selected the TOPSIS approach to find the excellent passenger automobile out of the five alternatives. The alternatives are analyzed with respect to their five selected attributes. The evaluated ranks by the TOPSIS method are shown in Table 7. The automobile TATA Nexon is the exceptional preference for the various different alternatives. It has the best safety results with affordable cost. The Harrier is the fifth preference but it also has good features but according to preferences it has been the last preference according to the priority of the attributes.

Table 7 Separation measures, relative closeness, ranking

Alternatives	Car name	Cost	Mileage	Safety Rating	Transmission	BHP	S_i^+	S_i^-	P_i	Ranks
1	Vitara Brezza	0.0699	0.1081	0.0808	0.0384	0.0681	0.0511	0.0973	0.6556	2
2	Tata Nexon	0.0672	0.1105	0.1010	0.0461	0.0780	0.0150	0.1111	0.8807	1
3	Harrier	0.1325	0.1038	0.0808	0.0461	0.1111	0.0856	0.0339	0.2835	5
4	Jeep Compass	0.1611	0.1079	0.1010	0.0461	0.1064	0.1009	0.0493	0.3283	4
5	Creta	0.0976	0.1270	0.0808	0.0461	0.0747	0.0587	0.0694	0.5416	3

7 Conclusion

The aim of selecting the passenger car problem is to select one of the best cars for any customer to understand the process of decision-making. All the cars which are chosen for evaluation are top-selling cars and choosing the best from them can be a complicated task among various conflicting criteria. The present work gives the simple and logical scientific method in taking a correct judgment for the selection of cars. The results of the process can be varied according to the customer's need and way of giving importance to different attributes in the pair-wise comparison matrix. The present methodology helps in correct decision-making in a scientific and logical manner by selecting a suitable alternative by considering both conflicting quantitative and qualitative selection criteria. The example presented has demonstrated the different attributes which are mainly focused on while buying a car. There are many different methods for decision-making other than TOPSIS which can also be applied to make a correct decision. These methods can be used to make the best decision in other domain problems also.

References

1. Srikrishna S, Reddy SA, Vani S (2014) A new car selection in the market using TOPSIS technique. Int J Eng Res Gen Sci 2(4):177–181
2. Sahu Y, Shukla N (2017Application of multiple criteria decision making mathematical model for selecting best automobile. Int J Sci Res Develop 5(4):1796–1801
3. Babu SR, Manoj V (2020) Selection of a four wheel passenger car using AHP and TOPSIS approach—Indian Scenario. Int J Adv Sci Technol 29(6):5542–5548
4. Fei L, Hu Y, Xiao F, Chen L, and Deng Y (2016) A Modified TOPSIS Method Based on *D* Numbers and Its Applications in Human Resources Selection, Published by Hindawi Publishing Corporation Mathematical Problems in Engineering, (16):1–14
5. Elsayed A, Dawood AKS, Karthikeyan R (2017) Evaluating alternatives through the application of Topsis method with entropy weight. Int J Eng Trends Technol 46(2):60–66
6. Kumar J, Soota T, Singh SK (2015) Selection of refrigerant using-TOPSIS method. Int J Sci Eng Res 14–19
7. Ebrahim SK, Omid NA, Tahmasebipour N (2017) Application of TOPSIS method in evaluation and prioritization of social stability in rural areas. J Appl Sci Environ Manage 21(1):49–56 (Case Study: Zidasht Basin)
8. Roszkowska E Multi-criteria decision making models by applying the TOPSIS method to crisp and interval data. Multi-Criteria Decis Making Models 200–230
9. Rahim R, Supiyandi S, Siahaan APU, Listyorini T, Utomo AP, Triyanto WA, Irawan Y, Aisyah S, Khairani M, Sundari S, Khairunnisa K (2018) TOPSIS method application for decision support system in internal control for selecting best employees. J Phys Conf Ser 1028:1–8 (2nd international conference on statistics, mathematics, teaching, and research)
10. Zhongyou X (2012) Study on the application of TOPSIS method to the introduction of foreign players in CBA games. Phys Procedia 33:2034–2039 (International conference on medical physics and biomedical engineering)
11. Bulgurcu B (2012) Application of TOPSIS technique for financial performance evaluation of technology firms in Istanbul stock exchange market. Procedia Soc Behav Sci 62:1033–1040 (Elsevier Ltd.)

12. Jamil N, Besar R, Sim HK (2013) A study of multicriteria decision making for supplier selection in automotive industry. J Indus Eng 13:1–22 (Hindawi Publishing Corporation)
13. Zulqarnain RM, Saeed M, Ahmad N, Dayan F, Ahmad B (2020) Application of TOPSIS method for decision making. Int J Sci Res Math Stat Sci 7(2):76–81
14. Govil N, Tripathi A, Kumari V (2019) Identification of best Indian entry–level segment SUV through TOPSIS method. Int J Rec Technol Eng 8(4):8237–8240
15. Jozaghi A, Alizadeh B, Hatami M, Flood I, Khorrami M, Khodaei N, Tousi EG (2018) A comparative study of the AHP and TOPSIS techniques for dam site selection using GIS: a case study of Sistan and Baluchestan province, Iran', Geosciences 8(494):1–23
16. Moradian M, Modanloo V, Aghaiee S (2019) Comparative analysis of multi criteria decision making techniques for material selection of brake booster valve body. J Traffic Transp Eng 6(5):526–534

Design, Fatigue Analysis, and Optimization of Propeller Shafts Using Finite Element Analysis

Athul Vijay, Manas P. Vinayan, A. Hafsana, and T. Jagadeesha

1 Introduction

The propeller shaft is a major component used in automobiles that transmits torque from the gearbox to the wheels. Driveshafts are designed to move in diverse working angles and effective lengths to facilitate the movements in suspension to transmit torque from the gearbox to wheels in a reliable, vibration-free package. This renders the design of drive shafts moderately complex. Propeller shafts may be constructed from steel, aluminium alloy, or carbon fibre composites. High-quality Steel (Steel SM45C) is conventionally used to construct propeller shafts because of its reliable properties. The propeller shafts are constructed in a tubular shape to minimize the weight without compromising the component's strength. Torque transmission through two or more angles is made possible by the use of a Universal Joint. In order to accommodate the change in the effective length of the driveshaft, splined slip joints may be used.

The Cross and Yoke design of universal joints provide angular mobility to the propeller shaft. The Cross (also called Trunnion) imparts internal support for the needle roller bearings, while Yoke carries the bearing cap. The bearing cap aims to prevent the entry of undesirable particles and avoid any subsequent damage to the roller. Moreover, it prevents leakage of the lubricants, sealing the bearings. Some

A. Vijay (✉) · M. P. Vinayan · A. Hafsana · T. Jagadeesha
Department of Mechanical Engineering, National Institute of Technology, Calicut, Kerala 671603, India
e-mail: athul_b180096me@nitc.ac.in

M. P. Vinayan
e-mail: manas_b180068me@nitc.ac.in

A. Hafsana
e-mail: hafsana_b180045me@nitc.ac.in

T. Jagadeesha
e-mail: jagdishsg@nitc.ac.in

universal joints are maintenance-free, where the joint is sealed for its service life. Others are fitted with a grease nipple for lubrication during an inspection. The tail shaft and the final drive assembly must move in agreement during the compression or rebound of the suspension. The variation of the separation between the tail shaft and final drive assemble correlates to the arc that the final drive follows. The slip joint coupled with the tail shaft helps to counterbalance this tendency.

Periodic stresses induced in the drive shaft during operation lead to fatigue in shafts. This fatigue results in the propagation of a crack in the shaft, ultimately causing shaft failure. Hence, the number of cycles that the drive shaft can undergo before fatigue failure occurs is essential in design. Also, it is crucial to consider the fatigue factor of safety to incorporate periodic stresses occurring during operation. In this way, fatigue analysis of drive shaft design can help foresee the failure of the machinery.

2   Research Background

Driveshafts or propeller shafts are an integral part of the most power-driven machines. However, these are subjected to cyclic loads, which may eventually induce fatigue failure. The untimely mechanical breakdown of drive shafts can lead to massive catastrophes. Therefore, analysis and optimization of drive shafts for improved structural and mechanical properties have been a subject of significance in many works of literature. Gujaran and Ghalop [1] investigated the drive shaft in paper converting machines using parameters like stress and deflection pertaining to combined bending and torsion. The fatigue life was examined using analytical and numerical methods. Pradhan et al. [2] studied fatigue failure in composite driveshafts, viz, Carbon Fibre (notably, the commercial variant Panex 30), and Epoxy resin. A comparative study was performed between the conventional steel drive shaft and recently developed composite shafts. The composite shaft displayed a higher safety factor and weight reduction, revealing an exemplary behaviour of composites in engineering applications. Sulthana et al. [4] utilized Finite Element Analysis (FEA) to predict the fatigue life of propeller shafts of heavy-duty trucks. One of the significant observations was that drive shafts tend to collapse at the domain of maximum stress concentrations, especially at the region of splines. Overloading was found out to be the root cause of driveshaft failure. Dharmadhikari et al. [5] studied the design and analysis of composite, two-piece propeller shaft using ANSYS software by incorporating Genetic Algorithm for optimization. The Genetic Algorithm (GA) was preferred over conventional optimization methods due to the availability of discrete design data in the domain of structural mechanics. Comparisons between the Bernoulli-Euler beam theory and Timoshenko beam theory indicated the reliability of Timoshenko theory, which considers the rotary inertial effect and transverse shear forces in calculations. Marudachalam et al. [6] employed Goodman Criteria for methodical optimization of the shaft in spinning machine subjected to cyclic load. Finite Element techniques were utilized for stress analysis. It was found that higher safety factors and endurance

limits were achieved by decreasing stress concentration factors resulting from the increase in fillet radii.

3   Design Aspects

The design parameters of propeller shafts in cars used for SAESUPRA INDIA are considered. The data pertaining to the design of the propeller shaft are given in Table 1.

High-quality Steel (Steel SM45C) is commonly used for constructing propeller shafts because of its reliable properties. The material properties of SM45C steel are given in Table 2.

For the analysis of composite shafts, Orthotropic Epoxy E-Glass of Grade G-10 that is normalized up to 60% fibre volume was used. The density of the composite is 2000 kg/m³. Von Mises failure criterion was used for the analysis of composite

Table 1 Design parameters of cars used for SAESUPRA INDIA

Parameter	Unit	Value
Torque transmission capacity (T)	Nm	320
Speed (N)	Rpm	7250
Outer diameter (d_o)	Mm	48
Length (L)	Mm	450

Table 2 Mechanical properties of SM45C steel

Mechanical properties	Symbol	Unit	Value
Young's modulus	E	GPa	207
Shear modulus	G	GPa	80
Poisson's ratio	μ	–	0.3
Density	P	Kg/m³	7850
Yield strength	S_y	MPa	460

Table 3 Mechanical properties of Epoxy E-Glass G-10

Mechanical properties	X/XY	Y/YZ	Z/XZ	Units
Young's modulus	45,000	10,000	10,000	MPa
Shear modulus	5000	3846.2	5000	MPa
Poisson's ratio	0.3	0.4	0.4	–
Tensile stress	1100	35	35	MPa
Compressive stress	−675	−120	−120	MPa
Shear stress	80	46.154	80	MPa
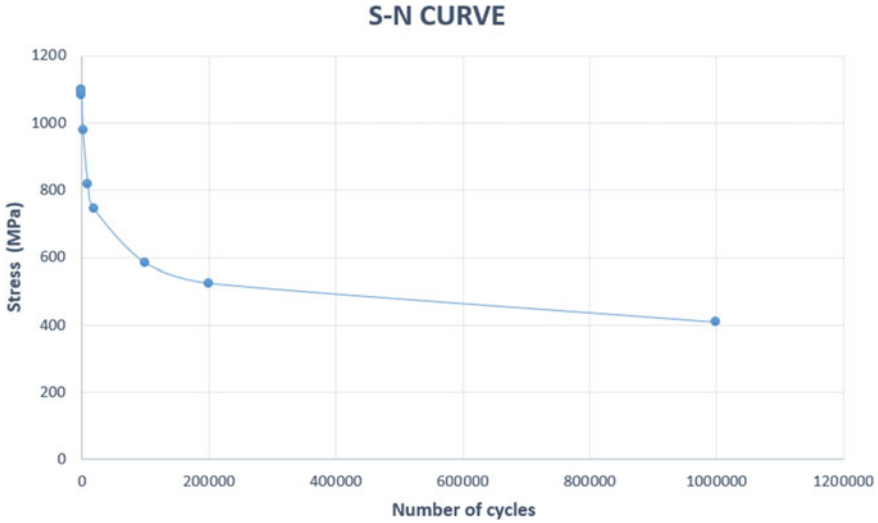
S-N CURVE

Fig. 1 *S-N* curve for epoxy E-glass

shafts. The mechanical properties of Epoxy E-Glass G-10 are given in Table 3. The *S-N* curve for Epoxy E-Glass is shown in Fig. 1.

4 Analytical Calculations for Solid Shaft

4.1 Torsional Strength

The primary load in the propeller shaft is torsion. The maximum shear stress, max τ_{max} in the propeller shaft is at the outer radius and is given by Torsion formulae as follows:

$$\tau = \frac{16M_t}{\pi d_0^3 (1 - c^4)} = \frac{16 * 320}{\pi * .048^3} = 14.736 \text{ MPa}$$

For a solid shaft, $c = 0$.
Mass of steel propeller shaft,

$$m = \frac{\rho \pi d^2 L}{4} = \frac{7850 \times \pi \times (0.048)^2 \times 0.45}{4} = 6.392 \text{ kg}$$

4.2 Design of Shaft for Fatigue Loading

The propeller shaft will be experiencing a force due to its own weight at the centre of the shaft.

Force due to the self-weight of the propeller shaft is,

$$P = mg = 62.708 \text{ N}$$

The shaft is free to move along the splined joint, and hence the reaction for is only the normal force at the two ends. The free body diagram of the propeller shaft is shown in Fig. 2.

The reaction forces (in the Y-direction) at points A and B are the same,

$$A_y = B_y = \frac{62.708}{2} = 31.354\text{N}$$

The bending moment at the centre of the shaft is,

$$M = A_y * \frac{0.45}{2} = 31.354 * \frac{0.45}{2} = 7.055\text{Nm}$$

The shear force diagram (SFD) and bending moment diagram (BMD) for the loading condition of the propeller shaft are given in Figs. 3 and 4, respectively.
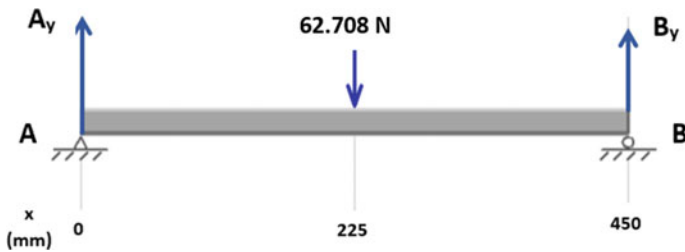
Fig. 2 Free body diagram of the propeller shaft
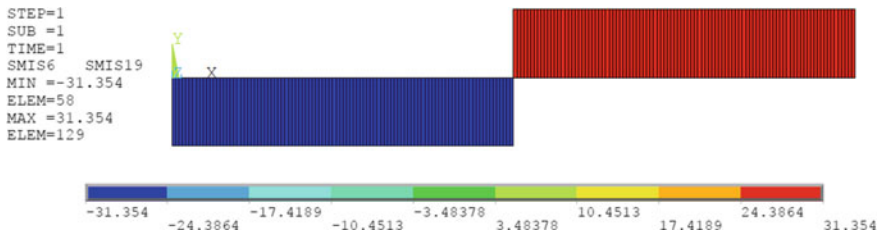
Fig. 3 Shear force diagram of the propeller shaft using ANSYS APDL
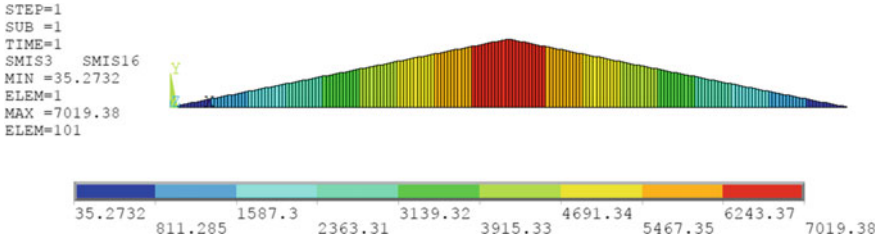
Fig. 4 Bending moment diagram of the propeller shaft using ANSYS APDL

4.3   Prediction of Fatigue Life

The maximum bending moment obtained from BMD is, $M_b(\text{max}) = 7.055$ Nm.
  The minimum bending moment on the system is, $M_b(\text{min}) = 0$ Nm.

4.3.1   Mean and Amplitude Stresses

Mean bending moment, $M_{\text{bm}} = \frac{7.055+0}{2} = 3.5275$ Nm.
  Amplitude of the bending moment, $M_{ba} = \frac{7.055-0}{2} = 3.5275$ Nm.
  Using Flexure formula,
  Mean normal stress, $\sigma_{xm} = \frac{32*M_{\text{bm}}}{\pi*d^3} = 324895.290 \text{N/m}^2$.
  Amplitude of the normal stress, $\sigma_{xa} = \frac{32*M_{ba}}{\pi*d^3} = 324895.290 \text{N/m}^2$.
  Mean torque on the shaft, $(M_t)_m = \frac{1}{2}[T+0] = 160$ Nm .
  Amplitude of torque on the shaft, $(M_t)_a = \frac{1}{2}[(M_t)\max - (M_t)\min] = 160$ Nm.
  Using Torsion formula,
  Mean shear stress induced in the shaft, $\tau_{xym} = \frac{16(M_t)_m}{\pi d^3} = 7.368$ MPa.
  Amplitude of shear stress induced in the shaft, $\tau_{xya} = \frac{16(M_t)_a}{\pi d^3} = 7.368$ MPa.
  Mean of the net normal stress induced in the shaft,

$$\sigma_m \sqrt{(\sigma_{xm} \times k_b)^2 + 3(\tau_{xym} \times k_t)^2} = 19.153 \text{ MPa}$$

Amplitude of the net normal stress induced,

$$\sigma_a = \sqrt{(\sigma_{xa} \times k_b)^2 + 3(\tau_{xa} \times k_t)^2} = 19.153 \text{ MPa}$$

The Von Mises stress developed in the shaft is, 19.153 Mpa.

4.3.2   Finding Factor of Safety of the Shaft

Endurance strength of shaft is,

$$Se = K_{load} \times K_{size} \times K_{surf} \times K_{temp} \times K_{reliability} \times K_d \times K_{st} \times S'_e$$

$$K_{load} = 1, K_{size} = 0.85, K_{surf} = A \times S_{ut}^{-0.265} = 4.51 \times 460^{-0.265} = 0.88827.$$

$$K_{reliability} = 0.897, K_{temp} = 1, K_d = \frac{1}{1 + 0.9 \times (1.44 - 1)} = 0.716, K_{st} = 1$$

$$S'_e = 0.5 \times S_{ut} = 0.5 \times 460 = 230 \text{ MPa}$$

Endurance strength of shaft,

$$S_e = 1 \times 0.85 \times 0.8827 \times 0.897 \times 1 \times 0.716 \times 230 = 111.531 \text{ MPa}$$

According to modified Goodman criteria,

$$\frac{S_a}{S_e} + \frac{S_m}{S_{yt}} = 1 \Rightarrow \frac{S_a}{111.531} + \frac{S_m}{460} = 1 \Rightarrow S_m = 89.7 \text{ MPa} = S_a$$

Fatigue factor of safety, FOS $= \frac{S_a}{\sigma_a} = \frac{89.7}{19.153} = 4.683$.

4.3.3 Number of Cycles Before Fatigue Failure Occurs

$$S_f = \frac{\sigma_a * S_{ut}}{S_{ut} - \sigma_m} = \frac{154.102 * 460}{460 - 154.102} = 20.033 \text{ Mpa}$$

Slope of S-N curve is, $m = \frac{-(\log(0.9 * S_{ut}) - \log S_e)}{3} = -0.1899$.
The equation of the S-N curve is, $\log S_f = m * \log N + \log(0.9 * S_{ut})$

$$\log N = \frac{\log S_f - \log(0.9 * S_{ut})}{m} = \frac{1.3017 - 2.617}{-0.1899} = 6.926$$

The number of cycles, $N = 8.433 \times 10^6$ cycles.
Thus, it is concluded that the propeller shaft is safe for infinite cycles.

5 Finite Element Modelling

In order to perform the Finite Element Analysis of solid and hollow variants of steel shafts subjected to fatigue load, the CAD model of the structure was modelled in Solidworks. The ANSYS Workbench software package, specifically ANSYS Discovery, was employed to carry out meshing, setup, and solving. Fatigue in the shaft occurs due to applied fluctuating load during operation. Figure 5 shows the
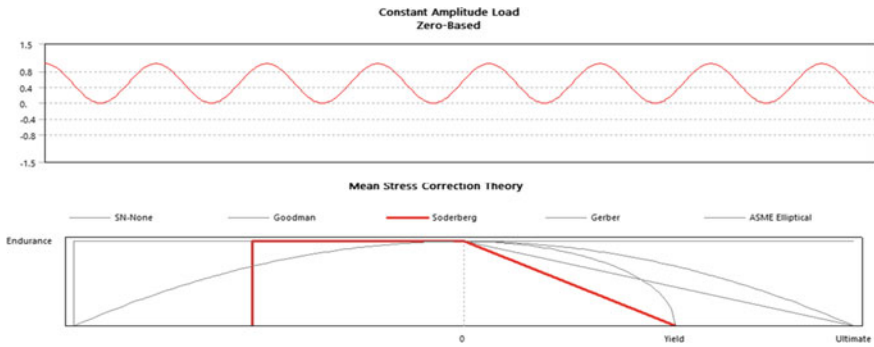
Fig. 5 Characteristics of fluctuating load

characteristics of the fluctuating load.

The CAD model was imported to Workbench, and the mesh was set up in ANSYS Mechanical. The tetrahedral mesh was selected for both solid and hollow shafts. For the hollow shaft, mesh size has a minimum edge length of 162 μm resulting in 29,126 nodes and 15,586 elements, as shown in Fig. 6. For the solid shaft, 32,118 nodes and 17,454 elements were generated, as shown in Fig. 7. Finer mesh was generated in the region of splines which is the critical area concerning higher stress concentrations. The Fatigue tool in ANSYS was used to determine the factor of safety and Fatigue life.

Figure 8 shows the composite propeller shaft used to determine the alternating stress modelled in ANSYS APDL.
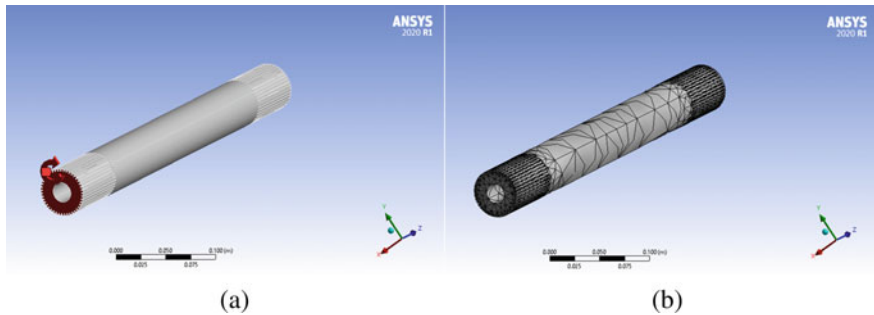
Fig. 6 **a** Hollow shaft—Boundary conditions **b** Hollow shaft—Mesh
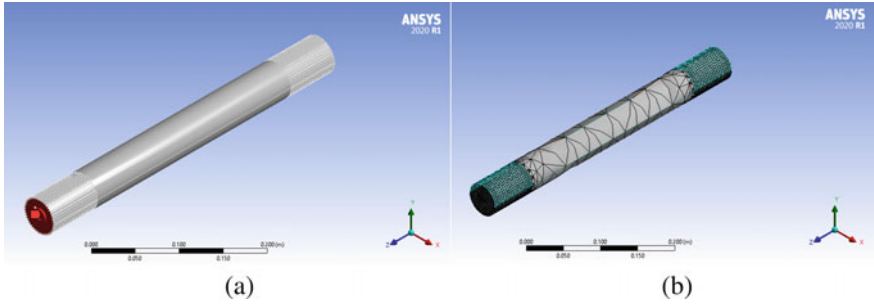
Fig. 7 a Solid shaft—Boundary conditions **b** Solid shaft—Mesh

Fig. 8 Composite propeller shaft modelled in ANSYS APDL
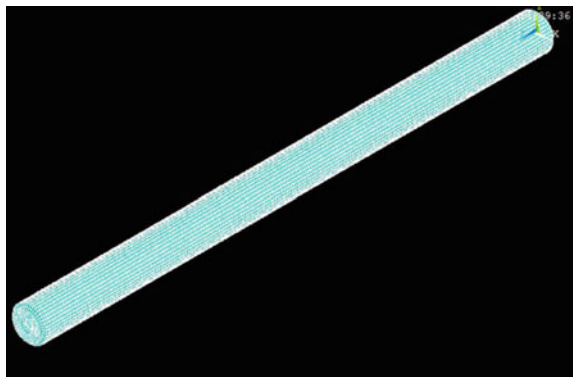
6 Results and Discussions

The maximum value of Von Mises stress obtained for hollow and solid shafts are 65.91 MPa and 70.67 MPa, respectively. The stress variation along the length of the shaft is given in Fig. 9.

The life of both the hollow and solid shafts is comparable and is in the range of 10^6 cycles.
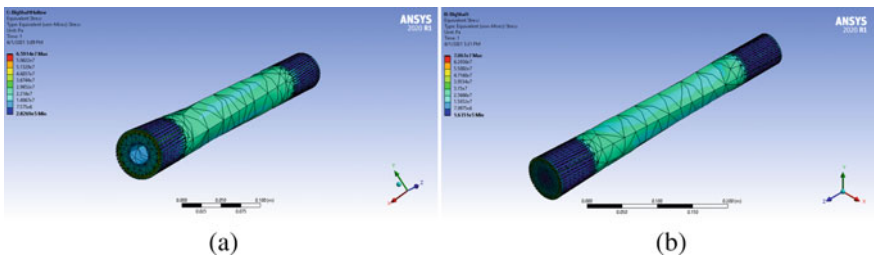
Fig. 9 Variation of stress **a** Hollow shaft **b** Solid shaft
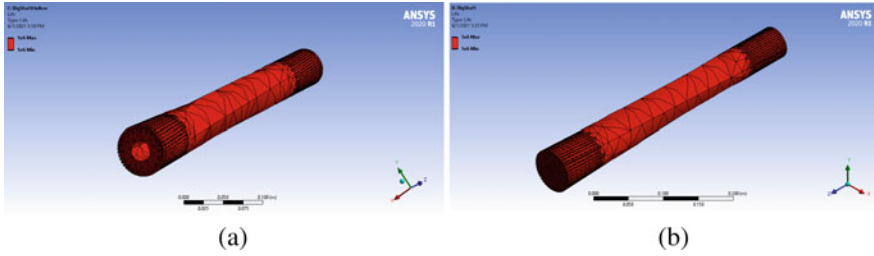
Fig. 10 Life **a** Hollow shaft **b** Solid shaft
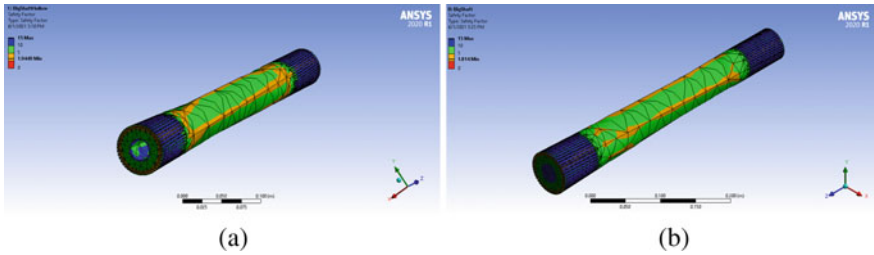
Fig. 11 Factor of safety **a** Hollow shaft **b** Solid shaft

Table 4 Results of Fatigue analysis of composite propeller shaft

Sl. No.	Ply orientation	Alternating Stress (MPa)
1	0°, 45°, 90°	81.6
2	0°, 90°, 45°	85.39
3	90°, 45°, 0°	82.8

Figure 11 shows the numerical results obtained from Fatigue analysis for factor of safety of both hollow and solid shafts. It is observed that the fatigue factor of safety of the hollow shaft is 1.9449, which is 7.2% greater than the fatigue factor of safety value obtained for the solid shaft (1.814).

The fatigue analysis of the composite propeller shaft was also done using ANSYS APDL. It was of Epoxy E-glass material and had three layers of 1, 2, and 3 mm thicknesses. The fatigue analysis of different ply orientations was compared, taking a constant diameter of the propeller shaft as 24 mm. The results are tabulated in Table 4.

7　Conclusions

Numerical study for the fatigue analysis of both solid and hollow propeller shafts was done using ANSYS. Also, analysis was carried out to understand the characteristics

of Composite shafts. It is found that the hollow shaft was better with the optimum diameter of the shaft as 48 mm with a 20 mm diameter hole through it. The factor of safety obtained in both cases was similar with 1.814 and 1.9449 for solid and hollow shafts, respectively. Although the material has been removed from the hollow shaft, the factor of safety was comparatively higher. Both the propeller shafts are showing infinite life, thereby making them suitable for extended use. The minimum factor of safety region for both propeller shafts was near the root of the spline teeth. This is due to the stress concentration occurring near the sharp corners of the spline. The interior of the shaft does not experience much stress. Therefore, it is safe to remove material from that region. Lightweight propeller shaft results in better fuel economy and better performance of the vehicle.

References

1. Gujaran S, Gholap S (2014) Fatigue analysis of drive shaft. Int J Res Aeronaut Mech Eng 2(10):22–28
2. Pradhan MN, Gaikwad HT (2015) Fatigue analysis of composite drive shaft. Int J Eng Res Technol 4(5):484–489
3. Pne Naveen R, Reddy B (2018) An analysis of composite drive shaft using ANSYS ACP. Int J Mech Prod Eng Res Develop 8(5):117–124
4. Parveen Sulthana P, Aruna K, Krishna Rao T, Shivakumar HG (2016) Design and analysis of drive shaft for heavy duty truck. Int J Res Eng Technol 5(1):52–57
5. Dharmadhikari SR, Mahakalkar SG, Giri JP, Khutafale ND (2013) "Design and analysis of composite drive shaft using ANSYS and genetic algorithm" a critical review 3(1):490–496
6. Deepan Marudachalam MG, Kanthavel K, Krishnaraj R (2011) Optimization of shaft design under fatigue loading using Goodman method 2(8)

Topological Optimization of Spiral Springs

Athul Vijay, Manas P. Vinayan, A. Hafsana, and T. Jagadeesha

1 Introduction

Spiral springs have evolved into state-of-the-art technology for energy storage. Flat spiral springs are manufactured by winding a band-shaped material to form a spiral around the centerline in a plane. These springs can store large amounts of energy in relatively lesser space, thus enabling them to be employed as power sources such as in watches and for power utilization in moving large objects.

Energy storage technologies have gained considerable attention in research, especially with the advent of clean energy technologies. An energy storage mechanism is inevitable for any power grid for the dynamic and reliable supply of energy from the source to the sink. Conventional storage systems include batteries, hydroelectric power storage, etc., prove to be less efficient in retaining capacity. Thus, mechanical storage mechanisms like flywheel-based and spring-based systems have gained interest in having better conversion and retaining efficiency.

The fundamental principle of elastic energy storage in flat spiral springs is that different forms of energy, such as electrical, chemical, and magnetic, can be converted into elastic potential energy of the spring and can be stored in the spring energy storage device. Hence, the design of the flat spiral springs plays a crucial role in the effectiveness and reliability of this energy storage method.

A. Vijay (✉) · M. P. Vinayan · A. Hafsana · T. Jagadeesha
Department of Mechanical Engineering, National Institute of Technology, Calicut, Kerala 671603, India
e-mail: athul_b180096me@nitc.ac.in

M. P. Vinayan
e-mail: manas_b180068me@nitc.ac.in

A. Hafsana
e-mail: hafsana_b180045me@nitc.ac.in

T. Jagadeesha
e-mail: jagdishsg@nitc.ac.in

Many surfaces in the geometry of flat spiral spring render it complex for analytical analysis for the deformation and energy stored per unit volume. Also, this kind of analysis is incapable of finding the stress variation for the whole spiral spring. Moreover, the natural frequency of the spring system as a whole is unable to be determined through analytical means. The analytical method is not applicable all over the spring for stress distribution and natural frequency. Thus, this work uses finite element analysis to study the spring characteristics of all the models and to perform the topology optimization. For this study, five variants of spiral spring are considered, namely I-beam-shaped spiral springs, no-holed springs, diamond-holed springs, oval-holed springs, and rectangular-holed springs.

2   Research Background

Current research and developments in energy storage in the form of mechanical elastic energy have shown that flat spiral springs are valuable elements for storing and providing the stored energy as per requirement. Hence, it is essential to analyze these energy storage components from the design point of view as the structure of these springs influences the effectiveness of energy storage. Tang et al. [1] conducted a finite element analysis of spiral springs used in mechanical elastic energy storage technology. The study focused on analyzing three types of spiral springs, and the first ten-order vibration modes of the spring are analyzed. Castellani et al. [2] discussed the prospective of mechanical spring systems for applications in energy storage. The benefits and limits of mechanical spring systems for storing macroscopic amounts of energy are assessed. The capability of these kinds of spring systems to be coupled with electrical and mechanical power storage and transmission systems is also discussed in the study. Chen et al. [3] used the elastic theory to study a spiral spring's deformation and natural frequency. Experimental analysis is also carried out as a part of the study and ensures that both the values of deformation and natural frequencies obtained by experimental and theoretical predictions match. Tang et al. [4] conducted studies on the methods to improve the energy storage density. Design of springs of two different cross sections was performed. Finite element analysis was used to analyze stress distribution and compare two kinds of spiral springs. Spiral torsion springs were studied analytically using certain variables in a study conducted by Munoz-Guijosa [5]. These variables had a direct correlation with the length of the strip used in the spring. The model is validated and is used to perform the parametric study to gain insights into spiral spring design.

Table 1 Mechanical properties of stainless steel

Sl. No.	Properties	Units	Value
1	Density, ρ	Kg/m^3	7750
2	Young's modulus, E	GPa	193
3	Poisson's ratio, γ	–	0.31

3 Methodology and Modeling

3.1 Material Considerations

The material of springs selected for the study is stainless steel. The reliable mechanical properties and the ability to resist corrosion make it suitable for the fabrication of energy storage springs. The mechanical properties of stainless steel are outlined in Table 1.

3.2 Modeling of Plane Spiral Spring

Plane spiral spring in its true form was modeled in SolidWorks 2020. The computer-aided drawing of the spiral spring designed for the analysis is shown in Fig. 1. The geometry of the spring is presented in Fig. 2.

3.3 Modeling of Spiral Spring Variants

3.3.1 Initial Optimized I-beam-Shaped Model

The spiral spring is modified at the end to have an I-beam structure. The model of I-beam optimized structure of the spiral spring is shown in Fig. 3.

3.3.2 Shape Optimization in Small Springs-No Hole

Small springs can be optimized by altering the shape of the cross section. The model of no-holed small spring is shown in Fig. 4

3.3.3 Shape Optimization in Small Springs-Oval Hole

The model of oval-holed small spring is shown in Fig. 5
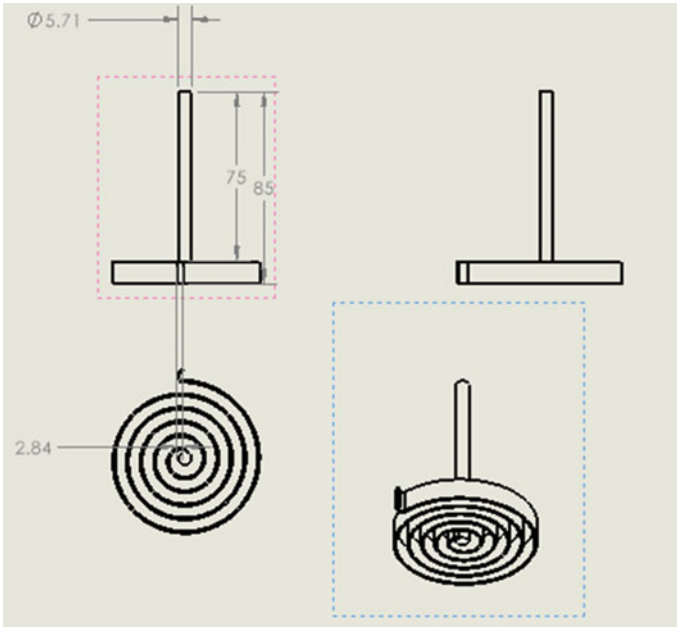
Fig. 1 Computer-aided drawing of the spiral spring
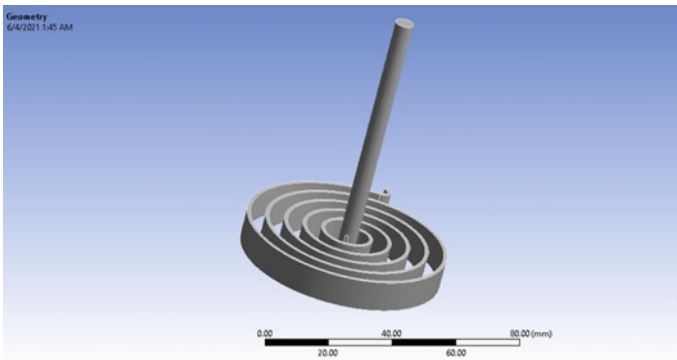
Fig. 2 Geometry of spiral spring

3.3.4 Shape Optimization in Small Springs-Diamond Hole

The model of diamond-holed small spring is shown in Fig. 6.

Fig. 3 Initial optimized I-beam-shaped model
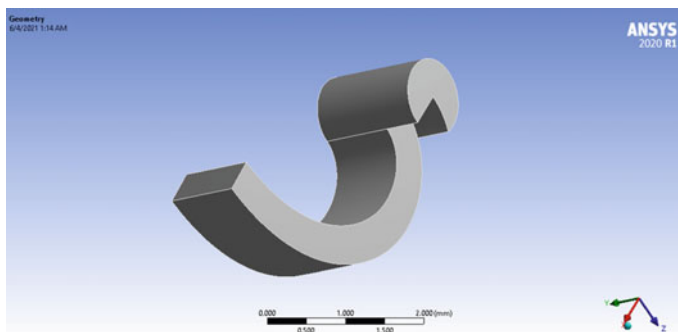
Fig. 4 Shape optimization in small springs-no hole
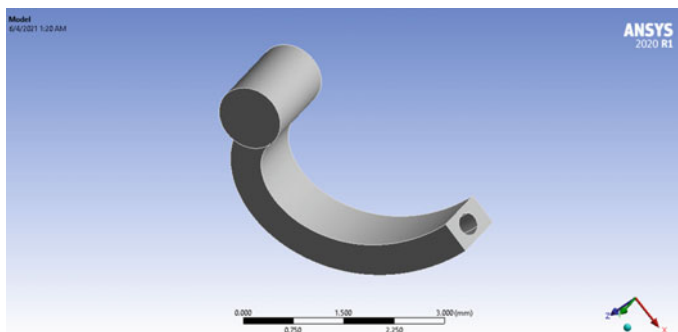
Fig. 5 Shape optimization in small springs-oval hole

3.3.5 Shape Optimization in Small Springs-Rectangular Hole

The model of rectangular-holed small spring is shown in Fig. 7.
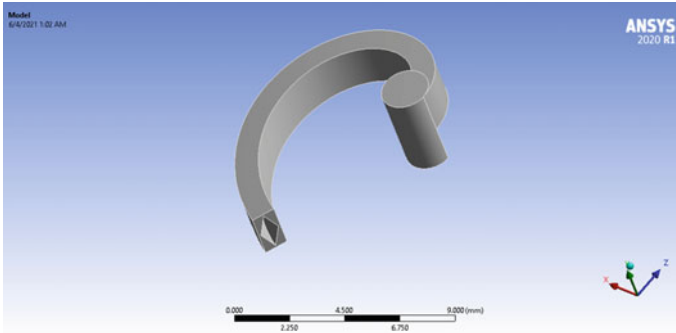
Fig. 6 Shape optimization in small springs-diamond hole
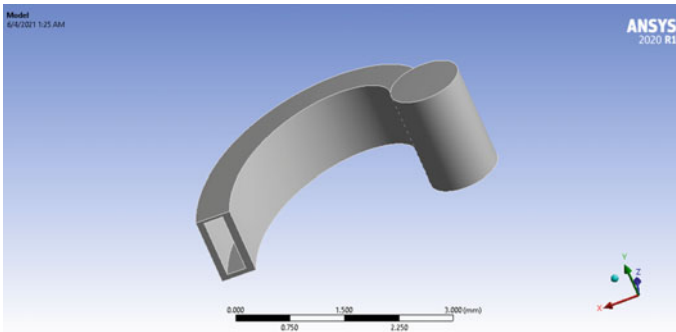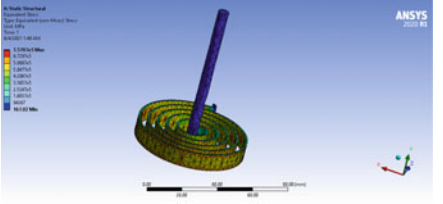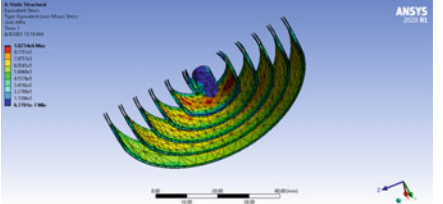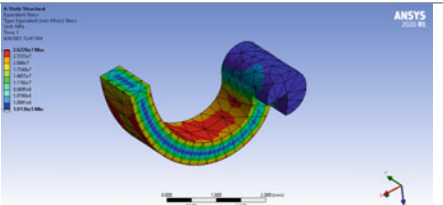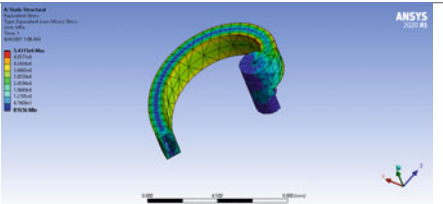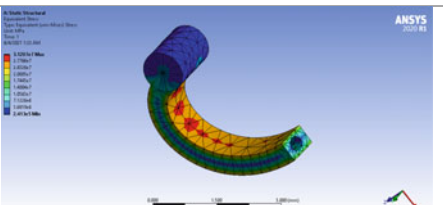
Fig. 7 Shape optimization in small springs-rectangular hole

4 Finite Element Analysis
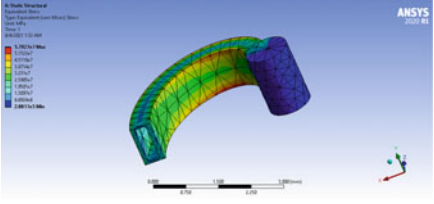
In order to perform the finite element analysis of variants of spiral springs subjected to load, the CAD model of the structure was modeled in SolidWorks. The ANSYS Workbench software was employed to carry out meshing, setup, and solving. For the meshing of the model, tetrahedral meshes are being employed. The spring is in the spring box of the energy storage device, its end is fixed to the spiral box, and its top is fixed to the mandrel. Hence, while assigning boundary conditions, the end of the spring is constrained, and the torque is exerted at the top of the spring. The values obtained from the analysis for the von Mises stress and Equivalent elastic strain are shown in Tables 2 and 3, respectively.

Table 2 Von Misses stresses for different models

Design model	Value (× 10^6 MPa)	Von Misses stress
Flat spiral spring	0.76	
Initial optimized model of I-Beam-shaped spiral spring	1.02	
No-holed small spring	26.23	
Diamond-holed small spring	5.43	
Oval-holed small spring	31.21	

(continued)

Table 2 (continued)

Design model	Value ($\times$ 10^6 MPa)	Von Misses stress
Rectangular-holed small spring	57.93	

5 Topology Optimization

While springs are employed for energy storage purposes, the weight of the springs can act as a barrier to their application in specific applications. Thus, it is essential to optimize the topology of the spring used without reducing its capacity of energy storage.

At the neutral axis of the spring section, the bending moment is equal to zero, which implies the spring torque does not produce work in this region. Accordingly, energy storage is also negligible near the neutral axis. Thus, it is imperative that an increase in storage energy density, i.e., energy storage per unit mass, is achieved by reducing the material near the neutral axis, establishing special sectioned spiral springs.

Under the applied load and constraint values, the topology density is optimized to remove the material from a no-holed small spring using the finite element method. Initially, finite element analysis was done for obtaining stress and strains for the given model (Fig. 8).
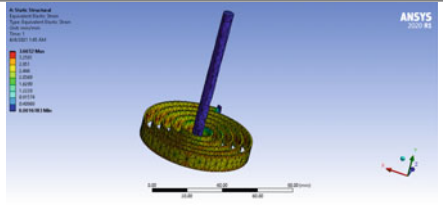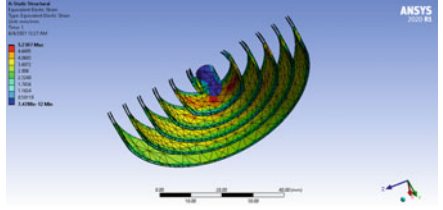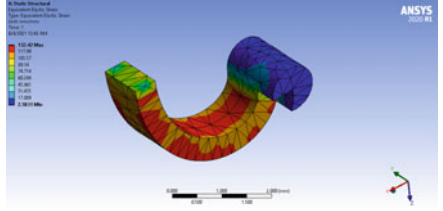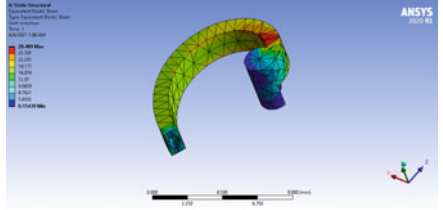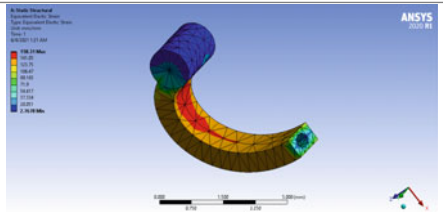
This analysis also revealed that the least stress and strain are along the neutral axis of the spring. Then design region for optimization is set accordingly, with a response constraint of 50% mass. The model is optimized, and the solution is found. The comparison between the original model and the optimized model is made using Fig. 9.

6 Results and Analysis

The strain energy values found out by finite element analysis of the spiral spring are given in Table 4.

The energy density value for the small spring variants is shown in Table 5. The values of mass for each model are obtained from ANSYS.

Table 3 Equivalent elastic strain for different models
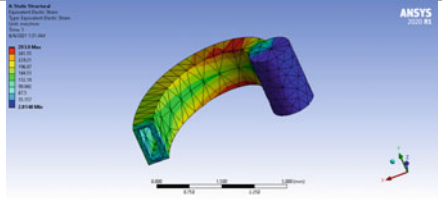
Design Model	Value (mm/mm)	Equivalent elastic strain
Flat spiral spring	3.66	
Initial optimized model of I-Beam-shaped spiral spring	5.23	
No-holed small spring	132.42	
Diamond-holed small spring	28.49	
Oval-holed small spring	158.31	

(continued)

7 Conclusions

Numerical analysis is conducted for five different variants of the spiral spring using ANSYS. The stress values developed in the spring, elastic strain, and energy density were found and tabulated. It is found that the energy density is highest for the spiral

Table 3 (continued)

Design Model	Value (mm/mm)	Equivalent elastic strain
Rectangular-holed small spring	293.9	
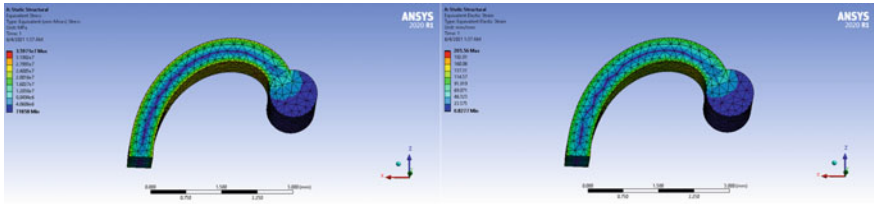
Fig. 8 Von Misses stress and equivalent elastic strain
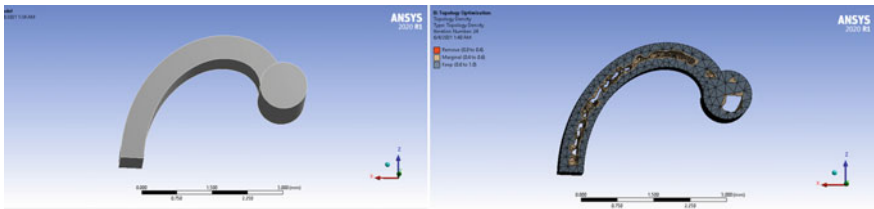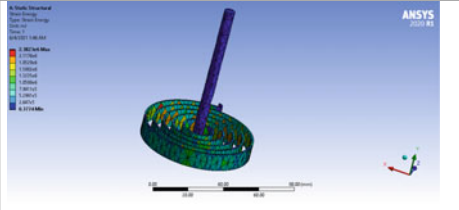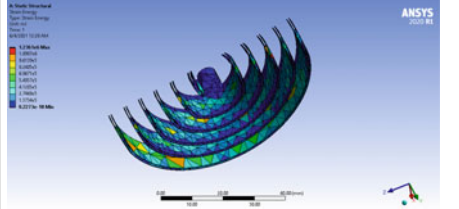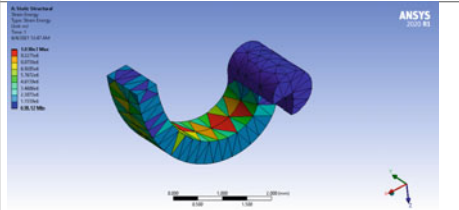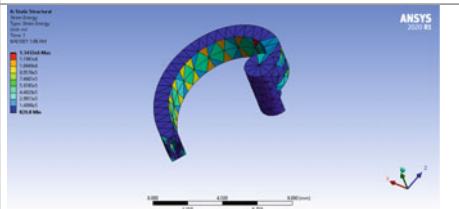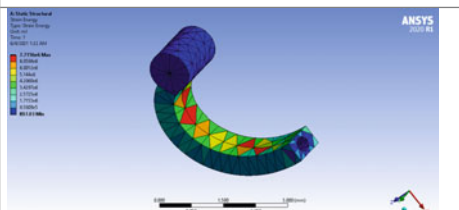
Fig. 9 Comparison between basic model and topologically optimized model

spring with rectangular hole and is lowest for the spiral spring with diamond hole. This is because the part near-neutral axis is underutilized for the storage of energy compared to the surface region of the spring, and removal of material in this area does not affect the energy storage potential of the spring. This is evident from the topological optimization carried out using finite element analysis. The comparison between the rectangular-holed small spring and topologically optimized small spring shows a definitive similarity in material removal region. The rectangular shape with its high energy storage density is best suited for energy storage applications where material mass is a constraint.

Table 4 Results of strain energy for different models

Design model	Value (KJ)	Strain Energy
Flat spiral spring	2.38	
Initial optimized model of I-Beam-shaped spiral spring	1.24	
No-holed small spring	10.38	
Diamond-holed small spring	1.34	
Oval-holed small spring	7.72	

(continued)

Table 4 (continued)
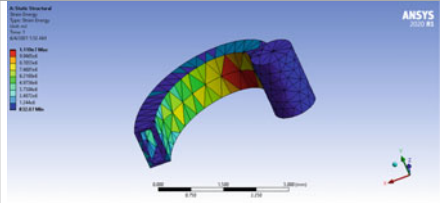
Design model	Value (KJ)	Strain Energy
Rectangular-holed small spring	11.19	

Table 5 Calculation of energy density

Design model of small spring	Total Energy (KJ)	Mass ($\times 10^{-5}$ kg)	Energy/unit mass (MJ/kg)
No-holed	10.38	2.6362	393.748
Oval-holed	7.72	2.1987	351.116
Diamond-holed	1.34	2.2889	58.543
Rectangular-holed	11.19	1.757	636.881

References

1. Tang J-Q, Wang Z, Mi Z, Yu Y (2014) Finite element analysis of flat spiral spring on mechanical elastic energy storage technology. Res J Appl Sci Eng Technol 7(5):993–1000
2. Rossi F, Castellani B, Nicolini A (2015) Benefits and challenges of mechanical spring systems for energy storage applications. Energy Procedia 82:805–810
3. Chen J-S, Chen I-S (2015) Deformation and vibration of a spiral spring. Int J Solids Struct 64-65:166–175
4. Tang J-Q, Wang Z, Mi Z, Yu Y (2014) Energy storage stress analysis spiral spring on mechanical elastic energy storage technology. In: International conference on mechatronics, electronic, industrial and control engineering
5. Muñoz-Guijosa JM, Caballero DF, Rodríguez V, de la Cruz J, Sanz LM, Echávarri J (2012) Generalized spiral torsion spring model. Machine and Mechanism Theory 51:110–130

The Lean-Based DMAIC Methodology for Optimization of Product Development Process (PDP)

Nikhil V. Patil, S. Komala, Snehal Nayakawade, and Jayant S. Karajagikar

1 Introduction

The word in the Japanese language for waste is Muda, which means "uselessness." Lean tools are designed to find out Muda in organizations and improve internal control. In other words, lean tools are used to find and eliminate processes that are not value-adding. Lean tools are utilized across many industries and organizations often leverage them together with six sigma methods. The lean product development is also a emerging concept, which applies lean concept in the product's development phase to reduce waste in both the development and manufacturing phases.

A literature review conducted using keywords related to lean, DMAIC and product development. As a result, some articles discussing methodologies by comparing lean and six sigma, their applications, and tools used in it were analyzed [1]. The application of DMAIC methodology in different industries and its uses was observed from the DMAIC review paper [2]. Also, there were articles that are using lean and six sigma for reduction of lead time [3], cycle time [4, 5], and process improvement. Literature review showed that lean and six sigma are the trending research topics for recent years. However, few researchers integrated both as Lean Six Sigma and documented how these techniques can achieve best-in-class results [6, 7]. One study also dealt with the DMAIC cycle-based LSS model for project management process

N. V. Patil (✉) · J. S. Karajagikar
Department of Manufacturing Engineering and Industrial Management, College of Engineering, Pune, India
e-mail: Patilnv19.prod@coep.ac.in

J. S. Karajagikar
e-mail: Jsk@prod.coep.ac.in

S. Komala
Visvesvaraya Technological University, Banglore, India

S. Nayakawade
Shivaji University, Kolhapur, India

improvement, but the author did not find anything related to product development process improvement [8]. Therefore, the idea was to prepare and apply the framework for design and development process improvement, which will be user-friendly and applicable to any product developing company.

Thus, the purpose of the study is to develop a framework, which will allow using lean based DMAIC approach for reducing the time of PDP. Till now, this paper presents an overview of lean. The upcoming section shows the methodology used in this study, followed by the proposed model for PDP optimization. The second last section shows the testing of the proposed model while the last discusses the conclusions of the study.

2 Lean Model for PDP Improvement

The proposed model for lean-based DMAIC methodology is shown in Fig. 1. It has five main phases: Define, Measure, Analyze, Improve, and Control (DMAIC). The main steps in DMAIC are sequential and specific tools support each step's output. The methodology is designed by conducting a literature survey to find similar methodologies and frameworks.
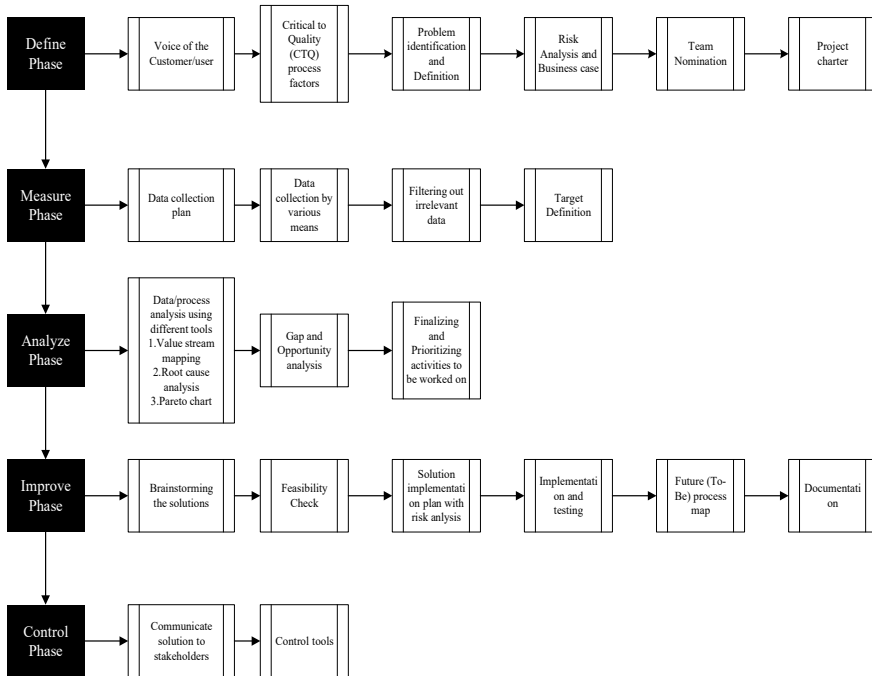
Fig. 1 Main steps for Lean Six Sigma in PDP improvement

The beginning of the DMAIC methodology is from the define phase, which focuses on defining the problem from a business perspective. In this, the input of the problem is taken from the customer or user through the voice of customer. To understand the problem, the current value stream map can be constructed or the SIPOC method can be used. Then project plan and milestones are prepared after doing risk opportunity management and business case calculation. From all, this user will get potential of the problem. So accordingly, team size and required expertise can be decided and team members from different domains can be nominated. Finally, at the end of the define phase, the project charter should be prepared, an official document containing the project scope and agreed targets to be achieved.

The second phase is the measure phase. It is essential because all inputs required for the process improvement are collected in this phase. So initially, a data collection plan should be prepared and followed by data collection by various means, which may include studying the process thoroughly, interviews, surveys, etc. Once the data is collected, data quality should be maintained by removing irrelevant data and working on relevant information only.

The third phase is one of the critical phases and aims to analyze all problems thoroughly by using different tools such as root cause analysis, value stream mapping, pareto chart. Once the analysis is completed, finalize, and prioritize the problems on which one can work based on their importance.

The cause of the problems defined in analyze phase needs to be treated, so there is an improvement phase. So initially, the solutions to the problem should be identified by using the best-suited problem-solving method. Once the solutions are available, then a feasibility study is conducted to check which solution is feasible and only feasible solutions can be implemented and tested. The last phase is the control phase, in which one has a goal to make sure that improvement is made as per plan and gains made from improvement are sustained till new technology and data show that there is a better way to operate the process.

3 Testing of Proposed Methodology

To test and validate the proposed model, it implemented in an Indian automotive electronics product supplier company, which comes under the "Make-to-Order" category of business. So once the company won the business from any customer to supply any electronic product, they start designing and developing the product at their design and development center. After the sample is developed and tested at the development location, the design is shared with the manufacturing facility for sample and series production. In this process, customers are also involved at many places to validate and give feedback on whether product being developed as per requirement. Once the product is ready, then it is delivered to the customer. For designing and developing the product in the company, there is a standard process established based on waterfall methodology and V model (Verification/Validation model), the process is known as Product Development Process (PDP). The PDP includes multiple phases, activities to

be done in various phases, standard document/templates to be prepared/maintained, the procedure to be followed, supporting software's, responsible person/domain for multiple activities and many more. As every product is different, so the exact process will not be followed for all, so tailoring and deviation for product-specific activities in PDP are allowed. After working on many project life cycles, it has been observed that more time is being spent in the design and development of product once the company won the business of customer project and this has severe implications on the business if not addressed immediately. Therefore, it was decided to reduce the duration of PDP/efforts in PDP by using lean-based DMAIC methodology.

3.1 Define Phase

In this phase, by VOC, there was input that PDP is taking more time due to which the whole product life cycle is being delayed. This has a significant impact on business because customer satisfaction is at the edge and effort spending is more than required. To work on it, in the initial stage, the design and development process of the company was thoroughly studied. To handle risk associated and find out business benefit behind process optimization, risk management and business case preparation were needed. So risk opportunity management was carried out containing the top five risks associated with this, its description if continued, its severity, strategy to tackle it and situation when risk will not be there. Business case preparation justifies undertaking work by evaluating benefits, cost, risk of alternatives available, and logic to prefer a specific solution. To prepare a business case, implementation efforts estimation, possible improvement potential, the cost associated with it, estimated cost saving due to it, problem in the process, current situation, and the future situation were considered. Also, it was committed that during the whole DMAIC cycle, quality and functional safety-related aspects of the product will not be touched anywhere.

3.2 Measure Phase

In the measure phase, data related to PDP was to be collected. Initially, the average time taken by PDP for the development of the product was estimated by finding out the duration taken by the process to develop different products to date and it was between 10000 and 13000 h depending on the type of product. To begin with data collection activity, there was a need to decide the method for data collection and plan for data collection in a respective way to collect useful data in the least time. Data collection was required to give the ideas of possible areas in PDP where effort reduction/time-saving is possible. So following type of data was expected.

- Longer duration activities in PDP (due to process/tools) where effort reduction is possible

- Non-value-adding activities/documentation in PDP
- Repetitive activity/content in documents in intra-domain/inter-domain, which can be eliminated to reduce efforts by eliminating one of the activity/document or by clubbing/linking activities/documents
- Lack of awareness/expertise in PDP execution
- Tool/software introduction
- Collaboration/roles of responsibility issues, which will result in effort reduction in PDP
- Anything apart from all above which will reduce efforts in PDP execution.

The approach adopted for data collection was interviewing PDP users, so the question set covering all the points mentioned above was prepared and input from the interviewing partner was noted. The data collected was containing ideas of the pain area where effort reduction is possible. The data was mixed type and processing was required on it to filter out irrelevant data. So each idea was checked whether that particular idea fits our criteria or not and if it is not fitting, then the particular ideas were dropped. After this, all ideas were categorized into six major groups named as below to make it easy to understand and focus on a specific type.

- High manual efforts
- Redundant work
- Non-value-adding efforts
- Process/tool unawareness
- Database/repository unavailability
- Unwanted delays.

3.3 Analyze Phase

The analysis phase is used to analyze the data with the deployment of relevant tools to arrive at the root causes of the defined problem. From the analysis, the individual group's contribution in more time consumption of PDP and total value-adding efforts spent in all ideas calculated by measuring each idea's current duration and possible effort reduction shown in Table 1.

The Ishikawa diagram drawn for root cause analysis is as shown in Fig. 2

To find a contribution from a particular category and value-adding time from ideas following graph shown in Fig. 3 was constructed.

Once the share of each type of idea in effort saving was clear, the category that easiest to implement ideas with maximum share in effort saving can be targeted for effort reduction. To find solutions for ideas to implement them, prioritization was required, and the basis for prioritization was the potential reduction of the respective idea. Therefore, pareto chart (Fig. 4) was used to prioritize the ideas for implementation as shown in Table 2.

Table 1 Activities contribution

1	Manual tolerance stack-up calculation	High manual efforts	48	24
2	Filling of design requirement checklist in the quotation phase	Redundant work	16	16
3	Repeated documentation of hardware design requirement review		150	80
4	Manually copying links in project documents	Non-value-adding efforts	20	20
5	Customer product requirement inputs into the requirement tracking tool		8	7.75
6	Missing features in existing design software compared to available in market		180	70
7	Unawareness on tailoring, deviation and technical cleanliness	Process/tool unawareness	37	36
8	Missing part library	Database/repository unavailability	24	16
9	Repository unavailability for standard software design and codes		18	18
10	Longer supplier approval process	Unwanted delay	176	136
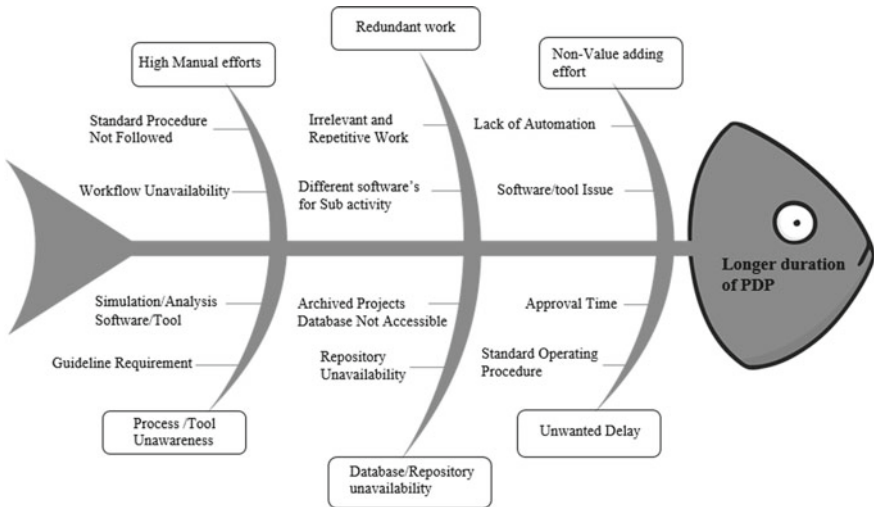
Fig. 2 Ishikawa diagram
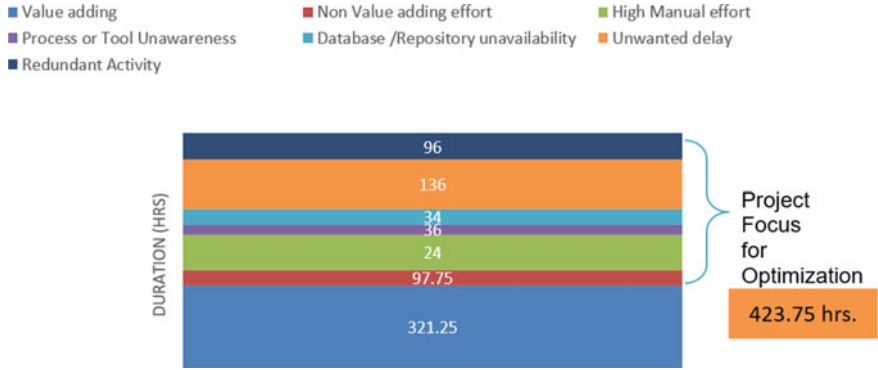
Fig. 3 Value Stream Mapping
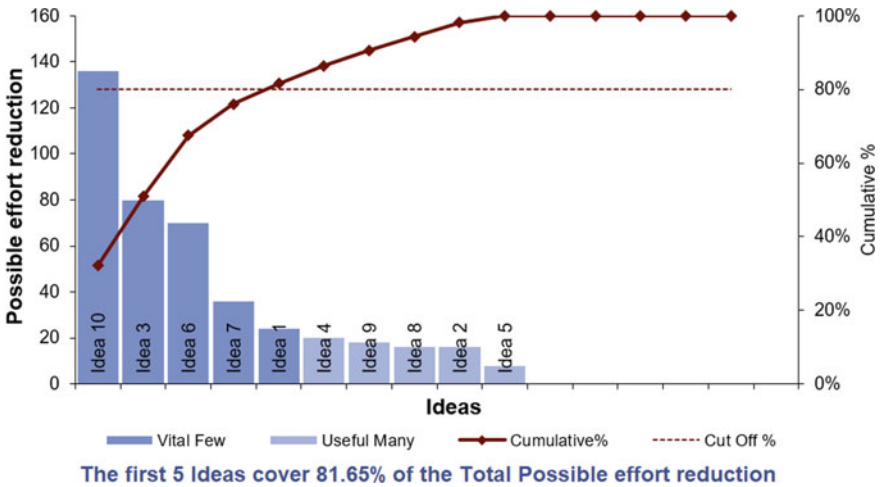
Fig. 4 Pareto chart

Table 2 Priorities

Priority	Idea No
First	10
Second	3
Third	6
Forth	7
Fifth	1
Sixth	4
Seventh	9
Eight	8
Ninth	2
Tenth	5

3.4   Improve and Control Phase

From analyze phase, the background and impact of each idea were clear. Now there was a need for a solution to each idea. To find out solutions brainstorming and expert opinion techniques were utilized. Solutions identified were thoroughly analyzed for their feasibility for implementation, time and cost constraints, potential risks involved, impact on legal requirements, etc. A Business case was also prepared for required ideas and presented to respective authority for their feedback and approval. Following is the summary of solutions proposed in Table 3.

Finally, the feasible solution implemented and tested according to their priority. Solution implementation helped to achieve 389.75 h effort reduction in PDP, which was almost 3% of total duration. There was considerable expenditure saving in

Table 3   Activities status

Problem category	Possible solutions	Feasibility Status
High manual efforts	1. Carry forward/automation/continuous improvement method 2. Different software and tools should be used to make iterations and modifications	Feasible
Redundant work	1. Redundant work which is not required at all should be eliminated 2. Redundant part for activity/document for work product should be eliminated or optimized	Feasible
Non-value-adding efforts	1. Non-value-adding steps/process eliminated	Feasible
Process/tool awareness	1. Training/awareness session for the use of available software in simulation/analysis, which could reduce manual effort 2. Awareness about the tailoring of process	Feasible
Database/repository unavailability	1. Creation of a central database, which will contain all details of each completed and ongoing projects in the company 2. Creation of database containing every detail for all required components 3. Creation of repository for standard software design and codes	Not feasible
Unwanted delays	1. Approval time should be reduced 2. Deviation should be created for standard operating procedure wherever required	Feasible

upcoming projects with faster delivery of customer projects without compromising the product's quality.

In the last phase of lean-based DMAIC methodology for the optimization of PDP modified process and its benefits were communicated to stakeholders and documented. Also, various measures and control tools were used to check, maintain, and achieve sustainable improvement in PDP.

4 Conclusion

The present article proposed, implemented, and verified a lean-based DMAIC methodology for Product Development Process (PDP) improvement at one of the automotive electronics products supplier companies. As per the nature of the study, some six sigma tools have been tested and adapted during the application of the proposed methodology, including VOC, root cause analysis, VSM, and pareto chart.

Through the proposed model, the study results show that PDP optimization can be achieved by continuous identification and analysis of efforts reduction opportunities, enabling process waste reduction, and organizational outcomes. There was 389.75 h of effort saving by using this approach, which was almost 3% of the total duration of PDP. As a result, time to market of product reduced and resource usage optimized without touching any quality-related aspect. It also indicates that the proposed approach is easy to use and adapt in any product developing company for sustainable improvement in PDP.

References

1. Ikumapayi OM, Akinlabi ET, Mwema FM, Ogbonna OS (2020) Six sigma versus lean manufacturing—an overview. Mater Today Proc
2. Jadhav GP, Jadhav SB, Bhagat A (2015) Six sigma DMAIC literature review. Int J Sci Eng Res
3. Gokulraju R, Vigneshwar K, Vignesh V (2016) A case study on reducing the lead time and increasing throughput by using value stream mapping. Int Res J Eng Technol (IRJET)
4. Wavhal SK, Mahadik SS, Angre AA, Shedge UK, Kashikar A (2017) A review on optimization of cycle time by using various techniques. IJEDR
5. S. Arun Vijay (2014) Reducing and optimizing the cycle time of patients discharge process in a hospital using six sigma dmaic approach. Int J Qual Res 8(2):169–182
6. Nandakumar N, Saleeshya PG, Harikumar P (2018) Bottleneck identification and process improvement by lean six sigma dmaic methodology. IConAMMA
7. Shahada TM, Alsyouf I (2012) Design and implementation of a lean six sigma framework for process improvement: a case study. IEEE
8. Tenera A, Pinto LC (2014) A lean six sigma (LSS) project management improvement model. Procedia Soc Behav Sci

Multi-response Optimization for Sustainable Turning of Ti–6Al–4V Alloy Using Taguchi-DEAR Methodology

Hariketan Patel, Jignesh Patel, Daksh Tandel, and Jhanbux Variava

1 Introduction

In the past few years, there was a rapid growth in the manufacturing production with reference to technological aspect, productivity, effectiveness, efficiency, planning, and capability due to the industrial revolution and economic development all around the globe [1]. The effort of recent technology is on increasing the production quantity with an ever-increasing energy demand while ensuring sustainability and improving quality. This craving for excellent quality has shifted our paradigm about the need for optimization in manufacturing industries. In the recent manufacturing era, energy, quality, and productivity have been drawing great attention as main domains of research [2].

Turning operations are found to be among the most widely used machining process for material removal applications in the majority of the industries [3]. It requires careful utilization of resources in modern manufacturing [4]. For quality turning of industrial part, good surface roughness profile [5], close dimensional tolerance [6], greater rate of material chipping [7], and exceptional lifecycle of cutting tool [8] are the key characteristics. The quality, productivity, tool life, efficiency, time, and cost of the turning process are constrained by the critical input parameters like depth of cut, rate of feed, turning speed, rake angle, job size dimensions, tool form and shape,

H. Patel (✉) · D. Tandel
Mechanical Department, GIDC Degree Engineering College, Navsari, India

D. Tandel
e-mail: drt.med@gdec.in

J. Patel
Mechanical Department, Mahatma Gandhi Institute of Technical Education and Research Centre, Navsari, India

J. Variava
Mechanical Department, Government Engineering College, Daman, India

category of material to be handled, the machine tool vibration, and type of coolant used [9].

Recent trends in the aerospace industry, superalloys are widely preferred about 45–50% of the overall material necessities in many military and commercial aircraft [10]. The titanium alloys are one of the superalloys, accountably adopted owing to their exceptional strength, decent fatigue, excellent resistance to creep, better resistance against corrosion with other mechanical properties enables them in functioning at higher temperatures over long times [11]. Ti–6Al–4V is among the group termed as hard materials as the machining is challenged by its grater chemical reactiveness, lower heat conductive capacity, comparatively higher hardness, strength, and the predisposition of built up edge during machining operations. The aim of the machining industry is to significantly reduce the cost of machined titanium components, by enhancing material chipping rates and production rate deprived of acquiring additional costs in terms of improved quality, lead time, tooling costs, etc. [12].

There are many strategies, multi-response optimization methods, and statistical tools like Taguchi Grey relational analysis (TGRA) [13], Analysis of Variance (ANOVA) [14], Response surface methodology (RSM) [15], artificial neural networks (ANN) [16] method and weights assign procedures are available to compute optimal solution of the turning operation parameters to achieve sustainable machining of the titanium alloy [17]. Multiple regression analysis and adaptive genetic algorithm approach are established to govern the machining parameters optimization [18].

A significant attention is shown by Data envelopment analysis ranking (DEAR) approach through the Taguchi technique in optimizing the multiple outputs to provide a simplest, systematic, effective, and structured method to the multiple outputs designs of experiment optimization, excellence with costing of turning operation [19]. DEAR method proposed by Charnes, in this method mathematical programming approach is used to investigate the relative characteristics effectiveness of output parameters through several input variables. DEAR technique deals through by integrating the preceding data or without the preceding data. Integrating the preceding data involves preceding information of the—process and expert. This technique can give incorrect results or influenced results in many investigations [20]. So, a method that operates deprived of preceding knowledge is examine higher consistent and yields better results. In many machining operation to compute the input characteristic optimization, the Taguchi-DEAR method has proved extensive accuracy [21].

It has been discovered that a wide range of efforts have been made in the area of multi-response optimization of Ti–6Al–4V employing TGRA, ANOVA, RSM, ANN, and GA. It is hard to get any literature to calculate the multi-response optimization of titanium bar by application of Taguchi-DEAR technique. In the current investigation data envelopment analysis based ranking with Taguchi technique is employed for multi-response decision optimization as it is reliable in its conclusive nature with respects to the maximization of MRR and tool life which improve energy consumption and productivity while minimizing cutting force and surface roughness, meeting cleaner and efficient production goals of benefiting the industry.

2 Materials, Methodology, and Experimentations

2.1 Selection of Materials and Its Parameters for Turning Operations

In the present investigation, a Ti–6Al–4V (grade 5) bar of 30 mm diameter was used as the work piece. The Ti–6Al–4V bar has the chemical compositions as presented in the Table 1. Table 2 shows the mechanical properties of the work piece material. In this experimental work, because of the importance of such input characteristics in the turning operation depth of cut, cutting speed, tool nose radius, and the feed rate of the tool have been designated as the input process parameters. The turning experiments were carried out with no lubrication conditions by means of Al_2O_3–ZrO_2 (Alumina–Zirconia) ceramic insert (ISO Designation: CNGN 120408 E040), rhombic form having rake angle of 0° without chip breaker as shown in the Fig. 1a.

Table 1 The chemical compositions of the Ti–6Al–4V bar

Element	V	Al	Fe	N	C	O	H	Ti
Wt%	4.1	5.9	0.11	0.01	0.01	0.15	0.004	Balanced

Table 2 The mechanical properties of the Ti–6Al–4V bar

Elongation [%]	Hardness [HV]	Tensile strength [MPa]	Elastic modulus [Gpa]	Yield strength [Mpa]	Fracture toughness [Mpa m$^{1/2}$]
14	350	990	115	1050	55

(a). Ceramic Insert

(b). Insert Tool Holder

(c). Turning Operation

(e). Tool Dynamometer

(d). Surface Roughness Tester
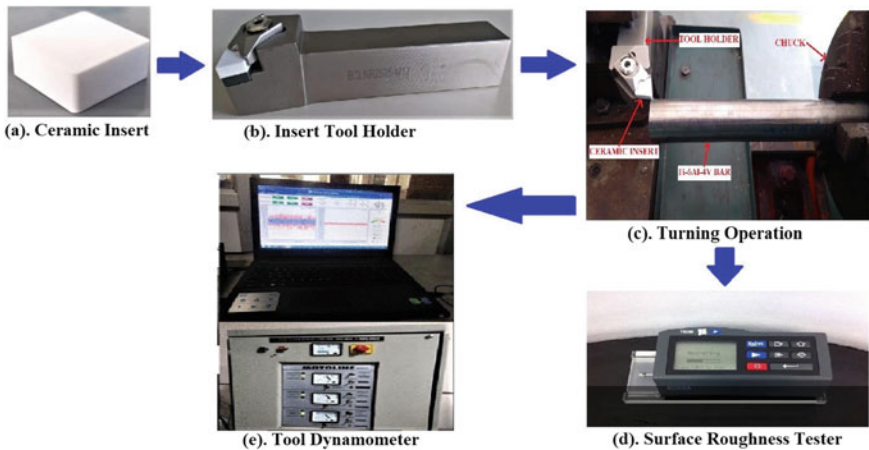
Fig. 1 Experimental setup

Table 3 Properties of Al$_2$O$_3$–ZrO$_2$ (Alumina–Zirconia) ceramic insert

Color	Density [g/cm^3]	Hardness [HV]	Fracture toughness [Mpa m$^{1/2}$]	Thermal conductivity [Cal/cm s °C]
White	4	1800	4.50	0.07

Table 4 Experimental parameters and their levels

Parameters	Unit	Level 1	Level 2	Level 3	Level 4
Cutting speed (CS)	m/min	25	50	75	100
Depth of cut (DOC)	mm	0.2	0.4	0.6	0.8
Feed rate (FR)	mm/rev	0.08	0.12	0.16	0.2
Nose radius (NR)	mm	0.4	0.8	1.2	1.6

The ceramic insert is supplied by Union Materials, South Korea, having properties as shown in Table 3. The insert tool holder with the designation BCLNR2525-M12 was used as shown in Fig. 1b. The CNC machine setup for turning experiments is as shown in the Fig. 1c. The CNC spindle had a power of a 21 kW with highest 5000 rpm speed. The turning input process parameters with their levels are selected in Table 4. A new insert tip was used for every turning operation run and each experiment was replicated two times for data repeatability.

2.2 Machining Responses

The cutting force, surface roughness, tool life, and material removal rate of the workpiece are the four response characteristics investigated in this study. Kistler (9272) type dynamometer as shown in Fig. 1e was attached straight to the source of the machine for measuring the force during machining. Times TR 200 [Fig. 1d], surface roughness tester measured roughness value for every turning operation for three times to take the average of values. The rate for removal of material has been found by relation as shown in Equation (1).

$$\text{MRR} = \frac{V \times f \times d}{60} \qquad (1)$$

where v is cutting speed in m/min, f is feed ate in mm/rev., and d is depth of cut in mm. The MRR unit is mm^3/s.

To improve the machinability of the turning operations, multi-response optimization was used to achieve lower cutting force, lower surface roughness, longer tool life, and higher material removal rate.

2.3 Orthogonal Array Selection

This investigation is carried out through four machining input performance characteristics including depth of cut, cutting speed, nose radius, and feed rate each at four levels. As indicated in Table 5, the L_{16} (4^4) orthogonal array was chosen based on the Taguchi's design for turning experiments.

3 Steps for DEAR Method (Data Envelopment Analysis Based Ranking)

The multi-response performance index is a group of definite experiment result response measurands that are recorded through the DEAR technique. The weighted total of the larger-the-preferable functional properties divided by the weighted total of smaller-the-preferable functional properties is termed as the MRPI. The MRPI value is utilized to compute and decide the set of optimality of input process parameters of a turning operation. The subsequent steps are integrated in the DEAR technique:

Table 5 Investigational outputs of turning process

Exp No.	Cutting speed	Depth of cut	Feed rate	Nose radius	Cutting force (CF)	Surface roughness (Ra)	Tool life (TL)	MRR
	(m/min)	(mm)	(mm/rev)	(mm)	(N)	(µm)	(s)	(mm³/s)
1	25	0.2	0.08	0.4	39.512	2.068	2423	162.75
2	25	0.4	0.12	0.8	50.712	2.69	2190	184.01
3	25	0.6	0.16	1.2	92.462	3.564	1985	193.78
4	25	0.8	0.2	1.6	110.892	4.263	1509	207.41
5	50	0.2	0.12	1.2	52.112	2.017	2048	215.04
6	50	0.4	0.08	1.6	68.512	2.049	1872	208.76
7	50	0.6	0.2	0.4	86.142	3.717	1691	239.32
8	50	0.8	0.16	0.8	131.652	3.972	1459	241.93
9	75	0.2	0.16	1.6	56.162	2.073	1601	240.79
10	75	0.4	0.2	1.2	86.522	3.25	1126	247.21
11	75	0.6	0.08	0.8	113.372	3.47	1269	251.42
12	75	0.8	0.12	0.4	135.072	3.949	999	243.93
13	100	0.2	0.2	0.8	69.312	2.304	931	260.98
14	100	0.4	0.16	0.4	74.762	3.442	813	274.96
15	100	0.6	0.12	1.6	106.522	3.464	457	257.91
16	100	0.8	0.08	1.2	177.462	3.653	367	262.12

3.1 Calculation of Weights for Distinct Response for Entire Turning Process

The proportion among every character measure during that investigative trial and the sum total of every investigative runs is used to determine the weight of each characteristic. The current investigation has beneficial maximization function necessities with higher-the-preferable for tool life and MRR, and non-beneficial minimization function requirements with lower-the-better for cutting force and surface roughness. The weight computation for each response is calculated as following Eqs. (2)–(5):

$$W_{TL} = \frac{TL}{\sum TL} \tag{2}$$

$$W_{MRR} = \frac{MRR}{\sum MRR} \tag{3}$$

$$W_{CF} = \frac{\frac{1}{CF}}{\sum \frac{1}{force}} \tag{4}$$

$$W_{Ra} = \frac{\frac{1}{Ra}}{\sum \frac{1}{Ra}} \tag{5}$$

3.2 For the Entire Turning Process, Convert Output Measurands into Weighted Data

Convert the output measurands data into weighted data by multiplying each observed output value with its own weight by using the following Eqs. (6)–(9),

$$T = TL \times W_{TL} \tag{6}$$

$$M = MRR \times W_{MRR} \tag{7}$$

$$F = Force \times W_{CF} \tag{8}$$

$$S = SR \times W_{Ra} \tag{9}$$

3.3 For Every Experiment, the Multi-response Performance Index Calculated as

The relative MRPI values were obtained by calculating the ratio of larger-the-preferable response to the smaller-the-preferable responses. The method to evaluate MRPI is presented in Eq. 10.

$$\text{MRPI} = \frac{M + T}{F + S} \tag{10}$$

4 Results and Discussions

For the experimental study, the turning processes of Ti–6Al–4V bar using ceramic inserts are conducted based on Taguchi L_{16} orthogonal array. All the 16 trial runs and their investigational outcomes are shown in Table 5.

4.1 Multi-response Decision Making of Turning Operations

The weights of measurands values are computed by use of Eqs. (6)–(9) using the investigational outputs as presented in Table 5 of all the experiments performed. The DEAR approach was used to determine the proportions of the distinct performance metrics using various parameters as presented in the Table 6. Table 6 represents the combined value of MRPI for each trial of all the input characteristics with all the levels through distinct combinations of machining input process parameters. The evaluated grades are computed by assemblage of all the MRPI grades at the conforming combination for every method parameter by means of Eq. (10). The highest value of MRPI for turning characteristics indicates that those input quality have the most influence on process improvements in any machining operations. Table 6 represents an optimum set of input characteristics of the turning operation is obtained when the depth of cut(DOC) is 0.2 mm, cutting speed (CS) is 25 m/min, the feed rate (FR) is 0.08 mm/rev., and nose radius (NR) is 0.4 mm respectively. The higher value of maximum—minimum from all levels of each parameter specifies the most inflating input characteristics on turning operation. From the Table 7, it is recognized that to govern the experimental runs the cutting speed has a highest impact due to its significance in computing the MRR and surface roughness over the tool life and cutting force of the specimens turning operation. It inferred that cutting speed has strong significance on obtaining turning measures because of its significance on computing output parameters in the turning operation. As a result, it

Table 6 MRPI values of experiments

Exp. No	Cutting force	Ra	TL	MRR	MRPI
1	0.122701	0.088023	0.106552	0.044078	52.75161
2	0.095602	0.067669	0.096306	0.049836	43.75205
3	0.052434	0.051075	0.087291	0.052482	36.46845
4	0.04372	0.0427	0.066359	0.056173	22.22315
5	0.093033	0.090248	0.090062	0.05824	39.15765
6	0.070763	0.088839	0.082322	0.056539	32.98286
7	0.056281	0.048972	0.074362	0.064816	28.08219
8	0.036825	0.045828	0.06416	0.065522	21.76094
9	0.086324	0.08781	0.070405	0.065214	25.53002
10	0.056034	0.056009	0.049516	0.066952	14.37457
11	0.042763	0.052458	0.055805	0.068093	17.4817
12	0.035893	0.046095	0.043931	0.066064	11.9285
13	0.069947	0.079006	0.040941	0.070682	11.24467
14	0.064848	0.052885	0.035752	0.074468	9.848976
15	0.045513	0.052549	0.020097	0.06985	5.407229
16	0.027319	0.04983	0.016139	0.070991	4.876776

Table 7 Response of Max.–Min. MRPI values in the turning experiments

Parameters	Levels				Max.–Min
	I	II	III	IV	
Cutting speed	155.1953	121.9836	69.31479	31.37765	123.817603
Depth of cut	128.6839	100.9585	87.43957	60.78937	67.89457853
Feed rate	108.0929	100.2454	93.60838	75.92458	32.16837293
Nose radius	102.6113	94.23936	94.87745	86.14326	16.46801747

was determined that the optimal input process parameters for turning Ti–6Al–4V bar with Al_2O_3–ZrO_2 ceramic inserts can improve the experimental outcome.

4.2 Analysis of Significant Process Parameters

The values attained for the output characteristics (Cutting force, SR, TL, and MRR) were analyzed to measure the effect of the input factors (CS, FR, DOC, and NR) on these responses. The main effects plot gives the investigation of the influence of the input characteristics on the measure of performance. In the main effect graph Fig. 2a–d depicts the pattern of every response parameter. The deviation of the response curve line from the horizontal line reveals the higher influence feature of

(a) (b)

(c) (d)
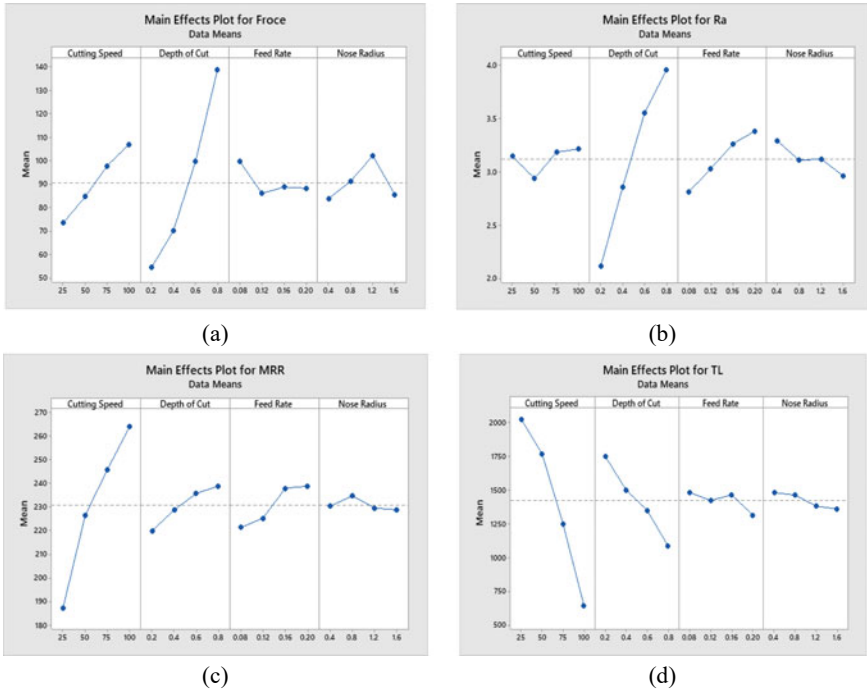
Fig. 2 The main effect plot of response parameters **a** Cutting Force, **b** Surface Roughness, **c** Tool life, and **d** MRR

the machining properties of the Ti–6Al–4V bar. The main effects plot demonstrates that when turning titanium alloy with a ceramic insert, the cutting speed has the highest impact in the cutting force, surface roughness, material removal rate, tool life, and MRPI values.

4.2.1 Measures of Turning Characteristics on Cutting Force [Fig. 2a]

The steep slope of the cutting speed and the depth of cut in the graph of mean effect plot of cutting force indicates that there is a significant increase in the cutting force value when both the cutting speed and the depth of cut increase. The strain hardening effect caused by extreme plastic deformations during the metal cutting process was accounted for this condition. The—cutting force initially decreases and then slightly increases when the feed rate increased because the volume of the material in contact with the cutting tool has risen. Furthermore, the amount of cutting force increases as the tool-work interaction length increase, leading to an increase in the value of the cutting force as the nose radius value start to increase. The optimum value of the cutting force (Fz) was 39.152 N attained when CS = 25 m/min, DOC = 0.2 mm FR = 0.08 mm/rev. and NR = 0.4 mm. The value of cutting force decreased with

the rising value of the feed rate because of the thermal softening of the workpiece. However, the cutting force increased with the increasing values of the depth of cut and chip width.

4.2.2 Measures of Turning Characteristics on Surface Roughness [Fig. 2b]

For every experimental run, the data of the surface roughness was quantified on four different positions of the turned surface. Then mean data was calculated. As both the depth of cut and the feed rate increased, the value of surface roughness increased. These values are expediently attributed to the very little amount of material ploughing at small depth of cut with small feed rates. The uncut chip thickness was low at small feed rates, and this specification can minimize plunging and termed out as a low surface roughness. Contradictorily, by increasing the feed rate, there is an increase in plunging effect that consequently associated in inferior surface quality finish. The value of surface roughness decreases initially and then slightly increases with rise of the value of the cutting speed. In contrast, with the increased value of nose radius there was decrease in surface quality finish value. To obtain optimal surface roughness of 2.068 µm, the obtained combinational conditions of the factors are CS = 25 m/min, DOC = 0.2 mm, FR = 0.08 mm/rev., and NR = 0.4 mm.

4.2.3 Measures of Turning Characteristics on MRR [Fig. 2c]

The MRR value is the primary factor to improve productivity in turning operation. MRR = $(v \times f \times d)/60$ mm^3/s. The trend of the mean curve of MRR for all four responses is almost the same except nose radius. The MRR increases with the increased values of the depth of cut, feed rate, and cutting speed. As the cut depth raised, heat generation at the tool-workpiece junction increased, suggesting a increased value of MRR. The MRR slightly increases with nose radius and then decreases with further increase in nose radius value. The optimal value of MRR is obtained at CS = 25 m/min, DOC = 0.2 mm, FR = 0.08 mm/rev., and NR = 0.4 mm.

4.2.4 Measures of Turning Characteristics on Tool Life [Fig. 2d]

The trend of the mean curve of tool life for all four responses is almost the same and toward downwards. The tool life decreases with an increased value of all four input parameters. The optimal tool life value is obtained at the CS = 25 m/min, DOC = 0.2 mm, FR = 0.08 mm/rev., and NR = 0.4 mm.

According to the overall effects of all performance parameters obtained from the mean curve, cutting speed increases the values of the cutting force and MRR, while it reduces the tool life and it has no significant effect on surface roughness. With the exception of the cutting force, increasing the value of the feed rate decreases the tool

Table 8 ANOVA of MRPI values

Source	DOF	Adj SS	Adj MS	F-value	% contribution
Cutting speed (CS)	3	2264.5	754.832	93.39	73.9373
Depth of cut (DOC)	3	599.13	199.709	24.71	19.56196
Feed rate (FR)	3	140.9	46.968	5.81	4.600471
Nose radius (NR)	3	33.96	11.32	1.4	1.108815
Error	3	24.25	8.082		0.791777
Total	15	3062.73			

S—2.84292, R-sq—99.21%, R-sq(adj)—96.04%

life and the cutting force while increasing the value of the feed rate decreases the surface roughness and the MRR. With the rise of depth of cut, there was rise in the values of the cutting force, surface roughness, and the MRR while there was fall in the tool life value. Because of incremental tool wear, strain hardening at high speeds, and material adherence at the cutting edge of the tool, this trend was observed for output variables, resulting in significant magnitudes of the—cutting force and the MRR for performance variables while turning at high speeds.

4.3 Most Influential Machining Parameter

The ANOVA is used to assess the accuracy of the created model and to analyze the effect of each machining parameters and their relative magnitudes on the objective function. From Table 8, ANOVA results exhibit that R-sq value of the experimental runs is 99.21%, and R-sq (adj.) value is 96.04%, representing that the established array has very high accuracy. Cutting speed was reported to be most significant machining factor, accounting for 73.95 percent of the total, followed by depth of cut and feed rate, which each accounted for 19.56 and 4.60% of the total. The nose radius has the lowest impact of 1.10% only.

4.4 Confirmation Experiment

After identifying the most optimum process parameters, the goal of the confirmation experiment is to verify the optimal process parameter combination obtained from the methodology. A validation experiment was carried out in this study using the optimum levels of significant variables. The cutting force, surface roughness, tool life, and MRR values from the validation tests assessed are 39.618 N, 2.095 μm, 2418 s, and 163.22 cm^3/s, respectively, at the optimum process parameters. The MRPI value for the confirmation experiment is deviated 1.2% from the normal MRPI

value. As a result, the optimal combination of the process parameters is evaluated as satisfactory in the current investigation.

5   Conclusions

The current investigation was based on the turning of Ti–6Al–4V bar with Al_2O_3–ZrO_2 ceramic insert in a dry machining environment. The L_{16} orthogonal array design was used to conduct the experiments. The performance input factors were depth of cut, cutting speed, feed rate, and nose radius. The output response measures were the cutting force, surface roughness, tool life, and material removal rate. The aim of this analysis was to examine the trade-offs among sustainability, productivity, and efficiency of turning operation under dry environment. The cutting force and tool life represent sustainability and efficiency, surface roughness, and material removal rate advocates for the productivity of the turning operation. To obtain optimal parameters, multi-objective optimization using the Taguchi-DEAR approach was used. ANOVA was used after process parameters were standardized to determine the relative significance of each input factor on objective functions. From the study, the following conclusion can be drawn:

- For the turning of Ti–6Al–4V, multi-response analysis using the Taguchi-DEAR approach helped to find an optimal solution that offers a trade-off between the four competing responses of input characteristics. The optimal condition yields the highest MRPI value with a feed rate of 0.08 mm/rev., a depth of cut of 0.2 mm, a cutting speed of 25 m/min, and a nose radius of 0.4 mm.
- The proposed approach is viewed as a hierarchical procedure, suggesting that the proposed optimization technique is a valuable tool for multi-objective cutting parameter optimization. This technique is simple to apply since it does not necessitate a large amount of computation and can be completed using Excel and Minitab software.
- From the ANOVA it is acknowledged that cutting speed, with a contribution of 73.93%, is the most critical characteristic, followed by depth of cut (19.56%), feed rate (4.60%), and nose radius (1.10%).
- It was also verified by the confirmation test, which revealed a 1.2% deviation from the average MRPI value.

This work can also be further integrated by other considerations such as tool tribology, cutting fluid used, tool geometry, cooling techniques, and cost constraints. It may also investigate at tool life under various cutting circumstances (dry, wet, and cryogenic), as well as chip morphology and mechanics of machining titanium alloy with the appropriate machine settings and parameter selection. The latest multi-objective optimization approach can be used to make machining and manufacturing operations more sustainable.

References

1. Khan MA et al (2020) Multi-objective optimization of turning titanium-based alloy Ti–6Al–4V under dry, wet, and cryogenic conditions using gray relational analysis (GRA). Int J Adv Manuf Technol 106(9–10):3897–3911. https://doi.org/10.1007/s00170-019-04913-6
2. Yi S, Jang Y, An AK, Jang YC (2018) Accepted manuscript. https://doi.org/10.1016/j.jclepro.2017.12.103.This
3. Abas M, Sayd L, Akhtar R, Khalid QS, Khan AM, Pruncu CI (2020) Optimization of machining parameters of aluminum alloy 6026–T9 under MQL-assisted turning process. J Mater Res Technol 9(5):10916–10940. https://doi.org/10.1016/j.jmrt.2020.07.071
4. Younas M et al (2019) Multi-objective optimization for sustainable turning Ti6Al4V alloy using grey relational analysis (GRA) based on analytic hierarchy process (AHP). Int J Adv Manuf Technol 105(1–4):1175–1188. https://doi.org/10.1007/s00170-019-04299-5
5. Gupta MK et al (2020) Machinability investigations of hardened steel with biodegradable oil-based MQL spray system. Int J Adv Manuf Technol 108(3):735–748. https://doi.org/10.1007/s00170-020-05477-6
6. Ul Haq M, Khan A, Gong L, Xu T, Meng L, Hussain S (2018) A comparative study of face milling of D2 steel using Al_2O_3 based nanofluid minimum quantity lubrication and minimum quantity lubrication. Adv Sci Technol Res J 12(1):99–105. https://doi.org/10.12913/22998624/85629
7. Khan AM et al (2019) Multi-objective optimization of energy consumption and surface quality in nanofluid SQCl assisted face milling. Energies 12(4). https://doi.org/10.3390/en12040710
8. Khan AM et al (2020) Energy-based cost integrated modelling and sustainability assessment of Al–GnP hybrid nanofluid assisted turning of AISI52100 steel. J Clean Prod 257. https://doi.org/10.1016/j.jclepro.2020.120502
9. Tascioglu E, Gharibi A, Kaynak Y (2019) High speed machining of near-beta titanium Ti-5553 alloy under various cooling and lubrication conditions. Int J Adv Manuf Technol. https://doi.org/10.1007/s00170-019-03291-3
10. Ramulu M, Branson T, Kim D (2001) A study on the drilling of composite and titanium stacks. Compos Struct 54(1):67–77. https://doi.org/10.1016/S0263-8223(01)00071-X
11. Arunachalam R, Mannan MA (2000) Machining Science and Technology machinability of nickel-based high temperature alloys. Mach Sci Technol 4(1):127–168 [Online]. Available: http://www.tandfonline.com/action/journalInformation?journalCode=lmst20%5Cn https://doi.org/10.1080/10940340008945703
12. Bermingham MJ, Kirsch J, Sun S, Palanisamy S, Dargusch MS (2011) New observations on tool life, cutting forces and chip morphology in cryogenic machining Ti–6Al–4V. Int J Mach Tools Manuf 51(6):500–511. https://doi.org/10.1016/j.ijmachtools.2011.02.009
13. Patel H, Patel J, Gajera B, Rana H (2021) Multi objective optimization in drilling of glass fiber/epe foam sandwich composite based on grey relational analysis, vol 16, no 60, pp 276–286. https://doi.org/10.24412/1932-2321-2021-160-276-286
14. Patel HB, Patel KC, Lad CB (2015) Application of ANOVA method in optimizing the parameters of drilling process of sandwich composite material, vol 3, no 01, pp 1241–1245
15. Davoodi B, Eskandari B (2015) Tool wear mechanisms and multi-response optimization of tool life and volume of material removed in turning of N-155 iron-nickel-base superalloy using RSM. Meas J Int Meas Confed 68:286–294. https://doi.org/10.1016/j.measurement.2015.03.006
16. Jafarian F, Taghipour M, Amirabadi H (2013) Application of artificial neural network and optimization algorithms for optimizing surface roughness, tool life and cutting forces in turning operation. J Mech Sci Technol 27(5):1469–1477. https://doi.org/10.1007/s12206-013-0327-0
17. Muthuramalingam T, Vasanth S, Vinothkumar P, Geethapriyan T, Rabik MM (2018) Multi criteria decision making of abrasive flow oriented process parameters in abrasive water jet machining using Taguchi–DEAR methodology. SILICON 10(5):2015–2021. https://doi.org/10.1007/s12633-017-9715-x

18. Reddy VV, Valli PM, Kumar A, Reddy CS (2015) Multi-objective optimization of electrical discharge machining of PH17-4 stainless steel with surfactant-mixed and graphite powder-mixed dielectric using Taguchi-data envelopment analysis-based ranking method. Proc Inst Mech Eng Part B J Eng Manuf 229(3):487–494. https://doi.org/10.1177/0954405414530904
19. Manoj M, Jinu GR, Muthuramalingam T (2018) Multi response optimization of AWJM process parameters on machining TiB_2 particles reinforced Al7075 composite using Taguchi-DEAR methodology. SILICON 10(5):2287–2293. https://doi.org/10.1007/s12633-018-9763-x
20. Zaremba LS, Smoleński WH (2000) Optimal portfolio choice under a liability constraint. Ann Oper Res 97(1–4):131–141. https://doi.org/10.1023/A:1018996712442
21. Sandeep MJ, Manjunath PGC, Chate GR, Parappagoudar MB, Daivagna UM (2019) Multi response optimization of green sand moulding parameters using Taguchi-DEAR method. Appl Mech Mater 895:1–7. https://doi.org/10.4028/www.scientific.net/amm.895.1

Comparative Study of Estimated Surface Roughness Using GA and PSO Techniques for Milling of Thin-Walled Structures

Shivang Shekhar and Tufan Chandra Bera

1 Introduction

The importance of thin-walled structures has led to an increased focus on the quality of these structures with applications in aircraft components and fuselages because of their lightweight and high load-carrying capacity. The manufacturing of these structures must be of high quality, which is quantified by the surface roughness value. The surface roughness of thin-walled structures is affected by uncontrollable factors such as chatter and vibration, which make it very difficult to correctly predict the surface roughness and make the selection process of machining parameters difficult. Several methodologies have therefore been developed to estimate the surface roughness accurately [2]. Techniques like RSM (Response Surface Methodology) have been used previously for mathematical modeling of surface roughness [1]. Response surface contours were created in [1] to find the optimal machining conditions for improving the surface finish, while at the same they also gave an idea about how the surface finish is impacted by the machining conditions. A similar idea was used in [6], with the exception that here both power consumption and surface roughness value were aimed to minimize. This was achieved by using grey relational analysis with Principal Component Analysis and RSM. Surface roughness for thin-walled structures has also been modeled previously by calculating how much the structure deforms dynamically along the path of the milling process, which can be calculated by solving the vibration equation for the structure and later substituting the milling path coordinates into the solution obtained [4].

S. Shekhar (✉) · T. C. Bera
Department of Mechanical Engineering, Birla Institute of Technology and Science Pilani, Pilani Campus, Rajasthan 333031, India
e-mail: f20170742@pilani.bits-pilani.ac.in

T. C. Bera
e-mail: tcbera@pilani.bits-pilani.ac.in

The use of AI (Artificial Intelligence) is another widely used method to estimate surface roughness. The use of the AI approach in such problems can involve using ANNs (Artificial Neural Networks), fuzzy logic, and expert systems to mimic the biological brains by learning from experimental data to make accurate predictions. Predictive models based on regression analysis and fuzzy logic were created in [8] to predict the surface roughness, but it was concluded in [7] that ANNs give better results than regression analysis and fuzzy logic-based prediction models in terms of accuracy. In the present study, an ANN model was created to predict the surface roughness data using the Neural Network Toolbox of MATLAB. Experimental data from the literature was used to train the neural network, and hypothesis tests were performed on the model to check the correctness of fit. Using this model then, the variation of surface roughness was also studied by keeping one parameter constant and by varying the other two parameters. A polynomial representing the surface fit for the surface roughness variation with the considered parameters was also calculated for each case, and PSO (Particle Swarm Optimization) was applied on each of these polynomial fits to obtain the minimum surface roughness for each case. Finally, both GA (Genetic Algorithm) and PSO were applied to the entire model to calculate the minimum surface roughness, which was found to be 49.95 μm by both techniques.

Previous works have focused on using ANN for surface roughness prediction but have not focused on estimating the surface roughness for milling of thin-walled structures much. This paper develops a surface roughness prediction model for milling of thin-walled structures using ANN and uses the same model to obtain surface plots of surface roughness which have mostly been obtained through RSM (Response Surface Methodology) in literature.

The rest of the paper is arranged in the following manner: ANN model for surface roughness prediction is developed in Sect. 2, Sect. 3 explains the experimental procedure, Sect. 4 discussed the results obtained, and Sect. 5 discusses the conclusions drawn from this study.

2 Estimation of Surface Roughness Using Artificial Neural Network

2.1 Theoretical Basis of Artificial Neural Networks

ANNs mimic the working of the biological brain, which consists of a vast number of interconnected neurons, just like our biological nervous systems. Our brain learns from the activities of the outside world by creating new links between neurons. Similarly, the ANNs mimic the working of the biological brain to make accurate predictions by learning from a dataset by adjusting weights and biases between the neurons. They are trained so that a specific input gives a particular output, and this training is done based on a set of target data and the output data. The neural networks are trained until it adjusts the values of weights and biases in the neural network

such that the difference between the actual output (output data) and the target data becomes minimum.

There are three main layers in an ANN, a layer that takes inputs from the outside world, a hidden layer, and an output layer, each containing some number of neurons. All the neurons in a layer are connected to all the neurons in the next layer via a connection having some weight value. The input layer takes inputs from the actual environment and transmits them to the next layer after multiplying them with a weight value and adding a bias value. The output is obtained with the help of summation and activation functions. The net input is calculated by the summation function, and "the activation function converts the neuron's weighted input to its output activation" [7]. The output layer accepts the result of the activation function and either gives the output or passes it to the relevant processing neuron. In each iteration of input, the error, which is the difference between the output obtained from the ANN, is calculated. To minimize this error, different training algorithms are applied.

2.2 Methodology

The data for the study was picked up from [5] to be used as training data for the surface roughness prediction model. The prediction model was created using an ANN for which the Neural Network Toolbox from MATLAB was used, and a neural network with three neurons in the input layer corresponding to the input values of milling parameters (nose radius, rake angle, and approach angle), ten neurons in the hidden layer, and one neuron in the output layer corresponding to the surface roughness was created. The choice of the number of neurons in the hidden layers depends on what number gives the best results, and in this case, ten neurons in the hidden layer gave the best results.

The Levenberg–Marquardt algorithm was used to train the model, and the training, testing, and validation percentage were chosen to be 80%, 10%, and 10%, respectively. This splitting of data can be anything depending on what gives the best ANN ([3, 7]). After training, the following regression plot was obtained, which shows the correctness of the model (Fig. 1).

The closer the value of R is to 1, the higher is the correlation between the ANN output and the target data, i.e., the experimentally observed data. Therefore, the overall value of R, which was obtained to be 0.92801, shows that this model was trained perfectly.

After the development of the ANN model, its goodness of fit was verified using the hypothesis tests. The next step was to study how the surface roughness value is affected by various parameters. To do this, out of the three parameters chosen, two parameters were taken at a time with the third parameter fixed, a surface fit for the variation of surface roughness was obtained. The following flowchart describes the method to obtain these plots (Fig. 2).

Once the surface roughness plots were obtained, an attempt was made to explain the nature of the surface plots, which will be discussed in the results section. At last,

Fig. 1 Regression plot for
the ANN
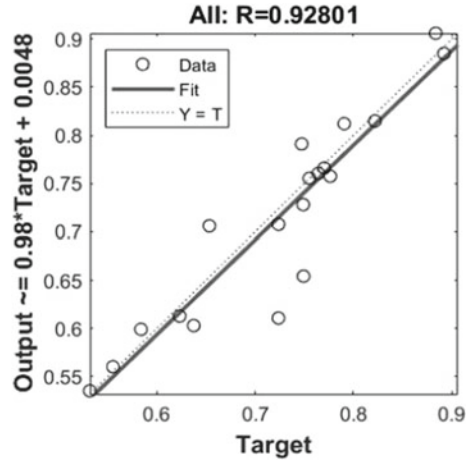
both GA and PSO were applied on the entire ANN model with all three parame-
ters (nose radius, rake angle, and approach angle) taken into consideration, and the
minimum surface roughness was obtained, and matching results were found from
both the approaches.

3 Experimental Procedure

For the present study, the work of [5] was taken as a case study. They performed a
set of machining operations to examine the surface roughness of the workpieces in
both physical and analytical ways. A profilometer was used to measure the surface
roughness physically, while a statistical software was used for analytical study.

The data used in this paper is for the thin-wall milling of a thin AL 6351 T6 work-
piece using High-speed steel (HSS) tooling. The elastic modulus of the workpiece
used was $69,000 \, \text{N/mm}^2$, and its length was 75 mm. A feed rate of 102 mm/rev., depth
of cut of 3 mm, and 30° helix angle of end mill were used. The approach angles of
60°, 75°, 90°; rake angles of $-3°$, $-6°$, $-9°$ and nose radii of 0.4, 0.8, and 1.2 mm
were used, and the surface roughness was evaluated using the Taylor Hobson Form
Talysurf 50 profilometer [5]. The measured values are listed in the Table 1.

4 Results and Discussion

The results obtained from the ANN are discussed below.

```
┌─────────────────────────────────────────────────────────────┐
│                  Choose the fixed parameter                   │
└─────────────────────────────────────────────────────────────┘
                             ⬇
┌─────────────────────────────────────────────────────────────┐
│              Fix the value of the fixed parameter             │
└─────────────────────────────────────────────────────────────┘
                             ⬇
┌─────────────────────────────────────────────────────────────┐
│   Create all possible combinations of the other two          │
│       parameters within the allowed range of parameters       │
└─────────────────────────────────────────────────────────────┘
                             ⬇
┌─────────────────────────────────────────────────────────────┐
│            Apply the ANN model on the obtained data set       │
└─────────────────────────────────────────────────────────────┘
                             ⬇
┌─────────────────────────────────────────────────────────────┐
│     Obtain the surface roughnesses for all the inputs of      │
│                        the dataset                            │
└─────────────────────────────────────────────────────────────┘
                             ⬇
┌─────────────────────────────────────────────────────────────┐
│   Determine the polynomial whose surface best fits the        │
│                 surface roughness data                        │
└─────────────────────────────────────────────────────────────┘
                             ⬇
┌─────────────────────────────────────────────────────────────┐
│   Plot the surface of that ploynomial with surface            │
│   roughness of the z-axis and the parameters on x and y axes  │
└─────────────────────────────────────────────────────────────┘
                             ⬇
┌─────────────────────────────────────────────────────────────┐
│   Apply PSO to obtain the optimal parameters for minimum      │
│                   surface roughness                           │
└─────────────────────────────────────────────────────────────┘
                             ⬇
┌─────────────────────────────────────────────────────────────┐
│   Repeat this process for another fixed value of the same     │
│                     fixed parameter                           │
└─────────────────────────────────────────────────────────────┘
                             ⬇
┌─────────────────────────────────────────────────────────────┐
│        Repeat this process with another fixed parameter       │
└─────────────────────────────────────────────────────────────┘
```

Fig. 2 Flowchart showing the process to obtain the surface plot showing the dependence of surface roughness on the two chosen parameters

4.1 Mathematical Structure of ANN

After several trials, it was clear that a neural network with ten neurons in the hidden layer makes the most accurate predictions of the surface roughness values. The feed-forward backpropagation was used to train the network, which updates the values of biases and weights until it minimizes the mean of all squared differences between the target and output values. Table 2 shows the final weights between the input neuron and the pth neuron in the hidden layer.

Table 1 Surface roughness data for the milling of AL 6351 T6 thin workpiece using HSS tool [5]

Experiment No	Nose radius (mm)	Approach angle (deg)	Rake angle (deg)	Surface roughness (μm)
1	0.4	60	− 9	0.5321
2	0.4	60	− 6	0.5555
3	0.4	60	− 3	0.5841
4	0.4	75	− 9	0.6233
5	0.4	75	− 6	0.6376
6	0.4	75	− 3	0.6536
7	0.4	90	− 9	0.7238
8	0.4	90	− 6	0.7239
9	0.4	90	− 3	0.7474
10	0.8	60	− 9	0.7489
11	0.8	60	− 6	0.7493
12	0.8	60	− 3	0.7551
13	0.8	75	− 9	0.7642
14	0.8	75	− 6	0.7702
15	0.8	75	− 3	0.7764
16	0.8	90	− 9	0.7906
17	0.8	90	− 6	0.8219
18	0.8	90	− 3	0.8836
19	1.2	60	− 9	0.892

Table 2 Weight values between an input neuron and the pth neuron in the hidden layer

pth neuron in the hidden layer	W_{1p}	W_{2p}	W_{3p}	bp
1	2.2385	1.9312	0.2782	− 3.0958
2	− 0.6923	1.9506	1.6867	2.6480
3	2.6631	− 1.1127	0.6969	− 1.8195
4	− 1.6904	1.4447	− 2.0245	1.1557
5	2.4612	0.0140	− 1.6749	− 0.6484
6	− 0.2786	2.9846	− 0.8171	− 0.3280
7	1.6519	1.9027	1.7556	0.6466
8	1.6519	− 1.8447	1.8908	1.4745
9	− 0.7748	1.8984	1.8949	− 2.6161
10	− 1.2451	2.9239	− 0.8072	− 2.7440

Table 3 Weights between the *p*th neuron in the hidden layer and the output neuron

*p*th neuron in the hidden layer	W_{po}
1	0.0066
2	− 0.1963
3	0.3399
4	− 0.1033
5	0.3326
6	0.6219
7	0.3767
8	0.3479
9	0.0155
10	− 0.2033

The bias value for the connections between the hidden and output layer was estimated as 0.581, and the weights between the *p*th neuron in the hidden layer and the output neuron (designated as 'O') are given in Table 3.

4.2 ANN Predicted Surface Roughness

The developed ANN model, when applied to the data from [5], gave the following results.

Table 4 shows that the developed ANN model predicted the correct surface roughness to a very large extent, with the mean relative error found to be only 3.65%. The Fig. 3 gives the pictorial representation of the same.

4.3 Hypothesis Tests on ANN Model

The hypothesis tests like t-test and f-test for mean and variance, respectively give us a way to estimate how well curve fitting has been done by the ANN. The Table 5 shows the p-value obtained from these tests.

"In all these tests, the *p*-values are greater than 0.05, which means that the null hypothesis cannot be rejected. These values also indicate that there is no significant evidence to conclude that the experimental data and the data predicted by the ANN model differ from each other" [7]. Therefore, it can be concluded from here that ANN can be successfully used for curve fitting for modeling purposes.

Table 4 Comparison between surface roughness values obtained through ANN and experimentally in [5]

Experiment No.	Nose radius (mm)	Approach angle (deg)	Rake angle (deg)	Ra (Exp) (µm)	Ra (ANN) (µm)	Relative error (%)
1	0.4	60	− 9	0.5321	0.5353	0.6066
2	0.4	60	− 6	0.5555	0.5605	0.8970
3	0.4	60	− 3	0.5841	0.5993	2.5999
4	0.4	75	− 9	0.6233	0.6130	1.6555
5	0.4	75	− 6	0.6376	0.6032	5.3977
6	0.4	75	− 3	0.6536	0.7060	8.0320
7	0.4	90	− 9	0.7238	0.6109	15.5968
8	0.4	90	− 6	0.7239	0.7077	2.2381
9	0.4	90	− 3	0.7474	0.7912	5.8627
10	0.8	60	− 9	0.7489	0.7282	2.7651
11	0.8	60	− 6	0.7493	0.6545	12.6555
12	0.8	60	− 3	0.7551	0.7555	0.0501
13	0.8	75	− 9	0.7642	0.7604	0.4919
14	0.8	75	− 6	0.7702	0.7661	0.5290
15	0.8	75	− 3	0.7764	0.7576	2.4187
16	0.8	90	− 9	0.7906	0.8122	2.7313
17	0.8	90	− 6	0.8219	0.8150	0.8436
18	0.8	90	− 3	0.8836	0.9061	2.5452
19	1.2	60	− 9	0.8920	0.8851	0.7756
Mean relative error						3.6514

Fig. 3 Experimental and ANN predicted data for surface roughness
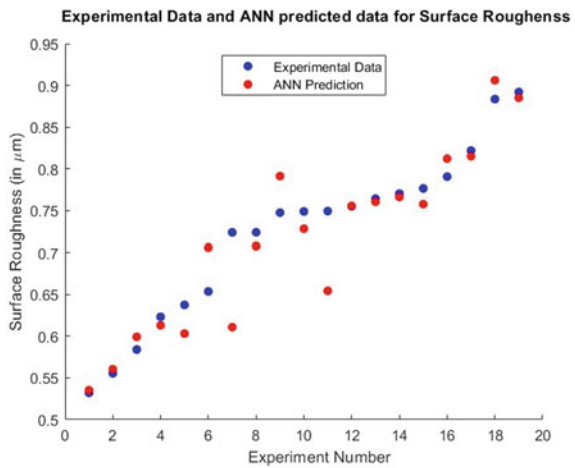
Table 5 Results of the hypothesis tests

Hypothesis test (with 95% CI)	P-value
Mean paired t-test	0.3536
Variance F-test	0.8154

4.4 Surface Fits for Surface Roughness Variation

The process shown in the flowchart in Fig. 4 was used to generate the surface fits for the variation of surface roughness with the two chosen parameters by fixing the third parameter. Three cases were considered by fixing the rake angle in the first case, nose radius in the second, and the approach angle in the third case. The surface plots for these are explained in the following sections.

4.4.1 Dependence of Surface Roughness Value on Nose Radius and Approach Angle

The following plots were generated by fixing the rake angle, taking all possible combinations of the other two parameters' values, and applying the ANN model to the generated data. The values of surface roughness are plotted on the z-axis, while those of approach angle and nose radius are plotted on the x and y-axis, respectively.

The above plots indicate that surface roughness increases with an increase in nose radius while it initially decreases slightly and then increases with an increase in approach angle. Usually, the surface roughness is expected to decrease with an increase in nose radius due to less chatter and less rubbing [5], but as evident, in the above plots, an opposite trend was observed here. "The surface roughness is expected to increase with an increase in approach angle due to an increase in the thickness of the uncut ridge" [9], and this trend is rightly observed except for the lower values of approach angle. The increase in surface roughness due to the increase in nose radius means that the influence of approach angle in determining the surface roughness is dominating over the effect of nose radius in determining the surface roughness. Similar behavior was observed in all three plots corresponding to the different constant values of rake angle.
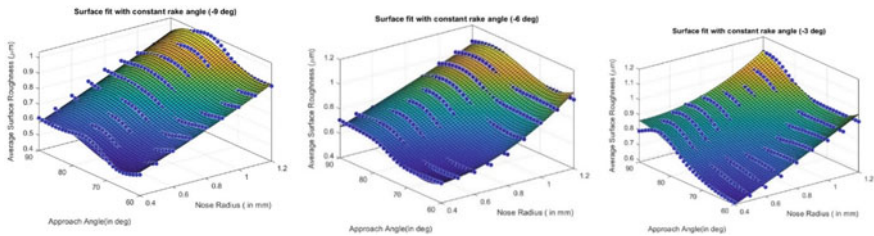
Fig. 4 Surface fit for dependence of surface roughness value on approach angle and nose radius
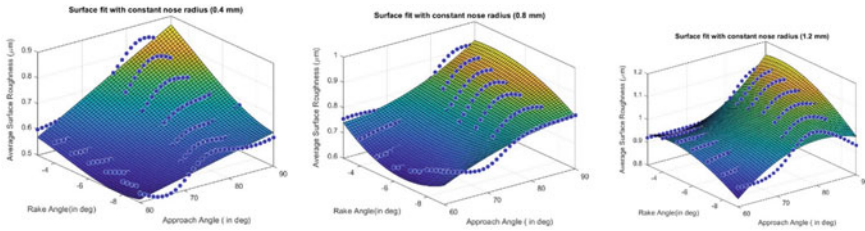
Fig. 5 Surface fit for dependence of surface roughness value on rake and approach angle

4.4.2 Dependence of Surface Roughness Value on Rake Angle and Approach Angle

The following plots were generated by fixing the nose radius and taking all possible combinations of the other two parameters' values, and applying the ANN model to the generated data. The values of surface roughness are plotted on the z-axis, while those of rake angle and approach angle are plotted on the x and y-axis, respectively (Fig. 5).

The plots above indicate that approach angle has a positive effect on the surface roughness value [9]. It was found to decrease with the increase in the magnitude of negative rake angle, which is in agreement with the conclusion in [10]. Compressive stresses induced due to the negative rake angle weaken the material's breaking, resulting in a better surface finish [10]. Another interesting thing to note is that as the value of nose radius is increased from 0.4 mm to 0.8 mm to finally 1.2 mm, the surface bulges inwards in the center. The effect of rake angle and approach angle becomes more parabolic compared to the linear-like behavior in the first case, which means too high a value of nose radius can deteriorate the surface finish in thin-walled structures, possibly due to higher chatter.

4.4.3 Dependence of Surface Roughness Value on Rake Angle and Nose Radius

The following plots were generated by fixing the approach angle and taking all possible combinations of the other two parameters' values, and applying the ANN model to the generated data. The values of surface roughness are plotted on the z-axis, while those of rake angle and nose radius are plotted on the x and y-axis, respectively (Fig. 6).

These plots also indicate that surface roughness decreases with the increase in the magnitude of negative rake angle due to the reasons discussed in the previous section and in [10]. However, the surface roughness unexpectedly increases with the increase in nose radius, which shows that other parameters like rake angle and approach angle have a more pronounced impact than the effect of nose radius. Too high a value of nose radius can be disadvantageous as well.
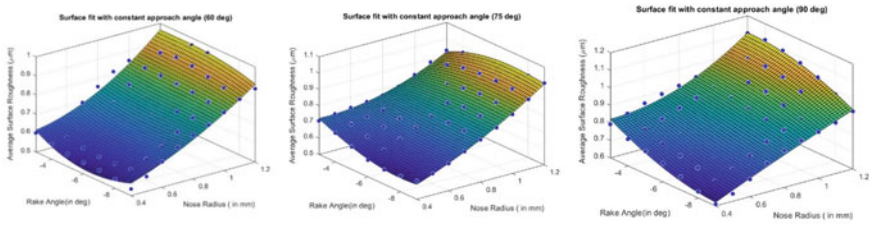
Fig. 6 Surface fit for dependence of surface roughness value on rake angle and nose radius

4.5 *Application of PSO on the Surface Plots*

The optimum points on the surface plots for minimum surface roughness were obtained by applying PSO on the polynomial representing the surface. The results of this optimization are summarized in Table 6.

Table 6 Optimum value of parameters for each surface plot

Surface plot	Optimum nose radius (in mm)	Optimum approach angle (in deg)	Optimum rake angle (in deg)	Surface roughness (in μm)
Constant rake angle (− 9°)	0.4	66.05	− 9	0.5130
Constant rake angle (− 6°)	0.4	64.89	− 6	0.5047
Constant rake angle (− 3°)	0.4	60	− 3	0.5791
Constant nose radius (0.4 mm)	0.4	60	− 7.7052	0.4993
Constant nose radius (0.8 mm)	0.8	60	− 6.6815	0.6294
Constant nose radius (1.2 mm)	1.2	60	− 9	0.8333
Constant approach angle (60°)	0.4	60	− 6.4240	0.5245
Constant approach angle (75°)	0.4	75	− 8.001	0.5847
Constant approach angle (90°)	0.4	90	− 9	0.6223
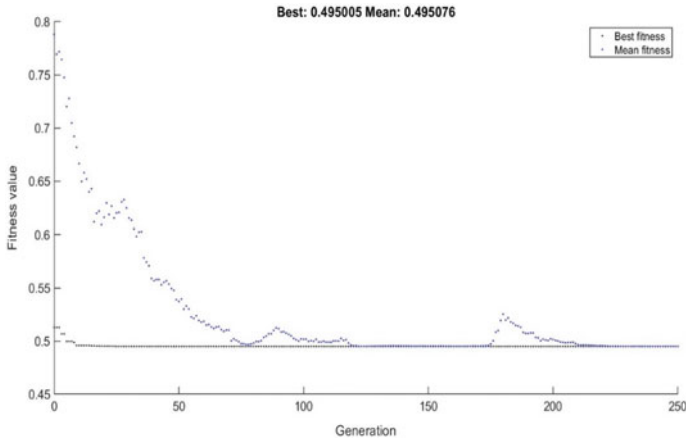
Fig. 7 Plot for variation of best fitness value during the GA process

4.6   Application of GA and PSO on the ANN Model

For the last part of the study, GA and PSO were applied to the developed ANN model to obtain the optimal parameters for the best surface finish. The optimal parameters were found to be 0.4950 µm for a nose radius of 0.4 mm, an approach angle of 66.1973°, and a rake angle of − 8.5133°. Both GA and PSO gave the same results, which show the validity of the correct optimal solution. The following best fitness plot was obtained when GA was applied to the neural network model (Fig. 7).

5   Conclusions

The following conclusions can be made from this study:

1. AI-based methods such as ANN, Neuro-fuzzy systems, and fuzzy systems can be very effective in building models to predict the surface roughness, as was observed in this study where only an error of 3.65% was found in predicting the surface roughness
2. Evolutionary algorithms such as GA and PSO are very effective in finding the optimum machining conditions for obtaining minimum surface roughness and can be employed in practical scenarios, which will reduce the costs of machining and improve the surface finish as well.
3. The effect of various machining parameters like rake angle, approach angle, and nose radius, in this case, can be easily studied with the help of surface plots, and it is possible that we may observe unexpected trends due to the combined effects of two factors or more pronounced effect of the other factor.

4. Surface plots showed the surface roughness to decrease with an increase in the magnitude of negative rake angle and increase with the approach angle. The effects of approach angle and rake angle dominated the impact of nose radius and that too high the value of nose radius can be disadvantageous.

Future work can be extended to explore the effects of other parameters such as feed rate, cutting speed, tool length on the surface finish for milling of thin-walled structures.

References

1. Alauddin M, El Baradie M, Hashmi M (1995) Computer-aided analysis of a surface-roughness model for end milling. J Mater Process Technol 55:123–127
2. Benardos P, Vosniakos GC (2003) Predicting surface roughness in machining: a review. Int J Mach Tools Manuf 43:833–844
3. Fausett L (1994) Fundamentals of neural networks: architectures, algorithms, and applications. Prentice-Hall, Englewood Cliffs, NJ
4. Fei J, Lin B, Yan S, Ding M, Zhang J, Ji C, Zhang X (2019) Modeling of surface roughness for manufactured thin-walled structure. J Eng Manuf 1216–1223
5. Hareendran M, Sreejith S (2018) A study on surface quality of thin-walled machined parts. Mater Today: Proc 5:18730–18738
6. Kant G, Sangwan KS (2014) Prediction and optimization of machining parameters for minimizing power consumption and surface roughness in machining. J Clean Prod 83:151–164
7. Kant G, Sangwan KS (2015) Predictive modelling and optimization of machining parameters to minimize surface roughness using artificial neural network coupled with genetic algorithm. Paper presented at 15th CIRP Conference on modelling of machining operations
8. Kovac P, Rodic D, Puckovsky V, Savkovic B, Gostimirovic M (2013) Application of fuzzy logic and regression analysis for modeling surface roughness in face milling. J Intell Manuf 24:755–762
9. Surya MS, Atla S (2015) Effect of approach angle in face milling using tungsten carbide tool. Int J Recent Adv Mec Eng (IJMECH) 4:2
10. Yang D, Wan Z, Xu P, Lu L (2018) Rake angle effect on a machined surface in orthogonal cutting of graphite/polymer composites. Adv Mater Sci Eng. https://doi.org/10.1155/2018/3601918

Optimization of EDM Process Parameter for Inconel 925 by Using Taguchi Method

Avadh Kumar, Rahul Vishwakarma, and S. K. Yadav

1 Introduction

Electrical discharge machining (EDM) is unconventional machining process in which material is removed by the collaboration of electrical and thermal energy. In this process, sparks are generated between work piece and tool, which are electrically conductive materials and submerged in the dielectric fluid [1]. In this process, material is removed from work piece due to erosion, melting and vaporization. A very narrow gap about 0.0250 mm is maintained between work piece and tool with the help of servo mechanism. Figure 1 shows the mechanical setup for EDM.

It is widely used in producing punches, dies, molds, aerospace, surgical components and automotive industries [2]. Inconel is nickel-based superalloy, which has excellent strength at very high temperature. It is used for high-temperature application in aerospace, jet engine, automotive and marine industries.

Jegan et al. [3] performed an experimental investigation on stainless steel AISI202. They have taken T_{on} and T_{off} process parameters and optimize MRR and SR by using GRA approach. They reported that discharge current plays a significant role for MRR. Ayesta et al. [4] performed machining (narrow slots) on aeronautical alloy C1023 by using EDM with process parameters spark current, pulse on time (T_{on}) and voltage. They calculated MRR and electrode wear rate. They reported that for minimum electrode wear, high-intensity current and more pulse time should be required. Koshy et al. [5] concluded that the machining with rotational tool in disk shape improves MRR and surface roughness because a tangential force acted on outer surface of disk which was responsible for cutting the material and generation of centrifugal force due to rotation. Nayak and Mahapatra [6] had conducted experiment on Inconel 718 using wire EDM, and they used artificial neural network to develop functional equation

A. Kumar (✉) · R. Vishwakarma · S. K. Yadav
Department of Mechanical Engineering, M. M. M. U. T., Gorakhpur, India

S. K. Yadav
e-mail: skyme@mmmut.ac.in

Fig. 1 Principle of EDM [1]
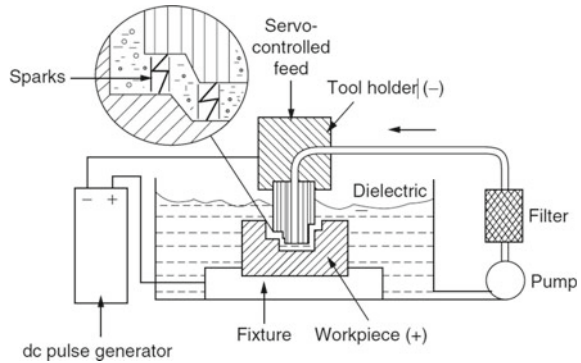
for input process parameters and response parameters. Rajyalakshmi and Ramaiah [7] carried out experimental investigation on Inconel 825 using wire cut EDM. They used Taguchi GRA for optimizing MRR and SR. They reported that by applying the GRA–Taguchi method, MRR increased and surface roughness reduced. Singh et al. [8] investigated effect of machining parameter on MRR, radial overcut, TWR and Ra in EDM of E31 tool steel. The experiments were performed with different tools. They concluded that copper and aluminum tool give higher MRR and lower radial overcut. Srivastava et al. [9] performed experimental work on EDM for Al MMC. They used RSM to optimize the response parameters. They found that peak current is most significant process parameter for responses. Vishwakarma et al. [10] reviewed the effect of different electrodes and dielectric fluids on metal removal rate and surface integrity of electrical discharge machining. They reported the use of different types of dielectric fluid and their effect on different electrodes.

2 Materials and Methods

2.1 Experimental Setup

ELECTRONICA-ELECTRAPLUS PS ZNC-make EDM machine was used for experimentation. All experiments were performed in advanced machining laboratory of our department. Positive polarity is used for all experiments. In this machine, EDM oil is used as a dielectric fluid (Fig. 2) [9].

Fig. 2 Setup of tool and work piece [MMMUT, MED, Gorakhpur]
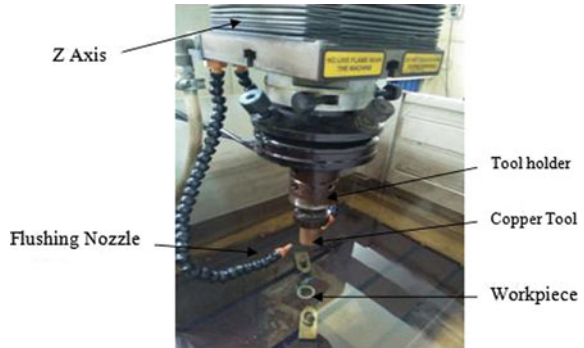
Table 1 Weight % of element of Inconel 925

Element	Ni	Cr	Mo	Cu	Ti	Mn	Si	Al	Fe
Weight %	42.95	20.13	2.68	1.17	2.12	3.0	0.5	0.4	Rest

2.2 Tool and Workpiece Materials

In this work, Inconel 925 was selected as work piece material of 100 mm × 50 mm × 4 mm. A copper electrode 18 mm diameter is used for experiments. Table 1 shows the weight % of element of Inconel 925.

2.3 Selection of Control Factors

In this experiment, design of experiment plays an important role. The concept of DOE was approached by the Taguchi. For the proper design of experiment, input variables are essential for the appropriate evolution of desired response. Selection of the response parameter and control factors for the design of experiment and for each control factor decides the level and each value of level by literature survey. Orthogonal array was decided on the basis of control factor and level. After experimentation, evaluate the MRR and measure the SR for each data. In this experiment, four input parameters, i.e., I_p, T_{on}, duty cycle and voltage were considered. As per DOE L27, orthogonal array (OA) was selected by using Taguchi method. Table 2 represents input variables and their levels.

Table 2 Input variable along with their levels

Variables	Coding	Level		
		1	2	3
Peak current (Ampere)	I_p	9	13	17
Pulse on time (μs)	T_{on}	300	400	500
Duty cycle (%)	τ	10	11	12
Voltage (Volt)	V	50	60	70

3 Results and Discussion

Minitab 18 software was used for analysis of the experimental data. This statistical tool was used to create orthogonal array L27 as per design of experiment. All the experiments were performed according to L27 orthogonal array. The calculated results of S/N ratio are shown in Table 3. The objective of this investigation is to minimize tool wear rate and maximize MRR.

Die-sinking EDM was used to perform all sinking operations on Inconel 925. In this experimental investigation, an 18 mm diameter copper tool was used.

Formula used for MRR calculation:

$$\text{MRR} = \frac{(W_i - W_f) * 1000}{t\rho}$$

where

W_i is initial weight of work piece (in gram).
W_f is final weight of work piece (in gram).
t is time used for machining (in minute).
ρ is work piece density.

The above formula is also used for TWR calculation.

Surface roughness tester is used to measure surface roughness.

Table 3 shows that maximum value of MRR is 30.0602 mm^3/min at Experiment no. 22, and the process parameters are peak current 17 A, pulse on time 400 μs, duty cycle 10 and voltage 70 ^{V}. For TWR, minimum value for tool wear rate is 0.0582 mm^3/min at Experiment no. 3; the process parameter is peak current 9 A, pulse on time 300 μs, duty cycle 10 and voltage 50 V; for surface roughness, minimum value is 9.50 μm at Experiment no. 9; the process parameter is peak current 9 A, pulse on time 500 μs, duty cycle 12 and voltage 70 V.

Fig. 3 shows main effect plot for means for MRR. MRR is considered for the condition as larger is better, so from Fig. 3, the optimum value of response is taken as larger value. So, peak current is 17 A, T_{on} is 400 μs, duty cycle is 10, and voltage is 60 V.

Table 3 Value of responses and S/N ratios

Experimental run	Peak current (A)	Pulse on time (µs)	Duty cycle (%)	Voltage (V)	MRR (mm³/min)	S/N ratio	TWR (mm³/min)	S/N ratio	SR (µm)	S/N ratio
1	9	300	10	50	8.5734	18.0682	0.0604	23.7776	11.6	− 21.2911
2	9	300	10	50	8.6956	18.0682	0.0744	23.7776	11.3	− 21.2911
3	9	300	10	50	7.0753	18.0682	0.0582	23.7776	11.9	− 21.2911
4	9	400	11	60	7.7491	18.8582	0.0637	23.6734	10.4	− 20.2015
5	9	400	11	60	8.6391	18.8582	0.0659	23.6734	10.3	− 20.2015
6	9	400	11	60	10.559	18.8582	0.0669	23.6734	10.0	− 20.2015
7	9	500	12	70	5.5535	15.2631	0.0689	22.4162	12.0	− 20.7073
8	9	500	12	70	6.4596	15.2631	0.0781	22.4162	10.9	− 20.7073
9	9	500	12	70	5.5133	15.2631	0.0797	22.4162	9.50	− 20.7073
10	13	300	11	70	8.0924	18.9657	0.0924	19.6870	12.5	− 22.7512
11	13	300	11	70	8.5714	18.9657	0.0930	19.6870	14.4	− 22.7512
12	13	300	11	70	10.4347	18.9657	0.1227	19.6870	14.2	− 22.7512
13	13	400	12	50	12.6807	22.6468	0.1171	18.2207	12.1	− 21.5216
14	13	400	12	50	14.8573	22.6468	0.1164	18.2207	12.5	− 21.5216
15	13	400	12	50	13.4105	22.6468	0.1339	18.2207	11.1	− 21.5216
16	13	500	10	60	11.0766	21.5756	0.1395	18.0468	11.0	− 20.9442
17	13	500	10	60	13.2575	21.5756	0.1275	18.0468	10.5	− 20.9442
18	13	500	10	60	11.9254	21.5756	0.1064	18.0468	11.9	− 20.9442
19	17	300	12	60	22.8571	27.0644	0.2455	12.8756	16.2	− 23.2419
20	17	300	12	60	23.2925	27.0644	0.2418	12.8756	14.1	− 23.2419

(continued)

Table 3 (continued)

Experimental run	Peak current (A)	Pulse on time (μs)	Duty cycle (%)	Voltage (V)	MRR		TWR		SR	
					MRR (mm³/min)	S/N ratio	TWR (mm³/min)	S/N ratio	SR (μm)	S/N ratio
21	17	300	12	60	21.6147	27.0644	0.1897	12.8756	13.1	− 23.2419
22	17	400	10	70	30.0602	28.9544	0.3013	11.2770	12.5	− 22.7291
23	17	400	10	70	28.6956	28.9544	0.2791	11.2770	14.2	− 22.7291
24	17	400	10	70	25.8507	28.9544	0.2343	11.2770	14.3	− 22.7291
25	17	500	11	50	18.4265	24.9997	0.2046	12.1788	14.3	− 23.1287
26	17	500	11	50	17.0033	24.9997	0.2489	12.1788	14.0	− 23.1287
27	17	500	11	50	18.0124	24.9997	0.2790	12.1788	14.7	− 23.1287
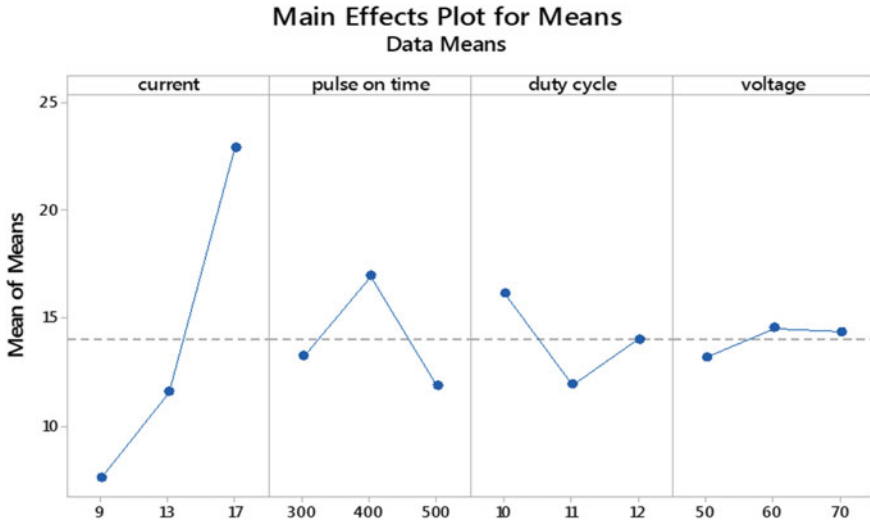
Fig. 3 Main effects plot for means (MRR)

Main effect plot for means of TWR is plotted in Fig. 4. The condition for the TWR is taken as the smaller is better, so from Fig. 4, the optimum value for TWR peak current is 9 A, pulse on time at 300 μs, duty cycle at 11 and voltage at 60 V.
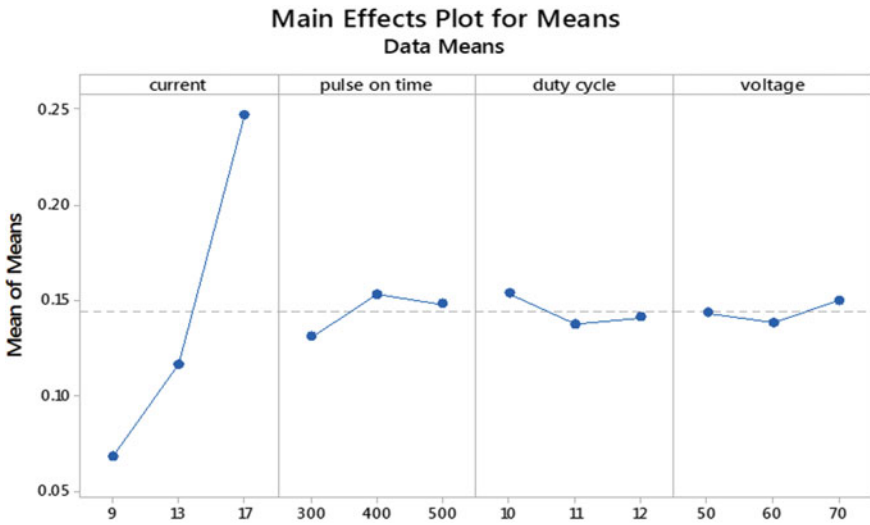
Fig. 4 Main effects plot for means (TWR)
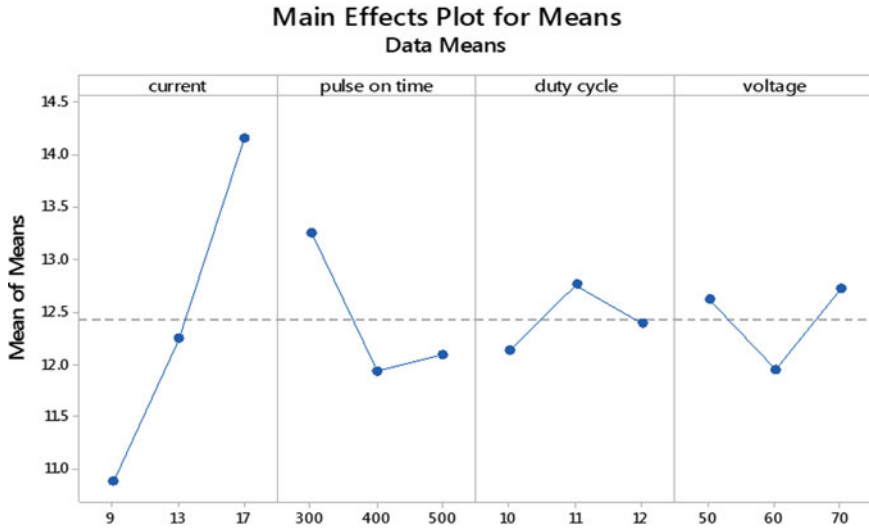
Fig. 5 Main effects plot for means (SR)

Main effect plot for S/N ratios of SR is plotted in Fig. 5. The condition for the SR is taken as the smaller is better, so from Fig. 5, the optimum value for SR peak current is 9 A, pulse on time at 400 μs, duty cycle at 10 and voltage at 60 V.

Analysis of Variance (ANOVA)

The results obtained by Taguchi method were not sufficient. ANOVA is used for effect of individual parameters in EDM.

Table 4 shows the ANOVA result for MRR. In this, P-value for I_p, T_{on} and duty cycle is less than 0.05. So, this model is significant.

Table 5 shows the ANOVA result for TWR. In this, P-value for I_p is less than 0.05. So, this model is significant.

Table 6 shows the ANOVA result for SR. In this, P-value for I_p and T_{on} is less than 0.05. So, this model is significant.

Table 4 ANOVA table for MRR

Input variable	DoF	Seq SS	% contribution (%)	Adj SS	Adj MS	F-value	P-value
I_p	2	1123.36	82.57	1123.36	561.68	387.77	0.00
T_{on}	2	122.29	8.99	122.29	61.15	42.21	0.00
τ	2	79.06	5.81	79.06	39.53	27.29	0.00
V	2	9.74	0.72	9.74	4.87	3.36	0.06
Error	18	26.07	1.92	26.07	1.45		
Total	26	1360.51	100.00				

Table 5 ANOVA table for TWR

Input variable	DoF	Seq SS	% contribution (%)	Adj SS	Adj MS	F-value	P-value
I_p	2	0.154	92.23	0.154	0.077	159.83	0.000
T_{on}	2	0.003	1.47	0.003	0.001	2.55	0.106
τ	2	0.001	0.75	0.001	0.001	1.31	0.295
V	2	0.001	0.35	0.001	0.0003	0.61	0.554
Error	18	0.009	5.19	0.009	0.0005		
Total	26	0.167	100.00				

Table 6 ANOVA table for SR

Input variable	DoF	Seq SS	% contribution (%)	Adj SS	Adj MS	F-value	P-value
I_p	2	48.792	62.50	48.792	24.396	29.41	0.000
T_{on}	2	9.401	12.04	9.401	4.700	5.67	0.012
τ	2	1.761	2.26	1.761	0.880	1.06	0.367
V	2	3.185	4.08	3.185	1.593	1.92	0.176
Error	18	14.933	19.13	14.933	0.830		
Total	26	78.072	100.00				

4 Conclusion

In the present work, Inconel 925 was machined by EDM. The aim of this experimental investigation was to optimize the input process parameters, i.e., peak current, duty cycle, pulse on time and voltage on the response parameters, i.e., MRR, TWR and SR by using Taguchi method. This experimental investigation gives the following conclusion:

i. For MRR, peak current is most important process parameter. Other process parameters also play an important role for MRR, but its effect is less than the peak current. The optimum process parameters are 17 A peak current, 400 pulse on time, 10 duty cycle and 60 V voltage.
ii. For TWR, peak current plays a significant role. Other process parameters also play an important role for TWR, but its effect is less than the peak current. The optimum machining parameter is 9 A current, 300 pulse on time, 11 duty cycle and 60 V voltage.
iii. Surface roughness is mainly affected by peak current. Effect of other process is less than the peak current. The optimum machining parameter is 9 A current, 400 pulse on time, 10 duty cycle and 60 V voltage

References

1. Kalpajian S, Schmid SR (2003) Material removal processes: abrasive chemical, electrical and high-energy beam; manufacturing processes for engineering materials. Prentice Hall, New Jersey
2. Ho KH, Newman ST (2003) State of the art electrical discharge machining (EDM). Int J Mach Tools Manuf 43(13):1287–1300
3. Jegan TM, Chenthil M, Anand D, Ravindran D (2012) Determination of electro discharge machining parameters in AISI202 stainless steel using grey relational analysis. Procedia Eng 38:4005–4005
4. Ayesta I, Izquierdo B, Sanchez JA, Ramos JM, Plaza S, Pombo I, Ortega N, Bravoe NH, Fradejas R, Zamakon I (2013) Influence of EDM parameters on slot machining in C1023 aeronautical alloy. Procedia CIRP 6:129–134
5. Koshy P, Jain VK, Lal GK (1993) Experimental investigations into electrical discharge machining with a rotating disk electrode. Precis Eng 15(1):6–15
6. Nayak BB, Mahapatra SS (2016) Optimization of WEDM process parameters using deep cryo-treated Inconel 718 as work material. Eng Sci Technol Int J 19(1):161–170
7. Rajyalakshmi G, Ramaiah PV (2013) Multiple process parameter optimization of wire electrical discharge machining on Inconel 825 using Taguchi grey relational analysis. Int J Adv Manuf Technol 69:1249–1262
8. Singh S, Maheshwari S, Pandey PC (2004) Some investigations into the electric discharge machining of hardened tool steel using different electrode materials. J Mater Process Technol 149(1):272–277
9. Srivastava A, Yadav SK, Singh DK (2021) Modeling and optimization of electric discharge machining process parameters in machining of Al 6061/SiC$_p$ metal matrix composite. Mater Today Proc 44(1):1169–1174
10. Vishwakarma R, Yadav SK, Kumar A, Krishna H (2017) Effect of different electrodes and dielectric fluids on metal removal rate and surface integrity of electric discharge machining: a review. Int J Eng Technol Sci Res 4(11):935–941

Use of Analytic Hierarchy Process Methodology for Analyzing Existing Motorcycle Helmet Design Concepts

S. R. Bajare, A. K. Bewoor, and H. P. Jagtap

1 Introduction

In India, wearing helmets while riding bicycles is the biggest problem. Riding a two-wheeler without wearing helmets has resulted in severe brain injuries as well as fatality. A report "ROAD ACCIDENTS IN INDIA—2017" published by Ministry of Road Transport and Highways, Government of India, shows that in 2017 most fatal accidents were those of two-wheeler riders accounting for 33% of deaths on Indian roads and 73.8% of them did not wear a helmet [1]. Also in 2018, approximately 43,600 two-wheeler riders not wearing helmets died in road accidents accounting for 28.8% of total fatal injuries in road accidents [2]. The figures mentioned here clearly indicate the importance of helmets in saving the lives of the rider. Major populous find wearing helmets uncomfortable, also there is a lack of ventilation, neck pain also storage problems are there [3, 4]. Because of these problems with existing helmets, it has become necessary to find smart alternatives. The steps shown in Fig. 1 can be followed to finalize the concept.

2 Problem Definition

Defining the problem statement accurately is the initial stage of the conceptual design process. In this case, the existing helmet model has many limitations viz. uneasiness, lack of ventilation, heavyweight hence causing neck pain, limited field of vision, hearing ability, storage, carriage problem, etc. The majority of bike riders do not opt

S. R. Bajare · A. K. Bewoor
MKSSS'S Cummins C.O.E. for Women, Pune, India
e-mail: siddhi.bajare@cumminscollege.in

H. P. Jagtap (✉)
Zeal College of Engineering and Research, Pune, India
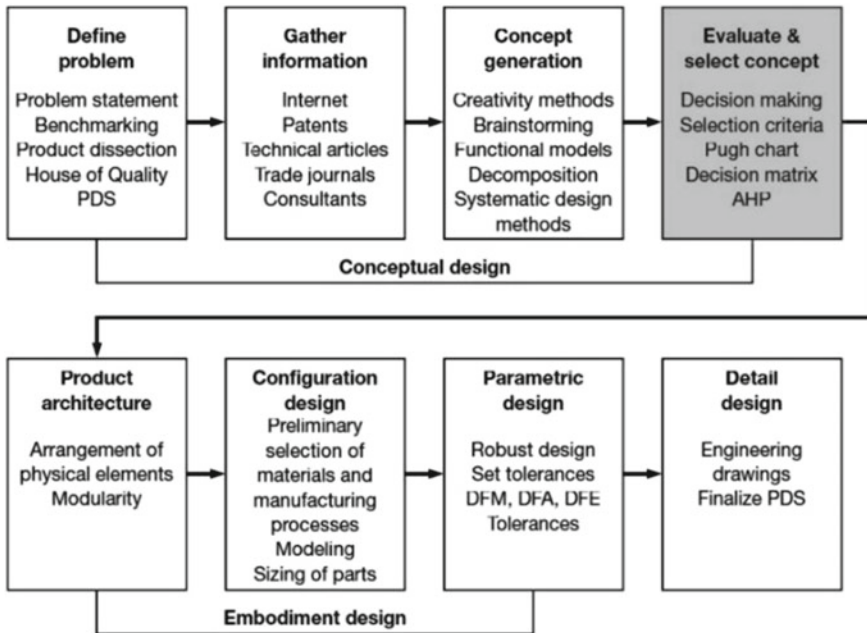
Fig. 1 Steps in the design process [5]

to wear helmets because of these reasons. Also, most widely used helmets are not made up of eco-friendly materials, thereby, not supporting the concept of environmental sustainability. There is a need for a smart alternative helmet that will overcome these problems. Also, in some states in India, the government has made wearing a helmet compulsory and it has increased the use of helmets among two-wheeler riders. Despite the increased use of helmet among rider's two-wheeler related Traumatic Brain Injuries (TBIs) has increased over the last few years [2]. Some mandatory tests are performed on the helmet to check its performance in critical loading conditions. From the interaction with domain experts and field experience, it is observed that the existing helmet protects the head in case of linear acceleration but fails to protect against angular acceleration and it is known that TBI is caused by angular acceleration. The brain is vulnerable to shear strain which is caused by the angular acceleration of the head. To idealize normal impact test, current safety standards [6] for two-wheeler helmets like ECE R22 have limits for peak linear acceleration. As per this standard, a helmet is dropped vertically at 0° and 45° angles on a flat anvil, and also the head of the dummy is constrained in order to prevent angular acceleration [7]. In the new version of ECE standards, i.e., ECE R22.06, angular acceleration will be considered [8]. Hence, a need can be sensed that a helmet has to satisfy both linear accelerations as well as angular acceleration criteria.

3   Review of Literature

Some appropriate literature that is published to date has been described beside the intention (a) to analyze different criteria considered in helmet testing (b) to identify different existing helmet design concepts.

3.1   Concepts Identified for Further Study

From the available literature following concepts of helmets are selected for the further evaluation process. (1) *Airbag Helmet*—In this helmet during an accident situation head protector is inflated and it acts as an Airbag cushion for the head. For detecting accidental situations sensors such as accelerometer, gyroscope and actuators are used [9] (Refer Fig. 2).

(2) *Helmets with Angular Impact Mitigation (AIM) System*—Helmet with Angular Impact Mitigation (AIM) system where EPS foam liner of the regular helmet is replaced with aluminum honeycomb liner [10] (Refer Fig. 3). (3) *Shell Helmet with*
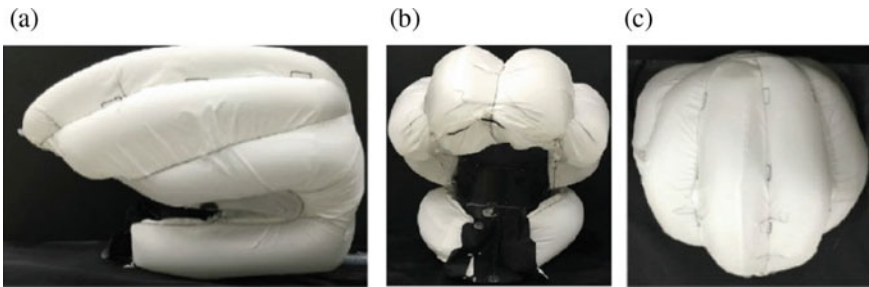
Fig. 2   a Top view **b** side view **c** front view of hovding in an inflated state
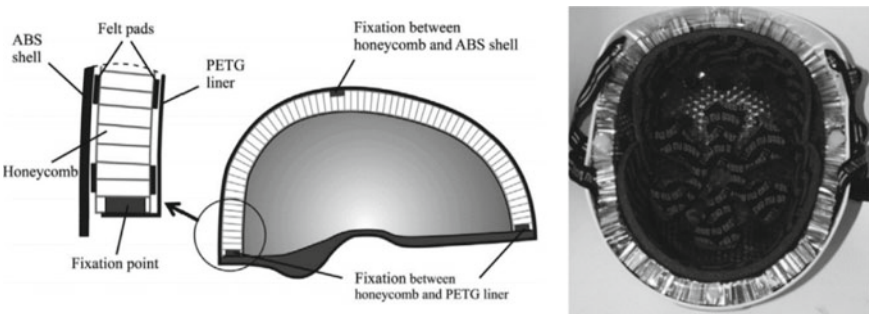
Fig. 3   Helmets with AIM system [10]
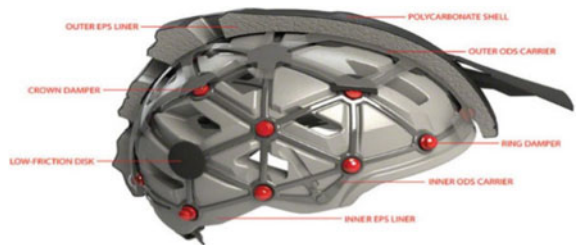
EPS foam—It is a regular two-wheeler helmet with a hard outer shell, and foam liner of Expanded Polystyrene (EPS) material and comfort padding [10] (Refer Fig. 4).

(4) *Helmets with multi directional impact protection system*—MIPS helmets mimic the brain's protection system for reducing the impact of rotational acceleration on the head. It uses a slip plane system that moves inside the helmet at the time of impact [12] (Refer Fig. 5).

Studied literature is presented in the form of the Table 1.

3.2 Need Identification

Need identification can be done in different ways and it can be represented in different forms. One of the standard ways to present it is the Kano model.

As shown in the Fig. 6 Kano model there are different types of requirements viz. must be, one-dimensional, attractive requirements. The customer feels satisfied or dissatisfied when these attributes are sufficient or insufficient, respectively [17, 18].

By using the Kano model, needs identified for helmet use are;

(A) **Basic Needs**

    (i)   The protection provided by the helmet to absorb acceleration in impacts during accidents,

    (ii)   Protection to the user from moisture and heat,

    (iii) Relative movement of the helmet w.r.t. the head (i.e., free play and slip, relative movement is not desired),

Table 1 Literature review of motorcycle helmets

Application	Concept/type	Parameter	Major conclusions
Bicycle	Shell helmet with EPS liner	1. Head injury criterion (HIC) [14] 2. Linear peak acceleration [14, 15] 3. Peak angular acceleration [15] 4. Material and design of helmet [15]	1. From the helmeted and unhelmeted impacts, it is clear that the helmet reduces injuries to the brain and skull by absorbing energy considerably for all impact configurations. 2. Helmeted impacts drastically reduce the potential for severe brain injury, peak linear head acceleration in all impacts. 3. Strain level depends on the loading conditions. Compared to the purely radial impact, angular impacts are riskier for more impact locations on the helmet.
Motorcycle	Airbag helmet	1. Translational acceleration [16, 9] 2. Angular acceleration [16, 9]	1. Angular acceleration is not included in the current bicycle helmet standards for certification, even though it is known as the dominant factor in causing brain injury. 2. From the test results, it is clear that rotational acceleration causes serious brain injuries like concussions, Diffuse Axonal Injury (DAI), etc. 3. The size and stiffness of the helmet are the important variables in designing a bike helmet which directly affects its energy absorption capacity. 4. As compared to MIPS, AIM, EPS helmets; Airbag helmet performed best and showed fewer results of shock absorption and oblique impacts.

(continued)

Table 1 (continued)

Application	Concept/type	Parameter	Major conclusions
Bicycle	AIM helmet	1. Translational acceleration [16, 12] 2. Angular acceleration [16, 12]	In the MIPS helmet, a slip liner is used which permits relative motion of sliding between head and helmet during impact hence results in reduced rotational acceleration of head as compared to EPS-based bicycle helmets
Bicycle		1. Linear peak acceleration [10] 2. Angular acceleration [10]	AIM helmets showed less linear as well as angular acceleration as compared to EPS-based bicycle helmets and hence provide better protection to severe brain injuries
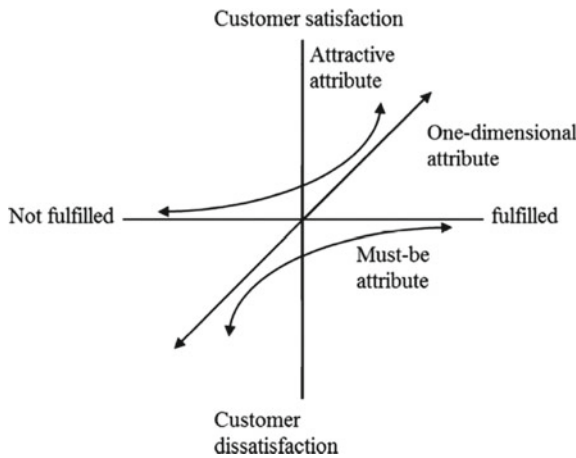
Fig. 6 Kano's model [17]

    (iv)   Field of vision accessible to helmet user through the helmet visor,
    (v)   Hearing ability while using the helmet

(B) **One-dimensional requirements**

    (i)   Cost of the helmet
    (ii)   Ventilation,
    (iii)   Comfort in the fit, carriage and storing the helmet
    (iv)   Weight of the helmet (less weight will reduce neck load)

    (v)   Restrictions on the head and neck movements (range of motion of the neck w.r.t. comfort)

    (vi)   Moisture resistant, non-biodegradable, washable and replaceable helmet liner material.

    (vii) Fog prevention and possible scratch protection of the visor

(C)   **Attractive requirements**

    (i)   Accommodation of additional accessories such as earphones, spectacles. inside the helmet,

    (ii)   Accommodation of hair bun, turban, etc. inside the helmet,

    (iii) Sustainable helmet material

    (iv) These identified needs will now be used further as criteria for the evaluation of helmet concepts.

3.3 Evaluation of Selected Concepts for Further Design Recommendations

In this step, different identified helmet design concepts/types (which are presented in the literature review section) are evaluated and a ranking of these helmet design concepts is done. For evaluating helmets different needs or requirements of helmet users which are identified by using the Kano model are used. Since there are more than one criteria for evaluation, multiple criteria decision making (MCDM) method is used for further analysis as the MCDM method efficiently assists decision-makers to choose the best alternative among all, by using different criteria. Analytical Hierarchy Process (AHP) is one of the MCDM methods which is most widely used [19]. In AHP, the problem is divided into Hierarchy in which objectives or goals are defined at the top level, the middle level consists of criteria and sub-criteria as well as option be defined at the lowest level. As per this method, pair-wise comparison of elements that are at the same level in the hierarchy is done. For comparing elements scale is used, where the importance of one element over another concerning a higher-level element is indicated by the scale.

The following steps will help in the formation of a Hierarchical structure for the problem by using the AHP method-

Step I   Create the Hierarchy of the problem.

Step II   Define the scale for scoring each criterion.

Step III   A comparison matrix is created based on the scale defined in step 2.

Step IV   Normalized matrix is formed by converting comparison matrix which is obtained in step 3 (Table 2).

Assume that X stand for the comparison matrix: $X = [x_{ij}]$; where i represents helmets ($i = 1, 2, …, n$) and j represents criteria ($j = 1, 2, …, m$).

The normalized matrix of X can be obtained by: $r_{ij} = \underline{x_{ij}}, j = 1, 2, 3, …, m$

Table 2 Explanation of intensities (scale) assignment of weights

Intensity	Definition of importance	Explanation
1	Same importance	The two elements (i, j) contribute equally to the goal
3	Moderate importance	Experience moderately favors one element over another
5	Strong importance	Experience strongly favors one element over another
7	Very strong importance	Experience very strongly favors one element over another
9	Extreme importance	Experience extreme favors one element over another
2, 4, 6, 8 used for intermediate values		

Step V   Between the n rating criteria, pair-wise comparison of relative importance is defined. As a result an *n*-by-*n* matrix $A(a_{ij})$ is obtained with $i, j = 1, 2, 3, \dots n$).

$$A = [a_{ij}]_{nxn}$$

where aij is representing the relative importance of criterion *i* for criterion *j* which is defined by user and $a_{ii} = 1$, $a_{ij} > 0$, $a_{ij} = 1/a_{ji}$. Also, when $a_{ij} = a_{ji} = 1$ it indicates that *i* and j have the same comparative weight.

Step VI   In this step, the consistency of the pair-wise comparison matrix is checked and calculates the weight of the different criteria adopted.

The above steps will be applied to the helmet selection process. In this study, the cost parameter is treated as constant since the Airbag helmet design is under the development phase (Fig. 7).

Step I—Creation of the Problem Hierarchy

A—Protection provided by the helmet to absorb linear acceleration in normal impacts during accidents, B—Protection provided by helmet to absorb angular acceleration in oblique impacts during accidents, C—Ventilation, D—Protection to the user from moisture and heat, E—Comfort in fitment, carriage, and storage of the helmet, F -Relative movement of the helmet w.r.t. the head (i.e., free play and slip, relative movement is not desired), G—Weight of the helmet (less weight will reduce neck load), H -Restrictions on the head and neck movements (range of motion of the neck w.r.t. comfort), I—Accommodation of additional accessories such as earphones, spectacles, etc. inside the helmet, J—Accommodation of hair bun, turban, etc. inside the helmet, K—Moisture resistant, washable, and replaceable helmet liner material and sustainable helmet material, L—Fog prevention and possible scratch protection of the visor, M—Field of Vision accessible to helmet user through the helmet visor, N—Hearing Ability while using the helmet.
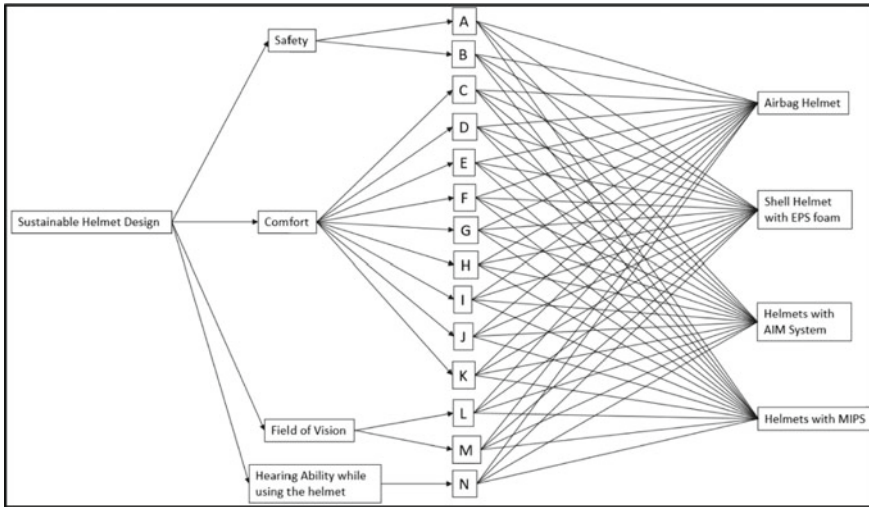
Fig. 7 AHP Hierarchy structure diagram

Criteria I: Safety

For assessing the impact of safety criteria on Sustainable Helmet Design, two parameters viz. (1) Protection provided by the helmet to absorb linear acceleration in normal impacts during accidents and (2) Protection provided by helmet to absorb angular acceleration in oblique impacts during accidents are used. The scale used for comparison: 1 for below- average impact, 2 for sufficient impact, 3 for good impact, and 4 for excellent impact on safety. The details of the analysis are given in Table 3.

Step III for Criteria I—A comparison matrix is calculated in this step and on the basis of scale which is defined above, the weight of each criterion is defined. When the row parameter is having more importance as compared to the column parameter, 3 is written in that particular cell. Similarly, 2 and 1 are written in the cell, when both

Table 3 Effect of safety criteria on helmet design evaluation

Helmets	Safety criteria	
	Protection provided by helmet to absorb linear acceleration in normal impacts during accidents	Protection provided by helmet to absorb angular acceleration in oblique impacts during accidents
Airbag helmet	4	4
Shell helmet with EPS foam	2	1
Helmets with AIM system	3	3
Helmets with MIPS	3	3

the parameters are of equal importance and column parameter is of more importance than row parameter, respectively [20] (Refer to Tables 4).

The impact of any particular criteria is evaluated by multiplying score with weight of that criterion. Overall Impact of Safety criteria on Helmet selection is calculated and given in Table 5

Table 6 represents the Scale of 1–4 which is given for scoring of this criteria and Table 7 represents the required score table which is formulated based upon the scoring in Table 6.

For Criteria II—Comfort, Criteria III—Field of Vision, and Criteria IV—Hearing Ability, the procedure shown for Criteria I will be followed, and a comparison matrix for Criteria II, Criteria III, and Criteria IV will be obtained.

Step IV   The score table/comparison matrix for all four criteria is specified in Table 8.

Table 4 Weight of safety criteria

	The protection provided by helmet to absorb linear acceleration in normal impacts during accidents	The protection provided by helmet to absorb angular acceleration in oblique impacts during accidents	Sum	Weight
The protection provided by helmet to absorb linear acceleration in normal impacts during accidents	2	3	5	0.625
The protection provided by helmet to absorb angular acceleration in oblique impacts during accidents	1	1	3	0.375

Table 5 Overall impacts safety criteria on helmet selection

	The protection provided by helmet to absorb linear acceleration in normal impacts during accidents	The protection provided by helmet to absorb angular acceleration in oblique impacts during accidents	Overall impact
Airbag helmet	2.5	1.5	4
Shell helmet with EPS foam	1.25	0.375	1.625
Helmets with AIM system	1.875	1.125	3
Helmets with MIPS	1.875	1.125	3

Table 6 Scale of measurement

Safety	Scale
3.5–4.00	4
2.5–3.4	3
1.5–2.4	2
0.5–1.4	1

Table 7 Comparison matrix for safety criteria

Helmets	Safety
Airbag helmet	4
Shell helmet with EPS foam	2
Helmets with AIM system	3
Helmets with MIPS	3

Table 8 Comparison matrix for helmets

	Safety	Comfort	Field of vision	Hearing ability
Airbag helmet	4	3	4	4
Shell helmet with EPS foam	2	2	2	2
Helmets with AIM System	3	2	2	2
Helmets with MIPS	3	2	3	3

A normalized matrix is calculated by converting the above comparison matrix which is given in Table 9.

Step 5   Between the n rating criteria, pair-wise comparison of the comparative weight is defined. As a result an n-by-n matrix $A(a_{ij})$ is obtained with $i, j = 1, 2, 3,… n$) as shown in Table 10

Where a_{ij} represents the relative importance of criterion i with respect to criterion j which is defined by user and $a_{ij} = 1$, $a_{ij} > 0$, $a_{ij} = 1/a_{ij}$. Also, when $a_{ij} = a_{ij} = 1$ it indicates that i and j have equal relative importance.

Step 6   In this step, the consistency of the pair-wise comparison matrix is checked and the weight of different criteria considered is calculated which is

Table 9 Normalized matrix

	Safety	Comfort	Field of vision	Hearing ability
Airbag helmet	0.333	0.333	0.364	0.364
Shell helmet with EPS foam	0.167	0.222	0.182	0.182
Helmets with AIM system	0.250	0.222	0.182	0.182
Helmets with MIPS	0.250	0.222	0.273	0.273

Table 10 Pair-wise comparison matrix

	Safety	Comfort	Field of vision	Hearing ability
Safety	1	5	3	3
Comfort	1/5	1	1/3	1/3
Field of vision	1/3	3	1	1
Hearing ability	1/3	3	1	1

Table 11 Eigenvector of multiple criterions

	Safety	Comfort	Field of vision	Hearing ability	4th root	Eigenvector
Safety	1	5	3	3	2.5900	0.5206
Comfort	0.2	1	0.33	0.333	0.3859	0.0776
Field of vision	0.333	3	1	1	0.9997	0.2009
Hearing ability	0.333	3	1	1	0.9997	0.2009

discussed below. All the entries in a particular row of the matrix are multiplied and the nth root of the product is calculated, where n represents the order of the matrix. Then all the calculated roots are added. This sum of calculated roots is used for normalizing each nth root for findings Eigenvector for that particular row as shown in Table 11.

Check for consistency

Every row of the comparison matrix is likewise multiplied as the matrix multiplication with the appropriate vector column. Values obtained for all the four rows after multiplication are: 2.1139, 0.3154, 0.8079, and 0.8079, resp.

By dividing the above values by corresponding Eigenvectors corresponding value of λ is calculated. λ_{max} is then obtained by taking an average of all the four values of λ. Here $\lambda_{max} = 4.0425$.

Formula for Consistency Index (CI) is, $CI = (\lambda_{max} - n)/(n - 1) = 0.0142$, also Consistency Ratio $CR = CI/RI$ where, $RI =$ Random Index and for $n = 4$, $RI = 0.9$. Hence, $CR = 0.0157$. Since the Consistency Ratio is less than 0.10, it can be concluded that the judgment is consistent.

For calculating weighted values for each of the alternatives, Eigenvectors will act as the relative weights since CR is less than 0.10. Eventually, the total weighted score is calculated and the corresponding rank of each helmet is found out, which is given in Table 12.

Table 12 Final ranks of helmet

	Safety	Comfort	Field of vision	Hearing ability	Weighted score	Rank
Airbag helmet	0.3333	0.3333	0.3636	0.3636	1.3939	1
Shell helmet with EPS foam	0.1667	0.2222	0.1818	0.1818	0.7525	4
Helmets with AIM system	0.2500	0.2222	0.1818	0.1818	0.8359	3
Helmets with MIPS	0.2500	0.2222	0.2727	0.2727	1.0177	2

4 Discussions

In the study under consideration, problems faced by motorcycle riders while using helmets are identified and from the literature review, four helmet design concepts are shortlisted for evaluation. Kano model is used for identifying the needs or requirements of motorcycle helmets. The Analytical Hierarchy Process (AHP) method, in which these identified needs are taken as evaluation criteria, is used for analyzing the ranking of the selected motorcycle helmet design concepts and results are obtained. It is seen from the result that the Airbag helmet design concept gains the highest preferential rank, while Shell helmet with EPS foam gains the lowest rank.

In the case of safety criteria, the Airbag helmet is absorbing impact caused by linear and angular acceleration during an accident to a larger extent and hence gains the highest rank in safety criteria. Also, helmet with MIPS system and helmet with AIM system absorbs accidental impact due to slip plane mechanism and Aluminum Honeycomb structure, respectively. But in the case of a Shell helmet with EPS foam, there is no mechanism for absorbing impact. And hence it gains the lowest rank in safety criteria. On the various sub-criteria of comfort viz. ventilation, weight, comfort in carriage and storage of helmet, etc. the Airbag helmet is having exceptionally good performance than other alternatives.

As the Airbag helmet gets deployed only at the ultimate moment of the accident, its cent percent performance is obvious on the criteria of field of vision and hearing ability, whereas all the remaining helmets will perform almost equally well for these two criteria.

5 Conclusions

From the analysis, it is argued that the Airbag helmet functions more salutary than other types of helmets as it provides more safety, more comfort as well as better performance on the criteria of the field of vision and hearing ability. Since the Airbag helmet design is in its initial development phase, cost parameter has not been considered in this analysis. In the present field practice, though Nylon is the

most widely used Airbag material [21], it being non-biodegradable, there is a scope to work on some sustainable substitute like biodegradable synthetic fabric for it. Also, the uncoated Airbag is an environmentally friendly option where instead of coating weaved Airbag fabric with neoprene or silicon it is kept uncoated [21].

References

1. Government of India, Ministry of road transport and highways transport research wing (2018) Road accidents in India 2017, 13 Jan 2021. Retrieved from https://www.morth.nic.in/sites/default/files/Road_Accidents_in_India_2017.pdf
2. Government of India, Ministry of road transport and highways transport research wing (2019). Road accidents in India 2018, 13 Jan 2021. Retrieved from https://www.morth.nic.in/sites/default/files/Road_Accidednts.pdf
3. Singh D (2014) Effects of "Use Helmet" Campaign and helmet laws on helmet use among college students in India. Eur Acad Res II(2)
4. Faryabi J, Rajabi M, Alirezaee S (2014) Evaluation of the use and reasons for not using a helmet by motorcyclists admitted to the emergency ward of shahid bahonar hospital in Kerman. Arch Trauma Res
5. Dieter GE, Schmidt LC. Engineering design. McGraw-Hill, New York
6. Halldin P (2018) CEN/TC 158 working group 11 shock absorption including measuring rotational kinematics
7. Bourdet N, Deck C, Mojumder S, Willinger R (2018) Comparative evaluation of DOT vs. ECE motorcycle helmet test method. IRCOBI Conf
8. Informal Working Group on UN Regulation No. 22 (2019) Proposal for the 06 series of amendments of regulation No. 22 (PROTECTIVE HELMETS), 13 Jan 2021. Retrieved from https://unece.org/DAM/trans/doc/2019/wp29grsp/GRSP-66-22e.pdf
9. Kurt M, Laksari K, Kuo C, Grant GA, Camarillo DB (2017) Modelling and optimization of airbag helmets for preventing head injuries in bicycling. Ann Biomed Eng 45(4)
10. Hansen K, Dau N, Feist F, Deck C, Willinger R, Madey SM, Bottlang M (2013) Angular impact mitigation system for bicycle helmets to reduce head acceleration and risk of traumatic brain injury. Accid Anal Prev 59
11. Shoei-helmets, 13 Jan 2021. Retrieved from https://www.shoei-helmets.com/technology/inside-a-shoei-helmet.html
12. Bliven E, Rouhier A, Tsai S, Willinger R, Bourdet N, Deck C, Madey SM, Bottlang M (2019) Evaluation of a novel bicycle helmet concept in oblique impact testing. Accid Anal Prev 124
13. RVE bike, 6D Helmets ATR-1Y Macro Youth Helmet, 13 Jan 2021. Retrieved from https://www.rvebike.com/product/6d-helmets-atr-1y-macro-youth-helmet-379207-1.htm
14. Cripton PA, Dressler DM, Stuart CA, Dennison CR, Richards D (2014) Bicycle helmets are highly effective at preventing head injury during head impact: Head-form accelerations and injury criteria for helmeted and unhelmeted impacts. Accid Anal Prev 70
15. Fahlstedt M, Halldin P, Kleiven S (2014) Importance of the bicycle helmet design and material for the outcome in bicycle accidents. In: Proceedings, international cycling safety conference, Sweden
16. Stigson H, Rizzi M, Ydenius A, Engstrom E, Kullgren A (2017) Consumer testing of bicycle helmets. IRCOBI Conf
17. Lin F-H, Tsai S-B, Lee Y-C, Hsiao C-F, Zhou J, Wang J, Shang Z (2017) Empirical research on Kano's model and customer satisfaction. PLoS ONE 12(9):1325–1330
18. Madzik P, Budaj P, Mikulas D, Zimon D (2019) Application of the kano model for a better understanding of customer requirements in higher education—a pilot study. Adm Sci (9)
19. Singh RK, Kulkarni M (2013) Criticality analysis of power—plant equipments using the analytic hierarchy process. Int J Indus Eng Technol (IJIET). ISSN 2277-4769 3(1–14)

20. Sumperet A (2010) Methodology for the assessment of the impact of existing high voltage lines in urban areas. Energy Policy386,036–386,044
21. Yao G (2015) Development of airbag fabrics by polyester filament. In: 3rd International conference on material, mechanical and manufacturing engineering

Optimization of Electrodischarge Machining Parameters Using Non-traditional Optimization Techniques

Kaushik Agarwal, Shishir Joshi, Divyansh Asudani, Dixit Savani, Deep Patel, Ashish R. Prajapati, Keyur P. Desai, and Harshit K. Dave

1 Introduction

Electrodischarge machining (EDM) has become a widely used non-traditional machining process. It is a thermoelectric process, during which a number of sparks are generated which leads to the removal of material from the workpiece. During this process, the dielectric liquid is employed, and also, the electrode and work material is immersed therein medium. These discharges evaporate a little amount of the workpiece's material, which is then washed away. The ability to process conductive specimens regardless of hardness with heat energy was a huge benefit in precision tooling and mould production. The EDM process is unaffected by the mechanical properties of the workpiece material, such as strength and brittleness, which is a significant advantage. Although a product's quality is important for a company's survival, material qualities and process parameters are as important in determining end product quality and manufacturing costs. To achieve the most efficient manufacturing conditions, process parameters must be optimized. The final product's quality is largely determined by the material and process characteristics. Conventional electrodes are used to drill a wide range of holes in orbital EDM. The gap between the electrode and the hole is greater here, which aids in the dielectric's induction to the rock bottom point of the exit. Due to the higher flushing of dielectric fluid, the recasting of removed material is reduced, which results in better surface properties of the workpiece. Overcut (OC), surface roughness (Ra) and tool wear rate (TWR)

K. Agarwal · S. Joshi (✉) · D. Asudani · D. Savani · D. Patel · A. R. Prajapati · K. P. Desai · H. K. Dave
Department of Mechanical Engineering, SVNIT, Surat, Gujarat, India

K. P. Desai
e-mail: kpd@med.svnit.ac.in

H. K. Dave
e-mail: hkd@med.svnit.ac.in

© The Author(s), under exclusive license to Springer Nature Singapore Pte Ltd. 2022
S. Kumar et al. (eds.), *Recent Advances in Manufacturing Modelling and Optimization*, Lecture Notes in Mechanical Engineering,
https://doi.org/10.1007/978-981-16-9952-8_30

are the foremost significant response parameters in the EDM process while lower values of OC and Ra are essential for the EDM process.

In the EDM process, the impact of processing factors on various response characteristics varies. Hence, the selection of an optimum combination of process parameters is difficult. As a result, an optimization approach is critical for this problem. Several researchers have conducted various studies to reinforce the performance of the EDM process using differing types of optimization techniques. Still suitable selection of processing parameters to realize the foremost effective process performance may well be a difficult task.

Several scholars have attempted to improve the EDM process using traditional optimization methods. El-Taweel [1], Tzeng and Chen [2] worked on response surface methodology, Luis et al. [3] performed multivariate analysis, and Taguchi analysis was administered by Kao et al. [4]. Traditional optimization techniques can only discover the best set of specified processing parameter combinations. As a result, if the best process parameter settings aren't found inside the provided parameter level combination, these procedures aren't the best option. Non-traditional optimization strategies frequently overcome the obstacles that traditional optimization approaches confront. Firefly algorithm (FA), particle swarm optimization (PSO), Rao algorithm, Jaya algorithm, genetic algorithm (GA) and teaching learning-based algorithm (TLBO) are a variety of non-traditional optimization techniques.

The genetic algorithm is a well-known optimization tool with numerous technical applications. Khalid [5] developed the idea of Electrical Discharge Machine utilizing Fuzzy Fitness Evolutionary Strategies Optimization (EDiMfESO), which he effectively optimized in terms of MRR, Ra, overcut (OC) and tool wear rate (TWR). The teaching–learning-based optimization (TLBO) algorithm, developed by Rao et al. [6], does not require any algorithm-specific parameters. Only a few basic controlling parameters, such as population size and generation number, are required for the TLBO algorithm to function. The TLBO method has gained a lot of traction among optimization specialists. Kennedy and Eberhart invented the particle swarm optimization (PSO) method, which is a metaheuristic algorithm based on the concept of swarm intelligence capable of tackling complicated mathematics problems in engineering [7]. The firefly algorithm (FA) was created in Cambridge by Xin-She Yang in 2008 and reported in Yang [8]. A metaheuristic algorithm is what it is. This algorithm is influenced by the flashing habit of fireflies to attract one another. Rao and more presented the self-adaptive Jaya method, which changes population sizes at random [9]. The SAMP-Jaya algorithm, which is a self-adaptive multi-population-based Jaya algorithm, was presented by Rao and Saroj [10]. The population was divided into varied numbers of sub-populations during this variant of the Jaya algorithm. The number of sub-populations was automatically updated when the fitness value increased. An alternative technique called the 'self-adaptive population Rao algorithm' is offered to avoid the need for population size adjustment. Rao algorithms were the inspiration for this algorithm. The Rao algorithms (Rao-1, Rao-2 and Rao-3) are three algorithm-specific parameter-less algorithms suggested by Rao

[11]. Rao algorithms are metaphor-less algorithms. These algorithms move the population throughout the search space based on population interactions with best, worst and randomly chosen solutions.

Mandal et al. [12] employed the non-dominating sorting genetic algorithm-II (NSGA-II) to optimize the EDM process parameters. Joshi and Pande [13] employed GA and artificial neural networks (ANN) to optimize input parameters in the EDM process for higher MRR and reduced TWR. Teimouri and Baseri [14] dispensed optimization using backpropagation neural network (BPNN) and ABC algorithm for dry EDM process. Dave [15] dispensed optimization of MRR was administered for helical path orbital EDM process of AISI 304 and Inconel 718 by TLBO and PSO techniques and performance of both the algorithms compared in terms of precision and rate of convergence. Das et al. [16] used weighted principal component analysis (WPCA) to optimize the multi-responses, viz. overcut and surface roughness in the EDM process. Majumder [17] made a trial to optimize the EDM performance using three algorithms, viz. SA, GA and PSO. They found that the performance of PSO is best as compared to other two algorithms. Aich and Banerjee [18] conducted research on the EDM process using various combinations of processing parameters, including current and pulse time MRR, as well as surface roughness.

According to a literature review, traditional and non-traditional optimization strategies were used to get the best outcomes for various EDM processes and variation responses. Traditional optimization methods can suffer from the drawback of locally optimal solutions, resulting in lower accuracy of the results.

In recent years, several non-traditional optimization methods are applied to optimize the EDM parameters, but the use of TLBO, PSO, Rao, Jaya and firefly algorithms is restricted. Therefore within the present work, one case study has been taken within which helical path orbital EDM process was disbursed to work out the influence of processing parameters, viz. current (I_p), pulse ON time (T_{on}), pulse OFF time (T_{off}), orbital speed (S_o), orbital radius (S_r), on the OC and Ra. The single-objective optimization problem and multiple optimization problem of helical path orbital EDM process are formulated to support experimental data and solved using five computational intelligent algorithms, viz. TLBO, PSO, Rao, Jaya and firefly.

2 Non-traditional Optimization Tools

We, individuals, have a natural tendency to follow the nature the character has solved complicated optimization problems, whenever we tend to fail to resolve them using traditional optimization ways. Some natural processes, like biological and physical processes are modelled by artificial means to develop optimization tools for determining the problems. An enormous literature is offered on non-traditional optimization tools. These ways involve teaching–learning-based optimization (TLBO), Jaya algorithm, Rao algorithm, firefly algorithm (FA), particle swarm optimization (PSO), evolutionary programming (EP), Tabu search and others. The operating principles of the number of these non-traditional optimization tools are explained below, in brief.

2.1 Optimization Algorithms

Most of the difficulties in the analysis, design, manufacturing and related problems can eventually be broken into the objective of determining the maximum and minimum values of the function. Optimization basically means achieving the best results in the provided set of constraints. For most design tasks, the ultimate goal is to simply maximize production efficiency or minimize manufacturing costs. The usage of optimization methods has many applications and can solve complex problems efficiently. In the past few years, various new optimization methods, viz. TLBO, PSO, Rao, Jaya and FA, have been identified.

2.1.1 Teaching–Learning-Based Optimization (TLBO)

Rao has established TLBO algorithms to solve optimization problems in various areas. It was tested on the standard benchmarking feature. They tested the TLBO optimization technique on numerous problems in various areas to check whether the results achieved were better than other evolutionary methods. In a few iterations, it was reported that the TLBO technique provided superior results as compared to other methods. Also, the TLBO algorithm did not need particular algorithm control factors.

The TLBO process consists of two parts. The first part contains the teacher stage, and the second part of the algorithm contains the student stage, respectively. In the teaching phase, students gather knowledge from the teachers, while in the student phase, students gather knowledge through the communications between themselves. TLBO algorithm steps to employ the optimization are:

Step 1 Initialization of input parameters of the algorithm.
Step 2 Create the population as per the number of design variables.
Step 3 Calculate the suitability of the population's viable solutions and place the solutions as per their fitness level.
Step 4 Change the result using the model of the learning of the students from the teacher.
Step 5 Change the result using the model of the learning of the students through their interaction.
Step 6 Repeat the process until the best solution is achieved.

2.1.2 Particle Swarm Optimization (PSO)

PSO is a widely known optimization technique which ensures the best combination of input processing conditions. It is motivated by the intelligence of swarm populations. In the year 1992, James Kennedy proposed the PSO algorithm. Genetic algorithms and evolution strategies were used in PSO. One can achieve better convergence and faster results in the least number of iterations through this algorithm. PSO technique

is centred on the computer simulations of the motion of organisms, namely schools of fish and flocks of birds. PSO uses a population of search points to examine the problem space. Each element tracks its coordinates in problem space and is referred to as a particle. To perform the optimization by PSO algorithm, the following steps are employed:

Step 1 Parameter limits are selected between the lower and higher values.
Step 2 The particle velocity created is randomly selected between the particle's higher and lower values.
Step 3 Next, the values of the objective function are calculated.
Step 4 Then, for the new particle position, the values of the function are again calculated.
Step 5 This procedure is repeated until the final solution has been achieved.

2.1.3 RAO Algorithm

Let $f(z)$ be the minimized objective function (or maximized). Assume that there are 'm' number of design variables and 'n' number of candidate solutions (i.e. population size, $s = 1, 2, …, n$) at any iteration p. Let the most effective candidate gets the most effective $f(z)$ result (i.e. $f(z)$best) in the complete candidate solutions, and the worst candidate gets the worst $f(z)$ result (i.e. $f(z)$worst) in the entire candidate solutions. If the result of the qth variable for the sth candidate during the pth iteration is Zq, s, p, then the result is altered according to the following equation.

$$Z'q, s, p = Zq, s, p + r1, q, p(Zq, \text{ best, } p - Zq, \text{ worst, } p)$$

Step 1 Initialization population, number of design variable and termination criteria.
Step 2 Recognize the best and worst of the population.
Step 3 Change the solution formed on a best and worst solution and random interaction.

$$Z'q, s, p = Zq, s, p + r1, q, p(Zq, \text{ best, } p - Zq, \text{ worst, } p)$$

Step 4 Change the result.
Step 5 Repeat the process until the best solution is achieved.

2.1.4 Jaya Algorithm

Let $f(z)$ be the minimized objective function (or maximized). Assume that there are 'm' number of design variables (i.e. $q = 1, 2, …, m$) and 'n' number of potential solutions (i.e. population size, $s = 1, 2, …, n$) at any iteration p. Let the most effective candidate gets the most effective $f(x)$ result (i.e. $f(z)$best) within the complete

candidate solutions, and the worst candidate gets the worst $f(z)$ result (i.e. $f(z)$worst) within the entire candidate solutions. If the result of the qth variable for the sth candidate during the pth iteration is Zq, s, p, then the result is altered according to the following equation.

$$Zq, \ s, \ p = Zq, \ s, \ p + r1q, \ p(Zq, \ best, \ p - |Zq, \ s, \ p|)$$
$$- r2, \ q, \ p(Zq, \ worst, \ p - |Zq, \ s, \ p|)$$

Step 1   Initialization population, number of design variables and termination criteria.
Step 2   Recognize the best and worst of the population.
Step 3   Change the solution formed on a best and worst solution and random interaction.

$$Z'q, \ s, \ p = Zq, \ s, \ p + r1q, \ p(Zq, \ best, \ p - |Zq, \ s, \ p|)$$
$$- r2, \ q, \ p(Zq, \ worst, \ p - |Zq, \ s, \ p|)$$

Step 4   Change the result.
Step 5   Repeat the process until the best solution is achieved.

2.1.5   Firefly Algorithm

Firefly algorithm (FA) is a metaheuristic algorithm. The flashing behaviour of fireflies to attract each other influences this algorithm. There are three rules that support it:

(i)   Because all fireflies are unisex, one attracts all auxiliary fireflies.
(ii)   A firefly's attraction is proportionate to its brightness. The fainter of two fireflies is attracted to (and hence goes towards) the brighter one. If there are no fireflies brighter than a certain firefly, then firefly will move at random.
(iii)   The brightness of a firefly decreases because the distance from it will increase. Light is absorbed after it travels through the medium, which causes this. As a result, the equation specifies the brightness (and attractiveness) of the firefly j as viewed by the firefly i.

$$\beta j(r) = \beta j(0)e - \gamma r2$$
$$r = |xi - xj| = [d\Sigma k = 1(xki - xkj)2](1/2)$$

where γ is a light absorption coefficient of the medium, r is the Euclidean distance between the firefly i and the firefly j, $\beta j(0)$ is the brightness of the firefly j at $r = 0$, and xi and xj are the locations of the fireflies i and j, respectively.

Step 1   Initialization population with objective function formulation.
Step 2   Calculate the fitness of each function of the firefly.

Step 3   Selection of best firefly with updated position.
Step 4   Evaluate attractiveness and update the intensity of light.
Step 5   Rank the fireflies and choose the best one.
Step 6   Repeat the process until the best solution is achieved.

3   Case Study

Major response parameters, viz. OC and Ra, during the EDM process are optimized using five computational intelligence optimization algorithms, TLBO, PSO, firefly, Rao and Jaya. A case study based on the previous work of Sudhanshu [19] on helical path orbital EDM is considered for optimization in the present study. The effect of five machine process parameters, viz. current (I_p), pulse ON time (T_{on}), pulse OFF time (T_{off}), orbital speed (S_o) and orbital radius (S_r), was investigated. Table 1 depicts the values of the parameters:

3.1   Objective Function

For the optimization of OC and Ra of EDM process, the fitness function model is determined by regression analysis. The functional relationship of both overcut and surface roughness individually and input parameters can be proposed using the following equations.

Surface roughness

$$Ra = 2.096 + 0.088 * (x(1))0.01633 * (x(2)) + 0.0511 * (x(3)) + 48.1 * (x(4))$$
$$+ 0.00004 * (x(2)).^2 + 0.000699 * (x(1)) * (x(2)) - 0.595 * (x(3)) * (x(4)); \tag{7}$$

Overcut

Table 1 Selected parameters with their levels

Parameters	Level		
	1	2	3
Current Ip [A]-(×1)	6	13	21
Pulse ON time Ton [µs]-(×2)	75	195	315
Pulse OFF time Toff [µs]-(×3)	32	82	135
Orbital Speed So [mm/s]-(×4)	0.05	0.09	0.13
Orbital Radius Sr [mm]-(×5)	0.50	1.00	1.50

$$OC = 0.0489 + 0.00043 * (x(1)) + 0.000017 * (x(2)) + 0.00057 * (x(3))$$
$$+ 0.498 * (x(4)) - 0.0068 * (x(5)) - 0.000132 * (x(1)).^2$$
$$+ 0.0275 * (x(5)).^2 + 0.000019 * (x(1)) * (x(2)) - 0.000075 * (x(2)) * (x(5))$$
$$- 0.00653763 * (x(3)) * (x(4)) \tag{8}$$

The bounds for the six variables are given in Eqs. (9) to (13).

$$6 \leq I \leq 21(A) \tag{9}$$

$$75 \leq t_{on} \leq 315(\mu s) \tag{10}$$

$$32 \leq t_{off} \leq 135(\mu s) \tag{11}$$

$$0.05 \leq So \leq 0.13(mm/s) \tag{12}$$

$$0.5 \leq Sr \leq 1.5(mm) \tag{13}$$

4 Single Objective Optimization

In the present work, optimization of OC and Ra has been carried out using five optimization techniques, viz. TLBO, Jaya, firefly, Rao and PSO. In TLBO, Jaya and RAO, there are only two parameters, viz. size of population and generation number, which are 10 and 30, respectively. While in the case of PSO, apart from these two parameters, other algorithm-specific parameters such as inertia coefficient, damping coefficient, personal acceleration coefficient and social acceleration coefficient also have to be defined, which are taken as 0.7, 0.8, 1.5 and 1.5, respectively. Similarly, in firefly algorithm, attraction coefficient base value, light absorption coefficient, mutation coefficient, mutation coefficient damping ratio are 2,1,0.2 and 0.98, respectively. The results of optimization of Ra and OC of EDM process using all above-stated algorithms are presented in Table 2.

In order to identify the best serving algorithm among the above discussed five algorithms, the basis of comparison can be brought down to two major characteristics, namely convergence of curve and success ratio.

Success ratio: It corresponds to the ratio of the frequency of minimum values of surface roughness or overcut obtained to the number of total iterations being carried out.

Convergence curve: It is a comparison of the stated minimum value obtained in the least number of iterations. The corresponding graphs of surface roughness and overcut are shown in Fig. 1

Table 2 Single objective optimization results

Optimization methods	Response	Value	Peak current	Pulse ON time	Pulse OFF time	Orbital speed	Orbital radius	Success ratio
TLBO	OC	0.05853	21	75	135	0.13	0.50	0.3667
	Ra	4.4127	6	151.7	135	0.13	–	0.2333
PSO	OC	0.05853	21	75	135	0.13	0.50	0.2333
	Ra	4.4127	6	151.7	135	0.13	–	0.5667
RAO	OC	0.05853	21	75	135	0.13	0.50	0.6
	Ra	4.4127	6	151.7	135	0.13	–	0.6
Jaya	OC	0.05853	21	75	135	0.13	0.50	0.7333
	Ra	4.4127	6	151.67	135	0.13	–	0.5667
FA	OC	0.05853	21	75	135	0.13	0.50	0.7333
	Ra	4.4127	6	151.7	135	0.13	–	0.5333
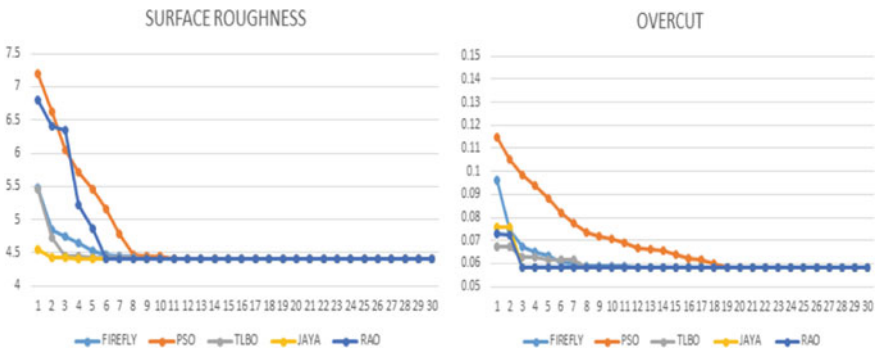
Fig. 1 Convergence curve

For both the objectives (minimization of surface roughness and overcut), the convergence curve shows that the Jaya algorithm has succeeded in achieving a minimum value 0.058535 µm (overcut) and 4.4137microns (surface roughness) in the least number of iterations. Moreover, the Jaya algorithm has shown maximum repeatability of the best result, as evident from the success ratio mentioned in Table 2.

5 Multi-objective Optimization

Finding a vector of decision variables while simultaneously optimizing (i.e. minimizing or maximizing) numerous objectives with a given set of constraints is known as multi-objective optimization. In this paper, two such objectives are examined simultaneously for multi-objective optimization, namely minimizing OC and Ra.

Table 3 Multi-objective optimization results at $B = 0.4$

Optimization method	Response	Value	Peak current	Pulse ON time	Pulse OFF time	Orbital speed	Orbital radius
TLBO	OC	0.0912	6	149.947	135	0.13	0.5
	Ra	4.4128					
PSO	OC	0.0913	6	150.535	135	0.13	0.5
	Ra	4.4128					
RAO	OC	0.0912	6	149.9496	135	0.13	0.5
	Ra	4.4129					
Jaya	OC	0.0911	6	149.0537	135	0.13	0.5
	Ra	4.4128					
FA	OC	0.0911	6	150.065	135	0.13	0.5
	Ra	4.413					

For multi-objective optimization, the weight technique is used in the current work. For multi-objective optimization, the objective functions from the previous section are combined. The following equation gives the normalized multi-objective function (f), which is formed by allocating distinct weight factors to various objectives:

$$f = A * (OC) + B * (Ra)$$

where A = constant between 0 and 1 $B = 1 - A$.

Table 3 shows this multi-objective optimization results obtained using the TLBO, PSO, RAO, FA and Jaya algorithm (Fig. 2).

Eventually, all algorithms provide similar results from the graph and we can see the most promising minimization is achieved when the weighted factor of Ra lies between 0.4 and 0.5. But drawing the curve similar to Pareto charts provides flexibility to users to observe the nature of curves and select different weighted factors that fulfil the requirement of different jobs easily.

6 Conclusion

The identification of optimal parameters for minimization of Ra and Oc on the work processed from raw AISI sheet fed to electric discharge machine was done using different non-traditional optimization techniques. Using these techniques, various combinations of process parameters, i.e. Ton, Toff, So and Sr, were obtained and different graphs were plotted to observe the trends. It was evident from the convergence curve of all the five algorithms for single-objective optimization, Jaya stands out by achieving the optimum value in the least number of iterations. The success ratio of all five algorithms further props up the superiority of the Jaya algorithm by achieving the highest success ratio. For multi-objective optimization, the most
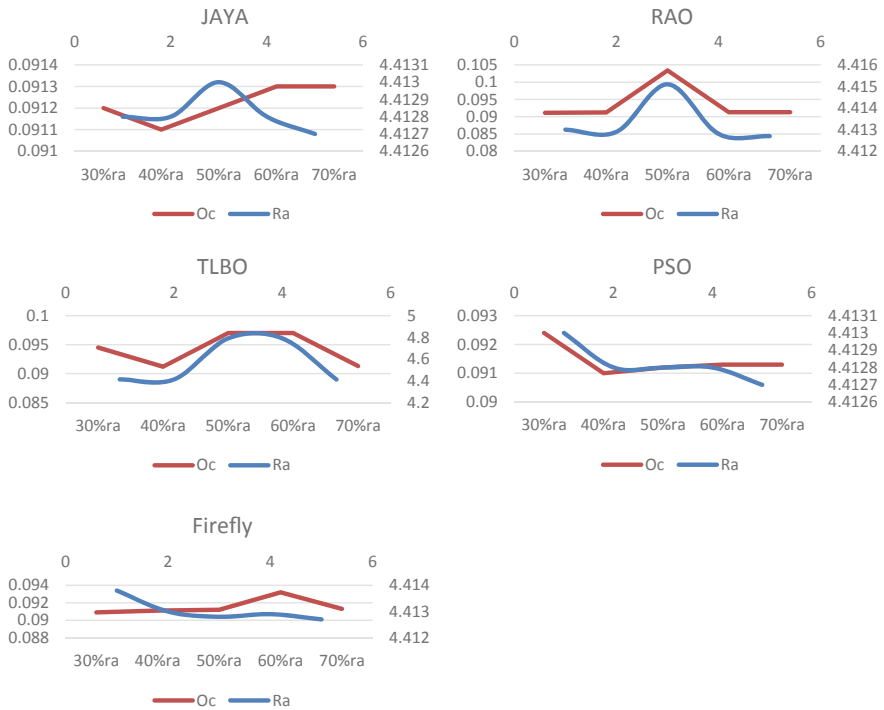
Fig. 2 Multiple objective optimization results

promising minimization for all algorithms is achieved when the weighted factor of Ra lies between 0.4 and 0.5. Moreover, the graph obtained as a result of multi-objective optimization serves to cater with different work requirements and hence provides flexibility to choose a vast range of parameter weightage.

References

1. El-Taweel TA (2009) Multi-response optimization of EDM with Al–Cu–Si–TiC P/M composite electrode. Int J Adv Manuf Technol 44(1–2):100–113
2. Tzeng CJ, Chen RY (2013) Optimization of electric discharge machining process using the response surface methodology and genetic algorithm approach. Int J Precis Eng Manuf 14(5):709–717
3. Luis CJ, Puertas I, Villa AG (2005) Material removal rate and electrode wear study on the EDM of silicon carbide. J Mater Process Technol 164:889–896
4. Kao JY, Tsao CC, Wang SS, Hsu CY (2012) Optimization of the EDM parameters on machining Ti–6Al–4V with multiple quality characteristics. Int J Adv Manuf Technol 47(1–4):395–402
5. Khalid NEA (2011) EDM using fuzzy for fitness evolutionary strategies optimization. In: Proceedings of the 15th WSEAS international conference on Computers, Corfu Island, Greece, 14–16 July 2011, pp 334–339

6. Rao RV, Savsani VJ, Vakharia DP (2011) Teaching–learning-based optimization: a novel method for constrained mechanical design optimization problems. Comput Aided Des 43(3):303–315

7. Kennedy J, Eberhart R (1995) Particle swarm optimization. In: Proceedings of ICNN'95—international conference on neural networks, vol 4, pp 1942–1948. https://doi.org/10.1109/ICNN.1995.488968

8. Yang XS (2009) Firefly algorithms for multimodal optimization. In: Watanabe O, Zeugmann T (eds) Stochastic algorithms: foundations and applications. SAGA 2009. Lecture notes in computer science, vol 5792. Springer, Berlin, Heidelberg. https://doi.org/10.1007/978-3-642-04944-6_14

9. Rao V, Ravipudi, More K (2017) Design optimization and analysis of selected thermal devices using self-adaptive Jaya algorithm. Energy Convers Manage 140:24–35. https://doi.org/10.1016/j.enconman.2017.02.068

10. Rao V, Ravipudi, Saroj A (2017) A self-adaptive multi-population based Jaya algorithm for engineering optimization. Swarm Evol Comput 37. https://doi.org/10.1016/j.swevo.2017.04.008

11. Rao V, Ravipudi (2020). Rao algorithms: three metaphor-less simple algorithms for solving optimization problems. Int J Indus Eng Comput 107–130. https://doi.org/10.5267/j.ijiec.2019.6.002

12. Mandal D, Pal SK, Saha P (2007) Modelling of electrical discharge machining process using back propagation neural network and multiobjective optimization using non-dominating sorting genetic algorithm-II. J Mater Process Technol 186(1–3):154–162

13. Joshi SN, Pande SS (2011) Intelligent process modeling and optimization of die-sinking electric discharge machining. Appl Soft Comput 11(2):2743–2755

14. Teimouri R, Baseri H (2012) Improvement of dry EDM process characteristics using artificial soft computing methodologies. Prod Eng Res Dev 6:493–504

15. Dave HK (2019) Optimization of orbital electro discharge machining parameters using tlbo and pso algorithms Vol. XI, No. 2/2019. Int J Mod Manuf Technol

16. Das MK, Kumar K, Barman TK, Sahoo P (2013) Optimization of surface roughness and MRR in EDM using WPCA. Procedia Eng 64:446–455

17. Majumder A (2015) Comparative study of three evolutionary algorithms coupled with neural network model for optimization of electric discharge machining process parameters. Proc Inst Mech Eng Part B J Eng Manuf 229(9):1504–1516

18. Aich U, Banerjee S (2016) Application of teaching learning based optimization procedure for the development of SVM learned EDM process and its pseudo Pareto optimization. Appl Soft Comput 39:64–83

19. Kumar S, Dave HK, Desai KP (2016) Experimental investigation on performance of different tool movement strategies in EDM process for boring operation. Int J Adv Manuf Technol 87(5–8): 1609–1620

Performance Improvement in Construction Industry by Using TOPSIS Method for Brick Material Supplier Selection

Sanket D. Alone, Pramod Naik, V. M. Athawale, and D. N. Raut

1 Introduction

Construction projects in today's world are becoming more and more intricate due to increased competition and consumer demands for better modern amenities, and to make completion of project possible in time, supply chain management has become crucial. Supply chain is the various linkages which are interconnected that facilitate swift and continuous flow of material according to the demand that emerges in the industry. The role of the supply chain management (SCM) in procurement of raw material for construction makes it important for maintaining the quality of the finished product and helps in increasing the profitability of the organization through the project. A construction project becomes successful by perfect collaboration between engineers, clients, contractors, and suppliers. Due to coordination between various stakeholders of the project and proper supply chain management, project attains its decided objectives. In every industry, a successful project is resultant of every factor working in the right direction during its each and every phase. As recent studies highlight, more than half of the project cost in construction project is done on the raw materials required for building purpose. If the procurement of these raw materials is done in the proper way using supply chain networks and considering its expenditure during the planning phase, then most appropriate supplier for particular raw material can be selected based on criterions previously decided, and due to that required quality can be achieved, and efficiency in the project can be improved. Supply chain management helps to make the process of procurement of materials cost-effective and on time. Supplier selection plays a momentous role in deciding the profitability of the project from organization point of view. Selection of raw material for construction purpose is crucial from the viable from the point of view

S. D. Alone (✉) · P. Naik · D. N. Raut
Department of Production Engineering, VJTI, Mumbai, India

V. M. Athawale
Department of Mechanical Engineering, Government College of Engineering, Nagpur, India

of maintaining customers trust. Proper evaluation and selection of building material supplier can increase product quality, reduce defects, and optimize costs. To select good material suppliers, determining core criteria for evaluating them is one of the most crucial economic decisions in the success of any construction contractors. As Majority of the research papers discusses about the quality, cost, and service as the most predominant factors for selection of supplier. The responses and suggestions provided by the experts are studied and reviewed.

The supplier selection problem is complicated due to the various aspects involved in it. The quality of the construction material becomes the most important aspect, there after comes the cost and least importance given to supplier relation. In this research, survey was undertaken involving civil engineering field experts to know about the most predominant criterions for selection of construction materials, in this case bricks. TOPSIS method was used to solve the issues related to supplier selection and ranking the supplier alternatives based on various criterions. While creating a supplier survey for the purchaser, it is to be decided which quality parameter to include. For most of times, quality, cost, and delivery time would be enough criterions, but for carrying out more critical and detailed survey in terms of supplier, a more advanced analysis covering more details of supplier alternatives need to be done. Many researchers in the field of supplier selection methods have come to the conclusion that there is no single approach as the best for the selection of alternatives from a given set, but different approaches should be used according to the situation. The prime objective of this research is to select the most appropriate supplier for supplying bricks for building construction purpose from the given set of criterions and alternatives.

DiakoulakiI et al. [1] discussed the use of critic method for selection of alternatives, critic method can be viewed as an promising method for weihts calculation. Khyomesh et al. [2] explained if the procurement of raw material required is done properly, then the productivity and efficiency of the project can be improved to great extent. Vimal et al. [3] applied TOPSIS method for selecting supplier in a manufacturing industry, and it proved to be a beneficial method. Don Amila Sajeevan Samarasinghe et al. [4] suggested an interplay between the measurable and non-measurable criteria which are important for selecting the best supplier. Review of supplier selection methods for the construction industry is carried out in this paper. Bhatt Rajiv and Bhatt Darshana [5] have listed seven criteria such as technical competence, financial competence, commercial and skilled management, quality, cost, delivery time, and trust for appropriate supplier determination. In this, TOPSIS and VIKOR methods are applied for best supplier selection. Renato Krohling and André Pacheco [6] proposed a method based on TOPSIS for carrying out ranking for supplier selection and compared algorithms based on it. The preceding work on taking decision for supplier selection issues has been revised, focusing on evaluation of decision matrix. Jitendra Kumar et al. [7] studied selection of refrigerant using TOPSIS, multicriteria approach to handle complex situations with multiple objectives, including the inaccurate and uncertain information. Esra Aytaç Adalı and Ayşegül TuşIşık [8] applied multi-attribute utility theory (MAUT) which is used for ranking alternatives, and CRITIC method is used for weighting criterions to solve selection problem for

contract manufacturer. Ayşegül Tuşlşık and Esra Aytaç Adalı [9] deal with the selection of apple which is most preferred among the alternatives for the production of apple juice is a complex task for food companies which is mainly based on acidity level and sweetness of processed product. Entropy method is used for determining the weights of different criterions. And ROV is used as ranking method. Girish Bhole and Tushar Deshmukh [10] give information about the application of various MCDM methods for their use in various scenarios where decision maker needs to know about characteristics of the method. Josy George et al. studied supplier selection decision-making problem in which both factors influencing quality and quantity are included. For selection of supplier, various methods and techniques have been developed for evaluation of supplier. Rabieha et al. [11] considered the criterions for supplier selection and also to determine the allocation of the resources so that optimum performance is ensured from the process as a whole. Roman Vavrek [12] dealt with TOPSIS method along with other methods, which is usually in association with use of several subjective and objective methods for their use in determination of weights of selected criteria. Yadav et al. [13] The Lean manufacturing process is observed for its application in various organizations. In this paper, hybrid fuzzy AHP and DEMATEL tools were used to identify and to evaluate the connections that exists among the various factors for application of Lean manufacturing. Pallav Kaneriya and Ankit Patel [14] pointed out that in construction industry, material cost is crucial in terms of project success. 10–12% cost is saved due to material management and purchase. Detailed study of factors mainly depicts factors affecting supplier selection in contractor companies. Deng et al. [15] Deng Entropy discusses the unique weighting approach used to calculate relative importance.

2 Methodology

2.1 CRITIC Method

The criteria importance through inter-criteria correlation method relies on the standard deviation proposed by Diakoulakil et al. [1] which uses correlation analysis to calculate the value of every criterion. The method primarily used to analyze the correlation to search for the disparity among various criterions. CRITIC method involves following steps:

It is assumed that there is collection of finite possible alternatives A_i^* and selected determination criteria C_{rj} within the problem.

1. The decision-making matrix X bears a resemblance to the effectiveness of various choices with comparison to other criterions that are used in the supplier selection problem.

$$X = \left[a_{ij}\right]_{m \times n} = \begin{bmatrix} a_{11} & \cdots & a_{1n} \\ \vdots & \ddots & \vdots \\ a_{m1} & \cdots & a_{mn} \end{bmatrix} \tag{1}$$

a_{ij} represents the effectiveness value of ith choice with respect to jth criterion.

2. The normalization of decision matrix is obtained using following equation:
    Beneficial criteria,

$$a^*_{ij} = \frac{a_{ij} - \min\left(a_{ij}\right) -}{\max\left(a_{ij}\right) - \min\left(a_{ij}\right)} \tag{2}$$

Non-beneficial criteria,

$$a^*_{ij} = \frac{\max\left(a_{ij}\right) - a_{ij}}{\max\left(a_{ij}\right) - \min\left(a_{ij}\right)} \tag{3}$$

where a^*_{ij} is the effectiveness value that is normalized for ith alternative with respect to jth criterion.

3. For determination of weightage of different factors, the variance of the criterion is obtained. Also, its relation with other criteria is checked. The weight of the jth criterion (w^*_j) is calculated as:

$$\sigma^*_j = \sqrt{\frac{\sum_{i=1}^{m}\left(r_{ij} - r_j\right)^2}{m}} \tag{4}$$

Correlation between criterions is included $= r_j$, correlation matrix criteria.

$$w^*_j = \frac{C_{rj}}{\sum_{j=1}^{n} C_j} \tag{5}$$

C_{rj} is the amount of details included in jth criterion determined as:

$$C_{rj}\sigma^*_j \sum_{j=1}^{n}\left(1 - r_j\right) \tag{6}$$

where σ_j is variance of the jth criterion and r_j is the parametric statistic matrix between the two criteria. The more the value of C_{rj} resembles that more amount of data is obtained from that particular criterion that ultimately means that the significance in relation with other is higher.

2.2 ENTROPY Method

Entropy method (Deng et al. [15]) is presented in the following steps. The initial assumption is that there is collection of finite possible alternatives, A_i^* and selected determination criteria C_{rj} within the problem.

The decision-making matrix X resembles the effectiveness of various choices with comparison to other criterions.

$$X = \begin{bmatrix} a_{11} & \cdots & a_{1n} \\ \vdots & \ddots & \vdots \\ a_{m1} & \cdots & a_{mn} \end{bmatrix} \tag{7}$$

a_{ij} represents the effectiveness value of ith choice with respect to jth criterion. The normalization of decision-making matrix is done based on beneficial and non-beneficial criteria.

Beneficial (maximization) criteria

$$r_{ij}^* = \frac{a_{ij} - \min(a_{ij})}{\max(a_{ij}) - \min(a_{ij})} \tag{8}$$

Non-beneficial (minimization) criteria

$$r_{ij}^* = \frac{\max(a_{ij}) - a_{ij}}{\max(a_{ij}) - \min(a_{ij})} \tag{9}$$

1. For each criterion, entropy values (e_j) are determined using equation stated below:

$$e_j^* = -\frac{\sum_{j=1}^m f_{ij}^* \ln f_{ij}^*}{\ln m} \text{ where } f_{ij}^* = \frac{r_{ij}^*}{\sum_{i=1}^m r_{ij}^*} 1 < e_j^* < 2 \tag{10}$$

In case, when all the f_{ij}^* values are equal, then max value for each criterion can be obtained.

2. The weights can be obtained by using

$$w_j^* = \frac{1 - e_j^*}{\sum_{j=1}^m 1 - e_j^*} \tag{11}$$

Entropy value resembles degree of disorder of the system.

2.3 TOPSIS Method

Technique for order of preference by similarity to ideal solution) (TOPSIS) is a multi-criteria decision analysis method, which was originally developed by Hwang and Yoon. TOPSIS selects that alternative which has the shortest geometric distance from the positive ideal solution and compares a collection of choices by considering weights for each criterion. The steps for the TOPSIS method are as given below:

Step 1   Generate the decision matrix with values of different criterion

$$X_{ij} = \begin{bmatrix} a_{11} & \cdots & a_{1n} \\ \vdots & \ddots & \vdots \\ a_{m1} & \cdots & a_{mn} \end{bmatrix} \tag{12}$$

Step 2   To calculate normalized matrix x_{ij} using the below formula:

$$x_{ij} = \frac{a_{ij}}{\sqrt{\sum_{j=1}^{j} a_{ij}^2}} \tag{13}$$

Step 3   To obtain the weighted normalized decision matrix by multiplying weights of different criteria as mentioned in following equation:

$$w_{ij} = x_{ij} x_{ij} \tag{14}$$

Step 4   To obtain the positive and negative ideal solution from following equations:

$$\mathrm{Ap}^* = \left\{ \left(\max w_{ij} / j \in j \right), \min w_{ij} / j \in j' \right\}$$
$$\mathrm{An}^- = \left\{ \left(\min w_{ij} / j \in j \right), \max w_{ij} / j \in j' \right\} \tag{15}$$

Step 5   To get the separation measures:

$$\mathrm{Sp}_i^* = \sqrt{\sum_{j=1}^{j} \left(\left(w_{ij} - w_j^* \right) \right)^2}; \ \mathrm{Sn}_i^- = \sqrt{\sum_{j=1}^{j} \left(\left(w_{ij} - w_j^- \right) \right)^2} \tag{16}$$

Step 6   To calculate the relative closeness to the ideal solution using following equation:

$$Cr_i = \frac{Sn_i^-}{Sn_i^- + Sp_i^*} 0 \leq Cr_i \leq 1 \tag{17}$$

Step 7   Calculate the overall score and choose the choice closest to 1.

3   Case Study on Brick Material Selection

Selection of best brick supplier for building construction purpose is done in this research work using a real-time example, based on the evaluation by the weights using CRITIC and entropy methods and then applying TOPSIS method to forecast the ranking alternative. Also, the effect of weights on ranking performance is observed. Six criteria are used among which four criteria belong to beneficial, i.e., compressive strength, flexural strength, volume and class of brick, and remaining criteria are non-beneficial criteria. Table 1 shows the decision matrix of brick supplier with their criteria values. Compressive strength of the brick is important as the load-bearing capacity of bricks depends on it. For good quality wall construction, bricks having more compressive stress should be used. The flexural strength of the brick is important for the resistance of brick against shear forces. During earthquake, the walls play important role as shear members for resisting the shock waves, and in that scenario, flexural stress of the bricks is most important. The density of bricks directly influences the dead load of the structure; the more dead load the more will be requirement for reinforcement which will ultimately increase the cost of the project. Hence, it is considered as non-beneficial criteria. The volume of the brick will directly decide the number of bricks that will be required for the masonry work of wall. The more the volume of bricks, less number of bricks will be required; the less labor work for building the wall is required, so it is a beneficial criterion. The class of brick is crucial criteria for determining the quality of the brick. The class of brick is decided based on various tests and higher the class the better the brick for construction purpose.

Table 1 Decision matrix of brick supplier selection

Criteria/alternative	Cost brick (₹)	Compressive strength (N/mm^2)	Flexural strength (N/mm^2)	Density of brick (kg/m^3)	Volume of brick (m^3)	Class of brick
Supplier 1 (S1)	8	8.5	0.05	1900	0.00153	5
Supplier 2 (S2)	12	12	0.07	1700	0.00216	5
Supplier 3 (S3)	6.5	6	0.06	1900	0.0020	3
Supplier 4 (S4)	32.5	4	0.03	650	0.0180	5
Supplier 5 (S5)	40	3	0.03	550	0.0180	5

3.1 Solution

The weights of different criteria are obtained using CRITIC and entropy methods as per the procedure mentioned above and are presented in Table 3. After weighted normalization, the relative closeness values from ideal solutions are calculated using TOPSIS methodology, and the obtained values are given in Table nine. The ranking performance by TOPSIS method with weights obtained by considered weighting methods is presented in Tables 2, 4, 5, 6, 7, 8, 9, and 10.

Table 2 Normalized matrix for TOPSIS method

Criteria/alternative	C	CS	FS	DB	VB	CB
S1	0.14839	0.51048	0.44194	0.57721	0.05960	0.47891
S2	0.22258	0.72068	0.61871	0.51645	0.08414	0.47891
S3	0.12056	0.36034	0.53033	0.57721	0.07790	0.28734
S4	0.60283	0.24022	0.26516	0.19746	0.70117	0.47891
S5	0.74195	0.18017	0.26516	0.16708	0.70117	0.47891

Table 3 Weights by CRITIC and entropy method

Criteria/method	C	CS	FS	DB	VB	CB
CRITIC	0.1339	0.1350	0.1989	0.1484	0.2447	0.1391
ENTROPY	0.0841	0.1312	0.3006	0.1965	0.1734	0.1142

Table 4 Weighted normalized matrix using CRITIC weights

Criteria/alternative	C	CS	FS	DB	VB	CB
S1	0.01987	0.06890	0.08790	0.08564	0.01458	0.06658
S2	0.02980	0.09728	0.12307	0.07663	0.02059	0.06658
S3	0.01614	0.04864	0.10548	0.08564	0.019069	0.03994
S4	0.08073	0.03242	0.05274	0.02930	0.17162	0.06658
S5	0.09936	0.02432	0.05274	0.02479	0.17162	0.06658

Table 5 Weighted normalized matrix using entropy weights

Criteria/alternative	C	CS	FS	DB	VB	CB
S1	0.01248	0.06700	0.13283	0.11339	0.01033	0.05466
S2	0.01872	0.09459	0.18597	0.10145	0.01459	0.05466
S3	0.01014	0.04729	0.15940	0.11339	0.01351	0.03279
S4	0.05071	0.03153	0.07970	0.03879	0.12161	0.05466
S5	0.06242	0.02364	0.07970	0.03282	0.12161	0.05466

Table 6 Positive and negative ideal solution for CRITIC weights

Criteria	C	CS	FS	DB	VB	CB
Ap*	0.01614	0.09728	0.12307	0.02432	0.17162	0.06658
An⁻	0.09936	0.02432	0.02432	0.08564	0.01458	0.03994

Table 7 Positive and negative ideal solution for entropy weights

Criteria	C	CS	FS	DB	VB	CB
Ap*	0.01014	0.09459	0.18597	0.02364	0.12161	0.05466
An⁻	0.06242	0.02364	0.02364	0.11339	0.01033	0.03279

Table 8 Separation measure using CRITIC and entropy weights

Critic	S1	S2	S3	S4	S5	Entropy	S1	S2	S3	S4	S5
Sp_i*	0.174	0.160	0.174	0.115	0.131	Sp_i*	0.155	0.132	0.152	0.130	0.138
Sn_i⁻	0.114	0.144	0.118	0.172	0.172	Sn_i⁻	0.129	0.1842	0.147	0.147	0.149

Table 9 Relative closeness values from ideal solution by TOPSIS method

Alternative	S1	S2	S3	S4	S5
CRITIC	0.3956	0.4731	0.4053	0.5989	0.5686
ENTROPY	0.4552	0.5814	0.4920	0.5298	0.5202

The selection criterions are cost/brick (C), compressive strength (CS), flexural strength (FS), density of brick (DB), volume of brick (VB), class of brick (CB).

Step 1   Criteria and alternative values in matrix form:
Step 2   Calculation of normalized matrix:
Step 3   Obtain weighted normalized matrix by multiplying with weights of criterions:
Step 4   Determine the positive and negative ideal solution:
Step 5   Calculate the separation measure:
Step 6   Calculate relative closeness to ideal solution:
Step 7   Calculate the overall score and rank of alternative:

Table 10 Ranking by TOPSIS using CRITIC and entropy weighting method

Supplier	S1	S2	S3	S4	S5
Ranking of TOPSIS using CRITIC weights	5	3	4	1	2
Ranking of TOPSIS using entropy weights	5	1	4	2	3

3.2   Result and Discussion

From Table 3, it can be observed that two weighting methods, namely CRITIC and entropy, gave different weights to criterions. After using these weights, TOPSIS method shows slight changes in the ranking. From Table 10, the ranking by TOPSIS method for different suppliers using CRITIC weights is 5-3-4-1-2, and using entropy weights, the ranking is 5-1-4-2-3. The suppliers S4 and S2 are the best choice by TOPSIS method when weights by CRITIC method and entropy method are applied to the same real-time example.

4   Conclusion

- After comparing the ranking obtained by considered MCDM method using CRITIC and entropy weighting methods, the result shows that slight variation in the ranking of suppliers. This variation in the ranking obtained is because of the methodology adopted in the two weighting methods.
- The obtained evaluation results are accordance with the expectations of the decision maker. The entropy weight and TOPSIS method which have high resolution and the calculation process are simple could objectively evaluate best brick supplier.
- In construction industry, the application of TOPSIS method can turn out to be very productive as the different suppliers are selected for different purposes which helps directly to improve the project performance in terms of cost and quality. The case study shows that the evaluation results obtained are reliable and are more coincident with the reality of construction industry.

References

1. DiakoulakiI D, Mavrotas G, Papayannakis L (1992) International Journal of Management Science 20(4): 467–474
2. Patel KV, Vyas CM (2011) Construction materials management on project sites. National Conference on Recent Trends in Engineering & Technology, May 2011
3. Vimal J, Chaturved V, Dubey AK (2012) Application of TOPSIS Method for supplier selection in manufacturing industry. Int J Res Eng Appl Sci 2(5)
4. Samarasinghe DAS, Tookey JE, Rotimi JOB, Thiruchelvam S (2012) Supplier selection in the construction material purchasing function. https://www.researchgate.net/publication/357 38531
5. Bhatt Rajiv, Bhatt Darshana (2014) Supplier selection for construction projects through 'TOPSIS' and 'VIKOR' multi-criteria decision-making methods. Int J Eng Res Technol 3(5)
6. Krohling RA, Pachecob AGC (2015) TOPSIS—an approach based on TOPSIS for ranking evolutionary algorithms. Procedia Comput Sci 55
7. Kumar J, Soota T, Singh SK (2016) Selection of refrigerant using-TOPSIS method. Int J Sci Eng Res 4(11)

8. Adalı EA, Işık AT (2017) Critic and Maut methods for the contract manufacturer selection problem. Eur J Multidiscip Stud 2(5)
9. Işık AT, Adalı EA (2017) The decision-making approach based on the combination of entropy and Rov methods for the apple selection problem. Eur J Interdiscip Stud 3(3)
10. Bhole GP, Deshmukh T (2018) Multi criteria decision making (MCDM) methods and its applications. Int J Res Appl Sci Eng Technol 6(5)
11. Rabieha M, Fadaei Rafsanjania A, Babaeia L, Esmaeili M, Iran (2018) Sustainable supplier selection and order allocation: an integrated delphi method, fuzzy TOPSIS, and multi-objective programming model. Sci Iranica, Indus Eng 26:2524–2540 (July 2018)
12. Vavrek R (2019) Evaluation of the impact of selected weighting methods on the results of the TOPSIS technique. Int J Inf Technol Decis Mak 18
13. Yadav G, Luthra S, Huisingh D, Mangla SK, Narkhede BE, Liu v (2019) Development of a lean manufacturing framework to enhance its adoption within manufacturing companies in developing economies. J Clean Prod 245:118726
14. Kaneriya P, Patel A (2020) Factor affecting of supplier selection in construction industry. Int Res J Eng Technol 07(06)
15. Deng Y (2015) Generalized evidence theory, Applied Intelligence, Second revision

Analyze and Optimize Thinning and Forming Force in Single Point Incremental Forming on AA6061-T6 Using the Finite Element Method

Vinod D. Golakiya, Mahesh K. Chudasama, and Harit K. Raval

1   Introduction

There are constant improvements in the nature of sheet metal products in today's sheet metal industries. Usually, conventional forming processes are used but frequent changes in design are not desirable for conventional forming process. Traditional forming methods such as deep drawing and stamping have high tooling costs and lead times. However, in recent years, the single point incremental sheet metal forming process (SPIF) has gradually replaced the traditional forming process. SPIF process is used for small batch production of metal sheet part, prototype, customized product especially in aerospace, biomedical applications, and household product at a lower cost as well as small lead time [1–4]. Three-dimensional (3D) shape products are formed (manufactured) in the SPIF process by highly localized plastic deformation layer to layer by feed provided to a generic tool controlled by a CNC machine, as shown in Fig. 1. When compared to a traditional stamping process, the SPIF process has more formability [5].

In incremental sheet metal forming (ISF), excessive thickness thinning, low geometric precision, and poor surface finish of formed parts remain challenges for industrial applications [6]. Sheet thickness thinning is the most serious of these problems because it leads to early component fracture. Since the formability of forming

V. D. Golakiya (✉)
Assistant Professor, Dr. S. & S. S. Ghandhi Government Engineering College Surat, Surat, India

V. D. Golakiya · M. K. Chudasama
Gujarat Technological University, Ahmedabad, Gujarat 382424, India

M. K. Chudasama
Assistant Professor, Government Engineering College Dahod, Dahod, India

H. K. Raval
Professor, Mechanical Engineering Department, S.V. National Institute of Technology, Surat, Gujarat 395007, India
e-mail: hkr@med.svnit.ac.in
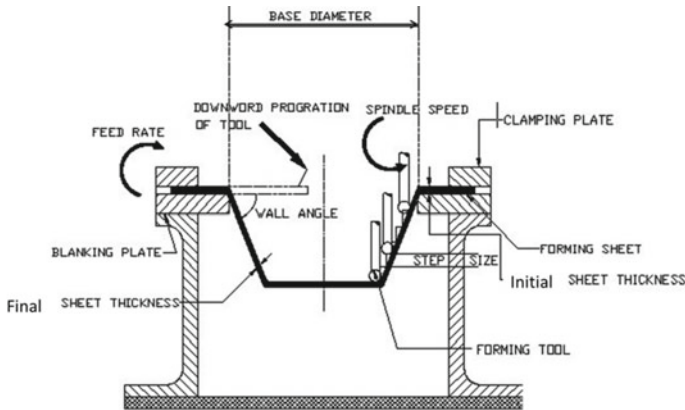
Fig. 1 Working principle of the SPIF process

parts is directly related to wall thickness thinning, understanding the thickness rule for forming parts is critical. Based on the literature, the sine law can be used to esti-mate the final wall thickness of a shaped element [7]. According to sine law, forming a component with a wall angle of 90° is impossible since the final wall sheet thickness is zero. However, using a different technique, researchers were able to successfully shape a component with a wall angle of 90°. Young and Jeswiet et al. [8] have been verified that sine law can be used as an approximation to predict thickness distribu-tion ISF process. This is clarified by Kegg [9], that an over spinning condition similar to that of shearing action could occur. Since thinning is a pioneer of failure, unpre-dicted failures will take place in the extreme thinning action. Liu et al. [10] found that multistages forming process is an effective method to avoid unnecessary thinning in specific area. This approach is unsatisfactory due to the increased time cost. Hussain and Gao [11] suggested the thinning limits of parts and used a generatrix curve shell in SPIF to calculate the final sheet thickness of parts using the sine law. Blaga et al. [12] have worked on experimentation on the strains and relative thinning. It has been noticed that step size and punch size are having the most influence on the strains and relative thinning. Xiao et al. [13] studied uniform thickness for the critical forming angle of a conical part in SPIF through experimental and numerical simulation. The sheet thickness of the formed part can accurately estimate by software. Mirnia et al. [14] used sequential limit analysis (SLA) to calculate the minimum thickness and studied at how step size and tool diameter affected the thickness distribution. Li et al. [15] performed a systematic finite element analysis of the ISF deformation process. To optimize and estimate thickness distribution, methods such as sequential limit analysis, response surface method, and finite element analysis were used. Further-more, Li et al. [16] investigated the effect of process parameter on thinning of formed parts in incremental forming using desirability function with reducing thinning rate. It showed that decreasing tool diameters and step size to decrease the thinning rate.

Estimating the amount of forming force in SPIF is a very crucial task, particularly when determining the best process parameters and selecting or designing equipment for the sheet forming process. It is also essential to understand the deformation failure mechanism as well as design factors such as tooling stiffness, jig and fixtures, component quality, and the machines used. As a result, estimating the maximum forces is crucial, not just for design purposes, but also for other critical factors. These reasons include maintaining the tooling machine, ensuring the safe use of hardware, and ensuring the quality of the parts produced [17]. Furthermore, depending on the shape of the component, the forming force causes pressure and stresses in the layer, which also determines the structural reliability of the final part [18]. Duflou et al. [17] showed that tool diameter, vertical step-downsize, wall angle, and the initial sheet thickness are mainly influenced on forming force and concluded that forming force increases with increase wall angle, vertical step, and sheet thickness. With a constant wall angle, Fillice et al. [19] identified various tangential force patterns, such as steady-state force trends, polynomial force trends, and monotonically decreasing force trends. Ambrogio et al. [20] concluded that probable fracture of the part is effectively considered after the peak value of force gradient, which may be considered an indication for forming limits. Petek et al. [21] analyzed results of influential various parameters on product deformation and the force size. Fiorentino et al. [22] have presented failure criterion as comparing the stresses developed on the material, which is calculated based on the ultimate strength of the material and forming forces. Through the manufacturing of a circular generatrix cone, Bagudanch et al. [23] revealed that formation force increases with step size and tool diameter while decreasing with higher spindle rpm. Li et al. [24] derived an efficient tangential force estimation model based on analysis of deformation. This model was validated by experimental tests to form a truncated cone as well as pyramid made of AA7075-O sheet with diffident step size. Arfa et al. [25] investigated the impact of helical and profile tool paths on forming a truncated cone shape on aluminum alloy AA3003-O sheet using simulation and experimental methods using ABAQUS commercial tools. The vertical forming force exerted by the forming tool was more stable for the helical tool direction.

Many researchers have done various experiments and simulations by varying different process parameters with different geometric form parts to study of thinning and force involved in single point incremental forming process. For sheet metal forming process, formability is an ability to form a part without fracture under plastic deformation. It is measured in different terms, i.e., maximum forming angle, thinning, and maximum forming depth. The shear deformation is primarily responsible for the thinning of the shape component, for which the sine law is insufficient in regulating and forecasting final sheet thickness. Further forming force is directly related to the quality of the formed part. The force prediction is a complex aspect due to nonlinear large displacement in SPIF process. SPIF process is regulated with different input parameters. Even the main challenge in single point incremental forming process is to select the most appropriate parameters; effective parameters to obtain a good quality form part. As a result, the aim of this study is to use the finite element method (FEM) to analyze and optimize the most important process parameters, such as wall angle,

step size, sheet thickness, tool radius, tool rotational speed, and feed on thinning and forming force. The SPIF process is simulated using ABAQUS-standard program and finite element simulation. In addition, the Taguchi method (TM) and ANOVA were used for systematic design of experiments (DOE) and analysis and optimization of simulation results, respectively.

2   Procedure

Single point incremental forming (SPIF) process is affected by many factors like material properties and operating parameters. Operating parameters are easily controllable while material properties and geometrical parameters are not easy to deal with. Material properties may vary from lot-to-lot for the same material. Therefore, it is more convenient to use the finite element method (FEM)-based tool to investigate such process by varying the process parameters to reduce the material cost of a blank sheet and tooling. In this work, AA6061-T6 has been selected as a blank sheet because it serves several advantages like excellent corrosion resistance, lightweight, recyclable, high ductility, and various applications in small batch-type industries like aerospace and defense. AA-6061-T6 alloy material size of 90 mm × 90 mm blank sheet is used to form axisymmetric truncate cone with a circular base diameter 50 mm and 15 mm depth with two -varying wall angle. Drawing of targeted (final) formed part is shown in Fig. 2, which is formed from flat sheet. The mechanical properties of AA6061-T6 sheet metal are summarized in Table 1. The mechanical properties are used as input data for a single point incremental forming process FEM simulation.

Literature shows that wall angle, step size, tool radius, feed, speed, work material, thickness of sheet, lubricant, tool path, etc., are the considerable important parameters which have a significant effect on different responses of SPIF process, i.e., formability, forming force, surface roughness, geometric accuracy, etc. [26]. In the present work, there are six basic parameters, i.e., wall angle, step size, tool radius, feed, speed, and thickness of sheet have been selected, which are affecting the thinning of formed part and average vertical forming force for the SPIF process. Table 2 lists all of the design parameters and their corresponding levels used across all of the simulations (experiments).

Taguchi method is a versatile method commonly used in engineering experiments for obtaining optimum and reliable results [27]. It is a well-developed design of experiment method to analyze complex and costly experiments. The experimental (simulation) design in this study provides a logical approach to determining the best possible settings of forming variables. Taguchi-based orthogonal array (OA) L_{18} design has been selected by using Minitab software, which includes three levels of five operating variables (step size, tool radius, feed, speed, and thickness of sheet) and two levels of one operating variable (wall angle). The experimental degree of freedom (DOF) must be less than the total degree of freedom of the orthogonal array (DOFOA) to be selected, i.e., DOF experiment DOFOA., i.e., DOF experiment ≤ DOFOA. In

Fig. 2 Target shape of a
final formed part (in mm)

FRONT VIEW

TOP VIEW
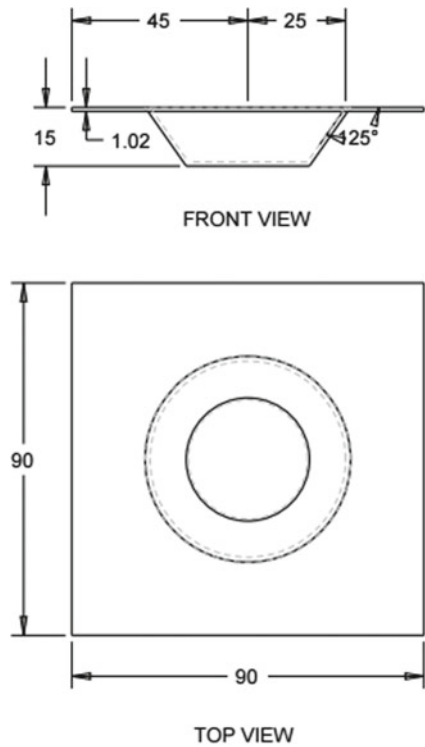
Table 1 Mechanical properties of AA 6061-T6

Yield strength-(MPa)	Young's modulus-(GPa)	Density (kg/mm^3)	Poisson ratio	Strength coefficient—(MPa)
270	68.9	2.7×10^{-6}	0.33	410

Table 2 Factors and their levels considered for simulation

Parameters (Factor)	Units	Levels		
Wall angle (A)	(deg)	55	65	–
Step size (B)	(mm)	0.5	1.0	1.5
Sheet thickness (C)	(mm)	1.024	1.62	2.052
Tool radius (D)	(mm)	3	4.5	6
Speed (E)	(rev/min)	0	250	500
Feed (F)	(min/min)	1000	2000	3000

the present investigation, L_{18} standard orthogonal array has been prepared to carry out for simulation, which satisfies the condition for selecting standard OA. The total DOF to conduct simulation is 12 is less than DOF of the orthogonal array. To identify significant parameter(s) of process response(s), an analysis of variance (ANOVA) was used, followed by the Taguchi method.

Thinning of wall is almost an unavoidable phenomenon in single point incremental sheet metal forming process. Hence, the thinning of sheet metal is required to study. In this work, thinning is considered as one of the response parameter and it is measured on the wall, where maximum thinning takes place along radial direction of final formed part (FEM-model) simulated by ABAQUS software. Other response, average vertical forming force is considered, which required a study of forming mechanism and equipment design purpose. The data for all two responses have been collected from finite element method (FEM) simulation.

For analysis of results, signal-to-noise ratios (η, dB) have been calculated for each responses. As wall thinning is a non-desirable response, expression for smaller the better (SB) condition has been employed. Similarly, average vertical forming force should be minimum, so this response also expressed in terms of signal-to-noise ratio has been employed as a smaller the better condition. The expressions of smaller the better are given below:

$$\eta_{SB} = -10 \log_{10}\left(\frac{1}{n}\sum_{i=1}^{r} y_i^2\right) \tag{1}$$

where y_i is the response value and $n =$ number of repetitions.

The results for both responses and Taguchi-based standard orthogonal array L18 are given in Table 3.

3 Finite Element Method Simulation

Single point sheet metal incremental shaping is a highly dynamic physical process characterized by layer-by-layer gradual plastic deformation. SPIF is a highly nonlinear process with nonlinear geometry, nonlinear material, and nonlinear interaction. It is difficult to predict the wall thinning of a formed part after the accumulation of metal deformation due to the numerous passes. The finite element approach (FEM) has made it easier to evaluate the thinning of a geometric form and reaction forces on the tool in the SPIF process over the last decade.

The ABAQUS/Explicit software finite element code is used in this study to compute the SPIF method since it can solve a nonlinear large plastic deformation. It can accurately simulate a long contact process cycle with large plastic deformation [25]. To simulate frustum cones made of aluminum alloy, finite element models are built. During process forming, the simulation results are expressed in terms of

Table 3 S/N ratio of response parameters

Exp. No	Input parameters						Signal-to-noise (S/N) ratios	
	A: Wall angle (ψ)	B: Step size-(ΔZ)	C: Sheet thickness (t)	D: Tool radius (r)	E: Speed (N)	F: Feed (f)	Thinning (TH)	Avg. Ver force (AVFF)
	deg	mm	mm	mm	rpm	mm/min	dB	dB
1	55	0.5	1.024	3	0	1000	5.88259	−58.4649
2	55	0.5	1.62	4.5	250	2000	6.70646	−64.3707
3	55	0.5	2.052	6	500	3000	7.67153	−69.6174
4	55	1	1.024	3	250	2000	7.84713	−57.1948
5	55	1	1.62	4.5	500	3000	7.93203	−65.2062
6	55	1	2.052	6	0	1000	7.86303	−68.9648
7	55	1.5	1.024	4.5	0	3000	7.12632	−57.3611
8	55	1.5	1.62	6	250	1000	7.69867	−66.4361
9	55	1.5	2.052	3	500	2000	8.59419	−66.8721
10	65	0.5	1.024	6	500	2000	2.89326	−59.1138
11	65	0.5	1.62	3	0	3000	4.47908	−64.2757
12	65	0.5	2.052	4.5	250	1000	5.92546	−68.0073
13	65	1	1.024	4.5	500	1000	3.73130	−59.2758
14	65	1	1.62	6	0	2000	4.10989	−63.8122
15	65	1	2.052	3	250	3000	5.73989	−67.1777
16	65	1.5	1.024	6	250	3000	4.25234	−57.8196
17	65	1.5	1.62	3	500	1000	5.88019	−64.5936
18	65	1.5	2.052	4.5	0	2000	5.67131	−67.6187

final geometry, reaction forces, product thinning, and so on. Analysis and optimization have been made of the simulation. The accuracy of the finite element process is determined by the constitutive laws used and the identification of their material parameters. Henrard et al. [28] did a finite element simulation of the SPIF process to predict tool reaction force. The result showed that the type of material hardening behavior, element type, and method of determining the parameters are affected by the prediction of forces. Material is considered to be elastoplastic isotropic. Anisotropic hardening rule (power law) was assigned to the material. The elastic part of sheet material's constitutive behavior is found to be isotropic and linear. This is expressed as given below:

$$\sigma = K\varepsilon^n \tag{2}$$

where σ = true stress (MPa), K = Strength coefficient and n = strain hardening—exponent.

An assembly model is consisted of three sub-models, i.e., bottom support, forming tool with hemispherical end, and deformable sheet blank. Figure 3 depicts an assembly model. At the start of the shaping process, the tool is found in the center of the sheet blank, and during the shaping period, the sheet blank is supported by the bottom support (fixture body). Support is assisted to reduce geometry error of final form part.

Material properties are not assigned to tool and support in the model, which is considered to be analytical rigid objects which lead to reducing computational time to determine the stress and strain. The section is selected as continuum shell and homogeneous. The thickness-reduced integration rule is taken as Gauss, and five
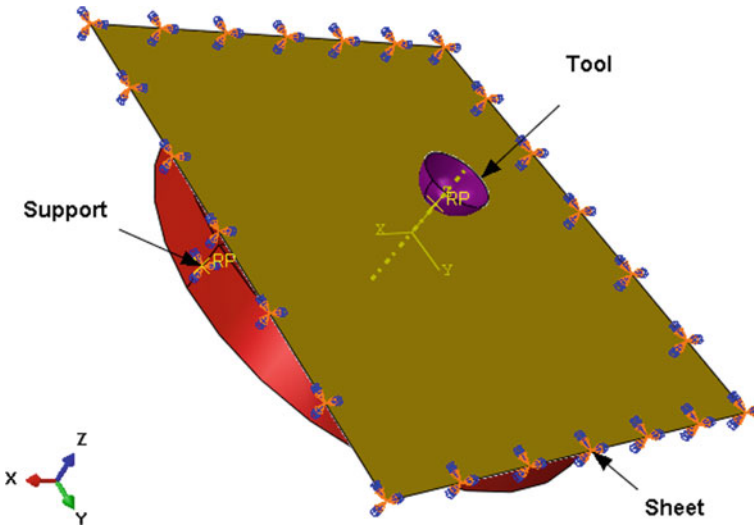
Fig. 3 Model of assembly with the boundary condition of SPIF process

thickness integration points are taken. In the present work, a quadrilateral S4R with 6 degrees of freedom per node type of shell element is used for the blank sheet. Support and forming tool do not to be divided due to the rigid body [25]. Mesh density number of sheet blank was chosen 8100 corresponding global sizes of element 1 mm × 1 mm for simulation purpose based on mesh sensitive analysis with mass scaling number 500.

One surface to other surface contact between forming tool (master surface) and blank (slave surface) was defined by the contact model. Classical isotropic Coulomb friction contact model was chosen because of the tangential behavior properties at tool and blank interface. This contact can be defined as the coefficient of friction (COF) in terms of average surface temperature. In the present work, a friction coefficient was specified 0.09 between contact surfaces [25]. Moreover, tool to sheet surface contact between support (master surface) and the blank (slave surface) was also the same contact properties as a tool and blank. Edges of sheet and support are assigned an encastred (fixed). The part will not have translational or rotational movement under that boundary condition. The mid surface area of the sheet is not supported and is kept free to deform. The tool trajectory determines the final form of the component in the SPIF process. The tool trajectory simulation for cone shape is described by a periodic amplitude curve. In the x-direction, the tool will follow $X = A1 \cos (2tn)$, and in the y-direction, it will follow $Y = B1 \sin (2tn)$, where $A1$ and $B1$ are the radii and it is the analysis step time. The motion of the tool will be generated by synthesizing the motion along X- and Y-directions. Finally, the tool moves over a blank sheet in Z-level spiral form.

The simulation produced has been validated with literature, i.e., Mugendiran [29]. The thickness of the shaped component is derived from the simulation outcome in order to evaluate its formability. As seen in Fig. 4, the thickness of the shaped component using FEM is observed to be between the experimental outcome from
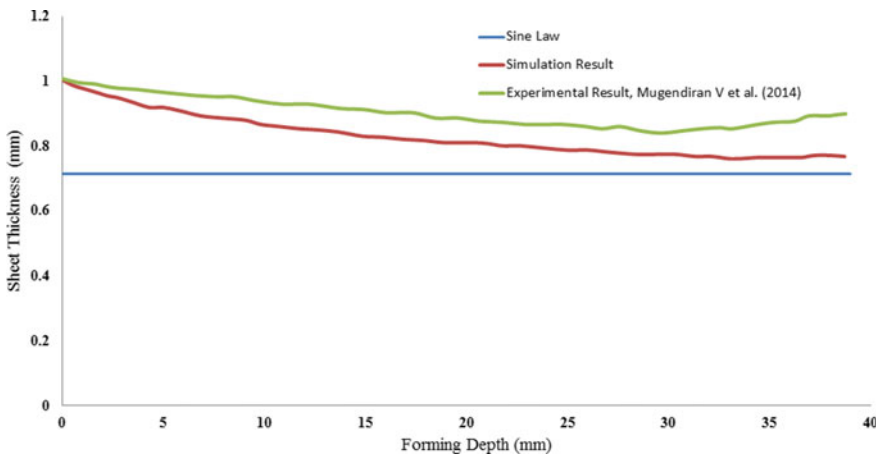
Fig. 4 Thickness of the formed part validated with literature

the literature [29] and the theoretical value according to the predict sine law model:

$$t_f = t_i \sin(90 - \Phi) \tag{3}$$

where t_f = final thickness of sheet, t_i = Initial thickness of sheet, and Φ = forming angle.

4 Result and Discussion

The current study looks into the thinning and shaping forces in the SPIF process. Thinning study is required to understand the fracture of formed part as thinning happens prior to fracture of part. The wall thickness of simulated form part is extracted from the simulation result as shown in Fig. 5. It has been noticed from simulated formed part that thinning is found to be drastically changing in deforming zone. As seen in Fig. 5, maximum thinning was observed in the middle zone of the deformed wall, while no thinning was observed at the bottom of the formed component. The thickness of the shaped component was assessed by choosing a particular point (node) along the Y-axis on the diameter path. Figure 6 depicts the thickness distribution of the virtual-shaped component along with the corresponding chosen direction. Moreover, the minimum thickness of the formed part has been selected along the node path for analysis purpose.

The second response of the SPIF process is average vertical forming force. A study of forming force is essential for design SPIF process equipment and to understand the

Fig. 5 Typically visualization of FEM form part thickness distribution
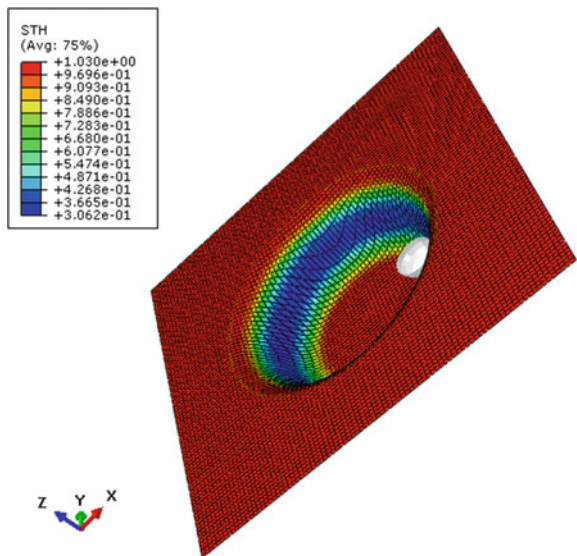
Fig. 6 Selected path for thickness measurement of model part
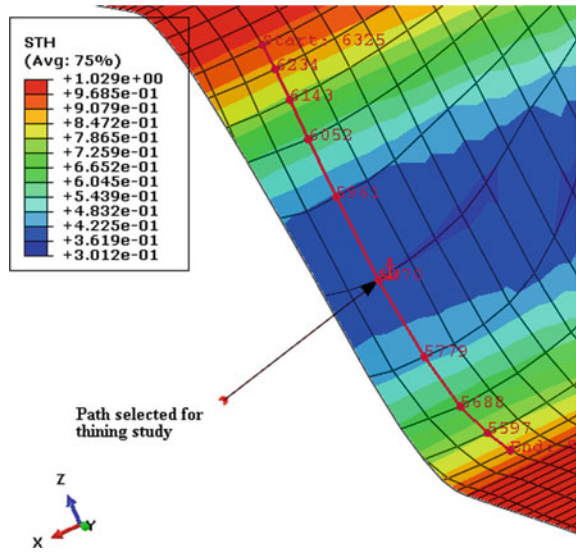
failure mechanism of formed part. In SPIF process, significantly a smaller amount forming forces are required than traditional forming processes [21]. According to the literature, a component of the tool's force in the vertical downward direction is significantly greater than the other two horizontal plain direction components of force. Hence, it is required to determine vertical downward component for safe employment of the machine tool equipment. Nature of forming force is dynamic, which is continuously varying along the time as shown in Fig. 7. The average value of vertical dynamic force is considered for the analysis of forming force.

Taguchi et al. [30] had reported that S/N (signal to noise) should be higher for better performance for any quality characteristics. Figures 8 and 9 show the major influence plots (graphs of S/N ratio) for thinning and vertical shaping force, respectively. Based on Taguchi approach, it can be seen from Fig. 8 that optimal performance thinning can be achieved at 55° wall angle (level-1), 1.5 mm step size (level-3), 2.053 mm sheet thickness (level-3), 3 mm tool radius (level-1), 250 rpm speed (level-2), and 3000 mm/min feed (level-3), i.e., A1-B3-C3-D1-E2-F3.

Further, at 65° wall angle (level-2), 1.5 mm step size (level-3), 1.024 mm sheet thickness (level-1), 3 mm 250 rpm speed (level-1), and 2000 mm/min feed (level-2), i.e., *A*2-*B*3-*C*1-*D*1-*E*1-*F*2 is an optimal condition for lower average vertical forming force Fig. 9.

In order to identify the factor having significant effect on responses, analysis of variance (ANOVA) at confidence interval of 95% has been carried out. If the *p*-value for a parameter is less than 0.05, the same can be considered as a significant factor [30]. Tables 4 and 5 represent the ANOVA results of thinning and average vertical forming force, respectively.

Table 4 shows that the most important parameter influence on component thinning is the wall angle. It contributes 69.52% in order to control the total variability.
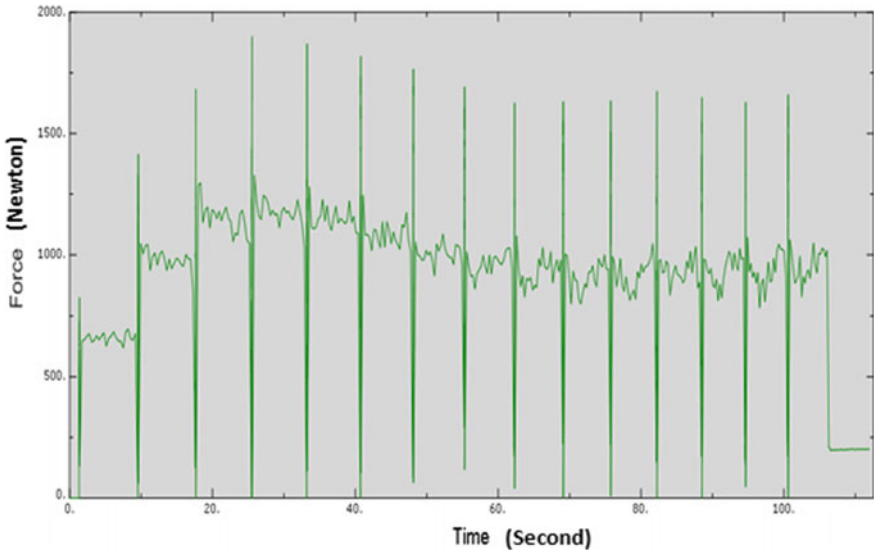
Fig. 7 Vertical forming force during SPIF forming

Signal-to-noise: Smaller is better
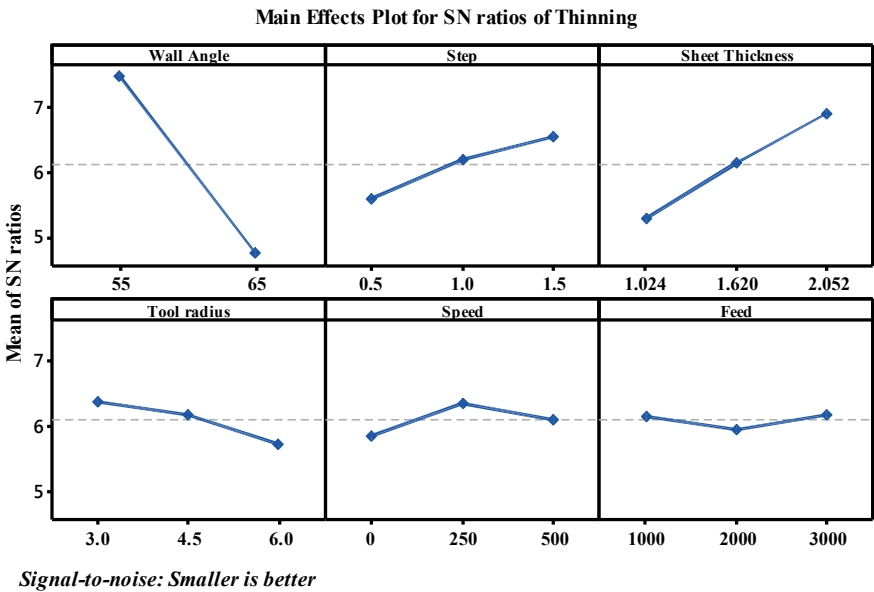
Fig. 8 Graph of S/N ratio of sheet thinning
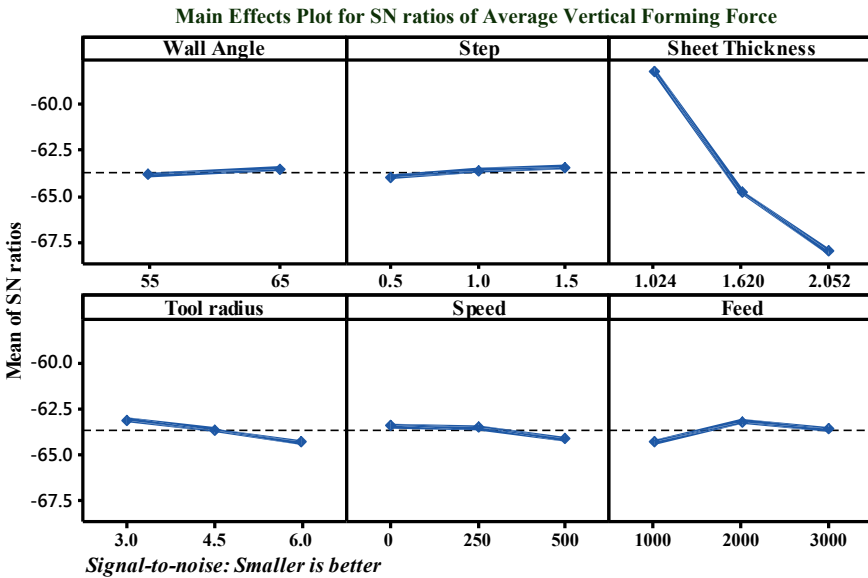
Fig. 9 Graph of S/N ratio of average vertical forming force

Table 4 ANOVA result for thinning of simulated form part

Factor	DOF	SS	MS	F-Value	P-Value	Percentage contribution
A: Wall angle	1	33.72	33.72	109.17	0.000	69.52
B: Step size	2	2.751	1.37	4.45	0.065	5.67
C: Sheet thickness	2	7.89	3.94	12.78	0.007	16.28
D: Tool radius	2	1.33	0.66	2.16	0.196	2.75
E: Speed	2	0.76	0.38	1.24	0.353	1.59
F: Feed	2	0.18	0.09	0.3	0.754	0.38
Error	6	1.85	0.30	–	–	3.82
Total	17	48.51	–	–	–	–

Table 5 ANOVA result for average vertical forming force

Factor	DOF	SS	MS	F-Value	P-Value	Percentage contribution
A: Wall angle	1	0.434	0.434	1	0.357	0.14
B: Step size	2	0.872	0.436	1	0.422	0.28
C: Sheet thickness	2	301.362	150.681	345.93	0	95.60
D: Tool radius	2	4.314	2.157	4.95	0.054	1.37
E: Speed	2	1.735	0.868	1.99	0.217	0.55
F: Feed	2	3.899	1.95	4.48	0.065	1.24
Error	6	2.613	0.436	–	–	0.83
Total	17	315.230	–	–	–	–

Subsequent factors are an initial thickness with 16.28% contribution and followed by step size, tool radius, speed, and feed of the total variability. According to the approximate model of sine law, the thinning is the function of the wall angle as well as the initial thickness of blank, which is in these results. Furthermore, Ham and Jeswiet [31] also reported that material thickness depicts a significant increase in formability for increasing material thickness. The increase in thickness contributed to the increase in formability as there is more material to deform.

From the ANOVA Table 5, it was observed that the initial thickness of the blank sheet has the largest percentage (95.6) contribution effect on the forming force. This was due to the vast volume of material that the tool had to shape as the thickness of the material increased, resulting in an increase in shaping force. While a thinner sheet needs less force to bend, it can break more easily than a dense sheet due to the thinner material. Further, forming force is increased for the larger size of the tool. The increased deformation area between the tool surface and the sheet blank on each pass is the cause for the rise in force when a larger tool is used. In comparison with a smaller tool, a larger tool has a larger deformation region and hence deformed more material for each step, resulting in higher force requirements. The effect of step size and wall angle on average vertical forming force is seen in Fig. 9. The average force increased as the step size and wall angle increased. This is due to at any instant; the reaction of sheet metal for local plastic deformation is increased. Same trend has been observed in the effect of rotational speed on average forming force in SPIF process simulates (Fig. 9). Metal becomes more ductile in nature with increasing the friction at tool–sheet interface due to higher rotational speed, which helps to decrease the forming force [32].

The validation of simulation was carried out using ABAQUS finite element tools for both response characteristics (thinning and forming force) at optimum levels of the process variables in order to verify the results obtained. The value of thinning and forming force was found to be 0.363 and 818 N, respectively. The signal-to-noise ratio was 8.8018 dB and -58.2550 dB, respectively, which is indicated the maximum value as compared to previous all simulated results.

5 Conclusions

In industries where batch style manufacturing and specialized prototype parts are made, single point sheet metal incremental forming can play an important role. The numerical investigation of AA6061 was carried out in this study because many input parameters have an effect on product quality. Simulations were run using a DOE that included input parameters (such as wall angle, sheet thickness, tool radius, step size, rpm, and feed) and two responses (i.e., thinning and forming force). ANOVA was also used to optimize process parameters using simulated results data. The following are the major points taken from the current study of a single point incremental forming process using the finite element approach.

- FE modeling and simulation for conical frustum of benchmarking problems were successfully done with ABAQUS 6.13 software, and their results are in good agreement with available literature result.
- In the deforming region, thinning is observed to be drastically changing. The middle region of the deformed wall shows the most thinning, while the bottom of the formed section shows no thinning. Based on Taguchi approach, the most significant process parameters influencing thinning is wall angle 69.72% followed by an initial thickness of 16.28% of the sheet. The ANOVA shows that step size and tool radius have little influence on thinning, while speed and feed have no effect.
- A smaller amount of the forces are required for forming in SPIF process than traditional forming processes. From the ANOVA analysis, it shows that the sheet thickness is the largest 95.6% of contribution on the effect on forming force.
- The optimum formation parameters are also confirmed with FEM-simulated validation tests. The thinning and shaping force values were found to be 0.363 and 818 N, respectively, which is the lowest value of all previously simulation results.

The results of this study show that optimizing a parameter will help reduce forming force and thin the shape component of sheet metal in a single point incremental forming process. Further ABAQUS Software (finite element method) is capable to simulate nonlinear behavior SPIF process to form sheet metal parts by minimum error without performing many experimental works. In the future, the authors will investigate the impact of these optimized parameters on actual industrial parts made of AA6061 T6 sheet parts that are not regular parts, such as cup and pyramid shapes, and with various materials.

References

1. Jeswiet J, Young D (2005) Forming limit diagrams for single-point incremental forming of aluminium sheet. Proc Inst Mech Eng Part B J Eng Manuf 219(4):359–364
2. Gulati V, Kathuria S, Katyal P (2015) A paradigm to produce customized ankle support using incremental sheet forming. J Eng Technol 5(1):14
3. Sbayti M, Bahloul R, Belhadjsalah H (2017) Numerical modeling of hot incremental forming process for biomedical application. In: International conference design and modeling of mechanical systems. Springer, Cham, pp 881–891 (Mar)
4. Gupta P, Szekeres A, Jeswiet J (2019) Design and development of an aerospace component with single-point incremental forming. Int J Adv Manuf Technol 103(9):3683–3702
5. Kurra S, Rahman NH, Regalla SP, Gupta AK (2015) Modeling and optimization of surface roughness in single point incremental forming process. J Market Res 4(3):304–313
6. Emmens WC, Sebastiani G, Van den Boogaard AH (2010) The technology of incremental sheet forming—a brief review of the history. J Mater Process Technol 210(8):981–997
7. Duflou JR, Verbert J, Belkassem B, Gu J, Sol H, Henrard C, Habraken AM (2008) Process window enhancement for single point incremental forming through multi-step toolpaths. CIRP Ann Manuf Technol 57(1):253–256
8. Young D, Jeswiet J (2004) Wall thickness variations in single point incremental forming. Proc Inst Mech Eng B 218(B11):204–210

9. Kegg Richard L (1961) A new test method for determination of spinnability of metals. J Eng Ind-T ASME 83(2):119–124

10. Liu B, Daniel WJT, Li Y, Liu S, Meehan PA (2014) Multi-pass deformation design for incremental sheet forming: analytical modeling, finite element analysis and experimental validation. J Mater Process Technol 214(3):620–634

11. Hussain G, Gao L (2007) A novel method to test the thinning limits of sheet metals in negative incremental forming. Int J Mach Tools Manuf 47(3–4):419–435

12. Blaga A, Bologa O, Oleksik V, Breaz R (2011) Influence of tool path on main strains, thickness reduction and forces in single point incremental forming process. Proc Manuf Syst 6(4):191–196

13. Xiao SC, Gao JZ, Jia LL, Xu L (2012) Research on critical forming angle of uniform thickness in single-path incremental forming for conical part. Forging Stamping Technol 1(37):49–54

14. Mirnia MJ, Dariani BM, Vanhove H, Duflou JR (2014) An investigation into thickness distribution in single point incremental forming using sequential limit analysis. Int J Mater Form 7(4):469–477

15. Li Y, Daniel WJT, Meehan PA (2017) Deformation analysis in single-point incremental forming through finite element simulation. Int J Adv Manuf Technol 88:255–267

16. Li Y, Chen X, Zhai W, Wang L, Li J, Guoqun Z (2018) Effects of process parameters on thickness thinning and mechanical properties of the formed parts in incremental sheet forming. Int J Adv Manuf Technol 98(9):3071–3080

17. Duflou J, Tunckol Y, Szekeres A, Vanherck P (2007) Experimental study on force measurements for single point incremental forming. J Mater Process Technol 189(1–3):65–72

18. Bagudanch I, Centeno G, Vallellano C, Garcia-Romeu ML (2013) Forming force in single point incremental forming under different bending conditions. Procedia Eng 63:354–360

19. Filice L, Ambrogio G, Micari F (2006) On-line control of single point incremental forming operations through punch force monitoring. CIRP Ann 55(1):245–248

20. Ambrogio G, Filice L, Micari F (2006) A force measuring based strategy for failure prevention in incremental forming. J Mater Process Technol 177(1–3):413–416

21. Petek A, Kuzman K, Kopač J (2009) Deformations and forces analysis of single point incremental sheet metal forming. Arch Mater Sci Eng 35(2):107–116

22. Fiorentino A (2013) Force-based failure criterion in incremental sheet forming. Int J Adv Manuf Technol 68(1–4):557–563

23. Bagudanch I, Perez-Santiago R, Garica-Romeu ML, Rodríguez C (2011) Forming force in SPIF of variable wall angle components: FEM modeling and experimental results. In: Proceedings of 10th international conference of technology of plasticity, pp. 541–546

24. Li Y, Daniel WJ, Liu Z, Lu H, Meehan PA (2015) Deformation mechanics and efficient force prediction in single point incremental forming. J Mater Process Technol 221:100–111

25. Arfa H, Bahloul R, BelHadjSalah H (2013) Finite element modelling and experimental investigation of single point incremental forming process of aluminum sheets: influence of process parameters on punch force monitoring and on mechanical and geometrical quality of parts. IntJ Mater Form 6(4):483–510

26. Gatea S, Ou H, McCartney G (2016) Review on the influence of process parameters in incremental sheet forming. Int J Adv Manuf Technol 87(1):479–499

27. Chen YH, Tam SC, Chen WL, Zheng HY (1996) Application of the Taguchi method in the optimization of laser micro–engraving of photomasks. Int J Mater Prod Technol 11(3–4):333–344

28. Henrard C, Bouffioux C, Eyckens P, Sol H, Duflou JR, Van Houtte P, Habraken AM (2011) Forming forces in single point incremental forming: prediction by finite element simulations, validation and sensitivity. Comput Mech 47(5):573–590

29. Mugendiran V, Gnanavelbabu A (2014) Comparison of FLD and thickness distribution on AA5052 aluminium alloy formed parts by incremental forming process. Procedia Eng 97:1983–1990

30. Taguchi G, Chowdhury S, Wu Y (2005) Taguchi's quality engineering handbook, 1st edn. Wiley, Hoboken, New jersey

31. Ham M, Jeswiet J (2008) Single point incremental forming. Int J Mater Prod Technol 32(4):374–387
32. Xu D, Wu W, Malhotra R, Chen J, Lu B, Cao J (2013) Mechanism investigation for the influence of tool rotation and laser surface texturing (LST) on formability in single point incremental forming. Int J Mach Tools Manuf 73:37–46

PSO-Based Single Objective Optimization of WEDM Process on SKD 11 Material

Sandip S. Patel and J. M. Prajapati

List of Symbols

MRR	Material removal rate
P, WF	Feed rate of wire
Q, Ton	Pulse on time
R, IP	Peak current
S, Toff	Pulse off time
T, WT	Tension of wire
U, SV	Spark gap set voltage
DF	Degree of freedom
MS	Mean square
RSM	Response surface methodology
φ	Diameter
CCD	Central composite design
SS	Sum of squares

1 Introduction

There is currently an expanding trend in manufacturing toward high-speed machinery even as the interest of composite materials with high hardness, excellent toughness, and properties of obstruction strength impact [1]. However,

S. S. Patel (✉)
Department of Mechanical Engineering, Government Engineering College, Patan, Gujarat, India

J. M. Prajapati
Department of Mechanical Engineering, Faculty of Technology & Engineering, M. S. University of Baroda, Baroda, Gujarat, India

machining of such materials is troublesome by ordinary machining measure [2]. Consequently, non-traditional machining measures are applied to the machine for such problematic machining materials. The wire discharge machining (WEDM) uses the thermoelectrical part to cut electrically conductive materials by a progression of unique sparkles generated in the presence of dielectric liquid between wire anode and workpiece, which allows a plasma channel for each electrical release as the dielectric liquid is ionized inside the hole [1]. In the case of sparkle release, there is a current stream through the workpiece hole wire terminal. The surface area where sparkles form is heated to colossally high temperatures as high as 20,000 °C. Thus, it dissolves and eliminates the surface area. A stream of dielectric liquids and a cooling medium flushes the eliminated particles in the form of debris. Thus, the disintegration of material happens. Assurance of the right machining conditions is an essential viewpoint to be considered while machining a section.

In EDM processes, the impact of processing parameters is diverse for different response characteristics. Therefore, the selection of a single optimum combination of process parameters is difficult. Hence, an optimization method is much needed for this problem. Several researchers have conducted various studies to improve the WEDM process's performance using different optimization techniques. Still appropriate selection of processing parameters to get the best process performance difficult task. For modeling and optimization of the WEDM process, a number of studies have used linear and nonlinear regression analysis [3–7], gray relation analysis [8–11], Taguchi-based gray analysis [11–14], response surface methodology [15–20], artificial neural network [21–25], genetic algorithm [18, 24–26], fuzzy logic [27, 28], adaptive neuro-fuzzy inference system[29], Taguchi-based utility approach [30], hybridized RSM and NSGA-II [31], Pareto optimization [32, 33], desirability function [32, 34], simulated annealing scheme [22], data envelopment analysis[35], principal component analysis [36], dimensionless analysis [37], and finite element analysis [24] to understand themethod's superior insight. Mukherjee et al. [38] researched, implemented, and compared various on-traditional methods of optimization, namely optimization of an ant colony, optimization based on biogeography, optimization of particle swarm, genetic algorithm, an algorithm of the sheep flock, and algorithms of an artificial bee colony for single and multi-objective optimizations [1, 38].

The literature review suggests that several researchers employed traditional and non-traditional optimization techniques to find optimal results for various responses to the WEDM process and its variants. Traditional optimization methods can suffer the disadvantage of locally optimal solutions, which led to reduced accuracy of the results. Several non-traditional optimization techniques that have been applied to optimize the WEDM parameters in recent years, but PSO algorithm's use is limited.

Presently, in the current examination, the point is to build the profitability joined with the machined test's ideal exactness and cost. Any creation company seeks the highest level of profitability, the smallest amount of cost, and the uppermost level of accuracy. As a consequence, it is vital to achieve the best configuration of process parameters in demand to acquire the best global result for increasing the WEDM concert [39]. Keeping in view the world-class execution, the machineability of SKD

Table 1 SKD 11 material chemical structure

Element	Ordinary (Max weight)	Actual (Max weight)
Fe	Balance	Balance
Cr	11–13%	12%
Mo	0.7–1.2%	0.8%
Si	0.6% max	0.3%
V	1.1 max	0.9%
Mn	0.6% max	0.4%
C	1.4–1.6%	1.5%

11 was used to improve the exhibition of WEDM by utilizing the development of single-streamlining approaches like particle swarm optimization.

1.1 Material of the Workpiece

In the present work, the high chromium and high carbon SKD 11 was taken as workpiece material having 12 mm height whose chemical composition was summarized in Table 1.

1.2 Experimental Arrangement and Devices for Measuring Performance

The tests are carried out on an Electronica Sprint cut wire EDM unit, which can be found at Darshan Wire Cut in Odhav, Ahmedabad. During the experimentation, different input control parameters such as Toff, IP, WF, Toff, WT, and SV were varied to see how they affected the material removal rate [40]. The wire is attached to the terminal of $-$ ve while the workpiece is protected by the terminal of $+$ ve. During the entire machining process, φ 0.25 mm of brass wire is kept constant. To grasp the workpiece on the computer table, a fixture is used to scale back any possibility of misalignment [40]. From the deionized water, electrode and workpiece are isolated. MRR is in charge of the financial aspects of machining as well as the production volume. It is determined by the following Eq. (1) [41].

$$MRR(mm^3/min) = width\ of\ cut \times average\ machining\ rate \times thickness\ of\ plate \tag{1}$$

Width of cut $= (Xs - Ys)$

Table 2 Process variables and their limits

Level	Feed rate of wire: P	Pulse on time: Q	Peak current: R	Pulse off time: S	Tension of wire: T	Spark gap set voltage: U
−α	4	110	160	50	4	10
−1	6	112	170	52	6	20
0	7	115	180	54	7	30
+1	8	118	190	56	8	40
+α	10	119	200	58	10	50

Xs = size of desired workpiece = 10 mm, Ys = after machining, the real workpiece size was determined with a digital vernier and a micrometer with a least count of one. On the AB, BC, and CD sides, it is measured at two random locations [1] and as a result, the actual size of the workpiece is equivalent to the numeral of the six values.

1.3 Input Process Variables and Their Levels Selection

Various input process variables, i.e., IP, Ton, SV, WF Toff, and WT on performance characteristics; material removal rate have been explored in this study. Based on the pilot experiment, capacity of machine, literature review, and manufacturer's machine manual, the input process variables and their ranges were chosen [40]. Table 2 illustrates the variables of the regulated input method and their limits in coded and actual values.

1.4 Design of Experiments

The Design expert 7 was used to form the design of experiments (DOE) and process optimization by response surface approach [40]. The RSM was liable to generate a second-order regression of y on x concerning response characteristics and process variables [42]. Besides regression investigation, "the experimentation helps the modeling of the favored response to frequent input process variables". The experiment was intended to allow for "the estimation of interaction and quadratic polynomial effects, as well as to provide data on the shape of the response curve" [40]. Fifty-two tests were directed by CCD using half replication for six input parameters with 1.565 as alpha value, referred to as realistic [40]. When there are a lot of input variables, it is a good idea to use it [43]. This 52-experiment design includes 32 factorial points (experimental turns 1–32), 12 axial points (experimental runs 33–44) to form a CCD with 1.565 as alpha for estimation of curvature effect, and eight center points (experimental runs 45–52) for pure error estimation at zero levels for

replication [40]. The randomization of experimental runs ensures that human predispositions are eliminated [40]. The experimental architecture matrix is shown in Table 3, which contains input variables as well as concert steps for the output reaction.

2 Particle Swarm Optimization for Single-Objective Optimization

The PSO was a metaheuristic technique that used a design-based optimization algorithm [44]. The algorithm was designed in 1995 by James Kennedy Russell Eberhart [45, 46]. Searching for the best solution is an intelligence of the swarm-based optimization approach of machine learning. PSO was a population-based technique in which each particle is a candidate solution, defined via its locations (xi) and velocity (vi). In multi-dimensional space, particles change their location (d) by flying. The particle's new position arises by changing its speed, i.e., $x_i = (x_{i1}, x_{i2} \ldots x_{id})$. Each iteration particle changes its location according to its greatest rank (pbest) and greatest location globally (gbest), viz. the experience of adjoining particles. Accordingly, the replacement velocity value for every particle is meant to support its current velocity [45]. In multi-dimensional space, the next location of each particle was determined using a changed velocity value. This method was repeated several times to update position and velocity, and iteration was stopped when the smallest error was reached [45]. PSO may be a method for stochastic optimization that supported the swarm intelligence and mobility. The PSO algorithm was utilized as per the following steps [45]:

Stage 1. Build the initial particle population (x) randomly across a three-dimensional plane (d).
Stage 2. For each particle, the objective function's value was calculated [44].
Stage 3. Also, decide the best position that any particle within the population has obtained so far, i.e., gbest.
Stage 4. Using Eqs. (2) and (3), find the modified velocity of each particle [46].

$$V_{id}^{j+1} = w \times V_{id}^{j+1} + c_1 \times r_1 \times \left(\text{pbest}_i - x_{id}^j \right) + c_2 \times r_2 \times \left(\text{gbest}_i - x_{id}^j \right)$$

(2)

$$w = w_{\max} - \frac{w_{\max} - w_{\min}}{iter_{\max}} \times (j + 1)$$

(3)

where c_1 and c_2 are constants, r_1 and r_2 are arbitrary numbers in the (0–1) range, j is the numeral of iterations, and itermax is the largest number of iterations, and w is the weight of inertia.
Stage 5. Using Eq. (4) to verify the present location of particles.

Table 3 Experimentation design matrix with resulting response values

S. No.	Order of execution	Factor P	Factor Q	Factor R	Factor S	Factor T	Factor U	Response I
		Feed rate of wire WF (m/min)	Pulse on time T_{on} (mu)	Peak current IP (A)	Pulse off time T_{off} (mu)	Tension of wire WT (mu)	Spark gap voltage SV (V)	MRR mm^3/min
1	15	6	112	170	52	6	20	4.428
2	40	6	118	170	52	8	20	8.7348
3	26	6	112	170	56	8	20	4.0656
4	9	6	118	170	56	6	20	8.2584
5	31	6	112	190	52	8	20	6.498
6	38	6	118	190	52	6	20	10.44
7	8	6	112	190	56	6	20	5.1642
8	45	6	118	190	56	8	20	8.2764
9	34	6	112	170	52	8	40	3.996
10	30	6	118	170	52	6	40	6.948
11	51	6	112	170	56	6	40	3.3108
12	14	6	118	170	56	8	40	5.7096
13	33	6	112	190	52	6	40	5.256
14	27	6	118	190	52	8	40	8.28
15	11	6	112	190	56	8	40	4.347
16	36	6	118	190	56	6	40	6.8076
17	20	8	112	170	52	8	20	4.5936
18	35	8	118	170	52	6	20	6.9552
19	24	8	112	170	56	6	20	3.6288
20	6	8	118	170	56	8	20	6.0876
21	47	8	112	190	52	6	20	5.1072
22	12	8	118	190	52	8	20	8.4216
23	46	8	112	190	56	8	20	3.975
24	28	8	118	190	56	6	20	6.6864
25	13	8	112	170	52	6	40	3.696
26	1	8	118	170	52	8	40	5.6448
27	18	8	112	170	56	8	40	2.772
28	48	8	118	170	56	6	40	4.6032
29	37	8	112	190	52	8	40	3.564
30	4	8	118	190	52	6	40	6.3684
31	44	8	112	190	56	6	40	3.42
32	22	8	118	190	56	8	40	5.4912

(continued)

Table 3 (continued)

S. No.	Order of execution	Factor P Feed rate of wire WF (m/min)	Factor Q Pulse on time T_{on} (mu)	Factor R Peak current IP (A)	Factor S Pulse off time T_{off} (mu)	Factor T Tension of wire WT (mu)	Factor U Spark gap voltage SV (V)	Response I MRR mm³/min
33	32	7	110	180	54	7	30	3.06
34	41	7	120	180	54	7	30	6.048
35	3	7	115	180	50	7	30	5.22
36	10	7	115	180	58	7	30	4.026
37	39	7	115	160	54	7	30	4.536
38	42	7	115	200	54	7	30	5.112
39	7	7	115	180	54	7	10	4.8048
40	49	7	115	180	54	7	50	3.7422
41	5	4	115	180	54	7	30	5.487
42	16	10	115	180	54	7	30	5.184
43	25	7	115	180	54	4	30	5.1642
44	43	7	115	180	54	10	30	5.673
45	19	7	115	180	54	7	30	5.4984
46	21	7	115	180	54	7	30	5.7462
47	17	7	115	180	54	7	30	5.664
48	52	7	115	180	54	7	30	5.394
49	50	7	115	180	54	7	30	5.796
50	29	7	115	180	54	7	30	5.724
51	2	7	115	180	54	7	30	5.5998
52	23	7	115	180	54	7	30	6.1236

$$x_{id}^{j+1} = x_{id}^{j} + v_{id}^{j+1} \tag{4}$$

Stage 6. Test the value of each particle's current objective function against the previous one. If the answer changes, keep this position; if it doesn't, keep it.

$$x_{id}^{j+1} = x_{id}^{j}$$

Stage 7. If the utmost value is reached by the sum of iteration, obey step 8; otherwise, take step 4.

Stage 8. The most recent gbest is the answer to the query [44].

3 Justification of the Projected Model

The experiments were designed to confirm the rationality of the model selected by predicting the value of the best possible parameters. The answer was calculated and compared to the value predicted.

4 Result and Discussion

In the current analysis, input process variables, i.e., Ton, WT, IP, Toff, SV, and WF were preferred based on introductory soundings and literature explorations. An overall 52 experiments, as suggested by CCD, were carried out, as per Table 3. The study of variance test for MRR is highlighted in Table 4.

This means that the F-value of the model is 81.88, and the p-value is 0.0001 [47], suggesting that "the model is significant" [1]. There is just a 0.01% chance that a "Model F-value" this large would arise due to noise. Furthermore, the 7.43 "lack of fit F-value" specifies that the lack of fit is important [40]. There is just a 0.01 percent chance that noise would trigger such a broad "lack of fit F-value." As a result, a quadratic model with a 95% confidence level is sufficient.

Table 4 ANOVA table for material removal rate

Source	SS	DF	MS	F-Value	Prob > F		Contribution %
Model	226.88	11	20.62	81.88	< 0.0001	Significant	
P-WF	19.57	1	19.57	77.72	< 0.0001		7.83
Q-T_{on}	134.17	1	134.17	532.72	< 0.0001		53.66
R-IP	13.89	1	13.89	55.17	< 0.0001		5.56
S-T_{off}	19.08	1	19.08	75.77	< 0.0001		7.63
T-WT	0.24	1	0.24	0.98	0.3245		
U-SV	26.95	1	26.95	107.00	< 0.0001		10.78
QU	1.97	1	1.97	7.82	0.0063		
PQ	3.38	1	3.38	13.45	0.0004		1.35
P^2	2.27	1	2.27	9.03	0.0034		0.91
S^2	1.87	1	1.87	7.45	0.0076		
T^2	3.39	1	3.39	13.49	0.0004		1.35
Residual	23.1	92	0.25				
Lack of fit	18.67	33	0.56	7.42	< 0.0001	Significant	
Pure error	4.49	59	0.07				
Cor total	250.05	103					

Standard deviation 0.50 R^2 0.9073 R^2_{Adj} 0.8963 R^2_{Pred} 0.8812

The other significant coefficient, R^2, known as the coefficient of determination, indicates less inconsistency between the expected values and the real values. The adjusted R^2 value of 0.8963 is reasonably close to the predicted R^2 value of 0.8812. In comparison to the pulse off, the pulse on time was found to be a highly influential parameter.

The regression equation for the material removal rate as a function of six process parameters was established with trial data and is specified below in terms of an important factor. The quadratic equation has omitted the insignificant coefficients of certain terms.

$$
\begin{aligned}
\mathrm{MRR} = {} & -88.78 + 1.16 \times T_{\mathrm{on}} - 0.254 \times T_{\mathrm{off}} + 0.043 \times IP0.762 \times +4.442 \times WF \\
& - 4.777 \times WT - 5.849 \times 10^{-3} \times T_{\mathrm{on}} \times SV - 0.076 \times T_{\mathrm{on}} \times WF \\
& - 2.50 \times 10^{-3} \times SV^2 + 0.275 \times WF^2 + 0.33 \times WT^2
\end{aligned}
\tag{5}
$$

The MRR is affected by the quadratic polynomial functions of wire feed rate, spark gap voltage, and wire tension. They can be used within the limits of control variables to forecast material removal rates.

4.1 Single Response Optimization for Maximization MRR

In this analysis, to find the optimal MRR, the PSO algorithm was used. The PSO program was run by MATLAB 7. The PSO algorithm involves the fixing of certain parameters. The overall number of iterations was known to be 100. Equation 5 provided the target feature adopted. Figure 1 displays PSO's convergence graph for MRR maximization. The PSO constraints consist of a number of elements, their location in the result space, and the inertia factors w, $c1$, and $c2$ [44]. The population

Fig. 1 PSO's convergence graph for MRR maximization
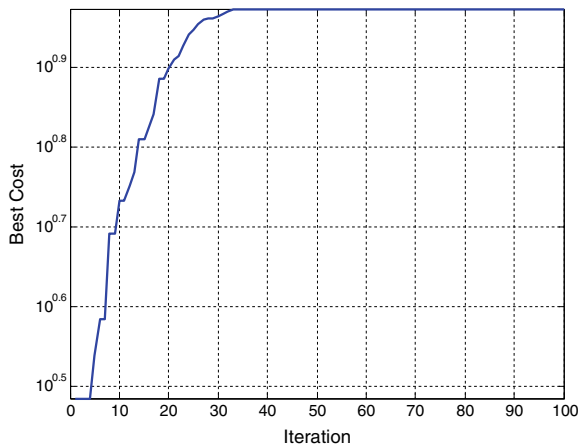
Table 5 Authentication of PSO forecast model

Type of optimization	Objective							Predicted result	Experimental result
		WF m/min	T_{on} (mu)	IP (A)	T_{off} (mu)	WT (mu)	SV (V)		
Single objective PSO	MRR	8	118	190	52	6	20	9.4234	9.3135

size in this research work was 50, describing the possible solution [43]. The w inertia factor varies between wmin and wmax, and 1.65 $c1$ and 1.75 $c2$ were taken.

The PSO system was used to optimize the single objective function (MRR), and it was discovered that T_{on} 118 (machine unit), T_{off} 52 (mu), SV 20 V, IP 190 A, WT 6 (mu), and WF 8 m/min were the best process parameters, with MRR reaching a limit of 9.4234 mm³/min.

4.2 Justification of Projected Results

The trials were conducted with optimal MRR combinations. Table 5 showed the comparison of results for MRR. Table 5 shows that the optimum combination of settings resulted in a 9.3135 mm³/min MRR.

5 Conclusion

- The rate of material removal is influenced by all of the input variables and their interactions. However, Ton, SV, and WF variables have a stronger impact on MRR. It is also worth noting that the relationship between feed rate of wire and pulse on time has a considerable effect on MRR.
- It can also be inferred that traditional and non-traditional manufacturing processes like milling, spinning, rotary ultrasonic, drilling, abrasive jet machining, facing, electrochemical machining, etc., can be appropriately applied to the PSO algorithm; the most effective use of PSO, however, is contingent on the algorithm's optimum set of controlled parameters.
- T_{on}-118 mu, T_{off}-52 mu, IP-190 A, WT-6 mu, SV-20 V, WF-8 m/min, and MRR 9.4234 mm³/min. The best global solution obtained by the use of the PSO relates to the beneficial consequences of MRR.

References

1. Dave HK (2019) Optimization of orbital electro discharge machining parameters using TLBO and PSO algorithms. Int J Mod Manuf Technol XI(2):1–6
2. Mathew B, Babu J et al (2014) Multiple process parameter optimization of WEDM on AISI304 using Taguchi grey relational analysis. Procedia Mater Sci 5:1613–1622
3. Rajyalakshmi G, Venkata Ramaiah P (2012) A parametric optimization using Taguchi method: effect of WEDM parameters on surface roughness machining on Inconel 825. Elixir Mechanical Engineering 43:6669–6674
4. Tosun N, Cogun C, Tosun G (2004) A study on kerf and material removal rate in wire electrical discharge machining based on Taguchi method. J Mater Process Technol 152(3):316–322
5. Mahapatra SS, Patnaik A (2007) Optimization of wire electrical discharge machining (WEDM) process parameters using Taguchi method. Int J Adv Manuf Technol 34(9–10):911–925
6. Yuan J, Wang K, Yu T, Fang M (2008) Reliable multi-objective optimization of high-speed WEDM process based on Gaussian process regression. Int J Mach Tools Manuf 48(1):47–60
7. Ikram A, Mufti NA, Saleem MQ, Khan AR (2013) Parametric optimization for surface roughness, kerf and MRR in wire electrical discharge machining (WEDM) using Taguchi design of experiment. J Mech Sci Technol 27(7):2133–2141
8. Khan NZ, Khan ZA, Siddiquee AN, Chanda AK (2014) Investigations on the effect of wire EDM process parameters on surface integrity of HSLA: a multi-performance characteristics optimization. Prod Manuf Res 2(1):501–518
9. Routara BC, Nanda BK, Patra DR (2009) Parametric optimization of CNC wire cut EDM using grey relational analysis. In: International conference on mechanical engineering, ICME09-RT-24
10. Majhi SK, Mishra TK, Pradhan MK, Soni H (2014) Effect of machining parameters of AISI D2 tool steel on electro discharge machining. Int J Curr Eng Technol 4(1):19–23
11. Lin KW, Wang CC (2010) Optimizing multiple quality characteristics of wire electrical discharge machining via Taguchi method-based gray analysis for magnesium alloy. J CCIT 39(1):23–34
12. Lal S, Kumar S, Khan ZA, Siddiquee AN (2015) Multi-response optimization of wire electrical discharge machining process parameters for Al7075/Al$_2$O$_3$/SiC hybrid composite using Taguchi-based grey relational analysis. Proc Inst Mech Eng Part B: J Eng Manuf 229(2):229–237
13. Bobbili R, Madhu V, Gogia AK (2015) Multi response optimization of wire-EDM process parameters of ballistic grade aluminium alloy. Eng Sci Technol Int J 18(4):720–726. https://doi.org/10.1016/j.jestch.2015.05.004
14. Jangra K, Jain A, Grover S (2010) Optimization of multiple-machining characteristics in wire electrical discharge machining of punching die using grey relational analysis
15. Haddad MJ, Tehrani AF (2008) Material removal rate (MRR) study in the cylindrical wire electrical discharge turning (CWEDT) process. J Mater Process Technol 199(1–3):369–378
16. Hewidy MS, El-Taweel TA, El-Safty MF (2005) Modelling the machining parameters of wire electrical discharge machining of Inconel 601 using RSM. J Mater Process Technol 169(2):328–336
17. Ghodsiyeh D, Davoudinejad A, Hashemzadeh M, Hosseininezhad N, Golshan A (2013) Optimizing finishing process in wedming of titanium alloy (Ti$_6$Al$_4$V) by brass wire based on response surface methodology. Res J Appl Sci Eng Technol. https://doi.org/10.17485/IJST/2012/V5I10/30915
18. Rajesh R, Anand MD (2012) The optimization of the electro-discharge machining process using response surface methodology and genetic algorithms. Procedia Eng 38:3941–3950
19. Sharma N, Khanna R, Gupta R (2013) Multi quality characteristics of WEDM process parameters with RSM. Procedia Eng 64:710–719
20. El-Taweel TA, Hewidy AM (2013) Parametric study and optimization of WEDM parameters for CK45 steel. Int J Eng Pract Res 2(4):156–169

21. Shandilya P, Jain PK, Jain NK (2013) RSM and ANN modeling approaches for predicting average cutting speed during WEDM of SiCp/6061 Al MMC. Procedia Eng 64:767–774

22. Yang SH, Srinivas J, Mohan S, Lee DM, Balaji S (2009) Optimization of electric discharge machining using simulated annealing. J Mater Process Technol 209(9):4471–4475

23. Guven O, Esme U, Kaya IE, Kazancoglu Y, Kulekci MK, Boga C (2010) Comparative modeling of wire electrical discharge machining (Wedm) process using Back propagation (BPN) and general regression neural networks (GRNN). Mater Technol 44(3):147–152

24. Joshi SN, Pande SS (2011) Intelligent process modeling and optimization of die-sinking electric discharge machining. Appl Soft Comput 11(2):2743–2755

25. Shandilya P, Tiwari A (2014) Artificial neural network modeling and optimization using genetic algorithm of machining process. J Autom Control Eng 2(4)

26. Rao TB, Krishna AG (2014) Compliance modelling and optimization of Kerf during WEDM of Al7075/SiCP metal matrix composite. Int J Mech Mechatron Eng 7(2):324–333

27. Diantoro M, Soepangkat BOP (2016) Optimization of multiple response characteristics in the WEDM process of Buderus 2379 ISO-B tool steel using Taguchi-Grey-Fuzzy logic method. In: Applied mechanics and materials, vol 836. Trans Tech Publications Ltd., pp 185–190

28. Sengottuvel P, Satishkumar S, Dinakaran D (2013) Optimization of multiple characteristics of EDM parameters based on desirability approach and fuzzy modeling. Procedia Eng 64:1069–1078

29. Maher I, Ling LH, Sarhan AA, Hamdi M (2015) Improve wire EDM performance at different machining parameters-ANFIS modeling. IFAC-PapersOnLine 48(1):105–110

30. Manjaiah M, Laubscher RF, Kumar A, Basavarajappa S (n.d.) Parametric optimization of MRR and surface roughness in wire electro discharge machining (WEDM) of D2 steel using Taguchi-based utility approach. https://doi.org/10.1186/s40712-016-0060-4

31. Zhang Z, Ming W, Huang H, Chen Z, Xu Z, Huang Y, Zhang G (2015) Optimization of process parameters on surface integrity in wire electrical discharge machining of tungsten tool YG15. Int J Adv Manuf Technol 81(5):1303–1317

32. Sarkar S, Sekh M, Mitra S, Bhattacharyya B (2008) Modeling and optimization of wire electrical discharge machining of γ-TiAl in trim cutting operation. J Mater Process Technol 205(1–3):376–387

33. Sarkar S, Mitra S, Bhattacharyya B (2005) Parametric analysis and optimization of wire electrical discharge machining of γ-titanium aluminide alloy. J Mater Process Technol 159(3):286–294

34. Maan V, Chaudhary A (2013) Optimization of wire electric discharge machining process of D-2 steel using response surface methodology. Int J Eng Res Appl (IJERA) 3(3):206–216

35. Sahu J, Mohanty CP, Mahapatra SS (2013) A DEA approach for optimization of multiple responses in electrical discharge machining of AISI D2 steel. Procedia Eng 51:585–591

36. Mohapatra KD, Sahoo SK (2015) Micro-structural analysis and multi-objective optimization in gear cutting process for AISI 304 stainless steel using wire EDM 26:978–993

37. Bobbili R, Madhu V, Gogia AK (2015) Modelling and analysis of material removal rate and surface roughness in wire-cut EDM of armour materials. Eng Sci Technol Int J 18(4):664–668

38. Mukherjee R, Chakraborty S, Samanta S (2012) Selection of wire electrical discharge machining process parameters using non-traditional optimization algorithms. Appl Soft Comput J. https://doi.org/10.1016/j.asoc.2012.03.053

39. Singh S, Garg D, Kumar S (2018) Investigation for obtaining the optimal solution for improving the performance of WEDM of super alloy Udimet-L605 using particle swarm optimization. Eng Sci Technol Int J 21(2):261–273. https://doi.org/10.1016/j.jestch.2018.03.005

40. Patel SS, Prajapati JM (2018) Experimental investigation of surface roughness and kerf width during machining of blanking die material on wire electric discharge machine. Int J Eng 31(10):1760–1766

41. Mohapatraa K, Satpathya M, Sahooa S (2017) Comparison of optimization techniques for MRR and surface roughness in wire EDM process for gear cutting. Int J Ind Eng Comput 8(2):251–262

42. Ingh S, Isra M (2016) A critical review of wire electric discharge machining, pp 249–266. https://doi.org/10.2507/daaam.scibook.2016.23
43. Guo WY, Chen LG, Cao Y (2013) Study on the optimization of absorption baffle with coating material. Adv Res Intell Syst Mech Eng 644:165–170. https://doi.org/10.4028/www.scientific.net/AMR.644.165
44. Kumar P, Gupta M, Kumar V (2019) Experimental analysis of WEDM machined surface of Inconel 825 using single objective PSO. J Phys Conf Ser 1240(1):012053 (IOP Publishing, July)
45. Shayan AV, Afza RA, Teimouri R (2013) Parametric study along with selection of optimal solutions in dry wire cut machining of cemented tungsten carbide (WC-Co). J Manuf Process 15(4):644–658
46. Zhang HC, Tang L, Yang QL (2011) Optimization of the ultrasonic wave-assisted extraction condition of peanut protein isolate. Adv Mater Res 189:3904–3911 (Trans Tech Publications Ltd.)
47. Sreebalaji VS, Kumar KR (2016) Artificial neural networks and multi response optimisation on EDM of aluminium (A380)/fly ash composites. Int J Comput Mater Sci Surf Eng 6(3–4):244–262

Slurry Abrasion Wear Assessment of Hybrid-Reinforced Polymer Composite Using Comparative Taguchi Gray Relational Analysis

Vikash Gautam, Aakash Sharma, Amar Patnaik, M. J. Pawar, Ashiwani Kumar, and Vikas Kukshal

1 Introduction

Tribology is known to be a vague term that deals with friction, lubrication, and wear. When one body has relative movement with other contacting body, friction is said to occur at the interface of both the bodies which further results in removal of materials from softer material body. This process of removal of material from the softer material body is known as wear [1].

There are many different types of wear such as adhesive wear, erosive wear, sliding wear, and fatigue wear, but as far as the components such as slurry pumps, slurry nozzles, and pipes in the power plants and mining industries are concerned, the most common type of wear among all is the abrasive wear [2]. Several research studies [3–5] inferred from their work that abrasive wear single-handedly contributes 50% of the total industry failures.

Studies on the wear due to abrasion of the stainless steel surface [6], mild steel [7], and glass/epoxy composites filled with aluminum oxide [8] have concluded that the abrasive size and slurry concentration have a direct impact on the abrasive wear rate.

V. Gautam (✉) · A. Sharma (✉)
Department of Mechanical Engineering, Swami Keshvanand Institute of Technology, Jaipur, India

A. Patnaik
Mechanical Engineering Department, Malviya National Institute of Technology, Jaipur, India
e-mail: apatnaik.mech@mnit.ac.in

M. J. Pawar
Mechanical Engineering Department, K. J. Somaiya College of Engineering, Mumbai, India

A. Kumar
Mechanical Engineering Department, Feroze Gandhi Institute of Technology, Lucknow, India

V. Kukshal
Mechanical Engineering Department, National Institute of Technology, Uttarakhand, India
e-mail: vikaskukshal@nituk.ac.in

Researchers have also reviewed the abrasive wear [9] in different polymer composites and inferred more on fiber-reinforced composites and less on filler-reinforced composites. Because of its low weight percentage in the composite material, the filler is considered less as a reinforcement material [10]. Surendra Kumar et al. in their work learned the slurry abrasive wear behavior of metal matrix composites incorporated with zirconium sand [11] and titanium carbide [12] under dry and wet sand conditions [13]. Various studies have shown that the considered need to determine the impact of various abrasives on the abrasive wear behavior of the composites is necessary to improve the cost efficacy of the machines used in slurry environment.

To solve disputed and uncertain industrial problems, Taguchi gray relational analysis has been extensively used. GRA based on Taguchi optimization technique is exploited in order to optimize the input design parameters for multi-criteria outputs such as wear rate [14]. Using this optimization technique, multi-criteria performance characteristics can be easily converted into simple gray relational grade (GRG) which can be further optimized by exploiting the Taguchi method in its pure form [15].

In the present work, titania particulates/granite dust is used as filler material to obtain granite dust/titania-filled hybrid-reinforced polymer composites. Further, the fabricated composites are tested for slurry abrasion resistance, and the results are optimized using multi-response Taguchi-based gray relational technique.

2 Experimental Details

2.1 Materials and Methodology

In the present study, conventional hand lay-up method is used to fabricate the granite dust/titania particulate-filled hybrid polymer composite specimens. For magnificent chemical and abrasion wear resistance, vinyl ester is used as a matrix material along with E-glass fiber as a reinforcement, which is predominantly a mixture of various oxides such as silica and alumina [16]. Further, Titania particulates and granite dust is used as a filler material for excellent abrasion resistant characteristics. Titania is purely an oxide of titanium, whereas granite dust [17] is a combination of various oxides.

The composition of vinyl ester in the composites is varied from 70 to 55% while E-glass fiber weight fraction is kept constant at 30%. The granite dust/titania weight fraction is varied from 5 to 15% in correspondence with the composition of vinyl ester (Table 1).

The vinyl ester matrix in 10 parts by weight is mixed with its corresponding hardener in 1 part by weight, i.e., in the weight ratio of 10:1, respectively. For easy removal of composites from the wooden mold of dimension 340 * 340 * 40 mm^3, silicon mold releasing spray has been applied. During the curing of the composites, the load of 40 kg is applied for about 24 h before their removal from the wooden mold. The casted composite specimens are post cured for another 24 h. Finally, the

Table 1 Notations and compositions of the specimens

Notations	Composition (by weight)
EGG-0	E-glass fiber (30%) + vinylester (70%)
EGT-5	E-glass fiber (30%) + vinylester (65%) + titania (5%)
EGT-10	E-glass fiber (30%) + vinylester (60%) + titania (10%)
EGT-15	E-glass fiber (30%) + vinylester (55%) + titania (15%)
EGG-5	E-glass fiber (30%) + vinylester (65%) + granite (5%)
EGG-10	E-glass fiber (30%) + vinylester (60%) + granite (10%)
EGG-15	E-glass fiber (30%) + vinylester (55%) + granite (15%)

diamond cutter is used for the cutting of composite specimen of desired size for slurry abrasion wear testing.

2.2 Slurry Abrasion Wear Assessment

Abrasion wear behavior of the obtained composite material specimens using slurry as a third-body abrasive is examined and speculated under varying operating parameters using the slurry abrasion test rig according to ASTM G105.

The slurry abrasion test rig (Fig. 1) consists of a rubber wheel ($\phi = 178$ mm and 50 HRC) that involves the abrasion of fabricated specimens with controlled size grit, a loading lever mechanism that involves the application of load on the standard test samples, a hopper that involves pouring slurry (abrasive particles and water mixture), and a control panel. This slurry flows in contact between the test specimen and the rubber wheel. This ongoing flow of slurry abrading the specimen surface

Fig. 1 Slurry abrasion test rig

which will be tested while making use of the lever arm mechanism, the specimen is pressed against the rubber rim for the evaluation of abrasion at a particular force. The applied force using the lever arm and the duration of the abrasion test are varied throughout the experimentation. The weight loss due to wear can be, then, estimated by weighing the test samples before and after the test. Slurry abrasion wear can be, thus, calculated on the basis of volumetric wear as follows:

$$W = \frac{\Delta M}{\rho} * S * N \tag{1}$$

where

ΔM	mass loss due to abrasion wear (gm).
ρ	density of the fabricated vinyl ester composites (gm/mm^3).
S	sliding distance of the composite (m).
N	applied load by lever mechanism (N).
W	abrasion wear rate (Nm/mm^3).

2.3 Taguchi's Design of Experiments

Since our goal is to get the best possible results by taking into account all levels of variables, so the optimization of the experimental setup is carried out in order to minimize the overall time and cost required for different tests. A comprehensive review of the literature infers that factors such as speed of the wheel, applied normal load, filler content, and grit size of the abrasives strongly affect the abrasive wear properties of the produced composite material. Therefore, the effects of the four variables are investigated using an orthogonal L16 design. Table 2 clearly mentions the control factors and various levels of input value assigned to them.

The experimental design is: The amount of filling is mentioned in the first column, the wheel speed in the second, the third column consists of normal load, and the fourth column is the size of the erodent while the columns that are remaining will be used to evaluate the experimental error. The columns of the orthogonal matrix are occupied by random values of assigned control factors. Table 3 shows the L16 Taguchi orthogonal array along with their notations used in the present work. Once the level

Table 2 Control factors, levels with their units

Control parameters	Levels			
	1	2	3	4
Wheel speed	100 RPM	150 RPM	200 RPM	250 RPM
Normal load	5 N	10 N	15 N	20 N
Abrasive size (μm)	106	150	212	300
Filler contents (%)	0	5	10	15

Table 3 L16 orthogonal array for Taguchi's design of experiment

S. No	Filler content (%)	Wheel speed (RPM)	Applied load (N)	Abrasive size (μm)	Notations
1	0	100	5	106	A0
2	0	150	10	150	B0
3	0	200	15	212	C0
4	0	250	20	300	D0
5	5	100	10	212	A5
6	5	150	5	300	B5
7	5	200	20	106	C5
8	5	250	15	150	D5
9	10	100	15	300	A10
10	10	150	20	212	B10
11	10	200	5	150	C10
12	10	250	10	106	D10
13	15	100	20	150	A15
14	15	150	15	106	B15
15	15	200	10	300	C15
16	15	250	5	212	D15

settings have been set, S/N ratio is required to examine the results of the experiment. There are predominately three S/N characteristics, i.e., lower-the-better, nominal-the-better, and higher-the-better. For analyzing the optimal degree of abrasive wear, the lower-the-better characteristic of the signal-to-noise ratio must be taken as follows:

$$\frac{S}{N} = -10\log\frac{1}{n}(y^2) \tag{2}$$

where

n Observation number
i   Observed value.

ANOVA is performed to determine important process parameters for the experiment. The S/N ratio and ANOVA analysis can be prominently exploited to find the optimal set of control factors. At last, a validation experiment is performed to test the perfect solution obtained in the design of the Taguchi experiment.

2.4 *Gray Relational Analysis*

The theory of the gray system, developed by Professor Deng, is proven to be a useful tool for treating the poor, discrete, and unreliable data. Between black and white set of information, the gray system consists certain details [18]. This is an effective way to evaluate the low data correlation between the sequences and can evaluate multiple variables.

For the evaluation of multi-performance characteristics, gray relational grade is obtained using GRA. As a result of the GRA, the multi-performance characteristic optimization, which is quite complicated, can be easily converted to simple gray relational grade [19].

Data preprocessing

The experiments were conducted as per Table 3 for calculating the slurry abrasion wear rate of granite dust/titania particulate-filled hybrid polymer composite specimen based on the Taguchi's orthogonal array. The experimental results of abrasion wear rate for granite dust-filled composites, and titania-filled composites were normalized in the strict range of 0 and 1 based on the characteristics of the calculated values. Since we are calculating the abrasion wear for granite/titania-filled polymer composites, the smaller-the-better characteristics are used for the set of experimentation performed. The experimental data is normalized for smaller-the-better characteristic as follows [20]:

$$\omega i * (k) = \frac{\max . \omega i°(k) - \omega i°(k)}{\max . \omega i°(k) - \min . \omega i°(k)} \tag{3}$$

where

i 1, …, m; (m = no. of experimental data).
k 1, …, n; (no. of operational parameters).

The symbol $\omega i * (k)$ denotes the sequence before the data preprocessing, $\omega i°(k)$ denotes the preprocessed data sequence, $max . \omega i°(k)$ and $min . \omega i°(k)$ denote the maximum and minimum value of $\omega i°(k)$, respectively.

The deviation sequences $\Delta i(k)$ for $i = 1$–16 and $k = 1$–2 are also calculated for the following Taguchi's orthogonal set of experiments.

Calculation of GRC

The gray relational coefficient experiment after data has been preprocessed for the kth operation in the ith set of is determined as follows:

$$\xi i(k) = \frac{\Delta \min . + \zeta \Delta \max .}{\Delta i(k) + \zeta \Delta \max .} \tag{4}$$

where $\Delta i = |\omega * (k) - \omega i * (k)|$

The sequence particularly used for referencing with the original sequence is denoted by $\omega * (k)$, and the original sequence is denoted by $\omega i * (k)$. The value of $\xi i(k)$ lies between the strict range of 0 and 1. The value gray relational coefficient $\xi i(k)$ can be 1 in some set of experiments. ζ represents the distinguishing coefficient whose value is defined in the range of 0 and 1; generally, the value of ζ is opted as 0.5.

Calculation of GRG

The gray relational grade, which is the optimal mean of gray relational coefficients, is calculated as below:

$$\gamma i = \frac{1}{n} \sum_{k=1}^{n} \xi i(k) \tag{5}$$

The symbol γi represents the GRG which denotes the association between the original and the reference sequence which further determines the ranking for the set of experiments. Table 4 depicts the calculated gray relational grade for the following L16 orthogonal array. Higher the value of gray relational grade, the closer the set of operating parameters to the optimality.

3 Results and Discussion

Abrasion tests were performed to investigate the influence of process parameters on response characteristics. Based on experimental results, the gray relational grade of response characteristics was determined for each change at different levels. The main impact of changes in the GRG process is plotted. Response plots are used to analyze the parametric effect on response properties. GRG transformation analysis (ANOVA) is used to classify important variables and measure their impact on response properties.

For average response characteristics, the optimal settings for the process are calculated from ANOVA tables and response graphs. Table 4 shows the experimental slurry abrasion wear results and their S/N ratios along with the gray relational coefficients. The ranks of optimal input parameters are also assigned, keeping in consideration the gray relational grades obtained from their respective coefficients.

In present research work, smaller is better S/N ratio condition was used. From S/N Ratio table, it was depicted that overall mean S/N ratio for granite-filled composites was -41.2555 and for titania-filled composites was -41.5945.

The main effects plot for S/N ratio of different input parameters with their levels for granite and titania hybrid composites were presented in Figs. 2 and 3. From both figures, it was depicted that 15% filler content, 100 RPM wheel speed, 5 N normal load, and 106 micron erodent size particles cause minimum wear rate for granite and titania-filled polymer composites. The above presented levels obtained minimum

Table 4 Experimental results and gray relational analysis of hybrid polymer composites

S. No.	Notations	Abra. wear (Granite) (gm/Kg)	S/N ratio (db)	Abra. wear (Titania) (gm/Kg)	S/N ratio (db)	GRC (Granite)	GRC (Titania)	GRG	Rank
1	A0	106	− 40.506	115	− 41.214	0.857	0.633	0.745	4
2	B0	119	− 41.510	120	− 41.583	0.529	0.542	0.536	10
3	C0	129	− 42.211	130	− 42.278	0.409	0.422	0.415	15
4	D0	139	− 42.860	142	− 43.045	0.333	0.333	0.333	16
5	A5	110	− 40.827	121	− 41.655	0.72	0.527	0.623	8
6	B5	108	− 40.668	115	− 41.214	0.782	0.633	0.707	5
7	C5	125	− 41.938	132	− 42.411	0.45	0.404	0.427	14
8	D5	123	− 41.798	128	− 42.144	0.473	0.441	0.457	13
9	A10	117	− 41.363	121	− 41.655	0.562	0.527	0.545	9
10	B10	121	− 41.655	127	− 42.076	0.5	0.452	0.476	12
11	C10	105	− 40.423	112	− 40.984	0.9	0.703	0.801	3
12	D10	111	− 40.906	116	− 41.289	0.692	0.612	0.652	6
13	A15	119	− 41.510	121	− 41.655	0.529	0.527	0.528	11
14	B15	113	− 41.061	115	− 41.214	0.642	0.633	0.638	7
15	C15	107	− 40.587	109	− 40.748	0.818	0.791	0.804	2
16	D15	103	− 40.256	104	− 40.340	1	1	1	1
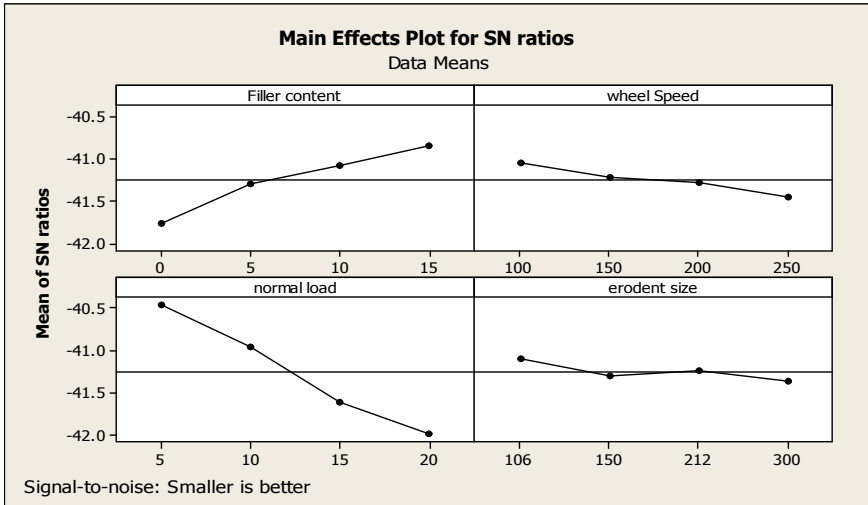
Fig. 2 Response graph of composite filled with granite
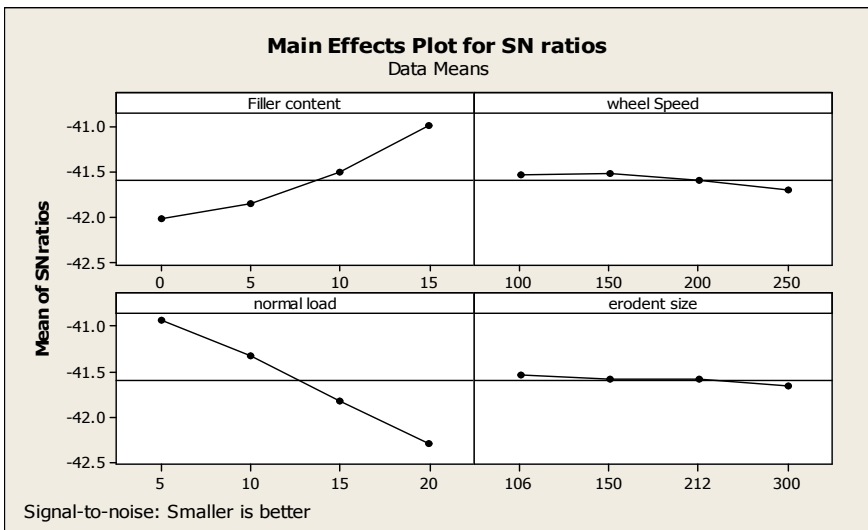
Fig. 3 Response graph of composite filled with titania

wear rate among all selected levels for individual factor for granite and titania-filled glass fiber-reinforced polymer composites. From the comparison of mean effect of S/N ratios of individual input parameters, it was clearly observed that filler content graph of 10% granite-filled composites was nearby to mean position; on the other hand, for titania filled composites, 15% was nearby to mean position. As far as erodent

size is concerned, mean effects plot for S/N ratio graph for 212 micron size granite-filled composites lies on mean line; on the other hand, for titania-filled composites, both 150 and 212 micron levels were on mean line.

3.1 ANOVA Analysis of Hybrid Polymer Composites

ANOVA tool was used to identify the most and least influence input parameter among all the selected input parameters. ANOVA analysis of hybrid polymer composites was presented in Tables 5 and 6. For titania-filled polymer composites, all factors contribute to output parameters, but the most significant factors were normal load and filler content with percentage contribution of 61.39 and 36.91%. On the other hand, least significant factors were wheel speed and erodent size with percentage contribution of 1.165 and 0.52%.

From Table for granite-filled glass fiber-reinforced polymer composites, the most significant factors were normal load and filler content with percentage contribution of 70.34% and 23.37% whereas, on the other hand, least significant factors were wheel speed and erodent size with percentage contribution of 4.26 and 2.02%.

Comparing the ANOVA results of both granite and titania-filled glass fiber-reinforced polymer composites. It was concluded that the order of most significant factor to least significant factor was same. The percentage contribution of each

Table 5 ANOVA of wear rate for titania filler hybrid composites

Source	DF	Seq. SS	Adj. SS	Adj. MS	F-Value	Percentage contribution
Filler content (%)	3	2.53259	2.53259	0.84420	21.86	36.91
Wheel speed (RPM)	3	0.08008	0.08008	0.02669	0.69	1.165
Normal load (N)	3	4.21042	4.21042	1.40347	36.35	61.39
Abrasive size (μm)	3	0.03620	0.03620	0.01207	0.31	0.52
Error	3	0.11584	0.11584	0.03861		
Total	15	6.97513				

Table 6 ANOVA of wear rate for granite filler hybrid composites

Source	DF	Seq. SS	Adj. SS	Adj. MS	F-Value	Percentage contribution
Filler content (%)	3	1.83644	1.83644	0.61215	22.51	23.37
Wheel speed (RPM)	3	0.33402	0.33402	0.11134	4.10	4.26
Normal load (N)	3	5.52554	5.52554	1.84185	67.74	70.34
Abrasive size (μm)	3	0.15891	0.15891	0.05297	1.95	2.02
Error	3	0.08157	0.08157	0.02719		
Total	15	7.93648				

factor was different on output performance of granite and titania-filled glass fiber-reinforced polymer composites such as normal load percentage for granite and titania-filled composites was 70.34 and 61.39, respectively, and filler content percentage for granite and titania filled composites was 23.37 and 36.91, respectively.

4   Conclusion

Some of the deductions were written according to the slurry abrasion wear experimentation as follows:

1. The titania particulate-filled hybrid polymer composites are fabricated successfully using the conventional hand lay-up technique and compared with the results of granite dust-filled E-glass fiber-reinforced vinyl ester-based polymer composites.
2. It was concluded that with the inculcation of granite dust/titania particulate in the virgin polymer composites, the slurry abrasive wear resistance of the newly fabricated composites infers significant improvement in the existing characteristics.
3. For granite dust-filled hybrid polymer composites, the most significant factors are normal load and filler content with 70.34 and 23.37% contribution, respectively, whereas the wheel speed contribution is limited to 4.26% followed by erodent size with 2.02%.
4. For titania particulate-filled hybrid polymer composites, the most significant factors are normal load and filler content with 61.39 and 36.91% contribution, respectively followed by wheel speed contribution limited to 1.16% and erodent size with 0.52%.
5. GRA technique is successfully applied to improve the experimental results and determine the rankings of the fabricated polymer composites.
6. According to GRA, the most impactful set of input parameters includes 15% granite dust/titania content, 5 N normal load, 250 RPM wheel speed, and 212 μm erodent size while the least significant parameters are for virgin polymer composites.

References

1. Sarfraj A, Thakare OP, Shrivastava R, Sharma S, Sapate SG (2018) A review on slurry abrasion of hard faced steels. Mater Today Proc 5:3524–3532
2. Petrica M, Katsich C, Badisch E, Kremsner F (2013) Study of abrasive wear phenomena in dry and slurry 3-body conditions. Tribol Int 64:196–203
3. Zumgahr K (1987) Microstructure and wear of materials. Elsevier Science Publishers Amsterdam
4. Stachowiak GW, Batchelor A (2002) Engineering trybology, 3rd edn. Elsevier, London

5. Stolarski TA (2000) Tribology in machine design. Butterworth-Heinemann, Oxford
6. Balasubramanian V, Varahamoorthy R, Ramachandran CS, Babu S (2008) Abrasive slurry wear behavior of stainless steel surface produced by plasma transferred arc hard facing process. Surf Coat Technol 202:3903–3912
7. Rathod A, Sapate SG, Khatirkar RK (2014) Scaling laws of wear by slurry abrasion of mild steel. Appl Mech Mater 446–447:126–130
8. Joshi AG, Prasannakumar M, Pasavarajappa S (2014) Influence of Al_2O_3 fillers on the slurry erosion behavior of glass/epoxy composites. Procedia Mater Sci 5:863–872
9. Unal H, Sen U, Mimaroglu A (2005) Abrasive wear behaviour of polymeric materials. Mater Des 26:705–710
10. Biswas S, Satapathy A, Patnaik A (2009) Erosion wear behavior of polymer composites: a review. J Reinfo Plast Compos. https://doi.org/10.1177/0731684408097786
11. Patel SK, Kuriachen B, Kumar N, Nateriya R (2018) The slurry abrasive wear behaviour and microstructural analysis of A2024-Sic-Zrsio4 metal matrix composite. Ceram Int 44(6):6426–6432
12. Patel SK, Nateriy R, Kuriachen B, Singh VP (2018) Slurry abrasive wear, microstructural and morphological analysis of titanium carbide and zirconium sand aluminium alloy (A5052) metal matrix composite. Mater Today Proc 5:19790–19798
13. Deng X, Huang L, Wang Q, Fu T, Wang (2020) Three-body abrasion wear resistance of tic-reinforced low-alloy abrasion-resistant martensitic steel under dry and wet sand conditions. Wear. https://doi.org/10.1016/j.wear.2020.203310
14. Alagarsamy SV, Ravichandran M, Meignanamoorthy M (2020) Multi-objective optimisation of dry sliding wear control parameters for stir casted Aa7075-TiO_2 composites using Taguchi-grey relational approach. Aust J Mech Eng. https://doi.org/10.1080/14484846.2020.1815997
15. Vinukumar S, Suresha B, Rajamurugan G, Megalingam A (2018) Mechanical and abrasive wear behavior of cenosphere filled carbon reinforced epoxy composites using Taguchi-Grey relational analysis. Mater Res Express 6(1)
16. Gautam V, Kumar A, Sharma A, Kumar D, Kumar A (2021) Tribological behaviour of hybrid reinforced vinyl ester based functionally graded materials. Mater Today: Proc 44(6):4682–4688
17. Sharma A, Gautam V (2021) Mechanical and wear characterization of epoxy resin-based functionally graded material for sustainable utilization of stone industry waste. In: Advances in manufacturing systems: select proceedings of RAM 2020, p 30
18. Perumal S (2020) Study of tribology behavior of hybrid composites of aluminium matrix using Taguchi gray relational analysis system. Int Res J Adv Sci Hub 2(11):53–59
19. Dharmalingam S, Subramanian R, Kok M (2013) Optimization of abrasive wear performance in aluminium hybrid metal matrix composites using Taguchi–grey relational analysis. In: Proceedings of the institution of mechanical engineers, Part J: Journal of engineering tribology https://doi.org/10.1177/1350650112467945
20. Julong D (1989) Introduction to grey system theory. J Grey Syst 1:1–24

Experimental Investigation and Optimization of PM-EDM by Using Al Powder on Tungsten Carbide

Shubham Najan and B. Rajiv

1 Introduction

EDM is widely used non-traditional machining process in this present manufacturing era. In normal EDM, workpiece and electrode are submerged in dielectric fluid. In powder-mixed EDM, two-phase dielectric is used, that is, the mixture of powder and dielectric liquid. The electro-discharge machining (EDM) has large application in the production of dies and molds [1]. EDM is useful to machine those materials which are tough to machine by the conventional machining process. Powder-mixed EDM helps to improve surface finish and MRR adequately as compared to conventional EDM. Study on EDM describes that the material removal rates are lesser in the EDM than the other conventional machining processes [2]. The main advantage of using EDM over conventional machining processes is very high surface finish rates. Because of its ability to process any conductive material, regardless of its strength attributes, EDM has found various applications in the die and tool making, aero-space, automotive, and surgical equipment manufacturing industries [3].

The advantage of using EDM is that there are no machining vibrations and mechanical stresses arises during machining due to no direct contact between the workpiece and tool material. Another benefit of using EDM over other conventional machining processes is that it can machine any geometry or profile. It can easily machine the intricate geometry which can be arduous to machine by some other machining processes. The limitation of the process is only the tool material and workpiece must be electrically conducted.

S. Najan (✉) · B. Rajiv
Department of Manufacturing Engineering and Industrial Management, College of Engineering, Pune. (COEP), Maharashtra 411005, India

2 Experimental Setup

The authors have done the experiments on smart CNC machine for PM-EDM, shown in Fig. 1.

The authors have used tungsten carbide as the workpiece material while copper as an electrode material. Dielectric used is EDM oil for experimentation. The powder used for PM-EDM process is fine aluminum powder. The powder can be used from 0 to 45 gm/l; however, during experiment, authors have used the powder from 0 to 9 gm/l in four levels as follows 0 gm/l, 3gm/l, 6gm/l, and 9gm/l. The authors have used circular as well as square type of electrodes in order to study the difference in MRR, TWR, and surface finish.

Authors manufactured separate EDM oil tanks for the purpose of powder mixing so that whole EDM oil do not get contaminated because of the powder. Manufactured tank used has a capacity of 25 L, made of cast iron, shown in Fig. 2. Aluminum powder is mixed with EDM oil, and experimentation is done. Fiber pipe is used for stirring purpose; the reason behind using the fiber pipe is nonconductive, so it will be safe for operator to use.

Fig. 1 Smart CNC EDM machine

Fig. 2 Separate powder-mixed tank

3 Experimental Conditions

For selecting the proper experimental parameters, number of trail experiments has been conducted by the authors by varying the different parameters such as increasing the peak current and decreasing the pulse on time and vice versa. The parameters put in the MINITAB software for L16 orthogonal array. In addition, appropriate EDM parameters are considered. The duty factor, which is the ratio of pulse duration to pulse cycle time, is critical to EDM efficiency. The duty factor is derived from the on-time and off-time. Number of DOE sheets are generated varying the parameters, number of trails has been done, after number of trails considering the surface finish, using standard parameters of EDM, the optimum DOE sheet is generated shown in Table three. Tungsten carbide (CW10 grade) was used as a workpiece material, and Table 1 lists their physical characteristics. Copper electrode, not only circular but also of square-shaped, was used for the experimentation purpose. Copper electrode is used due to its high material removal rate for rough machining (Tables 2 and 3).

Table 1 Physical properties of tungsten carbide

Properties	Tungsten carbide (WC–Co)
Melting point (°C)	2870
Density (g/cm^3)	15.7
Thermal expansion (°C)	5×10^{-6}
Hardness (HRA)	87.4
Elastic modulus (GPa)	648
Electrical resistivity (Ω cm)	17×10^{-6}

Table 2 Process parameters

Machining parameters	Level 1	Level 2	Level 3	Level 4
Peak current (Ip)	4	6	8	10
Pulse on time (T_{on})	4.0	5.0	7.5	10.0
Duty cycle (%)	50	65	80	95

Table 3 DOE sheet

Std order	Run order	Peak current	Ton	Duty cycle	Powder concentration
1	1	4	4.0	50	0
5	2	4	5.0	65	3
9	3	4	7.5	50	6
13	4	4	10.0	65	9
10	5	6	4.0	50	6
14	6	6	5.0	65	9
2	7	6	7.5	65	0
6	8	6	10.0	80	3
15	9	8	4.0	80	9
11	10	8	5.0	65	6
7	11	8	7.5	50	3
3	12	8	10.0	80	0
8	13	10	4.0	65	3
4	14	10	5.0	80	0
16	15	10	7.5	80	9
12	16	10	10.0	80	6

4   Results and Discussion

The graphical data showed in following figures was obtained after the experimentation. The authors have done experiments with both circular and square-type electrodes. The main effects plots for MRR of experimentation for squared electrode are shown in Fig. 3, whereas main effects plots for TWR are shown in Fig. 4.

Main effects plots for MRR shows the behavior of workpiece material, that is, tungsten carbide for different machining parameters. The response optimizer of the Minitab software was used to generate the main effects optimization plots displayed in Figs. 3 and 4 as well as in Figs. 5 and 6. The peak current (I_p) and powder concentration have tremendous impact on the MRR, as seen in the main effects' plots. MRR improves as powder concentration rises, but at large powder concentrations, MRR is nearly flat. The TWR reduces as the powder concentration rises.

All of these experiments show that errors being distributed randomly. The main effects plot in Figures illustrates that MRR increases as current increases. The effect of the gap voltage, the pulse, the duty factor on time, and duty factor is minimal. Surface roughness decreases as gap voltage is increased. In the instance of PM-EDM, the minimal value of SR was detected at the minimum value of T_{on}.

After the experimentation, the graphical data shown in the following figures was collected by using the Minitab software. Both round and square electrodes were used in the studies by the authors. Figure 5 shows the major effects plots for the MRR of the circular electrode experiment, whereas Fig. 6 shows the main effects plots for TWR.

Fig. 3 Main effects plots for MRR (squared)
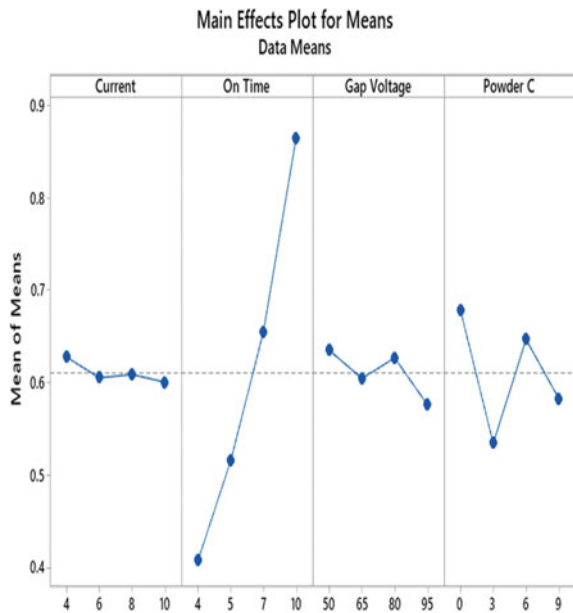
Fig. 4 Main effects plots for TWR (squared)
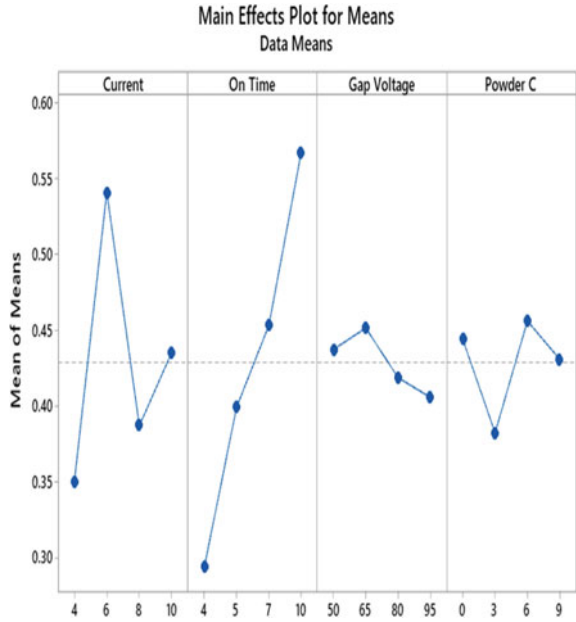
Fig. 5 Main effects plots for MRR (Circular)
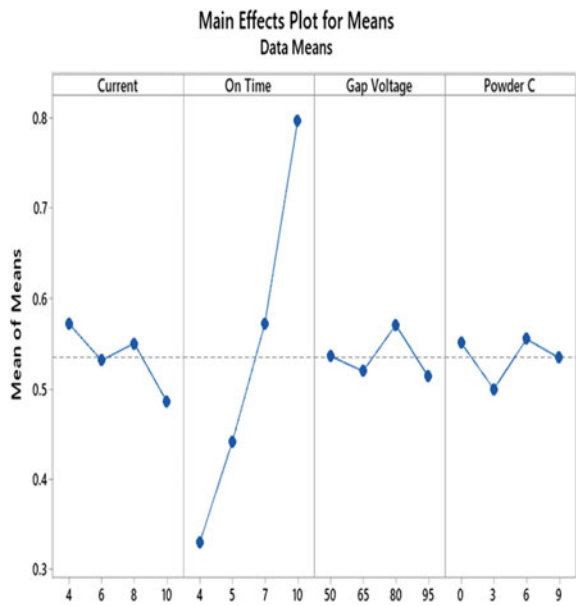
Fig. 6 Main effects plots for TWR (Circular)
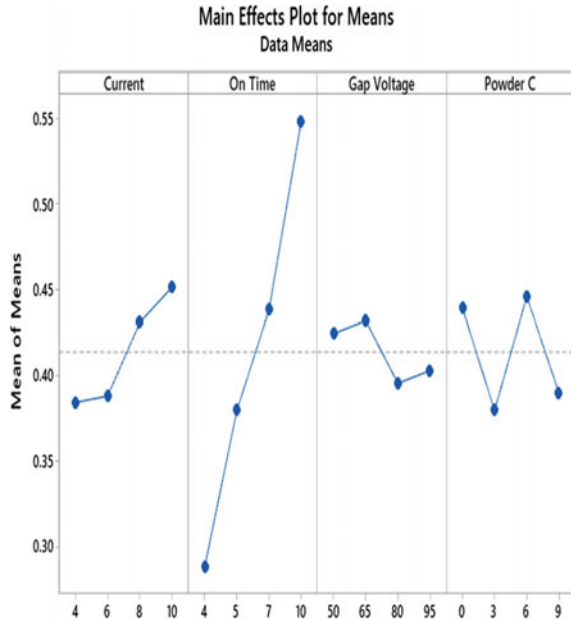
Following are the results obtained after the experimentation. The authors have done experiments with both circular and square type of electrodes. Authors have found that there is not much difference in MRR and TWR of two different shapes. The results of experimentation for square electrode are shown in Table 4, while outcomes of circular electrodes are shown in Table 5.

There are several optimization techniques used in EDM process like gray relational analysis, neural network method, genetic algorithm method, finite element method, artificial bee colony optimization, fuzzy set theory method. These methods play an important role in EDM optimization and data analysis. Here, authors have used gray relational analysis method for EDM optimization.

4.1 ANOVA and Regression Analysis

The regression analysis methodology is used to discover the most appropriate equation that represents the response parameters in relation to the input variables. The regression coefficient is a metric that shows how far the built-up connection is valid for ensuring output variable estimations while using output variable estimations, for which readings are not available in the range of least and most extreme output variable estimations.

ANOVA table is used to verify the significance of the regression model. It is determined whether the inclusion of a given parameter in the model is useful or

Table 4 Experimentation results for **square** electrode

Process parameters			Responses	
Peak current	T_{on}	Duty cycle	MRR (g/min)	TWR (g/min)
1	1	1	0.4917	0.2426
1	2	2	0.5021	0.2986
1	3	3	0.7323	0.3732
1	4	4	0.7846	0.4852
2	1	2	0.3975	0.4740
2	2	1	0.5147	0.5039
2	3	4	0.7344	0.5599
2	4	3	0.7742	0.6270
3	1	3	0.4456	0.2463
3	2	4	0.4896	0.3658
3	3	1	0.5670	0.3919
3	4	2	0.9332	0.5449
4	1	4	0.2950	0.2127
4	2	3	0.5545	0.4292
4	3	2	0.5858	0.4889
4	4	1	0.9667	0.6121

not utilizing the student's t-test. If the t-significant test's result is less than 0.05, the parameters are significant. Table 6 shows ANOVA for MRR of square electrode, while Table 7 displays ANOVA for TWR of square electrode.

P-values of less than 0.05 indicate significance of the parameters. Gap voltage and powder concentration are important parameters in this case.

The regression equation obtained for MRR of square electrode is as follows:

$$MRR = 0.256 - 0.00389\,Current + 0.07440\,On\,Time - 0.00104\,Gap\,Voltage - 0.00585\,Powder\,C$$

The significant parameters in the TWR ANOVA table are gap voltage and pulse on time. Following regression equation displays the relation between input parameters and TWR,

$$TWR = 0.177 + 0.0052\,Current + 0.0418\,On\,Time$$
$$- 0.00085\,Gap\,Voltage + 0.00115\,Powder\,C$$

Table 8 shows ANOVA for MRR of circular electrode, while Table 9 displays ANOVA for TWR of circular electrode.

P-values of less than 0.05 imply that the parameters are significant. In this scenario, the pulse on time and current are critical characteristics.

Table 5 Experimentation results for **circular** electrode

Process parameters			Responses	
Peak current	T_{on}	Duty cycle	MRR (g/min)	TWR (g/min)
1	1	1	0.3452	0.2948
1	2	2	0.4289	0.3247
1	3	3	0.7323	0.4292
1	4	4	0.7846	0.4889
2	1	2	0.3034	0.3172
2	2	1	0.5042	0.3471
2	3	4	0.5649	0.4180
2	4	3	0.7553	0.4703
3	1	3	0.3808	0.2538
3	2	4	0.4164	0.4180
3	3	1	0.5273	0.4367
3	4	2	0.8788	0.6159
4	1	4	0.2887	0.2874
4	2	3	0.4164	0.4292
4	3	2	0.4687	0.4703
4	4	1	0.7700	0.6196

Table 6 ANOVA table for MRR of square electrode

Source	DF	Seq SS	Contribution (%)	Adj SS	Adj MS	F-value	P-value
Regression	4	0.477126	87.43	0.477126	0.119281	19.13	0.000
Current	1	0.001213	0.22	0.001213	0.001213	0.19	0.668
On time	1	0.464933	85.20	0.464933	0.464933	74.57	0.000
Gap voltage	1	0.004828	0.88	0.004828	0.004828	0.77	0.398
Powder C	1	0.006151	1.13	0.006151	0.006151	0.99	0.342
Error	11	0.068581	12.57	0.068581	0.006235		
Total	15	0.545707	100.00				

Table 7 ANOVA table for TWR of square electrode

Source	DF	Seq SS	Contribution (%)	Adj SS	Adj MS	F-value	P-value
Regression	4	0.152644	59.15	0.152644	0.038161	3.98	0.031
Current	1	0.002142	0.83	0.002142	0.002142	0.22	0.646
On time	1	0.146994	56.96	0.146994	0.146994	15.34	0.002
Gap voltage	1	0.003269	1.27	0.003269	0.003269	0.34	0.471
Powder C	1	0.000238	0.09	0.000238	0.000238	0.02	0.878
Error	11	0.105430	40.85	0.105430	0.009585		
Total	15	0.258073	100.00				

Table 8 ANOVA table for MRR of circular electrode

Source	DF	Seq SS	Contribution (%)	Adj SS	Adj MS	F-value	P-value
Regression	4	0.493726	90.93	0.493726	0.123431	27.57	0.000
Current	1	0.011667	2.15	0.011667	0.011667	2.61	0.135
On time	1	0.481990	88.77	0.481990	0.481990	107.66	0.000
Gap voltage	1	0.000064	0.01	0.000064	0.000064	0.01	0.907
Powder C	1	0.000005	0.00	0.000005	0.000005	0.00	0.973
Error	11	0.049246	9.07	0.049246	0.004477		
Total	15	0.542971	100.00				

Table 9 ANOVA table for TWR of Circular electrode

Source	DF	Seq SS	Contribution (%)	Adj SS	Adj MS	F-value	P-value
Regression	4	0.152731	87.92	0.152731	0.038183	20.02	0.000
Current	1	0.011968	6.89	0.011968	0.011968	6.27	0.029
On time	1	0.137380	79.08	0.137380	0.137380	72.02	0.000
Gap voltage	1	0.002033	1.17	0.002033	0.002033	1.07	0.324
Powder C	1	0.001349	0.78	0.001349	0.001349	0.71	0.418
Error	11	0.020983	12.08	0.020983	0.001908		
Total	15	0.173714	100.00				

The regression equation obtained for MRR of circular electrode is as follows:

$$MRR = 0.135 - 0.01208\,\text{Current} + 0.07575\,\text{On Time}$$
$$- 0.000119\,\text{Gap Voltage} + 0.00017\,\text{Powder }C$$

Powder concentration, gap voltage, and peak current are the significant parameters noted in ANOVA for TWR. The relationship between input parameters and TWR is seen in the following regression equation.

$$TWR = 0.1264 + 0.01223\,\text{Current} + 0.04044\,\text{On Time} - 0.000672\,\text{Gap Voltage} - 0.00274\,\text{Powder }C$$

4.2 Gray Relational Analysis

Deng was the first to propose the gray theory, which was first proposed in 1982. This theory is helpful when dealing with incomplete or inaccurate data. For the estimation of the behavior of a discrete data problem and uncertainty system, the gray theory is a very powerful technique that needs very little knowledge.

According to the Gray theory, there are three forms of systems: black (no information), white (all information) and gray (imperfect information) are systems that need very little information to estimate the problem's conduct.

As there are two response parameters in this analysis, the multi-objective optimization technique has been used. Since, every response parameter had its own set of units in which it was measured. As a result, there was a significant need to normalize the data and turn the multiple responses into a single response. GRA was used to optimize the two responses in this study, namely MRR and TWR. Using the GRA methodology, the experimental results obtained in accordance with the DoE were analyzed to determine the optimum process parameters. It is essential to normalize the raw data in GRA. The normalized MRR can be expressed as, "The wider the better criterion, the higher the normalized MRR." It can be stated as,

$$Xi^*(k) = \frac{Xi^0(k) - minXi(k)}{max\,Xi(k) - minXi(k)} \tag{1}$$

And the smaller the parameters, the better the normalized TWR, which can be described as,

$$Xi^*(k) = \frac{max\,Xi(k) - Xi^0(k)}{max\,Xi(k) - minXi(k)} \tag{2}$$

where $Xi(k)$ is the sequence after data preprocessing, and $Xi^0(k)$ is the comparability sequence.

The next deviation series is determined as follows:

$$\Delta 0i\,(k) = |x0 * (k) - xi * (k)| \tag{3}$$

where $x0 * (k)$ represents the larger value of normalized data, and $xi * (k)$ represents the normalized data value of the ith experiment.

The gray relational coefficient is then estimated, and it is defined as follows:

$$\xi i\,(k) = \frac{\Delta min + (\in \times \Delta max)}{\Delta 0i(k) + (\in \times \Delta max)} \tag{4}$$

$\in$ Distinguishing or recognition coefficient, where $0i\,(k)$ is the variance sequence of the reference sequence $x0^*\,(k)$, and $xi * (k)$ is the comparability sequence.

After calculating the gray relational coefficient, the average of the gray relational coefficient is used to determine the gray relational grade. A higher gray relational grade indicates that the corresponding experiment has an ideal normalized value, and therefore ranks are assigned based on grades (Tables 10 and 11).

Table 10 Gray relational grade and its rank for **Square** electrode

S. No.	Coefficient		GRG	Rank
	MRR	TWR		
1	0.414195	0.873866	0.644031	4
2	0.419576	0.706876	0.563226	7
3	0.588952	0.563443	0.576198	6
4	0.648422	0.431877	0.54015	8
5	0.371084	0.442203	0.406644	16
6	0.426287	0.415672	0.420979	15
7	0.591129	0.373681	0.482405	12
8	0.635658	0.333333	0.484496	11
9	0.391913	0.860436	0.626175	5
10	0.413125	0.575017	0.494071	10
11	0.456597	0.536172	0.496384	9
12	0.9093	0.384073	0.646687	3
13	0.333333	1	0.666667	2
14	0.448967	0.488965	0.468966	13
15	0.468573	0.428571	0.448572	14
16	1	0.341522	0.670761	1

Table 11 Gray relational grade and its rank for **Circular** electrode

S. No	Coefficient		GRG	Rank
	MRR	TWR		
1	0.356061	0.816883	0.586472	5
2	0.396067	0.720646	0.558357	8
3	0.668214	0.510466	0.58934	6
4	0.757996	0.43756	0.597778	3
5	0.338963	0.74259	0.540776	10
6	0.440603	0.662201	0.551402	9
7	0.484523	0.526937	0.50573	12
8	0.704934	0.457937	0.581435	7
9	0.372045	1	0.686022	1
10	0.389531	0.526937	0.458234	14
11	0.456345	0.5	0.478173	13
12	1	0.335596	0.667798	2
13	0.333333	0.844804	0.589069	4
14	0.389531	0.510466	0.449998	15
15	0.418422	0.457937	0.438179	16
16	0.730593	0.333333	0.531963	11

Table 12 Main effects on mean gray relational grade for square electrode

Level	Current	On time	Gap voltage	Powder C
1	0.5809	0.5859	0.5580	0.5605
2	0.4486	0.4868	0.5163	0.5527
3	0.5658	0.5009	0.5390	0.5369
4	0.5637	0.5855	0.5458	0.5090
Delta	0.1323	0.0991	0.0418	0.0516
Rank	1	2	4	3

4.2.1 Main Effects on Gray Relational Grade

Table 12 shows main effects on mean gray relational grade for square electrode used for the experimentation purpose. The peak current (I_p) and powder concentration have a substantial impact on the MRR, according to an analysis of variance (ANOVA). Current is the most significant factor that affects the GRG followed by pulse on time and powder concentration.

5 Conclusion

EDM is one of the most common non-traditional manufacturing techniques for machining electrically conductive materials with high strength and hardness. PM-EDM is an advanced methodology that has a lot of potential and overcomes the disadvantages of traditional EDM. Various powder materials and dielectric combinations have been tested by several researchers.

The following are a few of the conclusions taken from this study:

1. When compared to the traditional EDM method, the additive powder-mixed dielectric used in PM-EDM plays a significant role in improving material removal rate and reducing tool wear.
2. The use of powder-mixed dielectric aids in the attainment of a mirror-like surface finish, while suspended additive powder particle alloying aids in the modification of surface characteristics and complete burr-free workpiece.
3. One of the revolutionary innovations that ensures better machining rates at desired surface quality and reduced tool wear rate is powder mixing into the dielectric fluid of EDM.
4. The conductive powder concentration in EDM oil improves the surface finish of the workpiece. Greater the powder concentration, ethical the surface finish. The optimum value for PM-EDM can be 9–45 gm/l.
5. There is not much remarkable difference between the MRR and TWR of the square and circular type of electrode. Regarding market availability, machining and other purposes selection of circular electrode are preferable.

References

1. Jamwal A, Aggarwal A, Gautam N, Devarapalli A (2018) Electro-discharge machining: recent developments and trends. Int Res J Eng Technol (IRJET) (2395) (0056-0072) 05(02) (Feb)
2. Kumar V, Kumar A, Kumar S, Singh NK (2018) Comparative study of powder mixed EDM and conventional EDM using response surface methodology. ICMPC_2018. Mater Today Proc 5:18,089–18,094
3. Talla G, Gangopadhyay S, Biswas CK (2014) Multi response optimization of powder mixed electric discharge machining of aluminium/alumina metal matrix composite using grey relation analysis. International conference on advances in manufacturing and materials engineering, AMME 2014. Procedia Mater Sci 5:1633–1639
4. Talla G, Sahoo DK, Gangopadhyay S, Biswas CK (2015) Modeling and multi-objective optimization of powder mixed electric discharge machining process of aluminum/alumina metal matrix composite. Eng Sci Technol Int J 2015:1–5

Experimental Study and Optimization of Tribological Properties of Blended Biodiesel

Naga Lakshmi Pavani Puvvada, Polarao Ronanki, and Srikiran Satuluri

1 Introduction

The increase demand of diverse biolubricants use made the origination for biodiesels. The pure or blended biodiesels are employed in numerous applications. Xiao and Liu [1] reviewed the lubricity property of biodesels and surmised that the velocity has effect on friction and wear compared to load and temperature. Dugala et al. [2] experimented the engine with different combinations of blended bio fuels extracted from the mahua and jatropha vegetable oils. During the study it is spotted that the blended biodeisels have shown better results concerning of emissions accompanying the operationsl performance. The combined properties can be gained if the biodiesels produced from the blended vegerable oils. Acharya et al. [3] examined and collated the storage and oxidation stabilities. Out of all combinations of blended bio diesels the mahua blended bio diesels have shown superior results contrast to jatropha and mineral oil combinations. Sundus et al. [4] reviewed various tribological characteristics of biodiesel to analyse the several issues associated with biodiesels. It is recognized that the stability of bio diesel has main concern to concentrate. Hamdan et al. [5] examined the tribological effect of diluted palm methyl ester in the engine lubricnats and noticed that friction modifier effect is higher where as the load bearing ability is less. Pavani et al. [6] presented the results of sysnthesis of bio lubricnats taken at various proportions. During the analysis it is found that the 90% mahua and 10% palm is exhibiting better tribological properties compared to other variations. Peng [7] examined the significant attributes of palm biodiesel and petro diesel combinations to examine wear and friction under boundary lubrication conditions.

N. L. P. Puvvada (✉) · P. Ronanki
Department of Mechanical Engineering, GMR Institute of Technology, Rajam, Srikakulam District 532127, Andhra Pradesh, India
e-mail: pavani.pnl@gmrit.edu.in

S. Satuluri
Department of Mechanical Engineering, Visakhapatnam, India

The outcome conveys that the friction, wear get increased with a rise in temperature, where as the lubricty is because of biodiesel concentrations rise. Taguchi experimental layout gives better combinations between the input variables and also minimises the repetitios. Maleque and Abdulmumin [8] reviewed the tribo corrosion behavior to realize the electrochemical and mechanical conditions. Wear and corrosion are dominant factors that influences the engine performance. Alves et al. [9] decided that the vegetable oils are replacement to the mineral oils and these biolubricants helps in the depletion of friction, wear. Arumugam and Sriram [10] discovered that the rapeseed oil bio lubricant and biodiesel extricated from the oil exhibits better tribological attributes and longer life. Saravanan et al., Godiganur et al., Raheman and Ghadge and Puhan et al., have explored the utilization of mahua bio diesel in the diesel engine as they have exhibited superior emission attributes and engine performace [11–14].

2   Preparation of Biodiesel

The biodiesel is prepared by taking Mahua, Palm and blended vegetable oils (90% M and 10% P). The 90% Mahua and 10% Palm vegetable oils have given better results compared to remaining possible combinations. Transesterification process is employed for the production of biodiesel. The process comprised to four basic steps as depicted in Fig. 1.

In the first step, acid treatment, raw oil is heated up to 60 °C and 100 ml methanol, 2–3 ml of sulfuric acid are added. Settling is done in decanter for 3 h. Pulp is separated from the oil (Fig. 2). Figure 3a represents the raw oil heating on the heater equipped with the stirrer. In next step, base treatment is performed at 60 °C. In this process a mixture of methanol and sodium hydroxide (sodium methoxide) is added to the acid treated oil. For making of sodium methoxide, 250 ml of methanol is used to dissolve 6–7.5 g of sodium hydroxide pellets (Fig. 3b). It's an exothermic reaction. Sodium hydroxide needs to handle carefully as its a highly explosive material. Settling is carried in decanter for about 6 h.

Fig. 1 Procedure followed for biodiesel preparation

Acid treatment followed by settling

Base treatment followed by settling

Water

Dehydration
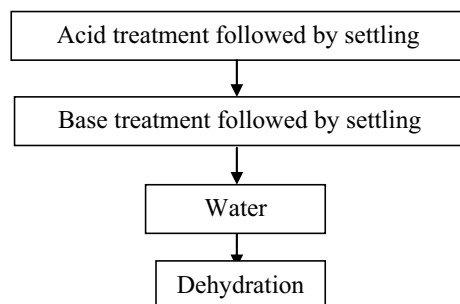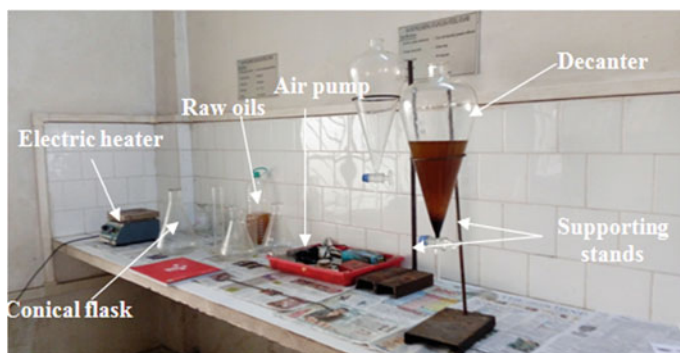
Fig. 2 Observational set up in production of biodiesel
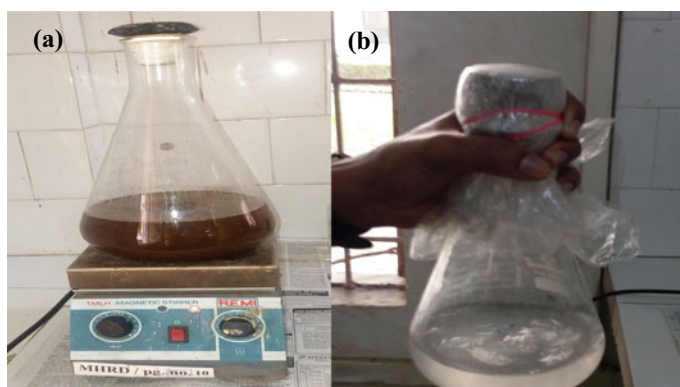
Fig. 3 **a** Heater with magnetic stirrer. **b** Methanol and sodium hydroxide pellets

In this process, the glycerin is settled at bottom as repredented in Fig. 4a and the settled glycerol will be drained out. In the time of the third step, as illustrated in Fig. 4b the base treated oil is washed with the distilled water by circulating the air by air motor. Based on the last step, dehydration, the separated oil is heated to 100º C to dehydrate the oil to finally obtain the biodiesel (Fig. 4c and d).

3   Testing of Biodiesel Characteristics

The prepared biodiesel samples are tested to reveal the properties like viscosity, density, flash point, fire point as appeared in Table.1. The achieved results are near to the standard values and further the Tribological properties are studied by considering rotational speed, normal load and tracking diameter at different levels.
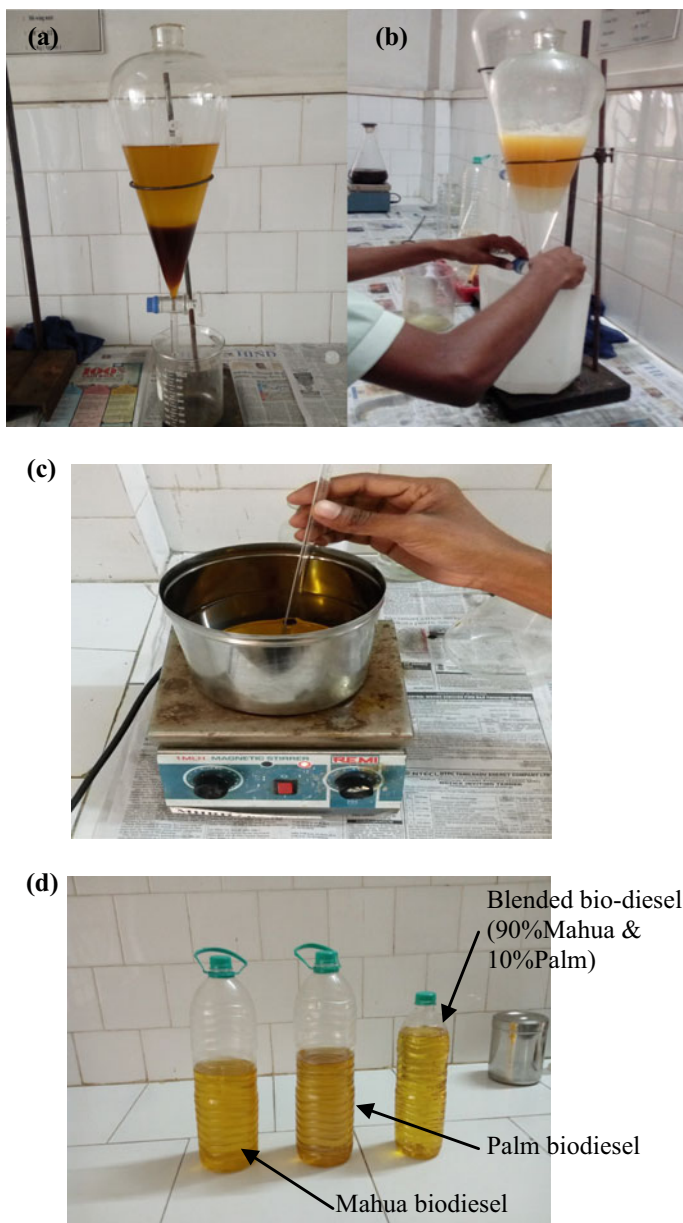
Fig. 4 **a** Seperation of biodiesel and glycerol. **b** Water wash. **c** Dehydration process. **d** Biodiesel prepared

Table 1 Properties of biodiesel

Biodiesel	Flash point (°C)	Fire point (°C)	Kinematic viscosity (mm^2/s)	Density (kg/m^3)
Mahua	202	210	9.0583	867.5
Palm	240	250	6.5642	857.426
Blended	196	200	12.67	857.298

4 Design of Experiments

With all possible combinations of input parameters (Table 2) and its levels an L_{16} ($4^{(3-1)}$) Taguchi orthogonal array is designed as illustrated in Table 3. Constant time 30 min is taken for all trials (Table 4).

Table 2 Parameters and their levels for wear test of AISI 1040 Steel

Input parameters/factors	Levels			
	1	2	3	4
Load (kg)	2	4	6	8
Sliding speed (rpm)	200	400	600	800
Track diameter (mm)	20	40	60	80

Table 3 Experimental conditions (Taguchi orthogonal array)

Experiment No.	Speed, N (rpm)	Load, P (kg)	Track diameter, D (mm)
1	200	2	20
2	200	4	40
3	200	6	60
4	200	8	80
5	400	2	40
6	400	4	20
7	400	6	80
8	400	8	60
9	600	2	60
10	600	4	80
11	600	6	20
12	600	8	40
13	800	2	80
14	800	4	60
15	800	6	40
16	800	8	20

Table 4 Experimental results showing wear

Exp. No.	Wear (μm)		
	Bio-diesels		
	Mahua	Palm	Blended
1	39	35	31
2	209	17	18
3	307	251	4
4	278	217	173
5	134	71	64
6	35	47	16
7	41	135	168
8	294	124	3
9	277	14	35
10	279	170	206
11	128	43	36
12	46	15	55
13	130	83	41
14	327	19	168
15	15	168	77
16	57	80	51

The AISI 1040 steel disc and aluminium pins are prepared as per the drawings revealed in Fig. 5. The disc and pin used for pin on disc experimentation are exhibited in Fig. 6. The experiments are conducted at several combinations of normal load, speed and track diameter values and the recorded values are shown in Tables 5 and 6. The total wear measured for all viable blended bio lubricants and bio diesel prepared from the best combinations are presented in Table 7. The results are plotted in the form of graphs as seen in Fig. 7.

The least wear rate occurred for the pair of bio-lubricants and bio-diesels at 90% **M and 10% P** combination.

5 Calculation of S/N Ratios

Wear

Among the three criterias used for the calculation of S/N ratios, the smaller the better criteria is used for wear, frictional force and coefficient of frction analysis. The ratios are calculated by the following equation

$$S/N = -10 \log\left(\sum y^2/n\right) \tag{1}$$

Fig. 5 CAD drawings of disc and pin used for the samples preparation (as per Ducom company wear tester specifications)
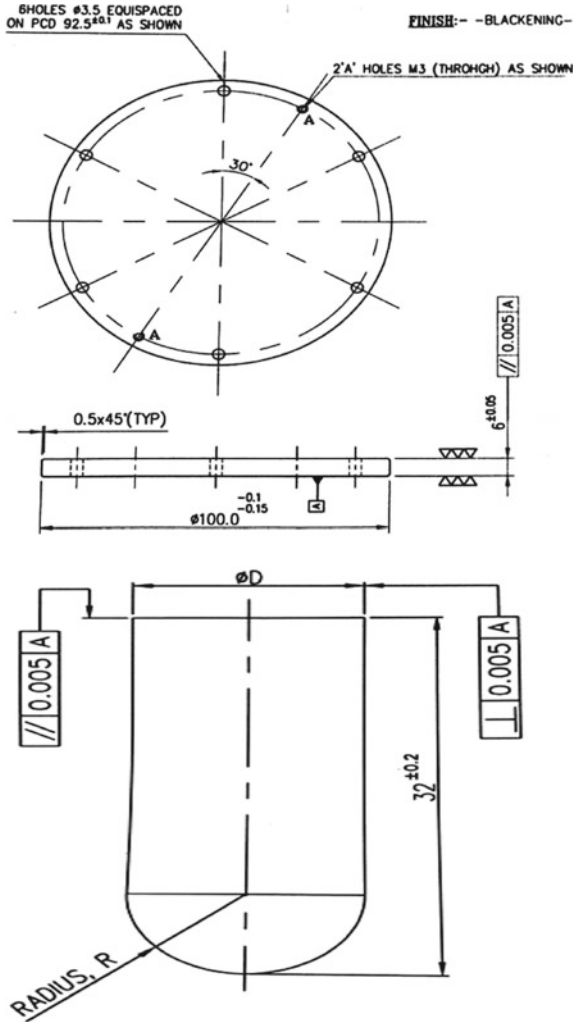
where y = data points i.e. the value of wear according to table and n = number of experiments = 16. The calculated ratios are represented in Table 8.

Frictional Coefficient (COF)

Like the wear the S/N ratios for Frictional coefficient are calculated using the smaller the better criteria. The calculated ratios are outlined in Table 9.

Frictional Force (F)

The calculated ratios as per Eq. (1) are drafted in Table 10.

From results shown in Tables 8, 9 and 10, the S/N ratios are used to discover the best condition from the designed experimental layout.
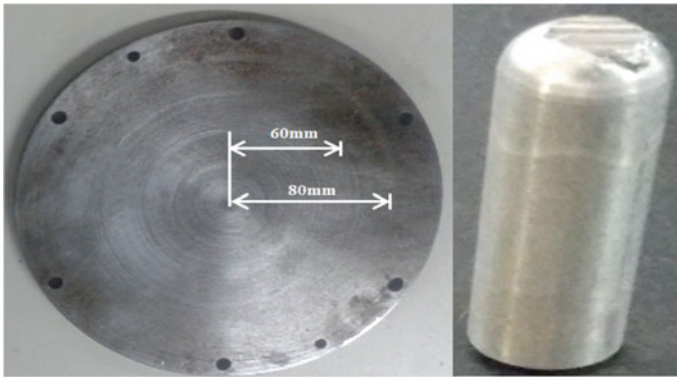
Fig. 6 AISI 1040 Steel disc with various tracks and aluminium pin used for test

Table 5 Experimental results showing frictional force

Exp. No.	Frictional force (N)		
	Bio-diesels		
	Mahua	Palm	Blended
1	2.1	2.6	2.4
2	2.6	6.5	5.6
3	4.6	8.6	8.2
4	8.9	11.6	8.2
5	1.3	2.6	2.2
6	3.2	5.2	5.2
7	4.3	7.8	6.1
8	6.1	9.7	9.1
9	1.1	2	1.6
10	2.5	4.5	3.1
11	4.1	7.8	7.6
12	5.2	10.6	9.7
13	1.2	2.0	1.1
14	2.5	3.5	3.0
15	3.3	7.0	6.9
16	5.4	9.8	9.2

6   Analysis of Variance

The variance calculation is analyzed using the sum of squares and mean squares. Tables 11,12 and 13 show the results of analysis of variance for signal to noise ratio using F-Test for Wear, Frictional coefficient and frictional force (using MINTAB).

Table 6 Experimental results showing frictional coefficient

| Exp. No. | Frictional coefficient | | |
| | Bio-diesels | | |
	Mahua	Palm	Blended
1	0.107	0.112	0.105
2	0.058	0.058	0.125
3	0.067	0.128	0.123
4	0.106	0.130	0.091
5	0.057	0.133	0.099
6	0.079	0.117	0.119
7	0.068	0.116	0.091
8	0.075	0.108	0.103
9	0.050	0.092	0.071
10	0.055	0.102	0.073
11	0.066	0.118	0.115
12	0.07	0.119	0.111
13	0.076	0.092	0.08
14	0.080	0.080	0.067
15	0.05	0.106	0.106
16	0.063	0.110	0.105

Table 7 Total wear of all the lubricants and bio-diesels under all the tribological environments

	Sample description	Total wear (μm)
Bio-lubricants	10% mahua & 90% palm	2102
	20% mahua & 80% palm	3433
	30% mahua & 70% palm	1482
	40% mahua & 60% palm	1602
	50% mahua & 50% palm	1210
	60% mahua & 40% palm	1334.7
	70% mahua & 30% palm	2958
	80% mahua & 20% palm	1535
	90% mahua & 10% palm	**934**
	Pure mahua	1944
	Pure palm	3253
Bio-diesels	Mahua bio-diesel	2596
	Palm bio-diesel	1489
	Blended bio-diesel	**1146**
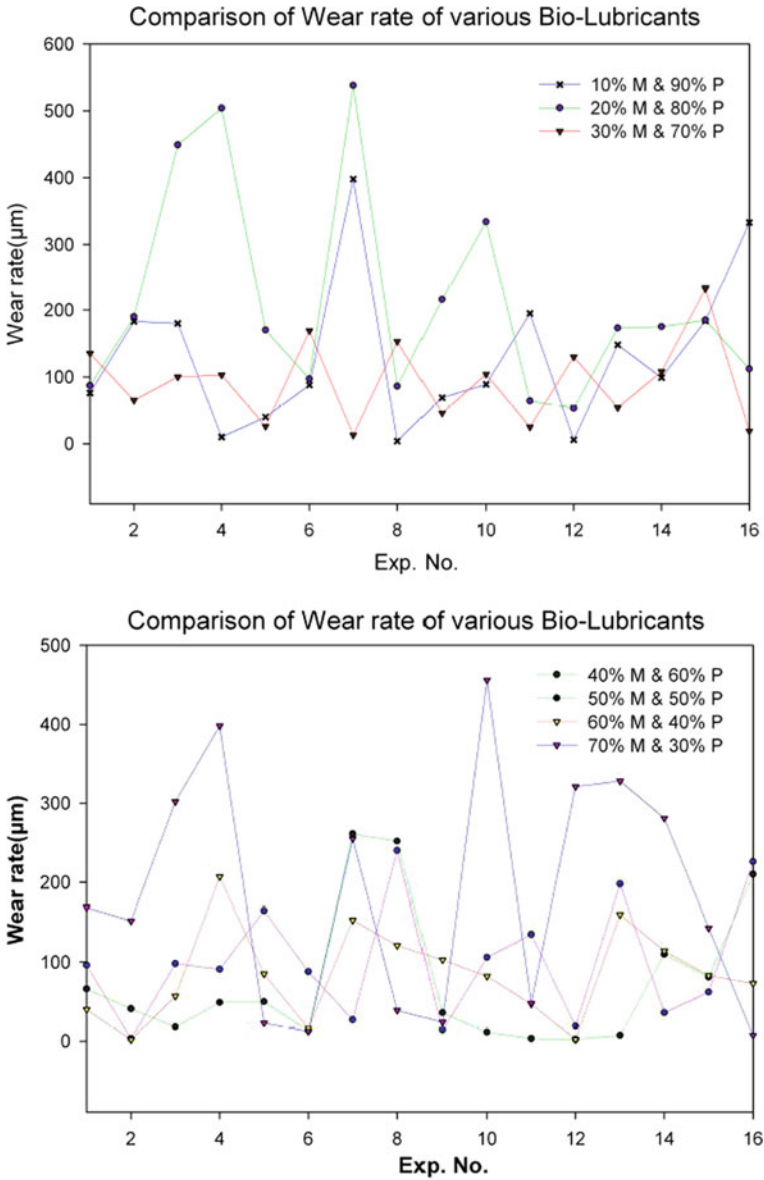
Fig. 7 Variation of wear rate under various combinations
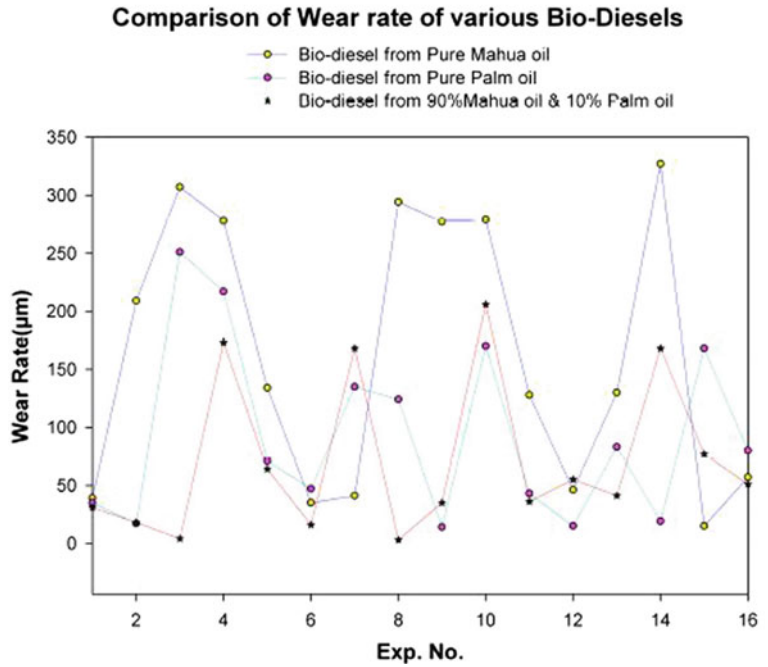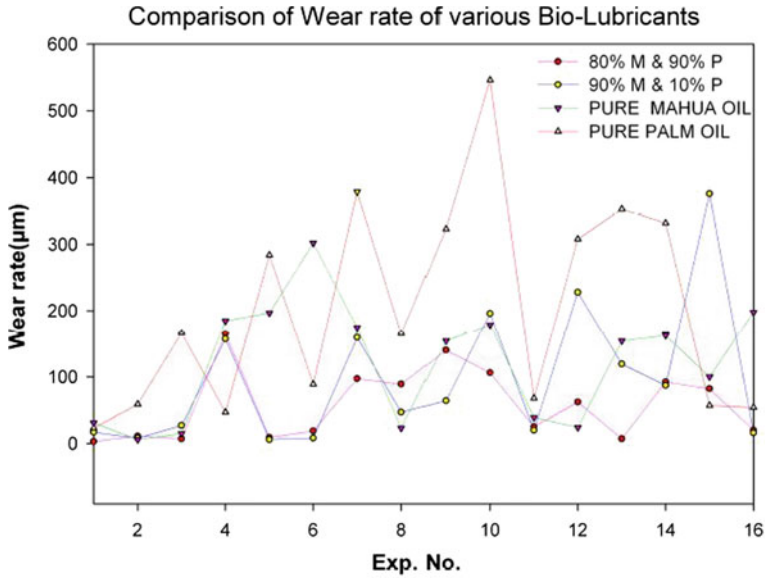
Fig. 7 (continued)

Table 8 S/N ratios of wear

S/N ratios at different levels	Factors		
	Speed (rpm)	Load (N)	Track dia (mm)
1	−28.804	−29.4516	−23.1934
2	−27.7737	−30.189	−33.0718
3	−38.787	−37.5449	−34.2458
4	−38.9719	−37.1502	−43.8254

Table 9 S/N ratios of COF

S/N ratios at different levels	Factors		
	Speed (rpm)	Load (N)	Track dia (mm)
1	−14.249	3.303	−10.123
2	−9.65474	−7.5430	−10.48
3	−11.7684	−14.06	−4.13
4	−1.4165	−11.164	−5.3502

Table 10 S/N ratios of F

S/N ratios at different levels	Factors		
	Speed (rpm)	Load (N)	Track dia (mm)
1	18.6622	29.190	14.935
2	23.44913	25.57	17.60
3	29.42345	17.014	29.47
4	16.14799	16.155	28.339

Table 11 Results of analysis of variance for wear

Parameters	Dof	Sum of squares	Mean sum of squares	F-ratio	% of P	Rank
Speed	3	29,673	9891	0.88	0.384	2
Load	**3**	**20,552**	**6851**	**0.57**	**0.518**	**1**
Track dia	3	61,344	20,448	2.38	0.09	3
Total	9	111,569			0.992	

Table 12 Results of analysis of variance for frictional coefficient

Parameters	Dof	Sum of squares	Mean sum of squares	F-ratio	% of P	Rank
Speed	3	22.12	7.374	1.01	0.386	2
Load	3	41.44	13.814	2.72	0.091	3
Track dia	**3**	**5.887**	**1.962**	**0.24**	**0.864**	**1**
Total	9	69.117			1	

Table 13 Results of analysis of variance for frictional force

Parameters	Dof	Sum of squares	Mean sum of squares	F-ratio	% of P	Rank
Speed	3	0.01869	0.006228	2.45	0.082	3
Load	3	**0.000609**	**0.000203**	**0.05**	**0.706**	**1**
Track dia	3	0.01269	0.004229	1.39	0.211	2
Total	9	0.031989			1.392	

To have the statistical validation of experimental results, ANOVA is done using minitab 16.0 software and the research reveals that the out parameter Wear is mostly influenced by the input parameter normal laod. Similarly, Frictional coefficient and friction load outputs are influenced by track diameter and load as shown in Tables 11, 12 and 13. The main effect plots of all output parameters are shown in Figs. 8, 9 and 10 inrespect of all input factors. Load is the most significant factor which effects the wear with a percentage contribution of 51.8% followed by speed (38.4%) and track dia (9%). Track dia is the most significant factor which effects the frictional
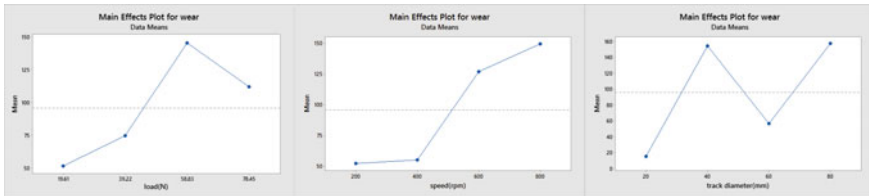
Fig. 8 Main effect plots of wear for all input factors
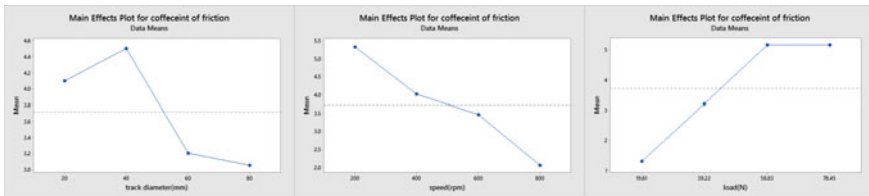
Fig. 9 Main effect plots of frictional coefficient for all input factors
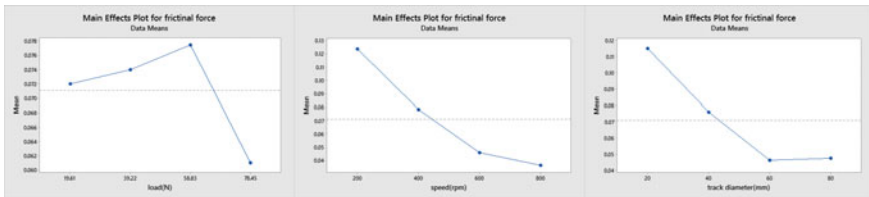
Fig. 10 Main effect plots of frictional force for all input factors
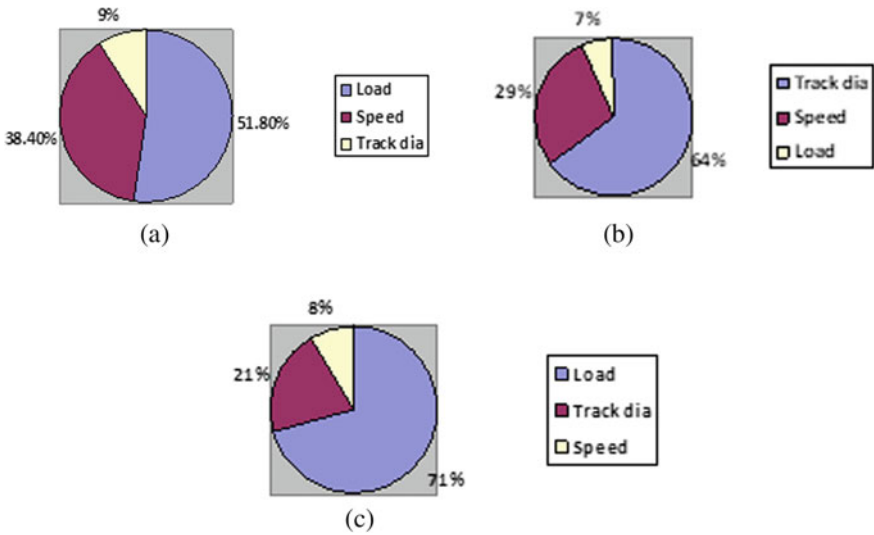
Fig. 11 Contribution of parameters. **a** Wear, **b** friction coefficient and **c** friction force

coefficient with a percentage contribution of 86.4% followed by speed (38.6%) and load (9.1%). Load is the most significant factor which effects the frictional force with a percentage contribution of 70% followed by track dia (21.1%) and speed (8.2%) respectively (Fig. 11).

7 Conclusion

The objective of current research is to investigate the performance of bio-lubricant and diesel prepared from the blended bio diesels. Taguchi methodology was used to identify the finest combination of Palm and Mahua blended bio-lubricants. It is also used in the preparation of bio-diesel from the best blend of the palm and mahua oil blended samples. According to the outcomes of these experimental investigations, the subsequent inferences are made.

- Blended bio-lubricants can be used as an alternative to the commercially available lubricants and it would be an added advantage of gaining the lubricating properties of two individual vegetable oils
- Taguchi methodology was found to be useful in identifying the best combination of machining parameters by minimizing the repetitions.
- The tribological performance of the Bio-diesel prepared using blended vegetable oils has better tribological properties than the bio-diesels prepared from individual vegetable oils.

- The analysis of experimental results show that wear rate is minimum with a bio-diesel prepared from the 90% Mahua and 10% Palm vegetable oil composition. So if bio-diesel prepared at this proportion can be used as an alternative to the commercially available lubricants.

References

1. Xiao H, Liu S (2020) Tribological properties of biodiesel: a review of recent advances. Energy Sources Part A: Recov Util Environ Effects 1–20
2. Dugala NS, Goindi GS, Sharma A (2020) Evaluation of physicochemical characteristics of Mahua (*Madhuca indica*) and Jatropha (*Jatropha curcas*) dual biodiesel blends with diesel. J King Saud Univ-Eng Sci
3. Acharya N, Nanda P, Panda S, Acharya S (2019) A comparative study of stability characteristics of mahua and jatropha biodiesel and their blends. J King Saud Univ—Eng Sci 31(2):184–190
4. Sundus F, Fazal MA, Masjuki HH (2017) Tribology with biodiesel: a study on enhancing biodiesel stability and its fuel properties. Renew Sustain Energy Rev 70:399–412
5. Hamdan SH, Chong WWF, Ng JH, Chong CT, Rajoo S (2017) A study of the tribological impact of biodiesel dilution on engine lubricant properties. Process Saf Environ Prot 112:288–297
6. Pavani PNL, Rao RP, Prasad CLVRSV (2017) Synthesis and experimental investigation of tribological performance of a blended (palm and mahua) bio-lubricant using the taguchi design of experiment (DOE). Synthesis 8(3)
7. Peng DX (2015) Effects of concentration and temperature on tribological properties of biodiesel. Adv Mech Eng 7(11)
8. Maleque A, Abdulmumin AA (2014) Tribocorrosion behaviour of biodiesel—a review. Tribology Online 9(1):10–20
9. Alves SM, Barros BS, Trajano MF, Ribeiro KSB, Moura EJTI (2013) Tribological behavior of vegetable oil-based lubricants with nanoparticles of oxides in boundary lubrication conditions. Tribol Int 65:28–36
10. Arumugam S, Sriram G (2012) Effect of bio-lubricant and biodiesel-contaminated lubricant on tribological behavior of cylinder liner–piston ring combination. Tribol Trans 55(4):438–445
11. Saravanan N, Nagarajan G, Puhan S (2010) Experimental investigation on a DI diesel engine fuelled with Madhuca Indica ester and diesel blend. Biomass Bioenergy 34(6):838–843
12. Godiganur S, Murthy CS, Reddy RP (2009) 6BTA 5.9 G2-1 Cummins engine performance and emission tests using methyl ester mahua (*Madhuca indica*) oil/diesel blends. Renew Energy 34(10):2172–2177
13. Raheman H, Ghadge SV (2007) Performance of compression ignition engine with mahua (*Madhuca indica*) biodiesel. Fuel 86(16):2568–2573
14. Puhan S, Vedaraman N, Ram BV, Sankarnarayanan G, Jeychandran K (2005) Mahua oil (Madhuca Indica seed oil) methyl ester as biodiesel-preparation and emission characterstics. Biomass Bioenergy 28(1):87–93

Evaluation of Alternate Material of a Bush for Reducing Fretting Wear Damage in a Bush-Pin Joint

T. Sawant, S. J. Joshi, D. V. Patel, D. B. Shah, and V. M. Bhojawala

1 Introduction

Fretting is a very minute vibratory motion at the contact surface between the elements and is a common phenomenon found in several assemblies of mechanical components that can considerably lessen the life cycle of components of the assembly. In the fretting wear, the produced debris generally confined at the contact surfaces and offers a load transmitting plateau [1]. The fretting wear can happen where two elements of assemblies are joined by bolts, rivets, or pins [2]. Wear growth at the contact between the components in machinery is owing to numerous factors such as the geometry of the elements in contact, loads and relative slip amplitude, structure of machines, friction at the contacting surface of components, rigidity and hardness of material, and defects due to geometric features of the contacting surfaces [3]. The phenomenon of fretting at the contact surfaces is very complex. And hence the measurement of the parameter is challenging in the experimental test. Owing to the advancement of simulation using the computer, the finite element analysis techniques are widely used for the study related to the fretting wear [4]. Ding et al. studied the growth of sub-surface stress field in case of fretting wear using simulation tool [5]. Lee and

T. Sawant · S. J. Joshi · D. V. Patel · D. B. Shah · V. M. Bhojawala (✉)
Departmental Mechanical Engineering, Institute of Technology, Ahmedabad 382481, India
e-mail: vipul.bhojawala@nirmauni.ac.in

T. Sawant
e-mail: 15mmed11@nirmauni.ac.in

S. J. Joshi
e-mail: s.j.joshi@nirmauni.ac.in

D. V. Patel
e-mail: dhaval.patel@nirmauni.ac.in

D. B. Shah
e-mail: dbshah@nirmauni.ac.in

Kim [6] investigated the reasons for fretting wear failure of bolt by means of FEA in pressure vessel and suggested to change the bolt material. Kim et al. [7] suggested numerical approach for simulating the progressive increase of wear in the vibrating metal to metal interaction. The wear rate is an input quantity for simulation using finite element software. Many researches have suggested the finite element analysis-based procedure for predicting the behavior of sliding wear [8, 9]. In the current work, alternate material of a bush for reducing fretting wear damage in a bush-pin joint of a flyer (a textile machinery component) is evaluated.

2 Failure of a Bush-Pin Joint

The flyer is rotating component in roving frame for producing yarn in textile manufacturing process. The constructional details of the flyer which consists of two arms, one hollow and other solid, are shown in Fig. 1 along with the details of presser with hollow arm of the flyer.

A steel tube passing through hollow arm facilitates the passage of thread. The thread, passing through the presser tip, is wound on the bobbin. The bobbin is mounted coaxially with flyer. The bobbin has reciprocating motion, whereas the flyer normally rotates at 1400 rpm. The presser rod is pivoted at two points on the hollow end of the flyer. The details of arrangement are shown in Fig. 1b. Normally, it takes ninety minutes for winding of a bobbin and this involves movement of presser finger from inner most position POS1 to outer most position POS2 as indicated in Fig. 2.
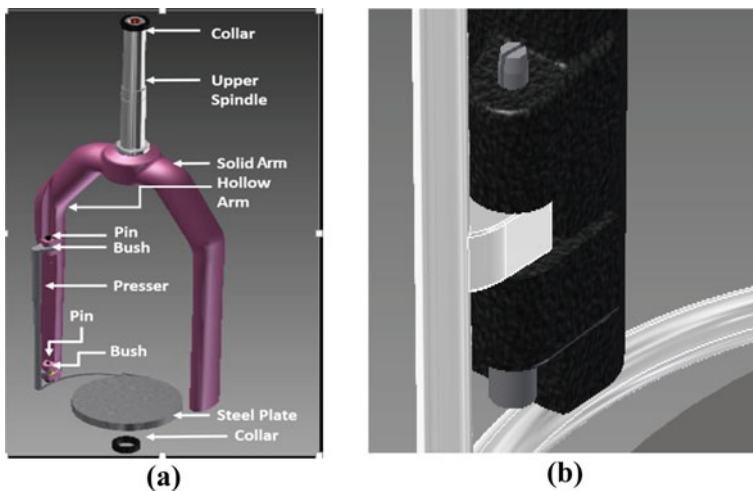
Fig. 1 a Schematic view of flyer; **b** details presser with hollow arm of the flyer
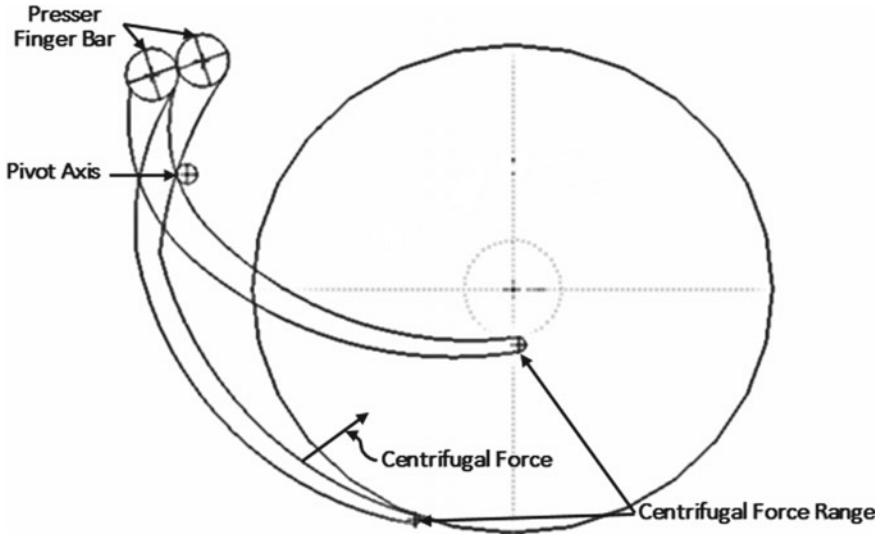
Fig. 2 Movement of presser finger during winding of a bobbin

As the roving frame operates continuously, the pivot points of the presser have bush and pin contact. It is present practice to use the bush made from polyamide (blended with 15% graphite) and pin from stainless steel SS304. Numerous failures of the bush and pin presser are reported resulting in wear and fracture of bush as well as wear of the pin (refer Fig. 3).

The wear further results in uneven force sharing between two pivot points and thus resulting in bending of presser as shown in Fig. 4a and the wear of presser flyer contact point as shown in Fig. 4b.
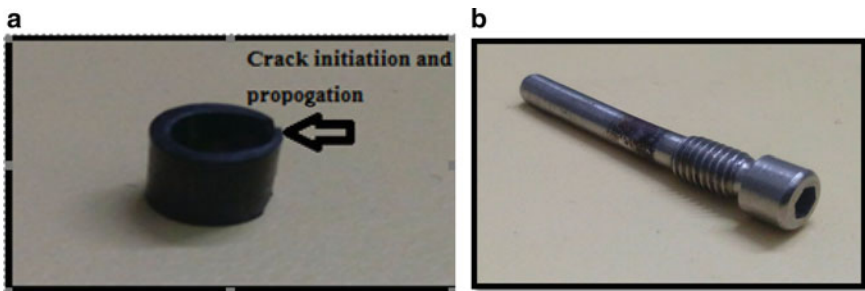
Fig. 3 a Wear and fracture of a bush; **b** wear of the pin
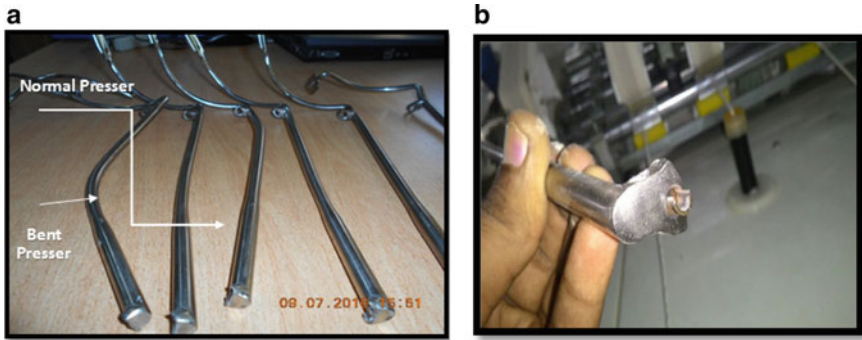
Fig. 4 **a** Uneven reaction force at upper and lower bush resulting in the binding of presser, **b** wear of the presser at its connection with hollow arm of flyer

2.1 Estimation of Wear Resistance of Bush

The radial wear of bush as per manufacturer's catalogue [10] is given in Eq. 1.

$$R = \text{Wear factor} \times \text{PV} \times \text{Running time} \tag{1}$$

P is pressure at contacting surfaces and V is velocity. The center of gravity of the presser is determined by constructing the solid model of it. It is noted that the center of gravity of the presser lies outside its geometry owing to its shape. The reaction at the upper and lower bush was determined resulting in the calculation of the pressure. As the velocity of the bush is very less, so is the resulting PV value. The running per year is 17520 h. The radial wear as estimated by Eq. (1) and for the presently used bush material is 0.005 microns which is quite good result. In spite of this, failures do occur leading to the need of force analysis using dynamic simulation and wear analysis using finite element analysis.

3 Dynamic Simulation

Dynamic simulation is performed to find out the reaction force at bush and presser force acting on the bobbin. The free body diagram of the presser with various forces acting on it during winding process is indicated in Fig. 5.

During the spinning process, the presser finger moves from innermost position to outermost position because of centrifugal force. Hence, it is required to study the force variation with respect to bobbin diameter. The force calculation will be useful in estimation of wear life.

During the dynamic simulation, the upper collar is given a rotational joint with the driving spindle of the flyer and lower collar is given rotational joint at the bottom
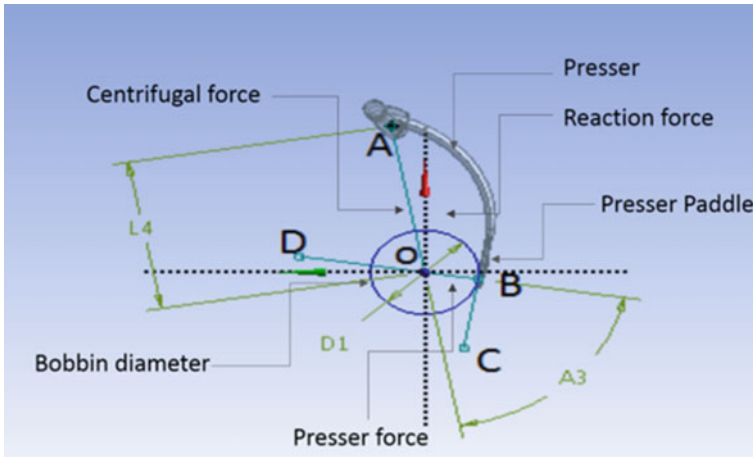
Fig. 5 Free-body diagram of pressure with forces acting during the winding operation

plate where the bobbin is mounted and rotated with separate drive. The spindle which drives flyer is given constraint with the hollow arm of the flyer. In order to give connection between the presser and arm of the flyer, two pins are placed into the hollow arm. The lower pin joint connection in the hollow arm with presser results in revolute joint whose motion is restricted throughout simulation. Based on the above constraints, the reaction forces are calculated at the upper and lower end of the presser where it is connected with hollow arm using the pin joint. The dynamic simulation is performed for the time span of 2 s at various bobbin diameter position. The presser force and reaction force for 50 mm bobbin diameter at lower end bush and upper end bush are shown in Figs. 6 and 7, respectively.

The variation of reaction force with bobbin diameter at upper bush and lower bush is shown in Table 1.

4 Wear Life Estimation

Wear of bush-pin joint of flyer is a serious issue because of concentrated reaction force acting at lower and upper bush ends coupled with rolling motion. Continuous operation, inaccessibility of bush ends, and size limit the use of liquid lubricants in this case. Polyamides blended with various dry film solid lubricants like molybdenum disulfide (MoS2), graphite, and PTFE are suitable in such situation as bush material. It is present practice to use polyamide (blended with 15% graphite) as bush material. It is clear from manufacturer's catalogue [10] that polyamide (blended with 15% graphite) is suitable for high temperature and high speed applications where as polyamide (blended with 15% graphite and 10% Teflon) is suitable especially as bush material up to 100 °C temperature for low speed applications. The bush-pin wear is simulated
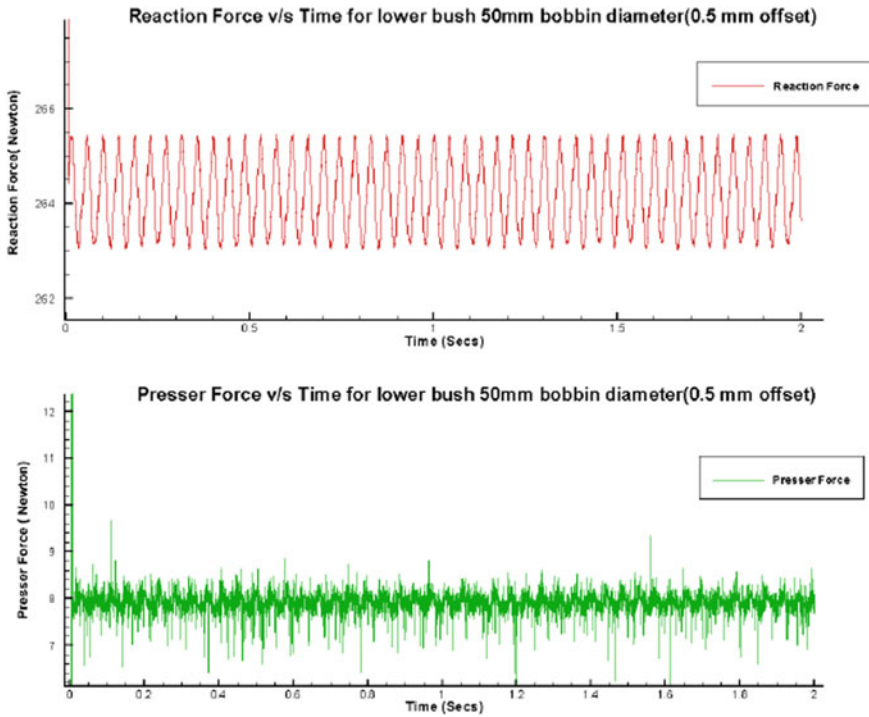
Fig. 6 Variation of presser force and reaction force at lower bush for 50 mm bobbin diameter

using ANSYS workbench using transient structural suite. The boundary conditions required to perform simulation are indicated in Fig. 8.

The revolute joint B is given on the entire bush surface and the pin is kept as fixed. Both the rotational joints can give rotation about the pin axis. The presser rotates through 250° angle in 90 min which corresponds to inner position (50 mm diameter) to outer position (150 mm diameter) of bobbin. The angle turned by presser and bush for 2 s is 0.090. Hence, the rotation provided to the bush during simulation is 0.090. During this simulation, in order to evaluate the reaction at the presser ends, the translation normal to contact surface is taken as free. The remaining degrees of freedom are constrained in the pin; the reaction forces are obtained from the simulation. The script is written in ANSYS for estimation of wear volume. The volume of material loss owing to wear for two different material is shown in Fig. 9. The calculated depth of wear is obtained by means of model developed in reference [11]. The wear depth is depicted in Fig. 10 for both the materials.

The wear life of the bush is calculated for maximum reaction force of 260 N. The wear life of bush as per wear volume criterion and wear depth criterion for the two materials is represented in Tables 2, 3, 4, and 5. The wear volume criterion results in life of 279 days for polyamide (blended with 15% graphite), which is more pragmatic and coincides with real-life observations. It is to be noted that wear
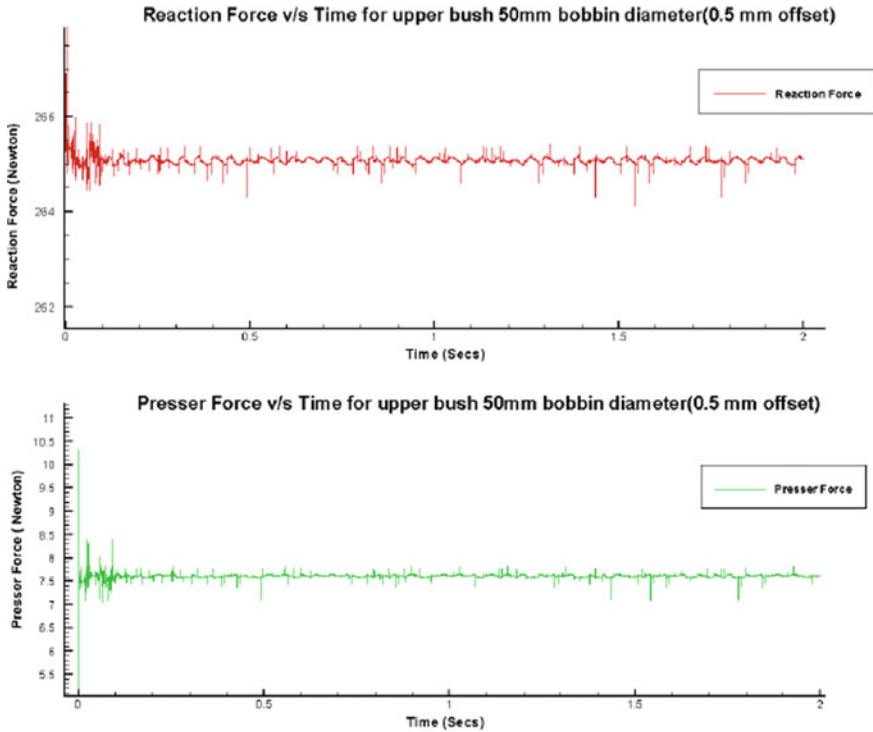
Fig. 7 Variation of presser force and reaction force at upper bush for 50 mm bobbin diameter

Table 1 Variation of reaction at upper bush and lower bush with the bobbin diameter

Bobbin diameter (mm)	Reaction of upper bush (N)	Reaction of lower bush (N)	Paddle force (kg)
50	264.5–266	268–265	0.7–0.8
70	270–274	275–274	0.7–0.9
90	272–275	273–275	0.8–1
110	274–278	274–277	0.7–0.9
130	275–276	274–275	0.7–0.8
150	264–268	272–274	0.8–1

life with polyamide (blended with 15% graphite and 10% Teflon) bush material is almost double when compared with polyamide (blended with 15% graphite) as bush material.

A: Transient Structural
Transient
Time: 2. s
5/4/2017 12:00 PM

A Force: 132.65 N
B Joint - Rotation: 9.e-003 °
C Displacement
D Joint - Rotation: 9.e-003 °

Surfaces on which joint D is acting
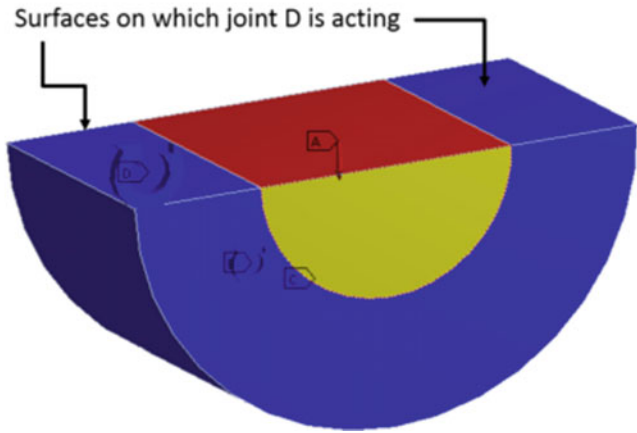
Fig. 8 Boundary conditions during wear volume calculation using ANSYS
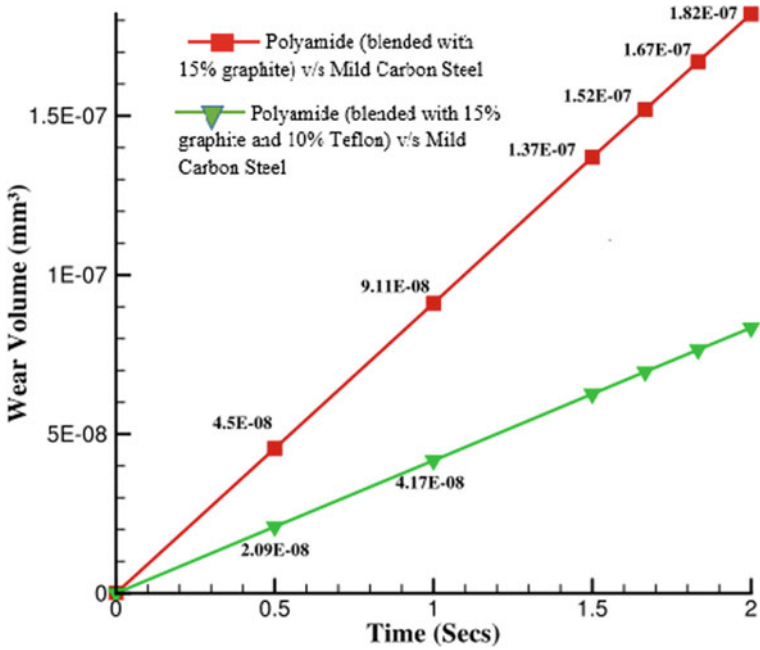
Fig. 9 Wear volume for two different bush materials
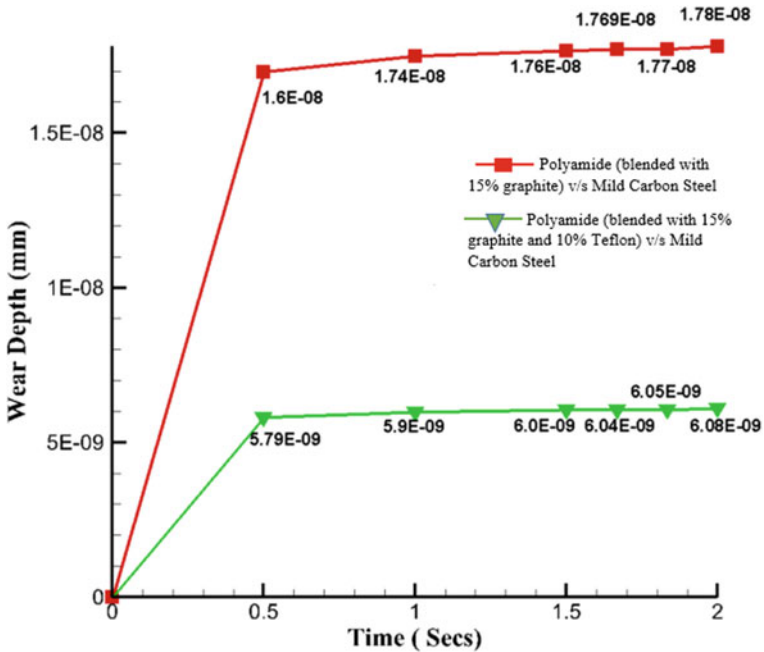
Fig. 10 Wear depth for the two bush materials

Table 2 Wear depth and life for polyamide (blended with 15% graphite)

Time (s)	Wear depth	Wear depth in 1 s (mm)	Wear depth in 1 day (mm)	Total days (life)
0	2.58E−34	2.33E−08	0.00200912	995
0.5	2.26E−08			
1	2.33E−08			
1.5	2.35E−08			
1.66	2.35E−08			
1.83	2.36E−08			
2	2.37E−08			

5 Conclusion

The issue of failure of the bush-pin joint of the flyer has been investigated. It is noted that wear rate is very low as per the calculations carried out with the guidelines provided in manufacturer's catalogue which is contradictory with the actual failures. Adopting the alternate route, dynamic simulation is carried out to find the variation for reactions at upper bush and lower bush with bobbin diameter. The wear analysis is performed using finite element analysis software, and life of the bush is calculated.

Table 3 Wear volume and life for polyamide (blended with 15% graphite)

Time (s)	Wear volume (mm^3)	Total volume (mm^3)	Wear volume loss in 1 s (mm)	Volume loss in 1 day (mm)	Total days (life)
0	0	4.4179	1.83E−07	0.015816	279
0.5	9.14E−08	4.4179			
1	1.83E−07	4.4179			
1.5	2.74E−07	4.4179			
1.66	3.05E−07	4.4179			
1.83	3.35E−07	4.4179			
2	3.66E−07	4.4179			

Table 4 Wear depth and life for polyamide (blended with 15% graphite and 10% Teflon)

Time (s)	Wear depth	Wear depth in 1 s (mm)	Wear depth in 1 day (mm)	Total days (life)
0	6.84E−35	8.54E−09	0.00073762	2711
0.5	8.16E−09			
1	8.54E−09			
1.5	8.62E−09			
1.6667	8.66E−09			
1.8333	8.67E−09			
2	8.71E−09			

Table 5 Wear volume and life for polyamide (blended with 15% graphite and 10% Teflon)

Time (s)	Wear volume (mm^3)	Total volume (mm^3)	Wear volume loss in 1 s (mm)	Volume loss in 1 day (mm)	Total days (life)
0	0	4.4179	8.40E−08	0.007259	609
0.5	4.21E−08	4.4179			
1	8.40E−08	4.4179			
1.5	1.26E−07	4.4179			
1.6667	1.40E−07	4.4179			
1.8333	1.54E−07	4.4179			
2	1.68E−07	4.4179			

It is found that bush made from (blended with 15% graphite and 10% Teflon) results in double life as compared to presently used bush material polyamide (blended with 10% graphite).

References

1. Ding J, McColl IR, Leen SB, Shipway PH (2007) A finite element based approach to simulating the effects of debris on fretting wear. Wear 263(1–6, special issue):481–491
2. Paul JS (1973) Evaluation of method for reducing fretting fatigue damage in 2024−T3 aluminium lap joint. Wear 26:1689–1699
3. Chevalier L, Eddhahak−Ouni A, Cloupet S (2009) On a simplified model for numerical simulation of wear during dry rolling contacts. J Tribolol 131(1):1–15
4. Han C, Zhang J (2014) Interference assembly and fretting wear analysis of hollow shaft. Sci World J 2014:919518
5. Ding J, Leen SB, McColl IR (2004) The effect of slip regime on fretting wear−induced stress evolution. Int J Fatigue 26(5):521–531
6. Lee YH, Kim HK (2011) Failure analysis of a pressure vessel bolt in a nuclear fuel fretting wear simulator. Eng Fail Anal 18(7):1735–1741
7. Kim NH, Won D, Burris D et al (2005) Finite element analysis and experiments of metal/metal wear in oscillatory contacts. Wear 258(11–12):1787–1793
8. Ashraf MA, Ahmed R, Ali O et al (2015) Finite element modeling of sliding wear in a composite alloy using a free−mesh. J Tribolol 137(3):1–15
9. Põdra P, Andersson S (1999) Simulating sliding wear with finite element method. Tribol Int 32(2):71–81
10. Pont D Using Vespel bearings design and technical data. Catalogue 1–16
11. Shil'ko SV (1986) Study of wear at cyclic compression using the numerical solution of the contact problems. J Friction Wear 7(6):52–56

Design and Analysis of Independent Suspension System of a FSAE Vehicle

Sanjay Lohar, Vaishnavi Patil, Sahil Save, and Rakeshkumar Thakur

1 Introduction

In any automotive vehicle, the suspension system plays a vital role in terms of human comfort and more over performance of vehicle present study proposes the procedure in designing a double wishbone suspension for FSAE cars [1]. Suspension system connects the vehicle to the wheel by means of linkages, dampers and hence allows their relative motions. Basic function of suspension systems is to support road handling as well as ride quality, which is a difficult task to achieve. It is important for the suspension system to keep the road and wheels intoned with the horizontal surface to the utmost amount as possible, because all rock bottom forces exert on the vehicle through the contact patches of the tires. The suspension system also protects the vehicle from physical and any damage from wear. Depending on various suspension system like dependent system, independent system and semi-dependent [2]. The independent suspension system is selected for the present study as this suspension system ensures all wheels for free movement after a prescribed path and allows greater control over the wheel travel.

The wheel suspension assumes a crucial role within the vehicle chassis it is the affiliation between the wheels and therefore the vehicle's body and it transfers and divides all forces and torques within the wheels and bodywork. The wheel suspension is supposed to form safe driving characteristics and thus the best possible comfort [3]. Driving axle transmits power to the wheels whereas the front axle transfers steering motions to the wheels. The main advantage of this type of suspension system is camber gain can be easily adjusted by using an unequal length of A-arms. Secondly, this configuration makes the suspension system more responsive as

S. Lohar · V. Patil (✉) · S. Save · R. Thakur
Department of Mechanical Engineering, Vidyavardhini's College of Engineering and Technology, Palghar District, Vasai (W) 401202, India

S. Lohar
e-mail: sanjay.lohar@vcet.edu.in

it needs to move less weight when it travels [4]. Considering all the parameters and advantages the double wishbone suspension is chosen for FSAE cars. It consists of (occasionally parallel) two wishbone formed arms to find the wheel. Each wishbone has two mounting points on the chassis and one joint at the knuckle. The vertical movement is managed by shock and spring which is connected to the wishbone. The weight is transmitted from the body to the cross member to the lower wishbone member. The wishbones position the wheels and transfer the vehicle load as well as acceleration, braking and cornering the forces.

2 Proposed System

For the process of designing the suspension system, a systematic approach and a well proven process is followed. Figure 1 depicts the flowchart of steps involved in design of suspension system, with identifying relevant rules from the FS rulebook.

2.1 Suspension Geometry

The design technique is driven by the Formula Bharat Rules, which verify many vogue parameters. In this system the low cross arm is longer than the higher cross arm. The arm length magnitude relation of the higher and lower cross arm dimension to ensure the camber rate is kept negligible to ensure the handling and stability. Here, the vehicle should be equipped with awfully operational suspension with shock absorbers at front and rear. The usable wheel travel of a minimum of 50.8 mm (2 in.),
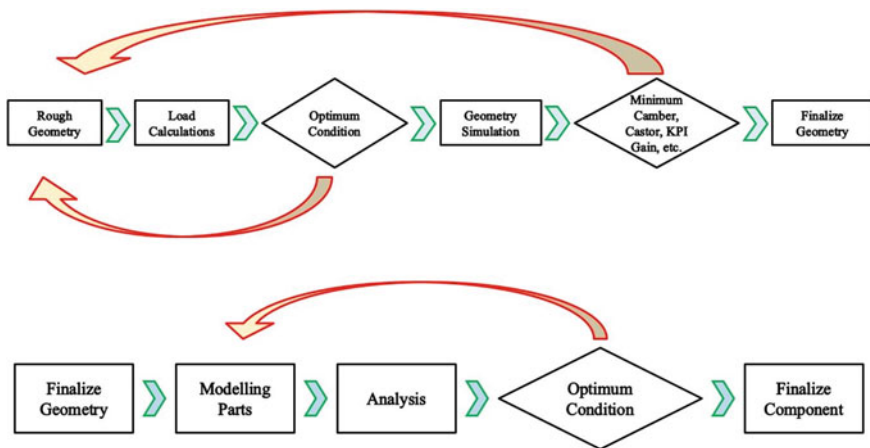
Fig. 1 Steps involved in design of suspension system

Fig. 2 Suspension geometry
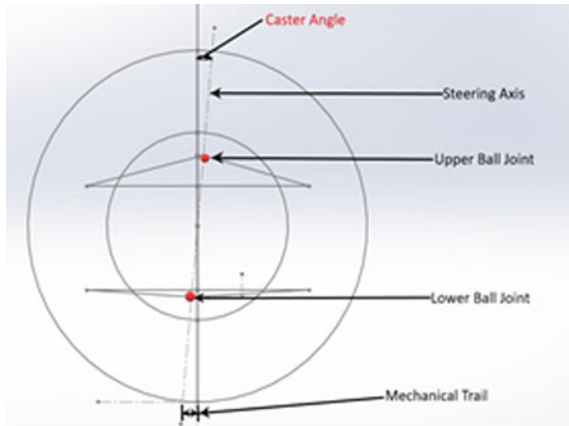
which consist of 25.4 mm (1 in.) jounce and 25.4 mm (1 in.) rebound, with driver sitting and minimum ground clearance needs to be 30 mm. The suspension geometry is obtained by considering the above parameters using Solid Works software (Fig. 2).

2.2 Knematic Analysis and Study

The optimum wheelbase, which is the length of the car between the center lines of the axle is bit difficult to define. The rule of thumb is short wheelbase cars are nimble and hence good at cornering on twisty circuits, whereas long wheelbase cars are more stable on fast straights. The weight transfer is critical to decide the optimum track-width which is nothing but the width of the car between the centers of the wheels. Weight transfer reduces as track-width increases, consequently it usually pays to adopt the widest track that regulations allow. A wide track also reduces the cornering roll. Decision for the wheelbase is driven by following parameters which includes rulebook, FSAE circuit, weight transfer, inertia, packaging, ergonomics report, etc. (Fig. 3).

3 Implementation Methodology

Once the selection of the wheelbase and track-width is done, further kinematic analysis is carried using the optimum K and its data is imported into MATLAB for further visualization. In this study the vehicle is given a maximum bump allowance of 30 mm, with some variation along the line and additional steering motion is added. Following parameters and appropriate values are considered for overview of kinematic motion analysis. The overall weight of car is considered 200 kg, weight distribution ratio
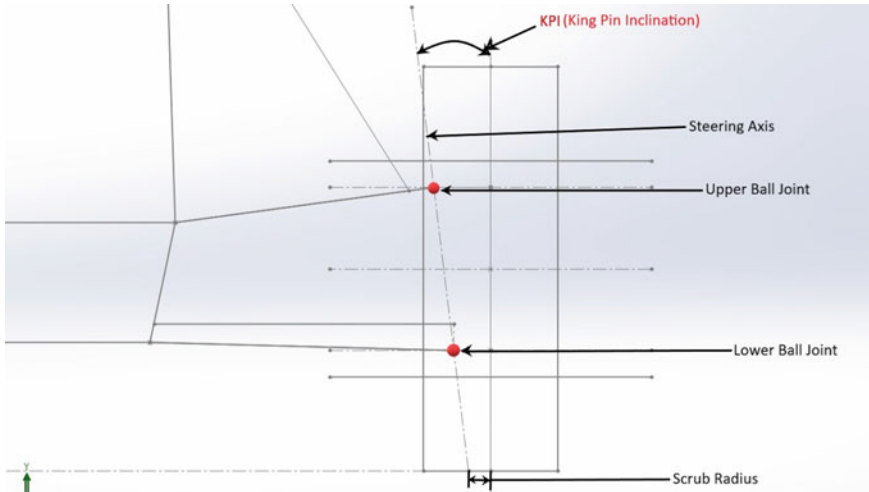
Fig. 3 Vehicle geometry

between front and rear wheel is taken as 47:53, wheelbase is taken as 1575 mm, whereas center of gravity height is taken as 310 mm from ground datum. The graph indicates considerable amount of half-track variation at both front and rear wheel. This variation is expected to increase even more during the cornering events, which lead to increase in tire temperature and wear (Fig. 4).

3.1 Designing of Components

Suspension geometry is created and tested under optimum conditions in MATLAB, components are CAD modeled using Solid Works software. The suspension assembly includes bell crank, extension shaft, roll housing, threaded shaft, adapter, mounting, etc.

The damper being the key part of the suspension system which regulates loads and contribute crucial part during vehicle travel [5]. The location of the damper mounting on the frame of the vehicle is decided only after considering by several restriction factors. The restriction includes the consideration of damper system to be mounted which ensures the working of assembly not affecting other subsystems. The restrictions also need to ensure the placement and the working of the damper system should not lead to high forces on the pushrod which may result in shear or buckling failure. The selection of damper is done by considering the spring design calculations using design data book [6].
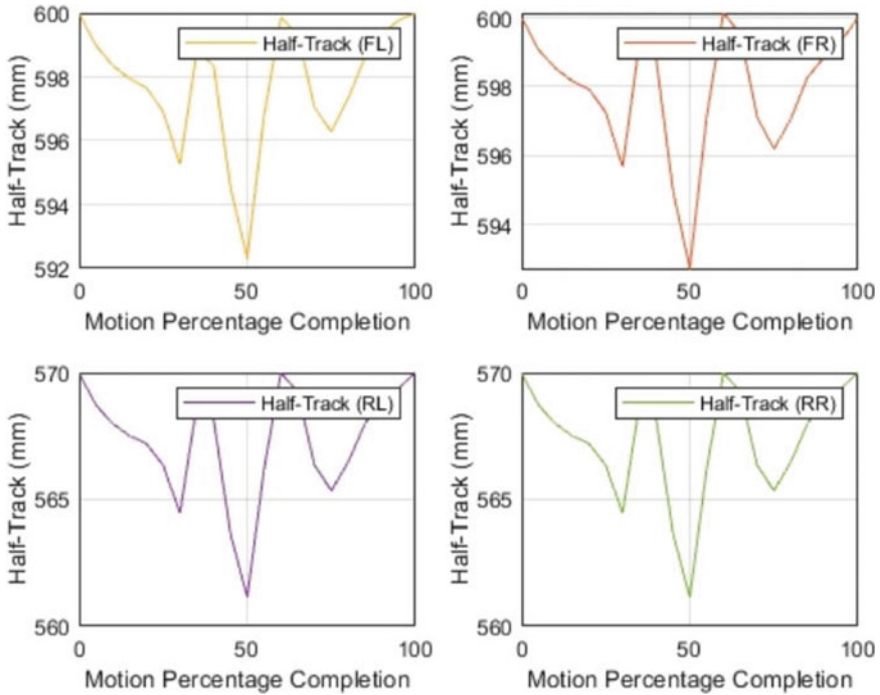
Fig. 4 Half-track variation in simulation

3.2 Loads and Forces

When the vehicle is subjected to acceleration, brake, or turn, the weight transfer occurs. This happens because the grip from the tire creates a force through which leads to effect on momentum and inertia of the vehicle. In the case of a turn, the car tries to continue to move in a straight line, but the tire generate enough force to pull the car around a specific curve, causing weight transfer to the outside of the car. We consider three components to evaluate weight transfer namely, Unsprung weight transfer, sprung weight transfer and total weight transfer.

3.2.1 Unsprung Weight Transfer

The first component, i.e., Unsprung weight transfer is calculated by considering the components which are directly connected to wheel of the vehicle

Weight transfer = Lateral force × weight × height of center of gravity/width

Table 1 Total weight transfer (lateral and longitudinal)

Parameters	CW (FL)	CW (RL)	CW (FR)	CE (RR)
N	562.11	1265.41	54.44	668.62
%	22.03	49.61	2.13	26.21

3.2.2 Sprung Weight Transfer

The second component, i.e., sprung weight transfer is the value at which the vehicle will tip over and will cause the suspension to make the body roll. Sprung weight transfer is calculated with two more sub parts which are,

Geometric Weight Transfer − Lateral force × weight × roll center height/width,
Elastic Weight Transfer − Lateral force × weight (C.G height − roll center height)/width.

3.2.3 Weight Transfer Calculation

For third component is calculated using MS Excel-based simulations, the lateral and longitudinal weight transfer is calculated for each of these weight distributions. The weight transfer is calculated for range of individual and combined value of lateral and longitudinal *g* forces ranging from 0.6 to 1.8 G. The calculations are shown for 47–53% weight distribution for front and rear of the vehicle (Table 1).

3.3 Forces on Suspension Hard Points

Double wishbone or A-arm force analysis is performed for an imaginary situation of combined acceleration and cornering. The maximum acceleration *g* force of 1.2 G and lateral G force of 1.6 G is used to perform the calculations. The coordinate system used are given below.

- *X* axis—Lateral force considered positive toward right when view from cockpit
- *Y* axis—Vertical force considered positive upwards when viewed from cockpit
- *Z* axis—Longitudinal force considered positive rearwards when viewed from cockpit.

For further calculation, the datum assumed is the center-point of the front axle. The values of *g* forces are obtained from previous logged data for separate runs. These *g* force values are combined and used as input for the weight transfer sheet to obtain the forces in 3 axes to recreate hypothetical worst-case scenario. The calculation consists of matrix multiplication using the below given equation,

$$\alpha^{-1} \times \beta = X \tag{1}$$

where, matrix α is a 6 by 6 matrix consisting of unit vectors and cross products, matrix β is a 6 by 1 column matrix consisting of the forces in the 3 axes and their moments at the centerline, and matrix X is a 6 by 1 column matrix consisting of the forces in each of the suspension (Table 2).

The material selection is done by considering suspension parameters obtained by design calculation. Based on suspension parameters solid modeling of key parts is done, followed by stress analysis conducted in Ansys. Material selection is done by considering factors like cost, availability of material, machinability, density, yield strength, tensile strength. FEA is conducted under identical loading conditions on suspension models to compare deformation and stress results.

Table 2 Sample output of forces on hard points under various conditions

Pure acceleration					Breaking performance				
			Force at					Force at	
β	0	Fx	Tie Rod	−1824.2	β	0	Fx	Tie Rod	−155.81
	1086.151	Fy	LCA-F	−369.82		326.315	Fy	LCA-F	866.427
	868.9206	Fz	LCA-R	1183.69		−522.104	Fz	LCA-R	−837.84
	198.6352	Mx	UCA-F	1604.23		−119.353	Mx	UCA-F	−1578.1
	−21.723	My	UCA-R	−1886.3		13.0526	My	UCA-R	1149.22
	27.15377	Mz	P ROD	1788.82		8.15787	Mz	P ROD	522.755
Cornering with acceleration					3G bump				
			Force at					Force at	
β	2166.667	Fx	Tie Rod	−1625.7	β	0	Fx	Tie Rod	−2446.3
	1113.807	Fy	LCA-F	−651.62		1912.95	Fy	LCA-F	1258.86
	1275.3	Fz	LCA-R	3287		0	Fz	LCA-R	−247.4
	291.5336	Mx	UCA-F	1785.13		0	Mx	UCA-F	−1200.2
	−31.8825	My	UCA-R	−5728.8		0	My	UCA-R	30.9081
	−467.455	Mz	P ROD	1037.68		47.8237	Mz	P ROD	3121.85

Steady state cornering				
			Force at	
β	0	Fx	Tie Rod	−3102
	2166.67	Fy	LCA-F	600.364
	661.32	Fz	LCA-R	727.579
	151.178	Mx	UCA-F	380.22
	−16.533	My	UCA-R	−1414
	54.1667	Mz	P ROD	3548.29
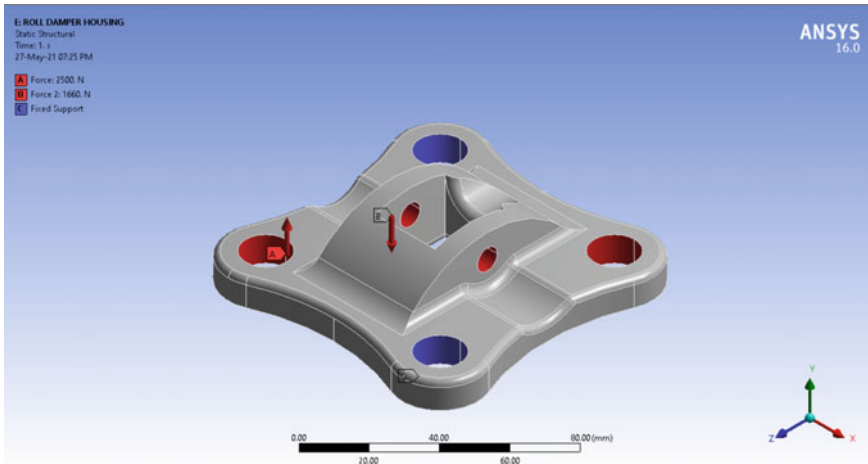
Fig. 5 Ansys of roll housing

3.4 FEA and Optimization of the Components

FEA software ANSYS is used to optimize the design which has been developed. This analysis helps us to design optimum part without sacrificing the structural rigidity. Factor of safety is decided considering the loads aspects, hence enabling it to optimize the component to its maximum potential. During the analysis stress and deformation of individual suspension components under defined conditions has been tested. The results of the stress analysis allowed further improvement in design. The analysis is performed on suspension components such as housing, adapter. To find out the value of factor of safety, the endurance limit of the material is used considering maximum stress in the component. For example, in the analysis of the roll damper housing the diagonal holes are set as fixed support and the other two are loaded with 2500 N force. The point at which damper is mounted is loaded with 1660 N force. The Images of analysis for the given parameter are in Figs. 5, 6, 7 and 8.

3.5 Adams Simulation

For dynamic and motion simulation of suspension system, Adams software is used. The purpose of this simulation is to check distribution of forces and loads while the vehicle is in motion and to improve performance and to validate design.

The value obtained from suspension geometry, Ansys and excel sheet calculations are used in simulation and the input bump of 0–30 mm with varying magnitude is given (Fig. 9).
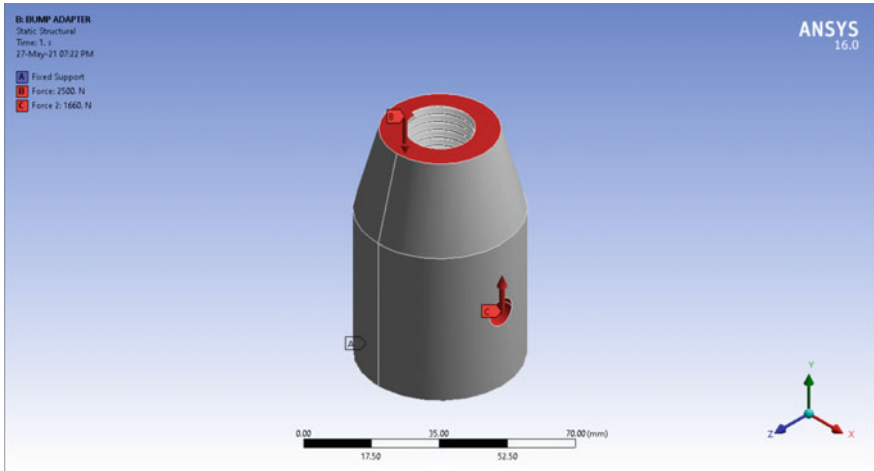
Fig. 6 Ansys of bump adapter
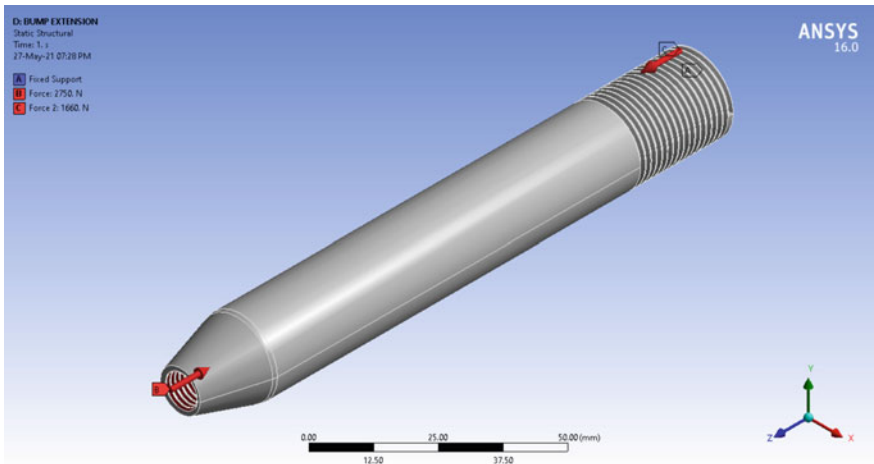
Fig. 7 Ansys of bump extension

4 Results and Discussion

4.1 Adams Simulation

Dynamic simulation of the suspension system is carried out using Adams software. The behavior of forces on the vehicle in motion is observed. Figures 10, 11 and 12 show that with a bump of 30 mm with the expecting load of 900 N. At high load, the tire tends to lose traction hence the suspension components needed to be designed to
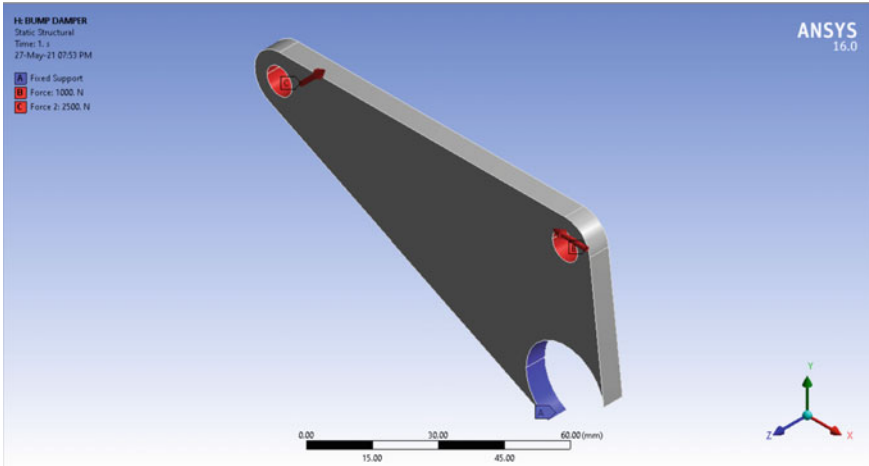
Fig. 8 Ansys of bump damper
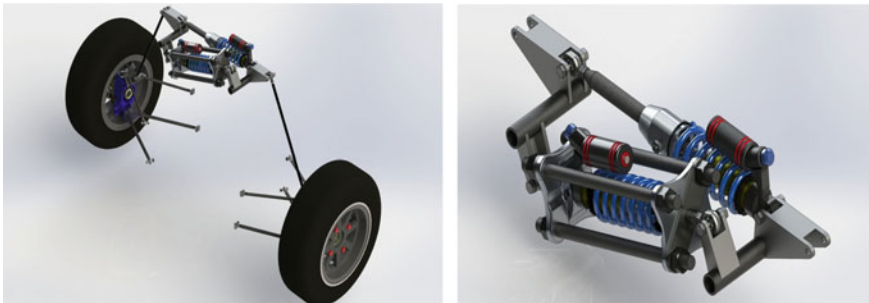
Fig. 9 Assembly of suspension system
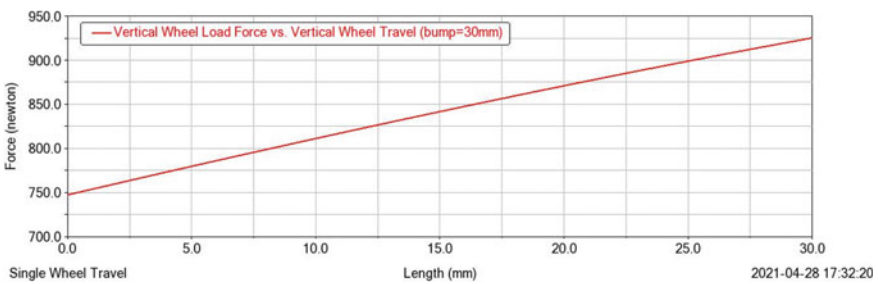
Fig. 10 Parallel wheel load versus wheel travel
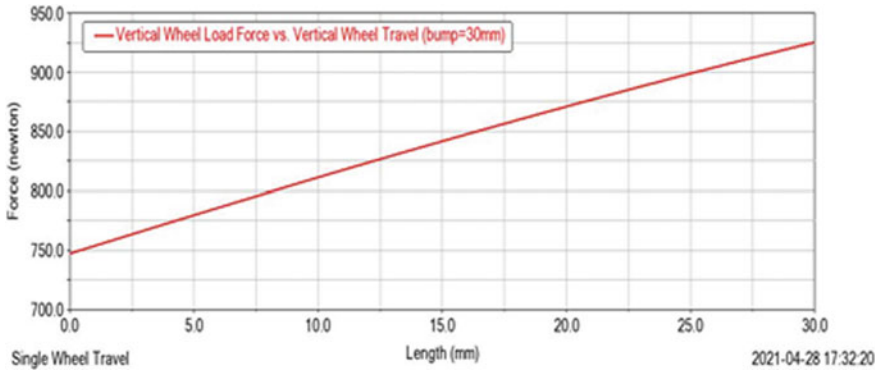
Fig. 11 Vertical wheel load versus single wheel travel
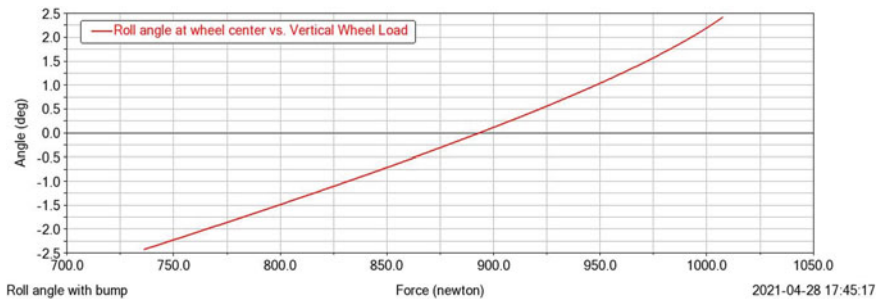
Fig. 12 Roll angle at wheel center versus vertical wheel force

overcome this shortcoming of the tire and maintain maximum traction. Availability of roll damper helps in adjusting the stiffness of the suspension thereby obtaining the required traction as per the demand of the driver and racing circuit. At actual, tracks where good chance of jounce and bounce are present then a moderate stiff suspension will help overcome traction as well as control problems.

4.2 FEA Analysis

Analysis of the suspension system components is carried out using Ansys software. Figures 13, 14, 15 and 16 are the results for components under max. Force of 2500 N due to weight transfer and 1660 N due to resistance by damper is applied. The results for deformation and factor of safety are obtained as mentioned in Table 3. The results obtained from Ansys show that the modeled components can sustain the forces acting on them. Hence, we consider the design to be safe.
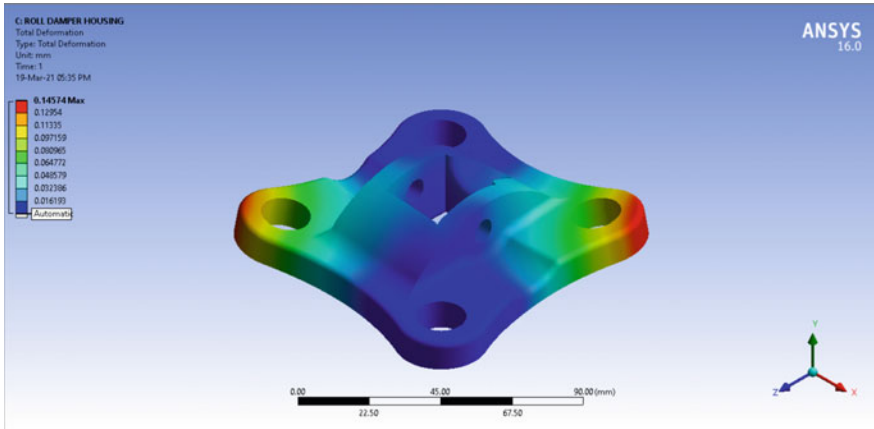
Fig. 13 Results of roll housing
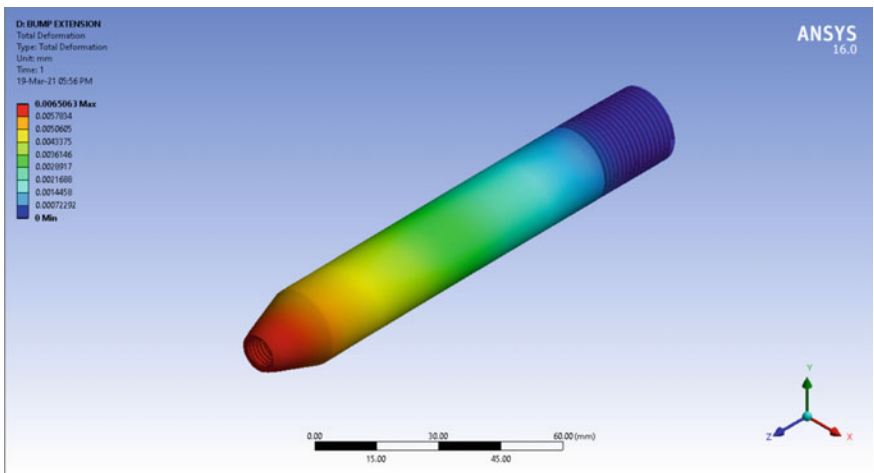
Fig. 14 Results of bump extension

5 Conclusion

Design and analysis of mechanical systems and subsystems within the FSAE vehicle norms is an important challenge. This paper focuses on designing a double wishbone which is the part of an independent suspension system for FSAE cars. One of the important aspects is to keep every part as lightweight as attainable, and easier to manufacture the vehicle via FEA and simulation software. Suspension properties when tested virtually on Adams are found to be satisfactory and under desired limit. The FEA result indicates that the suspension system performs safe and comfortable
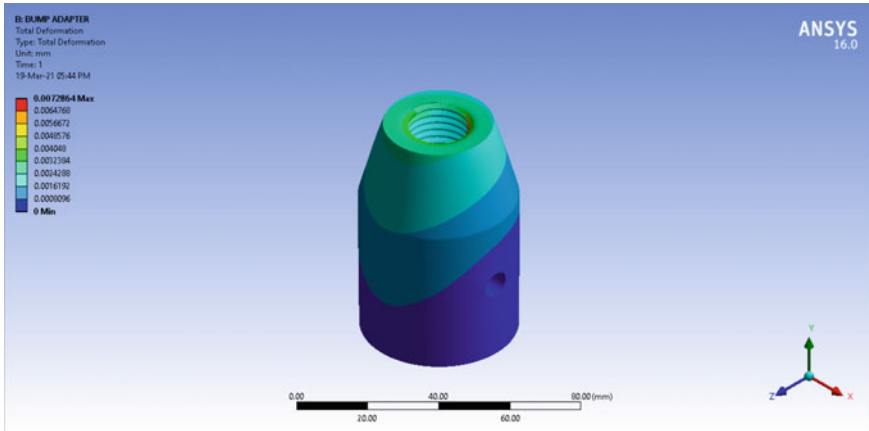
Fig. 15 Results of bump adapter
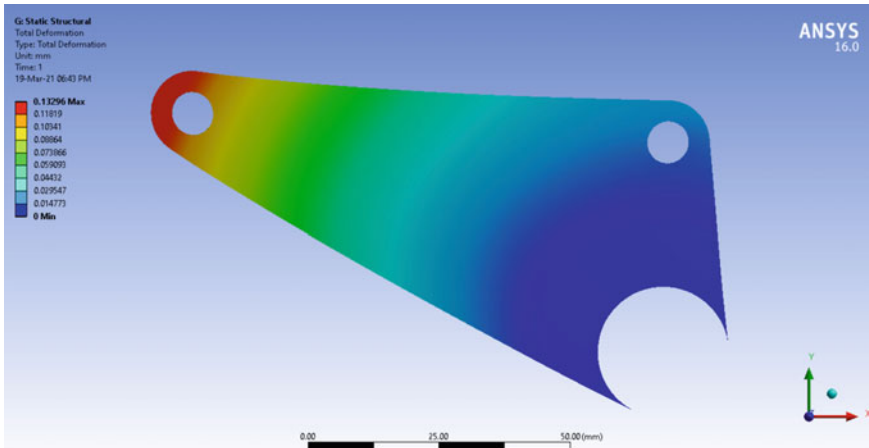
Fig. 16 Results of bump damper

in real track condition as desired within the boundary conditions. As suspension is essential for safety and handling of the motive force. Hence, a field trial is important before installation to a race vehicle. The result from ADAMS also suggests the vehicle to have good dynamic properties. The vehicle is predictable on track. This can help the driver to maneuver the vehicle as they desire.

Table 3 Results of forces on components

Components	Material	Forces	Results
Bump damper	Mild steel	A—2500 N B—1660 N C—fixed support	FOS—1.7 Deformation—0.14 mm
Roll damper	Mild steel	A—fixed support B—2500 N	FOS—1.3 Deformation—0.14 mm
Bump adapter	Al 6061 T6	A—fixed support B—2500 N C—1660 N	FOS—6.1 Deformation—0.007 mm
Bump extension	Mild steel	A—fixed support B—2500 N C—1660 N	FOS—3.4 Deformation—0.06 mm
Roll housing	Al 6061 T6	A—fixed support B—1660 N C—2500 N	FOS—3.4 Deformation—0.14 mm
Roll mounting	Mild steel	A—fixed support B—2500 N	FOS—1.8 Deformation—0.005 mm
Threaded shaft	Mild steel	A—2500 N B—fixed support	FOS—3.0 Deformation—0.08 mm

References

1. Balaji DS, Prabhakaran S, Umanath K (2017) Design and analysis of the double wishbone suspension system. J Adv Res Dyn Control Syst 9(2):987–993
2. Riduan M, Fahmi A, Tamaldin N, Sudrajat A, Ahmad F (2018) Review on active suspension system. SHS Web Conf 49(23):1–8
3. Wirawan JW, Sabino U, Aditra R, Alnursyah R, Rahman R, Sukmaji C (2018) Design analysis of formula student race car suspension system. In: AIP conference proceedings, Indonesia, p 030051
4. Samant S, Kumar S, Behera S, Kamal Jain K, Gandhi D, Sivapuram R, Kalita K (2015) Design of suspension system for formula student race car. Paper presented at 12th international conference on vibration problems, IIT Guwhati, 14–17 Dec 2015
5. Ahmad A, Hassaan Md, Nayeem F, Alam M (2020) Design & analysis of suspension system for a formula student vehicle. J Eng Technol (IRJET) 7(12):1629–1635
6. Achchagam K (2017) Design data: data book of engineers. PSG College of Technology, India

Experimental Investigations on the Machining of the Circular Profile Using Hermite and NURBS Interpolators by MACRO Programming Method

P. V. Savalia and B. B. Kuchhadiya

1 Introduction

In modern CAD/CAM systems, profiles for parts such as turbine blades, dies, car bodies, aerofoil models and vanes are usually modelled with parametric free-form curves. Since conventional CNC machines only provide linear and circular interpolators. The CAD/CAM systems have to segment a curve into huge numbers of small linearized segments and send them to CNC systems. Such linearized segments processed on CNC systems are undesirable in real applications because of the transmission errors between CAD/CAM and CNC systems, i.e. lost data and noise agitation may be unavoidable for the huge amount of data, the discontinuity of segmentation deteriorates surface accuracy and the motion becomes non-uniform and unsmooth. Yeh and Hsu [1] have stated that the chord error in interpolation depends on machining speed and radius of curvature. Chord accuracy between two interpolated points along parametric curves is generally difficult to achieve due to a non-uniform map between curves and parameters. Cheng et al. [2] have developed a real-time parametric interpolator with variable feed rate. Boujelbene et al. [3] have stated that a smaller program size is needed to achieve smaller chordal deviations, accurate geometrical dimensions, lower surface roughness. Pateloup et al. [4] have computed that when the real feed rate is improved, reducing machining time. Peng et al. [5] have studied the constant feed rate algorithm. The chord error is increasing dramatically with the increase of the feed rate. Ulker [6] has proposed an algorithm for NURBS to decrease the machining time and data. Liu et al. [7] have developed

P. V. Savalia (189999919064).

P. V. Savalia (✉)
Mechanical Engineering Department, Govt. Eng. College, Bhuj, Gujarat Technological Univeristy, Ahmedabad, India

B. B. Kuchhadiya
Mechanical Engineering Department, Shantilal Shah Eng. College, Bhavnagar, India

a real-time high-precision interpolation algorithm for a general-typed explicit parametric curve. Pateloup et al. [8] have adopted a new method for profiles formed of line segments and circle arcs, presenting discontinuities. The method is dedicated to the calculation for NURBS. Rahman and Feng [9] have generated a new constant feed rate-based toolpath for corner machining. Dhanda and Pande [10] have developed the curvature-based strategy using MACRO programming to decrease the surface roughness.

Considering the literature reviewed, it can be concluded that quality and cost are the main attributes in the field of manufacturing. Considering aesthetic aspects and design needs, machining of freeform various curve shapes is a necessity in today's manufacturing industries. Commercial CAM system to generate program blocks. Hence, there is an increase in program memory. With the MACRO approach, the program size is reduced. Further, analysis is done in terms of surface finish, machining time and ease of programming. The conventional toolpath of linear and circular segments have become the bottleneck for high-speed high-precision machining of freeform curves which will decrease the productivity and product surface finish. The MACRO programming method for CNC machines is required to machine freeform curves, which includes different parameters like numbers of control points, and feed rate to analyse shape accuracy, surface quality and machining time. CNC machines are required to enhance the quality of a product at a reasonable cost but preparatory codes on CNC machines provide automation but are restricted with a capacity to machine linear and circular toolpath (G01 and G02 or G03). However, various curved shape components are regularly used in industries and machining on CNC machine cause difficulty due to non-availability of appropriate preparatory function. However, various commercial CAD softwares are available to plot these curves in routine practice. Thus, understanding the CAD software is essential to machine the curved shape. The cutter location (CL) points on the curved profile are acquired by using CAD software and it will generate preparatory codes automatically from X- and Y-coordinates of the CL points on that curve. Cutter interpolates the toolpath linearly between two successive CL points of the segments. It results in the deviation of the toolpath from the actual curved profile to be machined, and the deviation of the tool is directly proportional to the curvature of the geometry. To reduce the deviation, the numbers of CL points are to be increased by increasing linear segments of the toolpath. Each linear segment to machine the curve is adding a single block in the part program; it will lengthen the part program and add to program memory size; and program memory size will be increased at the cost of the surface quality. To achieve better shape accuracy, parametric interpolation (MACRO programming) is required, the number of CL points can be enhanced without affecting program length in the case of MACRO programming and it can avoid the requirement of the CAD and CAM software. Any freeform curve which can be expressed by different mathematical expressions can be machined by MACRO programming. The MACRO program includes different parameters likewise numbers of control points, the segment of curves, machining time, etc.

This paper suggests various interpolation approaches for the machining of circular profile on a 3-axis CNC machine to study surface finishing and shape accuracy

(i.e. radial and chordal error for the desired toolpath). During the present study, different interpolation functions have been selected for the machining of circular profile (i.e. NURBS and Hermit curves). For that, the MACRO program is prepared to machine circular profile on MS and aluminium material to find out the effect of programing methods and interpolating curves on the surface roughness and shape accuracy. Surface roughness has been measured by surface roughness tester Mitutoyo SJ-210® and checks the shape accuracy of the profile by using AutoCAD®.

2 Methodology

CNC machine is an automatically controlled machine. The movement of the CNC machine's tool is controlled by instructions containing numbers and letters in sequence. This sequence to perform a particular predefined task is called a program. With the help of the program, CNC machines are required to enhance the quality of a product at a reasonable cost. For that, preparatory codes on CNC machines provide automation. But preparatory codes are restricted with a capacity to machine linear and circular interpolators (G01 and G02 or G03). Due to the non-availability of appropriate preparatory function, CNC machining of curved shape components causes difficulty. MACRO is a simpler form of instruction included in the part program. CNC systems support MACRO statements to allow utilization of variables and flow control structures (i.e. loops). Programmers can use logic to eliminate the redundant programming of machine functions, such as milling multiple pockets or freeform curves [11].

Freeform curves are widely used to interpolate aerospace, turbine blades automobile, consumer products, die manufacturing, etc. Increasing precision requirements for products have led to significant challenges for manufacturing industries due to the machining of the freeform curves [12]. The curves are either made of predefined equations like Bezier curve, B-spline, NURBS (Non-Uniform Rational B-Spline) and Hermit. In CAD, these types of curves can be easily plotted and transmitted with the help of a post-processor. For the transmitting of the profile curve from the CAD system to the CAM system, it is divided into small linear or circular segments. It results in the lost data and noise. The discontinuity of the curved toolpath due to linear segments deteriorates the surface quality and shape accuracy. To reduce the deviation of the toolpath, the numbers of linear segments are to be increased. Each linear segment to be machine is adding a single block in the part program. It will lengthen the part program and add to program memory size at the cost of the surface quality. MACRO programming significantly simplifies part programming by reducing part program length and hence program execution time. Hence, to achieve better shape accuracy, parametric interpolation (i.e. MACRO programming) is required. It allows the reuse of the program to machine freeform curves using various dimensions [11].

For representing freeform curves, NURBS is a mathematical tool that utilizes a basis spline. It combines properties in order to use it for the highly precise description
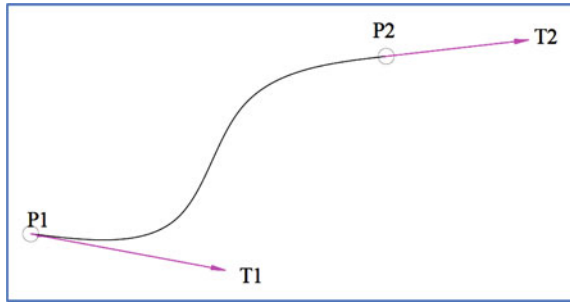
of free-forms during the design, for the calculation of complex tool trajectories, calculation of corrective re-machining steps and handling in a machine control system. A NURBS curve for parameter u is given by Eq. (1).

$$P(u) = \frac{\sum_{i=0}^{n} P_i N_{i,k}(u) w_i}{\sum_{i=0}^{n} N_{i,k}(u) w_i}, \quad 0 \le u \le 1 \tag{1}$$

Similarly, the Hermite curve (shown in Fig. 1) is spline, where every piece is a third-degree polynomial, by its values and initial derivatives at the endpoints of the equivalent domain interval. The Hermite curve is normally used for interpolation of numeric values defined at certain discrete values of coordinates $x_1, x_2, x_3, \ldots, x_n$, to achieve a smooth continuous function.

P_1 and P_2 are the start and endpoints of the Hermite curve, respectively, and T_1 and T_2 are the tangents to the start and endpoint, respectively. The Hermite curve is simple to calculate but also more powerful. They are used to well interpolate between control points.

During the present work, NURBS and Hermite interpolators are used to generate a circular profile (i.e. axis-symmetric regular close shape profile) using the spreadsheet to prepare user-defined part programming (i.e. MACRO programming). Vertical machining centre (VMC) is used to cut circular profiles on the workpieces of the materials M.S. and aluminium. The curved profiles are machined by the MACRO programming method using NURBS and Hermite interpolators. The machined surfaces are examined for surface quality by using a surface roughness tester (i.e. Mitutoyo SJ-210®). The machined curved tool paths are compared for the deviation from the actual profile using spreadsheet and CAD software.

The general form of Hermite interpolator is mentioned in Eq. (2).

$$P(u) = U M_h P_h \tag{2}$$

Matrix form of the Hermite curve is given by Eq. (3).

$$P(u) = \begin{bmatrix} u^3 u^2 u 1 \end{bmatrix} \begin{bmatrix} 2 & -2 & 1 & 1 \\ -3 & 3 & -2 & -1 \\ 0 & 0 & 1 & 0 \\ 1 & 0 & 0 & 0 \end{bmatrix} \begin{bmatrix} P_i \\ P_{i+1} \\ T_i \\ T_{i+1} \end{bmatrix} \tag{3}$$

From that, cutter location points on the Hermite curve can be calculated using Eq. (4)

$$P(u) = (2u^3 - 3u^2 + 1) P_i + (-2u^3 + 3u^2) P_{i+1} + (u^3 - 2u^2 + u) T_i + (u^3 - u^2) T_{i+1} \tag{4}$$

where $0 \le u \le 1$,

R is a radius of the circle, P and T denote control point and tangent vector, respectively, as shown in Table 1.

Table 2 mentions the values of X- and Y-coordinates of tangent vectors for all quadrants of circular profile.

Table 3 mentions the calculated values of X- and Y-coordinates of cutter location points of circular profile for the Hermite curve using Eq. (4).

Calculations can be made for quadratic NURBS using Eq. (5)

$$P(u) = \frac{\sum_{i=0}^{n} P_i N_{i,k}(u) w_i}{\sum_{i=0}^{n} N_{i,k}(u) w_i}, 0 \le u \le 1 \tag{5}$$

P_i = Control points $(n + 1)$ and degree of curve is $k - 1$,
each segment is influence by k,
Curve is made up of $n - k + 2$ segments.
Basis function can be calculated using Eq. (6),

$$N_{i,k}(u) = \frac{(u - t_i)}{(t_{i+k-1} - t_i)} N_{i,k-1}(u) + \frac{(t_{i+k} - u)}{(t_{i+k} - t_{i+1})} N_{i+1,k-1}(u) \tag{6}$$

Table 1 Values of control points and tangent vectors for Hermite curve

Range of parameter (u)	P_0	P_1	T_1	T_2
	(1, 0)	(0, 1)	(0, k)	(k, 0)
$u \in [0, 1]$	$2u^3 - 3u^2 + 1$	$-2u^3 + 3u^2$	$u^3 - 2u^2 + u$	$u^3 - u^2$

Table 2 Calculated tangent vectors for Hermite curve

Tangent vector	X-coordinate	Y-coordinate	Tangent vector	X-coordinate	Y-coordinate
T$_1$	0	49.71	T_3	0	−49.71
T$_2$	−49.71	0	T_4	49.71	0

Table 3 Calculated *X*- and *Y*-coordinates of cutter location points for Hermite curve

Quadrant	u	X-coordinate	Y-coordinate	Quadrant	u	X-coordinate	Y-coordinate
1	0	30	0	3	0	−30	0
	0.25	27.64	11.68		0.25	−27.64	−11.68
	0.5	21.21	21.21		0.5	−21.21	−21.21
	0.75	11.68	27.64		0.75	−11.68	−27.64
	1	0	30		1	0	−30
2	0	0	30	4	0	0	−30
	0.25	−11.68	27.64		0.25	11.68	−27.64
	0.5	−21.21	21.21		0.5	21.21	−21.21
	0.75	−27.64	11.68		0.75	27.64	−11.68
	1	−30	0		1	30	0

where $t_i \, (0 \leq i \leq n + k)$ is knot value

$$t_i = 0, \quad \text{if } i < k, \ t_i = i - k + 1, \quad \text{if } k \leq i \leq n \quad \text{and} \quad t_i = n - k + 2, \quad \text{if } i > n.$$

As, for example, number of control points are taken as 6, hence, $n = 5$ and control points per segment $(k) = 4$, $t_i \, (0 \leq t \leq n + k)$, t_i varies from 0 to $n + k \, (0 \leq t \leq n + k)$ (Table 4).

Calculation of *X*- and *Y*-coordinates of cutter location points of NURBS is done using Eq. (7)

$$P(u) = \frac{(1 - u)^2 \cdot w_0 \cdot P_0 + 2u(1 - u) \cdot w_1 \cdot P_1 + u^2 \cdot w_2 \cdot P_2}{(1 - u)^2 \cdot w_0 + 2u(1 - u) \cdot w_1 + u^2 \cdot w_2} \tag{7}$$

Table 5 mentions the values of *X*- and *Y*-coordinates of cutter location points of circular profile for quadratic NURBS.

Figure 2a and b shows the flowcharts to calculate coordinates of cutter location (CL) points of circular profile using Hermite and NURBS interpolators, respectively. The radius of a circle is taken as input. From the given input, *X*- and *Y*-coordinates of CL points are calculated.

Values of *X*- and *Y*-coordinates of CL points of circular profile can be found for the explicit function using Eq. (8)

$$P_x(u) = r \cos \theta, \quad P_y(u) = r \sin \theta \tag{8}$$

Table 4 Calculated knot value

t_0	t_1	t_2	t_3	t_4	t_5	t_6	t_7	t_8	t_9	t_{10}	t_{11}
0	0	0	1	1	2	2	3	3	4	4	4

Table 5 Calculated X- and Y-coordinates of cutter location points for quadratic NURBS

Quadrant	u	X-coordinate	Y-coordinate	Quadrant	u	X-coordinate	Y-coordinate
1	0	30	0	3	2	−30	0
	0.25	27.89	11.04		2.25	−27.89	−11.04
	0.5	21.21	21.21		2.5	−21.21	−21.21
	0.75	11.04	27.89		2.75	−11.04	−27.89
	1	0	30		3	0	−30
2	1	0	30	4	3	0	−30
	1.25	−11.04	27.89		3.25	11.04	−27.89
	1.5	−21.21	21.21		3.5	21.21	−21.21
	1.75	−27.89	11.04		3.75	27.89	−11.04
	2	−30	0		4	30	0

(a) Hermite interpolation

START

Input radius of circle, r

Set parameter $u = 0$, Quadrant $q = 0$ and Multiplication factor $mf = 0$

Calculate Tangent vectors T1, T2, T3 and T4 by using Hermite interpolation
$$T1 = \frac{[r\sin45 - r(-2u^3 + 3u^2)]}{[(u^3 - 2u^2 + u)]}, \quad T2 = \frac{[r\cos45 - r(2u^3 - 3u^2 + 1)]}{[(u^3 - u^2)]},$$
$$T3 = -T1 \text{ and } T4 = -T2 \qquad \text{where } u = 0.5$$

$q = q + 1$

Calculate cutter location point $P(u)$
$$P_x(u) = [r(2u^3 - 3u^2 + 1) + (u^3 - u^2)T_2]mf$$
$$P_y(u) = [r(-2u^3 + 3u^2) + (u^3 - 2u^2 + u)T_1]mf$$

$u = u + 0.01$

$u \le 1$ — Yes / No

$q = q + 1, u = 0$

Calculate cutter location point $P(u)$
$$P_x(u) = [r(-2u^3 + 3u^2) + (u^3 - 2u^2 + u)T_4]mf$$
$$P_y(u) = [r(2u^3 - 3u^2 + 1) + (u^3 - u^2)T_3]mf$$

$u = u + 0.01$

$u \le 1$ — Yes / No

$mf = -1, u = 0$

$q < 4$ — Yes / No

END

(b) NURBS interpolation

START

Input radius of circle, r

Set parameter $u = 0$

Calculate cutter location point $P(u)$
$$P_x(u) = \frac{r[(1-u)^2 + \sqrt{2}\,u(1-u)]}{[(1-u)^2 + \sqrt{2}\,u(1-u) + u^2]}, \quad P_y(u) = \frac{r[\sqrt{2}\,u(1-u) + u^2]}{[(1-u)^2 + \sqrt{2}\,u(1-u) + u^2]}$$

$u = u + 0.01$

$u \le 1$ — Yes / No

Calculate cutter location point $P(u)$
$$P_x(u) = \frac{r[-\sqrt{2}(u-1)(2-u) - (u-1)^2]}{[(2-u)^2 + \sqrt{2}(u-1)(2-u) + (u-1)^2]}, \quad P_y(u) = \frac{r[(2-u)^2 + \sqrt{2}(u-1)(2-u)]}{[(2-u)^2 + \sqrt{2}(u-1)(2-u) + (u-1)^2]}$$

$u = u + 0.01$

$u \le 2$ — Yes / No

Calculate cutter location point $P(u)$
$$P_x(u) = \frac{r[-(3-u)^2 - \sqrt{2}(u-2)(3-u)]}{[(3-u)^2 + \sqrt{2}(u-2)(3-u) + (u-2)^2]}, \quad P_y(u) = \frac{r[-\sqrt{2}(u-2)(3-u) - (u-2)^2]}{[(3-u)^2 + \sqrt{2}(u-2)(3-u) + (u-2)^2]}$$

$u = u + 0.01$

$u \le 3$ — Yes / No

Calculate cutter location point $P(u)$
$$P_x(u) = \frac{r[\sqrt{2}(u-3)(4-u) + (u-3)^2]}{[(4-u)^2 + \sqrt{2}(u-3)(4-u) + (u-3)^2]}, \quad P_y(u) = \frac{r[-(4-u)^2 - \sqrt{2}(u-3)(4-u)]}{[(4-u)^2 + \sqrt{2}(u-3)(4-u) + (u-3)^2]}$$

$u = u + 0.01$

$u \le 4$ — Yes / No

END

Fig. 2 Flowcharts for **a** Hermite and **b** NURBS interpolators of circular profile

Table 6 Calculated *X*- and *Y*-coordinates of cutter location points for explicit function

Angle (°)	X-coordinate	Y-coordinate	Angle (°)	X-coordinate	Y-coordinate
0	30	0	180	−30	0
22.5	27.716	11.48	202.5	−27.71	−11.48
45	21.21	21.21	225	−21.21	−21.21
67.5	11.48	27.716	247.5	−11.48	−27.71
90	0	30	270	0	−30
112.5	−11.48	27.716	292.5	11.48	−27.71
135	−21.21	21.21	315	21.213	−21.21
157.5	−27.71	11.48	337.5	27.716	−11.48
180	−30	0	360	30	0

Table 6 mentions the values of *X*- and *Y*-coordinates of cutter location points of circular profile for explicit function.

3　Experimental Setup

After the calculation, programming has been done to machine circular profile using explicit, NURBS and Hermite interpolator to compare with conventional part programming. After the programming, as shown in Fig. 3, actual machining is done using vertical machining centre-Siemens controlled-VMC 640.

Fig. 3 Vertical machining centre—Siemens controlled-VMC 640
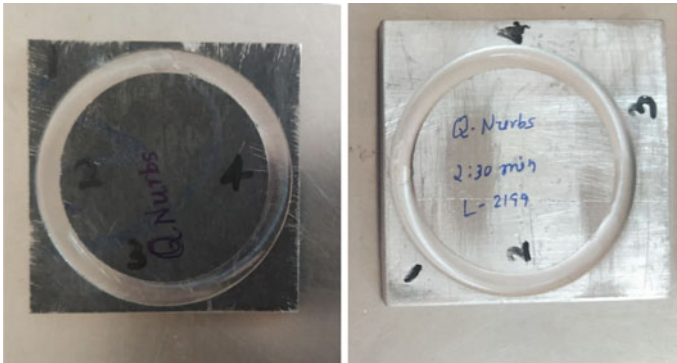
Fig. 4 Machined components (mild steel and aluminium)

Mild steel and aluminium materials are examined to cut circular profile using explicit, NURBS and Hermite interpolators as shown in Fig. 4.

Actual machining is done using a vertical machining centre to cut circular profile for the 400 cutter location points using conventional methods as well as MACRO programming methods using explicit function, NURBS and Hermite interpolators.

4 Result and Discussion

During machining, total machining time, cutting time, cutting length and file sizes are compared as shown in Table 7.

As mentioned in Table 7, the total machining time is almost the same for all the programming methods. For the circular profile machined with a conventional method, the number of lines is maximum (i.e. 411) and file size is the highest (16,711 bytes) while the number of lines is the least (i.e. 22) and program size is the lowest (468 bytes) in the case of the explicit function programming method.

A circular profile is machined using various programming methods such as explicit, NURBS and Hermite interpolator which is compared with circle plotted

Table 7 Comparative study for various programming methods

Programming method	No. of CL points	Machining time	Program length (blocks)	File size (bytes)
		Min:sec	No. of blocks	
Explicit-conventional	400	02:30	411	16,791
Explicit-MACRO	400	02:30	22	468
NURBS-MACRO	400	02:30	38	1421
Hermite-MACRO	400	02:30	39	982

with CAD software (i.e. AutoCAD$^{®}$) using circle command as shown in Fig. 5. The root mean square (RMS) value of error for different interpolators is shown in Table 8.

Table 9 shows a comparative study for shape accuracy in terms of root mean square (RMS) value of radial and chordal errors. It is clear that shape accuracy is
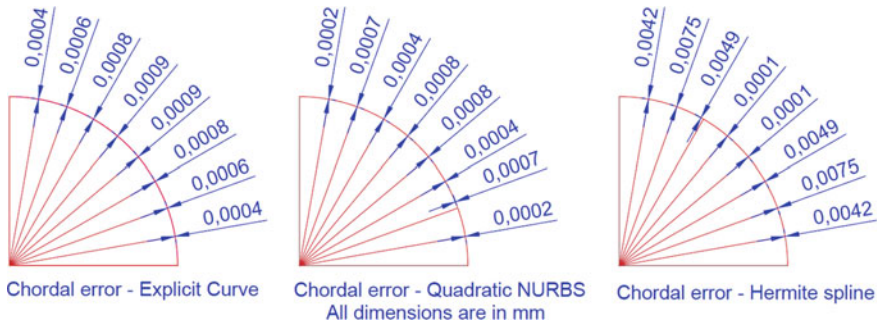
Fig. 5 Chordal error of circular profile

Table 8 Root mean square chordal error for explicit, NURBS and Hermite interpolators

Angle (°)	Chordal error (in mm)		
	Explicit curve	NURBS	Hermite spline
0	0	0	0
10	0.0004	0.0002	0.0042
20	0.0006	0.0007	0.0075
30	0.0008	0.0004	0.0049
40	0.0009	0.0008	0.0001
50	0.0009	0.0008	0.0001
60	0.0008	0.0004	0.0049
70	0.0006	0.0007	0.0075
80	0.0004	0.0002	0.0042
90	0	0	0
Error (RMS)	**0.0006**	**0.0005**	**0.0044**

Table 9 Comparative study for shape accuracy using various programming methods

Shape accuracy		
Programming method	Radial error (RMS) (in mm)	Chordal error (RMS) (in mm)
Explicit-MACRO	0	0.0006
NURBS-MACRO	0	0.0005
Hermite-MACRO	0.0041	0.0044
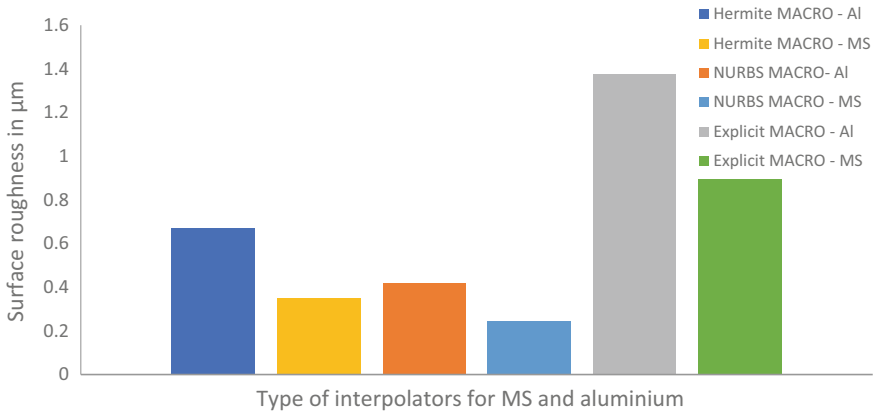
Fig. 6 Surface roughness of circular profile for different materials

maximum (i.e. least error) for the RMS value of radial error (i.e. 0 mm) and chordal error (0.0005 mm) while plotting circular profile with NURBS interpolator.

Figure 6 shows the comparison of cut circular profile surface roughness for the various materials (i.e. aluminium and mild steel) using the Hermite, NURBS and explicit interpolators.

It is clear that, during machining of the circular profile, surface roughness is minimum in the case of mild steel material cut with NURBS interpolator. It is found maximum when aluminium is cut with explicit function.

5 Conclusions

From the above discussion, important conclusions can be narrated as per the following:

- It is found that NURBS interpolations give a better surface finish than Hermite and explicit function. This is because, machining with the NURBS interpolation, the time for calculation of the cutter location (CL) point is more.
- Radial and chordal errors are the least in the case of NURBS interpolation compared to Hermite interpolation. The reason is whenever a single control point is moved, it affects only a local portion of the curve and control of the curve is very convenient in the case of NURBS.
- A better surface finish is observed while the circular profile is machined with MACRO programming. Due to the calculation of *X*- and *Y*-coordinates of the circular machined profile is required much time. It leads to less vibration in cutting tools.
- Surface roughness for the aluminium material is found higher than the surface roughness material for the mild steel material for the Hermite, NURBS and explicit

interpolators (i.e. Fig. 6). Aluminium is soft, gummy and sticks to cutting tools compared to mild steel, resulting in a built-up edge that adheres tool quality and tool life.

References

1. Yeh SS, Hsu PL (2002) Adaptive feed rate interpolation for parametric curves with confined chord error. J Comput Aided Des 34:229–237
2. Cheng C, Tsai M, Cheng M (2002) Real-time variable feed rate parametric interpolator for CNC machining. IFAC Proc Vol, 15th triennial world congress, Barcelona, Spain 35(1):109–114
3. Boujelbene M, Moisan A, Tounsi N, Brenier B (2004) Productivity enhancement in dies and molds manufacturing by the use of C1 continuous tool path. Int J Mach Tools Manuf 44:101–107
4. Pateloup V, Chanal H, Duc E, Ray P (2006) HSM-adapted tool path calculation for pocketing. Mach Sci Technol 10:181–196
5. Peng F, Chen X, Zhou Y, Li B (2008) NURBS curve interpolation algorithm adaptive to the machine's kinetic characteristics. Int J Mater Prod Technol 33(1/2):79–94
6. Ulker E (2012) NURBS curve fitting using artificial immune system. Int J Innov Comput Inf Control 8(4):2875–2887
7. Liu Q, Jin XJ, Long YH (2010) A real-time high-precision interpolation algorithm for general-typed parametric curves in CNC machine tools. Int J Comput Integr Manuf 23(2):168–176
8. Pateloup V, Duc E, Ray P (2010) B-spline approximation of circle arc and straight line for pocket machining. J Comput Aided Des 42:817–827
9. Rahman AKM, Feng H (2012) Effective corner machining via a constant feed rate looping tool path. Int J Prod Res 1–16
10. Dhanda M, Pande SS (2016) Tool path planning strategies for CNC machining of free form surfaces using surface properties. In: 6th international and 27th all India manufacturing technology, design and research conference (AIMTDR-2016), College of Engineering, Pune, 16–18 Dec 2016
11. ServoWorks CNC macro programming manual (2011) Soft Servo Systems, Inc., p 6.5
12. Lasemi A, Xue D, Gu P (2012) A freeform surface manufacturing approach by integration of inspection and tool path generation. Int J Prod Res 50(23):6709–6725

Analyzing Risk Factors of Reconfigurable Manufacturing System in Context of Industry 4.0 Using ISM-MICMAC Analysis

Rajesh Pansare, Manoj Palsodkar, and Madhukar Nagare

1 Introduction

The fourth industrial revolution (Industry 4.0) has stimulated several innovations like flexibility in manufacturing and services, quality in products, as well as customized production. These innovations are compelling manufacturing organizations to adopt the recent technologies that can fulfill the needs of a dynamic market, better quality at the lowest cost, and hence multi-skill employees at the workplace [1, 2]. Industry 4.0, also called a smart manufacturing system, is an advanced manufacturing paradigm where multiple products can be manufactured with the help of automation in production processes. It also considers information exchange, smart supply chain, reduced lead times, and many more that become a core competency of Industry 4.0 [3]. In these circumstances, the need of using intelligent products that are capable of self-maintenance, robustness, real-time control, and so on is highlighted by many researchers. The use of technologies like Cyber-Physical System (CPS), Radio Frequency IDentification (RFID), cloud manufacturing, etc., is playing a significant role in this era [4, 5]. However, according to Wang and Koren [6], Reconfigurable Manufacturing System (RMS) can meet these requirements of Industry 4.0.

R. Pansare (✉) · M. Palsodkar
Veermata Jijabai Technological Institute, Matunga, Mumbai 400019, India
e-mail: rajeshpansare@somaiya.edu

M. Palsodkar
e-mail: manojpalsodkar@somaiya.edu

K. J. Somaiya College of Engineering, Mumbai 400077, India

M. Nagare
Production Engineering Department, Veermata Jijabai Technological Institute, Matunga, Mumbai 400019, India
e-mail: mrnagare@pe.vjti.ac.in

© The Author(s), under exclusive license to Springer Nature Singapore Pte Ltd. 2022
S. Kumar et al. (eds.), *Recent Advances in Manufacturing Modelling and Optimization*,
Lecture Notes in Mechanical Engineering,
https://doi.org/10.1007/978-981-16-9952-8_40

The core characteristics of RMS (Modularity, Integrability, Customization, Convertibility, Scalability, and Diagnosability) enable it to provide the necessary flexibility, reconfigurability, etc.

Many RMS domain researchers contributed to the research on framework development and implementation methodologies. However, there are few examples of RMS being fully implemented in practice [7]. Furthermore, the initial investment required for RMS implementation is substantial; thus, it is necessary to identify the risks associated with RMS implementation so that they can be addressed at a specific stage of implementation. Keeping this in mind, the presented study has the following objectives:

i.   To conduct a thorough literature review and identify the risk factors associated with RMS implementation.
ii. To prepare a framework for identifying the specific stage at which the risk factor must be addressed.

With these goals in mind, an extensive literature review is conducted, and the risk factors associated with RMS implementation are identified. Following that, the Interpretive Structural Modeling (ISM) technique is used to generate the structural framework for the identified risk factors. This will assist RMS and Industry 4.0 practitioners in avoiding failures caused by the identified risk factors. The paper is divided into five sections, one of which is the current one. Section 2 discusses the literature review and the identified risk factors, while Sect. 3 explains the ISM method and its application to the current problem. Section 4 describes the results and discussions, whereas Sect. 5 summarizes the conclusion and future scope.

2 Literature Review

The primary goal of the literature review is to provide a snapshot of the work done in this domain. The peer-reviewed literatures were chosen for this study, and the results are shown below.

2.1 Risk Factors of RMS

Many RMS domain researchers have made significant contributions and attempted to develop various frameworks and methodologies. Their efforts have enhanced the concept of RMS and helped to improve the manufacturing system in a variety of ways in the era of Industry 4.0. At the same time, the researchers attempted to identify the risks associated with RMS implementation and to offer suggestions for mitigating these risks. Few researchers highlighted the financial loss as a result of the risk of RMS failing to improve its performance [6]. The above researcher emphasized that even after improving system scalability, there is no guarantee that this capacity will be fully

utilized. Furthermore, Abdi and Labib [7], emphasized the importance of the supply chain, the failure of which may affect the performance of the manufacturing system. Furthermore, management's role during implementation is critical, and unsupportive management may fail the manufacturing system [8, 9]. Furthermore, the availability of advanced technology is a critical factor during RMS implementation, and without it, most of the core characteristics are unable to meet. As a result, in the context of Industry 4.0, automation, advanced machinery, advanced communication, and so on, are necessary [10]. Employees may be resistant to cultural changes in the manufacturing system, and top management's role at this point is to try to convince them. Employee support will contribute to RMS's success [11]. RMS is specifically designed to meet the dynamic needs of the market, but there is a risk of complete overall market transformation [10]. There is also the possibility of a new competitor entering the market. In the context of Industry 4.0, the above two risks are critical and must be addressed at the appropriate stage of RMS implementation [12]. Few researchers identified process risks such as a lack of multi-skilled employees, strikes, decreased productivity, and so on [13]. Furthermore, the risk of failing to meet the required quality and flexibility of the manufacturing system cannot be overlooked [14]. Delays in product delivery, as mentioned by several researchers, may result in the loss of orders from those customers and are risky for the organization's future growth [13]. Table 1 concludes with a list of the identified risk factors.

The ISM method is described below for preparing the structural framework for the aforementioned risks.

2.2 ISM Process

When it comes to developing a structural framework, ISM is the best alternative, as many researchers have explored during their studies. As a result, the authors decided to use ISM to develop a structural framework for the aforementioned risk factors of RMS in the context of Industry 4.0. The steps to be taken to carry out the ISM process are outlined below [11, 15].

Step 1: Develop a contextual relationship between risk factors to create a Structured Self-Interaction Matrix (SSIM). In this matrix, the letters V, A, X, and O are used, where V represents one factor assisting another and A represents vice versa. X denotes that both factors help each other, whereas O denotes that there is no relationship. Finally, the Initial Reachability Matrix (IRM) is prepared.

Step 2: By removing transitivity from IRM, the Final Reachability Matrix (FRM) is created. This is followed by level partitioning, which prepares three sets: the reachability set, the antecedent set, and the intersection set.

Step 3: The digraph is developed from the level partitioning. The digraph depicts the relationship between various risk factors and the hierarchy from bottom to top.

Table 1 List of risk factors for RMS

Sr. No.	Risk factor	Code	Description	References
1	Financial loss risk	RF1	Due to the high cost of RMS implementation, there is a risk of loss, and any reconfiguration achieved should be economically beneficial	[6]
2	Supply chain risk	RF2	A flawed supply chain may cause product delivery to be delayed	[7]
3	Advanced technology risk	RF3	This indicates a lack of recent technology and the risk of further technological advancements	[10]
4	Unsupportive management risk	RF4	It highlights the need for strong support from top officials of the organization	[8]
5	Employee resistance risk	RF5	It is the resistance offered by human resources and the consequences of the same	[11]
6	Dynamic demand risk	RF6	It indicates the risk of rapidly changing customer needs and fluctuations in market demand	[10]
7	New competitor risk	RF7	The risk of the inclusion of a new competitor in the market is an important factor	[12]
8	Process risk	RF8	It indicates a risk of lack of skilled employees, productivity, strikes, etc.	[13]
9	Quality/flexibility risk	RF9	The inability of the system to meet required quality and flexibility	[14]
10	Delay risk	RF10	It indicates losses to the manufacturing system due to delays in product delivery	[13]

Step 4: The risk factor codes in the digraph have been replaced by the names of the actual risk factors. This is the structural framework.

Step 5: To obtain a cluster diagram, the MICMAC procedure is now followed.

3 Research Methodology and ISM Execution

This section discusses the procedures used to carry out research work. It also covers the various steps taken during the execution of ISM.
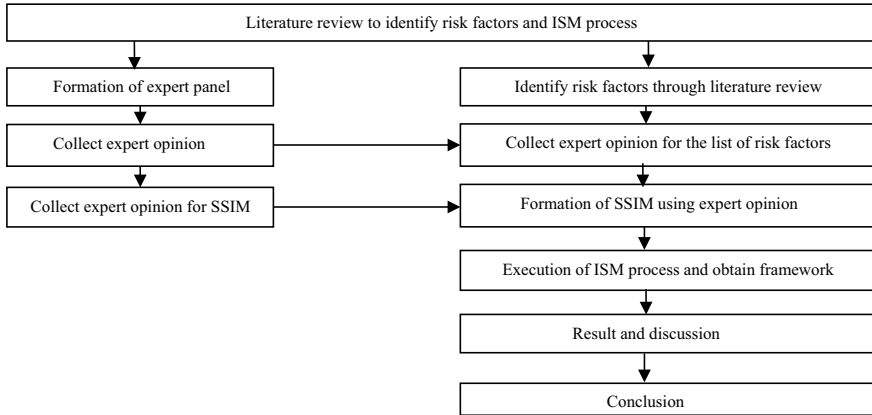
Fig. 1 Research methodology adopted

3.1 Research Methodology

The steps followed in the execution of research work are depicted using the flow chart as shown in Fig. 1.

The expert panel chosen is made up of ten members, seven from industry and three from academia. All experts were both experienced and qualified in the RMS and Industry 4.0 domains. The ISM process is carried out, according to expert opinion, as explained below.

3.2 ISM Steps and Case Application

The expert panel is asked to prepare an SSIM in which the relationships between various risk factors are identified and presented in Table 2.

Table 3 lists the various symbols used during SSIM and their meanings.

The procedure for ISM as mentioned in Sect. 2.2 is followed and level partitioning is obtained as shown in Table 4.

From the level partitioning, the digraph is obtained that shows the links of several risk factors. When the codes of a digraph are replaced by actual names of risk factors, the structural framework is obtained as shown in Fig. 2.

As shown in Table 4, there are a total of five levels obtained during level partitioning. The MICMAC process is now initiated to obtain a cluster diagram of RMS risk factors. Unsupportive management risk appears at the bottom of the structural framework, indicating that it is a strong input, whereas delay risk and quality/flexibility risk appear at the top, indicating that it is a strong output. Table 5 shows the Final Reachability Matrix (FRM), as well as the driving power and dependence power.

Table 2 SSIM for risk factors of RMS

Sr. No.	Name of risk factor	Code	RF10	RF9	RF8	RF7	RF6	RF5	RF4	RF3	RF2
1	Financial loss Risk	RF1	V	V	V	O	V	V	A	O	V
2	Supply chain risk	RF2	V	V	V	O	O	X	A	A	
3	Advanced technology risk	RF3	V	V	V	V	O	X	A		
4	Unsupportive management risk	RF4	V	V	V	V	O	V			
5	Employee resistance risk	RF5	V	V	V	V	X				
6	Dynamic demand risk	RF6	V	V	V	V					
7	New competitor risk	RF7	O	V	O						
8	Process risk	RF8	V	V							
9	Quality/flexibility risk	RF9	X								
10	Delay risk	RF10									

Table 3 Symbols and their meaning in SSIM

Entry in SSIM	(i, j) entry in initial reachability matrix	(j, i) entry in initial reachability matrix
V	1	0
A	0	1
X	1	1
O	0	0

As per the values obtained for driving power and dependence power, the cluster diagram is obtained as shown in Fig. 3.

The cluster diagram shows that there are no risk factors in cluster I, four risk factors in cluster II, two risk factors in cluster III, and four risk factors in cluster IV.

4 Results and Discussions

For selected risk factors, the ISM technique is used to obtain the structural framework. In addition, the MICMAC method is used to obtain driving power, dependence power, and the cluster diagram. The obtained results are discussed further below.

i. The structural framework shows that unsupportive management risk, financial loss risk, and advanced technology risk have the greatest impact on the

Table 4 Level partitioning of risk factors

Sr. No.	Name of risk factor	Code	Reachability set	Antecedent set	Intersection set	Level
1	Financial loss risk	RF1	1, 2, 5, 6, 8, 9, 10	1	1	II
2	Supply chain risk	RF2	2, 5, 8, 9, 10	2	2	III
3	Advanced technology risk	RF3	2, 3, 5, 7, 8, 9, 10	3, 5	3, 5	II
4	Unsupportive management risk	RF4	1, 2, 3, 4, 5, 7, 8, 9, 10	4	4	I
5	Employee resistance risk	RF5	2, 3, 5, 6, 7, 8, 9, 10	2, 6	2, 6	III
6	Dynamic demand risk	RF6	5, 6, 7, 8, 9, 10	6	6	III
7	New competitor risk	RF7	7, 9	7	7	IV
8	Process risk	RF8	8, 9, 10	8	8	IV
9	Quality/flexibility risk	RF9	9, 10	9	9	V
10	Delay risk	RF10	9, 10	9, 10	9, 10	V
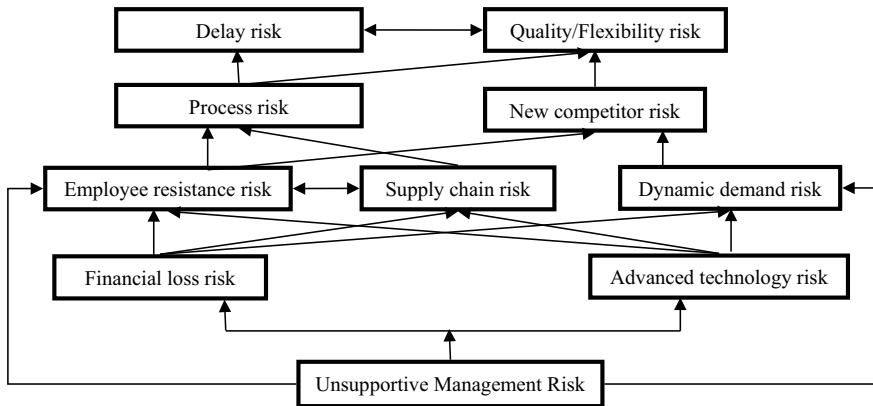
Fig. 2 Structural framework of RMS risk factors

remaining risk factors. This means that if these factors fail, other factors may suffer as a result, and practitioners must pay close attention to these factors. In addition, other factors have been identified, and their positioning in the structural framework emphasizes their relative importance during RMS implementation.

Table 5 FRM with driving power and dependence power

Sr. No.	Name of risk factor	Code	RF1	RF2	RF3	RF4	RF5	RF6	RF7	RF8	RF9	RF10	Driving power
1	Financial loss risk	RF1	1	1	0	0	1	1	0	1	1	1	7
2	Supply chain risk	RF2	0	1	0	0	1	0	0	1	1	1	5
3	Advanced technology risk	RF3	0	1	1	0	1	0	1	1	1	1	7
4	Unsupportive management risk	RF4	1	1	1	1	1	0	1	1	1	1	9
5	Employee resistance risk	RF5	0	1	1	0	1	1	1	1	1	1	8
6	Dynamic demand risk	RF6	0	0	0	0	1	1	1	1	1	1	6
7	New competitor risk	RF7	0	0	0	0	0	0	1	0	1	0	2
8	Process risk	RF8	0	0	0	0	0	0	0	1	1	1	3
9	Quality/flexibility risk	RF9	0	0	0	0	0	0	0	0	1	1	2
10	Delay risk	RF10	0	0	0	0	0	0	0	0	1	1	2
	Dependence power		2	5	3	1	6	3	5	7	10	9	
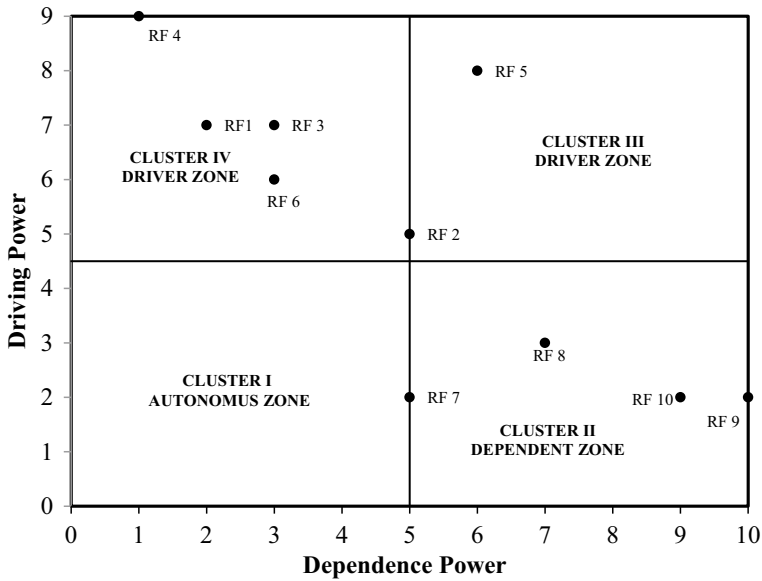
Fig. 3 Cluster diagram of RMS risk factors

ii.   In the structural framework, the position of delay risk and quality/flexibility risk is at the top. This demonstrates how these risk factors are heavily dependent on other risk factors. If the bottom-level factors are addressed, the top-level factors become safer and can be addressed with care. This implies that if bottom-level factors are addressed at each stage of RMS implementation, products can be delivered on time and with the necessary quality/flexibility.

iii. During RMS implementation, the role of employees, supply chain, and market forecasting that connects the bottom to the top cannot be overlooked. This implies that employee training, rewards and recognition, appropriate supply chain management, market analysis, and so on must be addressed at a specific stage of implementation to avoid process risk and, to some extent, to avoid the entry of new competitors into the market.

iv.   The risk factors that appear in clusters I (Autonomous Zone) have a low driving and dependence power, as well as disorganized characteristics. These factors do not affect other factors; however, no risk factors appear in this cluster during this cluster analysis. This implies that the risk factors shortlisted are accurate in the context of the chosen topic.

v.   The four risk factors, namely new competitors risk, process risk, quality/flexibility risk, and delay risk, appear in cluster II (Dependent Zone), indicating that these factors have a high dependence power but a low driving power. This means that these factors are dependent on other factors at the bottom level of the developed framework. These factors indicate output-related risks such as product delivery delays and poor quality/flexibility; thus, the

bottom-level factors must be addressed at the appropriate stage of RMS implementation. Furthermore, the risk factor new competitors risk is on the border, so out of the four factors in this cluster, the most care must be taken with this factor.

vi. The supply chain risk and employee resistance risk appear in cluster III (Linkage cluster), with high dependence power and driving power. This means that these risk factors are both highly influential and highly dependent. Because even minor changes in these risk factors have a large impact on other risk factors, top management must pay close attention to them during RMS implementation.

vii. Cluster IV (driver zone) contains four risk factors: financial loss risk, advanced technology risk, unsupportive management risk, and dynamic demand risk. This cluster is located in the cluster diagram's upper left corner and represents high driving power but low dependence power. This means that many other risk factors associated with RMS implementation are dependent on these risk factors. In practice, this means that if any of these risk factors fails, other risk factors may fail as well. Practitioners and decision-makers responsible for RMS implementation must pay close attention to these factors so that other risk factors are not put at risk.

5   Conclusion

In the presented work, an extensive literature survey is conducted, and ten risk factors for RMS implementation in the context of Industry 4.0 are identified, followed by a structural framework using the ISM technique. The following significant conclusions can be drawn from the presented work:

- According to the level partitioning and structural framework obtained, the risk of unsupportive management has a significant impact on RMS implementation and other identified risk factors. This emphasizes the critical role of top management in implementing RMS.
- As can be seen from the structural framework, financial support and advanced technology have their importance and have a large influence on other factors such as supply chain, employee, process, and so on.
- It is also worth noting that if risk factors at the bottom level are not addressed, top-level risk factors such as delay and quality/flexibility can suffer greatly.
- The driving and dependence power computed using MICMAC analysis emphasizes the interdependence of each risk factor with another.

References

1. Kipper LM et al (2021) Scientific mapping to identify competencies required by industry 4.0. Technol Soc 64
2. Yadav G, Luthra S, Jakhar SK, Mangla SK, Rai DP (2020) A framework to overcome sustainable supply chain challenges through solution measures of industry 4.0 and circular economy: an automotive case. J Clean Prod 254:120112
3. Germán A et al (2019) Industry 4.0 technologies: implementation patterns in manufacturing companies. Int J Prod Econ 210:15–26
4. Neal AD et al (2021) The potential of industry 4.0 Cyber Physical System to improve quality assurance: an automotive case study for wash monitoring of returnable transit items. CIRP J Manuf Sci Technol 32:461–475
5. Yadav G, Luthra S, Huisingh D, Mangla SK, Narkhede BE, Liu Y (2020) Development of a lean manufacturing framework to enhance its adoption within manufacturing companies in developing economies. J Clean Prod 245:118726
6. Wang W, Koren Y (2012) Scalability planning for reconfigurable manufacturing systems. J Manuf Syst 31(2):83–91
7. Abdi MR, Labib A (2017) RMS capacity utilisation: product family and supply chain. Int J Prod Res 55(7):1930–1956
8. Dixit AR, Gupta M (2013) Current status, enablers & barriers of implementing cellular manufacturing system in Indian industries. Adv Manuf 1(4):346–356
9. Yadav G, Desai TN (2016) Lean Six Sigma: a categorized review of the literature. Int J Lean Six Sigma 7(1):2–24
10. Kurniadi KA, Ryu K (2020) Maintaining sustainability in reconfigurable manufacturing systems featuring green-BOM. Int J Precis Eng Manuf Green Technol 7(3):755–767
11. Yadav G, Mangla SK, Luthra S, Rai DP (2019) Developing a sustainable smart city framework for developing economies: an Indian context. Sustain Cities Soc 47:101462
12. Koren Y et al (1999) Reconfigurable manufacturing systems. CIRP Ann Manuf Technol 48(2):527–540
13. Babu H, Bhardwaj P, Agrawal AK (2020) Modelling the supply chain risk variables using ISM: a case study on Indian manufacturing SMEs. J Model Manage
14. Poduval PS, Pramod VR (2015) Interpretive structural modeling (ISM) and its application in analyzing factors inhibiting implementation of total productive maintenance (TPM). Int J Qual Reliab Manage
15. Yadav G, Desai TN (2017) Analyzing Lean Six Sigma enablers: a hybrid ISM-fuzzy MICMAC approach. TQM J 29(3):488–510

Aerodynamic Drag Reductions of an Indian Tractor–Trailer Truck

Umangi Pathak and Mihir Solanki

1 Introduction

Today, however, effective aerodynamics is acknowledged as critical to any highway truck operation, primarily as a source of lower operating costs. When a vehicle moves, the air exerts a force on it that prevents it from moving. This force is known as aerodynamic drag, and it has a substantial impact on vehicle fuel consumption [1]. The aerodynamic drag of a vehicle is affected by its shape, frontal area and speed. The bigger the frontal area or speed of a vehicle, the greater the aerodynamic drag. Saving energy and protecting the global environment are two of the most significant goals of aerodynamic drag control studies [2]. The major goal of automobile engineers is to improve fuel efficiency. Reduced drag is vital in vehicle body development for improving fuel consumption and driving performance, and because an aerodynamically refined body is aesthetically pleasing, it will make a substantial contribution to increasing the vehicle's capacity [3].

There seems to be no motivation for heavy-duty trucks to have strong aerodynamics. Due to their bigger frontal area and bluff body design, heavy vehicles are aerodynamically inefficient when compared to other ground vehicles [4]. Fuel consumption for big vehicles can be reduced by changing truck designs to reduce aerodynamic drag [5]. It is possible that current truck drag coefficients might be lowered by up to 50%; this reduction in drag would reflect around a 25% reduction in fuel use at highway speeds; an estimated total savings of \$1.5 billion per year can be recognized in the USA alone for only a 6% reduced fuel use [6]. In this work,

U. Pathak (✉) · M. Solanki
Department of Mechanical Engineering, G.H. Patel College of Engineering and Technology, Vallabh Vidyanagar, India

M. Solanki
e-mail: mihirsolanki@gcet.ac.in

a comprehensive CFD study was conducted to investigate the influences of supple-mentary parts on drag reduction of heavy commercial vehicles using SolidWorks and Ansys package.

This article aims to;

- Identification and prioritization of trailer drag sources.
- Guidelines for improving trailer drag by the use of aerodynamic add-ons, trailer contouring, and tractor–trailer gap control, and
- Establishment of an effective computational approach for designing/analysis of heavy vehicles. This will be based on a summary of benchmarking efforts and results with the computational tools compared to experimental data.

In this research, a comprehensive CFD study is conducted to investigate the influ-ences of supplementary parts on drag reduction of trucks. Here, Sect. 2 represents the relevant literature review. In Sect. 3, an analysis of the based model Tata Signa 5530S tractor–trailer truck and modified model is presented. Section 4 highlights the results and discussion of this study, and Sect. 4(B) gives some ideas of future scope of study.

2 Literature Review

Ali and Mahmood (2013) [7]	• Used a 1/10th scaled model of a generic truck to work on reducing aerodynamic drag in generic trucks by adopting a geometrically designed rear cabin • To investigate the influence of these bumps on drag, we used the Taguchi or orthogonal array optimization methods. And plotted a curve for pressure distribution over the cabin using a SolidWorks model with and without bumps
Chowdhury et al. (2013) [2]	• Featured a wind tunnel research for commercial vehicles that used a 1/10th scale truck model to analyse the effects of aerodynamic changes on fuel savings • It is suggested that the front fairing alone can reduce roughly 17% of drag, while combinations of aerodynamic fairings in different portions of the truck body can reduce drag by up to 26%

<div align="right">(continued)</div>

(continued)

Drollinger (1987) [8]	• Discussed Volvo trucks and identified ways to improve the aerodynamics around a truck in order to reduce fuel consumption • Recommended for aerodynamic trailers for a significant reduction in drag force. When adding aerodynamic devices to the trailer, the undercarriage and the base of the vehicle experience the biggest drag effects. This demonstrates a large potential to improve the flow over side skirts and frame extension
Kim et al. (2017) [9]	• Designed cabs inspired by the cheetah's exterior fore body shape have been proposed to examine the probable effect of drag reduction on tractor–trailers • Cab design coefficients were quantitatively assessed using CFD simulation
Koike et al. (2004) [10]	• Aiming to investigate and quantify the aerodynamic influence of various fuel-saving measures used in heavy commercial vehicles, it was discovered that even modest modifications, such as a fairing on the front of the truck, can reduce drag by up to 20% at a 0° yaw angle • Furthermore, in light crosswinds with as little as a 5° yaw angle, with the addition of a full skirting along the truck, aerodynamic drag can be reduced by over 35%
Lee (2018) [11]	• Identified different aerodynamic solutions available for European tractor and semi-trailer layouts, summarizing their impact on aerodynamic drag, which leads to fuel consumption reduction • It was discovered that the results of aerodynamic methods employed to reduce fuel consumption in conventional trucks (CONV) utilized in the United States cannot be compared to cab over engine vehicles (CEV) used in Europe
Mohamed-Kassim and Filippone (2010) [6]	• Demonstrated the impacts of aerodynamic drag reduction devices on a large truck-trailer, as well as the evaluation of fuel economy for a standard and modified truck-trailer profile • It was determined that aerodynamic improvements to the basic truck-trailer result in a 21% reduction in drag and an improvement in fuel economy of roughly 4.2 L per 100 km at an average speed of 30 m/s

(continued)

(continued)

Tonpe et al. (2019) [12]	• Determination of the contribution of underbody flow, wheels, mirrors and gaps between the tractor and trailer on vehicle dynamics • It was discovered that Reynolds averaged Navier–Stokes computational fluid dynamics methods cannot capture unsteady and inherently time-dependent phenomena • CFD technologies that are more advanced than RANS and helpful in large-scale complex flow-fields are suggested

It has been discovered that there is a significant opportunity to work on drag reduction for Indian long trucks. As a result, the goal of this study is to serve as a good source of data for this type of aerodynamics investigation. Changes in velocity have an effect on drag. Drag force increases as velocity increases. A slight reduction in a vehicle's aerodynamic drag improves its performance and handling behaviour.

3   Methodology

Creo software is utilized for basic and modified model creation, and SolidWorks software is utilized for drag force, drag coefficient, lift force and drag reduction analysis. There are three basic ways for determining the advantage of aerodynamics: (i) computational fluid dynamics (CFD) simulations, (ii) wind tunnel testing (WTT) and (iii) track tests (TT) [13]. The study shows the drag coefficient is reduced when one or more the fairings are used. As a result, a 3D printed scale model of a trailer truck with various attachments is recommended, followed by a wind tunnel test. SolidWorks' CFD tool was used to simulate the impact of various add-on fairings [14]. To avoid vibration, the wind tunnel bracket should be stiffer. There are many solutions to minimize drag coefficient and many research papers concluded that but most of them did not took actual products into account [15]. No study has also optimized gap area of a truck which cannot be filled and responsible for most of the drag. Lastly, we will also work on the underbelly of trailer to reduce creation of vortex.

A.   **Problem Summary**

The geometry of a heavy tractor–trailer can have different geometrical configurations that contribute to drag force and can be articulated as a source of drag. This drag source can appear in the following ways:

The schematic of Fig. 1 depicts the principal percentage drag regions on a tractor–trailer truck which are the tractor front face, tractor–trailer gap, undercarriage/wheels and trailer base. As emission norms are becoming stringent, reduction in aerodynamic drag results in decreased emissions, in turn, improves the efficiency. In the designer's point of view, only the drag coefficient and frontal area can be controlled
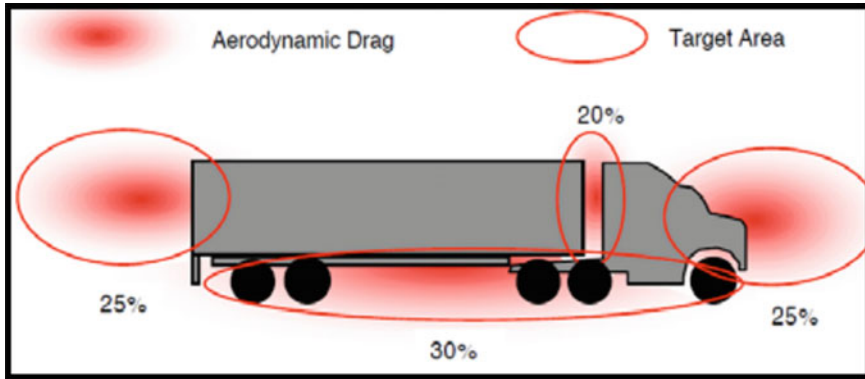
Fig. 1 Graphical representation of drag distribution for a tractor–trailer truck

[5]. Designing the vehicle considering the frontal area will result in the reduction of the aerodynamic drag force. This study focuses on Indian heavy-duty vehicle and tractor–trailer truck. India has a sizable and fast-growing commercial vehicles industry which is equal to many big nations. In Fiscal Year 2019, a total of 1,007,319 units were sold, with year-on-year growth of 17.5%. For whole analysis, we must use a truck made by Indian manufacturer who makes the vehicles as per Indian motor vehicle laws and to be used in India Commercial vehicles (CV) sector is divided into two segments of light commercial vehicles (LCV) and medium and heavy commercial vehicles (M&HCV). Tata Motors, the M&HCV goods carrier market leader Tata Motors sold a total of 181,265 trucks, to have a market share of 51.62%. So it makes sense to do our project on mass market manufacturer or market leader like Tata, and we are working on M&HCV or specifically semi-truck as it can carry the most amount of stuff in terms of fuel consumption per tonne of load carried. The standard shipping container is of 40 ft. capacity which is most widely used in logistics industry. In India, truck height is limited to 12 m. And all semi-trucks are segmented in terms of 10 tyre, 14 tyre, 18 tyre, 22 tyres based on their axle and tyre number while load on each axle is limited to 11.5 tonne per axle of 4 wheels. So, for 40 ft. container we need 18 tyre truck. Based on all the mentioned requirements, two models stand out which are Tata Prima and Signa. Prima is premium product and costly, while Signa is successor to their most successful semi-truck platform based on LPK Cab so we choose Tata Signa range. So we finally selected Tata Signa 5530S.

Dimensions of base model	
Tractor truck dimensions:	Trailer or container dimensions:
Length—6040 mm	King pin off set—914.4 mm
Width—2440 mm	Bed length—12,192 mm
Height—2790 mm	Height—3657.6 mm
Wheel base—3800 mm	Container width—2590 mm
Fifth tyre area—4100 mm	Tyre size—295 80 R 22.5, dia. 1043 mm
Tyre size—295 80 R 22.5, dia. 1043 mm	

(continued)

CAD modelling of base truck

The next step of the project is to make a 3D CAD model based on the dimensions, and its accuracy will affect the final results the most. So for this task we selected CREO 5.0 CAD modelling software (Fig. 2).

This is the point from which number crunching starts. For aerodynamic analysis or we can say fluid analysis of the body, we used ANSYS FLUENT software which is a fluid dynamics (CFD) software tool that includes physical modelling capabilities across a wide range of CFD and Multiphysics applications. It can be used to model flow, turbulence, heat transfer and reactions for industrial applications. In Ansys, we selected drag and lift analysis and the results for drag analysis are. And for this simulation, we are taking velocity of at inlet 22.222 m/s (80 kph) while max allowable simulation velocity is limited to 38.1888 m/s (140 kph) (Figs. 3 and 4).

In Fig. 5, we can see the cut section of the truck and simulation air is blocked by truck front and the whole surface of the container which is inducing more drag.

In Fig. 5, it is cut section on tyre of truck and we can see vacuum in underbelly and backside while the gape area is experiencing a cortex formation. It is observed that, the two intersecting vortex formation in middle and back while the amount of air displaced by the truck and trailer must be reduced.

For mitigating or reducing all the factors or improving all the areas, we must modify the geometry of the truck.

B. Proposed Model

Modification was proposed by our group to mitigate the problems and to reduce the drag. In various research papers, we read there were many ways to improve the aerodynamics and many of them were effective also but their feasibility in context of Indian market is questionable. So we came up with our own ideas, and we also borrowed some ideas from actual trucks in international market (Fig. 6).

(1) Tractor–trailer gap

Fig. 2 Initial base model design
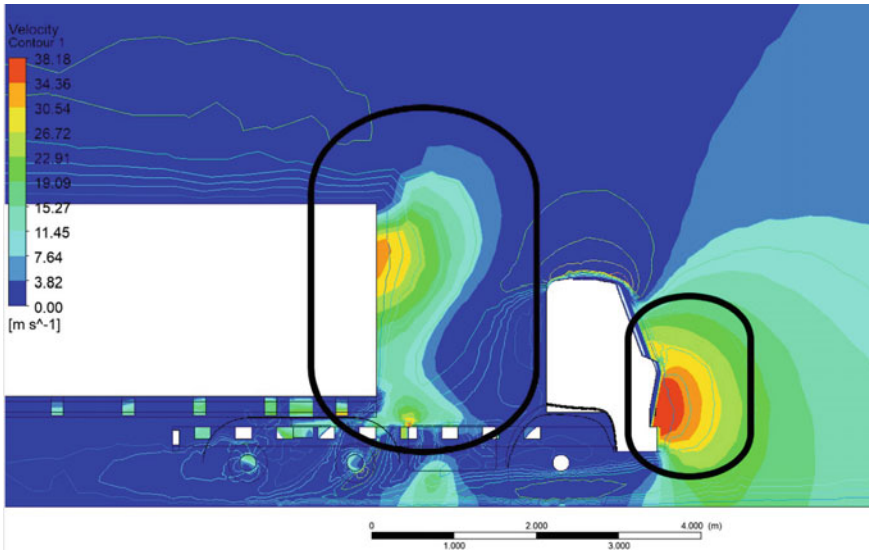
Fig. 3 Velocity contour analysis on base model
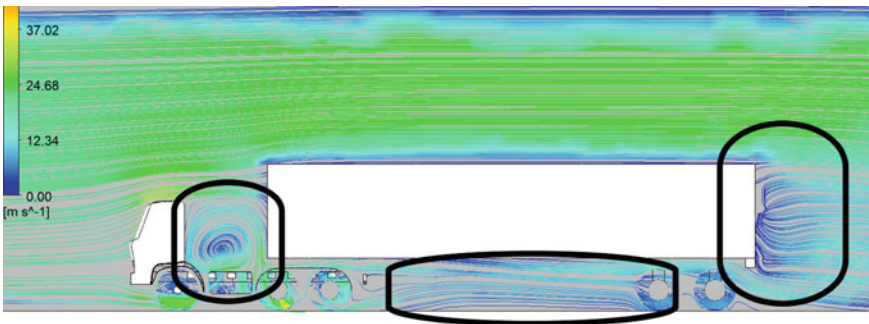
Fig. 4 Vacuum generation analysis on base model

This was the element as seen in simulation is inducing the most amount of drag and is subjected to vortex formation so looking at semi-trucks sold in American and European market we proposed a smooth geometry to match the trailer height. This geometry is made while keeping turning radius of the truck and related geometries in mind. This will guide the air over the surface of the container (Figs. 7 and 8).

(2) **Vacuum in the underbelly of truck**

The air interacting with tyres is also inducing drag while air is moving out abruptly so we covered the trailer sides and made a convergent divergent style of pattern to guide the air and increase its velocity so that the bundle layer formation is minimal and no disturbance is produced (Figs. 9 and 10).
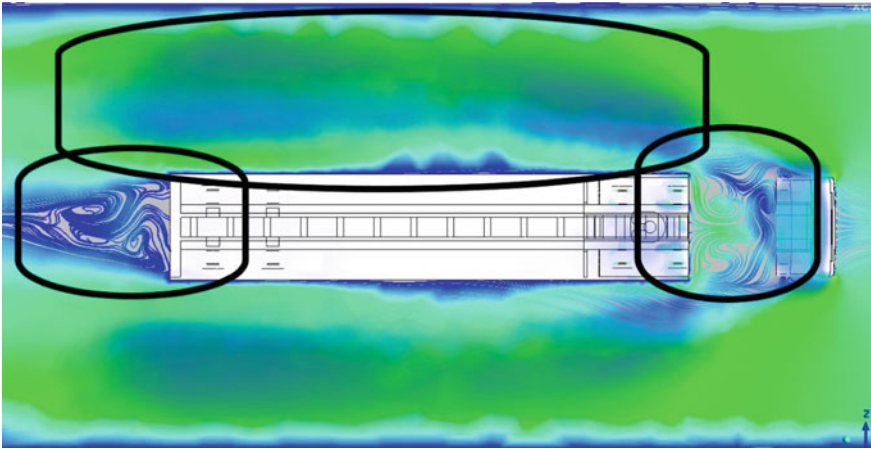
Fig. 5 Vortex formation analysis on base model
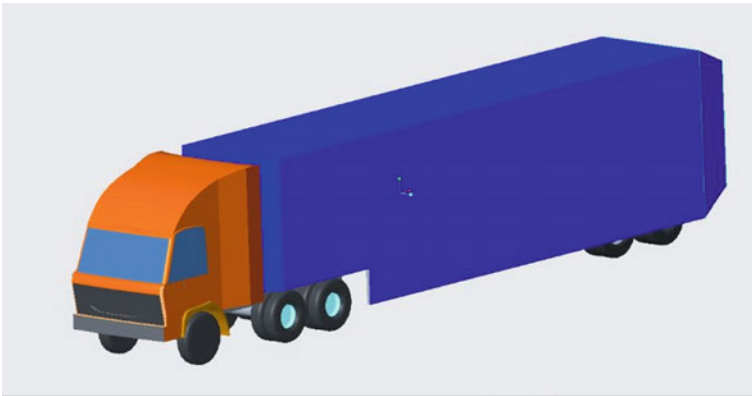
Fig. 6 Modified geometry of base model
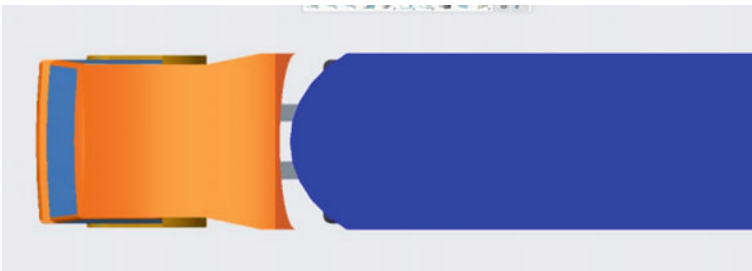
Fig. 7 Modified tractor–trailer gap

Fig. 8 Modified undercarriage wind deflector
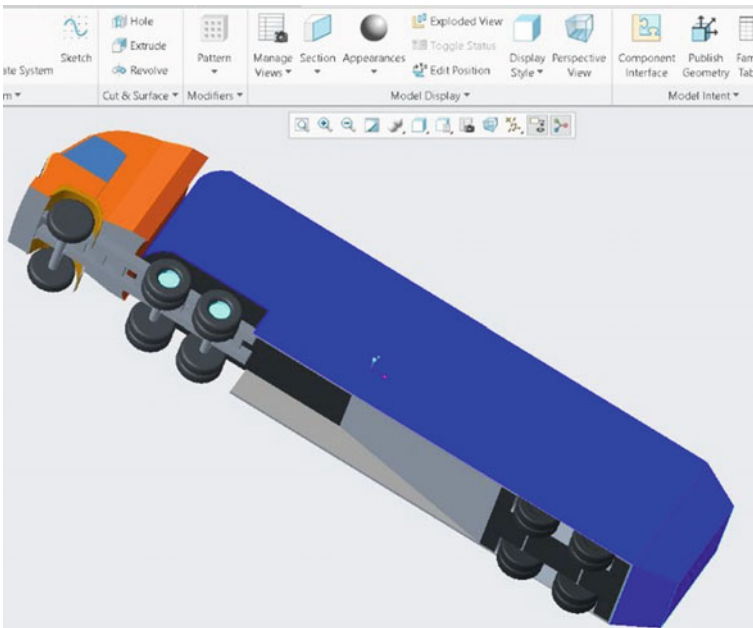
Fig. 9 Belly of trailer sides with convergent divergent style of pattern

4 Analysis of Modified Model

Figures 11 and 12 show reduced pressure at front and increased pressure at rear. A smooth exit of air and the vortex formation at the back because of vacuum is reduced.
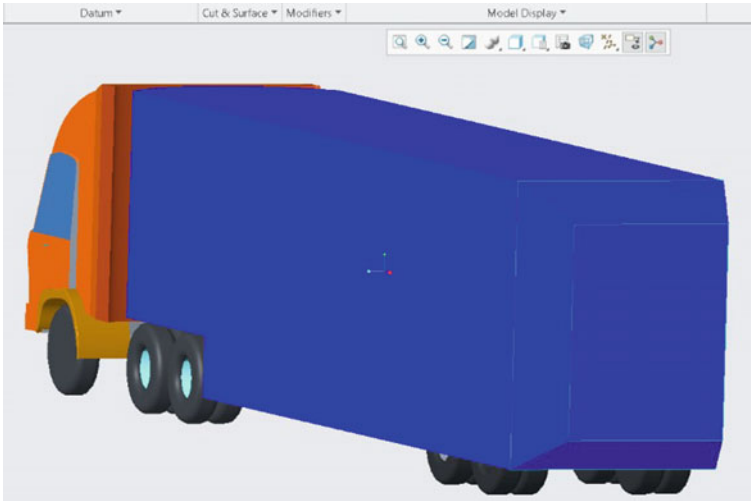
Fig. 10 Modified backside with wedge shape
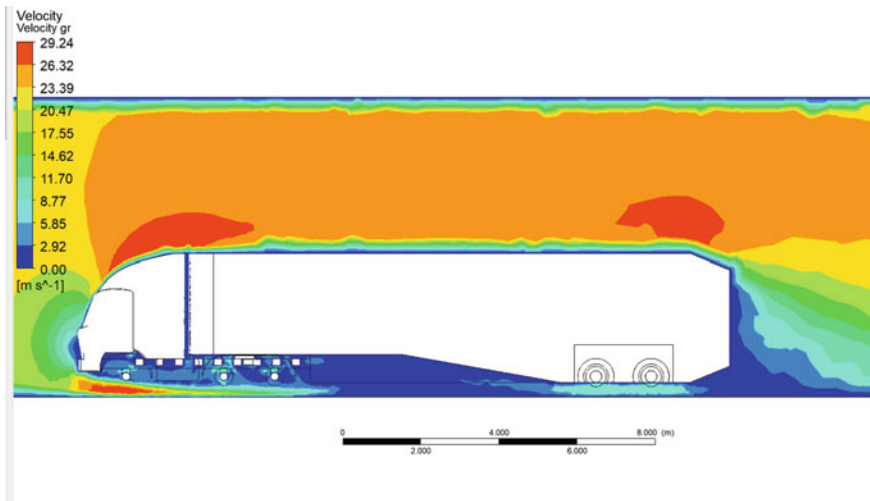
Fig. 11 Velocity contour analysis on modified model

A.   **Result and Discussion**

The lift generated by the truck is a small value 220.0873 N, and it increased to 393.7778 N which is double the original value but it is so small compared to the load carried by the truck so there won't be any measurable difference in the working of truck. Yet increase in lift can be considered success. And it will lift or reduce some minuscule amount of load from our wheels but such low
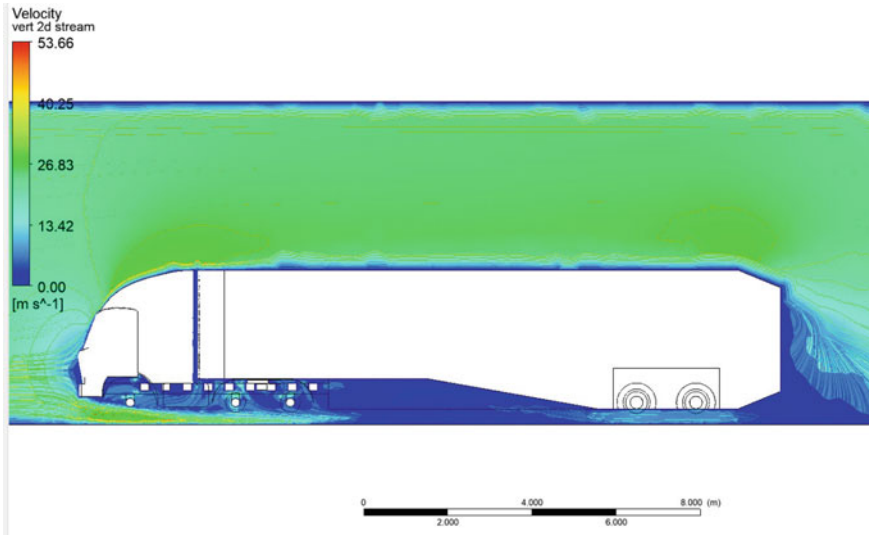
Fig. 12 Vacuum generation analysis on modified model

value won't even blip in sensors during wind tunnel testing at facilities of big corporations manufacturing these trucks as shown in Figs. 11 and 12.

Figure 13 represents side by side the air displaced is reduced and the dark blue or vacuum patches has also reduced which indicates lower vortex formation that certainly an improvement over original but to prove that drag has reduced we need drag force data. The disturbance in air at container wall is reduced while there is little to no air disturbance in the gap section yet it gap section still has some effect as it has to low pressure as observer in image above (Fig. 14).
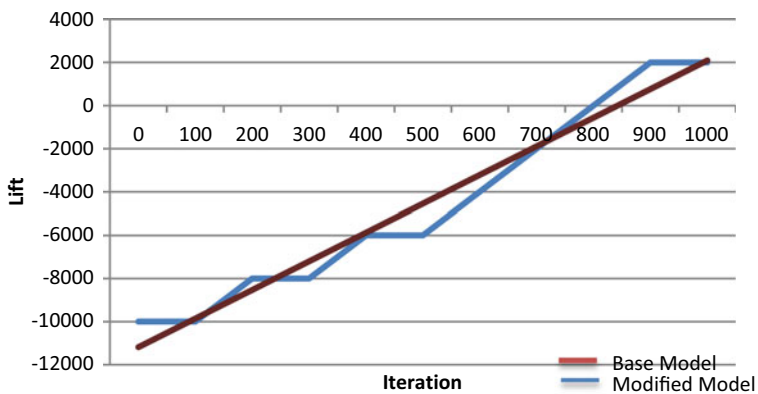
Fig. 13 Lift force verses number of iteration

Base Model   Modified Model
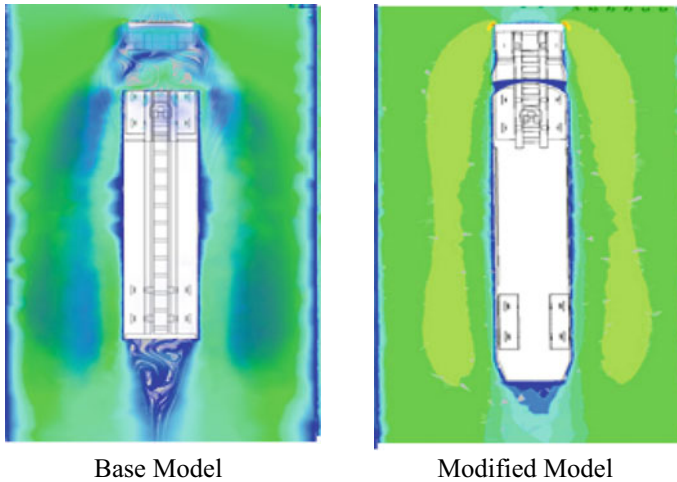
Fig. 14 Air curtain displaced by the containers

- The drag force acting on the front surface of truck was 4494.3867 N which was reduced to 3905.4911 N which can be called as a major milestone, but the difference is hard to find the graphs as they both look kind a same.
- Aerodynamic drag coefficient for our base model was 0.7337 which is a low value indeed but the modified model has drag coefficient as 0.6301. This reduction in drag coefficient can help to decrease the wind/air resistance of a vehicle.
- And, it finally helps to increase the fuel efficiency. Moreover, it also improves other performance characteristics such as handling and acceleration, reduced sensitivity to side winds and increased vehicle stability.

B. **Future Scope of Work**

The key focus of the aerodynamic analysis vehicle is that when we drive the truck on the road, the aerodynamics of the truck are influenced, and if we have done the arrangement on the truck that can have maximum drag reduction and maximize fuel economy. These can be accomplished with cab and trailer mounted equipment such as cab roof and side fairings, tractor and trailer side skirts, trailer-front fairings, vortex generators and base flaps. When we drive a truck or a vehicle, we often feel as if the vehicle is being pushed back, and as a result, it consumes a lot of fuel. Hence by reducing drag force, drag coefficient we can improve the performance of the vehicle. Modern and complex technologies, like active boundary-layer control approaches, have also been investigated for use on large trucks, with the promise of large drag reductions. Despite their availability, not all of these solutions have been widely adopted in the transportation business. Most of the time, practical considerations limit fleet operators' alternatives. Furthermore, there has been a significant increase in the breadth of work in truck aerodynamics study, particularly in India. Because

India is a developing country, there is a lot of research being done on this topic. As a result, there is a wide range of possibilities.

Over several decades, drag-reducing retrofits have matured to the point where considerable aerodynamic improvements can be produced. Heavy vehicle drag is typically decreased by optimizing airflow, reducing wake and flow separation and covering exposed underbody elements. Slight adjustments to tractors and trailers might result in much more drag reduction.

References

1. Khosravi M et al (2016) Investigation of fuel consumption and emissions of trucks by designing optimal body, pp 1789–1796
2. Chowdhury H, Moria H, Ali A, Khan I, Alam F, Watkins S (2013) A study on aerodynamic drag of a semi-trailer truck. Procedia Eng 56:201–205. https://doi.org/10.1016/j.proeng.2013.03.108
3. Hosravi M, Osaddeghi F, Veisi M, Hodayari-b A (2015) Aerodynamic drag reduction of heavy vehicles using append devices by CFD analysis. J Cent South Univ **22**(12), 4645–4652. https://doi.org/10.1007/s11771-015-3015-7
4. Rakibul Hassan SM, Islam T, Ali M, Islam MQ (2014) Numerical study on aerodynamic drag reduction of racing cars. Procedia Eng 90:308–313. https://doi.org/10.1016/j.proeng.2014.11.854.
5. Singh SN, Rai L, Puri P, Bhatnagar A (2005) Effect of moving surface on the aerodynamic drag of road vehicles. Proc Inst Mech Eng Part D J Automob Eng 219(2):127–134. https://doi.org/10.1243/095440705X5886.
6. Mohamed-Kassim Z, Filippone A (2010) Fuel savings on a heavy vehicle via aerodynamic drag reduction. Transp Res Part D Transp Environ 15(5):275–284. https://doi.org/10.1016/j.trd.2010.02.010
7. Ali IS, Mahmood AA (2013) Improvement of aerodynamics characteristic of heavy trucks. In: 3rd international conference on recent trends in engineering and technology, vol 7, no 3, pp 246–255 [Online]. Available at: http://escholarship.org/uc/item/63g6128j%5Cnpapers2://publication/uuid/55EF5EBD-7CB1-4E84-9889-EDAA3B6E65AD%0Ahttps://e-reports-ext.llnl.gov/pdf/741852.pdf
8. Drollinger RA (1987) Heavy duty truck aerodynamics. SAE Tech Pap. https://doi.org/10.4271/870001
9. Kim JJ, Lee S, Kim M, You D, Lee SJ (2017) Salient drag reduction of a heavy vehicle using modified cab-roof fairings. J Wind Eng Ind Aerodyn 164:138–151. https://doi.org/10.1016/j.jweia.2017.02.015
10. Koike M, Nagayoshi T, Hamamoto N (2004) Research on aerodynamic drag reduction. Mitsubishi Mot Tech Rev 16(2):11–16
11. Lee SW (2018) Computational analysis of air jet wheel deflector for aerodynamic drag reduction of road vehicle. Microsyst Technol 24(11):4453–4463. https://doi.org/10.1007/s00542-018-3992-1
12. Tonpe MH, Tadamalle AP, Burande DH (2019) Aerodynamic drag force analysis for light commercial vehicle. Acad Edu 8(07):696–701 [Online]. Available at: http://www.academia.edu/download/60144649/aerodynamic-drag-force-analysis-for-light-commercial-vehicle-IJERTV8IS07030820190728-91046-u8qrur.pdf
13. Hucho WH, Sovran G (1993) Aerodynamics of road vehicles, pp 485–537
14. Sudin MN, Abdullah MA, Shamsuddin SA, Ramli FR, Tahir MM (2014) Review of research on vehicles aerodynamic drag reduction methods. Int J Mech Mechatron Eng 14(2):35–47

15. Castellucci PJ, Salari K (2005) Computational simulation of tractor-trailer gap flow with drag-reducing aerodynamic devices. SAE Tech Pap no. 724. https://doi.org/10.4271/2005-01-3625

Analysis of Bending Abilities of Soft Pneumatic Actuator

Shreyas Chigurupati and Jeevan Balaji

1   Introduction

Soft robotics is expected to achieve USD 4965.06 million in the year 2025 in market value from USD 645.45 million in 2019, at compound annual growth rate (CARG) of 40.5% over the forecast period 2020–2025, and it has immense capabilities to offer in the military and medical field. But conformability of the robots to the object of interest having variation in size, shape, and orientation and new techniques for modeling and simulating soft structures are required as the conventional solutions are inappropriate for behavior of soft robots. In this context, many research works focused to develop the response of SPAs with internal fluidic channels governed by its morphology and the properties of the materials used in fabrication, but the analytical models were created making assumptions which lead to inaccurate results. The objective of the work was to create a model of the SPA with experimental testing of bending behavior based on morphology and examine the results.

TPU due to its hyper elastic nature was selected for the fused deposition modeling (FDM) of the actuator. Two prototypes were procured where the initial prototype mimicked the human finger, and upon experimental testing, the second prototype was procured with improved morphology for better bending. Solidworks and Abaqus software were used, respectively, for modeling and simulation of pneumatic-based soft actuator. The hyper elastic material was used for the analysis as it is best suited for nearly incompressible and nonlinear elastic material such as in our case TPU.

The experimental and simulation models are executed for different range of pressure. The safe loading range for pressure was found to be 0.01–0.05 MPa. The bending angles of the gripper finger for each pressure from the safe loading range were found to be 60°, 72°, 83°, 100°, and 121°, respectively. The bending angle of the actuator with gravity load alone was found to be 43°. With the development of various new manufacturing techniques and simulation software, the growth in field

S. Chigurupati (✉) · J. Balaji
Department of Mechanical Engineering, R V College of Engineering, Bengaluru 560059, India

of soft robots is certainly bound to be exponential. This data can also be used to create other types of end effectors for many other robotic applications. These next generations soft robots are expected to replace and create jobs that traditional robots in fields that they do not prevail in.

2   Review on Soft Pneumatic Actuation

Bio-inspired design of soft structures has capability to match and exceed the extraordinary multi-functioning of animals like starfish and octopus. Normally, conventional robots are made up of material (i.e., metals, plastics) which has an elasticity modulus more than the materials present in natural organisms (i.e., cartilage, muscle tissue). Viscoelastic materials exhibit viscous and elastic property; hence, including of viscoelastic materials will allow soft robotic structures to maintain stable and steady motion during dynamic loading. While selecting materials to fabricate soft actuators, it is crucial to identify fracture toughness, work energy density, and optimal viscoelastic material features [1]. Ecoflex has a high elongation at break and low young's modulus. Hence, it is being used for fabricating soft, elastic, pressure actuators, and medical applications due to its water repellency, low surface energy, thermal stability, and chemical inertness [2].

SPAs are structures composed of a pneumatic chamber, a frame constraint structure, and a body made by compliant materials. The pneumatic chamber is used to actuate the soft pneumatic actuator with deformation. The usage of SPA with its compliance nature allows for less complex analytical modeling and material characterization. Fabrics can be used in soft structures to improve stiffness, strength, and durability [3].

The pneumatic actuator fabricated from elastomer (elastosil M4601) compared to ecoflex 30 required $8\times$ more pressure and $1.5\times$ less change in volume [4]. Fabrics which are strong increase durability and strength of the soft components, which is valuable in soft structures, while fabrics which are elastic maintain elastic property and enhance strength [5]. Bending soft actuators are made up of silicone rubber, and a layer of strong fabric which is coated with silicone is attached to the underside surface. This fabric layer helps actuators to not extend in horizontal direction and to bend uniformly [6].

A wide range of multi-degree-of-freedom motions can be generated by using different fabrics and their layered arrangements when a thin pneumatic actuator is inserted between and inflated with pressurized air [7]. Dilibal et al. [8] compared three different SPAs using additive manufacturing and observed the highest tensile strength. Robinson et al. [9] used direct ink writing to 3D print the SPA model. Aliff et al. [10] developed a flexible robotic arm and observed the square trajectory using a compact control system. Elgeneidy et al. [11] have determined the bending abilities of the SPA using regression and neural network modeling. Wang et al. [12] developed a programmable pneumatic network actuator to perform complex operations. Dilibal et al. [8] compared experimental models of three different pneumatic actuators with

numerical models of the same. The numerical analysis was carried out in Marc Mentat software tool. The analysis of the actuators (which are of TPU material) are done based on three different mathematical models—(1) Neo-Hookean model, (2) Mooney–Rivlin model, and (3) Ogden model (the formulae for the same are shown below). Ogden model provides the best result that is like that of the experimental analysis. Ogden model uses principal stretches to depict large deformations for hyper elastic material models. The responses of both methods were equal when the applied pressure is 0.1–0.5 MPa.

$$W_{\text{neo - Hooken model}} = C_{10}.(I_1 - 3)$$

$$W_{\text{Mooney - Rivlin model}} = C_{10}.(I_1 - 3) + C_{01}.(I_2 - 3)$$

$$W_{\text{Ogden model}} = \sum_{k=1}^{N} \frac{\mu_k}{\alpha_k}.\left(\lambda_1^{\alpha_k} + \lambda_2^{\alpha_k} + \lambda_3^{\alpha_k} - 3\right)$$

where C is the material specific constant,
$\quad \lambda$ is the principal stretch ratio,
$\quad I$ is the strain variant.

Hassanin and Davis [12] developed an actuator which is based on a power augmented rehabilitation exoskeleton. The output of the experimental studies carried out is used for developing a mathematical model. The mathematical model is dependent on the geometrical parameters of the Extensor Bending Pneumatic Artificial Muscles (EBPAM). The output of the math model is force in terms of input pressure. This is done by placing a load cell at the free end of the actuator model. Three actuators of different lengths are considered for experimental studies. The experimental studies on the models depict that the bending angle increases with increase in input pressure. The formula for the force exerted is formulated as:

$$F = \frac{Pb^2}{8\pi n^2}\left(\frac{(\cos\theta + \cos\theta_{\text{max}})(\cos\theta\sin\theta + \sin\theta_{\text{max}}\cos\theta)}{\sin\theta} - \frac{(\sin\theta + \sin\theta_{\text{max}})^2}{2}\right)$$

where

$\quad P$ is the relative differential air pressure,
$\quad \theta$ is the braid angle,
$\quad b$ is the individual braid length,
$\quad n$ is the number of braids.

Polygerinos et al. [13] investigated the bending angle and the response force of the actuators that are used in rehabilitation glove by finite element methods before fabrication. The analytical model is compared to that of experimental model for verifying the results obtained. The FEM analysis is carried out in Abaqus 6.11 Computer

Aided Engineering package. The stress on the actuator is observed as shown in Fig. 1. The maximum bending angle was found to be 320 degrees which verifies the analytical value, and the maximum internal pressure was found to be 50 kPa. Robinson et al. [9] have developed soft integrated sensors which respond to tactile sense. Elastic moduli of silicone fabricated by different methods were analyzed. The value of elastic modulus of casted silicone model at 100% strain is larger (nearly 109 kPa) than that of 3D printed silicone (nearly 73 kPa) using direct ink writing (DIW). Aliff et al. [10] developed a robotic arm having master–slave control and trajectory control. The control system is processed by a PID controller. An analytical model confirms the
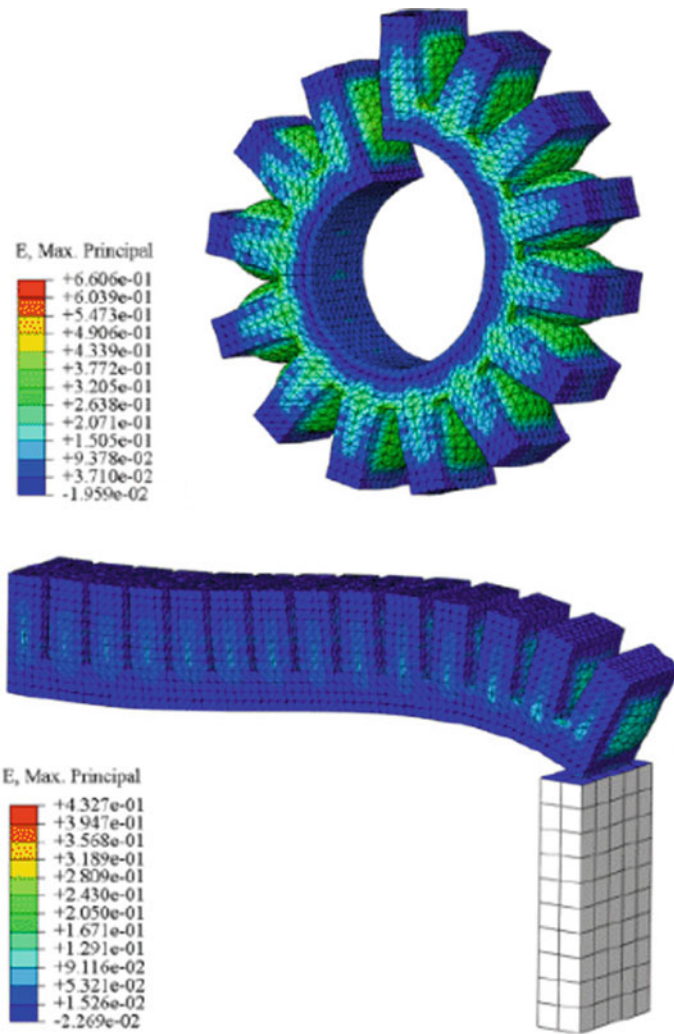
Fig. 1 FEM analysis of soft actuator

effectiveness of the system. Elgeneidy et al. [11] investigated a soft pneumatic actuator at different values of input pressures, and the feedback is collected by the flex sensors and pressure sensor that are inbuilt into the actuator. A high-speed camera is used to capture the image of actuation and use it for video motion analysis in Kinovea software. Later, this model was compared with a data-driven model resulting in same output. Wang et al. [14] demonstrated a programmable pneu-net actuator, which was analyzed for bending and twisting characteristics of the actuators by finite element analysis and later verified experimental model. For geometric models, SolidWorks 2016 (Dassault Systems S.A) was used, and the thermo-models were meshed in HyperMesh 13.0 (Altair) with C3D4H elements. The meshed models were then imported into Abaqus 6.14-4 (Dassault Systems S.A) for FEA simulations. Design of pneu-nets consists of two layers [15], top extensible layer and bottom inextensible layer, and two types are designed, one is "slow pneu-net" (sPN) and another "fast pneu-net" (fPN). The bending ability of soft actuator is undeniable, but the stiffness of the soft actuator cannot be increased much; hence, this leads to limiting the actuator to handle lighter objects [14]. The crawlers design [16] is bio-inspired which has six legs and has symmetrical movement. This soft pneumatic actuator can achieve two types of locomotion, one is locomotion by pushing the walls and another locomotion on flat surface.

3 Fabrication

The SPA's performance is closely linked to the manufacturing techniques used to produce the SPAs with good elastic quality and structure. Due to this reason, we can witness advancement in manufacturing techniques to produce soft structures such as soft lithography, additive manufacturing, shape deposition manufacturing, micro-injection molding and direct ink writing. We decided to fabricate the SPA directly instead of manufacturing mold and then casting. The best suitable manufacturing technique for this was found to be additive manufacturing which was able to produce directly printed actuators. The best suitable manufacturing technique for this was found to be additive manufacturing which was able to produce directly printed actuators. The manufacturing processes mentioned above are basically 2.5D, whereas a 3D inflatable elastic actuator is fabricable from additive manufacturing. Here, the actuators are printed directly rather than molds. Three types of additive manufacturing techniques are able to fabricate flexible structures. Stereo lithography is used to produce mm- to cm-sized bending actuators. For bigger (>10 mm) actuators, poly-jet printing can be used, which has the advantage that multiple materials can be printed. Other additive manufacturing techniques, selective laser sintering and FDM, have also been reported for fabricating bending actuator. We have used FDM in the printing of our components and shown in Fig. 2.

Fig. 2 Images of the gripper after fabrication

4 Design and Analysis of SPA

The ability to design and model soft actuators is particularly crucial because in soft robotics the motion path is typically programmed in the design of the actuator. The size and shape of the gripper for the SPA are decided by imitating the average size of a human finger. In the process of deciding the final dimensions of the gripper, two prototypes were fabricated. The gripper is attached to the robotic arm with the help of the clamp and the base. The gripper is firmly attached to the clamp with the use of adhesive.

Initially, the overall length of the gripper was decided to be 118 mm and the height of the gripper to be 18 mm with width 10 mm. Besides the length and height of the gripper, there are a number of other parameters such as chamber height, chamber wall thickness, number of chambers, sidewalls, and the air hole. The first prototype with the dimensions shown in the sectional view in Fig. 3 certain dimensions of the parameters of the SPA such as chamber height, chamber wall thickness, number of
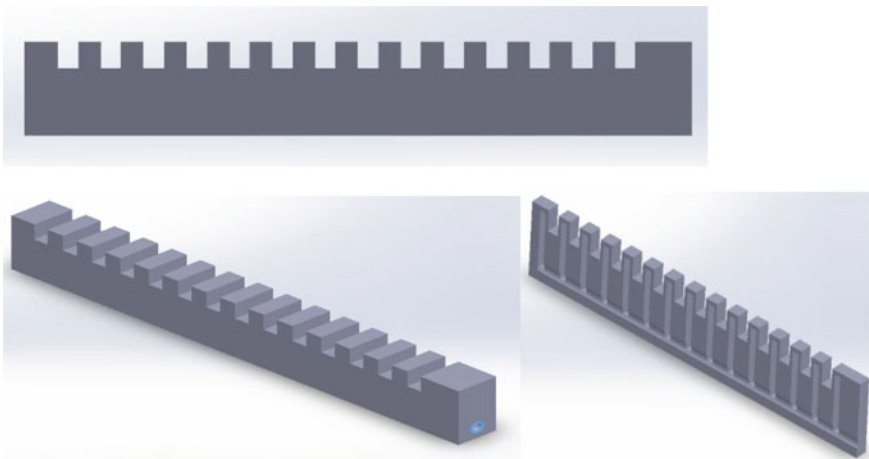
Fig. 3 SolidWorks view of first prototype with three different orientations
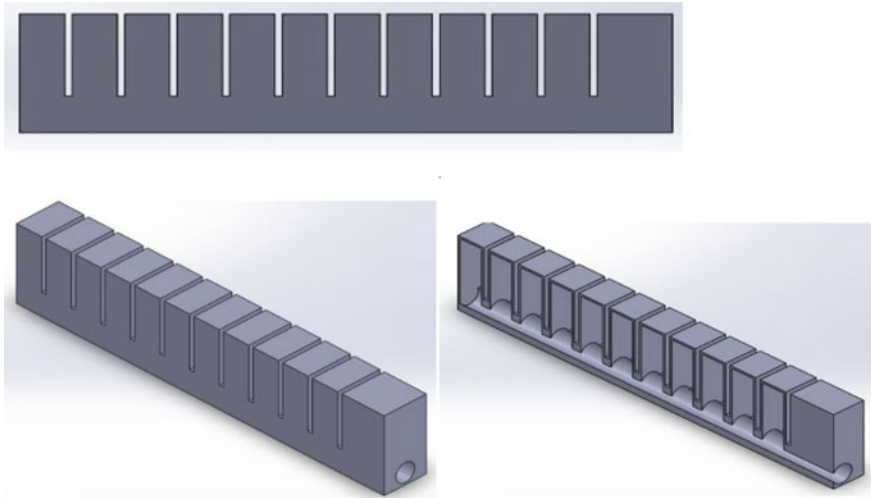
Fig. 4 SolidWorks view of second prototype with three different orientations

chambers, sidewalls, and the air hole after analysis is shown in Fig. 4 for the second prototype.

4.1 Material Selection

As we are using FDM for fabrication of the SPA, research on the materials used in FDM was done [1, 5, 6] and the commercial materials used in the FDM process are poly lactic acid (PLA), acrylonitrile butadiene styrene (ABS), polyethylene terephthalate (PET), thermoplastic polyurethane (NYLON, TPU), and polycarbonate (PC).

By comparing the properties of the materials listed above according to our application, TPU is mostly used for flexible application, PLA is a rigid material as well as ABS which is usually used for preparing mold for the resin, PET is heavier than PLA and ABS, and comparing properties like elongation at break, impact resistance, ease of printing, layer adhesion, and max stress. TPU material is selected based on its higher impact resistance, higher elongation at break, heat resistance up to 80 °C, high durability, decent max stress, and best flexibility compared to the rest.

ABS material is chosen as the material for the clamp and the base, as it is a very rigid material and has a high load bearing capacity. Since the clamp and base undergo less loads, this material was ideal solution. Also, fused deposition of ABS is very common, and the parts manufactured using this are extremely precise.

4.2   Analysis

Analysis consists of steps as follows:

- Importing the designed geometry
- Creating material
- Assigning material to gripper
- Adding loads
- Adding boundary conditions
- Meshing
- Submitting the job and viewing results

Before creating and assigning material, we need to select numerical material model for the hyper elastic material. There are three different hyper elastic numerical material models which are Yeoh, Ogden, Mooney–Rivlin, and Neo-Hookean models used for predicting the stress–strain behavior of hyper elastic material. Yeoh hyper elastic material model converges with the uniaxial tensile test results more than the other three hyper elastic models. Hence, Yeoh material model is used for the FEM analysis of the gripper. Loads acting on the gripper are gravity and pressure. Gravity load is subjected to the whole part of gripper, whereas the pressure load is subjected to the inner cavity surface as the pressure will be acting only on that surface as shown in Fig. 6.

Boundary conditions are the structural supports for specifying values like displacement and rotation variables at faces of the model and appropriate nodes. There is only one boundary condition in this analysis that is one end of the gripper being fixed as shown in Fig. 5 (Fig. 6).
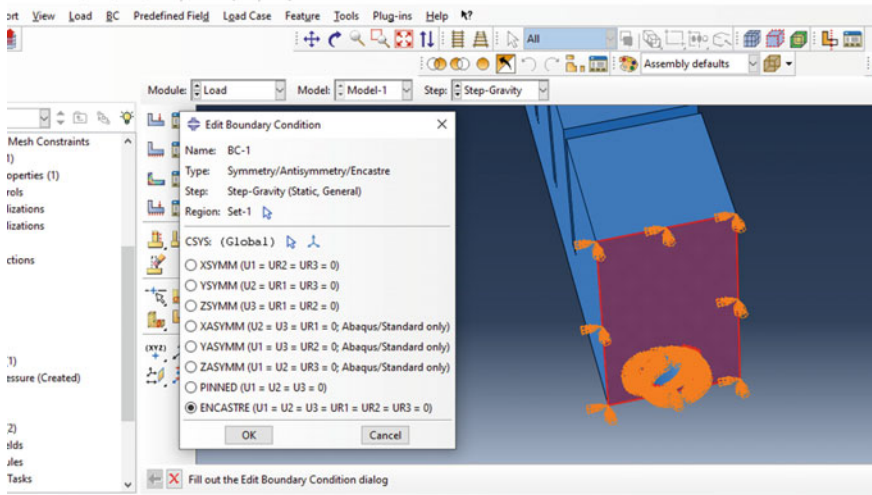
Fig. 5   Boundary condition of one end being fixed
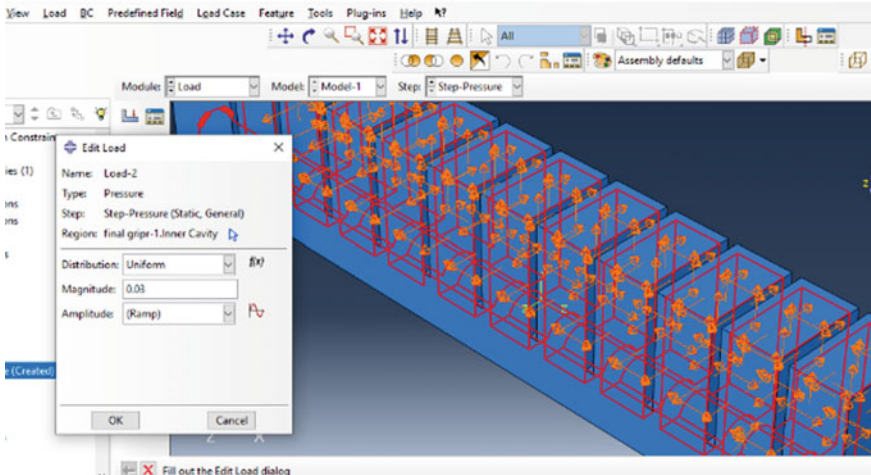
Fig. 6 Applying pressure to inner cavity

Meshing a model is an integral step in performing any simulation. Tetrahedral element type of mesh is used. As linear tetrahedron elements are much too stiff, which would be inappropriate for our case, Quadratic tetrahedral elements are used. The part is seeded with an approximate global size of 2.5. The model might turn out stiff due to high distortions if the size of the mesh is too small. On the other hand, bigger mesh sizes will not suit the model face.

One of the important factors of a good mesh is its aspect ratio, which is the measure of a mesh element's deviation from having all sides of equal length. Trial and error method is carried out to achieve the mesh aspect ratio to nearly "1"; this is obtained by changing the seeding repeatedly over the geometry. The average aspect ratio of a total of 13,072 tetrahedral elements is 1.75. The percentage of tetrahedral elements with aspect ratio greater than 3 is 6.35, where worst aspect ratio being 3.37. The average aspect ratio of a total of 540 triangular elements is 1.42. The percentage of tetrahedral elements with aspect ratio greater than 2 is 0, where worst aspect ratio being 1.42.

After meshing, total number of nodes are 23,407 and total number of elements are 13,612, of which 540 quadratic triangular elements of type STRI65 and 13,072 quadratic tetrahedral elements of type C3D10H. Part after meshing can be observed in an enlarged view in Fig. 7.

5 Results and Discussion

The hyper elastic soft materials such as TPU are sensitive to high loads. There is a high possibility that the material fails in the process due to high loading. Hence, the
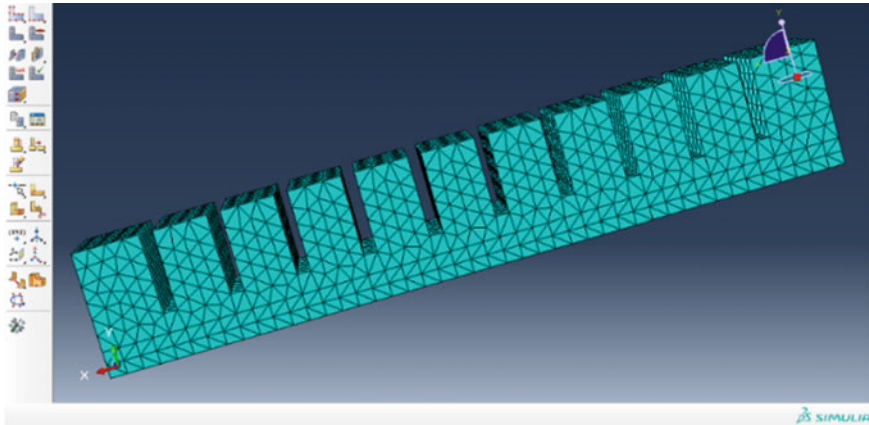
Fig. 7 Abaqus software view of part after meshing

main objective of this present study is to find the safe loading range for the gripper which is important, in our case the range of pressure. And from this range, we can find the wrapping space in turn determines the size of the objects that the gripper can hold from the bending angles of the individual fingers of the gripper. Therefore, with the help of Abaqus CAE software, we ran simulations with different input pressures to find out the safe loading range of pressure, bending angles, stress zones, and other relevant parameters.

The results obtained about the parameters of the SPA which affects the performance of the SPA in the process of selection of the gripper are explained in Table 1.

Due to the insufficient bending shown by the first Prototype, a new second Prototype is designed by altering certain dimensions of the parameters of the SPA such as chamber height, chamber wall thickness, number of chambers, sidewalls, and the air hole. By keeping the width and height of the gripper same, the overall length

Table 1 Gripper parameters and its influence on SPA

Parameter	Influence
Chamber height	Increased chamber height increases force output, but does not seem to affect the trajectory of the tip
Number of chambers	For fixed overall length, increasing the number of chambers decreases the required pressure
Chamber wall thickness	For fixed overall length, increasing the chamber wall thickness increases the required pressure (stiffer)
Side wall thickness	The thickness of the sidewalls must be thicker than the chamber wall thickness, so that they do not expand much in comparison
Overall length	Increasing overall length increases output force and deflection and size of the grasping object can be increased

was decreased to 87 mm to keep the number of chambers a whole number, and also because in the experimental testing of the first prototype, it was observed that the length of the first Prototype was more than required for the gripper holder. Thinner walls lead to an increased force output and requires less pressure for the actuator to reach max bending. The base of the SPA is made thick to facilitate one directional bending.

5.1 Test Case (1): Pressure 0.01 MPa

The actuator fixed on the one end was applied with two loads, gravity load and pressure load, where the gravity remains uniform throughout the testing of 9.81 N. The pressure of 0.01 MPa was applied for case 1. We can observe the results in Fig. 8, where Fig. 8a depicts the initial condition without any loads, Fig. 8b depicts the deformation or bending of the actuator with gravity alone, and Fig. 8c depicts the complete bending of the actuator for 0.01 MPa. The bending angle of an actuator is defined as the angle between when the actuator is in initial position and the line joining the ends of the actuator at complete bending. The bending angle for the Test Case 1 with 0.01 MPa is 60 degrees.

The color-coding of the stress in the actuator is shown in Fig. 9, where Fig. 9a depicts the color-coding of stress in the actuator for gravity alone and Fig. 9b depicts
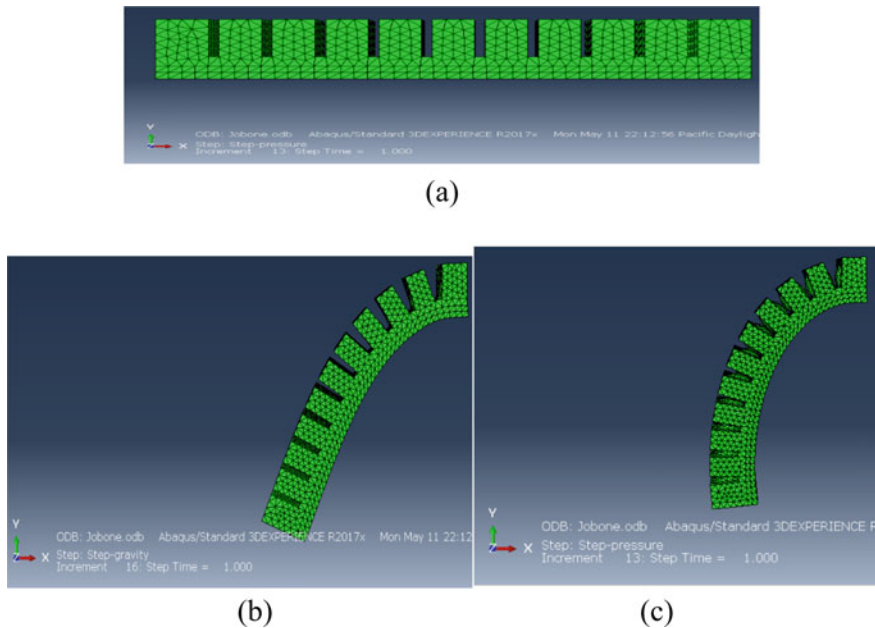
Fig. 8 Abaqus view of SPA **a** at initial condition; **b** at only gravity loading; **c** at 0.01 MPa
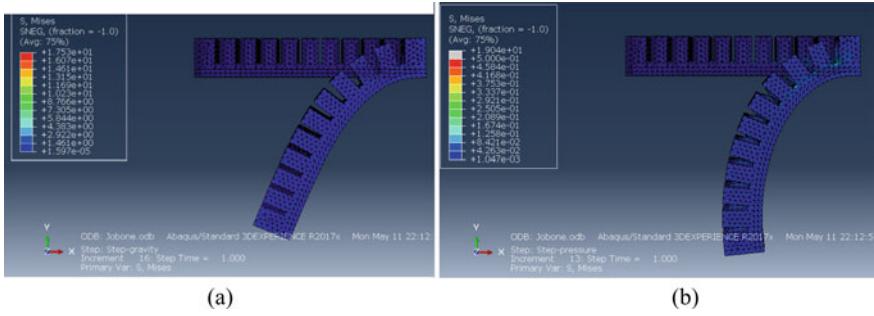
Fig. 9 Color-coding of stress in the actuator **a** only gravity load **b** at 0.01 MPa

the color-coding of the stress for 0.01 MPa pressure. Observing Fig. 9b, we can conclude that the load of 0.01 MPa pressure is under safe condition for working of the actuator. Hence, we conclude the Test Case 1 with positive results.

5.2 Test Case (2): Pressure 0.02 MPa

The pressure of 0.02 MPa was applied for Test Case 2. We can observe the results in Fig. 10, which depicts the complete bending of the actuator for 0.02 MPa. The
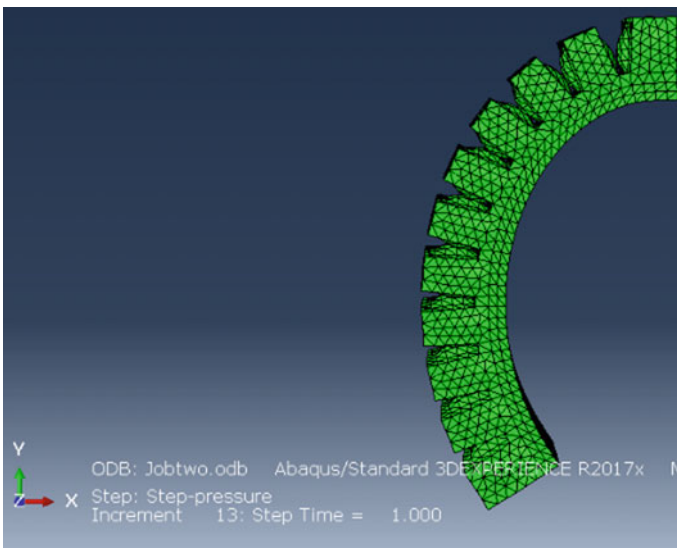
Fig. 10 Abaqus view of SPA at 0.02 MPa
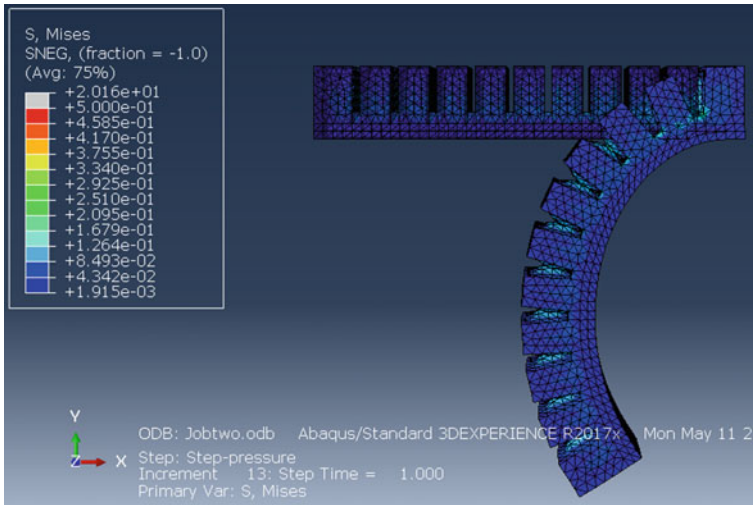
Fig. 11 Color-coding of stress in actuator at 0.02 MPa

bending angle for the Test Case 2 with 0.02 MPa was found to be 72°, where a little increase in the angle can be seen compared to the first case.

The color-coding of the stress in the actuator for 0.02 MPa pressure is shown in Fig. 11. Observing Fig. 11, we can conclude that the load of 0.02 MPa pressure is also under safe condition for working of the actuator and also the sides of the air chambers are seen to turn into light blue indicating the increase in stress which is very little; that is, the material of the actuator (TPU) can withstand the load of 0.02 MPa pressure as well. Hence, we conclude the Test Case 2 with positive results and increase the pressure to 0.03 MPa pressure in the next Test Case.

5.3 Test Case (3): Pressure 0.03 MPa

The pressure of 0.03 MPa was applied for Test Case 3. We can observe the results in Fig. 12, which depicts the complete bending of the actuator for 0.03 MPa. The bending angle for the Test Case 3 with 0.03 MPa was found to be 83°, where a curve shape can easily be visible.

The color-coding of the stress in the actuator is shown in Fig. 13, which depicts the color-coding of the stress for 0.03 MPa pressure. Observing Fig. 13, we can conclude that the load of 0.03 MPa pressure is also under safe condition for working of the actuator and also the sides of the air chambers are seen to turn into light green indicating the increase in stress which is little; that is, the material of the actuator (TPU) can withstand the load of 0.03 MPa pressure as well. Hence, we conclude the
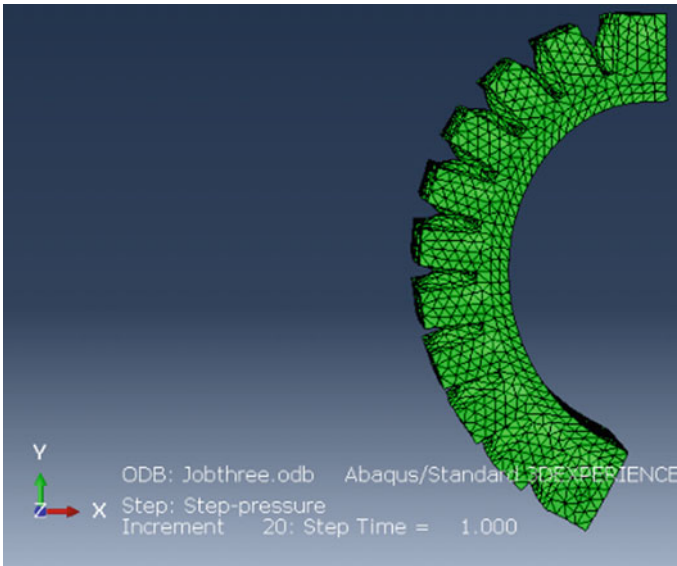
Fig. 12 Abaqus view of SPA at 0.03 MPa
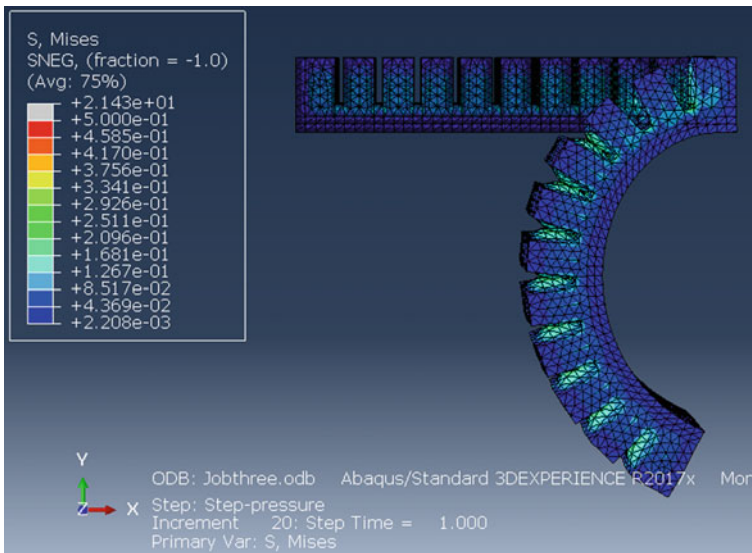
Fig. 13 Color-coding of stress at 0.03 MPa

Test Case 3 with positive results and increase the pressure to 0.04 MPa pressure in the next Test Case.

5.4 Test Case (4): Pressure 0.04 MPa

The pressure of 0.04 MPa was applied for Test Case 4. We can observe the results in Fig. 14 which depicts the complete bending of the actuator for 0.04 MPa. The bending angle for the Test Case 4 with 0.04 MPa was found to be 100°, where a curve shape can easily be visible. We can observe that the air chambers touch each other in turn pushing to create a force which makes the bending possible. The color-coding of the stress in the actuator for 0.04 MPa pressure is shown in Fig. 15. Observing Fig. 15, we can conclude that the load of 0.04 MPa pressure is also under safe condition for working of the actuator and also the sides of the air chambers are seen to turn into green evidently indicating the increase in stress; that is, the material of the actuator (TPU) can withstand the load of 0.04 MPa pressure as well. Hence, we conclude the Test Case 4 with positive results and increase the pressure to 0.05 MPa pressure in the next Test Case.
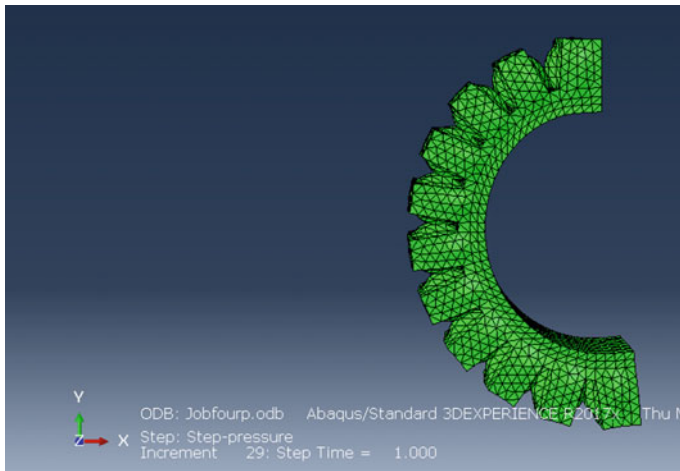
Fig. 14 Abaqus view of SPA at 0.04 MPa
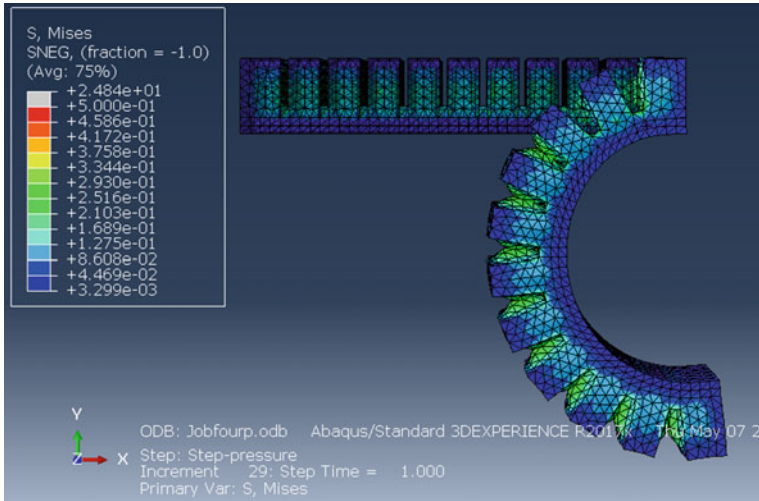
Fig. 15 Color-coding of stress at 0.04 MPa

5.5 Test Case (5): Pressure 0.05 MPa

The pressure of 0.05 MPa was applied for Test Case 5. We can observe the results in Fig. 16, which depicts the complete bending of the actuator for 0.05 MPa. The bending angle for the Test Case 5 with 0.05 MPa was found to be 121°.

The color-coding of the stress in the actuator for 0.05 MPa pressure is shown in Fig. 17. Observing Fig. 17c which is cross-sectional view, we can conclude that the load of 0.05 MPa pressure is under safe condition for working of the actuator
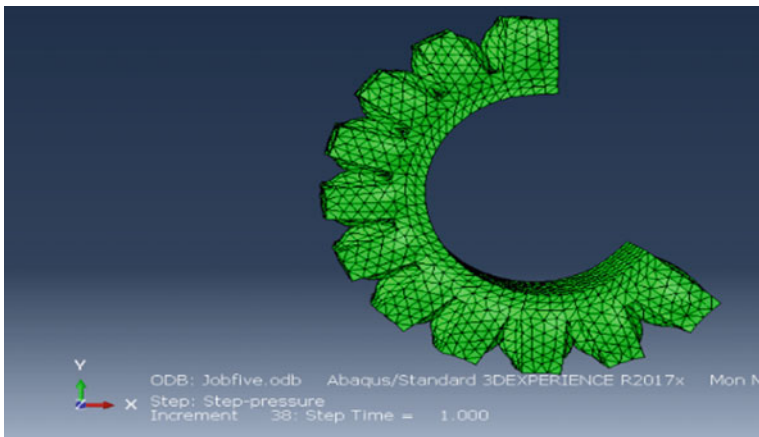
Fig. 16 Abaqus view of SPA at 0.05 MPa
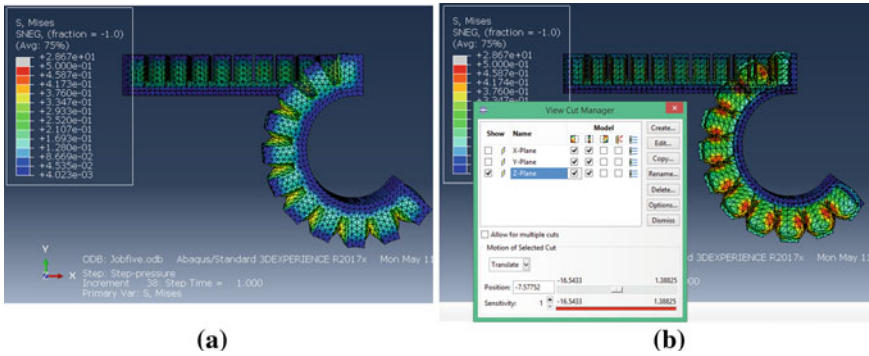
Fig. 17 Color-coding of stress in the actuator **a** at 0.05 MPa; **b** at 0.05 MPa with cross-sectional view perpendicular to Z axis

considering the factor of safety and also the air chambers are seen to turn into green at the middle and turn yellow and then orange toward the end evidently indicating the increase in stress. Hence, we conclude the Test Case 5 with positive results.

As mentioned earlier, the pressure exerted by the air on to the inner cavity of the SPA makes the hollow chambers to bulge, and in turn, the adjacent walls pushing each other cause the actuator actuate in the uni-direction when one end of the SPA is fixed. This phenomenon can be observed in Fig. 18, where with the help of view cut manager, the cavity of the SPA is cut in Z-plane for better visualization. The applied pressure, that is, 0.05 MPa for the soft pneumatic actuator, was observed to be under the material's limit.
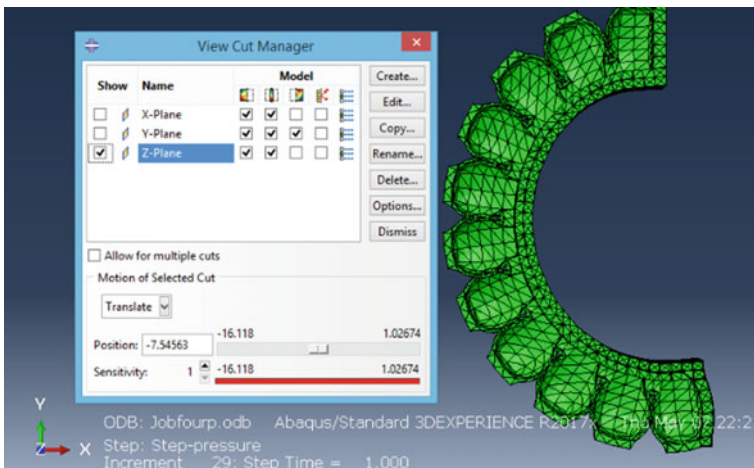
Fig. 18 Cross-sectional view from maximum bending position

The stress concentration is more at the center along the axis than at the ends. The stress concentration is highest between the walls of the air chambers due to the contact; hence, design of these chambers should be important. In Fig. 19, the color-coding of the spatial displacements at nodes is shown. The displacements according to Fig. 19 are less at the fixed end of the actuator and observed to increase along the actuator length uniformly to reach the peak at the other end.

Hence, we conclude the results with range of safe pressure, bending angles of the gripper finger for each pressure values applied from Test Case 1 to Test Case 5, which in turn provides the wrap space of the gripper for working. The loading range was found to be 0.01–0.05 MPa pressure as when we tried with 0.06 MPa pressure, the material failed, hence 0.01–0.05 MPa being the safe loading range. The bending angles of the gripper finger for each pressure loading are tabulated in Table 2. The bending angle of the actuator with gravity load alone was found to be 43°.
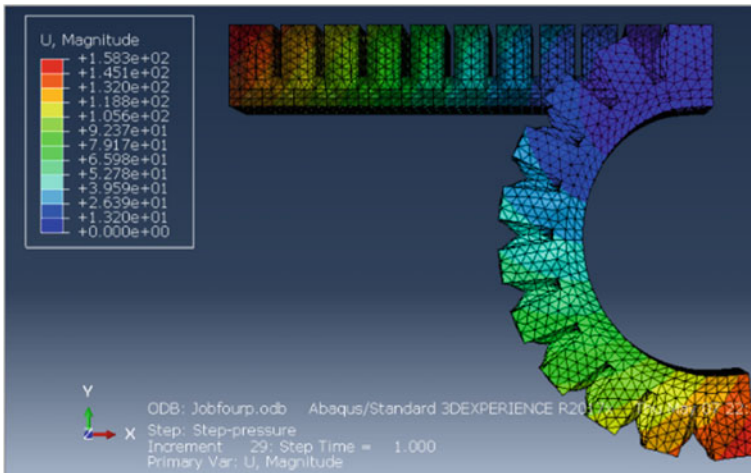
Fig. 19 Color-coding of spatial displacement at nodes

Table 2 Bending angles for different loads

Test case	Load	Bending angle (°)
	9.81 N	43
1	0.01 MPa	60
2	0.02 MPa	72
3	0.03 MPa	83
4	0.04 MPa	100
5	0.05 MPa	121

6 Conclusion and Future Scope

In view of the required applications and suitable experimental analysis conducted, TPU elastomer was chosen over PDMS elastomer. TPU having better physical properties and elastic properties. The design is based on average size of a finger. The chamber dimensions are optimized to an extent to get a best bending abilities and stiffness variations. This optimization was aided by some of the research works conducted by researchers working on pneumatic actuators. The design is conducted in SolidWorks 2018 version. The optimized design undergoes FEM analysis. This analysis is done in Abaqus CAE software. After obtaining the FEM bending analysis, the results are compared, and the design is then optimized until we obtain maximum bending abilities. The final design is then used for 3D printing. Out of various 3D printing process, FDM process is chosen for fabrication of the actuator. The actuators along with the clamps are made of TPU material and the base holder of the actuators is made up of ABS material. The ABS material is chosen as it is an efficient polymer. It also has a high resistance to facture. The FEM analysis is conducted for a single actuator. Four more actuators resembling this actuator are fabricated. After the fabrication is completed, assembly is done, and the actuators are connected to pressure regulator and to a 10-bar compressor through plastic hoses of diameter 4 mm. After the assembly is completed, experiments are conducted varying the pressure in the compressor through the pressure regulator. The gripper is then observed of gripping various objects of various stiffness. The data of various objects with various stiffness are recorded. The recorded stiffness of various objects is used to grip the object, irrespective of its morphology. These data can also be used to create other types of end effectors for many other robotic applications. Growth of a new generations of soft robots with increase in the complexity of the structures will be made possible by using the latest nonlinear simulation tools. Development of new and easy manufacturing techniques using highly elastic materials is a must to implement these complex and intricate designs. Soft robotic apparatus would be capable of functioning advanced applications in the absence of complex control systems. These will be characterized by soft compliance structures which would replace the application of robotic link and actuators. Soft robotics is proposed to employ important tasks in applications where conventional robots cannot prevail such as prosthetics, invasive surgery, and automation applications compiling delicate irregular objects. Due to the difference in nature of soft materials and hard materials, they might enable new application scope.

References

1. Coyle S, Majidi C, LeDuc P, Hsia KJ (2018) Bio-inspired soft robotics: material selection, actuation, and design. Extreme Mech Lett 22:51–59
2. Mosadegh B, Polygerinos P, Keplinger C, Wennstedt S, Shepherd RF, Gupta U, Shim J, Bertoldi K, Walsh CJ, Whitesides GM (2014) Pneumatic networks for soft robotics that actuate rapidly. Adv Funct Mater 2163–2170
3. Li Y, Chen Y, Yang Y, Wei Y (2016) Passive particle jamming and its stiffening of soft robotic grippers. University of Hong Kong and the Innovation and Technology Fund project. IEEE Trans Robot 1552–3098
4. Cho KJ, Koh JS, Kim S, Chu WS, Hong Y, Ahn SH (2018) Review of manufacturing processes for soft biomimetic robots. Int J Precis Eng Manuf 10(3):171–181
5. Gul JZ, Sajid M, Rehman MM, Siddiqui GU, Shah I, Kim KH, Lee JW, Choi KH (2018) 3D printing for soft robotics—a review. Sci Technol Adv Mater 19:243–262
6. FarzadLiravi ET (2018) A hybrid additive manufacturing method for the fabrication of silicone bio-structures: 3D printing optimization and surface characterization. Mater Des 138:46–61
7. Al-Fahaam H, Davis S, Nefti-Meziani S (2018) The design and mathematical modelling of novel extensor bending pneumatic artificial muscles (EBPAMs) for soft exoskeletons. Robot Auton Syst 99:63–74
8. Dilibal S, Sahin H, Celik Y (2018) Experimental and numerical analysis on the bending response of the geometrically gradient soft robotics actuator. Arch Mech 391–404
9. Robinson SS, O'Brien KW, Zhao H, Peele BN, Larson CM, Mac Murray BC, Van Meerbeek IM, Dunham SN, Shepherd RF (2015) Integrated soft sensors and elastomeric actuators for tactile machines with kinesthetic sense. Extreme Mech Lett 5:47–53
10. Aliff M, Dohta S, Akagi T, Li H (2012) Development of a simple-structured pneumatic robot arm and its control using low-cost embedded controller. In: International symposium on robotics and intelligent sensors 2012 (IRIS 2012). Procedia Eng 41:134–142
11. Elgeneidy K, Lohse N, Jackson M (2016) Data-driven bending angle prediction of soft pneumatic actuators with embedded flex sensors. IFAC-Papers Online 49–21:513–520
12. Wang T, Ge L, Gu G (2018) Programmable design of soft pneu-net actuators with oblique chambers can generate coupled bending and twisting motions. Sens Actuators A 271:131–138
13. Florez JM, Shih B, Bai Y, Paik JK (2014) Soft pneumatic actuators for legged locomotion. In: Proceedings of the 2014 IEEE international conference on robotics and biomimetics, 5–10 Dec 2014, Bali, Indonesia
14. Wang Y, Gregory C, Minor MA (2018) Improving mechanical properties of molded silicone rubber for soft robotics through fabric compositing. Soft Robot 5(3)
15. Cappello L, Galloway KC, Sanan S, Wagner DA, Granberry R, Engelhardt S, Haufe FL, Peisner JD, Walsh CJ (2018) Exploiting textile mechanical anisotropy for fabric-based pneumatic actuators. Soft Robot 5(7)
16. Sun Y, Song YS, Paik J (2013) Characterization of silicone rubber based soft pneumatic actuators. In: IEEE/RSJ international conference on intelligent robots and systems, 3–7 Nov
17. Vaicekauskaite J, Mazurek P, Vudayagiri S, Skov AL (2019) Mapping the mechanical and electrical properties of commercial silicone elastomer formulations for stretchable transducers. J Mater Chem C
18. Polygerinos P, Lyne S, Wang Z, Nicolini LF, Mosadegh B, Whitesides GM, Walsh CJ (2013) Towards a soft pneumatic glove for hand rehabilitation. In: 2013 IEEE/RSJ international conference on intelligent robots and systems (IROS), Tokyo, Japan, 3–7 Nov 2013
19. Alici G, Canty T, Mutlu R, Hu W, Sencadas V (2017) Modeling and experimental evaluation of bending behavior of soft pneumatic actuators made of discrete actuation chambers. Soft Robot
20. Schmitt F, Piccin O, Barbé L, Bayle B (2018) Soft robots manufacturing: a review. Front Robot AI 5

A Design for Assembly Framework Based on Subassembly Detection Method

V. S. S. Prasad, Anil Kumar Gulivindala, Sudhakar Uppada, Vykunta Rao Matta, M. V. A. Raju Bahubalendruni, and B. B. Biswal

1 Introduction

Design for assembly (DFA) promises reduced assembly efforts and simplifies product design and fabrication [1–3]. Since last few decades, DFA methodologies are drawn the attention of a multidisciplinary team of product designers, manufacturing, and assembly analysts. There exist several guidelines proposed by researchers to identify an appropriate combination of part-pairs with material and functional requirements [4]. However, the geometric feasibility of modified parts during the assembly is uncertain at the final stage [5–7].

The geometric feasibility concept is widely used in various engineering problems such as exploded view generation, assembly sequence planning, disassembly sequence planning, robot path planning, and computer animations [3, 8]. Assembly sequence planning is the process of obtaining a feasible assembly sequence of constituent parts through collision-free directions using necessary assembly attributes, namely liaison, geometric feasibility, stability, and mechanical feasibility [9]. In the early 70s, researchers followed graph-based methods to represent assembly contacts and precedence relations between the parts. Later, researchers have come

V. S. S. Prasad
Department of Mechanical Engineering, National Institute of Technology Tadepalligudem, Tadepalligudem 534101, Andhra Pradesh, India

A. K. Gulivindala (✉) · M. V. A. Raju Bahubalendruni
Department of Mechanical Engineering, National Institute of Technology Puducherry, Karaikal, U.T. of Puducherry, Puducherry 609609, India

S. Uppada · V. R. Matta
Department of Mechanical Engineering, GMRIT Rajam, Rajam 532127, Andhra Pradesh, India

B. B. Biswal
Department of Mechanical Engineering, National Institute of Technology Meghalaya, Shillong 793003, Meghalaya, India
e-mail: director@nitm.ac.in

up with matrix mode of data storage and representation, which drastically minimized the computational time [10–12]. The computer-aided assembly attributes were given priority due to its complex nature of interfacing with 3D-solid models [13–15]. Researchers have tried implementing searching techniques to identify an optimal feasible assembly sequence from a huge search space due to complex nature of multi-constraint NP-hard problem [16–21]. ASP was given more priority to solve direct assembly systems wherein finding stable subassemblies are difficult as the resulted outcome is a linear assembly sequence [22].

On the other hand, few researchers have come up with stable subassembly identification as part of assembly sequence planning [23]. The proposed research considers the subassembly-based assembly sequence generation and further implements material compatibility tests and functional requirements compatibility.

2 Design for Assembly Predicates

In order to perform design for assembly on a product, part contacts relations in the assembled state, mating part stability relations with reference to existent parts, function requirements of the product, material compatibility information, and assembly interference data are required. Representation and extraction of such data from the computer-aided design (CAD) models are discussed below.

2.1 Part Contact Relations

Part contact relations can be represented as non-directional graphs, wherein each part is represented in a node, and the contact between parts is signified by a connecting edge. The entire data can also be stored in a square matrix of size "$n \times n$," where the element values are represented by binary codes "0-for no contact" and "1-for surface contact" between pair of parts represented in the row and column.

2.2 Part Stability Relations

Part stability relations can be represented by directional graphs, where each part is represented in a node, and a directed edge is represented for the stability [1]. A single-sided directed edge indicates partial stability, and double-sided directed edge represents dynamic stability between the parts. The stability information between pair of parts can be stored in an "$n \times n$" square matrix in which an element can be given by three values 0, 1, and 2, respectively, indicate no-stable, partially stable, and permanent stable.

2.3   Material Compatibility Based on Functional Requirement

A functional requirement is the actual intention of the product to use in real-time. Material compatibility testing does verify a pair of parts made up of similar/dissimilar material/can be replaced by a single material. The material compatibility matrix is an "$n \times n$" square matrix consists 0, 1, 2 where 0—represents non-compatible due to functional requirement/nonexistence of replacing material; 1 represents partial compatibility where an industrial engineer takes the decision based on cost parameters and 2—represents high compatibility.

2.4   Assembly Interference Data

Assembly interference data are the most critical predicate, which gives the information about the possibility of assembling a component in the existence of other components in a specified direction. This data can be stored in a "$k \times n \times n$" three-dimension matrix where k—represents the number of possible directions and n—represents the total number of individual parts in a given assembly. The element values are typically binary codes "0—geometrically infeasibility" and "1—geometrically feasibility" of assembling a constituent part in the column in the presence of part specified in the row.

3   Design for Assembly Framework

The main objective of the proposed framework is to reduce the number of parts with the maximum possible part count reduction. A schematic representation of the design for assembly framework is shown in Fig. 1, which initially generates two-part assembly subsets using part-concatenation and tested for assembly stability. If there exists a dynamically stable relation with highest material compatibility, then the assembly subset (subassembly) will be treated as a single part and the redundant assembly subsets with altered patterns will be deleted. A non-existent part/subassembly is added at the further levels to create higher-order assembly subsets (subassemblies) and tested for assembly sequence predicates. The qualified subassemblies are further verified for formability. When a subassembly qualifies the formability test, the number of assembly levels is reduced by one and thus minimize the number of assembly levels.
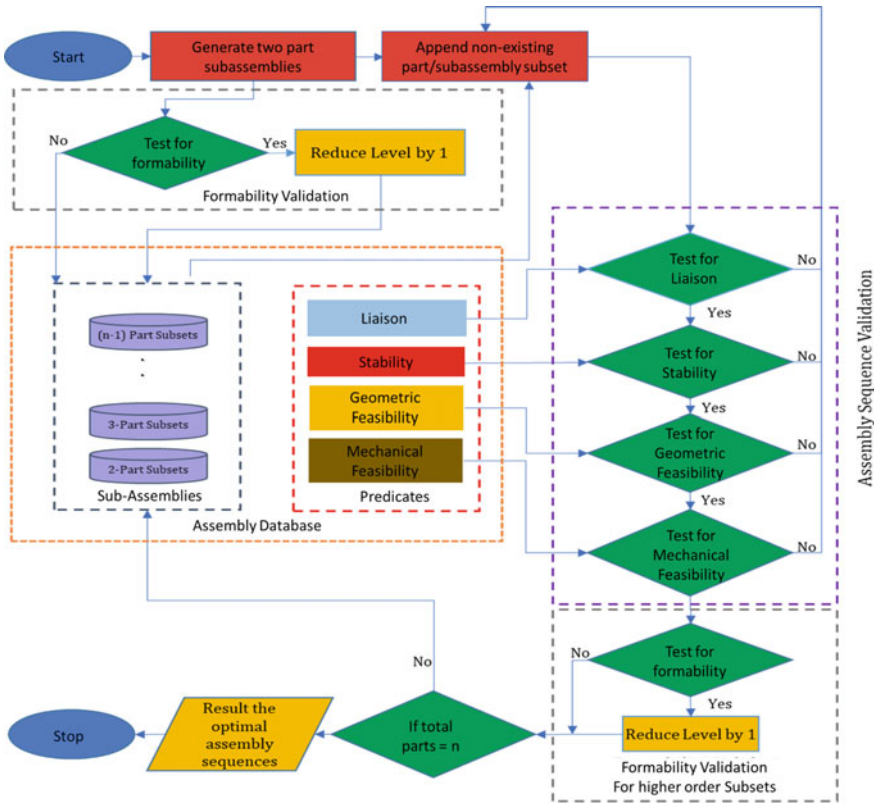
Fig. 1 Design for assembly framework

4 Implementation

A product made up 8 parts exploded view shown in Fig. 2a and assembled view in Fig. 2b is considered for implementation. The computer-aided programs have been written to extract the assembly predicate data through API. The resulted part contact relations, part stability relations, and assembly interference data are given below. The formability matrix is generated based on material compatibility and functional requirements of each individual part of the assembly.

The DFA framework resulted in 8—number of two-part assembly subsets with the possible state of subassemblies (static stable or dynamic stable), further formability query is applied on dynamically stable subsets to identify the possibility of merging the parts. For the 8-part pen product, three instances are identified as shown in Table 1. Table 1 also lists the number of assembly levels after querying for formability verification.

It can be observed from Table 1, based on formability criteria, the subassemblies (2-4), (6-7), (7-8) can be merged into a single parts with zero number of assembly

a. Exploded view   b. Assembled view
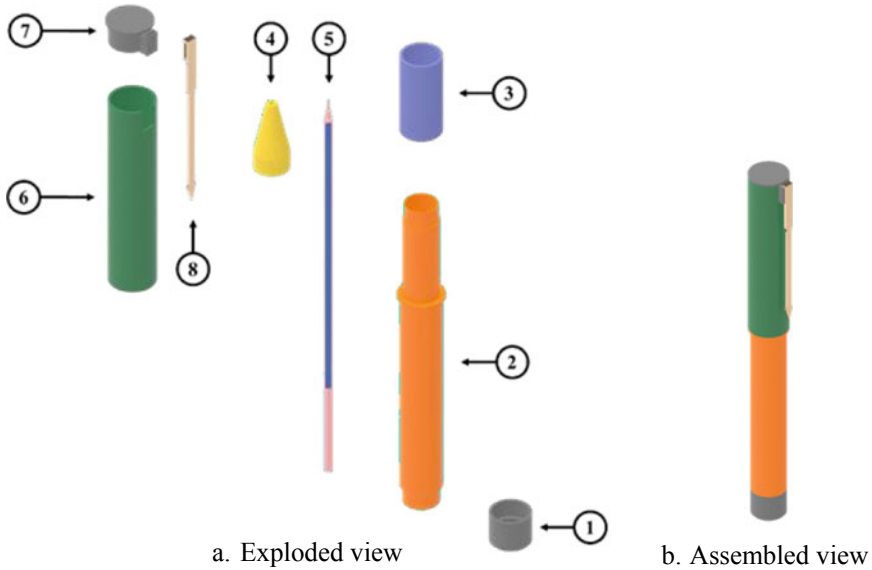
Fig. 2 Schematic representation of the 8-part pen

Table 1 List of two-part assembly subsets with number of assembly levels

S. No.	Assembly subset	State of sub-assembly	Formability	Number of assembly levels
1	(1-2)	Dynamically stable	No	1
2	[1-5]	Statically stable	-	1
3	(2-3)	Dynamically stable	No	1
4	(2-4)	Dynamically stable	Yes	0
5	(2-6)	Dynamically stable	No	1
6	[5-4]	Statically stable	-	1
7	(6-7)	Dynamically stable	Yes	0
8	(7-8)	Dynamically stable	Yes	0

levels. Appending a non-existent part to the two-part subassembly results three-part assembly subsets. If there is a subassembly to which a non-existent part cannot be assembled at higher levels are omitted as unfeasible assembly subsets by querying for "unfeasibility at a higher level." State of subassembly, formability, and number of assembly levels for 3-part subsets are listed in Table 2.

It can be observed from Table 2 that based on formability criteria, the subassembly ((6-7)-8) can be merged into a single part with zero number of assembly levels. At

Table2 List of three-part assembly subsets with number of assembly levels

S. No.	Assembly subset	An unfeasible assembly subset at higher levels	State of sub-assembly	Formability	Number of assembly levels
1	((1-2)-3)	No	Dynamically stable	No	2
2	((1-2)-4)	Yes	-	-	-
3	[(1-2)-5]	No	Statically stable	-	2
4	((1-2)-6)	No	Dynamically stable	No	2
5	[[1-5]-4]	Yes	-	-	-
6	((2-4)-3)	No	Dynamically stable	No	1
7	((2-3)-6)	No	Dynamically stable	No	2
8	((2-4)-6)	No	Dynamically stable	No	1
9	((2-6)-7)	Yes	-	-	-
10	[[5-4]-2]	No	Statically stable	-	2
11	((6-7)-8)	No	Dynamically stable	Yes	0

next higher-level assemblies, there is no further possibility of merging based on formability criteria and thus the resulted assembly sequences with the reduced part count are shown in Fig. 3.

From Table 1, it can be observed that the subsets (2-4), (6-7), (7-8) can be combined to form a single part. At higher levels, the only subset that can be combined to form a single part without violating the formability is ((6-7)-8), observed from Table 2. If the subset (2-4) is taken into consideration, at the higher level, it forms a subset ((2-4)-3) where it violates the functional requirement of the product if they combined into a single part. So, the framework not considered the subset ((2-4)-3) as a single part. The proposed framework resulted in the subsets which can be combined to form a single part without violating the functional requirement of the product are represented in Table 3.
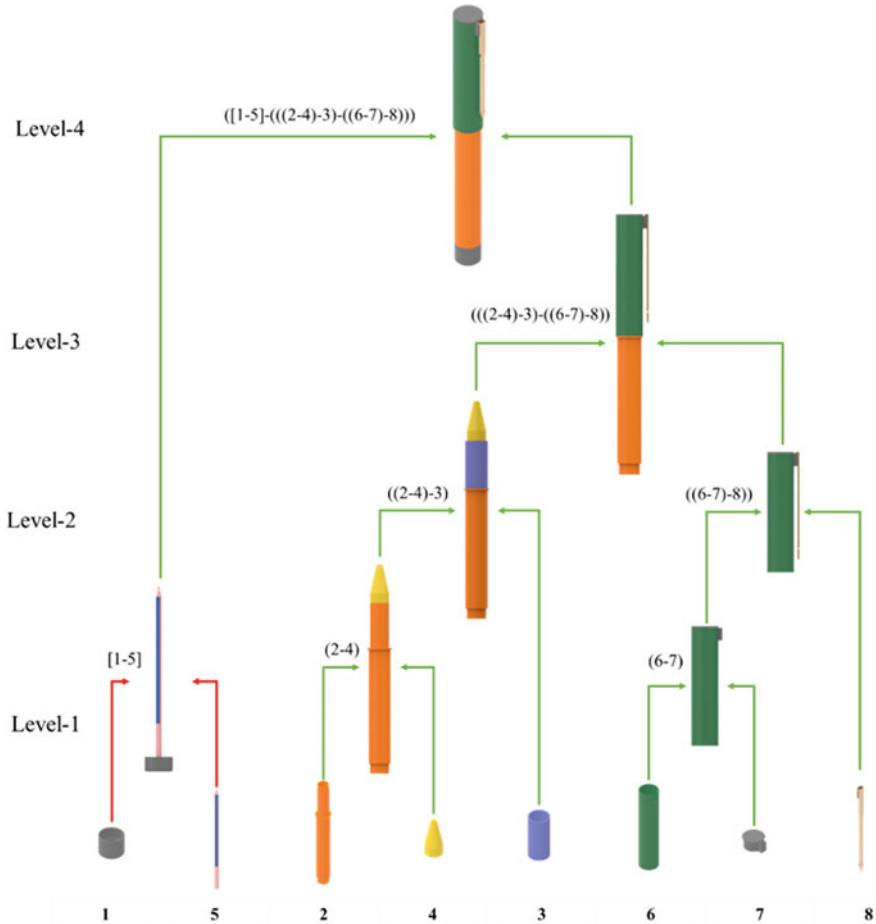
Fig. 3 Assembly sequences with the reduced part count

Table 3 Qualified assembly sets for merging

S. No.	Assembly subset	State of subassembly	Formability	Number of assembly levels
1	(2-4)	Dynamically stable	Yes	0
2	((6-7)-8)	Dynamically stable	Yes	0

5 Conclusion

A generalized framework of design for assembly (DFA) is proposed to merge the parts based on several criteria. The ASP-based integrated framework is proven in identifying the stable subassemblies for a given product based on the assembly attributes. Material compatibility and functional requirements queries have been developed to

validate the possibility of the assembly process in the physical environment. The method is proven in reducing the part count in large assemblies with multiple parts and reduces assembly/disassembly effort and time.

References

1. Kolur DK, Yadav S, Gulvindala AK, Bahubalendruni MVA (2020) A framework to facilitate automated assembly sequence planning in design strategies. Int J Perform Eng 16(10):1517–1524
2. Boothroyd G (1994) Product design for manufacture and assembly. Comput Aided Des 26(7):505–520
3. Bahubalendruni MR, Biswal BB, Kumar M, Nayak R (2015) Influence of assembly predicate consideration on optimal assembly sequence generation. Assem Autom 35(4):309–316
4. Fattahi P, Hosseini S, Jolai F (2013) Some heuristics for the hybrid flow shop scheduling problem with setup and assembly operations. Int J Ind Eng Comput 4(3):393–416
5. Bahubalendruni MR, Biswal BB (2017) A novel concatenation method for generating optimal robotic assembly sequences. Proc Inst Mech Eng C J Mech Eng Sci 231(10):1966–1977
6. Linn RJ, Liu H (1999) An automatic assembly liaison extraction method and assembly liaison model. IIE Trans 31(4):353–363
7. Shan H, Zhou S, Sun Z (2009) Research on assembly sequence planning based on genetic simulated annealing algorithm and ant colony optimization algorithm. Assem Autom 29(3):249–256
8. Bahubalendruni MR, Biswal BB (2016) A review on assembly sequence generation and its automation. Proc Inst Mech Eng C J Mech Eng Sci 230(5):824–838
9. Tseng HE, Li JD, Chang YH (2004) Connector-based approach to assembly planning using a genetic algorithm. Int J Prod Res 42(11):2243–2261
10. Bahubalendruni MR, Biswal BB (2018) An efficient stable subassembly identification method towards assembly sequence generation. Natl Acad Sci Lett 41(6):375–378
11. Wang JF, Liu JH, Li SQ, Zhong YF (2003) Intelligent selective disassembly using the ant colony algorithm. Ai Edam 17(4):325–333
12. Bahubalendruni MR, Biswal BB (2018) An intelligent approach towards optimal assembly sequence generation. Proc Inst Mech Eng C J Mech Eng Sci 232(4):531–541
13. Deepak BBVL, Bala Murali G, Bahubalendruni MR, Biswal BB (2019) Assembly sequence planning using soft computing methods: a review. Proc Inst Mech Eng Part E: J Process Mech Eng 233(3):653–683
14. Bahubalendruni MR, Varupala VP (2020) Disassembly sequence planning for safe disposal of end-of-life waste electric and electronic equipment. Natl Acad Sci Lett 1–5
15. Murali GB, Deepak BBVL, Bahubalendruni MR, Biswal BB (2019) Optimal robotic assembly sequence planning using stability graph through stable assembly subset identification. Proc Inst Mech Eng Part C: J Mech Eng Sci. 0954406219842908
16. Pan C, Smith SSF, Smith GC (2005) Determining interference between parts in CAD STEP files for automatic assembly planning. J Comput Inf Sci Eng 5(1):56–62
17. Shpitalni M, Elber G, Lenz E (1989) Automatic assembly of three-dimensional structures via connectivity graphs. CIRP Ann 38(1):25–28
18. Sinanoğlu C, Börklü HR (2005) An assembly sequence-planning system for mechanical parts using neural network. Assem Autom 25(1):38–52
19. Smith SSF, Smith GC, Liao X (2001) Automatic stable assembly sequence generation and evaluation. J Manuf Syst 20(4):225
20. Smith GC, Smith SSF (2002) An enhanced genetic algorithm for automated assembly planning. Robot Comput-Integr Manuf 18(5–6):355–364
21. Tseng HE, Li RK (1999) A novel means of generating assembly sequences using the connector concept. J Intell Manuf 10(5):423–435

22. Rodríguez I, Nottensteiner K, Leidner D, Durner M, Stulp F, Albu-Schäffer A (2020) Pattern recognition for knowledge transfer in robotic assembly sequence planning. IEEE Robot Autom Lett 5(2):3666–3673
23. Gulivindala AK, Bahubalendruni MR, Varupala VP, Sankaranarayanasamy K (2020) A heuristic method with a novel stability concept to perform parallel assembly sequence planning by subassembly detection. Assem Autom 40(5):779–787

Image Hashing Based on SHA-3 Implemented on FPGA

Argyrios Sideris, Theodora Sanida, Dimitris Tsiktsiris, and Minas Dasygenis

1 Introduction

The integrity of this transmission, as well as for any other transmission, is achieved via cryptographic functions of hashing. Cryptographic hash functions play a crucial role, in the modern world of digital communications and is an important technique used to safeguard the integrity of the information, when data are transmitted over a network.

Today, image data security is very important, especially in the domains of the military, meteorology, medical, intelligent robots, commercial, etc. Consequently, the design of an image hash functions has become the aim of the cryptographic community [1]. One of the techniques for protecting digital images and video from alterations or corruptions is watermarking. The hash functions can be used with great success in applications of content authentication and image/video watermark [2]. In addition, an image hash function would greatly facilitate searches and comparisons in large databases, in which several identical versions of an image can exist [3].

In this work, we designed and implemented the popular SHA3-256 (Keccak) algorithm in the Intel Arria 10 GX. We provide an approach based on the FPH2 component in our architecture, and we compare the two architectures: we have designed, with

A. Sideris (✉) · T. Sanida · D. Tsiktsiris · M. Dasygenis
Department of Electrical & Computer Engineering, University of Western Macedonia, 50131 Kozani, Greece
e-mail: asideris@uowm.gr

T. Sanida
e-mail: thsanida@uowm.gr

D. Tsiktsiris
e-mail: dtsiktsiris@uowm.gr

M. Dasygenis
e-mail: mdasyg@ieee.org

common evaluation criteria (entropy, NPCR, UACI, efficiency, and throughput) with other similar models.

This work has three main contributions:

- We implemented the design of the two-stage pipelined architecture for the SHA3-256 algorithm for 256×256 pixel images.
- We used the SHA-3 algorithm with an output length of 256-bit because it offers high security and which provides optimized performance and acceleration on FPGA board.
- We provide a design based on the FPH2 component in our architecture, which provides low cycle count.

The rest of this work is organized as follows: In Sect. 2, we present some research works which are suchlike to ours. In Sect. 3, we describe our implementation in detail for implementing SHA3-256 (Keccak) in 256×256 pixel images on FPGA. In Sect. 4, we present the experimental results and the performance evaluation of our design. Finally, in Sect. 5 we sum up the conclusions and future work of our implementation.

2 Related Work

From the literature review, we studied the implementation of our work, we selected two similar works for comparison. We selected the specific papers, because they are the state of the art architecture for image encryption using the SHA-3 algorithm up to date.

The authors in [4] propose a chaotic image encryption algorithm with double chaotic maps, SHA-3, and auto-updating system. SHA-3 is to compute the hash values to produce central results and initial condition of an logistic map. After that, the total permutation is implemented for the rows and columns of image to exchange pixels. As a result, the proposed algorithm can resist efficiently to known-plaintext attacks.

A secure and efficient image encryption algorithm is suggested in [5], using Keccak hash function with double two-dimensional Arnold chaotic maps. A standard encryption design is proposed with four random directions of shuffling, to avoid time consumption in the sorting operation for pixel position index in the permutation stage. The number results show that the proposed encryption algorithm can have top security and speeding implementation for the digital image communication.

In [6], the authors propose a pipelined SHA-3 architecture. The proposed SHA-3 architecture is simulated in ModelSim and implemented on a FPGA platform Xilinx Virtex-5. Results show the proposed architecture for the Keccak-512 algorithm needs 4.793 slices (area), achieves a 317.11 MHz maximum frequency, and demonstrates a 12.68 Gbps throughput and efficiency of 2.71 Mbps/Slices.

In contrast to these works, we present and implement two architectures of the algorithm SHA3-256, with the Nios II/f (fast) system on a chip (SoC). The first

architecture involves a two-stage pipeline and the second concerns an approach based on the FPH2 component in two-stage pipeline architecture. The two techniques we propose in this paper offer a secure SHA3-256 (Keccak) implementation. The proposed two-stage pipelined architecture with the FPH2 component outperforms existing implementations.

3 Implementation for Image Hashing

In this section, we analyze all the design components and we implemented for the SHA-3 256 (Keccak) algorithm. We use also for our experiments the Quartus II v18.1 Standard Edition (SE) software and the Terasic DE5a-Net board.

3.1 Embedded Processor—Nios II

The softcore Nios II processor is fully implemented in the FPGA. It is considered to be appropriate for most embedded applications and provides flexibility for cost-sensitive and real-time [7]. Nios II processor is available in two configurations: Nios II/e (economy) and Nios II/f (fast). The Nios II/f (fast) is optimized for the highest performance; this performance can be adjusted using custom instructions, hardware accelerators, and high bandwidth switch fabric. The Nios II/s (standard) is optimized for high performance, and Nios II/e (economy) is suitable for modest performance [8].

In our experiments, we used the Nios II/f processor. Some of its main characteristics are: contains a six-stage pipeline to provide maximum DMIPS/MHz, custom instructions, external interrupt controller and optional hardware multiply and disunite and shift options to improve performance.

3.2 Floating Point Hardware 2 (FPH2)

The Nios II architecture supports FPH2 component. The FPH2 provides low cycle count implementations. The custom floating point instructions include multiplication, subtraction, addition, float to integer conversion, square root integer to float conversion, and division operations.

Floating point divider needs more resources than other instructions, so we may choose to skip it if Nios II does not make much use of floating point division. Sometimes, we can rewrite our code to decrease or even cut split functions. If our algorithm requires division by a constant value, we can calculate the inverse and use a multiplication function at the critical speed of our code.

The custom instruction implementations provide minimum, maximum, negate, absolute, and comparisons. FPH2 is recommended by Intel rather than the legacy FPH1. It provides low clock cycle count, a smaller device footprint, and better performance. Additionally, the FPH2 component supports FPH1 operations and the reliable rounding [9].

3.3   System Architecture of the SHA3-256 Core

Our system architecture of the SHA3-256 is shown in Fig. 1. The architecture consists of the Control Unit, the bitrate XOR Input, the counter, a zero state, and the Keccak Round. The first architecture of the SHA-3 requires the initial zero state, which is maintained in the component zero state.

When processing a multi-block message, we used for feedback a multiplexer. The bitrate XOR Input component processes the XOR bits of the state matrix bitrate with the bits of the input block, which is the result of the padding process. The Control Unit is responsible for synchronizing, communicating, and controlling the data flow in the design. The Control Unit activates the counter by the control signal. The Keccak Round component is presented in the next subsection.
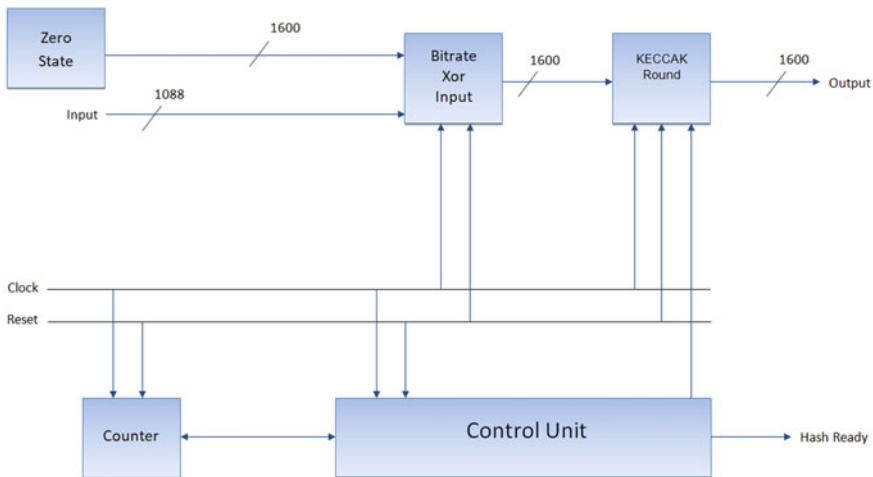
Fig. 1   System architecture for the SHA3-256 core
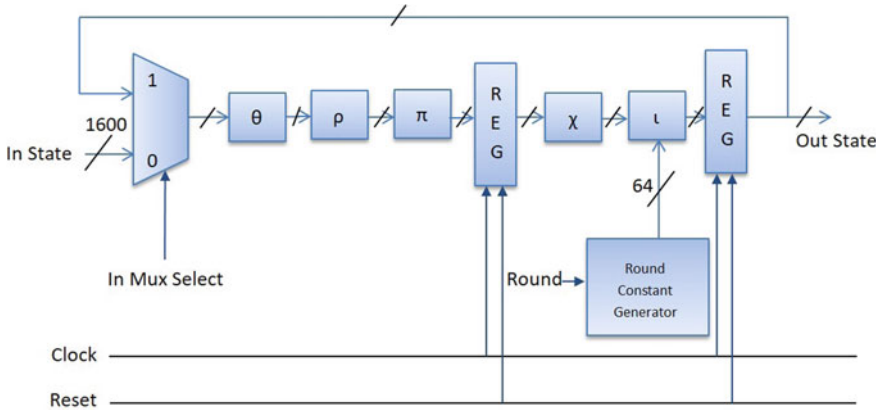
Fig. 2 Keccak Round with two-staged pipelined architecture

3.4 The Keccak Round Pipelined Architecture

The algorithm has 24 rounds, and each permutation round consists of 5 sequential phases. These phases called theta, rho, pi, chi, and iota denote as θ, ρ, π, χ, and ι. Algorithm takes each stage the state array and after applying the corresponding function, returns an updated state array. The two-staged pipelined architecture of the Keccak Round is shown in Fig. 2.

For the round's feedback, at the beginning of the round, there is a multiplexer 2 to 1. With the pipelined technique, we input two registers in each round. The first register is placed between sections π and χ, in order to limit the critical path in half. The second register is inserted at the end of the round. The two registers have two control signals the clock and reset. The round constants that are used in the ι are produced by the Round Constant Generator and are given in Table 1.

3.5 System Integration

The original image is grayscale and measures 256 × 256 pixels. The input block is stored in SDRAM memory. The block is then given as input to the SHA3-256 Core. The output block of the SHA3-256 Core is stored in SDRAM memory. All components were implemented in VHDL. We examined each VHDL file to vouch its correctness and functionality using a multitude of test benches. All tests were performed on each individual VHDL file using the simulator ModelSim 10.6d with valid input samples provided by NIST for the SHA3- 256 (Keccak) algorithm in [10]. Furthermore, we created and implemented the samples of all VHDL files, in the top module. In addition, we simulated the top module with valid input diagrams, provided by NIST for the SHA3-256 algorithm (Keccak) in [11]. After the correct verification

Table 1 Round constant generator RCi in iota function

RC	Values	RC	Values
0	0x0000000000000001	12	0x000000008000808B
1	0x0000000000008082	13	0XS00000000000008B
2	0x800000000000808A	14	0x8000000000008089
3	0x8000000080008000	15	0x8000000000008003
4	0X000000000000808B	16	0x8000000000008002
5	0x0000000080000001	17	0x8000000000000080
6	0x8000000080008081	18	0x000000000000800A
7	0x8000000000008009	19	0x800000008000000A
8	0x000000000000008A	20	0x8000000080008081
9	0x0000000000000088	21	0x8000000000008080
10	0x0000000080008009	22	0x0000000080000001
11	0x000000008000000A	23	0x8000000080008008

of the simulation results in ModelSim 10.6d, we proceeded to the implementation of the Nios II system.

The scheme of the processor was made using the designer platform. We used the Nios II/f (fast) core which provides high execution performance and maximize f_{MAX} performance of the processor core. The implemented components of the Nios II processor that we include: On-chip RAM, clock in 50 MHz, performance counter, DDR4 SDRAM controller, Peripheral ID System, JTAG-UART, PLL, and SHA3-256. On-chip RAM is used from the Nios II processor as operating memory. The complete implementation of our system that we designed with the processor Nios II is shown in Fig. 3.

4 Experimental Results for Image Hashing

We use the FPGA Arria 10 GX to perform our experiments. We designed a two-staged pipelined architecture and a two-staged pipelined architecture with the FPH2 component.

4.1 Entropy Analysis

The entropy of an image is a statistical measure and is utilized to indicate the randomness of the ciphered image. It describes the average information of an image source. The entropy $E(X)$ is calculated by using Eq. 1. X is the sample image, x_i is the possible value in X, and $P r(x_i)$ is the probability of $X = x_i$.
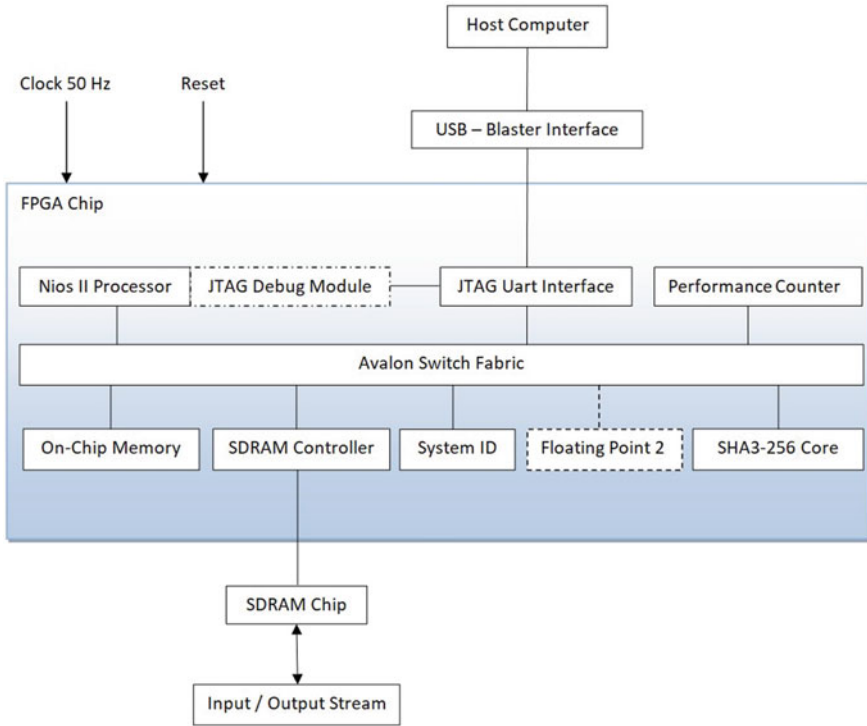
Fig. 3 Block diagram on the Intel Arria 10 GX

$$E(X) = \sum_{i=1}^{n} \Pr(x_i) \log_2 \Pr(x_i) \tag{1}$$

We computed the entropy to a plethora of hashed images. The results are shown in Table 2, where it is shown that the entropies of the hashed images are very close to 8. For a 256 grayscale image, the maximum entropy is $\log_2(256) = 8$. Thus, the proposed image hashing model is strong against entropy attacks.

Table 2 Entropies of hashed images

Images	This paper	Ye et al. (2016) [4]	Ye et al. (2016) [5]
Lena	7.9989	–	7.990
Camera man	7.9991	–	–
Peppers	7.9994	7.991	–
Boat	7.9993	7.991	7.991
Baboon	7.9995	7.992	7.992

4.2 NPCR and UACI Metrics

To measure the impact of changing one pixel in both the plain and the hashed images, we use the UACI and NPCR [12]. The UACI measures the intensity average, while the NPCR measure the number of distinct pixels between the two images. The NPCR is calculated by using Eq. (2), where D denotes the two-bit array with equal size as original image and hashed image, M × N defines the size of the image.

$$\text{NPCR} = \sum_{i=1}^{M} \sum_{j=1}^{N} D(i, j) \times \frac{100\%}{M \times N} \tag{2}$$

The UACI can be computed using Eq. (3), where C_1 denotes the first sample, C_2 is the hashed image, and $M \times N$ defines the size of the image in pixels.

$$\text{UACI} = \left[\sum_{i=1}^{M} \sum_{j=1}^{N} \frac{|C_1(i, j) - C_2(i, j)|}{255} \right] \times \frac{100\%}{M \times N} \tag{3}$$

Tables 3 and 4 show the results of the NPCR and the UACI of hashed images. The high values of the NPCR and UACI metrics indicate the greater security of hashing and better performance in resisting differential attacks.

Table 3 NPCR of hashed images

Images	This paper	Ye et al. (2016) [4]	Ye et al. (2016) [5]
Lena	99.6886	99.603	99.55444
Camera man	99.6543	99.641	99.59870
Peppers	99.6321	–	–
Boat	99.6420	–	99.62959
Baboon	99.6563	99.600	99.61586

Table 4 UACI of hashed images

Images	This paper	Ye et al. (2016) [4]	Ye et al. (2016) [5]
Lena	33.6818	33.432	33.39281
Camera man	33.6592	33.498	33.53431
Peppers	33.6326	–	–
Boat	33.6463	–	33.52958
Baboon	33.6531	33.428	33.40222

Table 5 Results of our two proposed architectures

Design	Throughput (Gbps) ($r = 1088$)	Efficiency (Mbps/slices) ($r = 1088$)	Frequency (MHz)	Area (slices)
Architecture with two-staged pipelined architecture	24.298	8.84	402	2746
Architecture with two-staged pipelined architecture and FPH2	35.593	11.92	458	2984

4.3   Efficiency and Throughput Metrics for Image Hashing

The throughput is computed using Eq. 4. In Eq. 4, bits are the bitrate size r, frequency is the maximum frequency reported by the tool, and clock cycles denote the latency of the circuit. Clock cycle represents the number of resumption needed of the five functions: theta, rho, chi, pi, and iota to generate the hash value.

$$\text{Throughput} = \frac{\text{Bits} \times \text{Frequency}}{\text{Clock cycles}} \tag{4}$$

Equation 5 shows how we calculate the efficiency:

$$\text{Efficiency} = \frac{\text{Throughput}}{\text{Area}} \tag{5}$$

The results of our two architectures for the SHA3-256 (Keccak) algorithm displayed in Table 5. In the implementation of a two-staged pipelined architecture, the number of clock cycles of the five functions is 18, while in the implementation of a two-staged pipelined architecture with the component FPH2 it is 14. The number of slices determines the utilization area. Four logic utilization (in ALMs) and eight storage elements are contained in every slice of FPGA board.

The proposed design of a two-staged pipelined architecture with the component FPH2 achieves the best efficiency and highest throughput. Because the number of clock cycles decreased and the maximum clock frequency increased.

5   Conclusion

In this paper, we focus our research on the optimal performance of the efficiency and throughput criteria of the SHA3-256 algorithm (Keccak) in 256×256 pixel images

in the Arria 10 GX using the processor Nios II/f (fast). We used the SHA-3 (Keccak) with an output length of 256 because it offers high security.

From our experiments, the implementation of a two-staged pipelined architecture with the FPH2 component area (slices) increased by 10.86% but simultaneously the maximum clock frequency increased by 11.39%, the number of clock cycles by 12, 85% resulting in an improvement in throughput increase by 14.64% and efficiency by 13.48%. The SHA3-256 (Keccak) algorithm offers us a good combination of speed, performance, and security.

As a future project, we will be working on image hashing according to the tree hashing which has a simpler architecture with fewer rounds (reduced to 12 and 14 rounds, out of the 24 that SHA-3 has) in order to examine the security of the image against the hashing process.

References

1. Agarwal S (2018) Secure image transmission using fractal and 2D-chaotic map. J Imaging 4(1):17
2. Swaminathan A, Mao Y, Wu M (2006) Robust and secure image hashing. IEEE Trans Inf Forens Secur 1(2):215–230
3. Monga V, Banerjee A, Evans BL (2006) A clustering based approach to perceptual image hashing. IEEE Trans Inf Forens Secur 1(1):68–79
4. Ye G, Huang X (2016) A secure image encryption algorithm based on chaotic maps and SHA-3. Secur Commun Netw 9(13):2015–2023
5. Ye G, Zhao H, Chai H (2016) Chaotic image encryption algorithm using wave-line permutation and block diffusion. Nonlinear Dyn 83(4):2067–2077
6. Mestiri H, Kahri F, Bedoui M, Bouallegue B, Machhout M (2016) High throughput pipelined hardware implementation of the KECCAK hash function. In: 2016 international symposium on signal, image, video and communications (ISIVC) IEEE, 2016, pp 282–286
7. Intel®FPGA (2020) Embedded design handbook [Online]. Available at: https://www.intel.com/content/dam/www/programmable/us/en/pdfs/literature/hb/nios2/edh_ed_handbook.pdf. Accessed 15 Jan 2021
8. © Intel Corporation (2018) Nios® II Processors for FPGAs. Intel® FPGA [Online]. Available at: https://www.intel.com/content/www/us/en/products/programmable/processor/nios-ii.html. Accessed 28 Jan 2021
9. Altera Corporation (2010) Using Nios II floating-point custom instructions [Online]. Available at: http://www.ee.nmt.edu/~erives/554_10/Altera_FloatingPoint.pdf. Accessed 30 Jan 2021
10. Intel®FPGA (2017) Nios II custom instruction user guide. © Intel Corporation [Online]. Available at: Nios II Custom Instruction User Guide (intel.com). Accessed 22 Jan 2021
11. NIST, Computer Security Resource Center. National Institute of Standards and Technology [Online]. Available at: https://csrc.nist.gov/projects/cryptographic-standards-and-guidelines. Accessed 5 Feb 2021
12. Wu Y, Noonan JP, Agaian S (2011) NPCR and UACI randomness tests for image encryption. Cyber J: Multidiscipl J Sci Technol J Sel Areas Telecommun (JSAT) 1(2):31–38

A Mechatronic Robotic Design to Aid Educational Learning Objectives in Primary and Secondary Schools

Dimitris Ziouzios, Antonios Chatzisavvas, Nikolaos Baras, Dimitrios Apostolou, and Minas Dasygenis

1 Introduction

Information and Communication Technologies (ICT) is a broader term for Information Technology (IT), which refers to all communication technologies, including the Internet, wireless networks, mobile phones, and computers. In recent years, researchers worldwide have been working on how Information and Communication Technologies (ICT) can be integrated and improve the educational process [1].

Mechatronics is a field that refers to the skill sets required in modern and advanced society. When intersecting engineering, electronics, and computer science, engineers create more straightforward, more straightforward, and intelligent systems. Mechatronics must be considered an essential foundation for the expected development of automation and manufacturing [2].

Robotics undoubtedly plays an essential role in science and our daily lives. For the educational process to evolve, robotics must be integrated into schools. This science helps teachers to incorporate new teaching methods and to present even more topics to students. It is an innovative approach to assisting students to engage in the use of new technologies. Students' abilities for observation, analysis, modeling, and control

D. Ziouzios (✉) · A. Chatzisavvas · N. Baras · M. Dasygenis
Electrical and Computer Engineering, University of Western Macedonia, Kozani, Greece
e-mail: dziouzios@uowm.gr

A. Chatzisavvas
e-mail: achatzisavvas@uowm.gr

N. Baras
e-mail: nbaras@uowm.gr

M. Dasygenis
e-mail: mdasygenis@uowm.gr

D. Apostolou
Industrial Design, Politecnico di Milano, Polytechnic University of Milan, Milan, Italy

531

of various physical tasks are developed [3]. In addition, educational robotics paves the way for both teachers and children to study Science, Technology, Engineering, Arts, Mathematics (STEAM) and other fields, such as teamwork, problem-solving, and cultivating collaborative and critical thinking skills [4]. An important finding is that the use of technology, even in preschool settings, plays an essential role in shaping the character and personality of the child [5].

Our work aims to build an innovative and low-cost robot that can be used for training purposes. Our robot is made of plastics that can be printed even on a home 3D printer.

The structure of our work: The second chapter presents other research projects. Section 3 explains our implementation, and Sect. 4 explains our conclusions.

2 Related Work

In this section, we highlight a project similar to ours, pinpointing the strong and weak points while comparing it with our contribution to this field.

Blue Frog has created buddy [6], a robotic system with the ability to interact socially. The robot consists of four microphones, a thermal camera, a 3D camera, an 8-inch touch screen, two speakers, three obstacle sensors, and six ground sensors. The robot, which is 56 cm high, can move and rotate its head. Also, its software is based on Android.

Buddy consists of desires and emotions that are influenced by its environment and are perceived by its sensors. Even though it is similar to ours, it lacks the programmability and expandability characteristics found in our project.

Another implementation comes from Embodied, who created a Moxie [7], a social partner for children aged 6–9. Moxie has a microphone camera screen, hug sensors, and touch sensors in its hands. The robot is 40 cm high. The robot's ability to display various expressions on its screen helped the development team conclude that using Moxie in education in children on the autism spectrum develops children's self-esteem and sociability. The major drawback is its cost, totaling over 2000$.

STIMEY [8] was developed as part of the European Horizon 2020 program. STIMEY is a social robot that can shake its head and arms. It consists of a screen in front of which depicts his expressions. On the back, you place an Android smartphone that takes over its functions. The lack of technical documentation makes it unrealistic to duplicate by a third party.

Breazeal et al. created the Jibo [9] robot, which has a height of 27 cm. He can move his body, but he cannot move. Its head rotates 360° and up and down like a human head. The Jibo head has a screen, two speakers, and one microphone. The robot, with its two cameras, detects the child is which is paying attention to it. So with specialized scenarios, they managed to help the child stay focused. The robot contains particular functions and training scenarios.

LuxAI SA created the QTrobot [10], which is about 63 cm high. QTrobot is a social robot that has a screen that displays its expressions. He has 12 degrees of

freedom and can shake both his head and his arms. The QTrobot has a 3D RealSense camera mounted on the front and a microphone layout. QTrobot is a robot that can help children on the autism spectrum. Children pay more attention to the robot, imitate the robot as much as a human does, and participate in various activities with him. Its weak point is again the cost of acquiring this unit, which makes it infeasible for educators.

Summing up, a universal disadvantage of most implementations is the absence of wheels for their movement. All are handicapped in movement and are stationary, limiting usability, as observed in our experiments. Many implementations offer software development kit (SDK) for application development but are limited to a single programming language. In our implementation, we present a robot with two wheels so that it can move. Furthermore, it can move the head and arms. The robot has been developed with open-source standards to support applications in any popular programming language.

3 Our Implementation

With our implementation, we aim to develop a sense of empathy, a critical component of social knowledge [11]. Goleman [12] characterizes empathy as a distinct dimension of emotional intelligence. It defines empathy as the awareness of other people's positive and negative emotions, understanding, and expressing one person's interest in the other's concerns. Empathy is a fundamental element of education. Several interventions have been implemented to cultivate empathy, following various approaches such as experiential learning and teaching [13].

The philosophy of the design process and frames (guidelines) in EDU Robot is driven by core ideas and practical considerations such as safety, energy efficiency, educationally oriented ethics, easy construction, and scalability.

Our starting point of designing the robot was our intention to 3D print all exterior parts to reduce the manufacturing cost. Robust construction combining high-strength 3D printed parts with additional metal pillars allows us to gain internal space for electronic components and at the same time gives the robot a high level of rigidity. A combination of simplified methods of design makes the robot very easy to fit its parts together. Mainframes in hands and soldiers with additional covers are giving to the robot for carrying educational-oriented assembly method, easily constructible from kids. Hands are made for plug-and-play accessories such as umbrellas, tools, music instruments, and many more.

The humanoid robot aims to assist in the educational process by utilizing various scenarios that help the teacher. During the design of the robot, particular emphasis was placed on the safety of its users. The goal was to create a robot that could express various emotions that children can perceive (Fig. 1). The robot software was developed supporting open templates to customize them and develop their custom scripts. An information system and a remote-control application were also developed for the complete control of the robot.

Fig. 1 3D schematic of our
robot
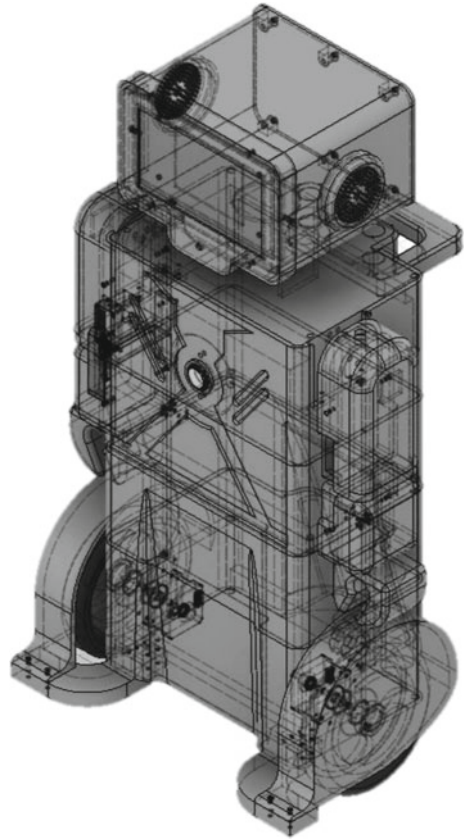
In the back, we find a multipurpose plug handle for transportation that becomes a backpack cradle expanding internal space and give us plenty of store capabilities for our power supply cable and accessories. The rear wheel is adjustable in height (Z-axis) from users to level the movement as flat as possible for e precise movement.

All parts of the robot were created by the process of rapid prototyping. Polylactic acid or common PLA is the material used to build the original model which is biodegradable and bioactive thermoplastic. We printed all parts of the robot with infill 15%, 0.2-layer height. During the printing process, the nose temperature was 215 °C and the bed at 65 °C.

Extra chassis with the two main motors is fitted with flexible isolators to prevent grainy motion and delivers a smooth ride. Concerning the physical characteristics of the robot is perfect for storage and transportation with a high of 60 cm and total weight of only 15 kg using a Li-ion battery, which has way less weight from common battery types and quicker charging time.

The robot was designed by our laboratory robotics, embedded and integrated systems (ROBIS) from scratch using open source and open hardware technologies.

We have incorporated controller software, acting like a brain, a brain, into the head of our robot-like humanoid (Fig. 2). Our design was also focused on high responsive head and shoulder sensors detecting action from users. Stereo audio and visual feedback with led indicators and a central button operation make the experienced user-friendly, aiming mainly at kids with special needs such as autism and every enthusiast child. The robot carries a Raspberry Pi 4. This is a low-cost and moderate performance computational board that is very popular in embedded and robotic projects. The Linux operating system of this board gives programming flexibility, while its connectivity adapters of Wi-Fi 2.4 GHz, Wi-Fi 5 GHz, Bluetooth 5.1, and LAN make it an ideal selection for our project, fulfilling all our use cases.

The "face" of the robot is a 7″ touch screen with a resolution of 800 × 480 pixels. Our robot has a built-in camera that, combined with our developed machine vision algorithms, can detect faces and objects. Furthermore, its array of microphones enables the robot to pinpoint the general direction of the sound source. This big touch-screen in the head gives us plenty of space for feedback information and software capabilities involving kids to use the robot as a stand-alone integrated system.
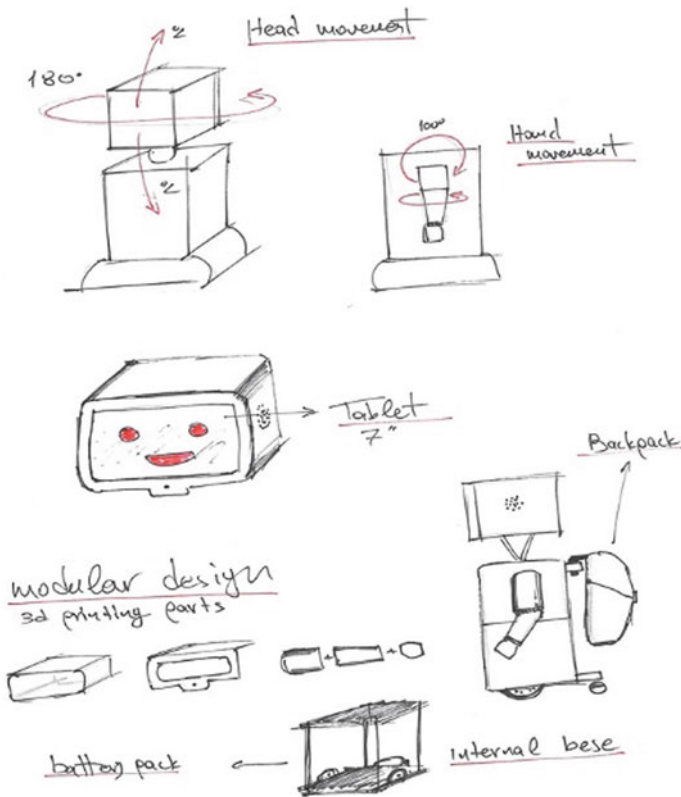
Fig. 2 Sketch of our robot

Sensors under the bottom of the robot control the precise movement. It stops instantly when it must avoid injuring itself if a gap is detected. The wheel cover is the main feature to prevent kids from injuring their hands and fingers. Front protective spoilers also keep robots free from falling. From the beginning of our concept, we have kept cables hidden for safety reasons and durability.

4   Conclusions

Our research work aims to transform the educational process into a better experience for the trainees, especially children aged 4–7. Also, utilizing our robot's capabilities could be a great tool in the hands of teachers for kids with special needs and primarily for individuals with ASD. Using the user-friendly python programming language, the teachers can develop their scenarios, and our 3D printed blueprints will be available in Q4 2021, so anybody who owns a 3D printer and is interested in our project can contribute.

Furthermore, the research team has created ten scenarios ready for the classrooms, which will be soon available for download from our platform. Unfortunately, due to the pandemic COVID-19 lockdown, it was impossible to test our scenarios in a real classroom. We hope during the following months to be able to do our experiments. That is why we prepared to test all of our scenarios in a real classroom and record students' reactions, levels of knowledge acquisition, and how the students feel about being trained by a robot. Our scope is to create a cost affordable robot for anyone to build and utilize in primary education.

References

1. Yelland NJ, Gilbert CL (2013) iPlay, iLearn, iGrow. A report for IBM. Victoria University, Melbourne
2. Eisenberg M, Oh H, Hsi S, Gross M (2015) Paper mechatronics: a material and intellectual shift in educational technology, pp 936–943. https://doi.org/10.1109/ICL.2015.7318153
3. Depover C, Karsenti T, Komis B (2010) Teaching using technology. Kleidarithmos, Athens
4. Eguchi A (2014) Robotics as a learning tool for educational transformation. In: Proceedings of 4th international workshop teaching robotics, teaching with robotics and 5th international conference robotics in education
5. Blackwell CK, Wartella E, Lauricella AR, Robb M (2015) Technology in the lives of educators and early childhood programs: trends in access, use and professional development from 2012 to 2014. Center on Media and Human Development at Northwestern University, Evanston, IL
6. Foley LM (2013) Digital storytelling in primary-grade classrooms. Unpublished Ph.D. Dissertation, University of Arizona State, USA
7. Milliez G (2018) Buddy: a companion robot for the whole family. In: HRI '18: companion of the 2018 ACM/IEEE international conference on human-robot interaction
8. Hurst N, Clabaugh C, Baynes R, Cohn J, Mitroff D, Scherer S (2020) Social and emotional skills training with embodied moxie

9. Christodoulou P, Reid A, Pnevmatikos D, Rioja-Del-Rio C, Fachantidis N (2020) Students participate and evaluate the design and development of a social robot
10. Scassellati B, Boccanfuso L, Huang C-M, Mademtzi M, Qin M, Salomons N, Ventola P, Shic F (2018) Improving social skills in children with ASD using a long-term, in-home social robot. Sci Robot
11. Costa A, Louise C, Rodríguez Lera F, Ziafati P, van der Torre L, Steffgen G (2018) More attention and less repetitive behaviors using a robot with children with autism
12. Goleman D (2011) Emotional intelligence. Pedio, Athens
13. Mittenberger RG (2015) Behavior modification: principles and procedures, 6th edn. Cengage Learning, Boston, MA

Irrigation Pumping Scheme Based on Solar PV and Zeta Converters with PMBLDC Motor

Ayan Banik and Anubrata Sengupta

1 Introduction

Due to the decline of fossil resources worldwide, India has been witnessing a severe energy crisis. It has been found that renewable-based electricity has immense potential to solve most of the future energy demands in a sustainable, environmentally friendly way. Renewable energy sources shall fuel and drive India's growing energy need, as they are limitless and thus have ample opportunity to harness. There is a need for affordable, reliable alternative fuels to produce electricity that can last a long time, such as renewable energy sources that shall definitely help India. Renewable energy sources are the conceivable foundation, and the inherent usage of non-conventional energy sources would offset energy sources that contain carbon incentives, reducing global warming to a significant degree. The majority of the world's population lives in remote and rural parts with insufficient access to sanitation. Electric hydropumps are used to drain deep underground water in many places. However, where energy is unavailable, diesel engines have historically been used to fuel electric pumps. Periodic servicing and maintenance are needed for these generators, which are both expensive and time-consuming. However, in order to prevent a collapse, it is essential to do so. One of the best approaches to solve this issue is to build solar energy pumps, as diesel-operated pump is both inefficient and releases harmful gases, i.e., significantly polluting the atmosphere with high carbon footprint.

A. Banik (✉)
Department of Electrical Engineering, National Institute of Technical Teachers' Training and Research, Kolkata, India

A. Sengupta
School of Illumination Science Engineering and Design, Jadavpur University, Kolkata, India

2 Literature Survey

In today's world, we are on the verge of facing an acute energy crisis due to the constant depletion of conventional sources and rapid industrialization. During this worldwide crisis hour, harnessing green sustainable energy can provide an alternative eco-friendly, cost-effective resource to meet future energy demand. Solar PV's role and future perspective are impressive among all renewable energy, and the opportunity is endless. In this work, the authors have attempted to investigate a unique novel approach of employing PMBLDC motor with Zeta converter in the irrigation domain to increase its effectiveness and dependency over traditional sources. In simple words, the approach is to design, study, and explore the proposed innovative irrigation pumping scheme powered by solar PV in collaboration with Zeta converters-based PMBLDC motor. An intensive literature review has been performed to uphold the present research scenario in this domain. M. Dubey et al. (2018) have developed control of a soft-switching-based boost converter for PMBLDC motor drive dependent on solar power, which has significantly helped to choose PMBLDC motors over other available motor drives like servo and stepper [1]. In 2017, Gotkhinde et al. [2] have undergone transient and harmonic analysis and its influence over PMBLDC motor. This research significantly proves the unwanted THD minimization techniques. Dubey et al. [3] have presented a beautiful result-driven case study of solar-powered PMBLDC motor drive with Z-source inverter in the year 2018. In 2017. Joy et al. have performed contemporary research on PMBLDC drive devices utilizing FLC, energy harvesting, and efficient consumption by regenerative braking and motoring modes of service [4]. The result and observations have proven efficient brushless DC motor and its smooth operation. Fasil [5] has out-of-box innovation to determine the finite element model-based design synthesis for axial flux PMBLDC motors. K. Manikandan et al. in 2020 have impersonated, a novel case study on, "Sepic and Zeta converters" by particle swarm optimization performance [6]. In 2020, Lima et al. have designed, developed, and fabricated an all-new DC–DC double Zeta quadratic converter [7].

Authors in their previous work have already worked over different fault detection techniques and investigated complex unexplored dimensions of solar PV [8–10]. Authors have been committed to exploring greener sustainable energy harnessing new generation technologies, which shall benefit humanity in multiple dimensions, including waste to energy conversion techniques. It is expected that this work shall be beneficial for energy-efficient irrigation using cutting-edge new generation technologies [11, 12].

3 Proposed Technology

The simplified block diagram of the proposed model has been shown and explained. This novel topology consists primarily of (a) solar photovoltaic array, (b) Zeta
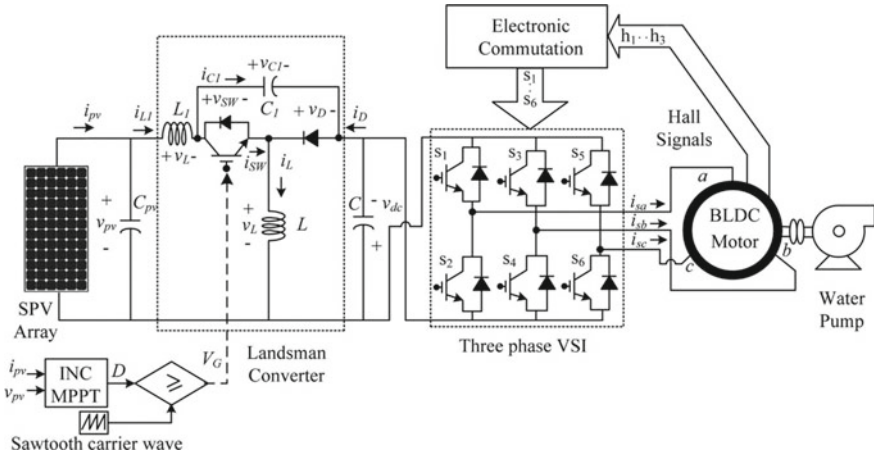
Fig. 1 Model of solar PV array and Zeta converter-based irrigation system employing PMBLDC

converter, (c) voltage source inverters, (d) brushless DC motor, and (e) water pumps as seen in Fig. 1.

The water pump requires electricity, which is provided by a solar array. A Zeta converter and a VSI are used to deliver the provided energy to the water pump. The photovoltaic array then serves as the control source for the Zeta topology. A pulse generator powers the Zeta converter. IGBT switching pulse for Zeta converter, the pulse generator is used to produce switches utilizing the INC-MPPT algorithm. The INC-MPPT receives voltage and current signals as input from the SPV series. The actual switching pulse is then produced by comparing the duty cycle to a high-frequency carrier wave. As a consequence, the optimum amount of power is extracted, increasing the PV array's performance. A Zeta converter's DC output is converted to AC through VSI, and this AC power is fed to the PMBLDC motor, which drives the water pump attached to its shaft. An encoder is integrated into the PMBLDC motor. The VSI, which is used to power the engine, is controlled by the electric commutation of the PMBLDC motor. Fundamental frequency switching is used to control the VSI. As a result, high-frequency switching errors are reduced, improving the proposed water pumping system's performance.

As seen in the previous figure, Fig. 1, a DC connection capacitor is associated between the Zeta converter and the inverter to provide a steady voltage at the inverter's input end, making the voltage ripple-free. The attached DC connection capacitor is huge. Its working temperature heavily influences the existence of a DC connection capacitor. It also costs between 5 and 15% of the overall cost of a BLDC engine. As a result, it is a goal to reduce the expense of the motor by removing the DC connection capacitor, which causes torque ripple at the motor's output. The torque ripple that results from removing the DC connection capacitor is reduced using a new system. This eradication aids in reducing the cost and scale of the engine. A ceramic capacitor and a switch with a parallel diode have been used to replace the DC

connection capacitor between the Zeta converter and the inverter. Each apparatus's operating principle is as follows:

3.1 Solar Photovoltaic (PV) Array

Solar irradiation with a capacity of 200 W/m^2 and above must be used to power the solar water pumping device. We are considering up to 1500 ^{W}/m^2 in this article, calculated under standard test conditions. PV arrays are constituted of many solar panels arranged in a group to absorb as much sunshine as possible and turn it into valuable energy. To get the necessary power production from a solar array, the number of modules in series and parallel must be adequate (Fig. 2).
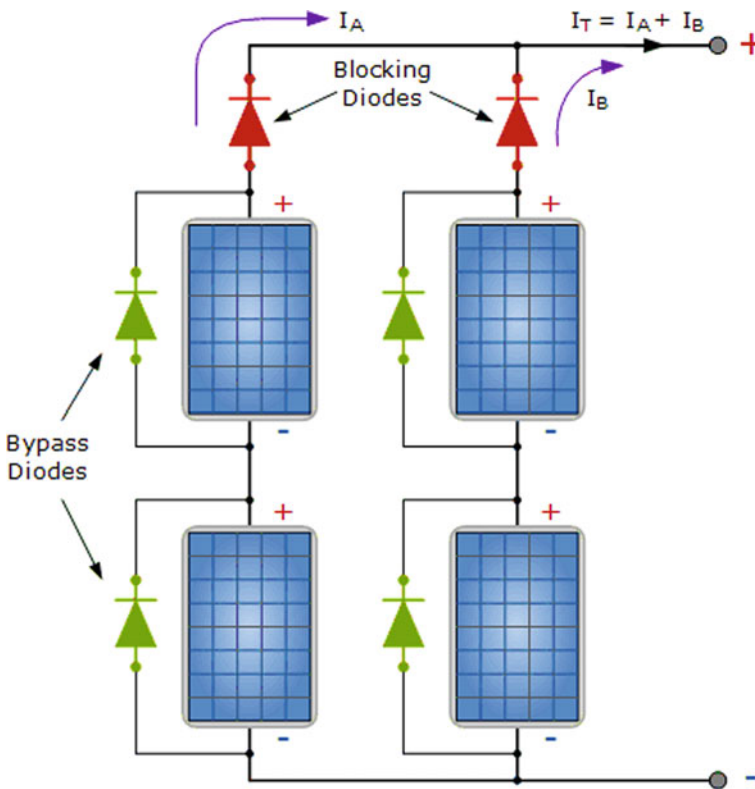
Fig. 2 Schematic block diagram of solar PV array configuration/architecture

3.2 Zeta Converter

In the recommended configuration, Zeta converter is installed after the solar PV array; a Zeta converter is a fourth-order DC–DC converter that will step the output voltage up and down as per specific criteria. It is a buck-boost converter of some kind. As seen in Fig. 1, it consists of two inductors and two capacitors (3) (Fig. 3).

It has been employed to get as much output out of the SPV series with the most negligible power loss. The job ratio of the converter determines the output voltage. As used for SPV applications, this converter has the following benefits: traditional buck, boost, buck-boost, CUK, and Sepic converters.

1. It outperforms standard buck-boost converters in terms of performance and voltage gain;
2. It has a broader service ratio spectrum than every other converter;
3. It has a non-inverted production. This property removes the need for an associated circuit for negative voltage sensing, reducing device complexity and the risk of system slowdown;
4. It has a higher power factor, lower input current distortion, lower output current ripple, and a broader output spectrum, as well as a constant and ripple-free output current. It has a good performance quality and is cost-effective;
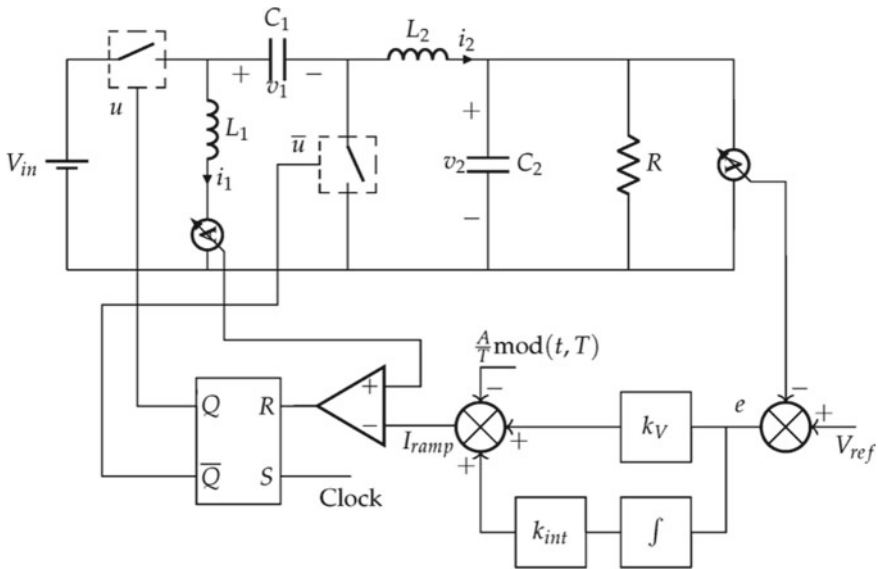
Fig. 3 Typical layout of Zeta converter
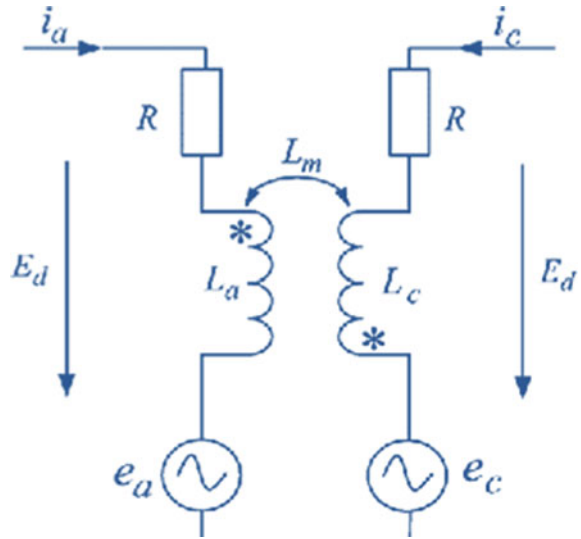
3.3 PMBLDC Motor

A PMBLDC motor is a modernized brushless DC motor that is electronically commutated. The stator has three coil windings, and the rotor has a single pole pair. The controller sends current pulses to the motor windings, which in turn power the motor's speed and torque. When it comes to solar-powered systems, the PMBLDC motor significantly outperformed. It has several benefits over brushed counterparts, including increased power, reduced maintenance, good durability, lower noise, long working life, high ruggedness, and outstanding performance over an extensive speed range (Fig. 4).

4 Proposed Tropology Control

The proposed topology can be scientifically influenced and regulated in either of the two ways, which have been elaborated and discussed underneath.

4.1 INC-MPPT Algorithm

The most widely used and powerful INC-MPPT technique is used in solar photovoltaic applications to adjust usable power and control the soft starting of BLDC motors which the BLDC motor experiences decreased current at startup. The gradual

conductance method is founded on the following observation: At the MPP, the difference in power concerning the change in voltage is equivalent to zero. It was created to address the flaws in the Perturb and observe, the PPT technique. The MPP is calculated using the incremental conductance equation, which compares the incremental conductance of solar PV arrays. The output voltage is the MPP voltage, while these two are equal. Before the irradiation varies and the procedure is replicated, the controller retains this voltage.

4.2 Electronic Commutation

The critical phases are accommodated every 60° for continuous motor rotation in the PMBLDC motor by six-step commutation or trapezoidal regulation. Three Hall effect signals are produced by the motor's inbuilt encoder depending on the rotor location. Three EMF signals are produced from these three Hall effect signals. Based on various combinations of three EMF signals, six switching pulses are produced, which are then fed into six VSI switches, resulting in BLDC motor control (Table 1).

5   Result and Observation

Simulation model and their corresponding result have been exhibited and discussed (Fig. 5).

Table 1   Switching sequence for the electronic commutation of DCBLDC motor

	Hall signal			Switching sequence					
	H1	H2	H3	S1	S2	S3	S4	S5	S6
NA	0	0	0	0	0	0	0	0	0
	0	−1	1	0	0	0	1	1	0
0–60	−1	1	0	0	1	1	0	0	0
60–120	−1	0	1	0	1	0	0	1	0
120–180	1	0	−1	1	0	0	0	0	1
180–240	1	−1	0	1	0	0	1	0	0
240–300	0	1	−1	0	0	1	0	0	1
300–360	0	0	0	0	0	0	0	0	0

Fig. 5 MATLAB simulation of solar PV array and Zeta converter-based irrigation system

5.1 Pumping Operation Using PMBLDC Motor

The simulation model of PV array and Zeta converter-based water pumping system using PMBLDC motor is shown in Fig. 6. The starting and steady-state behaviors of PV array, Zeta converter, PMBLDC motor, water discharge at 1500 W/m^2 are shown in Fig. 6.

The simulation model of PMBLDC motor that has driven PV array-fed water pumping system operating Zeta converter with torque ripple compensation is shown in Fig. 7.

The specific dynamic behavior of solar PV array, Zeta converter, PMBLDC motor, water discharge at 1500 W/m^2 has been shown in Fig. 8.

6 Specific Outcome and Discussion

The author in this paper has attempted to showcase the unique integration of solar PV, Zeta converter, and PMBLDC motor arrangement in such a way that shall formulate a cost-effective and energy-efficient pumping system for the next generation. The paper has been structured in the manner that is introduction, followed by a literature survey, and, finally, a comprehensive discussion with the proposed scheme. In the MATLAB simulation, the output result has been obtained under two different circumstances and then compared. The program was run in an ideal condition in the first condition, only employing a Zeta converter. In the latter case, the BLDC motor has been upgraded with torque ripple compensation which significantly shows
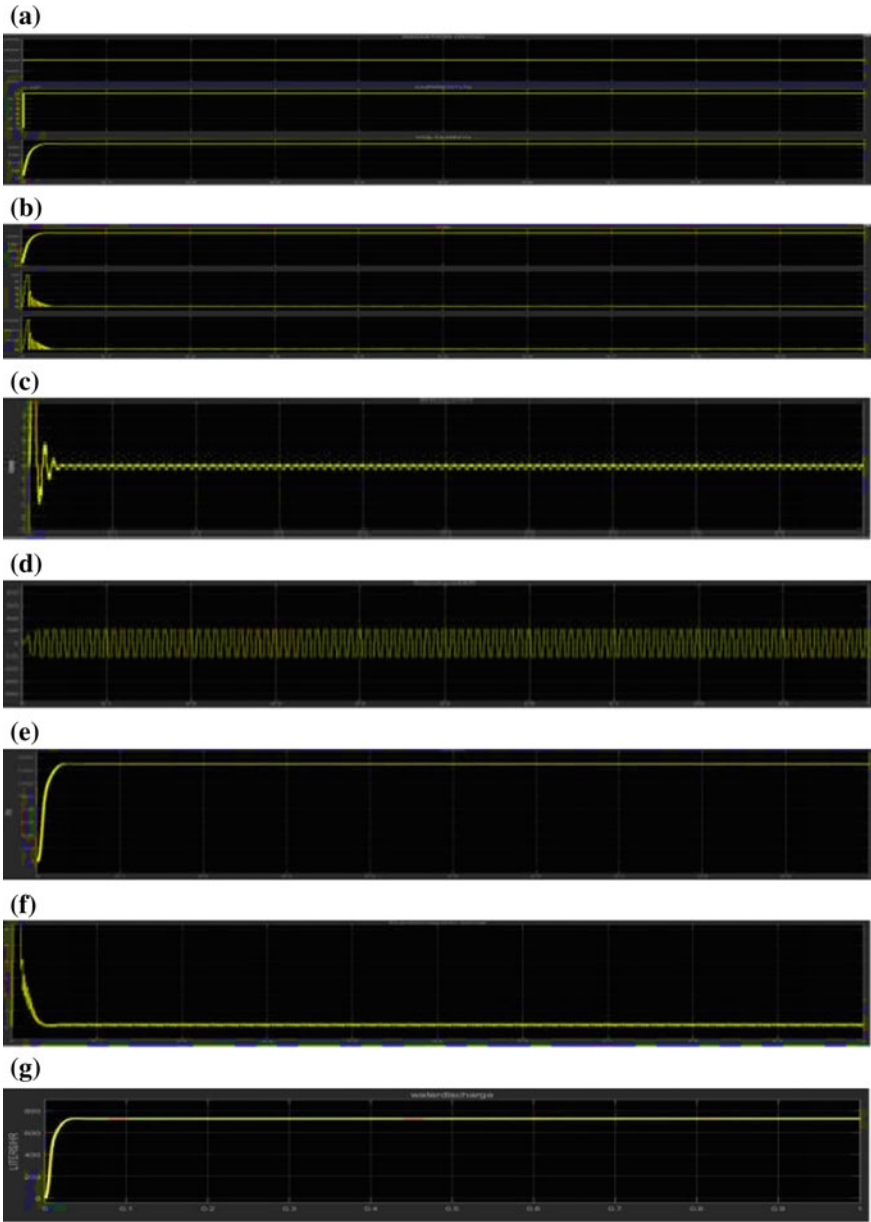
Fig. 6 **a** Solar PV array output waveform nature. **b** Zeta converter output waveform nature. **c** Stator current output waveform nature. **d** Back EMF output waveform nature. **e** Rotor speed output waveform nature. **f** Electromagnetic torque output waveform nature. **g** Nature of water discharge flow.
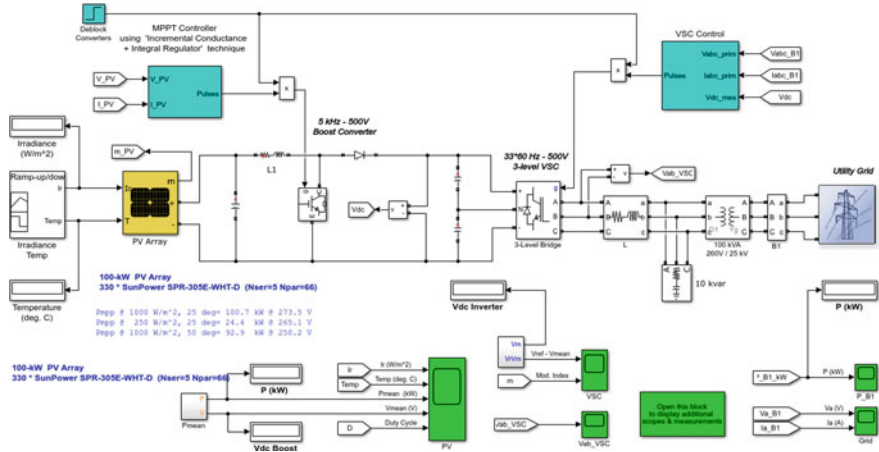
Fig. 7 MATLAB simulation model of solar PV array and Zeta converter-based irrigation system using exclusive BLDC motor with torque ripple compensation

better results. The comparison was made under seven parameters: solar PV array, Zeta converter, stator current, back EMF, rotor speed, electromagnetic torque output nature, and water discharge flow. The most remarkable feature is its output stability under varying physical conditions.

7 Conclusion

Through the usage of a Zeta converter and a PMBLDC drive, this paper provides a cost-effective outcome for the concept of developing and implementing an easy, fruitful, and efficient system for water pumping that can be used in a variety of applications such as irrigation, household drinking water. The device is designed, planned, and simulated here to account for spontaneous and instantaneous solar irradiance fluctuations. The system's suitability can be demonstrated by evaluating its startup, steady-state, and dynamic nature. This machine will prove to be a blessing to humanity, especially to farmers, as it will offer a slew of benefits, including no fuel costs and significantly low maintenance costs, saves time and effort, increases farm production, extraordinarily trustworthy, and long-lasting, environmentally sustainable, and improves the overall quality of living as income rises. We hope this study helps the potential young, dynamic researcher from various fields of science and engineering to get engrossed in this domain and further explore novel ideas to solve real-world challenges using cutting-edge utility technologies.

(a)

(b)

(c)

(d)

(e)

(f)

(g)
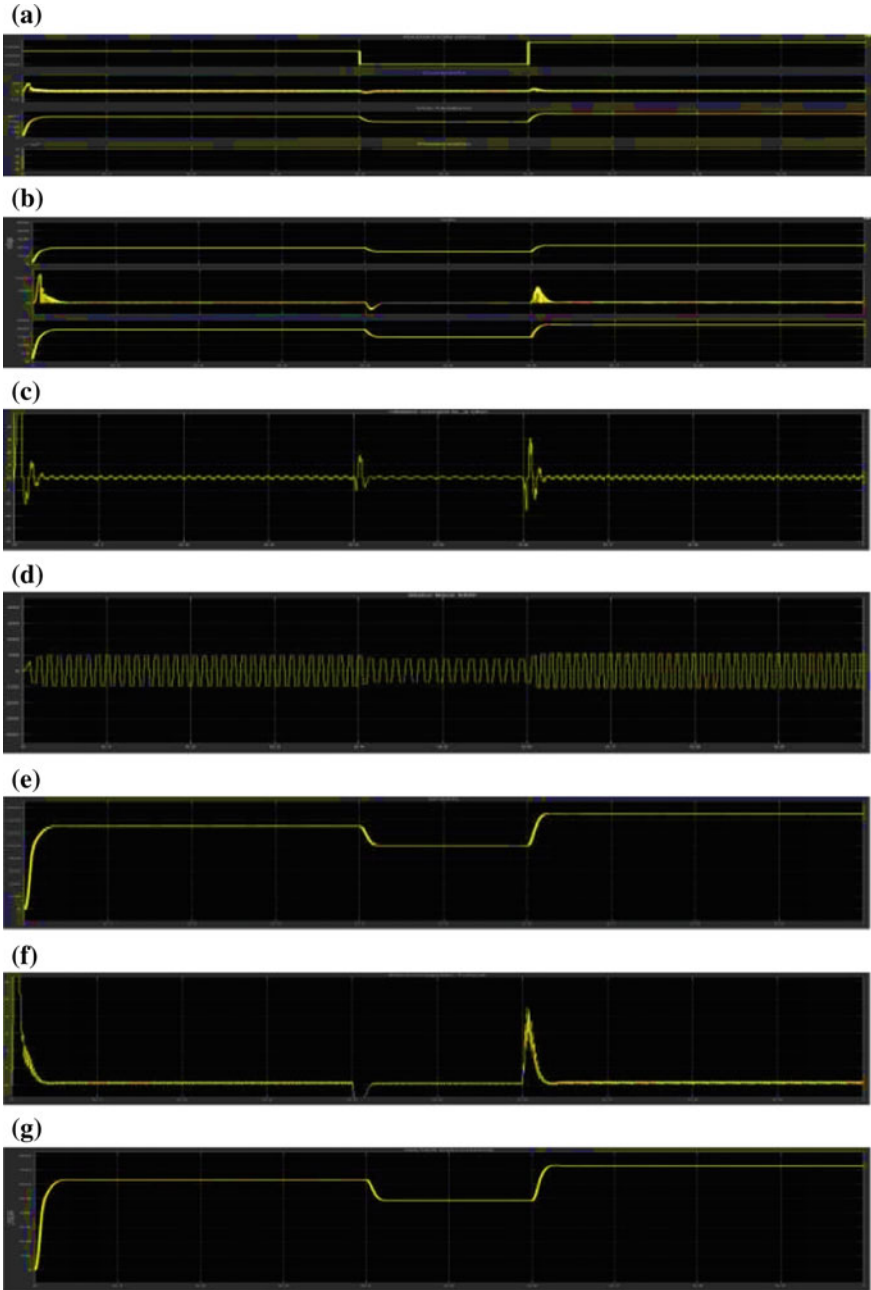
Fig. 8 **a** SPV array output waveform nature. **b** Zeta converter waveform nature. **c** Stator current output waveform nature. **d** Output waveform nature of back EMF. **e** Rotor speed output waveform nature. **f** Electromagnetic torque output waveform nature. **g** Water discharge output waveform nature.

References

1. Dubey M, Sharma S, Saxena R (2018) Control of solar power based soft switched boost converter for PMBLDC motor drive. In: 2018 IEEE International Conference on Power Electronics, Drives and Energy Systems (PEDES), pp 1–5. https://doi.org/10.1109/PEDES.2018.8707674

2. Gotkhinde SS, Jadhav PR (2017) Harmonic analysis of PMBLDC motor drive. In: 2017 Second International Conference on Electrical, Computer and Communication Technologies (ICECCT), pp 1–4. https://doi.org/10.1109/ICECCT.2017.8117966

3. Dubey M, Sharma S, Saxena R (2018) Z-source inverter based solar-power driven PMBLDC motor drive. In: 2018 IEEE 8th Power India International Conference (PIICON), pp 1–5. https://doi.org/10.1109/POWERI.2018.8704470

4. Joy J, Ushakumari S (2017) Energy harvestation and effective utilization by regenerative braking and motoring modes of operation in a PMBLDC drive system using FLC. In: 2017 IEEE Region 10 Symposium (TENSYMP), pp 1–5. https://doi.org/10.1109/TENCONSpring.2017.8069991

5. Fasil M, Mijatovic N, Jensen BB, Holboll J (2016) Finite-element model-based design synthesis of axial flux PMBLDC motors. IEEE Trans Appl Superconductivity 26(4):1–5, Art no. 0602905. https://doi.org/10.1109/TASC.2016.2537743

6. Manikandan K, Sivabalan A, Sundar R, Surya P (2020) A study of landsman, sepic and zeta converter by particle swarm optimization technique. In: 2020 6th International Conference on Advanced Computing and Communication Systems (ICACCS), pp 1035–1038. https://doi.org/10.1109/ICACCS48705.2020.9074164.

7. Banik A, Ranga J, Shrivastava A, Kabat SR, Marthanda AVGA, Hemavathi S (2021) Novel energy-efficient hybrid green energy scheme for future sustainability. In: 2021 International Conference on Technological Advancements and Innovations (ICTAI), pp. 428–433. https://doi.org/10.1109/ICTAI53825.2021.9673391

8. Das TK, Banik A, Chattopadhyay S, Das A (2019) FFT based classification of solar photo voltaic microgrid system. In: 2019 Second International Conference on Advanced Computational and Communication Paradigms (ICACCP), pp 1–5. https://doi.org/10.1109/ICACCP.2019.8882995

9. Banik A, Sengupta A (2021) Scope, challenges, opportunities and future goal assessment of floating solar park. In: 2021 Innovations in energy management and renewable resources, pp 1–5. https://doi.org/10.1109/IEMRE52042.2021.9386735

10. Das TK, Banik A, Chattopadhyay S, Das A (2019) Sub-harmonics based string fault assessment in solar PV arrays. In: Chattopadhyay S, Roy T, Sengupta S, Berger-Vachon C (eds) Modelling and simulation in science, technology and engineering mathematics. MS-17 2017. Advances in Intelligent Systems and Computing, vol 749. Springer, Cham. https://doi.org/10.1007/978-3-319-74808-5_25

11. Banik A, Shrivastava A, Potdar RM, Jain SK, Nagpure SG, Soni M (2022) Design, modelling, and analysis of novel solar PV system using MATLAB. Mater Today: Proc, vol 51, Part 1, pp 756–763, ISSN 2214-7853. https://doi.org/10.1016/j.matpr.2021.06.226

12. Das TK, Banik A, Chattopadhyay S, Das A (2021) Energy-efficient cooling scheme of power transformer: an innovative approach using solar and waste heat energy technology. In: Ghosh SK, Ghosh K, Das S, Dan PK, Kundu A (eds) Advances in Thermal Engineering, Manufacturing, and Production Management (ICTEMA 2020). Lecture Notes in Mechanical Engineering. Springer, Singapore. https://doi.org/10.1007/978-981-16-2347-9_17

Design, Development and Control of SCARA for Manufacturing Processes

Harshit K. Dave, Mihir D. Chanpura, Sanket J. Kathrotiya, Dixit D. Patolia, Dhaval D. Dodiya, and Paresh S. Kharva

1 Introduction

Industrial manipulators are used for doing repetitive tasks or tasks that require high precision and speed difficult to achieve by humans. Industrial robots automate many tasks that range from material handling to assembly, welding, painting and performing remote surgeries. SCARA robots' core concept is that they have a basic frame with high speed, accuracy and precision manipulation in the plane by using the third prismatic joint for pick and place missions. The SCARA is primary choice of industries due to high speed and accuracy. SCARA is commonly used for sorting, assembly, soldering, and pick and place applications [1]. This SCARA robot is suitable for applications where the manipulator must move in fixed coordinates. This paper presents the design and fabrication of SCARA that can be programmed and modified for various manufacturing processes like welding, drilling, 3D printing and EDM.

Urrea et al. [2] presented design, implementation and control of SCARA manipulator with 6 degrees of freedom. Ogulmuş et al. [3] presented the modelling and position control of SCARA type 3D printer which is simulated using MATLAB. Gamaralalage et al. [4] presented conversion of SCARA into hybrid manufacturing workstation which can perform additive and subtractive manufacturing processes using single setup. This also provides derived equations for inverse kinematics that are used in this paper. Shevkar et al. [1] fabricated 3 DOF SCARA using stepper motors and also investigated motor selection procedure and inter-step delay. Sinha et al. [5] developed Arduino code for extracting Cartesian coordinates from G-code

H. K. Dave · M. D. Chanpura (✉) · S. J. Kathrotiya · D. D. Patolia · D. D. Dodiya · P. S. Kharva
Mechanical Engineering Department, Sardar Vallabhbhai National Institute of Technology, Surat, Gujarat, India

H. K. Dave
e-mail: hkd@med.svnit.ac.in

551

which is used in this paper. The other studies [6–8] are about development and control of SCARA manipulator.

2   Development

Considering the applications of the robot, the following points are considered for the designing of the robot:

1. The robot should be as light and as rigid as possible, within the constraints.
2. It should be of 3 degree of freedom (DOF).
3. Load carrying capacity of the robot should be minimum of 5 kg.
4. The maximum reach of the manipulator should be approximately 600 mm.
5. Controlling resolution should be of 0.5 mm, and angular resolution should be less than 1°.

2.1   CAD Design

The CAD model of the SCARA manipulator is developed in SOLIDWORKS software. It is having a prismatic, revolute, revolute (PRR) structure. It is having kinematics of three degrees of freedom, 3-DOF. The outermost link of the arm is called an elbow link, and the inner link is called a shoulder link. The joint between those two is called an elbow joint, and the other pivot point is called a shoulder joint. The length of a shoulder link is 300 mm, length of an elbow link without any attachment is 258 mm, and a maximum vertical displacement of the manipulator is 325 mm (Fig. 1).

Two motors for the *X–Y*-direction actuation are placed near the pivot points of respective links. The motor for the elbow actuation is mounted on a mild steel plate which then is mounted on a 3D printed provision attached with a shoulder link. This complex design is introduced in order to provide a little adjustment during assembly to ensure the tightening of the belt (Fig. 2).

The vertical movement is provided by attaching the lead screw with spring flexible coupler with the stepper motor. The lead screw with 8 mm of the diameter and 2 mm of pitch is used for vertical power transmission. By the belt pulley mechanism, the power from the motor is transmitted to the link as shown in Fig. 3. According to the required speed reduction and torque amplification, pair of pulleys resulting in speed ratio of 3:1 is selected. Pulleys are having 20 and 60 teeth, respectively, for motor and linkage. Timing belts and timing pulleys are used here in order to avoid any slip, which is necessary for high precision applications.

A vertically reciprocating platform is attached with a stationary column with a lead screw and supported with the help of linear bearings on aluminium rods. The whole platform can be moved up/down with the help of stepper motor mounted on
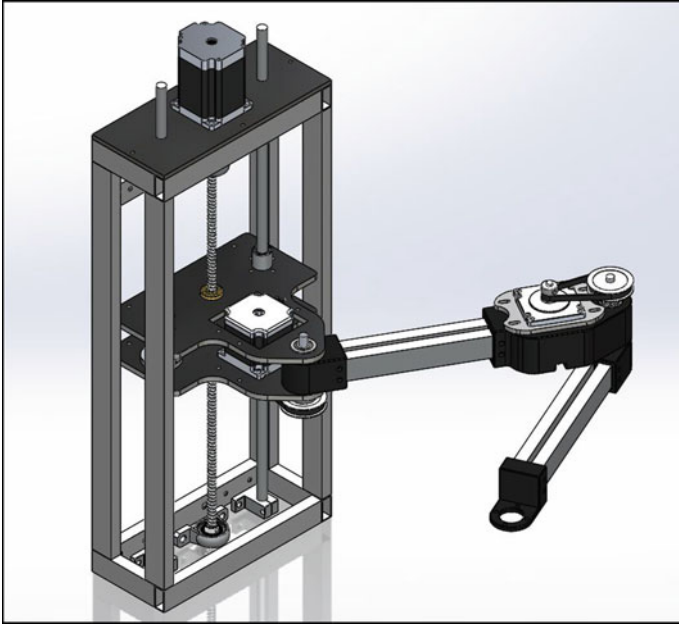
Fig. 1 Developed CAD design of SCARA
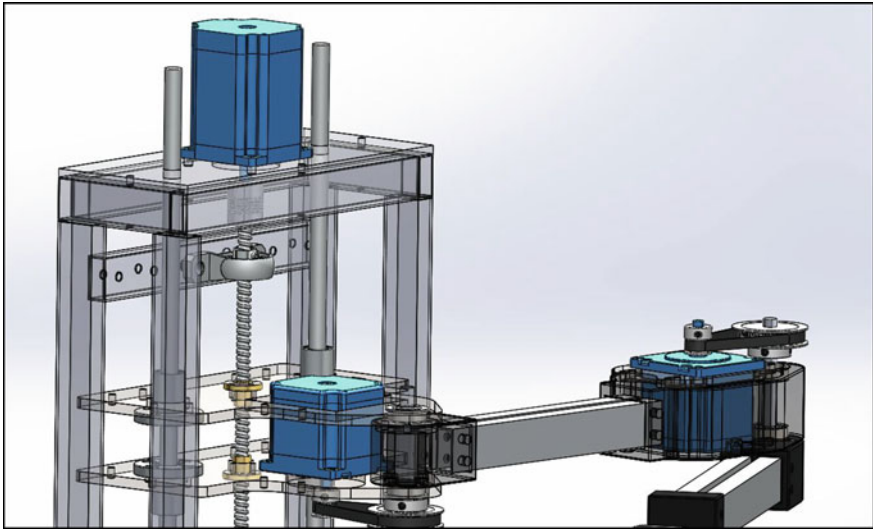
Fig. 2 Motor placement
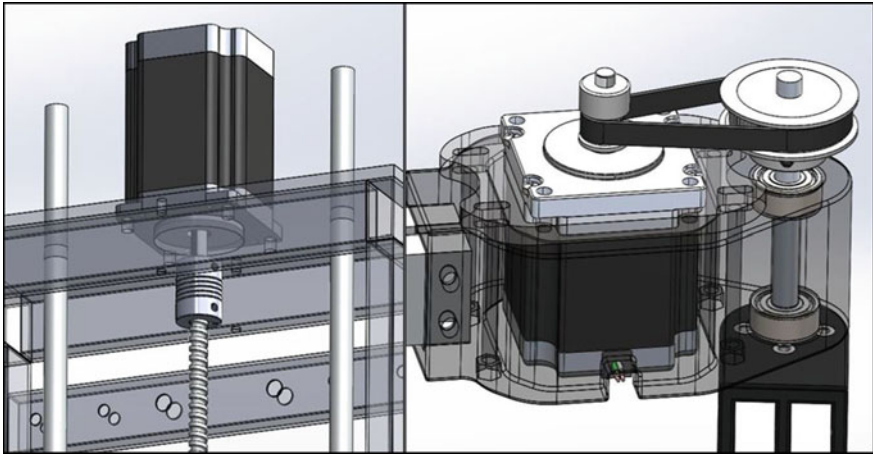
Fig. 3 Power transmission

a top. The end effector of the manipulator is designed in such a way that it can be attached with different attachments of tools required for the job.

2.2 Attachments

Usually, robotic arms are used for doing single type of task, because there is no mechanism for changing the end effector. In this design, different types of tool can be attached as per requirement of any particular task (Figs. 4 and 5).
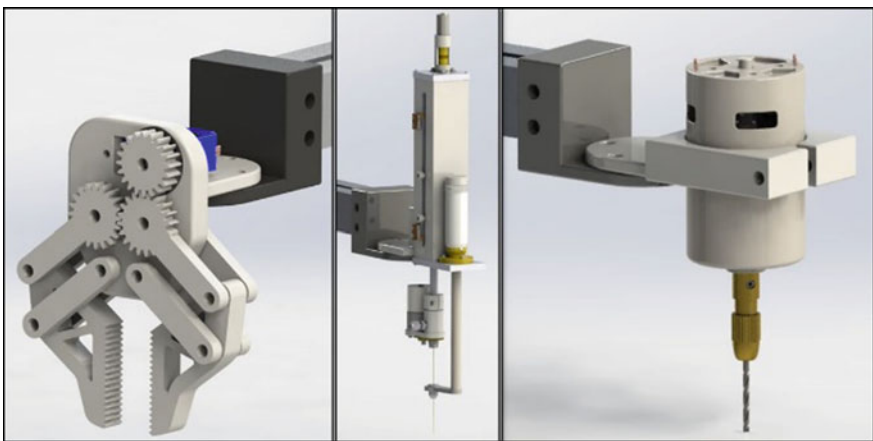
Fig. 4 (1) Gripper attachment, (2) EDM attachment, (3) Drilling attachment
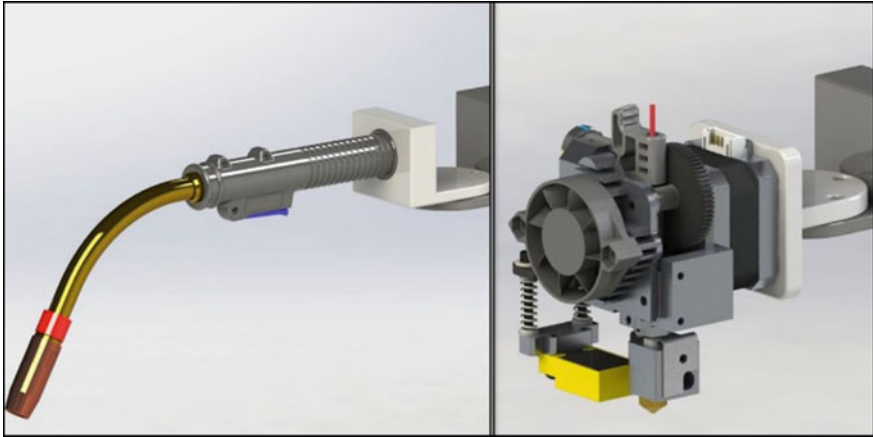
Fig. 5 (4) Welding attachment, (5) 3D Printing attachment

2.3 Structural Analysis

An important part of the manipulator is the arm. In this design, the arm is a combination of three parts, two of which are 3D printed parts for the joints, and the other part consists of two parallel $1'' \times \frac{1}{2}''$ aluminium box sections. The acting load at the end effector due to the attachment or the operational conditions directly acts upon these aluminium links. Thus, finite element analysis is carried out for these links using SOLIDWORKS software (Figs. 6, 7, 8, 9 and 10; Tables 1 and 2).
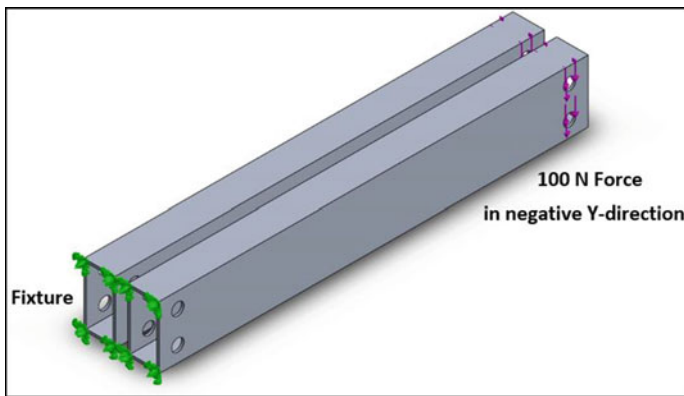
Fig. 6 Fixture and load
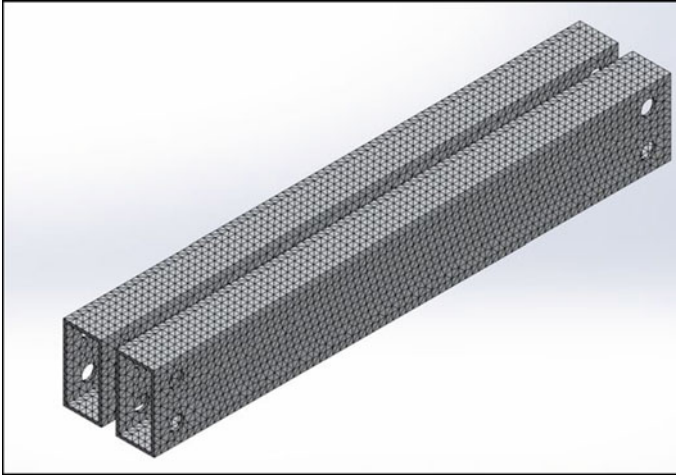
Fig. 7 Meshed model
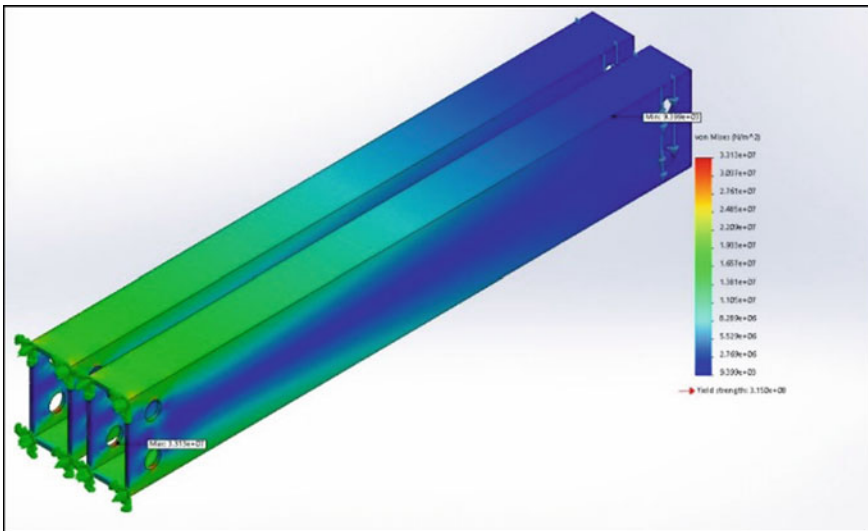
Fig. 8 Von Mises stresses

2.3.1 Study Results

The minimum factor of safety – FOS is found out to be 9.51, considering that, the design is declared safe (Table 3).
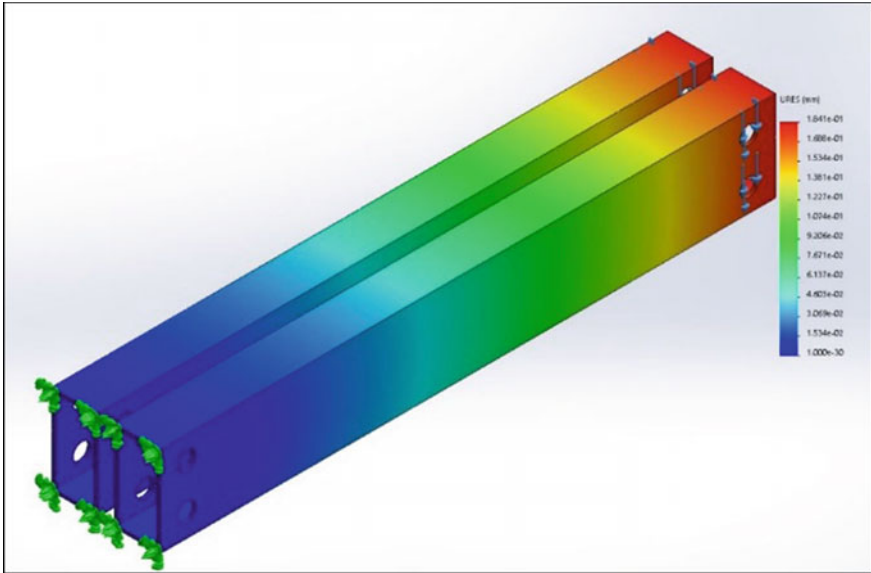
Fig. 9 Resultant displacement
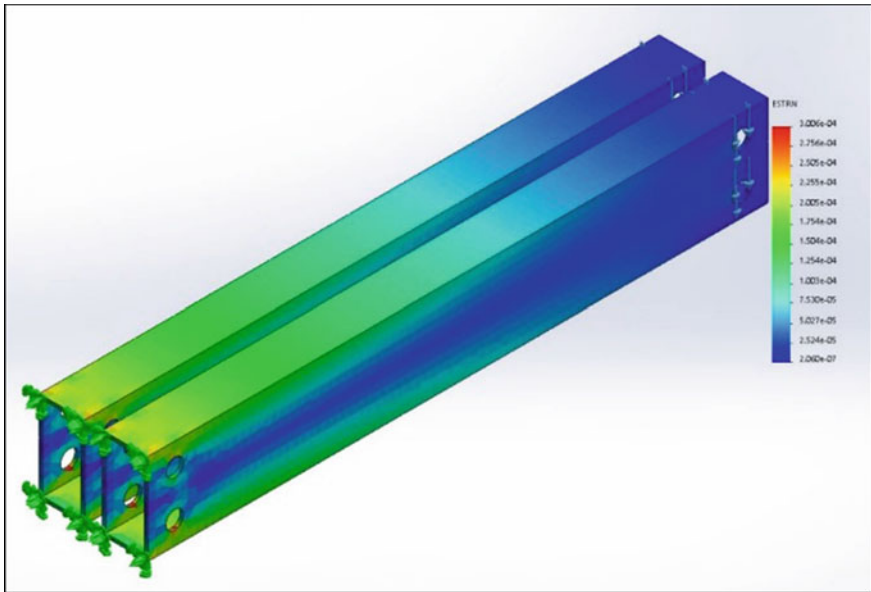
Fig. 10 Equivalent strain

Table 1 Material properties

Parameter	Value
Model type	Linear elastic isotropic
Default failure criterion	Max von Mises stress
Yield strength	3.15e+08 N/m^2
Tensile strength	3.8e+08 N/m^2
Elastic modulus	7.9e+10 N/m^2
Poisson's ratio	0.34
Mass density	2680 kg/m^3
Shear modulus	2.6e+10 N/m^2

Table 2 Mesh information

Parameter	Value
Jacobian points	4 Points
Element size	2.2346 mm
Tolerance	0.1117 mm
Total nodes	60,525
Total elements	29,903
Maximum aspect ratio	6.4142

Table 3 FEA study results

Name	Min value	Max value
Von Mises stress	9.399e+03 N/m^2	3.313e+07 N/m^2
Resultant displacement	0.000e+ 0 mm	1.841e−01 mm
Equivalent strain	2.06e−07	3.01e−04
Factor of safety—FOS	9.51e+00	3.35e+04

2.4 Construction of SCARA

Materials are selected for manufacturing the SCARA based on their ease of availability, cost, strength vs weight ratio and manufacturability. The manipulator is designed considering some non-conventional manufacturing technologies like additive manufacturing technology, laser cutting as well as conventional technology such as machining. Fused deposition modelling (FDM) with polylactic acid (PLA) is used for 3D printing some components at the joints and the entire gripper mounted on the end effector. For some parts, we have used laser-cut mild steel plates. The vertical stationary column on which the whole arm is mounted is made of $1'' \times \frac{1}{2}''$ rectangular aluminium box section (Fig. 11).

Fig. 11 Constructed SCARA
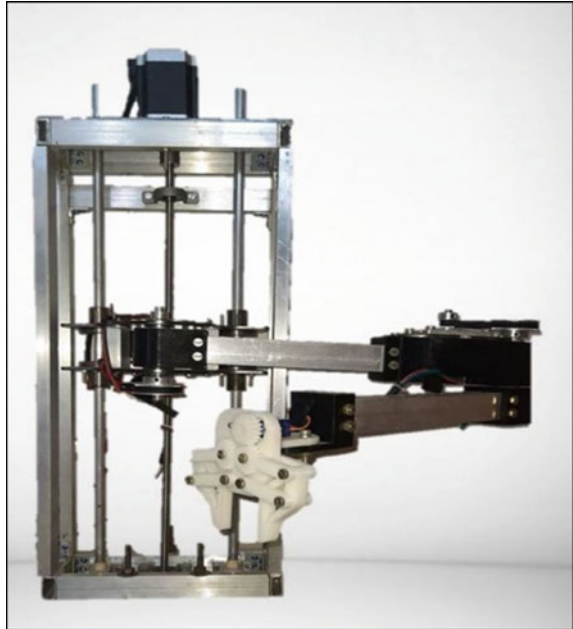
3 Hardware

Considering the research objective to make SCARA available for different manufacturing processes, an easily reprogrammable and open-source control unit is required; thus, Arduino Mega with an 8-bit ARMS processor is used as a processing unit of SCARA. After considering the requirement of high torque and precision, NEMA 23 bipolar motor is selected for all actuation. Specification of NEMA 23 is given in Table 4.

Based on high rated current 2.8A required for NEMA 23 TB6600 stepper motor driver is selected. The TB6600 drivers enable the motor to micro-step in $1, \frac{1}{2}, \frac{1}{4}, \frac{1}{8}, \frac{1}{16}, \frac{1}{32}$ steps.

Table 4 NEMA 23 motor specification

Parameter	Value
Holding torque	1.9 N m (19 kg cm), 1 N m (10 kg cm)
Step angle	1.8°
Rated current	2.8 A per phase
Resistance of coil	1.13 Ω
Weight	1 kg, 0.6 kg
Shaft diameter	6.35 mm

4   Control Logic

Following control logic can be used for different manufacturing operations (Fig. 12).

4.1   *Generating G-code and Extracting Coordinates from G-code*

G-code is generated from any G-code firmware like Cura or any other CAM software. For extracting coordinates from G-code, inbuilt library functions of Arduino will be used. One string line of G-code is considered one string. One string is also divided into substring, consisting of G01, X12, Y13, etc. The number after G determines the type of command. Numbers after X, Y and Z determine the position of the end effector or tool.

Fig. 12   Control logic
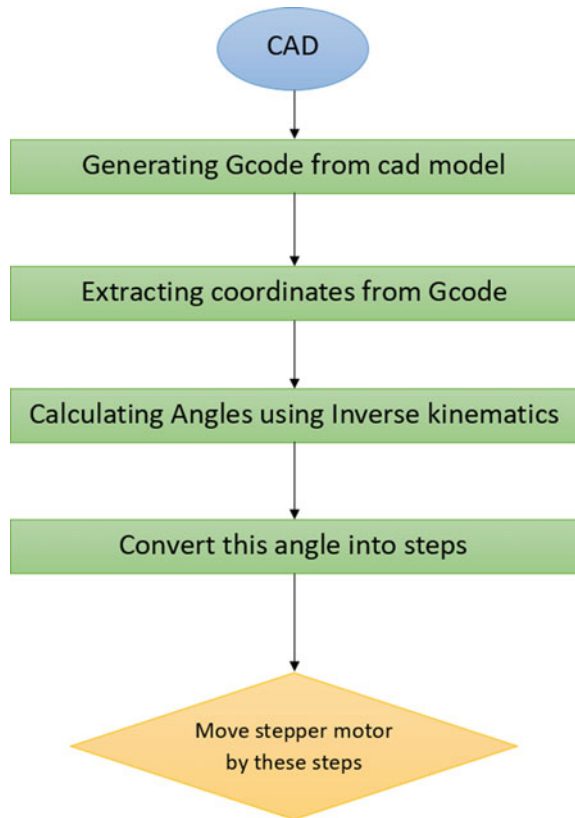
Fig. 13 Coordinate extraction logic

```
1
2  for (int i=1;i<a;i++)
3  {
4      if (d.charAt(i)=='G')
5      {
6      cmd=(d.substring(i+1).toInt();
7
8      }
9
10      if(cmd==1 || cmd==0)
11      {
12        if(d.charAt(i)=='X')
13        {
14          x=(d.substring(i+1)).toFloat();
15        }
16
17        if(d.charAt(i)=='Y')
18        {
19          y=(d.substring(i+1)).toFloat();
20        }
21
22        if(d.charAt(i)=='Z')
23        {
24          z=(d.substring(i+1)).toFloat();
25        }
26      }
27  }
```

For extraction of coordinates from G-code given logic (Fig. 13) will be used [5]. If in one string 'G' character is found, then the character next to the G will be saved in the cmd variable (line 6). If G01 or G00 command is used, then the value of cmd will be 1 or 2, which will be checked in line 10. The next substring starts with the character 'X' (line 12). The value after 'X' will be saved in the 'x' variable (line 14). The same computation is done for the y-coordinate and z-coordinate. These coordinates are given as input to the inverse kinematics function to find the angle of two links. If G02 or G03 command is used, the points of the arc can be found from interpolation.

4.2 Inverse Kinematics

Equations for θ_1 and θ_2 are as below [4] (Fig. 14),

$$\theta_2 = \cos^{-1}\left[\frac{P_x^2 + P_y^2 - L_1^2 - L_2^2}{2L_1L_2}\right] \qquad (1)$$

$$\theta_1 = \cos^{-1}\left[\frac{P_x(L_1 + L_2C_2) + P_y(L_2S_2)}{P_x^2 + P_y^2}\right] \qquad (2)$$

Fig. 14 Line diagram of
SCARA
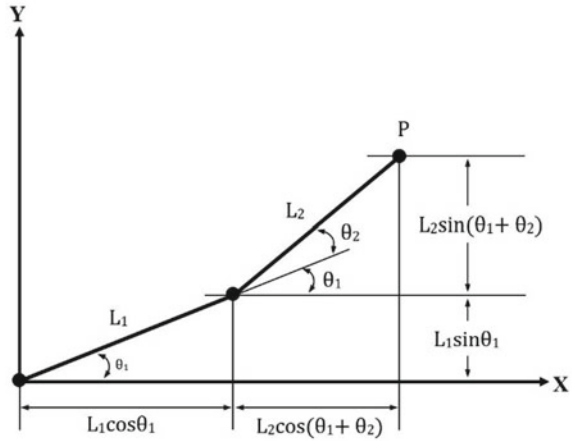
where $C_2 = \cos\theta_2$ and $S_2 = \sin\theta_2$.

4.3 Converting Angle into Steps

For one rotation of the stepper motor shaft, 200 steps are required if micro-steeping
is not used. However, if micro-stepping with 16 sub-steps is used, then to complete
one revolution of the motor shaft, 3200 steps (16 * 200 steps) will be required. So, it
can be concluded that a 1-degree rotation of the shaft will need 3200/360 steps. We
will use belt transmission with a transmission ratio of 1: 3, so to rotate the link by
1-degree to 3-degree rotation of the motor will be required. So, 3 * 3200/360 steps
per 1-degree revolution of link. So, by using this concept, steps will be calculated
for any θ_1 or θ_2.
   if micro-stepping with 16 sub-steps is used,

$$\text{steps} = \frac{\text{angle} \times 3 \times 3200}{360} \tag{3}$$

if micro-stepping is not used,

$$\text{steps} = \frac{\text{angle} \times 3 \times 200}{360} \tag{4}$$

4.4 Moving Stepper Motor by These Steps

The controller generates the pulse as output. This output is given to the stepper motor driver as input. The stepper motor generates current with pulses, as shown in the figure. Speed of the stepper motor increases with an increase in the frequency of these pulses. The circuit diagram made using fritzing software, for controlling the NEMA 23 stepper motor using the TB6600 driver is shown in Fig. 15.

5 Result and Validation

SCARA can be simplified and can be represented by a line diagram as shown in Fig. 14. The line diagram has two links, shoulder link L_1 and elbow link L_2. Point P represents the position of an end effector. Now using SOLIDWORKS, we can find the angles required to move (θ_1 and θ_2) for various test positions. We can also find θ_1 and θ_2 for same positions using Arduino code (Fig. 16).

This code can be used for debugging as well as validation. We can compare deviation from the actual position of the end effector (Figs. 17 and 18).

Since the angles match the data from the SOLIDWORKS software and the Arduino application, we may conclude that SCARA does not need more debugging.
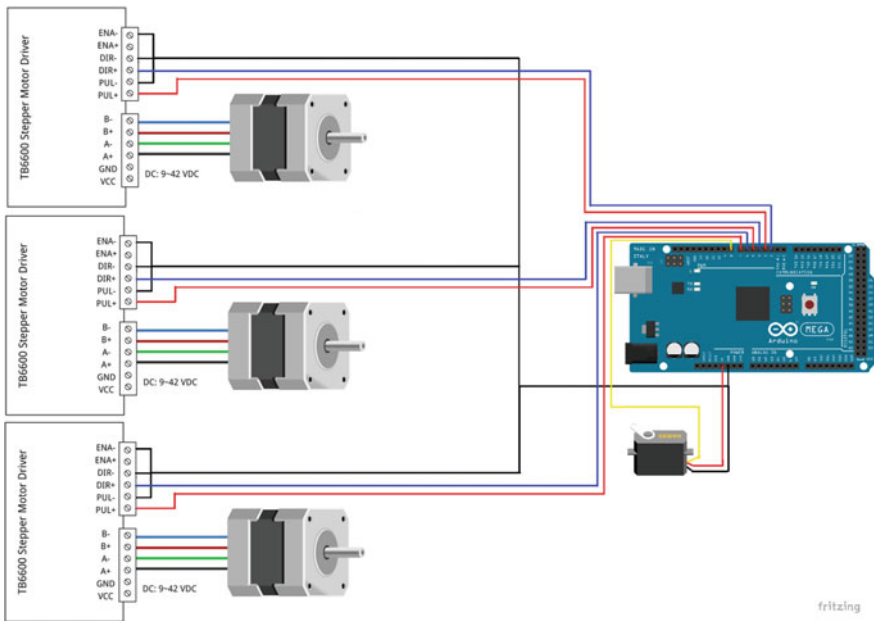
Fig. 15 Circuit diagram

```
1   #include <AccelStepper.h>
2   AccelStepper Soulder(1,3,2);
3   AccelStepper Elbow(1,4,7);
4   AccelStepper zAxis(1,5,8);
5   float theta1aDegree;
6   float theta2aDegree;
7   void setup() {
8     float px = 0;
9     float py = 550.0;
10    float pz = 100.0;
11    float screw_pitch = 4.0;
12    float l1=300.0;
13    float l2=250.0;
14    float gear_ratio=3;
15    float STEPS = 1600.0; // Number of steps on stepper motor
16    float ctheta2=(px*px+py*py-l1*l1-l2*l2)/(2*l1*l2);
17    float stheta2=sqrt(1-ctheta2*ctheta2);
18    float ctheta1 = (px * (l1 + l2 * ctheta2) + py *l2 * stheta2) / (px*px + py*py);
19    float theta1ar=atan2(sqrt(1-ctheta1*ctheta1),ctheta1);
20    float theta1br=atan2(sqrt(1-ctheta1*ctheta1)*(-1),ctheta1);
21    float theta1a=theta1ar*STEPS/(2.0*M_PI);
22    theta1aDegree =theta1ar*360/(2.0*M_PI);
23    float theta1b=theta1br*STEPS/(2.0*M_PI);
24    float theta2ar=atan2(sqrt(1-ctheta2*ctheta2),ctheta2);
25    float theta2br=atan2(sqrt(1-ctheta2*ctheta2)*(-1),ctheta2);
26    float theta2a=theta2ar*STEPS/(2.0*M_PI);
27    theta2aDegree =theta2ar*360/(2.0*M_PI);
28    float theta2b=theta2br*STEPS/(2.0*M_PI);
29    Soulder.setSpeed(1600.0);
30    Elbow.setSpeed(1600.0);
31    zAxis.setSpeed(1600.0);
32    Soulder.setMaxSpeed(1600.0);
33    Elbow.setMaxSpeed(1600.0);
34    zAxis.setMaxSpeed(1600.0);
35    Soulder.setAcceleration(800.0);
36    Elbow.setAcceleration(800.0);
37    zAxis.setAcceleration(800.0);
38    Soulder.moveTo(theta1a);
39    Elbow.moveTo(theta1a);
40    zAxis.moveTo(pz*screw_pitch);
41  }
42  void loop() {
43    Serial.println('Angle of first link');
44    Serial.println(theta1aDegree);
45    Serial.println('Angle of second link');
46    Serial.println(theta2aDegree);
47    Soulder.run();
48    Elbow.run();
49    zAxis.run();
50  }
```

Fig. 16 Arduino code for point navigation

Fig. 17 Comparison of data extracted from Arduino with data extracted from SOLIDWORKS for L_1
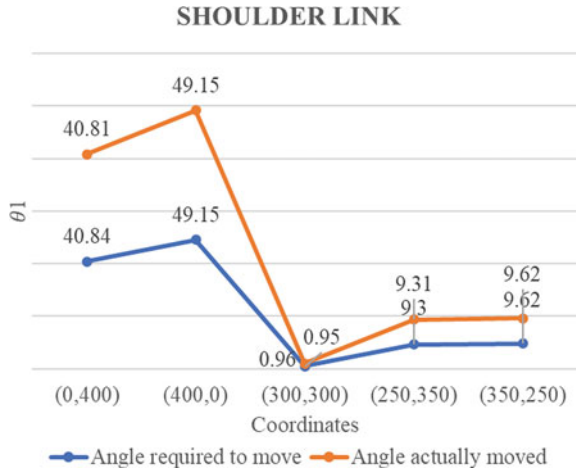
Fig. 18 Comparison of data extracted from Arduino with data extracted from SOLIDWORKS for L_2
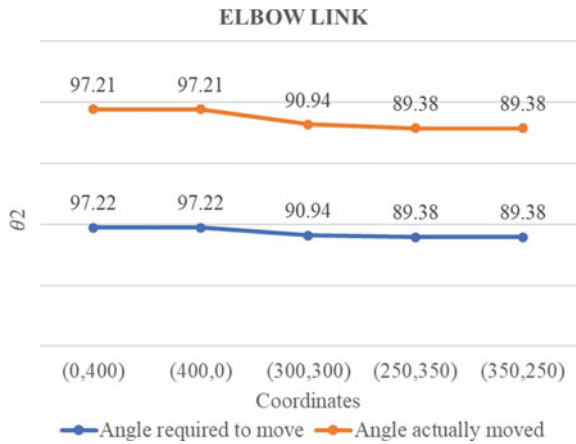
5.1 Test Results of SCARA

Testing of SCARA is done by taking various coordinates as inputs and then observing final position of end effector.

Following are result images of end effector positions changing from initial position (0,0) to final position (300,300) mm (Fig. 19).

Following are result images of the end effector positions changing from an initial position (0,0) to final position (424,424) mm (Fig. 20).
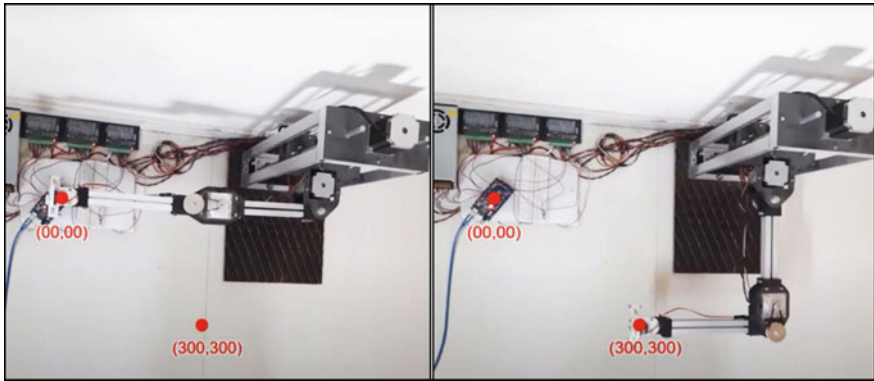
Fig. 19 (1) (0,0) Position, (2) (300,300) Position
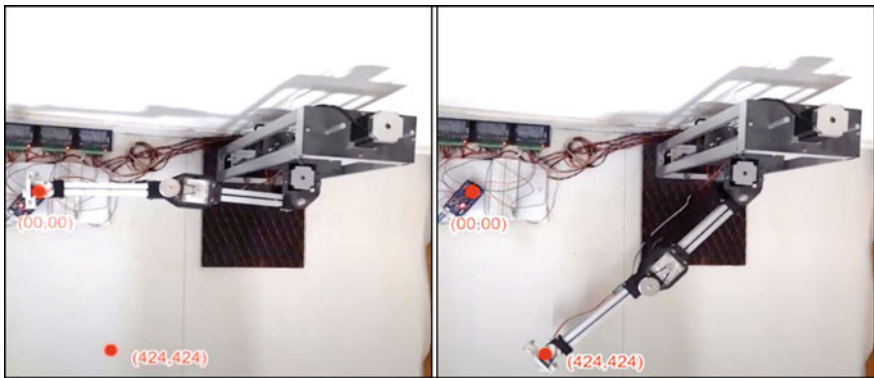
Fig. 20 (1) (0,0) Position, (2) (424,424) Position

6 Conclusion

The aim, which was to construct a SCARA robotic arm that could be used in manufacturing processes like spot welding or drilling, was accomplished. SCARA may also be reprogrammed to adapt to a wide range of production processes and functions, according to the research. This may be very useful in an industrial setting.

However, shown below, there is scope for improvements in the SCARA robotic arm system's design and implementation,

1. The robotic arm's degrees of freedom can be expanded in order to extend its workspace and thereby make it more flexible.
2. Motors with higher torque ratings can be used to operate the joints, ensuring that the robotic arm stays in place even though the motors are not powered by electricity.

3. Adding proximity sensors and/or camera with image processing to the robotic arm can allow for object recognition and collision avoidance.
4. The SCARA robotic arm can be controlled wirelessly using Bluetooth module or Wi-Fi module.

References

1. Shevkar P, Bankar S, Vanjare A, Shinde P, Redekar V (2019) A desktop SCARA robot using stepper motors, pp 132–139
2. Urrea C, Cortés J, Pascal J (2016) Design, construction and control of a SCARA manipulator with 6 degrees of freedom. J Appl Res Technol
3. Ogulmuş AS, Çakan A, Tınkır M (2016) Modeling and position control of SCARA type 3D printer. Model. Position Control SCARA Type 3D Print 5(12):140–143
4. Gamaralalage S, Jesus P, Šormaz D (2018) Conversion of the SCARA robot into a hybrid manufacturing workstation. Procedia Manuf 17:62–69
5. Sinha AK (2017) Development of arduino code for SCARA robotic arm. Int J Res Eng Technol 06(04):45–50
6. Jha P, Biswal BB (2014) A neural network approach for inverse kinematic of a SCARA manipulator. IAES Int J Robot Autom 3(1):52–61
7. Ghuffar S, Iqbal J, Mehmood U, Zubair M (2014). Design, simulation and fabrication of a 5-dof robotic arm (with implementation of inverse kinematics) ORIDATE Ademola Ayodeji
8. Manasra A, Salaymeh A, Natsheh Y (2018) Design, control and implementation of SCARA robot for sorting missions with machine vision

Design and Development of Dewatering Screw Press

P. G. Chitte, Prajwal Tapsi, and Bhagyesh B. Deshmukh

1 Introduction

Municipal solid waste that contains water as its constituent causes big problems in waste disposal or proceeding in any kind of dewatering. A huge quantity of sludge is generated from industry, households and agriculture. Treating the waste as a part of the household waste by anaerobic digestion has gained consideration both from the public and municipalities. There are numerous methods used for pre-treatment of the sludge by screw press, pressure press, disc screen, shredder magnet and food waste disposers are most commonly used. Particularly, there is a trend in using new pre-treatment methods as steps towards sustainable sludge treatment.

The dewatering screw press is one of the most efficient and widely accepted ways to separates liquids from solids. Belt press, centrifuge or filter paper press are usually replaced by screw press as it is more efficient in many aspects as compared to these machines. Dewatering screw press consists of a slow revolving screw that accomplishes dewatering by continuous compression of the sludge between a screen and pressure plate with the help of gravitational drainage of the filtrate [1].

Other than using screw presses for dewatering cattle dung, it can also be used as an oil expeller [2]. Oil processing, uses of biodiesel fuels, pressing soybeans or babassu nuts, screw press, can be used. Various innumerable oilseeds have been processed for over 120 years. Screw presses are now used in different applications of industry such as starch/sorbitol, processing of food and paper and also in the handling of material involving screw conveyor in dairies [3].

P. G. Chitte · P. Tapsi (✉) · B. B. Deshmukh
Mechanical Engineering Department, Walchand Institute of Technology, Solapur, Maharashtra, India

2   Literature Review

Dewatering screw press consists of a slow revolving screw that accomplishes dewatering by continuous compression of the sludge between a screen and pressure plate with the help of gravitational drainage of the filtrate. Materials that tend to be difficult to dewater and leading to trapping a large amount of liquid filtrate in them are dewatered using screw presses.

Feed is transferred manually or with the help of a pump into the screw via feed inlet. Feed inlet lets us control the flow to the sludge before entering the other section of the screw press by optimizing the flow using an overflow. The feed sludge can be pre-treated according to the requirement or processed raw to increase the efficiency of the screw press. Various pre-treatment processes for feed are used, e.g. flocculation. This is strictly dependent on the type of feed and the efficiency required.

The helix of the screw is surrounded by plates that are self-cleaning filter or mesh-type filter. This ensures that continuous filtration takes place while the screw is rotating. Concerning AOS treatment solutions having a dewatering screw process in an industrial or municipal wastewater treatment plant can increase the efficiency of the amount of water recycled for use, and decreasing the volume of dewatered sludge. This efficient wastewater treatment solution is one worth considering for an area that needs to conserve water or treat waste efficiently [3].

There are some of the features of dewatering screw press referred from Engr. Dr I. Nnanna, Okeahialam, Solomon I. and Okoro Humphrey O [4]

a.   Very simple processing.
b.   Very low investment in the system.
c.   Energy-efficient for dewatering.
d.   The system can be programmed to make the operation more convenient.
e.   Different flocculating that makes sludge dewatering easier.
f.   Uniform and accurate dispensing, saving costs.

From Engr. Dr I. Nnanna, Okeahialam, Solomon I. And Okoro Humphrey O, in the technology of screw press, a coarse screw is implied for converting drive wheel rotation into a greater force moment. The screw press body consists of long cylindrical material that holds and supports the filter, surrounding a screw assembly with a fixed diameter right from the feed to discharge. Full-length screw with flights is having constant pitch combined with a cylindrical container having a constant diameter.

From the feed end, the initial section of the dewatering drum is called the thickening zone, where the initial solid–liquid separating process takes place from where the majority of the filtrate is discharged through the screen. The initial section is having a filtration region with low pressure. Screw pitch and the gap between the cylindrical barrels increase its internal pressure. And at the end of the screw, the pressure plate increases the pressure, to discharge dry sludge cake at the discharge end.

As the sludge moves through the press with the help of a revolving screw, the feed slurry is pushed into the open end section of the press known as the dewatering

zone where the screw is present. This is the thickening region of the press, where the sludge accumulates resulting in increased pressure over the barrel and the pressure plate simultaneously for maximum dewatering through the screen.

In the final squeezing section, at the discharge end of the screw, a manual pressure plate restricts the discharge of the filter cake, by applying a back pressure that enhances the dewatering of the cake. A small gap between the screen and the pressure plate allows the dewatered cake to escape in the form of dewatered sludge. This continuous compression by the screw results in efficient dewatering [5].

3 Design of Dewatering Screw Press

3.1 Design Considerations

Material Considerations

a. The density of material stainless steel AISI 302- 65 kg/m^3
b. Yield stress of SS (δo) $=$ 386.105 N/mm^2
c. The material factor of cow dung $=$ 1
d. Ultimate tensile strength $=$ 715.7 N/mm^2

Design Considerations:

a. Flight diameter and shaft diameter as 140 and 70 mm as low capacity are required as output.
b. Speed of screw (n) $=$ 60 rpm, as high compression is required along with high torque

   The slower the screw speed, the efficient the dewatering. Prolonged residence time in the screened area resulting from lower screw speed allows the sludge for more thorough dewatering. This also minimizes the chances of clogging, as the speed is less the amount of material accumulation is considerably low as compared to that of the accumulation of the sludge at a higher speed and thus, unfortunately, resulting in a reduced capacity. Higher speed can result in inefficient dewatering and stress on the gearbox increasing the chances of clogging and failure.
c. The factor of inclination (C) $=$ 1, as it depends on the angle of the screw (β) to horizontal (Table 1)

d. Loading efficiency (Ψ) value for cow dung should be taken from 0.25 to 0.3 or 25–30% as cow dung is a mildly abrasive material (Fig. 1).

Table 1 Factor of inclination [5]

β degrees	0	5	10
C	1.0	0.9	0.8
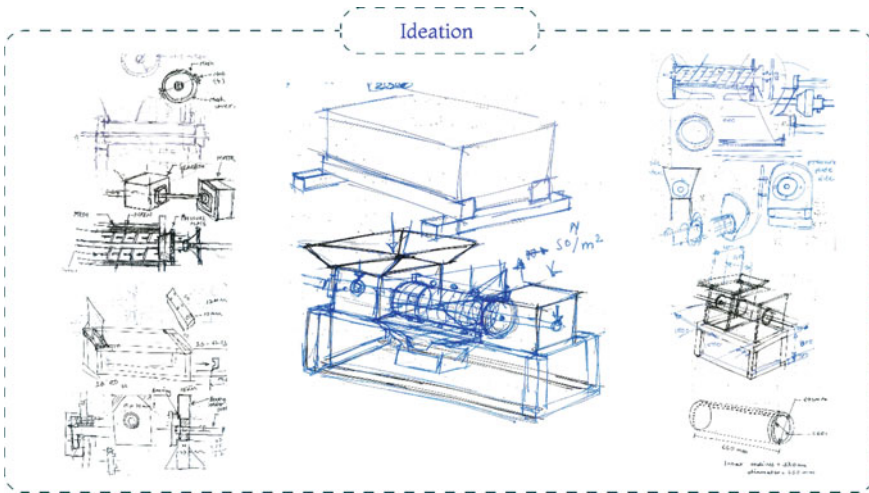
Fig. 1 Ideation process

3.2 Mathematical Calculations

Design of a screw press for dewatering of cattle dung slurry is carried out by the following data [5, 6].

The diameter of the screw or flight diameter conveyor is the overall outer diameter of the screw which is seen in image five above represented by "D"; On the other hand, shaft diameter is the inner diameter of the screw where flights are attached represented by "d" and pitch is the distance between screw threads and is commonly used with inch sized products and specified as threads per inch represented by "S" (Table 2).

With the help of the above mathematical calculations, we can say that the design safe.

Table 2 Result from mathematical calculations

S. No.	Parameter	Output
1	Capacity of screw	857 kg/h
2	Power required to drive screw	2.595 Kw
3	Torque received on the screw shaft	48.75 Nm
4	Load propulsion speed	0.105 m/s
5	Load per metre length of the screw	10^3 N
6	Design of the pressure to be developed by the screw thread	103 N/m^2
7	Design for pressure of the mesh	20.412 $\times$ 106 N/m^2
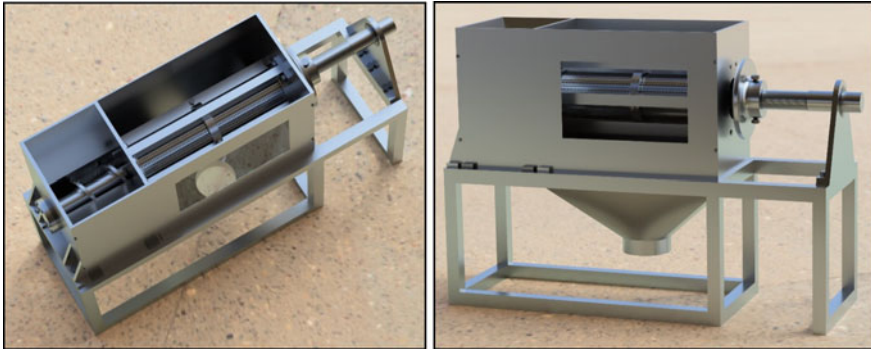
Fig. 2 3D modelling of dewatering screw press

3.3 Three-Dimensional Modelling of Dewatering Screw Press

Modelling, rendering and drafting of dewatering screw press are carried out in Autodesk Fusion 360 (Fig. 2).

3.4 Computer-Aided Drafting of Dewatering Screw Press

Computer-aided drafting has been developed of dewatering screw press for more detailing and better understating (Fig. 3).

4 FEA Analysis of Dewatering Screw Press

Following are the FEA results generated by Fusion 360 for the analysis of the screw, screw and pressure plate and the base frame for the two materials: stainless steel 302 (SS 302) and stainless steel 304 (SS 304) (Tables 3 and 4).

Static Structural Analysis—Screw (Stainless Steel 304)

See Figs. 4, 5, 6 and 7.

Static Structural Analysis—Screw (Stainless Steel 302)

See Figs. 8, 9, 10, 11 and Table 5

From the results above, we can conclude that the best-suited material for the screw is stainless steel 302. These results also state that the screw can sustain all the loads required (considering the FOS), derived from the mathematical calculations safely, and hence we can conclude that the design for the screw is safe.
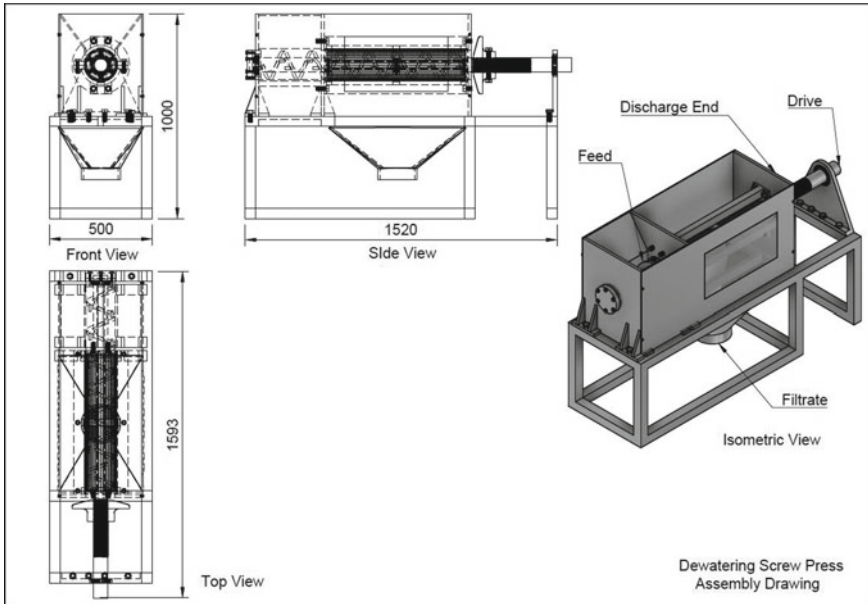
Fig. 3 Computer-aided drafting of dewatering screw press

Table 3 Material of construction for screw

Material properties	Stainless steel 302	Stainless steel 304
Yield strength	386.105 Mpa	215 Mpa
Tensile strength	715.672 Mpa	505 Mpa
Density	8000 kg/m^3	8000 kg/m^3

Table 4 Loads for screw

Loads	Magnitude	Direction
Gravity	9.807 m/s^2	$-Z$
Pressure	392,800 Pa	Perpendicular to screw Flights
Moment	150 N m	$-Y$
Hydrostatic pressure	655 kg/m^3	Over the screw length

5 Conclusion

From the above design process, we can conclude that,

1. A screw press has been designed for separating solids and liquid contained in the cow dung slurry at a rate of 857 kg/h, with 60 rpm, at 30% of loading capacity (as suggested in manufacturer CatLog) with a factor of safety of 2.5.
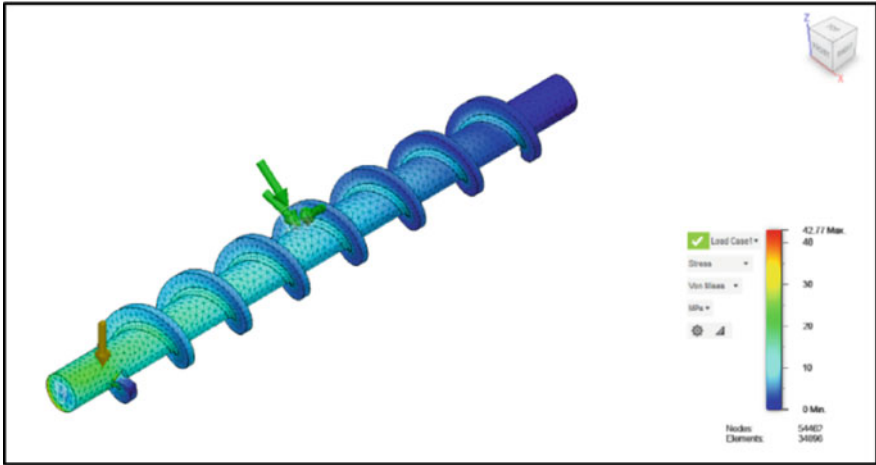
Fig. 4 Von Misses stress SS 304
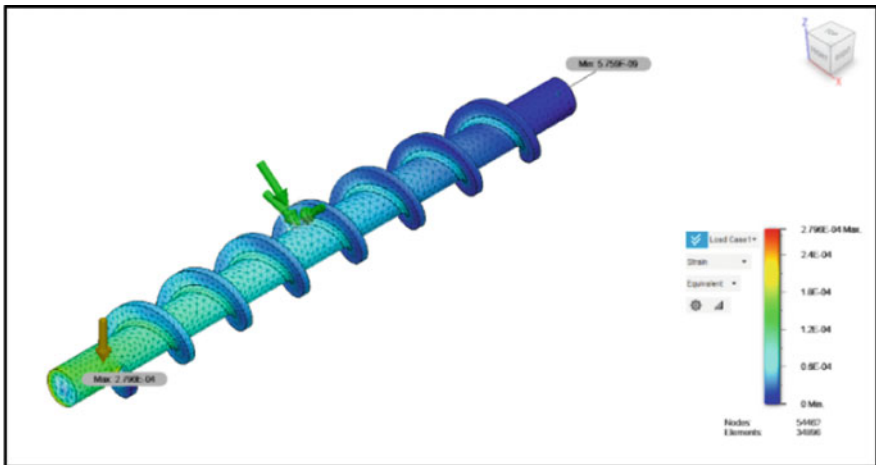
Fig. 5 Strain SS 304

2. A three-phase 5 HP motor to be used coupled with a reduction gearbox to provide a minimum necessary torque of 48.75 Nm to attain the required capacity.
3. Perforation size for the screen is found to be Ø 3 mm as optimum in size.
4. Design equipment should be used for generating a slurry of dry biomass with a moisture content of 36% to the weight to that of initial moisture content of up to 70% of weight before dewatering the biomass.
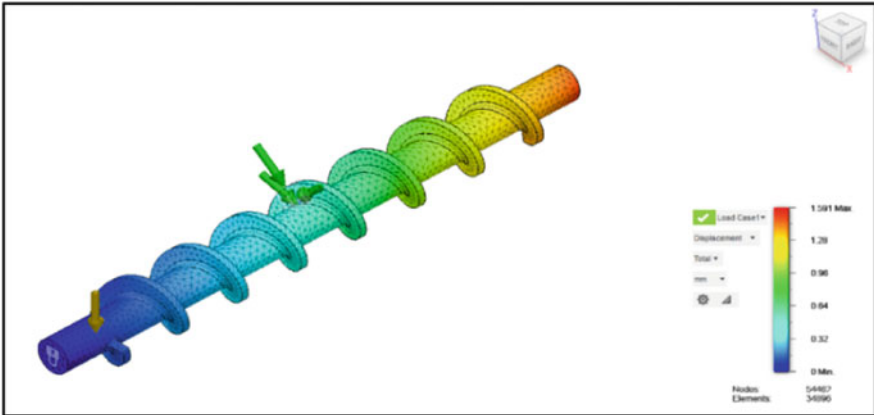
Fig. 6 Displacement SS 304
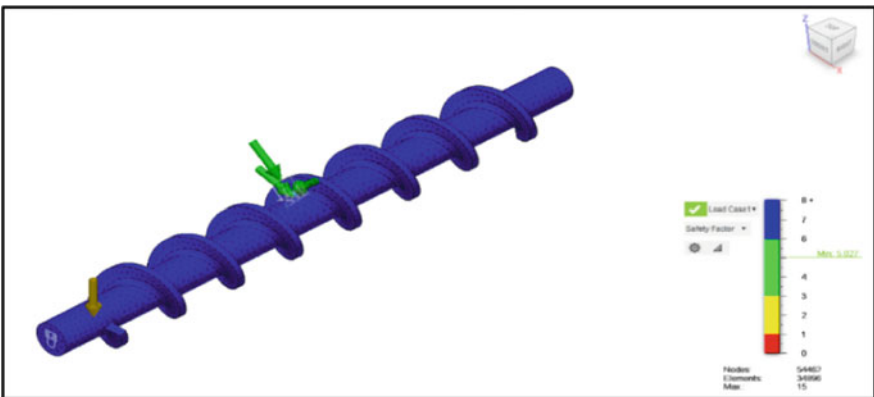
Fig. 7 Factor of safety SS 304
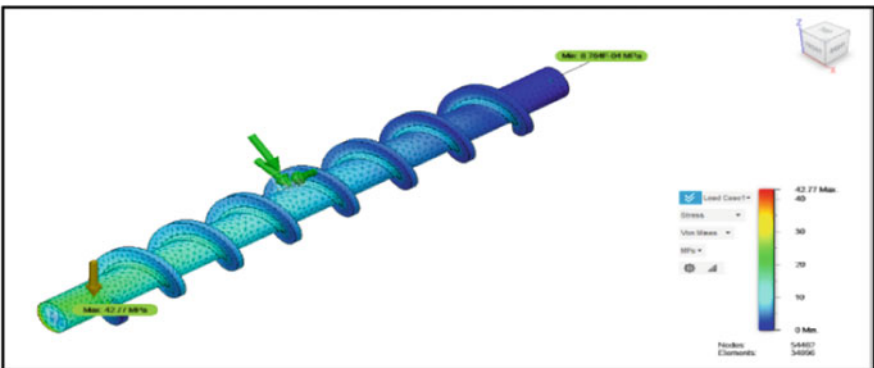
Fig. 8 Von Misses stress SS 302
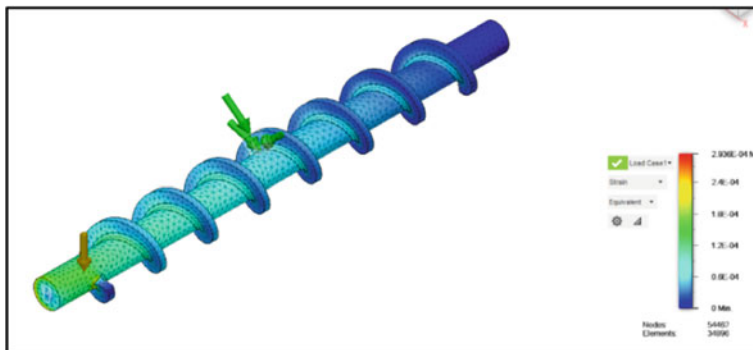
Fig. 9 Strain SS 302
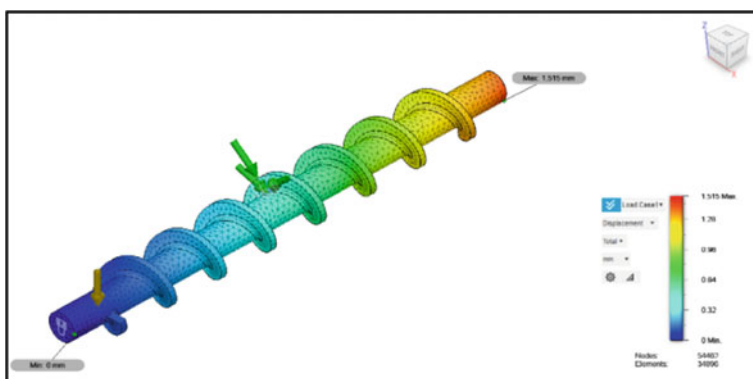
Fig. 10 Displacement SS 302
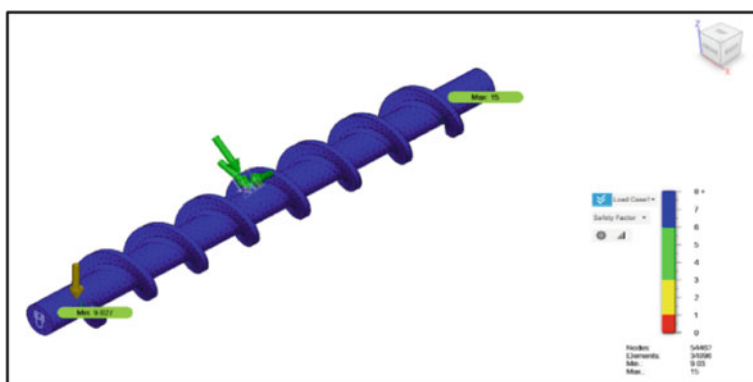
Fig. 11 Factor of safety SS 302

Table 5 Result summary for screw

Parameter	SS 302		SS 304	
	Minimum	Maximum	Minimum	Maximum
Factor of safety				
Factor of safety	9.027	15	5.027	15
Stress				
Stresses (MPa)	8.764×10^{-4}	42.77 MPA	8.764×10^{-4}	42.77
Displacement				
Total (mm)	0	1.515	0	1.591
Reaction force				
Total (N)	0	1417	0	1417
Strain				
Equivalent	5.759E−09	2.796E−04	6.048E−09	2.936E−04

References

1. Mumbi AW, Li F, Fridah M, Batzorig U (2017) An assessment of multi-plate screw press in dewatering process of sludge treatment. Int J Adv Res 740–747
2. Wang H, Aguirre-Villegas HA (2019) Physical properties of dairy manure pre-and post-anaerobic digestion. www.mdpi.com/journal/applsci
3. Adetola OA, Olajide JO, Olalusi AP (2020) Development of a screw press for palm oil extraction. Int J Sci Eng Res 1416–1422
4. Nnanna I, Okeahialam SI, Okoro Humphrey O (2016) Design and fabrication of a groundnut oil expelling machine. Am J Eng Res (AJER) 46–57
5. Habib Ullah Khan Md., Mondal D, Hoque S (2016) Design and construction of oil expeller press with structural analysis of screw with ansys. In: International conference on mechanical, industrial and energy engineering, 160363, pp 1–6.
6. Kataria Mahendra B, Khunt H, Kondhiya P (2018) Design of a screw press for dewatering of cattle dung slurry. Int J Sci Develop Res (IJSDR) 296–304

Moving Object Tracking in 2D Using State Estimation

Bhavika G. Balani, Bansari B. Nayak, and Sneh Soni

1 Introduction

The main purpose of this project is to learn about state estimation and types of system models, and to implement a state estimation algorithm for an application using MATLAB software. State estimation is used in different fields in various applications. Many works are going on in the field of state estimation. There are mainly two types of systems on which we apply estimation algorithms, which are stochastic and deterministic. Further it is categories into different classifications. For all those systems, there are different algorithms that we can use to estimate the states as a single algorithm cannot be used for every kind of system. Some of the examples of state estimation algorithms are Kalman filter, Moving Horizon Estimation, Particle Filtering, Wiener Filter, etc. From all these algorithms, in this paper, we mainly focus on the two algorithms, which are the Kalman filter and Moving Horizon Estimation (MHE). For the linear systems, the Kalman filter works very well, while for the nonlinear systems, algorithms like MHE and also other versions of the Kalman filter are used. MHE works best when we include inequality constraints. From the literature study, for nonlinear and constrained processes, MHE can be called an extension of the Kalman filter [1]. We can get the data from any device like SCADA, PLC, or any sensor device from the algorithm implementation. Algorithms like Kalman filter and MHE also include the process and measurement noises for the estimation.

In this project, we have taken the object tracking example to implement the state estimation algorithm, i.e., Kalman filter to track the required object. Recently, a lot of research is going on in applications such as video surveillance, video navigation, and video compression using object tracking [2]. We have also used some image processing tools to obtain the trajectory of the required object. After getting the trajectory, we have implemented the estimation algorithm using MATLAB software. The MATLAB results conclude that the algorithm works very well.

B. G. Balani · B. B. Nayak · S. Soni (✉)
Instrumentation and Control Department, Nirma University, Ahmedabad, India

2 Need of State Estimation

As the name itself suggests, state estimation means estimating the state of the system. When considering the accurate definition of the state estimation is considered, then state estimation means estimating the internal state of the system from the given measurements of input and output of the system. It is the method of propagating the probability distribution function (pdf) of the system's state over time and updating the pdf with the help of measurements received from the system [3]. All the states of the system may not be measured directly. Other parameters also affect the dynamics of the system and the output. So, we need to estimate those parameters and for that, we need a state estimator. State estimation is used in many different applications in various fields like security, weather forecasting, stock market, medical, control systems, power plants, etc. In the control system, state estimation is used in trajectory or path tracking of any object like satellite, rocket, missile, etc.

3 Types of System Model

The system model can be classified as shown in Fig. 1. There are primarily two types of system models, which are deterministic and stochastic (probabilistic) systems. The main differences between deterministic and stochastic system are as follows:

A deterministic system is purely an ideal system or condition, whereas a stochastic system is a realistic system or condition. In the deterministic system, we neglect any process or measurement noise, whereas in a stochastic system, we consider the process and measurement noise. To estimate state in deterministic systems, we use state observers, whereas for stochastic systems, we use state estimators. Both these classifications can be further subdivided into two categories. The former is based on time dependency, which is static and dynamic. When we talk about time, we can choose it as continuous or discrete. Similarly, the dynamic can be further divided into two categories, i.e., continuous and discrete.
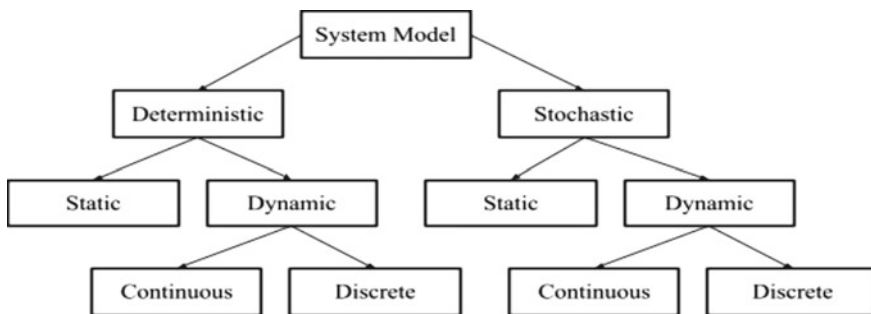
Fig. 1 System model classification [4]

4 State Estimation for Deterministic System

Deterministic systems are ideal systems as we do not include any uncertainty or noise, which is always there in real-life systems. So, when we use a state estimator for the deterministic systems, we call it a state observer. Let us take an example of a rocket as shown in Fig. 2, where we need to estimate the internal temperature as we cannot place the temperature sensor internally because of the high temperature, so instead of internal temperature, we measure the external temperature. Rocket fuel is taken as an input and the rocket's mathematical model is related to all three parameters: fuel, internal, and external temperature. Both input and the system's mathematical model are the known elements.

With the same initial conditions and input, we can estimate the external temperature with the help of the system's mathematical model. When the external temperature matches with the estimated external temperature, we can get the estimated internal temperature, which will converge to the internal temperature of the real system. We have to minimize the difference between the estimated and the real internal temperature and for that, we will apply the feedback loop as shown in Fig. 3, where we will try to minimize the error between the estimated external temperature and the measured external temperature, where K is the controller gain.

The error dynamics of the state observer (e_{obs}), i.e., error between estimated internal temperature and the measured internal temperature, is

$$e_{\text{obs}}(t) = e^{(A-KC)}e_{\text{obs}}(0)$$

Fig. 2 Closed-loop connection
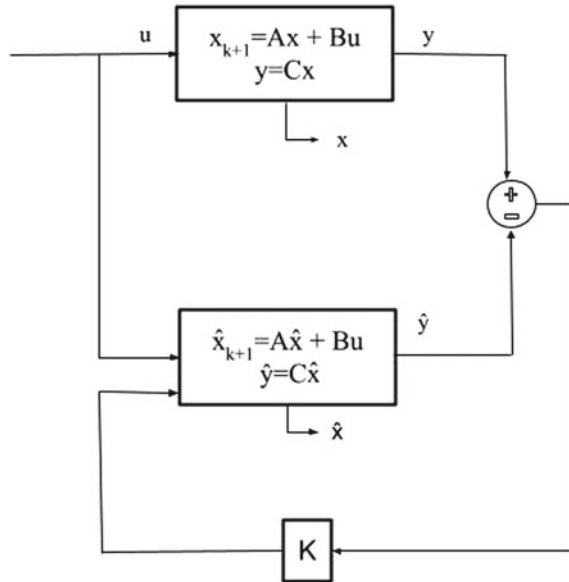
From the above equation, we can say that if (A-KC) < 0, then e_{obs} tend to 0 as t tends to ∞. So, $\hat{x}$ tends to x which means the error will eventually die and the rate at which it dies can be controlled by the K, i.e., controller gain.

5 State Estimation for Stochastic System

Real systems are not that ideal and have noises and errors for which we'll use state estimators. There are many different algorithms used in state estimation for stochastic systems from which we'll discuss the Kalman filter algorithm and the Moving Horizon Estimation (MHE) algorithm.

5.1 Kalman Filter Algorithm

Kalman filter is an iterative algorithm. It uses a series of measurements that are observed over time, which include noises, i.e., process noise, measurement noise, and other inaccuracies to provide an estimation of unknown variables or states. While using this algorithm, we have the input statistical properties, properties of the uncertainty, and the mathematical model of the system. The Kalman filter was introduced by R. E. Kalman in 1960. It became the classic concept for optimal estimation [5]. Kalman filter is also known as Linear Quadratic Estimation. It uses

the set of computations containing noise and other inaccuracies observed over time [6].

The Kalman filter can be broken down into two main steps which are prediction and update as shown in Fig. 4. *A* is the state matrix, *B* is the input matrix, and *C* is the output matrix when the system is modeled in the state-space representation. *K* is Kalman gain. *P* is the estimated covariance matrix, *Q* is the process covariance matrix, and *R* is the measurement covariance matrix. *X* is the state vector. In the Kalman filter, states and noise are assumed to satisfy Gaussian distribution [7]. With some initial state and covariance estimates, we predict the state and covariance at kth instant using $(k-1)$th instant, and then, by calculating the Kalman gain, we will update both state and covariance. The value of *K* is very important as it will shift our state and covariance values to the side where the error is less, that is, if the prediction has less error, then the state and covariance calculation will put more weightage on the prediction values, and if the actual measured values have less error, then the state and covariance calculation will put more weightage to the measured values. This process goes on continuously. So, the role of the Kalman filter in this application is that this filter looks at an object as it moves, and it takes information on the state of the object at the precise moment. Then, it uses this information to predict where the object is in the next frame [8].

For the nonlinear systems, there are extensions of the Kalman filter like Extended Kalman filter, Unscented Kalman filter, Quadrature Kalman filter, Adaptive Kalman filter, etc.

Time Update(Predict)

1. Project of the state ahead
   $$\hat{x}_{k+1} = A\,\hat{x}_k + Bu_k$$

2. Project the error covariance ahead
   $$P_{k+1} = AP_k A^T + Q$$

Initial estimates for $\hat{x}_k$ and P_k

Measurement Update(Correct)

1. Compute the kalman gain
   $$K = \frac{P_{k+1}C}{CP_{k+1}C^T + R}$$

2. Update estimate with measurement y_k
   $$\hat{x}_{k+1} = \hat{x}_{k+1} + K(y_{k+1} - \hat{y}_{k+1})$$

3. Update the error covariance
   $$P_{k+1} = (I - KC)P_{k+1}$$
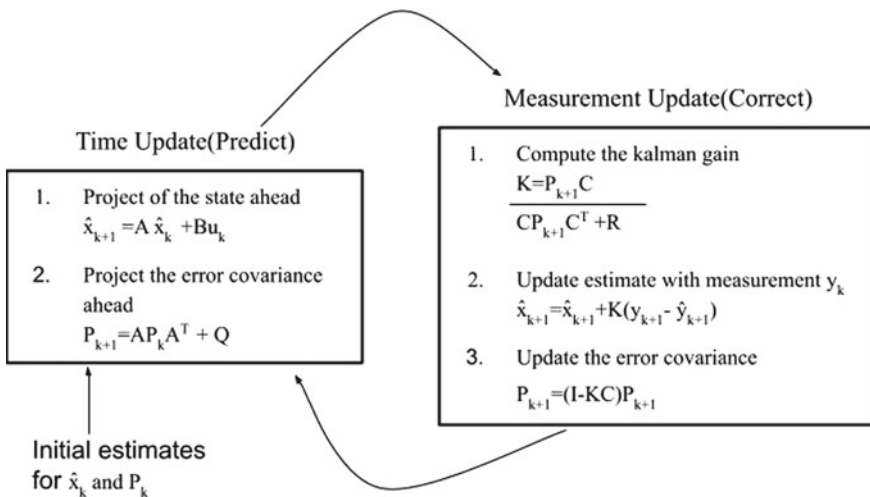
Fig. 4 Kalman filter operation [9]

5.2　Moving Horizon Estimation (MHE)

Moving Horizon Estimation (MHE) is an optimization strategy for process monitoring and state estimation. The MHE only considers a limited amount of past data. One of the main advantages of MHE is the possibility to incorporate system knowledge such as constraints in the estimation. The basic idea of MHE is to estimate the state trajectory using only the past N measurements, where N is referred to as the length of the horizon window. MHE reduces to the Kalman filter under certain simplifying conditions [1]. The application of MHE is generally to estimate measured or unmeasured states of dynamic systems (Fig. 5).

MHE is a multivariable estimation algorithm that uses an internal dynamic model of the process, a history of past measurements, and an optimization cost function over the estimation horizon to calculate the optimum states and parameters. For object tracking problems, the Moving Horizon Estimation (MHE) approach is preferred as in MHE, we can treat the physical constraints on the target motion as some useful knowledge [10].

The fundamental idea of Moving Horizon Estimation is that the current state of the system is based on a finite sequence of N past measurements while incorporating information from the dynamic system equation. This is formulated as an optimization problem, where the finite sequence of states, algebraic states, and inputs are optimization variables. These sequences are determined, such that the initial state of the sequence is coherent with the previous estimate, the computed measurements match the true measurements, and the dynamic state equation is obeyed. One advantage of MHE is also the possible incorporation of further constraints on estimated variables. These can be used to enforce physical bounds, e.g., fractions between 0 and 1.

6　Application of State Estimation

State estimation has so many applications in different areas such as weather forecasting, stock market, radar tracking, etc. We have discussed object tracking as an

Fig. 5 Estimation window for MHE [1]
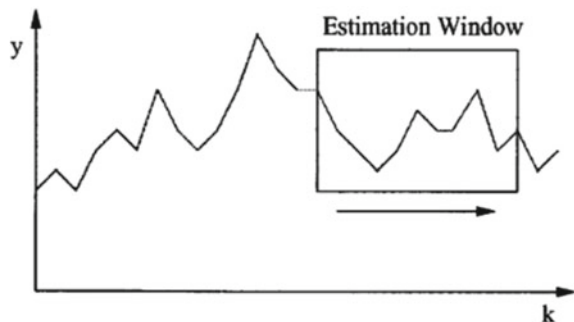
application of state estimation where we have used the Kalman filter algorithm. One may see the Kalman filter as the least fluctuation estimation algorithm for dynamic systems. With the increasing demand for target tracking, the Kalman filter has also gained much attention from researchers [5].

6.1 Object Tracking

Object tracking is used in a wide variety of applications including navigation process, video surveillance, emerging technologies like augmented reality, and many others [7]. In this example, we have taken a video in which there is a moving object (car) and our goal is to estimate the car's location. To extract the locations of the required object, i.e., car from the video, we have used image processing. This whole process can be divided into two steps, i.e., tracking and estimation.

6.1.1 Tracking

To track the object, we have to detect the object. For any video surveillance, detecting an object is the first and an important step [2]. This step is further divided into three steps which are conversion, extraction, and trajectory.

Conversion

The first step is converting the video from which the object must be tracked into a sequence of images or frames to apply image processing tools on each image or frame.

Extraction

After converting the video into the sequence of images, the next step is to treat each image separately. The image can be treated as an array or matrix of pixels ordered in rows and columns. In an 8-bit grayscale image, each image element value corresponds to an intensity that varies from 0 to 255. So, our required element, i.e., the car, has also some unique features or say pixels which we need to extract.

First, we have to eliminate the background of the required object, i.e., car. For that, we will take some images that have just background and not required objects in them and then take the average of those images. This will give us the smoothened background template. After that, we will subtract that background template from each image to get the image that contains only the required object. This way we will get the subtracted image. After getting the subtracted image, we will use a Gaussian filter to smoothen out the image. In the end, we will apply the histogram thresholding which will help us in calculating the location of the car. Histogram thresholding will transform the image into the binary image where there will be 1 on the pixel places of the object, i.e., car, and other than that, there will be 0 as we will put the threshold value of the object's pixel's intensity value.
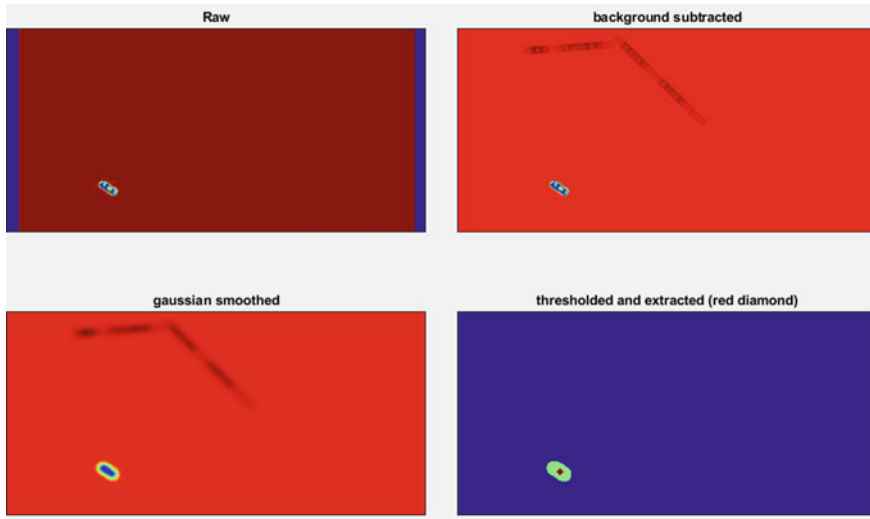
Fig. 6 MATLAB results for pre-estimation

Trajectory

After getting the thresholded image, we will calculate the location of the object. We will use a center of the mass method where we will average the x-coordinates of all the 1's and similarly for y-coordinates. In this way, we will get the approximate x and y coordinate of the object. When we will repeat all the steps for every image, we will get the whole path or trajectory of the car.

In Fig. 6, the results of all the steps are shown. In the thresholded image, the red diamond is just shown to see the car's location more clearly.

6.1.2 Estimation

After getting the trajectory, we will use that information as the measured output at every instance for the Kalman filter algorithm to estimate the object's path. The system's model will be as follows:

State equation

Our goal is to track an object and an object is moving in a couple of directions. It can move in the *x*-direction and also in the *y*-direction, so the Kalman filter has to be applied in two dimensions. Two dimensions are *x* and *y*-direction. Here, we use the standard equations of motion, i.e.,

$$s = ut + \frac{1}{2}at^2,$$
$$v = u + at$$

So, the equations of position and velocity in the x-direction will be

$$x_{t+1} = x_t + v_t t + \frac{1}{2}at^2$$
$$v_{t+1} = v_t + at$$

As we are going for two dimensions, so we will use another set of equations, one for the y position and one for the y velocity. So, we are just going to change our matrices a little bit.

$$\begin{bmatrix} x \\ y \\ \dot{x} \\ \dot{y} \end{bmatrix} \begin{bmatrix} 1 & 0 & T & 0 \\ 0 & 1 & 0 & T \\ 0 & 0 & 1 & 0 \\ 0 & 0 & 0 & 1 \end{bmatrix} \begin{bmatrix} \frac{T^2}{2} \\ \frac{T^2}{2} \\ T \\ T \end{bmatrix} a$$

System dynamics will be as follows:

$$\bar{x}_t = Ax_{t-1} + Bu_t + E_x$$
$$\bar{t}_t = C\bar{x}_t + E_t$$

6.1.3 MATLAB Results

After applying a Kalman filter to the system with the random process and measurement noise using MATLAB software, we get the result as shown in Fig. 7. The red circle on the object, i.e., car, represents the Kalman tracking, and the green circle represents the actual measurement of the object. From the result, one can conclude that for this system, the Kalman filter is working very well. It tracks the trajectory or the path of the object successfully.

7 Conclusion

In this work, following significant outcomes were received,

- State estimation for the deterministic and stochastic systems was introduced.
- The Kalman filter, state estimation algorithm was discussed in detail and the concept of Moving Horizon Estimation was introduced.
- Implementation of the Kalman filter was also shown with an example of object tracking in 2D using MATLAB software.
- The pre-estimation steps required for the tracking process also explained in detail. As shown in the MATLAB results, the Kalman filter was successful in tracking the object.
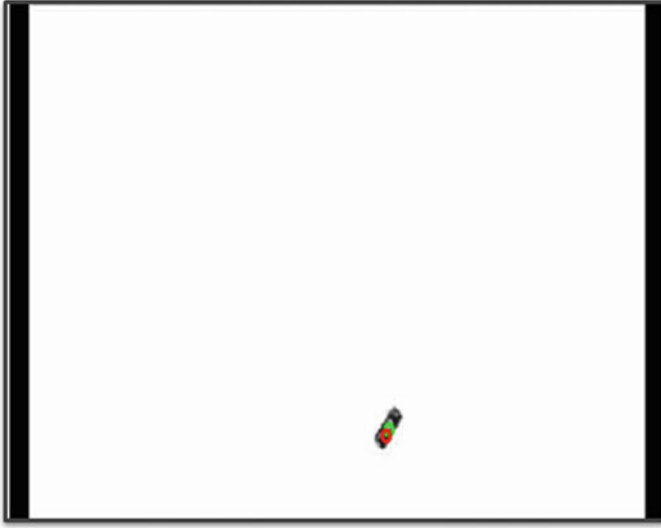
Fig. 7 MATLAB results of object tracking using Kalman filter

- The implementation of the Moving Horizon Estimation algorithm for object tracking will be future work.

References

1. Rao CV, Rawling JB (2002) Constrained Process monitoring: moving-horizon approach. AIChE J 8
2. Li Q, Li R, Ji K, Dai W (2015) Kalman Filter and its application. In: 8th international conference on intelligent networks and intelligent systems. IEEE
3. Shyamalagowri M, Rajeswari R (2016) Unscented Kalman filter based nonlinear state estimation case study—nonlinear process control reactor (continuous stirred tank reactor). In: 2016 10th international conference on intelligent systems and control (ISCO). IEEE.
4. Fakharian A, Gustafsson T, Mehrfam M (2011) Adaptive Kalman filtering based navigation: An IMU/GPS integration approach. In: International conference on networking sensing and control. IEEE
5. Li H, Huang L, Zhang R, Lv L, Wang D, Li J (2020) Object tracking in video sequence based on Kalman filter. In: 2020 international conference on computer engineering and intelligent control. IEEE
6. Bukey CM, Kulkarni SV, Chavan RA (2017) Multi-object tracking using kalman filter and particle filter. In: 2017 IEEE international conference on power, control, signals, and instrumentation engineering. 978-1-5386-0814-2/2017
7. Vasekar SS, Shah SK (2018) A method based on background subtraction and Kalman Filter algorithm for object tracking. In: 2018 fourth international conference on computing communication control and automation (ICCUBEA), IEEE.

8. Salhi A, Ghozzi F, Fakhfakh A (2020) Estimation for motion in tracking and detection objects with Kalman Filter, dynamic data assimilation. Dinesh G Harkut, IntechOpen. https://doi.org/10.5772/intechopen.92863
9. Masdari M, Kheazri H (2020) Efficient offloading schemes using Markovian models: a literature review. Research Gate
10. Jiao Z, Li W, Zhang Q, Wang P (2015) Tracking for the maneuvering target based on multiple models and moving horizon estimation. In: 2015 IEEE international conference on information and automation, pp 1936–1941. https://doi.org/10.1109/ICInfA.2015.7279605

CMS Implementation Framework Development and Validation for the Manufacturing Industry

Vikrant Sharma and B. D. Gidwani

1 Introduction

Cellular manufacturing (CM) is a process for improving job shop and batch shop operations. By preparing a group of parts on a group (cell) of machines, CM enables the benefits of a product-oriented manufacturing system to be realized in a medium volume, medium variety environment. The CM, which clusters machines, is devoted to a family of similar components [1]. While CM does not yet have the versatility of job shops to produce a wide variety of items, it has a high production rate and an efficient flow [2]. In the current batch production environment, demand for the product is determined by an endless number of variables, including volume, product mix, and new product development [3]. By reducing work-in-progress inventory and lead times, CM improves productivity and delivery performance, thereby assisting manufacturing industries in remaining competitive [4].

V. Sharma (✉)
Mechanical Engineering Department, SET, Mody University of Science and Technology, Lakshmangarh, India

B. D. Gidwani
Mechanical Engineering Department, RTU, Kota, India
e-mail: bgidwani@rtu.ac.in

As stated previously, the advantages of cellular manufacturing make it an attractive option for manufacturing industries, particularly in countries like India. In recent years, India's competitive environment has compelled industries to review various procedures to make complete updates to changing customer needs. Manufacturing industries are now focusing on intelligent processes that boost productivity without sacrificing product quality [5]. The improvement of manufacturing plant layout and design has been identified as a growing area of interest in this reference. As a result, many industries in India have attempted to adapt to cellular manufacturing through group technology rather than batch production, which remains a dominant manufacturing mode in Indian manufacturing industries.

This paper aims to introduce a novel conceptual framework that is specifically tailored to the needs of Indian manufacturing firms. Additionally, this article discusses the validation process for the proposed CM implementation framework. The purpose of framework validation is to determine whether the factors considered when engaging in CM implementation are considered.

2 Literature Review

The concept of cellular manufacturing is not quite contemporary. It is often dated back to the 1960s when the Langston Company in Camden, New Jersey, a producer of semi-custom heavy machinery for the paper industry, running in a traditional job shop mode. Applications of cellular manufacturing are prevalent in both academic and industrial settings. Although the concept of cellular manufacturing was introduced decades ago through the use of terms such as group technology and lean manufacturing, research in this field has accelerated over the last two decades.

Researchers have identified numerous approaches to cell manufacturing design over time. The review of the literature reveals a strong bias toward cell formation issues [6–10]. The establishment of production cells enables the decomposition of an extensive job shop production system into a series of smaller, more manageable subsystems [11]. As a result, the design of CMS is a critical manufacturing principle that has received recent research attention [12].

Additionally, frameworks to assist practitioners in designing and implementing cellular manufacturing have been evaluated to determine the model's effectiveness by introducing a manufacturing cell within Australia's largest manufacturer of electrical accessories and surveying its outcomes [13]. Another attempt at reconfiguring the production system to a CM-based system has been made, demonstrating superior workflow, efficiency, and other characteristics compared to the previous system [14].

A review of the literature revealed that there is no solid framework for the Indian manufacturing industry. This study provides a solid framework for CMS implementation to address this research gap, which is validated using a SWOT analysis.
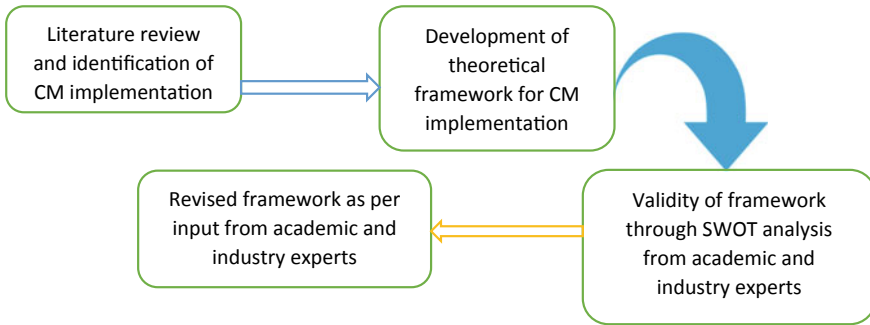
Fig. 1 Methodology

3 Methodology

This paper is a follow-up to the author's previous paper [15]. In this study, the author proposed an implementation model for visualizing cellular manufacturing system (CMS) prioritization using analytic hierarchy process (AHP) and analytic network process (ANP) techniques. Four enabler dimensions and 17 CM attributes were evaluated in the proposed study.

In the present study, the theoretical framework of CMS implementation is being developed to facilitate CMS implementation in Indian industries. SWOT analysis is used to validate this framework. Figure 1 depicts the study's methodology.

4 Theoretical Framework and Validation

As shown in Fig. 2, the author developed a theoretical framework for CMS implementation in this study, which is of great managerial importance. The framework has the following three phases.

Phase 1: Conceptual and Training Phase

This is the kick-off phase in which the staff responsible for CMS implementation is chosen, expanded, and trained. The team is informed of critical CMS knowledge and information. The benefits of the project should be emphasized so that each member understands why the project is necessary. As a result, it is reasonable to anticipate an increase in understanding of the CMS and the mindset aspect.

Phase 2: Design and implementation Phase

Select from the available literature or develop a cell design method appropriate for the objective during this phase. Involve all trained employees in the process of cell design. Create a database of product/part families and machine cells. Define CMS performance assessment matrices and metrics for performance improvement. To
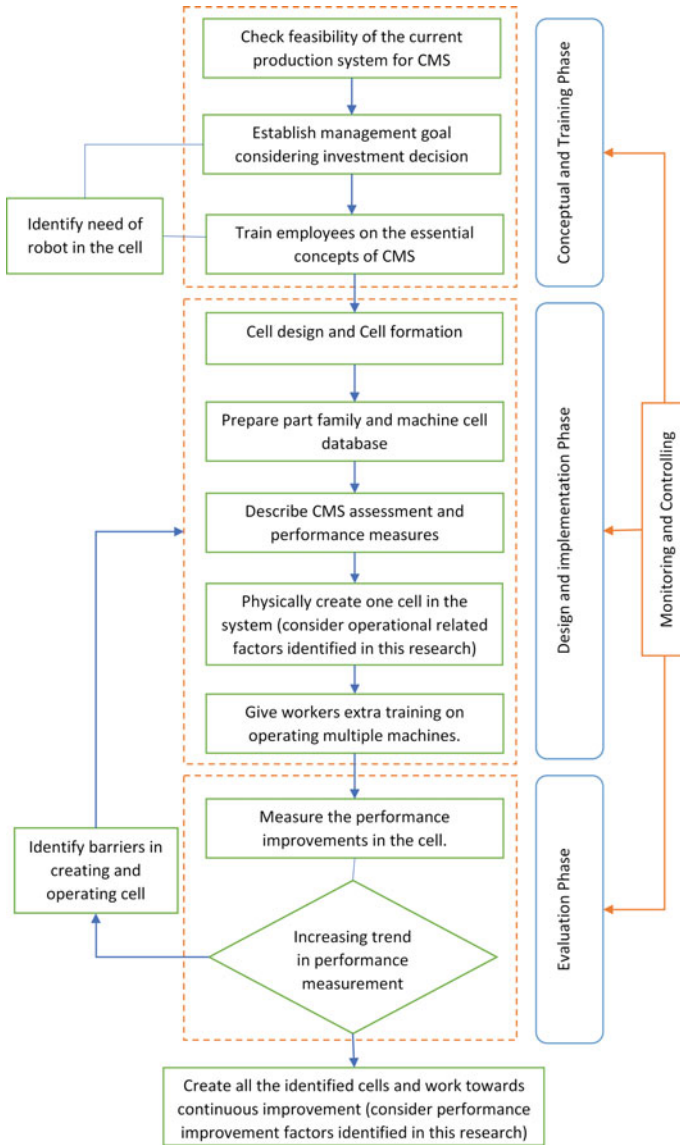
Fig. 2 Theoretical framework

begin, physically create one cell in the system. Consider operational factors when establishing this cell as identified by [15]. Employees must be trained to operate multiple machines within the cell. If management has decided to install an integrated robotic cell, then the worker must be trained appropriately.

Table 1 Operational and performance improvement related factors [15]

Operational factors	Level scheduling	Process improvement factors	Lean manufacturing
	Total productive maintenance		Quality improvement/six sigma
	Setup time reduction or elimination plans		Computer integrated Manufacturing
	Line balancing		Value-added analysis
	Workplace organization plans		Flexibility
	Robotics (RO)		Agile manufacturing
			Concurrent engineering

Phase 3: Evaluation Phase

This evaluation is a continuous process of validating implementation outcomes and closing the gap between evidence and practice. Assess the cell's performance improvements and also identify barriers to cell creation and operation.

If the performance measures show an upward trend, apply the technique to other cells and work toward continuous improvement using the performance improvement factors discovered by [15]. Operational and performance improvement related factors are provided in Table 1.

4.1 SWOT Analysis for the Framework's Validity

Validation is the process of determining whether a tool is fit for its purpose. SWOT analysis is used to describe a business's strengths, weaknesses, opportunities, and threats. It appeared to have originated in management literature and was developed by researchers at Stanford University [16]. SWOT analysis was chosen because it is a highly effective methodology for analyzing and validating existing frameworks via experts and is the only one that provides strengths, weaknesses, opportunities, and threats [17–19].

Twelve experts have distributed the questionnaire, which included the proposed framework and a blank SWOT analysis matrix. It was distributed electronically. Table 2 contains a list of experts, their experience, and their designation. Table 3 summarizes the SWOT analysis and expert recommendations.

In summary, as determined by input from experts conducting SWOT analyses, the proposed framework's strength is that it applies to the Indian batch manufacturing industry. Additionally, experts emphasize the framework's robustness and readability. Considering the experts' identified weaknesses and opportunities, the proposed framework has been modified and is depicted in Fig. 3.

Table 2 Experts for SWOT analysis

Expert	Experience (years)	Designation
IE 1	10	Assistant Engineering Manager
IE 2	13	Engineer—Quality and Business Excellence
IE 3	15	Sr. Manager, Manufacturing Engineering
IE 4	10	R&D Engineer
IE 5	08	Quality engineer
IE 6	17	Plant Manager
IE 7	16	Assistant General Manager
IE 8	10	Senior Manufacturing Engineer
AE 1	28	Professor
AE 2	24	Professor
AE 3	20	Associate Professor
AE 4	14	Associate Professor

IE Industry expert, *AE* Academic expert

5 Conclusion

The purpose of this study was to propose a theoretical framework for the implementation of a CMS. The proposed framework was validated through the input of twelve experts via a SWOT analysis. The research is novel in that it develops a conceptual framework for evaluating the implementation effort and benefits of CM in the Indian manufacturing industry. This framework provides a non-prescriptive framework for incorporating CM into an organization's business strategy. The final framework will be tested and applied in a real-world work environment to refine further and eliminate any framework weaknesses.

Table 3 SWOT analysis summary

S, W, O, T	Data extract	Expert
Strength	Framework is applicable to Indian industry	AE 1, IE 6
	Performance measure are contemporary	AE 1
	May be implemented in batch production	AE 1, AE 4, IE 4
	Robust, stable, clearly presented, and focused on implementation	AE 2, AE 3, AE 4, IE 5, IE 6
	Promotes lean manufacturing	AE 3
	Easy way to analyze and observe the current performance level of a plant (Cell)	IE 1, IE 8

(continued)

Table 3 (continued)

S, W, O, T	Data extract	Expert
	KPIs can be monitored	IE 1
	CMS framework results in increased efficiency compared to traditional manufacturing	IE 2, IE 3, IE 4
	The CMS framework promotes a great deal of benefits if it is employed as expected	IE 5
	Improve quality and work life balance to worker	IE 7
	Focus on employee (workers) involvement through rigorous trainings	IE 8
Weakness	Performance measure should be clearly defined	AE 1, IE 8
	Practically not tested	AE 2
	Cost of implementation needs to be considered	AE 2, AE 3, IE 2
	Monitoring of performance of cells regularly	AE 4
	High level of skill enhancement program/training like TPM, Agile framework, VA analysis, WPO, lean manufacturing found missing for cell associates	IE 1, IE 3, IE 6, IE 7
	CMS framework may not be applicable for all production systems	IE 2, IE 4
	Wrong part families identified	IE 3, IE 5
Opportunity	Can consider in I 4.0	AE 1
	Cost saving	AE 2, AE 3
	To and Fro communication system like DMS (daily monitoring system) KPIs within all levels of hierarchy should be implemented	IE 1
	Timely rewards and reorganization to engage more and more associates	IE 1
	In conceptual and training phase, goal alignment within management and worker union is missing	IE 1
	Effective techniques and software tools for identifying part families and machine cells database	IE 2, IE 6
	CMS assessments and performance measures should be correctly defined and described for effective CMS implementation	IE 2
	Operation efficiency by robotics	IE 3, IE 5

Table 3 (continued)

S, W, O, T	Data extract	Expert
	Flexibility and agility in manufacturing	IE 3
	Horizontal deployment across operations	IE 3
	IoT can be helpful for cellular manufacturing system	AE 4, IE 4
	Employee (workers) involvement during cell design	IE 8
Threat	None	AE 1, AE 4, IE 4
	Resistance to change	AE 2, AE 3, IE 1
	Transition to CMS can be arduous, so needs to be planned carefully	AE 3
	Insufficient funds or capacity from management can have an impact in implementing CMS framework	IE 2, IE 6, IE 7
	Workers should be properly trained for CMS implementation	IE 2
	Effective feedback mechanism for identifying improvement objectives	IE 2
	Non-availability of expert resources during implementation	IE 3
	Wrong mindset of staff	IE 3
	Management and employee support	IE 4
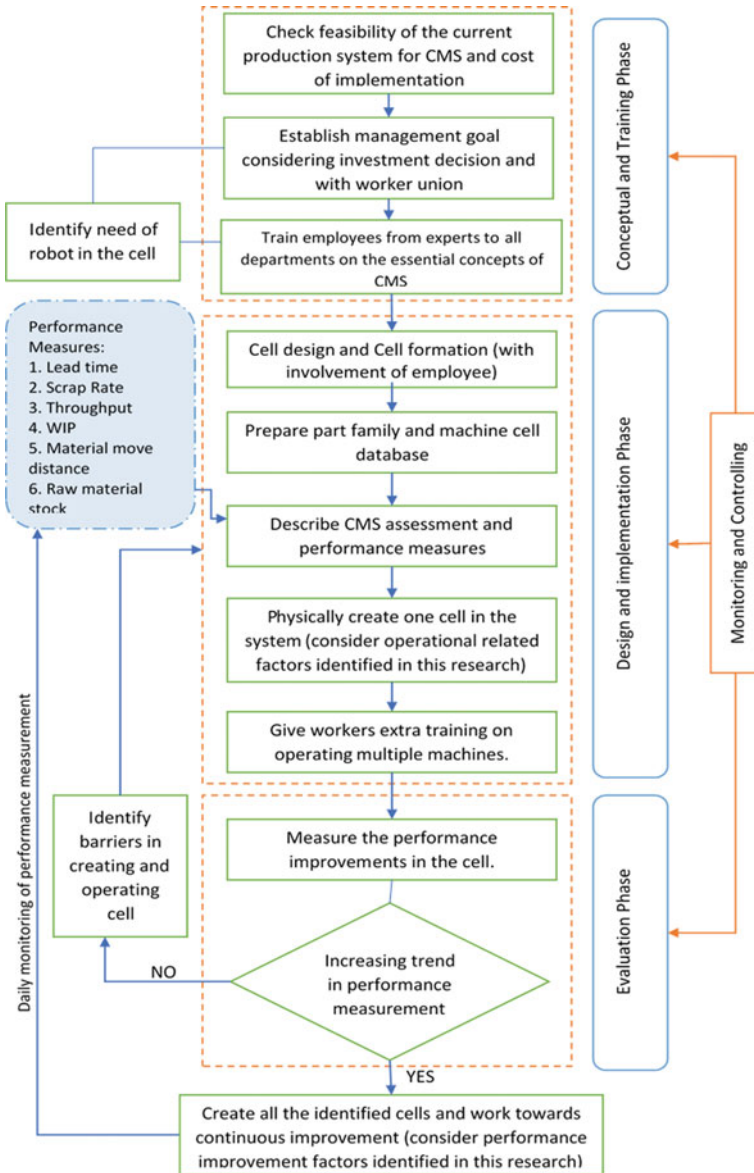
Fig. 3 Revised theoretical framework

References

1. Dekkers R (2018) Group technology: amalgamation with design of organizational structures. Int J Product Econ 200:262–277
2. Liu C, Wang J, Leung JYT (2018) Integrated bacteria foraging algorithm for cellular manufacturing in supply chain considering facility transfer and production planning. Appl Soft Comput J 62(1):602–618
3. Kesavan V, Kamalakannan R, Sudhakarapandian R (2019) Heuristic and meta-heuristic algorithms for solving medium and large scale sized cellular manufacturing system NP-hard problems: a comprehensive review. Mater Today Proc. https://doi.org/10.1016/j.matpr.2019.05.363
4. Chaudhuri B, Jana RK, Pranab K (2020) A review on the multi-objective cell formation problem in cellular manufacturing systems. Int J Manuf Technol Manage 34(2):188–209
5. Kumar S, Malhotra V, Kumar V (2020) To find the suitability of CMS in Indian industries in comparison of other manufacturing system using AHP technique. Int J Process Manage Benchmarking 10(3):367. https://doi.org/10.1504/ijpmb.2020.107937
6. Papaioannou G, Wilson JM (2010) The evolution of cell formation problem methodologies based on recent studies (1997–2008): review and directions for future research. Eur J Oper Res 206(3):509–521
7. Arora PK, Haleem A, Singh MK (2013) Recent development of cellular manufacturing systems. Sādhanā 38(3):421–428
8. Sharma V, Gidwani BD, Meena ML (2019) Cellular Manufacturing: Literature review and trends. J Manuf Technol Res 11(1–2):49–79
9. Wu L, Li L, Tan L, Niu B, Wang R, Feng Y (2020) Improved similarity coefficient and clustering algorithm for cell formation in cellular manufacturing systems. Eng Optim 52(11):1923–1939. https://doi.org/10.1080/0305215X.2019.1692204
10. Goli A, Babaee E, Aydin NS (2021) Fuzzy integrated cell formation and production scheduling considering automated guided vehicles and human factors. IEEE Trans Fuzzy Syst. https://doi.org/10.1109/TFUZZ.2021.3053838
11. Garbie IH (2011) Converting traditional production systems to focused cells as a requirement of global manufacturing. J Serv Sci Manag 4(3):268–279. https://doi.org/10.4236/jssm.2011.43032
12. Sakhaii M, Tavakkoli-Moghaddam R, Bagheri M, Vatani B (2016) A robust optimization approach for an integrated dynamic cellular manufacturing system and production planning with unreliable machines. Appl Math Model 40(1):169–191. https://doi.org/10.1016/j.apm.2015.05.005
13. Fraser K, Harris H, Luong L (2007) 'Improving the implementation effectiveness of cellular manufacturing: a comprehensive framework for practitioners. Int J Prod Res 45(24):5835–5856
14. Silvio CS, Marta CM, Fabio AF (2013) A practical methodology for cellular manufacturing systems design an industrial study. Trans Control Mech Syst 2(4):198–211
15. Sharma V, Gidwani BD, Sharma V, Meena ML (2019). Implementation model for cellular manufacturing system using AHP and ANP approach. Benchmark Int J 26(5):1605–1630
16. Mishra RP, Anand G, Kodali R (2007) Strengths, weaknesses, opportunities, and threats analysis for frameworks of world-class maintenance. Proc Inst Mech Eng Part B: J Eng Manuf 221(7):1193–1208. https://doi.org/10.1243/09544054jem810
17. Antony J (2012) A SWOT analysis on Six Sigma: some perspectives from leading academics and practitioners. Int J Product Perform Manag 61(6):691–698
18. Mishra RP, Chakraborty A (2014) Strengths, weaknesses, opportunities and threats analysis of lean implementation frameworks. Int J Lean Enterprise Res 1(2):162. https://doi.org/10.1504/ijler.2014.066833
19. McLean RS, Antony J (2017) A conceptual continuous improvement implementation framework for UK manufacturing companies. Int J Qual Reliab Manage 34(7):1015–1033. https://doi.org/10.1108/ijqrm-02-2016-0022

Design of Water Pumping System with Off-Grid Connected Solar PV Array Driven Permanent Magnet Synchronous Motor

Mahadasyam Naveen and Rajiv Kumar Sharma

1 Introduction

Mostly water pumping system used for agriculture and industrial application [1] and most farmers are from rural area sectors. In rural areas using of traditional grid connected power supply leads to long period of power cuts during the farming period (i.e., during day time). For overcoming this issue's, since from decade renewable energy power generation came into existence and also by using renewable energy sources, carbon emission can also reduce and can be mitigate to the issues of global warming [2]. Among so many renewable energy sources, solar energy sources are utilized for so many applications due to less maintenance and availability of sunlight most of the day time throughout the year, capital and operating cost are turn down [3]. In this research, a solar PV array was employed to power a voltage source inverter and operate a PMSM. Permanent magnet synchronous motors and brushless dc motors are commonly utilized in solar water pumping systems [4, 5] and among them PMSM is more reliable due to the following advantages like higher efficiency, high power to weight ratio, higher air gap flux density, less torque ripples, less harmonics, high torque to inertia ratio are the fewer advantages to stand out from the brushless dc motor and induction motor [5].

In PMSM driven solar water pumping system also had a few challenges, they are speed control of PMSM is complex and difficult to control due to interlink between flux and torque. Due to this speed control of PMSM is too complex. Vast techniques are used in so many literatures to control the speed of PMSM, among them Direct

M. Naveen (✉)
Department of Center for Energy and Environment Engineering, National Institute of Technology, Hamirpur, Hamirpur, Himanchal Pradesh, India
e-mail: 19m706@nith.ac.in

R. K. Sharma
Department of Mechanical Engineering, National Institute of Technology, Hamirpur, Hamirpur, Himanchal Pradesh, India

torque control and vector control are mostly used techniques for speed control of PMSM. Among these two methods DTC technique is simple design than vector control technique [6]. Various kind of modified techniques has been developed for both DTC and vector control techniques, but there are few flaws like increased in cost effectiveness or increased in hardware components and doesn't mitigate harmonics in torque and flux ripples [7–10].

Modified vector control has been introduced for mitigating the complex control technique more reliable and by using extra torque control loop will reduce the over-burden on controlling of speed. Feed forward term is used to improve the overall system reaction [11].

After design the speed control of synchronous motor next crucial part is to get the most power out of the photovoltaic array. These may be done by watching the maximum power point on the PV array's power and voltage curve, which fluctuates from zero to open circuit voltage. The outputs of solar PV arrays are mostly affected by sun irradiance and temperature, like if solar irradiance varies it's effect the current of the solar PV array and voltage remains unaltered. If temperature changes voltage of the PV array changes and current remains unaltered [12]. So, PV array power depends on solar irradiation and temperature. Various MPPT techniques are introduced for both on-grid and off-grid systems. Accordingly, various system configuration and climate changes many MPPT techniques are introduced in various literature. They can be classified into many forms like online, offline and hybrid mode of methods [13] or they can be classified into analogy, digital and hybrid methods [14]. Incremental conductance algorithm, In the literature, perturbation and observation algorithms, fuzzy logic, neural networks, open circuit voltage, and short circuit current are examples of MPPT approaches. Only P&O and incremental conductance approaches are employed in a solar water pumping systems. P&O is simple and straightforward to use, however it has the downside of causing the SPV array voltage to fluctuate at maximum output (MPP). These oscillations leads to the disturbance at MPP and creates steady state oscillations. These disadvantage leads to power loss and it is ineffective and inefficient for extracting maximum power [15]. While in an INC maximum power point tracking (MPPT) has a wide range of operation under quickly changing climate conditions [16–18]. INC MPPT gives accurate and fast response than P&O MPPT. INC method has a good tracking behavior under transient condition. But has some limitation due to oscillations under steady state condition. To overcome this issue use variable step size incremental conductance (VSS-INC). According to the conditions use large and small step sizes to improve transient and steady state conditions [19]. This MPPT approach is utilised for single stage topologies, which eliminates the need for a DC-DC converter and enhances overall system efficiency while lowering cost and space.

The VSS-INC MPP Technique and Modified vector control for speed control of the PMSM are used to model this solar water pumping system in Matlab software under various climate conditions. By taking the data of Irradation and temperature of Hamirpur (H.P) location through NASA Site and analyze according to that data.

2 System Configuration and Operation:

Figure 1 depicts the SWP device setup. An SPV series, a three-phase voltage source inverter (VSI), a PMSM, and a water pump make up this machine (from left to right). A diode (D) is inserted between the SPV array and the VSI to prevent any reverse current from going through it. The SPV array is made up of a suitable number of series and parallel SPV module combinations. As photons strike the SPV array's surface, they emit electrical energy. The produced electrical energy is sent through VSI's DC connection. Power processing is handled by the VSI. It rotates the PMSM, which is connected to the pump, transferring electrical energy to rotational mechanical energy.

$$P_{pv} = P_{cdc} + P_m \tag{1}$$

where P_{pv}, P_{cdc}, P_m are the PV array Power, DC link capacitor power, motor power output.

$$P_{cdc} = V_{dc} * C_{dc} * \frac{dV_{dc}}{dt} \tag{2}$$

$$P_{pv} = V_{dc} * C_{dc} * \frac{dV_{dc}}{dt} + T_m * W_m \tag{3}$$

where T_m, W_m are the motor torque and speed. During steady state V_{dc} remains constant. Therefore, P_{cdc} is remains zero.

$$P_{pv} = P_m \tag{4}$$

$$P_{pv} = T_m * W_m \tag{5}$$
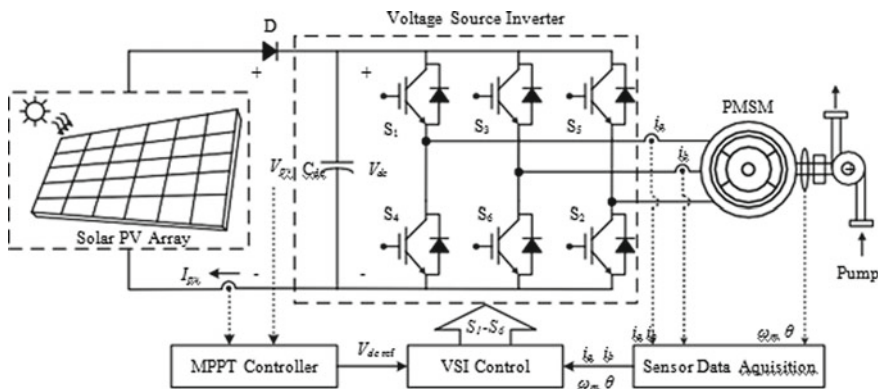
Fig. 1 Solar water pumping system driven PMSM

For pump load type,

$$T_m \propto W_m{}^2 \tag{6}$$

$$P_{pv} \propto W_m{}^3 \tag{7}$$

$$P_{pv} = K_m * W_m{}^3 \tag{8}$$

where K_m is pump load constant.

According to reference, the SPV array power (P_{pv}) is proportional to the cube of the motor speed (Wm) (8). For accurate MPPT monitoring, the reference motor speed (W_r) must be maintained in this case. Be accessed correctly For this scheme, ref is divided into two parts; W_{r1} and W_{r2}, as shown in Fig. 2b. W_{r1} is derived from the DC relation voltage regulator The SPV array voltage is used by the VSS-INC algorithm. As inputs, voltage (V_{pv}) and current (I_{pv}) are used to produce a reference DC voltage. The reference voltage (V_{dcr}) required for MPP service. The DC component voltage (V_{dc}) for a single stage scheme is now the same as V_{pv}. They are interchangeable and have the same meaning. The difference between V_{dc} ref and V_{dc} is passed to the DC link voltage controller, which adjusts W_{r1} to zero the DC link voltage error. The FFT is a property of the SPV control (P_{pv}). Since W_{r2} is a clear reference, Any adjustment to the role of P_{PV} without the use of a controller Changes in P_{PV} cause changes in Wr₂, making the mechanism more faster. By adding Wr₁ and Wr₂ which leads to generation of W_r. MVC is used to power it. For this, W_m and W_r are compared and difference between them gives the speed error which is gives the input to the speed PI controller. The speed controller's contribution is referred to as a reference electro-magnetic torque (Ter). The modified vector control is split into two parts. The first part involves estimating electro-magnetic torque, while the second part involves producing currents and, in turn, swapping signals for the voltage source inverter (VSI).Control diagram of SWPS as shown in Fig. 2
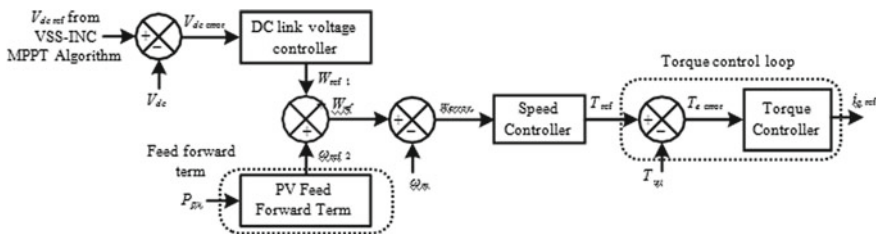
Fig. 2 Modified vector control

3   System Design

1. PV Array Design:-Design of PV array plays a crucial role for the entire solar water pumping system. Design should be more economical and reliable for the SWPS user. For design of PV array use the 'KYOCERA KC200GT' PV module and this modeling of PV array is done by venkatramana [20]. For good operation, PMSM necessary rating will be 7.8 kw. By including losses in an intermediate stages Solar PV array is designed for 8.4 kw.

- Number of PV modules required are

$$N = \frac{Pmpp}{Pmp} = 8400/200.143 \approx 42 \tag{9}$$

- Number of PV modules connected in series are

$$Ns = \frac{Vmpp}{Vmp} = 560/26.3 \approx 21 \tag{10}$$

- Number of SPV modules connected in parallel per string

$$Np = \frac{Pmpp}{Ns * Vmp * Imp} = 8400/(21 * 26.3 * 7.61) \approx 2 \tag{11}$$

2. Design of DC Link Capacitor:-DC link capacitor is design properly because it is a replacement of DC-DC converter and the formulae to calculate dc link capacitor is as follows

$$C_{dc} = I_o/(2 * W_e * \Delta V_{dc})$$
$$= \frac{8400/560}{(2 * 2 * 3.14 * 50 * 0.02 * 560)} = 2132 \ \mu F \tag{12}$$

where $W_e = 2 * 3.14 * 50$ rad/s, ΔV_{dc} is a % ripple voltage taken as 2% of V_{dc}, $I_o = Pmpp/V_{dc}$, C_{dc} approximately taken as 2200 μF.

4   System Control Strategy

This SWP system's control is split into two sections. The first section focuses on getting the most power out of the solar PV array. The permanent magnet synchronous motor's speed regulation is the subject of the second half. First method is achieved by using VSS-INC method to extract maximum power whereas second one is achieved by Modified vector control. In these control uses three PI controller to reduce errors. By comparing V_{dc} reference to V_{dc}, one PI controller is used to reduce the error

for DC connection voltage. Vdcerror is used as an input to the PI controller, and the error can be minimised by changing the K_p and K_i values. Similarly speed and torque errors can be reduced by PI controller and to reduce the burden on the speed control of PMSM. The word SPV feed forward is often used to speed up system response.

4.1 Variable Step Size Incremental Conductance Algorithm

Variable step size is used in an incremental conductance technique ensure to improve the tracking accurate MPP without losing extra power. This method operate by using larger step size under transient condition to give fast dynamic response and smaller step size under steady state condition to reduce the oscillations while approaching near to the maximum power point. This technique's output is Vdcref, which is compared to the DC link voltage and fed into the DC link voltage power (i.e., PI controller).The algorithm of VSS-INC is as shown in below Fig. 3.
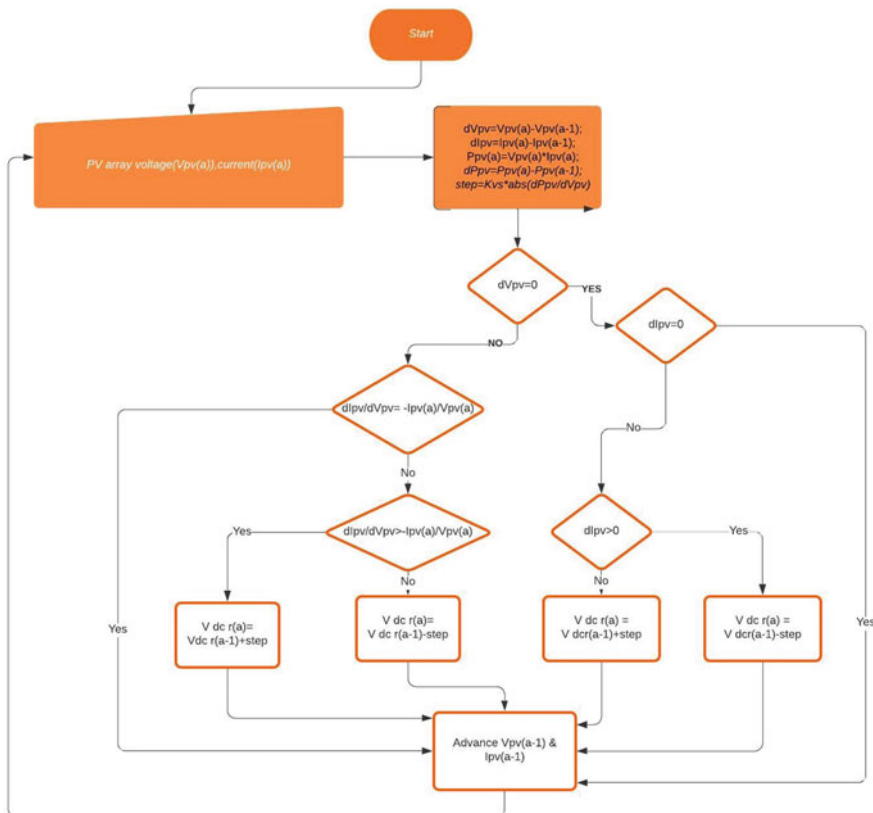
Fig. 3 Algorithm of Variable step size incremental conductance

The generalized equation is

$$V_{dc}\ ref(a) = V_{dc}\ ref(a-1) \pm step \qquad (13)$$

The value of step is calculated as

$$Step = k * dP_{pv}/dV_{pv} \qquad (14)$$

where k is the step size constant, dP_{pv} and dV_{pv} are the PV array power and voltage at ith and $I - 1$th samples respectively.

Step size value is greatly affects the operation of the maximum power extraction from PV array. During transient condition uses step max for the fast dynamic response. During starting uses the step max which is the upper limit of the VSS-INC and close to the MPP the dP_{pv}/dV_{pv} approximately tends to zero. Their should to some crossing point to change from step max.

$$i.e.,\ \ K < step\ max /(dP_{pv}/dV_{pv})_{at\ step\ max} \qquad (15)$$

4.2 Modified Vector Control

These controls are subdivided into two sections once more. The first is to estimate the torque, and the second is to produce current and generate a switching signal to the voltage source inverter using hysteresis current power. The control diagram is seen in the Fig. 4.

(1) Estimation of Electromagnetic Torque (Test)

Estimation of Electromagnetic Torque is estimated by stationary reference frame.
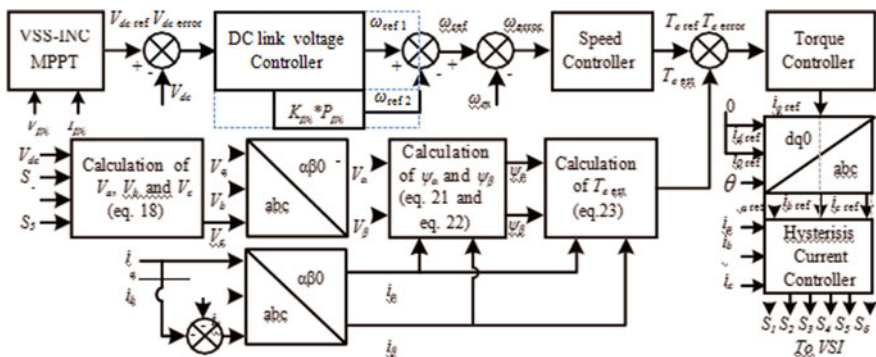
Fig. 4 Overall control diagram of solar water pumping system

By V_{dc}, VSI Switching signal S_1, S_3, S_5 obtained require V_a, V_b, V_c by equations below 16, 17, 18

$$V_a = \frac{V_d}{3}(2S_1 - S_3 - S_5) \tag{16}$$

$$V_b = \frac{V_d}{3}(2S_3 - S_1 - S_5) \tag{17}$$

$$V_c = \frac{V_d}{3}(2S_5 - S_1 - S_3) \tag{18}$$

Three phase voltages and currents are converted into stationary reference frame voltages (V_1, V_2) and currents (I_1, I_2) using clark's transformation are given as,

$$V_1 = \frac{1}{3}(2V_a - V_b - V_c) \quad V_2 = \sqrt{3}(V_b - V_c) \tag{19}$$

$$I_1 = \frac{1}{3}(2I_a - I_b - I_c) \quad I_2 = \sqrt{3}(I_b - I_C) \tag{20}$$

By above clark's transformation currents and voltages, we can get stationary flux (Φ_1, Φ_2)

$$\Phi_1 = \int (V_1 - R_s * I_1) + \Phi_{10} \tag{21}$$

$$\Phi_2 = \int (V_2 - R_s * I2) + \Phi_{20} \tag{22}$$

where R_s is the stator resistance, $\Phi_{10,20}$ are the initial stationary flux's.

T_{est} is calculated by the below mentioned equation

$$T_{est} = \frac{3}{2}p(\Phi_1 * I_2 + \Phi_2 * I_1) \tag{23}$$

where p is the number of pole pairs.

(2) *Generation of reference i_q axis current and switching signals*

V_{dc} reference generated by VSS-INC is compared by V_{dc} at an instant and the error is determined by the difference of both voltages at an instant 'i'.

$$V_{dc\ error} = V_{dc\ ref}(i) - V_{dc}(i) \tag{24}$$

This error is fed to a DC link voltage PI controller to reduce error and convert to W_{ref1}.

W_{ref1} is estimated as below mentioned equation

$$W_{\text{ref}\,1}(i) = W_{\text{ref}\,1}(i-1) + K_{p1}(V_{\text{dc err}}(i) - V_{\text{dc err}}(i-1)) + K_{i1}V_{\text{dc err}}(i)$$

where K_{p1}, K_{i1} are the proportional and integral constants of the PI controller.
$W_{\text{ref}\,2}$ are generated by feed forward term,

$$W_{\text{ref}\,2} = K_{\text{pv}} * P_{\text{pv}} \tag{25}$$

where K_{pv} is a constant of feed forward term. It is the ratio of the rated speed to the rated power. It is selected by obtaining the maximum stability of the system.

The reference motor speed is the sum of both speeds

$$W_{\text{ref}} = W_{\text{ref}\,1} + W_{\text{ref}\,2} \tag{26}$$

W_{ref} is compared with actual motor speed W_{m} at the ith instant error

$$W_{\text{error}}(i) = W_{\text{ref}}(i) - W_{\text{m}}(i) \tag{27}$$

With this speed error gives input to the PI controller and the output given as reference Electro -magnetic torque ($T_{\text{e ref}}$)

$$T_{\text{e ref}}(i) = T_{\text{e ref}}(i-1) + K_{p2}(W_{\text{error}}(i) - W_{\text{error}}(i-1)) + K_{i2}W_{\text{error}}(i) \tag{28}$$

where K_{p2}, K_{i2} are the proportional and integration constants used in PI controller of speed.

$T_{\text{e ref}}$ is compared with T_{est} at the ith instant and gives the error

$$T_{\text{error}}(i) = T_{\text{e ref}}(i) - T_{\text{est}}(i) \tag{29}$$

This error is fed to torque PI controller and gives the output as $i_{\text{q ref}}$,

$$i_{\text{q ref}}(i) = i_{\text{q ref}}(i-1) + K_{p3}(T_{\text{error}}(i) - T_{\text{error}}(i-1)) + K_{i3}T_{\text{error}}(i) \tag{30}$$

where K_{p3}, K_{i3} are the proportional and integral constants used in PI controller of Torque.

In this way $i_{\text{q ref}}$ is generated and also speed of the motor is operated below rated speed because of the main field flux cannot be reduced. $i_{\text{d ref}}$ is operated at zero which leads to operate at unity power factor. By using dq0 to abc transformation block given the input as $i_{\text{q ref}}$ and get the output as three phase current (i.e.,$i_{a\text{ ref}}$, $i_{b\text{ ref}}$, $i_{c\text{ref}}$).By using hysteresis current controller compare reference currents ($i_{a\text{ ref}}$, $i_{b\text{ ref}}$, $i_{c\text{ ref}}$) and actual motor currents (i_a, i_b, i_c) and generating pulse width modulation gives the output as required switching signals to the switches for IGBTs and is fed to voltage source inverter as a gate pulses to operate. This controller gives the faster response and easy to design.

5 Simulation Results

The complete solar water pumping system is simulate in the MATLAB software and its performance is studied under different type of solar irradiation.

Figure 5a, b represents the PV array and PMSM parameters under 1000 W/m². Figure 5c, d represents the PV array and PMSM parameters under 500 W/m².

Figure 5a–d operates at solar irradiation of 1000 W/m² and 500 W/m² at a standard test condition of temperature 25 °C. In both the cases transient period is very low and quickly attains the steady state condition at 0.01 s. By using VSS-INC MPP technique gives the better time response (i.e., fast response to settle in the final value). PMSM parameter takes long time to settle compare with PV array parameters due to starting of motor takes some time for building flux and start of a rotor.
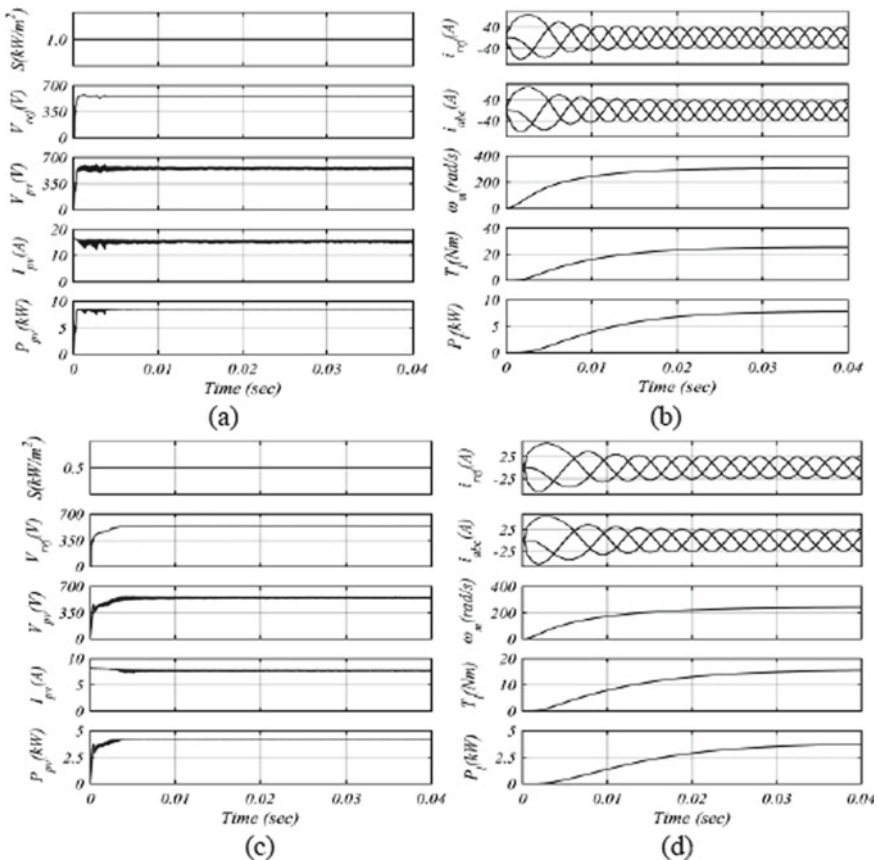
Fig. 5 a, b Simulation results of 1000 W/m² PV array parameters and PMSM parameters. **c, d** Simulation results of 500 W/m² PV array and PMSM parameters respectively.

This PMSM has a large time constant due to this settling at the steady state condition takes time. With these can be pump water to the 2 and half acres of the land. By taking an insolation and temperature of Hamirpur location data from the NASA of the real time provides the average insolation ranging from 6000KW-h/m²/day to 8000 KW-hr/m²/day and temperature ranging from 20 to 25 °C in the month between march to September as shown in Fig. 6.

(a)

(b)
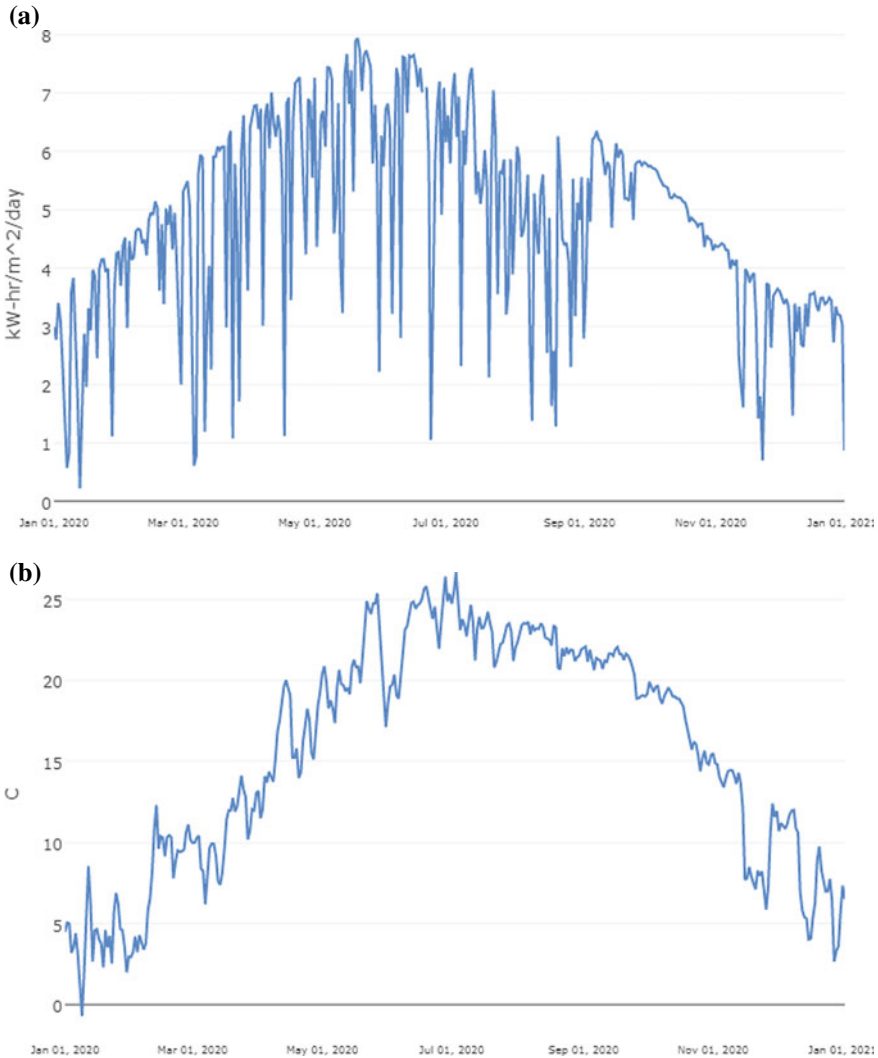
Fig. 6 **a** Hamirpur (H.p) Insolation data throughout the year from NASA site. **b** Hamirpur (H.p) Temperature data throughout the year from NASA site

With these inputs extract more power from the same PV array panels than before with the standard insolation of 1000 W/m^2 and temperature of 25 °C and with proportional improve in the PMSM specifications can be utilized for approximately 3–4 acres of land. Which is 2 times improvement in the system with almost same specifications and configuration of the solar panels. From October to February insolation levels are higher than standard but temperature are quiet low that is below 10 °C. This will give more current and low voltage and its impact on overall power output but improves panel's efficiency by providing cooling to the panels. These benefits can improve in both sides of customers as well as manufactures.

6 Conclusion

The PV array fed water pumping system driven PMSM has been simulated in 'Matlab software'. By using VSS-INC MPPT can extract maximum power without losing the transient and steady state behavior compared with the INC MPPT which has more power losses. For speed control of PMSM uses modified vector control. In these modified vectors control uses extra control loop for torque which improves torque response and also reduce the overburden on speed control. In this way speed control of PMSM with modified vector gives efficient control technique. By using feed forward term improves system response because it's operates directly by taking input as power of PV array. In these by using required amount of DC link capacitor can removes the usage of DC-DC converter which leads to reduce the system conversion stages and improves the system by economically.

References

1. Choudhary P, Srivatava RK, De S (2017) Solar powered induction motor based water pumping system: A review of components, parameters and control methodologies. In: 2017 4th IEEE Uttar Pradesh section international conference on electrical, computer and electronics *(UPCON)*. IEEE, pp 666–678
2. Mamat R, Sani MSM, Sudhakar KJSOTTE (2019) Renewable energy in Southeast Asia: policies and recommendations. Sci Total Environ 670:1095–1102
3. Meyer J, Von Solms S (2018) Solar powered water security: an enabler for rural development in Limpopo South Africa. IEEE Access 6:20694–20703
4. Kumar R, Singh B (2019) Grid interactive solar PV-based water pumping using BLDC motor drive. IEEE Trans Ind Appl 55(5):5153–5165
5. Murshid S, Singh B (2019) Implementation of PMSM drive for a solar water pumping system. IEEE Trans Ind Appl 55(5):4956–4964
6. Niu F, Li K, Wang Y (2015) Direct torque control for permanent-magnet synchronous machines based on duty ratio modulation. IEEE Trans Industr Electron 62(10):6160–6170
7. Varshney A, Singh B (2018) Direct torque controlled synchronous reluctance motor drive for PV array fed water pumping. In: 2018 IEEMA Engineer Infinite Conference (eTechNxT). IEEE, pp 1–6

8. Shukla S, Singh B (2018) Single-stage PV array fed speed sensorless vector control of induction motor drive for water pumping. IEEE Trans Ind Appl 54(4):3575–3585
9. Li J, Ren H, Wang S, Fang Y (2020) Integral Sliding mode control for PMSM with uncertainties and disturbances via nonlinear disturbance observer. In: 2020 39th Chinese Control Conference (CCC). IEEE, pp 2055–2060
10. Murshid S, Singh B (2020) An improved SMO for position sensorless operation of PMSM driven solar water pumping system. In: 2020 IEEE International Conference on Power Electronics, Smart Grid and Renewable Energy (PESGRE2020). IEEE, pp 1–5
11. Zhang Z, Guo H, Liu Y, Zhang Q, Zhu P, Iqbal R (2019) An improved sensorless control strategy of ship IPMSM at full speed range. IEEE Access 7:178652–178661
12. Prakash G, Pradeepa S (2018) Design and modeling of MPPT for solar based power source. In: 2018 4th International Conference on Electrical Energy Systems (ICEES). IEEE, pp 624–629
13. Podder AK, Roy NK, Pota HR (2019) MPPT methods for solar PV systems: a critical review based on tracking nature. IET Renew Power Gener 13(10):1615–1632
14. Chandel SS, Naik MN, Chandel R (2015) Review of solar photovoltaic water pumping system technology for irrigation and community drinking water supplies. Renew Sustain Energy Rev 49:1084–1099
15. Elgendy MA, Zahawi B, Atkinson DJ (2014) Operating characteristics of the P&O algorithm at high perturbation frequencies for standalone PV systems. IEEE Trans Energy Convers 30(1):189–198
16. Singh B, Mishra AK, Kumar R (2016) Solar powered water pumping system employing switched reluctance motor drive. IEEE Trans Ind Appl 52(5):3949–3957
17. Pokharel M, Ghosh A, Ho CNM (2018) Small-signal modelling and design validation of PV-controllers with INC-MPPT using CHIL. IEEE Trans Energy Convers 34(1):361–371
18. Yang L, Yunbo Z (2019) A novel improved variable step size INC MPPT method for PV systems. In: 2019 Chinese Control and Decision Conference (CCDC). IEEE, pp 5070–5073
19. Sahoo RR, Singh M (2016) Analysis of variable step incremental conductance mppt technique for PV system. IOSR J
20. Venkatramanan D, John V (2019) Dynamic modeling and analysis of buck converter based solar PV charge controller for improved MPPT performance. IEEE Trans Ind Appl 55(6):6234–6246

Experimental and Flow Simulation Study of VARTM Process

Maulik V. Shah and Vijaykumar P. Chaudhary

1 Introduction to VARTM Process

Since last two decades, VARTM process has become prominent technology for manufacturing the polymer matrix composites (PMC). It is a closed-mold process which helps in reducing volatile organic compounds (VOC) emission, leads to high quality and repeatability, and also provides flexibility and scalability of open-mold hand layup processing with high fiber volume fraction. Primarily, VARTM process plays key roles in promoting the quality, cost-effective, and very large complex composite structures. VARTM processes are widely used in different sectors such as marine, energy, and infrastructure building, wherein aerospace and defense industries in major.

In order to obtain high fiber volume fraction composite laminate, it is necessary to have complete mold filling with sufficient saturation of fiber mat. So, VARTM process can be critical in such situation where improper resin infiltration in the fiber mat results dry spots and faulty parts. To realize decent quality product, various process parameters need to be correctly set like the numbers of injections and venting ports with its locations, vacuum pressure, resin viscosity, and many more [1–3].

The present study focuses on manufacturing of fiber laminates by the VARTM process and verifying flow simulation model of resin infusion using input parameters taken from experiment. This flow simulation study is to simulate VARTM infiltration process and accomplished using the computational fluid dynamics (CFD) software ANSYS FLUENT. In order to optimize the process parameter and further improvement in the process, a CFD resin flow model can be useful [4, 5].

M. V. Shah (✉) · V. P. Chaudhary
Department of Mechanical Engineering, Chandubhai S. Patel Institute of Technology, Charotar University of Science and Technology, CHARUSAT Campus, Changa, Gujarat, India
e-mail: maulikshah.me@charusat.ac.in

V. P. Chaudhary
e-mail: vijaychaudhary.me@charusat.ac.in

2 VARTM Experimentation

2.1 Materials

In this work, the woven basalt fabric is used to make composite laminate and supplied by Composites Tomorrow. Basalt fabric has a tensile strength of 2500 MPa, the areal weight of 400 g/m^2, and the fiber density of 2.7 g/cc. Each layer of basalt fabric thickness is 0.344 mm. The mixing fluid used in the experiment was an epoxy resin supplied by Atul Ltd. The resin was chosen for its relative ease of use and having low viscosity for high performance applications. The epoxy resin having initial mix viscosity at 25 °C of 400–600 MPas, the specific gravity of 1.10–1.20 g/cm^3, and pot life at 25 °C of 6–8 h has been considered. Similarly, hardener comes with the epoxy resin having mixing ratio of 1:0.42. Typical properties of epoxy resin system have tensile strength of 40–45 MPa and flexural strength of 80–120 MPa. The glass transition temperature of epoxy resin system is 190–220 °C. The other consolidate materials like release agent, peel ply, perforated sheet, high permeable medium, PVC infusion channel, vacuum bag, sealant tape, vacuum pump, T-joint pipe, PVC hose, and breather sheet have been provided by GBT Composites Technology Ltd. The peel ply applied as a last material in stack up sequence and peeled from the laminate after curing and left textured surface which is free from any contamination. The perforated sheet is used to separate and release the laminate from the vacuum stack following the cure. It also allows resin and volatiles to bleed come out of the laminate. High permeable medium accelerates the resin flow inside the vacuum stack. Breather sheet ensures the air to be easily extracted and absorbs excess resin came from the laminate [6].

2.2 Experimental Setup

The VARTM process can be divided into several steps. At the first, the mold tool considered in this study is aluminum flat plate with high surface finish. Next, three times release agent layers have been applied over the mold surface at 15 min of interval, which allows demolding of the cured composite laminate from the mold tool. Meanwhile, the basalt fabric has been put in the microwave oven for 10 min for 100 °C to remove moisture content. The schematic diagram of VARTM process is shown in Fig. 1.

The preform was formed by stacking the ten layers of plain weave basalt fabric sheet. The square-shaped basalt fabric layers having size of 300 mm × 300 mm have been kept over the mold surface. Next, peel ply and perforated sheet have been kept on the top of the basalt fiber preform. A layer of high permeable medium has been placed on the perforated sheet. The infusion PVC channel is then located at one side of the mold, which is connected to the high permeable medium and the resin bucket using T-joint connection. The vacuum sealant tape has been mounted around
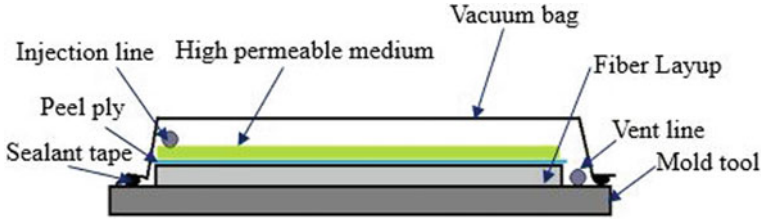
Fig. 1 Schematic diagram of VARTM Process [1]

the mold to make it leak proof. The vacuum pump is connected to another end of the preform through vent line along with breather sheet. The size of high permeable medium is kept shorter than the basalt fabric layer such that it must not cover the edges near the outlet. Sometimes, second layer of high permeable medium (nearly half in the size than first one) is also placed to accelerate the flow in case of more thickness preform. At the end, a vacuum bag is used to envelope the stacking and attached with vacuum sealant tape. To begin with the operation, resin inlet valve to be kept closed while the vacuum is applied through the vent line to remove the air inside the mold cavity. This process should remain on for 15 min before the resin infusion leads to compress the preform. The initial leakage has been checked for 5 min by monitoring the pressure drop occurred in the vacuum system. The inlet valve has been opened to make resin flow inside the mold cavity. The step-by-step procedure has been demonstrated in Fig. 2. Once the mold got completely filled with resin, the inlet valve is closed. Subsequently, the vacuum pump is kept running for 24 h until the resin cures. Then, whole system has been kept under 70 °C temperature by

Fig. 2 Experimental setup of VARTM process with necessary steps

convection heat through air heater which helps to increase the rate of curing process. The rest of the accessories have been removed after the curing process. At last, flat laminate of BFRP has been demolded from the aluminum mold [7, 8].

3   VARTM Model Development

The VARTM process has to deal with two fundamental models: first, resin flow through the fiber layup, and second, compaction and relaxation of the fibers under the vacuum.

3.1   Resin Flow Model

This model traces the flow of resin through the high permeable medium and the fiber stacking. By considering as a quasi-steady state condition, the governing equation for the incompressible resin flow can be defined by following continuity Eq. (1),

$$\nabla u = 0 \tag{1}$$

The movement of the resin while saturating the fibrous preform is calculated as the flow of an incompressible fluid through a permeable medium. Usually, flow through the porous media can be modeled using Darcy's law Eq. (2),

$$u = -\frac{K}{\mu} * \nabla p \tag{2}$$

where the fluid velocity is u, resin viscosity is μ, pressure gradient is p, and permeability is K.

3.2   Compaction Model

During the flow of resin in the fiber layup, due to the nature of flexible vacuum bag, variable compaction pressure has been generated on the fiber layers. The total atmospheric pressure is balanced by the resin pressure and compaction pressure by the fiber. It can be written as Eq. (3),

$$P_{atm} = P_{comp} + P_{resin} \tag{3}$$

where P_{atm} is the atmospheric pressure outside of the mold cavity, P_{comp} is the compaction pressure applied to the fiber layup, and P_{resin} is the resin pressure [4, 9–11].

4 Numerical Simulation

The complete VARTM process has been simulated as two-phase flow through a porous medium in ANSYS FLUENT software. A multiphase volume of fluid (VOF) model has been taken to trace the resin flow patterns. A Euler explicit time-dependent formulation was used for getting the solution of the VOF method [12]. The 2D geometry of preform has been modeled in ANSYS workbench geometry module as per experimental details. Linear 2D quadrilateral elements were used to create the finite element mesh.

Boundary conditions are applied as: the inlet pressure of 1013.25 mbar at inlet position and outlet pressure of 0 mbar at outlet position. In this study, the resin flow is uniform across the width of flat layers as it is defined as "wall." As an input data to the FLUENT, the other important parameters such as resin velocity, pressure jump coefficient, average permeability, resin density and viscosity, and final laminate thickness have been provided. The simulation model assumed that the properties of resin remained constant during the infusion process. The value of pressure jump coefficient has been calculated using all input values. The "porous jump" boundary condition in FLUENT is used to model thin layers with known velocity (pressure-drop) characteristics [13].

The flow front location, resin pressure distribution, and resin filling pattern at different locations are obtained using time-dependent approach in simulation results. These simulation results are compared with the experimental results. Figure 3 shows the flow sequence in actual VARTM experiment at different interval of time, and Fig. 4 shows the predicted resin flow pattern at different interval of time by simulation approach. In Fig. 4, the red color represents resin rich volume which is fully saturated,

(a)   (b)   (c)
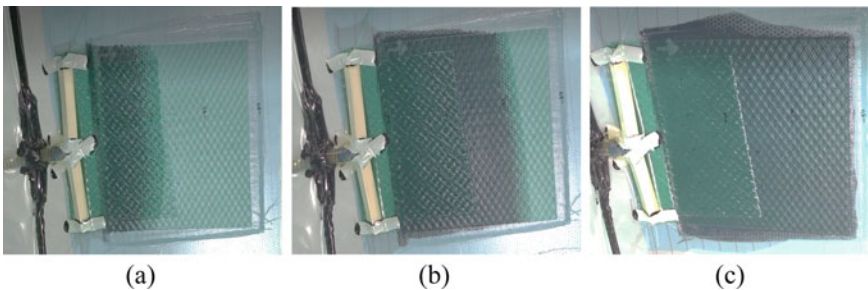
Fig. 3 Measured flow sequence in actual VARTM experiment **a** at 50 s, **b** at 200 **s,** and **c** 400 s, respectively
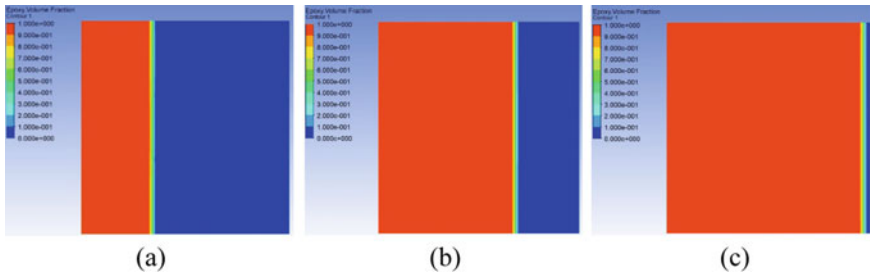
Fig. 4 Predicted resin flow pattern by simulation approach **a** at 50 s, **b** at 200 s, and **c** 400 s, respectively

and apparently, blue color represents resin empty volume which is completely dry [5].

This study has envisaged the 1D flow comparisons for VARTM through experiment and simulation. The detailed method has shown for fabricating the composite panel without void generation and premature resin gelation, while reducing the mold fill time and wastage of resin. The total resin infusion time was measured as 450 s as opposed to simulated infusion time of about 432 s. The simulation model did not predict a total wet-out of the preform at the same filling time because the simulation model results were based on constant permeability values.

5   Conclusion

The BFRP flat laminate has been manufactured using VARTM manufacturing process. In this experiment, plain weave basalt fabric layers with epoxy resin have been used. It has been observed in the beginning of experiment, the resin flow is quite fast due to the high permeable medium. Afterward, the resin flow velocity decreases because of enlarging viscosity, lower pressure gradient, and capillary forces. A simulation model of the VARTM process was developed using the CFD software package ANSYS FLUENT. The two-dimensional model used the VOF two-phase resin-air model to track the resin flow patterns and the infusion times of basalt preform during the resin infusion stage of the VARTM. The predicted resin flow patterns and infusion time by CFD simulation model are well agreed with measured flow sequence obtained during the manufacturing of BFRP panel. The percentage deviation in the infusion time between the experimental and simulation approach has been found within 5%.

References

1. Shah M, Chaudhary V (2020) Flow modeling and simulation study of vacuum assisted resin transfer molding (VARTM) process: a review. In: IOP conference series: materials science and engineering, vol 872, No. 1, p 012087
2. Hancioglu M, Sozer EM, Advani SG (2020) Comparison of in-plane resin transfer molding and vacuum-assisted resin transfer molding 'effective' permeabilities based on mold filling experiments and simulations. J Reinf Plast Compos 39(1–2):31–44
3. Hindersmann A (2019) Confusion about infusion: an overview of infusion processes. Compos Part A Appl Sci Manuf 126:105583
4. Adhikari D, Gururaja S, Hemchandra S (2021) Vacuum infusion in porous preform with different mould configurations: flow simulation and experimental validation. J Reinf Plast Compos 40(7–8):321–338
5. Tuncol G, Loos AC, Cano RJ (2011) Simulation of resin infusion in the manufacture of fiber metal laminates by VARTM. In: Proceedings of the ICCM 2011, vol 18
6. Fracassi FT, Donadon MV (2018) Simulation of vacuum assisted resin transfer molding process through dynamic system analysis. J Compos Mater 52(27):3759–3771
7. Kedari VR, Farah BI, Hsiao KT (2011) Effects of vacuum pressure, inlet pressure, and mold temperature on the void content, volume fraction of polyester/e-glass fiber composites manufactured with VARTM process. J Compos Mater 45(26):2727–2742
8. Gajjar T, Shah DB, Joshi SJ, Patel KM (2020) Analysis of process parameters for composites manufacturing using vacuum infusion process. Mater Today Proc 21:1244–1249
9. Gajjar T, Shah DB, Joshi SJ, Patel KM (2020) Experimental study of thickness gradient and flow simulation in VARTM process. Fibers Polymers 21(2):384–391
10. Song X, Loos AC, Grimsley B, Cano R, Hubert P (2004) Simulation of the vacuum assisted resin transfer molding process. Southern Illinois University at Carbondale Materials Technology Center; July 1
11. Stolz J, Fideu P, Herrmann A (2017) Extended physics modeling of the resin flow during vacuum infusion processes. In Proceedings of the COMSOL conference
12. Fluent 17.2 User's Guide, 17.3.1 Overview and Limitations of the VOF Model, Ansys Inc.
13. Fluent 17.2 User's Guide, 6.3.20 Porous Jump Boundary Conditions, Ansys Inc.

Electrically Operated Hygiene Bin to Simplify the Initial Stage of Diaper Composting

Dipti N. Kashyap, Rounak Choudhury, Pranav Thete, Savita Baviskar, and Pravesh Khatwani

1 Introduction

The world's population has been steadily increasing for the last 7 decades. According to UNICEF, in India every day 67,385 babies are born. Hence, India contributes for one-sixth of the world's infant birth. Thus, it leads to the consumption of more and more products especially the use of diapers which has been the main concern for environment as these diapers once used are disposed unprocessed. In 2020, the diaper market of India rose to 1.25 billion US dollars considering that all the leading brands in the states like Maharashtra, Delhi NCR, Tamil Nadu and others states by the survey conducted by IMARC, which predicted the trend is set to increase. As a matter of fact, the data suggested that all the children born are not privileged by birth. Thus, to use diapers in a developing country such as India assumptive calculating if a baby usage of least a diaper a day and there would be 50,000 of them and a baby diaper would weigh at least 300gm which is 1.5 tonnes of waste that these babies would produce in subsequent days to come. More than 90% of used diaper's go to the municipal corporation or are disposed carelessly on some abandoned land. This could add to burden on our environment which will take more than 400 years to discompose which is not a good indicator, as it shall release harmful pathogens while in the process. Hence, there is an urgent need for some technique to decompose these used diapers. Zulfikar, Wiwit Aditama, Nasrullah [1] discussed various methods and composition of material in accordance with experimenting composting temperature, composting moisture, composting time period and composting PH value and quality of compost and had come up with Takakura method which included taking 5 diapers with different ratios along with organic waste and then moisturised with sugar and salt solution and kept for 5–7 days, and then it was put in Takakura mixture which was taken into sack for 2 weeks also known as normalisation process. This makes the decomposition of

D. N. Kashyap (✉) · R. Choudhury · P. Thete · S. Baviskar · P. Khatwani
Department of Mechanical Engineering, Yeshwantrao Chavan College of Engineering, Nagpur, India

the diapers by microorganisms most successful with 40% diaper and 60% organic waste which could turn out to be useful in agriculture. Navarro Ferronato, Máximo Lucio Nova Pinedo and Vincenzo Torretta [2] discussed the various assessment techniques for analysing baby diaper composting in Bolivia. In this method, diapers were mixed with things such as cow dung, activated bacteria and red earthworm. These samples were kept in hermetically sealed container, and the previous method was repeated again and again; some of them were mixed with components. It was found that components which were mixed with cow dung took 60 days to decompose, whereas one that was mixed with earthworm and activated bacteria took 70 days to decompose but the hydrogel remains as it is. Hence, the hydrogel needs cow dung to decompose. Hence, the results were obtained. Joan Colon, Luz Ruggieri, Antoni Sanchez, Aina Gonzalez and lgnasi Puig [3] discussed composting of diaper waste with municipal waste. Where they studied diaper source-separated organic fraction of municipal solid waste (OFMSW) and OFMSW without diaper. So, the evolution of routine parameters and biological activity were monitored. The result showed that both the compost was identical in every term with no pathogenic micro-organism but the OFMSW with 3% of disposable diaper was tested with slightly higher level of zinc which can prevent the use large amounts of diaper mixed with OFMSW. Norihiro Itsubo [4] discussed a new technology for closed-loop recycling of used paper diapers which are first- crushing, washing and separation technology, second-ozone treatment technology, third-SAP reactivation technology and fourth-verification of the quality and safety of recycled product. These all are the conventional ways to reduce the diaper waste with the other waste generated locally but also increased the use of diaper and the other hygiene product which signifies that the conventional ways would take time to process that amount of waste. So, the incineration bins were introduced to solve the problem. A study by TQH consulting for the NFSSM Alliance published a report in 'MENSTRUAL WASTE DISPOSAL IN INDIA' on March 2020 of all the actions taken by the government to promote waste disposal system and a brief study report whether all in India have taken place, with briefed norms and specification to use a public incinerator. But one cannot run from the fact that the gases produced from these techniques are harmful for an individual and also for the environment. The study by 'Chintan environmental research and action group' concluded that burning sanitary product released high toxic 'dioxins gas' which had been a reason for multiple health problems. So, the incinerators may produce energy and reduce the waste at the same time but also could release are much more harmful than expected. Therefore, keeping some of the main points in mind Kosemund [5] discussed all the risks before and after the diaper had been used to exposure-based risk assessment used by procter and gamble for absorbent hygiene product. Gerba [6] discussed the occurrence of enteric pathogenic viruses and protozoan parasite in composted municipal domestic solid waste and their concentration had increased by the addition of diapers by 2-3 folds. One out of 19 samples collected after 175 days of ageing were found positive for Salmonella. This indicated that the pathogens were destroyed during composting or present one organism per 40-50 gm of compost. Using this information, one could think of producing biogases and compost at the same time De Rycke [7] discussed that if the diaper has been composted with solid

paper product and biowaste, it would result in high-quality compost and also the life cycle of a disposable diaper. Therefore, in existing economy setting up identical but separate biogas plant where the diaper can be recycled with biowaste, this way would contribute to the waste management. Location of manure produced can be used for the non-fruit bearing plant would make the environment eco-friendlier. Khoo [8] discussed the different technologies used to process a diaper in large quantity and stated three main processes—landfill, incineration and recycling—and explained used diaper composition of waste as it briefed about the mechanism of enzymatic biodegradation. So, it discussed the machine available and all of them were capable to process the waste when applied in a bulk but the process should have been carried out at household level which could have reduced the use of resources and then carried out to the plant for further process. Hence, electrically operated hygiene bin is introduced to carry out the initial processing at the house. This machine is capable of scraping off the pulp part of the diaper leaving the outer layer separated so it could retrieve afterword for recycling it as a plastic material. The scraped-out pulp of the diaper is collected in a bin which can be dumped in the environment so that it becomes easy for the nature to play its part.

2 Components of Electrically Operated Hygiene Bin

I. Inner drum or diaper holding drum: The inner drum is provided to hold the diaper in place so that during processing the diaper remains intact, which reduces chances of disruption in the process.
II. Outer drum: Outer drum is appointed to hold all the ongoing processes together and to provide a layer of protection so that the operator won't feel uncomfortable at the time.
III. Cutter: Cutter is the main component of the machine, and the cutters here are identical to earth auger bit with sharp edges so that it is capable of making significant cuts on the used diapers.
IV. Wire Brush: The wire brush is less dense than typical wire brushes available so that it can scratch out the diaper upper surface after the cuts.
V. Scraper: It can be distinguished as a teethed horizontal plate located at the end of the process and opposite to the first cutter on the inner drum with 0.5–0.6 cm clearance, and it is meant to ensure that nothing is left after the process is complete.

3 Methodology
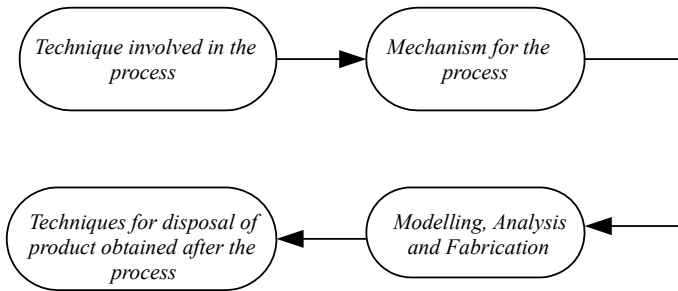
3.1 Technique Involved in the Process

- The process used to hold the diaper on the inner drum is initiated by simple magnets and can increase or decrease according to the size of the diaper as there are number of grooves appointed in which the magnet will get fitted without interrupting the path of cutter.
- The cutter selected here resembles the spiral geometry (earth auger) because of which irrespective of diaper placed on the inner drum the cutter will successfully make the cut on it.
- Length of the cutter selected is longer than the inner drum and is equal to the outer drum so the diaper is capable to process adult diaper at a time.
- A teethed scraper is appointed at the end of the process so that anything left on the diaper will be taken off of it before the next rotation and will carry on until it is less than the clearance provided between the scraper and the inner drum.
- Gears are used so that all the cutter including the wire brush will rotate at the same time.

3.2 Mechanism for the Process

There will be two separate motors, one will rotate the inner drum and the other will rotate the cutters and the wire brush. The cutters along with the wire brush will rotate simultaneously with the help of spur gear.
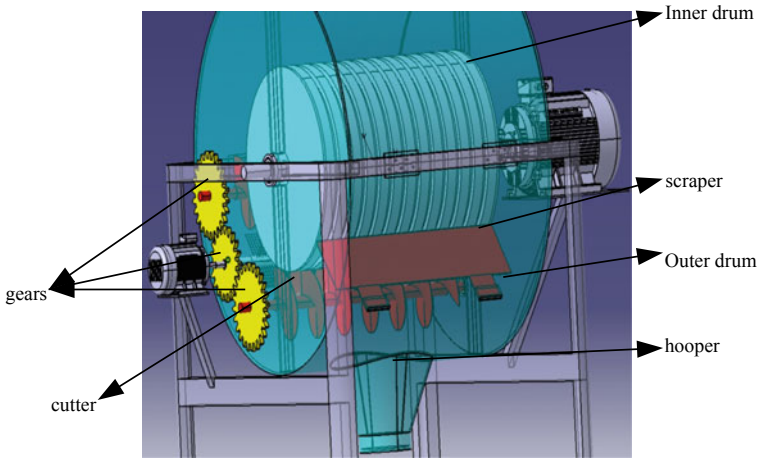
Fig. 1 Different parts of the electrically operated hygiene bin

3.3 Modelling, Analysis and Fabrication

3.3.1 Modelling

The modelling is done on CATIA software (Figs. 1 and 2).

3.3.2 Analysis

Analysis was done on Ansys software.

1. Gear analysis (Figs. 3 and 4):

To conduct the analysis on the gear a torque of 30Nm was applied and was found that the design was safe for operation.

2. Cutter analysis (Figs. 5 and 6):

To conduct the analysis on the cutter, a force of 2000 N was applied and the stress and deformation on different parts were noted.

3. Drum analysis (Figs. 7 and 8):

The stress and deformation on the drum of were recorded on different parts after the application of 2000 N.

Fig. 2 Full vision of the
electrically operated hygiene
bin
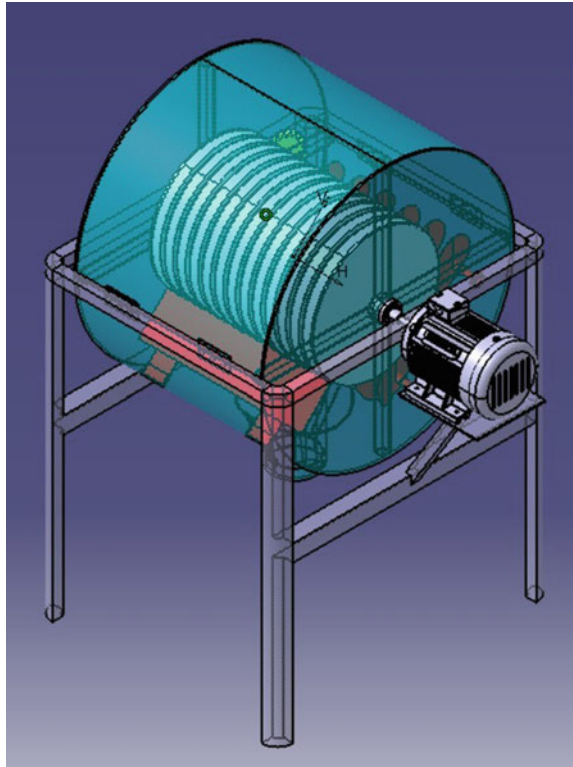
3.3.3 Fabrication

As some of the machine parts are selected as per the availability in the market. The
parts such as the cutter selected here for the machine are identical to the earth auger
bit available in the market. And some parts such as the inner drum the outer drum are
to be manufactured as per the specification of the diaper required to be processed.
Both the drum are made up of sheet metal SAE1010 cold-drawn carbon steel. And
the gears are made up of grade SAE1025.

3.4 Cellulose Removal and Composting Technique

There are many introduced techniques for the disposal of the used disposable diaper
from which the techniques mainly used are incineration and landfills and the tech-
nique now adopted by few are composting; but in this technique, one has to take great
efforts where individual conducting the technique have to pill the diaper first then
put it for composting. The machine introduced will do all the work to be done on the
diaper and will provide the inner material which can be composted. As known that
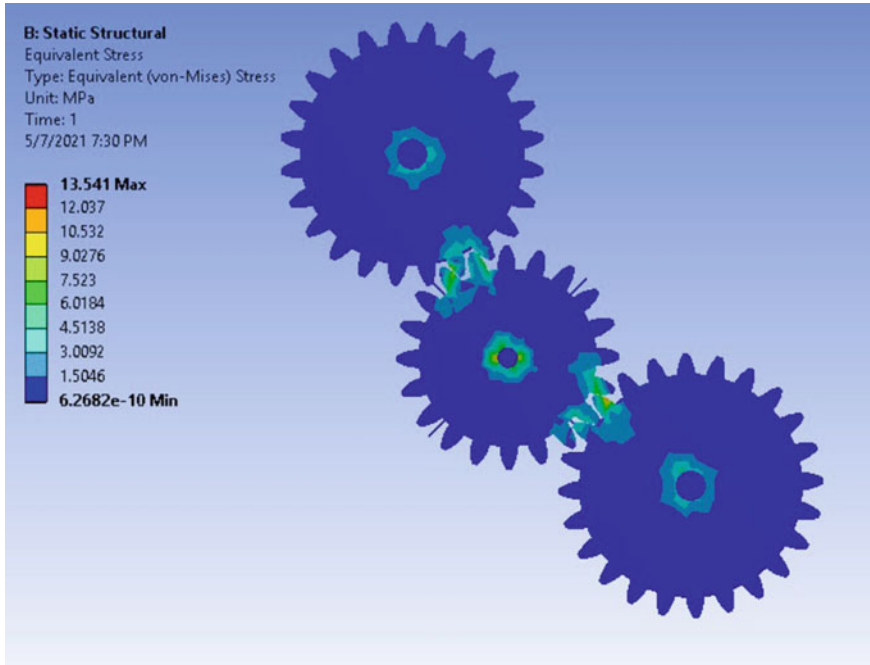
Fig. 3 Gear stress analysis

Indian government has introduced the collecting of wet and dry waste separately, where wet waste is vegetable leftover, garden waste and all the waste that can be composted into manure and the dry waste is generally paper and plastic product as the paper may contain plastic or they may be printed so is not collected with the wet waste. If this waste is converted into compost, it can contribute to the environment, and the other way, it is to send this waste into the biogas generation plant where it can be turned into manure, and at the same time, biogas will also be generated which is effectively generated can reduce the needs of our natural occurring gases. And the plastic generated from the process can be recycled with the other plastic waste.

4 Different Aspects of the Diapers and Composting

4.1 Aspects

Different diaper brands claim for different comfort that these products provide to the customer but the fact is all the product in the market have the similar core material that is the absorbent and the cellulose. There are the two most important components that are to be dealt with to convert the disposable diaper into a compost. The thickness
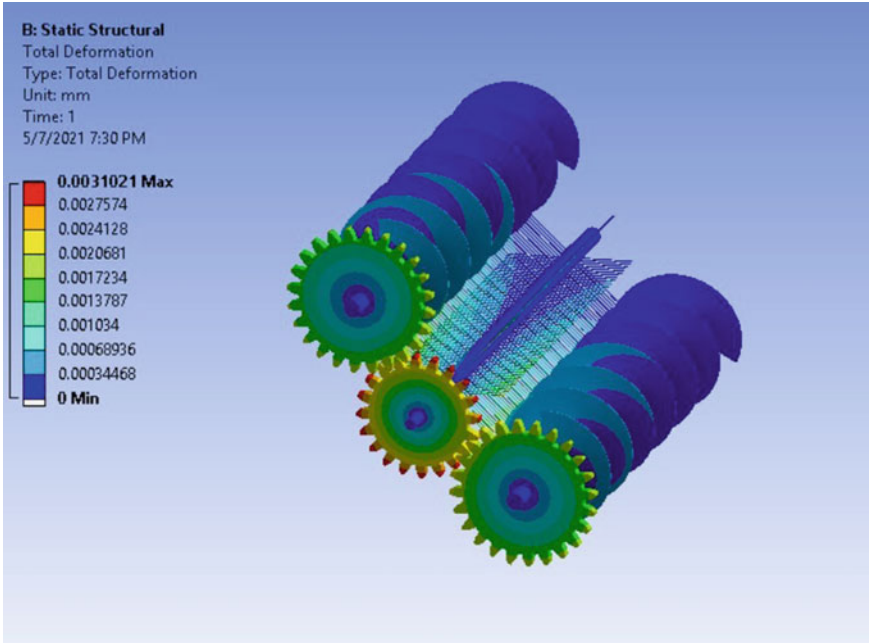
Fig. 4 Gear deformation analysis
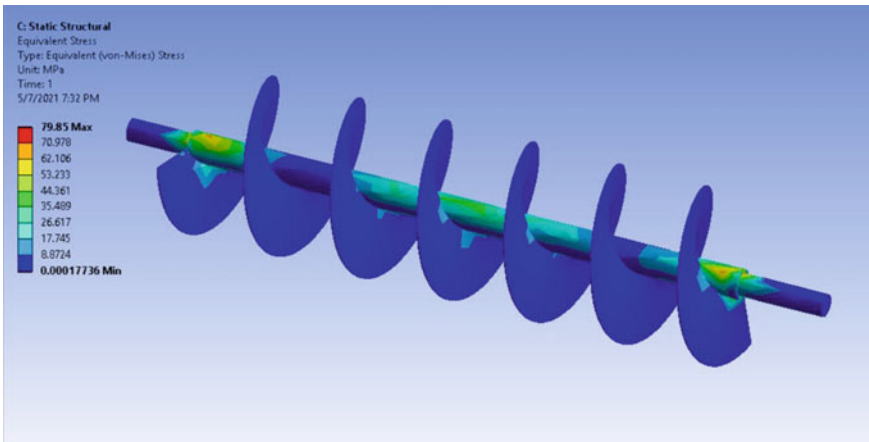
Fig. 5 Cutter stress analysis
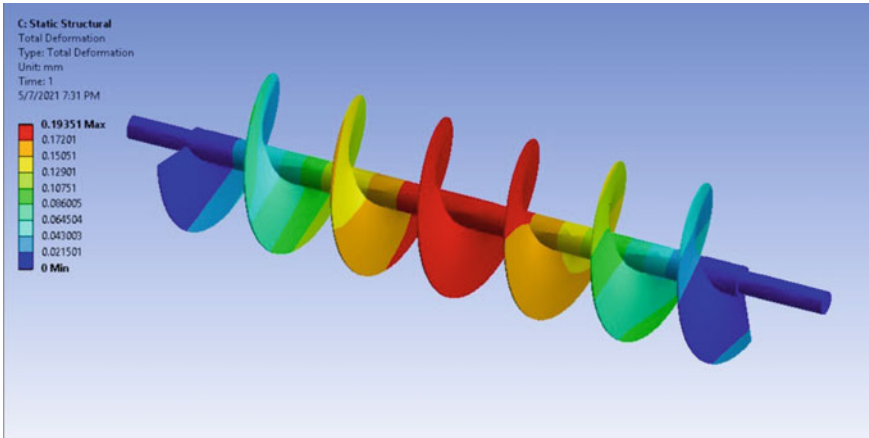
Fig. 6 Cutter deformation analysis
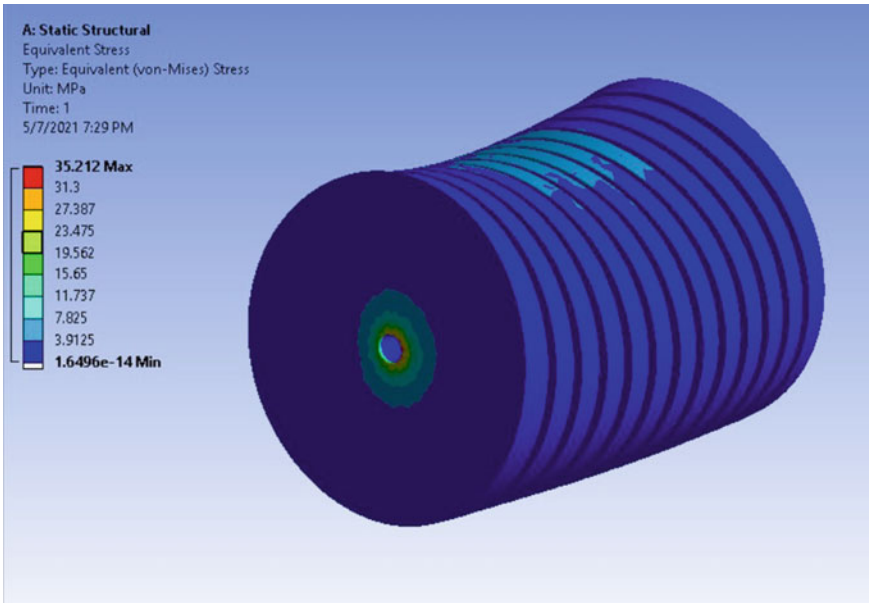
Fig. 7 Stress analysis of drum

of the diaper is one more aspect to look after to carry out the process easily. Diapers'
thickness may vary accordingly to the size and company, i.e. for a small size of
baby diaper, thickness comes between 1.5 and 2cm, and that for the adult diaper, the
thickness is 3.5cm to 4cm; this thickness was determined; when the diaper was in
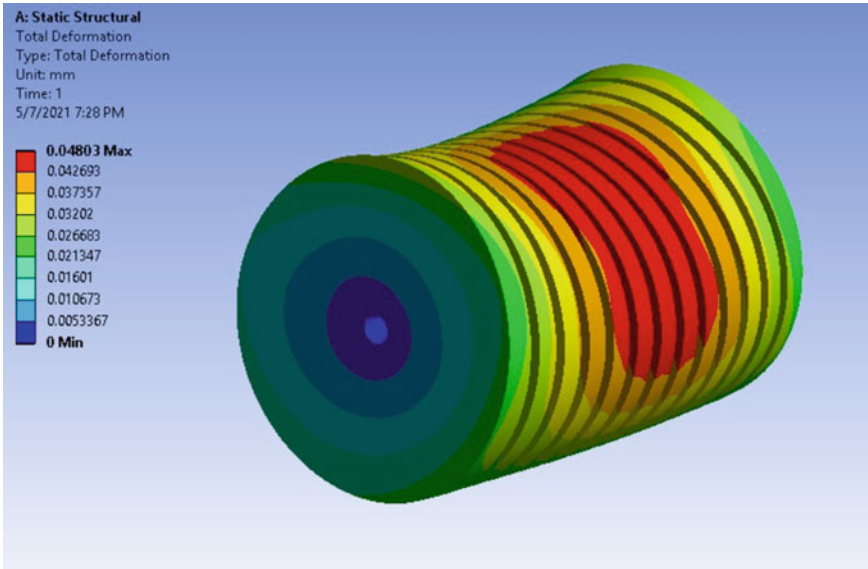
Fig. 8 Deformation analysis of drum

their folded form, the conclusion was taken after taking two samples of each baby diaper and adult diaper when they are not used (Fig. 9).

Inner layer of the diaper (absorbent layer):

- This layer is responsible for holding up the liquid till it is changed with a new one. This layer is combined with cellulose to make it comfortable for the user.

Fig. 9 Thickness of the diaper while the diaper is in folded condition

- The cellulose is a nature obtained product or can be made artificially; the preferred way is to make this artificially as this should be in abundance to insure the continuous production.
- Cellulose is biodegradable in nature and is only the part which consumes most of the diaper composition.
- Superabsorbent in diaper mostly is sodium poly-acrylate; this is also called as water- lock as the name it can hold 100–1000 times of liquid to its mass, and the chemical formula is (C3H3NaO2)*n*.
- Sodium poly-acrylate is hard to be degraded in nature. Wilske [12] discussed the degradation of superabsorbent polymer (SAP) in different agricultural soil and at different temperature; no significant changes were recorded due to the variation in temperature in 12 weeks. After conducting the experiment, suggestion was made that the poly-acrylate main chain degrades in the soil at a rate of 0.12–0.24% per 6 months.
- Sodium poly-acrylate is responsible for soil hardening and is capable of causing all the environmental issues that can be caused by plastic; once the powder is converted to gel, after absorbing water it is dumped into soil and is either not degradable if at all at very slow rate if the applied quantity is in bulk resulting pollution. It can also affect adversely to human, if enters into human body, it can also absorb blood which is not good that the following points were disused at https://english.mathrubhumi.com

4.2 Composting

Steps were conducted to verify how SAP performs in soil.

- Step 1—Selection of soil: as the availability garden soil was selected for the process (Fig. 10).
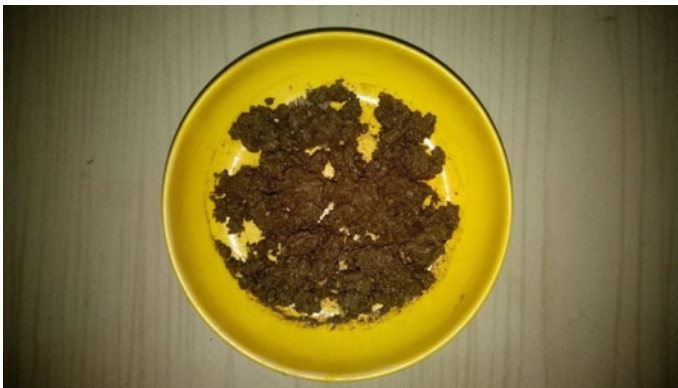
Fig. 10 Garden soil with nominal moisture contain

- Step 2—Taking SAP from the diapers: here 2 cm × 2 cm of diaper inner part was taken to conduct the step, and two samples were taken to monitor the after results. The first sample was taken a whole sheet of the given above dimension, and the second sheet was shredded into small pieces (Figs. 11 and 12)
- Step 3-Results: both the containers were opened after a duration of 4 months, and it was observed that there was no moisture contained in both the container and a hard mass of garden soil was recovered. After crushing both the retrieved sample separately, it was hard to detect the difference between both of them (Fig. 13).
- Step 4—SAP Sample: the sample was collected to observe if there are any changes, if the SAP is soaked in water for 6 months. And the observation was made that there are no changes in it. It still contains the amount of water that it was used at the initial stage (Fig. 14).

Fig. 11 SAP samples

Fig. 12 Container to contain the samples for further consideration. Sample A: Not Mixed (a layer of inner diaper material is clearly visible). Sample B: Mixed (as it is thoroughly mixed with the garden soil the sample is not clearly visible

Fig. 13 Results of both the samples

Fig. 14 SAP soaked in water

- All the samples were collected from the single diaper, and the same company was pampers (Fig. 15).
- After the machine has done its part, the leftover will be collected in a bin. The bin used is with some changes, and the changes are to be done because after gradual disposal of leftover into the bin water (urine that is collected in the diaper) will squeeze from the cellulose. If there is no way to pass out this water, there is a high

chance that the collected material will smell bad. So, perforation at the bottom-most layer is made and another container is provided to collect the water that comes out (Fig. 16).

- At a time, 5–6 kg of material can be collected in the drum. Before the collection takes place, the operator should put any brown paper or cardboard pieces or blank white paper (should not be a newspaper) should be kept on the bottom surface of the drum for better result. The operator of the machine can also put kitchen waste into the machine, dried leaves especially Neem leaves will give much better result as it acts as an insecticide. After the collection, the collected material should be spread on the ground so that it can get full heat of the sunlight and should be left at least for a month. This will help in killing all the pathogens and the unwanted bacteria. Most important the land used to spread this material should not have any fruit-bearing plant and also should be free from public.

Fig. 16 Perforated bin with bottom urine collector
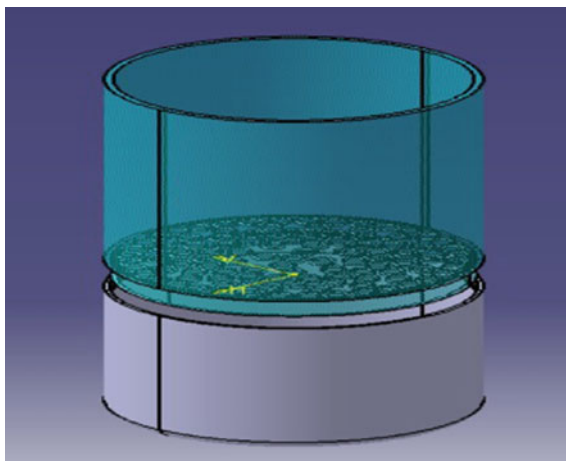
5   Conclusion

The different aspects of diaper waste were studied along with the different disposal techniques for diaper waste. Presently, incinerator is used for easy disposal which will contribute to air pollution. The proposed model is capable of separating the compostable cellulose from diaper's upper layer and composting of the same with the garden soil. It will help in reducing the huge waste generated due to increasing the number of diaper usage in the country and can be developed commercially for small geographical areas.

References

1. Zulfikar Z, Aditama W, Nasrullah (2019) Decomposition process of disposable baby diapers in organic waste with Takakura Method. Int J Sci Healthcare Res 4(1). ISSN: 2455-7587
2. Ferronato N, Pinedo MLN, Torretta V (2020) Assessment of used diapers composting in Bolivia. MDPI Sustain 12:5055.https://doi.org/10.3390/su12125055
3. Colon J, Ruggieri L, Sanchez A, Gonzalez A, Puig I (2010) Possibilities of composting disposable diaper with municipal solid waste. Res Gate Waste Manage Res 29(3):249–259. https://doi.org/10.1177/0734242X10364684
4. Itsubo N, Wada M, Imai S, Myoga A, Makino N, Shoatake K (2020) Life cycle assessment of the closed-loop recycling of used disposable diaper. MDPI; Resources 9:34. https://doi.org/10.3390/resources9030034
5. Kosemund K, Schlatter H, Ochsenhrit JL, Krause EL, Marsman DS, Erasala GN (2008) Safety evaluation of super absorbent Baby Diaper. Elsevier. https://doi.org/10.1016/j.yrtph.2008.10.005
6. Gerba CP, Huber MS, Naranjo J, Rose JB, Bradford S (1994) Occurrence of enteric pathogens in composted domestic solid waste containing disposable diapers. Sci Direct, Waste Manage Res 13(4):315–324

7. Rycke AD, Lentz R, Franke M, Prinsen WA (1998) Diapers recycled as compost. integrated soil and sediment research: a basis for proper protection. Soil Environ 1. Springer, Dordrecht, pp 713–723. https://doi.org/10.1007/978-94-011-2008-1_154

8. Khoo SC, Phang XY, Ng CM, Lim KL, Lam SS, Ma NL (2018) Recent technologies for treatment and recycling of used disposable baby diapers. Sci Direct Process Safety Environ Protect 123(2019):116–129

9. Anderson GF (1991) Recycling the components of used single use human waste collecting and/or absorbing products. United States Patent, Patent number: 4,990,244

10. Cina Y (1994) Process of recycling of disposable diapers and the machine components thereof. United States Patent, Patent number: 5,322,225

11. Bartlett BL, Woodenville W (1994) Disposable diaper recycling process. United States Patent, Patent number: 5,292,075

12. Wilske B, Bai M, Lindenstruth B, Bach M, Rezaie Z, Frede H-G, Breuer L (2013) Biodegradability of poly-acrylate super absorbent in agricultural soil. Springer, Berlin. https://doi.org/10.1007/s11356-013-2103-1

Evaluation of Criteria for Developing Renewable Energy Sources in India

Himanshu Prajapati, Ravi Kant, and Chirag Solanki

1 Introduction

Energy is an essential key factor for economic improvement of nation. It plays an important role in economic, social, and personal advancement across the globe. The worldwide consumption of energy is likely to increase faster with the growth of the population, majority of which comes from the fossil fuels. This causes emission of greenhouse gases, which leads to increase the average temperature of earth causing global warming and climate changes. Renewable energy is the best option to fulfill the energy demand [1]. Renewable energy has a lot of benefits such as, inexhaustible, sustainable, and eco-friendly energy. Renewable energy has a reliance to diminish the dependency on fossil fuels by growing sustainable power sources [12]. Figure 1 shows the types of renewable energy sources which have high potential to fulfill the need to energy consumption.

India is the second most populous and seventh largest country in the world with high potential of renewable energy sources. India has the access to about 900 GW of renewable energy, which are nearly 750 GW from solar energy, 102 GW from wind energy (at 80-m height), 20 GW from small hydro, and 25 GW from bio energy [10–12]. It is exceptionally essential to prepare the advancement plans to use renewable energy sources in current Indian power sector to mitigate the bad effect of pollutants on the ecosystem and to meet the current and future energy demands.

H. Prajapati (✉)
Assistant Professor, Mechanical Engineering Department, Maharishi Markandeshwar Engineering College, Maharishi Markandeshwar (Deemed to be University), Mullana-Ambala, Haryana 133207, India

R. Kant
Mechanical Engineering Department, S. V. National Institute of Technology, Surat, Gujarat 395007, India

C. Solanki
Carriage Repair Workshop, Indian Railway, Bhavnagar, India

639
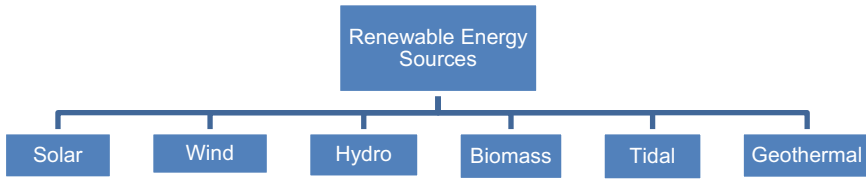
Fig. 1 Types of renewable energy sources

The adoption of renewable energy to fulfill the required need of energy will be the best solution to overcome the issue of global warming and climate changes, but the availability of renewable energy is restricted to the geography of a particular location. Hence, the selection of a particular renewable energy sources is a challenging task which requires rigorous efforts. Therefore, the aim of this research is to prioritize the available criteria for the selection of appropriate renewable energy sources in India. The Shannon entropy weighing method is adopted in this study to build a tool to help in selecting best available renewable energy sources.

2 Literature Review

The article were surveyed from the databases of Google Scholar and Scopus for selection of evaluation criteria based on its frequency of application in energy sector and also by India's present economic and environmental situation. Extensive review was carried out related to multi-criteria decision-making methods and its applications in energy selection and ranking of renewable energy, on the advancement of renewable energy and selection of best alternatives. Strantzali and Aravossis [2] observed that most used evaluation criteria are efficiency, availability of resources, reliability, maturity, and installed capacity as technical criteria; operation and maintenance cost, capital cost and electric cost as financial criteria; carbon dioxide emission, land requirement, and ecological impacts as environmental criteria; job opportunities, benefits to society, and social acceptance as social criteria. The authors also stated that it ought to be noticed that the recurrence of criteria of a measure in the literature does not imply that it is the essential factor to be considered. It helps to review all the criteria and to select evaluation criteria based on the objectives of project. There are ten evaluation criteria selected for analysis of renewable energy in India listed in Table 1.

Table 1 Evaluation criteria for analysis of renewable energy in India

Perspectives	Code	Criteria	Code	Description	References
Financial	C_1	Capital cost (Rs. crores/MW)	C_{11}	It comprises of absolute expenditure used in building up a power plant including the labor work, apparatus installation, framework etc.	[1, 3–5]
		Operation and maintenance cost (Rs. Lakhs/MW)	C_{12}	It incorporates the plant performing expenses including salaries of the representatives, cost of the parts required for maintaining purposes etc.	
		Electric cost (Rs./kWh)	C_{13}	It is expected expenses in power production by power plant	
Technical	C_2	Efficiency (%)	C_{21}	It is the ratio of total output energy to total input energy	[3, 5–7]
		Capacity factor	C_{22}	It is the proportion of the total electricity produced during a time period to electrical energy that could be generated at continuous full power operation in same time period Annual total generation/(installed capacity * 365 * 24 h/day)	
		Installed grid power capacity (MW)	C_{23}	It is maximum power generating capacity designed for power plant	
Environmental	C_3	CO_2 emission (gm/kWh)	C_{31}	It is average carbon dioxide emission during manufacturing, transportation, and installation of set up	[1, 3, 5, 6],
		Land requirement (ha./MW)	C_{32}	It comprises of the land used to set up a power plant	
Social	C_4	Useful life (years)	C_{41}	It is the life span of plant in years	[1, 3, 5, 6, 8],
		Employment (Person/MW)	C_{42}	It is expected person required to set up and operate a power plant	

3 Shannon Entropy Weighing Multi-criteria Decision-Making Method

Zou et al. [9] described that entropy was initially an idea in thermodynamics and was utilized to ascertain the disorderliness of the system, that is, to figure the level of disorder. Later, it was adopted as a multi-criteria decision-making method. Lee and Chang [5] suggested that Shannon entropy is highly recommended objective weighing method.

Assuming n criteria ($C_1, C_2, C_3, \ldots, C_n$) and m alternatives ($A_1, A_2, A_3, \ldots, A_m$) in problem, set up an initial decision matrix A_{ij} having components as a_{ij}.

Step1: The normalization of decision matrix is carried out by dividing each element by the sum of all ith values.

$$r_{ij} = \frac{a_{ij}}{\sum_{i=1}^{m} a_{ij}} \quad \text{where } i = 1, 2, 3, \ldots, m \tag{1}$$

Step 2: Determine value of constant k where $k = k = 1/l$ nm.

Step 3: Computing entropy

$$e_j = -k \sum_{i=1}^{m} r_{ij} * \ln r_{ij} \quad \text{where } j = 1, 2, 3, \ldots, n \tag{2}$$

Step 4: Calculating relative importance of each criterion

$$w_j = \frac{1 - e_j}{\sum_{j=1}^{n}(1 - e_j)} \quad \text{Where } j = 1, 2, 3, \ldots, n \tag{3}$$

4 Calculation and Results

The data collected for this research is summarized from various literatures, national, and international governmental organizations. The Central Electricity Authority India (CEA) and Ministry of New and Renewable Energy (MNRE) are the Indian Government organizations which provide numerous data related to determine energy status of India on their official websites. The five alternative sources of renewable energy selected for the analysis based on current energy policy are large hydro (A1), small hydro (A2), solar PV (A3), wind (A4), and biomass (A5). The value of selected evaluation criteria is presented in Table 2. The average and derived values are considered for evaluation criteria. This will also act as initial decision matrix required for calculations.

Table 2 Data on India's renewable energy sources (initial decision matrix)

	C_{11}	C_{12}	C_{13}	C_{21}	C_{22}	C_{23}	C_{31}	C_{32}	C_{41}	C_{42}
A_1	10.4	26	2.75	70	35	45,403.4	7.6	6.6	35	1.746
A_2	6.76	32	2.6	70	30	4593.15	9	6.6	35	1.746
A_3	5.5	14.45	11	15	14	28,180.7	97	8	25	0.715
A_4	6	10.25	3.125	30	17	35,626	8	10	25	0.417
A_5	5.7	40	4.25	35	64	9103.5	22	15	20	0.63
$\sum A_{ij}$	34.36	122.7	23.725	220	160	122,906.75	143.6	46.2	140	5.254

Table 3 Normalized decision matrix

	C_{11}	C_{12}	C_{13}	C_{21}	C_{22}	C_{23}	C_{31}	C_{32}	C_{41}	C_{42}
A_1	0.3027	0.2119	0.1159	0.3182	0.2188	0.3694	0.0529	0.1429	0.2500	0.3323
A_2	0.1967	0.2608	0.1096	0.3182	0.1875	0.0374	0.0627	0.1429	0.2500	0.3323
A_3	0.1601	0.1178	0.4636	0.0682	0.0875	0.2293	0.6755	0.1732	0.1786	0.1361
A_4	0.1746	0.0835	0.1317	0.1364	0.1063	0.2899	0.0557	0.2165	0.1786	0.0794
A_5	0.1659	0.3260	0.1791	0.1591	0.4000	0.0741	0.1532	0.3247	0.1429	0.1199

Normalizing the decision matrix by dividing every element of each column by their respective sum of all elements (Table 3).

Compute the constant k using Eq. 1, where $m = 5$ (number of alternatives); therefore, $k = 0.621$. The value of entropy e_j is calculated according to Eq. 2 and is given in Table 4.

The relative importance of each criterion is calculated using Eq. 3 and is given in Table 5.

The final ranking of the criteria is given based on the obtained weights of individual criteria. Table 6 shows the ranking of criteria and the table is arranged in the decreasing weights of perspectives.

Shannon entropy result shows that financial criteria are having highest relative importance followed by technical, environmental, and social criteria. It is observed that most important criteria is CO_2 emission followed by electric cost, land requirement, operation, and maintenance cost, capacity factor, useful life, capital cost, efficiency, employment, and installed grid power capacity. The CO_2 emission and land requirement have negative impact on environment. The capital cost, electric cost, and operation and maintenance cost, land requirement, and CO_2 emission are non-beneficial criteria, so lower values are desired. The efficiency, capacity factor, installed grid power capacity, useful life of pant and employment opportunities are beneficial criteria, so the higher values are required.

Table 4 Computation of entropy

	C_{11}	C_{12}	C_{13}	C_{21}	C_{22}	C_{23}	C_{31}	C_{32}	C_{41}	C_{42}
A$_1$	−0.3617	−0.3288	−0.2498	−0.3644	−0.3325	−0.3679	−0.1555	−0.2780	−0.3466	−0.3661
A$_2$	−0.3199	−0.3505	−0.2423	−0.3644	−0.3139	−0.1228	−0.1736	−0.2780	−0.3466	−0.3661
A$_3$	−0.2933	−0.2519	−0.3564	−0.1831	−0.2132	−0.3377	−0.2650	−0.3036	−0.3076	−0.2714
A$_4$	−0.3047	−0.2074	−0.2670	−0.2717	−0.2382	−0.3590	−0.1609	−0.3313	−0.3076	−0.2011
A$_5$	−0.2980	−0.3654	−0.3080	−0.2925	−0.3665	−0.1928	−0.2874	−0.3652	−0.2780	−0.2543
$\sum_{i=1}^{m} r_{ij} * \ln r_{ij}$	−1.5776	−1.5040	−1.4235	−1.4760	−1.4642	−1.3801	−1.0424	−1.5561	−1.5864	−1.4590
e_j	0.2246	0.2042	0.1551	0.2263	0.2065	0.2285	0.0966	0.1726	0.2152	0.2273

Table 5 Relative criteria weight

	C11	C12	C13	C21	C22	C23	C31	C32	C41	C42	$\sum$
$1-e_j$	0.7754	0.7958	0.8449	0.7737	0.7935	0.7715	0.9034	0.8274	0.7848	0.7727	8.0431
w_j	0.0964	0.0989	0.1050	0.0962	0.0987	0.0959	0.1123	0.1029	0.0976	0.0961	

Table 6 Ranking of criteria

Perspectives	Weight	Criteria	Code	Weight	Rank
Financial	0.3004	Capital cost	C11	0.0964	7
		Operation and maintenance cost	C12	0.0989	4
		Electric cost	C13	0.1050	2
Technical	0.2908	Efficiency	C21	0.0962	8
		Capacity factor	C22	0.0987	5
		Installed grid power capacity	C23	0.0959	10
Environmental	0.2152	CO_2 emission	C31	0.1123	1
		Land requirement	C32	0.1029	3
Social	0.1936	Useful life	C41	0.0976	6
		Employment	C42	0.0961	9

5 Conclusions

To maintain the environmental structure, there is a need to find out a way to overcome the energy demand. So, the adoption of renewable energy sources to generate energy is the best solution available. The criteria were selected and prioritized that rate the best available renewable energy sources according to geography of location. This study provides guidance to energy policy makers for implementation and development of new plans of renewable energy in India.

The future scope of this study include identification of more number of criteria which may have significant impact on current renewable energy status of India. Also, the renewable energy sources can also be ranked with the help of these selected criteria and data.

References

1. Kannan D, Moazzeni S, Mostafayi Darmian S, Afrasiabi A (2020) A hybrid approach based on MCDM methods and Monte Carlo simulation for sustainable evaluation of potential solar sites in east of Iran. J Cleaner Prod 279:122368
2. Strantzali E, Aravossis K (2016) Decision making in renewable energy investments: a review. Renew Sustain Energy Rev 55:885–898

3. Wu Y, Xu C, Zhang T (2018) Evaluation of renewable power sources using a fuzzy MCDM based on cumulative prospect theory: A case in China. Energy 147:1227–1239

4. Al H, Kassem A, Awasthi A, Komljenovic D, Al-Haddad K (2016) A multicriteria decision making approach for evaluating renewable power generation sources in Saudi Arabia. Sustain Energy Technol Assess 16:137–150

5. Lee HC, Chang CT (2018) Comparative analysis of MCDM methods for ranking renewable energy sources in Taiwan. Renew Sustain Energy Rev 92:883–896

6. Chatterjee K, Kar S (2018) A multi-criteria decision making for renewable energy selection using Z-numbers in uncertain environment. Technol Econ Dev Econ 24(2):739–764

7. Çolak M, Kaya İ (2017) Prioritization of renewable energy alternatives by using an integrated fuzzy MCDM model: a real case application for Turkey. Renew Sustain Energy Rev 1(80):840–853

8. Yazdani-Chamzini A, Fouladgar MM, Zavadskas EK, Moini SHH (2013) Selecting the optimal renewable energy using multi criteria decision making. J Bus Econ Manag 14(5):957–978

9. Zou ZH, Yi Y, Sun JN (2006) Entropy method for determination of weight of evaluating indicators in fuzzy synthetic evaluation for water quality assessment. J Environ Sci 18(5):1020–1023

10. Ministry of New and Renewable Energy (Government of India) https://mnre.gov.in/. Accessed on 1 Nov 2020

11. Ministry of Power (Government of India) https://powermin.nic.in/. Accessed on 1 Nov 2020

12. National Solar Mission https://mnre.gov.in/file-manager/annual-report/2016-2017/EN/pdf/4.pdf. Accessed on 1 Nov 2020

Modelling and Analysis of PCB Vibration

Vinay Shewale and Surbhi Razdan

1 Introduction

All vehicles are subjected to range of excitation from the road and engine. Electrical packages used in vehicles need to be designed in a way such that they can resist them. Component failure due to vibration has been observed, thus compromising the reliability of the system. All contemporary vehicles have a large number of electronic packages they need to be isolated from the excitation to prevent resonance [1]. The response of PCBs to vibration is required for accurate prediction of reliability. The previous work indicates that addition of stiffeners higher directional loads can be resisted [2]. Multiple load paths are introduced by use of stiffeners which ensure that component is protected against damage and crack growth under compressive loads and bending loads. Various methods have been proposed by different researchers to control the vibration encountered by the PCB. These methods depend on the applications. There are various methods which can be used to reduce the vibrations depending upon the application where it is used.

1.1 Stiffener

Somashekar [3], Sakri [4] study PCB plates with different stiffeners location by FEM under free vibration. Response of the PCB to vibration considering them to be supported at various locations was studied, and analysis was carried for PCB with and without mountings. The material of PCB as well as of stiffeners is assumed to be homogeneous and isotropic in nature [1, 4]. The material is also assumed to

V. Shewale (✉) · S. Razdan
School of Mechanical Engineering, Dr. Vishwanath Karad, MIT-WPU, Pune, India

S. Razdan
e-mail: surbhi.razdan@mitwpu.edu.in

be linearly elastic in nature, and thickness of the plate and stiffeners is assumed to be uniform. The thickness is assumed to be small in compared to the length of the PCB. Therefore, the effect of shear stress and rotary inertia is assumed to be negligible. Sakri and Prashanth [4, 5] worked on free vibration analysis of PCB for buckling by mounting stiffened plates at various positions. References [6, 7] in this analysis, researchers analyzed the response of ECU unit stiffeners applied in a mesh form modal analysis was carried out for obtaining natural frequency and mode shapes. The failure region was predicted using mode shapes, and it was observed that addition of stiffeners the effective stiffness leads to avoid the resonance condition [8].

1.2 Modifying the Support Condition

Somashekar and Harikrishnan [3] analyzed the vibrational response of PCB by modifying the critical area such as fixing condition and obtain the effect of change in number of support conditions at the critical areas. Arabi and Venkat Siva Rao [1, 8] worked on calculating the response of isotropic and anisotropic PCB. They also studied the effect of increasing the space between supports on the response. They obtained the optimal position of supports [5]. The effect of location of components on the vibratory behaviour of PCB is studied [9]. Two degree of freedom analytical model of PCB is analyzed numerically, and results are compared with finite element model. Dipam [10] worked on to optimize support location so the natural frequency of vibrating structures is within the operating range, and the method used by him is such that the lower modes of vibrational are eliminated by introduction of extra supports. Multilayer complex PCB dynamic response was calculated for isotropic and anisotropic PCB, and therefore, the results were not similar, also by increasing the spacing between the fixation points, natural frequency was increased but only till optimized limits [1, 2]. Changing the condition from screw support to edge support will increase the natural frequency of the PCB [11].

1.3 Material and Mountings on PCB

The natural frequency is a function of mass and stiffness of the system therefore mounted components on the PCB will increase the natural frequency if stiffer components are mounted on it rather than heavier which in turn would also safe material [11, 12]. Multilayer complex PCB dynamic response was calculated for isotropic and anisotropic PCB, and therefore, the results are not similar hence accurate results might be obtained by considering actual properties [11]. Obtained shows that the rubber spacers reduce the vibrations by almost 2.5–3 times as compared to plastic spacers. Aglietti [13] worked on outer casing of PCB and gave alternate design based

on carbon fibre reinforcement layers for the outer casing. Other factors such as radiation protection required are achieved along with weight reduction is also achieved when compared with the original design [14].

2 Introduction to the Problem

All vehicles are subjected to range of frequency excitation from the road and engine. A plane PCB and PCB with ribs/stiffeners attached with various configurations are analyzed for external vibrations to avoid resonance condition in the operating range. The operating range frequency is up to 4–500 Hz depending upon the engine RPM and road condition. The stiffeners are bonded to the PCB using VHB tape which has thermal resistant property. The material used for stiffeners is aluminium 7075 which is much lighter than steel but as strong as it. The material of PCB board is FR4 which is flame resistant. The assumptions made are

(a) The material used for PCB board and stiffeners is homogeneous, isotropic, and linearly elastic.
(b) Thickness of PCB board and stiffeners is uniform

The material properties considered are as follows:

FR4 (glass-reinforced epoxy laminate material): modulus of elasticity $(E) =$ *18,400 MPa*, Poisson's ratio $(\mu) = 0.11$, density $(\rho) = 1.840e-09$ tonnes/mm^3.

Aluminium7075: modulus of elasticity $(E) = 71,700$ *MPa*, Poisson's ratio $(\mu) = 0.33$, density $(\rho) = 2.810e-09$ tonnes/mm^3.

The dimensions of PCB board and stiffeners are

PCB board (150 * 100 * 1.5) mm, stiffener horizontal position (150*5*25) mm, and stiffener vertical position (100 * 5 * 25) mm.

3 Natural Frequency of the Plate with and Without Stiffeners

The analysis used the approach of finite element method using Ansys and HyperMesh for numerical analysis and comparing it with experimental results. The following four cases are considered for comparing the results of the analysis.

Case 1: Simple PCB without stiffeners.
Case 2: PCB with vertical stiffeners.
Case 3: PCB with horizontal stiffeners.
Case 4: PCB with plus (horizontal + vertical) stiffeners.
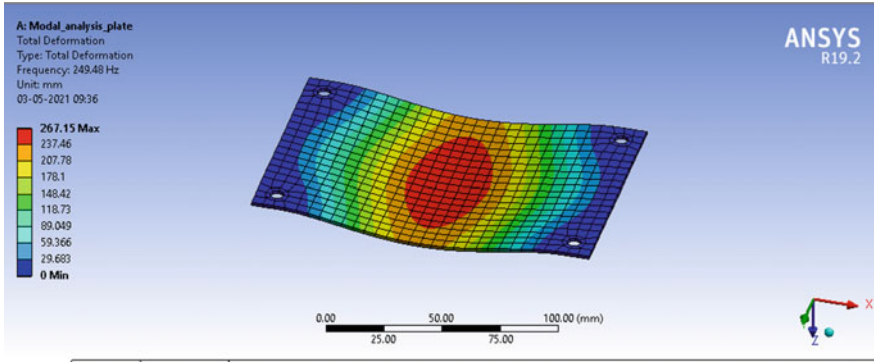
Fig. 1 Deformation and natural frequency for PCB without stiffeners (Ansys)
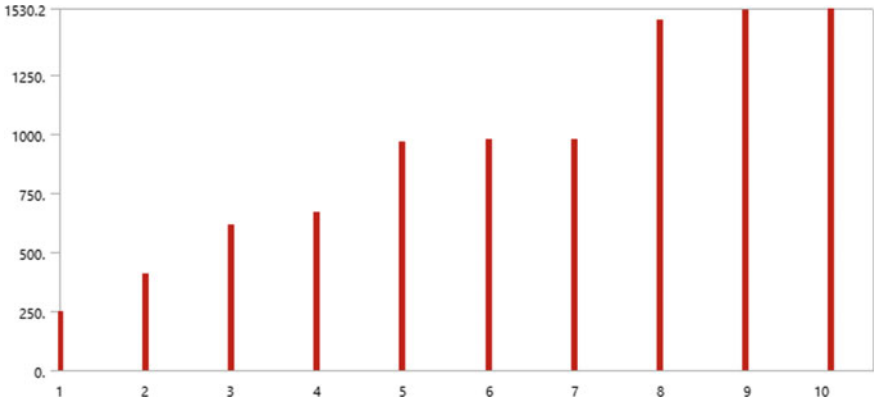
Fig. 2 Natural frequencies at various mode shapes PCB without stiffeners (Ansys)

3.1 Simple PCB Without Stiffeners

See Figs. 1, 2, 3, and 4

3.2 PCB with Vertical Stiffeners

See Fig. 5, 6,7, 8, and 9.
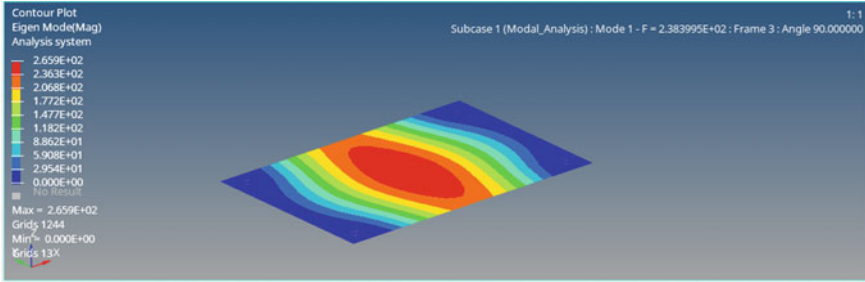
Fig. 3 Deformation and natural frequency for PCB without stiffeners (HyperMesh)

Subcase	Mode	Frequency	Eigenvalue	Generalized Stiffness	Generalized Mass
1	1	2.383995E+02	2.243729E+06	2.243729E+06	1.000000E+00
1	2	3.890986E+02	5.976944E+06	5.976944E+06	1.000000E+00
1	3	5.966984E+02	1.405625E+07	1.405625E+07	1.000000E+00
1	4	6.581644E+02	1.710128E+07	1.710128E+07	1.000000E+00
1	5	9.234844E+02	3.366812E+07	3.366812E+07	1.000000E+00
1	6	9.465727E+02	3.537266E+07	3.537266E+07	1.000000E+00
1	7	9.477780E+02	3.546280E+07	3.546280E+07	1.000000E+00
1	8	1.416471E+03	7.920906E+07	7.920906E+07	1.000000E+00
1	9	1.459318E+03	8.407355E+07	8.407355E+07	1.000000E+00
1	10	1.504971E+03	8.941616E+07	8.941616E+07	1.000000E+00

****

Fig. 4 Natural frequencies at various mode shapes PCB without stiffeners (HyperMesh)
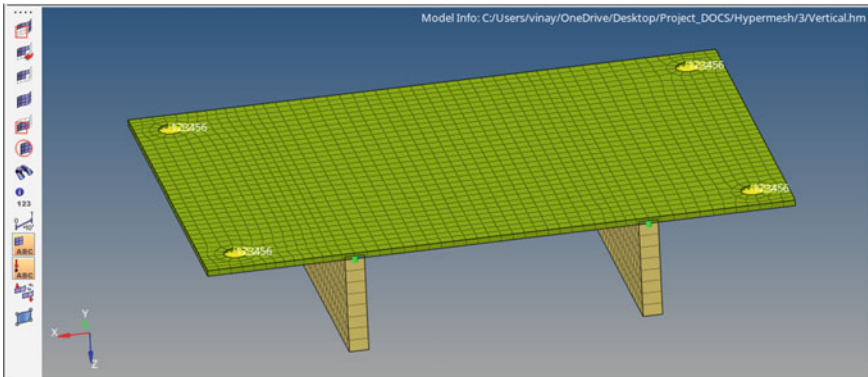
Fig. 5 PCB with vertical stiffeners

3.3 PCB with Horizontal Stiffeners

See Figs. 10, 11, 12, 13, and 14.
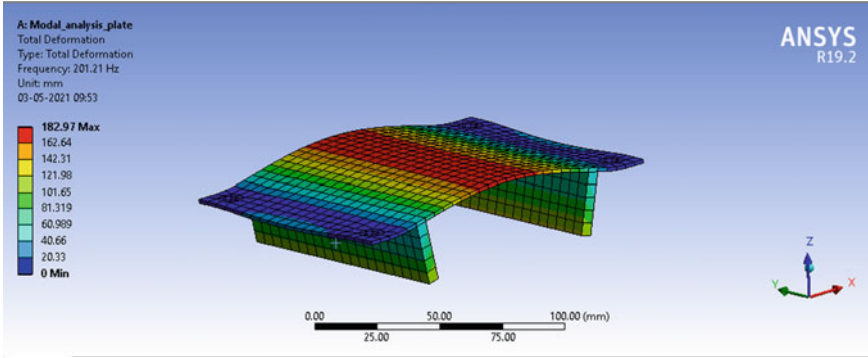
Fig. 6 Deformation and natural frequency for PCB with vertical stiffeners (Ansys)
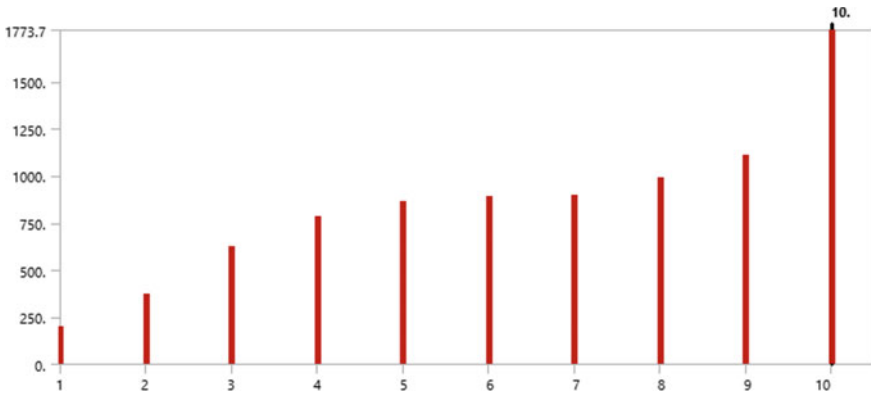
Fig. 7 Natural frequencies at various mode shapes PCB with vertical stiffeners (Ansys)
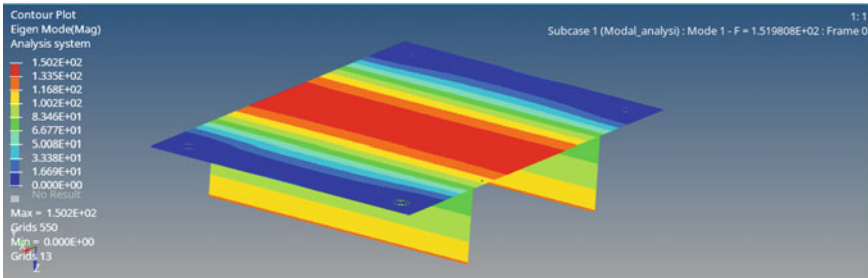
Fig. 8 Deformation and natural frequency for PCB with vertical stiffeners (HyperMesh)

Subcase	Mode	Frequency	Eigenvalue	Generalized Stiffness	Generalized Mass
1	1	1.519808E+02	9.118793E+05	9.118793E+05	1.000000E+00
1	2	3.001084E+02	3.555625E+06	3.555625E+06	1.000000E+00
1	3	3.617119E+02	5.165178E+06	5.165178E+06	1.000000E+00
1	4	4.220167E+02	7.031031E+06	7.031031E+06	1.000000E+00
1	5	5.133741E+02	1.040465E+07	1.040465E+07	1.000000E+00
1	6	5.535416E+02	1.209651E+07	1.209651E+07	1.000000E+00
1	7	1.028945E+03	4.179689E+07	4.179689E+07	1.000000E+00
1	8	1.045158E+03	4.312442E+07	4.312442E+07	1.000000E+00
1	9	1.190978E+03	5.599733E+07	5.599733E+07	1.000000E+00
1	10	1.192526E+03	5.614297E+07	5.614297E+07	1.000000E+00

Fig. 9 Natural frequencies at various mode shapes PCB with vertical stiffeners (HyperMesh)
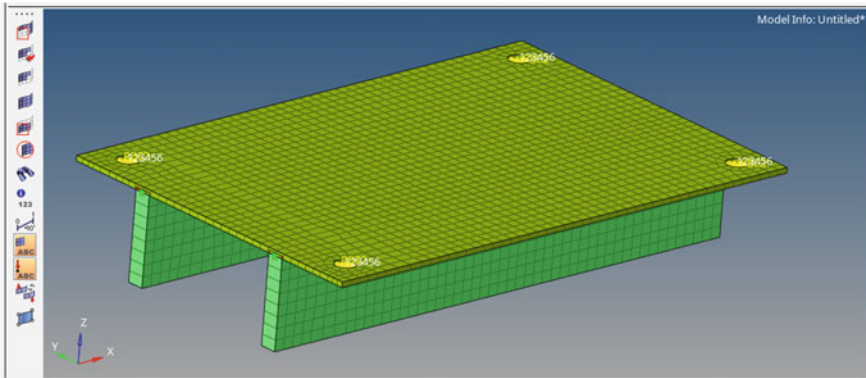
Fig. 10 PCB with horizontal stiffeners
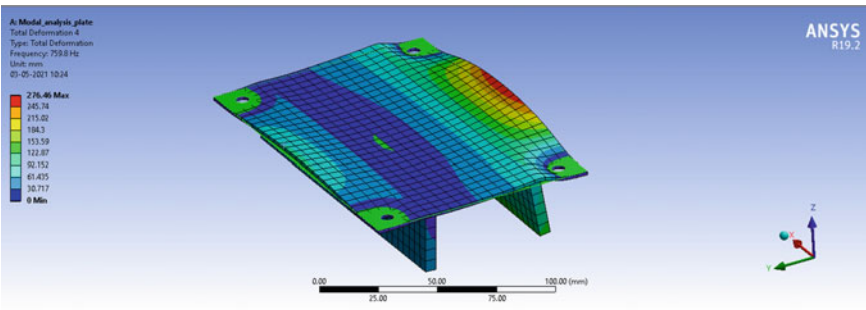
Fig. 11 Deformation and natural frequency for PCB with horizontal stiffeners (Ansys)

3.4 PCB with Plus Stiffeners

See Fig. 15, 16, 17, 18, and 19.
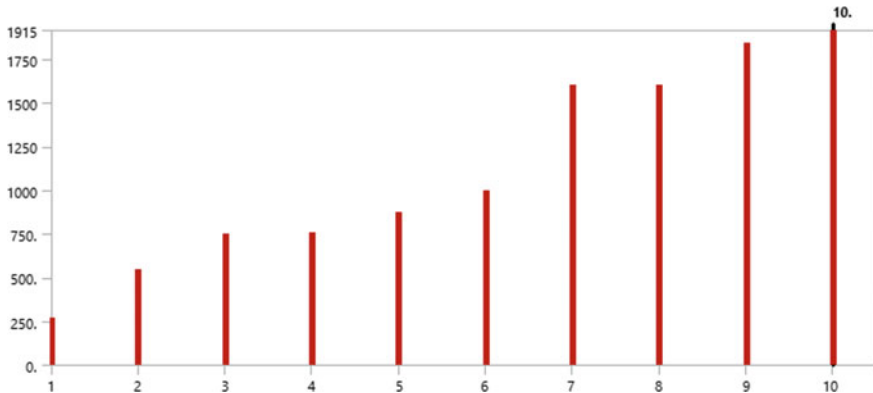
Fig. 12 Natural frequencies at various mode shapes PCB with horizontal stiffeners (Ansys)
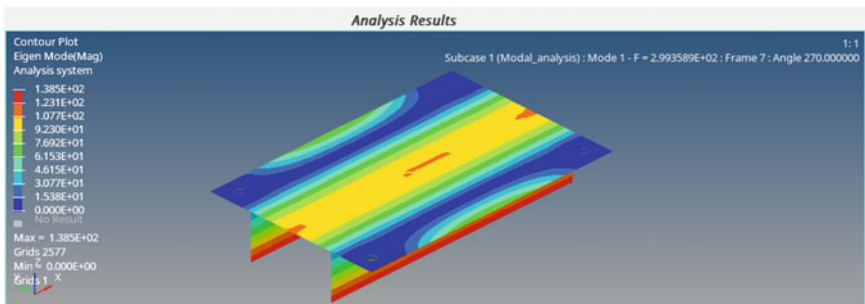
Fig. 13 Deformation and natural frequency for PCB with horizontal stiffeners (HyperMesh)

Subcase	Mode	Frequency	Eigenvalue	Generalized Stiffness	Generalized Mass
1	1	2.993589E+02	3.537889E+06	3.537889E+06	1.000000E+00
1	2	5.416697E+02	1.158321E+07	1.158321E+07	1.000000E+00
1	3	8.062183E+02	2.566049E+07	2.566049E+07	1.000000E+00
1	4	8.085382E+02	2.580838E+07	2.580838E+07	1.000000E+00
1	5	9.943848E+02	3.903631E+07	3.903631E+07	1.000000E+00
1	6	1.109067E+03	4.855961E+07	4.855961E+07	1.000000E+00
1	7	1.509953E+03	9.000908E+07	9.000908E+07	1.000000E+00
1	8	1.515579E+03	9.068111E+07	9.068111E+07	1.000000E+00
1	9	1.832971E+03	1.326390E+08	1.326390E+08	1.000000E+00
1	10	1.886210E+03	1.404558E+08	1.404558E+08	1.000000E+00

Fig. 14 Natural frequencies at various mode shapes PCB with horizontal stiffeners (HyperMesh)

The variation of natural frequency with respect to different mode shapes for PCB with and without stiffeners is shown in the above figures. Modal analysis is performed to calculate the natural frequency of vibration or modes of vibration of any given component to avoid the resonance condition during the dynamic operation. In results, elemental strain energy (ESE) is also calculated along with modal analysis. Elemental
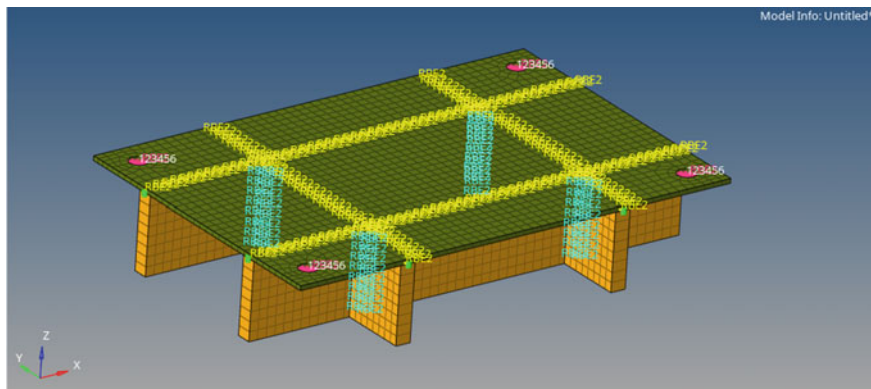
Fig. 15 PCB with plus stiffeners
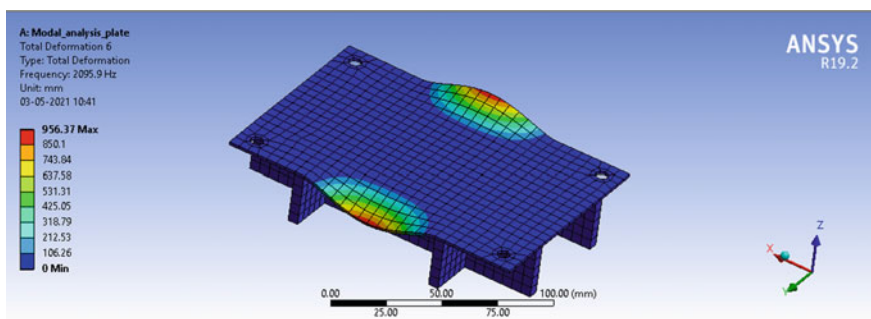
Fig. 16 Deformation and natural frequency for PCB with plus stiffeners (Ansys)
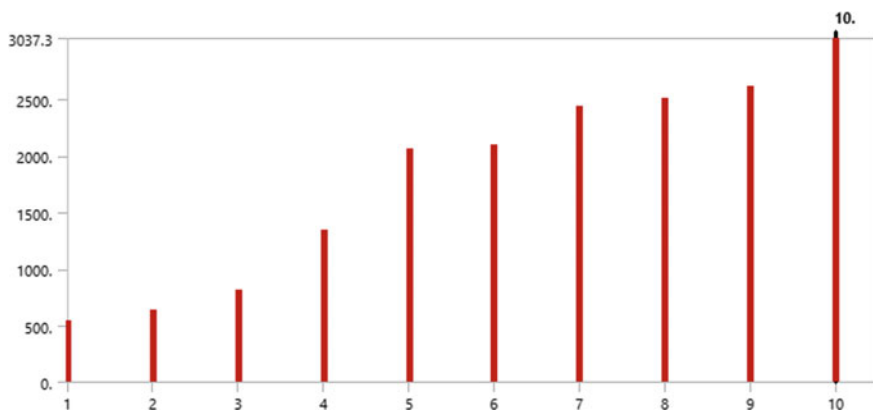
Fig. 17 Natural frequencies at various mode shapes PCB with plus stiffeners (Ansys)
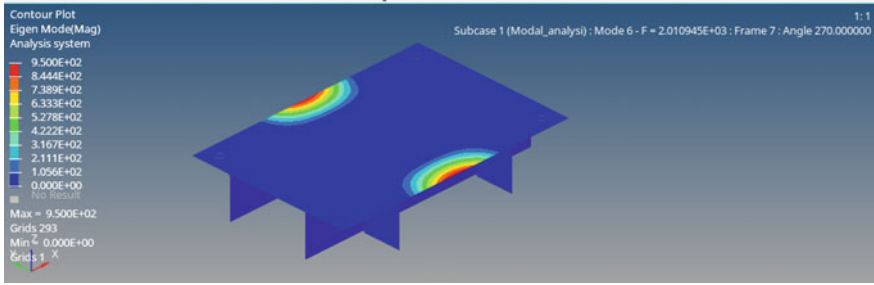
Fig. 18 Deformation and natural frequency for PCB with plus stiffeners (HyperMesh)

```
                                     Generalized   Generalized
Subcase  Mode   Frequency    Eigenvalue    Stiffness      Mass
     1     1   7.005615E+02  1.937547E+07  1.937547E+07  1.000000E+00
     1     2   7.699695E+02  2.340490E+07  2.340490E+07  1.000000E+00
     1     3   1.056535E+03  4.406845E+07  4.406845E+07  1.000000E+00
     1     4   1.501970E+03  8.905989E+07  8.905989E+07  1.000000E+00
     1     5   1.972682E+03  1.536292E+08  1.536292E+08  1.000000E+00
     1     6   2.010945E+03  1.596467E+08  1.596467E+08  1.000000E+00
     1     7   2.144873E+03  1.816197E+08  1.816197E+08  1.000000E+00
     1     8   2.224254E+03  1.953117E+08  1.953117E+08  1.000000E+00
     1     9   2.252133E+03  2.002386E+08  2.002386E+08  1.000000E+00
     1    10   3.143381E+03  3.900802E+08  3.900802E+08  1.000000E+00
```

Fig. 19 Natural frequencies at various mode shapes PCB with plus stiffeners (HyperMesh)

strain energy shows the areas where reinforcement needs to be done to avoid failure of structure during vibration at a particular frequency. Elemental strain energy plots show the location of maximum strain at that particular frequency. Hence, from the results, we get an idea about where the PCB needs to be reinforced so as to avoid the resonance condition (Table 1).

Table 1 Natural frequency comparison for mode frequency

Mode	Natural frequency (Hz)		% error
	Ansys	HyperMesh	
PCB w/o stiffeners	249.48	238	4.62
PCB with vertical stiffeners	168	151.9	10.5
PCB with horizontal stiffeners	269	299	10.3
PCB with plus stiffeners	630	700.56	10

Table 2 Comparison of the natural frequency of PCB without stiffeners analytically and by FEA (Ansys)

Results	Mode number					
	1	2	3	4	5	6
Analytical	281	462	693	702	1011	1023
FEA (Ansys)	249.5	409.5	616.53	670	968	977

4 Mathematical Model

By using Kirchhoff's theory for dynamic analysis of thin plates helps us in determining the propagation of waves in the thin plates which helps us study about vibration modes. This theory is used to describe mathematical systems for transverse vibrations. According to Kirchhoff plate theory, the equations for calculating natural frequency based on differential equations with the help of finite element method for thin plates are given by

$$\omega_{mn} = \sqrt{\frac{D}{\rho h} \left[\left(\frac{m\pi}{s}\right)^2 + \left(\frac{n\pi}{b}\right)^2 \right]},$$

where D is flexural rigidity:

$$D = \frac{Eh^3}{12(1 - \vartheta^2)}$$

where ω_{mn} = natural frequencies, ρ—density, a, b—length and width of plate, h—thickness of plate which is constant. The material properties and dimensions that are considered for the analysis of PCB without stiffeners are

FR4 (glass-reinforced epoxy laminate material), modulus of elasticity $(E) = 18,400\ MPa$, Poisson's ratio $(\mu) = 0.11$, density $(\rho) = 1.840e$-09 tonnes/mm3. The dimensions of PCB board: PCB board (150 * 100 * 1.5) mm (Table 2).

5 Conclusions

The vibration analysis of the PCB plate is performed considering the operating conditions of the automobile. Initially, PCB is considered as a homogeneous, isotropic plate. For a PCB, the modal analysis is carried to know the natural frequencies and deformations at various mode shapes. The elemental strain energy is calculated to analyze where the PCB should be reinforced. The PCB is used in automobile applications, and the operating range is calculated based upon the RPM of the engine and external vibrations (road conditions) subjected to it. The external frequency range considered is up to 4–500 Hz depending upon the engine RPM. Data from various

sources confirm that the vibrations in lower frequency range are the main reason for resonance condition which may lead to the failure of PCB.

Hence, by comparing the above results for various configurations, it is observed that the lower frequency range is avoided by (20–50) Hz for horizontal stiffeners and (250–300) Hz by using plus stiffeners. PCB with vertical stiffeners natural frequency is reduced due to the deformations coinciding deformable modes. Analytical results using Kirchhoff's plate theory, and FEA results in Ansys for PCB without stiffeners for first 6 modes vary by (10–14) % because of the assumptions made in the Kirchhoff's plate theory and FEA error for capturing real-life conditions.

References

1. Arabi F, Gracia A, Delétage JY, Frémont H (2018) Vibration test and simulation of printed circuit board. In: 2018 19th International conference on thermal, mechanical and multi-physics simulation and experiments in microelectronics and microsystems
2. Bhat AJ, Bhope DV (2016) Effect of stiffeners on natural frequencies of plate. Int Res J Eng Technol (IRJET), pp 1048–1053
3. Somashekar VN, Harikrishnan S, Aejaz Ahmed PSM, Kamesh D (2016) Vibration response prediction of the printed circuit boards using experimentally validated finite element model. Procedia Eng
4. Sakri MI, Mohanram PV (2015) Protecting printed circuit boards from harsh vibrations. IJIRSET 4(9):9045–9050. https://doi.org/10.15680/Ijirset.2015.0409110
5. Prashanth MD (2018) Vibration Analysis of printed circuit boards: effect of boundary condition. In: AIP conference proceedings, p 1943. https://doi.org/10.1063/1.5029594
6. Mirajkar P, Thorat PML (2019) A research on vibration analysis & optimization of housing for ECU in automobile using FEA & FFT analyser. Int Res J Eng Technol (IRJET) e-ISSN: 1633–1640
7. Prashant P, Yadav S, Sen S, Mishra S (2020) Vibration analysis and optimization of housing for ECU in automobile using FEA. 13(2):789–793
8. Venkat, Siva Rao PV, Singh K, Srikrishna A, Ranganath (2016) Vibration analysis of printed circuit board plate with varying boundary conditions. Indian J Sci Technol 9(34). https://doi.org/10.17485/Ijst/2016/V9i34/100916
9. Braz B, De C, Bussamra FL, De S (2017) An enhanced random vibration and fatigue model for printed circuit boards. Latin Am J Solids Struct 14(13):2402–2422. https://doi.org/10.1590/1679-78253163
10. Patel DS, Pathan SS, Bhoraniya IH (2012) Influence of stiffeners on the natural frequencies of rectangular plate with simply supported edges. Int J Eng Res Technol (IJERT) 1. ISSN: 2278-0181
11. Bhavi IG, Sakri M (2016) Analytical and experimental investigations on a vibrating Pcb with heavy mounted components. Research Gate March.
12. Azam SA, Fragoso A (2020) Experimental and numerical simulation study of the vibration properties of thin copper films bonded to Fr4 composite. Appl Sci (Switzerland), 10(15). https://doi.org/10.3390/App10155197
13. Aglietti GS (2002) A lighter enclosure for electronics for space applications. Proc Inst Mech Eng Part G J Aerospace Eng 216(3):131–142
14. Kakade NT, Gangwani PDG (2014) Design and optimization of sheet metal enclosure with the help of behaviour modelling, pp 39–42
15. Shankar VPK, Sairajan KK (2015) Experimental investigation of particle damper-based vibration suppression in printed circuit board for spacecraft applications. J Aerospace Eng

16. Pitarresi JM, Primavera AA (2014) Comparison Of modeling techniques for the vibration analysis of printed circuit cards. J Electron Packag Trans ASME 114(4):378–383
17. Amy RA, Aglietti GS, Richardson G (2009) Reliability analysis of electronic equipment subjected to shock and vibration—a review. Shock Vibr 16(1):45–59. https://doi.org/10.3233/Sav-2009-0453
18. Ren G, Li B, Li D, Jiao Y (2015) Modal analysis of the printed circuit board based on finite element method. In: Iccset 2014, pp 150–154. https://doi.org/10.2991/Iccset-14.2015.32
19. Kovtun I, Boiko J, Petrashchuk S, Kałaczyński T (2018) Theory and practice of vibration analysis in electronic packages. In: Matec Web Of Conferences, 182. https://doi.org/10.1051/Matecconf/201818202015
20. Pingan D, Yating Y, Ezhong G, Bo L (2005) Finite element modeling for computer motherboard modal analysis. IEEE International conference on mechatronics and automation. ICMA 2005, July, pp 2101–2105. https://doi.org/10.1109/Icma.2005.1626887
21. Yuxun Z, Scanff E, Dasgupta A (2006) Vibration durability comparison Of Sn37pb Vs Snagcu solders. American Society of Mechanical Engineers, Electronic and Photonic Packaging, pp 1–8. https://doi.org/10.1115/Imece2006-13555
22. Vandevelde B, Gonzalez M, Limaye P, Ratchev P, Beyne E (2007) Thermal cycling reliability of Sn-ag-cu And Sn-pb solder joints: a comparison for several Ic-packages. Microelectron Reliab
23. Tee TY, Luan JE, Pek E, Lim CT, Zhong Z (2004) Novel numerical and experimental analysis of dynamic responses under board level drop test. In: Eurosime 2004. IEEE, pp 133–140.
24. Hv P (1991) An overview of NOPD: a passive damping technique. Shock Vib Dig 1:4–10
25. Hv P (1992) Structural damping enhancement via non-obstructive particle damping technique. Asme J Vibr Acoust 114:101–105
26. Ong JH, Lim GH (2000) A simple technique for maximizing the fundamental frequency of vibrating structures. J Electron Packaging, Trans ASME 122(4):341–349 10.1115/1.1289632
27. Timoshenko Sp, Krieger Sw (1959) Theory of plates and shells. Mcgraw Hill, New York, pp 1–591
28. Singh Yadav DP, Sharma AK, Shivhare V (2015) Effect of stiffeners position on vibration analysis of plates. Int J Adv Sci Technol 80:31–40
29. World Economic Forum (WEF), Mnif S, Feki C, Abdelkafi I, Terziyan V, Gryshko S, Golovianko M, et al (2018). Russ J Econ 48(2):123–154
30. Supported, S., & Approach, A. (2008). Vdem Onstr Vibatonsinpte Numelemen Mel. Slts Radom. 1178–1183.
31. Tang W, Ren J, Feng G, Xu L (2007) Study on vibration analysis for printed circuit board of an electronic apparatus. In: Proceedings of the 2007 IEEE international conference on mechatronics and automation (ICMA 2007), pp 855–860. https://doi.org/10.1109/Icma.2007.4303657
32. Hadim H (2016) Multidisciplinary design and optimization methodologies in electronics packaging : state-of-the-art. 130 (September 2008), pp 1–10. https://doi.org/10.1115/1.2957459
33. Lu W, Xiao-Kai C, Qing-Hai Z (2016) Muti-objective topology optimization of an electric vehicle's traction battery enclosure. Energy Procedia 88:874–880. https://doi.org/10.1016/J.Egypro.2016.06.103
34. Luan J (2007) Dynamic responses and solder joint reliability under board level drop test. 47:450–460. https://doi.org/10.1016/J.Microrel.2006.05.012
35. Mohd Nan NM, Idris MA, Bukhari MZ (2005) Board level reliability (Blr) – board design, test and application. In: 4th International conference on recent advances in mechanical & materials engineering. Icramme 2005, May
36. Veprik AM, Babitsky VI (2000) Vibration protection of sensitive electronic equipment from harsh harmonic vibration. J Sound Vibr 238(1):19–30. https://doi.org/10.1006/Jsvi.2000.3098

A Review on Multi-stage Incremental Sheet Forming

Nikhil Bari and Shailendra Kumar

1 Introduction

Single point incremental forming (SPIF) was invented in early 1990, and after that the process has proven to be a promising technology. It allows forming of customized products. SPIF is a flexible sheet metalworking used to form complex parts without fabricating specific die and punch, and thus reduces overall cost of product. SPIF is performed on computerized numerical control (CNC) machine to form highly accurate parts. Localized plastic deformation is imposed on sheet blank by numerically programmed spherical end tool. The sheet is held between clamping plates and backing plates. The deformation produced with SPIF process is higher than that of deep drawing and stretch forming. Therefore, the formability is higher. Park et al. [1] explained the deformation mechanism in their study. There have been controversies in the mode of deformation of SPIF. Many researchers claimed that deformation is due to stretching instead of shearing, whereas others claimed the converse. Skjoedt et al. [2] proved that the mode of deformation in the SPIF process is stretching, rather than shearing. In the last two decades, intensive research has been done in SPIF process. Jeswiet et al. [3] presented a study on the advances and development of SPIF on asymmetric components in SPIF and opened various opportunities of research in the domain of SPIF process. Micari et al. [4] presented the comprehensive literature review regarding different shapes, dimensional accuracy and future scopes in SPIF. Echrif et al. [5] classified the types of SPIF based on the kind of method, number of stages, supporting system, number of forming tools used, etc. Incremental sheet metal forming (ISF) is classified into two types SPIF and two-point incremental forming (TPIF). As shown in Fig. 1c, d, dedicated die is used to support the forming component. The process is known as TPIF, and if the sheet is supported by a blank holder only, then the process is known as SPIF. If the counter tool is used

N. Bari · S. Kumar (✉)
Department of Mechanical Engineering, Sardar Vallabhabhai National Institute of Technology, Surat, India

Fig. 1 Types of ISF [5]
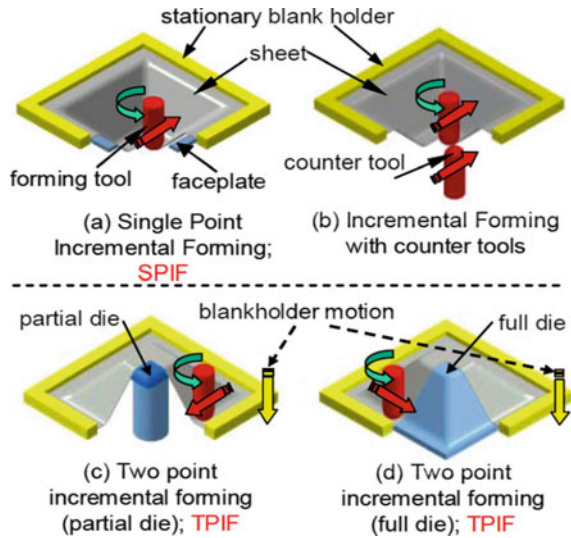
besides forming tool, the process is classified as double side incremental forming (DSIF), Fig. 1b. Hybrid single point incremental forming (HSPIF) is a combination of stretch forming and incremental sheet forming. Incremental sheet forming can also be classified on the basis of number of stages used to form a component. In the single stage, the whole component is formed in single pass, whereas the multi-stage single point incremental forming (MSPIF) takes more than one passes to form a component.

Apart from many advantages, there are certain limitations of SPIF like maximum forming angle, non-uniformed thickness distribution and geometrical accuracy. Duflou et al. [6] analysed different limitations of SPIF processes such as geometrical inaccuracy. Many researchers have made efforts to make the ISF process more suitable in the industry. Panjwani et al. [7] developed a supporting fixture to increase geometrical accuracy. Li et al. [8] presented the comprehensive literature on multi-stage increment forming to improve geometrical accuracy. Higher forming wall angle is one of the primary concerns of the SPIF process.

Hirt et al. [9] developed an equation (Eq. 1) known as 'sine law' which relates the final thickness of component (t_f) with initial thickness of sheet (t_0). With a wall angle θ_f (Fig. 2)

$$t_f = t_0 \sin\left(90° - \theta_f\right) \tag{1}$$

This relation limits the excessive thinning beyond particular wall angle. They also proved that the deformation made of SPIF is close to plane strain condition. Blank material, shape of components, and thickness of the blank limits the maximum wall angle many researcher investigated on maximum wall angle of different materials. Mikari and Ambrogio [10] developed a methodology to select a standard shape for

Fig. 2 Schematic of MSPIF
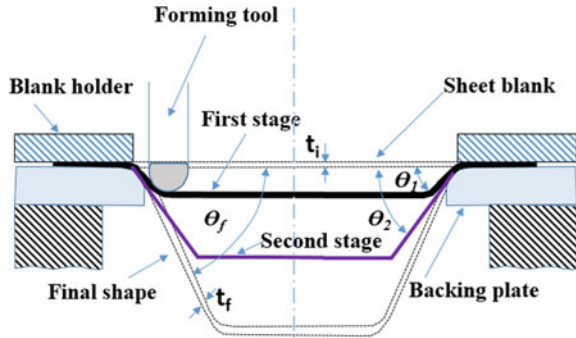
determining the maximum wall angle. After this, many researchers have found the maximum possible wall angle formed for material in a single stage.

The maximum possible wall angle in a single pass and non-uniform thickness distribution is observed to be improved in the MSPIF process. The final angle θ_f is formed with intermediate stages with wall angle of θ_1 and θ_2!. Other arrangement is same as SPIF. The reason behind higher thickness distribution of MSPIF is that large portion of volume is included while forming. Strain hardening is observed during forming which changes the mechanical properties of the material, hence decreasing deformation capacity of material. While in MSPIF strain hardening is distributed in number of stages and increases the deformation capacity, MSPIF is one of the most effective solutions to reduce the excessive thinning.

The development of MSPIF in research domain was started from 2000. There are numerous applications of MSPIF in various sectors. Because of the nature of the process, it is one of the most flexible sheet metal forming processes. Worldwide researchers have applied their efforts to improve the response characteristics of the MSPIF process to make it industry-acceptable standards. Some researchers have investigated the use of forming process to various industry-specific free form shapes like vehicle headlight reflector, generatrix shapes for piping, etc.

Present work contributes a comprehensive review of the MSPIF process. Efforts made by worldwide researchers are critically reviewed mainly focusing on the effect of MSPIF on geometrical accuracy, thickness distribution, surface roughness, numerical simulation and applications in various sectors. Finally, scope for future research work is discussed.

2   Literature Review

MSPIF has three important challenges, namely geometrical accuracy, surface roughness and rigid body translations. Literature related to different domains is classified based on different responses like geometrical accuracy, surface roughness and numerical simulation.

2.1 Geometrical Accuracy

Geometrical error is the degree of deviation between desired shape and actual part after forming. Geometrical accuracy is one of the main responses in MSPIF process. It is observed that the geometrical accuracy of parts formed with MSPIF is better than SPIF process. Many researchers have worked to determine the most influencing parameters on geometrical accuracy. Ambrogio et al. [11] experimentally studied the effect of parameters on geometric error, and they reported that step depth and tool diameter are most influencing parameters. Duflou et al. [6] compared the MSPIF component with CAD model of the same component. Nirala et al. [12] also observed that geometrical accuracy of MSPIF component reduces with generation of stepped features. Otsu et al. [13] studied the effect of changing of wall angle per stage on the geometric accuracy and also compared the accuracy with the components formed with single-stage forming. Li et al. [14] analysed the effect of stepping rate on geometrical accuracy and reported that the geometrical accuracy increases with increase in stepping rate provided that stepping rate value should be in range of 50 to 250 mm/min. They investigated the influence of change of materials on geometrical accuracy and reported that change of material has major influence on geometrical accuracy. Li et al. [15] experimentally investigated the effect of strength coefficient (K) and feed rate (v_1) on geometrical accuracy of component formed with MSPIF strategy. Suresh et al. [16] compared the geometrical accuracy of each stage with the geometrical profile obtained by FEA simulation. Dai et al. [17] investigated the influence of process parameters on geometrical accuracy to form a non-axisymmetric component using multi-stage strategy. They reported that step depth, rotational speed and feed rate are the significant process parameters on geometrical accuracy. They also increased the geometrical accuracy using multi-stage strategy. Vignesh et al. [18] explained the influence of tool path, forming strategies on geometrical accuracy. Gajjar et al. [19] investigated the effect on influence of process parameters on geometrical accuracy and reported that number of stages and incremental depth are significant process parameters for geometrical accuracy.

From the available literature, it is observed that geometrical accuracy of multi-stage process is a major concern. Stepped features formed at bottom increase overall depth of the part formed with MSPIF. Because of this, the actual shape deviates from the desired shape; hence, the geometric error increases. It is also noted that the process parameters like total number of stages, material type and stepping rate are the most influencing parameters on geometrical accuracy. Prediction of intermediate geometry helps in monitoring the process. Efforts are made to predict the intermediate shapes in MSPIF, but still there is no full proof approach to predict the geometry with analytical approach. However, MSPIF process gives better geometrical accuracy than SPIF.

2.2 Numerical Simulation

In past few years, considerable efforts have been made in the field of metal forming. Finite element method (FEM) simulations are helpful to evaluate process mechanism. No theoretical model is reliable to predict the MSPIF process; however, several assumptions are made to make the prediction possible. The formability of components formed with MSPIF can be predicted by considering strength and thickness of the sheet blank, contact point between forming tool and sheet. Due to involvement of friction, deformation, material flow and other factors, prediction of material properties is complex. Therefore, a literature review of numerical simulation methods like FEM, finite difference method (FDM) and finite volume method (FVM) of MSPIF process has been discussed in the present article. From evaluation of MSPIF strategies, and their deforming mechanics, it become mandatory to apply a FE model which contains an accurate fracture criterion.

Iseki [20] used a FEM model to determine bulging height, stress distribution and strain. The analysis-based shell theory of plane strain distribution. Duflou et al. [6] predicted the geometrical accuracy numerically. They reported that there seems an error in prediction of geometry of the bottom surface. FEA model of frustum cone was evaluated by Li et al. [21] to simulate MSPIF, and formability was investigated. Liu et al. [22] validated feasibility of models M1 and M2 by finite element analysis. The TPIF process was simulated using FE modelling to analyse the thickness strains and material flow mechanism, and the FEA simulation and results obtained by experiments were matching. Wu et al. [23] performed the FEA modelling to prove FLSD for MSPIF component. They accurately modelled the depth of fracture point and FLSD. Suresh et al. [16] studied the FEA for thickness distribution, forming strains and geometric accuracy. Zhu et al. [24] validated the formability of the process by using numerical simulations. Li et al. [25] established a highly precise FEA model to predict the fracture in material during MSPIF process. The model was based on modified Mohr–Coulomb criterion. Wu et al. [23] performed FEA simulation to analyse geometrical deviation and thickness distribution variation by stepped features. Zhu and Liu [26] used FEA modelling to simulate thickness distribution of the component formed with virtual body strategy.

From the literature related to numerical simulation, it is observed that different techniques can be applied on various materials which are difficult by experimental analysis. Many material constants which are useful in predictive model can be determined easily using FEA simulations. Thickness strains easily and accurately predict from FEA simulations. Complex phenomenon like rigid body translation in MSPIF is accurately simulated using FEA simulations.

2.3 Surface Roughness

Surface quality is one of the major challenging areas of SPIF. The SPIF forms a component with number of parallel contours which creates the localized plastic deformation. The distance given between two successive contours creates tool marking, and therefore, the surface roughness of SPIF process is poor than conventional deep drawing. In SPIF, tool moves from a particular location only single time but due to multi-stage deformation, tool has to move several times from same location, creating extra tool marks on sheet surface. But in the literature very less study has been reported regarding surface roughness on MSPIF process, whereas much research has been reported regarding SPIF process. It was noted that surface quality is directly affected by feed rate and step depth. Ambrogio et al. [27] studied the effect of step depth on surface finish of SPIF process and reported that lesser incremental depth and lesser amount of wall angle reduce the surface roughness. Durante et al. [28] investigated the effect of tool rotation on SPIF process. They found its effect on surface roughness, and they also reported that effect of tool rotation is mainly significant for friction coefficient and horizontal component of force but not on surface finish. Skjoedt et al. [2] observed a phenomenon of surface wear with increasing forming stages. Palumbo et al. [29] studied the effect of temperature and tool rotation on titanium alloy in SPIF on car door shell geometry. They concluded that surface roughness increases as the step depth and tool rotation increase. Raju and Narayanan [30] investigated the optimization technique using combination of Taguchi grey relational analysis (TGRA) and response surface methodology (RSM) to identify optimum process parameters for better surface finish. They concluded that feed rate was the most dominant parameter for all output response presented in study, with next dominant parameters incremental depth and tool size. The experiments confirmed that the hybrid optimization technique improved in grey rational grade (GRG) value. Raju et al. [31] studied the effect of multiple sheets on surface roughness on commercially pure aluminium sheet. Results showed that surface roughness significantly affects by number of sheets. Kumar et al. [32] investigated the influence of parameters on surface finish of AA2024-O sheet and reported that average surface roughness value of conical geometry increases with a decrease of tool size and corner radius of the forming tool. An increase in wall angle has an adverse effect on surface finish. Kumar et al. [33] studied the process parameters step size, tool size and tool rotation on average surface finish of SPIF components. The average surface roughness of part increases with respect to decrease in tool size and tool rotation. However, surface roughness decreases with respect to a decrease in step depth. Vijaykumar et al. [34] investigated the effect of parameters on surface quality and concluded that surface roughness increases with increase in feed of tool. Gajjar et al. [19] investigated the effect of process parameters on surface quality of MSPIF component and reported that forming stages and step depth have significant effect on surface roughness. Mulay et al.[35] investigated the influence of various lubricants on SPIF. The efforts were made to get better surface finish, and they concluded that

the corrosion is higher in full deformed sheet than initial sheet and also reported that residual stress is major factor for corrosion.

From the literature review, it is observed that very less work has been done in the field of surface properties on MSPIF process. Researchers have reported that increasing wall angle in single stage decreases the surface finish of parts formed with MSPIF process. It is also found that increase in forming stages increases the surface roughness. Therefore, experimental investigation must be carried out to determine most influencing parameters on surface roughness in MSPIF process. Also, parametric optimization should be performed to minimize surface roughness.

3   Scope for Future Research

Researchers from all over the world have worked to improve MSPIF process suitable for industries. But still formability, thickness distribution and rigid body translation of MSPIF components are major limitations in MSPIF. From thorough study of the available literature, the scope for research is identified as given under.

i.   Optimization of process parameters should be performed to minimize surface roughness in MSPIF process.
ii.   Most of the research in MSPIF and SPIF is carried out for axisymmetric parts. Investigation on automobile parts, aerodynamic shapes and more practical geometries should be performed.
iii. Research efforts are required to reduce the stepped features without decreasing the wall thickness to minimize surface roughness in MSPIF process.
iv.   Further study is required on effect of spring back on geometrical accuracy in MSPIF process.
v.   Effect of different tool materials on surface properties of parts formed by MSPIF process should be studied.
vi.   Effect of number of forming stages on geometrical accuracy and thickness distribution in MSPIF process should be investigated.

4   Conclusion

Research papers published during 2000 to 2021 have been reviewed in the present work. The literature review is presented in three sections—geometrical accuracy, numerical simulation and surface roughness. It is found that MSPIF forming strategies greatly influence the properties of formed component. Based on the critical literature review, scope for future research work has been discussed.

References

1. Park JJ, Kim YH (2003) Fundamental studies on the incremental sheet metal forming technique. J Mater Process Technol 140(1–3):447–453
2. Skjødt M, Silva MB, Martins PAF, Bay N (2010) Strategies and limits in multi-stage single-point incremental forming. J Strain Anal Eng Des 45(1):33–44
3. Jeswiet J, Micari F, Hirt G, Bramley A, Duflou J, Allwood J (2005) Asymmetric single point incremental forming of sheet metal. CIRP Ann 54(2):88–114
4. Micari FABRIZIO, Ambrogio G, Filice L (2007) Shape and dimensional accuracy in single point incremental forming: state of the art and future trends. J Mater Process Technol 191(1–3):390–395
5. Echrif SBM, Hrairi M (2011) Research and progress in incremental sheet forming processes. Mater Manuf Processes 26(11):1404–1414
6. Duflou JR, Verbert J, Belkassem B, Gu J, Sol H, Henrard C, Habraken AM (2008) Process window enhancement for single point incremental forming through multi-step toolpaths. CIRP Ann 57(1):253–256
7. Panjwani D, Priyadarshi S, Jain PK, Samal MK, Roy JJ, Roy D, Tandon P (2017) A novel approach based on flexible supports for forming non-axisymmetric parts in SPISF. Int J Adv Manuf Technol 92(5):2463–2477
8. Li X, Han K, Li D (2018) Multi-stage two point incremental sheet forming. J Phys Conf Ser 1063(1):012064
9. Hirt G, Junk S, Witulski N (2002) Incremental sheet forming: quality evaluation and process simulation. In: Proceeding of the 7th ICTP conference, pp 925–930
10. Micari F, Ambrogio G (2004) A common shape for conducting incremental forming tests. In: 1st Incremental forming workshop, University of Saarbrucken, vol 9
11. Ambrogio G, Costantino I, De Napoli L, Filice L, Fratini L, Muzzupappa M (2004) Influence of some relevant process parameters on the dimensional accuracy in incremental forming: a numerical and experimental investigation. J Mater Process Technol 153:501–507
12. Nirala HK, Jain PK, Roy JJ, Samal MK, Tandon P (2017) An approach to eliminate stepped features in multistage incremental sheet forming process: Experimental and FEA analysis. J Mech Sci Technol 31(2):599–604
13. Otsu M, Ogawa T, Muranaka T, Yoshimura H, Matsumoto R (2017) Improvement of forming limit and accuracy in friction stir incremental forming with multistage forming. Procedia Engineering 207:807–812
14. Li Z et al (2017) Analysis of geometrical accuracy based on multistage single point incremental forming of a straight wall box part. Int J Adv Manuf Technol 93(5):2783–2789
15. Li Z, Lu S, Chen P (2017) Improvement of dimensional accuracy based on multistage single point incremental forming of a straight wall cylinder part. Int J Precis Eng Manuf 18(9):1281–1286
16. Suresh K, Regalla SP, Kotkundae N (2018) Finite element simulations of multi stage incremental forming process. Mater Today: Proc 5(2):3802–3810
17. Dai P, Chang Z, Li M, Chen J (2019) Reduction of geometric deviation by multi-pass incremental forming combined with tool path compensation for non-axisymmetric aluminum alloy component with stepped feature. Int J Adv Manuf Technol 102(1):809–817
18. Vignesh G, Pandivelan C, Narayanan CS (2020) Review on multi-stage incremental forming process to form vertical walled cup. Mater Today: Proc 27:2297–2302
19. Gajjar S, Sisodia V, Jagtap R, More K, Kumar S (2020) Experimental investigation on geometric accuracy and surface roughness of formed part in multistage single point incremental forming (SPIF) process. In: Innovative design, analysis and development practices in aerospace and automotive engineering. Springer, Singapore, pp 209–222
20. Iseki H (2001) An approximate deformation analysis and FEM analysis for the incremental bulging of sheet metal using a spherical roller. J Mater Process Technol 111(1–3):150–154
21. Li J, Geng P, Shen J (2013) Numerical simulation and experimental investigation of multistage incremental sheet forming. Int J Adv Manuf Technol 68(9–12):2637–2644

22. Liu Z, Daniel WJ, Li Y, Liu S, Meehan PA (2014) Multi-pass deformation design for incremental sheet forming: analytical modeling, finite element analysis and experimental validation. J Mater Process Technol 214(3):620–634
23. Wu S, Ma Y, Gao L, Zhao Y, Rashed S, Ma N (2020) A novel multi-step strategy of single point incremental forming for high wall angle shape. J Manuf Process 56:697–706
24. Zhu H, Li J (2018) Tool path generation for the five-axis CNC multi-stage incremental forming. Int J Adv Manuf Technol 95(9):3197–3213
25. Li Z, Lu S, Zhang T, Feng T, An Z, Xue C (2020) Numerical prediction of ductile fracture in multi-stage single point incremental forming based on phenomenological modified Mohr–Coulomb. Measurement 154:107505
26. Zhu H, Liu, L. (2021). Research the CNC incremental forming of straight-wall parts based on a virtual auxiliary body. J Mater Process Technol 288:116841
27. Ambrogio G, De Napoli L, Filice L, Gagliardi F, Muzzupappa M (2005) Application of incremental forming process for high customised medical product manufacturing. J Mater Process Technol 162:156–162
28. Durante M, Formisano A, Langella A, Minutolo FMC (2009) The influence of tool rotation on an incremental forming process. J Mater Process Technol 209(9):4621–4626
29. Palumbo G, Brandizzi M (2012) Experimental investigations on the single point incremental forming of a titanium alloy component combining static heating with high tool rotation speed. Mater Des 40:43–51
30. Raju C, Narayanan CS (2016) Application of a hybrid optimization technique in a multiple sheet single point incremental forming process. Measurement 78:296–308
31. Raju C, Haloi N, Narayanan CS (2017) Strain distribution and failure mode in single point incremental forming (SPIF) of multiple commercially pure aluminum sheets. J Manuf Process 30:328–335
32. Kumar A, Gulati V, Kumar P (2018) Effects of process parameters on surface roughness in incremental sheet forming. Mater Today Proc 5(14):28026–28032
33. Kumar A, Gulati V, Kumar P (2018) Investigation of surface roughness in incremental sheet forming. Procedia Comput Sci 133:1014–1020
34. Vijayakumar MD, Chandramohan D, Gopalaramasubramaniyan G (2020) Experimental investigation on single point incremental forming of IS513Cr3 using response surface method. Mater Today Proc 21:902–907
35. Mulay A, Ben S, Ismail S (2020) Lubricant selection and post forming material characterization in incremental sheet forming. In: IOP conference series: materials science and engineering. IOP Publishing, vol 967, no 1, p 012072
36. Kim TJ, Yang DY (2000) Improvement of formability for the incremental sheet metal forming process. Int J Mech Sci 42(7):1271–1286
37. Iseki H, Naganawa T (2002) Vertical wall surface forming of rectangular shell using multistage incremental forming with spherical and cylindrical rollers. J Mater Process Technol 130:675–679
38. Young D, Jeswiet J (2004) Wall thickness variations in single-point incremental forming. Proc Inst Mech Eng Part B J Eng Manufacture 218(11):1453–1459
39. Wu M, Zha G, Zirui G (2017) FEA of vertical parts formed with multistage incremental sheet metal forming based on the forming limit stress diagram. Int J Adv Manuf Technol 93(5):2155–2160
40. An ZG, Yan D, Qie JJ, Lu ZL, Gao ZY (2020) Effect of process parameters on formability of a AZ31 magnesium alloy thin-walled cylindrical part formed by multistage warm single-point incremental forming. Front Mater 7:151. https://doi.org/10.3389/fmats

Realization of a Compliant Mechanism-Based Compensation Technique for Multiplexer Filter of Communication Space Payload

Krunal J. Shah and A. R. Srinivas

1 Multiplexer Filter

Multiplexers are used in satellite communication transponders to enable combining or multiplexing of very high-power amplified signals into a single waveguide. Multiplexer consists of two or more channels connected by single manifold. All the channels are consisting of cavity filters. The multiplexer is one type of microwave filter which segregates different radio frequencies (RF) of microwave energy to different channels according to the bandwidth allocation. These signals are received from the terrestrial networks and are transmitted by the multiplexers to an antenna which are then beamed back to a different terrestrial and ground networks. A single-channel filter is made up of cavities, irises, adapters and brackets [1] (Fig. 1).

K. J. Shah (✉)
Mechanical Engineering Department, A D Patel Institute of Technology, Anand, Gujarat, India
e-mail: me.kjs@adit.ac.in

A. R. Srinivas
Space Application Centre, ISRO, Ahmedabad, India
e-mail: arsrinivas@sac.isro.gov.in
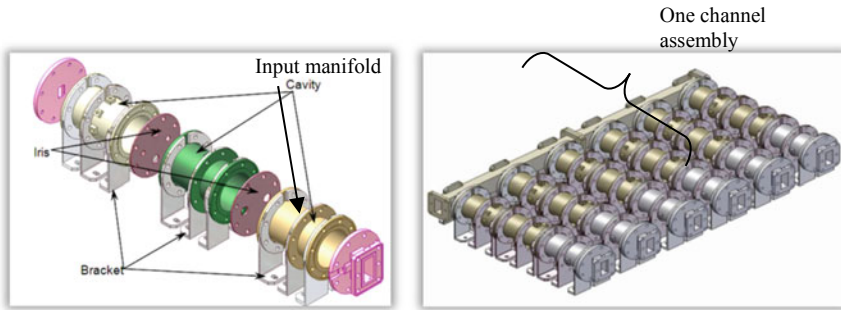
Fig. 1 Multiplexers

2 Need for Compensation

As the multiplexers have to deal with the filtration process of the radio frequency waves, the dimensions of the filter cavity should remain unchanged while processing. During this operation, due to radio frequency waves, resistance heating of the cavity occurs and thermal excursion takes place because of heating, and this will cause the change in dimension of the filter cavity. To avoid this dimension change, there is a need for some compensation mechanism for compensating this dimension change and nullifying the effect on the filtration process.

3 Conventional Methods of Compensation

Many solutions have been proposed using two dissimilar materials utilizing the advantage of different CTE's of the material. But most of the time, they involve complex joints and assemblies, develop stress/strain in the joints owing to the presence of the dissimilar materials when subjected to the temperature excursion which every satellite components has to withstand. These solutions also form heavy structures, complicated manufacturing processes, produce insufficient compensation, etc. and in general make the approaches techno-economically unfeasible for spacecraft components [2, 3].

Based on the disadvantage of the above approach, a novel and innovative solution has been proposed as a compliant mechanism to compensate the volume change of the multiplexer cavity. Using the benefit of geometrical advantage of the compliant mechanism, the over compensation can also produce and that will help to correct the uncontrollable expansion. A compliant mechanism is a joint less, single piece, lightweight, easy to realize system. In addition to this compliant, systems are inexpensive and can have almost infinite life expectancy without ever needing lubrication, and this will increase the attention of its use in aerospace applications [4, 5].

4 Design Optimization Methodology of Compliant Mechanism

A compliant mechanism can be defined as a single-piece flexible structure which uses elastic deformation for force or motion transmission. A novel optimization methodology for the design of compliant mechanism has been carried out. The design process for the present application starts with the structural optimization-based approach. The synthesis process is divided into two steps.

1. Topology optimization
2. Dimension/gage optimization.

The synthesis process starts with the topology optimization, and with the optimized topology, dimension/gage synthesis process has been carried out. The topology serves as the input for the dimension optimization process [4, 6].

5 Design Process

For the present application, the design domain of 50X50 mm in size and 2 mm thick with required loading and boundary conditions has been considered (Fig. 2).

The model has been created in HyperMesh software; topology optimization has been carried out, and optimized topology is then sent to the CAD software for dimension optimization. The number of iterations has been carried out to get the optimized geometry. The output geometry from the topology optimization gives only the desired direction of the actuation. The amount of output actuation is not amplified.

The dimensions are then fine-tuned by caring out number of iterations with varying the dimensions of the topology given by Altair's OptiStruct [7] (Fig. 3).

Table 1 shows results of both structures of mechanism, i.e., before and after the structural optimization.

As a result of mechanism's dimension optimization, the actuation of the mechanism has been amplified seven times compared to the initial structure's actuation at given loading condition. The optimized mechanism shows geometric advantage, i.e., ratio of the output actuation to the input actuation more than 2 (Fig. 4).

To accommodate the mechanism on the diaphragm of the multiplexer, following parts have to be introduced, namely holding ring, recovery disk and push rod. After introduction of these parts, the final mechanism will become a fully compliant mechanism as shown in Fig. 5 (Fig. 6).

An assembly of compliant mechanism with the multiplexer filter has been modeled in CAD software. The thermo-structural analysis has been carried out considering all the constraints that would exist while at the real situation (Fig. 7).

(a)

(b)

(c)

(d)
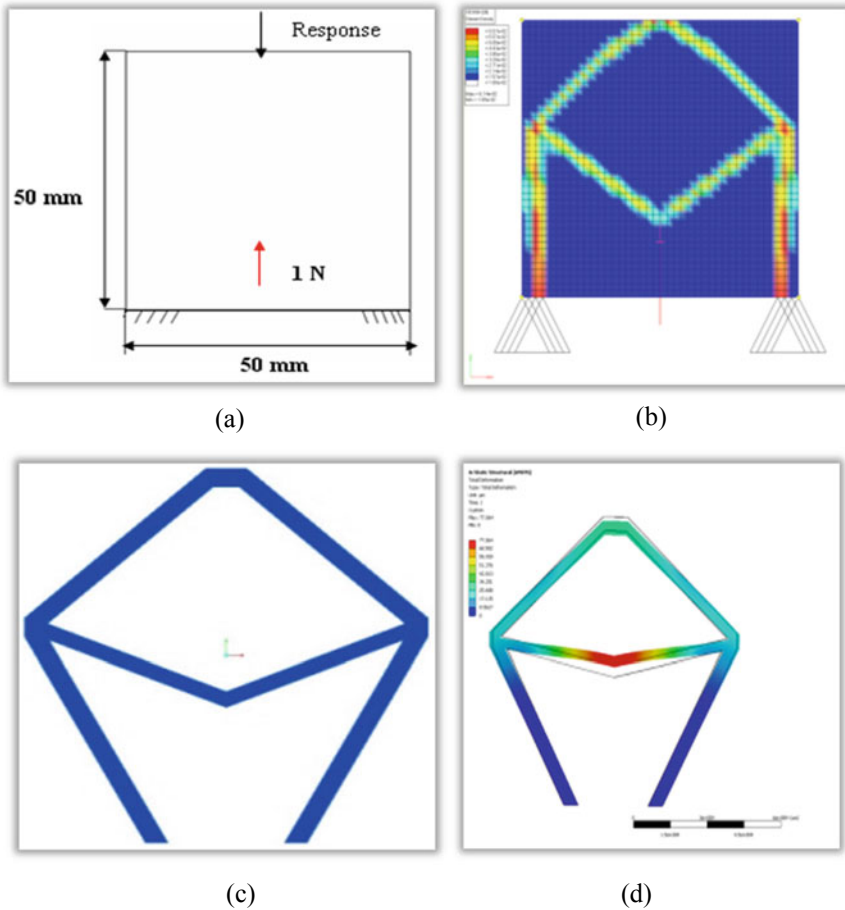
Fig. 2 Optimization process steps **a** boundary conditions, **b** topology optimization result in Hyper-Works, **c** CAD geometry from optimization result, **d** static structural analysis result of optimized CAD model

The numerical analysis has been carried out using ANSYS software. The environment has been developed to create a real-time situation. As stated earlier, the problem is not of only single domain; multi-domain problem has been formulated. As a result, steady-state thermal analysis has been carried out followed by static structure analysis. In steady-state thermal analysis, the domain/multiplexer cavity has been heated to achieve the 60 °C temperature which is considered for the real-time situation analysis (Figs. 8 and 9).

At the design stage, the concept of the mechanism is to give the amplified amount of output displacement, and the designed mechanism also proves it numerically by implementing it on to the multiplexer cavity.

(a)   (b)
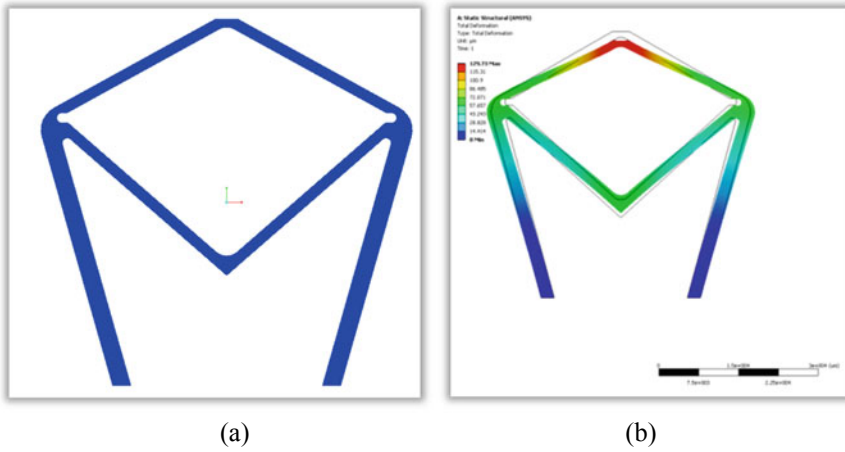
Fig. 3 Final optimized mechanism **a** optimized design, **b** structural analysis result

Table 1 Before and after dimension optimization [8]

S. No.	Description	Input (deflection at load end) (μm)	Output (deflection at desired end) (μm)	G.A (geometric advantage)
1	Initial structure	32	24	0.75
2	Optimized structure	78	165	2.11

6 Realization

The realization of the mechanism is also carried out with the conventional fabrication process. The material chosen for the realization is AL 6061 T6. The realized model is as shown in Fig. 10.

7 Experimentation

The experimentation with thermal loading has also been carried out. To measure the actual effect due to heat load, measurement of the displacement at the two ends (i.e., plunger end and top end) of the complaint mechanism has been carried out. Table 2 shows the comparison of the numerical analysis and experimental results (Figs. 11 and 12).

(a) Main body

(b) Holding ring

(c) Push rod

(d) Recovery disc
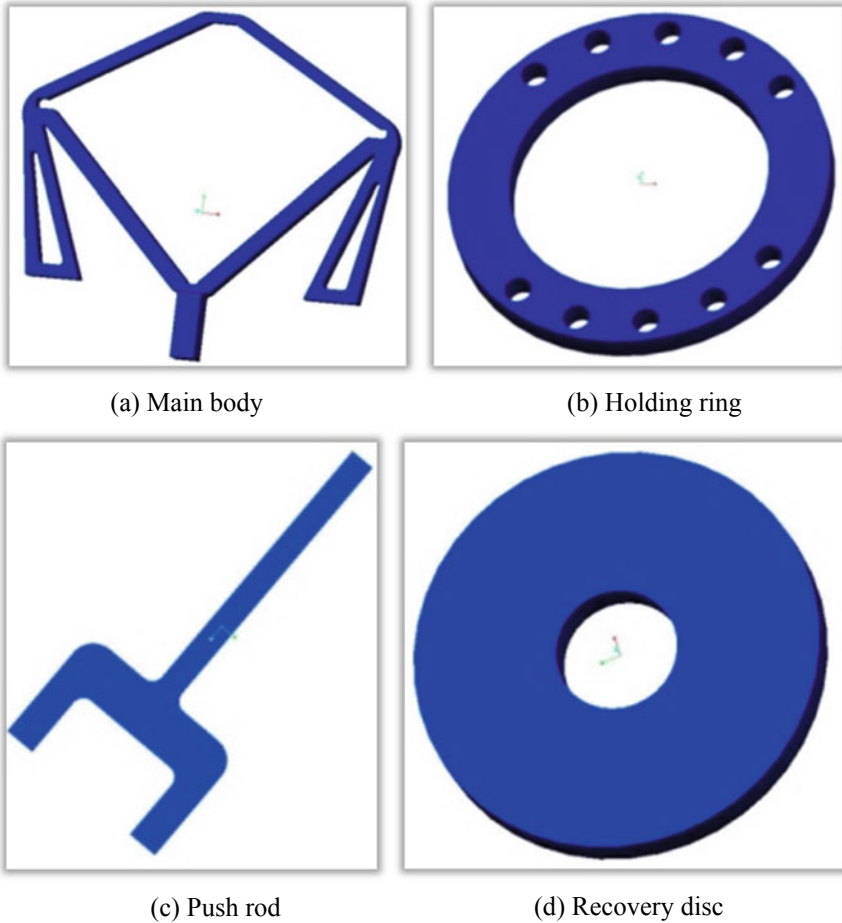
Fig. 4 Individual parts of the final mechanism

8 Conclusions

The results show that the concept of the design, developments and realization of the compliant mechanism-based compensation technique for multiplexer filter of communication space payload has been proved successfully.

- A fully numerical-based novel methodology has been developed which uses a two-step synthesis process that starts with topology optimization and size optimization.

Fig. 5 CAD model of optimized compliant mechanism

Fig. 6 Simulation model of optimized compliant mechanism
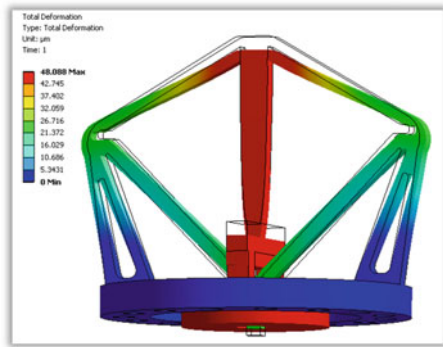
- Numerical simulation of compensating effect has been demonstrated using CAE tools. The compensation effect has been measured using manufactured prototype and is in close match with the numerical results.
- These results have proved that the designed compliant mechanism can be used as an alternative against conventional methods of compensation.
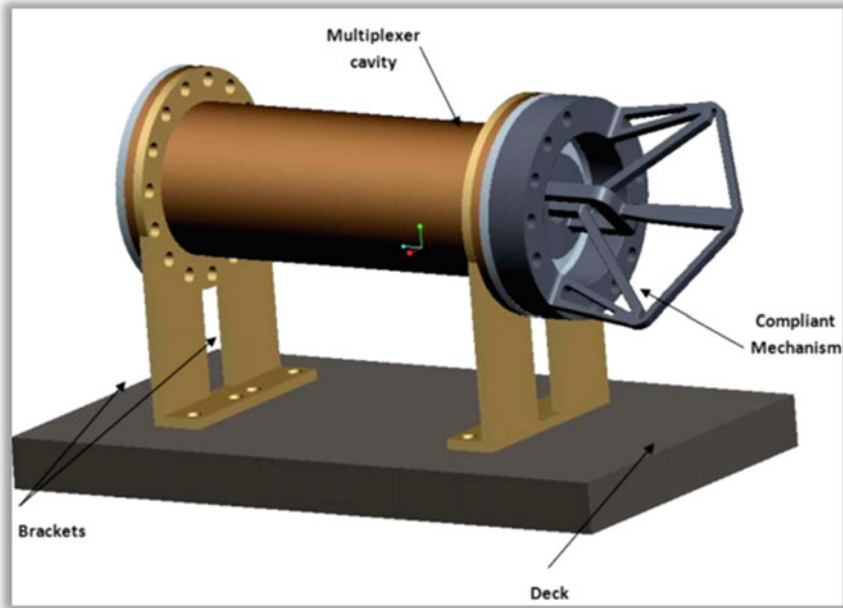
Fig. 7 CAD model of multiplexer cavity with compliant mechanism
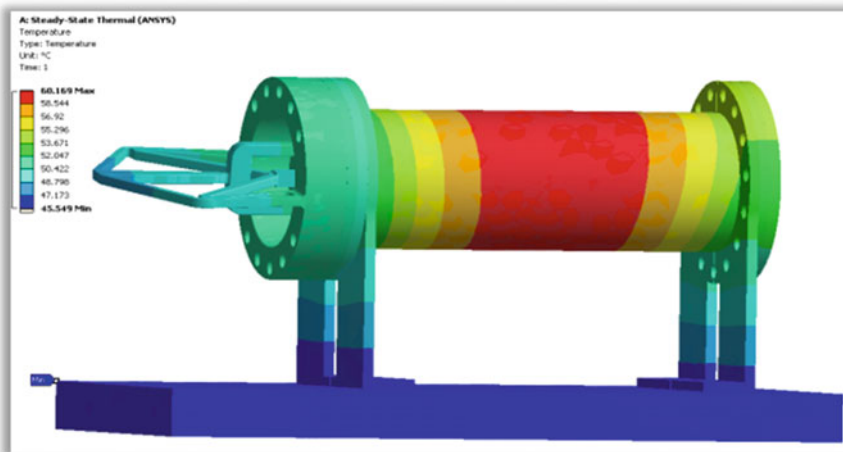
Fig. 8 Thermal analysis plot shows the cavity temperature
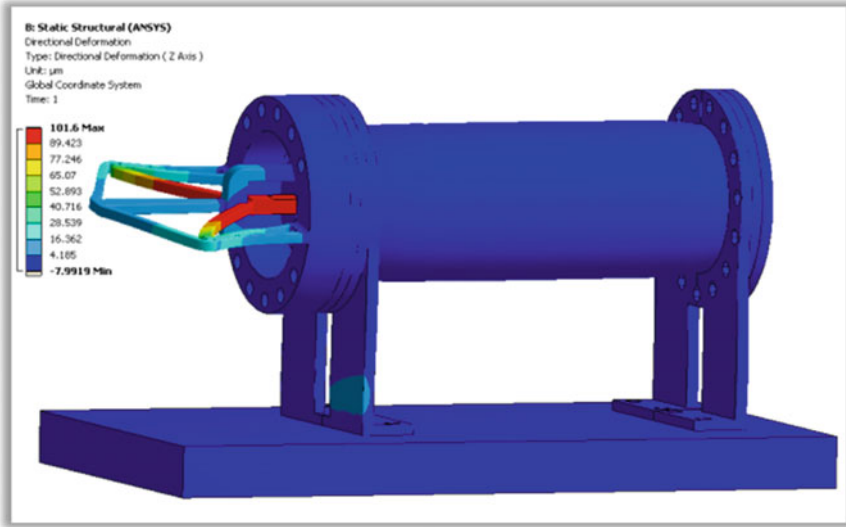
Fig. 9 Structural deformed plot of multiplexer cavity with compliant mechanism
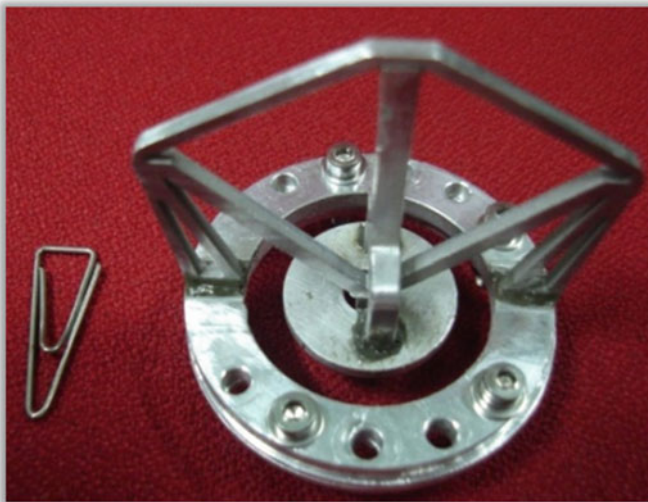
Fig. 10 Realized compliant mechanism with AL 6061 T6 material

Table 2 Experimental result table

	Displacement at the plunger end (μm)	Displacement at the top end (μm)	Geometric advantage (μm)
Numerical	20.1	9.9	2.03
Experimental	15	7	2.14
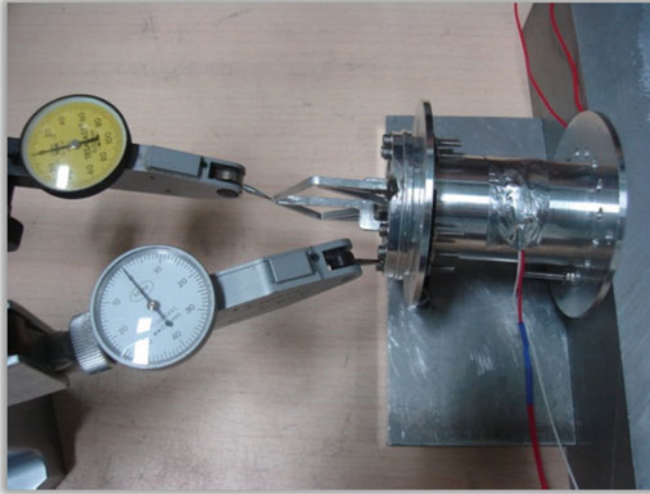
Fig. 11 Actual thermal experimentation
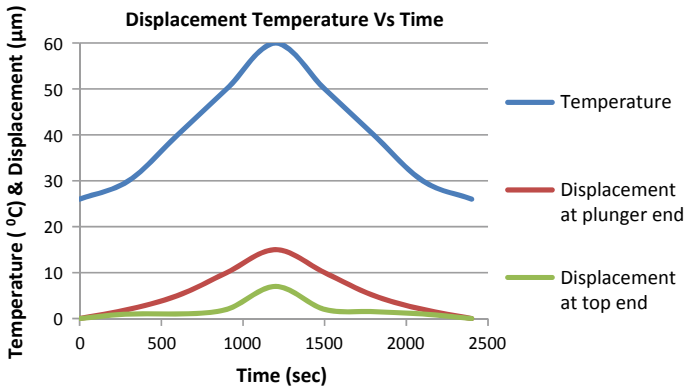
Fig. 12 Experimental result plot

References

1. Orlov P (1979) Fundamentals of machine design, vol 1, 1st edn. MIR publishers, Moscow
2. Srinivas AR (1993) Thermo elastic behavior and analysis of dissimilar joints. ReportNo.SAC/SPG/INS/TR03, Space application centre, ISRO, Ahmadabad
3. Nelson CW (1979) Thermal stresses in bonded joints. IBM J Res Dev 23(2)
4. Shuib S, Ridzwan MIZ, Kadarman AH (2007) Methodology of compliant mechanisms and its current developments in applications: a review. Am J Appl Sci 4(3):160–167
5. Lu KJ, Kota S (2002) Compliant mechanism synthesis for shape-change applications: preliminary results. Department of Mechanical Engineering, University of Michigan, Ann Arbor, MI 48109, SPIE vol 4693

6. Hetrick JA (1999) An energy efficiency approach for unified topological and dimensional synthesis of compliant mechanisms a dissertation report. University of Michigan
7. Shah KJ et al (2011) A novel optimization methodology for design of compliant mechanism of a space payload system. In: ICISET(International conference on innovative science and engineering technology), vvp engineering collage, Gujarat, India
8. Wang MY, Cheny S (2009) Compliant mechanism optimization: analysis and design with intrinsic characteristic stiffness. The Chinese University of Hong Kong Shatin, NT, Hong Kong
9. Shah KJ et al (2011) Realization of an optimized compliant mechanism for thermal compensation of communication space payload subsystem. In: Hyperworks technology conferenc, The Westin, Pune
10. Lu KJ, Kota S, Design of compliant mechanisms for morphing structural shapes. Department of Mechanical Engineering, University of Michigan, Ann Arbor, MI 48109-2125, USA

Characteristic Features Developed After Sheet Metal Processing of ARMCO Iron Using Constrained Groove Pressing Process

Vindala Poojitha, T. Raghu, and V. Pandurangadu

1 Introduction

Severe plastic deformation (SPD) is a name given to a group of methods working on a common principle of processing ultra-fine-grained materials without any change in geometry of the deformed samples. SPD can be adopted for manufacturing various engineering components such as bolts, small turbine blades, landing gears, connecting rods, micro-gears, circuit breakers, and biomedical implants. Most established methods in severe plastically deforming materials include equal channel angular pressing (ECAP) [1], high pressure torsion (HPT) [2], accumulative roll bonding (ARB) [3], repetitive corrugation and straightening (RCS) [4], constrained groove pressing (CGP) [5], etc. Among these, CGP is considered to be a potential method in fabricating materials that are in the form of a sheet. CGP process follows a sequence where sheet sample is grooved and flattened in closed dies. The uniqueness of this die design is that it constrains the sheet movement so that there is negligible change in its dimension. Since 2002, several investigations are well documented [6, 7] on CGP and its expertise in attaining increased refinement in grains and improved properties in both cubic and hexagonally close packed materials. Few of the CGP studies have also revolved around the influence of die design on a strained sample in terms of structural and mechanical properties [8, 9]. In this study, some of the features developed during constrained groove pressing of ARMCO Fe sheet are presented. The reasons for such observations are discussed and compared with other reports available in literature on this severe plastic deformation process.

V. Poojitha (✉) · V. Pandurangadu
Department of Mechanical Engineering, Jawaharlal Nehru Technological University Ananthapur (JNTUA), Ananthapuramu 515002, Andhra Pradesh, India

T. Raghu
Aeronautical Materials Division, Defence Metallurgical Research Laboratory (DMRL), Kanchanbagh, Hyderabad 500058, Telangana, India

2 Experimental Procedures

ARMCO Fe of 5 mm sheet thickness was subjected to CGP process, carried out using a set of corrugated dies and flat dies [10]. Every cycle of CGP constitutes two passes with four pressings of alternate corrugation and straightening, resulting in an effective strain of ~1.16 [11]. Higher strain of ~4.64 was attained in this work by carrying out eight passes of CGP corresponding to sixteen pressings at ambient temperature. A metallographic study was performed on the samples following a standard procedure, and micrographs were obtained using optical microscopy.

3 Results and Discussions

This section presents certain peculiar features observed after CGP process of ARMCO Fe sheet that are grouped as macroscopic and microscopic observations.

3.1 Macroscopic Observations

After CGP process, undulations were formed on the sheet surface as shown in Fig. 1. This distinctive feature is because of the CGP die profile especially the groove die design. However, for applications, it is necessary that sample surface is flat and smooth. This specification has created a need to fabricate a severe plastically deformed material with better surface finish. A conventional metal forming processes can be subsequently carried out to remove these undulations. Interestingly, in a study on Al alloy [12] subjected to a single cycle of CGP, undulations were seen, and to clear these surface irregularities, a mild skin pass rolling was suggested.

Additionally, micro-cracks were found on the sheet surface due to the increased stress accumulated regions after constant occurrence of corrugated pressings.
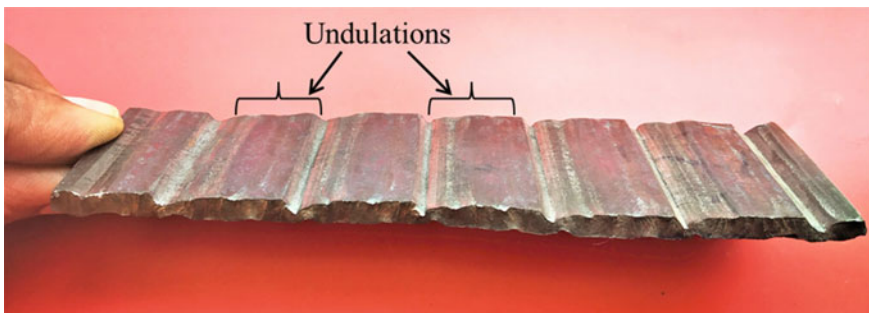
Fig. 1 Appearance of undulations on a constrained groove pressed ARMCO Fe sheet

Fig. 2 Formation of micro-cracks on the constrained groove pressed ARMCO Fe sheet

Figure 2 depicts a sheet surface with few of the micro-cracks circled in red. It is important to note that the formation of micro-cracks can restrict the amount of effective strain induced. This is clearly evident in the present study as sheet sample could not be processed beyond sixteen pressings. Earlier investigations have also reported such observations in a CGP processed materials [13]. Peng et al. [13] mentioned about formation of a cracked brass sheet after four CGP pressings. To resolve this issue of crack formation, appropriate heat treatments and die design modifications were carried resulting in more pressings without fracture.

Compared to this, present study was successful in achieving more cycles of CGP attributing it to the lubrication of sheet using antifriction coating before the commencement of CGP process. Furthermore, this imposition of higher strains in a material can thereby allow improved grain refinement and superior mechanical properties [14].

3.2 Microscopic Observations

An interesting CGP microstructural feature has appeared in this severe plastically deformed sample. Figure 3 is an optical micrograph of CGP processed ARMCO Fe sheet revealing flow lines with grains arranged in a wave pattern. These patterns are seen to have covered majority of the sample area. For the purpose of easy identification, red colored curves are marked along these flow arrangements. This observation is consistent with few other investigations published on CGP of pure Cu [15] and an aluminum alloy [16]. A common reasoning specified for this microstructural change is its corrugated die structure. While undergoing large plastic strains during corrugation, grain formation and change in its morphology are followed along these paths.
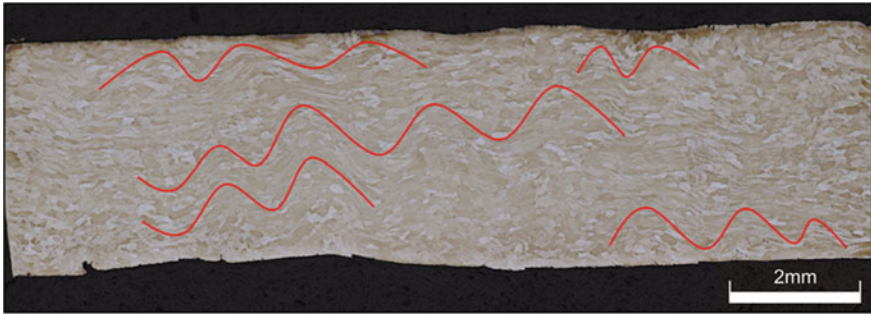
Fig. 3 Optical micrograph of ARMCO Fe sheet subjected to sixteen pressings

4 Conclusion

ARMCO Fe sheet subjected to sixteen pressings resulted in three distinct observations grouped as macroscopic and microscopic observations. In the scientific literature, their occurrence is reasoned to the characteristic groove die design. The pronounced observations in deformed sample are found to influence in the following two ways: firstly, the undulations developed on the surface might make it unsuitable for a structural application. Secondly, micro-cracks formed are proven to limit the capability of the material to undergo more number of CGP pressings. In the present work, ARMCO Fe sheet could not take effective strain beyond ~4.64, which can be attributed to micro-crack formation. Some basic metal forming processes may help reduce their impact on the largely strained sheet material.

References

1. Zenji Horita, Furukawa M, Langdon TG, Nemoto M (1998) Equal-Channel angular pressing (ECAP): a novel method for microstructural control. Mater Jpn
2. Vorona D, Sharafutdinov AV, Krasilnikov NA (2006) High strength and ductility of nanostructured Al Alloy 2024 subjected to high pressure torsion. Solid State Phenom
3. Krallics G (2004) An examination of the accumulative roll-bonding process. J Mater Process Technol
4. Rajinikanth V, Arora G, Narasaiah N, Venkateswarlu K (2008) Effect of repetitive corrugation and straightening on Al and Al–0.25Sc alloy. Mater Lett
5. Zrník J, Kovarik T (2008) Miroslav Cieslar. Microstructure and properties of aluminium processed by constrained groove pressing, Materials Science Forum
6. Ghorbanhosseini S, Fereshteh-Saniee F, Sonboli A (2019) An experimental investigation on the influence of elevated-temperature constrained groove pressing on the microstructure, mechanical properties, anisotropy and texture of 2024 Al sheets. J Alloy and Compd
7. Hoseini-Athara MM, Mahmudia R, Prasath Babub R, Hedströmb P (2019) Microstructural evolution and superplastic behaviour of a fine-grained Mg–Gd alloy processed by constrained groove pressing. Mater Sci Eng A
8. Niranjan G, Uday C (2010) Improvement in drawability (R Value) of an aluminum alloy subjected to groove pressing. Mater Sci Forum

9. Kazeminezhad M, Hosseini E (2010) Optimum groove pressing die design to achieve desirable severely plastic deformed sheets. Mater Des

10. Khodabakhshi F, Kazeminezhad M (2011) The effect of constrained groove pressing on grain size, dislocation density and electrical resistivity of low carbon steel. Mater Des

11. Shin DH, Park J-J, Kim Y-S, Park K-T (2002) Constrained groove pressing and its application to grain refinement of aluminium, Mater Sci Eng A328

12. Khakbaz F, Kazeminezhad M (2012) Strain rate sensitivity and fracture behaviour of severely deformed Al–Mn alloy sheets. Mater Sci Eng

13. Kaiping P, Su L, Shawb LL, Qian K-W (2007) Grain refinement and crack prevention in constrained groove pressing of two-phase Cu–Zn alloys. Scripta Materialia

14. Azushima A, Kopp R, A. Korhonen, Yang DY, Micari F, Lahoti GD, Groche P, Yanagimoto J, Tsuji N, Rosochowski A, Yanagid A (2008) Severe plastic deformation (SPD) processes for metals. Manuf Technol

15. Wang Z-S, Guan Y-J, Liang P (2014) Deformation efficiency, homogeneity, and electrical resistivity of pure copper processed by constrained groove pressing, Rare Metals

16. Jandaghi MR, Pouraliakbar H (2017) Study on the effect of post-annealing on the microstructural evolutions and mechanical properties of rolled CGPed aluminum-manganese-silicon alloy. Mater Sci Eng A

Design and Analysis of Piston Comparing Different Materials

Ankitkumar Rajpurohit, Krunalkumar Patel, Jimitkumar Naik, Meet Bhatt, Mukund Sondagar, and Sagarsingh Kushwah

1 Introduction

In the year 1866, the piston was invented by Nicholas August Otto, a German scientist. It falls under one of the major mechanical components. The mechanical devices such as gas compressors, reciprocating pumps, and pneumatic cylinders, amongst other associated mechanisms, are considered crucial parts of the reciprocating kind of engine to help convert chemical energy from the combustion of fuel to useful mechanic work [1]. The application of the piston is to provide the vehicle for transferring gas expansion to the crankshaft employing the connecting rod. A piston is essentially an up and down cylindrical plug. Piston rings are provided in order to ensure that the cylindrical wall is well sealed. Figure 1 depicts the basic picture of the piston's cross-section with its terminology [2].

The piston is used as a plug that tightens the gas which causes compression, suction, expansion, and drainage in the cylinders. Also, the key function of the piston is to receive and transmit to the connecting rod the thrust produced by the gas explosion in the cylinder [3]. Furthermore, the role of the piston is important to guide and support the connecting rod's small end and carry the lateral thrust produced because of the rod's obliquity [4].

Now, to study the piston, it is very important to know the major forces acting over it. The following are the major forces: 1. due to fuel gases' compression, 2. force produced as a result of the fuel gas explosion, 3. thermal load, 4. friction on the side wall, 5. t the crankpin, friction and forces exist, and 6. due to the high frequency of piston reciprocation, there is an inertia force [5].

A. Rajpurohit · M. Sondagar
Automobile Engineering Department, L. D. College of Engineering, Ahmedabad, Gujarat, India
e-mail: mukundsondagar33@gmail.com

K. Patel · J. Naik · M. Bhatt · S. Kushwah (✉)
Mechanical Engineering Department, R. N. G. Patel Institute of Technology, Bardoli-Navsari Road, Surat, Gujarat, India
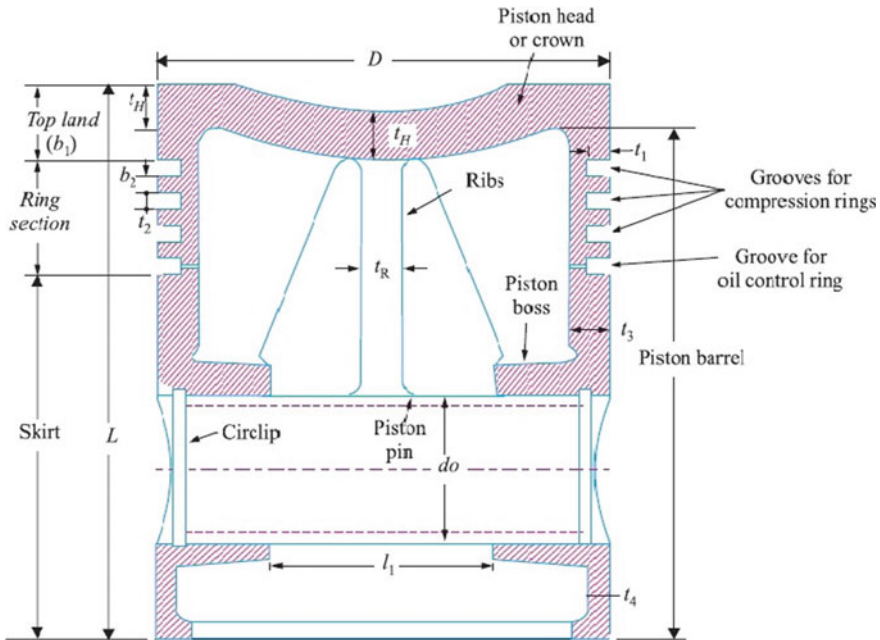
Fig. 1 Piston's cross-section with its nomenclature

2 Piston's Failure Mode

The piston failure can be classified into two methods: 1. wrought-out failure and 2. wrong-out failure. There are several reasons for these two kinds of failure which are discussed herein brief [6].

The wrought-out failure can be caused by running the unmixed fuel. On the skirt with the highest damage, the piston above is heavily squeezed at the embrace side [7]. All this damage is caused by direct fuel. Due to a lack of lubrication on the piston, the cylinder wall is seized. Another major reason for wrought failure is due to overspeeding the engine. The ring land is broken by the development of the high frequency of vibration [8]. Detonation and heat seizure is another reason for the wrought failure. The detonation heat caused the piston to be so hot, the rings stuck, and the piston gets seized [9].

In a similar way, there is various cause for the wrong failure. One of the causes is debris damage caused by the air filter. Due to debris coming through the air filter system, the damage on this skirt is caused. The scrubbed off marks are all formed on the lower part of the skirt showing extreme wear. Only on the intake side, this kind of damage is found in the piston. Damage caused by failure of bearing is another kind of wrong-out failure. The failure of the body bearings or the main bearings is the consequence of fine scratches on the skirt and the bottom intake skirt. Small but hard rollers and retention cages break loose, causing damage to the piston [10].

3 Methodology

Table 1 shows the specifications of a four-stroke single-cylinder Bajaj Pulsar 220 cc engine. The dimensions of the piston are demonstrated in Table 2. From the dimension, the 3D modelling was done in SOLIDWORKS software which is shown in Fig. 2.

Further, finite element analysis was performed over the 3D model by importing the model into the ANSYS Workbench (Simulation Software). The FEA is the simulation by means of the numerical technique called the finite element method (FEM) [13, 14]. It demonstrates whether a product break uses or works the way it has been designed. In the product development process, what happens when the product is used is predicted. FEA works by dividing a real object into a large number of finite

Table 1 Engine specification

Parameters	Values
Engine type	Four-stroke, petrol engine
No. of cylinders	Single cylinder
Induction	Air-cooled type
Maximum torque (T)	19.12 N-m at 7000 rpm (N)
Maximum power	15.51 kW at 8500 rpm
No. of revolutions/cycle	2
Compression ratio	9.5:1

Table 2 Dimensions of piston

Parameters	Values
Bore (D) (mm)	67
Stroke (L) (mm)	62.4
Length of connecting rod (mm)	124.8
Displacement volume (Cm^3)	220
Thickness of piston head (t_h) (mm)	7.735
Piston rings radial width (b) (mm)	1.834
Axial thickness (h) (mm)	1.284
Width of top land (h_1) (mm)	7.735
Ring lands (h_2) (mm)	0.963
Length of the skirt (L_S) (mm)	40.2
Thickness of piston barrel at the open end (t_2) (mm)	2.186
Thickness of piston barrel at the top end (t_1) (mm)	8.774
Piston pin diameter (d_o) (mm)	20.1
Piston boss diameter (1.5 d_o) (mm)	30.15

Fig. 2 3D model of piston

elements. FEA assists in the prediction of product behaviour that has many physical effects such as fluid flow, vibration, stress, heat transfer and motion [15, 16].

After importing the model in ANSYS, the next step is to assign the material or material properties to it. The materials selected for comparison are A2618, Al-GHS 1300 and Ti-6Al-4 V. After that, the meshing(discretisation) is performed (Fig. 3). The mesh size and shape were kept 5 mm and tetrahedral.

Applying the boundary conditions is the next step. The pressure of 13.65 MPa is applied at the piston head. Frictionless support is applied at the piston pin hole as the pin can freely rotate inside the hole. At the edges of the piston pin hole, the fixed supports shall be applied. The static structure analysis was performed for the materials assigned to the piston [11]. Deformation, equivalent elastic strain and von Mises stress were obtained as the output (result). In addition, steady-state thermal analysis was also performed, where the piston head temperature was kept 200 °C. The temperature of piston edges was 125 °C [12]. The temperature distribution and total
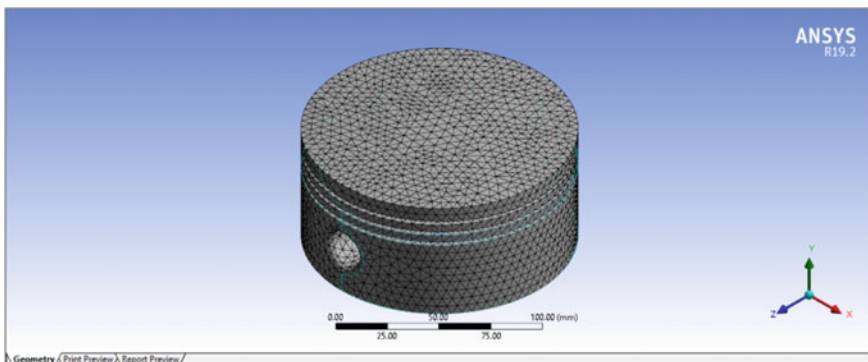
Fig. 3 Meshing of piston

heat flux were obtained as the output. Moreover, the combined thermo-mechanical analysis was performed, where both pressure and thermal loads were applied.

4 Results and Discussion

The results of static structure analysis for material A2618 are shown in Figs. 4, 5 and 6, respectively. Similarly, for the other two materials, the results were obtained. Table 3 depicts the results of the materials for static structural analysis.

The results of the steady-state thermal analysis for material Al-GHS 1300 are shown in Figs. 7 and 8. Similarly for the other two materials, the results were obtained. Table 4 depicts the results of the materials for steady-state thermal analysis. Moreover, the results of the combined thermo-mechanical analysis are shown in Table 5.

As it can be observed from the tables, the maximum stress occurs in A2618 alloy (534.13 MPa), while the minimum is in Ti-aI-4 V alloy (441.13 MPa). The maximum
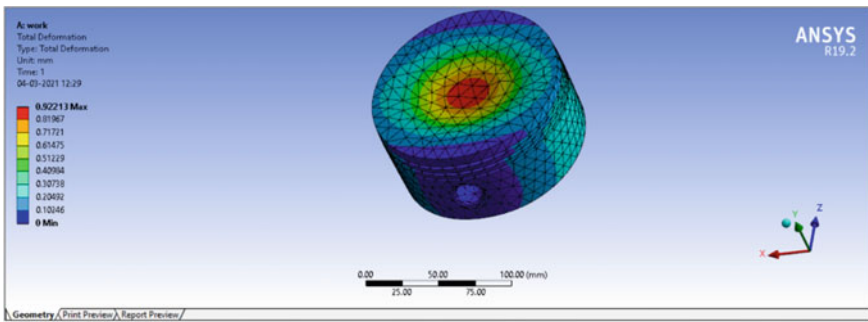
Fig. 4 Deformation of A2618
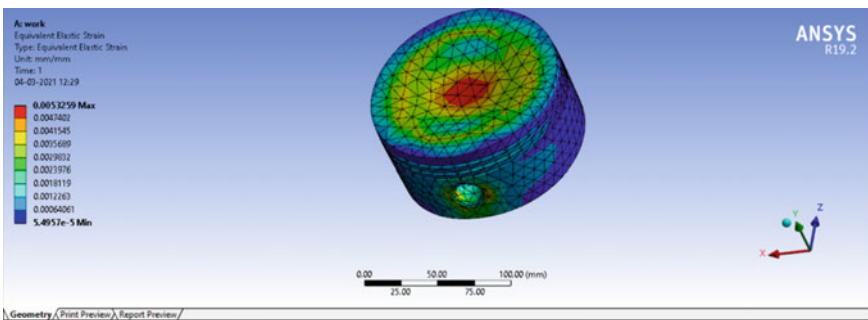
Fig. 5 Equivalent elastic strain of A2618
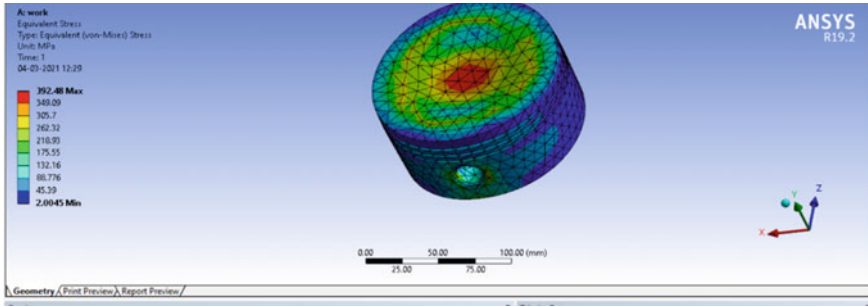
Fig. 6 Von Mises stress of A2618

Table 3 Results of static structural analysis

Parameters	A2618	Al-GHS 1300	Ti-6Al-4 V
Equivalent stress (MPa)	392.48	410.53	409.97
Total deformation (mm)	0.92213	0.73504	0.62442
Equivalent elastic strain (mm/mm)	0.0053529	0.004951	0.0042318
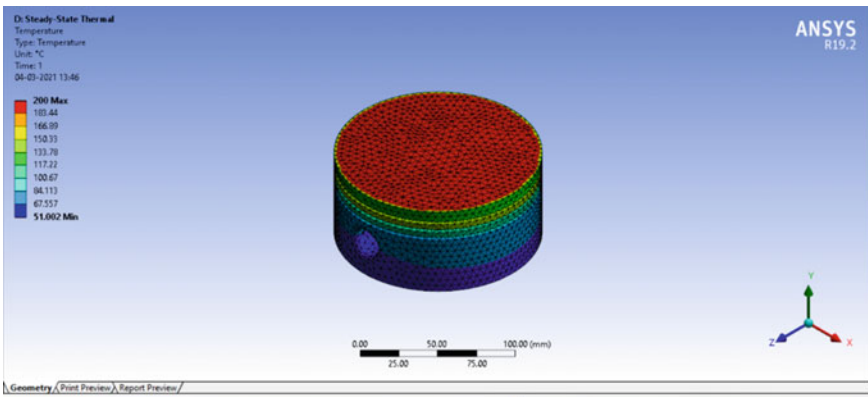
Fig. 7 Temperature distribution of Al-GHS 1300

total deformation is in A2618 alloy (0.66871 mm) and minimum in Ti-6Al-4 V alloy (0.42287 mm).

5 Conclusion

The titanium alloy (Ti-6Al-4 V) is commonly used in supercar piston, and it is assumed that it can also be used in motorcycles if used in such high-performance cars.
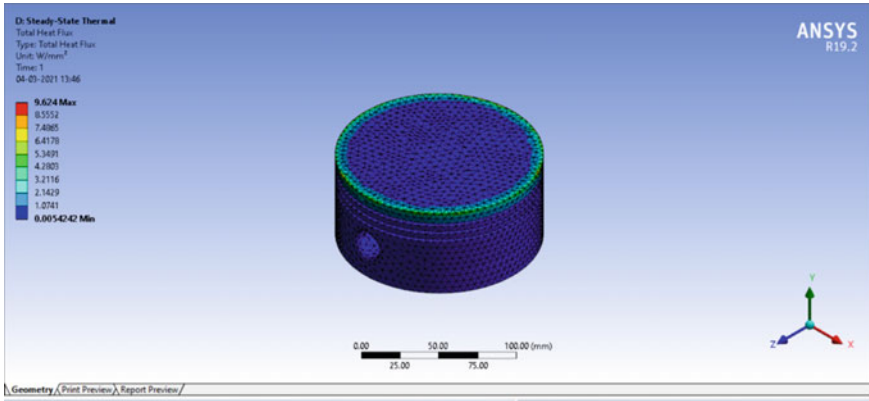
Fig. 8   Total heat flux of Al-GHS 1300

Table 4   Results of steady-state thermal analysis

Parameters	A2618	Al-GHS 1300	Ti-6Al-4 V
Heat flux (W/mm^2)	11.79	9.624	0.58542

Table 5   Results of combined thermo-mechanical analysis

Parameters	A2618	Al-GHS 1300	Ti-6Al-4 V
Equivalent stress (MPa)	534.13	553.9	441.13
Total deformation (mm)	0.66871	0.52231	0.42287
Equivalent elastic strain (mm/mm)	0.0079986	0.0060526	0.0038931
Heat flux (W/mm^2)	11.789	9.624	0.58542

The material properties of titanium alloy were also the same, and the above analysis shows clearly that this is an alternative. Based on our results, the titanium alloy was concluded to be Bajaj Pulsar 220 cc's best piston material of all three. For the following reasons:

- Total deformation of Ti-6Al-4 V alloy is least.
- Stress generation of Ti-6Al-4 V alloy is the least.

This result is due to the Bajaj Pulsar 220 cc's piston design. In order to make titanium alloy a practicable option, it is not necessarily important to make any changes to the piston design which may lead to a change to the overall design of the engine beyond the scope of this work. Still, a lot can be accomplished. The same is also possible with other motorcycles/vehicles. These materials can also be analysed for other than thermal and structural. These materials can also be compared by cost such as production costs and machining costs.

References

1. Feng SS (2014) An experimental and numerical study of finned metal foam heat sinks under impinging air jet cooling. Int J Heat Mass Transf 77:1063–1074
2. Calbureanu MX (2013) The finite element analysis of the thermal stress distribution of a piston head. Int J Mech 7(4):467–474
3. Srikanth RS (2013) Thermal Analysis and optimization of I.C. engine piston using finite element method. Int J Innov Res Sci Eng Technol 2(12):7834–7843
4. Bhagat AR (2012) Thermal Analysis and Optimization of I.C. Engine Piston Using Finite Element Method. Int J Mod Eng Res 2(4):2919–2921
5. Belov NA, Eskin DG, Avxentieva NN (2005) Constituent phase diagrams of the Al–Cu–Fe–Mg–Ni–Si system and their application to the analysis of aluminium piston alloys. Acta Mater 53(17):4709–4722
6. Arsha AG, Jayakumar E, Rajan TPD, Antony V, Pai BC (2015) Design and fabrication of functionally graded in-situ aluminium composites for automotive pistons. Mater Des 88:1201–1209
7. Yang Y, Li Y, Wu W, Zhao D, Liu X (2011) Effect of existing form of alloying elements on the micro hardness of Al–Si–Cu– Ni–Mg piston alloy. Mater Sci Eng 528(18):5723–5728
8. Medrano FJT, Gruzleski JE, Samuel FH, Valtierra S, Doty HW (2008) Effect of Mg and Sr-modification on the mechanical properties of 319-type aluminium cast alloys subjected to artificial aging. Mater Sci Eng 480(1–2):356–364
9. Raghukiran N, Kumar R (2015) Effect of scandium addition on the microstructure, mechanical and wear properties of the spray formed hypereutectic aluminium–silicon alloys. Mater Sci Eng 641:138–147
10. Hernandez FCR, Sokolowski JH (2006) Thermal analysis and microscopically characterization of Al–Si hypereutectic alloys. J Alloy Compd 419(1–2):180–190
11. Singh AP, Agarwal AK (2012) Combustion characteristics of diesel HCCI engine: an experimental investigation using external mixture formation technique. Appl Energy 99:116–125
12. Harshavardhan B, Mallikarjuna JM (2015) Effect of piston shape on in-cylinder flows and air fuel interaction in a direct injection spark ignition engine-A CFD analysis. Energy 81:361–372
13. Wang YX, Gao H (2010) Fatigue strength and analysis of diesel engine piston on finite element analysis. Adv Mater Res 156:1086–1089
14. Nie Y (2010) Finite element modeling and analysis for key parts of a new type internal combustion engine. Int Conf Comput Appl Syst Model 8:81–184
15. Silva FS (2006) Fatigue on engine pistons—a compendium of case studies. Eng Fail Anal 13:480–492
16. Huang ZL, Wang K, Zhang ZM, Li B, Xue HS, Yang DZ (2015) Effects of Mg content on primary Mg2Si phase in hypereutectic Al−Si alloys. Trans Nonferrous Met Soc China 25:3197–3203

Application of 7-Step Problem-Solving Methodology for Defect Elimination: A Case Study in an Automotive Industry

A. K. Bewoor, Mitali U. Kharul, Saloni G. Gosavi, and Tanvi J. Kuray

1 Introduction

Today, the automotive sector plays a significant role in determining the competitiveness of nations in the world. With advancements in technologies and a shift toward computer-integrated systems, auto-manufacturing companies face volatile economic conditions, including global competition, the ever-increasing customer demand for high-quality products. To remain competitive and relevant, companies are continuously looking for ways to reduce product failure and cost with improved product quality.

Quality is one of the most critical factors that determine a company's success. It adds to the product's value and helps the company present a competitive product in the market. Production of defect-free and quality products is crucial since defective products would otherwise lead to customer dissatisfaction, decreased sales, low financial profits, and greater cost to the company [1]. Defects arise when the product or service fails to meet the requirements. To minimize the defects and achieve improved product quality, increased efficiency, and effectiveness of the production process, manufacturers have started implementing different problem-solving methodologies (PSMs). These different problem-solving methods and approaches help the companies understand the issues at hand and provide procedural structure to reach solutions for tackling the problem in a systematic step-by-step manner, and help attain improved results in a short period. A few of many such techniques that companies use for such decision-making processes reported in published literature are 7-Step Problem-Solving Methodology (7SPSM), Design For Six Sigma (DFSS), Define-Measure-Analyze-Improve-Control (DMAIC) Model, Plan-Do-Check-At (PDCA) Cycle, and the Eight Disciplines (8Ds) method. Each step of these techniques has

A. K. Bewoor · M. U. Kharul (✉) · S. G. Gosavi · T. J. Kuray
Mechanical Engineering Department, Cummins College of Engineering for Women, Pune, India

A. K. Bewoor
e-mail: anand.bewoor@cumminscollege.in

an integrated approach. Considering this, different inter-disciplinary teams come together to find a solution that will be profitable to the company. A review of various aspects of such selected PSMs is presented in the next section.

2 Literature Review

The effectiveness of several PSMs was reported by earlier researchers. Several companies such as Toyota Production System, Ford Motor Company, General Motors, Delphi Automotive, Caterpillar, Honeywell, TC India Private Limited, and more are adopting lean manufacturing and Six Sigma tools for continuous improvement [2–4]. Major OEMs such as Toyota, Ford, Fiat Chrysler Automobiles, and other manufacturing firms have been implementing the PDCA cycle for problem-solving and reducing defects [5–7]. There is a vast amount of literature supporting the use of the 8D developed by Ford Motors [1, 5, 8] and the DMAIC model [9] for problem-solving in various industries. Fiat Chrysler Automobile has been using the 7SPSM across all its plants as a problem-solving approach that has been an integral part of their World Class Manufacturing model [5].

The comparison of different PSMs concerning various aspects is reviewed in Tables 1, 2, and 3. An intensive training and research period was engaged to get familiarized with the failure, the system in which the failure occurred, and the surrounding systems and their interactions. Table 1 discusses case studies based on different methodologies. Table 2 compares selected PSMs by mapping of steps followed during their implementations. Table 3 discusses the scopes of selected PSMs with respect to different factors.

3 Case Study

The study reported in this paper is regarding a multinational manufacturing company in the automotive field that designs, manufactures, distributes, and services engines and related components. The company has a broad service network spread over the country, and the employees have domain expertise to provide high-quality repairs, planned maintenance, and upgraded solutions.

3.1 Need for Identification

The company is involved in manufacturing of different components and technologies related to engine systems, gas flow system being one of them. The flanges of the gas flow system are sealed tight with clamp assemblies [16], which allow the flow of gases at high temperature and pressure during the operation. Internal and external

Table 1 Literature review

S. No	PSMs	Remarks
1	7-Step Problem-Solving Methodology [5]	• Mapping of steps used in different methodologies • Methodology validated in Tofas, an automobile manufacturer • After implementation, the company experienced: - Average increase in quality - Decrease of lead time - Increase in overall effectiveness in production • Method showed promising results for both current models and new model launches
2	DMAIC [9]	• DMAIC is applicable to well-structured and semi-structured problems but not to ill-structured problems • Six Sigma is a versatile and structured method • Characteristics, limitations, and directions where the DMAIC approach could be improved
3	PDCA [10]	• Use of PDCA in supplier selection • Its importance in the current business environment • Implementation of PDCA in the framework of supplier selection and implementation model
4	Six Sigma [3]	• Causes of failure of Six Sigma • Success of Six Sigma depends on the correct sequence of Six Sigma elements • Case study for an effective guide of implementation of Six Sigma
5	8D [11]	• An excellent tool for solving the problem as well as for preventing defects from reoccurring • Total rejection percentage reduced to 6.57% from 37.95% after the implementation of 8D

customers are reporting complaints regarding noise being produced from the exhaust system. Considering the fact that on-field failure of the product might lead to unsafe accidents, it became essential to curb the damage and produce an effective solution. Moreover, the noise produced was due to the escape of exhaust gases at high working temperature and pressure. Thus, it was necessary to ensure that safety and air purity are not compromised and the performance of the system is not affected. Hence, it was decided to adopt problem-solving techniques that would help in determining the root cause of the failure systematically.

Table 2 Mapping of steps in different methodologies [12–14]

7SPSM	6 Step method	8D	DMAIC	PDCA
Step 1: identify the problem	Verify fault	D1: form the team	Define: define project goal and deliverables	Plan
Step 2: identifying and prioritizing the possible causes	Collect information	D2: define the problem	Measure: measure the process to determine current performance; quantify the problem	
Step 3: take short-term action		D3: develop an interim containment action		
Step 4: determine failure causes	Evaluate evidence	D4: define and verify root causes	Analyze: analyze and determine the root cause(s) of the defects	
Step 5: select and verify the solution	Carry out the tests in a logical sequence	D5: choose and verify permanent corrective actions	Improve: improve process performance by addressing and eliminating the root causes	Do
Step 6: implement permanent solution	Rectify problem	D6: implement and validate corrective actions		
Step 7: monitor and prevent reoccurrences	Check all systems	D7: prevent recurrences	Control: control the improved process and future process performance	Check and Act
		D8: recognize team and individual contributions		

Table 3 Comparison of scope [15]

Factors for comparison	7-Step	8D	DMAIC	PDCA
Problem solving process	Yes	Yes	No	Yes
Provides containment action	Yes	Yes	Yes	Yes
To be followed sequentially	No	Yes	Yes	Yes
Provides structure	Yes	Yes	Yes	Yes
Data-driven	Yes	Yes	Yes	Yes
Standard toolbox available	No	No	Yes	No

Corrective actions taken by the company involved forming a cross-functional team that conducts discussions regularly, working toward a common goal. The company follows a data-driven approach while implementing problem-solving methodologies to curb the issues being faced. The company has implemented company-wide quality management systems like ISO 9001 and TS16949. The company has been practicing performance improvement and problem-solving techniques like 5S and Kaizen. It has also been working with data-driven approaches like Six Sigma and 7SPSM. The company's experiences in tackling problems in the past had revealed that the 7SPSM had produced the best results in a short period.

3.2 Methodology Adopted

The 7-step problem-solving technique provides a structured approach and helps to deliver the best possible outcomes and solutions to problems. The 7-Step Problem-Solving Methodology offers an effective approach for problems where the solution is not apparent. The 7-step method is a reactive problem-solving methodology and is applied when a correction is to be made to a plan due to recurrences of any of the five evils. The reactive evils can be any one of defects, delays, mistakes, wastes, and accidents. These reactive problems require an orientation toward the weaknesses that undermine the successful operation of standardized processes.

3.3 The 7-Steps Problem-Solving Methodology

Any problem that we see is far deeper rooted than what it seems. It is crucial that we collect all the background information on the issue, get acquainted with the root causes, and then start working toward it. As proposed in Table 4, the sequential implementation of the 7SPSM is used in association with various system engineering tools and techniques for the same.

Table 4 Tools and techniques used in 7SPSM [13]

Steps	Description	Tools used
Step 1	Identify the problem	5W1H
Step 2	Identify and prioritize possible causes	Pareto chart, cause-effect diagram, fault tree analysis, boundary diagram, Parameter diagram
Step 3	Take short-term action	
Step 4	Determine failure causes	
Step 5	Select and verify the solution	Pugh matrix, DFMEA
Step 6	Implement permanent solution	
Step 7	Monitor and prevent recurrences	Check-sheet, audit

3.3.1 Step 1. Identify the Problem

The company's foremost task is the detailed identification of the problem or failure that occurs. The problem is addressed with the 5W1H questioning method (Who, What, When Where, Why, and How) [5, 17], which helps in better understanding of the loss of function and the failure mode. Comparison is made between the current working of the system and the ideal working, and it is checked by how much the variation from the norm is tolerable. As mentioned previously, customers complained of noise from the exhaust system. Upon inspection, the main problem was a failure in the clamps being used, which led to leakage of exhaust gases, and hence, the noise was being produced. Data related to clamp failure location, intake and exhaust manifold configuration, stage at which failure was reported, and several other factors were collected. These activities helped in documenting a concise and quantifiable problem statement and identify the severity of the failure.

3.3.2 Step 2: Identify and Prioritize Possible Causes

The task here is to understand the mechanism of failure with respect to the three realities (Real Parts, Real Place, and Real Situation). The cross-functional team systematically derives all possible causes of the problem. It investigates why the problem went undetected during the design and analysis phase to understand whether the problem has occurred after eventual repairs [5]. Step 2 is then concluded by formulating a prioritized list of possible causes of the product problem/failure mode based on the severity of damages caused by them. This involves using Pareto Charts (Fig. 1) with the data collected in the previous step to indicate the frequency of defects and their cumulative impact. Failure causes like design failures, quality defects, excessive stresses, and alignment issues are identified, and a cause-effect diagram (Fig. 2) is developed with these causes to get an idea of the inter-relationship between the causes. Using physics and logical approach, fault tree analysis is prepared to identify all the system failures and their hierarchy. Based on their severity, damage caused by them, and their effect on the system, possible assignable causes are obtained.

3.3.3 Step 3: Take a Short-Term Action

Since the cross-functional team is familiar with the product/process, possible short-term corrective actions must be undertaken to control the problem and prevent its expansion. These actions should be taken to protect the customer from the problem until permanent collective measures are implemented. In addition, this corrective action should make sure that no further problems arise on its implementation. This step is proposed to stop the failure outcome from proving to be irrecoverable before the problem can be solved. Replacement of the failed clamps with new clamps when the vehicles were brought to the service touchpoints of the company was thought to
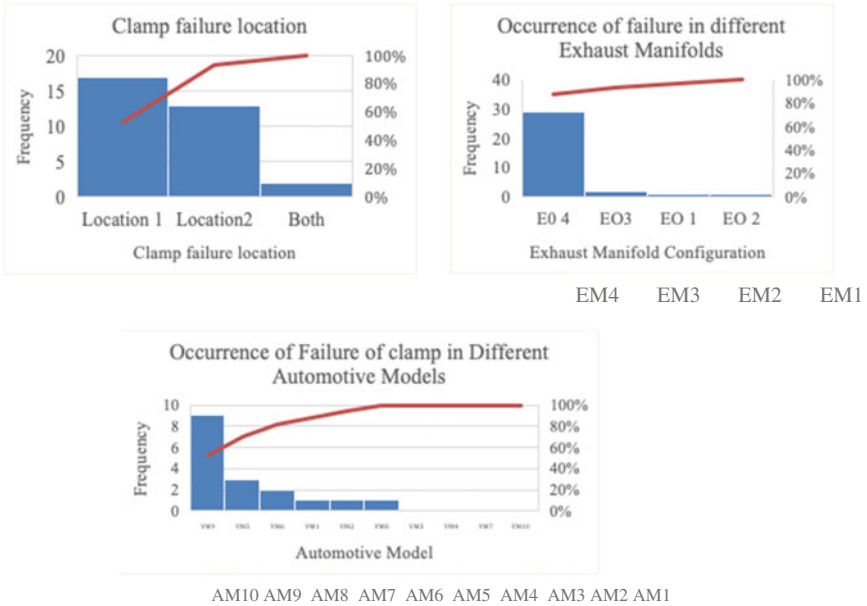
Fig. 1 Pareto charts
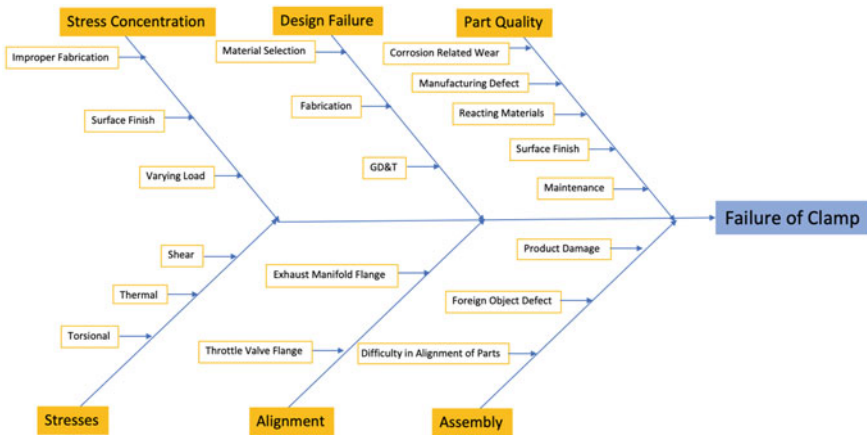
Fig. 2 Cause-Effect diagram

be the best possible interim corrective action. For this, the service centers had to be stocked with spare clamps for quick replacements.

NOISE 1: Piece to Piece Variation	NOISE 2: Change Over Time	NOISE 3: Customer Usage	NOISE 4: External Environment	NOISE 5: System Interaction
Manufacturing & Assembly process	Weld fatigue	Fuel Quality	Ambient temperature	Heat Shield
Welding process	Wear in clamp material	Speed	Road vibrations	Exhaust
Clamping force	Chemical aging	Improper maintanence and upkeep	Road debris	Oil contamination
Orientation	Corrosion		Air	Backpressure
Surface finish - clamp	Loosening of Parts		Water	Powertrain Vibrations
			Salt	

INPUT SIGNAL	SYSTEM	IDEAL FUNCTION
Mass		Leakproof transfer of gases
Flow gas	Clamp Assembly	Efficient clamping
Energy		
Thermal		
Pressure		
Mechanical		
Chemical		

CONTROL FACTORS	ERROR STATES
Mechanical	Abnormal Noise levels
Clamp material	Gas leakage
Gas Pressure	Cracking of clamp
Gas temperature	
Alignment of flanges	
Weld Strength	

Fig. 3 Parameter diagram

3.3.4 Step 4: Determine Failure Causes

This step involves systematically conducting tests to demonstrate a correlation between the possible causes and the observed failure modes using the data obtained in Step 2. This step was initiated using the boundary diagram, which helped in studying the different interactions like mass flow, fluid flow, and reaction forces between the system and its adjacent subsystems. Fault tree analysis helped to identify the causes in detail by progressing from left to right of the tree. This also helped in getting a detailed analysis of all the possible causes. The parameter diagram (Fig. 3) helped in studying the different noise sources like the piece to piece variation, external environment, change over time, customer usage, system interactions as well as the input signals, ideal functions, the error states, and the controlling factors of the system. It was observed that most of the failures were caused by excessive stresses developed on the clamp and due to flange misalignment. The different causes that were contributing to these two failures were further studied in detail. Simulation study validated that flange misalignments led to excessive stress generation on clamp.

3.3.5 Step 5: Select and Verify the Solutions

After thorough analysis, the team should be able to objectively demonstrate the effect of each of the causes identified previously [5]. This helps to understand all the aspects of the problem and helps in initiating proper corrective actions. The current system is modeled in SOLIDWORKS and simulated in Ansys. Since the main contributing factors for the excessive stresses being developed on the clamp were design and material aspects of the clamp, they were studied in greater detail. Different design alternatives with modifications in the thickness and filets were modeled and analyzed, and their results for different engine temperatures were plotted. Desirable results were also obtained by changing the material grade. To solve the issue of misalignment of flanges, different flange designs were tested. Determination of which

potential solutions are more effective or 'better' than others is done by using the Pugh Matrix, a scoring matrix used for concept selection. All the design alternatives are rated for different parameters like size, weight, cost, manufacturability, ease of assembly, function, life, strength, and safety. The alternative that fares the best in all the parameters is selected for implementation. At the end of this step, a combination of the clamp with optimum dimensions and good strength along with the flange type that prevents misalignment was selected.

3.3.6   Step 6: Implement Permanent Solution

The potential solutions narrowed down with the help of Pugh Matrix were implemented in the initial system. Before the implementation, it is imperative that we thoroughly check that the problem has been understood completely, all the constraints and factors affecting the failures were taken into consideration, and all the possible alternatives were studied. This was facilitated by implementing Design Failure Mode and Effect Analysis (DFMEA). All the possible modes of failure of the existing system are listed by prioritizing them out along with their effects, severity, and frequency of occurrence. With these data, the Risk Priority Number (RPN) is calculated for each mode. Further, the same exercise is carried out for the system with our implemented corrective solution, and RPN is calculated. By comparing these two RPNs, we can effectively understand if our solution is successful in preventing the failure.

3.3.7   Step 7: Monitor and Prevent Recurrence

In this step, it is ensured that the underlying systemic or process issues which led to the problem have been addressed. The implemented solution is continuously monitored to check whether it is preventing failures with the help of check-sheets. The check-sheets consist of several parameters such as flow rate of gases, vibrations, and noise which are used to validate the solutions. The system is also checked for any recurrences of failures. At the end of this step, the long-term effectiveness of the permanent solution is quantified, and verification of the effectiveness of the implemented solution is confirmed.

4   Conclusions

Several automotive companies have started adopting standard approaches for failure diagnosis in recent years. This paper discusses a case study of the successful implementation of 7SPSM in an automotive company for solving a problem in the exhaust gas flow system. The tools used in the different phases of the seven steps contribute majorly toward an effective and complete understanding of the problem considering all the underlying factors. The diagnostic process was carried out efficiently once the

main causes were identified, such as the excessive axial pressure on the clamp and low yield strength of the material being used. The solution most effective, feasible, and most compatible with the system was chosen through the Pugh Matrix. The 7-step diagnosis provides a standardized, methodical, and disciplined approach to understand the root causes, identify their effects, and implement solutions that are effective and help increase the system's efficiency. The case study shows that 7SPSM could provide an effective method for solving problems where the solution is not obvious. Considering the damage caused by the failure, it is imperative that we reach the root causes and solve them as soon as possible.

References

1. Realyvásquez-Vargas A, Arredondo-Soto KC, García-Alcaraz JL, Macías EJ (2020) Improving a manufacturing process using the 8Ds method. A case study in a manufacturing company. Appl Sci 10(7):2433
2. Bayou ME, Korvin AD (2008) Measuring the leanness of manufacturing systems-a case study of ford motor company and general motors. J Eng Tech Manage 25(4):287–304
3. Chakravorty SS (2009) Six Sigma programs: an implementation model. Int J Prod Econ 119(1):1–16
4. Bewoor AK, Pawar MS (2010) Mapping macro/micro level critical links for integrating Six Sigma DMAIC steps as a part of company's existing QMS: an Indian SME case study. Inte J Six Sigma Competitive Adv 6(1/2):105–131
5. Altinisik A, Hugul O (2020) The seven-step failure diagnosis in automotive industry. Eng Fail Anal 116:104702.https://doi.org/10.1016/j.engfailanal.2020.104702
6. Darmawan H, Hasibuan S, Purba HH (2018) Application of Kaizen concept with 8 steps PDCA to reduce in line defect at pasting process: a case study in automotive battery. Int J Adv Sci Res Eng 4(8). https://doi.org/10.31695/IJASRE.2018.32800
7. Realyvásquez-Vargas A, Arredondo-Soto KC, Carrillo-Gutiérrez T, Ravelo G (2018) Applying the plan-do-check-act (PDCA) Cycle to reduce the defects in the manufacturing industry. A case study. Appl Sci 8(11):2181
8. Disciplines of Problem Solving. https://quality-one.com/8d/. Referred on 02 May 2021
9. Mast JD, Lokkerbol J (2012) An analysis of the Six Sigma DMAIC method from the perspective of problem solving. Int J Prod Econ 139(2):604–614
10. Chan FTS, Chan HK (2004) Development of the supplier selection model-a case study in the advanced technology industry. Proc Inst Mech Eng Part B J Eng Manuf 218(2) https://doi.org/10.1177/095440540421801213
11. Atigre PS, Shah AP, Patil VR (2017) Application of 8D Methodology for Minimizing the Defects in Manufacturing Process: A Case Study. Int J Eng Res Technol 6(9):123–126
12. Denton T (2006) Advanced automotive fault diagnosis, 2nd edn. Elsevier Ltd., Linacre House, Jordan Hill, Oxford OX2 8DP, UK
13. Bewoor A, Sapkal S, Dhaygude P (2021) Mapping of Lean Six Sigma with 8D problem solving methodology to improve productivity and safety: a case study. In: Paper presented at the 4th international conference on innovations in mechanical engineering (ICME-2021), Guru Nanak Institutes Hyderabad, 27 Feb 2021
14. Kulkarni VA, Bewoor AK (2009) Quality Control, 1st edn. Wiley India Pvt. Ltd., New Delhi, India
15. Which project structure should we choose. https://houseofsixsigma.com/which-project-structure-should-we-choose/. Referred on 28 Apr 2021
16. Everything you need to know about V-band clamps. https://www.enginelabs.com/engine-tech/exhaust/v-band-clamps-from-race-parts-solutions/. Referred on 18 Oct 2020

17. Effective problem solving. https://structx.com/Article002-7_Step_Problem_Solving.html. Referred on 10 Apr 2021

Ergonomic Risk Assessment of Rubber Tappers Using Rapid Entire Body Assessment (REBA)

Abi Varghese, Vinay V. Panicker, Jeffry Abraham, Jobin Gimmi, Judson Tom, and Kevin Desini

1 Introduction

Natural rubber is one of the most essential polymers for human society [13]. As a global commodity, rubber finds extensive applications in major industries, especially in the automotive, aerospace and medical sectors [1]. Natural rubber is harvested by a technique referred to as rubber tapping in which thin slices of the rubber tree's outer bark are scraped off to allow the milky, white liquid to ooze out of the inner layer [12]. A channel is incised along an oblique curve inclined at an angle of 30–35° to the horizontal in order to cut through the highest possible number of latex vessels. A sharpened V-shaped knife (Michie-Golledge) is lodged into the tree's bark to a minor depth and then pulled out with jerky, to-and-fro movements. The cut progresses downward from the left to the right direction [8]. The latex exudes from the bark, flows through the cut-out channel and then drips into a collecting cup placed below it [2].

Tapping is an ergonomically hazardous occupation since it involves awkward body postures with simultaneous physical exertion [15]. In addition, fast-paced

A. Varghese (✉) · V. V. Panicker
Department of Mechanical Engineering, National Institute of Technology Calicut, Calicut, Kerala, India

V. V. Panicker
e-mail: vinay@nitc.ac.in

A. Varghese · J. Abraham · J. Gimmi · J. Tom · K. Desini
Department of Mechanical Engineering, Amal Jyothi College of Engineering, Koovappally, Kanjirappally, Kottayam, Kerala, India
e-mail: jeffryabraham2021@me.ajce.in

J. Tom
e-mail: judsontom2021@me.ajce.in

K. Desini
e-mail: kevindesini2021@me.ajce.in

cyclic work, static and asymmetric postures are very common in rubber tapping, exposing tappers to many MSD risk factors [10, 16]. The hand perhaps faces a greater ergonomic risk since its posture and movement while tapping involves high degrees of flexion and/or extension of the wrists, repeated deviation from the midline, twisting, strenuous exertion and mechanical stress [9, 11]. With the ageing of the tree, tapping will have to be performed along different circumferential sections and at varying heights to allow previously tapped sections to recover. One section is usually tapped for a period of 5 years [13]. As a consequence, tapping will eventually have to be performed at levels nearer to the ground, for which the rubber tapper's trunk will have to be in a degree of forward bending with flexion of arms and wrists. Similarly, tapping at heights near or above the shoulder level also requires flexion and abduction of upper arms along with the usual risky postures in the wrists [14]. Since rubber tappers usually tap around 300 trees per day, these ergonomically awkward postures are repeated continually for hours [2]. These ergonomic problems can contribute to musculoskeletal disorders (MSDs) in rubber tappers.

Musculoskeletal disorders (MSDs), as the name suggests, are disorders resulting in pain, injury or discomfort across the human musculoskeletal system, specifically affecting the ligaments, joints, tendons, nerves, muscles and other supporting structures. A survey was conducted by Meksawi et al. among rubber tappers in Southern Thailand to gauge the prevalence of ergonomic risk levels and MSDs, among them [7]. Work activities of 427 rubber tappers were videotaped to analyse postures with the Rapid Upper Limb Assessment method (RULA). The study revealed that 52.9% of rubber tappers surveyed suffered from lower back pain. The RULA grand score averaged at 5.25 indicating the need for swift medical evaluation and alterations in work habits.

A case-control study was conducted by Pramchoo et al., also in Thailand, to point out physical determinants associated with the rubber tapping operation that can lead to Carpal tunnel syndrome (CTS) [8]. Here also, Rapid Upper Limb Assessment (RULA) [6] was performed to examine postures of the wrists and hands. It was confirmed that in addition to demographic factors, latex collection and tapping trees at or below knee level are contributing causes of CTS in rubber tappers. The study also found that awkward wrist postures were correlated with the level of tapping—tapping at a height above the chest level required flexion and/or extension of the right wrists, radial and/or ulnar flexion and twisting of the left wrists more frequently among right-handed tappers.

In the light of the above findings, the same team proposed an ergonomic design for a tapping knife to enhance posture of the wrist and avert or lessen symptoms of CTS in rubber tappers [9]. They conducted a study to assess variations in the severity of symptoms of Carpal tunnel syndrome after adopting the novel tool. It was found that the ergonomic intervention was effective since the improved design of the knife led to a decrease in severity scores for all symptoms.

The prevalence of MSDs among rubber tappers was also studied by Kayla Stankevitz et al. in the island of Sri Lanka [10]. Three hundred participants were surveyed to measure MSDs and determine the probable causative factors. Furthermore, the Quick Exposure Check instrument (QEC) was implemented in a group of 90 tappers

to ascertain their exposure to ergonomic risks [3]. According to the results, 66% of tappers experienced at least one MSD over a year prior to data collection. The most commonly affected regions included the back (43%), shoulders (28.3%) and neck (19.3%). Furthermore, the QEC analysis results showing high or extreme levels of risk exposure in the shoulders (94.2%), back (96.7%) and neck (83.3%) are in line with the aforementioned findings.

Another study by Doi et al. to investigate the prevalence of MSDs among Malaysian workers involved in rubber tapping also showed similar trends [4]. Here, Nordic Musculoskeletal Questionnaire (NMQ) was used for the investigation, and results asserted that MSDs were most prevalent in the lower back (74.4%) among rubber tappers followed by shoulders (53.5%), neck (48.8%) and wrists/hands (48.8%).

Therefore, it is evident that rubber tappers are either already suffering from MSDs or at risk of experiencing them in the near future. This can be attributed to the ergonomically awkward postures demanded by the rubber tapping occupation—repeated lateral bending, twisting, flexion and/or extension of arms, wrists, neck and trunk. Another observation from the literature review is that most studies have used RULA as the assessment tool to evaluate working postures and the ergonomic risks they pose to rubber tappers. This study aimed to implement Rapid Entire Body Assessment (REBA) [5] to examine the whole body and estimate the prevalence of ergonomic risk levels among rubber tappers in Kerala, India, and their vulnerability to MSDs in different body segments.

2 Materials and Methods

2.1 Study Population

This study was carried out mainly among rubber farmers in the northern district of Kozhikode in Kerala, India. Twenty-five rubber tappers participated after they were informed of the purpose of the study and the data collection methods involved. Data collection was initiated only after receiving oral consents. The inclusion criteria for the selection of rubber tappers were as follows: the worker should (a) be a regular tapper, (b) have a minimum experience of one year in rubber tapping and (c) be 18 years old or above.

2.2 Data Collection

Interviews were conducted in-person based on a Standard Nordic Questionnaire to collect information pertaining to the work activity of rubber farmers and their demographic details. During the interview, upon request, participants rated the level

of pain and/or discomfort they experienced in different body parts while performing the tapping operation. The rubber tapping work of each worker was observed directly and also recorded on video. Video-based posture analysis was conducted with the ergonomic assessment tool, REBA.

2.3 Rapid Entire Body Assessment (REBA)

The REBA [5] is a posture analysis system that evaluates the risk of musculoskeletal injuries in the entire body and is sensitive to a variety of tasks. In accordance with the aim of developing a field posture analysis tool requiring minimal equipment, REBA is a pen and paper method consisting of a single page worksheet to evaluate body postures by integrating static and dynamic muscle loading factors and a coupling factor (the factor that accounts for the manner of interaction with the load).

The body is segmented into two groups: Group A and Group B. Group A comprises the neck, trunk and legs, whereas the wrists, upper arms and lower arms belong to Group B. Each of these body parts is scored according to the degree of flexion and/or extension maintained by them. Postures involving higher angles will usually be given higher scores, which can be further increased if the body part involved is subjected to twisting, side flexion, rotation, etc. The upper arm score can be reduced if its weight is supported or the posture is gravity assisted. Scores for each body part will range from 1 to anywhere between 2 and 6. A higher score implies a greater level of discomfort and risk of MSDs.

Sixty posture combinations are possible in Group A, whereas in Group B, only 36 are possible. The combinations can be brought down to nine scores in each group. A 'force/load' score is added to the score assigned to the Group A posture combination while a 'coupling' score is added to the Group B posture score, resulting in Scores A and B, respectively. Table C combines the A and B scores to produce score C.

In the final step, the REBA score is acquired after adding an activity score to score C. The REBA score sheet is shown in Fig. 1. The levels of MSD risk and the consequent conclusions corresponding to the final REBA scores are tabulated in Table 1.
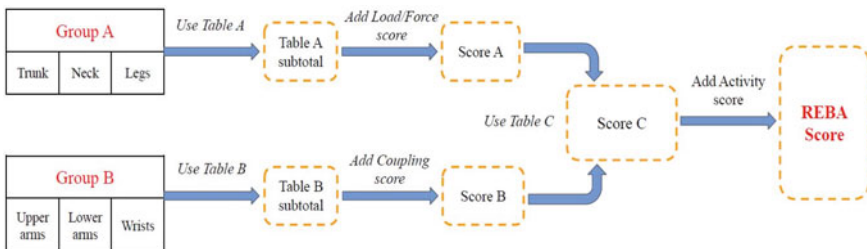
Fig. 1 REBA score sheet [5]

Table 1 REBA score and action requirement [5]

REBA score	Risk level	Action (including further assessment)
1	Negligible	Not necessary
2–3	Low	May be necessary
4–7	Medium	Necessary
8–10	High	Necessary soon
11+	Very high	Necessary now

3   Result and Discussion

It is observed in Table A that about 60% of the participants have a score equal to or greater than 4, showing that the postures of their group A body segments are associated with a significant level of risk of MSDs and will require changes. It is because these body parts have to undergo significant flexion, extension and deviation from non-neutral positions, especially when different tapping heights are involved. Score A is equal to Table A score in all subjects since the neck, trunk and legs usually do not experience any load during the tapping procedure. 36% of the subjects have a Score B greater than 4, indicating that the postures of Group B body segments considered along with the coupling factor do pose some amount of ergonomic risk and will require further investigation. It can be seen that Score B is one unit higher than Table B subtotal in almost all cases. This is because, while tapping, one hand holds the handle while the other supports the blade. The blade is supported usually by the dominant hand with only a few fingers. Hence, the handhold is not ideal, and a coupling score of 1 is added to Table B subtotal score.

An enormous proportion (84%) of participants have REBA scores in the 4–7 bracket, who are at a medium risk level of MSDs and in need of necessary changes after further investigation. Furthermore, the remaining rubber tappers are at a high level of risk of MSDs, having REBA scores in the 8–10 range. For them, remedial actions are necessary and will have to be implemented soon to avoid serious physical injury. Figures 2 and 3 illustrate how angles of flexion and/or extension in some body parts are measured for posture analysis.

The results of the posture analysis, including the scores obtained at significant points along the REBA scoring sheet, are presented in Table 2.

It can be easily understood that the level of tapping has a strong influence on both Scores A and B. It is observed that when tapping is done below the shoulder level, the neck will have to maintain a degree of flexion with simultaneous twisting and/or side flexion to get a clear view of the cut. This increases the postural score of the neck.

The circumference of the tree's trunk is segmented into two or maybe three sections, and tappers may not be able to perform the cut along one such circumferential section while standing in a fixed position. Although the tree bark is sheared off with jerky, to-and-fro motions of the blade, workers try to move laterally along
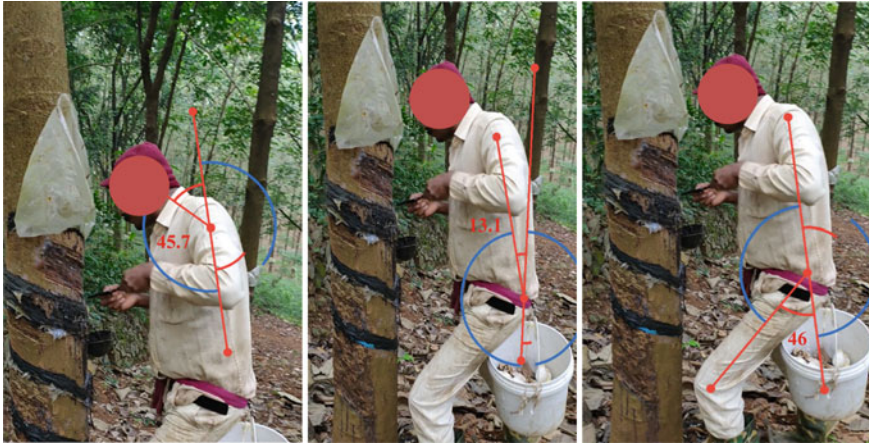
Fig. 2 Posture score for table A, **a** neck, **b**, trunk, **c** leg
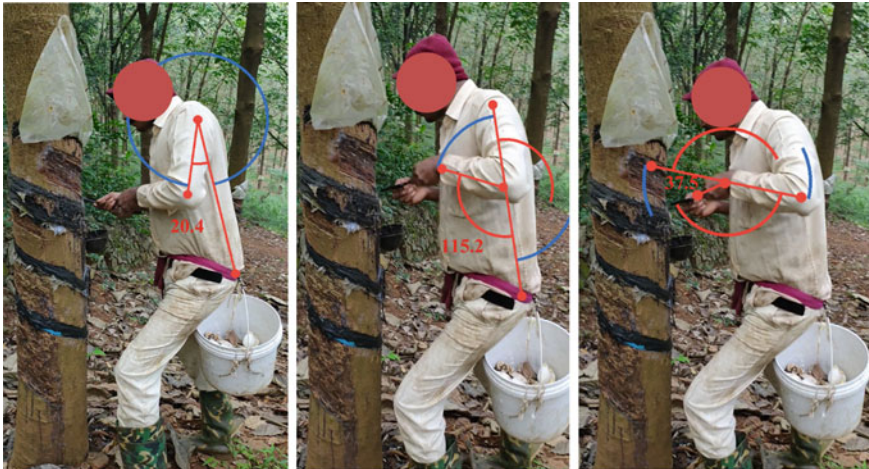
Fig. 3 Posture score for table B **a** upper arm, **b** lower arm, **c** wrist (deviation)

the channel to perform a single, continuous cut. It has been observed that many of them bend their left knee to cross their left leg over to the right side as one step in the rightward lateral movement. This results in flexion of the knee(s) and tappers sometimes transition through an unstable posture in which their legs are crossed. This bending in knees will be greater at tapping heights near or below the waist level, leading to an increase in the score associated with the legs.

In addition, rubber tappers have to flex their trunk to a great extent to tap trees at such heights. The slope of the land can also contribute to an increase in the score of

Table 2 Posture analysis results

Subject No.	Table A subtotal	Score A	Table B subtotal	Score B	Score C	REBA score
1	4	4	3	4	4	5
2	5	5	2	3	4	5
3	6	6	3	4	4	5
4	2	2	3	4	3	4
5	4	4	3	4	4	5
6	3	3	2	3	3	4
7	3	3	2	3	3	4
8	7	7	4	5	9	10
9	6	6	4	5	8	9
10	5	5	5	6	7	8
11	4	4	2	3	4	5
12	4	4	6	6	6	7
13	4	4	4	4	4	5
14	4	4	2	3	4	5
15	3	3	7	7	6	7
16	5	5	4	5	6	7
17	1	1	9	10	7	8
18	2	2	5	6	4	5
19	2	2	5	6	4	5
20	4	4	3	4	4	5
21	3	3	2	3	3	4
22	5	5	3	4	5	6
23	3	3	3	4	3	4
24	4	4	3	4	4	5
25	3	3	2	3	3	4

the legs. While tapping in uneven terrain or on a hillside, one leg may have to be in a raised position with a flexed knee. All these factors greatly influence score A.

Similarly, the flexion required in the upper arm also depends on the tapping height. Upper arms have to be greatly flexed to tap at heights at or above shoulder level and even below waist level, thereby increasing score B. In a nutshell, the REBA score is correlated to the tapping height.

To the best of our knowledge, no previous studies have used REBA to conduct the posture analysis of rubber tappers, making the current study the first one to do so. However, there are some limitations in this study that need to be considered. The REBA tool does not assess the force exerted by the arms and wrists, thereby ignoring the physical exertion markedly present in these parts during rubber tapping. Furthermore, it does not consider the duration spent on different work tasks. Novel

ergonomic assessment tools need to be designed specifically for this occupation to address such drawbacks.

4   Conclusion

The study confirms that rubber tapping is an occupational hazard exposing multiple body parts to ergonomic risks as confirmed by scores greater than 4 at multiple points along the REBA score sheet for a significant number of participants. 84% of rubber tappers surveyed were at medium risk of MSDs since they had REBA scores in the 4–7 range, whereas the remaining were at an even greater risk and required corrective measures in the near future. Furthermore, it can be concluded that the REBA score is correlated to the level of tapping. It would be beneficial to develop and implement programmes based on ergonomic and occupational health improvement to mitigate the risk of MSDs in this occupation.

References

1. Association of natural rubber producing countries (ANRPC) (2017) Report on rubber production. www.anrpc.org
2. Boonphadh P (2008) The perceived effects of work on health of rubber farmers in southern Thailand. Massey University, New Zealand
3. David G, Woods V, Li G, Buckle P (2008) The development of the quick exposure check (QEC) for assessing exposure to risk factors for work-related musculoskeletal disorders. Appl Ergon 39:57–69
4. Doi MAC, Yusuff RM, Leman Z (2007) A preliminary study of prevalence of musculoskeletal disorders among Malaysian rubber tappers. Age 45:25–78
5. Hignett S, McAtamney L (2000) Rapid Entire body assessment (REBA). Appl Ergon 31:201–205
6. McAtamney L, Corlett EN (1993) RULA: a survey method for the investigation of work-related upper limb disorders. Appl Ergon 24(2):91–99
7. Meksawi S, Tangtrakulwanich B, Chongsuvivatwong V (2012) Musculoskeletal problems and ergonomic risk assessment in rubber tappers: a community-based study in southern Thailand. Int J Ind Ergon 42(1):129–135
8. Pramchoo W, Geater AF, Tangtrakulwanich B (2020) Physical ergonomic risk factors of carpal tunnel syndrome among rubber tappers. Arch Environ Occup Health 75(1):1–9
9. Pramchoo W, Geater AF, Harris-Adamson C, Tangtrakulwanich B (2018) Ergonomic rubber tapping knife relieves symptoms of carpal tunnel syndrome among rubber tappers. Int J Ind Ergon 68:65–72
10. Stankevitz K, Schoenfisch A, de Silva V, Tharindra H, Stroo M, Ostbye T (2016) Prevalence and risk factors of musculoskeletal disorders among Sri Lankan rubber tappers. Int J Occup Environ Health 22(2):91–98
11. Udom C, Janwantanakul P, Kanlayanaphotporn R (2016) The prevalence of low back pain and its associated factors in Thai rubber farmers. J Occup Health 58(6):534–542
12. Udom C, Kanlayanaphotporn R, Janwantanakul P (2019) Predictors for nonspecific low back pain in rubber farmers: a 1-year prospective cohort study. Asia Pacific J Public Health 31(1):7–17

13. Van Beilen JB, Poirier Y (2007) Establishment of new crops for the production of natural rubber. Trends Biotechnol 25(11):522–529
14. Varghese A, Panicker VV (2021) Computer-Aided ergonomic analysis for rubber tapping workers. In: Advanced manufacturing systems and innovative product design: select proceedings of IPDIMS 2020. Springer Singapore, pp 293–302
15. Varghese A, Panicker VV (2020) Ergonomic evaluation of rubber tapping workers using postural ergonomic risk assessment. In: 18th Annual international ergonomics conference 'humanizing work and work environment' (HWWE)
16. Velásquez S, Valderrama S, Giraldo D (2016) Ergonomic assessment of natural rubber processing in plantations and small enterprises. Ingeniería y competitividad 18(2):233–246

Influence of Solvent Content in Screen Printing Inks for Plastics on Rubbing Fastness Properties

G. Vladic, N. Kasikovic, G. Bosnjakovic, D. Novakovic, and B. Banjanin

1 Introduction

Screen printing is the most versatile printing technique considering its industrial applications, ink types that can be used, as well as variety of substrates that it is suitable for (paper, textile, ceramic, plastic, etc.). It is applicable in industrial manufacturing but also in artistic applications for single-item production. Screen printing is the process in which ink is forced through a screen mesh which carries the stencil onto the substrate [1].

One of the materials which is increasingly being used as printing substrate is polyvinyl chloride (PVC) foil. The basic application of this type of foil is in the advertising graphic for outdoor and indoor use, so they are often exposed to external influences. This paper investigates the resistance of screen-printed PVC foils to external influence [2]. Investigations of mechanical effects of screen-printed textile products indicated that rubbing process has a significant impact on the color fastness. By varying the screens and types of the inks, it was concluded that oil-based inks and lover mesh count of the screen could produce better colorfastness on textile substrate, thus resulting in longer lasting printed products [3].

G. Vladic · N. Kasikovic (✉) · G. Bosnjakovic · D. Novakovic · B. Banjanin
Department of Graphic Engineering and Design, Faculty of Technical Sciences, University of Novi Sad, Novi Sad, Serbia
e-mail: knemanja@uns.ac.rs

G. Vladic
e-mail: vladicg@uns.ac.rs

G. Bosnjakovic
e-mail: gordana.delic@uns.ac.rs

D. Novakovic
e-mail: novakd@uns.ac.rs

B. Banjanin
e-mail: bojanb@uns.ac.rs

719

Prints made on the PVC substrate are usually exposed to various environmental influences during their use. Some of those influences are wetting, UV light exposure, rubbing, etc. All of them result in the color change of the print during exposure [4]. In contrast to wetting and UV exposure, rubbing can produce most dramatic changes in short time or even remove ink from the substrates surface completely exposing original substrate color. Amount of the damage to the print other than ink and substrate characteristics are highly dependable on the abrasiveness of the rubbing medium and force applied. Rubbing conditions in experimental setting is defined for some substrates, for example textile rubbing tests are defined by ISO 105-D02:2016 standard [5].

Screen printing inks are mainly "conventional curing", they cure in room temperature or heated air. Inks are chosen by consideration of substrate screenability (ability to pass through screen mesh but not seep without pressure) and intended use. Basic components of the screen printing ink are resins, fillers, and solvent. Resins are film former of an ink, and they are chosen to be suitable with substrate material and intended use. Typically, resins intended for use with PVC substrates are vinyl based, although there are also alkyd, ester, epoxy, and other resins. Compatibility with solvents and fillers is also considered. Fillers are usually inert materials used to carry color pigments or to thicken ink so it is screenable. Fillers may also to some extent improve opacity and adhesion to substrates. The main characteristics of solvents for screen printing are solvent power, flash point, boiling range, and toxicity. Solvent power is the ability of a solvent to dissolve a particular resin. The flash point is the temperature at which solvent vapor escaping from a liquid will form a combustible mixture with air and ignite when exposed to an open flame [6].

Screen printing inks intended for PVC substrates mainly cure by solvent evaporation accompanied with thermosetting, oxidation, polymerization, or penetration.

Toxicity of organic solvents is significant factor. Solvent-based inks are considered the least environmentally friendly due to the highly volatile solvents given off during printing and drying. Result of solvent evaporation is air pollution, and it must be taken into consideration on the local level to achieve healthy work invariant. This pollution is not significant on the larger scale. The petroleum-based binder used in many solvent-based inks could be replaced with renewable resources such as vegetable oil or soy. The downsides are that the inks dry very slowly, are less durable, and still contain solvents emitting VOCs during printing [7].

2 Experimental

Variation of the materials used in the printing process and their influence on the rubbing fastness is the main interest of this paper. Investigation on how rubbing fastness of printed plastics is influenced by varying four levels of solvent content in screen printing inks, three different screen printing mesh count, and two different substrates was done using 24 printed specimens subjected to automatized rubbing process.

2.1 Materials

Two printing substrates used for this experiment were self-adhesive PVC foils ORACAL 641 Economy Cal soft PVC film with glossy surface and ORACAL 551 High Performance Cal Polymeric PVC film with glossy surface. Technical data of both materials is given in Table 1.

Screen printing ink used was Tiflex, pc noir coloriflex, encre polycolor: 3,992,035 with composition as given in Table 2. Appropriate solvent was added to the ink in the increasing manner from 0% (ink previously contains from 2.5% up to 10% of solvent) up to 40% of the total volume of the ink.

Deposition of the ink was done using conventional screen printing technique. SEFAR mesh was used, and in three variations of screen printing mesh count, 40 threads/centimeter, 90 threads/centimeter, and 165 threads/centimeter, characteristics of screen printing mesh are shown in Table 3. Synthetic rubber squeegee 75 shore was used.

Table 1 Technical data of printing substrates [8, 9]

Parameters	ORACAL® 641 Economy Cal, white glossy	ORACAL® 551 High Performance Cal, white glossy
Thickness* (without protective paper and adhesive)	75 µm	70 µm
Dimensional stability (FINAT TM 14)	Adhered to steel, no measurable shrinkage in cross-direction, in length 0.4 mm max	Adhered to steel, no measurable shrinkage in cross-direction, in length 0.2 mm max
Temperature resistance***	Adhered to aluminum, − 40 °C to +80 °C	Adhered to aluminum, − 50 °C to + 90 °C (short-term, max. 24 h, at + 100 °C)
Water resistance	Adhered to aluminum, after 48 h/23 °C	Adhered to aluminum, after 100 h/35 °C
Adhesive power* (FINAT TM 1, after 24 h, stainless steel)	16 N/25 mm	18 N/25 mm
Tensile strength (DIN EN ISO 527)	Along: min. 19 MPa Across: min. 19 MPa	Along: min. 19 MPa Across: min. 19 MPa
Elongation at break (DIN EN ISO 527)	Along: min. 130%	Along: min. 130%
Shelf life**	2 years	2 years
Application temperature	> +10 °C	> +8 °C

*,**,***High

Table 2 Composition of the printing ink [10]

Tiflex, pc noir coloriflex, encre polycolor: 3,992,035	
Name	%
3-Ethoxypropionate D'ethyle	25< = × %<50
Cyclohexanone	10< = × %<25
Solvent Naphtha (Petroleum), Light AROM	2.5<= × %<10
Noir de Carbone	2.5<= × %<10
Diacetone Alcohol	2.5 <= × %<10
Mesitylene	0<= × %<2.5
Toluene	0<= × %<2.5

2.2 Method

Samples were printed according to the ink manufacturer instructions (except solvent content), honoring recommended drying and fixating process. Variation of the three screen printing mesh, ink composition increasing the percentage of solvent in four increments 0%, 15%, 30%, 40% (after that screenability was not achievable), and two different printing substrates were used. The patches of color were printed on to the substrate, adequate for testing, with dimensions 40 mm × 150 mm.

Electronic ckrockmeter Testex textile instrument LTD. TF411 was used for testing color fastness to dry rubbing. The rubbing head had a diameter of 16 mm, vertical pressure of 9 N, rubbing stroke of 104 mm. First test was done according to the ISO 105 × 12/D02 standard in the absence of the standard specialized for PVC self-adhesive foils. Mentioned standard is intended for textile materials, and after 2000 consistent stroke, cycles did not produce any noticeable changes on the surface of the print. This can be explained by better adhesion of the ink to the surface of PVC substrate than in the case of textile material. Modification to the methodology was made in order for rubbing treatment to produce noticeable effect. Several abrasive materials were tested, and general-purpose synthetic nonwoven abrasive scouring pad was amounted on the rubbing head.

Scans of the samples were taken after printing and after 10, 30, 50, 80, 110, 160, 310 rubbing cycles. Scanning was done using Canon CanoScan 5600F at 800 spi.

Having in mind size of the samples and size of the rubbing head, area of the 1 cm2 was cropped at resolution 300 pixels/cm where rubbing effect will be monitored and objectively quantified by image analysis. In total, 192 samples suitable for image analysis were made. Scans were converted to grayscale suitable for later analysis. Quantification of the rubbing result was done using ImageJ software through histogram analysis and reporting minimal, maximal, and mean value of pixels [11]. In grayscale system, value of the pixel is reported on scale from 0 to 255. Having in mind black color of the ink and white color of the surface, it can be concluded that lighter color of the print is the result of pigment removal by rubbing.

Table 3 Characteristics of screen printing mesh

Screen printing mesh: Sefar

Mesh number	Mesh count (/cm)	Thread diameter nominal (μm)	Weave	Tolerance of mesh count (± n/cm)	Mesh opening (μm)	Open area (%)	Mesh thickness (woven) (μm)	Tolerance of mesh thickness (μm)	Theoretical ink volume (cm³/m³)
165/420–31 PW	165	31	1:1	4.0	29	23	47	3	7
90/230–40 PW	90	40	1:1	2.5	68	37	61	4	23
40/103–80 PW	40	103	1:1	1.2	166	44	163	9	64

3 Results and Discussion

There are two possible effects of increasing amount of solvent in the printing ink. First is that by increasing the amount of solvent, less pigment is present on the surface of the substrate, and it will have less rubbing cycles to remove the pigment. Second is that increasing the amount of solvent will result in better bonding between ink and substrate by partly dissolving the surface of printing surface. Images in Fig. 1. show progression of pigment removal caused by rubbing. Observing the rows, it can be noticed that, as expected, with higher number of rubbing cycles, more pigment is removed. By analysis of images in columns, it can be noticed that there are some differences caused by increasing amount of solvent, but those differences must be further analyzed by objective method as they are not obvious and consistent.

Averaged numerical values describing the changes caused by different solvent amount obtained by image analysis are shown in Table 4.

In case of Oracal 551substrate printed using 40 t/cm, screen average of mean values across all rubbing repetitions is dropping from 25.4 down to 22 which means it indicates that prints with higher amount solvent are darker or that less pigment is removed from the surface in prints with higher amount of solvent. Similar but with less significant difference (dropping from 24.2 down to 21.9 can) be observed in case of Oracal 551 substrate printed using 90 t/cm screen. Prints made by using 165t/cm show similar results across all variations of solvent amount in ink. It is also important to note that 165 t/cm is fine screen intended for printing fine details, and there were some problems with adhesion of the screen ad substrate while printing such a big spot of color.

Analysis of the prints made on the material Oracal 641 did not show significant differences caused by amount of solvent in the ink. In case of prints made on this material using 40t/cm screen difference of the average values which is 1, prints
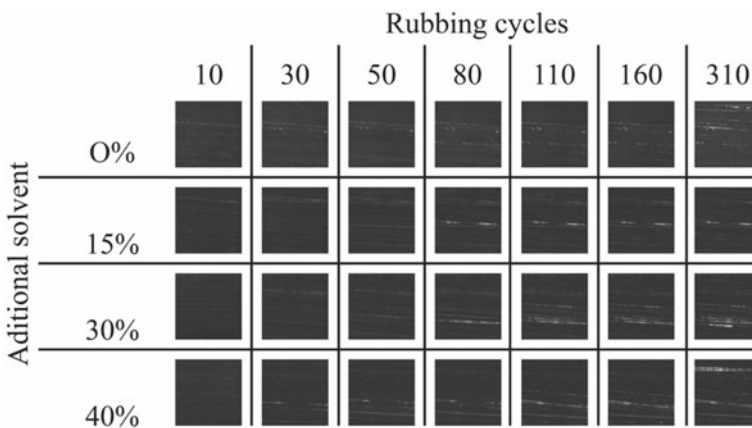
Fig. 1 Rubbing progression on prints made using 165/420-31 PW on ORACAL® 641 Economy Cal self-adhesive foil

Table 4 Averaged numerical values obtained by image analysis

Mean	Min	Max	Mean	Min	Max	Mean	Min	Max	Mean	Min	Max
Oracal 551_0%_40 t/cm			Oracal 551_15%_40 t/cm			Oracal 551_30%_40t/cm			Oracal 551_40%_40 t/cm		
25.4	16.8	117.0	23.4	15.8	78.6	22.8	15.9	87.8	22.0	15.9	76.3
Oracal 551_0%_90 t/cm			Oracal 551_15%_90 t/cm			Oracal 551_30%_90 t/cm			Oracal 551_40%_90 t/cm		
24.2	16.8	91.4	23.3	16.6	80.5	23.2	16.3	91.9	21.9	16.1	75.6
Oracal 551_0%_165 t/cm			Oracal 551_15%_165 t/cm			Oracal 551_30%_165 t/cm			Oracal 551_40%_165 t/cm		
27.4	18.4	133.5	28.0	17.8	166.9	26.1	17.4	166.9	28.2	17.6	161.5
Oracal 641_0%_40 t/cm			Oracal 641_15%_40 t/cm			Oracal 641_30%_40 t/cm			Oracal 641_40%_40 t/cm		
28.1	17.9	81.5	27.1	17.5	80.5	27.1	17.3	80.0	27.8	19.1	75.1
Oracal 641_0%_90 t/cm			Oracal 641_15%_90 t/cm			Oracal 641_30%_90 t/cm			Oracal 641_40%_90 t/cm		
25.7	17.3	75.8	25.5	17.3	81.5	24.8	16.6	81.0	25.0	17.0	84.3
Oracal 641_0%_165 t/cm			Oracal 641_15%_165 t/cm			Oracal 641_30%_165 t/cm			Oracal 641_40%_165 t/cm		
27.4	18.9	130.6	25.7	17.1	138.8	25.4	16.9	142.6	25.9	17.1	151.9

made using 90 t/cm screen have difference less than 1 and prints made using 165 t/cm have greatest difference of 2 but always following trend of prints made with ink without additional solvent being the lightest. It is important to note that there is no pronounced trend between inks with added solvent dependent on amount of solvent, and the values are similar in all variations. Material Oracal 641 did not show problems with adhesion between screen and substrate in case of the screen with 165 t/cm. This was resulted by composition differences which could also explain greater differences in case of material Oracal 551 which could be more prone to be dissolved with solvent and resulted in better bonding of ink and substrate surface.

4 Conclusion

Solvents are regularly added to ink during screen printing process in order to archive screenability by adjusting ink viscosity. This study was not considering visual reproduction quality, and it was only concerned with rubbing fastness. The amount of solvent in the ink also influences the pigment volume deposited on the substrate surface, but also, it helps bonding of the ink to the surface by partly dissolving the surface. These two concepts are opposing, and this study has offered the answer which of them is dominant in relation to removing the pigment by rubbing process. Inks with no additional solvent showed least resistance to rubbing in all combinations of substrate material and screen thread count. Differences between inks

with added solvent were not significant, and more refined study oriented on that subject could offer additional answers. Differences between materials suggest that amount of solvent affects bonding only if material is dissolvable with solvent used. Reducing amount of solvent in the ink is also responsible to the environment, especially effecting air condition in the workspace, so it should be considered when possible.

References

1. Novaković D, Kašiković N (2013) Propusna štampa. FTN Izdavaštvo, Novi Sad
2. Delić G, Tatović I, Petrović S, Banjanin B, Vasić J (2018) Resistance of screen-printed PVC foils to external influence. Mach Des 10(3):129–134
3. Vladić G, Kašiković N, Spiridonov I, Boeva R, Pintier I, Stančić M (2017) The colorimetric and microscopic analysis of differences in colorfastness to rubbing process caused by different composition of screen print inks. Bul Chem Commun 49(L):158–162
4. Kašiković N, Vladić G, Pál M, Novaković D, Đurđević S (2015) Uticajni parametri na kvalitet otiska dobijenog tehnikom sito štampe na PVC folije In: J Ziljak Vujic (eds), 14. Tiskarstvo i Dizajn, Akademija Tehničkih Znanosti Hrvatske Centar za grafičko inženjerstvo, Zagreb, Croatia, p 12
5. ISO 105-D02:2016 Textiles—tests for colour fastness—part D02: colour fastness to rubbing: organic solvents. Available from: https://www.iso.org/standard/65211.html. Accessed 22 Sept 2019
6. Aydemir C, Ayhan Özsoy S (2020) Environmental impact of printing inks and printing process. J Graph Eng Des 11(2):11–17
7. Nazdar Ink Technologies. Available from: https://www.nazdar.com/en-us/Environmental-Health-and-Safety-Docs-FAQ/QuestionID/47/AFMID/4076. Accessed 22 Sept 2019
8. ORACAL® 641 Economy Cal. Available from: https://www.orafol.com/products/europe/en/technical-data-sheet/oracal-641-economy-cal-3550-technical-data-sheet-europe-en.pdf. Accessed 22 Sept 2019.
9. ORACAL® 551 High Performance Cal. Available from: https://www.orafol.com/products/europe/en/technical-data-sheet/oracal-551-high-performance-cal-id3474-technical-data-sheet-europe-en.pdf. Accessed 22 Sept 2019
10. TIFLEX, PC NOIR COLORIFLEX, ENCRE POLYCOLOR—3992035. Available from: https://www.tiflex.com/fds/uploads/archives/3992035_R2_GB.pdf. Accessed 22 Sept 2019
11. Screen printing mesh: Sefar. Available from: https://www.sefar.com/data/docs/zh/10855/PS-PDF-SEFAR-PET1500-AL-EN.pdf?v=1.8. Accessed 22 Sept 2019

An ISM Framework for Agile New Product Development Process Risk Elements: Industry 4.0 Perspective

Manoj Palsodkar, Rajesh Pansare, and Madhukar Nagare

1 Introduction

The global consumer behavior and a narrowing window of opportunity for businesses are forcing organizations for quick and efficient product development (PD). At the same time, it is necessary to maintain product quality, suitability to market needs, and high competitiveness. The NPD consists of series of steps that allow the creation of a product from ideation of concept through manufacturing, and here the majority of product goals are set [1]. Cooper [2] reported that approximately 40% of new creations are predicted to fail at the introduction to the market, despite all quality measures; only one from seven to ten new product ideas are commercially successful; whereas [3] mentioned that hardly 10% of businesses report that their NPD efforts help them to meet their annual profit goals proving that NPD is a risky activity with high failure costs. In the present era of Industry 4.0, organizations have started using emerging technologies like big data, rapid prototyping, cloud computing, industrial Internet of things, and cyber-physical systems to develop new products [4]. Arromba et al. [5] cited, in the scenario of Industry 4.0, these digital technologies have an impact on NPD performance, and [6] quoted organizations should make changes significantly, in their NPD procedure for smart invention. With the growth avenues presented by Industry 4.0 capabilities and the highly competing

M. Palsodkar (✉) · R. Pansare
Veermata Jijabai Technological Institute, Matunga, Mumbai 400019, India
e-mail: manojpalsodkar@somaiya.edu

R. Pansare
e-mail: rajeshpansare@somaiya.edu

K. J. Somaiya College of Engineering, Mumbai 400077, India

M. Nagare
Production Engineering Department, Veermata Jijabai Technological Institute, Matunga, Mumbai 400019, India
e-mail: mrnagare@pe.vjti.ac.in

environment, leading-edge companies are attempting the ANPD process for physical product development, which originated in the software industry in the 1990s [7].

Simply adopting ANPD will not solve the current problems; instead, organizations should direct their efforts toward risk management resulting in fewer chances of failure [8]. To reduce their impact on the overall NPD process, risk factors emerge while ANPD adoption must be identified early in the process, followed by the creation of a risk management plan [3]. As a result, the authors have carried out the said research work with the following objectives:

i.   To find out potential risk elements having a significant effect on decisions during ANPD;
ii.   To evaluate and create interrelationships between possible risk elements using ISM; and
iii. To establish a risk element structural framework that takes into account both driving and dependence power.

This research has been divided into five sections including the current section. The ANPD literature is examined in the second section. Section three elaborates on the research methodology as well as a case application. Section four summarizes the above-mentioned research methodology's results and discussions; Section five discusses the research's conclusions, implications, as well as future scope.

2 Literature Review

This segment examines the ANPD concept, the associated risks, and the steps taken to model them using a hybrid ISM-MICMAC analysis.

2.1 ANPD Risk Elements

The majority of the organizations still use traditional PD processes such as stage-gate with structured timelines, rigid design evaluations, "gates" used while decision making, no interdisciplinary teams, and a new product creation which require a minimum of three years [9]. Industry 4.0 is a collection of advanced technologies for PD and manufacturing. Producing smart and connected products necessitate significant changes, particularly in the product development process. Organizations that create smart products must now use the most appropriate product development approaches [6].

Considering this, many organizations have attempted various alternate methodologies to enhance, speed up, and reconstruct their current PD methodology [2], agile new product development being one of them. It is understood as a collection of tools and strategies that allow for the rapid reconfiguration of products and related practices in response to changing customer needs [10]. With the increase in product

variety, demand, complexity, as well as global competition, the emphasis on ANPD has increased, and ANPD risk management has thus become an important concern for organizations under the current circumstances [11]. For effective ANPD execution, the decision-maker must understand the various risk elements. A literature review on ANPD risk elements has been conducted and discussed in this section.

Park [12] has identified five different risks, performance factors of NPD, and presented a conceptual framework for risk and performance management along with lessons for effective risk management. Oehmen et al. [13] used empirical research to investigate the integration of risk management practices with NPD programs, as well as their relationship with different aspects of successful risk management. The findings suggested conducting more research about the impact of risk management practice on the success of the NPD program. Salvati et al. [14] discovered a positive relationship between the organization, market, technology, and commercial risk management and NPD performance metrics and recommended that NPD project team members must optimize the NPD process. Further [15] investigated medical device development process risks and developed an interaction model based on the relevant relationship among these risk sources. However, [11] reviewed the risks pertinent to agile project management practices adoption and identified the best response strategies. It is also recommended that the risks involved while using a hybrid methodology for NPD be pinpointed to assess the impact on project success.

Even though many researchers have worked in the field of risk identification and developing risk response strategies for the NPD domain, none have worked on identifying the interrelationships between them. The authors of this study attempted to identify various risk elements through a literature review, followed by brainstorming among the authors, and finally gathering expert opinion. The final list of risk elements is given in Table 1.

2.2 Interpretive Structural Modeling and MICMAC Analysis

ISM being a framework-oriented procedure that allows practitioners to develop frameworks for the interrelationships within a diverse set of elements in mixed circumstances [15]. The ISM-MICMAC process is carried out as discussed by [17]:

Step 1: The interrelationship between the risk elements i and j was described by using four fixed notations (V, A, X, O) to investigate REs for the development of the SSIM.

1. V- RE_i assists in obtaining RE_j;
2. A- RE_j will assist in achieving RE_i;
3. X- RE_i as well as RE_j will help for mutual attainment;
4. O- RE_i as well as RE_j has no relationship.

Table 1 ANPD risk elements

S. No.	Risk element	Code	Risk triggers	Reference
1	Human resource risk	RE1	Resistance to change, insufficient training for employee, difficulty in performing the tasks	[11, 16]
2	Financial support risk	RE2	Product development budget constraint, unstable product price	[17]
3	Ineffective planning risk	RE3	Fear of failure, unsatisfied stakeholder, variation in development time, costs	[13, 18]
4	Corporate incompatibility risk	RE4	Failure to meet the goals, insufficient resources for research and development, poor employee performance, poor communication across the organization	[11, 12]
5	Supply chain management (SCM) risk	RE5	Failure of a supplier, errors in supplier commitment, supply source inflexibility	[19]
6	NPD process risk	RE6	Inadequate identification of NPD scope, poor end-user involvement, improper competition assessment	[15, 20]
7	Advanced technology risk	RE7	Technology adoption, poor product design and development, system integration, intellectual property rights	[12, 14]
8	Competitiveness risk	RE8	Small market section, short product life because of changing customer requirements, competitor's market entry	[15]
9	Responsiveness risk	RE9	Creates adoption challenges, lower product development speed, poor customer satisfaction	[11]
10	Delay risk	RE10	Delay in new product introduction, product rejection, slow response to a shift in demand	[15]

Step 2: Transform the SSIM to a binary matrix that reflects the initial reachability matrix (IRM). SSIM notations (V, A, X, O) are converted into binary forms (0 and 1) as per the following:

- In SSIM if (i, j) = V, then in IRM (i, j) = 1 and (j, i) = 0
- In SSIM if (i, j) = A, then in IRM (i, j) = 0 and (j, i) = 1
- In SSIM if (i, j) = X, then in IRM (i, j) = 1 and (j, i) = 1
- In SSIM if (i, j) = O, then in IRM (i, j) = 0 and (j, i) = 0

Step 3: Following the preparation of the IRM, the next step is to remove transitivity. The fundamental constitution of ISM is relational transitivity. If a risk element RE1 is relevant with a risk element RE2, and RE2 is relevant with a risk element RE3, then RE1 must be relevant with RE3.

Step 4: Following the removal of transitivity, the next step is level partitioning. The reachability and antecedent sets are prepared. The intersection set having common risk elements of reachability and antecedent set are identified. Following the preparation of these three sets, the next step is to determine their levels.

Step 5: By referring to the level partitioning, a digraph is developed which shows the relationship between various risk elements and the hierarchy from bottom to top. The final step of ISM is to structure the REs at various levels by replacing codes in the digraph.

Step 6: In MICMAC analysis, the sixth step is used for quantification and distribution of the ANPD risk elements considering their driving and dependent power.

3 Research Methodology and Execution of ISM

This section discusses the methodology used to conduct research. It also goes over the various steps that must be taken during the execution of ISM-MICMAC analysis.

3.1 Research Methodology

The flowchart shows the steps followed for the conduction of this research work. The expert panel is made up of eight experts, six from industry, and two from academia. The ISM-MICMAC investigation procedure for this research work is carried out by collecting input from a panel of experts (Fig. 1).

3.2 ISM-MICMAC Analysis and Case Application

The short-listed risk elements were presented to the expert panel, and based on their opinion, ten risk elements for the ANPD process were selected as given in Table 1. The entire ISM process was explained to the experts, and the final VAXO analysis table is created (Table 2).

Table 3 shows the final level partition of the FRM.

Finally, each RE in ISM is to be placed at various stages via level partitioning of the FRM. The structural framework of RE that reflects the interrelationship between the risk elements is shown in Fig. 2.
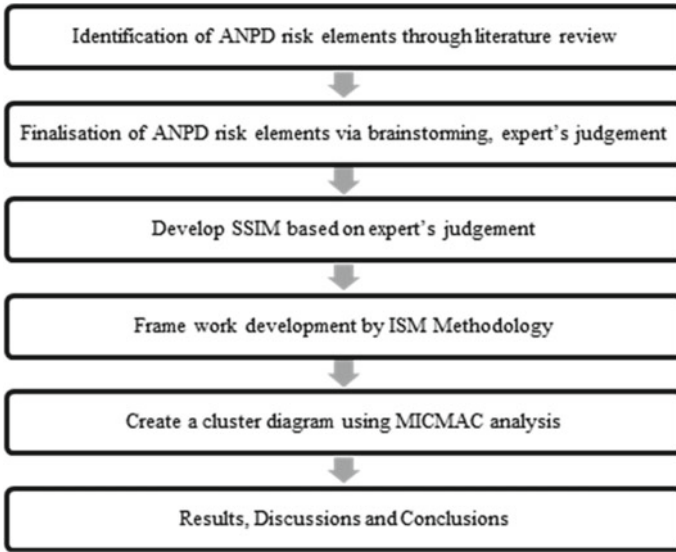
Fig. 1 Research methodology

Table 2 ANPD risk SSIM

Code	RE10	RE9	RE8	RE7	RE6	RE5	RE4	RE3	RE2
RE1	O	O	O	V	V	V	A	X	X
RE2	O	O	O	V	V	V	A	X	
RE3	O	O	O	V	V	V	A		
RE4	V	V	V	V	V	V			
RE5	V	V	V	X	X				
RE6	V	V	V	X					
RE7	V	V	V						
RE8	V	X							
RE9	V								
RE10									

By defining the partition levels, practitioners are often unable to make appropriate decisions for ANPD adoption; thus, understanding the driving as well as dependence power of REs used for the framework is required [17]. Finally, MICMAC analysis is added to address the aforementioned problem. Table 4 shows FRM with driving as well as dependence power.

As shown in Fig. 3, the ANPD risk elements are assigned to different quadrants based on the FRM information to analyze their driving as well as dependence power.

Table 3 Final level partition of FRM

Code	Reachability set	Antecedent set	Intersection set	Level
RE1	1,2,3,5,6,7	1,2,3,4	1,2,3	II
RE2	1,2,3,5,6,7	1,2,3,4	1,2,3	II
RE3	1,2,3,5,6,7	1,2,3,4	1,2,3	II
RE4	1,2,3,4,5,6,7,8,9,10	4	4	I
RE5	5,6,7,8,9,10	1,2,3,4,5,6,7	5,6,7	III
RE6	5,6,7,8,9,10	1,2,3,4,5,6,7	5,6,7	III
RE7	5,6,7,8,9,10	1,2,3,4,5,6,7	5,6,7	III
RE8	8,9,10	4,5,6,7,8,9	8,9	IV
RE9	8,9,10	4,5,6,7,8,9	8,9	IV
RE10	10	4,5,6,7,8,9,10	10	V
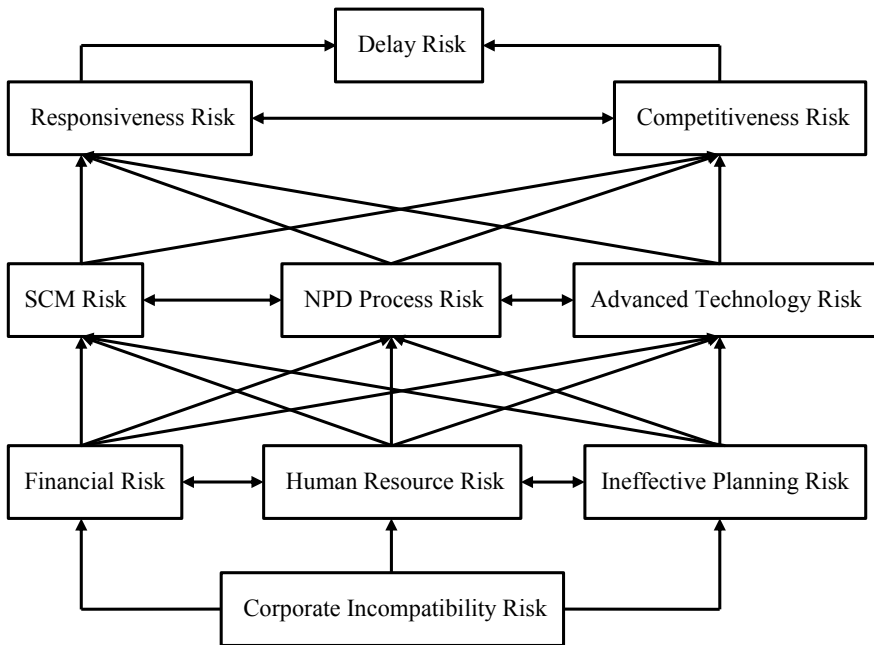
Fig. 2 Structural framework of REs

4 Results and Discussions

The model developed through the ISM approach depicts a structural framework of risk elements as well as their interrelationship. In this model, there are five levels. The results obtained are discussed below.

Table 4 ANPD risk elements FRM

Code	RE1	RE2	RE3	RE4	RE5	RE6	RE7	RE8	RE9	RE10	Driving power
RE1	1	1	1	0	1	1	1	0	0	0	6
RE2	1	1	1	0	1	1	1	0	0	0	6
RE3	1	1	1	0	1	1	1	0	0	0	6
RE4	1	1	1	1	1	1	1	1	1	1	10
RE5	0	0	0	0	1	1	1	1	1	1	6
RE6	0	0	0	0	1	1	1	1	1	1	6
RE7	0	0	0	0	1	1	1	1	1	1	6
RE8	0	0	0	0	0	0	0	1	1	1	3
RE9	0	0	0	0	0	0	0	1	1	1	3
RE10	0	0	0	0	0	0	0	0	0	1	1
Dependence power	4	4	4	1	7	7	7	6	6	7	
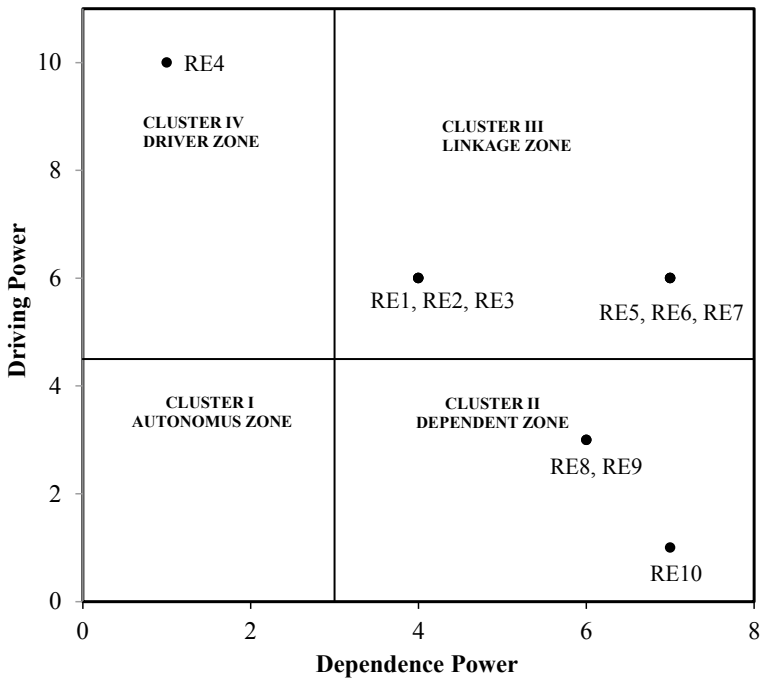
Fig. 3 Cluster diagram of ANPD REs

i.   The bottom-most level is occupied by "corporate incompatibility risk", while "financial support risk", "human resource risk", and "ineffective planning risk" occupy the fourth level. Because such risk elements have a significant driving power, any variation in such risk elements will create a noteworthy effect across the remaining risk elements. Such risk elements should be ANPD practitioners' top focus.

ii. The third level includes three risk elements: "supply chain management (SCM) risk", "NPD process risk", and "advanced technology risk". These risk elements are linked to one another as well as to other risk factors, and they have a strong driving as well as dependence power. The particular findings imply that changes in pair of risk elements will have a direct influence on the other risk elements.

iii. The risk elements "responsiveness risk" and "competitiveness risk" are placed second from the top, indicating that they are influenced by certain risk elements.

iv. The model indicates that the risk element "delay risk" has been elevated to the first level. This risk element is highly dependent on other risk elements. Figure 3 shows the distribution of risk elements according to the clusters and is described below.

v.   Cluster I: This cluster is made up of autonomous risk elements with low driving as well as dependence power. Such elements are somewhat detached from the system. None of the risk elements are recognized as autonomous elements in this case.

vi. Cluster II: It is composed of elements having high dependence but a little driving power, also termed as elements of criticality. In this case, the risk elements "competitiveness risk", "responsiveness risk", and "delay risk" are identified as the dependent elements. To address and mitigate these issues, a strategic plan is required.

vii. Cluster III: Linkage risk elements are having high driving as well as dependence power. Due to their unpredictable nature, any step performed on them may create an impact on the remaining risk elements along with the feedback effect. Risk elements like "human resource risk", "financial support risk", "ineffective planning risk", "supply chain management (SCM) risk", "NPD process risk", and "advanced technology risk" have been identified in this region. When decision-makers take action about them, it has the potential to have a significant impact on the ANPD process.

viii. Cluster IV: The driving risk element in the ANPD process is "corporate incompatibility risk", which has strong driving and weak dependence power. As a result, practitioners must conduct in-depth analysis to determine the root causes.

5   Conclusions and Future Scope

According to the literature review, the researchers identified several risks for various industries and countries. For the creation of the structural framework, ten potential risk elements related to ANPD are figured out in consultation with experts. The ISM–MICMAC methodology is used to investigate the interrelationships and related consequences of every risk element. The conclusions are as follows:

- Six risk elements have been identified as belonging to the linkage cluster. The significance of this third quadrant is that any alteration in the risk elements creates an impact on others. As a result of this circumstance, these risk elements are unstable.
- Organizations face a variety of risks as a result of globalization, technological advancement, and other factors. Although the risks associated with ANPD cannot be eliminated, their impact could be minimized by detecting, comprehending, and investigating the risk elements.
- Organizations, in particular, require a detailed strategy for ANPD implementation, and this article indicates a clear idea of ANPD risks, as well as the implications.
- The ISM model developed would aid ANPD practitioners and decision-makers in recognizing the most serious threats that necessitate immediate action.
- This study would help practitioners make decisions by assisting them in choosing risk management strategies to create a comprehensive and efficient ANPD process.
- In the future, potential risk elements, as well as sub-risk elements, can be recognized, evaluated, and ranked using various approaches. Although the ISM methodology was used to create an interrelationship structure between ANPD risk elements, this model is yet to be statistically validated. This model could be validated in the long term utilizing quantitative tools like structural equation modeling (SEM), etc.

References

1. Leite M, Baptista AJ, Ribeiro AMR (2016) A road map for implementing lean and agile techniques in SMEs product development teams. Int J Prod Dev 21(1):20–40
2. Cooper RG (2018) The drivers of success in new-product development. Ind Mark Manag 76(January):36–47
3. Chauhan AS, Nepal B, Soni G, Rathore APS (2018) Examining the state of risk management research in new product development process. EMJ Eng Manag J 30(2):85–97
4. Wijewardhana GEH, Weerabahu SK, Nanayakkara JLD, Samaranayake P (2020) New product development process in apparel industry using industry 4.0 technologies. Int J Product Perform Manag
5. Arromba IF et al (2020) Industry 4.0 in the product development process: benefits, difficulties and its impact in marketing strategies and operations. J Bus Ind Mark 36(3):522–534
6. Barrane FZ, Ndubisi NO, Kamble S, Karuranga GE, Poulin D (2020) Building trust in multi-stakeholder collaborations for new product development in the digital transformation era. Benchmarking 28(1):205–228

7. Cooper RG, Sommer AF (2018) Agile–Stage-Gate for manufacturers: changing the way new products are developedintegrating agile project management methods into a stage-gate system offers both opportunities and challenges. Res Technol Manag 61(2):17–26

8. Conforto EC, Amaral DC (2015) Agile project management and stage-gate model—a hybrid framework for technology-based companies. J. Eng Technol Manag JET-M 40(2015):1–14

9. Cooper RG, Sommer AF (2016) Agile-Stage-Gate: new idea-to-launch method for manufactured new products is faster, more responsive. Ind Mark Manag 59:167–180

10. Gurumurthy A, Kodali R (2012) An application of analytic hierarchy process for the selection of a methodology to improve the product development process. J Model Manag 7(1):97–121

11. Galli BJ, Lopez PAH (2018) Risks management in agile new product development project environments. Int J Risk Conting Manag 7(4):37–67

12. Park YH (2010) A study of risk management and performance measures on new product development. Asian J Qual 11(1):39–48

13. Oehmen J, Olechowski A, Robert Kenley C, Ben-Daya M (2014) Analysis of the effect of risk management practices on the performance of new product development programs. Technovation 34(8):441–453

14. Salavati M, Tuyserkani M, Mousavi SA, Falahi N, Abdi F (2016) Improving new product development performance by risk management. J Bus Ind Mark 31(3):418–425

15. Rane SB, Kirkire MS (2017) Interpretive structural modelling of risk sources in medical device development process. Int J Syst Assur Eng Manag 8:451–464

16. Yadav G, Desai TN (2016) Lean six sigma: a categorized review of the literature. Int J Lean Six Sigma 7(1):2–24

17. Yadav G, Desai TN (2017) Analyzing lean six sigma enablers: a hybrid ISM-fuzzy MICMAC approach. TQM J 29(3):488–510

18. Yadav G, Mangla SK, Luthra S, Rai DP (2019) Developing a sustainable smart city framework for developing economies: an Indian context. Sustain Cities Soc 47(February):101462

19. Narkhede BE, Raut RD, Roy M, Yadav VS, Gardas B (2020) Implementation barriers to lean-agile manufacturing systems for original equipment manufacturers: an integrated decision-making approach. Int J Adv Manuf Technol 108(9–10):3193–3206

20. Yadav G, Luthra S, Huisingh D, Mangla SK, Narkhede BE, Liu Y (2020) Development of a lean manufacturing framework to enhance its adoption within manufacturing companies in developing economies. J Clean Prod 245:118726

Application of Polymer Composite for Weight Reduction in the Automobile Sector Toward a Sustainable Development

Anand S. Baldota, Vishal J. Dulange, Shahrukh S. Patel, and Manoj W. Bhalwankar

1 Introduction

The automotive industry is one of the oldest industries in today's world. Due to it being a customer sensitive industry, it has been continuously evolving and adapting to become more sustainable and meet the demands of the customers. These changes can also be seen in the automobiles that are being manufactured.

Sustainable development consist of three pillars: environment, economic, and social. Sustainability can be achieved by redesigning the product, developing manufacturing processes, moving toward a better fuel source, and so on. Stella et al. in their attempt to present an analysis framework for sustainable development in automobiles mention how the selection of material during the design phase has an effect on the sustainability of the product due to its material weight [1]. The current work focuses on the use of lightweight material for weight reduction, for sustainable development in an automotive application [2].

Lightweight materials consist of advanced materials, nanomaterials, and composites. Based on the matrix, composites could be a metal matrix, ceramic matrix, and polymer matrix. These polymer composites are widely used in the automobile industry as they give a balanced performance in the strength to weight, safety, and

A. S. Baldota · V. J. Dulange · S. S. Patel
MIT Academy of Engineering, Alandi, Pune, India
e-mail: asbaldota@mitaoe.ac.in

V. J. Dulange
e-mail: vjdulange@mitaoe.ac.in

S. S. Patel
e-mail: sspatel@mitaoe.ac.in

M. W. Bhalwankar (✉)
School of Mechanical and Civil Engineering, MIT Academy of Engineering, Alandi, Pune, India
e-mail: mwbhalwankar@mitaoe.ac.in

comfort categories. They are also easy to utilize in design and economic manufacturing [3]. It has been reported that polymer matrix composite has been used in the automotive industry since the 1991s. Their application has seen a consistent rise throughout the history of the automotive industry, starting with hand layup bodies for limited production of sports cars up to the most sophisticated injection-molded air intake manifold. In the early days, Ford had developed an experimental car from hemp fiber-filled soya composites as early as the 1940s. He further stated that glass cloth-reinforced allyl composites were used in 1941 in the United States of America (USA). It was also reported that during World War II, in Britain, the material for the fuselage of Spitfire aircraft was replaced from aluminum to flax fiber-reinforced phenolic composites, due to the insufficient supply of aluminum. The application was extended to other sports car bodies and sporting goods [4]. The application of high-performance polymer materials allows more freedom in design, and in many cases, only these materials can allow safe geometrical or economic solutions for the construction of parts. The average global polymer usage is 120 kg/vehicle [3].

With the increasing awareness about the environment and global warming, recycling as one of the approaches of the end of life waste management of the polymer has been in full bloom [5, 6]. With the increasing awareness about the environment, global warming, and reduction in non-renewable resources, the use of polymer composites opens up the new way toward the sustainability of the automobiles/cars. It has been proved that every 10% reduction in total vehicle weight produces 3–7% better fuel economy, thereby reducing harmful emissions by 5–6% [1, 7]. This work tries to provide a brief overview of the use of polymer composites for weight reduction as an alternative for sustainable development in the automobile industry.

2   Weight Reduction Using Polymer Matrix Composite Material

An automobile consists of different types of constructional materials including polymers and polymer composite. In a report by Lucintel in 2017 on average, the polymer constituted about 24.4% weight percent of an automobile, and this is expected to grow in the upcoming years [8]. Abdelraoof Mayyas et al. suggested the possible use of fiber-reinforced polymer (FRP) for BiW using quality function deployment and analytical hierarchy process for roof, outer hood, outer trunk, quarter panel, front fender, door, wheelhouse, and floor weight reduction [9]. Polymers have a higher strength to weight ratio over conventional materials along with excellent chemical stability. Weight reduction of up to 60% has been reported by the application of polymers instead of metals [10]. Significant weight can be reduced although the use of polymers is restricted due to challenges of operating temperatures, insufficient heavy load carrying capacity, and manufacturing cycle time. Continuous improvements are made to extend the use of polymers in the automobile sector, and some of them are the use of coupling agents, surface treatment of fibers, nanofillers, nucleating agents,
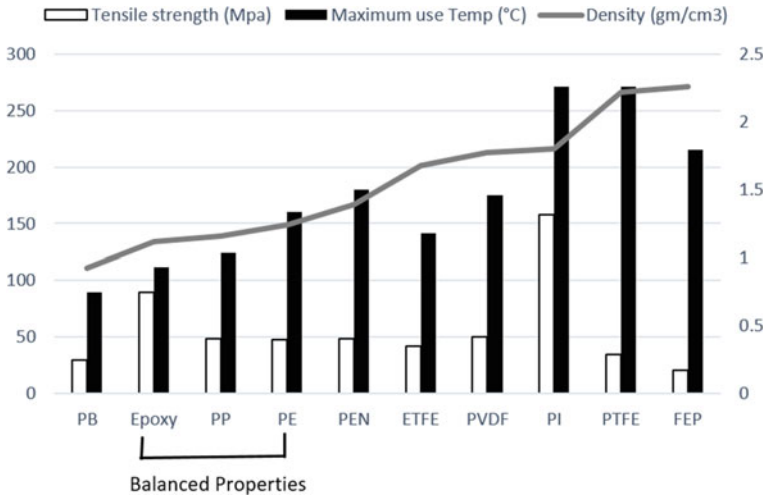
Fig. 1 Properties of polymers [12]. *PP* polypropylene; *PE* polyethylene, *PTFE* polytetrafluo-roethylene, *PI* polyimide, *PEN* polyethylene-2,6-naphthalene dicarboxylate, *PB* polybutylene, *PVDF* polyvinylidene difluoride, *ETFE* ethylene tetrafluoroethylene, *CF* carbon fiber, *GF* glass fiber, *FEP* fluorinated ethylene propylene

and hybridization of fillers. Vespel® is a trademark name of polyimide composite which can sustain temperatures of 300 °C without any change in the property making it suitable for high-temperature applications [11].

The below image depicts tensile strength, density, molding, and the temperature of polymers, which directly impact overall composite weight (Fig. 1).

PI exhibits higher tensile strength as well as temperature stability although due to its higher density its application is limited. PP, epoxy, and PE show better filler matrix adhesion as compared to other polymers, also their maximum use temperature ranges from 100–150 °C due to the balanced properties of PP, PE, and epoxy, and it has versatile applications ranging from interior of automobile to the engine compartments parts whose applications are shown in Fig. 2.

Polymers are reinforced with particles, fiber, sheets, whiskers, and flakes. Fibers and sheets provide better mechanical properties as compared to particles because of the higher aspect ratio which enables the transfer of load effectively. Upon use, fibers fall into three major categories. (1) Fibers used in high-end applications where performance is a primary concern, e.g., monocoque (2) middle end where along with performance cost reduction is also major point out, e.g., door panels, rooftop (3) cost reduction is more emphasized than performance, e.g., underbody shields. Synthetic fibers have exceptional mechanical properties as compared to natural fibers, thus they have been majorly used in high and middle-end applications, e.g., Formula 1 racing car panels. Carbon fiber and aramid have exceptional specific strength in the range of 3500 Mpa. Cost, availability, and recyclability limit the use of synthetic fibers, in general automotive components. These drawbacks have been overcome with the
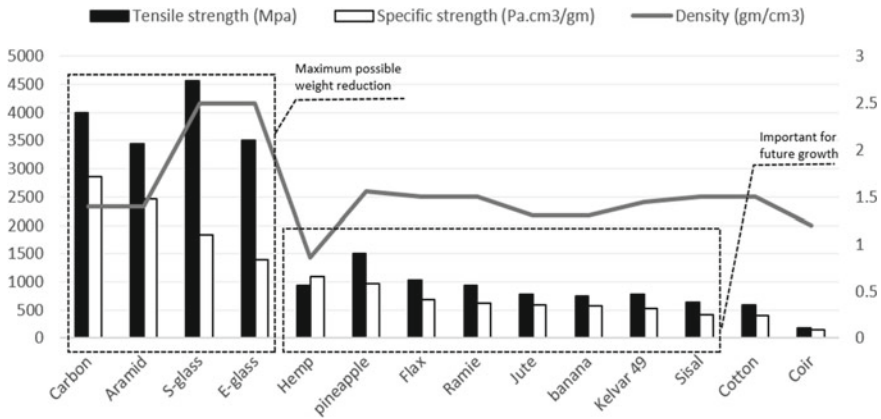
Fig. 2 Properties of fibers [13]

use of natural fibers as a replacement for synthetic fibers. Automobile floors are one such application.

Natural fibers contain cellulose fibers which can be harnessed and used as a reinforcement in composites. Some fibers are harvested from agricultural waste.

In recent years, these fibers are explicitly planted for textile, paper, and composite industries. Natural fibers show lesser strength as compared to synthetic fibers in the range of 900 Mpa but sufficient enough to be used in general automotive applications. Due to higher strength in this category, hemp, pineapple, and flax fibers find major applications in automotive body panels, interiors, casings, etc.

Synthesis methods for both the fibers vary thus limiting the use in the application. Table shows the key processes involved in the manufacturing of the composite and their applications (Table 1).

In applications such as monocoque chassis where high specific strength is required, only carbon fiber-reinforced polymer (CFRP) is a possible candidate as performance is the prime factor of consideration among other polymer composites. However, glass and natural composites find their application in door panels, hoods, etc., due to their balanced strength to weight ratio and lesser cost. Considering specific

Table 1 Key processes and application of glass composite, carbon composite, and natural composite [9]

Parameter	Glass composite	Carbon composite	Natural composite
Key processes	Compression molding, injection molding, resin transfer molding (RTM)	Prepreg layup, resin infusion	Compression molding
Key applications	Intake manifold, hood, door module, radiator end tank, oil pan	The monocoque, hood, door panel, roof, body panels	Door panel, seatback, load floor, interior panels, underbody shields
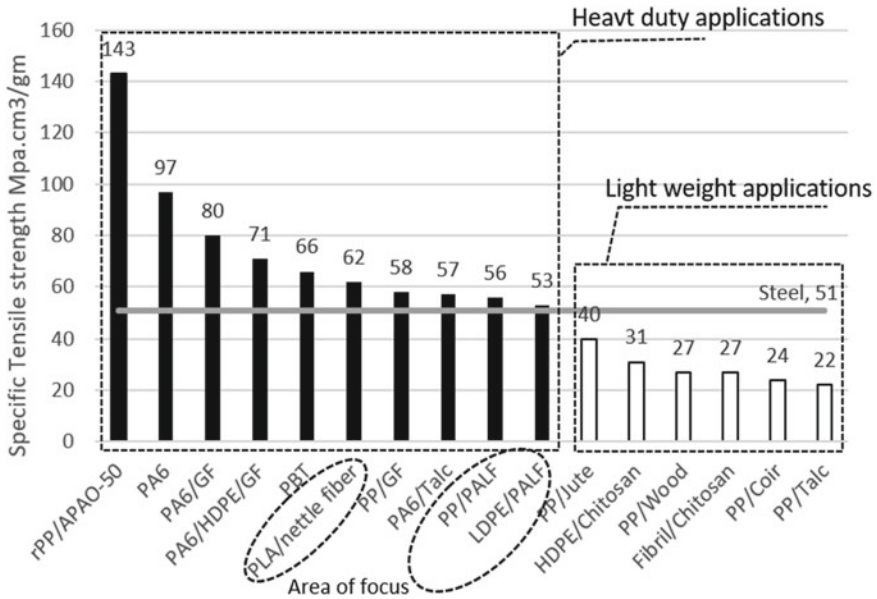
Fig. 3 Comparison of specific strength of PMC [14–23]

tensile strength as a sole property for application, Fig. 3 shows the % weight reduction possible by the use of polymer composites for a component instead of steel.

The positive value of the percentage weight saving shows the possibility of weight reduction by using the polymer matrix composite (PMC) instead of steel requiring equal strength as steel as required for the application. A negative value shows excess weight is added by the use of PMC instead of steel requiring equal strength as steel as required for the application. Amorphous polyalphaolefin (rPP/APAO-50) shows the maximum possible weight saving of 179% compared to that of steel and PP with talc and coir shows the least with −58 and −53% compared to that of steel.

PA6 positively affects weight reduction as a matrix displaying better filler matrix adhesion and copolymer adhesion. Talc with PP hurts the specific strength, but the same talc when added as a filler with PA6 shows a weight reduction of 12%, and this shows a better filler matrix adhesion as can be seen in PA6 and Talc as compared to PP. The above data does not include the effect of CF as filler on the weight reduction on the PMC. Nettle fiber is a natural fiber that shows promising weight reduction. PALF reinforced with PP also has weight reduction by 10 percent. These are natural fibers with promising applications. Much more emphasis will be given to them in the future.

3 Application of PMC in the Automotive Sector

With recent developments in the manufacturing systems and increasing environmental concerns, Original Equipment Manufacturers (OEMs) are exploring PMCs for weight reductions. Significant weight reductions have been observed in the automotive industry. Table 2 highlights these findings.

Due to ease and flexibility in manufacturing techniques, polymer components are replacing the traditional steel components by eliminating the need for fasteners, weldings, and other features which can be directly embedded in the mold casting them as a single component. Oil filter modules employed in Hyundai are such an example where weight reduction up to 43% was observed. As mentioned earlier, synthetic fibers are used in heavy-duty applications such as monocoque, frames (super and sub), and beams for excellent weight reduction although due to the economic concerns sustainable development is limited in this sector providing a fiber research gap for use of natural fibers in automotive applications.

Table 2 Weight reduction in automotive applications

S. No.	Application	Composite	Weight reduction obtained	Reference
1	Bumper beam	E-glass fiber epoxy composite	60%	[10]
2	Mono cell tub	CFRP	Component weight reduced to 80 kg	[24]
3	Monocoque	CFRP	23%	[24]
4	Superframe	CFRP	50%	[25]
5	Subframe	CFRP	10 kg weight reduction	[25]
6	Door modules	PP-LGF composite	2 kg weight reduction	[26]
7	Engine oil filter module	PA-GF composite	43% weight reduction	[26]
8	Engine cam cover	PA 66 with GF composite	2.5 kg weight reduction	[26]
9	Leaf spring	Epoxy glass fiber	Up to 80% of weight saving	[27]

Table 3 Application of PMC in the automotive industry [29]

S. No.	PMC	Application	Automobile		Reference
			company	Model	
1	Soy resin	Steel gull-wing doors	John deere	Harvester works	[28]
2	Wood fiber	The floor area of the pilot sport utility vehicle	Honda	SUV	
3	Kenaf and flax	Package trays and door panel inserts	General motor	Saturn L300s	
4	Wood fiber	Seatbacks for the	Cadillac	DeVille	
5	Wood fiber	Cargo area floor	GMC	Envoy	
6	Wood fiber	Cargo area floor	Chevrolet	TrailBlazer	
7	Corn resin	Goodyear tires	Ford	Fiestas	
8	Wood fiber	Sliding door inserts	Ford	Freestar	
9	Soy resin	Body panels	John Deere	Tractors	
10	Wheat straw-PP	Storage bins	Ford	Flex	[30]
11	Hemp–propylene	Front grill	Ford	Montagetreager	
12	Jute fiber	Interior door panels	Mercedes-Benz	1994 E-Class	
13	Polyester/flax	Engine encapsulations	Mercedes-Benz	EvoBus	
14	Sisal	Rear panel shelves	Mercedes-Benz	C-Class	
15	Abaca-PP	Spare tire wheel covers	Mercedes-Benz	A-Class	
16	poly lactic acid (PLA) + sugarcane + kenaf	Spare tire cover	Toyota	RAUM 2003	
17	PP + kenaf	Door trims	Toyota	Mazda	
18	Soy	Seat foams	Toyota	2008 Rav-4	
19	PP/PLA	Side trims, door scuff plates, toolbox area, floor finishing plate, and package trays	Toyota	Lexus CT200h	
20	Flax fiber	Inner door panels	Toyota	1995 Opel Corsa	

(continued)

Table 3 (continued)

S. No.	PMC	Application	Automobile		Reference
			company	Model	
21	Polyethylene terephthalate (PET)	Luggage compartment lining	Toyota	Lexus-CT200	
22	PU + flax/sisal	Hybrid mats	VW	A2	
23	PLA, nylon/flax	Floor mats	Mitsubishi	-	
24	Coconut shells	Structural guard	Ford	F-250	[31]
25	Coconut shells + rubber + MgSi fiber	Rear decklid appliqué brackets and side-door cladding	Ford	Mustang	
26	PP + Wheat straw	Quarter-trim bins	Ford	Flex CUV	
27	PP + Rice hulls	Electrical cowl brackets	Ford	F-Series pickups	
28	Acrylonitrile butadiene styrene (ABS) + cork	Laminates	Hyundai	Azera	
29	PET + crushed scoria	Trim panels	Hyundai	Kia Pride	
30	Advanced thermoplastic polyolefin	Step assist	GMC	Safari	[32]
31	Nylon 6	Timing belt	Toyota	–	
32	Nylon 6	Engine covers	Mitsubishi	GDI engines	
33	CFRP	Hood, roof panel with a full-width body spoiler, rocker panels, and air splitters	Chevrolet	ZR1, Z06	[24]
34	Ultramid polyamide + GF	Engine mounts, integrated hydraulic mounts	BMW	550i,750i	[26]
35	Ultramid PA6 + GF	Oil pan	Chrysler	5.7 L Hemi engines	
36	Hemp mats	Body panels	Kestrel electric	-	

3.1 Polymer Composite Application in the Automobile Industry

Table 3 summarizes the use of PMC in the automotive industry. The application variety can be seen from the interior of automobiles, their floorings, support structures, door panels, up to their exterior.

Ford, Volkswagen, and Toyota are leading researchers in the use of NF as reinforcement in PMC for automotive applications.

4 Research Gap/Future Scope

In the last few decades, significant research has been carried out in enhancing the properties of polymer composites using synthetic reinforcements. The results observed were promising for their applications. Although due to environmental concerns, their ineffectiveness in recycling has been the cause to explore new materials for generalized applications. This identified gap can be eliminated by exploring the use of natural fibers in polymer composites as reinforcements. As discussed above, incorporating nettle fiber along with PLA has significantly improved the tensile strength of the composites. Similarly, natural fibers, such as PALF, bamboo, wood fibers, and banana fibers, find their application in light-duty applications. Emphasizing these fibers can increase the application area of composites. Techniques such as the use of coupling agents, hybridization of fibers, use of nanofillers reinforcements, enhancement of surface morphology of fiber reinforcements, functionalization of the fillers, and matrix can be incorporated for enhancing the properties of these fillers/matrix, thus expanding the scope of applications.

5 Conclusion

Many techniques have been used by automakers for the sustainable development of the automobile. Downsizing, redesigning, electrification, use of better fuel sources, and use of lightweight materials are the most sought methods that automakers adopt. The above literature survey demonstrates the use of PMC in the automotive sector for sustainable development. PMC has helped in the smart designing of the automotive component, considered very crucial in weight reduction due to the flexibility of manufacturing. It can be observed that a gradually increasing trend of the use of fiber-reinforced polymer matrix composite in the automotive sector is being formed. Enhancing the properties of the PMC by coupling them with reinforcements has helped to extend the applications in the auto industry. But there is still a need for extensive research in the application of the reinforced PMC in automobiles, as the use of natural fiber-reinforced PMC has shown better results, concerning the economic

impact, environmental impact, and health hazards than the synthetic fiber-reinforced PMC.

Hence, it can be concluded that the use of polymer composites for weight reduction is one of the viable options for the sustainable development of the automotive industry, which has the potential to satisfy all three criteria of the environment, economic, and society of sustainability. Furthermore, based on the results shown in the above literature; the usage of the natural fiber-reinforced PMC in the automotive industry needs to be researched extensively, to explore its full application potential.

References

1. Stoycheva S, Marchese D, Paul C, Padoan S, Juhmani A, Linkov I (2018) Multi-criteria decision analysis framework for sustainable manufacturing in automotive industry. J Clean Prod 187:257–272
2. Mhapankar MM (2018) Weight reduction technologies in the automotive industry. https://www.aranca.com/knowledge-library/special-reports/ip-research/weight-reduction-technologies-in-the-automotive-industry. Accessed 7 May 2021
3. Patil A, Patel A, Purohit R (2017) An overview of polymeric materials for automotive applications. Mater Today Proc 4(2A):3807–3815
4. Sapuan SM (2017) Composite materials. In: Sapuan SM (ed) Composite materials. Butterworth-Heinemann, pp 57–93
5. Francis R, Gopalan GP, Sivadas A (2016) Introduction. Recycl Polym 1:1–10
6. Rajab MA, Shaban SY, Hussen LJ (2018) Recycling and improving the environmental impact of plastic waste. Am J Eng Res 7(11):131–134
7. Wang L-G, Zhang N (2015) Sustainable development of China's commercial vehicles. Adv Manuf 3:37–41
8. Fitzgerald B, Mazumdar S (2018) Major light weighting trends shaping the automotive industry
9. Mayyas A, Shen Q, Mayyas A, Abdelhamid M, Shan D, Qattawi A, Omar M (2011) Using quality function deployment and analytical hierarchy process for material selection of body-in-white. Mater Des 32(5):2771–2782
10. Adesina OT, Jamiru T, Sadiku ER, Ogunbiyi OF, Beneke LW (2019) Mechanical evaluation of hybrid natural fibre–reinforced polymeric composites for automotive bumper beam: a review. Int J Adv Manuf Technol 103:1781–1797
11. These 4 high temp plastics can take the heat-craftech industries—high-performance plastics. https://www.craftechind.com/heat-resistant-plastics/. Accessed 7 May 2021
12. Gorter T, Reinders AHME (2012) A comparison of 15 polymers for application in photovoltaic modules in PV-powered boats. Appl Energy 92:286–297
13. Jose JP, Joseph K, Advances in polymer composites: macro- and microcomposites—state of the art, new challenges, and opportunities, In: Thomas S, Kuruvilla J, Malhotra SK, Goda K, Sreekala MS (eds) Polymer composites. Wiley, pp 1–16
14. Varga LJ, Bárány T (2020) Development of polypropylene-based single-polymer composites with blends of amorphous poly-alpha-olefin and random polypropylene copolymer. Polymers 12(6):1429
15. Mortazavian S, Fatemi A (2015) Effects of fiber orientation and anisotropy on tensile strength and elastic modulus of short fiber reinforced polymer composites. Composites Part B Eng 72:116–129
16. P. Santos P, Amarasekera J, Moraes G, Plastics S (2008) Natural fibers plastics composites for automotive applications. In: Paper presented at automotive composites conference on the road to lightweight performance (ACCE 2008), pp 492–500

17. Palabiyik M, Bahadur S (2002) Tribological studies of polyamide 6 and high-density polyethylene blends filled with PTFE and copper oxide and reinforced with short glass fibers. Wear 253(3–4):369–376
18. Kumar N, Das D (2017) Fibrous biocomposites from nettle (Girardinia diversifolia) and poly(lactic acid) fibers for automotive dashboard panel application. Compos B Eng 130:54–63
19. Chollakup R, Tantatherdtam R, Ujjin S, Sriroth K (2011) Pineapple leaf fiber reinforced thermoplastic composites. Effects of fiber length and fiber content on their characteristics. J Appl Polym Sci 119:1952–1960
20. Chand N, Dwivedi UK (2006) Effect of coupling agent on abrasive wear behaviour of chopped jute fibre-reinforced polypropylene composites. Wear 261(10):1057–1063
21. Daramola OO, Taiwo AS, Oladele IO, Olajide JL, Adeleke SA, Adewuyi BO, Sadiku ER (2021) Mechanical properties of high density polyethylene matrix composites reinforced with chitosan particles. Mater Today Proc 38(2):682–687
22. Kweon H, Ha HC, Um IC, Park YH (2001) Physical properties of silk fibroin/chitosan blend films. J Appl Polym Sci 80:928–934
23. Ayrilmis N, Jarusombuti S, Fueangvivat V, Bauchongkol P, White RH (2011) Coir fiber reinforced polypropylene composite panel for automotive interior applications. Fibers Polym. 12:919
24. Jacob A (2011) Carbon fibre use increasing in the automotive industry—materials today, mater. Today. https://www.materialstoday.com/composite-applications/news/carbon-fibre-use-increasing-in-the-automotive/. Accessed 9 July 2020
25. Bakewell J (2018) The case for carbon fiber | article | automotive manufacturing solutions. https://www.automotivemanufacturingsolutions.com/automation/the-case-for-carbon-fibre/36250.article. Accessed 9 July 2020
26. Stewart R (2020) Rebounding automotive industry is welcome news for FRP sector—materials today. https://www.materialstoday.com/composite-applications/features/rebounding-automotive-industry-is-welcome-news/. Accessed 9 July 2020
27. Ganesan K, Kailasanathan CK, Kumarasamy Y (2015) Analysis of composite leaf spring enhanced with nanoparticles. Carbon Sci Technol 7:34–42
28. James H, Dan H (2006) Natural-fiber-reinforced polymer composites in automotive applications. JOM 58:80–86
29. Djafari Petroudy SR (2017) Physical and mechanical properties of natural fibers. In: M Fan, Feng Fu (eds) Advanced high strength natural fibre composites in construction. Woodhead Publishing, pp 59–83
30. Akampumuza O, Wambua PM, Ahmed A, Li W, Qin X-H (2017) Review of the applications of biocomposites in the automotive industry. Polym Compos 38:2553–2569
31. Malnati P (2018) Recycled waste products get new life as lightweight cost-effective auto parts. Plast Eng 74:18–25
32. Edser C (2002) Auto applications drive commercialization of nanocomposites. Plast Addit Compound 4(1):30–33

Predicting Remaining Useful Life of Capping and Filling Machine Using Exponential Degradation Model with Web Server Deployment

Devang J. Gajjar, Shrey A. Shah, and Sneh Soni

Abbreviations

BPM   Bottles per minute
RUL   Remaining useful life
OPC   Open Platform Communication
SQl   Structured Query Language
DSN   Data source name
PCA   Principal component analysis
PLC   Programmable logic controller
HMI   Human–machine interface
VFD   Variable frequency drive
FTP   File Transfer Protocol
ODBC   Open Database Connectivity
GUI   Graphical user interface
SLMP   Seamless Message Protocol

1 Introduction

Maintenance had always been an important factor in industries, and a lot of money is spent on it; where predictive maintenance has been a boom in recent times, it helps in increasing the lifetime of equipment by many years and henceforth increases its efficiency, productivity, and reliability alongside decreasing downtime caused by unexpected failures caused by several hazards like fire, short circuit, pharmaceutical hazards, plant shutdowns, etc. [1], enabling monetary gains and feasibility for the

D. J. Gajjar · S. A. Shah · S. Soni (✉)
Instrumentation and Control Department, Nirma University, Ahmedabad, India

organization. It implements the strategy of data analytics to analyze the state of equipment by comparing it with a ton of historic sensor data eventually predicting the time after which maintenance has to be done with minor ambiguity based on data. Unplanned or reactive maintenance can have estimated costs of up to $50 billion per year in big enterprises. This is where predictive maintenance comes into play. On the other hand, when preventive maintenance [2, 3] was implemented in an industry, then around 70% of the time transmitters had no problems, and when predictive maintenance was implemented, that figure rose to 90% [4].

In this project, we are using the vibration data of the accelerometer to analyze the state of the system and to determine the remaining useful life to ultimately maintain its health by doing maintenance at regular time intervals. The basic flow of operation is programming PLC to obtain sensor data, saving that real-time sensor data in tabular format to SQL database using an OPC server, and accessing the database from MATLAB using ODBC connector feeding the data to algorithm which processes the signal and extracts necessary data for post-processing for remaining useful life (RUL) determination using exponential degradation model. These results are shown graphically to the user in the form of an app and also deployed on MATLAB Web app server so that people not having MATLAB can monitor the health of the machine through a Web site accessible through a specific URL from any device connected to a local area network.

2 Filling and Capping Machine

Filling and capping machine is an automated system generally used in pharmaceutical industries to fill medical liquids and apply caps on bottles of various sizes operating without any human intervention at speeds up to 300 bottles per minute (BPM). The filling machine involves a linear conveyor and a rotational cam follower, and gear-based assembly driven by the main motor. Two pneumatic cylinders are used to stop a set of eight bottles on the conveyor, and the mechanically synced assembly fills these bottles with the liquid stored in the storage tank. In such a manner, bottles are filled continuously, and the liquid stored in a tank is stirred to maintain desired pharmaceutical standards.

Capping machine [5] (refer Fig. 1) kept in series with the filling machine comprises a linear conveyor along with assembly consisting of a star wheel (to accumulate the bottles and caps) and a rotational CAM-based multi-head screw capping assembly driven by conveyor motor and main motor, respectively, also like capping machine, and here conveyor motor and main motor are linearly synchronized to achieve desired BPM set by the user. A cap vibrator provides the required caps, and the whole assembly's height can be adjusted as per the size of the bottle (Fig. 2).

These systems are controlled via FX5U PLCs, and FR-D700 VFDs are used to drive motors. GS2110 HMI screen subsequently provides access for a user to control the whole system based on the level of control granted to him by the administrator from levels like admin, manager, supervisor, and operator depending on industrial
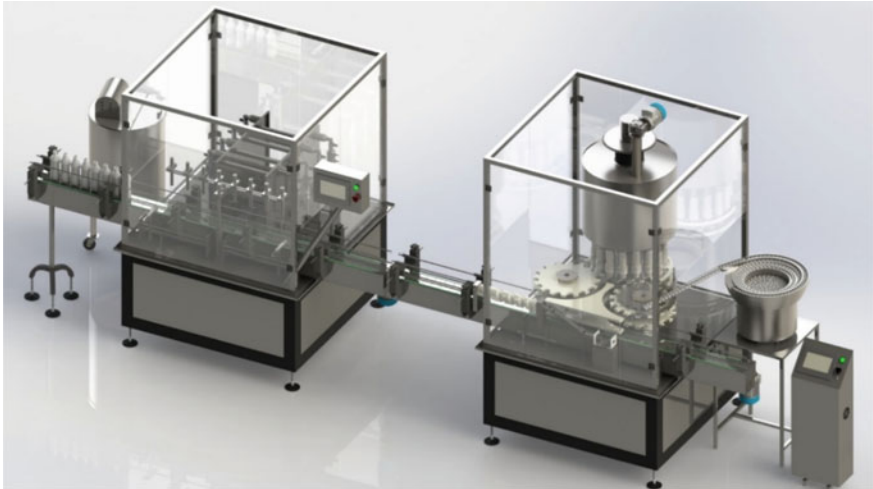
Fig. 1 Capping machine (right) and filling machine (left)
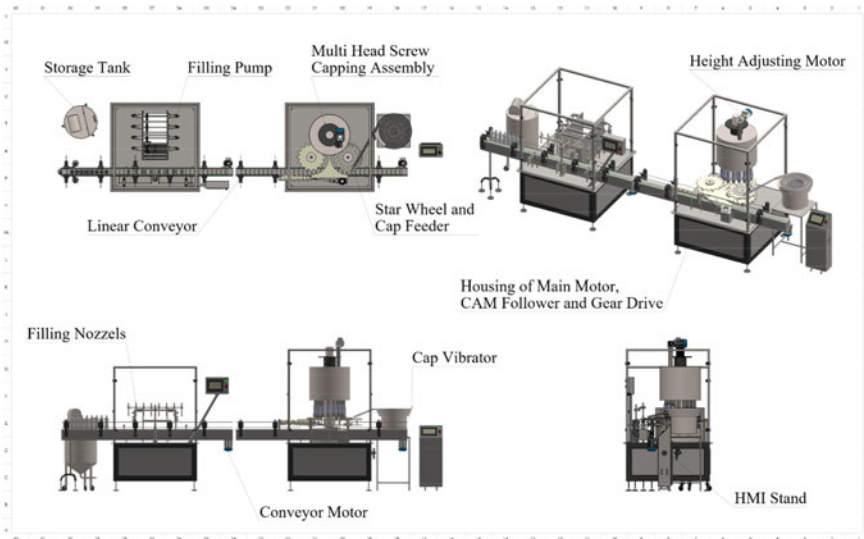
Fig. 2 Various subassemblies of the capping and filling machine

standard. The regularly generated is logged and transferred from HMI to the laptop using the File Transfer Protocol (FTP) [6] subsequently MODBUS-based inverter protocol is used to update the parameters of VFD directly from HMI, saving manual efforts.

3 Data Acquisition Via KEP Server

The process of predicting RUL begins from collecting real-time sensor data. KEP server is a platform that provides users with OPC [7] and other industrial-friendly protocols such as ODBC and SLMP. It acts as a single source where all the automation data can be accumulated for different applications [2]. Generally, OPC [8] offers an interface between software (in OS) and hardware (controllers) and helps in real-time monitoring, control, and data transfer. It helps in creating a connection between PLC and SQL database in our case. The connection between KEP server [9] and PLC is established through TCP/IP protocol [7] and a port number by providing an IP address of the same series as the IP of PLC. The PLC side settings involve the inclusion of the SLMP module which is for the connection of PLC with external devices (Figs. 3 and 4).

However, the connection between KEP server and MariaDB SQL can be done using the ODBC driver of MariaDB SQL which is a standard database driver using

Fig. 3 Tags monitored by KEP server
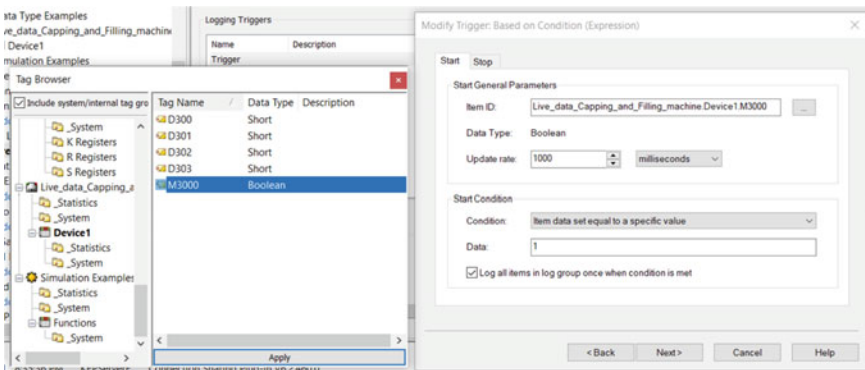
Fig. 4 KEP server settings for logging 6 s data when a signal to log data is given by PLC

industry standard ODBC API. Furthermore, the database source name (DSN) has to be configured in the KEP server along with the table name and the samples to be collected by a triggering condition. This is accomplished by using the data logger functionality of the KEP server to successfully create a real-time connection between PLC and SQL database.

4 MariaDB SQL Database

MariaDB SQL server is a popular open-source relational database that works on MySQL statements. A database can be created, and hence, a DSN can be formed using MariaDB. MariaDB is used as a database, and structured tables with sensor data from PLC are created in it (Fig. 5).

The table formed has the following columns: Numeric ID, Name, Value, Quality, and Timestamp (refer Fig. 6). Numeric ID refers to the number of data, Name is the register whose data is logged into the KEP server, Value is the value of that register, Quality determines the quality of the connection between PLC and KEP server (connected or disconnected), and Timestamp is the time when the value of the register is recorded.

This table is then finally connected with MATLAB using the database connector in MATLAB for further processing.
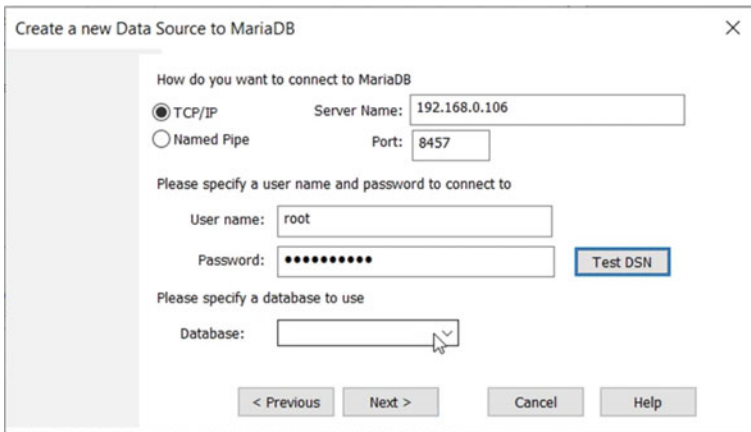
Fig. 5 ODBC driver setting for MariaDB connection

Fig. 6 Example of a table created by the KEP server to log data in SQL

5 Deployment of Predictive Maintenance Algorithm

MATLAB itself is used to get the data from MariaDB SQL in tabular format for processing in the predictive maintenance algorithm and to host the results on the Web site using MATLAB Web app server and in the form of GUI designed in App Designer. The data is collected by configuring DSN in MATLAB and selecting the appropriate database or with the help of the Database Explorer App in MATLAB.

MATLAB App Designer is an app for creating UIs for scripts running in the back end which can further be packaged and deployed as a stand-alone Web site using the MATLAB Web app server. Our UI consists of the result data in the form of a plot, the speed of the conveyor, stirrer motor speed, main motor speed, and the RUL with the highest probability. A "live" button is present which when selected would get the real-time data from the machine through the PLC process along with the historical data saved from operation since day 1 and updates both plots and speed indicators.

Predictive maintenance is one of the three types [2] of maintenance that holds high regard in the industry [3]. The primary source of running the algorithm is MATLAB's predictive maintenance toolbox. The algorithm utilizes the exponential degradation model to predict the RUL [10]. The exponential degradation model uses a threshold value to evaluate RUL based on health indicators (features extracted from sensor data). This model implements a continuous-time exponential degradation model [11] given as follows:

$$h(t) = \varphi + \theta e^{\left(\beta t + \epsilon - \frac{\sigma^2}{2}\right)} \tag{1}$$

where $h(t)$ = health indicator, φ = y intercept, β = slope of Gaussian distribution, θ = slope of lognormal distribution, ϵ = Gaussian white noise, and σ = standard deviation.

The data set for this is collected from an accelerometer-based vibration sensor mounted on a bearing of the capping assembly (a very critical component of the capping machine), and it includes data for vibration of the shaft. Daily the vibration signal for 6 s duration is collected once the main motor reaches a steady state. The steps involved in executing the predictive maintenance algorithm are as follows:

- Import this data to MATLAB and store it in the form of a MAT file for future reference.
- Explore data to find a pattern that leads to degradation [12]. In our case, as the system approaches failure, the vibration signal gets aggressive.
- The next step is to find the key indicators/features which triggered this impulsiveness [13]. In our case, these indicators were peak-to-peak value, spectral kurtosis, etc. Certain mathematical features such as mean, standard deviation, and skewness also hold as key indicators, which might cause this outcome [14].
- So as a part of post-processing, derive all the above-mentioned variables from the signal (sensor data) and process them further to remove noise using filters like moving mean filter to smooth the signal [15].
- Then find the importance ranking of each feature to simplify the further task. This is done by finding the monotonicity of all the features and comparing it. Where monotonicity for a particular feature is near to 1, then it means it holds a high rank and is more important, and if it is near to 0, then vice versa. By calculating this, it was found that Kurtosis held the highest rank followed by a few other features. The features with a monotonicity value less than 0.35 were eradicated which ultimately reduced the number of variables that affect the outcome [12].
- Further dimension reduction is required for simplification, and it is done using the principal component analysis (PCA) [16]. Normalization of features using mean and standard deviation is required before executing PCA [12]. The principal components, which have the highest effect, are then considered as the health indicator for the system. The threshold is considered as the least value of this health indicator.
- Finally, the exponential degradation model is implemented by giving the values to different constants which are involved in the model as described in Eq. 1. This model gives the output values of estimated RUL, confidence interval of RUL, and probability density function of RUL. While performing degradation in the model as the value of health indicator crosses the threshold, it concludes the prediction [12, 16]. These obtained results are plotted in the app whenever data is updated or the "Live" button is pressed (refer Fig. 7).
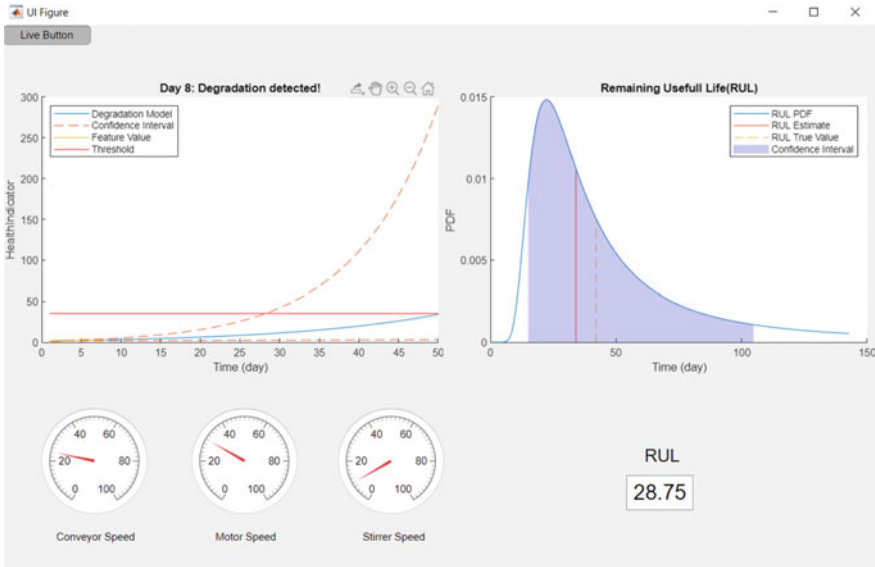
Fig. 7 Designed GUI as a MATLAB application to monitor real-time machine parameters and RUL prediction

6 MATLAB Web App Server

MATLAB Web app server provides a medium for Web apps in MATLAB to be accessed on a system without having MATLAB [17] installed by deploying it in the form of a Web site. Once the MATLAB App is designed, it is packaged in the ".ctf" format using the MATLAB compiler. This MATLAB app is now a deployable Web app. The files are further copied in the "apps" folder of the Web server to upload the Web app on the Web app server. The Web server has to be then configured by providing it with a free port number (by default 9988), start-up timeout, and session timeout. A secure connection can also be established by using the SSL option enabling HTTPS extension instead of HTTP in URL. This generates a URL to access the home page of our Web app server. The URL accessible by any device on the local area network is in the form of or http://user:PortNumber/webapps/home/index.html IP address replaced by host's user name.

This Web server runs only on an Ethernet-based local area network or on the same Wi-Fi connection between the server and clients (Fig. 8).

The above figure shows the configuration window of this Web app server and the simplicity it provides to use it.
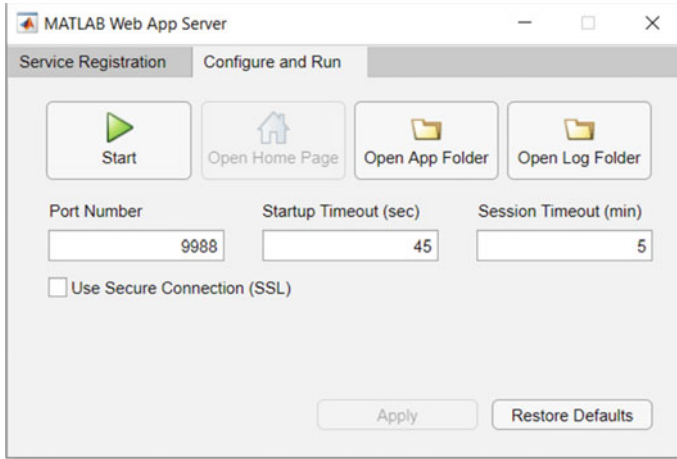
Fig. 8 Web app server configuration window

7 Results

As the algorithm performs prognostics on sensor data, desired output of estimating the remaining useful life of the system is obtained and represented in the form of these plots.

The plot comprises the value of the health indicator which follows the degradation model as shown by the blue line. The red line indicates the threshold value which signifies that when the value of the health indicator crosses it, the prediction is done and the computation is concluded to determine the final RUL. The plot on the right side indicates the probability density function based on the estimated RUL of the system (refer Fig. 9), and even for sake of simplicity, we are showing no days remaining before the part failure for a user to prepare the maintenance process.

The same thing is deployed on the Web server through which anyone on the same network (LAN) can access the Web site and all the calculations on sensor data are performed daily on a computer where the Web server is hosted and updated for users (generally management team) to plan down time and reduce it. This Web site can be accessed by anyone on the Internet as of the host device (see Fig. 9).

The Web site is accessible from any kind of device which can open a Webpage as over here we have also tested it on a Raspberry Pi microcontroller (which deploys a form of Linux) through which the Web site was accessed (Fig. 10).
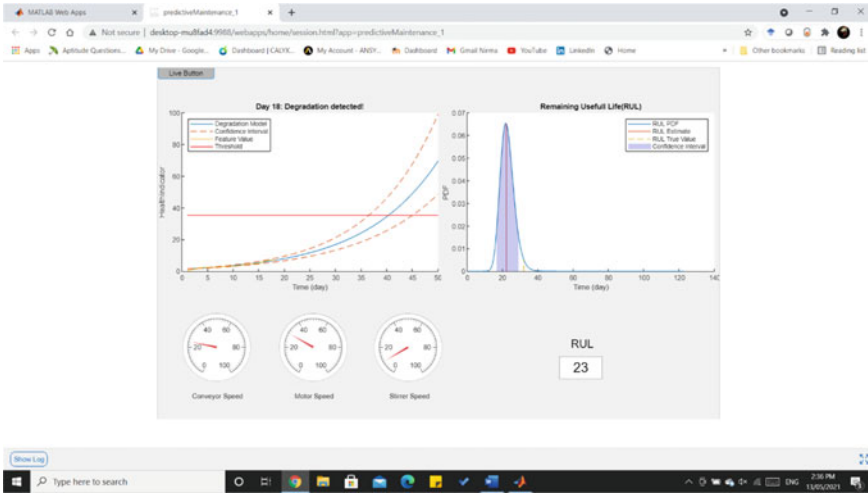
Fig. 9 Predictive maintenance result plot and RUL estimation on Web server
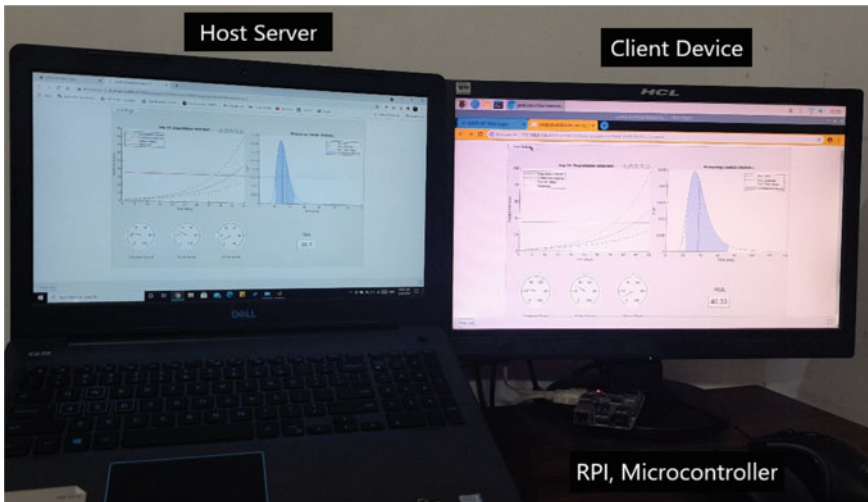
Fig. 10 Web site accessed by the user using microcontroller (RPI 3b+) in Raspbian OS, demonstrating Web site accessibility by any device present in same local area network as of host device

8 Conclusion

Processing the sensor data using technologies like prognostics and data analytics is deployed in the form of an algorithm. Remaining useful life of the system can be predicted where simple historical failure data or sensor data collected during

healthy working conditions and slight tuning based on the system are required. Such prediction of the system's health in real time helps in reducing physical hazards caused by a part failure and maximizes the productivity of the system boosting the quality of work done and leveraging monetary benefits gained through consistent operation machines along with ease to plan maintenance cycles.

Exponential degradation model assured proper prognostics of assembly part feeding health indicator derived based on the process of features extraction, feature ranking, and principal component analysis from the collected data of accelerometer-based vibration sensor. Due to the presence of healthy condition, sensor data threshold values were derived by the algorithm eliminating manual error caused by threshold estimation and increased the confidence interval of RUL prediction in results. Deployment in the form of an App provides ease to the user. The availability of functionality like Web servers helps to access the results by any device connected in the same local area network. Due to the scalability of this technology by minor changes, it can be used for a vast range of systems ranging from small bearings to whole aircraft engines simply by the usage of proper sensors.

Future Work
Currently, the proposed project is deployed locally requiring a computer, which can be accessed globally by deploying this algorithm on MATLAB production server and connecting it with AWS or Microsoft Azure for storing data and hosting a Web site securely accessible by anyone through the globe via the Internet. We can use unsupervised learning once we have a large amount of data set collected by the current system for more accurate predictions and also deploy that on the cloud [18]. The proposed algorithm can be implemented with minor modifications for other machine's prognostics.

References

1. Alhasadi R (2020) Licensed under creative commons attribution CC BY industrial hazards and safety measures in pharmaceutical industries
2. Jezzini A, Ayache M, Elkhansa L, Makki B, Zein M (2013) Effects of predictive maintenance (PdM), proactive maintenance (PoM) & preventive maintenance (PM) on minimizing the faults in medical instruments. In: 2013 2nd International conference on advances in biomedical engineering, Tripoli, Lebanon, pp 53–56. https://doi.org/10.1109/ICABME.2013.6648845
3. Wickern MZ, Vincent (2019) Challenges and reliability of predictive maintenance. https://doi.org/10.13140/RG.2.2.35379.89129.
4. Hashemian HM (2011) State-of-the-Art predictive maintenance techniques. IEEE Trans Instrum Meas 60(1):226–236. https://doi.org/10.1109/TIM.2010.2047662
5. Violante M, Sinapi P (2019) Digital twin for a single head capping machine
6. Rahim R, Lubis S, Wibowo P, Harahap AKZ, Suleman A, Sihombing EE, Harputra Y, Rambe MR, Siahaan APU, Her-Mansyah H, Riswanto A, Prasnowo M, Djanggih H, Karinda K, Nasrudin N, Wilda I (2018) Prototype file transfer protocol application for LAN and Wi-Fi communication. Int J Eng Technol (UAE) 7:345–347
7. Dongjiang L, Ruiqi S (2011) Implement of communication between configuration software and OPC server based on Modbus/TCP. In: IEEE 2011 10th international conference on electronic

measurement & instruments, Chengdu, China, pp 218–221. https://doi.org/10.1109/ICEMI.2011.6037717

8. Liping Z, Aiqun Z, Yunsheng Z (2007) On remote real-time communication between MATLAB and PLC based on OPC technology. In: 2007 Chinese control conference, Zhangjiajie, China, pp 545–548.https://doi.org/10.1109/CHICC.2006.4346760

9. Ćwikła G, Foit K (2017) Problems of integration of a manufacturing system with the business area of a company on the example of the integrated manufacturing systems laboratory. MATEC Web Conf 94:06004. https://doi.org/10.1051/matecconf/20179406004

10. Zhou R, Serban N, Gebraeel N (2011) Degradation modeling applied to residual lifetime prediction using functional data analysis. Ann Appl Stat 5. https://doi.org/10.1214/10-AOAS448

11. Gebraeel N (2006) Sensory-Updated residual life distributions for components with exponential degradation patterns. IEEE Trans Autom Sci Eng 3(4):382–393. https://doi.org/10.1109/TASE.2006.876609

12. Anis MD (2018) Towards remaining useful life prediction in rotating machine fault prognosis: an exponential degradation model. 1–6. https://doi.org/10.1109/CMD.2018.8535765.

13. Fernandes M, Canito A, Bolón-Canedo V, Conceição L, Praça I, Marreiros G (2019) Data analysis and feature selection for predictive maintenance: a case-study in the metallurgic industry., Int J Inf Manage 46. ISSN 0268-4012

14. Ali JB, Saidi L, Harrath S, Bechhoefer E, Benbouzid M (2018) Online automatic diagnosis of wind turbine bearings progressive degradations under real experimental conditions based on unsupervised machine learning. Appl Acoust 133:167–181. https://doi.org/10.1016/j.apacoust.2017.11.021

15. Saxena A, Celaya J, Roychoudhury I, Saha B, Saha S, Goebel K (2012) Designing data-driven battery prognostic approaches for variable loading profiles: some lessons learned. 10

16. Sehgal S, Singh H, Agarwal M, Bhasker V, Shantanu (2014) Data analysis using principal component analysis. In: 2014 International conference on medical imaging, m-health and emerging communication systems (MedCom), Greater Noida, India, pp 45–48. https://doi.org/10.1109/MedCom.2014.7005973

17. Suzana U (2006) MATLAB web server and m-file application. 2088–2092. https://doi.org/10.1109/EPEPEMC.2006.4778715

18. Wang J, Zhang L, Duan L et al (2017) A new paradigm of cloud-based predictive maintenance for intelligent manufacturing. J Intell Manuf 28:1125–1137

Performance Assessment of Internet of Things Implementation in Fleet Management Project—Schedule of Rate: An Oil Marketing Company Case Study

Anudeep G. Chandak, D. N. Raut, and Gunjan Yadav

1 Introduction

The usage of Internet of Things (IoT) is being rapidly increasing in all sectors and not restricted to any specific domain. Almost all the sectors, viz. healthcare, utilities, automotive, government organization, manufacturing, etc., have seen extensive exposure to the IoT. Due to industrialization and globalization, companies are coming up with best technologies and then can to provide the best customer satisfaction. The private and commercial fleet market has been severely underserved by technology, and hence, technological enhancement in fleet management plays a vital role in boosting transportation business. The recent demand of the customer involves better accountability, real-time data availability, remote operation, etc.

This research paper guides a stepwise walkthrough of the factors causing hindrance to the change of the fuel prices. The term RSP, i.e., Retail Sale Price, defines the change of the fuel prices by establishing the connection in between the retail outlet and Host of Server (HoS) of ABC company. The prices of fuel are determined by the Oil Marketing Companies (OMCs) by considering the crude oil price, taxation, gross refining margin (GRM), etc. Crude oil is being a commodity and the prices of it keeps on fluctuating, and hence, the fuel prices must be changed on daily basis.

A. G. Chandak (✉) · D. N. Raut
Production Engineering Department, Veermata Jijabai Technological Institute (VJTI), Mumbai, Maharashtra, India
e-mail: agchandak_m19@ci.vjti.ac.in

D. N. Raut
e-mail: dnraut@pe.vjti.ac.in

G. Yadav
Mechanical Engineering Department, Swarnim Startup and Innovation University, Gandhinagar, Gujarat, India
e-mail: hod.me@swarrnim.edu.in

1.1 Literature Review

The research conducted by Gupta et al. [1] on the 'IoT-based smart petrol pump' involves wet stock management through web server where the architecture involves hardware component measuring fuel level at filling station and communicating to the central server. The motive to establish the network in-between the server and filling station the website takes fuel level as the input from the hardware installed at the filling station and data is communicated to admin and user admin having editable option, whereas user can only view the data. In another research by Hubert Shanthan [2] on 'Filling Fuel Quantity Measurement Systems Using Internet of Things,' the work emphasizes to check the fraudulence happing at the fuel filling station through the dispensing units are been digitalized. The IoT application involves measuring quantity of fuel while dispensing through sensors and sending communication to user post filling. Research fellow Naveen Kumar et al. [3] and team explored an another IoT application, i.e., 'IoT-based retail automation of fuel station and alert system'; they highlighted the pain area of customer while filling the fuel the operator diverting customer attention while filling fuel and refill the fuel without resetting the nozzle setting and also established a system where the hourly data of sales and stock was been provided to owner. Ravichandran [4] gave his contribution in IoT usage by his research work on 'IoT in Fuel Station and Service Station Location' which involves identifying the fuel level in vehicle tank and locating the nearest fuel filling station to it. The architecture consists of three dialog boxes such as map, vehicle statistics, and service station. The system has ability to notify the threshold of fuel level in vehicle tank and tell the fuel filling station in its proximity. A behavioral study was been carried out by Harida et al. [5] on 'Internet of Things (IoT) Enabled Automation: A Shift toward Smart Fuel Stations' which involves measuring the operational efficiency prior to and post deployment of IoT in petrol pumps a survey-based research work considering factors cost, security, time payment ease using paired t-test. Model was proposed providing the extensional framework for automating the operation of petrol pumps. Vijyakumar et al. [6] added his contribution to IoT application in fleet management work with his topic 'IoT-based smart fuel monitoring system.' The research work involves remote monitoring and data collection system deployed at the site of the fuel storage tank. The computer takes fuel tank level information from the sensor, analyzes the data using sensor edge, and finds the pattern in it by edge analytics technology. It has full connectivity and compatibility with Internet Android mobile. There is a need of error robust fleet management because the scalability in transportation business is increasing so considering the data generated out of it should have the least error and infrastructure cost involved and a research was done on Yadav et al. [7] on 'Lean Six Sigma: a categorized review of the literature' which drives us to the importance of emerging aspects, trends and importance of Lean Six Sigma through reviewing the published literature over multiple parameters for an ameliorating and trenchant view. The finding of this came out as LSS is growing rapidly, covering various disciplines and domains with a great focus on LSS tools and techniques; empirical research is dominant with more emphasis on case

study approach; and growing gap between manufacturing- and service-focused articles implies return of LSS to manufacturing as its initial base. Financials are the key for any business, and the gross refining margin (GRM) is one factor which decides fuel prices; hence, some insights were gathered by the research work by Yadav et al. [8] on 'Development of a lean manufacturing framework to enhance its adoption within manufacturing companies in developing economies' which emphasized on the studying and proposing the lean manufacturing framework and also documented the drivers of lean manufacturing among the manufacturing industries of emerging economies. Pump manufacturing was sector chosen to implement the lean manufacturing models, and organizational performance metrics were documented. The sole is to prevent the theft happening gas filling station. Exploring the other application of IoT Yadav et al. [9] came up with research topic 'A framework to overcome sustainable supply chain challenges through solution measures of Industry 4.0 and circular economy: An automotive case.' The study figured out 28 Sustainable Supply Chain Management (SSCM) challenges and developed the framework which was analyzed through hybrid BWM-ELECTRE approach and proposed 22 solution measures of Industry 4.0 and circular economy. Effective strategies to overcome SSCM adoption failures were also suggested. A study by Yadav et al. [10] exploring indicators of circular economy adoption framework through a hybrid decision support approach as fuel being a commodity which affects the economy on nation appreciable the fuel prices are something we more critical element to keep on inflation rate of the country. The research came with the 31-circular economy (CE) indicator and proposed the framework to an Indian manufacturing company to improve the CE adoption process; the study was quantified by the hybrid BMW—DEMATAL approach which demonstrated intensity and interrelationship among the CE indicators. So, we had some testimonial for adoption of IoT in fleet management system a study by Bag et al. [11] on 'Key resources for Industry 4.0 adoption and its effect on sustainable production and circular economy: An empirical study helped how the IoT Industry 4.0 has served the manufacturing sector and adoption of industry 4.0 has a positive relationship with sustainable production.' Sustainable production can help to develop circular economy capabilities and this finding of study was supported by developing testable model using RBV theory as a theoretical lens and suggestion were made to the manufacturing firm to engage suppliers into various R&D programs to develop successful CE business models.

1.2　Finding and Exploring New Area for IoT Implementation in Fleet Management

The research scholars have figured out various ways in implementing IoT in fleet management system which ultimately focused on the pain areas of the end user and owner operating the fuel filling station. Moving ahead we could see that all research area involves IoT implementation post setting of the fueling price; i.e.,

once the fuel prices are fed into the dispensing unit and later measures are taken to implement IoT so as improve the efficiency customer satisfaction, check fraudulence, etc. Implementing IoT before feeding the fuel price motivates to study the newer area IoT implementation before setting the fuel prices.

The change in the fuel price is important so as check the manual intervention of price change by the owner of the filling station. Also, there may be an arbitrage issue related to fuel prices, say for example on day 1 the fuel price were 89 INR per lit and on day 2 fuel price decreased to 88 INR per lit, so if fuel prices are not updated at the fuel filling station through server the sale will happen will old price which is higher than the actual that should be on day 2.

1.3 How the Fueling Price Change

a. The fuel prices are decided a day before on which they are implemented; the data is uploaded in the master server, i.e., ABC's Host of Server (HoS) with its validity; i.e., the price will be only for duration 6:00 A.M. to 5:59 A.M (23-h 59 min.).

b. The ABC HoS will send the price value to forecourt controller (FCC)
     FCC is an electronic device; it is placed in the cabinet or says the office at the fuel filling station. Now each dispensing unit has a communicating device called nano-pass interface router (nPIR) and CnPIR—the central nano-pass interface router—which is placed in cabinet through Zigbee networking protocol; the communication is established in between the ABC company HoS and the CnPIR through, and fueling price is feed to it which later is communicated to all the nPIR installed at the dispensing units at the filling station.

c. Whenever the price will be pushed by the server, the FCC will accept it; this action is termed as 'price queried.'

d. The FCC will send the acknowledgement to the HoS server confirming that the price has been received this is termed as 'retail sale price (RSP) Queried.'

e. In the morning 6:00 AM, the FCC must change the fuel price in the system, i.e., the fuel filling station and same need to confirm the HoS that the fuel price is been updated and will be valid for the duration mentioned, i.e., 6:00 AM to 5:59 AM (next day) 'retail sale price (RSP) queried and acknowledged.'

After knowing the process flow of price update activity, we came across two major cases which affect the retail sale price (RSP) not happen and they were:

i. RSP Queried but NOT Acknowledge: The price is pushed by HoS to the FCC and FCC acknowledge that the price has been received; while changing the fuel price in the morning at 6:00 AM, the FCC did not communicate and acknowledge about the price change to the HoS.

ii. RSP Not queried: The price from the HoS was pushed to the FCC but FCC didn't acknowledge that the updated fueling price was received to him.

Benefit of the technology lies in its successful rollout, and in the current scenario, the system seems to be disjoint and needs to focus on increasing scalability and access; reduction in IT cost and infrastructure needs and achieve integrated fueling system.

To address problem, data was collected from all the retail outlet of ABC company over span of 85 day in between Jan 6th, 2021, and May 12th, 2021, the data was collected for 2440 retail outlet (RO) in India, which involves finding out the factors affecting RSP not to happen.

There were numerous factors that were listed while having daily review with field execution team of XYZ automation company and were broadly classified under four broad heading, viz. no connectivity problem arriving due to the very small aperture terminal (VSAT), geographical constraint, data usage of the SIM card provided for establishing the connectivity between RO and HoS. Second, factor was intermediate connectivity which occurs due geographical constraints, weather impact on specific instances. Third was hardware failure problem which consist of any problem related to architectural component involved in the price change process. The fourth and the last was operational issues which cover issues related to events which involves human intervention (fuel filling station dealer of ABC company or service delay and problems from XYZ automation company's field execution team) (Fig. 1).

After investigating, the most (as it is an in-exhausted list) of the factors and classifying them into three broad categories, viz. hardware, operational issues, and connectivity, a statistical technique needs to apply so as quantify the dominance of each factor which was affecting the RSP not happening.
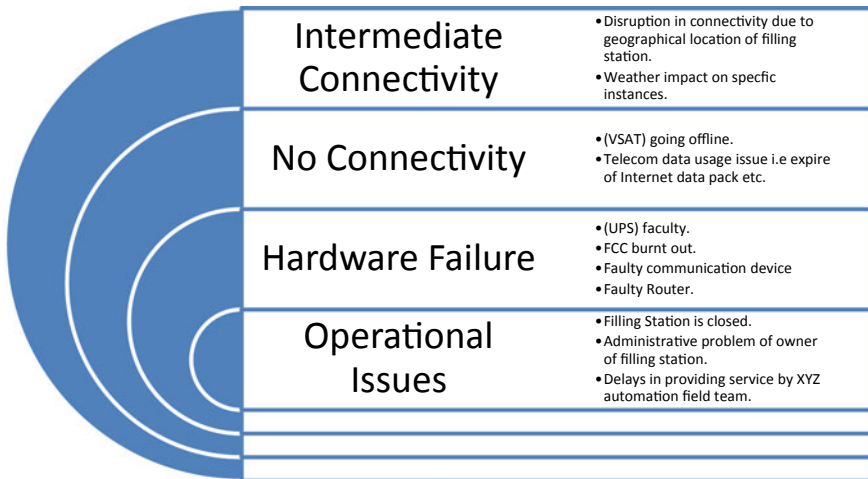
Fig. 1 Classification of the factors affecting the RSP not happening

1.4   Framing Multiple Regression Statistical Model

While choosing a statistical method, the case was structured as:

$$A \text{ dependent variable: RSP Not happening} \quad \text{say} \, 'Y' \qquad (1)$$

$$\text{Independent variable: Intermediate Connectivity} \quad \text{say} \, 'X_1' \qquad (2)$$

$$\text{No Connectivity} \quad \text{say} \, 'X_2' \qquad (3)$$

$$\text{Hardware Failure} \quad \text{say} \, 'X_3' \qquad (4)$$

$$\text{Operational Issues} \quad \text{say} \, 'X_4' \qquad (5)$$

Multiple regression analysis is adopted when there is one dependent variable which is presuming to be function of a two or more independent variables.

Framing the regression equation as:

$$Y = b_0 + b_1 X_1 + b_2 X_2 + b_3 X_3 + b_4 X_4 \qquad (6)$$

b_1, b_2, b_3, b_4 are the regression coefficients and b_0 is the intercept value.

By using excel data analysis tool the feasibility, accuracy of the model, and significance of independent variable was determined.

- The overall regression accuracy is determined by the r^2. It is measure which tell about how the variation in dependent variable Y dependent on the independent variables of the model.
- Significance F determines that the regression is not chance and tell about the realness of the model.
- P-Value tells us about the significance of the factor lesser the P-value stronger is the independent variable affecting the dependent variable.
- Residual is the difference between the actual value of dependent variable and predicted value of dependent variable.
- Here the confidence level is 95%, and hence, the significance level 5% 'α' $= 0.05$.

After solving the regression equation on 85 samples (i.e., the data collected for 85 days), the following results were drawn.

2 Results and Discussion

See Table 1.

The coefficient of determination r^2 values ranges from 0 to 1 in the above case, and the values come out to be 0.9989 which shows the independent variable Y; i.e., 'RSP not Happening' strongly depends on the independent, viz. intermediate connectivity (X_1), no connectivity X_2, hardware failure X_3, and operational issue X_4 (Table 2).

The significance factor comes out to be 6.6956×10^{-118} which is far smaller than the significance level $(\alpha = 0.05)$ this implies that the result out of regression analysis are not obtained by chance and lower significance factor show realness of result. (Table 3).

The regression equation comes out to be (Table 4):

$$Y = 0.8433 + 0.9989X_1 + 0.9349X_2 + 2.1018X_3 + 0.3115X_4 \qquad (7)$$

The t-test values of independent variables support the prominence of 'Intermediate Connectivity' factor as it has the highest value of 241.6822 followed by 'No Connectivity' and 'Hardware Failure' having values 50.0100 and 21.9243, respectively. The least value is of the factor 'Operational Issue' having value of 1.2698.

Table 1 Regression statistics

Sr. No	Description	Notation	Value
1	Coefficient of Determination	r^2	0.9989
2	No. of observation	n	85
3	Parameter (i.e., b_0, b_1, b_2, b_3, b_4)	k	5

Table 2 ANOVA

Sr. No	Description	Degree of freedom (d_f)	Significance F
1	Regression	$k - 1 = 4$	6.6956×10^{-118}
2	Residual	$n - k = 80$	
3	Total	$n - 1 = 84$	

Table 3 Calculation of regression coefficient

Sr. No	Parameters	Coefficient	Coefficient value
1	Intercept	b_0	0.8433
2	Intermediate connectivity (X_1)	b_1	0.9989
3	No connectivity (X_2)	b_2	0.9349
4	Hardware Failure (X_3)	b_3	2.1018
5	Operational Issues (X_4)	b_4	0.3115

Table 4 Determination of standard error and probability value

Sr. No	Parameters	Standard Error	t-Stat	P-value
1	Intercept	1.1677	0.7222	4.722×10^{-1}
2	Intermediate connectivity (X_1)	0.0041	241.6822	2.4523×10^{-116}
3	No connectivity (X_2)	0.0187	50.0100	4.0527×10^{-62}
4	Hardware failure (X_3)	0.0959	21.9243	1.4346×10^{-35}
5	Operational issues (X_4)	0.2454	1.2698	2.0785×10^{-1}

The P-values for the independent factor intermediate connectivity (2.4523×10^{-116}); no connectivity (4.0527×10^{-62}); hardware failure (1.4346×10^{-35}) is lesser than 0.05 and the significance level 'α'. This shows these factors are strongly influencing the independent variable 'RSP Not Happening' in order.

The P-Value and t-stat values give the priority order of factors influencing the RSP rate.

$$\text{Intermediate Connectivity} > \text{No Connectivity} > \text{Hardware Failure}$$

The factor 'Operational Issues' has P-Value (0.20785) which is greater than the significance level 0.05 (α) which implies this not a strong influencing factor and could be ignored while making any forecast (Figs. 2, 3, 4, 5, and Table 5).

The regression line of 'Intermediate Connectivity' has slope m of 0.9871 close to the '1'; this shows the direct relation of in-between 'RSP Not Happening' and 'Intermediate Connectivity' factor.

The slopes of 'No Connectivity' regression line and 'Hardware Failure' line are 1.1276 and 1.6590, respectively; though the slope are positive, they are not so close

Fig. 2 Intermediate connectivity line fit plot
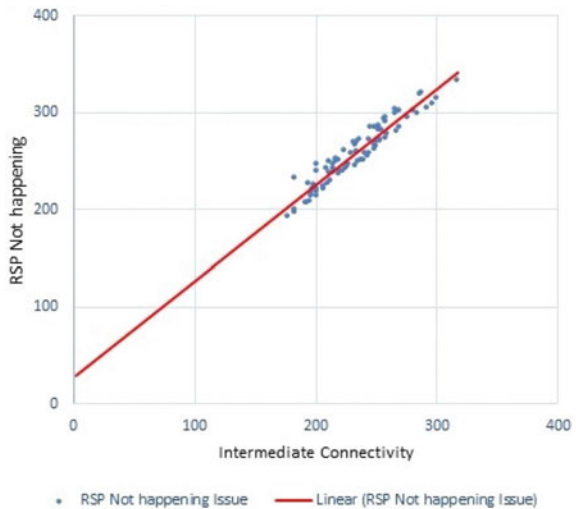
Fig. 3 No connectivity line fit plot
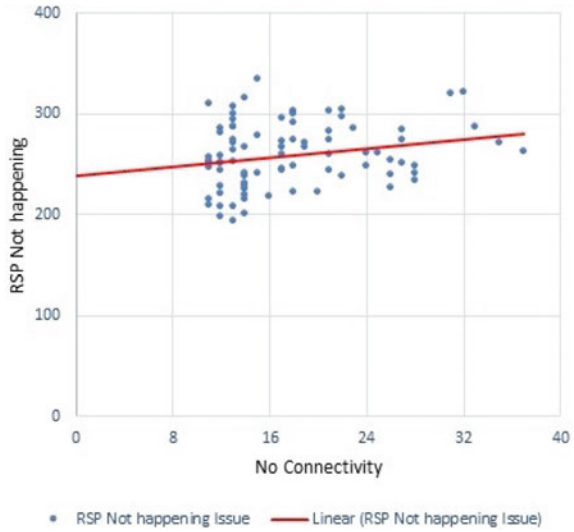
Fig. 4 Hardware failure line fit plot
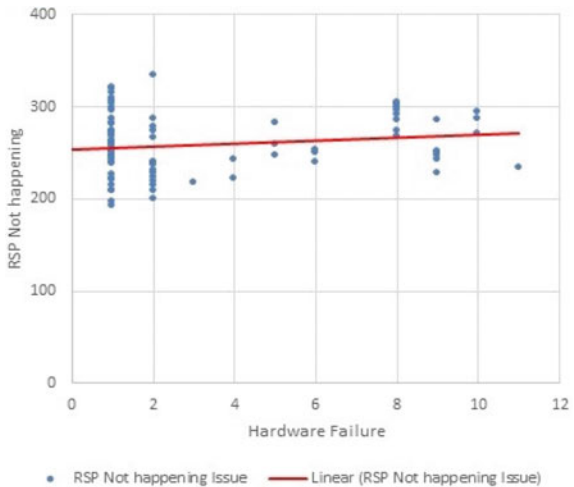
to unity. This implies that there is no direct relation in-between these factors and 'RSP Not Happening' factor.

The slope of regression line for 'Operational Issue' is -0.4172 which is a negative slope and could not justify the relation as if 'Operational Issue' would increase the 'RSP Not Happening' will decrease which is not the case.

The r^2 (Coefficient of determination) values for factors 'Intermediate Connectivity,' 'No Connectivity,' 'Hardware Failure,' 'Operational Issue' are $0.9101, 0.0513, 0.0281, 0.0003$.

Which again shows the most determining factor sequence as:

Fig. 5 Operational issue
line fit plot
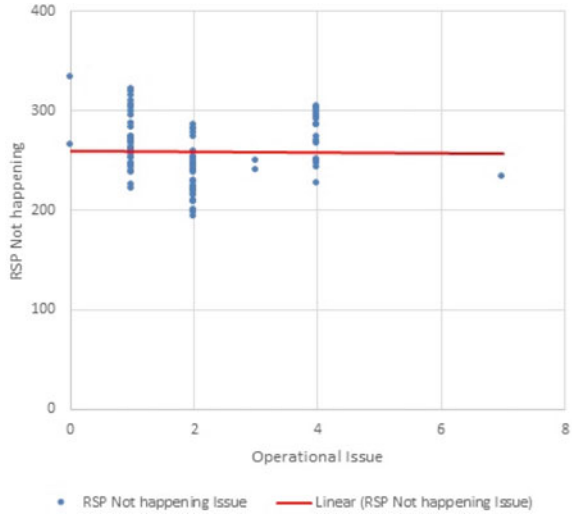
Table 5 Regression lines description

Sr. No	Independent Factor	Regression Line '$y = mx + c$'	r^2 value
1	Intermediate connectivity	$y = 0.9871x + 27.95$	0.9101
2	No connectivity	$y = 1.1276x + 238.84$	0.0513
3	Hardware failure	$y = 1.6590x + 253.44$	0.0281
4	Operational issue	$y = -0.4172x + 259.83$	0.0003

Intermediate Connectivity > No Connectivity > Hardware Failure > Operational Issue.

3 Conclusion

The major cause of intermediate connectivity is due to the network connectivity medium that Very Small Aperture Terminal (VSAT) so as improve the RSP rate of ABC OMC, XYZ automation company upgraded the retail outlets (ROs) with WFCC commissioning and providing 4G SIM router set-up for better connectivity.

In some geographies (dense forest, hilly region) of ABC company's, retail outlet VSAT proved to be better means of connectivity as telecom network is not that strong in it.

The data handling capacity of the ABC company server (HoS) should be improved.

References

1. Gupta P, Patodiya S, Singh D (2016) Department of Computer Science Engineering and Jasmeet Chhabra, Achman Shukla Department of Electronics & Communication Engineering from Jaypee University of Information Technology Himachal Pradesh, IoT based Smart Petrol Pump. In: 2016 fourth international conference on parallel, Distributed and Grid Computing, January 2016
2. Hubert Shanthan BJ (2016) Research Scholar, Dept. of Computer Science Dr. L. Arockiam Associate Professor, Dept. of Computer Science A. Dalvin Vinoth Kumar Research Scholar, Dept. of Computer Science from St. Joseph's College (Autonomous), Tiruchirappalli, Filling fuel quantity measurement systems using internet of things. Int J Innov Res Adv Stud (IJIRAS) 3(13), Dec 2016, ISSN: 2394–4404
3. Naveen Kumar P, Kumaresan P, Babu Sundaresan Y (2017) School of information technology and engineering, VIT University, IoT based retail automation of fuel station and alert system. In: 14th ICEST IOP conference series: material science and engineering 263:042072
4. Ravichandran S (2016) IOT in fuel station and service station location. Int J Control Theor Appl
5. Harida M, Pillai SV (2019) Assistant Professor CET School of Management, College of Engineering, Trivandrum, India, Internet of Things (IoT) Enabled automation: a shift towards smart fuel stations. Int J Eng Sci Comput
6. Vijayakumar P, Ganesan V, Patwari P, Singh R, Sharmila A, Tayade PP, Rajashree R, Tamilselvi M (2019) IoT based smart fuel monitoring system. Int J Recent Technol Eng (IJRTE) 8(2). ISSN: 2277–3878
7. Yadav G, Desai TN (2016) Lean Six Sigma: a categorized review of the literature. Int J Lean Six Sigma 7(1)
8. Yadav G, Luthra S, Huisingh D, Mangla SK, Narkhede BE, Liu Y (2020) Development of a lean manufacturing framework to enhance its adoption within manufacturing companies in developing economies. J Cleaner Prod 245(1):118726
9. Yadav G, Luthra S, Jakhar SK, Mangla SK, Rai DP (2020) A framework to overcome sustainable supply chain challenges through solution measures of industry 4.0 and circular economy: an automotive case. J Cleaner Prod 254:120112
10. Yadav G, Mangla SK, Bhattacharya A, Luthra S (2020) Exploring indicators of circular economy adoption framework through a hybrid decision support approach. J Cleaner Prod 277:124186
11. Bag S, Yadav G, Dhamija P, Katarina KK (2021) Key resources for Industry 4.0 adoption and its effect on sustainable production and circular economy: an empirical study. J Cleaner Prod 281:125233

Design Enhancement and Vibration Analysis of Bladeless Wind Turbine

Japagna N. Agnihotri, Monil M. Bhamare, Mihir H. Amin, Kishan D. Patel, and Dattatraya G. Subhedar

1 Introduction

Energy is one the fundamental need in our day-to-day life for improvement of human development as chief in terms of economic growth, social and productivity. Nowadays, fossil fuel and other non-renewable resources produce global warming and huge environment pollution which affect negative impact on earth and surrounding atmosphere. So, everyone is looking to utilize clean and green renewable energy resources by innovative technologies. Renewable energy also referred as sustainable energy which cannot run out and comes from natural resource such as Wind Power Energy, Solar Energy, Hydroelectric Power, Biomass Energy, Geothermal Energy, Tidal Energy are processes that are continuously day by day refilled.

One of the cleaner, efficient and reliable sources of renewable energy is Wind Energy. Nowadays, Wind Energy transformation or conversion system progress towards being a focal point in current research and development for maximum enhancement and utilization of renewable energy resources. The scientists and researchers are continuously endeavoured to boost novel optimization approach on every design parameter for harvesting Wind Power Efficient Energy.

J. N. Agnihotri · M. M. Bhamare · M. H. Amin (✉) · K. D. Patel · D. G. Subhedar
Mechanical Engineering Department, Chandubhai S. Patel Institute of Technology, CHARUSAT University, Nadiad-Petlad Road, Changa, Gujarat 388421, India

D. G. Subhedar
e-mail: dattatraya.me@charusat.ac.in

2   Literature Review

Brief study of Vortex induced vibration was explained effectively by various wind generation method to achieve maximum energy from bladeless wind turbine. Limitations and various problem of conventional wind power harvesting system was discussed properly. For production better Electrical Energy, piezoelectric material is novel approach in the oscillation of bladeless wind turbine or wind power harvesting system [1, 2].

Modelling of bladeless wind turbine was present effectively. With novel approach, detailed study of every components like Mast, Rack and pinion, pulley, spring was discussed. To obtain maximum displacement, FEA analysis performed. Air flow around mast was studied by computational fluid dynamics approach [3]. By using parametric study, computer aided design of bladeless wind turbine was optimized. Static structure analysis was analysed with finite element method and computational fluid dynamics analysis was done effectively. The main aim was to obtain maximum defection for bladeless wind and material optimization (by utilizing Composite Material) for achieving maximum Electrical Energy. Experimental results were discussed briefly with comparison of ANSYS simulation [4]. Optimization of mast design was carried out to achieve maximum output frequency. Theoretical calculation has done properly for Tapered Oscillation Cylinder structure [5, 6].

New technique was used via Piezoelectric sensor to harvest Electrical Energy from undesired ground vibration. Details study and experiment were performed to utilize Electrical Energy from unwanted vibration [7].

With the help of Alya code, scaled model of bladeless wind energy generator was simulated by Multi-code coupling approach and loose coupling algorithm. Numerical result and experiment data are good and accurate with less than 10% relative error [8, 9].

Main factor such as mass ratio, damping coefficient and the Reynolds number was investigated for harvesting energy by VIV of circular cylinder. Mathematical model was demonstrated for circular cylinder undergoing Vortex induced vibration [10]. Several experiment has performed to understand the Vortex induced vibration phenomenon tapered cylinder shaped. Effect of different taper ratio was testing on different types of cylinder properly. The comparison of linear tapered cylinder (wider range) and uniform cylinder was done effectively [11].

The setup is comparatively simple and can be placed at compact places such as farm, open land and high rise commercial building. As the vibration are generated by wind which is a natural resource our prototype is eco-friendly comprising of clean and free energy. It is not noisy. It does not require a highly skilled labour for operation. They can be placed at close intervals. Multiple prototypes can be installed in same area required for one conventional windmill which leads to higher overall amount of power generated from the site. The concept of the prototype can be stated as one-time investment after installation, giving quick return after investment. Transportation is feasible as they are no heavy and large components.

3 Effect of Vortex Shedding and Vortex Induced Vibrations (VIV)

Vortex shedding is a broadly going on happening relevant to almost any bluff (no streamlined) frame immersed in a fluid flow. Since any actual fluid float is viscous, there can be a huge boundary layer on the surface of the bodies for all; however, the least Reynolds number move. At a few points alongside the surface of the bodies, there will be detachment of the boundary layer will arise, relying on the precise geometry of the surface. This uncoupled layer, which confine the wake and loose stream, will generally tend to cause on fluid rotation, for the reason that its outer side, in touch with the free-stream, actions quicker than its internal side, in touch with the wake.

The non-linear resonance phenomenon referred to as Vortex Induced Vibration (VIV) as shown in Fig. 1 has a lot importance in numerous domains of mechanical engineering. For example, it could be discovered in civil systems, like narrow chimneys stacks, high rise constructions, electric powered electricity strains or bridges, to call a few. It is likewise standard in offshore systems or with inside the tubes of warmth change devices. Due to its realistic and research-based interest, VIV has caused a massive variety of essential studies. Usually, VIV is taken into consideration as an unwanted effect, as it could severely have an effect on the structural integrity or the authenticity of performance, however alongside this document we are able to see that if the vibration is substantial, it could be used to extract beneficial power from the encircling flow.

Fig. 1 Vortex shedding effect from top
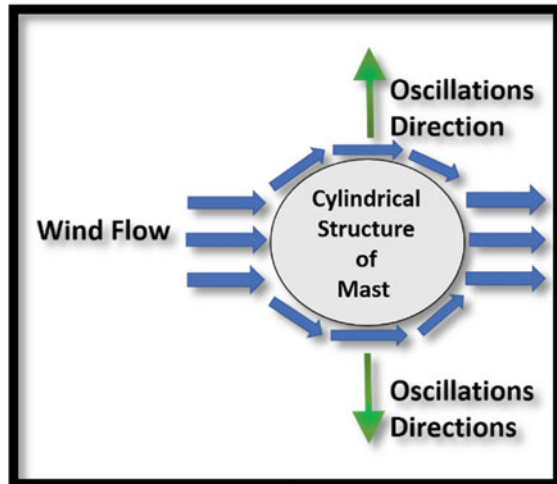
3.1 Reynolds Number

In general, flow parameter that affects the behaviour of vortex shedding has been observed to be the Reynolds number of flow as given in Eq. (1).

$$R_e = \frac{U.D}{v} \tag{1}$$

where

R_e = Reynolds number

U = free-steam velocity

D = cylinder diameter

V = fluid kinematic viscosity.

U is the free-stream velocity, D is the cylinder diameter and v is the fluid kinematic viscosity. The regime that is targeted in this project is known as the "fully turbulent vortex street", with Reynolds number in the range of (300 < Re < 3 × 10^5).

$$v = \frac{\mu}{\rho} \tag{2}$$

3.2 Strouhal Number

Strouhal number (S_t) is a non-dimensional number as given in (3).
    Describe vortex shedding frequency to oscillating flow mechanism.

$$S_t = \frac{f_s.D}{U} \tag{3}$$

where

f_s = vortex shedding frequency.
    Strouhal number will be used as a constant value in this project as the Reynolds number falls in the middle of constant. Strouhal number region which is 0.2 for subcritical flow.

4   Numerical Investigation

The proposed model is designed using Solid works software. The several main components of the proposed model of bladeless wind turbine are base plate, outer cylindrical base, rod, inner cylindrical support, Mast, clamps and anchors and alternator. And vibration analysis in terms of acceleration using accelerometer and natural frequency of the design with total deformation of the rod is done using modal analysis.

4.1   Structure and Geometry

The base plate grips the structure and mainly confines the outer and inner cylinder from the bottom. It is generally made up of high density material to bear the load of the setup. The outer cylindrical base is anchored at the top of base plate. Similarly, an inner cylindrical support which is basically hollow from inside is placed inside the outer cylindrical base and on the top of base plate. The outer and inner cylindrical base is made up of high density thermo plastic polymers such as HDPE, they are clamped as they are required to remain stationary as shown in Fig. 2. The Fig. 3 shows the main components of the bladeless wind turbine.

The rod is a key component in the bladeless wind turbine, it is made up of highly flexible and durable materials such as carbon fibres/glass fibres. For the given structure rod is made up of carbon fibre reinforced material (CFRP). The rod is anchored in the centre of the base plate at the bottom and top of the rod is attached with mast such that it supports the mast.
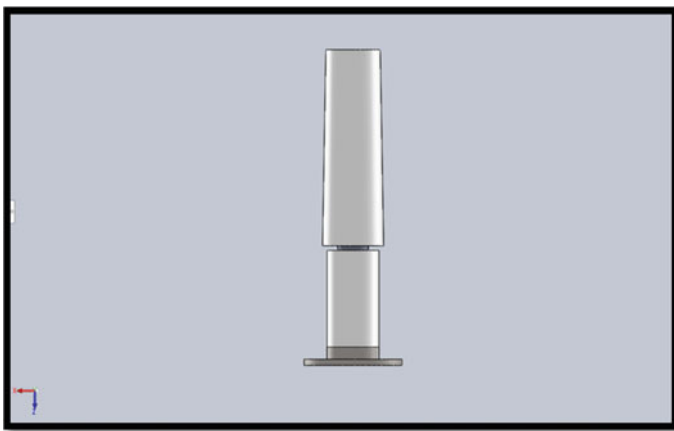
Fig. 2   3D model of bladeless wind turbine
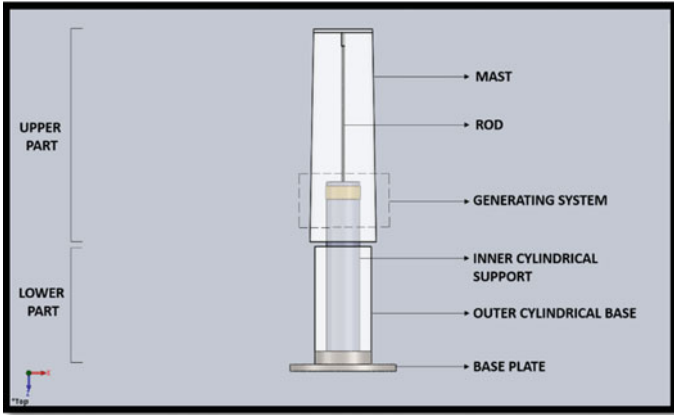
Fig. 3 Components of BWT

The mast is a tapered cylindrical structure which is the upper body of the bladeless wind turbine, it is deigned such as it has ability to oscillate and to remain unconstrained. The mast is made up of light weighted, low density polymers such as nylon. The maximum amplitude of oscillation can be obtained at the mast.

The model designed is symmetrically from all sides because the wind can impinge from any direction and the isometric view is as shown in Fig. 4. The alternator is used for generating electricity which is placed inside the structure. The diameter of outer and inner cylindrical base is kept lower than the diameter of mast for the mast to oscillate freely reducing the restriction of motion and a gap is maintained between the mast and outer cylindrical base.
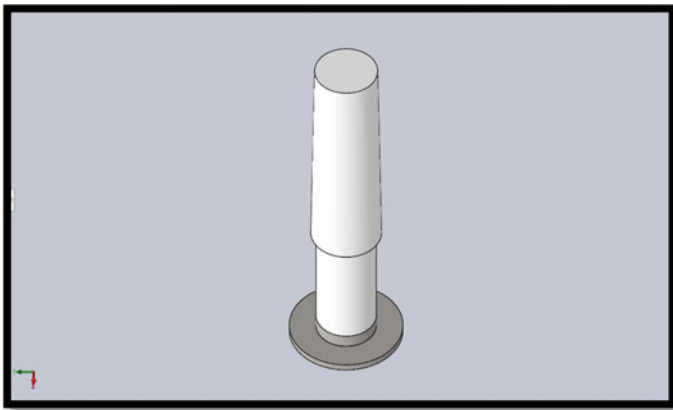
Fig. 4 Iso-view of BWT

5 Electromagnetic Generation System

The generation of electrical energy is done using alternating system working on the principle of electromagnetic induction. The working of alternating system resembles to the working of a linear alternator. The conversion is done from oscillatory motion occurring due to vibration into electrical energy and obtaining electrical power from it. For the given structure copper wire windings are used as electric conductor as copper shows outstanding electrical properties. The alternator comprises of rare earth permanent magnets, copper wire windings and electrical circuit consisting rectifiers, capacitors, voltage regulator, storage device. The principle of electromagnetic induction states that EMF, i.e. electromotive force is induced across the electric conductor due to change in magnetic field. It suggests that the component generating electric field should remain stationary and component possessing magnetic field should be moving at the same time or vice versa.

The setup of generation system is constructed such a way that following the principle of electromagnetic induction, when the wind strikes the mast due the oscillation of mast movement occurs and from that movement the magnetic field lines gets cut and change in magnetic field occurs and from that EMF induces. The generation system in the given structure of bladeless wind turbine is having the magnets placed on the periphery of inner cylindrical support and copper wire is winding across moving component inside the magnetic field generated by magnets. The other approach for the generating system can be done by inter changing the positions of the magnets and copper wire with each other. The electric circuit can be attached with end of copper wire windings for converting the induced EMF into voltage and obtaining electrical power output.

The magnets used are permanent magnets made up of Neodymium ($Nd_2Fe_{14}B$) material of grade N45, the higher the grade the better the magnetic strength as the EMF induced is directly proportional to the flux density of magnetic field, so for more amount of EMF strong magnetic field is suggested. The EMF induced using electromagnetic induction depends upon the number of turns of electrical conductor so the number of turns on the copper wire windings should be as much as possible. The EMF induced using electromagnetic induction is given as in (4).

$$\varepsilon = Blv \sin\theta \tag{4}$$

$$\varepsilon_{\max} = Blv \quad (\sin 90 = 1) \tag{5}$$

where

ε = induced electromotive force (EMF)

B = flux density of the magnetic field

l = length of the electrical conductor

Fig. 5 Flow chart of working mechanism

v = velocity of the conductor

θ = angle by which the conductor cuts the magnetic field.

6 Working Methodology of Bladeless Wind Turbine

The bladeless wind turbine works on the mechanism of converting oscillations generated due to vibration into electrical energy without using blades or any rotating part unlike conventional wind turbine. The wind from any direction strikes the mast surface will get departed and sheared off. Due to the impingement of wind on mast, the mast and rod which are attached together starts oscillating, which results in generation of vortex shedding. The flow of working process is as shown in Fig. 5.

The rod endures vibration from vortex shedding effect, as the rod is anchored from bottom and attached from topmost part and made up of flexible material it results in higher amount of oscillation. The electrical conductor which is placed inside a magnetic field is in connection with the rod. When the mast starts to oscillate the electrical conductor will also move along inside the magnetic field. This oscillatory motion will cut the magnetic field lines with a velocity v and as per the principle of electromagnetic induction an EMF will get induced across the electrical conductor and the electrical output will be obtained as per the generation system.

7 Results and Discussion

Vibration analysis is done for the given structure of bladeless wind turbine to find the natural frequency and acceleration of the oscillating components, i.e. mast. Two analysis method were used such as acceleration motion of the mast due to impingement of air on it using accelerometer and secondly modal analysis for obtaining frequency and total deformation of oscillating components. The results are discussed the sections given below.
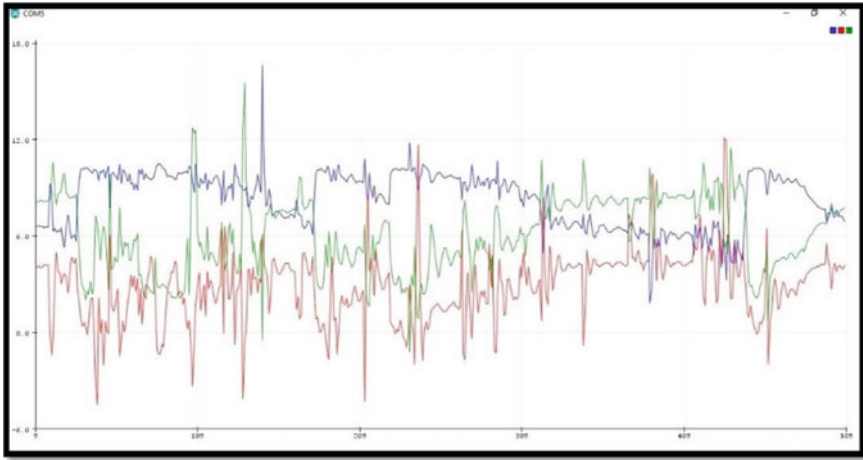
Fig. 6 Acceleration versus time graph using Arduino UNO

7.1 Vibration Analysis Using Accelerometer

The vibration analysis is done for obtaining frequency in the form of acceleration using Arduino UNO and accelerometer sensor. The Arduino UNO board is used and sensor for acceleration measurement such as ADXL345 accelerometer is used connected with the Arduino UNO board with circuit and programme required for given correspondence and application. ADXL345 is a 3-axis accelerometer to acceleration in X, Y and Z direction. The accelerometer is attached with the moving component, i.e. mast and Arduino UNO is connected to computer to obtain the following graph as shown in Fig. 6.

The Fig. 6 shows acceleration of the oscillation component in *X*, *Y* and *Z* direction occurring due to striking of air on mast. The output obtained is that the peak value from the graph at *X*-axis shows the average acceleration of 5 m/s^2. The output obtained is that the peak value from the graph at *Y*-axis shows the average acceleration of 9 m/s^2 and the output obtained is that the peak value from the graph at *Z*-axis shows the average acceleration of 6 m/s^2 for initial 60 s obtained from Fig. 6.

7.2 Modal Analysis Using ANSYS Software

ANSYS software, version R19.2 was used to perform modal analysis of the structure of BWT to find natural frequency of the structure. The bottom part, i.e. the outer base and base plate is held with fixed support. Total deformation is also obtained for the given structure obtained as shown in Fig. 7. Frequencies are obtained of the structure for 10 modes and the graph is obtained as shown in Fig. 8 and Table 1.
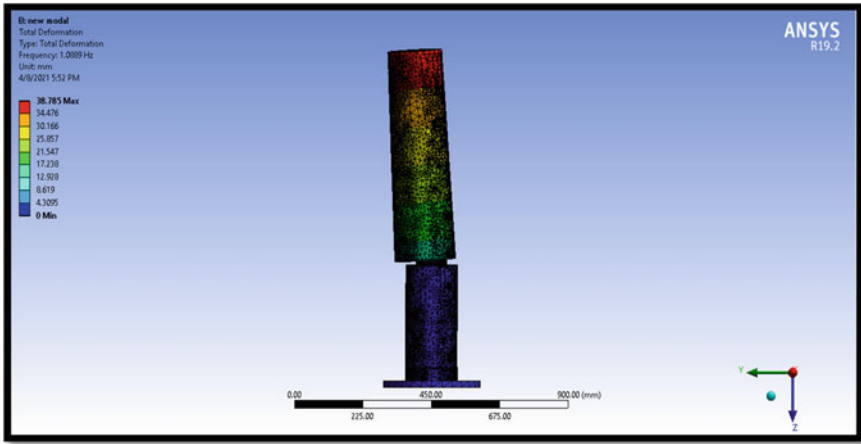
Fig. 7 Total deformation of the structure

Fig. 8 Mode frequencies
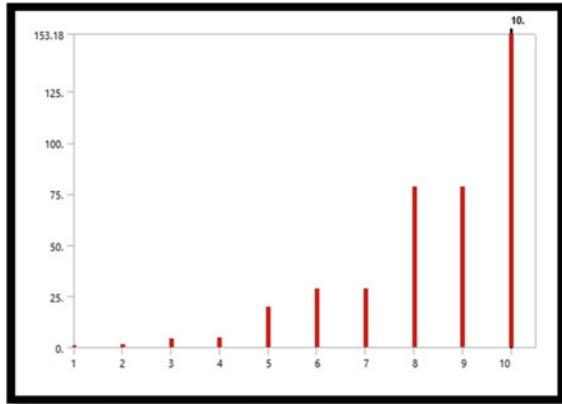
Table 1 Corresponding modal frequency

Mode	Frequency [Hz]
1	1.0889
2	1.2001
3	4.0604
4	4.7582
5	19.515
6	28.827
7	28.859
8	78.597
9	78.703
10	153.18

The modal analysis is used to determine the normal modes and normal shapes, and it helps to understand all other dynamic analysis. The performed modal analysis finds out if a design change will improve the dynamic performance of the system. Patch conformation method was used on the outer structure for meshing with tetrahedron elements as its capability of ignoring the points within the body that does not have any relationship with the computation, number of elements were 65,203 and number of nodes were 242,931.

In current work authors performed modal analysis for 10 modes having first mode frequency of 1.0889 Hz showing total deformation of 38.785 mm from the mean position. The maximum vibration occurs at natural frequency which is generally tried to minimize but on the contradictory in this case to attain more vibration the system should vibrate close to the natural frequency of the system. So, the structure was designed in such a way that the natural frequency coincides with excitation frequency, the first mode of frequency obtained is lower in comparison therefore the initial excitation frequency for oscillations is attained rapidly. The total deformation obtained is comparatively more which ultimately results in a greater number of oscillations for vibration.

Onkar D Kshirsagar et al. found maximum deformation of 9.1281 mm at third condition of static structural analysis after analysing their results it was observed that if the design is optimized to achieve more deformation, then significant improvement can be obtained [4].

Mr. Satish Raghuwanshi et al. designed bladeless wind turbine and performed modal analysis of their design for 6 modes. The first mode showed frequency of 9.2905 Hz showing the total deformation of 8.2786 mm [12]. The deformation obtained with different structure of mast gives different deformation of the oscillating structure, from this it can be deduced that from the enhanced design of mast comparatively more deformation is obtained than the conventional design generally used.

8 Conclusions

It is apparent that vibration is one of the major drawbacks in any system which reduces the life span and also increases maintenance cost, so in this current research work new design has been proposed that will utilize this vibration as an advantage to generate electricity and is providing a new innovative approach in designing bladeless wind turbines. This novel design has been optimized by creating a symmetric enclosed surface with integrated design and using polymer nylon as material with lowest density, so it is light in weight, and is also based on the concept of electromagnetic induction to produce vibration. This new design can be proven effective in an innovative way of fabricating modern generation non-conventional type of windmills and the production cost will be much less than the conventional type windmills. This new design has been simulated in ANSYS/modal analysis, and adxl345 accelerometer connected to Arduino UNO board attached with vibrating components

and validated natural frequency with the result obtained from ANSYS. Numerical investigation gave better idea about required parameter such as total deformation, acceleration, natural frequency for vibration which in turn helped to optimize design to harvest better amount of oscillations for vibration.

References

1. Gohate G, Bobde S, Khairkar A, Jadhav S (2016) Study of vortex induced vibrations for harvesting energy. Int J Innov Res Sci Technol 2(11):374–378
2. Williamson CHK, Govardhan R (2004) Vortex-induced vibrations. Annu Rev Fluid Mech 36:413–455
3. CAE design and analysis of bladeless wind turbine. Int J Emerg Technol Innov Res 5(5):21–25. (www.jetir.org), ISSN: 2349-5162 May 2018
4. Kshirsagar OD, Gaikwad AB Design and analysis of vortex bladeless windmill for composite material. J Indus Mech 4(2)
5. Aru V, Chavan N, Chaudhari U, Dange C Design & Analysis of Vortex bladeless. ISSN: 2395-1621. www.ierjournal.org
6. Chaudhari CC, Shriram MA, Unhale SG, Nirmal RS (2017) Fabrication of vortex bladeless windmill power generation model. Int J Sci Technol Eng 3(12):52–56
7. Garimella RC, Sastry VR, Mohiuddin MS (2015) Piezo-Gen-An approach to generate electricity from vibrations. Procedia Earth Planetary Sci 11:445–456
8. Bodkhe VD (2018) Design and Development of Vortex Blade less Wind Turbine. Int J Trend Sci Res Develop (ijtsrd) 2(3):2460–2462. ISSN: 2456–6470
9. Cajas García JC, Houzeaux G, Yáñez DJ, Mier-Torrecilla M (2016) SHAPE project vortex bladeless: parallel multi-code coupling for fluid-structure interaction in wind energy generation
10. Barrero-Gil A, Pindado S, Avila S (2012) Extracting energy from vortex-induced vibrations: a parametric study. Appl Math Model 36(7):3153–3160
11. Seyed-Aghazadeh B, Carlson DW, Modarres-Sadeghi Y (2015) The influence of taper ratio on vortex-induced vibration of tapered cylinders in the crossflow direction. J Fluids Struct 53:84–95
12. Raghuwanshi S, Pandey A (2020) Design and fabrication of vortex bladeless wind turbine. Chandrashekhar singh and Pandey, Ayush and shrivastava, akriti and sonanis, amol and banwariya, mayank (24 May 2020)

Evaluating the Barriers of Circular Supply Chain Implementation Using Pythagorean Fuzzy DEMATEL Method

Swapnil Lahane and Ravi Kant

1 Introduction

In the today's growing and competitive business environment, every manufacturing organization worldwide is looking to adopt sustainable practices into its supply chain model. This is because of several issues such as waste generation, climate change, global warming, resource shortage and deteriorating environmental conditions [1]. The current economic model is based on "take–make–use–dispose" philosophy [2]. This model ignores the value recovery aspects of sustainability, produces substantial amount of waste and creates resource scarceness issues; as a result, the manufacturing environment gets polluted continuously and affects the product life cycle management [3]. Thus, to overcome such issues, recently, the circular supply chain (CSC) has gained considerable attention among the community of researchers, practitioners and policy planners. CSC acts as sustainable solution approach to earlier dominant linear supply chain model. CSC integrates the circular economic (CE) principles into manufacturing organizations' supply chain [4]. CSC is based on value gain approach of CE, such as reusing, recycling, remanufacturing, redesigning, repairing and reducing. CSC focuses on various sustainability areas such as industrial symbiosis, eco-industrial park, product service system, industrial ecology, process integration, end of life management and life cycle assessment [5]. It offers several sustainable benefits to manufacturing organization. The developed nations have set their goals to adopt CE practices in supply chain operations. These nations have formulated an action plan towards CSC implementation, aiming to reduce the carbon footprint across the supply chains and ensure the continued use of resources in a closed-loop manner [6]. Thus, the gross domestic product (GDP) of the European Union (EU) economy has increased by 0.5% and produces several employment

S. Lahane (✉) · R. Kant
Mechanical Engineering Department, Sardar Vallabhbhai National Institute of Technology, Ichchhanath, Surat, Gujarat 395007, India

opportunities by adopting the principles of CE [7]. The EU had come up with legislative and non-legislative measures to achieve its targets of waste reduction throughout the entire product life cycle management.

In contrast to this, CSC concept in emerging economies is at the nascent stage, especially in India. There is the absence of stringent laws, regulation policies and strategies to adopt CSC effectively [7]. Also, the India is the second largest populated nation in the world. It generating enormous amount of waste every day by large volume [8]. Thus, India has substantial potential to obtain innovative and sustainable growth by adopting CE in supply chain processes. However, despite several benefits, the adoption of CSC in manufacturing industries is a challenging and difficult task due to several barriers, which hamper its implementation. From the previous literature, it has been seen that very less research has been performed in the area of CSC implementation in the context of emerging economies using any decision-making approach. Therefore, this research aims to recognize and evaluate the barriers to CSC implementation. This research proposes PF-DEMATEL approach to achieve the set research objective. PF-DEMATEL is used to evaluate the interrelationship and identifies the cause and effect group between the selected CSC barriers. This research provides the suitable direction for industrial practitioners to effectively adopt CSC management along with policy recommendations to the concerned stakeholders.

This paper is organized as follows: Sect. 2 presents the literature review on CSC barriers. Solution methodology adopted in this study is presented in Sect. 3. Section 4 presents the results of this study. Discussion on result is presented in Sect. 5. Section 6 concludes the paper.

2 Literature Review

The literature review is considered a backbone of any research work; thus, this research work adopts systematic literature review approach for this study. This research is used the SCOPUS database for article search. The combination of keywords, such as "circular economy and barriers", "circular supply chain and barriers", is used for data collection. The total of fifteen significant CSC implementation barriers is finalized through literature review and experts input. The list of selected barriers to CSC implementation is illustrated in Table 1.

3 Solution Methodology

This research proposes Pythagorean fuzzy sets (PFSs) in the classical DEMATEL method. The imprecision and ambiguity associated with human judgement in decision-making are effectively handled by PFSs as compared to other fuzzy sets. It allows the large freedom to experts to articulate their views on decision-making

Table 1 List of selected CSC barriers (CSCB)

CSCB Code	CSC barriers	Brief description	References
CSCB1	Lack of ecological laws, regulations and policy standards towards circularity adoption	The government agencies must come forward and develops the stringent laws, policies and regulation towards the CSC adoption	[9–12]
CSCB2	Lack of economical resources and facilities	There is a need for adequate financial support from funding agencies; otherwise, it makes a hurdle in CSC adoption and implementation, especially in the context of developing economies	[9, 13–15]
CSCB3	Low acceptability for second-hand products	The negative attitude of people towards acceptance of recycled/ remanufactured products hampers the CSC implementation	[11, 16–18]
CSCB4	Lack of support from government and funding agencies towards subsidies, incentives, tax rebate policies for endorsement of circular practices in an organization	Preferential tax benefits and loans for waste reduction and energy saving helps to uphold the CSC activities in business organizations	[9, 10, 12, 19]
CSCB5	Lack of suitable performance measurement systems	The standards performance measuring system helps to improve the socio-economic and environmental performance of organizations	Experts opinion
CSCB6	Lack of training and awareness programmes on CSC management	The government agencies must arrange the training and awareness programmes to the members of supply chain of various business organizations. It may help to promotes the circularity practices in manufacturing sectors	[12, 17, 19]
CSCB7	Lack of technological infrastructure and marketing strategy for remanufactured goods and secondary market	The sufficient technological infrastructure and proper marketing strategies are required to adopt CSC successfully	[8, 12, 19]

Table 1 (continued)

CSCB Code	CSC barriers	Brief description	References
CSCB8	Lack of economic benefits in short-run	If a business organization focuses on ecological aspects, it would certainly have some loss of financial value. It would be understandable that be deficient in financial earnings in short-run will also increase short-term cost	[6, 10, 11, 17]
CSCB9	Lack of organizations willingness to adopt ecological management system	The environment management system in industries plays a crucial role in managing the environmental aspects. It helps to improve the sustainability of organizations	[1, 9, 10, 12]
CSCB10	Lack of knowledge, skills and awareness towards CSC adoption	The adoption of CSC requires high technical skills, expertise, knowledge and involvement of stakeholders, however, which are lagging in current business practices	[6, 9, 11, 12, 20]
CSCB11	Lack of vision and tactical plan to adopt circularity in supply chain	The clear vision and tactical plan are needed for effective adoption of CSC management. Otherwise, it may keep the industries away from its adoption	[1, 9, 10, 12]
CSCB12	Lack of upfront investment costs for CSC adoption	For adoption of several circularity practices in an manufacturing firms require a huge capital investment, and it is a challenging task for many organizations in developing economies due to the lack of sufficient funds	[6, 8, 12, 17]
CSCB13	Nonexistence of proper information management system	The efficient, systematic information system helps track the recycled materials and improves the organization's overall performance. However, implementation of such a system is still missing in manufacturing sector of emerging economies	[6, 10, 12, 18, 21]

Table 1 (continued)

CSCB Code	CSC barriers	Brief description	References
CSCB14	Lack of adequate collection centres and recycling plants	For value creation and value propositions of waste plastic products needs sufficient in-house collection centres and recycling plants	Experts opinion
CSCB15	Lack of support and commitment from top management of an organization towards CSC implementation	A sustainable, innovative strategy is required to adopt the CSC concept in the industry, which could be possible only with committed management support	[9, 12, 13, 20]

problems [2]. Thus, this research proposes the PF-DEMATEL technique for the evaluation of CSC barriers.

3.1 PF-DEMATEL

DEMATEL technique is extensively used for building the structural model in decision-making problems [22]. It is generally used to evaluate the interrelationship and identifies the causal dependency among the selected variables. However, the classical DEMATEL is unable to handle the uncertainty associated with the subjective opinion of experts. Thus, this research employs the PFSs in DEMATEL. This is the first research that evaluates the barriers to CSC implementation using the PF-DEMATEL method to the best of our knowledge. In recent times, PF-DEMATEL has been employed in various areas such as solid waste management [22] and probabilistic safety analysis in process industry [22]. The steps involved in PF-DEMATEL are as follows [23]:

Step 1: Construct the initial direct relationship matrix (Z) by pairwise comparisons using the Eq. (1):

$$
Z_m = [Z_{ij}]_{n \times n} = \begin{array}{c} \\ C_1 \\ \vdots \\ C_n \end{array} \begin{bmatrix} C_1 & \dots C_n \\ (0,0) & \dots \left(\mu_{m_{1n}}, \vartheta_{m_{1n}} \right) \\ \vdots & \vdots \\ \vdots & \ddots & \vdots \\ \left(\mu_{m_{n1}}, \vartheta_{m_{n1}} \right) \dots & (0,0) \end{bmatrix} \tag{1}
$$

Step 2: Covert the initial direct relationship matrix (Z) into Pythagorean fuzzy direct relationship matrix with the help of linguistic terms (Table 2).

Step 3: Compute the weighted initial direct–relation matrix using Eq. (2):

Table 2 Linguistic variable in Pythagorean fuzzy sets [23]

Linguistic terms	Rating scale in crisp number	Rating scale in Pythagorean fuzzy sets
Very low influence	0	(0, 0)
Low influence	1	(0.1, 0.9)
Medium low influence	2	(0.2, 0.9)
Medium influence	3	(0.4, 0.6)
Medium high influence	4	(0.5, 0.7)
High influence	5	(0.7, 0.2)
Very high influence	6	(0.9, 0.1)

$$\lambda_m Z_m = \begin{bmatrix} \lambda(0,_m 0) & \ldots \lambda_m P_{1n} \\ \vdots & \vdots \\ \lambda_m P_{n1} & \ldots \lambda_m (0, 0) \end{bmatrix} \tag{2}$$

where $\lambda_m P_{ij} = \sqrt{1 - (1 - \mu_{ij}^2)^\lambda}$, $(\vartheta_{ij})^\lambda$ is the weighted PFS element.

Step 4: Compute the aggregated matrix using Eqs. (3) and (4);

$$\lambda_{m1} Z_{m1} \oplus \lambda_{m2} Z_{m2} = \begin{bmatrix} \lambda_{m_1} P_{Z_{m_1}}, 11 \oplus \lambda_{m_2} P_{Z_{m_2}}, 11 \ldots & \lambda_{m_1} P_{Z_{m_1}, 1n \oplus \lambda_{m_2} P_{z_{m_2}}, 1n} \\ \vdots & \vdots \\ \lambda_{m_1} P_{Z_{m_1}}, n1 \oplus \lambda_{m_2} P_{Z_{m_2}}, n1 & \lambda_{m_1} P_{Z_{m_1}, nn \oplus \lambda_{m_2} P_{z_{m_2}}, nn} \end{bmatrix} \tag{3}$$

where $\lambda_{m_1} P_{Z_{m_1}}, ij \oplus \lambda_{m_2} P_{Z_{m_2}}, ij$

$$= \sqrt{\mu_{\lambda_{m_1}}^2 Z_{m1} + \mu_{\lambda_{m_2}}^2 Z_{m2} - \mu_{\lambda_{m_1}}^2 Z_{m1} \mu_{\lambda_{m_2}}^2 Z_{m2}}, \vartheta \lambda_{m_1} Z_{m1} \vartheta \lambda_{m_2} Z_{m2} \tag{4}$$

Step 5: Construct total average crisp matrix using Eq. (5)

$$A = \begin{bmatrix} a_{11} & \ldots & a_{1_n} \\ \vdots & \ddots & \vdots \\ a_{n1} & \ldots & a_{nn} \end{bmatrix} \tag{5}$$

where $a_{ij} = \mu_{P_z, ij}^2 - \vartheta_{P_z, ij}^2$.

Step 6: Develop the normalized average crisp matrix (X) using Eq. (6):

$$X = s \cdot A \tag{6}$$

where

$$s = \frac{1}{\max 1 \le i \le n \sum_{j=1}^{n} a_{ij}} \quad i, j = 1, 2, \ldots, n.$$

Step 7: Construct the total–relation matrix (T) using Eq. (7).

$$T = X(I - X)^{-1} \tag{7}$$

where I is the identity matrix.

Step 8: Compute the sum of rows and columns separately using Eqs. (8) and (9).

$$\text{Sum of row, } R_i = \sum_{j=1}^{n} t_{ij} \tag{8}$$

$$\text{Sum of Column, } C_j = \sum_{i=1}^{n} t_{ij} \tag{9}$$

Step 9: Compute the prominence (P_i) and net effect (E_i) of the criteria using Eqs. (10) and (11).

$$P_i = R_i + C_j \tag{10}$$

$$E_i = R_i - C_j \tag{11}$$

4 Results

In this section, firstly, the introduction to case company and its problem statement is presented which is followed by calculations and results part is discussed.

4.1 The Case Company and Problem Statement

This research identifies the Indian automobile part manufacturing company to analyse the effectiveness of proposed research method. The name of the case organization is not disclosed due to the issue of authentication. It was established in 1996 and is presently located in Aurangabad in the state of Maharashtra. Selected company has annual turnover of US \$20.4 million and having over 5000 employees. This organization manufactured various plastic components of automobile. This organization aims to manufacture safe, environmentally concerned and user-friendly products, but they fail to balance the organization's economic, environmental and social performance. The selected case organization is also facing problems of solid waste management.

They do not have in-house recycling and remanufacturing facilities. Thus, the case company's management is looking to adopt a sustainable strategy such as CSC into their business unit. As effective CSC implementation improves organizational performance in three dimensions of sustainability. However, the adoption of CSC in actual practice is a challenging task for the organization's management, as they face several hurdles to its implementation. These hurdles are known as barriers that hamper the CSC implementation. Therefore, the case organization executives are fascinated in evaluating the barriers to CSC adoption.

4.2   Calculations and Results

In this subsection, PF-DEMATEL is used for the evaluation of CSC barriers. Initially, decision-makers asked to fill the questionnaire required for pairwise comparison of CSC barriers. The decision-making (DM) panel of the case organization consists of five experts, namely head (production department), head (environmental and quality department), lead (maintenance department), head (waste management department) and senior manager (logistics department). Selected experts are highly qualified and expertise in waste management practices. The DM experts used a relative scale of PF-DEMATEL for pairwise comparison (Table 2). Further, the decision matrix mode is calculated to obtain a single decision matrix before proceeding for further calculations. Following steps in Sect. 3.1, the calculations were made. Table 3 presents

Table 3 Final result of PF-DEMATEL method

CSC barriers	R	C	$P_i = R + C$	$E_i = R - C$	Ranking of barriers based on $R + C$
CSCB1	1.3031	0.8883	2.1914	0.4148	3
CSCB2	1.0345	0.4036	1.4381	0.6309	10
CSCB3	0.8081	1.3413	2.1494	−0.5332	4
CSCB4	1.2665	1.2269	2.4934	0.0396	2
CSCB5	−0.0749	1.0812	1.0063	−1.1561	14
CSCB6	0.6095	0.8158	1.4253	−0.2063	11
CSCB7	0.5858	1.0242	1.6100	−0.4384	8
CSCB8	0.0302	0.7072	0.7374	−0.6770	15
CSCB9	0.9227	0.6406	1.5633	0.2821	9
CSCB10	0.6532	0.6165	1.2697	0.0367	13
CSCB11	1.7914	0.2996	2.0910	1.4918	5
CSCB12	0.6165	0.6544	1.2709	−0.0379	12
CSCB13	0.7787	1.0718	1.8505	−0.2931	6
CSCB14	0.6947	0.9494	1.6441	−0.2547	7
CSCB15	1.7261	1.0253	2.7514	0.7008	1
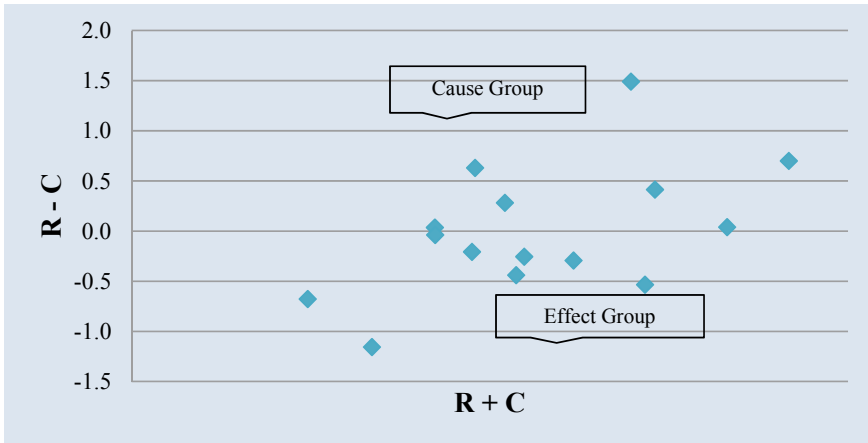
Fig. 1 Cause and effect diagram

the final result of PF-DEMATEL method. Based on "$R - C$" value, CSC barriers are classified as cause and effect group's barriers. The prominence ($R + C$) scores and effect ($R - C$) of each barrier are plotted on the graph as shown in Fig. 1.

5 Discussion

The result finding of the PF-DEMATEL provides the significance order of each barrier and categorized the CSC barriers into two groups. The ascending order of the barrier's importance is calculated based on the increasing value of "$R + C$". From Table 3, the selected CSC barriers are categorized based on "$R - C$" values into two distinct groups, namely cause and effect. The cause/influential group consists of seven CSC barriers, namely CSCB11, CSCB15, CSCB2, CSCB1, CSCB9, CSCB4 and CSCB10. These cause barriers are having a high influenced on the CSC adoption. Similarly, the effect/influenced group contain the eight CSC barriers, namely CSCB12, CSCB6, CSCB14, CSCB13, CSCB7, CSCB3, CSCB5 and CSCB8. The selected CSC barriers to CSC implementation are ranked based on "$R + C$", and it is presented in Table 3. These effect group barriers are the benefits to CSC implementation in organizations. Thus, for the improvement in effect group barriers there is need to have improvement in cause group barriers first. This is because of the effect group barriers having a higher dependency on influential group barriers. From the result, it can also be seen that "lack of support and commitment from top management of an organization towards CSC implementation" (CSCB15) is the most significant barrier and "lack of economic benefits in short run" (CSCB8) is the least important barrier to CSC adoption. Thus, without the support and guidance of top management of the

organization, it would be tough to implement CSC effectively in the business environment [6]. The result and graph obtained in this method are again discussed with same decision-making panel for obtaining the practical implications of the study.

Further, the research outcomes assist government agencies to develop preferential tax incentive plans for those who are willing to adopt CE in supply chain operation of business organizations. Such initiatives may help to increase the organization's interest towards implementation of CSC management. Also, decision-makers of the organization are recommended to perform training and awareness programmes to enhance their stakeholders' skills and knowledge for remanufacturing and recycling activities [10]. This will help industrial practitioners in understanding the most prominent barrier to CSC adoption and assist them in developing and formulating efficient strategies for successful adoption of CSC management.

6 Conclusions, Contribution and Recommendations for Future Research

Most of the manufacturing organizations in developing economies are comes under a severe threat of unsustainable development. It is caused because of various issues such as waste generation, resource scarcity, climate change and environmental degradation problems. Thus, the adoption of CSC in the industry becomes critical. It acts as a sustainable solution approach to overcome the earlier linear supply chain pattern where a lot of wastes are dumped into the landfill without any recovery. However, the firms in developing economies face several challenges and difficulties in adopting CSC in actual practice. The variables that restrict the organizations from the implementation of CSC are known as barriers. Therefore, this research aims to identify and evaluates the CSC barriers in the perspective of emerging economies. The fifteen CSC barriers were identified and selected through literature review and experts input. PF-DEMATEL technique was used for the evaluation of interrelationship and casual dependency among the selected CSC barriers.

Further, selected CSC barriers were categorized into cause and effect groups. Seven CSC barriers belonged to the cause group and eight CSC barriers were organized in the effect group. The slight improvement in cause group barriers will enhance the adaptability of effect group barriers. Thus, effect/influenced group barriers are largely dependent on cause group barriers. This research outcome helps the business professionals that seek to implement CSC into their business. Also, assist them to develop effective strategies to overcome the negative impact of barriers on CSC implementation. This research has its constraints which can be accepted as open door for future research. This study used subjective opinions of experts for analysis; any biasing may affect the research's final result. Thus, this result can be validated through a simulation-based model such as structural equation modelling in future research. This research also focused on a single case organization from India; in future, this study can be extended to other geographical locations of developing economies

based on a similar CSC barrier set. Further, in future studies, selected CSC barriers can be analysed using other advanced MCDM techniques like SWARA, WASPAS, COPRAS, TODIM, ELECTREE, BWM, TOPSIS, VIKOR and PROMETHEE under a Pythagorean fuzzy environment.

References

1. Batista L, Bourlakis M, Liu Y, Smart P, Sohal A (2018) Supply chain operations for a circular economy. Prod Plann Control 29(6):419–424
2. Lahane S, Kant R (2021) Evaluation and ranking of solutions to mitigate circular supply chain risks. Sustain Prod Consumption 27:753–773
3. Farooque M, Zhang A, Thürer M, Qu T, Huisingh D (2019) Circular supply chain management: a definition and structured literature review. J Clean Prod 228:882–900
4. Lahane S, Kant R, Shankar R (2020) Circular supply chain management: a state-of-art review and future opportunities. J Clean Prod. https://doi.org/10.1016/j.jclepro.2020.120859
5. Merli R, Preziosi M, Acampora A (2018) How do scholars approach the circular economy? a systematic literature review. J Clean Prod 178:703–722
6. Mangla SK, Luthra S, Mishra N, Singh A, Rana NP, Dora M, Dwivedi Y (2018) Barriers to effective circular supply chain management in a developing country context. Prod Plann Control 29(6):551–569
7. Goyal S, Esposito M, Kapoor A (2018) Circular economy business models in developing economies: lessons from India on reduce, recycle, and reuse paradigms. Thunderbird Int Bus Rev 60(5):729–740
8. Kumar V, Sezersan I, Garza-Reyes JA, Gonzalez ED, Moh'd Anwer AS (2019) Circular economy in the manufacturing sector: benefits, opportunities and barriers. Manage Decis 57(4):1067–1086
9. Urbinati A, Franzò S, Chiaroni D (2021) Enablers and barriers for circular business models: an empirical analysis in the Italian automotive industry. Sustain Prod Consumption 27:551–566
10. Khandelwal C, Barua MK (2020) Prioritizing circular supply chain management barriers using Fuzzy AHP: case of the Indian plastic industry. Glob Bus Rev. https://doi.org/10.1177/097215 0920948818
11. Tura N, Hanski J, Ahola T, Ståhle M, Piiparinen S, Valkokari P (2019) Unlocking circular business: a framework of barriers and drivers. J Clean Prod 212:90–98
12. Govindan K, Hasanagic M (2018) A systematic review on drivers, barriers, and practices towards circular economy: a supply chain perspective. Int J Prod Res 56:278–311
13. García-Quevedo J, Jové-Llopis E, Martínez-Ros E (2020) Barriers to the circular economy in European small and medium-sized firms. Bus Strateg Environ 29(6):2450–2464
14. Kazancoglu I, Kazancoglu Y, Kahraman A, Yarimoglu E, Soni G (2020) Investigating barriers to circular supply chain in the textile industry from Stakeholders' perspective. Int J Log Res Appl. https://doi.org/10.1080/13675567.2020.1846694
15. Lieder M, Rashid A (2016) Towards circular economy implementation: a comprehensive review in context of manufacturing industry. J Clean Prod 115:36–51
16. D'Agostin A, de Medeiros JF, Vidor G, Zulpo M, Moretto CF (2020) Drivers and barriers for the adoption of use-oriented product-service systems: a study with young consumers in medium and small cities. Sustain Prod Consumption 21:92–103
17. Zhang A, Venkatesh VG, Liu Y, Wan M, Qu T, Huisingh D (2019) Barriers to smart waste management for a circular economy in China. J Clean Prod. https://doi.org/10.1016/j.jclepro. 2019.118198
18. Shi J, Zhou J, Zhu Q (2019) Barriers of a closed-loop cartridge remanufacturing supply chain for urban waste recovery governance in China. J Clean Prod 212:1544–1553

19. Agyemang M, Kusi-Sarpong S, Khan SA, Mani V, Rehman ST, Kusi-Sarpong H (2019) Drivers and barriers to circular economy implementation. Manag Decis 57(4):971–994
20. Guldmann E, Huulgaard RD (2020) Barriers to circular business model innovation: a multiple-case study. J Clean Prod. https://doi.org/10.1016/j.jclepro.2019.118160
21. Masi D, Kumar V, Garza-Reyes JA, Godsell J (2018) Towards a more circular economy: exploring the awareness, practices, and barriers from a focal firm perspective. Prod Plann Control 29(6):539–550
22. Yazdi M, Nedjati A, Zarei E, Abbassi R (2020) A novel extension of DEMATEL approach for probabilistic safety analysis in process systems. Saf Sci 121:119–136
23. Abdullah L, Goh P (2019) Decision making method based on Pythagorean fuzzy sets and its application to solid waste management. Complex Intell Syst 5(2):185–198

Disruptions in Indian Supply Chain Due to COVID-19

Parthiv V. Shah, Bhavin J. Prajapati, Jitesh J. Panchal, and Shivangi Thakker

1 Introduction

The coronavirus disease 2019 outbreak is an unprecedented pandemic in its scale as well as severity to human beings. The global markets have experienced a long empty stretch in terms of suppliers [1]. Businesses mainly dependent on global suppliers are facing a crisis in product management and procurement. The adverse effects of this pandemic on the SCM domain are as dangerous as any earthquake or a tsunami [2]. Unforeseen by any economic model, the pandemic has overturned these strategies into business scramble leading to global shutdowns. In our research, we would be carrying out analysis by applying ISM to find out the most impacting disruptions of the global supply chain and giving appropriate solutions to it. This study aims to research various parameters affecting each other indirectly/directly and ultimately on the global supply chain. For the point of view to general information, it is estimated approximately that global manufacturing and export loss is about $228 billion due to disturbances brought by the coronavirus waves on the global supply chain. This loss is significant, and hence, strategies to cope up and probably eliminate these disruptions become quite important and critical.

P. V. Shah · B. J. Prajapati (✉) · J. J. Panchal · S. Thakker
Somaiya Vidyavihar University, Mumbai, Maharashtra, India
e-mail: bhavin.jp@somaiya.edu

P. V. Shah
e-mail: parthiv.vs@somaiya.edu

J. J. Panchal
e-mail: panchal.jj@somaiya.edu

S. Thakker
e-mail: shivangiruparel@somaiya.edu

2 Literature Review

2.1 *Supply Chain Challenges*

The coronavirus outbreak had been proclaimed a pandemic by the World Health Organization, causing a gigantic effect on individuals' lives and families. While nobody realizes exactly how long this will proceed for, one thing that is sure is that supply chains are facing challenges across the globe, due to which disruptions are likely to persist for many months [3]. Initial challenges in supply chains began with the supply end closing setups within China. That situation at length gave rise to insufficiency of hardware causing descending businesses—cloth, spare parts, consumables and many more elements belonging to a technical domain. These after-effects in various parts of the world resulted in some enterprises to halt their production or even cease operations. Additionally, contrary supply chains were shaken owing to the stringent lockdown policies and regulations that inhibited not only the growth and progress of rural products and industrial merchandise but also hampered the operations of existing small- and large-scale enterprises.

2.2 *Interpretive Structural Modeling (ISM)*

Interpretive Structural Modeling (ISM) is one of the popular strategies used for distinguishing relations shown by straightforward elements that identify an affair. Considering any perplexing subject viable, elements can be recognized with respect to a matter. These prompts or roundabout relations shared by elements depict a situation undeniably accurately contrast to a single factor brought into segregation. Subsequently, ISM forms bits of knowledge to collect conclusions of the relations. This modeling starts with a recognition of all factors that are pertinent to a particular subject or affair. Afterward, an evaluative thinking plan of action. Right there, a pertinent auxiliary relation is selected [4].

Being resolved upon the element sets along with context-oriented relations, a structural self-interaction matrix (SSIM) is constructed depending upon couple equivalence of individual strands. The following step includes the conversion of the above-obtained matrix to a reachability matrix (RM), where its transition gets examined. After inserting these transitions, a matrix is achieved. Then, the allocation of elements and a rooted primary matrix version named ISM is inferred [5].

The above approach is demonstrative since the acumen of these accumulated factors decides the relationship between the components. Basically, it depends on shared relationships; a broad design comes under separation, out of a mind-boggling set of elements. It can be called an indicative procedure since the specific relationships along with the formations shared are portrayed in the graphical representation. This assists with forcing requests together with the stance on complications of relations surrounded by varied elements in a model substructure [6, 7].

3 Data Collection and Methodology

3.1 Data Collection

Our group studied a variety of research papers regarding supply chain management and its worldwide impact due to COVID-19. Through brainstorming sessions, we found various disruptions in this domain due to this pandemic which are tabulated within Table 1.

After collection of these factors, a questionnaire was prepared which consisted of the factors—disruptions in supply chain. Respondents had to rate the impact of each disruption based on a scale of 1–5 where 1 being the least affected and 5 being the most affected. Responses of 20 industry experts were taken into account. The sectors they belonged to are shown in Fig. 1.

The total ratings of each disruption were found by adding the individual ratings given by each respondent. These calculated sums were eventually used to formulate the SSIM. All the factors and their respective ratings are displayed in Table 2.

3.2 Methodology

Warfield built up a strategy that incorporates efficient utilization of some rudimentary ideas of chart hypothesis and Boolean polynomial math so that when carried out in a man machinery-dependent manner, hypothetical, applied and arithmetical influence is imposed to build coordinated diagrams [22] (a portrayal of the progressive design of the framework). This philosophy has in any event two alluring properties when contrasted with the comparative methodologies, namely severity in perception of not preferring from the user that interpretation of modern arithmetical intelligence and performance in terminology of economizing in PC era.

Specialists from corporate and the scholarly background are counseled in understanding the idea of context-oriented dependency among the elements. Implementation of the following four factors signifies the course of connection between two factors (m and n): (a) V if factor m impacts factor n, (b) A if factor n will impact factor m, (c) X if factors m and n will impact one another and (d) O if factors m and n are inconsequential. Table 3 shows SSIM produced for factors acting as obstacles [23].

The reachability matrix is made from the SSIM. Images V, A, X or O of the SSIM are supplanted by 1's or 0's to make a reachability matrix. Rules followed are: (a) If the (m, n) spot of SSIM is V, at that point the (m, n) spot of the reachability network gets 1 and (n, m) spot gets 0. (b) If the (m, n) spot of the SSIM is A, at that point (m, n) spot of the reachability grid gets 0 and (n, m) spot gets 1. (c) If the (m, n) spot of SSIM is X, at that point the (m, n) spot of the reachability network gets 1 and the (n, m) spot gets 1. (d) If the (m, n) position of the SSIM is O, at that point (m, n)

Table 1 Disruption in supply chain due to COVID-19

Disruptions [source]	Description
Ban on transportation (import/export) [8]	Due to immediate lockdown scenario, movement of logistics was also prohibited by government of all countries
Restrictional policies [9]	Certain restrictional policies implemented on specific products/country from any governing authority
Sealed borders [10]	Due to implement of lockdown in the whole world, not only at international, national but even at regional level "demands and supplies" were not feasible
Shutdown of public transport [11]	To avoid social gathering in pandemic, unavailability of public transport led to halts in production
Lack of labor [8]	Economic recession led to migration of workers across the country, which in turn led to labor shortages
Living in informal sector [12]	For people staying on the outskirts, the equivalent is tiresome, increasing chances of lower productiveness
Panic purchasing [13]	Upon restraining the quantity of purchase permitted by each buyer, companies across globe struggled to meet the demand
Shortage of M/c or equipment [14]	Suppliers of machineries/equipment to small manufacturers were lacking in their shipment services due to unprecedented pandemic
Raw material unavailability [14]	As lockdown was implemented, transportation and procurement of raw materials were certainly a disruption
Delayed deliveries [15]	Delivery delays are probable to disrupt the businesses that work with JIT premise
Contamination of products [16]	Manufacturing plants suffered from contamination issues due to warehouse shutdowns
Fall in quantity arrivals [10]	Aggregate arrivals for goods like fruits and vegetables fall by 20% in many cities
Shutdown of factories [17]	Only essential services/products flow was permitted, which led to disproportion of all other non-essential productions/services
Particular dependency [18]	Being dependent on only one source/suppliers for product/services at times (e.g., pandemic) when they are not available is a major lead to disruption in supply chain
Sub-standard quality [17]	Rising demand of supplies led to compromise of quality, disturbing the supply chain for both suppliers as well as customer end

(continued)

Table 1 (continued)

Disruptions [source]	Description
Abolishment of contracts [19]	E-commerce platforms suspended many sellers' contracts on their platform
Lack of service and maintenance issues [20]	Lack of maintenance workers for machines which otherwise would have been in operating conditions led to malfunction
Lack of technological development [21]	On-hand businesses, applying traditional strategies, were forfeited in pandemic situations (being in a digital world)
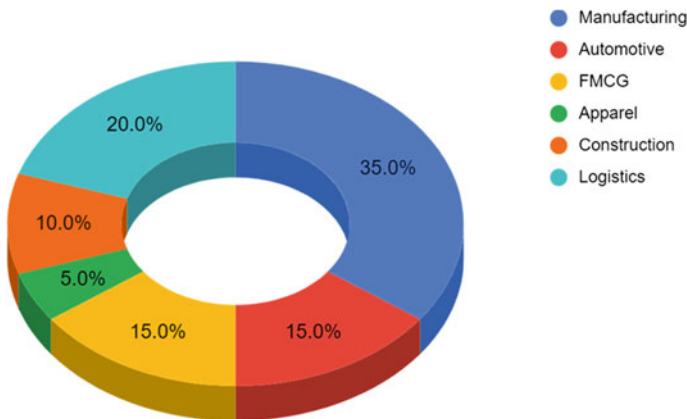
Fig. 1 Respondents' classification (sectorwise)

spot of the reachability matrix gets 0 and (*n*, *m*) spot gets 0 [23, 24]. Table 4 shows reachability matrix acquired using SSIM.

From the reachability matrix, reachability sets as well as antecedent sets are created for all respective factors. The reachability set contains factor itself along with factors which impact it, though antecedent set contains the factor itself as well as different factors that impact it. Intersection set for every factor contains regular variables within reachability set as well as antecedent set. A factor is positioned on high level on condition that reachability as well as intersection sets is equivalent [23, 24]. Table 5 shows the level partition, using which the digraph was generated as displayed in Fig. 2.

4 Results and Analysis

Eighteen disruptions are identified and analyzed which caused hindrance in the Indian supply chain due to the pandemic. Based on the level partitions obtained using ISM,

Table 2 Factor ratings based on the survey

Factors	Rating
Ban on transportation (import/export)	60
Restrictional policies	67
Sealed borders	63
Shutdown of public transport	60
Lack of labor	55
Living in informal sector	59
Panic purchasing	57
Shortage of machine/equipment	58
Raw material unavailability	60
Delayed deliveries	57
Contamination of products	60
Fall in quantity arrivals	56
Shutdown of factories	58
Particular dependency	58
Sub-standard quality	57
Abolishment of contracts	58
Lack of service and maintenance issues	59
Lack of technological development	58

the diagraph is developed wherein nine levels represent the corresponding factors starting from most affecting at top (i.e., Level 1) to least affecting at bottom (i.e., Level 9). The following factors occupy bottom levels of ISM-based models, as they possess higher driving power. Restriction policies (F3), sealed borders (F4), lack of technological development (F18), ban on transportation (import/export) (F2), shutdown of public transport (F13), contamination of products (F14), living in informal sector (F15), shutdown of factories (F6), lack of service and maintenance issues (F9), raw material unavailability (F10), panic purchasing (F17), abolishment of contracts (F11). The remaining six factors have strong dependency power; therefore, they occupy the upper levels of the model generated on the basis of ISM. These factors are shortage of machine/equipment (F4), particular dependency (F7), fall in quantity arrivals (F16), lack of labor (F1), delayed deliveries (F12), sub-standard quality (F8). The obstacle present at Level 9 is F3 which is restrictional policies. On Level 8, the factors are F5 and F18. Advanced technologies can be used to make systems capable of adapting to sudden changes by some level of automation. F2 occupies Level 7 which throws light on the ban of transportation. At Level 6, factors F13, F14, F15 imply that the storage facilities should be clean and safety practices are being followed. Additionally, accommodation and other emergency provisions can be made for people living in informal sectors. Level 5 has F6, F9, F10, F17 which indicates that online deliveries and quick restocking are important. Consider supplanting

Table 3 SSIM of disruptions affecting supply chain

Factors	F1	F2	F3	F4	F5	F6	F7	F8	F9	F10	F11	F12	F13	F14	F15	F16	F17	F18
1. Lack of labor	1	A	A	O	A	O	O	O	V	O	A	O	A	O	A	O	O	A
2. Ban on transportation		1	A	V	A	V	V	O	V	V	V	V	V	V	O	V	V	A
3. Restrictional policies			1	V	V	V	V	O	V	V	V	V	V	V	V	V	A	V
4. Shortage of machine/equipment				1	A	V	A	O	A	O	A	O	O	O	O	V	A	A
5. Sealed borders					1	V	V	V	O	V	V	V	V	V	V	V	V	O
6. Shutdown of factories						1	V	V	A	A	V	V	A	V	O	V	V	A
7. Particular dependency							1	O	O	A	A	O	O	O	O	V	O	A
8. Sub-standard quality								1	A	A	O	O	O	A	O	A	O	A
9. Lack of service and maintenance issues									1	A	V	V	A	V	A	V	O	A
10. Raw material unavailability										1	O	V	O	A	O	A	A	A
11. Abolishment Of contracts											1	V	A	A	A	A	V	O
12. Delayed deliveries												1	A	A	O	A	A	A
13. Shutdown of public transport													1	V	O	V	O	O
14. Contamination of products														1	O	V	V	A
15. Living in informal sector															1	O	V	V
16. Fall in quantity arrivals																1	A	A
17. Panic purchasing																	1	O
18. Lack of technological development																		1

Table 4 Reachability matrix of disruptions affecting supply chain

Factors	F1	F2	F3	F4	F5	F6	F7	F8	F9	F10	F11	F12	F13	F14	F15	F16	F17	F18
Lack of labor	1	0	0	0	0	0	0	0	1	0	0	0	0	0	0	0	0	0
Ban on transportation	1	1	0	1	0	1	1	0	1	1	1	1	1	1	0	1	1	0
Restrictional policies	1	1	1	1	1	1	1	0	1	1	1	1	1	1	1	1	0	1
Shortage of machine/equipment	0	0	0	1	0	1	0	0	0	0	0	0	0	0	0	1	0	0
Sealed borders	1	1	0	1	1	1	1	1	0	1	1	1	1	1	1	1	1	0
Shutdown of factories	0	0	0	0	0	1	1	1	0	0	1	1	0	1	0	1	1	0
Particular dependency	0	0	0	1	0	0	1	0	0	0	0	0	0	0	0	1	0	0
Sub-standard quality	0	0	0	0	0	0	0	1	0	0	0	0	0	0	0	0	0	0
Lack of service and maintenance issues	0	0	0	1	0	1	0	1	1	0	1	1	0	1	0	1	0	0
Raw material unavailability	0	0	0	0	0	0	1	1	1	1	0	1	0	0	0	0	0	0
Abolishment of contracts	1	0	0	1	0	0	1	0	0	0	1	1	0	0	0	0	1	0
Delayed deliveries	0	0	0	0	0	0	0	0	0	0	0	1	0	0	0	0	0	0
Shutdown of public transport	1	0	0	0	0	1	0	0	1	0	1	1	1	1	0	1	0	0
Contamination of products	0	0	0	0	0	0	0	1	0	1	1	1	0	1	0	1	1	0
Living in informal sector	1	0	0	0	0	0	0	0	1	0	1	0	0	0	1	0	1	1
Fall in quantity arrivals	0	0	0	0	0	0	0	1	0	1	1	1	0	0	0	1	0	0
Panic purchasing	0	0	1	1	0	0	0	0	0	1	0	1	0	0	0	1	1	0
Lack of tech. dev	1	1	0	1	0	1	1	1	1	1	0	1	0	1	0	1	0	1

Table 5 Level partitioning

Factors	Reachability set	Antecedent sets	Intersection set	Level
F1	1, 9	1, 2, 3, 5, 11, 13, 15, 18	1	**2**
F2	1, 2, 4, 6, 7, 9, 10, 11, 12, 13, 14, 16, 17	2, 3, 5, 18	2	**7**
F3	1, 2, 3, 4, 5, 6, 7, 9, 10, 11, 12, 13, 14, 15, 16, 18	3, 17	3	**9**
F4	4, 6, 16	2, 3, 4, 5, 7, 9, 11, 17, 18	4	**3**
F5	1, 2, 4, 5, 6, 7, 8, 10, 11, 12, 13, 14, 15, 16, 17	3, 5	5	**8**
F6	6, 7, 8, 11, 12, 14, 16, 17	2, 3, 4, 5, 6, 9, 10, 13, 18	6	**5**
F7	4, 7, 16	2, 3, 5, 6, 7, 10, 11, 18	7	**3**
F8	8	5, 6, 8, 9, 10, 14, 16, 18	8	**1**
F9	4, 6, 8, 9, 11, 12, 14, 16	1, 2, 3, 9, 10, 13, 15, 18	9	**5**
F10	6, 7, 8, 9, 10, 12	2, 3, 5, 10, 14, 16, 17, 18	10	**5**
F11	1, 4, 7, 11, 12, 17	2, 3, 5, 6, 9, 11, 13, 14, 15, 16	11	**4**
F12	12	2, 3, 5, 6, 9, 10, 11, 12, 13, 14, 16, 17, 18	12	**1**
F13	1, 6, 9, 11, 12, 13, 14, 16	2, 3, 5, 13	13	**6**
F14	8, 10, 11, 12, 14, 16, 17	2, 3, 5, 6, 9, 13, 14, 18	14	**6**
F15	1, 9, 11, 15, 17, 18	3, 5, 15	15	**6**
F16	8, 10, 11, 15, 17, 18	2, 3, 4, 5, 6, 7, 9, 13, 14, 16, 17, 18	16	**3**
F17	3, 4, 10, 12, 16, 17	2, 5, 6, 11, 14, 15, 17	17	**5**
F18	1, 2, 4, 6, 7, 8, 9, 10, 12, 14, 16, 18	3, 15, 18	18	**8**

The bold significance as name implies level partitioning, the outcome of performing ISM methodology is to obtain levels for all factors, which is most important to analyse all the factors

preventive maintenance with predictive support utilizing "little information" from a particular machine for condition observing and creating a notification when things rot. F11 is at Level 4. It signifies that e-commerce platforms should pay attention to crisis management. The top levels and their solutions are described in detail as follows.

Sub-standard Quality (Level 1, F8)

Mainly caused due to: procurement of low-quality raw materials, lack of acquisitions of machine power, unevenness of manufacturing process, less sales (in some cases).

Solutions: Educational and awareness—Various educational and awareness programs should be carried out virtually giving knowledge about material handling and procurement [25]. Supply Chain Integrity—The supply chain should be made crystal clear from the point of procurement to the point of public outlets. Product
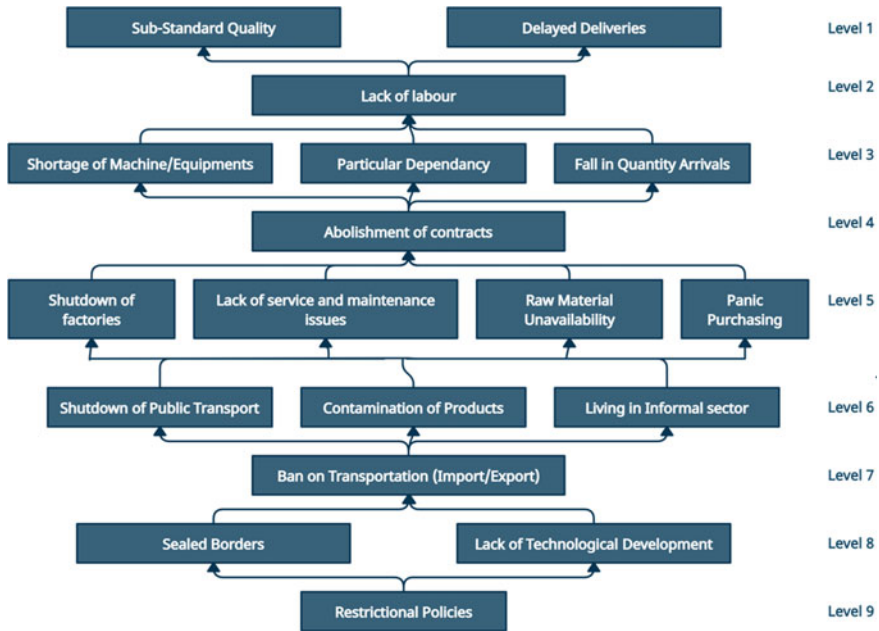
Fig. 2 Digraph of factors

Sales Forecast—The forecasting of the demand and need of the products should be carried out in a legit and disciplined manner in order to avoid over-stocked positions.

Tuning of Production Machines (in some cases): The machines used in manufacturing of products should be tuned properly to avoid any product deterioration.

Delayed Deliveries (Level 1, F12)

Mainly caused due to: restrictions imposed in containment zones, lack of resources available to process the order in such times, over-demand fulfillment attempts that cause lack of visibility of order delivering processes.

Solutions: mentioning the brand name on the vehicle and providing passes so that delivery man of essential services is not restricted and allowed to deliver the products. Study the situation and pre-informing the customer about the time accordingly so that there is no disbelief in seller–customer relation and help dealing with the situation. Ensuring proper tuning of the vehicle being used to deliver the products timely, so that there is no midway breakdown. Updating the stock quantity timely so that the new customer has an alternative source, and the existing customers do not have to face this problem.

Lack of labor (Level 2, F1)

Mainly caused due to: lack of owned residences which leads to returning of the employees to their respective native places. Also for employees living nearby the

organization, there is a sense of fear developed from getting infected, and also transportation restrictions play a role in causing this problem.

Solutions: Government-owned busses are lying, utilizing these busses by taking contracts so that laborers can be transported by maintaining social distance [26].

Creating awareness programs about safety arrangements in factories, and inculcating employees about these safety measures helps in removing fears and misconceptions.

Operational strategies should be changed to ensure minimum contact and proper sanitation so that workers are safe and can contribute toward the organization.

Shortage of Machine/Equipment (Level 3, F4)

Mainly caused due to: over-reliance on China, lockdown and limited production.

Solutions: avoiding reliance on one particular source and finding alternatives. Retooling of the equipment to produce different products can be a new strategy to cope up with this shortage [27].

Particular Dependency (Level 3, F7)

Mainly caused due to: beliefs and buyer customer relations, unavailability of alternative resources, shutdowns of outlets.

Solutions: The customer should move toward an online shopping approach where various alternatives are found. The organization should have and maintain a good relation and name in the whole market so that alternative sellers approach the organization readily.

Always try and explore new contracts and sellers to acquire an idea of selecting the most promising and profiting seller.

Fall in Quantity Arrivals (Level 3, F16)

Mainly caused due to: imposition of national lockdown policies, reliance on one source [28], over-stocking (panic purchasing).

Solutions: researching about the alternative suppliers.

Inventory management, optimal order quantity, reorder points should be analyzed timely.

5   Conclusions and Limitations

The supply chain has been influenced by the coronavirus pandemic in numerous ways. This paper introduces an Interpretive Structural Modeling (ISM) that links all the 18 disruptions of supply chain and classifies them into 5 categories. After performing extensive research, we came up with such disruptions which had a gigantic impact on the supply chain. We have also made an attempt to propose possible solutions for the identified disruptions which can bring improvements to the same. Generally speaking, it is recommended that the manufacturers cooperate to distribute assets and commence mutually in the crisis and spotlight more on essential variety and

capacity, as opposed to zeroing in on luxurious standards, to aid more patrons. The commitment of this study lies for the most part in portraying the particular estimates that can be received by organizations in different nations, in order to avoid disruptions in the supply chain. This study may likewise help distinguish successful and effective risk control measures during pandemic outbreaks.

Since there might be numerous factors to an issue or issue intricacy expansions in ISM philosophy, these models are not genuinely approved. Structural equation modeling (SEM) additionally usually recognized as a straight primary affinity procedure has the ability of assessing the legitimacy of such speculative models [29].

References

1. Gua D, Wang D, Hallegatte S et al (2020) Global supply-chain effects of COVID-19 control measures. Nat Hum Behav 4, 577–587
2. Dave HK, Rajpurohit SR, Patadiya NH, Dave SJ, Thambad SS, Srinivasn VP, Sheth KV (2019) Compressive strength of PLA based scaffolds: effect of layer height, infill density and print speed. Int J Mod Manuf Technol 11(1):21–27
3. The effects of COVID-19 on trade and global supply chains. International Labour Organization, June 2020. https://www.ilo.org/wcmsp5/groups/public/---dgreports/---inst/documents/publication/wcms_746917.pdf
4. Jharkharia S, Shankar R (2005) IT- Enablement of supply chains: Understanding the barriers. J Enterp Inf Manag 18(1):11–27
5. Agarwal A, Shankar R, Tiwari MK (2006) Modeling agility of supply chain. Indus Mark Manage 36:443457
6. Sage AP (1977) Interpretive structural modeling: methodology for large scale systems. McGraw-Hill, New York, NY
7. Singh MD, Shankar R, Narain R, Agarwal A (2003) An interpretive structural modeling of knowledge management in engineering industries. J Adv Manage Res 1(1):28–40
8. Xu Z, Elomri A, Kerbache L, El Omri A (2020) Impacts of COVID-19 on global supply chains: facts and perspectives. IEEE Eng Manage Rev 48(3):153–166, 1 third quarter
9. Singh S, Kumar R, Panchal R, Tiwari MK (2020): Impact of COVID-19 on logistics systems and disruptions in food supply chain. Int J Prod Res
10. Mahajan K, Tomar S COVID-19 and supply chain disruption: evidence from food markets in India, Am J Agric Econ
11. Tirachini A, Cats O (2020) COVID-19 and public transportation: current assessment, prospects, and research needs. J Public Transp 22(1)
12. Sharma A, Gupta P, Jha R (2020) COVID-19: impact on health supply chain and lessons to be learnt. J Health Manag 22(2):248–261
13. Paul SK, Chowdhury P (2020) Strategies for managing the impacts of disruptions during COVID-19: an example of toilet paper. Glob J Flex Syst Manag 21:283–293
14. Rao C (2020) Supply DIsruption due to Covid-19. Indus Eng J 13. https://doi.org/10.26488/IEJ.13.5.1256
15. Unnikrishnan A, Figlozzi M (2020) A Study of the Impact of COVID-19 on home delivery purchases and expenditures, Working Paper
16. Chowdhury M, Sarkar A, Paul SK et al (2020) A case study on strategies to deal with the impacts of COVID-19 pandemic in the food and beverage industry. Oper Manag Res
17. Sharma A, Adhikary A, Bikash Borah S (2020) Covid-19's impact on supply chain decisions: strategic insights for NASDAQ 100 firms using twitter data. J Bus Res

18. Donato M, Ahsan K, Shee H (2015) Resource dependency and collaboration in construction supply chain: literature review and development of a conceptual framework. Int J Procurement Manage 8(3)
19. Amazon & the Covid-19 crisis. Global Union
20. Shafi M, Liu J, Ren W Impact of COVID-19 pandemic on micro, small, and medium-sized enterprises operating in Pakistan. Research in Globalization
21. Queiroz MM, Ivanov D, Dolgui A et al (2020) Impacts of epidemic outbreaks on supply chains: mapping a research agenda amid the COVID-19 pandemic through a structured literature review. Ann Oper Res
22. Warfield JW (1974) Developing interconnected matrices in structural modelling. IEEE Trans Syst Men Cybern 4(1):51–81
23. Mathiyazhagan K, Govindan K, NoorulHaq A, Geng Y (2013) An ISM approach for the barrier analysis in implementing green supply chain management. J Clean Prod 47:283–97
24. Tripathy S, Sahu S, Ray PK (2013) Interpretive structural modelling for critical success factors of R& D performance in Indian manufacturing firms. J Model Manag 8(2):212–240
25. WHO Global Surveillance and Monitoring System for substandard and falsified medical products ISBN 978-92-4-151342-5
26. Mukherjee P, Prakash S Covid-19: innovative solutions required for labour shortages. Disruptions in supply chain of essential commodities
27. COVID-19 Impact on global machine tool market by machine type (Cutting and Forming), Automation type (CNC and Conventional), industry (Automotive, Sheet Metal, Capital Goods and Energy), Sales channel (Direct Sales, Events & Exhibitions and Dealer & Distributor) and Region—Global Forecast to 2021, AT 7618 Apr 2020
28. WH (2021) The economic times. 20 Apr 2021
29. George JP, Pramod VR (2013) Mapping of steel re rolling mills, a practitioner's perspective. J Organisational Manage (AIMA) XXIX:45–50

Reverse Logistics Performance Metrics: An Evaluation by Pythagorean Fuzzy Decision-Making Trial and Evaluation Laboratory Method

Himanshu Prajapati and Ravi Kant

1 Introduction

In India, growing public interest in e-commerce in the recent years and its easy return policy has burdened sellers with product returns. Reverse logistics has gained attention in the recent years due to increased waste generation, shorter product life and high returns [1]. To handle these organizations today are focussing on introducing reverse logistics in its supply chain. Reverse logistics is defined as, "The process of planning, implementing and controlling the efficient, effective inbound flow and storage of secondary goods and related information opposite to the traditional supply chain direction for the purpose of recovering value and proper disposal" [2]. Reverse logistics has significant impact on enhancing organization's income but very few literatures discussed the performance of reverse logistics [3]. Performance measurement is essential for the success of the business [21]. Measurement of reverse logistics performance is a prime issue in reverse logistics literature and the metrics of measuring reverse logistics performance are not autonomous but interrelated. Reverse logistics performance measurement is generally the way towards measuring the productivity and viability of reverse logistics operations. Reverse logistics performance can be greatly improved if measured and monitored [4]. Therefore, the context of this research is to identify the reverse logistics performance metrics (RLPM) and to find the causal relationship between them. The identification of RLPM represents an important step that addresses a significant advance in embracing a coordinated and exhaustive way to deal with reverse logistics performance.

H. Prajapati (✉)
Assistant Professor, Mechanical Engineering Department, Maharishi Markandeshwar Engineering College, Maharishi Markandeshwar (Deemed to be University), Mullana-Ambala, Haryana 133207, India

R. Kant
Mechanical Engineering Department, S. V. National Institute of Technology, Surat, India

The research proceeds with the identification of RLPM from the thorough literature view. The Scopus database was searched with suitable keywords to find the articles primarily focussed on reverse logistics performance. Thereafter, the Pythagorean fuzzy decision-making trial and evaluation laboratory (PFDEMATEL) is used to build and analyse a structural model derived using RLPM. DEMATEL is widely used multi-criteria decision-making (MCDM) method to develop the causal relationship between variables, and Pythagorean fuzzy sets are employed to handle the uncertainty in decision-making [5]. The proposed framework is employed on an automobile part manufacturer company based in India.

The structure of article is as follows: Sect. 2 presents the past literature on reverse logistics performance metrics and highlights the research gap. Section 3 presents the proposed PFDEMATEL method in detail. Section 4 presents the empirical case to construct causal diagram followed by conclusions in Sect. 5.

2 Literature Review

Reverse logistics implementation is a very complex process (starting from adopting right standards, appropriate human resource, strategic procurement of returns, and performing the operation of reuse, refurbishing, remanufacturing, etc.) so as measuring its performance. Reverse logistics can enhance a firm's status but depends on its overall performance. A comprehensive literature survey shows the scarceness of work done particularly focussed on reverse logistics performance measurement and metrics. Agrawal et al. [4] found a few studies on performance measurement but was limited to either economic performance or environmental performance. They extend their study to collect several factors of social aspects to complete the triple bottom line aspects of reverse logistics performance and prioritize the selected RLPM. Few authors [3, 6–8] have used balanced scorecard approach to define reverse logistics goals and performance metrics. Although balance scorecard helps to identify and check the internal factors on the basis of strategic, operational and financial measures it does not consider external factors directly related to reverse logistics performance such as stakeholder's perspective. Several other authors developed mathematical models based on meta-heuristics [9], statistical analysis [10] and intelligent algorithms [11].

The literature assessment finds a limited study on reverse logistics performance metrics based on MCDM environment. The previous study was also limited to find RLPM of particular area (such as financial, environmental or social performance). This study selects the RLPM based on overall organization's performance. Also, this research develops causal relationship between RLPM in a MCDM environment using advanced Pythagorean fuzzy sets. Table 1 shows the selected RLPM with its description and reference.

Table 1 Reverse logistics performance metrics

Code	RLPM	Description	References
PM1	Reverse logistics network with volume flexibility	This type of reverse logistics network structure can handle quantity uncertainty, good capacity utilization and enhances recovery efficiency	[10, 15, 19, 20]
PM2	Integrate reverse logistics with organization's goal	This helps in developing organizational strategy focussed on reverse logistics and support during decision-making. It also helps to better manage organizations' resources according to reverse logistics implementation	[19, 21]
PM3	Innovation and Growth	Continuous improvement and learning bring efficiency in the reverse logistics operating domain of an organization	[8, 19]
PM4	Transportation and Logistics cost optimization	Transport and logistics have a great impact on product cost. A good RL helps in optimizing these costs	[10, 14]
PM5	Reduced disposal cost	RL helps in limiting core disposal rate, thereby giving cost benefits	[9, 13, 14]
PM6	Enhance productivity and performance	By doing proper quality management and control, standardization, and benchmarking, reverse logistics enhance efficiency of organization	[7, 19, 20]
PM7	Better customer experience and satisfaction	Incorporating customer's feedback and handling returns efficiently enhances customer satisfaction responsiveness	[6, 7, 13, 14, 18, 20]
PM8	Sustainable culture	It arises from environmental sustainability, social and sustainable growth, and moral and ethical responsibilities resulting from environmental regulations	[7–9, 13, 14, 18, 19]
PM9	Follow environmental legislation	Implementing reverse logistics satisfies the law requirements of the country, thereby saving from legal actions	[9, 17]

(continued)

Table 1 (continued)

Code	RLPM	Description	References
PM10	Reverse MRP	Reverse MRP helps to maintain optimum inventory levels, thereby reducing costs	[6, 15, 16]
PM11	Advanced information and communication technology solutions and infrastructure	Reverse logistics implementation involves advance technologies and infrastructure which helps in overall organizations development. It also reduces reverse logistics lead time	[13, 14, 16, 18, 19]
PM12	Enhanced core product ratio	Increasing core product ratio shows reverse logistics successful implementation	[13]
PM13	Sustainable production and consumption	A proper implemented reverse logistics practice should enhance waste reduction, decreased scrap rate, material recovery from waste, use of recycled material and proper disposal of end-of-life products	[7, 14–16]
PM14	Reduced New component cost	Reuse of used products and its parts reduces the use of new components, thereby reducing cost	[13, 15]

3 Pythagorean Fuzzy Decision-Making Trial and Evaluation Laboratory Method

DEMATEL is widely used MCDM technique developed to solve complex and inter-related criteria and to develop causal relationship between them. It then identifies the criteria in cause and effect groups to develop a meaningful structural model [5]. DEMATEL method utilizes matrices and directional graphs (diagraph) to show the contextual relationship, degree of influenced and influential impact, and importance level of factors [12]. Though DEMATEL has various benefits it cannot handle the uncertainty in the expert's opinion. This limitation was successfully handled by grey sets and intuitionistic fuzzy sets but have a limitation on arithmetic addition and hesitation degree. These limitations were handled by introducing Pythagorean fuzzy sets to DEMATEL. The following are the steps of newly developed PFDEMATEL method.

Step 1: An initial direct relationship matrix (Z) is prepared by pair-wise comparisons in terms of influences and directions between criteria.

Table 2 Linguistic variable and rating scale of Pythagorean fuzzy sets

Linguistic terms	Rating scale in crisp number	Rating scale in Pythagorean fuzzy sets
Very low influence	0	(0, 0)
Low influence	1	(0.1, 0.9)
Medium low influence	2	(0.2, 0.9)
Medium influence	3	(0.4, 0.6)
Medium high influence	4	(0.5, 0.7)
High influence	5	(0.7, 0.2)
Very high influence	6	(0.9, 0.1)

$$
Z_m = [Z_{ij}]_{n \times n} = \begin{array}{c} \\ C_1 \\ \vdots \\ C_n \\ \end{array} \begin{bmatrix} C_1 & \dots C_n \\ (0,0) & \dots \left(\mu_{m_{1n}}, \vartheta_{m_{1n}}\right) \\ \vdots & \vdots \\ \vdots & \ddots \quad \vdots \\ \left(\mu_{m_{n1}}, \vartheta_{m_{n1}}\right) \cdots & (0,0) \end{bmatrix}
$$

Step 2: Convert matrix (Z) into Pythagorean fuzzy direct relationship matrix by providing respective Pythagorean fuzzy numbers from Table 2.

Step 3: Calculate weighted initial direct relation matrix using Eq. 1

$$
\lambda_m Z_m = \begin{bmatrix} \lambda(0,_m 0) & \dots \lambda_m P_{1n} \\ \vdots & \vdots \\ \lambda_m P_{n1} & \dots \lambda_m(0,0) \end{bmatrix} \tag{1}
$$

where $\lambda_m P_{ij} = \sqrt{1 - (1 - \mu_{ij}^2)^\lambda}, (\vartheta_{ij})^\lambda$ is the weighted Pythagorean fuzzy set element.

Step 4: Calculate the aggregated matrix using Eqs. 2 - 3

$$
\lambda_{m1} Z_{m1} \oplus \lambda_{m2} Z_{m2} = \begin{bmatrix} \lambda_{m_1} P_{Z_{m_1}}, 11 \oplus \lambda_{m_2} P_{Z_{m_2}}, 11 \dots & \lambda_{m_1} P_{Z_{m_1}, 1n \oplus \lambda_{m_2} P_{Z_{m_2}}, 1n} \\ \vdots & \vdots \\ \lambda_{m_1} P_{Z_{m_1}}, n1 \oplus \lambda_{m_2} P_{Z_{m_2}}, n1 & \lambda_{m_1} P_{Z_{m_1}, nn \oplus \lambda_{m_2} P_{Z_{m_2}}, nn} \end{bmatrix} \tag{2}
$$

where $\lambda_{m_1} P_{Z_{m_1}}, ij \oplus \lambda_{m_2} P_{Z_{m_2}}, ij$

$$= \sqrt{\mu_{\lambda_{m_1}}^2 Z_{m_1} + \mu_{\lambda_{m_2}}^2 Z_{m_2} - \mu_{\lambda_{m_1}}^2 Z_{m_1} \mu_{\lambda_{m_2}}^2 Z_{m_2}}, \; \vartheta \lambda_{m_1} Z_{m_1} \vartheta \lambda_{m_2} Z_{m_2} \qquad (3)$$

Step 5: Construct total average crisp matrix by defuzzification function using Eq. 4

$$A = \begin{bmatrix} a_{11} & \cdots & a_{1_n} \\ \vdots & \ddots & \vdots \\ a_{n1} & \cdots & a_{nn} \end{bmatrix} \qquad (4)$$

where $a_{ij} = \mu_{P_z,ij}^2 - \vartheta_{P_z,ij}^2$.

Step 6: Develop the normalized average crisp matrix (X).

$$\text{The crisp matrix } X = x_{ij} = s.A \qquad (5)$$

where $0 \le x_{ij} \le 1$ and

$$s = \frac{1}{\max 1 \le i \le n \sum_{j=1}^n a_{ij}} \quad i, \; j = 1, \; 2, \; ..., \; n.$$

Step 7: Develop total relation matrix (T) using Eq. 6.

$$T = X(I - X)^{-1} \qquad (6)$$

where I is the identity matrix.

Step 8: Calculate the sum of rows and the sum of columns using Eqs. 7, 8. It is denoted as R_i and C_j within the total relation matrix T through $T = t_{ij}$, where $i, j = 1, 2…, n$.

$$\text{Sum of row, } R_i = \sum_{j=1}^n t_{ij} \qquad (7)$$

$$\text{Sum of Column, } C_j = \sum_{i=1}^n t_{ij} \qquad (8)$$

Step 9: Compute the prominence (P_i) and net effect (E_i) of the criteria using Eqs. 9 - 10.

$$P_i = R_i + C_j \qquad (9)$$

$$E_i = R_i - C_j \qquad (10)$$

The positive value of E_i shows the net effect (cause) of the criteria on the system and the negative value represents the net effect (effect) on the criteria caused by the system.

4 Empirical Case of an Indian Manufacturing Company

The PFDEMATEL approach has been applied to evaluate the performance metrics of an Indian manufacturing company which has recently implemented reverse logistics in its supply chain. The aim of the organization towards implementation of reverse logistics is to implement sustainability in its supply chain and to move towards circular economy. Five experts were chosen from various departments who are involved with reverse logistics operation in the organization. The profile of the experts and their weight score is shown in Table 3.

The RLPM that influences reverse logistics performance is retrieved from the literature and is given in Table 1. The weights to the RLPM are provided by experts in the field related to reverse logistics operation in the selected Indian manufacturing industry. An online interview was conducted with the expert's individually to obtain the pair-wise comparison matrix between RLPM based on linguistic scale in Table 2. The obtained five linguistic matrixes were then evaluated using the steps of PFDE-MATEL method in Sect. 3. The initial direct relationship matrix Z_1 as developed from the responses received from E1 is given in Table 4.

Similarly, four other similar matrices were developed using responses from E2, E3, E4 and E5. The weights of expert are calculated using Eq. 11 and are summarized in Table 3.

$$\text{Expert weight} = \lambda_m = \frac{\text{Expert weight score}}{\text{Total weight}} \quad (11)$$

Table 3 Experts demographic details and weight score

Expert	Designation	Department	Experience	Expert's weight score	Expert's weight
E1	Senior manager	Reverse logistics operations	20 years	0.80	0.2500
E2	Senior engineer	Purchase	7 years	0.45	0.1406
E3	Senior engineer	Production	7 years	0.40	0.1250
E4	General manager	General management	12 years	0.75	0.2344
E5	Senior manager	Sales and marketing	13 years	0.80	0.2500

Table 4 Initial direct matrix (Expert 1)

PM	PM1		PM2		PM3		–	–	–	–	PM12		PM13		PM14	
PM1	0	0	0.7	0.2	0.9	0.1	–	–	–	–	0.7	0.2	0.5	0.7	0.9	0.1
PM2	0.7	0.2	0	0	0.9	0.1	–	–	–	–	0.4	0.6	0.7	0.2	0.7	0.2
PM3	0.7	0.2	0.7	0.2	0	0	–	–	–	–	0.4	0.6	0.7	0.2	0.4	0.6
PM4	0.4	0.6	0.7	0.2	0.7	0.2	–	–	–	–	0.7	0.2	0.9	0.1	0.7	0.2
PM5	0.4	0.6	0.5	0.7	0.7	0.2	–	–	–	–	0.1	0.9	0.4	0.6	0.4	0.6
PM6	0.7	0.2	0.4	0.6	0.7	0.2	–	–	–	–	0.7	0.2	0.9	0.1	0.7	0.2
PM7	0.4	0.6	0.4	0.6	0.9	0.1	–	–	–	–	0.4	0.6	0.7	0.2	0.9	0.1
PM8	0.9	0.1	0.4	0.6	0.2	0.9	–	–	–	–	0.4	0.6	0.4	0.6	0.7	0.2
PM9	0.7	0.2	0.7	0.2	0.5	0.7	–	–	–	–	0.7	0.2	0.7	0.2	0.7	0.2
PM10	0.9	0.1	0.9	0.1	0.9	0.1	–	–	–	–	0.4	0.6	0.1	0.9	0.9	0.1
PM11	0.9	0.1	0.7	0.2	0.9	0.1	–	–	–	–	0.9	0.1	0.7	0.2	0.9	0.1
PM12	0.2	0.9	0.5	0.7	0.9	0.1	–	–	–	–	0	0	0.9	0.1	0.7	0.2
PM13	0.9	0.1	0.9	0.1	0.9	0.1	–	–	–	–	0.9	0.1	0	0	0.4	0.6
PM14	0.4	0.6	0.1	0.9	0.9	0.1	–	–	–	–	0.9	0.1	0.7	0.2	0	0

The weighted initial direct relationship matrix is calculated using Eq. 1 and is given in Table 5. Similarly, calculations were made for matrices from E2, E3, E4 and E5.

The aggregated matrix for the five experts is calculated using Eqs. 2 and 3 and is shown in Table 6.

Table 5 Initial direct relationship matrix (E1)

PM	PM1		PM2		–	–	PM13		PM14	
PM1	0.0000	0.0000	0.1750	0.0500	–	–	0.1250	0.1750	0.2250	0.0250
PM2	0.1750	0.0500	0.0000	0.0000	–	–	0.1750	0.0500	0.1750	0.0500
PM3	0.1750	0.0500	0.1750	0.0500	–	–	0.1750	0.0500	0.1000	0.1500
PM4	0.1000	0.1500	0.1750	0.0500	–	–	0.2250	0.0250	0.1750	0.0500
PM5	0.1000	0.1500	0.1250	0.1750	–	–	0.1000	0.1500	0.1000	0.1500
PM6	0.1750	0.0500	0.1000	0.1500	–	–	0.2250	0.0250	0.1750	0.0500
PM7	0.1000	0.1500	0.1000	0.1500	–	–	0.1750	0.0500	0.2250	0.0250
PM8	0.2250	0.0250	0.1000	0.1500	–	–	0.1000	0.1500	0.1750	0.0500
PM9	0.1750	0.0500	0.1750	0.0500	–	–	0.1750	0.0500	0.1750	0.0500
PM10	0.2250	0.0250	0.2250	0.0250	–	–	0.0250	0.2250	0.2250	0.0250
PM11	0.2250	0.0250	0.1750	0.0500	–	–	0.1750	0.0500	0.2250	0.0250
PM12	0.0500	0.2250	0.1250	0.1750	–	–	0.2250	0.0250	0.1750	0.0500
PM13	0.2250	0.0250	0.2250	0.0250	–	–	0.0000	0.0000	0.1000	0.1500
PM14	0.1000	0.1500	0.0250	0.2250	–	–	0.1750	0.0500	0.0000	0.0000

Table 6 Aggregated matrix (E1)

PM	PM1		PM2		–		PM13		PM14	
PM1	0.0000	0.0000	0.7000	0.2000	–	–	0.5000	0.7000	0.9000	0.1000
PM2	0.7000	0.2000	0.0000	0.0000	–	–	0.7000	0.2000	0.7000	0.2000
PM3	0.7000	0.2000	0.7000	0.2000	–	–	0.7000	0.2000	0.4000	0.6000
PM4	0.7047	0.2953	0.7000	0.2000	–	–	0.9000	0.1000	0.7000	0.2000
PM5	0.2500	0.8250	0.5000	0.7000	–	–	0.4000	0.6000	0.4000	0.6000
PM6	0.6578	0.2562	0.4000	0.6000	–	–	0.9000	0.1000	0.7000	0.2000
PM7	0.4000	0.6000	0.4000	0.6000	–	–	0.7000	0.2000	0.9000	0.1000
PM8	0.9000	0.1000	0.4000	0.6000	–	–	0.6719	0.2766	0.6500	0.3250
PM9	0.5500	0.5750	0.7000	0.2000	–	–	0.7000	0.2000	0.7000	0.2000
PM10	0.8500	0.1250	0.9000	0.1000	–	–	0.1000	0.9000	0.9000	0.1000
PM11	0.9000	0.1000	0.7000	0.2000	–	–	0.7000	0.2000	0.9000	0.1000
PM12	0.3922	0.6703	0.5000	0.7000	–	–	0.9000	0.1000	0.7000	0.2000
PM13	0.9000	0.1000	0.5250	0.4750	–	–	0.0000	0.0000	0.4000	0.6000
PM14	0.6547	0.3203	0.1000	0.9000	–	–	0.7000	0.2000	0.0000	0.0000

Total average crisp matrix and normalized matrix are then calculated using Eqs. 4 and 5. The matrices are given in Tables 7 and 8. The total relationship matrix is then calculated using Eq. 6 and is given in Table 9.

Summation of row R and summation of column C from total relationship matrix (Table 9) is calculated. R represents degree of influential impact, and C represents degree of influenced impact. The relative importance of each RLPM is calculated from the $R + C$ value and is known as prominence vector (P_i), whereas $R–C$ value is known as relational vector (E_i). The RLPM having positive relational vector is classified into cause groups, whereas RLPM having negative relational vector is classified in effect group. Table 10 shows the R value, C value, prominence vector, relational vector, priority order, cause group and effect group. A causal relationship diagram also known as cause–effect diagram (Fig. 1) is prepared with P_i on its horizontal axis and E_i on its vertical axis. The result shows seven RLPMs each in cause and effect group.

It is apparent from Table 10 that the importance order of RLPM is based on prominence vector (P_i), and RLPMs are divided into cause and effect group based on relational vector (E_i). The RLPM according to importance is reverse logistics network with volume flexibility (PM1) followed by transportation and logistics cost optimization (PM4), advanced information and communication technology solutions and infrastructure (PM11), innovation and growth (PM3), sustainable production and consumption (PM13), reduced new component cost (PM14), enhance productivity and performance (PM6), better customer experience and satisfaction (PM7), integrate RL with organization's goal (PM2), follow environmental legislation (PM9), reverse MRP (PM10), enhanced core product ratio (PM12), reduced disposal cost (PM5) and sustainable culture (PM8).

Table 7 Total average crisp matrix

PM	PM1	PM2	PM3	PM4		PM11	PM12	PM13	PM14	Σ
PM1	0.0000	0.4500	0.8000	0.4500	–	0.8000	0.4500	-0.2400	0.8000	6.5700
PM2	0.4500	0.0000	-0.1461	0.3671	–	0.8000	-0.2000	0.4500	0.4500	5.1710
PM3	0.4500	0.4500	0.0000	0.4500	–	-0.2000	-0.2000	0.4500	-0.2000	3.2600
PM4	0.4094	0.4500	0.4500	0.0000	–	0.4500	0.4500	0.8000	0.4500	5.2094
PM5	-0.6181	-0.2400	0.4500	0.8000	–	-0.2000	-0.8000	-0.2000	-0.2000	-0.8413
PM6	0.3671	-0.2000	0.3671	0.4500	–	-0.8000	0.4500	0.8000	0.4500	3.4012
PM7	-0.2000	-0.2000	0.8000	0.3006	–	0.4500	-0.2000	0.4500	0.8000	1.7513
PM8	0.8000	-0.2000	-0.4200	-0.2000	–	-0.2000	0.0344	0.3749	0.3169	-0.4438
PM9	-0.0281	0.4500	-0.2400	0.4500	–	0.4500	0.4500	0.4500	0.4500	3.9919
PM10	0.7069	0.8000	0.8000	0.2241	–	-0.2000	-0.2000	-0.8000	0.8000	3.5816
PM11	0.8000	0.4500	0.6594	0.8000	–	0.0000	0.8000	0.4500	0.8000	8.4234
PM12	-0.2955	-0.2400	0.8000	-0.2000	–	-0.2000	0.0000	0.8000	0.4500	2.2254
PM13	0.8000	0.0500	0.6594	0.5267	–	-0.2400	0.8000	0.0000	-0.2000	4.6267
PM14	0.3260	-0.8000	0.8000	0.5775	–	-0.2000	0.8000	0.4500	0.0000	2.7535
Σ	3.9677	1.2200	5.7798	4.9960		0.7100	2.6344	4.2349	5.1669	8.4234

Table 8 Normalized average crisp matrix

PM	PM1	PM2	PM3	PM4			PM11	PM12	PM13	PM14
PM1	0.0000	0.0534	0.0950	0.0534	–	–	0.0950	0.0534	−0.0285	0.0950
PM2	0.0534	0.0000	−0.0173	0.0436	–	–	0.0950	−0.0237	0.0534	0.0534
PM3	0.0534	0.0534	0.0000	0.0534	–	–	−0.0237	−0.0237	0.0534	−0.0237
PM4	0.0486	0.0534	0.0534	0.0000	–	–	0.0534	0.0534	0.0950	0.0534
PM5	−0.0734	−0.0285	0.0534	0.0950	–	–	−0.0237	−0.0950	−0.0237	−0.0237
PM6	0.0436	−0.0237	0.0436	0.0534	–	–	−0.0950	0.0534	0.0950	0.0534
PM7	−0.0237	−0.0237	0.0950	0.0357	–	–	0.0534	−0.0237	0.0534	0.0950
PM8	0.0950	−0.0237	−0.0499	−0.0237	–	–	−0.0237	0.0041	0.0445	0.0376
PM9	−0.0033	0.0534	−0.0285	0.0534	–	–	0.0534	0.0534	0.0534	0.0534
PM10	0.0839	0.0950	0.0950	0.0266	–	–	−0.0237	−0.0237	−0.0950	0.0950
PM11	0.0950	0.0534	0.0783	0.0950	–	–	0.0000	0.0950	0.0534	0.0950
PM12	−0.0351	−0.0285	0.0950	−0.0237	–	–	−0.0237	0.0000	0.0950	0.0534
PM13	0.0950	0.0059	0.0783	0.0625	–	–	−0.0285	0.0950	0.0000	−0.0237
PM14	0.0387	−0.0950	0.0950	0.0686	–	–	−0.0237	0.0950	0.0534	0.0000

The cause–effect diagram (Fig. 1) illustrates reverse logistics network with volume flexibility (PM1), integrate RL with organization's goal (PM2), transportation and logistics cost optimization (PM4), follow environmental legislation (PM9), reverse MRP (PM10), advanced information and communication technology solutions and infrastructure (PM11), and sustainable production and consumption (PM13) are the RLPM associated with the cause group. RLPM related with the cause group affects the entire framework and their presentation has enormous effect on organization's targets. The effect group constitutes RLPM, namely innovation and growth (PM3), reduced disposal cost (PM5), enhance productivity and performance (PM6), better customer experience and satisfaction (PM7), sustainable culture (PM8), enhanced core product ratio (PM12) and reduced new component cost (PM14). These RLPMs are the factors which are affected by the cause group factors.

5   Conclusion

Reverse logistics adds value to the organization, and its effective management enables the organization to cut costs, increase profits, a sustainable competitive advantage, improve internal processes and increase customer satisfaction. However, to be effective, the performance of reverse logistics is to be measured. Implementing a reverse logistics performance measurement system through RLPM to measure the productivity and viability of activities is the primary condition to improve and accomplish business excellence [21]. This research selects 14 RLPM from the available reverse logistics literature to find its relative importance and their contextual relationship.

Table 9 Total relationship matrix

PM	PM1	PM2	PM3	PM4		PM11	PM12	PM13	PM14	Σ = R
PM1	0.0000	0.0552	0.0981	0.0552	–	0.0981	0.0552	–0.0294	0.0981	**0.8059**
PM2	0.0552	0.0000	–0.0179	0.0450	–	0.0981	–0.0245	0.0552	0.0552	**0.6343**
PM3	0.0552	0.0552	0.0000	0.0552	–	–0.0245	–0.0245	0.0552	–0.0245	**0.3999**
PM4	0.0502	0.0552	0.0552	0.0000	–	0.0552	0.0552	0.0981	0.0552	**0.6390**
PM5	–0.0758	–0.0294	0.0552	0.0981	–	–0.0245	–0.0981	–0.0245	–0.0245	**–0.1032**
PM6	0.0450	–0.0245	0.0450	0.0552	–	–0.0981	0.0552	0.0981	0.0552	**0.4172**
PM7	–0.0245	–0.0245	0.0981	0.0369	–	0.0552	–0.0245	0.0552	0.0981	**0.2148**
PM8	0.0981	–0.0245	–0.0515	–0.0245	–	–0.0245	0.0042	0.0460	0.0389	**–0.0544**
PM9	–0.0035	0.0552	–0.0294	0.0552	–	0.0552	0.0552	0.0552	0.0552	**0.4897**
PM10	0.0867	0.0981	0.0981	0.0275	–	–0.0245	–0.0245	–0.0981	0.0981	**0.4393**
PM11	0.0981	0.0552	0.0809	0.0981	–	0.0000	0.0981	0.0552	0.0981	**1.0333**
PM12	–0.0362	–0.0294	0.0981	–0.0245	–	–0.0245	0.0000	0.0981	0.0552	**0.2730**
PM13	0.0981	0.0061	0.0809	0.0646	–	–0.0294	0.0981	0.0000	–0.0245	**0.5675**
PM14	0.0400	–0.0981	0.0981	0.0708	–	–0.0245	0.0981	0.0552	0.0000	**0.3378**
Σ = C	**0.4867**	**0.1497**	**0.7090**	**0.6128**		**0.0871**	**0.3232**	**0.5195**	**0.6338**	

Table 10 Prominence vector, the relational vector, cause and effect of RLPM

PM	R	C	$R + C$	$R–C$	Importance order	Cause	Effect
PM1	0.8059	0.4867	1.2926	0.3192	1	✔	
PM2	0.6343	0.1497	0.7840	0.4847	9	✔	
PM3	0.3999	0.7090	1.1089	−0.3091	4		✔
PM4	0.6390	0.6128	1.2519	0.0262	2	✔	
PM5	−0.1032	0.5889	0.4857	−0.6921	13		✔
PM6	0.4172	0.4222	0.8394	−0.0050	7		✔
PM7	0.2148	0.5810	0.7958	−0.3662	8		✔
PM8	−0.0544	0.3755	0.3211	−0.4300	14		✔
PM9	0.4897	0.2902	0.7799	0.1995	10	✔	
PM10	0.4393	0.3146	0.7540	0.1247	11	✔	
PM11	1.0333	0.0871	1.1204	0.9462	3	✔	
PM12	0.2730	0.3232	0.5961	−0.0502	12		✔
PM13	0.5675	0.5195	1.0870	0.0481	5	✔	
PM14	0.3378	0.6338	0.9716	−0.2960	6		✔
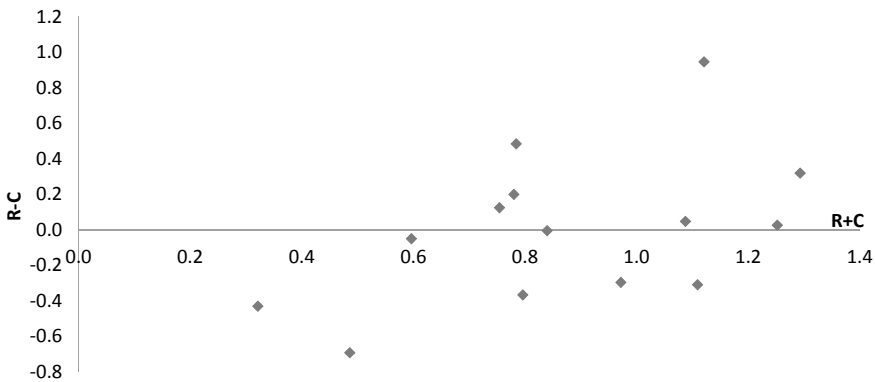
Fig. 1 RLPM causal relationship diagram

This research also develops a causal relationship diagram to segregate the RLPM in cause and effect groups using PFDEMATEL. The most important RLPM is reverse logistics network with volume flexibility (PM1). The findings of this study can aid managers in comprehending the RLPM that must be addressed in order to effectively evaluate reverse logistics performance. The findings also may assist managers in implementing an efficient and scalable reverse logistics system that improves an organization's overall profitability.

The study has a drawback in that, like all MCDM applications, it requires subjective decisions. Despite the fact that the model used can account for ambiguities, the results cannot be generalized. Although the selected RLPM are generalized and

can fit to other industries, the result of this study is still based on the responses from a single selected case organization. These limitations open a way for future development on this research.

References

1. Prajapati H, Kant R, Shankar R (2019) Prioritizing the solutions of reverse logistics implementation to mitigate its barriers: a hybrid modified SWARA and WASPAS approach. J Cleaner Prod 240:118219
2. Fleischmann M (2001) Quantitative models for reverse logistics. Lecture Notes in Economics and Mathematical Systems, Springer-Verlag, Berlin, p 501
3. Shaik MN, Abdul-Kader W (2014) Comprehensive performance measurement and causal-effect decision making model for reverse logistics enterprise. Comput Ind Eng 68:87–103
4. Agrawal S, Singh RK, Murtaza Q (2016) Triple bottom line performance evaluation of reverse logistics. Compet Rev 26(3):289–310
5. Abdullah L, Goh P (2019) Decision making method based on Pythagorean fuzzy sets and its application to solid waste management. Complex Intell Syst 5(2):185–198
6. Maheswari H, Yudoko G, Adhiutama A, Agustina H (2020) Sustainable reverse logistics scorecards for the performance measurement of informal e-waste businesses. Heliyon. 6(9):e04834
7. Ravi V, Shankar R, Tiwari MK (2005) Analyzing alternatives in reverse logistics for end-of-life computers: ANP and balanced scorecard approach. Comput Ind Eng 48(2):327–356
8. Shaik M, Abdul-Kader W (2012) Performance measurement of reverse logistics enterprise: a comprehensive and integrated approach. Meas Bus Excell 16(2):23–34
9. Kannan G (2009) A metaheuristics-based decision support system for the performance measurement of reverse supply chain management. Int J Bus Perform Manag 11(1–2):152–169
10. Yogi KS (2015) Performance evaluation of reverse logistics: a case of LPG agency. Cogent Bus Manag 2(1):1063229. https://doi.org/10.1080/23311975.2015.1063229
11. Pandian GR, Abdul-Kader W (2017) Performance evaluation of reverse logistics enterprise–an agent-based simulation approach. Int J Sustain Eng 10(6):384–398
12. Shao J, Taisch M, Ortega-Mier M (2016) A grey-decision-making trial and evaluation laboratory (DEMATEL) analysis on the barriers between environmentally friendly products and consumers: practitioners' viewpoints on the European automobile industry. J Clean Prod 112:3185–3194
13. Bag S, Gupta S (2019) Examining the effect of green human capital availability in adoption of reverse logistics and remanufacturing operations performance. Int J Manpow 41(7):1097–1117
14. Agrawal S, Singh RK (2020) Outsourcing and reverse supply chain performance: a triple bottom line approach. Benchmarking Int J 28(4):1146–1163
15. Fernando Y, Tew MM (2016) Reverse logistics in manufacturing waste management: the missing link between environmental commitment and operational performance. Int J Integr Supply Manag 10(3–4):264–282
16. Mahadevan K (2019) Collaboration in reverse: a conceptual framework for reverse logistics operations. Int J Prod Perform Manag 68(2):482–504
17. Mimouni F, Abouabdellah A (2016) Proposition of a methodology to evaluate the performance of the production process via performance indicators of both the production process and reverse chain process. ARPN J Eng Appl Sci 11(13):8468–8474
18. Mahindroo A, Samalia HV, Verma P (2018) Moderated influence of return frequency and resource commitment on information systems and reverse logistics strategic performance. Int J Prod Perform Manag 67(3):550–570

19. Panjehfouladgaran H, Shirouyehzad H (2018) Classification of critical success factors for reverse logistics implementation based on importance-performance analysis. Int J Prod Qual Manag 25(2):139–150
20. Škapa R, Klapalová A (2012) Reverse logistics in Czech companies: increasing interest in performance measurement. Manag Res Rev 35(8):676–692
21. Fernandes SM, Rodriguez CM, Bornia AC, Trierweiller AC, Silva SM, Freire PD (2018) Systematic literature review on the ways of measuring the of reverse logistics performance. Gestão & Produção 25(1):175–190

Project Scheduling Using Linear Programming, CPM and Crashing Time Technique

Takshay V. Sayre, Keshav Kumar, Divyansh A. Waghmare, Yash S. Deshpande, and Vishal A. Bhosale

1 Introduction

Project management can be defined as implementing certain processes and principles for initiating, planning, implementing and managing the way new programs or changes are made in an organization.

When a particular project is lagging behind the given schedule time, it is difficult for the project manager to finish the given project in the given schedule. In case if there is a termination fee set when a project manager cannot complete the project in the given time frame, then the project manager comes under lot of pressure to reduce the duration of the project. Project time can usually be reduced by providing additional resources to one or more critical activities of the project in the course of time. However, providing additional resources increases the cost of the whole project. Therefore, the decision to crash the project involves trading overtime costs [1].

The objectives of this paper are as follows:

1. Scheduling of PMRP using linear programming, CPM, crashing time technique and LINDO software.
2. To develop a model that finds a proper trade-off between time and cost to hasten the execution process.

CPM, network design, time saving and storage costs are applied in the planning of the PMRP. Final solution is evaluated using the LINDO system.

T. V. Sayre (✉) · K. Kumar · D. A. Waghmare · Y. S. Deshpande · V. A. Bhosale
MIT Academy of Engineering, Pune, India

V. A. Bhosale
e-mail: vabhosale@mitaoe.ac.in

2 Literature Survey

Many studies were led in the area of project scheduling and time cost trade-off. Agyei [2] studied at Angel Estates and Construction Ltd situated in Ghana. Here both the CPM and PERT techniques are considered for calculating the time and cost of the project. Geda [1] found that a straightforward system is used to solve project crash problems in terms of a fixed cost and delay fee. Microsoft Excel is used for solving linear programming models. Project scheduling is a part of project management which uses scheduling techniques such as Gantt charts, CPM, project evaluation and review technique (PERT) to solve and generate reports for the project. Time cost trade-off problems can be solved by using CPM/PERT and linear programming [3]. LINDO software is an alternative to excel for solving linear programming. Linear programming is used to optimize the time duration during the project for solving the linear programming. LINDO software is a better option than Excel [4].

Genetic algorithm is also used for solving the resource-constrained problems. The multi-mode resource-constrained project scheduling problem (MRCPSP) is solved by using the genetic algorithm [5]. Heuristic sequencing rules have been considered to solve in-resource-constrained problems. A heuristic algorithm is used to solve a problem in a faster and more efficient way [6]. The network scheduling techniques are used for time, resources and cost scheduling. Advanced mathematical models are more effective in case of construction scheduling [7]. A case study was done for reducing the completion time for constructing a 50 m cube biogas plant in Iran using CPM. There are many activities used that are connected through network diagrams [8]. For shortening project duration which is achieved at a lower total cost, the duration of activities acts as discrete non-increasing functions of the cost. The outcome of this leads to the discrete time/cost trade-off problem (DTCTP) [9]. A multi-objective evolutionary algorithm (e-MOEA), used for optimal time cost trade-off solutions, illustrates the methods using an automotive case study [10].

3 Methodology of Project

Following are the steps:

1. Collection of data—the data for the project was collected from various journals and research papers.
2. Project network—it is the network created for the implementation of the project in proper order and sequence.
3. CPM—critical path method is used to understand the critical activities and non-critical activities.
4. Tabulating normal time duration and cost of each activity.
5. Finding the cost time slope of each activity
6. Formulating linear programming (LP) model—To minimize the objective function and find the optimal solution.

4 Implementation

4.1 Data Collection

This study implemented linear programming technique for a chosen case organization (PMRP). From Swargate to PCMC is corridor 1 which is 16.59 km with addition to underground path of 5.0 km and elevated path of 11.50 km. Corridor 1 has 15 stations including six underground and nine elevated stations. The first column indicates the activity serial number, second column represents description of each activity, the third column provides the activity code, the fourth column represents predecessors, the fifth column represents the normal duration of each activity, and the sixth column represents the normal cost of each activity [12]. Table 1 represents a project with normal time cost data [11, 12].

4.2 CPM

The CPM is a very effective scheduling method for big projects. In this method (CPM), the duration of activity is in proportion with the amount of resources assigned to that given activity. So, the duration of activity and project can be varied by changing the amount of allocation of resources.

Critical path—the sequence of project activities from start to end. It gives minimum possible time for the completion of project.

By using forward pass, earliest start time was calculated. The earliest start time of first activity is 0.

Earliest Start$_{j\,=}$ Max$_i$ (Earliest Start$_{i\,+}$ Duration$_{ij}$)
and by using backward pass, latest finish time was calculated.
Latest finish$_{i\,=}$ Min$_j$ (Latest finish$_j$ – Duration$_{ij}$).
Critical Path: $1 - 2 - 6 - 7 - 8 - 9 - 10 - 11 - 12 - 13 - 14 - 15 - 16 - 17$.
     $A - F - G - I - J - K - L - M - N - P - R - S - T$.
     $= 9 + 3 + 4 + 12 + 3 + 36 + 6 + 4 + 3 + 5 + 2 + 2 + 1$.
     $= 90$ (months).

The CPM network diagram is shown in Fig. 1.

Before applying CPM, the duration of project was 122 months. After applying CPM, the duration of project was calculated as 90 months. So, project duration was crashed by 32 months using CPM.

Slack is the difference of time between LS and ES or LF and EF. It gives the amount of delay in an activity without having an impact on the project duration. Activities whose slack is zero are considered as critical activities because zero slack means the activity cannot be delayed without changing the project duration.

The slack of each activity along with ES, EF, LS and LF is shown in Table 2.

Table 1 Collected data

| No	Activity	Code	Predecessor(s)	Normal Time (Months)	Normal cost (In Cr)
1	Survey	A	–	9	250
2	Sanction/approval	B	A	3	20
3	Planning and timetable	C	B	4	10
4	Architecture and design	D	C	3	30
5	Approval of area	E	A	9	25
6	Auction for tender	F	A	3	10
7	Contracts and authorization	G	F	4	30
8	Financial planning and evaluation	H	E	6	100
9	Resource and man power	I	G	12	1350
10	Alignment and formation	J	I	3	901.21
11	Construction of viaducts, stations, depot and P-way	K	D, H, J	36	1445.9
12	Electrification work	L	K	6	1300
13	Technical team/wagons assembly and rolling stock	M	L	4	805.62
14	EM works	N	M	3	543.04
15	Signal and telecommunication works	O	L	6	276.63
16	Power supply and traction	P	O, N	5	207.23
17	Automatic fare collection	Q	P	1	81.82
18	Metro trials	R	P	2	50
19	Approval of NMC and NIT	S	R	2	20
20	Launch and inauguration	T	Q, S	1	5
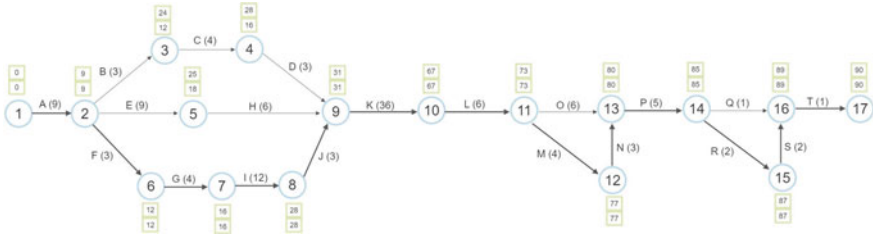
Fig. 1 Network diagram

Table 2 Slack activities

Activity	Duration	Earliest start ES	EF = ES + Duration	LS = LF − Duration	LF	Slack (LS − ES)	Critical
A	9	0	9	0	9	0	Yes
B	3	9	12	21	24	12	No
C	4	12	16	24	28	12	No
D	3	16	19	28	31	12	No
E	9	9	18	16	25	7	No
F	3	9	12	9	12	0	Yes
G	4	12	16	12	16	0	Yes
H	6	18	24	25	31	7	No
I	12	16	28	16	28	0	Yes
J	3	28	31	28	31	0	Yes
K	36	31	67	31	67	0	Yes
L	6	67	73	67	73	0	Yes
M	4	73	77	73	77	0	Yes
N	3	77	80	77	80	0	Yes
O	6	73	79	74	80	1	No
P	5	80	85	80	85	0	Yes
Q	1	85	86	88	89	3	No
R	2	85	87	85	87	0	Yes
S	2	87	89	87	89	0	Yes
T	1	89	90	89	90	0	Yes

4.3 Crashing Data

Some important terms required for crashing data are stated below.

Normal time: Duration required to complete each activity.
Crash time: Duration under which the activity has to be completed after crashing.
Normal cost: Normal cost of each activity.

Crash cost: Normal cost + additional cost required to crash the activity for the given duration.

ΔC: (Crash cost–Normal cost)

Δt: (Normal time–Crash time)

$U_i = \frac{\Delta C}{\Delta t}$: Cost time slope.

Cost time slope indicates the variation in cost of the activity if the duration of activity is to be varied.

The cost time slopes of activities along with crash time and crash cost are shown in Table 3.

4.4 Linear Programming

The problem has been framed as a linear programming model as follows:

Assume Z be the total cost of crashing activities. Here Z is to be minimized subjected to the constraints.

$\sum_{i=1}^{n} U_i X_i$ (objective function)

$X_i =$ Amount of times that each activity i will be crashed

$Y_i =$ Start time of activity I (This variable is not required for the activity which starts the project)

U_i is the cost time slope.

Objective function:

Objective function is to minimize the total cost of crashing activities

$$\text{Minimize } Z = 10X_A + 5X_B + 2.5X_C + 5X_D + 4X_E + 2X_F$$
$$+ 3.333X_G + 10X_H + 100X_I + 300X_J + 50X_K + 166.66X_L$$
$$+ 150X_M + 40X_N + 26.667X_O + 33.334X_P + 0X_Q$$
$$+ 10X_R + 5X_S + 0X_T \tag{1}$$

In this study, three major constraints are considered such as maximum reduction, non-negativity, start time and project duration.

Max reduction constraints:

$$\text{Crash time constraints:} X_i \leq \text{Allowable crashing time for activity } i \tag{2}$$

Maximum crash time cannot exceed Δt.

$X_A \leq 5$	$X_K \leq 12$
$X_B \leq 1$	$X_L \leq 3$

(continued)

(continued)

$X_C \le 2$	$X_M \le 2$
$X_D \le 2$	$X_N \le 1$
$X_E \le 5$	$X_O \le 3$
$X_F \le 1$	$X_P \le 3$
$X_G \le 3$	$X_Q \le 0$
$X_H \le 2$	$X_R \le 1$
$X_I \le 4$	$X_S \le 1$
$X_J \le 1$	$X_T \le 0$

Non-negativity constraints:

$$\text{Non - negative constraints : All decision variables must} \ge 0. \qquad (3)$$

$X_i \ge 0$ where $i = $ A, B, C…, T
$Y_i \ge 0$ where i = A, B, C…, T
Start time constraints:

Start time of this activity $(Y_i) = $ (start time $+$ normal duration $-$ crash duration)
for this immediate predecessor. $\qquad (4)$

For example, activity C has predecessor as activity B whose duration is $3 - X_B$.
So, the start time constraint of activity C is $Y_C \ge Y_B + 3 - X_B$. Therefore, activity cannot start unless activity B is completed.

For example, activity P has predecessor as activity O and activity M. The duration of activity O is $6 - X_O$, and for activity M is $3 - X_N$, so the start time constraint of activity P is $Y_P \ge (Y_O + 6 - X_O)$ and $Y_P \ge (Y_M + 3 - X_N)$.

Activities with one immediate predecessor	Activities with two immediate predecessor	Activities with three immediate predecessor
$Y_B \ge (0 + 9 - X_A)$	$Y_P \ge (Y_O + 6 - X_O)$	$Y_K \ge (Y_D + 3 - X_D)$
$Y_C \ge (Y_B + 3 - X_B)$	$Y_P \ge (Y_M + 3 - X_N)$	$Y_K \ge (Y_H + 6 - X_H)$
$Y_D \ge (Y_C + 4 - X_C)$	$Y_T \ge (Y_Q + 1 - X_Q)$	$Y_K \ge (Y_J + 3 - X_J)$
$Y_E \ge (Y_A + 9 - X_A)$	$Y_T \ge (Y_S + 2 - X_S)$	
$Y_F \ge (Y_A + 9 - X_A)$		
$Y_G \ge (Y_F + 3 - X_F)$		
$Y_H \ge (Y_E + 9 - X_E)$		
$Y_I \ge (Y_G + 4 - X_G)$		
$Y_J \ge (Y_I + 12 - X_I)$		
$Y_L \ge (Y_K + 36 - X_K)$		
$Y_M \ge (Y_L + 6 - X_L)$		

(continued)

Activities with one immediate predecessor	Activities with two immediate predecessor	Activities with three immediate predecessor
$Y_N \geq (Y_M + 4 - X_M)$		
$Y_O \geq (Y_L + 6 - X_L)$		
$Y_Q \geq (Y_P + 5 - X_P)$		
$Y_R \geq (Y_P + 5 - X_P)$		
$Y_S \geq (Y_R + 2 - X_R)$		
$Y_{finish} \geq (Y_T + 1 - X_T)$		

Project duration constraints:

Project completion constraints : $Y_m \leq$ project completion date after extension,

$$(5)$$

where m is the last activity of that project.

Suppose the project manager of the project wants to complete the project the project under 70 months.

Assume Y_{finish} and the predecessor of Y_{finish} is Y_T, i.e., the last activity of the project $Y_{finish} \leq 70$.

5 Computation

LINDO software is used to calculate the optimal solution for the given linear programming problem. The results obtained from the LINDO software are presented in Fig. 2.

6 Result and Analysis

In this case study, the projected problem is optimized using LINDO software, and the solution is given in Table 4.

From this table, the first column represents the variables, second column represents the value of the variables, and the 3rd column represents the reduced cost. Earlier, the total time duration was 90 months, and estimated total cost was 7461.45 cr was required for the project to be completed.

After performing the cost time trade-off method, we get Table 4 which shows that the extra cost of 357.0020 cr is to be sustained in order to crash the activities and finish the project by 20 months.

Table 3 Crashing data

	Activity	Code	Predecessor(s)	Normal time (months)	Crash time	Normal cost (In Cr)	Crash cost	ΔC	Δt	$U_i = \frac{\Delta C}{\Delta t}$
1	Survey	A	–	9	4	250	300	50	5	10
2	Consent/authorization	B	A	3	2	20	25	5	1	5
3	Work plan and time schedule	C	B	4	2	10	15	5	2	5/2
4	Designing and architecture	D	C	3	1	30	40	10	2	5
5	Area approval	E	A	9	4	25	45	20	5	4
6	Tender auction	F	A	3	2	10	12	2	1	2
7	Contract signing	G	F	4	1	30	40	10	3	10/3
8	Finance and evaluation	H	E	6	4	100	120	20	2	10
9	Resource and man power	I	G	12	8	1350	1750	400	4	100
10	Alignment and formation	J	I	3	2	901.21	1201.21	300	1	300
11	Construction of viaducts, stations, depot and P-way	K	D, H, J	36	24	1445.9	2045.9	600	12	50
12	Electrification work	L	K	6	3	1300	1800	500	3	500/3
13	Technical team/wagons assembly and rolling stock	M	L	4	2	805.62	1105.62	300	2	150
14	EM works	N	M	3	2	543.04	583.04	40	1	40

(continued)

Table 3 (continued)

	Activity	Code	Predecessor(s)	Normal time (months)	Crash time	Normal cost (In Cr)	Crash cost	ΔC	Δt	$U_i = \frac{\Delta C}{\Delta t}$
15	Signal and telecommunication works	O	L	6	3	276.63	356.63	80	3	80/3
16	Power supply and traction	P	O, N	5	2	207.23	307.23	100	3	100/3
17	Automatic fare collection	Q	P	1	1	81.82	0	0	0	0
18	Metro trials	R	P	2	1	50	60	10	1	10
19	Approval of NMC and NIT	S	R	2	1	20	25	5	1	5
20	Launch and inauguration	T	Q, S	1	1	5	0	0	0	0

Fig. 2 Result in Lindo

So, the project time is reduced from 90 to 70 months, i.e., 20 months, and the total cost of the project increased from 7461.45 cr to 7818.452 cr in order to complete the project in desired time. The percentage decrease in time is 22.22%, and the percentage increase in cost is 4.56%.

For activity A, the value of X_A from the table is 5, so this indicates that activity A should be crashed for 5 months, similarly it applies to other activities in order to finish the project in 70 months.

For activity A, the value of Y_A from the table is 0, so this indicates that the start time of activity A is 0. Similarly for activity B, the value of Y_B is 4, it indicates that the start time of activity is 4. As activity A is the predecessor of B, it means that it will only start when activity A is completed.

The reduced cost may be inferred as the amount of penalty you need to pay to introduce a variable into the solution. For activity B, the value of crash time is 0, and the value of reduced cost is 5. So for crashing activity B, additional cost of 5 Cr is required.

Since Y_{Finish} is equal to 70, this indicates that the whole project would finish within 70 months.

Table 4 Result of LINDO software

VARIABLE	VALUE	Reduced COST
X_A	5	0
X_B	0	5
X_C	0	2.5
X_D	0	5
X_E	0	4
X_F	1	0
X_G	3	0
X_H	0	10
X_I	0	50
X_J	0	250
X_K	2	0
X_L	0	116.660004
X_M	0	150
X_N	0	40
X_O	3	0
X_P	3	0
X_Q	0	0
X_R	1	0
X_S	1	0
X_T	0	0
Y_A	0	50
Y_B	4	0
Y_C	15	0
Y_D	19	0
Y_E	7	0
Y_F	4	0
Y_G	6	0
Y_H	16	0
Y_I	7	0
Y_J	19	0
Y_K	22	0
Y_L	56	0
Y_M	62	0
Y_N	66	0
Y_O	62	0
Y_P	65	0
Y_Q	68	0

(continued)

Table 4 (continued)

VARIABLE	VALUE	Reduced COST
Y_R	67	0
Y_S	68	0
Y_T	69	0
Y_{FINISH}	70	0

7   Conclusion

This paper focused on the method of project scheduling in PMRP. The PMRP was studied as a linear programming model and optimized with the help of LINDO software.

The following points can be concluded from this paper:

- Using CPM method, the project duration was decreased to 90 months to finish the project; however, the original project time was 122 months.
- In order to decrease the time, furthermore the cost time trade-off method was used which resulted in project time decreasing to 70 months, i.e., 22.22% decrease (90 to 70 months) and an extra cost of 357.0020 Cr is sustained, i.e., 4.56% increase.

The above prepared schedule using cost time trade-off method is considerably shorter than the original schedule. This planned schedule is a very beneficial and feasible option. This method can be used in various bigger projects like construction project.

References

1. Geda MW (2014) A linear programming approach for optimum project scheduling. Int J Eng Res Technol 3(10):1271–1275
2. Agyei W (2015) Project planning and scheduling using PERT and CPM techniques with linear programming: case study. Int J Sci Technol Res 4(8):222–227
3. Vyas RS (2013) Project management using crashing CPM network to get project completed on time. Int J. Eng Res Technol (IJERT) 2(2):1–12
4. Elmabrouk OM (2012) Scheduling project crashing time using linear programming technique. In: Proceedings of the 2012 international conference on industrial engineering and operations management Istanbul, Turkey 3–6 July 2012
5. Hartmann S (2001) Project scheduling with multiple modes: a genetic algorithm. Ann Oper Res 102:111–135
6. Davis EW, Patterson JH (1975) A Comparison of heuristic and optimum solutions in resource-constrained project scheduling. Manage Sci 21(8):944–955
7. Ahuja V, Thiruvengadam, (2004) V Project scheduling and monitoring: current research status. Constr Innov 4(1):19–31
8. Zareei S (2018) Project scheduling for constructing biogas plant using critical path method. Renew Sustain Energy Rev 81:756–759
9. De P, Dunne EJ, Ghosh JB, Wells (1995) CE The discrete time-cost tradeoff problem revisited. Europ J Opera Res 81:225–238

10. Meier C, Yassine AA, Browning TR, Walter U (2016) Optimizing time–cost trade-offs in product development projects with a multi-objective evolutionary algorithm. Res Eng Design 27:347–366. https://doi.org/10.1007/s00163-016-0222-7
11. Uparkar SS, Chawre SS, Rehpade RS, Jha NR, Sahu AJ, Chhabriya BM, Ballav KS (2020) Analysis of Nagpur metro rail project using CPM, PERT and crashing. Int J Adv Sci Technol 29(8):4055–4064
12. Delhi metro rail corporation LTD. (2015) Final detailed project report for Pune metro rail project client: Pune Municipal Corporation http://www.pmc.gov.in/informpdf/Metro/DPR_Metro_NOV_2015.pdf

Experimental Study of Effect of Process Parameters on Surface Roughness and Dimensional Accuracy of Parts Fabricated by Fused Deposition Modelling

Shailendra Kumar, Swapnil Vyavahare, and Jyothi Kootikuppala

1 Introduction

Additive manufacturing is a new approach that gained industry and research interest because of the ability to build lighter, stronger and complex parts as suitable for end user. Conner et al. [1] stated that with increase in costs for customization in conventional manufacturing, there is necessity to increase focus on AM. These techniques are categorized into seven groups [2]. In 1988, Crump had patented FDM which is one of the AM techniques [3]. It has become popular because of its ability to use wide range of materials to fabricate parts economically. But, the parts fabricated by FDM show low-dimensional accuracy and surface finish when compared with another AM techniques. In recent times, several studies for obtaining better surface finish and dimensional accuracy in FDM fabricated specimens are made.

Anitha et al. [4] fabricated models using acrylonitrile butadiene styrene (ABS) to investigate the effect of parameters on surface roughness. They showed that the significance of build layer height is higher and indicated a strong inverse relation between surface finish and thickness of layer. Campbell et al. [5] showed that the different AM processes have varied surface roughness for different build orientations, and also for some models, the staircase effect does not affect surface roughness. Semi-empirical model was developed to find factors that affect surface roughness, and it showed that layer height, part orientation are significant [6]. Adaptive slicing and genetic algorithm are used to determine optimum orientation of part. [7]. Lee et al. [8] have conducted an experimental study on catapult-shaped ABS and found that layer height, air gap and raster angle affect elastic performance of specimen. Horvath et al. [9] revealed that minimum value of layer thickness and higher value of part temperature are required for low surface roughness of FDM parts. Wang et al. [10] analysed surface roughness on trapezoidal ABS specimen. They concluded

S. Kumar (✉) · S. Vyavahare · J. Kootikuppala
Department of Mechanical Engineering, Sardar Vallabhbhai National Institute of Technology, Surat, India

that by selecting optimal settings, surface roughness has increased by 62.27%. Ahn et al. [11] studied surface roughness of ABS fabricated specimen with filament of elliptical cross section. The surface roughness values at different surface angles and layer thickness are obtained and compared with proposed model. They showed that surface roughness for FDM process is accurately predicted using the proposed model. Galantucci et al. [12] carried out experiments on ABS prototype in two levels where one is by manufacturing only and other is carried by chemical bath and found that surface finish is better for parts that underwent chemical treatment. Sood et al. [13] observed that deviation in length and width dimensions are negative in value, whereas deviation in thickness direction is positive for FDM built ABS P400 parts. Nancharaiah et al. [14] investigated the dimensional accuracy of ASTM D695 standard FDM specimen of ABS material. The investigation revealed that layer height, road width show major influence on part accuracy. Chang and Huang [15] studied profile error and aperture of extrusion in parts made from FDM process. It is observed that profile error can be minimized by selecting large contour widths and small contour depths. Zhang and Peng [16] made an empirical formula which states relation among process parameters and deformation, accuracy of ABS specimen. They found the optimal values for process parameters for minimizing dimensional error and deformation. Gorski et al. [17] have conducted an experimental study to find role of parameters in effecting dimensional accuracy and repeatability of specimens. They revealed that built orientation affects dimensional accuracy and repeatability of specimens directly. Luzanin et al. [18] studied influence of temperature, extrusion speed on surface roughness of prismatic part of PLA material and revealed that low surface roughness is observed at low extrusion speed and high extrusion temperature. Raol et al. [19] carried out an experimental investigation on polycarbonate parts and found that part orientation and layer height have significant effect. Mohamed et al. [20] used I-optimality criteria and developed mathematical models to understand the relation of process parameters and accuracy of the part. They concluded that I-optimal criteria gave better results than traditional methods, and the results are within acceptable range for industrial applications. Beniak et al. [21] carried out research work on dimensional accuracy of trapezium and cylindrical shaped PLA specimens fabricated by FDM and noted that layer height and extrusion temperature are influencing parameters.

The above literature review shows that several studies are being carried out to improve surface finish and dimensional accuracy of parts. However, further study is required to investigate the effect of FDM parameters on quality characteristics of parts having complex features. Therefore, the objective of the present study is to study the effect of parameters on responses such as surface finish and dimensional accuracy of fabricated specimens.
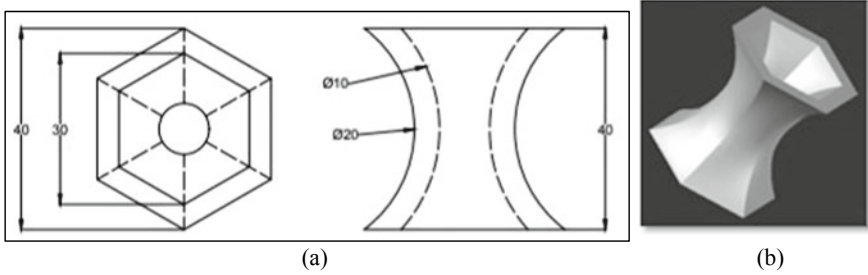
Fig. 1 **a** 2D drawing of specimen with dimensions (All dimensions are in mm.); and **b** 3D CAD model of specimen

2 Experimental Details

The current study contains different steps such as computer-aided design (CAD) modelling of specimen, design of experiment (DOE), manufacturing of parts and measuring responses.

2.1 CAD Modelling

This study includes the part having 6 curved surfaces. The specimen is having hexagonal face on both sides and circular shape at centre. The part is modelled using Autodesk Inventor 2020 software and is saved as stereolithography (STL) format file. The specimen is shown in Fig. 1.

2.2 Experimental Design

Process parameters, namely layer thickness, build orientation, extrusion temperature and raster width, are considered for current study. Table 1 shows levels of process parameters which are based on available FDM machine and literature review. A

Table 1 Selected levels of process parameters

S. No.	Process parameters	Units	Levels			
			1	2	3	4
1	Layer thickness	Mm	0.1	0.15	0.2	0.25
2	Build orientation	Degree	0	30	60	90
3	Extrusion temperature	°C	195	200	205	210
4	Raster width	Mm	0.5	0.6	0.7	0.8

Table 2 Constant parameters and their values

S. No.	Parameter	Units	Value
1	Raster angle	degree	0
2	Print speed	mm/s	40
3	Infill density	%	25
4	Infill pattern	type	Grid
5	Wall thickness	mm	1
6	Base plate adhesion	type	Brim
7	Temperature of base plate	°C	70

detailed experimental study is designed using L_{16} Taguchi orthogonal array by using Minitab and Design-Expert software. The Taguchi orthogonal matrix suggested a total of 16 runs. Constant parameters are given in Table 2.

2.3 Specimen Fabrication

FDM machine (Make: Prusa) used for current study is shown in Fig. 2. It has 0.8 mm nozzle diameter. Its rectangular print surface has area of 200×200 mm with maximum print velocity of 300 mm/s. Slicing of the model is done using the CURA software. PLA material is considered as feedstock material. It is supplied by M/s Positron Additive Ltd., Pune as 1.75 mm diameter filament.

The earlier saved STL file is imported to CURA 4.4 to obtain the file in G-CODES as per design of experiment. The GCODE files are loaded in the FDM machine for printing the parts. Specimens with part orientation w.r.t Y-axis from 0° to 90° are shown in Fig. 3. While fabricating parts, support structures of same feedstock material are built during the fabrication process. In total, 16 parts are fabricated as shown in Fig. 4.

2.4 Measurement of Responses

Surface roughness of manufactured parts is measured to find average surface roughness (R_a) with Mitutoyo Surftest SJ-310 surface roughness tester. Dimensions of parts are calculated with the help of a vernier caliper having range of 0–150 mm with 0.05 mm least count. The error in dimension (%) in width is found using Eq. 1. Similarly, dimensional accuracy for height and outer diameter is measured.

$$\delta w = \frac{\text{Width of CAD model } - \text{ Width of manufactured part}}{\text{Width of CAD model}} \times 100\% \quad (1)$$
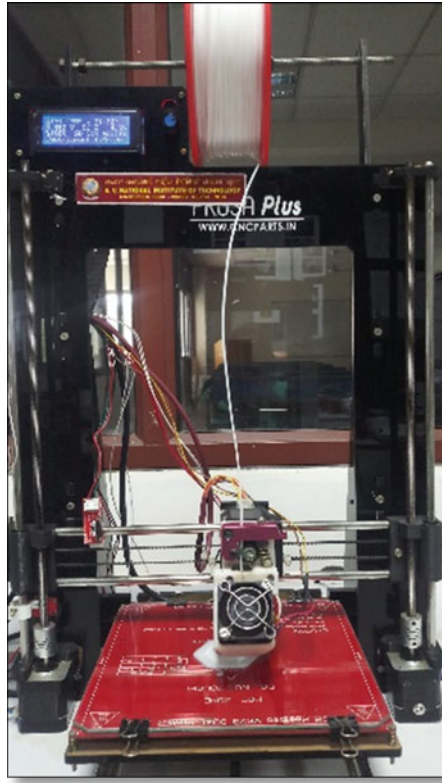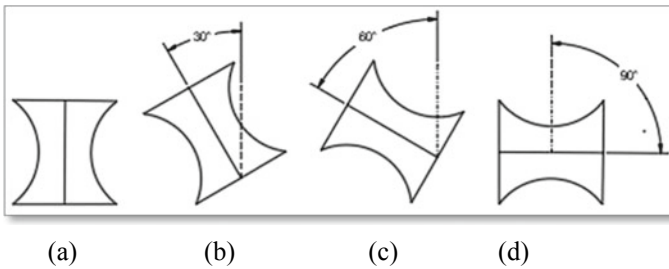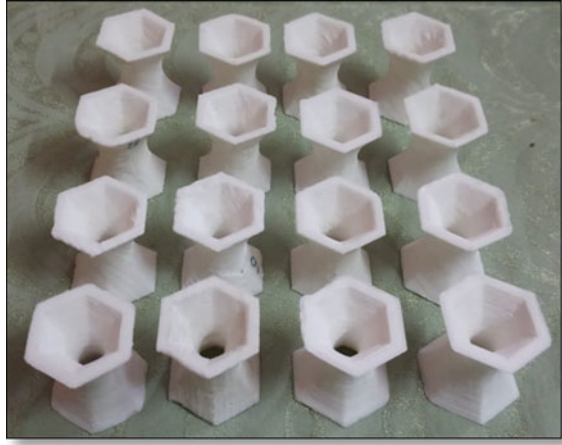
Fig. 2 Prusa plus FDM machine

(a)   (b)   (c)   (d)

Fig. 3 Parts showing build orientations **a** 0° **b** 30° **c** 60° **d** 90°

Reading is taken for curved surfaces excluding the surfaces having contact of support structures and the mean value of R_a is considered in this study. Experimental results are given in Table 3.

Fig. 4 Specimens fabricated
by FDM

3　Results and Discussion

Obtained responses are analysed using Minitab software. Surface roughness values of fabricated specimens vary from 11.986 to 22.036 µm for outer curved surface and 13.062–21.056 µm at inner curved surface regions. Dimensional error is obtained between 0.12 and 1.63% in height, 1.64–3.96% in width and 0.25–2% in diameter of fabricated specimens. Overall data of mean and standard deviation of measured responses is calculated (Table 4). ANOVA is carried out to find the effect of selected factors on measured responses (Table 5).

3.1　Surface Roughness (Curved Faces of Outer Surface)

Main effect plots on outer curved region are in Fig. 5. It is noted that all factors influence the surface roughness of parts. As in Table 5, layer height and part orientation are to be considered as most influential. It is observed that as layer height increases, surface roughness also increases which is caused by staircase effect [4, 6, 22]. Build orientation decides the stacking sequence of layers and also need of support structures, thus affecting the overall surface finish of the part [7, 23].

　　The interaction plot for surface roughness on outer curved region is shown in Fig. 6. Synergistic interaction exists between layer height and remaining parameters [24].

Table 3 Experimental design with results

Run	Layer thickness	Build orientation	Extrusion temp	Raster width	R_a (outer surface)	R_a (inner surface)	δw	δd	δh
	mm	deg	°C	mm	micron	micron	%	%	%
1	0.10	0	195	0.5	16.827	15.860	2.08	0.25	1.00
2	0.10	30	200	0.6	13.827	13.139	2.61	1.75	0.50
3	0.10	60	205	0.7	17.139	13.062	3.29	0.25	1.00
4	0.10	90	210	0.8	11.986	14.378	3.38	0.50	0.50
5	0.15	0	200	0.7	18.279	17.275	1.64	0.75	1.63
6	0.15	30	195	0.8	16.278	16.916	2.08	0.50	0.12
7	0.15	60	210	0.5	18.737	16.136	3.53	0.25	0.25
8	0.15	90	205	0.6	17.416	17.125	2.80	0.25	0.88
9	0.20	0	205	0.8	20.610	19.523	1.84	1.25	0.25
10	0.20	30	210	0.7	20.598	19.771	3.29	1.00	0.12
11	0.20	60	195	0.6	19.736	17.121	3.57	1.50	0.25
12	0.20	90	200	0.5	20.590	18.181	3.43	0.25	0.12
13	0.25	0	210	0.6	22.036	20.309	2.95	1.75	1.50
14	0.25	30	205	0.5	21.313	21.056	3.72	2.00	0.12
15	0.25	60	200	0.8	20.675	18.124	3.43	0.75	0.25
16	0.25	90	195	0.7	21.353	20.226	3.96	0.25	0.12

Table 4 Data of mean and standard deviation along with factor levels

Factor	Levels	R_a (outer surface)		R_a (inner surface)		δw		δd		δh	
		μ	σ	μ	σ	μ	σ	μ	σ	μ	σ
Layer thickness	0.10	14.94[a]	2.47	14.11[a]	1.313	2.838	0.613	0.688	0.718	0.750	0.289
	0.15	17.678	1.082	16.863	0.507	2.512	0.828	0.438	0.239	0.719	0.688
	0.20	20.383	0.432	18.649	1.235	3.031	0.806	1	0.54	0.188[a]	0.072
	0.25	21.344	0.556	19.929	1.26	3.514	0.436	1.187	0.826	0.500	0.669
Build orientation	0	19.44	2.33	18.24	2.04	2.126[a]	0.576	1	0.645	1.094	0.624
	30	18	3.56	17.72	3.51	2.923	0.726	1.313	0.688	0.219	0.188
	60	19.071	1.512	16.11	2.19	3.454	0.128	0.688	0.591	0.438	0.375
	90	17.84	4.26	17.48	2.43	3.394	0.474	0.312[a]	0.125	0.406	0.359
Extrusion Temp	195	18.55	2.41	17.531	1.88	2.923	0.989	0.625	0.595	0.375	0.421
	200	18.34	3.21	16.68	2.4	2.778	0.85	0.875	0.629	0.625	0.685
	205	19.12	2.15	17.69	3.48	2.911	0.809	0.938	0.851	0.562	0.439
	210	18.34	4.45	17.65	2.86	3.285	0.246	0.875	0.661	0.594	0.624
Raster width	0.5	19.37	2.01	17.81	2.4	3.188	0.75	0.688	0.875	0.375	0.421
	0.6	18.25	3.5	16.92	2.94	2.983	0.418	1.313	0.718	0.781	0.544
	0.7	19.342	1.967	17.58	3.28	3.043	0.987	0.562	0.375	0.719	0.732
	0.8	17.39	4.15	17.24	2.18	2.681	0.843	0.75	0.354	0.281	0.157

Notes [a]Minimum value for mean; μ—Mean; σ—standard deviation

Table 5 ANOVA analysis of factors

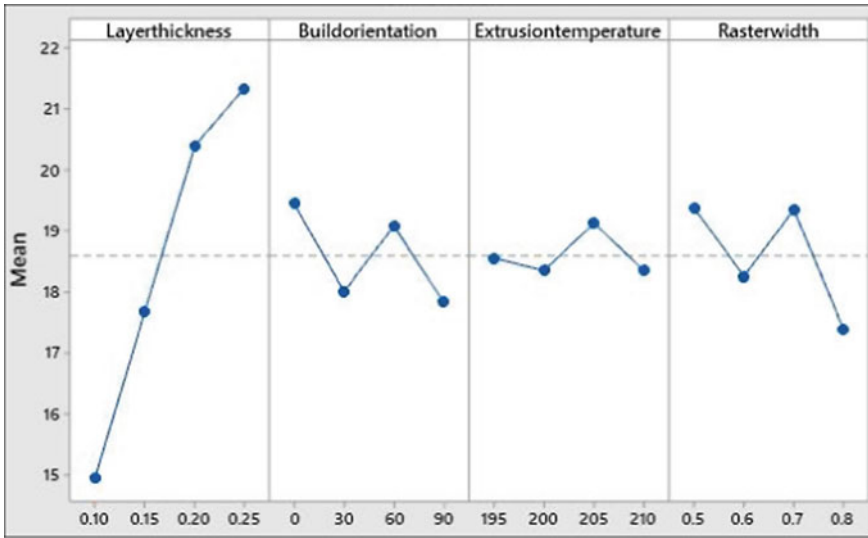| Factor	R_a (outer surface)		R_a (inner surface)		δw		δd		δh	
	F	P	F	P	F	p	F	P	F	P
Layer thickness	5.08	<0.05	22.46	<0.05	7.73	<0.05	1.13	0.456	1.610	0.289
Part orientation	13.96	<0.05	57.79	<0.05	6.8	<0.05	1.2	0.387	1.440	0.322
Extrusion temp	1.04	0.4389	7.51	<0.05	14.56	<0.05	1.99	0.217	3.120	0.109
Raster width	0.227	0.8741	2.07	0.2062	1.83	0.2423	0.205	0.887	0.269	0.845

Fig. 5 Main effects plots of factors vs surface roughness on curved faces of outer surface
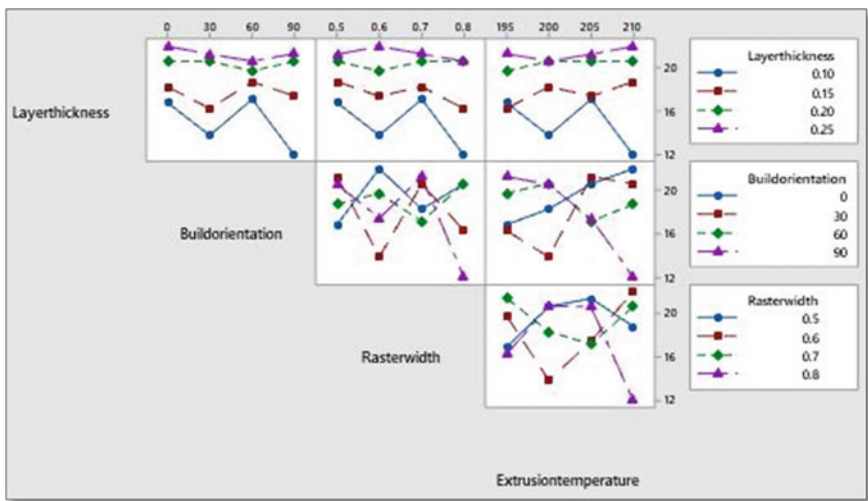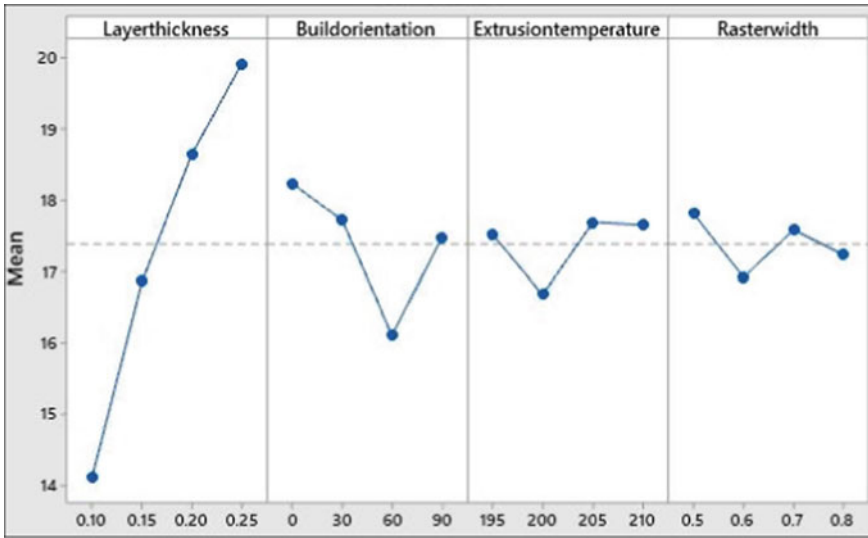

Fig. 6 Interaction plot for surface roughness on curved faces of outer surface

3.2 Surface Roughness (Curved Faces of Inner Surface)

Main effect plots showing inner curved region are shown in Fig. 7. As shown in Figs. 7 and 8, trends for inner curved region are similar to outer curved region except for build orientation. It is observed that for 60° part orientation, surface roughness

Fig. 7 Main effects plots of factors vs surface roughness on curved faces of inner surface
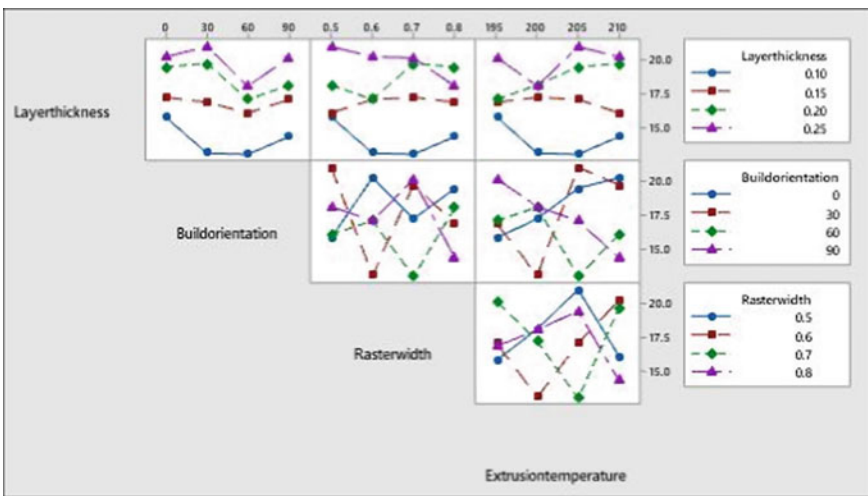
Fig. 8 Interaction plot for surface roughness on curved faces of inner surface

on curved faces of outer surface is higher than curved faces of inner surface. Layer thickness and orientation of part affect the surface roughness [25, 26]. From Table 4, it is noted that overall mean of surface roughness for curved faces of outer surface is higher than the overall mean of surface roughness for curved faces of inner surface. From Fig. 8, it is observed that synergistic interaction exists between layer thickness and other parameters.
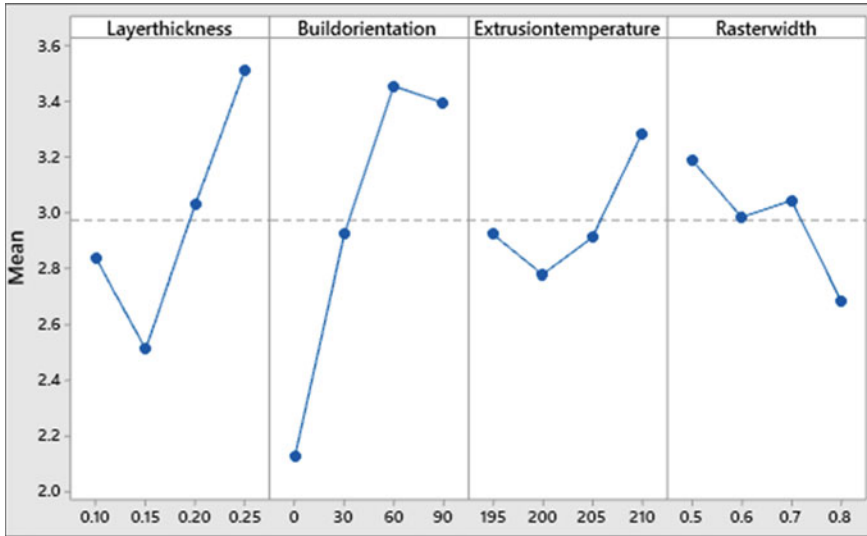
Fig. 9 Main effects plots of factors vs accuracy in the direction of width

3.3 Dimensional Accuracy in the Direction of Width (Curved Faces of Outer Surface)

Main effect plots in the direction of width are in Fig. 9. Least accuracy is obtained at intermediate value for layer thickness and extrusion temperature. From Table 5, it is observed that layer height, orientation of part and extrusion temperature are significant along width. Minimum accuracy is observed at 0° build orientation and 0.8 mm raster width. Layer thickness, orientation of part are the significant parameters for dimensional accuracy [10, 21, 27, 28].

Interaction plots in the direction of width are in Fig. 10. Severe interactions are observed between all the process parameters. From Table 5, it is noted that there is a major influence of layer thickness, orientation of part and extrusion temperature ($p < 0.05$).

3.4 Dimensional Accuracy of Diameter (Curved Faces of Outer Surface)

Main effect plots for diameter are in Fig. 11. Accuracy is minimum at intermediate values of layer thickness and raster width. The deviations in diameter are less than the deviations in width direction. Accuracy along diameter initially increases, then decreases as part orientation and raster width increases. Interaction plots of diameter are in Fig. 12. Severe interactions between each factor are observed.
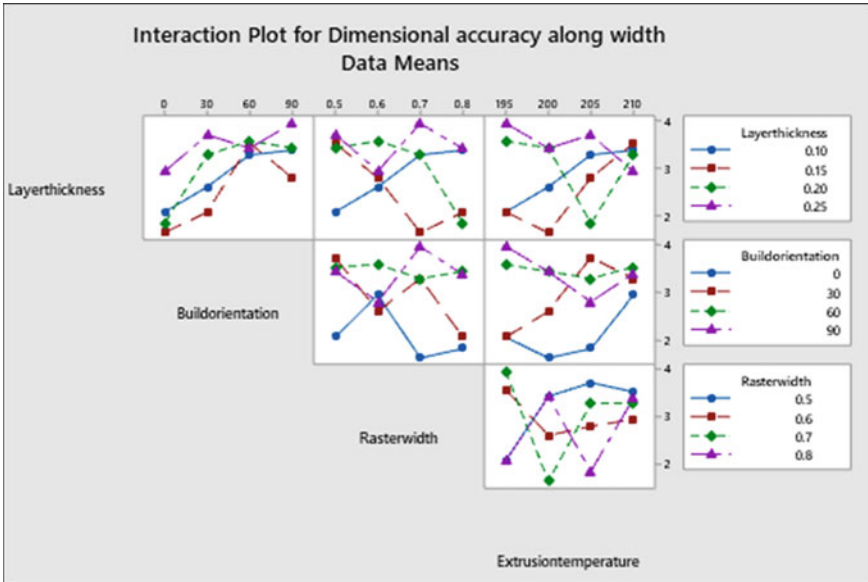
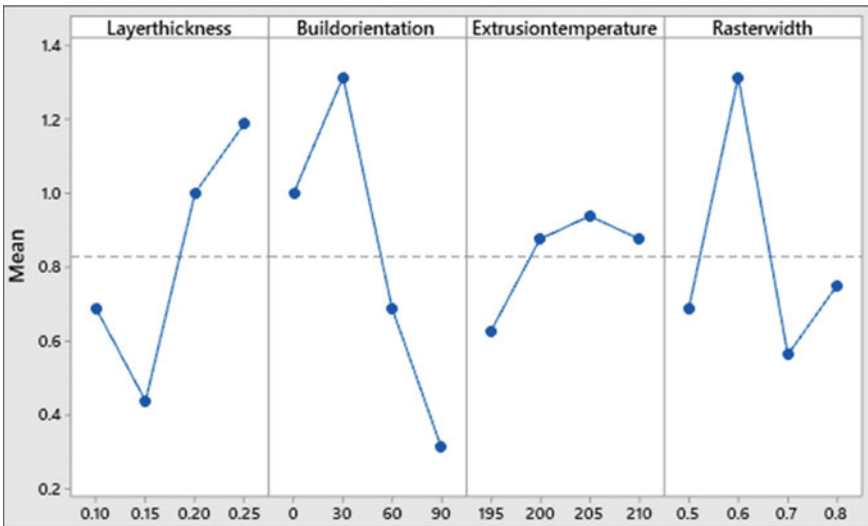**Fig. 10** Interaction plot in the direction of width

Fig. 11 Main effects plot of factors versus accuracy of diameter
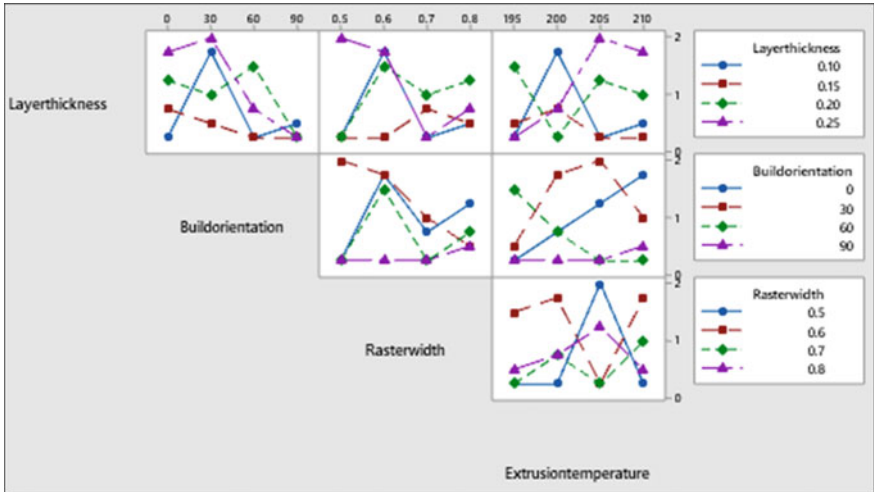
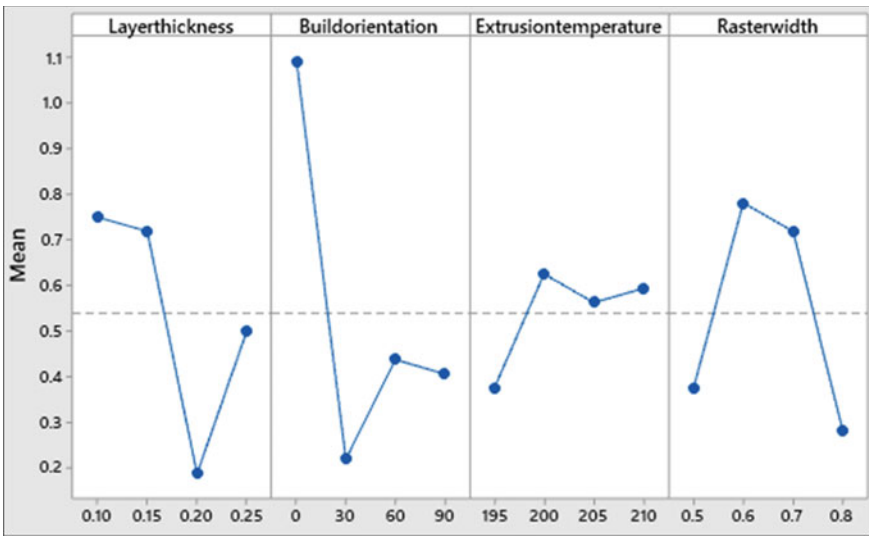**Fig. 12** Interaction plot of diameter

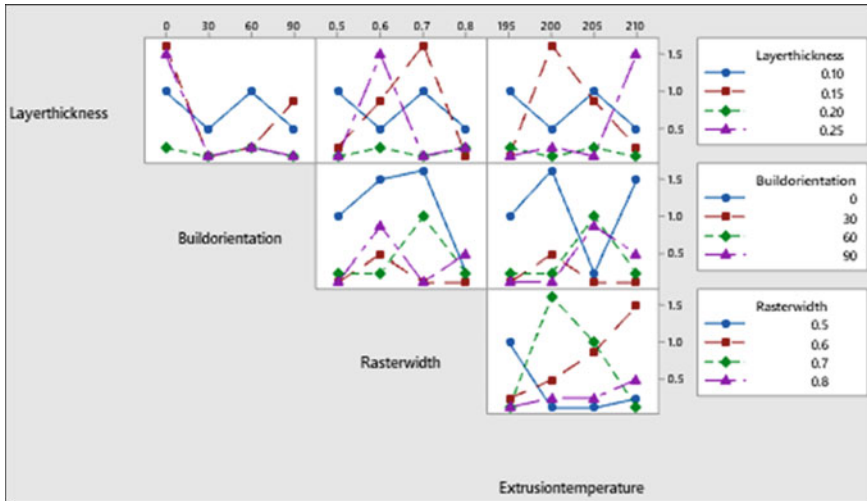**Fig. 13** Main effects plots of factors vs accuracy in the direction of height

Fig. 14 Interaction plot in the direction of height

3.5 Dimensional Accuracy in the Height Direction (Curved Faces of Outer Surface)

Main effect plots in the direction of height for dimensional accuracy are given in Fig. 13. Maximum deviation is observed at intermediate level for extrusion temperature and raster width. Maximum deviation is observed at 0° build orientation because specimen is fabricated on base plate using support structures. Minimum deviation is observed at 195 °C temperature and 0.8 mm road width.

Interactions plot in height direction for dimensional accuracy is depicted in Fig. 14. There exist severe interactions between all the factors. No synergistic interaction between any factors is observed.

4 Conclusion

The present paper describes an experimental study of effect of process parameters on surface roughness and dimensional accuracy of parts fabricated by FDM technique. The findings from this study are listed as follows -

(i) Layer thickness and part orientation are major factors affecting the specimens' surface roughness. Surface roughness increases with layer height. It first decreases and then increases as part orientation and raster width increases.

(ii) Dimensional accuracy in the direction of width is mostly influenced by layer height, part orientation and extrusion temperature. The deviation in dimensions initially decreases, then increases as layer height increases. With increase in

part orientation dimensional accuracy initially increases and then decreases. With increase in extrusion temperature dimensional accuracy first decreases and then increases.

References

1. Conner BP, Manogharan GP, Martof AN, Rodomsky LM, Rodomsky CM, Jordan DC, Limperos JW (2014) Making sense of 3-D printing: Creating a map of additive manufacturing products and services. Addit Manuf 1:64–76
2. Li H, Wang T, Sun J, Yu Z (2018) The effect of process parameters in fused deposition modelling on bonding degree and mechanical properties. Rapid Prototyping J 24(2):80–92
3. Vyavahare S, Teraiya S, Panghal D, Kumar S (2020) Fused deposition modelling: a review. Rapid Prototyping J 26(1):176–201
4. Anitha R, Arunachalam S, Radhakrishnan P (2001) Critical parameters influencing the quality of prototypes in fused deposition modelling. J Mater Process Technol 118(1–3):385–388
5. Martorelli CM, Lee HS (2002) Surface roughness visualization for rapid prototyping models. Comput-Aided Des 34:717–725
6. Pandey PM, Reddy NV, Dhande SG (2003) Improvement of surface finish by staircase machining in fused deposition modelling. J Mater Process Technol 132(1–3):323–331
7. Thrimurthulu K, Pandey PM, Reddy NV (2004) Optimum part deposition orientation in fused deposition modeling. Int J Mach Tools Manuf 44(6):585–594
8. Lee BH, Abdullah J, Khan ZA (2005) Optimization of rapid prototyping parameters for production of flexible ABS object. J Mater Process Technol 169(1):54–61
9. Horvath D, Noorani R, Mendelson M (2007) Improvement of surface roughness on ABS 400 polymer using design of experiments (DOE). Mater Sci Forum 561–565:2389–2392
10. Wang CC, Lin TW, Hu SS (2007) Optimizing the rapid prototyping process by integrating the Taguchi method with the Gray relational analysis. Rapid Prototyping J 13(5):304–315
11. Ahn D, Kweon JH, Kwon S, Song J, Lee S (2009) Representation of surface roughness in fused deposition modeling. J Mater Process Technol 209(15–16):5593–5600
12. Galantucci LM, Lavecchia F, Percoco G (2009) Experimental study aiming to enhance the surface finish of fused deposition modeled parts. CIRP Ann Manuf Technol 58(1):189–192
13. Sood AK, Ohdar RK, Mahapatra SS (2009) Grey Taguchi method for improving dimensional accuracy of FDM process. Mater Des 30(10):4243–4252
14. Nancharaiah T, Raju D, Raju V (2010) An experimental investigation on surface quality and dimensional accuracy of FDM components. Int J Emerg Technol 1(2):106–111
15. Chang DY, Huang BH (2011) Studies on profile error and extruding aperture for the RP parts using the fused deposition modelling process. Int J Adv Manuf Technol 53(9–12):1027–1037
16. Zhang J, Peng A (2012) Process-parameter optimization for fused deposition modelling based on Taguchi method. Adv Mater Res 538–541:444–447
17. Górski F, Kuczko W, Wichniarek R (2013) Influence of process parameters on dimensional accuracy of parts manufactured using fused deposition modelling technology. Adv Sci Technol Res J 7(19):27–35
18. Luzanin O, Movrin D, Plan M (2013) Experimental investigation of extrusion speed and temperature effects on arithmetic mean surface roughness in Fdm. J Technol Plast 38(2):179–190
19. Raol TS, Dave KG, Patel DB, Talati VN (2014) An Experimental Investigation of effect of process parameters on surface roughness of fused deposition modeling built parts. Int J Eng Res Technol 3(4):2270–2274
20. Mohamed OA, Masood SH, Bhowmik JL (2016) Optimization of fused deposition modeling process parameters for dimensional accuracy using I-optimality criterion. Measur J Int Measur Confederation 81:174–196

21. Beniak J, Krizan P, Soos, Matus M (2019) Research on shape and dimensional accuracy of FDM produced parts. IOP Conf Ser Mater Sci Eng 501(1)
22. Narang R, Chhabra D (2017) Analysis of process parameters of fused deposition modeling (FDM) technique. Int J Future Revolution Comput Sci Commun Eng IJFRCSCE 41–48 (Oct 2017)
23. Vasudevarao B, Natarajan DP, Henderson M, Razdan A (2000) Sensitivity of RP surface finish to process parameter variation. In: Solid freeform fabrication proceedings. The University of TX, Austin, TX, pp 251–258
24. Vyavahare S, Kumar S, Panghal D (2020) Experimental study of surface roughness, dimensional accuracy and time of fabrication of parts produced by fused deposition modelling. Rapid Prototyping J 26(9):1535–1554
25. Durgun I, Ertan R (2014) Experimental investigation of FDM process for improvement of mechanical properties and production cost. Rapid Prototyping J 20(3):228–235
26. Alsoufi MS, Elsayed AE (2017) How surface roughness performance of printed parts manufactured by desktop FDM 3D printer with PLA+ is influenced by measuring direction. Am J Mech Eng 5(5):211–222
27. Alafaghani A, Qattawi A, Alrawi B, Guzman A (2017) Experimental optimization of fused deposition modelling processing parameters: a design-for-manufacturing approach. Procedia Manuf 10:791–803
28. Wu J (2018) Study on optimization of 3D printing parameters. IOP Conf Ser Mater Sci Eng 392(6)